PROCEEDINGS OF THE

INTERNATIONAL CONFERENCE ON

18TH Environmental Degradation of Materials in Nuclear Power Systems – Water Reactors

August 13–17, 2017

Marriott Portland Downtown Waterfront

Portland, Oregon, USA

Volume 2

EDITED BY:

John H. Jackson · Denise Paraventi · Michael Wright

TMS

Springer

The Minerals, Metals & Materials Series

John H. Jackson · Denise Paraventi
Michael Wright
Editors

Proceedings of the 18th International Conference on Environmental Degradation of Materials in Nuclear Power Systems – Water Reactors

Volume 2

TMS

Springer

Editors
John H. Jackson
Idaho National Laboratory
Idaho Falls, ID
USA

Denise Paraventi
Naval Nuclear Laboratory
Pittsburgh, PA
USA

Michael Wright
Chalk River Laboratories
Canadian Nuclear Laboratories
Chalk River, ON
Canada

ISSN 2367-1181 ISSN 2367-1696 (electronic)
The Minerals, Metals & Materials Series
ISBN 978-3-319-68453-6 ISBN 978-3-319-68454-3 (eBook)
https://doi.org/10.1007/978-3-319-68454-3

Library of Congress Control Number: 2017956373

Printed on acid-free paper

This Springer imprint is published by Springer Nature
The registered company is Springer International Publishing AG
The registered company address is: Gewerbestrasse 11, 6330 Cham, Switzerland

Preface

The production of electricity from nuclear power reactors occupies a central role in meeting worldwide energy requirements. As of January 2017, there are 450 power reactors operating in 30 countries. The industry continues to grow, despite setbacks. There are 60 new construction projects underway in 15 different countries. The great majority of the new reactors are being built in countries with emerging economies. For the USA, western Europe, and Japan, although there are some new construction projects, the emphasis is on maintaining capacity and extending the operating lives of existing reactors. Of the worldwide fleet of 450 power reactors, 273 of them have been in service for over 30 years and 67 have been in service for over 40 years.

If nuclear power is going to continue making a contribution to worldwide energy demands, power plants must be operated in a safe and cost-effective manner. Central to safety and reliability goals for these plants is effective materials degradation management. Effective materials degradation management must include the maintenance of operating plants, prolongation of the lifetime of plants, and choice and use of materials in new plants.

Environmentally induced materials degradation represents a significant fraction of materials-related problems in today's nuclear power plant operation. Under extended lifetime to 60 years or potentially longer, understanding materials degradation will be even more important as these issues are of concern for both economic and safety reasons. Understanding today's materials problems is also critical for the future in the advanced reactor sector.

The purpose of the "Environmental Degradation of Materials in Nuclear Power Systems" conference series is to foster an exchange of ideas about such problems and their remedies. The conference series has been running since 1983. The meetings cover materials problems facing nickel base alloys, stainless steels, ferritic steels, zirconium alloys, and other alloys in water environments of relevance. Components covered include heat transport system pressure boundary components, reactor vessels and internals, steam generators, fuel cladding, irradiated components, fuel storage containers, and balance of plant components and systems. The scope and emphasis of the individual conferences have varied over the past 30 years

as different challenges arose and were resolved. Reflecting the growing concerns over materials aging in general, this, the 18th conference in the series, includes a session dedicated to cable insulation aging and concrete aging.

This conference featured the presentation of 164 papers, spread over 25 sessions. The conference was attended by over 200 scientists and engineers from 17 countries, representing power plant operators, reactor vendors, regulators, national laboratories, research institutes, universities, and other organizations affiliated with the nuclear and nuclear service industries.

However, this year's meeting was sadly missing one of its longest serving and most influential contributors. January 2017 saw the passing of Dr. Roger Washburne Staehle (1934–2017). Roger was an international giant in the field of metallurgy and corrosion. Roger made enormous scientific and engineering contributions to these fields, and he contributed to every one of the Environmental Degradation meetings and personally attended the majority. Roger studied metallurgical engineering at The Ohio State University (OSU), graduating in 1957. After college, he worked for Admiral Hyman Rickover, the father of the US Nuclear Navy, something Roger was immensely proud of. A successful and influential academic career followed, with a major focus on materials degradation in commercial nuclear power. In his later career, as an international consultant, mentor, and instigator, Roger was an aggressive advocate for the best experimental and analytical techniques. Roger was also a champion of international information exchange. Over his last 20 years, Roger focused considerable efforts to build collaborative interactions in China.

Returning to the current meeting, the organizers recognize the help of a dedicated group of individuals who made this 18th edition of the conference a success and these proceedings possible. The Program Committee and Session Chairs listed in this volume's front matter played vital roles in organizing the sessions and conducting paper reviews. These activities required a significant commitment of their time, and they are greatly appreciated. The organizers are thankful to their respective employers for making them available for participating in planning, organizing, and serving at the conference.

Special thanks go to the Technical Program Chair, John Jackson of Idaho National Laboratory, and the Assistant Technical Program Chair, Denise Paraventi of the (Bettis) Naval Nuclear Laboratory for their tireless efforts in ensuring the success of this conference.

Finally, we thank The Minerals, Metals & Materials Society (TMS) for their assistance with conference planning, paper review, and publication of these proceedings.

Michael Wright
General Conference Chair

In Memoriam

Roger Washburne Staehle (February 4, 1934–January 16, 2017)

It is with great sadness that we mark the passing of Dr. Roger W. Staehle, an international giant in the field of metallurgy and corrosion. Roger made enormous scientific and engineering contributions to these fields, but was best known for his friendship, generosity, and drive to support and recognize the work of others—no one "out-gave" Roger.

Roger became ill after a fall during his morning walk in the snow and ice. He died several weeks later with members of his family at his bedside. He is survived by his brother, George, and his children, Elizabeth, Eric, Sara, Erin, and William.

Roger Staehle studied metallurgical engineering at The Ohio State University (OSU), graduating in 1957 as the president of his senior class. After college, Roger fulfilled his Navy ROTC obligation on the staff of Admiral Hyman Rickover, who was the father of the US Nuclear Navy. Following this extensive education in nuclear technology, he returned to get his Ph.D. at OSU under the distinguished guidance of Prof. Mars Fontana. He graduated in 1965 and immediately joined the

metallurgical engineering faculty. Roger founded the Fontana Corrosion Center (FCC) and built it into one of the largest and most influential academic corrosion laboratories in the world. By the end of the 70s, he had a group of over 40 people in the FCC, with a major focus on materials degradation in commercial nuclear power. He left OSU in 1979 to become Dean of the Institute of Technology at the University of Minnesota (College of Science and Engineering), a position he held until 1983. Roger remained very active to the end as a consultant specializing in the degradation of materials in nuclear reactors.

Roger received many awards for his accomplishments. He was a fellow of NACE International and The Electrochemical Society and received the W.R. Whitney Award from NACE. He was elected to the US National Academy of Engineering in 1978, when he was 44 years old, one of the youngest to be elected to NAE at that time. Roger served as the editor for *CORROSION* journal from 1973 to 1981.

Roger devoted enormous energy to coordinating and supporting research throughout the world. He made hundreds of trips to many countries, including Russia, Japan, China, Korea, Europe, South Africa, South America, the Middle East, investing consistently and heavily in promoting international collaborations. He was sufficiently proficient in Russian at one time to be able to lecture in that language. Among the early examples of his efforts to develop international collaborations was his organization of major international conferences.

Roger also promoted international collaboration by inviting and hosting innumerable prominent experts, as well as early-career scientists, to OSU, and it had a dramatic impact on the thinking and progress throughout the world (including the USA), in addition to fostering the careers of many dozens of international scientists.

Roger was heavily engaged in the International Cooperative Group on Environmentally Assisted Cracking, whose charter is to promote international exchange of information, emerging data, and the best experimental techniques for addressing cracking in high-temperature water environments. In the last 20 years, Roger focused considerable efforts to build collaborative interactions in China, aimed primarily but not exclusively on issues related to materials degradation in commercial nuclear power reactors. He initiated and organized four major symposia in China, the first of which was “Materials Problems in Light Water Nuclear Power Plants: Status, Mitigation, Future Problems” in 2005. Roger was single-handedly responsible for attracting the best of the world’s experts in each aspect of each symposium, and each symposium attracted about 200 engineers and scientists from throughout China.

In 2008, Roger conceived and organized a conference on stress corrosion crack (SCC) initiation in Beaune, France, involving about 130 scientists. The week-long conference was designed to exchange ideas, define critical experiments, and discuss experimental technique. Many similar efforts were instigated by Roger in areas such as lead and sulfur effects in steam generators, alloys with improved SCC resistance. In 2010, Roger undertook a massive effort to bring together world experts in diverse fields who could speak to the issues of fundamental understanding and modeling of SCC. The series of four annual meetings brought together about 40 international

experts for a week-long workshop. Roger realized the importance of such a meeting, defined the content, identified and invited the experts, and solicited support from about a dozen agencies and companies.

These are but a few examples of Roger's selfless, energetic efforts to promote international collaboration, which are in turn but a fraction of his efforts in consulting, educating, lecturing, mentoring, writing award nominations and references, etc. It is difficult to imagine a world without Roger's presence, friendship, vision, and energy.

Peter L. Andresen, Ron Latanision, and Gerald S. Frankel
First Published by NACE in CORROSION—Vol. 73, No. 3

Contents

Part V BWR SCC and Water Chemistry

Part VI Zirconium and Fuel Cladding

About the Editors/Organizers

Technical Program Chair: John Jackson, Idaho National Laboratory

Dr. John H. Jackson is a Distinguished Staff Scientist/Engineer at the Idaho National Laboratory (INL) in Idaho Falls, Idaho. He currently has dual responsibility as the Gateway for Accelerated Innovation in Nuclear (GAIN) Technical Interface and as the Industry Program Lead for the Nuclear Science User Facilities (NSUF). In these capacities, John works closely with the DOE Office of Nuclear Energy and the nuclear industry to ensure that DOE facilities are used effectively to maintain the current reactor fleet and to enable innovation. John has nearly twenty years of experience in the areas of mechanical testing and fracture mechanics. He also has over three years of experience in extreme environment materials characterization and drilling mechanics at the ExxonMobil Upstream Research Company in Houston, Texas. John holds Ph.D. (2001) and M.S. (1998) degrees in Mechanical Engineering from the University of Washington, Seattle, WA, and a B.S. in Mechanical Engineering Technology (1995) from Central Washington University in Ellensburg, WA.

Assistant Technical Program Chair: Denise Paraventi, Naval Nuclear Laboratory

Dr. Denise Paraventi is an Advisor Engineer at the Bettis site of the Naval Nuclear Laboratory in Pittsburgh, PA, and has worked at Bettis since 2000. Her career has been dedicated to testing to understand environmental degradation of materials in nuclear power systems, primarily focused on stress corrosion cracking of nickel-based alloys and corrosion fatigue of austenitic stainless steels. She has extensive experience with mechanical and high-temperature autoclave testing of these materials. She has also been involved with Electric Power Research Institute (EPRI) efforts to evaluate Alloy 690 stress corrosion crack growth rates for use in commercial industry disposition curves. Denise holds a Ph.D. in Materials Science and Engineering from the University of Michigan in Ann Arbor and a B.S. degree in Metallurgical Engineering from Michigan Technological University in Houghton, Michigan.

Conference General Chair: Michael Wright, Canadian Nuclear Laboratories

Dr. Michael Wright has worked at the Canadian Nuclear Laboratories' (CNL) Chalk River site since 1993. His career at Chalk River has exposed him to a wide range of degradation issues and materials: nickel alloys, ferritic steels, stainless steels, aluminum, and zirconium. Mike has applied his expertise largely to corrosion and cracking issues (fatigue, creep-cracking, hydride cracking, stress corrosion cracking, and corrosion fatigue), but he has also worked on assessments of irradiation embrittlement of aluminum- and nickel-based alloys. Much of his work has been in direct support of utility operations largely related to steam generators or primary heat transport system degradation issues. He has also provided support for nuclear operations at the Chalk River site (e.g., high-level-waste storage-tank corrosion, research-reactor vessel repair). Mike is currently working in a business development role at CNL. Before moving to Canada, and the nuclear industry, Mike worked for four years at The Welding Institute (TWI) in the UK

where he led welding-related commercial research projects and failure investigations. Work at TWI started Mike's career-long interest in environmentally assisted cracking. Mike holds a Ph.D. from Birmingham University (UK) for research on fatigue of aerospace alloys.

Organizing Committee for Environmental Degradation Conferences

Todd Allen, Third Way and University of Wisconsin
Peter Andresen, Andresen Consulting
Steve Bruemmer, Pacific Northwest National Laboratory
Jeremy Busby, Oak Ridge National Laboratory
Thierry Couvant, Electricite de France
Ian de Curieres, IRSN
Pal Efsing, Vattenfall, Sweden
Ulla Ehrnsten, VTT Technical Research Centre of Finland
Lionel Fournier, AREVA, France
Steve Fyfitch, AREVA, USA
Barry Gordon, Structural Integrity Associates Inc.
Catherine Guerre, CEA
En-Hou Han, Institute of Metal Research, China
Ron Horn, GE-Hitachi, retired
Il Soon Hwang, Seoul National University, Korea
Gabriel Ilevbare, Idaho National Laboratory
John Jackson, Idaho National Laboratory
Anders Jenssen, Studsvik, Sweden
Renate Kilian, AREVA, GmbH
Hong Pyo Kim, KAERI, Korea
Peter King, PJ King Consulting, Canada
Stuart Medway, AMEC Foster Wheeler
Dave Morton, Naval Nuclear Laboratory
Larry Nelson, JLN Consulting
Greg Oberson, US Nuclear Regulatory Commission
Denise Paraventi, Naval Nuclear Laboratory
Hans-Peter Seifert, PSI, Switzerland
Robert Tapping, Canadian Nuclear Laboratories

Gary Was, University of Michigan
Yutaka Watanabe, Tohoku University
Mike Wright, CNL, Canada
TK Yeh, Nat Tsing Hua University, Taiwan
Toshio Yonezawa, Tohoku University, Japan

Session Chairs and Co-chairs

Note The primary session chair is italicized.

Zirconium and Fuel Cladding
Jacki Stevens, AREVA Inc.
Evan Dolley, GE Global Research
George Jiao, University of Michigan

Accident Tolerant Fuel Cladding
Gary Was, University of Michigan
Bruce Pint, Oak Ridge National Laboratory
Cem Topbasi, Electric Power Research Institute

Cables and Concrete Aging and Degradation–Cables
Leo Fifield, Pacific Northwest National Laboratory
Robert Duckworth, Oak Ridge National Laboratory
David Rouison, Kinectrics

Cables and Concrete Aging and Degradation–Concrete
Thomas Rosseel, Oak Ridge National Laboratory
Joe Wall, Electric Power Research Institute

BWR SCC and Water Chemistry
Bob Carter, Electric Power Research Institute
Earl Johns, Naval Nuclear Laboratory
Susan Garcia, Electric Power Research Institute

Plant Operating Experience
Maria-Lynn Komar, Kinectrics Inc.
Peter King, PJKing Consulting Inc.

Irradiation Damage–Nickel Based and Low Alloy
Mychailo Toloczko, Pacific Northwest National Laboratory
Maxim Gussev, Oak Ridge National Laboratory
Myles Connor, General Electric–Hitachi

Irradiation Damage–Stainless Steel
Larry Nelson, JLN Consulting
Sarah Davidsaver, AREVA GmbH
Anna Hojna, Centrum vyzkumu Rez

Irradiation Damage–Swelling
Frank Garner, Radiation Effects Consulting
Cheng Sun, Idaho National Laboratory
Sebastien Teysseyre, Idaho National Laboratory

PWR Ni Alloy SCC–Alloy 600 Mechanistic
Steve Bruemmer, Pacific Northwest National Laboratory
Thierry Couvant, EDF
Tony Horner, Rolls Royce plc

PWR Ni Alloy SCC–Alloy 690 Mechanistic
Stuart Medway, AMEC Foster Wheeler
Matt Olszta, Pacific Northwest National Laboratory
Hannu Hänninen, Aalto University

PWR Ni Alloy SCC–SCC
Bogdan Alexandreanu, Argonne National Laboratory
Sonya Pemberton, AMEC Foster Wheeler
Grace Burke, The University of Manchester

PWR Ni Alloy SCC–Initiation
Dave Morton, Naval Nuclear Laboratory
Ziqing Zhai, Pacific Northwest National Laboratory
Meg Audrain, US Nuclear Regulatory Commission

PWR Ni Alloy SCC–Aging Effects
Tyler Moss, Naval Nuclear Laboratory
Peter Chou, Electric Power Research Institute
Dan Schreiber, Pacific Northwest National Laboratory

IASCC Testing–Initiation and Growth
Peter Andresen, Andresen Consulting
Yiren Chen, Argonne National Laboratory
Colin Judge, Canadian Nuclear Laboratory

IASCC Testing–Characterization
Anders Jenssen, Studsvik Nuclear AB
Masato Koshiishi, Nippon Nuclear Fuel Development
Mike McMurtrey, Idaho National Laboratory

PWR Stainless Steel SCC and Fatigue–Fatigue
Denise Paraventi, Naval Nuclear Laboratory
Barry Gordon, Structural Integrity Associates Inc.
Renate Killian, AREVA GmbH

PWR Stainless Steel SCC and Fatigue–SCC
Gabriel Ilevbare, Idaho National Laboratory
Keith Leonard, Oak Ridge National Laboratory
Elaine West, Knolls Atomic Power Laboratory

PWR Secondary Side
Ian De Curieres, IRSN
Jared Smith, Canadian Nuclear Laboratory
Brent Capell, Electric Power Research Institute

Special Topics II: Processes
Ulla Ehrnstén, VTT Technical Research Centre of Finland Ltd.
TK-Yeh, National Tsing Hua University
George Young, Dominion Engineering

Welds, Weld Metals, and Weld Assessments
Catherine Guerre, CEA
Bryan Miller, Naval Nuclear Laboratory
Hans Peter Seifert, Paul Scherrer Institute

PWR Oxides and Deposits
Cecilie Duhamel, MINES ParisTech
Fabio Scenini, The University of Manchester

General SCC and SCC Modeling
Raj Pathania, Electric Power Research Institute
David Tice, AMEC Foster Wheeler
Jean Smith, Electric Power Research Institute

Stainless Steel aging and CASS
Steve Fyfitch, AREVA Inc.
Jeremy Busby, Oak Ridge National Laboratory
TS Byun, Pacific Northwest National Laboratory

Special Topics I: Materials
Pål Efsing, Ringhals AB
Rory Kennedy, Idaho National Laboratory
Peter Hosemann, University of California, Berkeley

Part I
Cables and Concrete Aging and Degradation–Cables

Simultaneous Thermal and Gamma Radiation Aging of Electrical Cable Polymers

Leonard S. Fifield

Abstract Elevated temperature is the primary source of aging for nuclear power plant electrical cable insulation and jacketing, but gamma radiation is also a significant contributor to structural changes that result in loss of polymer mechanical and electrical properties in affected plant locations. Despite many years of research, the combined degradation effects of simultaneous exposure to thermal and radiation stresses are not well understood. As nuclear operators prepare for extended operation beyond initial license periods, a predictive understanding of exposure-based cable degradation is becoming an increasingly important input to safety, licensing, operations and economic decisions. We focus on carefully-controlled simultaneous thermal and gamma radiation aging and characterization of the most common nuclear cable polymers to understand relative contributions of temperature, time, dose and dose rate to changes in cable polymer material structure and properties. Improved understanding of cable performance in long term operation will help support continued sustainable nuclear power generation.

Keywords Cables · Nuclear · Polymers · Thermal aging · Gamma aging · Simultaneous aging

Introduction

Both boiling water reactor and pressurized water reactor nuclear power plant (NPP) designs contain hundreds of miles of electrical cable within their containment buildings [1] and several hundreds of miles of cable in the plants outside of the containment buildings. Cable is used primarily for control functions, but also for instrumentation, power and communication [2]. Cable constructions include a metal

L.S. Fifield (✉)
Pacific Northwest National Laboratory, Richland, WA, USA
e-mail: Leo.fifield@pnnl.gov

L.S. Fifield
Washington State University, Pullman, WA, USA

J.H. Jackson et al. (eds.), *Proceedings of the 18th International Conference on Environmental Degradation of Materials in Nuclear Power Systems – Water Reactors*, The Minerals, Metals & Materials Series, https://doi.org/10.1007/978-3-319-68454-3_1

conductor and dielectric insulation layer, but can also include ground/drain wires, semiconducting screens, a metallic shield, and a polymeric jacket [3]. The most prevalent materials used for cable insulation in U.S. NPP containment applications are cross-linked polyethylene (XLPE) and ethylene-propylene rubber (EPR); and the most common cable jacketing materials are chlorosulfonated polyethylene (CSPE) (Hypalon®), polychloroprene (neoprene), and chlorinated polyethylene [4].

Suitability of cable materials for use in the NPP application was originally demonstrated by cable manufacturers through environmental qualification (EQ). EQ testing included demonstration of adequate cable performance following exposure to severe environmental conditions meant to simulate long term service conditions in an accelerated laboratory setting. For cables used in containment, expected service conditions include both elevated temperature and gamma irradiation. In one example, thermal durability performance during operation for 40 years (350,000 h) at 49 °C was extrapolated from performance over testing from 1000 to 8000 h at temperatures from 180 to 121 °C [5]. Radiation resistance of cables was determined through exposure to a total gamma dose selected to bound the expected total 40 years exposure, such as, in the same example, 11 Mrad (110 kGy).

The EQ testing performed by most cable vendors involved exposure to accelerated thermal aging first, followed by exposed to the total gamma dose [6]. Actual exposure of cables to these environmental stresses in service, however, occurs simultaneously. The combined effects of thermal and radiation aging applied sequentially may not be the same as those applied simultaneously if the simultaneous presence of these stresses promotes a different degradation mechanism than occurs when they are applied one at a time [7]. We are exploring cable insulation material aging parameters including temperature, gamma total dose, applied dose rate, and sequential versus simultaneous thermal and gamma exposure to better understand cable material aging and degradation behavior. A better understanding of these factors, combined with accurate knowledge of actual service conditions of cables in NPPs, will facilitate predictive understanding of cable aging that will enable efficiency in cable aging management.

XLPE Cable Insulation Material Studied

The electrical cable insulation most commonly found in containment in U.S. NPPs is Firewall® III XLPE manufactured by The Rockbestos Company (now RSCC) [2]. Firewall® III XLPE-insulated cable was purchased for the studies described here from RSCC with product code I46-0021. This product, seen in Fig. 1, has two XLPE-insulated conductors, one white and one gray, metallic shield and a CSPE overall jacket. Straw specimens of the white XLPE insulation suitable for tensile testing were obtained by removal of the shielding, jacket and conductor.

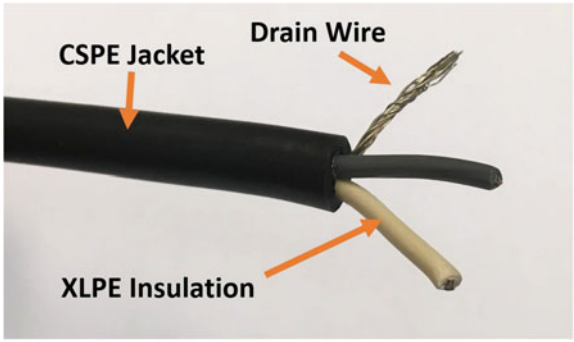

Fig. 1 Photo of RSCC XLPE two conductor cable with CSPE overall jacket

Differential Scanning Calorimetry

White XLPE was heated from 50 to 350 °C at a rate of 10 °C/min while heat flow in the sample was monitored using differential scanning calorimetry, as plotted in Fig. 2. Phase transitions are noted in the polymer material around 113–123 °C. Operating service temperatures are well below the temperatures of these transitions. If accelerated aging is used for service life prediction of this material at temperatures above which these transitions occur, it may be important to verify that aging and degradation mechanism are consistent in the different regimes [8].

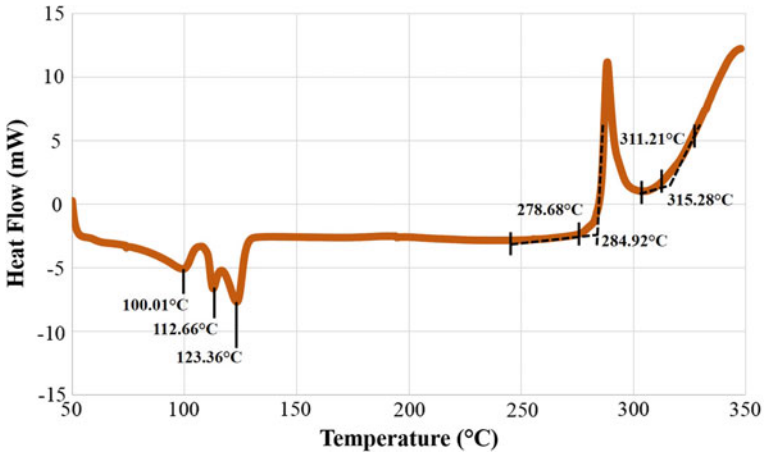

Fig. 2 Plot of heat flow response with temperature for unaged white XLPE insulation

Thermal and Gamma Radiation Aging

XLPE specimens were thermally aged in forced air, mechanical convection ovens at three temperatures: 60, 90, and 115 °C. Gamma irradiation aging was accomplished using the High Exposure Facility (HEF) in the Radiological Exposures & Metrology Laboratory at the Pacific Northwest National Laboratory. A Co-60 source in the HEF provided the gamma radiation. Specimens were loaded into mechanical convection ovens placed in the gamma beam to control specimen temperature during irradiation, as seen in Fig. 3. Dose rate was selected by controlling specimen distance from the source [9]. Actual dose rates were measured at the sample locations within the oven using an ion gauge detector.

Oxidation Induction Time

Oxidation induction time (OIT) measures the relative time that a polymer sample takes to exhibit an exothermic event when presented with an oxidizing environment at elevated temperature and can be a sensitive measure of polymer aging and of antioxidant concentration. XLPE samples were heated at 15 °C/min to 230 °C in helium atmosphere. Upon reaching 230 °C, the samples were held for 2 min before the carrier gas was changed to oxygen. Each sample was held under these conditions until an exothermic event occurred indicting oxidative reaction. Figure 4 plots OIT for XLPE specimens exposed to 115 °C and to 115 °C under gamma irradiation of 350 Gy/h [10]. From this data the acceleration of degradation in the presence of radiation can be observed.

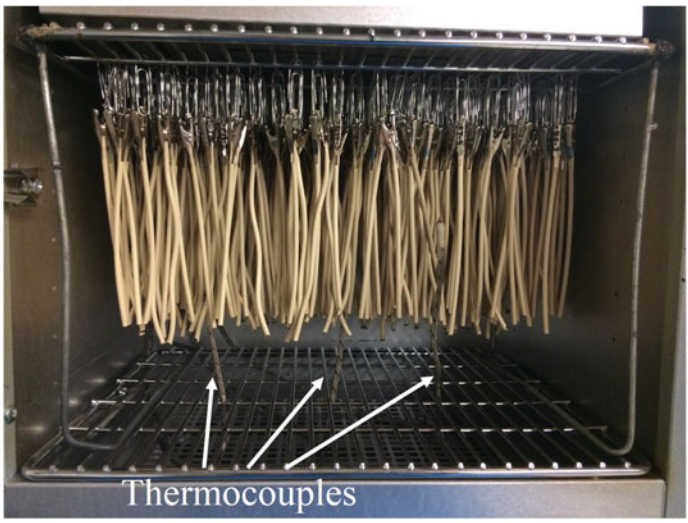

Fig. 3 Photo of oven chamber containing rack of XLPE specimens

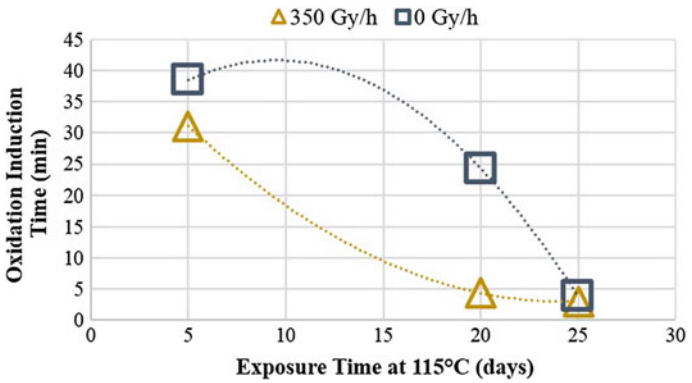

Fig. 4 Plot of OIT for XLPE aged at 115 °C with and without 350 Gy/h gamma irradiation

Gel Fraction and Uptake Factor

The gel fraction (percent gel or "% gel") of a sample is a relative measurement of the homogeneity of the XLPE polymer network [11]. When crosslinking dominates aging in a polymer network, the gel fraction increases. The uptake factor of a sample indicates how easily a sample swells. When polymer chain scission dominates during aging, the uptake factor increases as solvent is absorbed more readily. The gel fraction and uptake factor therefore share an inverse relationship: as gel fraction increases, uptake factor decreases and vice versa. These quantities were measured for XLPE incubated in mixed xylenes at 110 °C. The outputs of the process are sample masses: initial aged sample (Wa), sample swollen by the solvent (Ws), and samples after drying (Wd). Gel fraction is defined as the ratio of dried weight to initial weight. Uptake factor is defined as the ratio of swollen weight to dried weight.

$$Gel\ Fraction = \frac{W_d}{W_a} \times 100 \quad Uptake\ Factor = \frac{W_s}{W_d}$$

Crosslinking in XLPE is seen to occur with exposure to 350 Gy/h gamma radiation as evidenced by the increase in gel fraction plotted in Fig. 5. The effect is seen to increase proportionally with exposure temperature over the range investigated. Similarly, chain scission is also seen to progress under these conditions as revealed by the decrease in uptake factor with exposure seen in Fig. 6.

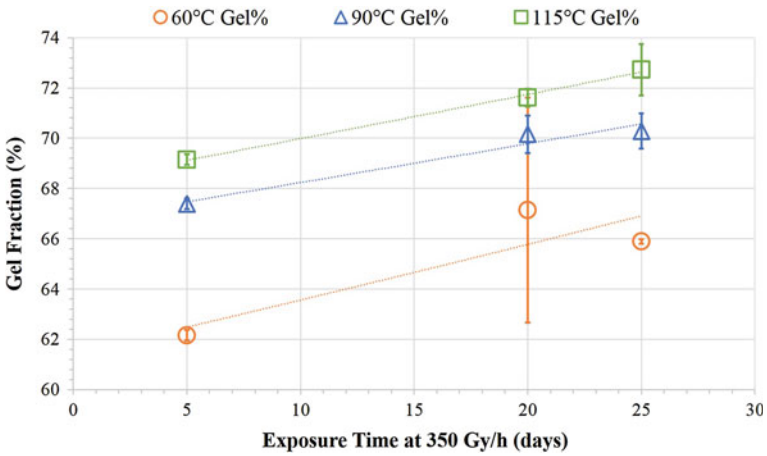

Fig. 5 Plot of gel fraction values of XLPE aged at 350 Gy/h at 60, 90 and 115 °C

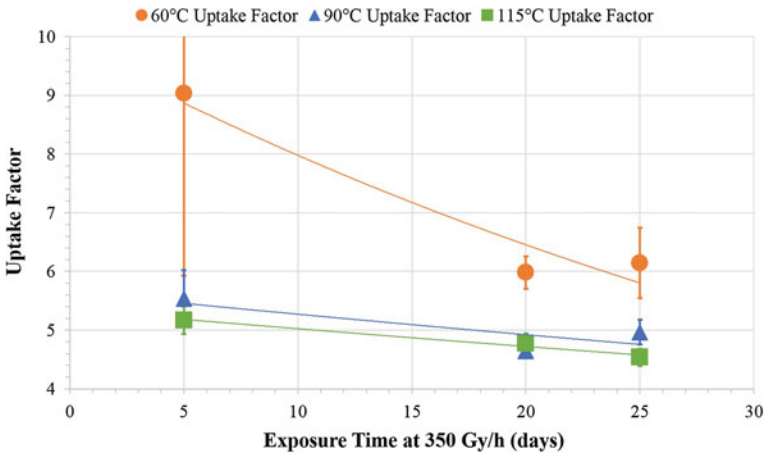

Fig. 6 Plot of uptake factor values of XLPE aged at 350 Gy/h at 60, 90 and 115 °C

Scanning Electron Microscopy

The heterogeneous nature of the polymer composite that comprises the XLPE-based insulation is visible in the scanning electron microscope image in Fig. 7. In addition to XLPE, the insulation material also contains inorganic and organic fillers for color, flame resistance and other functions [12]. Future investigation of changes in XLPE composite microstructure with aging is expected to inform understanding of aging mechanisms.

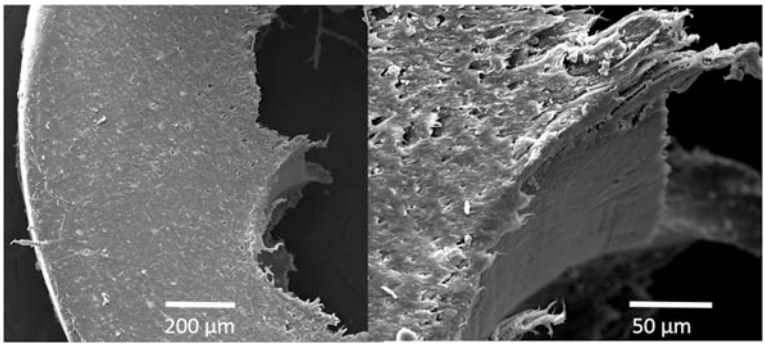

Fig. 7 Scanning electron microscope images of XLPE at two magnifications

Conclusion

Electrical cables used for power, instrumentation and control within nuclear power plant containment buildings are often exposed to elevated temperatures and gamma irradiation during their service life that may extend for several decades. Understanding changes in cable polymer insulation and jacketing materials that occur with exposure over time enables development and use of cable condition monitoring technology and informs operator repair, replacement and assessment frequency decisions. XLPE is the most common polymer insulation material in low voltage cables in containment and is therefore a priority material for research to understand cable aging behavior.

We are investigating the relative effects of temperature, gamma total dose, gamma dose rate, and sequential versus simultaneous exposure of thermal and radiation stress on XLPE and other materials to advance the practical understanding of cable aging behavior. Results described here demonstrate some of the detectable changes in XLPE with aging that are informing our predictive understanding. Material changes with gamma radiation exposure are seen to track with exposure temperature for the material, dose rates, and temperatures considered. Work is ongoing in our group to study the effects of gamma irradiation at ambient and service temperatures.

Acknowledgements Funding for this work has been provided by the Materials Aging and Degradation Pathway of the U.S. Department of Energy Office of Nuclear Energy Light Water Reactor Sustainability Program and the Nuclear Energy University Program. Data described herein was obtained with the assistance of Birgit Schwenzer, Miguel Correa, Ian Childers, Shuaishuai Liu, Mark Murphy and Andy Zwoster. The Pacific Northwest National Laboratory is operated by Battelle for the United States Department of Energy under Contract DE-AC05-76RL01830.

References

1. A. Ahmed, S.P. Carfagno, G.J. Toman, Inspection, Surveillance, and Monitoring of Electrical Equipment inside Containment of Nuclear Power Plants—with Applications to Electrical Cables (Report NUREG/CR-4257, U.S. Nuclear Regulatory Commission, 1985)
2. R.F. Gazdzinski et al., Aging Management Guideline for Commercial Nuclear Power Plants-Electrical Cable and Terminations (Report SAND96-0344, Sandia National Laboratories, 1996)
3. S.W. Glass, L.S. Fifield, T.S. Hartman, Evaluation of Localized Cable Test Methods for Nuclear Power Plant Cable Aging Management Programs (Report PNNL-25432, Pacific Northwest National Laboratory, 2016)
4. J.J. Carey, Low-voltage Environmentally-Qualified Cable License Renewal Industry Report; Revision 1 (Report EPRI TR-103841, Electric Power Research Institute, 1994)
5. BIW, Bostrad 7E Cables, Flame and Radiation Resistant Cables for Nuclear Power Plants (Report No. B 915, Rev. 1., BIW Cable Systems, Inc., 1984)
6. M. Subudhi, Literature Review of Environmental Qualification of Safety-Related Electric Cables (Report NUREG/CR-6384, Vol. 1, U.S. Nuclear Regulatory Commission, 1996)
7. J.T. Busby et al., Expanded Materials Degradation Assessment (EMDA), Volume 5: Aging of Cables and Cable Systems (Report NUREG/CR-7153, Vol. 5, U.S. Nuclear Regulatory Commission, 2014)
8. K.T. Gillen, R. Bernstein, Review of Nuclear Power Plant Safety Cable Aging Studies with Recommendations for Improved Approaches and for Future Work (Report SAND 2010-7266, Sandia National Laboratories, 2010)
9. L.S. Fifield, S. Liu, N. Bowler, Simultaneous Thermal and Gamma Radiation Aging of Cable Polymers, in *IEEE Conference on Electrical Insulation and Dielectric Phenomena (CEIDP)* (Toronto, ON, 2016), pp. 11–14
10. L.S. Fifield et al., Characterizing Oxidation of Cross-linked Polyethylene and Ethylene Propylene Rubber Insulation Materials by Differential Scanning Calorimeter (Report PNNL-25172, Pacific Northwest National Laboratory, 2016)
11. M. Celina, G.A. George, Characterisation and degradation studies of peroxide and silane crosslinked polyethylene. Polym. Degrad. Stab. **48**, 297–312 (1995)
12. S. Liu, L.S. Fifield, N. Bowler, Towards Aging Mechanisms of Cross-linked Polyethylene (XLPE) Cable Insulation Materials in Nuclear Power Plants, in *IEEE Conference on Electrical Insulation and Dielectric Phenomena (CEIDP)* (Toronto, ON, 2016), pp. 935–938

Principal Component Analysis (PCA) as a Statistical Tool for Identifying Key Indicators of Nuclear Power Plant Cable Insulation Degradation

Chamila C. De Silva, Scott P. Beckman, Shuaishuai Liu and Nicola Bowler

Abstract This paper describes the use of Principal Component Analysis (PCA) as a statistical method to identify key indicators of degradation in nuclear power plant cable insulation. Seven kinds of single-point data and four kinds of spectral data were measured on cross-linked polyethylene (XLPE) that had undergone aging at various doses and dose rates of gamma radiation from a cobalt 60 source, and various elevated temperatures. To find the key indicators of degradation of aged cable insulation, PCA was used to reduce the dimensionality of the data set while retaining the variation present in the original data set. For example, PCA reveals that, for material aged at 90 °C, elastic modulus shows a positive correlation with total dose while mass loss, oxidation induction time and density show negative correlations with the same parameter.

Keywords Aged XLPE · Characterization methods · Principal component analysis

Introduction

The world is in a constant need for energy. To satisfy the increasing demand for energy it is necessary to consider the use of all types of energy sources. Nuclear energy plays an important role in the diverse supply of electricity due to its high reliability, efficiency and ability to maintain clean air by not emitting greenhouse gases. Currently there are 99 operating nuclear power reactors in the United States.

C.C. De Silva (✉) · S. Liu · N. Bowler
Iowa State University, Ames, IA 50010, USA
e-mail: chamila@iastate.edu

N. Bowler
e-mail: nbowler@iastate.edu

S.P. Beckman
Washington State University, Pullman, WA 99164, USA
e-mail: scott.beckman@wsu.edu

J.H. Jackson et al. (eds.), *Proceedings of the 18th International Conference on Environmental Degradation of Materials in Nuclear Power Systems – Water Reactors*, The Minerals, Metals & Materials Series, https://doi.org/10.1007/978-3-319-68454-3_2

The oldest operating reactor is in Oyster Creek, New Jersey, in operation from 1969 [1]. It takes 10–15 years to plan and build a Nuclear Power plant (NPP). Continued safe operation of existing NPPs is, therefore, desirable to meet energy demands in the country. Nuclear power plants in the USA receive an initial license from Nuclear Regulatory Commission (NRC) allowing them to operate for 40 years. At the end of the 40 years, the nuclear power plant operating companies can apply for a 20-year license extension (with potential for subsequent license extension for 20 years). License extension of NPPs is a critical process since it is needed to ensure that all the instruments and components of a NPP are safe and at a reliable operational level for another 20 years. Out of all the components of a NPP, the items that are most vulnerable for radiation and thermal degradation are power cables and concrete components [2]. In this study, we are concentrating on degradation of insulation materials in low-voltage instrumentation and control cables in NPPs.

Principal Component Analysis (PCA) [3, 4] is a standard statistical tool used in analyzing multidimensional data. It is widely used in almost all areas of research where manipulation of large numbers of attributes is necessary. It is a non-parametric method useful for obtaining relevant information from a complex data set.

In this study, we have applied the method of PCA to data obtained from different materials characterization methods to identify the key indicators of degradation in nuclear power plant cable insulation. In addition, we have explored the use of PCA as a method of identifying outliers and grouping in the data set.

Sample Preparation

To understand the damage done by persistent radiation and heating to cable insulation material, several characterization methods were performed on samples that had undergone accelerated aging. The accelerated aging was done at the High Exposure Facility at Pacific Northwest National Laboratory. The samples were prepared and aged under Co-60 radiation at 90 °C [4]. The samples used in aging are commercially available white XLPE cable insulation material extracted from RSCC 2/C 16AWG cable (product code 146-0021). The samples that are identified as with-conductor (WC) are intact, with the conducting wire inside the insulator, whereas those identified as ‘straw’ samples have the conductor removed from the insulation. The samples were aged for different dose rates varying from 120 to 540 Gy/h and for different periods of 5, 10, 15, 20, and 25 days (Table 1). The total radiation dose received by the samples at 90 °C ranges between 0 and 324 kGy for total radiation time of 0 to 25 days. Figure 1 shows a set of white XLPE insulation samples aged at 90 °C.

Table 1 Characterization data measured on XLPE WC samples aged at 90 °C ordered by increasing total dose

Row number	Days exposed (Days)	Dose rate (Gy/h)	Total dose (kGy)	OIT (min)	IM (Nm^{-1})	Straw % mass loss	WC % mass loss	EAB	WC density (g/cm^3)	Straw density (g/cm^3)
1	0	0	0.0	48.5	102.6	0.00	0.00	2.5	1.32	1.34
2	5	130	15.6	45.9	104.5	0.08	0.78	1.6	1.35	1.40
3	5	140	16.8	42.1	105.6	0.10	0.01	2.1	1.32	1.39
4	5	230	27.6	37.1	107.3	0.04	0.03	2.2	1.33	1.38
5	10	130	31.2	37.3	101.6	0.07	0.02	2.1	1.33	1.38
6	10	140	33.6	35.7	102.5	0.05	0.00	1.5	1.30	1.39
7	5	350	42.0	35.4	106.5	0.08	0.03	1.3	1.33	1.40
8	15	120	43.2	32.3	102.9	0.09	0.04	1.7	1.32	1.39
9	15	150	54.0	30.2	103.3	0.06	0.01	1.5	1.33	1.40
10	10	230	55.2	30.2	105.6	0.07	0.02	1.3	1.34	1.37
11	20	120	57.6	28.0	105.2	0.07	0.03	1.5	1.33	1.37
12	15	170	61.2	27.7	107.2	0.09	0.03	1.9	1.33	1.39
13	20	140	67.2	26.3	108.2	0.09	0.04	1.5	1.33	1.40
14	20	150	72.0	25.5	106.7	0.09	0.03	1.6	1.32	1.38
15	25	120	72.0	27.4	103.1	0.04	0.02	1.1	1.34	1.40
16	15	210	75.6	25.5	105.6	0.09	0.02	1.5	1.32	1.39
17	25	130	78.0	25.2	101.6	0.02	0.02	1.4	1.33	1.39
18	25	130	78.0	26.1	104.2	0.03	0.00	1.9	1.31	1.39
19	15	230	82.8	25.9	106.0	0.09	0.01	1.8	1.32	1.39
20	25	160	96.0	23.2	101.9	0.05	0.02	2.2	1.34	1.39
21	25	170	102.0	23.3	103.7	0.07	0.02	1.9	1.34	1.40
22	10	450	108.0	26.8	102.0	0.04	−0.01	1.8	1.33	1.39
23	15	300	108.0	23.2	110.7	0.01	0.01	1.8	1.34	1.40
24	25	180	108.0	21.3	101.5	0.06	0.02	2.2	1.34	1.39
25	20	230	110.4	22.7	108.6	0.03	0.01	2.0	1.34	1.39
26	25	200	120.0	19.0	102.4	0.06	0.00	1.4	1.34	1.39
27	25	210	126.0	18.4	101.5	0.05	0.00	1.8	1.34	1.40
28	25	240	144.0	19.2	101.7	0.01	0.01	1.9	1.33	1.39
29	15	450	162.0	17.0	114.0	−0.01	0.01	1.4	1.32	1.40
30	20	350	168.0	14.6	110.4	0.07	0.01	1.0	1.32	1.41
31	25	280	168.0	15.5	104.7	−0.01	0.01	1.0	1.32	1.37
32	25	300	180.0	15.2	105.3	0.00	−0.01	1.5	1.33	1.38
33	20	380	182.4	14.8	112.5	0.01	0.01	1.1	1.33	1.38
34	15	540	194.4	15.0	115.1	0.01	−0.01	0.9	1.34	1.39
35	25	350	210.0	12.5	105.1	0.00	−0.01	1.7	1.34	1.38
36	25	490	294.0	11.8	104.8	−0.08	−0.05	1.0	1.34	1.38
37	25	540	324.0	10.7	111.8	−0.10	−0.05	1.5	1.34	1.37

Fig. 1 Samples thermally aged at 90 °C and radiation aged at dose rate 230 Gy/h for 5 days. Samples labeled A–C are straw samples and sample D (with-conductor, WC) is intact, containing the central conductor

Statistical Analysis Method

PCA is used to reduce the dimensionality of a data set, which consists of a large number of interrelated attributes, while retaining as much of the variation present in the original data set as possible [5, 6]. This is done by linear transformation of an original set of attributes into a smaller set of attributes called principal components (PCs). Principal components are uncorrelated and ordered so that the first few retain most of the variation present in all of the original attributes. The basic steps of a PCA are given [7–9] in Fig. 2 and are described in the paragraphs.

The first step in PCA is to construct the data table that we are going to analyze, this is done by identifying the attributes (dimensions) of interest for the experiment. Then, the number of samples that are needed to measure the attributes is determined. The latter step is important since there should be a greater number of samples than the number of dimensions in order to obtain a reduced dataset that represents the original data set without missing variations in any important dimensions. For example, in this study we have ten dimensions for each of 37 samples. We are interested in observing the variations of only seven of those dimensions, however, because the other three dimensions (days exposed, dose rate, and total dose) are present in the data set to convey more information about the aging conditions of each sample. Hence, we use a matrix of 37 $\times$ 7 for analysis.

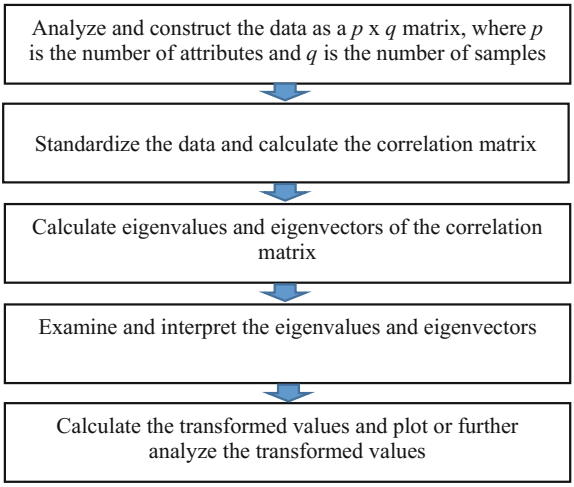

Fig. 2 Flow chart of the basic steps of PCA

PCA is a least-squares method, which assigns large coefficients to the PCA output to attributes with large variance. Since the data set contains attributes of different units and scales it as necessary to standardize the data matrix so that each dimension has variance 1.0. This scaling makes all coordinate axes, corresponding to the various dimensions, have the same length, which in turn gives each attribute the same influence on the PC model. A covariance matrix is calculated using the scaled values. The covariance matrix is a symmetric matrix which can be used to describe the original data set. The eigenvectors of this data set are orthogonal and the eigenvalues are ordered in descending order.

The cumulative percentage of eigenvalues gives the percent variability of the data set. The values of the eigenvectors (original dimension) of each PC (which vary from −1 to +1) can be interpreted as an index of the combined action or contrast of the original dimensions. We select only the PC that contribute the greatest variability to the data, which allows us to reduce the dimensionality of the data significantly.

The ability to present data findings in a few informative plots is one of the very attractive features of PCA. The score plot of PC shows the groupings of samples, outliers and other patterns in the data set. Loading plots make it possible to identify which attribute is corresponding to outliers, if any, and which attributes are responsible for grouping of samples. The directions in the score plot correspond directly to the direction in the loading plot. Hence, superposition of the two types of plot gives a simultaneous display of both objects and attributes. It is a choice of the user to inspect these two plots as one or two separate plots.

In this study, PCA is used to identify characterization methods that show maximum variation and to extract key indicators of aged cable insulator material. The anticipated outcome of applying PCA is to develop a small number of PCs, lower than the number of measurement types, to provide a reasonable characterization of the data set measured on the aged polymer material. The JMP Pro 12 software is used for the analysis presented here [10].

Characterization Methods

The seven attributes (dimensions) analyzed in this study are obtained from five characterization methods that provide values of mass loss, elongation-at-break, modulus (measured by surface indentation), mass density, and oxidation induction time. Mass loss and density are measured for both straw samples and samples with conductor (WC), giving four dimensions of data. The other characterization methods were applied only to straw samples, giving three dimensions of data.

Mass Loss

Mass loss is a physical change that can give information about possible oxidation reactions occurring in the material during the aging process. The weight of each sample was recorded both before and after the nuclear/thermal aging process. Mass loss was calculated by subtracting final mass from initial mass. Mass loss is presented as a percentage of initial mass.

Elongation-at-Break

Elongation-at-break (EAB) tests were conducted on tubular straw samples following the procedure outlined in IEC/IEEE 62582-3. The tubular samples are prepared by removing the conductor from lengths of the insulation material. The overall length of a sample is 60 mm. End tabs are needed to prevent breakage of the sample in the grips of the tensile testing machine that are tightened evenly and firmly to avoid slippage between the sample and the grips. The end tab is gray cross-linked polyethylene tubing with an inner diameter of 0.3175 mm and a length of 10 mm. The gauge length, that is the length between the two end tabs, is 30 mm. The testing strain rate is 50 mm/min. The load exerted on the sample and the corresponding distance between the grips are recorded until the sample breaks.

Indenter Modulus

Indenter modulus (IM) is a nondestructive, measurement technique that has shown a correlation with thermal and gamma aging [11]. IM measurements were carried out on samples with conductor (WC) using an indenter polymer aging monitor (IPAM) from the Analysis and Measurement Services Corporation. The indenter probe is clamped onto a wire and during operation; a rounded pyramidal tip is pressed into the cable insulation with increasing force while the insulation deformation is recorded in millimeters. The resulting IM is reported in units of Nm^{-1}.

Density

Density is a physical property that can give insights into the crosslinking and/or oxidation reactions take place during the aging process. Two experiments were carried out using "straw" samples and WC samples. For the cables with conductors, the insulation was cut using a wire cutter and pulled out as a straw. The density of each cable insulation material was measured using Archimedes' principle, which

states that every solid body immersed in a fluid loses weight by an amount equal to that of the fluid it displaces. Each sample was cut to 1 cm long and then cut lengthwise into three pieces, which were used for measurements. The samples were cut lengthwise to avoid the buildup of air bubbles inside the straw, once immersed in the liquid. Experiments were carried out using ethanol as the immersing liquid. Ethanol was used to avoid the forming of bubbles.

Oxidation Induction Time (OIT)

Oxidation Induction Time (OIT) is a measure of the amount of thermo-oxidative stabilizers present in a commercial polymer such as the XLPE studied here. In this study, the static OIT method, which has high sensitivity for the degree of stabilization, is used. The tests were conducted using a TA Instruments Q2000 differential scanning calorimeter (DSC). Samples with masses approximately 10 mg each were heated at 15 °C/min from ambient to 230 °C in nitrogen gas at a flow rate of 50 ml/min. When the sample reached the temperature of 230 °C, the temperature was held constant for 2 min and then the gas was changed to oxygen at the same flow rate as nitrogen. The sample is held at the constant temperature of 230 °C until the exothermic oxidation reaction occurred. The oxidation reaction is identified by the increase in heat flow over a given threshold value of 5 mW/g. A typical DSC plot showing how OIT is obtained is given in Fig. 3. The oxidation induction time is measured from the time the purge gas is switched from nitrogen to oxygen to the time that the heat flow increases by 0.1 mW/g.

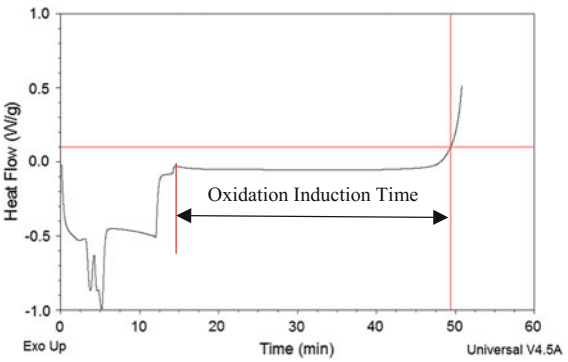

Fig. 3 OIT plot for sample exposed for a total dose of 54.0 kGy

Results and Discussion

Data

Table 1 gives all the information that is needed to describe each sample analyzed in this study. Each sample is identified by its row number. The number of days exposed, dose rate and total dose describe the aging condition of each sample. Table 1 also shows all the characterization data that results from application of the methods mentioned above, for samples aged at 90 °C.

Effect of Total Dose on Irradiated Samples

Following the steps of the flow chart shown in Fig. 2, the eigenvalues and the eigenvectors of the correlation matrix are calculated and presented in Tables 2 and 3 respectively. The eigenvalues represent the strength of the PCs and the eigenvectors show the coefficients in linear combination of the original attributes (dimensions) that contribute to each PC.

The seven eigenvalues given in Table 2 are ordered according from the highest to the lowest variability. It is important to decide the number of PCs that have practical significance. One of the simple but arbitrary rules-of-thumb is to consider the principal components, which have eigenvalues of one or greater as having practical significance. In this case, therefore, the first three components, which account for about 77% of the total variability, can be taken as components of practical significance.

The values of the eigenvectors are given in Table 3. The eigenvectors are scaled from +1 to −1. The attributes that have significant positive or negative value (the bolded values in the table) work as an index of agreement or disagreement of change in the original attributes. For example, the first principal component gives high positive values to both WC and straw % mass loss, OIT and EAB. Hence, the first PC gives information about the mass loss effect on thermal characterization

Table 2 Eigenvalues of the correlation matrix

Principal component	Eigenvalue	Percentage of variability component cumulative	
		Component	Cumulative
1	2.7638	39.483	39.483
2	1.5736	22.481	61.963
3	1.0387	14.839	76.802
4	0.6847	9.781	86.583
5	0.5089	7.271	93.854
6	0.2719	3.884	97.738
7	0.1584	2.262	100.000

Table 3 Eigenvectors for all seven principal components

	PC 1	PC 2	PC 3	PC 4	PC 5	PC 6	PC 7
OIT	**0.50107**	−0.23316	−0.1774	0.16977	−0.00796	**0.77198**	0.19559
IM	−0.30855	0.30988	**−0.40112**	**0.73429**	0.30052	0.07236	−0.11469
Straw % mass loss	**0.50059**	**0.35424**	0.06073	0.03384	−0.14397	−0.01697	**−0.77335**
WC % mass loss	**0.46638**	**0.34052**	0.03407	**0.32564**	−0.31791	**−0.40447**	**0.54285**
EAB	**0.34958**	**−0.40728**	**0.31522**	0.23824	**0.67578**	−0.31174	−0.04406
WC density	−0.24943	0.01729	**0.80145**	**0.39736**	−0.25226	0.26946	−0.03217
Straw density	0.03459	**0.66483**	0.2472	**−0.33192**	**0.51723**	0.25523	0.22991

PC principal component

method and on mechanical characterization methods. The second PC relates to straw density, mass loss in both straw and WC samples versus EAB, which relates to physical property versus mechanical property. The third PC gives information about the relationship between WC sample density and IM data, recalling that IM characterization was applied to samples with conductor intact. In addition, the third PC shows a relationship between IM and EAB, which represents the relationship between mechanical properties of WC and straw samples.

The first three principal components described above give some indications about the nature of the differences in aged samples. In Fig. 4, a loading plot of selected PCs depict the above eigenvectors for easy interpretation.

The score plot gives information about grouping or outliers and other patterns in the sample set. Analyzing the score plot given in Fig. 5a, it is clear that this data matrix can be grouped by high and low total dose. The higher total dose samples are towards the left side of the plot and the lower total dose samples are towards the right side of the plot. This segregation indicates that the radiation could substantially affect the results of characterization methods. PCA is a least-squares method, which means that outliers may influence the results unduly. It is essential to find and eliminate outliers before making the final PCA analysis, therefore. There are two possible outliers appearing in the score plot of Fig. 5a, labeled as 'Row: 1' and 'Row: 2'. Row: 1 represents the pristine sample, which has not been exposed to thermal, or radiation aging. As a result, one should expect this sample to possess deviant properties in comparison with the aged samples. On the other hand. Row: 2 represents a sample exposed to thermal and gamma radiation aging but whose characterization properties deviate from those of the rest of the aged samples. This sample is regarded as an outlier, therefore. Directions in the score plot correspond directly to the directions in the loading plot (Fig. 5b). The Row: 2 sample is vertically separated from the other samples. Consider overlapping the score plot and

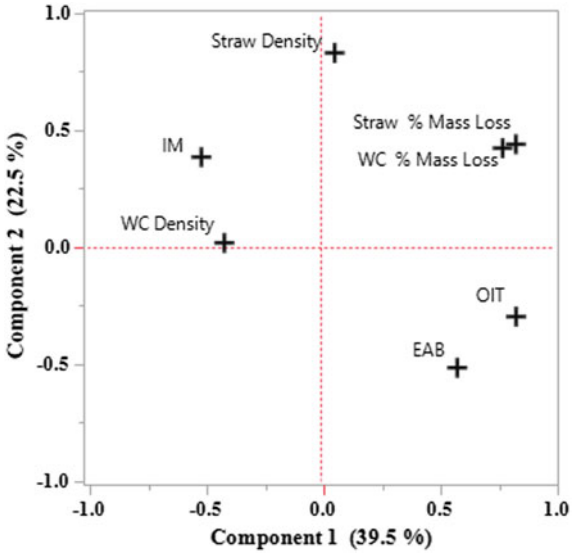

Fig. 4 Loading plot of first two PCs, which contribute to 76.8% of the total variance

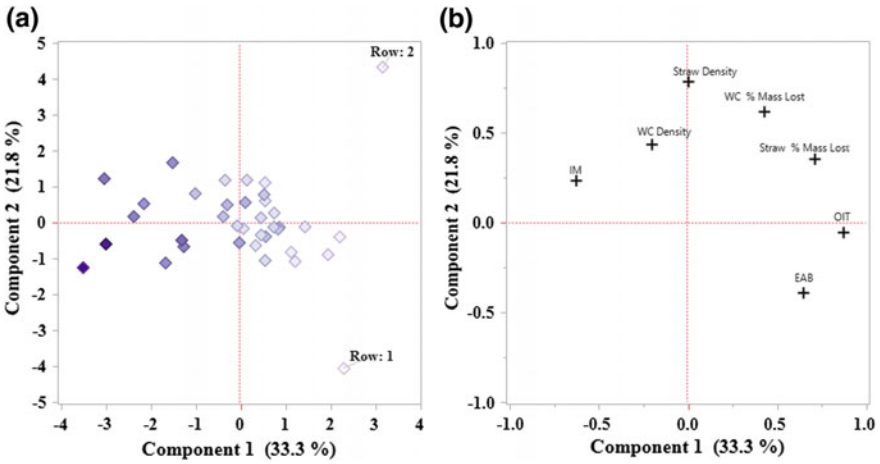

Fig. 5 **a** Score plot of the first two PCs gives information about grouping of samples. Samples in the score plot are color coded from dark to light, where the darkest symbol represents the sample with maximum total dose of 320 kGy and the lightest symbol represents 15.6 kGy. The color density variation shows the variation of the total dose. The two possible outliers are labeled according to their row number in Table 1. **b** Loading plot of first two PCs shows the variation of original attributes on those PCs. Attributes that cause the outlier are identified by overlapping figure (**b**) with figure (**a**)

loading plot. The attributes that are in the same area as the outlier are the attributes that cause the outlier. Therefore, attributes far from zero in the vertical direction are responsible for the outlier of Row 2. In this case, straw density and WC % mass loss are the attributes that cause Row 2 to be an outlier.

Figure 6 shows a score plot calculated after removing the Row: 2 sample from the data set. Comparing Figs. 5a and 6, removing the outlier leads to a much better separation on samples that are in between very high and very low total dose. Before removing the outlier, the samples that were exposed to very high and very low total dose are separated to left and right side of the score plot while the samples that are in between the two extremes do not have a clear separation. After removing the outlier, the separation of the samples in between the two extremes becomes more visible. The eigenvalues and eigenvectors given in Tables 2 and 3, the loading plot of Fig. 4, and the superposition of score and loading plots shown in Fig. 7 are all derived from calculations made after removing the outlier.

For simultaneous analysis of the attributes and objects the score and loading plots can be superposed, Fig. 7.

By looking at the positions of highly radiated samples in the plot of Fig. 7, it is easy to understand which attributes are responsible for separation of samples according to the total dose. OIT, EAB, straw, and WC % mass loss are aligned with lower total dose to higher total dose, the positive eigenvector values of these attributes in Principal Component 1 indicates that they negatively correlate with increasing total dose. On the other hand, IM data, which has a negative eigenvalue, is superimposed in Fig. 7 upon samples of higher total dose, indicating positive correlation with increasing total dose. The eigenvalue of straw density is extremely small on the horizontal axis, indicating that straw density shows no correlation with

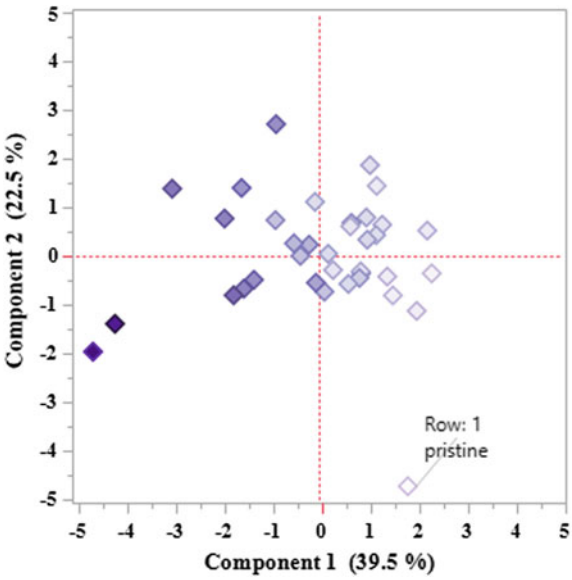

Fig. 6 Score plot of the same data as shown in Fig. 5a, calculated after removing the outlier at Row: 2

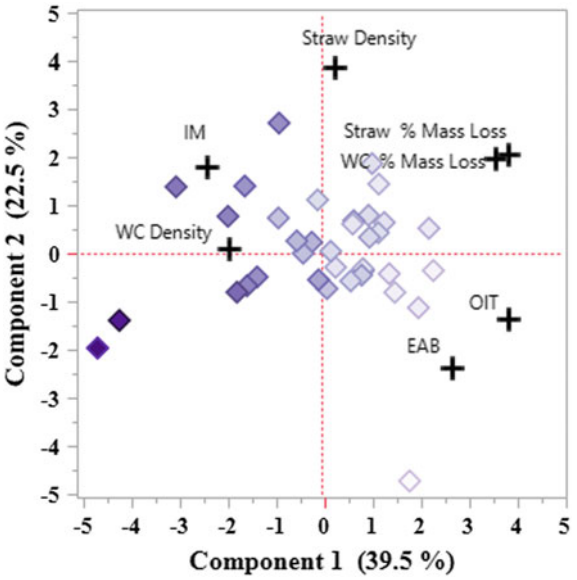

Fig. 7 Superposition of score and loading plots

total dose. By contrast, WC density shows a moderate correlation with the increase of total dose.

Conclusions

Applying PCA to a high-dimension data matrix reduces the dimensions of the data set by means of introducing a new set of attributes called principal components. Viewing the data through this new data set enables the user to identify outliers, grouping and other patterns in the data set. The graphical mode represents collated information, about both attributes and sample set. As an example, PCA was applied in this work to thermally and gamma radiation-aged XLPE cable insulation material. Out of seven attributes that were used, OIT, EAB, straw, and WC % mass loss show a negative correlation with increase total dose in the samples and IM shows a positive correlation with increase total dose. In future work, we will examine the effect of dose rate on aged cable insulation materials.

Acknowledgements This work was funded by the DOE Office of Nuclear Energy's Nuclear Energy University Programs under contract number DENE0008269 and the DOE Office of Nuclear Energy's Light Water Reactor Sustainability Program. Exposure experiments were conducted at Pacific Northwest National Laboratory, which is operated by Battelle for the US DOE under contract DE-AC05-76RL01830.

References

1. The official website of the Nuclear Energy Institute: https://www.nei.org/Knowledge-Center/Nuclear-Statistics/US-Nuclear-Power-Plants. Accessed 14 July 2017
2. D.J. Naus, C.B. Oland, B.R. Ellingwood, Report on Aging of Nuclear Power Plant Reinforced Concrete Structures. Division of Engineering Technology Office of Nuclear Regulatory Research U.S. Nuclear Regulatory Commission Washington, DC. Report number NUREG/CR-6424 ORNL/TM-13148 (1996)
3. K. Pearson, On lines and planes of closest fit to systems of points in space. Philos. Mag. **11**, 559–572 (1901)
4. L.S. Fifield, S. Liu, N. Bowler (in preparation) Method of simultaneous thermal and gamma radiation aging of cable polymers. Rad. Phys. Chem
5. H. Hotelling, Analysis of a complex of statistical attributes into principal components. Educ. Psychol. 417–441 https://doi.org/10.1037/h0071325 (1933)
6. J.V. Gulmine, L. Akcelrud, Correlation between structure and accelerated artificial ageing of XLPE. Eur. Polym. **42**, 553–562 (2006)
7. J.N.R. Jeffers, Two case studies in the application of principal component analysis. J. R. Stat. Soc. Ser. C. Appl. Stat. **16**(3), 225–236 (1967)
8. I.T. Jolliffe, *Principal Component Analysis* (Springer Verlag, New York, 2002)
9. S. Wold, K. Esbensen, P. Geladi, Principal component analysis. Chemometr. Intell. Lab. Syst. **2**, 37–52 (1987)
10. JMP® (1989–2007) Version 12.0.1. SAS Institute Inc., Cary, NC
11. E.M. Arvia, R.T. Sheldon, N. Bowler, A Capacitive Test Method for Cable Insulation Degradation Assessment. in *Paper presented at the Annual Report Conference on Electrical Insulation and Dielectric Phenomena*, Des Moines, Iowa, pp. 19–22 Oct 2014 (2014)

How Can Material Characterization Support Cable Aging Management?

David Rouison, Marzieh Riahinezhad and Anand Anandakumaran

Abstract Low voltage (LV) power, control and instrumentation cables are essential to the safe and reliable operations of nuclear power plants (NPPs). However, considering the huge consumption of cables in NPPs, it is impractical and cost prohibitive to replace cables when they reach the end of their design life. As a result, condition monitoring and aging management of cables is critically important for the life extension of NPPs. The aging of LV cables is characterized by the degradation of the polymeric insulation and jacket materials leading to their mechanical failure or the loss of their ability to withstand critical conditions. This paper focuses on studying material characterization techniques (already existing and new) to monitor the change in polymeric material properties and also to establish a general framework between material properties and ageing conditions that could assist in predicting the condition of cables and estimating their remaining life.

Keywords Low voltage cables · Condition monitoring · Aging · Material properties · Polymer characterization

Introduction

Nuclear Power Plants (NPPs) in Europe and North America are reaching the end of their design life and for the most part, entering periods of extended operation. To achieve continued reliability and safe operation, NPPs have been paying particular attention to major components and structures and performed detailed condition assessments to determine if replacements or repairs are required. Electrical cables have been identified as essential components to the operation of the plants. The huge number of cables, especially Low voltage (LV) power, control and instrumentation cables, supporting the operation of each nuclear unit renders any large scale replacement impractical and cost prohibitive.

D. Rouison (✉) · M. Riahinezhad · A. Anandakumaran
Kinectrics Inc., 800 Kipling Ave., Toronto, ON M8Z 5G5, Canada
e-mail: david.rouison@kinectrics.com

J.H. Jackson et al. (eds.), *Proceedings of the 18th International Conference on Environmental Degradation of Materials in Nuclear Power Systems – Water Reactors*, The Minerals, Metals & Materials Series, https://doi.org/10.1007/978-3-319-68454-3_3

In order to mitigate the risks of failure of LV cables, significant research has been carried out on cable insulation and jacket materials starting in the 1980s by national research laboratories and utilities. This effort included condition assessment of cables collected in the field and comparison to the expected level of degradation based on environmental qualification tests data, which highlighted the influence of radiation dose and synergistic effects between radiation and thermal exposure [1]. The failure and degradation mechanisms of the main families of cable insulations and jackets were clarified and reported in various industry reports of which only a few are referenced in this paper [2–6].

The degradation of LV cables is generally characterized by a loss of mechanical and physical properties of the polymeric materials used for the insulation and jacket. This degradation is driven by exposure to adverse environments, generally high temperature, ionizing radiation, mechanical stresses, and moisture. The loss of ductility of the insulation in particular would ultimately lead to cracking and failure of the cables. Based on this knowledge, various material-based test methods were developed over the years to assess and monitor the condition of the insulation and jacket materials. Comparatively, medium voltage cable failures have been found to be the result of electrically induced aging mechanisms, hence electrical-based test methods have been developed to assess and monitor cables' condition in the field. As NPP approached their period of extended operations, regulators [7–11] and industry groups [12, 13] issued guidelines for the implementation of cable aging management programs, which included these material test methods as condition monitoring tools in the field and in the laboratory.

Recent research in the field of cable material degradation added further complexity to the aging management of these components. The result of these works demonstrated that the environmental qualification tests performed at high temperatures to simulate and accelerate the ageing of cables often involve chemical degradation mechanisms with higher activation energy than the degradation mechanisms occurring at typical operation temperatures [14–17]. Furthermore, the mechanism of diffusion limited oxidation, which also results in slower apparent rate of aging at higher temperatures, was also found to be a factor when the thickness of the material reaches a certain limit [16, 17]. These findings put further emphasis on the need to obtain mechanical and physical test data in the field to properly assess the condition of cables in adverse environments, since aging models based on laboratory experiments under high temperatures and high dose rates cannot be fully relied upon.

In recent years, the focus of LV cable testing research has switched to the development of electrical-based techniques to determine the condition of the insulation material. Broadband dielectric spectroscopy and frequency domain reflectometry techniques have shown promise to identify local and bulk material degradation [18–23]. However, at this stage, these methods cannot yet accurately relate these findings to the exact condition of the cable, and much less predict its remaining life. Therefore, material-based techniques remain the most reliable and accurate methods to achieve accurate evaluation of LV cables in the field. This

paper discusses the applicability of the most commonly used material test methods in the laboratory and in the field by providing multiple examples.

Electrical Cable Materials

A wide range of insulating materials is used for LV applications. The choice of material is primarily driven by mechanical requirements and environmental conditions such as exposure to certain fluids, high temperatures or radiation. In NPPs, the most commonly used insulation materials are crosslinked polyethylene (XLPE) and ethylene propylene rubber (EPR) based compounds. Plasticized polyvinyl chloride (PVC) compounds are also used extensively for outside containment operations in Canadian and certain European plants [3, 10]. Other materials can be found in plant settings, such as silicone rubber, butyl rubber or Tefzel for instance, but usually in much smaller quantities and for specialty applications. The cable jackets, which are mainly used for mechanical protection of the insulated wires, also come in a variety of materials in NPPs. A number of materials are based on halogenated polymers with inherent flame retardant properties, such as chlorosulfonated polyethylene (CSPE), polychloroprene (CR), chlorinated polyethylene, or PVC. Other types of jacket materials include crosslinked polyolefin materials (XLPO).

The aging characteristics of the various insulation and jacket materials are specific to each material family. For instance plasticized compound will lose ductility when subjected to high temperature as a result of loss of plasticizer. Other materials will harden as a result of additional crosslinking of the polymer backbone. Similar differences exist when materials are subjected to ionizing radiation. These different mechanisms translate into different mechanical and physical behavior as the materials age. For this reason several material-based condition monitoring and characterization techniques were developed over the years to determine the condition of LV cables in the laboratory and in the field [6, 11–13].

Test Methods

The gold standard for the assessment of aged LV cable insulation and jacket materials is tensile elongation at break. It was established by various sources that the end of life of a LV cable insulation corresponds to a tensile elongation of 50% [6, 7]. This value was defined as the minimum ductility required from the insulation to withstand a design basis accident event without failure. Based on this premise, all other techniques developed are compared or correlated to elongation at break results. Among those techniques, this paper focuses on the ones which have been deployed successfully in the field to assess the condition of cables and have supported laboratory investigations of aged cables.

Near Infrared Spectroscopy

Fourier Transform Near Infra-Red (FTNIR) instruments equipped with a fiber optic reflectance probes have been used for over two decades on over 10,000 installed cables in CANDU plants as a technique to analyze LV cables. The insulation or jacket materials are scanned with the probe in the NIR region and the resulting spectrum provides a fingerprint of the chemical structure of the compound in that region. It is a non-destructive technique that can be used on any polymers of light colour. Models were developed to directly correlate the chemical changes produced by the oxidative aging of PVC, XLPE, and EPR as measured by NIR to elongation at break [24]. Partial least square chemometric analysis techniques were used to develop the calibration curves for thermally and radiation aged insulation materials [24]. Practically, the cable insulation is scanned five times and the average spectrum will be compared to a library of insulation formulations found in CANDU plants. If the material matches one of the formulations for which a model exists, the spectrum is processed by the analysis software and compared to the model to obtain an estimate of the elongation at break. This method can also discriminate between thermal and radiation aging effects for a material like PVC.

Mid Infrared Spectroscopy

Fourier Transform Mid Infra-Red (FTIR) instruments equipped with an attenuated total reflectance crystal are used to characterize the chemical composition of materials. The insulation or jacket materials are scanned with the instrument in the mid-IR region and the resulting spectrum provides a fingerprint of the chemical structure of the compound in that region. FTIR is a non-destructive technique that can be used on any polymer. A portable unit was recently commercialized which expanded the applicability of this technology. The technique is still mostly used in the laboratory to determine the composition of cable materials and to assess the presence of aging markers, such as oxidation peaks.

Indenter Modulus

The EPRI (Electric Power Research Institute) indenter uses an anvil which is driven into the cable jacket or insulation at a constant speed while recording force and deformation depth [25–27]. The reported indenter modulus is the ratio of the deformation force to the deformation depth with an average of at least 5 measurements from the same sample.

Elongation at Break

Tensile strength and elongation at break tests follow various international standards such as ASTM D470 or D2633, or IEC 62852-3. Tests are performed on tubular insulation or die cut jacket tensile specimens at a constant grip separation speed.

Oxidation Induction Time

The oxidative stability (effectiveness of antioxidants) can be measured using Differential Scanning Calorimeter (DSC). The time to the onset of exothermic oxidation, oxidation induction time (OIT), is used as the measure of oxidative stability and is particularly applicable to XLPE and EPR compounds. Similarly, the onset temperature for oxidation, oxidation induction temperature (OITP), can be also used as the measure of oxidative stability.

Results and Discussion

In the laboratory, a large number of material-based destructive and non-destructive characterization techniques can be used to elucidate the condition of LV cables. Figure 1 shows one power and one control cable received in the laboratory after being discovered in a severely degraded condition during an outage. These cables are part of a powertrack subjected to regular operation. They displayed a significantly damaged section, characterized by severe cracking of the jacket. The insulation and jacket of the degraded and reference cables were analyzed by FTIR. The spectra for the power cables are provided in Figs. 2 and 3. The main peaks of the insulation material (Fig. 2) are consistent with an EPR material with the vibrations for the methylene group in the 3000–2850 cm^{-1}, 1450 cm^{-1} and 725 cm^{-1} regions, and the vibration for the methyl group around 1380 cm^{-1}. Analysis of the insulation in the degraded section of the cable revealed the presence of a large stretch around 3400 cm^{-1} and additional peaks in the 1650 cm^{-1} region. These peaks can be attributed to hydroxyl and carbonyl groups in the material. These groups are likely the product of oxidation of the insulation. The spectra for the jacket material (Fig. 3) were found to be most consistent with a CSPE material (also known by the trade name Hypalon) with the vibrations for the methylene group in the 3000–2850 cm^{-1} and 1450 cm^{-1} regions, and the peaks for the sulfonyl chloride group around 1370 cm^{-1} and 1150 cm^{-1}. Analysis of the jacket in the degraded section of the cable also revealed the presence of oxidation products. In general, both power and control cables were found to be made of EPR insulation and CSPE jacket.

For both cables, the jackets cracked as a result of bending of the cables during the application. The cause of the cracking was attributed to severe embrittlement of

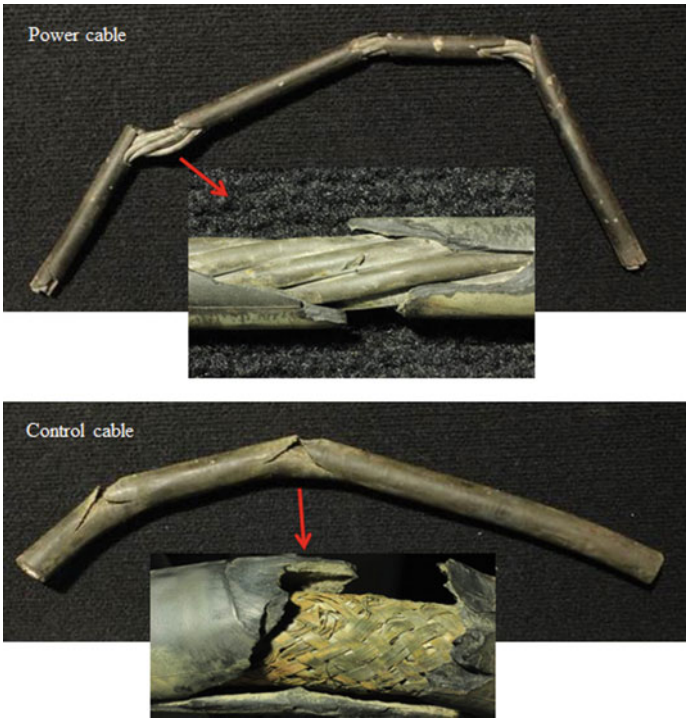

Fig. 1 Failed power (top) and control (bottom) cables

the jacket, as noted by a significant drop in elongation at break and increase in indenter modulus (Table 1). The level of embrittlement of the jacket was noted to be more severe on the power cable. In addition, the power cable exhibited significant discolouration of the insulation and jacket material. This discolouration and the embrittlement of the insulation and jacket are characteristic of thermal ageing. Presence of oxidation by-products in the degraded material confirmed degradation of the material through a thermo-oxidative process. The results of the examination of the power and control cables indicated that their degradation was likely the result of an external source of heat. The heat source was most likely closer to the power cable as this cable was more brittle and discoloured than the control cable. For this type of application, radiation may have been a contributing factor but was not the dominant ageing mechanism.

Material testing in the laboratory can also support condition assessment of cables in the field when samples can be collected and sent for evaluation. The ability to perform destructive testing in the laboratory, such as elongation at break or OIT, increases the accuracy of the cable assessment. To illustrate this point, a number of safety related LV sacrificial cables were removed from the vault of a NPP after 12 and 22 years of operation to assess their conditions in comparison to available baseline data. The insulation of these cables was tested for NIR, OIT, OITP and

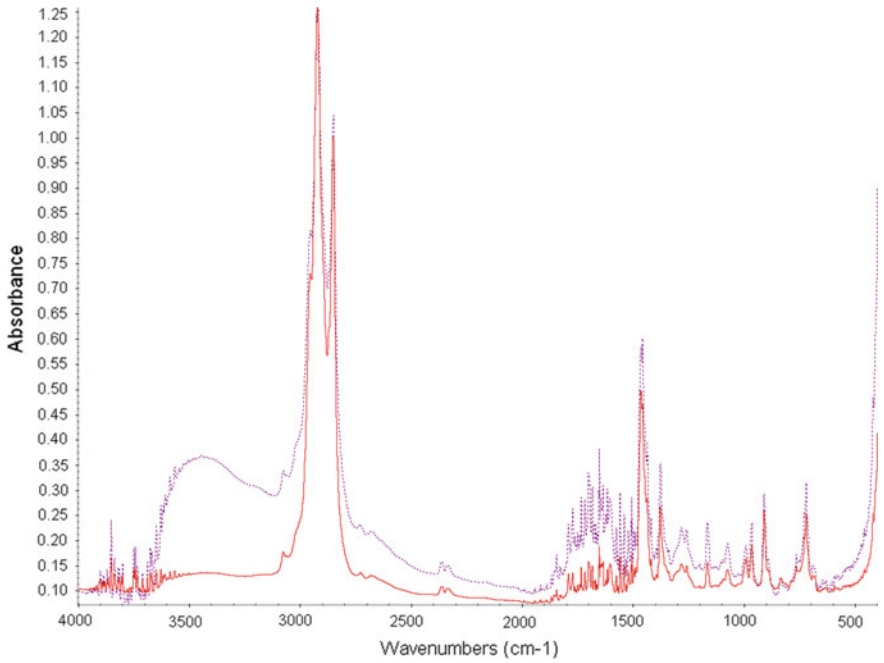

Fig. 2 FTIR of the insulation from the degraded (purple dashed curve) and reference section (red solid curve) of the power cable

elongation at break, while the jacket's indenter modulus and elongation at break were measured.

The formulation of the insulation materials was characterized by NIR and compared to the Kinectrics database, which includes date for environmentally qualified cables. The insulation materials matched various XLPE and EPR compounds listed in the database and confirmed the fingerprint of each cable. Visual inspections of the cables did not reveal any visible discolouration, inferring that these cables experienced minimal heat exposure. Representative results of OITP, OIT, and elongation at break tests for the insulation materials are shown in Table 2. Tensile test results indicated that the XLPE and EPR insulation materials retained at least 95% and 80% of their initial unaged elongation values, respectively. The OIT and OITP results indicated a decrease in the level of stabilization against oxidative aging. However, the OIT values of above 5 min for the 22-years aged samples, indicate that the XLPE and EPR insulation materials were still protected against thermal and radiation induced oxidative aging.

The indenter modulus, a key indicator of heat-induced hardening, was measured for cable jackets (see Table 3), and the results suggested it had not significantly increased for the PVC and CSPE jackets. The elongation at break values for the cable jacket showed some loss of ductility for a number of cables over the 22 years of operation.

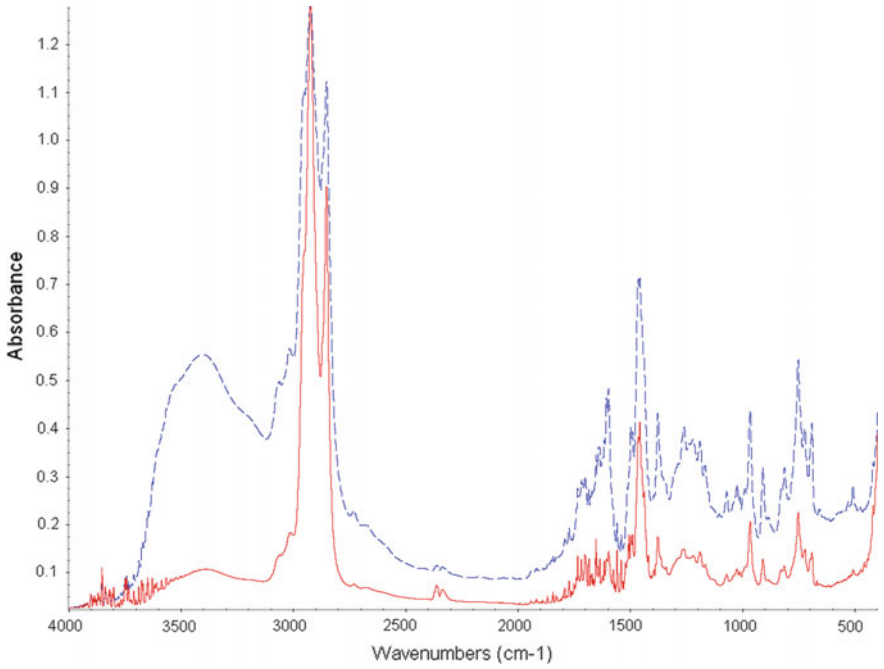

Fig. 3 FTIR of the jacket from the degraded (blue dashed curve) and reference section (red solid curve) of the power cable

Comparison of the elongation values for the insulation and jacket materials and the jacket indenter data with the elongation trends of thermal, radiation, and radiation plus thermal aged cables in the Kinectrics database, provided supplementary insight into the extent of exposure from the environment. It was estimated that the XLPE and EPR insulations were exposed to a radiation field of 10 Mrad or less and a thermal environment of approximately 40 °C during the 22 years of field aging. Jacket materials which exhibited low elongation or high indenter modulus values experienced a radiation dose close to 10 Mrad and/or experienced the effects of a thermal environment for a long period of time. The safety-related cables included in this work were qualified for in-service environments with 50 Mrad or higher and 40 years or longer at 75 °C. Therefore, the results of this evaluation indicated that the samples had not been exposed to high levels of radiation, or long periods of high temperature, and can therefore remain in operation for longer times.

The NIR spectra collected on these cables were used to predict the elongation values of the XLPE and EPR insulation materials evaluated in this study using available models [24]. Table 4 presents the actual and predicted elongation values based on NIR along with the Mahalanobis distance (M-Distance) for insulation materials. The M-Distance is a statistical measure of the difference between sample data and the calibration-set data. Generally a value in the region of 3 and below indicates that the model is statistically representative of the sample. Table 4 results

Table 1 Elongation at break and indenter modulus results

	Power cable				Control cable			
	Jacket		Insulation		Jacket		Insulation	
Sample ID	Degraded section	Reference section	Degraded section	Reference section	Degraded section	Reference section	Degraded section	Reference section
Elongation at break (%)	N/A[a]	344 ± 38	132 ± 14	214 ± 30	N/A[a]	231 ± 10	225 ± 17	202 ± 21
Indenter modulus (N/mm)	150.0	11.0	18.7	19.6	36.2	10.8	19.9	20.0

[a]Not appropriate for tensile test

Table 2 Insulation material test data

Insulation type	OITP (°C)			OIT (min)			Elongation (%)		
	22 years	12 years	Baseline	22 years	12 years	Baseline	22 years	12 years	Baseline
Cable 1 (XLPE)	272.2 ± 1.4	281 ± 1	278 ± 1	8.5 ± 2 @240 °C	19 ± 3 @240 °C	23 ± 4 @240 °C	335 ± 42	283 ± 37	346 ± 34
Cable 2 (EPR)	230 ± 0.9	249 ± 1	260.5 ± 1	Not Available	11 ± 1 @230 °C	17 ± 1 @230 °C	250 ± 13	251 ± 11	240 ± 21
Cable 3 (XLPE)	274.3 ± 0.1	275 ± 4	275 ± 2	10.1 ± 2 @240 °C	15 ± 3 @240 °C	20 ± 3 @240 °C	276 ± 18	268 ± 23	244 ± 18
Cable 4 (EPR)	253.4 ± 6.6	250.5 ± 0.5	259 ± 1	15.8 ± 5 @230 °C	18 ± 6 @230 °C	20 ± 3 @230 °C	279 ± 12	320 ± 21	210 ± 10
Cable 5 (XLPE)	211.4 ± 1.3	218.5 ± 0.5	220 ± 1	6.7 ± 1 @190 °C	11 ± 3 @190 °C	8 ± 1 @190 °C	318 ± 62	292 ± 10	255 ± 19
Cable 10 (EPR)	245.7 ± 7.6	258.5 ± 0.5	264.2 ± 5	7.3 ± 1 @230 °C	20 ± 5 @230 °C	15 ± 3 @230 °C	182 ± 19	227 ± 15	211 ± 10

Table 3 Jacket material test data

Jacket type	Indenter modulus (N/mm)			Elongation (%)		
	22 years	12 years	Baseline	22 years	12 years	Baseline
Cable 1 (PVC)	27.4 ± 2	27.8	32	202 ± 12	280 ± 28	301 ± 16
Cable 2 (PVC)	23.2 ± 3	Jacket split open	13.8	171 ± 18	247 ± 12	290 ± 17
Cable 3 (CSPE)	14.3 ± 1.8	Loose jacket	10	177 ± 26	312 ± 14	383 ± 15
Cable 4 (PVC)	20 ± 2.2	25.2	21	257 ± 11	268 ± 35	256 ± 8
Cable 5 (CSPE)	27.5 ± 2.8	21.8	22	230 ± 7	254 ± 22	309 ± 18
Cable 10 (PVC)	26 ± 3	30.6	Too Large	92 ± 15	321 ± 8	300 ± 46

Table 4 Actual and NIR predicted elongation values of common cable types

Cable ID	Actual elongation (%)	NIR predicted elongation at break (%)	M-Distance
Cable 1 (XLPE)	335 ± 42	301	0.68
Cable 2 (EPR)	250 ± 13	238	1.5
Cable 3 (XLPE)	276 ± 18	307	0.83
Cable 4 (EPR)	279 ± 12	242	0.73

show that the NIR-predicted elongation values are consistent with the measured values within the uncertainties in the elongation measurements of ± 15%. The above data further validates the NIR models for predicting the condition of in-service cables in situ.

In the field, non-destructive methods are required to determine the condition of cables without the need to obtain a sample. The EPRI indenter and NIR spectroscopy can be deployed to provide a full assessment of cables in situ. The indenter modulus is generally conducted on elastomeric jacket materials to locate any degradation. The jacket is most often made with compounds less thermally stable than the underlying insulation. As such degradation of the jacket can be used as a leading indicator of the thermal aging of the whole cable. NIR spectroscopy is used to determine the chemical composition of the jacket and insulation and find out if these materials are listed in the Kinectrics cable material database in order to get access to the environmental qualification data of the cables. If the tested insulation matches on the compound in the database, historical environmental qualification data can then be used to support the condition assessment. Moreover, if the material is found to match one of the NIR models currently available, then its elongation at break can be estimated as demonstrated in the previous example [24]. This combined approach with the indenter and NIR has the advantage of providing a complete assessment of the cable materials and is sensitive to the two main modes of aging encountered in NPPs, namely thermal and radiation exposure.

This methodology has been applied to the examination of installed cables. A number of LV cables at a NPP were chosen for a baseline evaluation. The cables were located in predominantly thermal, radiation and thermal plus radiation environments. NIR spectroscopy was first used to identify the cables' insulation and determine if they matched with a known compound. Indenter modulus was measured on the cables with elastomeric jackets and, for cables with known insulations, the elongation at break was estimated by NIR spectroscopy. Representative results from thermal, radiation, and thermal plus radiation environments are presented in Tables 5, 6, and 7.

Nuclear qualified XLPE and EPR insulations were the major cable types evaluated. Limited number of cables were PVC insulated and primarily used in telephone applications and LDPE insulated used for coaxial cables. The nuclear qualified cables had yellow PVC jackets and the other cables had black PVC or CSPE jackets. The condition of the cables was evaluated for continued service under different environments namely: thermal only, radiation only, and combined thermal plus radiation environments.

None of the cables exhibited cracking or discolouration during visual inspection. A few cables were contaminated with lubricants and a couple of cables exhibited mold growth due to dampness. The indenter modulus values did not show any evidence of PVC jacket hardening. Additionally, the elongation values of the nuclear grade XLPE and EPR insulated cables were in the range of unaged values showing only minimal aging. Similarly, the PVC and LDPE insulated cables, which were more prone to aging in nuclear-plant environments, also showed minimal deterioration in the elongation values.

Table 5 Condition monitoring of cables subjected to thermal environment

Cable number	Jacket color	Ambient temp (°C)	Indenter modulus (N/mm) jacket	Typical indenter modulus @ 25 °C (N/mm)	NIR predicted elongation at break (%)	Actual elong. (%)
Cable 1 (XLPE)	Black (Hypalon)	33	8.6	10	282	No samples
Cable 2 (XLPE)	Yellow	30	19.8	20.5–27.8	320	No samples
Cable 3 (XLPE)	Yellow	27.6	16.4	20.5–27.8	315	No samples
Cable 4 (EPR)	Yellow		N/A	N/A	217	236
Cable 5 (PVC)	Light grey	29	17.2 & 12.6	Not known Values similar to unaged PVC	N/A	218
Cable 6 (LDPE)	Black	26.8	24.1	22.8–40.2	N/A	No samples

Table 6 Condition monitoring of cables subjected to radiation environment

Cable number	Jacket color	Ambient temp. (°C)	Indenter modulus (N/mm) jacket	Typical indenter modulus[1] @ 25 °C (N/mm)	NIR predicted elongation at break (%)	Actual elong. (%)
Cable 7 (XLPE)	Yellow	25.1 °C	23.7	20.5–27.8	322	No samples
Cable 8 (PVC)	Light grey	25.9 °C	15.3	Not known Values similar to unaged PVC	N/A	186
Cable 9 (XLPE)	No Access	N/A	No Access	19.3–30.6	294	324
Cable 10 (XLPE)	Yellow	26.7 °C	20.3	20.5–27.8	327	No samples

Table 7 Condition monitoring of cables subjected to radiation and thermal environment

Cable number	Jacket color	IM (N/mm) jacket	Typical indenter modulus @ 25 °C (N/mm)	NIR predicted elongation at break (Ins) %	Actual elong. (%)
Cable 11 (EPR)	No Access	No Access	Not Applicable	201	176 Limited sample length
Cable 12 (LDPE)	Black	19.3	22.8–40.2	Not Applicable	>512
Cable 13 (XLPE)	No Access	No Access	Not Applicable	278	400

In some instances installed cables cannot be analyzed by NIR because of their dark colour or simply because they are not in the material database. In such instance, the field condition assessment often has to rely on a single test, most often the indenter modulus. Despite this limitation, accurate assessments can still be achieved if the jacket materials can be identified.

In another cable condition assessment, the indenter modulus readings were obtained for 50 installed cables and representative results are tabulated in Table 8. The values have not been corrected to account for the effect of elevated temperatures. If corrected, at an ambient temperature of 24 °C, the modulus values would be slightly higher. The cables were located in trays with the power cables placed in the top tray (A) near the ceiling, and the instrumentation cables placed in the bottom tray (F). The control cables were located in between the power and instrumentation cables in two separate trays (trays C and D). Random indenter measurements were conducted in each available tray.

Table 8 Field indenter modulus results

Cable ID	Ambient temp (°C)	Jacket color	Average indenter modulus
C-01	27.6	Black	206
C-04	27.6	Black	198.4
C-07	27.6	Black	229
F-10	28.2	Black	18.9
F-15	28.2	Black	172
F-18	28.2	Purple	40.6
F-22	28.2	Black	24.4
A-027	28.2	Black	241
A-028	28.2	Black	208
D-034	28.2	Black	108.1
D-035	28.2	Black	124.4
D-036	28.2	Black	58.4

The cables were inspected and no evidence of cracking, swelling, or any deposits was found. The measured indenter readings showed a general pattern regardless of the tray location. Power and control cables placed in the top two trays showed higher modulus values than the control cables and the instrumentation cables placed in the bottom two trays. Indenter modulus values below 100 N/mm indicated a minimal level of aging. However, the values in the 200 N/mm range suggested that the cables have been significantly aged and will not be able to withstand an accident event and remain functional. The data predicted that any manipulation of these cables could result in cracking of the jacket and insulation. Moreover, operation of these cables in a wet environment could also lead to electrical failure.

The assessment performed with the indenter showed that a number of cables had been significantly aged. The power and control cables on the top two trays (A & C) were found to display the worst level of aging and should therefore receive high priority consideration going forward.

Conclusions

The aging of LV cables is driven by material degradation as a result of exposure to adverse environments, such as high temperature, high radiation, moisture, mechanical stresses or contaminants. Hence, a number of material-based characterization techniques were developed over the years to support the aging management of cables in NPPs. The extension of the operating life of a majority of North American and European plants reinforced the need to accurately determine the condition and, when possible, the remaining life of electrical cables since their replacement is complex and cost prohibitive. This paper demonstrated that measurement of the indenter modulus and use of NIR in the field, supplemented with

adequate aging models and material database, can provide sufficient data to estimate the elongation at break of the insulation and confidently assess the condition of the cables. These techniques can also be used in the laboratory, along with FTIR, elongation at break and oxidation induction time and temperature measurements, to do a complete and accurate characterization of a failed or removed cable. Despite their proven applicability and usefulness to assess the condition of cable insulation and jacket materials, these techniques have also known limitations. For instance, NIR does not work on dark coloured materials and the EPRI indenter cannot monitor degradation of hard, non-elastomeric materials such as XLPE. To overcome these limitations, new material-based portable techniques are being investigated to monitor aging markers. FTIR, for instance, is a very promising technique since it can measure, non-destructively, the presence of oxidation by-products in the polymer structure. These material tests also require some knowledge about the environmental conditions affecting the cable, to ensure the assessment is performed at the most conservative location. Recent research on electrical-based techniques, namely dielectric spectroscopy and frequency domain reflectometry, has also shown great promise to determine the condition of dielectric materials. However, despite the potential of these technologies, it appears that developing acceptance criteria for the large number of LV cable materials and designs will be challenging. In the meantime these electrical tests will probably provide new insight about the state of the cables being investigated and allow more efficient and targeted deployment of the established material characterization methods.

References

1. NUREG/CR-2877 (SAND81-2613), K.T. Gillen, R. L. Clough, L.H. Jones, Investigation of Cable Deterioration in the Containment Building of the Savannah River Nuclear Reactor (1982)
2. NUREG/CR-5461 (SAND89-2369), M. J. Jacobus, Aging of Cables, Connections, and Electrical Penetration Assemblies Used in Nuclear Power Plants (1990)
3. SAND96-0344, R.F. Gazdzinski, W.M. Denny, G.J. Toman, R.T. Butwin, Aging Management Guideline for Commercial Nuclear Power Plants—Electrical Cable and Terminations (1996)
4. IAEA-TECDOC-1188, Assessment and Management of Ageing of Major Nuclear Power Plant Components Important to Safety: In-containment Instrumentation and Control Cables, Vol. I and II (2000)
5. NUREG/CR-6794 (BNL-NUREG-52673), M. Villaran, R. Lofaro, Evaluation of Aging and Environmental Qualification Practices for Power Cables Used in Nuclear Power Plants (2002)
6. SAND2005-7331, K. T. Gillen, R. A. Assink, R. Bernstein, Nuclear Energy Plant Optimization (NEPO) Final Report on Aging and Condition Monitoring of Low-Voltage Cable Materials (2005)
7. National Regulatory Commission Document NUREG/CR-7000, M. Villaran, R. Lofaro, Essential Elements of an Electric Cable Condition Monitoring Program (2010)
8. National Regulatory Commission Document NUREG-1801, Rev. 2, Generic Aging Lessons Learned (GALL) Report (2010)

9. National Regulatory Commission Document REGULATORY GUIDE 1.218, Condition Monitoring Techniques for Electric Cables Used in Nuclear Power Plants (2012)
10. Canadian Nuclear Safety Commission Report RSP-084, P. Lindsay, S. Benson, Ageing Management of Cable in Nuclear Generating Stations (2012)
11. IAEA NP-T-3.6, Assessing and Managing Cable Ageing in Nuclear Power Plants (2012)
12. EPRI Report 1021629, Plant Support Engineering: Aging Management Program Development Guidance for Instrument and Control Cable Systems for Nuclear Power Plants (2010)
13. EPRI Report 1020804, Plant Support Engineering: Aging Management Program Development Guidance for AC and DC Low-Voltage Power Cable Systems for Nuclear Power Plants (2010)
14. N. Fuse, H. Homma, T. Okamoto, Remaining Issues of the degradation models of polymeric insulation used in nuclear power plant safety cables. IEEE Trans. Dielectr. Electr. **21**(2), 571 (2014)
15. T. Seguchi, K. Tamura, T. Ohshima, A. Shimada, H. Kudoh, Degradation mechanisms of cable insulation materials during radiation-thermal ageing in radiation environment. Radiat. Phys. Chem. **80**, 268–273 (2011)
16. SAND 2010-7266, K.T. Gillen, R. Bernstein, Review of Nuclear Power Plant Safety Cable Aging Studies with Recommendations for Improved Approaches and for Future Work (2010)
17. K.T. Gillen, R. Bernstein, M. Celina, Challenges of accelerated aging techniques for elastomer lifetime predictions. Rubber Chem. Technol. **88**(1), 1–27 (2015)
18. E. Linde, L. Verardi, D. Fabiani, U.W. Gedde, Dielectric spectroscopy as a condition monitoring technique for cable insulation based on crosslinked polyethylene. Polym. Testing **44**, 135–142 (2015)
19. Y. Ohki, N. Hirai, Effects of the structure and insulation material of a cable on the ability of a location method by FDR. IEEE Trans. Dielectr. Electr. Insul. **23**(1), 77 (2016)
20. EPRI Report 1015209, Plant Support Engineering: Line Impedance Resonance Analysis for the Detection of Cable Damage and Degradation, 2007
21. H.M. Hashemian, B. Mcconkey, G. Harmon, C. Sexton, Methods for testing nuclear power plant cables. IEEE Instrum. Meas. Mag. **16**(5), 31 (2013)
22. PNNL-25432, S.W. Glass, L.S. Fifield, T.S. Hartman, Evaluation of Localized Cable Test Methods for Nuclear Power Plant Cable Aging Management Programs (2016)
23. ADVANCE—Publishable Summary, Ageing Diagnostics and Prognostics of low—voltage I&C cables (2013)
24. K. Anandakumaran, Condition Monitoring of Low-Voltage Cables, CANDU Owners Group (GOG) Reports, COG-06-4063, March, 2007 and COG-07-4056 (2008)
25. EPRI Report NP-7348, Cable Indenter Aging Monitor (1991)
26. EPRI Report 1008211, Initial Criteria Acceptance Concepts and Data for Assessing Longevity of Low-Voltage Cable Insulations and Jackets (2005)
27. EPRI Report TR-104075, Evaluation of Cable Polymer Aging through Indenter Testing of In-plant and Laboratory-Aged Specimens. EPRI (1996)

Aqueous Degradation in Harvested Medium Voltage Cables in Nuclear Power Plants

R.C. Duckworth, A. Ellis, B. Hinderliter, E. Hill and M. Maurer-Jones

Abstract For medium voltage (MV) power cables with voltages between 5 and 35 kV that provide power to emergency and safety support systems in nuclear power plants (NPPs), degradation and failure of cables due to water exposure has occurred. Systematic studies of current NPP MV cable systems are being carried out to determine and characterize cable-aging mechanisms and provide greater accuracy to models being developed to predict MV cable field performance to support existing cable aging management and monitoring programs. To validate models based on representative laboratory specimens, samples from harvested MV cable systems are being subjected to accelerated aging and degradation from humid conditions and submergence. Degradation will be characterized via partial discharge and voltage endurance testing of the cable and induced water tree growth in insulation. The technical approach to be used for the testing harvested MV cable samples is presented.

Keywords Cross-linked polyethylene · Water degradation · Medium voltage cables

Introduction

For nuclear power plants (NPPs), medium voltage (MV) power cables provide auxiliary power for safety systems to continue operation in the event of an emergency. These cables with voltages between 5 and 35 kV travel from off-site power networks, emergency diesel generators, and battery backup systems to the safety busses and allow for short-term, uninterrupted reactor operations. While these cables do not operate on a regular basis, they are required to meet the same lifetime

R.C. Duckworth (✉) · A. Ellis
Oak Ridge National Laboratory, One Bethel Valley Rd, Oak Ridge, TN 37830, USA
e-mail: duckworthrc@ornl.gov

B. Hinderliter · E. Hill · M. Maurer-Jones
University of Minnesota-Duluth, 1305 Ordean Ct, Duluth, MN 55812, USA

J.H. Jackson et al. (eds.), *Proceedings of the 18th International Conference on Environmental Degradation of Materials in Nuclear Power Systems – Water Reactors*, The Minerals, Metals & Materials Series, https://doi.org/10.1007/978-3-319-68454-3_4

performance and reliability requirements as in-plant, lower voltage instrument and control (I&C) cables which is 40 years for the initial plant operating license in the US.

One issue that has affected the reliability of MV power cables in NPPs is their exposure to water while energized. While MV power cables in NPPs are installed in either underground concrete ducts and conduits, direct-buried in the ground, or within the support buildings on the plant to mitigate environmental exposures and to protect from direct lightning strikes [1], water has collected in different locations and geometries within these structures and has resulted in the submergence of cables for extended periods of time beyond their original specifications. This submergence has led to cable failures prior to the end of their 40-year lifetime as shown in Fig. 1 from surveys performed by the Nuclear Energy Institute [1] and the Nuclear Regulatory Commission (NRC) [2]. To set the context of a MV power cable failure at a NPP, the loss of a circulating water pump and two non-safety related 4.16 kV substations at Davis Bessie [3] occurred following a fault in a MV power cable that had been submerged for an extended period. While the risk is currently managed by the redundancy of electrical and operating systems to prevent damage to the NPPs and allow for issues to be address during planned outages, the development of a predictive model for degradation of MV power cables due to water exposure would benefit the efficient operation and maintenance of the existing MV power cable networks.

A Department of Energy (DOE) Nuclear Energy University Partnership (NEUP) between the University of Minnesota-Duluth (UMD) and Oak Ridge National Laboratory (ORNL) has been formed to develop a mechanistic model through the analysis of degradation of harvested MV power cable insulation relative to laboratory chemically equivalent insulations with respect to insulation type and exposure conditions. Once this model has been benchmarked in collaboration with organizations like the Plant Engineering Group at the Electrical Power Research Institute (EPRI), it will be provided to stakeholders in NPP cable aging management programs for assessment of their current MV power cables. This paper

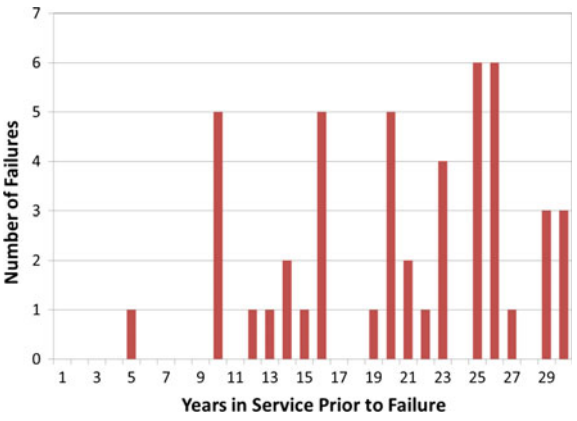

Fig. 1 Distribution of MV power cable failures with respect to years to failure from NEI survey of existing NPPs [1]

provides the context for the current technical approach with respect to previous basic and applied MV insulation and cable research.

Basic and Applied MV Power Cable Research—An Academic and Utility Perspective

Performance degradation of MV power cables due to water exposure has not solely been an NPP issue. This phenomenon was found during initial underground installation of MV power cables and early failures of cross-linked polyethylene (XLPE) from the late 1960s to the mid-1970s due to moisture and submergence [4–6]. These failures were attributed to a combination of water and electrical stress across the insulation system which resulted in the formation of water trees through polymer chain breakdown. This breakdown led to cable failure or reduction in ac breakdown strength that could leave insulation vulnerable to voltage switching transients or surges from lightning strikes [7].

The possible mechanisms for water trees and the related polymer chain breakdown vary by manufacturer and insulation type. For XLPE and tree-resistant XLPE (TR-XLPE) insulations, polymer chain breakdown occurs in the following sequence: (1) electrolysis of water, (2) initiation of degradation, (3) catalysis of degradation by metal ions, (4) chain scission resulting in ketone and carboxylate ion formation, and (5) further conversion of ketones to carboxylate ions [8, 9]. The growth and size of water trees (10–100 μm long) have also been quantified with respect to water exposure chemistry [10] and semiconducting and impurity ions [11–13]. These effects are lessened in TR-XLPE, which contains an additive that creates hydrophilic areas that essentially siphon the water away from the hydrophobic insulation [14]. For ethylene-propylene rubber (EPR), the process of water tree growth is different due to the clay fillers and impurities within the insulation [14–16]. These additions impact the chemical structure of the EPR causing a reduction in the probability of water tree initiation, but they have enhanced water tree growth once it is initiated. While improvements in water tree growth have been realized through the implementation of various process improvements [17–21], the challenge remains to correlate the degradation due to water exposure in harvested MV power cable insulation.

In parallel with the study of water tree growth mechanisms in insulations, a large applied research effort on global cable performance degradation due to water exposure was carried out by utilities, manufacturers, and supporting test organizations. This effort included the development of environmental qualification testing that would enable long-term cable performance with respect to its exposure to water to be calculated accurately since many of MV power cable failures were happening prior to the end of their 40-year life. Because qualification testing involves accelerated aging, its effectiveness is influenced by determination of cable degradation mechanisms and the manner in which these mechanisms are influenced by aging

parameters such as voltage, temperature, and frequency. Bartinkas et al. [22] found degradation in MV power cables from water exposure to be attributed to the permeation of water, initiation of water trees, their growth, and eventual electrical breakdown. This degradation was found to be influenced by electrical stress (voltage and frequency), temperature, water characteristics, and time, where the effects of these various parameters were coupled. For example, temperature affects the permeation of water into the insulation, but not water tree initiation. With respect to temperature and electrical stress for MV power cables that underwent accelerated aging in water, a drop in test voltage from 34.6 to 26 kV increased cable life by a factor of 2.0 to 3.7 depending on material, and a drop in test temperature from 90 to 75 °C increased cable life by a factor of 2.0 [23]. With these studies, as well as many others, two standards emerged for accelerated life testing. The Accelerated Water Treeing Testing (AWTT) [24, 25] was developed to test MV power cables in conduits and quantify the water tree resistance of the insulation. The Accelerated Cable Life Test (ACLT) [26] quantifies cable performance with respect to operating conditions for either a time-to-failure or retention of ac breakdown strength of the insulation and provides configuration recommendations on full immersion of MV power cables. Both standards provide an evaluation of the cable insulation performance with respect to water exposure and the specific standard that is utilized depends on the nature of the information that is required by the end-user whether it is a manufacturer or NPP cable aging management program operators.

Applied MV Power Cable Research—A Nuclear Industry Perspective

Given the increasing number of MV power cable failures in NPPs prior to end of their 40-year lifetime, growth in nuclear-specific MV power cable research has occurred. This growth coincided with the increased attention this problem has received from the NRC after several instances of MV power cable failures [3, 27] due to water. The NRC works with the NPP operators to review and assess the instances of MV power cable failures and develops compliance criteria. These compliance criteria include best practices for the monitoring of cable conditions and the surrounding environment [2, 28], which includes active water level monitoring and removal of water through active pumping or mitigation in problem areas as appropriate. In addition, the NRC also periodically documents the state of knowledge in the area of water degradation in MV power cables through the assistance of organizations such as NEI [1] and Sandia National Laboratory (SNL) [29, 30] to assure the current knowledge gaps are identified and their relative consequences on plant operation are documented. A recent assessment by SNL [30] identified knowledge gaps in chemical and physical degradation theories, pathways,

and understanding as well as a need for fundamental studies in the area of accelerated aging of field aged cables.

The Plant Engineering group at EPRI works with cable aging management program managers at NPPs around the world to harvest low voltage and MV cables in order to perform forensic characterization and accelerated aging of MV cables [31–34]. The outcomes of this work have led to a polymer database on MV power cables [35] and the vetting of high voltage techniques for condition monitoring of MV power cables. One method that is rapidly gaining acceptance is a low frequency (0.1 Hz), high-voltage dissipation technique often referred to as tan δ. This method tracks the cable performance as a function of voltage for a wide range of cable degradation mechanisms including water [36]. While a portion of the EPRI work on MV power cable exposure to water has examined water tree growth in EPR compounds, their work, as well as work performed by the NRC, has also evaluated MV power cable exposure from a functional standpoint to determine and manage the exposure limits as well as to develop techniques to monitor cable performance. A predictive model for cable insulation degradation would add a layer of understanding that could reduce unnecessary removals or reveal environmental conditions that need to be addressed in future installations.

ORNL—UMD MV Power Cable Accelerated Aging Technical Approach

Despite an extensive amount of work has been performed by the utility, academic, and nuclear industry, a predictive model that integrates the different chemical and electrical degradation mechanisms to estimate the remaining useful life for NPP MV power cables is needed. The approach for the ORNL—UMD project to develop this model has two parallel tracks. The first track utilizes representative, harvested XLPE and EPR MV power cables from nuclear power plants and applies an accelerated aging methodology to examine the cable performance as a function of water composition, temperature, time, and electrical stress. The second track uses lab-equivalent XLPE and EPR cable insulation samples with variations in polymer compositions to conduct equivalent accelerating aging conditions in order to determine the chemical origins or possible accelerants to degradation. The focus of this paper is to describe the first track that utilizes harvested cables. Details of the sample preparation and supporting characterization methods are presented elsewhere [37].

Harvested XLPE and EPR MV power cables were provided to ORNL and UMD by EPRI through their working relationship with cable aging management programs at NPPs and are representative of MV power cable currently in use. Examples of the harvested XLPE and EPR cable cross-sections are given in Fig. 2. The XLPE cables were manufactured by Cablec in 1990 and are rated for use at an operating voltage V_o = 15 kV with an insulation thickness of 4.44 mm. The EPR cables were

manufactured by Okonite in 1974 and 2015 and rated for use at 5 kV. Given the spectrum of cable age, results from the accelerated aging and subsequent characterization is expected to be reflective of the historical improvements in cable insulation and processing.

The first step for each insulation type will be to determine the influence of preconditioning on the cable chemical composition. For the accelerated aging of unaged, newly manufactured MV cables, preconditioning is a recommended process [26] where a cable is heated to 90 °C in circulating air for 12 days to minimize the chemical variation within the insulation that is caused by residual curing agents or other chemicals. Given the variation in ages for these harvested cables, it is not clear whether these chemical variations would still be present and influence accelerated aging. To verify the chemical variation of the insulation, short sections of cable will be removed and the chemical structure due to natural aging and preconditioning at 90 °C for 12 days will be analyzed via Fourier transform infrared reflectometry (FTIR) and thermogravimetric analysis to determine the impact of pre-conditioning. If a measurable difference is found due to chemical variation, preconditioning will be performed on each cable prior to termination and testing.

The accelerated aging methodology to be used for the testing of these MV power cable is similar in configuration and instrumentation to current ACLT guidelines [26] but is adjusted to maximize the number of harvested cables (provided by EPRI) to be exposed to the different conditions. For a given voltage ($3V_o$), frequency (60 or 600 Hz), and water temperature (75 or 90 °C), four 3.6 m (12′) long U-shaped sections of cable will be terminated and evenly spaced into a circular fiberglass tank that has an inner diameter of 1.83 m and a depth of 0.60 m. Prior to immersion in tap water, the cable insulation integrity and the integrity of the terminations will be baselined via partial discharge and AC withstand at $2.5V_o$ and 60 Hz. The cable will be removed and replaced if the partial discharge is greater than 5 pC or the failure of the insulation or termination is observed.

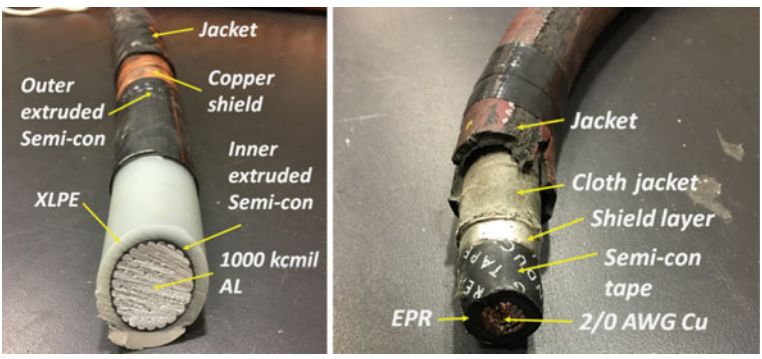

Fig. 2 Cross-section of harvested XLPE (left) and EPR (right) MV power cables

To evaluate water exposure, tap water will be added to 75% of the tank height and the baseline liquid level and water resistivity will be measured and subsequently monitored for reduction from water insulation permeation and evaporative losses. Building water was selected over de-ionized water per the recommendation of current ACLT guidelines [26] and the inconclusive effects of water ion concentration on accelerated aging. Multiple immersion heaters surrounded by stainless steel ground planes will raise the water temperature up to either 75 or 90 °C over a period of four hours to minimize non-uniformity of the temperature along the length of the cable. Temperature along the cable length will also be monitored with thermocouples embedded into the cable jacket.

After equilibrium is reached, the AC voltage will be ramped to $3V_o$, which is 26.0 kV (three times phase-ground) for a 15 kV rated cable and 8.66 kV for a 5 kV rated cable. Partial discharge for each cable will be monitored until a failure is observed or the set period of aging is reached. For aging at a frequency of 60 Hz, a cable removal is planned for every 60 days of exposure with the last cable removed after 240 days of exposure. The time of exposure will be reduced by a factor of 10 for measurements done at 600 Hz applied via a 40 kV programmable high voltage amplifier. Prior to removing the test articles from the tank the temperature of the tank will be reduced slowly to avoid any temperature non-uniformity. After removal an AC breakdown test for the cable will be performed. Upon location of the breakdown along the cable length, the cable will be sectioned into shorter samples varying in lengths between 15 and 50 cm for study of water tree resistance and their growth per ASTM D3756 [38] and ASTM D6097 [39], cross-sectional FTIR characterization along the insulation depth via microtome samples of 50 µm using a chemical processing protocol like Boggs [12] of water tree initiation sites, and ac breakdown along the length of the cable. The goal is to quantify chemical and electrical mechanisms of degradation in the cable performance as a whole, compare the findings with previous non-nuclear cable aging studies for consistency, and develop a model that consistently predicts the cable performance in light of water exposure.

Conclusions

The ORNL—UMD technical approach for the development of a model that accurately accounts for aqueous cable aging mechanisms in MV power cables for current NPPs requires systematic accelerated aging and characterization. Previous work on MV power cables by both the utilities and nuclear industry has emphasized the importance of the water composition, frequency, and temperature to quantify the formation of water trees within the insulation that can lead to degradation. A technical approach for the testing of harvested MV power cables from NPPs has been formulated to maximize the amount of information that can be obtained from testing of the currently available MV power cables. This data will serve as a baseline so the degradation mechanisms that are observed for lab-created,

equivalent polymer insulation samples with varying material compositions can be connected to the actual MV insulation. Ultimately these results as well as the supporting model will be compared to those obtained by NPP cable aging programs, the NRC, and EPRI research programs to determine the boundaries for water exposure in MV power cable degradation more clearly.

Acknowledgements This manuscript has been authored by UT-Battelle, LLC under Contract No. DE-AC05-00OR22725 with the U.S. Department of Energy. The United States Government retains and the publisher, by accepting the article for publication, acknowledges that the United States Government retains a non-exclusive, paid-up, irrevocable, world-wide license to publish or reproduce the published form of this manuscript, or allow others to do so, for United States Government purposes. The Department of Energy will provide public access to these results of federally sponsored research in accordance with the DOE Public Access Plan (http://energy.gov/downloads/doe-public-access-plan).

This work was conducted as a collaborative project between ORNL and UMD and is supported by the Department of Energy (DOE) Office of Nuclear Energy NEUP. Special appreciation is given to Drew Mantey of EPRI and Bodgan Fryszczyn and staff at Cable Techology Laboratories for their guidance and feedback on the test program and for providing harvested MV cable samples they obtained as part of their harvesting activities with existing nuclear power plants.

References

1. Medium Voltage Underground Cable White Paper, Nuclear Energy Institute, NEI 06-05, ML12338A536 (2006)
2. Generic Letter 2007-01, Nuclear Regulatory Commission, ML082760385 (2008)
3. Davis-Beese Nuclear Power Station Inspection Report No. 05000346/2004017, Nuclear Regulatory Commission, ML050310426 (2004)
4. T. Miyashita, Proceedings 1969 IEEE-NEMA Electrical Insulation Conference (Boston, 1969), pp. 131–135
5. J.H. Lawson, W.A. Thue, in *IEEE International Symposium on Electrical Insulation*, pp. 100–104 (1980)
6. R. Bartinkas, H.C. Doepken, R.M. Eichhorn, G.W. Rittman, W.D. Wilkens, IEEE Trans. Power App. Sys. **PAS-99**(4), 1575–1586 (1980)
7. P. Cox, R. Fleming, F. Krajick, S. Boggs, Y. Cao, IEEE Electr. Insul. Mag. **32**(3), 24–28 (2016)
8. J.J. Xu, S.A. Boggs, IEEE Electr. Insul. Mag. **10**(5), 29–37 (1994)
9. J.J. Xu, Ph.D. Dissertation, Univ. of Conn. Storrs, CT, 1994
10. N. Yoshimura, F. Noto, K. Kikuchi, IEEE Trans. Electr. Insul. **EI-12**(6), 411–417 (1977)
11. A. Garton, J.H. Groeger, J.L. Henry, IEEE Trans. Electr. Insul. **25**(2), 427–435 (1990)
12. M.S. Mashikian, J.H. Groeger, S. Dale, E. Ildstad, Conf. Rec. 1988 Inter. Symm on Electr. Insul., pp. 314–321, 1989
13. S.A. Boggs, M.S. Mashikian, IEEE Electr. Insul. Mag. **10**(1), 23–28 (1994)
14. S. Boggs, J. Xu, IEEE Electr. Insul. Mag. **17**(1), 23–27 (2001)
15. J. Xu, A. Garton, IEEE Trans. Diel. Electr. Insul. **1**(1), 18–24 (1994)
16. Plant Engineering: Medium-Voltage Cable Failure Mechanism, Update 7, EPRI, Palo Alto, CA, Report No. 3002005323 (2015)
17. M.S. Mashikian, EPRI, Palo Alto, CA, EPRI Final Report No. EL-4398 (1986)
18. J. Xu, A. Garton, Annual Report—Conference on Electrical Insulation and Dielectric Phenomena, pp, 648–653, 1993

19. S. Ramachandran, R.A. Reed, Papers—Rural Electric Power Conference, pp. B4–B47, 2003
20. S. Boggs, Proceedings of Conference on Electrical Insulation and Dielectric Phenomena (CEIDP) **2**, 547–551 (2000)
21. M.A. Martin, R.A. Hartlein, IEEE Trans. Power App. Sys. **PAS-99**(4), 1597–1605 (1980)
22. R. Bartinkas, R.J. Densley, R.M. Eichhorn, IEEE Trans. Power Del. **6**(3), 929–937 (1991)
23. R. Lyle, IEEE Trans. Power. Del. **3**(2), 434–440 (1988)
24. Specification for Extruded Dielectric Shielded Power Cables Rated 5 Through 46 kV, Association of Edison Illuminating Companies, AEIC CS 8 (2013)
25. Concentric Neutral Cables Rated 5 Through 46 kV, Insulated Cable Engineers Association, ICEA S-94-649 (2013)
26. IEEE Guide for Accelerated Aging Tests for Medium-Voltage (5 kV–35 kV) Extruded Electric Electric Power Cables Using Water-Filled Tanks, Institute of Electrical and Electronics Engineers, IEEE Std. 1407 (2007)
27. Information Noice 2002-12: Submerged Safety-Related Electrical Cables, Nuclear Regulatory Commission (2002)
28. Generic Aging Lessons Learned (GALL) Report, Nuclear Regulatory Commission, NUREG-1801, Rev. 2 (2010)
29. Aging Management Guideline for Commercial Nuclear Power Plants—Electrical Cable and Terminations, Sandia National Laboratories, SAND96–0344 (1996)
30. J. Brown, R. Bernstein, G. Von White II, S. Glover, J. Neely, G. Pena, K. Williamson, F. Zutavern, F. Gelbard, Sandia National Laboratories, SAND2015-1794 (2015)
31. Plant Support Engineering: Failure Mechanism Assessment of Medium-Voltage Ethylene Propylene Rubber Cables—Rev. 1, Electrical Power Research Institute, Palo Alto, CA, Report No. 1018777 (2009)
32. Plant Support Engineering: Medium-Voltage Cable Failure Mechanism—Update 2, Electrical Power Research Institute, Palo Alto, CA, Report No. 1021069 (2009)
33. Plant Support Engineering: Medium-Voltage Cable Failure Mechanism—Update 3, Electrical Power Research Institute, Palo Alto, CA, Report No. 1022965 (2011)
34. Plant Support Engineering: Medium-Voltage Cable Failure Mechanism—Update 4, Electrical Power Research Institute, Palo Alto, CA, Report No. 1024894 (2012)
35. Plant Engineering: Cable Polymer Handbook—Medium Voltage Insulation, Electrical Power Research Institute, Palo Alto CA, 30020053222015 (2015)
36. Plant Engineering: Evaluation and Insights from Nuclear Power Plant Tan Delta Testing and Data Analysis—Update, Electrical Power Research Institute, Palo Alto CA, 3002005321 (2015)
37. E. Hill, B. Hinderliter, M. Maurer-Jones, R. Duckworth, in *Medium Voltage Cable Insulation for Nuclear Power Plants: An Approach to Sample Preparation*, to be presented at the 18th Intl. Conf. on Env. Deg. Mat. Nucl. Pow. Systems, Portland, OR, 2017
38. Standard Test Method for Relative Resistance to Vented Water-Tree Growth in Solid Dielectric Insulating Materials, ASTM International, ASTM D6091-16 (2016)
39. Standard Test Method for Evaluation of Resistance to Electrical Breakdown by Treeing in Solid Dielectric Materials Using Diverging Fields, ASTM International, ASTM D3756-97 (2010)

Frequency Domain Reflectometry Modeling and Measurement for Nondestructive Evaluation of Nuclear Power Plant Cables

S.W. Glass, L.S. Fifield, A.M. Jones and T.S. Hartman

Abstract Cable insulation polymers are among the more susceptible materials to age-related degradation within a nuclear power plant. This is recognized by both regulators and utilities, so all plants have developed cable aging management programs to detect damage before critical component failure in compliance with regulatory guidelines. Although a wide range of tools is available to evaluate cables and cable systems, cable aging management programs vary in how condition monitoring and nondestructive examination is conducted as utilities search for the most reliable and cost-effective ways to assess cable system condition. Frequency domain reflectometry (FDR) is emerging as one valuable tool to locate and assess damaged portions of a cable system with minimal cost and only requires access in most cases to one of the cable terminal ends. This work examines a physics-based model of a cable system and relates it to FDR measurements for a better understanding of specific damage influences on defect detectability.

Keywords Cable modeling · Frequency domain reflectometry · Nondestructive evaluation

Introduction and Background

As nuclear power plants consider applying for second, or subsequent, license renewal to extend their operating period from 60 to 80 years, it is important to understand how the materials installed in plant systems and components will age during that time and develop aging management programs to assure continued safe operation under normal and design basis events (DBE). Normal component and system tests typically confirm the cables can perform their normal operational function. The focus of the cable test program, however, is directed toward the more demanding challenge of assuring the cable function under accident or DBE. The

S.W. Glass (✉) · L.S. Fifield · A.M. Jones · T.S. Hartman
Pacific Northwest National Laboratory, 999, Richland, WA 99352, USA
e-mail: Bill.Glass@pnnl.gov

J.H. Jackson et al. (eds.), *Proceedings of the 18th International Conference on Environmental Degradation of Materials in Nuclear Power Systems – Water Reactors*, The Minerals, Metals & Materials Series, https://doi.org/10.1007/978-3-319-68454-3_5

industry has adopted 50% elongation at break (EAB) relative to the unaged cable condition as the acceptability standard. All tests are benchmarked against the cable EAB test. EAB, however, is a destructive test so the test programs must apply an array of other nondestructive examination (NDE) tests to assure or infer the overall set of the cable's system integrity.

One test that is gaining favor within the industry is frequency domain reflectometry (FDR). This is a low-voltage nondestructive test that can be applied at a cable end. Testing from the cable end is important because local inspection all along the cable length is frequently difficult since cables are routed within trays, conduits, underground, and through walls. The FDR technique has been shown to locate cable insulation damage due to thermal, radiation, environmental, and mechanical damage [1]. However, understanding the degree and extent to which damage will produce detectable results has not been fully quantified. Experimental validation of the wide range of possible cable damage scenarios requires a non-trivial investment of time and resources because not only must cable segments be artificially aged or damaged, but this damage must be located within relatively long (>15 m) cable lengths to allow meaningful FDR measurements. In order to maximize the opportunity to validate FDR across a wide spectrum of conditions, a physics-based modeling approach has been developed to generate FDR responses for various cable geometries, lengths, and simulated cable anomalies. This model has been benchmarked with several experimental verification cables in which well-understood damage mechanisms were compared with the model predictions.

FDR Theory

Frequency domain reflectometry is a nondestructive electrical inspection technique used to detect, localize, and characterize subtle impedance changes in power and communication system conductors along the length of a cable from a single connection point. FDR is based on the interaction of electromagnetic waves with conductors and dielectric materials as they propagate along the cable. The technique uses the principles of transmission line theory to locate and quantify impedance changes in the cable circuit. These impedance changes can result from connections, faults in the conductors, or degradation in the cable polymer material [2, 3]. For the measurement, two conductors in the cable system are treated as a transmission line through which a low-voltage, swept-frequency waveform is propagated. As the excitation signal is swept over the frequency range and the associated electromagnetic wave travels down the cable, the impedance response is recorded at each frequency to characterize the wave interaction with the conductors and surrounding dielectric materials. The remote end of the cable can be terminated in any impedance that is different from the cable characteristic impedance, but is often grounded or open-circuited during the test.

Because the applied signal is low-voltage, the test is nondestructive and poses no special safety concerns to operators, assuming that routine electrical safety

procedures are followed. In most cases, it is only necessary to de-energize the cables and de-termination is not required since the FDR measurement can be made even with a load connected. Typically, however, at least one end of the cabling is de-terminated to connect the FDR measurement system. The need to only de-terminate one cable end can be an advantage over other techniques by shortening the required test time and minimizing the risk of improper re-termination. Frequently, however, both ends of the cable are de-terminated and any residual charge is bled to minimize the risk of residual charge shock.

Figure 1 shows a linearly increasing "chirp" sinusoidal waveform that is representative of the type of excitation signal used in the FDR technique. The excitation signal can be generated for transmission into the cable using an analog circuit such as a voltage-controlled oscillator or using a digital circuit such as a direct digital synthesizer.

For most practical applications, a simplified form of transmission line theory analysis is sufficient. In transmission line theory, the electric fields in a circuit relate to distributed (per unit length) capacitance and the magnetic fields relate to distributed inductance. The resistance of the metallic conductors and dielectric loss in the insulation attenuate the signal as it propagates along the cable.

A schematic representation of the standard transmission line model is shown in Fig. 2, where the distributed circuit elements representing an infinitesimally short length may be cascaded with similar elements to model the overall behavior of the line. In the FDR method, an inverse Fourier transform coupled with the cable

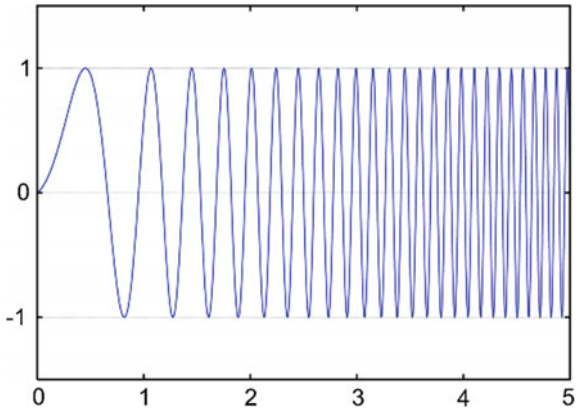

Fig. 1 Example FDR excitation in which the signal frequency increases through the chirp interval

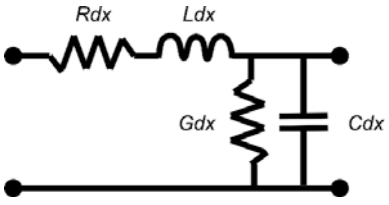

Fig. 2 Transmission line circuit model consisting of distributed impedance elements over an infinitesimally short length

velocity factor is used to develop the range domain data, which contains information on the wave interactions with the cable's resistive, inductive, and capacitive elements and which identifies the physical location of signal reflections [4].

The FDR technique has inherent advantages that can potentially yield better sensitivity to cable degradation than traditional time domain reflectometry (TDR), which is best suited for identifying open and short circuit conditions in conductors [5]. For example, FDR is less susceptible to electrical noise and interference due to the availability of filtering and noise-reducing algorithms in the frequency domain. This can lead to increased sensitivity and accuracy. Additionally, FDR is better suited for identifying and characterizing a series of multiple degradations occurrences in long cables, because TDR pulses may have difficulty continuing in the forward direction after multiple significant reflections.

Spatial resolution is an important parameter for detection and localization of cable defects. The range resolution is a function of the frequency bandwidth (BW), the speed of light (c), and the velocity factor (VF) of the cable [3]:

$$\text{Resolution (m)} = (c \times VF) / (2 \times BW) = 1.5 \times 10^8 \times (VF/BW) \quad (1)$$

where c = 3E8 m/s. The cable's velocity factor is a value less than unity and is inversely related to the square root of the dielectric constant of the insulation material. As an example, using a 200 MHz FDR bandwidth to inspect a coaxial cable with a velocity factor of 66% results in a 0.5 m resolution as shown below:

$$\text{Resolution} = (3 \times 10^8 \text{m/s} \times 0.66)/(2 \times 200 \times 10^6) = 0.5 \text{ m} = 1.6 \text{ ft.} \quad (2)$$

Figure 3 shows a simplified diagram and example data processing flow for an FDR system, which collects and processes the cable data for aging/damage evaluation.

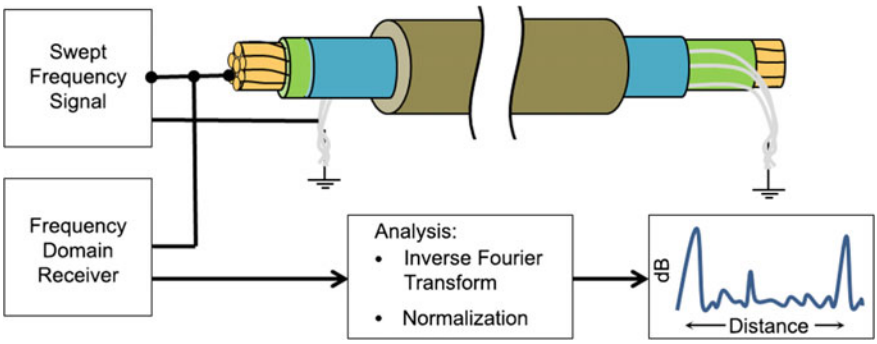

Fig. 3 Block diagram of FDR instrument and cable test arrangement

Cable and FDR Modeling Prior Work

Cable modeling has been extensively used for cable system design. Commercial finite element modeling (FEM) packages include dedicated electromagnetic modules that are tailored for cable modeling and analysis [6, 7]. These software packages offer both two- and three-dimensional modeling capability. Design inputs include conductor material and geometry, insulation permittivity and geometry, and signal frequency. This allows for calculation of multiple parameters relative to cable design including electric and magnetic field strengths for the given input and the effective cable capacitance per unit length. Many researchers have used these modeling tools to predict cable characteristics and performance and to characterize defects in cables. Given the amount of literature available in the area, representative examples are summarized below that were judged to be most relevant to the current simulation study.

As early as 1984, commercial FEM tools like ANSYS were used at Fermi National Accelerator Laboratory to calculate transmission line impedances and capacitance for two conductor systems [8]. Cases considered included coaxial, off-centered coaxial, and two-paired conductor systems.

Chen et al. [9] applied FEM tools to characterize a water-tree damaged section of cable insulation and to image the altered electric field in the region of the water tree. The model was parametrically varied to characterize capacitance of the water-tree affected area versus the percent growth of the water tree across the insulation.

Collaborators from Sebha University and Glasgow Caledonian University used COMSOL software to characterize the electric field for an 11 kV armored cross-linked polyethylene (XLPE) cable insulation containing air-filled void defects [10]. The 2D electrostatic simulation showed a map of the electric field strength within the XLPE cable insulation. The void defect strongly affected the electrostatic field strength and geometric distribution.

Researchers at Sandia National Laboratory have studied submerged medium-voltage cable systems. As part of this effort, they have presented a circuit model for a coaxial cable [11]. This work includes a review of several references where circuit models are developed.

Fantoni has published extensively on the Line Resonance Analyzer (LIRA) FDR method including measurement examples and modeling associated with NDE. One significant report includes a discussion of the LIRA simulator in which cables are modeled using cascaded equivalent circuit-model segments [12]. Most of the segments are similar and represent undamaged cable. The circuit model values are estimated based on inputs that include segment length, conductor material and diameter, insulation conductivity, and wire inductance. The characteristics of a damaged segment are different primarily due to the change in cable capacitance within the damaged segment. The LIRA simulator applies the same kind of input to this circuit model as is used in the measurement instrument to simulate the theoretical cable measurement response. The commercial version of this LIRA simulator is one of the methods used to predict cable responses in this work.

FDR Simulation Methodology

An electromagnetic/circuit co-simulation approach based upon ANSYS High Frequency Structure Simulator (HFSS) as the electromagnetic FEM simulator and ANSYS Nexxim as the circuit simulator was used to model scenarios representative of nuclear power plant cable systems. ANSYS HFSS was used to rigorously solve Maxwell's equations for 3D models representing damaged and undamaged cable sections. The frequency-domain scattering parameters were extracted from each HFSS model to provide physics-based building blocks, which can be combined to investigate a variety of defect scenarios. The simulated FDR response for a specific scenario was obtained from an ANSYS Nexxim circuit model with cascaded scattering parameter datasets corresponding to damaged or undamaged cable sections.

An example circuit schematic is shown in Fig. 4 where the FDR input port is on the upper left and the defect cable segments are the four scattering parameter blocks in the center. In all simulation cases, the cable layout is assumed to be straight along the entire length of the cable run. The frequency domain simulation response was converted to the range domain using an inverse Fourier transform in order to plot the cable signature. This approach provided a computationally efficient method to study the FDR response using detailed 3D models of cable runs, which can be many electrical wavelengths long.

As mentioned in the previous section, an approach based on circuit analysis of cascaded transmission line segments is used in the commercially available LIRA simulator. In this simulation tool, available cable types are limited to coaxial or twisted pair configurations. Physical parameters such as conductor size, insulation type, and cable dimensions are used to describe the cable to be studied. For coaxial cable, a damaged segment can be represented by changing the insulation dielectric constant. For twisted pair cable, a damaged segment can be represented by a change

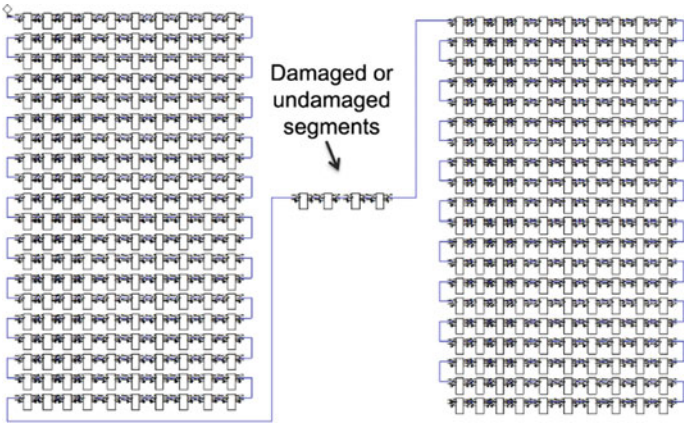

Fig. 4 Example FDR co-simulation model showing cascaded scattering parameter blocks containing FEM results for damaged or undamaged cable segments

Table 1 Cable parameters considered in FDR simulation models

Parameter	600 V Shielded triad cable	RG-58 Coaxial cable
Conductor	Copper, 16 AWG, 1.52 mm diameter, 76 mm lay length (twist rate)	Copper, 0.91 mm diameter
Insulation	EPR, Dk = 3, 0.64 mm thick	PE, Dk = 1.98, 1.02 mm thick
Shield	Copper	Copper
Jacket	CPE, Dk = 2.25, 1.14 mm thick	PVC, Dk = 2.7, 0.75 mm thick
Outer diameter	8.31 mm	4.95 mm
Loss	Insulation Df = 0.025	0.161 dB/m at 100 MHz

PE polyethylene, *PVC* polyvinyl chloride

in the distributed capacitance. The simulator uses these inputs to calculate an FDR response for the overall cable scenario.

Two cable types were modeled in this study—(1) an RG-58 coaxial cable and (2) a General Cable flame-retardant ethylene-propylene rubber/chlorinated polyethylene (FR-EPR/CPE) three-conductor shielded cable. The relevant design parameters shown in Table 1 were used to model the 3D cable geometries in ANSYS HFSS. The coaxial cable was modeled in the LIRA simulator by entering the physical dimensions while the triad cable was approximated in the LIRA simulator as a twisted pair using the distributed circuit parameters.

Validation of Simulation Results

The ANSYS cable simulations were validated using measurements obtained with a vector network analyzer (VNA) and a Wirescan LIRA system of damaged and undamaged cables. These instruments have been previously evaluated and shown to provide similar results [1]. The LIRA system used here has an upper frequency limit of 100 MHz, while the VNA can be used to collect data over a much larger frequency range. The electromagnetic/circuit co-simulation approach was successfully benchmarked against the measured responses and the LIRA simulator for FDR bandwidths of 100 and 200 MHz.

An initial comparison was performed using a 100 ft. section of coaxial RG-58 flexible cable with a 1.5 in. long gouge of the insulation material located at 50 ft. This defect consisted of removing the upper half of the PVC jacket, the outer copper conductor, and the polyethylene insulation as shown in Fig. 5. In the circuit simulation, a randomized impedance tolerance having a standard deviation of 0.25% was applied to the undamaged segments to generate a noise floor, which represents the stochastic nature of the fabrication tolerances of this cable. As shown

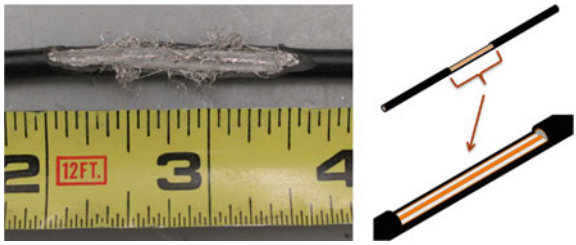

Fig. 5 (left) RG-58 coaxial cable with 1.5 in. long mechanical damage; (right) corresponding ANSYS HFSS finite element model of damaged section

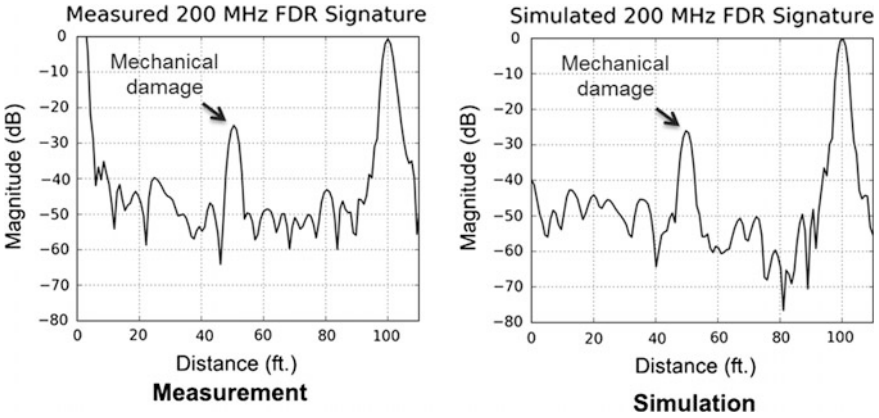

Fig. 6 (left) VNA measurement and (right) ANSYS simulation of 1.5 in. long damaged section at the halfway point of a 100 ft. RG-58 coaxial cable

in Fig. 6, the ANSYS simulation results and FDR measurements for peaks (above −40 dB) agree well. Differences at lower levels are attributed to the random noise simulation and the random noise from the cable fabrication.

A similar assessment was performed using a 100 ft. section of General Cable FR-EPR/CPE shielded 600 V three-conductor cable [13]. In this case, a 3.5 in. long segment of the cable jacket was removed at the 50 ft. location as shown in Fig. 7.

Fig. 7 (left) Damaged 3.5 in. section at the halfway point of a 100 ft. three-conductor shielded 600 V EPR cable; (right) corresponding ANSYS HFSS finite element model of damaged section

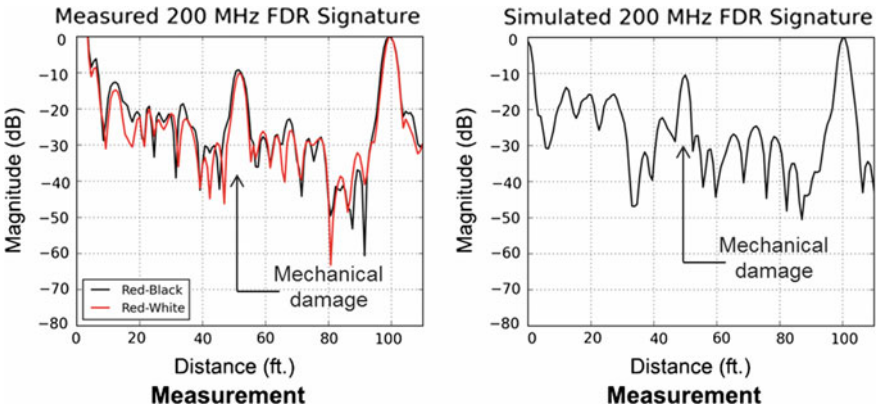

Fig. 8 (left) VNA measurement; (right) ANSYS simulation of damaged 3.5 in. section in the center of 100 ft. three-conductor shielded EPR cable

In the circuit simulation, a randomized impedance tolerance having a standard deviation of 2% was applied to the undamaged segments to generate a noise floor, which represents the stochastic nature of the fabrication tolerances of this cable. The ANSYS simulation results and VNA measurements are in good agreement as shown in Fig. 8.

Cable FDR Simulation Study

Insulation Dielectric Constant

The simulation models of the RG-58 coaxial cable and FR-EPR/CPE shielded triad cable were parametrically analyzed to assess the impact of a uniform change in cable insulation dielectric constant. Because the insulation dielectric constant is related to the distributed capacitance, this parameter can impact the FDR response if the change is significant compared to the cable fabrication tolerances. In both cases, a progressive increase in dielectric constant from 1 to 5% was modeled for a 1 ft. segment centered along a 100 ft. cable, as could be expected for thermal or radiation damage that impacts a short section of a cable.

It is important to note that signal noise can impact the ability of the FDR method to detect defects, which create small changes in insulation dielectric constant over short sections of cable. An important contributor to the FDR noise floor is the cable fabrication tolerance, which produces small, random fluctuations in electrical parameters along the cable length. These small differences in cable construction (twist rate, conductor or insulation dimensions, dielectric properties, etc.) can set a threshold for the FDR defect response. For the coaxial cable model, a randomized impedance tolerance having a standard deviation of 0.25% was applied to the

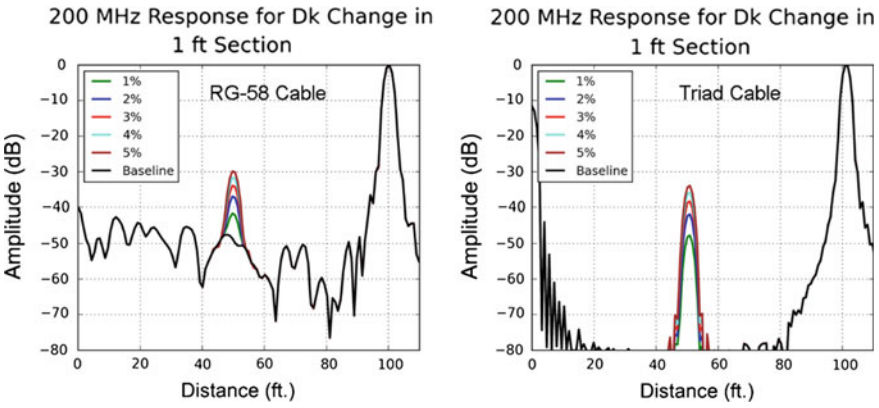

Fig. 9 ANSYS simulation results for 1 ft. defect segment with increased insulation dielectric constant at halfway point of 100 ft. (left) RG-58 coaxial cable and (right) shielded triad cable

undamaged segments to generate a noise floor representative of laboratory measurements. For the triad cable model, no stochastic noise was added to the simulation so that very small reflections would be visible. The noiseless simulated FDR results shown here for the triad cable scenarios should be interpreted accordingly, and is not associated with a specific dynamic range that will limit detection in a cable measurement.

The simulation results for both cable types are shown in Fig. 9. As expected, the peak amplitude increased with increased insulation dielectric constant over the 1 ft. segment. Fabrication tolerances are better controlled for coaxial cables than for multi-conductor cables having helical twists, which may impact the ability of the FDR method to detect the reflection peaks shown for the triad cable. The peak levels due to equivalent percentage changes are also lower for the triad cable. This is because the electric field between the two test wires in this cable type is not completely contained within its insulation, as is the case for coaxial cable.

Defect Length

To evaluate the influence of defect length on the FDR response, the shielded triad cable model was adjusted to include a range of defect lengths in the center of a 100 ft. cable. The defect sections were represented by a uniform 5% change in insulation dielectric constant. Relatively short defects ranged from 0.25 to 2 ft. and longer defects ranged from 3 to 10 ft. The similarly grouped FDR responses were divided into relatively short damage lengths of <1 wavelength and relatively long damage lengths of ≥ 1 wavelength at the highest frequency. At 200 MHz, the electrical wavelength for the triad cable is approximately 3 ft.

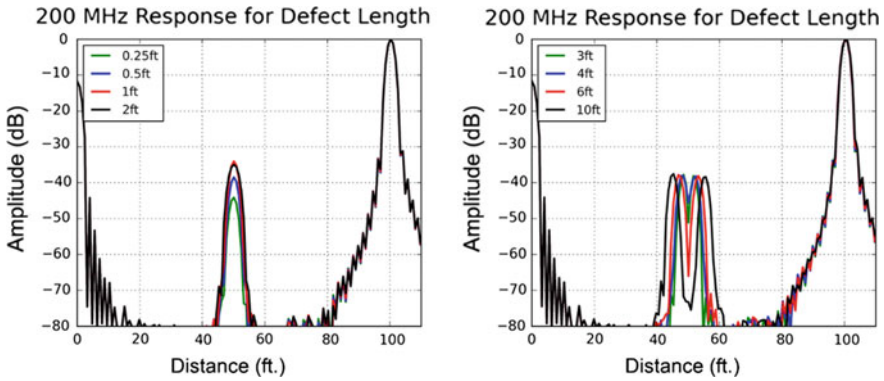

Fig. 10 ANSYS simulation results for 5% increase in insulation dielectric constant for (left) relatively short defect lengths (<1 wavelength at maximum frequency) and (right) relatively long defect lengths in shielded triad cable

The simulation results for these two groups are shown in Fig. 10. For the relatively short defects, the reflection peak decreased in amplitude as the length decreased from the maximum peak observed for defects approximately 0.5 wavelengths long. This length is equivalent to the spatial resolution of the FDR spectrum. In the 200 MHz simulations, the peak amplitudes dropped by 5–10 dB from the maximum peak values associated with the 1 to 2 ft. damaged segments. This trend was consistent in the 100 and 200 MHz ANSYS simulations as well as the 100 MHz LIRA simulation for the triad cables.

For the longer defects, two distinct peaks were observed in the FDR response at the beginning and end of the defect segment. This is due to the defect length being greater than the spatial resolution of approximately 1.5 ft. The amplitudes of these peaks were approximately 3 dB lower than the maximum single peak, because the energy was separated into two reflections. The significance of these observations is that the length of an assumed uniform cable degradation should be considered during a peak amplitude calibration of FDR tests for assessing the degree of cable damage. Particularly short defects will produce lower amplitude responses than defects that are on the order of a half-wavelength at the highest frequency of the FDR.

Defect Distribution

The previous section noted the influence of defect length on the FDR response. It was observed that longer defects with abrupt changes in insulation dielectric constant (which is equivalent to capacitance) produced significant responses at the beginning and end of the damaged area. These responses are due to the impedance discontinuities represented by these junctions. In order to investigate defect scenarios in which the change in cable electrical characteristics is of a more gradual

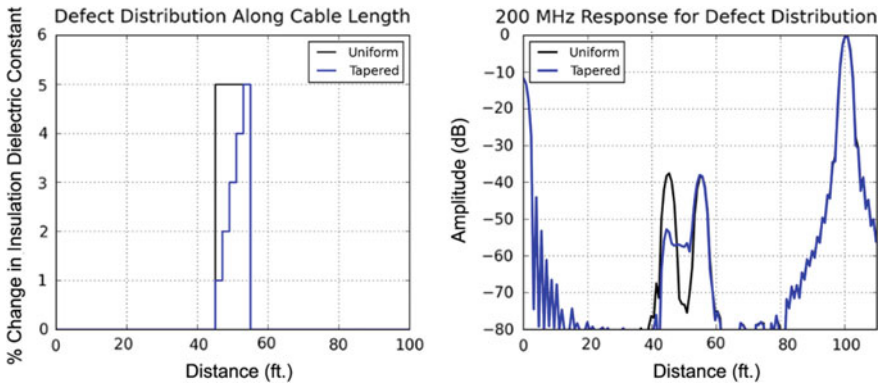

Fig. 11 (left) A uniform 5% capacitance change from 45 to 55 ft. (black) versus a tapered change (blue); (right) corresponding ANSYS simulation results (Color figure online)

nature, tapered increases in the insulation dielectric constant along a defect were compared to the uniform step changes.

Simulation results for an example linearly tapered (ramped) profile along a 10 ft. section of a 100 ft. cable are shown in Fig. 11. The maximum change in the insulation dielectric constant is 5% in both cases. The amplitude response at the beginning of the ramped segment is approximately 15 dB below the uniformly damaged segment. This is because the gradual change in impedance along the cable smoothly transitions the electromagnetic wave between the undamaged and damaged segments. However, the amplitude response at the end of the ramped segment is equal to the uniformly damaged segment. This is due to the impedance change that occurs at this junction as the wave abruptly transitions back to the undamaged section. The two distinct peaks present in the FDR response for the uniform defect are separated by approximately 3 wavelengths along the cable.

Quantifying the effect of reflection peak variations under typical field conditions where a damage profile may be impossible to predict would be difficult. However, it can be understood that a ramped damage profile may exhibit an FDR response level different than a uniform damage profile.

Conclusions

Additional cable configurations have been modeled and verified by test. These cases are more fully documented in [14]. Significant conclusions from this cable FDR simulation study include:

- Defect length had an important influence on the FDR amplitude response. The maximum amplitude occurred for defect lengths on the order of 0.5 wavelengths at the highest frequency, which corresponded to the spatial resolution for the sweeps.

This is an explanation for the relatively small FDR amplitude responses for mechanical cable damage, because most mechanically damaged segments only extend for a short length.

- For longer damage segments consisting of a uniform change in a parameter such as dielectric constant (and thus local capacitance), the FDR response separated into two distinct peaks centered on the ends of the damaged segments. This began to occur when the defect section length was greater than the system resolution. The amplitude of the two peaks was smaller than the amplitude of a similarly damaged segment, which was approximately 0.5–1 wavelengths at the maximum frequency of the FDR spectrum.
- When the damage profile was tapered rather than occurring as a step-condition change, the peak FDR amplitude was reduced. This was due to the gradual impedance change that reduces the reflection from the tapered portion of the defect segment. If the length of the defect segment was below the spatial resolution, the effect of a tapered damage profile was to simply reduce the amplitude of the single reflection.

Future Work

Work continues for parametric variation of the model to assess various cable conditions that may be encountered within a plant plus select laboratory empirical tests to confirm the model predictions. Parametric case variations include:

- Mechanical damage
- Thermal aging damage effectively increasing the insulation dielectric constant
- Cable end termination conditions (open, shorted, impedance-loaded)
- Multiple defects within a cable segment compared to a single defect
- Location of a defect (near or well removed from the test instrument)
- Effect of adding cable with identical and slightly dissimilar impedance to the beginning and/or end of a test segment, thereby attempting to minimize the effect of the cable-end shadow and increasing flaw sensitivity near cable ends.

This basic modeling approach may also be extended to other frequency-based cable test technologies that are gaining credibility in the cable test industry such as dielectric spectroscopy and joint time frequency domain reflectometry.

References

1. S.A. Glass et al., *Bulk Electrical Cable non Destructive Examination Methods for Nuclear Power Plant Cable Aging Management Programs* (Report PNNL-25634, Richland, Washington, Pacific Northwest National Laboratory, 2016)

2. C. Furse et al., Frequency-domain reflectometry for on-board testing of aging aircraft wiring. IEEE Trans. Electromagn. Compat. **45**(2), 306–315 (2003). doi:10.1109/TEMC.2003.811305
3. Mohr and Associates, in *Application Note: TDR vs. FDR: Distance-to-Fault* (Mohr and Associates, Richland, Washington, 2010). Available at http://www.mohr-engineering.com/TDR_vs_FDR_Distance_to_Fault-A.php
4. J. Minet et al., A generalized frequency domain reflectometry modeling technique for soil electrical properties determination. Vadose Zone J. **9**(4), 1063–1072 (2010). doi:10.2136/vzj2010.0004
5. K.L. Murty (ed.), in *Materials Ageing and Degradation in Light Water Reactors: Mechanisms and Management* (Cambridge, United Kingdom, Woodhead Publishing, 2013)
6. ANSYS, in *Application Brief: Power Cable Analysis* (Canonsburg, Pennsylvania, ANSYS, Inc., 2014). Available at http://resource.ansys.com/staticassets/ANSYS/staticassets/resourcelibrary/techbrief/ab-power-cable-analysis.pdf. Accessed 29 March 2017
7. A. Strikwerda, in *Model Cables and Transmission Lines in COMSOL Multiphysics* (Burlington, Massachusetts, COMSOL, Inc., 2016). Available at https://www.comsol.com/blogs/model-cables-and-transmission-lines-in-comsol-multiphysics/. Accessed 29 March 2017
8. M.K. Johnson, *Calculation of Transmission Line Impedances Using the ANSYS Finite Element Program* (Report TM-1270, Batavia, Illinois, Fermilab, 1984). Available at http://lss.fnal.gov/archive/tm/TM-1270.pdf
9. Q. Chen et al., Capacitance of water tree modeling in underground cables. J Power Eng **2**(11), 9–18 (2014). doi:10.4236/jpee.2014.211002
10. M. Alsharif et al., FEM Modeling of Electric Field and Potential Distributions of MV XLPE Cables Containing Void Defect (Paper presented at the 2012 COMSOL Conference, Milan, Italy, 10–12 October 2012). Available at https://www.comsol.com/paper/fem-modeling-of-electric-field-and-potential-distributions-of-mv-xlpe-cables-con-13431
11. J. Brown et al., *Submerged Medium Voltage Cable Systems at Nuclear Power Plants: A Review of Research Efforts Relevant to Aging Mechanisms and Condition Monitoring* (Report SAND2015—1794, Albuquerque, New Mexico, Sandia National Laboratories, 2015). doi:10.2172/1177756
12. P.F. Fantoni, A. Nordlund, *Wire System Aging Assessment and Condition Monitoring* (*WASCO*) (Report NKS-130, Roskilde, Denmark, Nordic Nuclear Safety Research 2006)
13. General Cable, in *Industrial Cable, SPEC 4325* (General Cable, 2016). Available at http://viewer.epaperflip.com/Viewer.aspx?docid=848fb272-4ff4-45b2-b702-a69e0113edcc#?page=38. Accessed 29 March 2017
14. S.A. Glass et al., *Physics-Based Modeling of Cable Insulation Conditions for Frequency Domain Reflectometry* (*FDR*) (Report PNNL-26493, Richland, Washington, Pacific Northwest National Laboratory, 2017)

Aging Mechanisms and Nondestructive Aging Indicator of Filled Cross-Linked Polyethylene (XLPE) Exposed to Simultaneous Thermal and Gamma Radiation

Shuaishuai Liu, Leonard S. Fifield and Nicola Bowler

Abstract Aging mechanisms and a nondestructive aging indicator of filled cross-linked polyethylene (XLPE) cable insulation material used in nuclear power plants (NPPs) are studied. Using various material characterization techniques, likely candidates and functions for the main additives in a commercial filled-XLPE insulation material have been identified. These include a mixture of brominated components such as decabromodiphenyl ether and Sb_2O_3 as flame retardants, ZnS as white pigment and polymerized 1,2-dihydro-2,2,4-trimethylquinoline as antioxidant. Gas chromatography-mass spectrometry, differential scanning calorimetry, oxidation induction time and measurements of dielectric loss tangent are utilized to monitor property changes as a function of thermal and radiation exposure of the cable material. The level of antioxidant decreases with aging by volatilization and chemical reaction with free radicals. Thermal aging at 90 °C for 25 days or less causes no observable change to the cross-linked polymer structure. Gamma radiation causes damage to crystalline polymer regions and introduces defects. Dielectric loss tangent is shown to be an effective and reliable nondestructive indicator of the aging severity of the filled-XLPE insulation material.

Keywords Filled cross-linked polyethylene · Aging mechanisms · Gas chromatography-mass spectrometry · Differential scanning calorimetry · Oxidation induction time · Dielectric loss tangent

S. Liu (✉) · N. Bowler
Iowa State University, Ames, IA 50010, USA
e-mail: sliu1@iastate.edu

L.S. Fifield
Pacific Northwest National Laboratory, WA 99352 Richland, USA

J.H. Jackson et al. (eds.), *Proceedings of the 18th International Conference on Environmental Degradation of Materials in Nuclear Power Systems – Water Reactors*, The Minerals, Metals & Materials Series, https://doi.org/10.1007/978-3-319-68454-3_6

Introduction

Cross-linked polyethylene (XLPE)-based polymer composites are the most widely used cable insulation material in United States nuclear power plants (NPPs) [1]. The XLPE matrix in these materials contains various fillers and additives. Cables used in NPPs can be exposed to radiation at elevated temperatures. The integrity of the cable insulation is critical for the reliable operation of the cables and consequently for the safe operation of the NPPs. The study of the degradation of cable insulation materials under radiation and at elevated temperatures is important for gaining a fundamental scientific understanding of the aging mechanisms and for developing effective safety inspection methods. A review of prior work in this area was recently published by Bowler and Liu [2]. In this work, candidate components of the studied filled-XLPE insulation are identified, aging mechanisms are studied and a nondestructive indicator of the aging severity is identified.

Sample Preparation

White XLPE insulation material was obtained from a commercially available nuclear-grade instrumentation cable consisting of two 16AWG conductors, a laminated aluminum/polyester shield, drain wire, and a chlorosulphonated polyethylene jacket. The cable was purchased from RSCC (product code I46-0021). The cable jacket was removed to expose the XLPE-insulated wires. The average inner and out diameter of the XLPE insulation layer were measured under an optical microscope to be 1.46 and 2.76 mm, respectively, resulting in an average wall thickness of 0.65 mm. For accelerated aging, samples were hung by clips on a rack placed in an oven located in the exposure zone of a Co-60 source in the High Exposure Facility (HEF) at Pacific Northwest National Laboratory (PNNL). Simultaneous thermal and gamma radiation aging of the samples was achieved through placement of the oven in the radiation environment and control of the oven temperature. The dose rate to each individual sample was selected by controlling sample distance from the radiation source. Various radiation doses to the samples were achieved by aging them for different periods of time. Details of the accelerated aging process and sample preparation can be found in our previous paper [3].

Materials Characterization

A variety of materials characterization tests were conducted on pristine, 90 °C thermally-only aged and simultaneously thermal (90 °C) and gamma radiation (540 Gy/h) aged XLPE insulation materials in order to (1) identify the composition of

the filled-XLPE sample material; (2) study material aging mechanisms under these exposures; and (3) find a reliable and prominent nondestructive aging severity indicator.

Scanning Electron Microscopy (SEM)

SEM was conducted on the fracture surface of pristine XLPE material. The fracture surface was prepared by breaking the sample immediately upon removal from liquid nitrogen following 5 min immersion. The surface was coated with 5 nm of iridium prior to examination to avoid sample charging. The fracture surface was imaged using an FEI Quanta-FEG-250 SEM operated at 10 kV.

Pyrolysis Gas Chromatography—Mass Spectrometry (Pyrolysis GCMS)

An evolved gas analysis (EGA) using pyrolysis GCMS was conducted. The GCT is an accurate mass time-of-flight (TOF) mass spectrometer coupled to an Agilent 6890 gas chromatograph (GC). The Electron ionization (EI) source is used in this study. The Frontier 3030D pyrolyzer is mounted on the Back Inlet of the GC. A sample of 0.2 mg was heated in the pyrolyzer at 220 °C for 2 min and then heated to 700 °C at 20 °C/min. The GC was held isothermally at 320 °C during the run.

Oxidation Induction Time (OIT)

OIT was measured using a TA Instruments Q800 differential scanning calorimeter. Ten mg of sample material was heated at a rate of 15 °C/min from ambient temperature to 230 °C in helium flowing at 50 mL/min. When the temperature of 230 °C was reached, the specimen was held in helium isothermally for 2 min, after which the atmosphere was changed to oxygen maintained at the same flow rate. The specimen was then held at 230 °C until the oxidative reaction was revealed on the thermal curve. The threshold defining the oxidative reaction is heat flow of 0.1 W/g above the baseline.

Differential Scanning Calorimetry (DSC)

A DSC Q800 from TA Instruments was also used to perform standard calorimetry. In helium atmosphere, a temperature program of heating (cycle 1), cooling (cycle 2)

and re-heating (cycle 3) was performed using a sample mass of 5 mg. In cycle 1, the temperature was ramped from 20 to 160 °C at 10 °C/min, after which the temperature was held isothermally at 160 °C for 2 min. In cycle 2, the temperature was ramped from 160 °C back to 20 °C at 10 °C/min, after which the temperature was held isothermally at 20 °C for 2 min. In cycle 3, the temperature was ramped again from 20 °C up to 160 °C at 10 °C/min.

Dielectric Loss Tangent

Dielectric loss tangent is a dielectric property of an insulating material and is frequency-dependent. An Agilent 4980A LCR meter and 16451B dielectric test fixture were used to measure the dielectric loss tangent of the XLPE insulation materials. An electrode of 10 mm in diameter was used and the dielectric properties were measured over a frequency range of 10^5 to 10^6 Hz. For complex permittivity, at a particular frequency,

$$\varepsilon(\omega) = \varepsilon'(\omega) + i\varepsilon''(\omega) \tag{1}$$

the dielectric loss $\varepsilon''(\omega)$ is the imaginary part of the permittivity, and the loss tangent is defined as

$$\tan\delta = \frac{\varepsilon''}{\varepsilon'} \tag{2}$$

Loss tangent of the pristine and aged XLPE insulation materials were measured in this study.

Results

Composition Analysis

An SEM image of the cross-section of the studied XLPE cable insulation material is shown in Fig. 1. It can be seen that the XLPE cable insulation is a composite material containing filler particles of various sizes. Further characterization of the material using energy dispersive X-ray spectroscopy (EDX, not shown), pyrolysis GC-MS, Fourier transform infrared spectroscopy (FTIR, not shown), carbon-hydrogen elemental weight ratio testing (C–H testing, not shown) and thermogravimetric analysis (TGA, not shown) indicate that the primary fillers consist of a mixture of brominated flame retardants such as decabromodiphenyl ether (DBDE), Sb_2O_3, ZnS and polymerized 1,2-dihydro-2,2,4-trimethylquinoline (pTMQ). The calculated weight percentages of these components are listed in Table 1. For brevity, detailed data

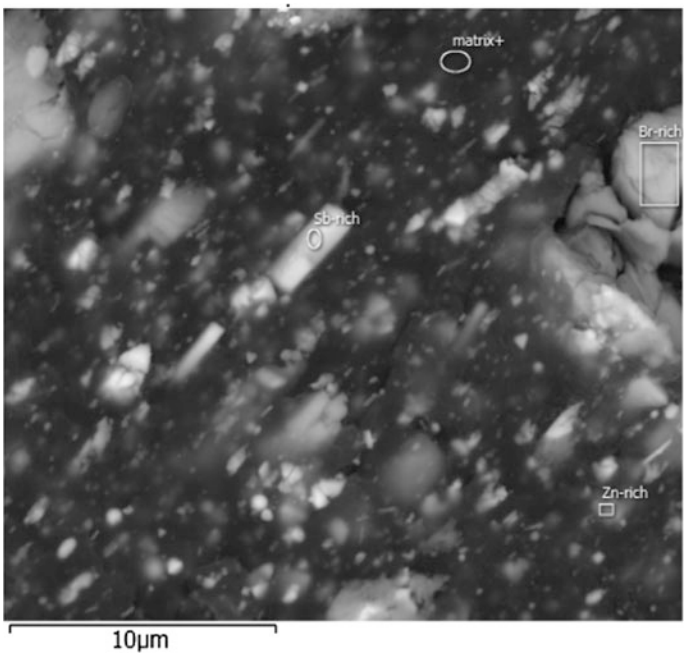

Fig. 1 SEM image (5000×) of the cross-section of pristine XLPE insulation material

Table 1 Composition of the commercial, filled, cross-linked polyethylene

Identified component (probable function)	Weight percentage (%)
XLPE (polymer base)	56–60
Brominated components (e.g. DBDE, flame retardant)	~15
Sb_2O_3 + ZnS (flame retardant and colorant)	<20
pTMQ (antioxidant)	<3
Others	2–6

supporting the identification and weight percentage calculation of these components are not provided here, but will be published separately. DBDE and Sb_2O_3 are likely included to function as flame retardants [4], ZnS as white pigment [4] and polymerized 1,2-dihydro-2,2,4-trimethylquinoline as antioxidant [5].

Characterization Results

EGA data taken on pristine and aged XLPE materials (aging condition: 540 Gy/h for 25 days at 90 °C) are shown in Fig. 2. Antioxidant fragments start to come out of the samples near the program starting temperature of 220 °C, fragments of

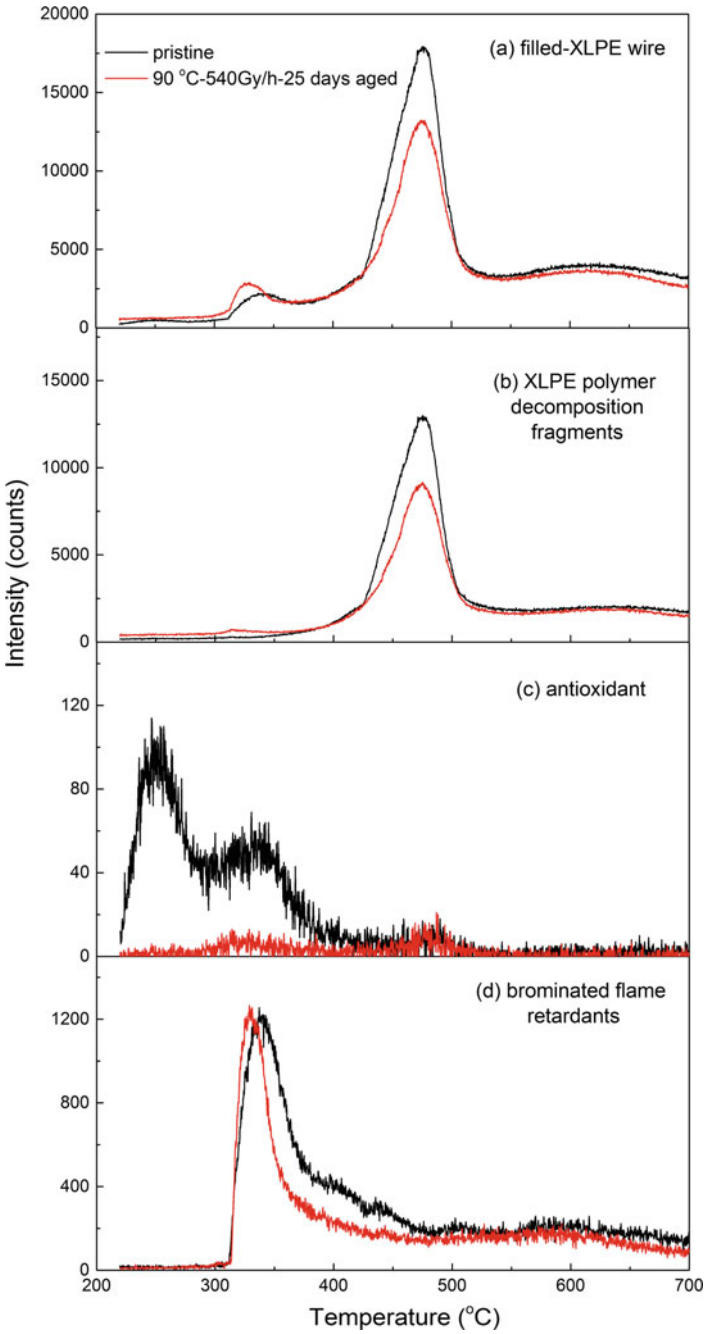

Fig. 2 EGA data for **a** pristine and aged XLPE wire; **b** the fragments of the decomposition of the XLPE polymer chains; **c** the fragments of the decompositions of the antioxidant; and **d** the fragments of the decomposition of flame retardant decabromodiphenyl ether (DBDE). Note that the antioxidant curve shown in **c** is obtained by summing the mass intensity given by the different fragments of pTMQ; similarly the flame retardant curve shown in **d** is obtained by summing the mass intensity given by DBDE and its fragments

brominated flame retardant DBDE start to come out at about 300 °C, and XLPE polymer decomposition fragments start to come out at about 300 °C. Figure 2a shows a significant decrease in the intensity of the aged material compared with that of the pristine material, which is mainly caused by the intensity decline in the decomposition fragments of the XLPE polymer matrix, as shown in Fig. 2b. Figure 2c shows a significant decrease of the antioxidant in the aged material in comparison with the pristine XLPE.

OIT results for pristine, 90 °C thermally-only aged, and simultaneously 90 °C thermal and 450 Gy/h gamma radiation aged filled-XLPE materials are shown in Fig. 3. OIT of pristine material is 45.2 min. When the material is aged thermally at 90 °C for 20 days, the OIT decreases to 40.1 min, dropping by approximately 11%. When the material is simultaneously aged thermally at 90 °C and by gamma radiation at 450 Gy/h for 20 days, the OIT decreases to 11.8 min, dropping by approximately 74%.

DSC cooling and re-heating curves of pristine, thermally only aged (aging conditions: 90 °C for 10 and 25 days), and simultaneously thermal and gamma radiation aged materials (aging conditions: 540 Gy/h at 90 °C for 10 and 25 days) are displayed in Fig. 4 and 5. It is shown in the cooling curve of pristine material that three exothermic signals are observed, with their maxima at 93.4, 102.6 and 115.9 °C. Figure 4a shows the cooling curves of pristine and thermally only aged materials, no significant difference is observed. Similar observations are made for their re-heating curves as in Fig. 4b. Figure 5a shows the cooling curves of pristine and simultaneously thermal and gamma radiation aged materials, it is observed that the peaks initially at 102.6 and 115.9 °C shift to lower temperatures, and the magnitude of the peak at 93.4 °C declines. Similar observations are made for re-heating curves as in Fig. 5b, in which the peaks shift to lower temperatures and the curve between the temperature range of about 100–120 °C gets flatter compared with pristine XLPE.

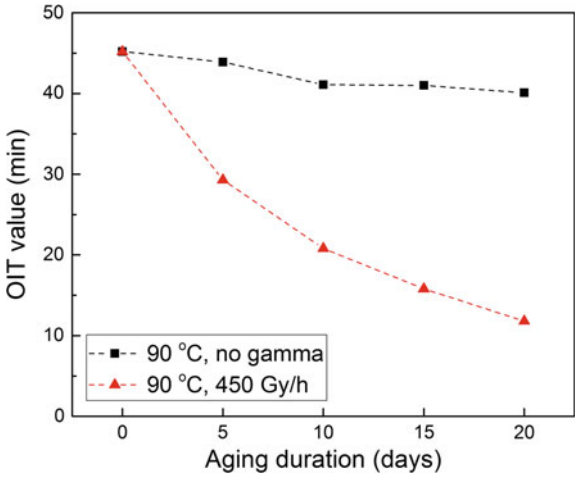

Fig. 3 OIT of filled-XLPE aged at 90 °C for various durations (5, 10, 15 and 20 days), at the dose rates of 0 and 450 Gy/h. The uncertainty is less than 2 min

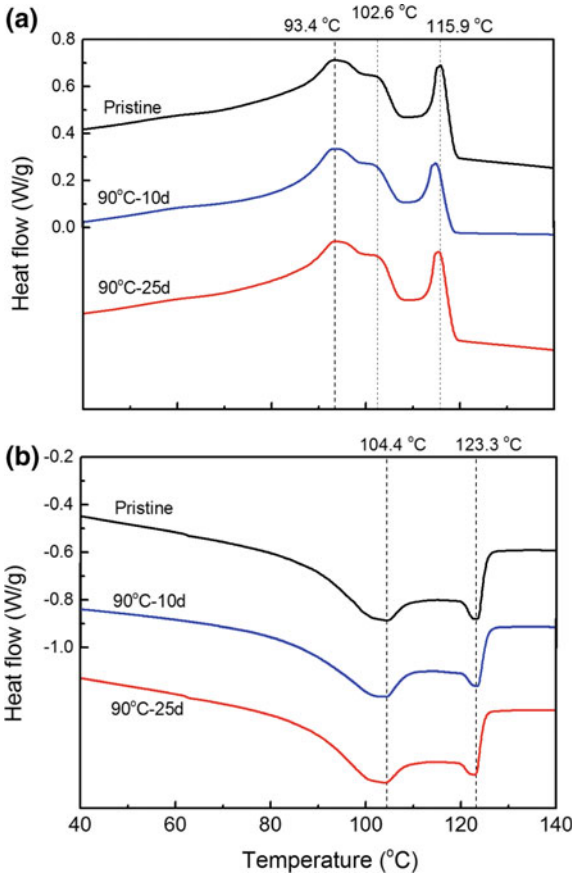

Fig. 4 Cooling (**a**) and re-heating (**b**) DSC curves of XLPE insulation materials that were thermally-only aged at 90 °C for durations of 10 and 25 days

The loss tangent of pristine and differently aged XLPE cable material over the frequency range of 10^5–10^6 Hz is exhibited in Fig. 6. At the frequency of 10^6 Hz, the loss tangent is 4.4×10^{-4} for pristine material, increasing to 7.4×10^{-4} (an increase of 68.2%) when the material is exposed to aging for 10 days, and to 1.2×10^{-3} (an increase of 172.7%) at exposure for 25 days. When no gamma radiation is present in the aging process at 90 °C for 25 days, the loss tangent is observed to decrease from 4.4×10^{-4} to 3.88×10^{-4} (a decline of 11.8%).

Interpretation

GC-MS and OIT results indicate that the aging process consumes antioxidants in the material. As has been discussed in section 1.4.1, the XLPE material appears to include pTMQ as an antioxidant. The melting temperature of pTMQ ranges from

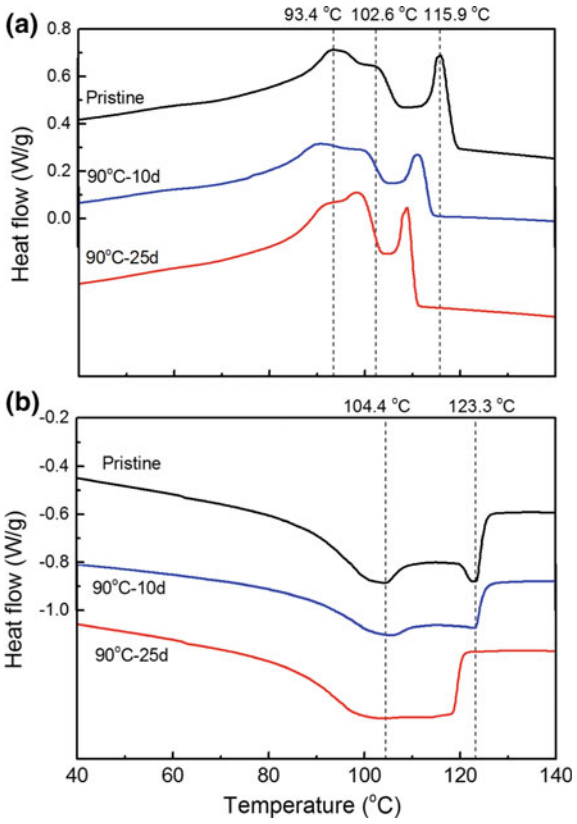

Fig. 5 Cooling (**a**) and re-heating (**b**) DSC curves of XLPE insulation materials aged at 90 °C for durations of 10 and 25 days at the dose rate of 540 Gy/h

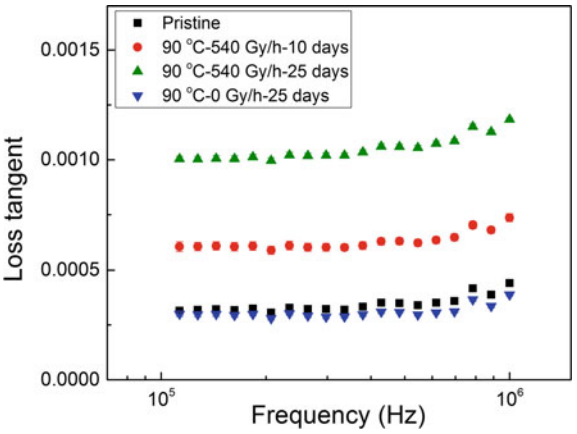

Fig. 6 Loss tangent of four sets of differently aged XLPE materials. (Note that the uncertainty is calculated by standard deviation of 5 measurements for each sample, the error bars are in the plot but too small to be seen.)

72 to 94 °C [6]. When the XLPE material studied here is thermally-only aged at 90 °C, loss of pTMQ antioxidant takes place. When the material is simultaneously aged by gamma radiation at 90 °C, thermal decomposition, evaporation or sublime take place, on the one hand, and, on the other, the gamma radiation breaks the polymer bonds and generates free radicals, which consume the antioxidants by chemical reaction. This explains why the OIT value decreases about seven times quicker when gamma radiation is present in the aging process. Compared with the DSC curves of pristine material, no significant change is observed for those of 90 °C thermally-only aged materials, indicating that when the material is thermally-only aged at 90 °C for 25 days or less, no significant changes take place in the polymer structures. When gamma radiation is involved in the aging process, however, the recrystallization peaks in the cooling curves and melting peaks in the re-heating curves shift to lower temperatures, indicating that the crystals formed during the cooling process are weaker. It is very likely that gamma radiation breaks the crystals to some extent and introduces defects, free radicals and chain branching in the crystals, making the crystals smaller and/or less perfect and hence melt at lower temperatures. When the material is thermally-only aged at 90 °C, a decrease in loss tangent is observed. When the material is simultaneously aged by thermal and gamma radiation, there is an increase in its loss tangent. Free radicals contribute to the conductivity of the material. When the material is at elevated temperature, there is a competing process between the generation and consumption of the free radicals. When no gamma radiation is involved in the aging process, the process of free radicals consumption by reacting with the antioxidant dominates over the free radicals generation process. When gamma radiation is involved in the aging process, the process of free radicals generation dominates leading to a larger number of defects and may account for the elevation in observed dielectric loss as the material ages. Dielectric loss is therefore promising as a reliable nondestructive indicator of the aging severity for the commercial XLPE cable insulation materials studied here.

Conclusions

The studied commercial XLPE cable insulation material is a composite with XLPE as polymer matrix and various fillers including antioxidant [polymerized 1,2-dihydro-2,2,4-trimethylquinoline (pTMQ)], flame retardants [decabromodiphenyl ether (DBDE) and Sb_2O_3], and white pigment (ZnS). The level of antioxidants decreases with aging by volatilization and chemical reaction with free radicals. When thermally aged at 90 °C for 25 days or less, no significant changes are caused in the polymer structure. When gamma radiation is present in the aging process, gamma radiation causes damage to the crystals and introduces defects, free radicals and chain-branching in the crystals, which causes the crystals to melt at lower temperatures. Consumption of free radicals dominates over their generation when the material is thermally aged, while the generation of free radicals dominates over their consumption when the material is exposed to gamma radiation. Dielectric

loss tangent is proved to be sensitive to the aging severity for the studied commercial XLPE cable insulation material and may hold promise as a nondestructive indicator of such. A paper including more characterization results of a larger sample set aged at a broader range of aging conditions is in preparation, which will give a clearer picture of the aging mechanisms taking place in irradiated XLPE, and further examine dielectric loss as a suitable nondestructive indicator of XLPE aging due to gamma radiation exposure.

Acknowledgements This research is being performed using funding received from the DOE Office of Nuclear Energy's Nuclear Energy University Programs under contract number DENE0008269 and the DOE Office of Nuclear Energy's Light Water Reactor Sustainability Program. Exposure experiments were conducted at Pacific Northwest National Laboratory which is operated by Battelle for the US DOE under contract DE-AC05-76RL01830.

References

1. Electric Power Research Institute (EPRI), Low-Voltage Environmentally-Qualified Cable License Renewal Industry Report; Revision 1. TR-103841 (1994)
2. N. Bowler and S. Liu, Aging Mechanisms and Monitoring of Cable Polymers. Int. J. Prognostics Health Manage., ISSN 2153-2648, pp. 1–12, 2015
3. L.S. Fifield, S. Liu, N. Bowler, Simultaneous Thermal and Gamma Radiation Aging of Cable Polymers. IEEE Conference on Electrical Insulation and Dielectric Phenomena, Toronto, Canada, October 16–19, 2016
4. M. Sheridan, *The Vanderbilt Rubber Handbook* (R.T. Vanderbilt Company Inc, Norwalk, CT, 2010), p. 431
5. M. Ash, Handbook of Green Chemicals, p. 22, Synapse Info Resources, 2004
6. Chemical Book. http://www.chemicalbook.com/ChemicalProductProperty_EN_CB3222852.htm

Successful Detection of Insulation Degradation in Cables by Frequency Domain Reflectometry

Yoshimichi Ohki and Naoshi Hirai

Abstract We have succeeded in detecting the degradation of cable's polymeric insulation well before its continual use becomes risky. Degradation of organic polymers is mainly caused by oxidation if the ambience around the cable contains oxygen. When organic polymers are oxidized, polar carbonyl groups are formed, by which the permittivity is increased. This in turn decreases the characteristic impedance of a polymer-insulated cable. If we inject electromagnetic waves in a very wide frequency range into the cable and measure the ratio of reflected power to injected power, the information on the effects of the characteristic impedance changes is included in the frequency spectra of the ratio. If we do inverse Fourier transform, we can convert the data to a time domain. Therefore, we can know the degraded portion by multiplying the velocity of electromagnetic waves in the cable.

Keywords Insulation diagnosis · Condition monitoring · Aging · Polymeric insulation · Characteristic impedance · Fault location · Cable

Introduction

Since the occurrence of the terrible Fukushima accident, the safety of nuclear power plants (NPPs) has been a matter of even serious public concern. Electric cables play various key roles in safe operation of NPPs at their normal stages and until their

Y. Ohki (✉)
Department of Electrical Engineering and Bioscience,
Waseda University, Ohkubo, Shinjuku-Ku, Tokyo, Japan
e-mail: yohki@waseda.jp

Y. Ohki · N. Hirai
Research Institute for Materials Science and Technology,
Waseda University, Ohkubo, Shinjuku-Ku, Tokyo, Japan

Y. Ohki
Joint Major in Nuclear Energy, Waseda University,
Ohkubo, Shinjuku-Ku, Tokyo, Japan

J.H. Jackson et al. (eds.), *Proceedings of the 18th International Conference on Environmental Degradation of Materials in Nuclear Power Systems – Water Reactors*, The Minerals, Metals & Materials Series, https://doi.org/10.1007/978-3-319-68454-3_7

safe termination after the occurrence of unexpected abnormalities. In this respect, periodical inspection or condition monitoring of the integrity of cables is truly important. The integrity of cables is in most cases endangered by the degradation of their polymeric insulation. In this presentation, the authors show that they have succeeded in detecting the degradation of cable's polymeric insulation at an early stage, well before continual use of the cable in a NPP becomes risky.

Principle of the Method

The fault location and degradation detection method that the authors have been developing is based on a kind of frequency domain reflectometry (FDR). For almost all the organic polymers being used for cable insulation, their degradation induced by radio-active rays or by a high temperature is mainly caused by oxidation as long as the ambience around the cable contains air or oxygen. When organic polymers are oxidized, carbonyl groups are formed. Since carbonyl groups are polar, the dielectric permittivity of the polymer increases. This in turn decreases the characteristic impedance of a cable insulated with the polymer. If we transmit electromagnetic wave or an electric pulse through the polymer-insulated cable, the wave would be reflected where the characteristic impedance changes. By detecting this reflection, we can know the portion where the cable insulation is degraded.

The method to measure the time to the occurrence of reflection directly is called time domain reflectometry (TDR). The authors found that TDR did not give a good result [1]. Therefore, in the present method, a kind of FDR is used. Its principle is briefly summarized in Fig. 1. First, the cable to be tested is connected to a terminal of a network analyzer or an impedance analyzer, an example of which is shown in Fig. 2. If the cable is coaxial, it can be connected directly to a type N connector of the analyzer. In the case of a multi-core cable, any two cores are connected via alligator clips to the connector. Then, electromagnetic waves in a very wide frequency range, e.g. from 100 kHz to 1 GHz are inputted to the cable, and their ratios of reflected power to inputted power, which is equivalent to the square of parameter

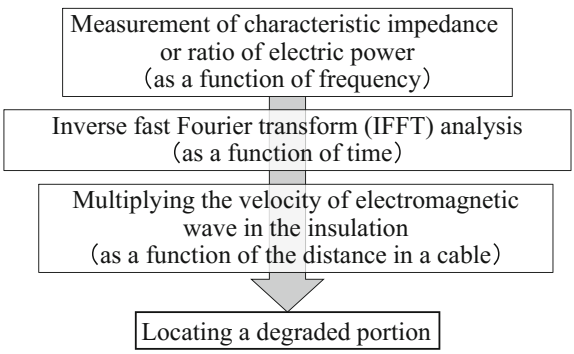

Fig. 1 Brief principle of the present measurement which is a kind of FDR and IFFT analysis

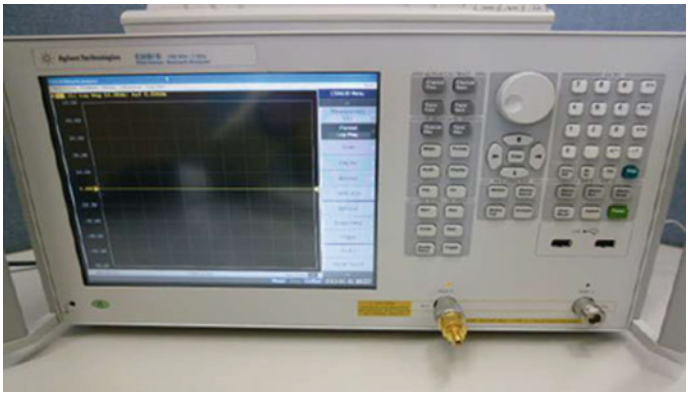

Fig. 2 Network analyzer used in the method

S_{11} in a two-port model, are measured. If we do inverse Fourier transform, we can convert the data to a time domain. Therefore, we can know the degraded portion or point of abnormality by multiplying the velocity of electromagnetic waves in the cable. If a cable insulation is oxidized for its entire length, the cable length appears as if it were lengthened, since the electromagnetic wave travels more slowly if the dielectric permittivity of cable insulation becomes higher. Therefore, we can also monitor, detect, or locate the degradation of cable insulation regardless of whether it is localized at a certain point or it stretches over the entire length of a cable.

Background and History of Development

In the 1970s, de facto standard test methods of polymer-insulated cables in NPPs were IEEE Standards 323 and 383 [2]. An investigation committee was set in April 1978 in the Institute of Electrical Engineers of Japan (IEEJ) to examine the applicability of these two IEEE standards to NPPs in Japan and to make proper amendments if necessary. The chairman of that committee was Prof. K. Yahagi of Waseda University. One of the authors of the present article (YO), who had obtained his doctorate under the supervision of Prof. Yahagi one month before the start of the committee, joined the committee as an assistant secretary. The committee published a Japanese standard [3], which is still being used as a commendable test method to evaluate the aging resistance of polymeric insulation of cables for NPPs.

With this relationship, Nuclear and Industrial Safety Agency of Japan asked him (YO) in 2005 to be a committee member to check the adequacy of life extension of NPPs. Through the activities in this committee, he gradually noticed that there was no truly reliable fault location method for cable insulation. Therefore, he started to develop the fault location method that is being discussed in this article in around 2009.

First, IFFT was not used in the fault location. The characteristic impedance spectrum as a function of frequency obtained by injecting electromagnetic waves with various frequencies was analyzed using a software for simulating responses of electromagnetic waves in electric circuits. By conducting simulation attempts for several equivalent circuit models with fault points, we can know the position of a fault that happened in a cable insulation. Figure 3 shows an example of such impedance spectra obtained in early days of the development [4]. In this case, the polymeric insulation of the cable was peeled off partly at a position around the middle point of the cable length. Although not shown here, similar spectra can be obtained for the phase of frequency response or the imaginary part of complex characteristic impedance. By analyzing these two spectra, we can judge whether the cable is degraded and can estimate a rough position of the degradation.

However, the above-mentioned process needs complex procedures and the resultant spatial resolution is not good. Therefore, the authors developed a new method. The introduction of IFFT was first reported in a Japanese domestic conference in September 2010 [5], in an international conference in September 2010 [6], and in a peer-reviewed journal in December 2013 [7]. Figure 4 shows a typical result reported in these media [5–7]. At that time, the frequencies of electromagnetic waves applied to the test were from 1 to 110 MHz.

Then, various improvements were done. Some examples are,

(1) search for the most adequate window function for IFFT [8],
(2) improvement of a connector to connect a test cable to an impedance (or network) analyzer,
(3) clarification of the effect of termination of the cable end whether it is open, short-circuited, or terminated with a resistor having the same impedance as the test cable [9], etc.

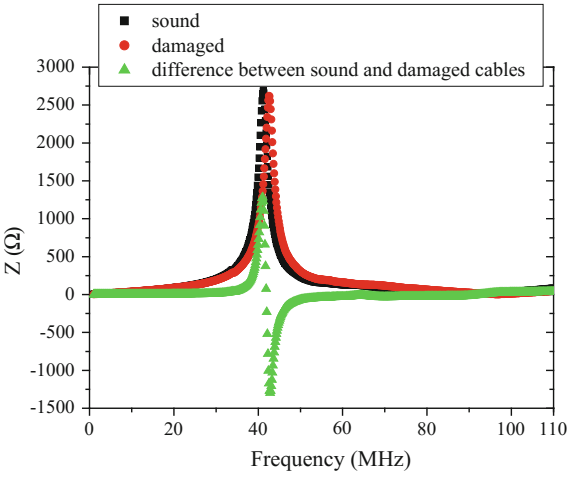

Fig. 3 Impedance spectra of sound and damaged cables measured by FDR method obtained in an early day of our attempts to develop a reliable location method of cable fault

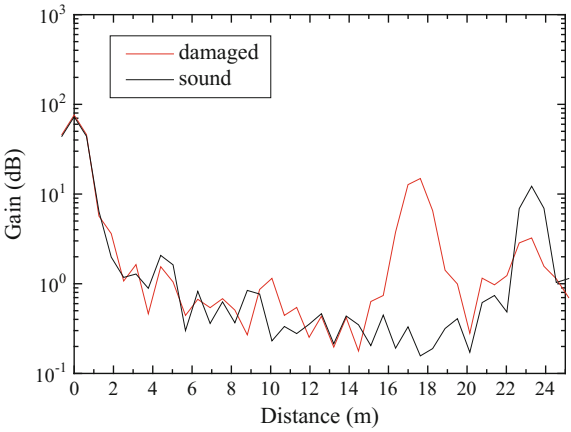

Fig. 4 Gain/position spectra obtained by a combination of FDR and IFFT in an early day of our attempts to develop a reliable location method of cable fault

Several Examples of Results Obtained in Recent Study

Figure 5 shows the ability of this method to locate an aged portion in a cable [10]. For this purpose, we aged a three-conductor power cable of 50 m long insulated with flame-retardant ethylene propylene rubber (FR-EPDM) at 120 °C in air with and without co-exposure to ^{60}Co γ-rays. As a result, we can clearly locate the aged portion as shown in Fig. 5, even when the degree of degradation is below the level that is assumed to be critical for its continuing use in NPPs [2]. That is, according to the criteria described in [2], cables insulated with FR-EPDM and manufactured by the same company as that of the cable for Fig. 5 can be used in NPPs until the absolute value of tensile elongation-at-break (EAB) of the FR-EPDM falls to 230%. Although not shown here, the EAB of the same FR-EPDM was confirmed to be about 400%, well above this criterion, after it had been gamma-irradiated to 312 kGy [10].

The authors have also succeeded as shown in Fig. 6 in detecting the position of a hole, which had been filled with a water solution of NaCl, in a coaxial cable insulated with cross-linked polyethylene [11]. The presence of the hole with the NaCl solution located at around 20 m from the cable end is clearly shown in the differential spectrum before and after the inclusion of the solution. The background of this location attempt is that the water treeing is classified as one of the several important phenomena of degradation of electrical insulation to be watched regularly in NPPs [12, 13]. Namely, this result indicates that a vented water tree can be detected by this method.

Furthermore, as for the ability to locate the portion in a cable where the temperature becomes high temporally, Fig. 7 indicates that we can locate very clearly a portion as short as 2.5 cm along a coaxial cable insulated with low-density polyethylene (LDPE) where the temperature is raised only by 5 °C for a short period.

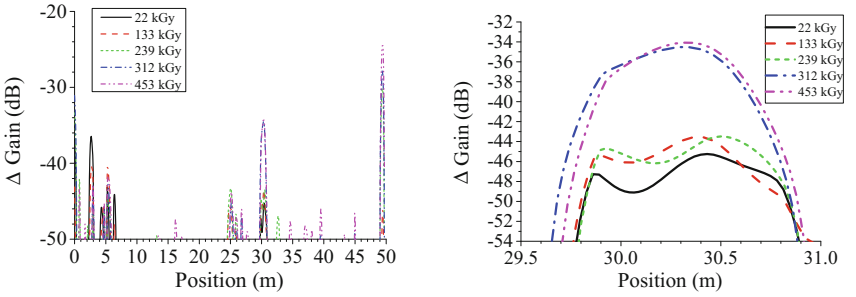

(a1) Differential spectra over the entire cable length (a2) Differential spectra around the γ-irradiated part

(a) 1 MHz - 300 MHz

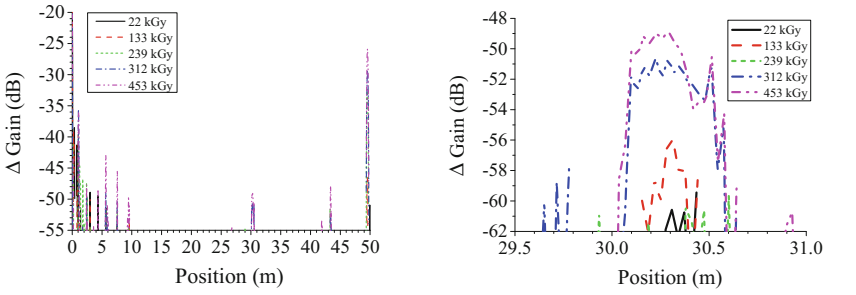

(b1) Differential spectra over the entire cable length (b2) Differential spectra around the γ-irradiated part

(b) 1 MHz - 1.5 GHz

Fig. 5 Differential spectra obtained for a 50-m triplex FR-EPDM cable as a function of the position in the cable and the total dose. The spectra were obtained by subtracting spectra obtained before the γ-irradiation from those obtained during the γ-irradiation. The cable had been irradiated by γ-rays at 120 °C at a position about 30 m from its end. Measurements were done during the γ-irradiation. The highest measurement frequencies are 300 MHz (**a**) and 1.5 GHz (**b**). (a1) and (b1) spectra over the entire cable length, (a2) and (b2) those around the γ-irradiated part

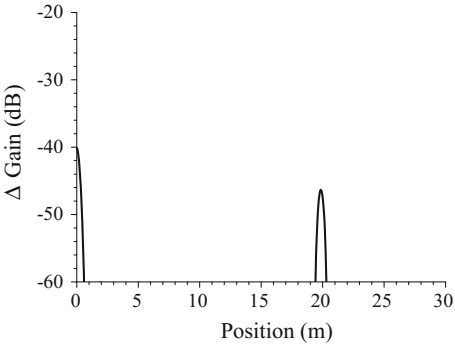

Fig. 6 Differential spectrum of a 29-m coaxial cable with a through hole, obtained before and after the hole had been filled with a NaCl solution at a position about 20 m from the terminal. The measurement was done in a frequency range from 1 to 400 MHz

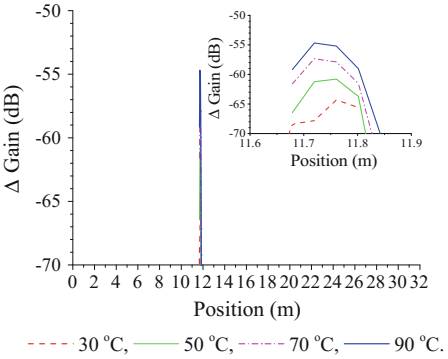

Fig. 7 Differential spectra obtained by subtracting the spectrum of an LDPE coaxial cable of 32 m long at 25 °C from the spectra obtained when a 2.5-cm portion at 11.7 m from the measuring terminal was heated to various temperatures. The measurements were done in a frequency range from 1 MHz to 1.5 GHz

As mentioned above, this method detects the point where the cable's characteristic impedance shows a change. The impedance change induced by the temperature increase of the insulation by 5 °C is less than 0.1% [7]. This indicates that the present method has a high sensitivity to a temperature change of polymeric insulation in a cable, even if it occurs temporally [7, 14].

Since our FDR-IFFT method utilizes reflection of electromagnetic waves at a position where the cable's characteristic impedance changes, it can also detect degradation or occurrence of some temporal extraordinary event even if it happens over the entire cable length, by observing the signal due to the reflection of electromagnetic waves at the cable end. To demonstrate this, the FDR-IFFT measurements were conducted while the entire cable temperature of a 30-m coaxial cable insulated with LDPE put in a heating chamber was raised to 60 and 90 °C. Figure 8 shows the result [15]. Here, the abscissae show the spectra as a function of time before we multiply the velocity of electromagnetic waves in the cable. The large signals appearing around 150 ps correspond to the position of the cable end. These signals are enlarged in Fig. 8b. When the entire cable temperature is raised, the signal appears early. That is, the cable length appears as if it were shortened at high temperatures. The fact is that the permittivity of the LDPE insulation was lowered and the velocity of electromagnetic waves travelling in the cable became fast. This means that we can recognize the degradation of this cable even when it stretches over the entire cable length.

This research was partly supported by the Nuclear Regulation Authority in Japan as a part of the Ageing Management Program for System Safety.

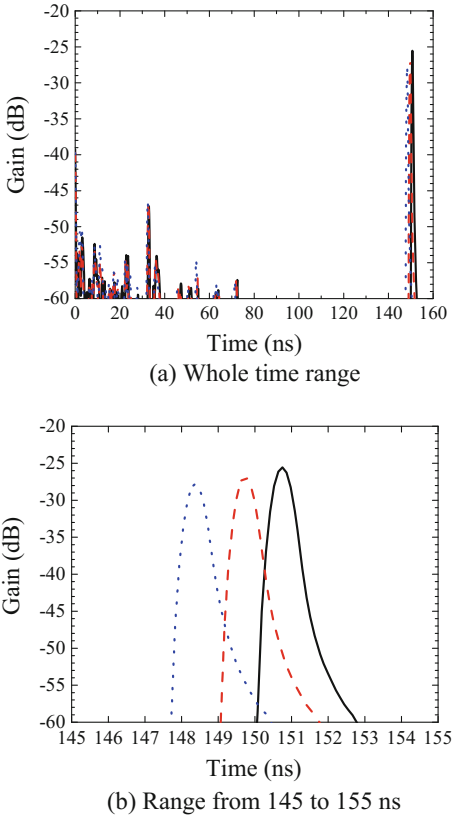

Fig. 8 Inverse Fourier-transformed spectra obtained while the temperature of a 30-m coaxial cable insulated with LDPE was raised to 60 and 90 °C. solid line: 20 °C, red dashed line: 60 °C, blue dotted line: 90 °C (Color figure online)

References

1. N. Hirai, T. Yamada, Y. Ohki, Comparison of broadband impedance spectroscopy and time domain reflectometry for locating cable degradation. Paper presented at the 2012 international conference on condition monitoring and diagnosis, Bali, 25 September 2012, B-3, pp. 229–232
2. T. Yamamoto, T. Minakawa, Final Report of the Project of 'Assessment of Cable Aging for Nuclear Power Plants' (Report JNES-SS-0903, 2009)
3. Institute of Electrical Engineers of Japan, Recommended Practice for Methods of Environmental Test and Flame Resistance Test for Electrical Wires and Cables for Nuclear Power Plants. Tech. Rep. (Division II) IEEJ 139, (1979) (In Japanese)
4. Y. Ohki, N. Hirai, T. Yamamoto, Need for condition monitoring and diagnosis of electric wires and cables used in nuclear power plants. Paper presented at the 2008 international conference on condition monitoring and diagnosis, Beijing, 23 April 2008, L2-08
5. Y. Ohki, N. Hirai, Localization of a damaged portion in electric cable by broadband impedance spectroscopy and FFT analysis. Paper presented at the 2010 annual conference of fundamentals and materials society, IEE Japan, Okinawa, 13 September 2010, 390 (In Japanese)

6. Y. Ohki, N. Hirai, Broadband impedance spectroscopy as a tool to evaluate the integrity of cable insulation. Paper presented at the 2010 international conference on condition monitoring and diagnosis, Tokyo, 8 September 2010, B3-5, pp. 313–316
7. Y. Ohki, T. Yamada, N. Hirai, Precise location of the excessive temperature points in polymer insulated cables. IEEE Trans. Dielectr. Electr. Insul. **20**(6), 2099–2106 (2013)
8. T. Yamada, N. Hirai, Y. Ohki, Sensitivity of broadband impedance spectroscopy as a location method of cable degradation. Paper presented at the joint technical meeting on dielectrics and electrical insulation and electric wire and power cable, IEE Japan, Tokyo, 22 February 2012, DEI-12-055/EWC-12-003 (In Japanese)
9. T. Yamada, N. Hirai, Y. Ohki, Effect of terminating impedance on the fault location in a cable by frequency domain reflectometry. Paper presented at the 2013 annual meeting, IEE Japan, Nagoya, 22 March 2013, 212 (In Japanese)
10. Y. Ohki, N. Hirai, Condition monitoring for predictive maintenance of cables insulated with FR-EPDM by frequency domain reflectometry. Paper presented at the 2014 international conference on condition monitoring and diagnosis, Jeju, 22 September 2014, OD1-1, pp. 57–60
11. T. Yamada, N. Hirai, Y. Ohki, Improvement in sensitivity of broadband impedance spectroscopy for locating degradation in cable insulation by ascending the measurement frequency. Paper presented at the 2012 international conference on condition monitoring and diagnosis, Bali, 24 September 2012, B-4, pp. 677–680
12. Atomic Energy Society of Japan, Code on implementation and review of nuclear power plant ageing management programs: 2008, (AESJ-SC-P005E, July 2012)
13. IAEA, Safety Reports Series No. 82, Ageing Management for Nuclear Power Plants: International Generic Ageing Lessons Learned, (IGALL, 2015)
14. Y. Ohki, N. Hirai, Effects of the structure and insulation material of a cable on the ability of a location method by FDR. IEEE Trans. Dielectr. Electr. Insul. **23**(1), 77–84 (2016)
15. N. Hirai, Y. Ohki, Abnormality detection over the whole cable length by frequency domain reflectometry. Paper presented at the 2017 annual meeting, IEE Japan, Toyama, 17 March 2017, 264 (In Japanese)

Capacitive Nondestructive Evaluation of Aged Cross-Linked Polyethylene (XLPE) Cable Insulation Material

Z.H. Shao and N. Bowler

Abstract Cross-linked polyethylene (XLPE) is used widely as insulation material in low-voltage instrumentation cables deployed in nuclear power plants (NPPs). Suffering from degradation due to exposure to heat and radiation, the insulating properties of the material gradually degrade, which may imperil the safe operation of NPPs. In this paper, a new capacitive sensing method is introduced for nondestructive evaluation of aged instrumentation cable with XLPE insulation. The capacitive sensor is capable of measuring capacitance of cable materials and may potentially be employed to extract the dielectric properties of insulation material from those of the entire cable. Interdigital capacitive sensor designs are targeted that maximize sensitivity to changes in the dielectric values of the cable polymers.

Keywords Capacitive sensor · Nondestructive evaluation · Nuclear cable · Polymer degradation

Introduction

Approximately 1000 km of power, control, instrumentation and other cables are found in nuclear power plants (NPPs) and cross-linked polyethylene (XLPE) is used widely as insulation material in low-voltage instrumentation cables. Due to exposure to heat, radiation and other environmental factors over extended periods of time, the properties of XLPE insulation material gradually degrade and the integrity of whole cable may be imperiled, potentially preventing successful reactor shut-down following loss-of-coolant event in containment. Degraded cable polymers may therefore prevent license extension that permits NPPs to operate beyond

Z.H. Shao (✉) · N. Bowler
Iowa State University, Ames, IA 50011, USA
e-mail: zshao@iastate.edu

N. Bowler
e-mail: nbowler@iastate.edu

J.H. Jackson et al. (eds.), *Proceedings of the 18th International Conference on Environmental Degradation of Materials in Nuclear Power Systems – Water Reactors*, The Minerals, Metals & Materials Series, https://doi.org/10.1007/978-3-319-68454-3_8

their initial design life [1]. Hence it is desirable to monitor insulation degradation and to predict the remaining-useful-life of the cable if possible.

A significant amount of research effort has been devoted to the evaluation of XLPE insulation material in NPP cable. Also, different kinds of evaluation methods have been developed that define or evaluate the condition of the insulation. Traditional mechanical methods, such as elongation-at-break (EAB) [2], are widely used for evaluation of nuclear cable polymers but have the drawback of being destructive. More recently, indenter measurements have been developed that measure a mechanical modulus of the cable jacket nondestructively, that correlates to material state. Some electrical testing methods have also been developed, such as partial discharge (PD) [3], volume electrical resistivity [4], and frequency domain reflectometry (FDR) [5]. But these methods have some deficiencies including the need for complex instrumentation and access to the central conductor of the cable.

Capacitive sensing offers some advantages for in situ nondestructive evaluation of the insulation material in nuclear cables, due to its sensitivity to the relative permittivity (dielectric constant) of the material and, for certain sensor configurations, not requiring access to the central conductor of the cable. Recently, some principles about the interdigital capacitive sensor design, mainly about parameters of sensor digits, have been investigated [6–8]. However, many of them concentrate on the single layer cable. Commonly, a basic cable comprises a central conductor, formed from copper or aluminum strands that are often tin-coated, covered by a polymeric electrical insulation layer, protected by a plastic jacket. For instance, a signal-core instrumentation cable used in NPPs may contain a structure comprising: a multi-strand conductor, one insulation layer (XLPE) and one jacket layer (chlorosulfonated polyethylene (CSPE)), each with two characteristic parameters: thickness t and permittivity ε, as indicated in Fig. 1. This paper will focus on the parameter design of an interdigital capacitive sensor for nondestructive evaluation of a two-layer cable with the structure illustrated in Fig. 1.

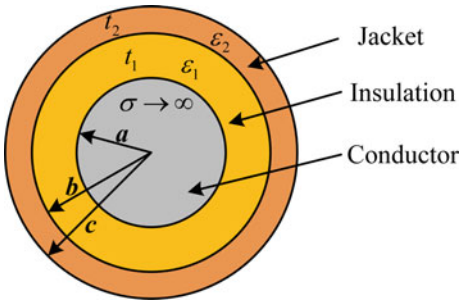

Fig. 1 Schematic diagram of the cross-section of a single-core XLPE cable, showing polymeric insulation and jacket layers

Modeling

Sensor Configuration

The interdigital capacitive sensor designed in this paper consists of odd number (denoted as N) of electrode digits, with length l (mm) in the z-direction and arc-width w (mm) in the -direction, arranged on the outer surface of the XLPE cable with a separation of g (mm) from each other. All electrode digits are deposited on a thin substrate layer which is itself deposited on a metal ground plane in order to repress any electrical noise from the surrounding environment, as depicted in Fig. 2. A suitable material for the sensor substrate layer is polytetrafluoroethylene (PTFE) with a small thickness denoted as t_s, and for background plane is copper with a small thickness denoted as t_g.

In a practical implementation of this sensor design, N sensor electrode digits (blue color in Fig. 2) are connected to one voltage supply terminal and the other $(N + 1)$ sensor electrode digits (red color in Fig. 2) are connected to another terminal such that a potential difference exists between certain of the sensor digits. The measured output of the sensor is the capacitance between two terminals.

Capacitance and Sensitivity

According to electromagnetic theory, the capacitance of the system interrogated by the sensor shown in Fig. 2 depends on the characteristic electrical parameters of each dielectric layer, the thickness and curvature of each layer, and the electrical and geometrical parameters of the system. Hence, a mathematical model of the sensor configuration (including output capacitance and other characteristic parameters) can be represented by the following relation (1),

$$C = f(a, \varepsilon_1, t_1, \varepsilon_2, t_2, w, g, l, N) \tag{1}$$

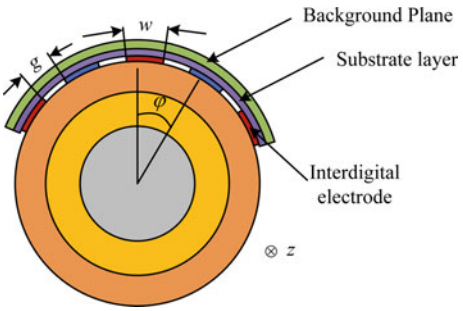

Fig. 2 Concept diagram of the cross-section of an XLPE cable, as shown in Fig. 1, with an interdigital capacitive sensor applied to its outer surface (color figure online)

where some parameters, such as $\varepsilon_1, t_1, \varepsilon_2, t_2$, are related to the cable itself, Fig. 1, and the dielectric properties of the polymers are expected to change during their aging process. Other parameters, such as a, w, g, l, N, are related to the sensor configuration. Note, in general, permittivity and capacitance will be complex numbers that are functions of frequency.

In practice, the parameters of the sensor itself and the geometrical parameters of a particular cable employed in an NPP may be independently known or assumed, such that only the dielectric properties $\varepsilon_1, \varepsilon_2$ and their changes during degradation need be inferred from nondestructive measurement. For these reasons, the sensor designed in this paper, for the nondestructive evaluation of aged XLPE cable insulation, concentrates on the relation between output capacitance C and XLPE insulation permittivity ε_1. This means that the designed sensor should maximize sensitivity S of the sensor defined as follows, in relation (2).

$$S = \frac{\partial C}{\partial \varepsilon_1} \tag{2}$$

Simulation Setting and Sensitivity Calculation

In this section, interdigital sensors with different parameters (w, g, N) are presented and their capacitance and sensitivity are calculated via the finite element method. From the results of the simulations, optimal parameters can be found in order to maximize S. The parameters of cable used in the simulation are based on a particular cable supplied by the RSCC company [9], and the detailed information about this cable is provided in Table 1. Fixed parameters employed in the simulation of the interdigital sensor are listed in Table 2 whereas the parameters w, g, and N are permitted to vary in order to optimize the sensor sensitivity to the insulation permittivity variation.

Using finite element methods (AC/DC packages of COMSOL™), the charge density on each electrode can be calculated, for given values of assigned electrical

Table 1 Cable parameters

Company	Cable type	Total diameter (mm)	Jacket		Insulation	
			Thickness (mm)	Material	Thickness (mm)	Material
RSCC	P62-3902	14.49	1.143	CSPE	1.4	XLPE

Table 2 Sensor parameters

	Thickness, t_e (μm)	Material
Electrode	17.8	copper
Substrate	25.4	PTFE
Back plane	17.8	copper

potential, and geometrical and electrical parameters. Then the capacitance between two electrodes can be calculated using Eq. (3), where Q is the total charge on one electrode and V is the potential difference between them.

$$C = \frac{Q}{V} \tag{3}$$

In the simulation, the relative permittivity of the jacket is set to 3.85 [9] and that of the substrate is set to 2.1 [10]. The relative permittivity of XLPE insulation is allowed to vary between 1 and 10. The sensitivity is calculated using the approximation expressed in relation (4).

$$S \approx \frac{\Delta C}{\Delta \varepsilon_1} \tag{4}$$

Here, an interdigital sensor with the parameters w = 1 mm, g = 1 mm, and N = 5 is used as an example to illustrate the process of simulation: mesh, potential distribution, field distribution and sensitivity calculation. The mesh for simulation is depicted in Fig. 3a, and mesh grid density is automatically increased around the sensor to improve solution accuracy. The potential and electric field distribution are depicted in Fig. 3b, wherein the color represents potential distribution and the arrows show the direction and strength of electric field. It is clearly depicted in Fig. 3b that, in this example, there are five digits arranged around the outer surface of the cable: three negative digits connected to 0 V (the dark blue regions) and two positive digits connect to 1 V (the red regions). The electric field strength decreases toward the inner region of the cable, which means that the strength of the electric field is higher in the jacket layer than in the insulation.

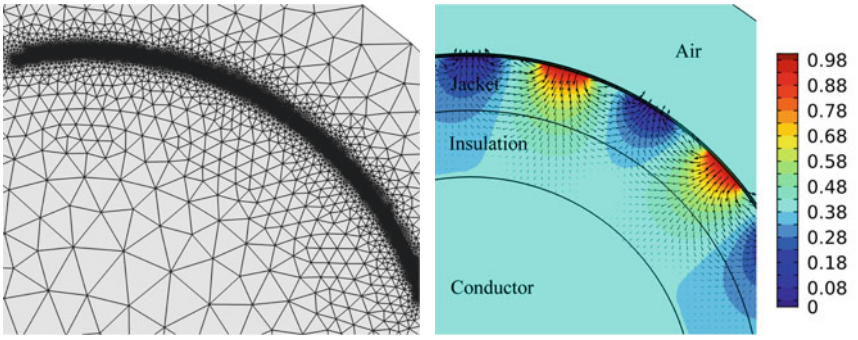

(a) Mesh distribution (b) Potential and field distribution

Fig. 3 COMSOL™ simulation results for sensor with parameters (see Fig. 2) w = 1 mm, g = 1 mm, and N = 5. Other calculation parameters are listed in Tables 1 and 2 (color figure online)

Results

In this section, results of sensitivity calculations described in the previous section are presented. The capacitance and sensitivity per unit length for different values of XLPE relative permittivity are plotted in Fig. 4. As the permittivity of XLPE is approximately 2.5 in new cables, the sensitivity at $\varepsilon_1 = 2.5$ is taken into consideration in ensuing discussions.

Univariate Effects

Digit Width (*W*)

The effect of digit width *w* on sensor sensitivity is depicted in Figs. 5a through (d), with the digit width changing from 0.25 mm to 2 mm for various digit seperations *g* and digit numbers *N*. As is shown in the figures, the sensitivity increases with digit width and the increase becomes faster for larger width.

Digit Separation (*G*)

The effect of digit seperation *g* on sensor sensitivity is depicted in Figs. 6a through (d), with digit seperation changing from 0.25 mm to 2 mm for various digit widths *w* and digit numbers *N*. It is shown that the sensitivity increases with digit seperation. However, the increase becomes slower when the digit seperation *g* is larger.

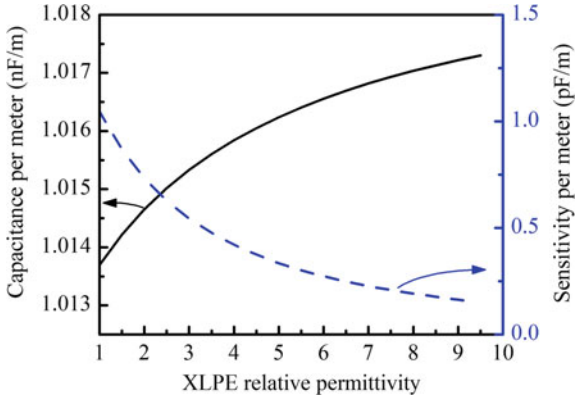

Fig. 4 Output capacitance and sensitivity curves for sensor with parameters (see Fig. 2) $w = 1$ mm, $g = 1$ mm, and $N = 5$. Other calculation parameters are listed in Tables 1 and 2

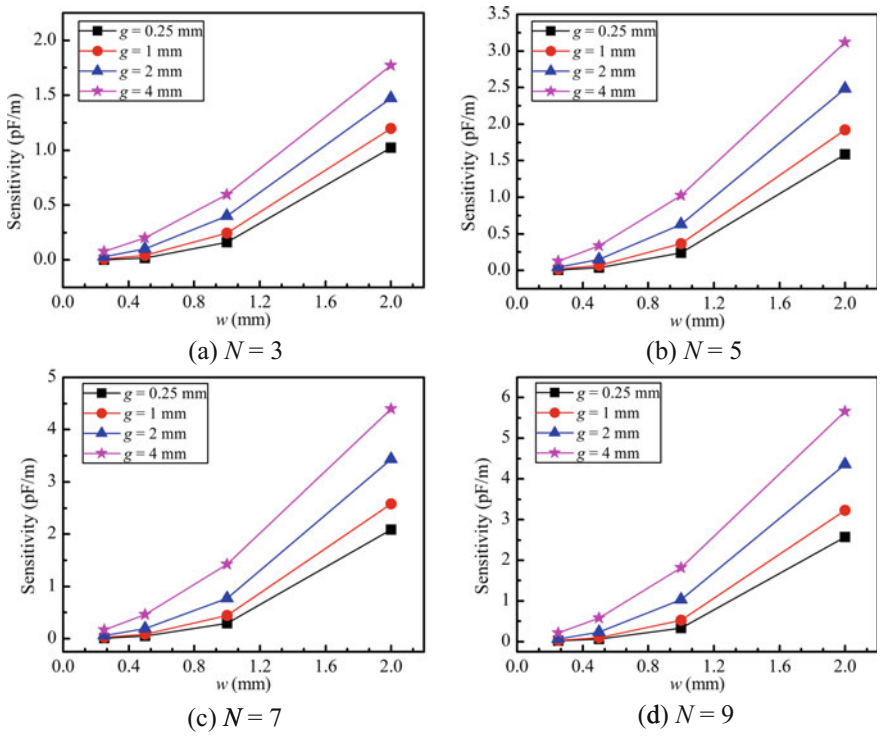

Fig. 5 Sensor sensitivity, Eq. (4), as a function of digit width w for various digit seperations g and digit numbers N. Other calculation parameters are given in Tables 1 and 2

Digit Number (N)

Investigating the effect on sensor sensitivity of the number of digits N, we select N to be an odd number: 3, 5, 7, 9. Then, the effect of N on the sensor sensitvity is depicted in Fig. 7, where other calculation parameters are listed in Tables 1 and 2. It can be seen that sensor sensitivity increases with digit number.

It can be concluded, therefore, that when designing a sensor for nondestructive evaluation of a cable insulation layer concealed beneath a plastic jacket, the sensor's digital width, digital seperation, and number of digits should be as large as possible in order to increase the sensor sensitivity. But there is a trade-off between sensor sensitivity S and output capacitance C, because the output capacitance is reduced as the digital separation increases, and C cannot fall below a certain threshold limited by the measurement device.

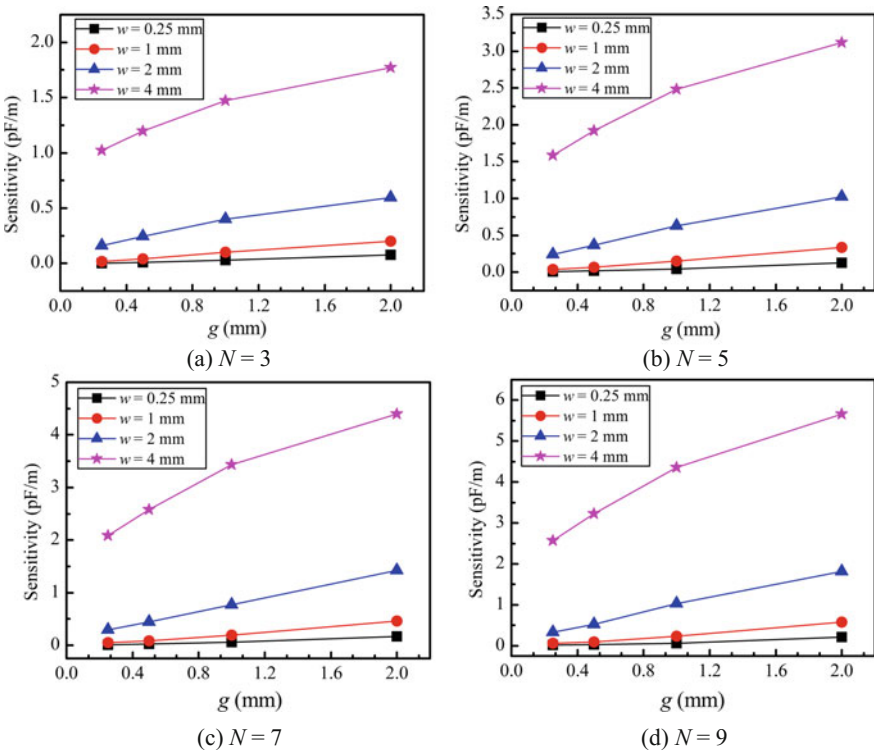

Fig. 6 Sensor sensitivity, Eq. (4), as a function of digit seperation g for various digit widths w and digit numbers N. Other calculation parameters are given in Tables 1 and 2

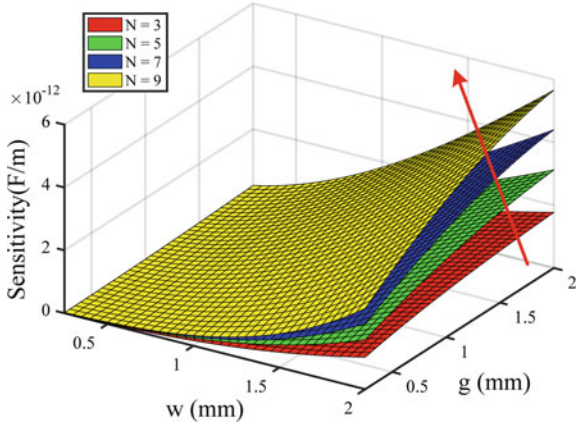

Fig. 7 Sensor sensitivity, Eq. (4), as a function of digit number N. Other calculation parameters are given in Tables 1 and 2

Combined Effect

The sensor parameters w, g and N are constrained in practice by the geometrical parameters of cable as shown in relation (5), where M is a length determined by the arc length of the sensor region, which is in turn constrained by the accessibility of the cable. Typically, only part of the cable surface is accessible, which means that M should be some fraction of the circumference of the cable.

$$Nw + (N - 1)g < M \tag{5}$$

Due to the constraint expressed in relation (5), considering the effects of w, g and N seperately on sensor sensitivity and capacitance is necessary but not sufficient for interdigital sensor design. When designing the interdigital sensor, the combined effect, including w, g, N, and relation (5) should all be taken into consideration as follows.

In the following discussion, M is assumed as 17 mm, which is approximately 37.5% of the cable surface. The combined effect of varying w and g for various N is depicted in Fig. 8a through (d), with digit number changing from three to nine. Figure 8 shows contour plots of sensitivity with w and g, and the dotted line represents the constraint defined by relation (5). As it is depicted, the gradient of sensitivity is larger along the width direction than that along the seperation direction. Therefore, larger width w and smaller seperation s gives higher sensitivity (at least for g > 0.5 mm). In addition, due to relation (5), the constraint line given by $Nw + (N-1)g = M$ moves towards the origin (0, 0) as N changes from three to nine. In Fig. 8, the sensitivity near the constraint line decreases from approximately 6.0 pF/m ($N = 3$) to approximately 1.5 pF/m ($N = 9$) as N increases (as indicated on the figures).

Therefore, N should be three when considering the combined effect including constraint relation (5). For $N = 3$, large w with small g will obtain high sensitivity, as depicted in Fig. 8. In summary, $N = 3$, $w = 5.5$ mm, $g = 0.3$ mm, should be optimal design parameters for the cable configuration considered here, and this sensor has a sensitivity of approximately 6.0 pF/m to changes in permittivity of the insulation layer when $\varepsilon_1 = 2.5$. Then, the output capacitance and the sensitivity of interdigital sensor with parameters, $N = 3$, $w = 5.5$ mm, $g = 0.3$ mm, are depicted in Fig. 9. It can be seen that this sensor has a sensitivity of 6.0 pF/m and output capacitance of 2.8 nF/m at $\varepsilon_1 = 2.5$. Here, both sensitivity and output capacitance use the unit F/m because COMSOL 2D package is used in the simulation. If the sensor is 2.5 cm long, the output capacitance and sensitivity are $C = 70$ pF and $S = 0.15$ pF.

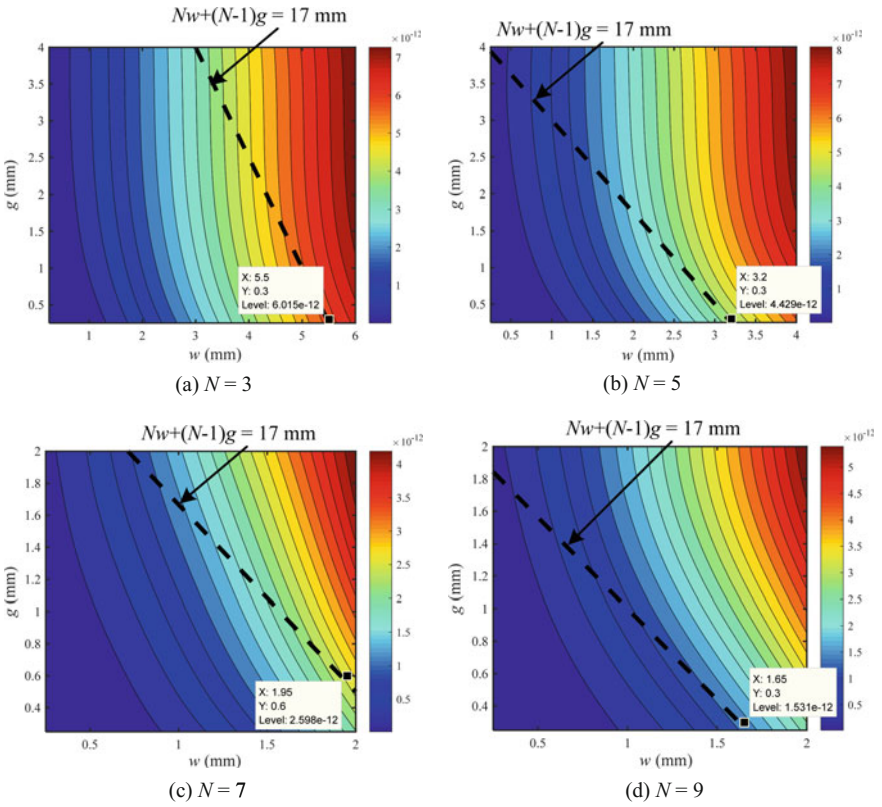

Fig. 8 Sensor sensitivity, Eq. (4), as a function of w, g, and N. Other calculation parameters are given in Tables 1 and 2

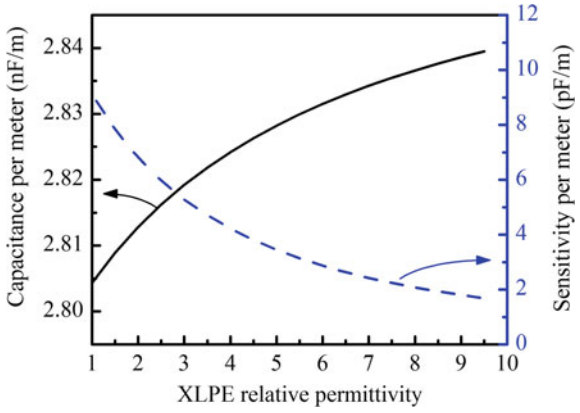

Fig. 9 Output capacitance and sensitivity curves for a sensor with w = 4 mm, g = 2.5 mm, N = 3, and other parameters given in Tables 1 and 2

Conclusions

A new capacitive interdigital sensor has been designed for nondestructive evaluation of XLPE insulation of aged instrumentation cable used in nuclear power plant. The capacitive sensor is designed for maximum sensitivity to the dielectric properties of insulation material situated beneath a cable jacket. The sensitivity of this capacitive sensor to dielectric properties of XLPE insulation is investigated as a function of sensor parameters w, g, and N. According to the effects of sensor parameters on sensitivity, interdigital capacitive sensor designs that maximize sensitivity to changes in the dielectric properties of the XLPE insulation material in jacketed cables are presented. Optimal design parameters for nondestructive evaluation of the XLPE insulation layer for the cable configuration considered here are found to be $N = 3$, $w = 4$ mm, and $g = 1$ mm, when the available cable surface available for inspection is assumed to be 37.5% of the full circumference. With these assumptions, a sensitivity of 4.66 pF/m and output capacitance of 2.09 nF/m are determined for the sensor, when the insulation relatively permittivity is assumed to be $\varepsilon_1 = 2.5$. In future work, pristine and aged cables of various types will be tested with custom-designed sensors whose design process will take into account the cable materials and geometry, as in the example given in this work.

Acknowledgements This work was funded by the United States Department of Energy under contract number DE-NE0008269.

References

1. N. Bowler, S.S. Liu, Int. J. Prognostics Health Manage., **6**, 1–12 (2015)
2. J.V. Gasa, Z. Liu, M.T. Shaw, Polym. Degrad. Stab., **87**(1), 77–85 (2005)
3. C. Desai, K. Brown, M. Desmulliez, A. Sutherland, in *2008 Annual Report Conference on Electrical Insulation and Dielectric Phenomena*, pp. 17–20, 2008
4. I.Y. Kim, C.S. Goo, J.H. Lee, B.S. Jin, M.K. Kang, Y.D. Shin, in *2012 International Conference on High Voltage Engineering and Application (ICHVE)* (2012), pp. 68–71
5. C. Furse, Y.C. Chung, R. Dangol, M. Nielsen, G. Mabey, R. Woodward, IEEE Trans. Electromagnetic Compatibility **45**(2), 306–315 (2003)
6. T.M. Chen, J.R. Bowler, N. Bowler, Appl. Phys. Lett. **104**(3), 032901 (2014)
7. E.M. Arvia, R.T. Sheldon, N. Bowler, in *Electrical Insulation and Dielectric Phenomena*, 2014, Annual Report Conference on, pp. 514–517 (2014)
8. R.T. Sheldon, N. Bowler, IEEE Sens. J. **14**(4), 961–970 (2014)
9. World Wide Web, www.r-scc.com/catalog?indID=6. Accessed 1 April 2017
10. World Wide Web, en.wikipedia.org/wiki/Polytetrafluoroethylene. Accessed 1 April 2017

Tracking of Nuclear Cable Insulation Polymer Structural Changes Using the Gel Fraction and Uptake Factor Method

Miguel Correa, Qian Huang and Leonard S. Fifield

Abstract Cross-linked polyethylene (XLPE) cable insulation samples were exposed to heat and gamma radiation at a series of temperatures, dose rates, and exposure times to evaluate the effects of these variables on material degradation. The samples were tested using the solvent incubation method to collect gel fraction and uptake factor data in order to assess the crosslinking and chain scission occurring in polymer samples with aging. Consistent with previous reports, gel fraction values were observed to increase and uptake factor values to decrease with radiation and thermal exposure. The trends seen were also more prominent as exposure time increased, suggesting this to be a viable method of tracking structural changes in the XLPE-insulated cable material over extended periods. For the conditions explored, the cable insulation material evaluated did not indicate signs of anomalous aging such as inverse temperature effect in which radiation-induced aging is more severe at lower temperature. Ongoing aging under identical radiation conditions and at lower temperature will further inform conclusions regarding the importance of inverse temperature effects for this material under these conditions.

Keywords Cable-aging · XLPE · Gel fraction · Uptake factor · Crosslinking · Inverse temperature effect

Introduction

Cable performance degradation leading to failure is a concern for continued long term operation of nuclear power plants past their original forty year licensee and initial twenty year license renewal periods [1]. In nuclear power plants cables can be exposed to gamma radiation, as well as to moderately high temperature

M. Correa · Q. Huang · L.S. Fifield (✉)
Pacific Northwest National Laboratory, Richland, WA, USA
e-mail: leo.fifield@pnnl.gov

L.S. Fifield
Washington State University, Pullman, WA, USA

J.H. Jackson et al. (eds.), *Proceedings of the 18th International Conference on Environmental Degradation of Materials in Nuclear Power Systems – Water Reactors*, The Minerals, Metals & Materials Series, https://doi.org/10.1007/978-3-319-68454-3_9

environments [2]. Laboratory accelerated aging has been applied to cable materials to simulate material evolution over long service life and to understand relationships between environmental stresses and material changes in multi-stress environments [3]. Here we describe recent efforts at the Pacific Northwest National Laboratory (PNNL) to use the metrics of gel fraction and solvent uptake factor to monitor changes in cross-linked polyethylene (XLPE) insulation material condition and identify behavior that does not fit into simple models of stress intensity and material change.

Elevated temperature and gamma irradiation were used to accelerate XLPE material aging. These stresses have been observed to produce oxidation embrittlement in XLPE [4]. Though elevated, temperatures were selected below the major phase transitions to better replicate service aging [5]. Gamma radiation dose rates were kept relatively low to again avoid artificial effects characteristics of laboratory aging that are not representative of aging in the plant [6]. Similarly, aging was performed with simultaneous exposure to both radiation and heat as would be the case during service aging rather than with sequential exposure [7]. A key goal of the aging studies is improved understanding of the relative importance of the aging factors employed in inducing material change [8].

The gel fraction of a sample is a relative measurement of the homogeneity of the polymer network. A gel fraction value of 100% would correspond to a network with all polymer chains connected [9]. Gel fraction values less than 100% indicate the portion of the material that not part of the network and thus reveal a heterogeneous overall network. Gel fraction increases with aging as new crosslinks form. The uptake factor of a sample indicates how easily the sample swells in a solvent. When polymer chain scission occurs, uptake factor values increase reflecting more facile solvent absorption. The gel fraction and uptake factor therefore often share an inverse relationship: as gel fraction increases, uptake factor decreases and vice versa. The objective of this work is to identify the trends in gel fraction and uptake factor of simultaneously aged XLPE.

Experimental

Material

The material studied was white XLPE insulation from a two-conductor, shielded and jacketed RSCC Firewall® III Instrumentation Cable (product code I46-0021). The material is described by the manufacturer as exhibiting enhanced thermal stability and radiation resistance and is qualified for Class 1E nuclear service. The XLPE has a thickness of 0.64 mm and was aged in 100 mm insulation "straws" with internal conductor removed.

Sample Aging and Preparation

XLPE samples were held at different temperatures (60, 90, and 115 °C) in a mechanical convection, air circulating oven for a series of exposure periods (5, 10, 15, 20, and 25 days). The oven was placed in Co-60 gamma radiation beam in the High Exposure Facility (HEF) within the Radiological Exposures & Metrology (REM) Laboratory at PNNL. Gamma dose rate was controlled (from 116 to 540 Gy/hr) by placement of samples at designated distances from the source by means of ordering on rows of a rack within the oven. Specimens of ~1 cm in length and 0.025 g in mass were cut form the aged samples. Specimens were placed inside open scintillation vials and preconditioned overnight at room temperature and 44% relative humidity in a vessel containing a saturated salt solution of K_2CO_3 (see Fig. 1) prior to testing.

Swollen Sample Measurement

The gel fraction and solvent uptake factor were measured using a solvent incubation method similar to the ASTM standard [10], but at smaller scale and without completely sealing incubation containers to avoid pressure build up hazard. Preconditioned specimens were immersed in xylenes (>99%) in a 200:1 weight ratio of solvent to XLPE sample (e.g. 0.025 g cable sample was combined with 5 mL of xylenes). Vials containing specimen and solvent were capped with spacers in order to create a reproducible seal during heating that avoided pressure buildup. Capped vials were heated at 110 °C on a hot plate, as seen in Fig. 2, for 24 h. After 24 h, the vials were transferred one-by-one to a heating mantle held at 110 °C to maintain swollen specimen temperature during transfer. Once in the heating mantle, the septum cap was removed and the cable sample was transferred to a new tared vial using tweezers. Once sealed, the specimen and tared vial were

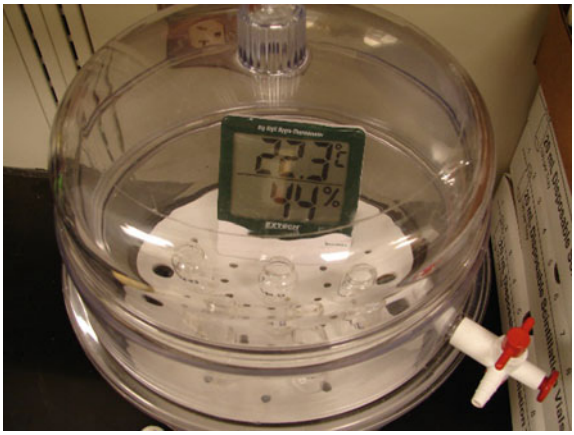

Fig. 1 Vessel used to pre-condition samples overnight at 44% humidity and room temperature

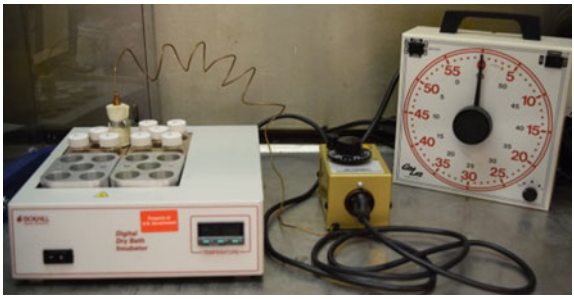

Fig. 2 Hot plate attached to thermostat and timer

allowed to cool to room temperature for 15 min before their mass was recorded. Mass values from three replicate samples were used to produce each data point. The ASTM test method specifies use of at least two specimens per data point.

Dried Sample Measurement

After measuring the weight of the capped vial containing the swollen specimen, the vial cap was removed and replaced with aluminum foil. The vial was placed inside an oven and held under vacuum at 100 °C for 24 h. Following the 24 h drying, the specimen and vial were removed from the oven and the cap was replaced on the vial. After 15 min equilibration to room temperature, the specimen and vial were massed. The mass of dried specimens were also determined independent of the tared vial they were dried in.

Results

Gel Fraction

The gel fraction of each specimen is calculated:

$$Gel\,Fraction = \frac{W_d}{W_a} \times 100$$

where W_d is the mass of the dried sample and W_a is the mass of the aged sample before the swelling procedure. From the data collected it is readily visible that the gel fraction increases when samples are thermally treated to higher temperatures. When all other factors were held constant, the data had no outliers and always showed 60 °C samples to have lower gel fraction than 90 °C samples, and the 115 °C samples always had higher gel fraction than the 90 °C samples as seen on Fig. 3. Similarly, the data show a consistent trend regarding days of exposure. Samples that were treated longer had

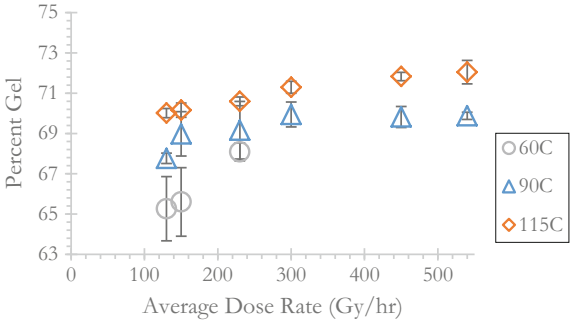

Fig. 3 Plot of average dose rate (Gy/hr) versus gel fraction of specimen. All samples plotted here were aged for 15 days, at either 60, 90, or 115 °C

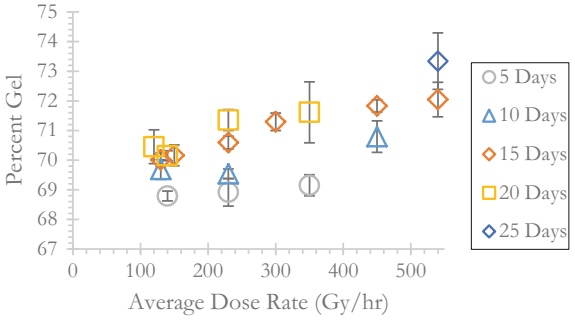

Fig. 4 Plot of dose rate (Gy/hr) versus gel fraction of XLPE specimen. Data plotted is from specimens aged at 115 °C for either 5 days, 10 days, 15 days, 20 days or 25 days

higher percent gel (25 > 20 >15 >10 > 5 days) when temperature and average dose rate were held constant as seen on Fig. 4. Both of these trends suggest that longer and higher thermal exposure leads to higher gel fraction, and thus higher degree of crosslinking.

More scatter is observed when looking only at the effect of dose rate. For data sets sharing the same length of exposure, it appears that specimens exposed to higher dose rates exhibit higher gel fraction. This general trend appears to hold for all of the exposure periods considered. Figure 4 reveals the effect dose rate on gel fraction of specimens heated at 115 °C. Trends for specimens similarly aged at 60 and 90 °C (not shown) are less clear as changes in gel fraction were less dramatic at these lower temperatures.

Uptake Factor

Specimen uptake factor is defined here as:

$$UptakeFactor = \frac{W_s}{W_d}$$

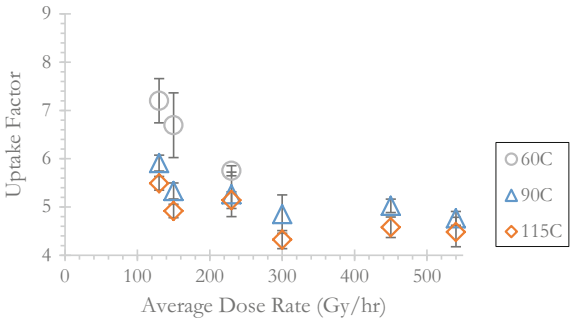

Fig. 5 Plot of average dose rate (Gy/hr) versus uptake factor of sample. All specimens were aged for 15 days at either 60, 90, or 115 °C

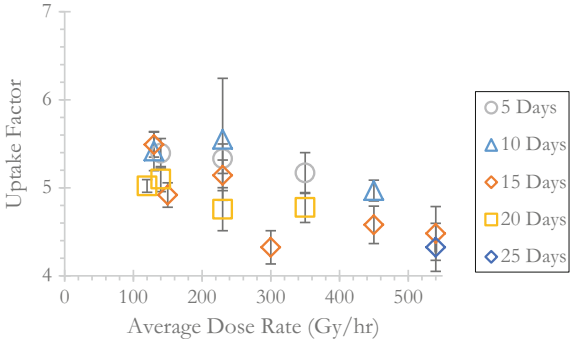

Fig. 6 Plot of average dose rate (Gy/hr) versus uptake factor of specimen. All samples were aged at 115 °C for either 5 days, 10 days, 15 days, 20 days, or 25 days

where W_s is the mass of the swollen gel sample and W_d is the mass of the dried sample. From the data plotted in Fig. 5 it can be seen that, for 15 day exposure, uptake factor decreases with increasing temperature and with increasing dose rate. Similarly in Fig. 6, uptake factor is seen to decrease with exposure time and dose rate at 115 °C.

Similar trends for effect of temperature, dose rate and duration were observed for both gel fraction and uptake factor. Uptake factor values exhibited more scatter than gel fraction values due to the dependence of uptake factor data on swollen specimen mass. The swollen specimen mass is prone to greatest measurement error due to reliance on the swollen specimen transfer step. Specimens are constantly cooling while they are transferred between solvent-filled and empty vials following incubation. As the specimen temperature decreases, the amount of solvent inside the swollen specimen decreases as seen by the visibly decreasing size of the sample. The small size of the specimens increases variability in this manual step, and is a probable cause of scatter in the uptake factor data. Larger samples or an alternate transfer method might decrease scatter in the uptake factor data in future studies.

Conclusion

Cable aging via thermal and radiation exposure involves induced polymer chain cross-linking and chain scission as reflected in gel fraction and uptake factor measurements. In this work, gel fraction values were seen to increase with XLPE insulation exposure time and temperature in the presence of gamma radiation. Gel fraction was also observed to increase with dose rate, however this trend exhibited more scatter and was more difficult to identify in all data sets. Uptake factor for XLPE insulation samples was observed to decrease with exposure time, temperature and dose rate. The uptake factor values had more scatter across all data sets, which could be attributed to the experimental method of specimen transfer following solvent incubation. Anomalous aging behavior, such as increased gel factor or decreased uptake factor with radiation exposure at lower temperature in the presence of radiation, was not observed.

References

1. K.T. Gillen, R.A. Assink, R. Bernstein, Condition monitoring approaches applied to a polychloroprene cable jacketing material. Polym. Degrad. Stab. **84**, 419–431 (2004)
2. K.T. Gillen, R.A. Assink, R. Bernstein, M. Celina, Condition montioring methods apllied to degradation of chlorosulfonated polyethylene cable jacketing materials. Polym. Degrad. Stab. **91**, 1273–1288 (2006)
3. K.T Gillen, R.A Assink, R Bernstein, Nuclear energy plant optimization (NEPO) final report on aging and condition monitoring of low voltage cable materials (Report SAND2005-7331, Sandia National Laboratories, 2005)
4. K. Anandakumaran, W. Seidl, P.V. Castaldo, Condition assessment of cable insulation systems in operating nuclear power plants. IEEE Trans. Dielectr. Electr. Insul. **6**(3), 376–384 (1999)
5. J. Boguski, G. Przybytniak, Benefits and drawbacks of selected condition monitoring methods applied to accelerated radiation aged cable. Polym. Test. **53**, 197–203 (2016)
6. K.T. Gillen, R. Bernstein, R.L. Clough, M. Celina, Lifetime predictions for semi-crystalline cable insulation materials: I. Mechanical properties and oxygen consumption measurements on EPR materials. Polym. Degrad. Stab. **91**(9), 2146–2156 (2006)
7. Verardi, L.; Fabiani, D.; Montanari, G. In *The influence of accelerated aging procedures on the correlation of electrical and mechanical properties of LV nuclear power plant cables*, 2014 IEEE conference on electrical insulation and dielectric phenomena (CEIDP), IEEE: 2014; pp 506–509
8. D. Andjelkovic, N. Rajakovic, Influence of accelerated aging on mechanical and structural properties of cross-linked polyethylene (XLPE) insulation. Electr. Eng. **83**(1), 83–87 (2001)
9. M. Celina, G.A. George, Characterisation and degradation studies of peroxide and silane crosslinked polyethylene. Polym. Degrad. Stab. **48**, 297–312 (1995)
10. ASTM, Determination of Gel Content and Swell Ratio of Crosslinked Ethylene Plastics, Test Standard ASTM D2765-11, ASTM International, 2011

Degradation of Silicone Rubber Analyzed by Instrumental Analyses and Dielectric Spectroscopy

Yoshimichi Ohki, Naoshi Hirai, Daomin Min, Liuqing Yang and Shengtao Li

Abstract Silicone rubber (SiR) was gamma irradiated at 125, 145 and 185 °C or thermally aged at 220, 250 and 280 °C and the resultant changes in performance were evaluated. It has become clear from instrumental analyses that crosslinking via oxidation of silicon atoms and chain scission are induced by gamma rays. Furthermore, from the temperature dependence of real relative permittivity at high frequencies, the thermal expansion coefficient was found to become smaller with the increase in dose. These results can be understood well by the chemical and structural changes in SiR induced by the degradation.

Keywords Degradation · Aging · Complex permittivity · Gamma rays · SiR · High temperature

Introduction

For electric cables in nuclear power plants (NPPs), degradation of their electrical insulation by heat and radio-active radiation is a matter of serious concern, since it may cause various malfunctions such as loss of controllability of machines [1–3]. To conduct condition monitoring of cables highly reliably, thorough understanding of the degradation behavior of cable insulation is important [3–5]. In safety-related

Y. Ohki (✉)
Department of Electrical Engineering and Bioscience,
Waseda University, Shinjuku, Tokyo 169-8555, Japan
e-mail: yohki@waseda.jp

Y. Ohki · N. Hirai · D. Min · L. Yang
Research Institute for Materials Science and Technology,
Waseda University, Shinjuku, Tokyo 169-8555, Japan

Y. Ohki · D. Min · L. Yang · S. Li
State Key Laboratory of Electrical Insulation and Power Equipment,
Xi'an Jiaotong University, Xi'an 710049, Shaanxi, China

J.H. Jackson et al. (eds.), *Proceedings of the 18th International Conference on Environmental Degradation of Materials in Nuclear Power Systems – Water Reactors*, The Minerals, Metals & Materials Series, https://doi.org/10.1007/978-3-319-68454-3_10

cables in NPPs, flame-retardant ethylene-propylene-diene copolymer (EPDM), silicone rubber (SiR), and flame-retardant cross-linked polyethylene are mainly used for electrical insulation [1, 2].

Tensile elongation at break (EAB) is often used as an index of degradation for verifying the integrity of cable insulation in NPPs [5, 6]. The reason for this is that mechanical properties deteriorate severely with the progress of degradation for rubber materials such as EPDM and SiR, although their electrical properties are less sensitive to degradation. However, the electrical properties still contain much information on the degradation behavior of respective materials. In this paper, the degradation behavior of SiR is discussed based on the results of various instrumental analyses and complex permittivity spectra obtained experimentally.

Experiments

The SiR used for the research was bought from two Japanese manufacturers of cables for NPPs and it has the same quality as the SiR being used for the cable insulation in NPPs. This also means that the sample may contain the same additives as those used for cable insulation. One important point on this is that additives are usually rarely added to SiR in comparison to EPDM to which various additives are generally added, although it is difficult to obtain such kinds of information directly from the manufacturers. The SiR samples were of the shape of a sheet with a thickness of about 550 μm. Some sheets were aged thermally at 220, 250 and 280 °C for 500, 900, 1350 and 1500 h in air. Some other sheets were aged simultaneously by heat and radiation of gamma-rays at 125, 145 and 185 °C for 500, 900, 1350 and 1500 h at a dose rate of 150 Gy/h in air. Using these samples, various instrumental analyses, which will be mentioned in the following section, were conducted.

For the measurements of complex permittivity, sheets irradiated by gamma-rays at 145 and 185 °C were used. An aluminum electrode with a diameter of 20 mm was pasted on either side of the sample with silicone oil similarly to our previous work [7, 8]. Then the sample sheet put in a vacuum chamber with a pressure below 5 Pa was measured by an impedance analyzer (126096, Solartron) by applying an ac voltage of $3V_{rms}$ in very wide frequency and temperature ranges such as from 10^{-2} to 10^{4} Hz and from 100 to 200 °C, respectively.

Several Important Experimental Results

Detailed results obtained by instrumental analyses and related discussion developed in this research can be seen elsewhere [9]. In this section, only several important experimental results are reviewed.

For any substance, its chemical structure is a basic factor influencing its various properties. Regarding this, Fourier-transform infrared (FT-IR) attenuated total reflection (ATR) spectra were compared before and after the aging. Figure 1a shows the spectra induced in sample sheets after the thermal or concurrent aging for 1500 h, while Fig. 1b shows the changes in absorbance of peaks at 785 and 1006 cm^{-1}, which are respectively assigned to Si–CH_3 and Si–O–Si. The number of Si–O–Si increases clearly, showing a marked contrast to that of Si–CH_3. This increase of Si–O–Si and the simultaneous decrease of Si–CH_3 clearly indicate that O forms a chemical bond with the Si atom that lost a terminal group of CH_3. This is a kind of oxidation of Si, which forms a cross-linked structure.

Figure 2a compares solid state ^{29}Si nuclear magnetic resonance (NMR) spectra measured before and after the thermal or concurrent aging for 1500 h. Letters D, T and Q represent that two, three and four oxygen atoms form chemical bonds with one Si atom, respectively [10]. If many Si atoms form chemical bonds with one oxygen atom, a signal should appear at 5 ppm, but no such signals are seen in the spectra. This indicates that very scarce Si atoms form one bond with oxygen. Figure 2b compares the abundance of D, T and Q before and after the aging of two types for 1500 h. The unaged sound sample reasonably exhibits a strong signal of D. However, the unaged sample has signal Q, which is difficult to imagine from the chemical structure of SiR. The reason for this is most likely the presence of talc, an additive commonly used in varieties of organic and inorganic polymers [11]. From these results, it is clear that signal T, which is an indicator of cross-linking, appears and becomes stronger with the progress of aging.

For the purpose of obtaining information on the crosslinking degree, swelling ratio was measured. Chips of SiR, obtained by cutting a sample sheet, were kept in

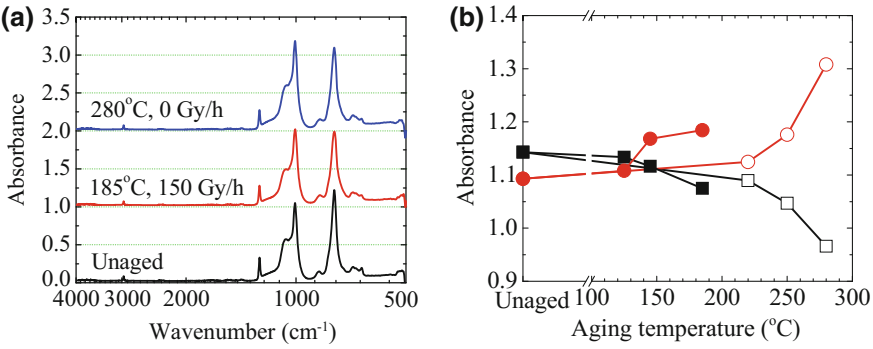

Fig. 1 **a** FT-IR ATR spectra observed for silicone rubber sheets unaged, aged thermally for 1500 h, and aged concurrently by heat and radiation for 1500 h. Each spectrum is shifted vertically by one to increase the visibility. **b** Change in FT-IR ATR absorbance as a function of aging temperature, observed for silicone rubber aged for 1500 h: Si–CH_3 (white square) and Si–O–Si (red circle) for ageing only by heat; Si–CH_3 (filled square) and Si–O–Si (filled red circle) for ageing concurrently by heat and radiation at a dose rate of 150 Gy/h

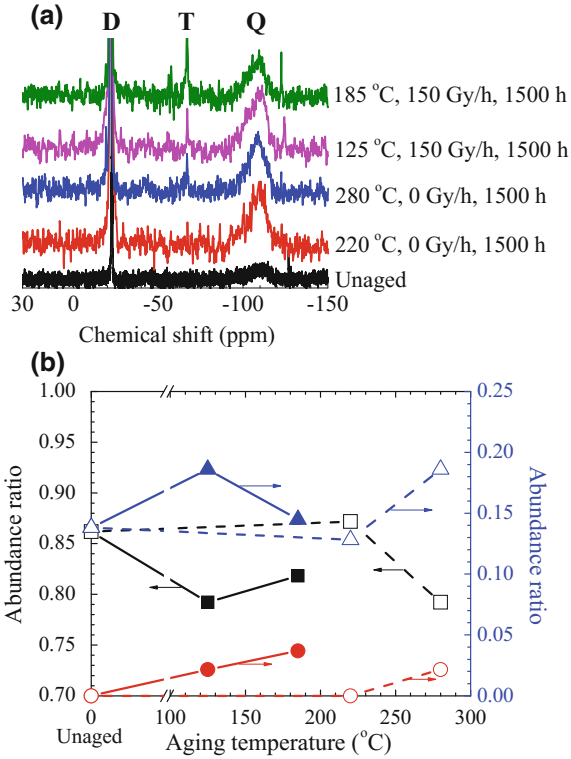

Fig. 2 **a** ^{29}Si–NMR spectra observed for silicone rubber unaged, aged thermally, and aged concurrently by heat and radiation for 1500 h. Spectra are shifted vertically to increase the visibility. **b** Abundance ratios of D (white square) (on the left ordinate) and T (red circle) and Q (blue triangle) (on the right ordinate) in silicone rubber degraded only by heat; D (filled square) (on the left ordinate) and T (filled red circle) and Q (filled blue triangle) (on the right ordinate) in silicone rubber degraded concurrently by heat and radiation (Color figure online)

toluene for 24 h at room temperature and the resultant change in volume was measured by the Archimedes method. As shown in Fig. 3, the swelling ratio decreases significantly by the aging. Swelling ratio depends directly on the amount of toluene that permeated into SiR, which becomes difficult by the cross-linking. Therefore, Fig. 3 indicates clearly that the sample becomes more densely cross-linked with the progress of aging.

In addition to chemical properties, the mechanical properties of the SiR were examined as a function of aging through indenter modulus and EAB. Figure 4 shows results obtained by an indenter. The indenter is a measuring device that gives an indicator to estimate the surface hardness of a solid substance. It inserts a metal needle tip called indenter at a speed of 0.08 mm/s and its modulus is defined as a derivative by depth of the force needed to push the tip into a sample. The modulus becomes high if the surface is rigid. We used two IEEE-standardized indenter tips with diameters of 0.79 and 0.56 mmϕ [12]. In Fig. 4, symbols and error bars represent the averages and standard deviations of indenter moduli measured six times for each sample. Their standard deviation is usually narrower than the width

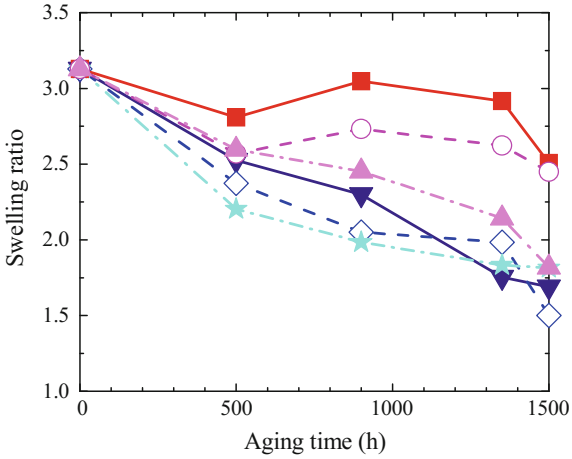

Fig. 3 Swelling ratios measured after silicone rubber had been aged only by heat at 220 (filled red square), 250 (red circle), and 280 °C (filled rose triangle) or concurrently by heat and radiation at 125 (filled cool black inverted triangle), 145 (blue diamond), and 185 °C (filled aqua star) with a dose rate of 150 Gy/h (Color figure online)

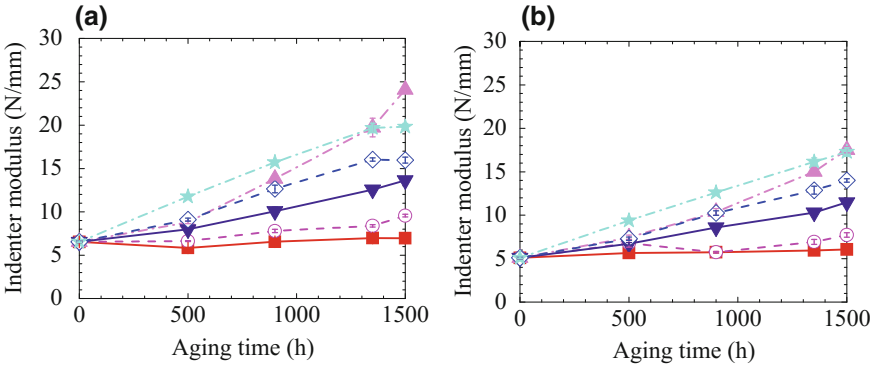

Fig. 4 Changes in average (symbol) and standard deviation (top and bottom of the vertical bar) of indenter modulus as a function of aging time. The measurements were done using the indenters with tip diameters of 0.79 mmϕ (**a**) and 0.56 mmϕ (**b**). The silicone rubber samples had been aged only by heat at 220 (filled red square), 250 (red circle), and 280 °C (filled rose triangle) or concurrently by heat and radiation at 125 (filled cool black inverted triangle), 145 (blue diamond), and 185 °C (filled aqua star) with a dose rate of 150 Gy/h (Color figure online)

of the corresponding symbol. Except for the thermal aging at 220 °C, the modulus is increased by the aging. Figure 5 shows the average and standard deviation of EAB measured five times for each sample according to the ISO Standard 37 [13] using a dumbbell-shaped test piece at a tensile speed of 500 mm/min. The error bars are often very small, which makes it difficult to find them. It is clearly shown

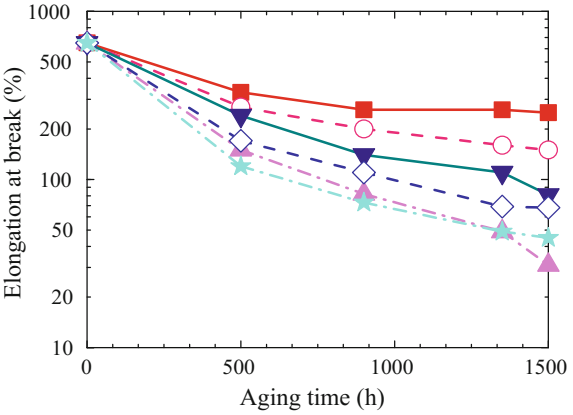

Fig. 5 Changes in elongation at break (EAB) as a function of aging time for silicone rubber aged only by heat at 220 (filled red square), 250 (red circle), and 280 °C (filled rose triangle) or concurrently by heat and radiation at 125 (filled cool black inverted triangle), 145 (blue diamond), and 185 °C (filled aqua star) with a dose rate of 150 Gy/h (Color figure online)

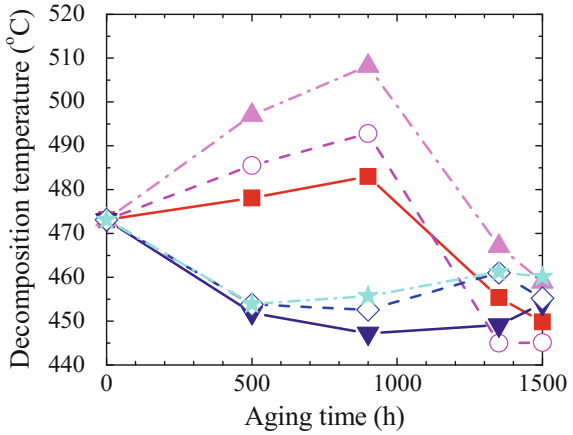

Fig. 6 Changes in decomposition temperature as a function of aging time for silicone rubber aged only by heat at 220 (filled red square), 250 (red circle), and 280 °C (filled rose triangle) or concurrently by heat and radiation at 125 (filled cool black inverted triangle), 145 (blue diamond), and 185 °C (filled aqua star) with a dose rate of 150 Gy/h (Color figure online)

that EAB decreases with the increase in aging. These results indicate that the sample surface becomes rigid by the aging.

Figure 6 shows thermal decomposition temperature T_D estimated by the measurements of thermogravimetry/differential thermal analysis (TG/DTA). If the samples were aged only by heat, T_D increases first up to the aging time of 900 h, which is followed by a sharp decrease. When samples were aged concurrently in heat and gamma radiation, TD decreases at an early stage of aging mainly up to 500 h and then increases slightly.

Through careful examination of the functional dependence of chemical and mechanical properties presented in Figs. 1, 2, 3, 4, 5 and 6, the degradation mechanism of SiR can be considered as follows. The results shown in Figs. 1, 2 and 3 clearly indicate that SiR becomes degraded by forming a cross-linked structure, which is preceded by breaking of Si-C bonds and oxidation of Si atoms [14].

Formation of the cross- linked structure should make the SiR hard and brittle, which in turn results in increase in indenter modulus and decrease in relative mechanical strength as shown in Figs. 4 and 5. The increase in T_D at a relatively weak thermal aging stage shown in Fig. 6 seems to be due to the formation of cross-linked structures, while the following significant decrease in T_D indicates the decomposition of SiR. Furthermore, the quite different aging-time dependence of T_D between the thermal aging and the concurrent aging indicates that pure thermal aging causes mainly cross-linking at its early stage, which is followed by decomposition. On the other hand, the decomposition starts much earlier in the concurrent aging by heat and gamma radiation.

Dielectric Spectroscopic Analysis of Degradation

As mentioned in Section "Experiments", we measured complex permittivity spectra as a function of frequency in very wide temperature and frequency ranges. Figure 7 shows a typical result. By fitting the spectra to theoretical equations as shown by solid curves, we can obtain valuable information on the effects of degradation of SiR on its electrode polarization, instantaneous polarization, intensity of dielectric relaxation due to hopping of ions, and dc conductivity. We will try to reveal the details of this in the near future. For the time being, only the effect of aging on the volume thermal expansion coefficient β of SiR is discussed here.

In general, charge transport inside a solid insulating material and resultant accumulation of charge in front of electrodes exert various influences on complex permittivity behavior of the material. Because the charge transport in electrically insulating organic polymers becomes active at high temperatures and because the

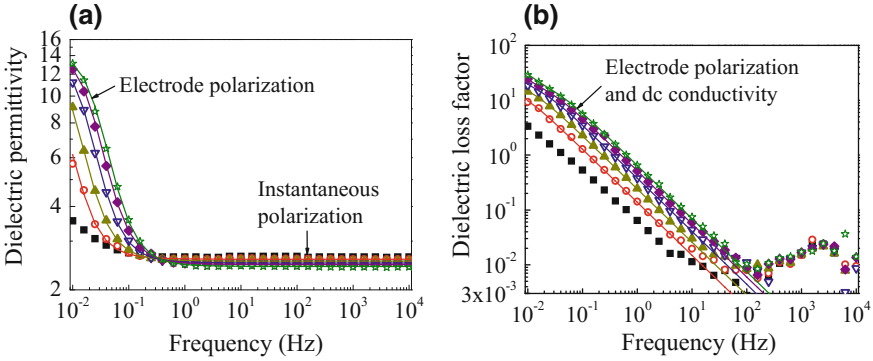

Fig. 7 **a** Dielectric permittivity and **b** dielectric loss factor for unaged silicone rubber measured at different temperatures. 100 °C (filled black square), 120 °C (red circle), 140 °C (filled army green triangle), 160 °C (white inverted triangle), 180 °C (filled blue purple diamond) and 200 °C (Ao star) (Color figure online)

charge accumulation becomes easy at low frequencies, both the real and imaginary parts of complex permittivity of many polymers become very large at high temperatures and low frequencies [15–17]. In contrast to such low-frequency spectra, instantaneous polarization processes such as electronic polarization and atomic polarization become dominant in high-frequency spectra. The real permittivity in this high-frequency range may depend negatively on temperature, especially in nonpolar organic polymers [15, 17]. The reason for this is thermal expansion of polymers, which reduces the density of polarizable atoms and molecules. It is well known that the following Clausius-Mossotti relation is satisfied between the density ρ and the real part of complex permittivity or dielectric constant $\varepsilon_{r\infty}$ due to instantaneous polarization:

$$\frac{\varepsilon_{r\infty}-1}{\varepsilon_{r\infty}+2}=\frac{\rho N_A}{3\varepsilon_0 M}(\alpha_E+\alpha_A). \tag{1}$$

Here, α_E is the electronic polarizability and α_A is the atomic polarizability, while M is the molecular weight and N_A is the Avogadro constant.

As mentioned above, if a polymer expands thermally, its density ρ decreases, which in turn decreases its $\varepsilon_{r\infty}$. Therefore, we can estimate β based on the data shown in Fig. 7 and Eq. 1 [15, 17]. It is clearly demonstrated in Fig. 8 that β decreases with the increase in dose irradiated by gamma rays and also with the increase in temperature at which the gamma irradiation was conducted. As mentioned above, if SiR is degraded, it becomes densely cross-linked. This should make the volume expansion difficult. Therefore, the negative temperature dependence and negative dose dependence of β shown in Fig. 8 are consistent with the above-mentioned degradation mechanism of SiR clarified through the various instrumental analyses.

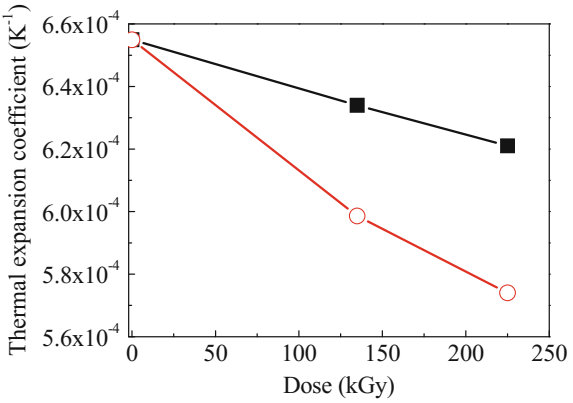

Fig. 8 Thermal expansion coefficients β calculated using Eq. (1) and dielectric permittivity spectra obtained for silicone rubber aged concurrently with gamma radiation at a dose rate of 150 Gy/h for different periods at 145 °C (filled black square) and 185 °C (red circle) (Color figure online)

Conclusion

Based on the results obtained by conducting various instrumental analyses, the degradation mechanism of SiR by heat or concurrently given gamma radiation was deduced. It has also become clear that the volume expansion coefficient, estimated from the dielectric spectroscopic analysis, becomes smaller as SiR is more severely degraded. This finding supports the degradation mechanism of SiR clarified by the instrumental analyses.

References

1. Japan Nuclear Energy Safety Organization, The Final Report of the Project of 'Assessment of Cable Aging for Nuclear Power Plants (Report JNES-SS-0903, 2009), pp. 1–4
2. A. Shimada et al., Degradation Distribution in insulation materials of cables by accelerated thermal and radiation ageing. IEEE Trans. Dielectr. Electr. Insul. **20**(6), 2107–2116 (2013)
3. Y. Ohki, N. Hirai, Effects of the structure and insulation material of a cable on the ability of a location method by FDR. IEEE Trans. Dielectr. Electr. Insul. **23**(1), 77–84 (2016)
4. Y. Ohki, T. Yamada, N. Hirai, Precise location of the excessive temperature points in polymer insulated cables. IEEE Trans. Dielectr. Electr. Insul. **20**(6), 2099–2106 (2013)
5. Brookhaven National Laboratory, Assessment of Environmental Qualification Practices and Condition Monitoring Techniques for Low-Voltage Electric Cables: Condition Monitoring Test Results (Report NUREG/CR-6704, vol. 2, United States Nuclear Regulation Commission, 2000), pp. 6(1)–6(3)
6. International Electrotechnical Commission, Nuclear Power Plants—Instrumentation and Control Important to Safety—Electrical Equipment Condition Monitoring Methods—Part 3: Elongation at Break (Standard IEC/IEEE 62582-3, 2012)
7. L.X. Zhang et al., Damage Effects and mechanisms of proton irradiation on methyl silicone rubber. Mater. Chem. Phys. **83**, 255–259 (2004)
8. X.T. Li et al., Space charge formation and charge transport in epoxy resin at varied temperatures. IEEJ Trans. Fundam. Mater. **135**(2), 88–93 (2015)
9. S. Hanada et al., Experimental investigation of the degradation mechanism of silicone rubber exposed to heat and gamma rays. High Voltage (2017). doi:10.1049/hve.2017.0009
10. A. Labouriau et al., NMR and ATR-FTIR spectroscopic investigation of degradation in RTV siloxane foams. Polym. Degrad. Stab. **92**(3), 285–292 (2006)
11. T. Izutsu et al., Estimation of talc contents in ethylene-propylene-diene copolymer by terahertz absorption spectroscopy. IEEJ Trans. Fundam. Mater. **136**(2), 81–85 (2016)
12. International Electrotechnical Commission, Nuclear Power Plants—Instrumentation and Control Important to Safety—Electrical Equipment Condition Monitoring Methods—Part 2: Indenter Modulus (Standard IEC/IEEE 62582-2, 2016)
13. International Standardization Orgnization, Rubber, Vulcanized or Thermoplastic-Determination of Tensile Stress-Strain Properties (Standard ISO 37, 2011)
14. A.A. Miller, Radiation chemistry of poly-dimethyl-siloxane. I. crosslinking and gas yields. J. Am. Chem. Soc. **82**(14), 3519–3523 (1960)

15. D. Min et al., Dielectric spectroscopic analysis of degradation in ethylene-propylene-diene copolymer. IEEE Trans. Dielectr. Electr. Insul. **23**(6), 3620–3630 (2016)
16. Friedrich Kremer, Andreas Schonhals, *Broadband Dielectric Spectroscopy* (Springer, Berlin, 2003)
17. Y. Hasegawa, J. Takihana, Y. Ohki, Estimation of thermal expansion coefficients of polymeric insulating films from temperature dependence of dielectric permittivity. Jpn. J. Appl. Phys. **53**(7), 071501(1)–071501(4) (2014)

Part II
Cables and Concrete Aging and Degradation–Concrete

Automated Detection of Alkali-Silica Reaction in Concrete Using Linear Array Ultrasound Data

Dwight A. Clayton, Hector Santos-Villalobos, N. Dianne Bull Ezell, Joseph Clayton and Justin Baba

Abstract This paper documents the development of signal processing and machine learning techniques for the detection of Alkali-silica reaction (ASR). ASR is a chemical reaction in either concrete or mortar between hydroxyl ions of the alkalis from hydraulic cement, and certain siliceous minerals present in some aggregates. The reaction product, an alkali-silica gel, is hygroscopic having a tendency to absorb water and swell, which under certain circumstances, leads to abnormal expansion and cracking of the concrete. This phenomenon affects the durability and performance of concrete cause significant loss of mechanical properties. Developing reliable methods and tools that can evaluate the degree of the ASR damage in existing structures, so that informed decisions can be made toward mitigating ASR progression and damage, is important to the long-term operation of nuclear power plants especially if licenses are extended beyond 60 years. The paper examines the differences in the time-domain and frequency-domain signals of healthy and ASR-damaged specimens. More precisely, we explore the use of the Fast Fourier Transform to observe unique features of ASR damaged specimens and an automated method based on Neural Networks to determine the extent of ASR damage in laboratory concrete specimens.

Keywords Nondestructive evaluation · Alkali-silica · Ultrasound

D.A. Clayton (✉) · H. Santos-Villalobos · N.D.B. Ezell · J. Clayton · J. Baba
Oak Ridge National Laboratory, Oak Ridge, TN, USA
e-mail: claytonda@ornl.gov

J.H. Jackson et al. (eds.), *Proceedings of the 18th International Conference on Environmental Degradation of Materials in Nuclear Power Systems – Water Reactors*, The Minerals, Metals & Materials Series, https://doi.org/10.1007/978-3-319-68454-3_11

Automated Data Analysis of Cracking Due to Alkali-Silica Reaction in Concrete

Synthetic Aperture Focusing Technique (SAFT) [1–3] is method usually employed for the reconstruction of time of flight signals, such as with radar applications, medical ultrasound, and industrial non-destructive evaluation (NDE). For NDE, one of SAFT outputs is a cross-sectional image or a "b-scan" of the interior of the specimen of interest. SAFT is the prefer method in NDE due to its reconstruction speed. The alkali-silica reaction (ASR) is a major source of concrete matrix degradation via pressure expansion that leads to cracking within the concrete structure. Figure 1 shows SAFT [4, 5] reconstructions for ASR- and non-ASR-damaged specimens. Specimens impacted by ASR, Fig. 1a, tend to show increased reflections due to the multiple ASR scatters inside the specimen. Because the large size of a typical nuclear power plant (NPP) structure makes manual human data interpretation costly and time consuming, we pursued the development of automated classification techniques for the nondestructive detection and localization of ASR in reconstructed ultrasound tomography images. We investigated frequency domain–based methods for feature extraction using the Hilbert transform indicator (HTI) as a classification metric. We also investigated automated classification based on neural network algorithm training that classified non-ASR and ASR samples based on features that were found to correlate with time and frequency domain features. Such techniques could be integrated with a mechanized ultrasound system that could "crawl" the surface of an NPP structure in search of ASR cracking and performing real time data analysis.

Frequency Domain Methods and Classification Features

The frequency content in the averaged A-scan data obtained from representative non-ASR and ASR samples is presented in Fig. 2 for both raw and smooth spectra, and the most significant time period regimes are evident in this plot. Figure 2a, b

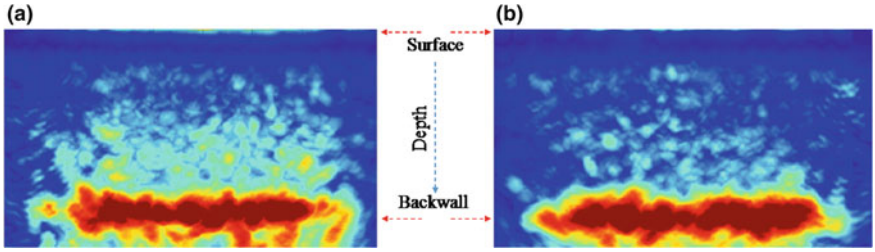

Fig. 1 Synthetic aperture focusing technique reconstruction for **a** alkali-silica reaction (ASR) and **b** non-ASR damaged specimens

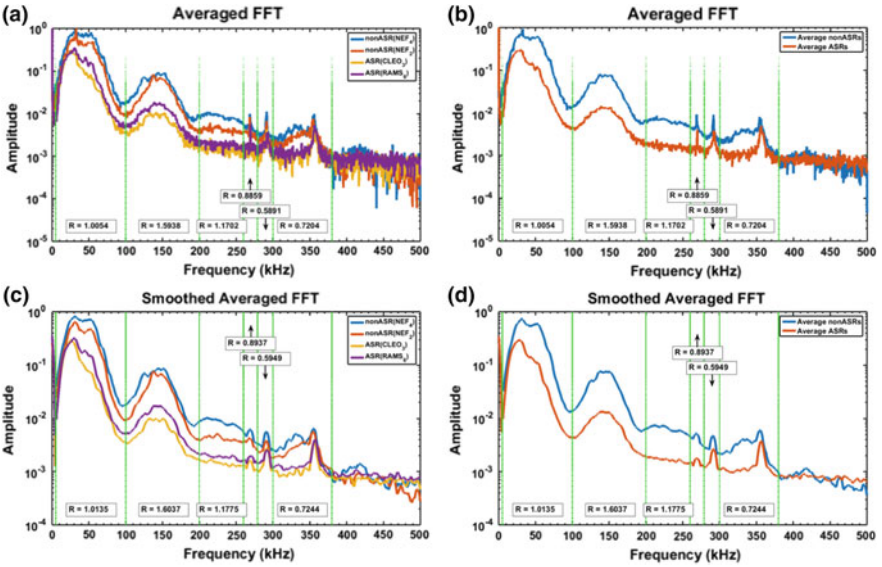

Fig. 2 Fast Fourier transform (FFT) spectral analysis results for four representative cases: **a** and **b** show the raw spectral data and **c** and **d** the smoothed data. "R" is the ratio of non-ASR (alkali-silica reaction) amplitudes to ASR amplitudes

represent the raw spectral data while Fig. 2c, d represent the smoothed data. "R" is the ratio of non-ASR to ASR of summed fast Fourier transform (FFT) amplitudes within regions demarcated by the vertical green lines. The characteristic peaks within certain bands are summarized in Table 1. The first regime is the cross-talk zone that encompasses the first 60 μs time-shift period. The second regime is the backwall reflectance zone that follows the cross-talk regime and encompasses the rest of the signal acquisition time duration. A closer examination of each of these regimes and zones follows.

The results in Table 1 reveal that the trends are consistent for both smoothed and unsmoothed FFT spectra. The greatest difference between ASR and non-ASR

Table 1 Averaged values for all 45 probe pair combinations for the most representative non-ASR (alkali-silica reaction) and ASR samples based on Hilbert transform indicator-value classification

Unsmoothed				Smoothed			
f (kHz)	R	Δ-value	Δ-rank	f (kHz)	R	Δ-value	Δ-rank
5–100	1.0054	0.0054	6	5–100	1.0135	0.0135	6
100–200	1.5938	0.5938	1	100–200	1.6037	0.6037	1
200–260	1.1702	0.1702	4	200–260	1.1775	0.1775	4
260–279	0.8859	0.1141	5	260–279	0.8937	0.1063	5
279–300	0.5891	0.4109	2	279–300	0.5949	0.4051	2
300–380	0.7204	0.2796	3	300–380	0.7244	0.2756	3

R non-ASR/ASR

samples is in the 100–200 kHz time-shift spectral band. These results are consistent with the wavelet decomposition results that highlighted the significance of the 150 kHz peak. Note that the results obtained from Fig. 2 and tabulated in Table 1 normalize the summation of spectral band amplitude by the total signal amplitude summation, i.e., they represent a ratio based on the total signal energy factor within a given spectral bandwidth.

A more in-depth investigation of the primary non-ASR versus ASR difference frequency band of 100–200 kHz (time-shifted units) is presented in Table 2. The data shows that the characteristic difference represented in this bandwidth emanates from the signal that has traversed the sample thickness between 1.5 and 3 times. This means that ASR damage has a compounding effect on the amplitude of the received signals. Although this technique is effective for specimens with a high degree of ASR damage, further investigation is needed to determine the sensitivity of the technique. Note for this document, the reference to high and low degrees of ASR damage is relative based on the HTI values.

Detection with the Hilbert Transform Indicator

Recent efforts on detection of cracking due to ASR damage used the HTI technique [6, 7] for ASR damage detection. The reasoning behind HTI is that the Hilbert transform will compute the envelope of a received signal. The envelope of specimens with low or none cracking damage are assumed to produce an envelope with less cycles than those specimens with high cracking damage [4]. The HTI index as a function of time is defined as

$$HTI(t) = \int \frac{HT(s(t))}{\max(HT(s(t)))} dt,$$

where s is the measured signal and HT is the Hilbert transform operator. Clayton et al. [7] reported HTI results on four specimens, Nefertiti, King Tut, Cleopatra, and Ramses, with average HTI of 70.63, 71.52, 105.94, and 105.69, respectively. The Nefertiti specimen was considered sound, while the King Tut had some ASR damage, and the Cleopatra and Ramses were considerably damaged. For our ANN training experiments, we were interested in the ASR-related features embedded in

Table 2 Averaged values for all 45 probe pair combinations for the most representative non-ASR (alkali-silica reaction) and ASR samples based on Hilbert transform indicator-value classification

f (kHz): units time-shifted	Time period (μs)	Path length [m]	Probe spacing [m]		Reflections (8″ thick)	
			Max	Avg	Max	Avg
100	10	24.6782	0.360	0.200	3.0	3.0
200	5	12.3391	0.360	0.200	1.5	1.5

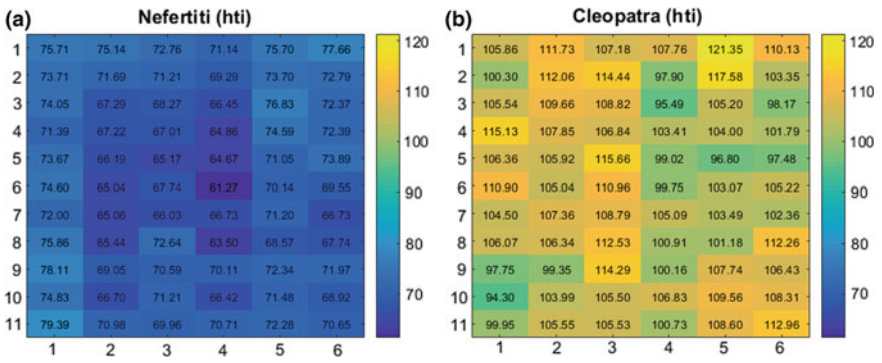

Fig. 3 Average Hilbert transform indicator (HTI) from back wall signals for the **a** Nefertiti (control) and **b** Cleopatra (ASR affected) specimens

the reflections from the back wall, which we expected to be largely modulated by the ASR defects. The HTI values of the cropped signals (i.e., time series corresponding to a back wall reflection.) provide more separation between healthy and unhealthy specimens, as shown in Fig. 3. The HTI method was used to identify cross-sections with high probably of damage. The values returned by the HTI method where used to assess the features of interest in the frequency domain as discussed next and for training of the ANN as discussed in Section "Machine Learning–Based Classification Features/Methods". The FFT plots in Fig. 2 are for cross-sections of the specimens where the HTI values where high for specimens with ASR and low for specimens with no ASR. Recall that this use of HTI is relative and is not an absolute measurement of damage.

Machine Learning–Based Classification Features/Methods

Artificial Neural Network Background

The basis of an artificial neural network (ANN) is the neuron. Similar to a biological neuron, artificial neurons (see Fig. 4), accept a variety of inputs and "fire" when the integrated inputs reach a triggering threshold value. Each neuron has a predefined number of inputs and outputs. Each input has a corresponding weight that is multiplied by the received input signal. If the sum of the weighted inputs is above the threshold for that neuron the neuron fires a signal. The weights assigned to the inputs and the neuron threshold are refined through training. Essentially, each individual rule represents a neuron, a combination of two rules represents a neural connection, and each serial combination of rules between the original inputs and the overall ANN output represents a layer. The neural connections can be layered, i.e., the connections can be hidden from the original inputs and/or the overall ANN output.

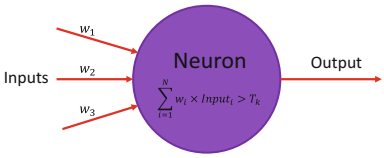

Fig. 4 Illustration of neuron connections and weights

Typically, the neurons and their layered connections are created via a training process where representative cases are provided as inputs to create internal sets of rules for classification. The ANN learning process entails determination of the appropriate weighting of each neuron to achieve correct classification of the known samples of the training data set. After the training is accomplished, other known samples not used in the original training data set, i.e., the validation data set, can be run through the ANN and the classification results compared to the true values to determine the classification error rate. If the classification error rate for the validation data set does not meet an acceptable tolerance level, then more characteristic samples are needed to rebuild and retrain the ANN. Upon achieving an acceptable error rate tolerance level, the ANN is ready to be applied to unknown samples, i.e., test data sets, for classification.

A major strength of using ANNs is robustness in the presence of noise, as the correct output can be achieved via the training process of adjusting neural weights, thus minimizing its impact. Fundamentally, an ANN is a nonlinear process that uses numerous nonlinear (i.e., multidimensional), multiple relationships (i.e., multivariable) within the data to achieve a classification. This contrasts with a linear method that uses a few well defined linearly related variables and is thus inherently susceptible to noise. An underlying requirement for ANN success is the use of a sufficient number of well demarcated samples for training. ANN performance directly correlates to the quality of the training data set. A notable downside of using ANNs is that the practical and/or physical basis for a given rule (i.e., neuron) or result (i.e., output) is not readily obvious. At times, this makes it difficult to achieve meaningful insights.

Development of an Artificial Neural Network Algorithm/Method for Detection of Cracking Due to Alkali-Silica Reaction

For the specific application of ASR detection, with robustness to noise in mind, we developed an ANN-based automated classification algorithm for non-ASR versus ASR samples. A single input (an A-scan from a transducer pairing) is passed to 10 neurons, whose output is then weighted and summed to predict the classification label as damaged or undamaged. The training data set consisted of the raw A-scan signals of the 45 linear array (MIRA) transducer pairing combinations from previously classified representative samples (i.e., ground truth). As shown in Fig. 5,

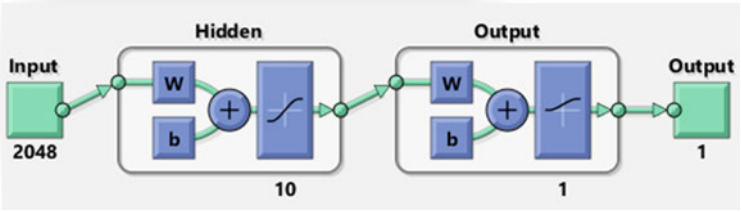

Fig. 5 Visualization of the implemented network

a single-layer ANN with 10 interior neurons and one output neuron was used to define an ANN classification based on the appropriate weighting to ensure the accurate prediction of non-ASR and ASR ground truth samples used for the training.

For the training set, we used data from one undamaged concrete sample—the Nefertiti specimen. All six regions of the specimen were included in the data set. For ASR damage data, we used two specimens—the Ramses and Cleopatra specimens [8]. For the Ramses and Cleopatra specimens, we included the odd and even positions, respectively. The complete data set was then randomly subdivided into three subsets: 70% training, 15%, validation and 15% testing data sets. The ANN receives an ultrasound time series and classifies the signal as 0 for undamaged, 1 for damaged. The confusion matrix in Fig. 6 summarizes the results for our training and testing. The algorithm correctly classified the testing data set more than 95% of the time.

It was observed that false positives (i.e., classifying a healthy specimen as damaged) were below half of a percent, while there was an order of magnitude increase in false negatives (i.e., classifying a damaged specimen as healthy). This increase in false negatives may be due to mislabeling of the ground truth data. The significance of the classification could be enhanced by changing the ANN training to a regression problem (i.e., the ANN will return a floating-point value similar to HTI) and consider the damage estimates of neighboring regions as part of the classification of a region of interest. Recall that the ANN considers each transducer pairing time series as a sample. This may be problematic as known classification labeling is at the ultrasound system position level and not at the level of each time series. In other words, every pairing is labeled with the same classification label even though each pairing traces a different path through the sample. It is possible for ASR damage to be present in a scan position but not in the path of a specific transducer pairing. Consequently, the training data sets were regrouped by transducer pair distance.

The right axis in Fig. 7 shows the error rate for each transducer pair distance set. The prediction error presented is based on the average results from 50 independent networks that were trained on different randomly selected training, validation, and testing data sets. As such, the contribution of statistical errors has been minimized to achieve a better comparison between pairings. Still, note that the error stays

Fig. 6 Confusion matrices for the data set in four categories: training set,validation set, testing set, and total

below 5% for all distances apart from the group with the lowest number of available samples—the maximum pairing distance. Therefore, the results for this group should be discarded, as data from more specimens are required. However, this may explain the increase in the number of false negatives in the overall tests.

Extracting Meaningful Insights from the Artificial Neural Network Algorithm/Method for Detection of Cracking Due to for Alkali-Silica Reaction

The results of the ANN weightings for each of the aforementioned pretreatments are presented in Fig. 8 with each colored line representing an individual neuron. A few insights are revealed from these plots. First, the networks do not diverge in

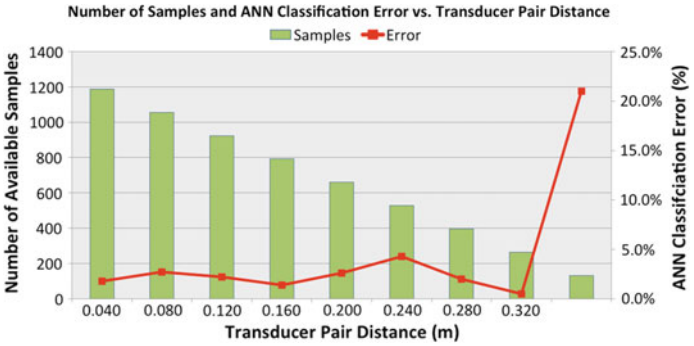

Fig. 7 Size of data set for each of the nine possible probe-space pairings and the artificial neural network (ANN) prediction error

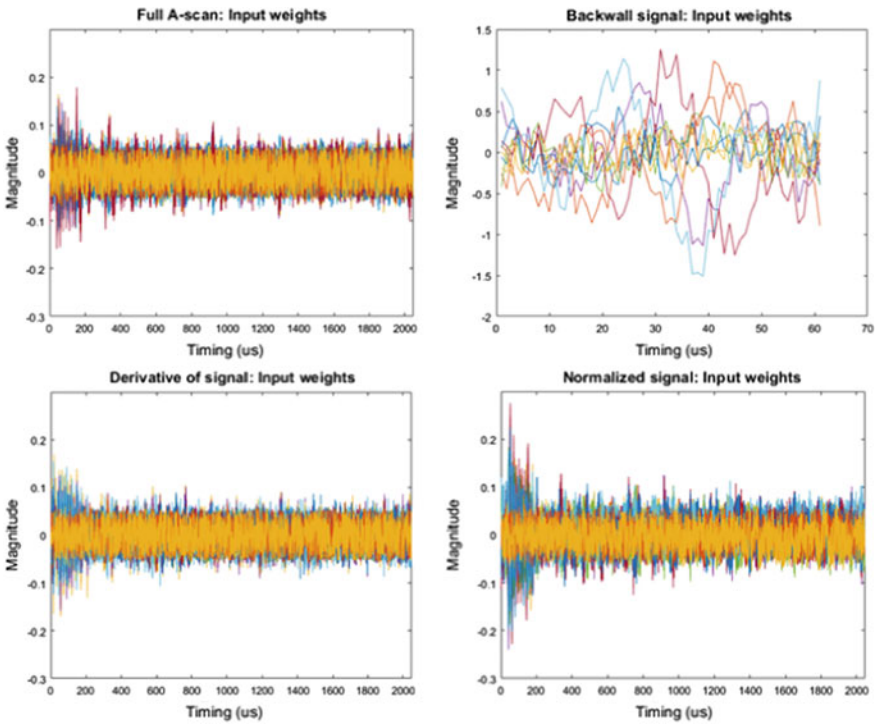

Fig. 8 Weights of each neuron in the network after training on the specified data set

amplitudes for the independent treatments but instead exhibit similarities for various epochs in the time series, i.e., time domain features. In particular, the weightings for the networks of the original raw and normalized signals exhibit the same pattern, with strong weights in the region containing the cross-talk and the back wall reflection signals. They also share significant weighting of the second

Fig. 9 Confusion matrices for the data set in four categories: training set, validation set, testing set, and total

reflection signal that is in the vicinity of 400 μs. Therefore, the experiments were repeated for time series samples with high back wall reflection likelihood.

Figure 9 shows the classification error rates when using the original and post-processed data for training. The data set consisted of the initial signal, the back wall signal, the derivative of the signal, and the normalized signal. The postprocessed data results were assembled in three groups: the derivative of the raw time series, the standard score normalized time series, and the truncated time series that was selected for back wall reflected samples. All results were comparable, with best ANN classification performance when the network was trained with the normalized signals.

Conclusions

As a result of ASR, water is absorbed, leading to swelling, abnormal expansion, and cracking of concrete. This in turn leads to significant loss of mechanical properties, severely impacting the durability and performance of concrete structures.

A technique for the automated data analysis for the detection of cracking generated by ASR in concrete specimens is documented. In comparing both methods, the ANN technique shows great potential with classification accuracy above 95%. Further assessment of these techniques should be performed with a larger set of specimens to confirm and validate the results presented in this report. Note that these approaches are extensible to the detection of additional defects and damage in heavily reinforced, thick concrete structures.

Acknowledgements This work was funded by the U.S. Department of Energy Office of Nuclear Energy under the Light Water Reactor Sustainability program.

References

1. Z. Shao, L. Shi, Z. Shao, J. Cai, Rev. Sci. Instrum. **82**, 073708 (2011)
2. B.J. Engle, J.L.W. Schmerr, A. Sedov, AIP Conf. Proc. **1581**, 49 (2014)
3. G. Dobie, S.G. Pierce, G. Hayward, NDTE Int. **58**, 10–17 (2013)
4. J.A. Jensen et al., Synthetic aperture ultrasound imaging. Ultrasonics **42**, e5–e15 (2006)
5. M.-L. Li, W.-J. Guan, P.-C. Li, Improved synthetic aperture focusing technique with applications in high-frequency ultrasound imaging. IEEE Trans. Ultrason. Ferroelectr. Freq. Control **51**(1), 63–70 (2004)
6. K. Freeseman, K. Hoegh, L. Khazanovich, Characterization of concrete at various freeze-thaw damage conditions using SH-waves. AIP Conf. Proc. **1706**(1) (2016) (020017-1-8)
7. D.A. Clayton, L. Khazanovich, L. Salles, *Linear Array Ultrasonic Test Results from Alkali-Silica Reaction (ASR) Specimens*, ORNL/TM-2016/159, Oak Ridge National Laboratory (2016)
8. R.N. Swamy (ed.), *Characterization of ASR damage in concrete using nonlinear impact resonance acoustic spectroscopy technique* (Van Nostrand Reinhold, New York, NY, 1992), pp. 1–28

Coupled Physics Simulation of Expansive Reactions in Concrete with the Grizzly Code

Benjamin W. Spencer and Hai Huang

Abstract The Grizzly code is being developed under the US Department of Energy's Light Water Sustainability program as a tool to model aging mechanisms and their effects on the integrity of critical nuclear power plant components. An important application for Grizzly is the modeling of aging in concrete structures, which can be due to a number of mechanisms. Initial focus in this area has been on modeling expansive reactions due to alkali-silica reactions or radiation-induced volumetric expansion. Grizzly is an inherently multiphysics modeling platform that naturally permits including the effects of multiple coupled physics in a simulation. Models have been developed for transport of heat and moisture in concrete, and these have been coupled and used as inputs to models for expansive reactions. This paper summarizes this capability, and demonstrates it on a representative structure.

Keywords Concrete · Alkali-silica reaction · Multiphysics simulation

Introduction

The fleet of commercial power reactors provides a significant portion of the reliable, emission-free electrical power in the United States. Many of the components in nuclear power plants are subjected to harsh operating environments, and experience degradation over time. Because of the resources and time involved in constructing new nuclear power plants, to maintain this nuclear generating capability, continued operation of existing plants is essential. The U.S. Department of Energy's Light Water Reactor Sustainability (LWRS) program is performing research and devel-

B.W. Spencer (✉)
Fuels Modeling and Simulation, Idaho National Laboratory,
P.O. Box 1625, Idaho Falls, ID 83415-3840, USA
e-mail: benjamin.spencer@inl.gov

H. Huang
Energy and Environment Science and Technology, Idaho National Laboratory,
P.O. Box 1625, Idaho Falls, ID 83415-3840, USA

J.H. Jackson et al. (eds.), *Proceedings of the 18th International Conference on Environmental Degradation of Materials in Nuclear Power Systems – Water Reactors*, The Minerals, Metals & Materials Series, https://doi.org/10.1007/978-3-319-68454-3_12

opment to address issues associated with aging, supporting the safe and economical long term operation of existing commercial light water reactors (LWRs).

The ability to assess the effects of aging mechanisms on nuclear power plant components is an important part of this effort. To that end, a simulation code known as Grizzly is being developed under the LWRS program. Grizzly can perform physics-based predictive simulations of aging mechanisms, as well as their effects on the safe operation of those components. Development priority in Grizzly is directed at those components that are most critical and for which mitigation is most expensive. Initial development was primarily focused on simulation of embrittlement and its effects in reactor pressure vessels [1].

More recently, efforts have also been undertaken to develop tools to predict degradation mechanisms in concrete components. Many critical nuclear power plant structures are constructed of reinforced or prestressed concrete. These are subjected to many of the same degradation mechanisms experienced by other civil concrete structures, in addition to some that are unique to the nuclear reactor environment. The Expanded Materials Degradation Assessment (EMDA) effort [2] recently identified these mechanisms and prioritized research needs based on the lack of current knowledge and the importance of those mechanisms.

Alkali-silica reaction (ASR) is a degradation mechanism common to many civil concrete structures, but was identified by the EMDA as one of the high priority research areas because of its potentially large impact on containment structures. ASR is a chemical reaction between alkali and hydroxyl ions in the cement pore water and amorphous siliceous materials in aggregates. These reactions produce a gel that expands when it comes in contact with water, leading to volumetric expansion of the concrete. This volumetric expansion can cause local and global structural damage. The rate of ASR is dependent on the local temperature and moisture content, as well as the stress state. Higher humidity and temperature accelerate the reaction, while compressive stresses slow down the expansion. Stresses redistribute the expansion in an anisotropic manner, with greater expansion occurring in the directions with lower compressive stress. The susceptibility of concrete to ASR is highly dependent on the composition of the aggregates—some aggregates are much more reactive than others.

ASR, like many other concrete degradation mechanisms, depends on multiple coupled physical phenomena. Numerical simulation of ASR requires a capability to model coupled equations of heat and moisture transfer and mechanical deformation. This paper provides a summary of the governing equations and constitutive models, models for ASR and accompanying volumetric expansion. It also discusses the implementation of those models in Grizzly's coupled physics solution environment, and the application of these models to an idealized engineering-scale model of a concrete structure. The assembly of the models used here is documented by [3], and more details of the Grizzly implementation are provided in [4]. This represents a foundational capability that will be expanded upon to address other degradation mechanisms in the future.

Governing Equations

Modeling ASR requires the solution of partial differential equations (PDEs) for three field variables of interest: temperature (T), pore relative humidity (H), and displacement (u). The equations for heat transfer, moisture transport, and mechanical deformation that govern the solution of those variables are summarized here.

Heat Transfer

Heat transfer in concrete is governed by the following equation [3, 5]:

$$\rho C \frac{\partial T}{\partial t} = \nabla \cdot (k \nabla T) - C_w \mathbf{J} \nabla T + C_a \frac{\partial W}{\partial H} \frac{\partial H}{\partial t} + Q, \tag{1}$$

The terms in this equation, in order, represent the transient behavior, conduction, convective transport, pore wall adsorption, and volumetric heat sources. In this equation, ρ is the density, C is the specific heat, and k is the thermal conductivity of concrete. C_w is the mass density and isobaric (constant pressure) heat capacity of liquid water, and $\mathbf{J}$ is the moisture flux, $-D_h \nabla \mathbf{H}$. W is the water (moisture) content per unit volume of material, C_a is the heat absorption of free water, $\frac{\partial W}{\partial H}$ is the moisture capacity per unit volume, Q is the rate of heat per unit volume generated within the body, and t is the time.

A number of models have been developed for the coefficients in Eq. 1 such as the specific heat and thermal conductivity as a function of concrete characteristics, temperature, and relative humidity, and are documented in detail in [4].

Moisture Transfer

Moisture diffusion is formulated based on pore water relative humidity in the following governing equation [3]:

$$\frac{\partial W}{\partial H} \frac{\partial H}{\partial t} = \nabla (D_h \nabla H) + \nabla (D_{ht} \nabla T) + \frac{\partial W_d}{\partial t}, \tag{2}$$

The terms in this equation, in order, represent the transient behavior, Fickian diffusion, Soret diffusion, and paste dehydration. In this equation, P_{vs} is the saturated vapor pressure ($P_{atm} e^{\left(4871.3 \frac{T-100}{373.157}\right)}$, where T is in K), and P_{atm} is the standard atmospheric pressure (101.325 Pa). D_h is the moisture diffusivity (also referred as humidity diffusivity), D_{ht} is the moisture diffusivity under temperature gradients,

and W_d is the total mass of free evaporable water released into the pores by dehydration of the cement paste.

The moisture capacity $\partial W/\partial H$ and moisture diffusivity D_h both depend on H, making it highly nonlinear. Because H is dependent on T, moisture diffusion and heat transfer must be solved as a coupled set of equations. Similar to the heat transfer model, multiple models have been developed for the coefficients in Eq. 2, and are documented in detail in [4].

Mechanical Deformation

Mechanical deformation is governed by the stress equilibrium equation:

$$\nabla \cdot \boldsymbol{\sigma} + \rho \boldsymbol{f} = 0 \tag{3}$$

where $\boldsymbol{\sigma}$ is the stress tensor and $\boldsymbol{f}$ is the vector of body forces such as gravity per unit mass (such as from gravity). A mechanical constitutive model is used to compute stress as a function of strain $\boldsymbol{\epsilon}$. The simplest such model is an elastic model, where $\boldsymbol{\sigma} = \boldsymbol{E}\boldsymbol{\epsilon}$, and $\boldsymbol{E}$ is the elasticity tensor. For geometrically linear analysis, the strain can be computed from the displacement, $\boldsymbol{u}$, as $\boldsymbol{\epsilon} = \frac{1}{2}(\nabla \boldsymbol{u} + (\nabla \boldsymbol{u})^T)$. To account for the effects of strains induced by intrinsic phenomena, such as thermal expansion or swelling, those strains are added to $\boldsymbol{\epsilon}$ prior to the stress calculation.

Alkali-Silica Reaction Models

The method used in Grizzly for computing ASR-induced strains is based on the approach of Saouma and Perotti [6], which adds stress-dependent effects to a model originally proposed by Ulm et al. [7]. This first involves solving ASR kinetics equations to compute the extent of reaction. Once that is known, the strains induced by ASR are computed and applied to the total strain tensor.

Alkali-Silica Reaction Kinetics

The extent of ASR reaction is represented by the variable ξ, which varies from 0 to 1, where 1 represents fully reacted material. The following differential equation describes the evolution of ξ at a given material point as a function of stress, temperature, and a set of parameters describing the concrete:

$$t_C(\theta,\xi)\cdot\frac{d\xi}{dt}=\tau_C(\theta)\cdot\frac{1+exp[-\tau_L(\theta,I_\sigma,f_c')/\tau_C(\theta)]}{\xi+exp[-\tau_L(\theta,I_\sigma,f_c')/\tau_C(\theta)]}\cdot\frac{d\xi}{dt}=1-\xi, \tag{4}$$

where θ is the temperature (used instead of T to be consistent with [7] and [6]), and the characteristic and latency times $\tau_C(\theta)$ and $\tau_L(\theta,I_\sigma,f_c')$ are expressed as:

$$\tau_C(\theta)=\tau_C(\theta_0)exp[U_C(1/\theta-1/\theta_0)] \tag{5}$$

$$\tau_L(\theta,I_\sigma,f_c')=f(I_\sigma,f_c')\tau_L(\theta_0)exp[U_L(1/\theta-1/\theta_0)] \tag{6}$$

Here θ_0 is the reference temperature (the temperature at which stress-free ASR experiments are carried out), I_σ is the first invariant of the stress tensor, f_c' is the uniaxial compressive strength of concrete, and U_L and U_C are thermal activation energy constants for the latency and characteristic times, respectively.

Per [6], compressive stress slows ASR, and this effect is accounted for in $f(I_\sigma,f_c')$, which modifies the latency time, and is computed as:

$$f(I_\sigma,f_c')=\begin{cases}1 & if \quad I_\sigma>0\\ 1+\alpha\frac{I_\sigma}{3f_c'} & if \quad I_\sigma\le 0\end{cases} \tag{7}$$

Based on experimental data, a value of 4/3 is suggested for the constant α by [6] based on the triaxial experiments of [8]. This has no effect under tensile stress, but increases latency time under compressive stress.

Equation 4 is solved in an incremental form for the updated value of ξ at each integration point at each time step using local Newton iterations.

Alkali-Silica Reaction Induced Strains

After determining the increment in ASR ($\Delta\xi$) for a step, the volumetric strain increment $\Delta\varepsilon_{vol}^{ASR}$ is then computed as:

$$\Delta\varepsilon_{vol}^{ASR}=\Gamma_t(f_t',\sigma_I|COD)\;\;\Gamma_c(\bar{\sigma},f_c')\;\;g(H)\;\;\Delta\xi\;\;\varepsilon^{\infty}(\theta_0) \tag{8}$$

where $\Gamma_t(f_t',\sigma_I|COD)$ is a function that reduces ASR expansion due to tensile cracking, $\Gamma_c(\bar{\sigma},f_c')$ is a function that reduces ASR expansion due to compressive stresses, $g(H)$ is a function that decreases expansion when there is reduced water content, and $\varepsilon^{\infty}(\theta_0)$ is the maximum unrestrained volumetric expansion at a reference temperature. In these functions, f_t' is the tensile strength of the concrete, COD is the crack opening displacement, $\bar{\sigma}$ is the ratio between the hydrostatic stress and compressive strength of concrete.

Microcracks form in concrete under compressive or tensile loading, which leads to ASR gel being adsorbed in those microcracks. In the present work, cracking is

not included, so the $\Gamma_t(f'_t, \sigma_I | COD)$ term in Eq. 8 is set to 1.0. If cracking is included in the model, [6] documents a procedure to compute that term to take the effects of cracking into account.

The function that accounts for reduction of ASR expansion under compressive stress is [6]:

$$\Gamma_c = \begin{cases} 1 & if \quad \bar{\sigma} \leq 0 \quad \text{tension} \\ 1 - \frac{e^{\beta}\bar{\sigma}}{1+(e^{\beta}-1)\bar{\sigma}} & if \quad \bar{\sigma} > 0 \quad \text{compression} \end{cases} \tag{9}$$

$$\bar{\sigma} = \frac{\sigma_I + \sigma_{II} + \sigma_{III}}{3f'_c} \tag{10}$$

where the exponent β is an empirical constant (between -2 and 2 according to [6] and $\bar{\sigma}$ is the ratio between the hydrostatic stress and compressive strength of concrete.

The function $g(H)$ in Eq. 8 accounts for the dependency of gel expansion on the water in concrete [6]:

$$g(H) = H^m, \tag{11}$$

where the exponent m is an empirical constant and H is the relative humidity in concrete. $g(H)$ can vary between 0 and 1.

Figure 1 shows representative histories of the evolution of ASR predicted by this model over time using varying values of the parameters $\tau_C(\theta_0)$ and $\tau_L(\theta_0)$ to illustrate their effect on the response. This shows how increasing $\tau_C(\theta_0)$ increases the duration of time over which the reaction occurs, while increasing $\tau_L(\theta_0)$ delays the beginning of the reaction.

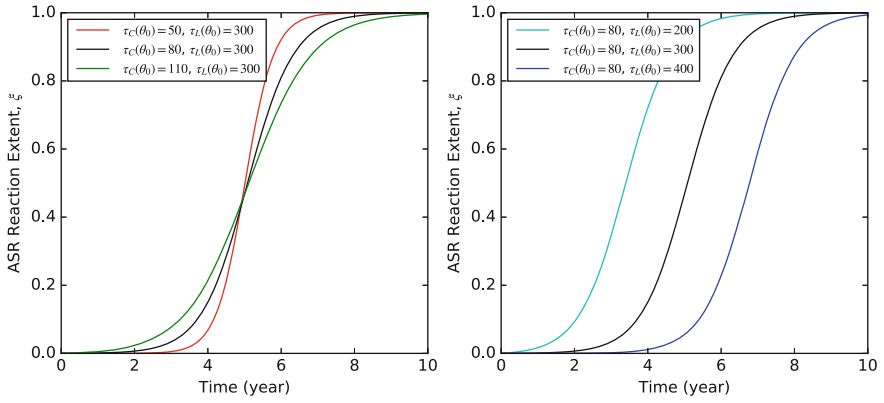

Fig. 1 Time history of ASR reaction extent, showing the effect of varying $\tau_C(\theta_0)$ (left) and $\tau_L(\theta_0)$ (right), with $\theta_0 = 37.85\,^{\circ}\text{C}$, under conditions where temperature is held constant at $20.0\,^{\circ}\text{C}$ and relative humidity is constant at 0.5

Anisotropic ASR Strains and Weights in Principal Directions

The final step in the approach of [6] is to distribute the strains due to ASR in the principal stress directions. ASR will cause higher strains oriented in the principal stress directions that are more tensile. An eigensolver is used to determine the principal stress directions, and the procedure of [6] is used to distribute the ASR-induced strains in those directions.

Multiphysics Solution Environment

Because the progression of ASR is dependent the solution of PDEs describing multiple coupled physics, solving the governing equations outlined in the previous sections must be done a solution environment that is capable of solving such problems. The MOOSE simulation framework developed at Idaho National Laboratory was developed specifically to solve coupled physics problems on parallel computers. MOOSE's development has been primarily motivated by applications to nuclear fuel performance and reactor physics [9], but it has been also applied to a wide variety of other applications, and the framework is publicly available under open source licensing. Grizzly is based on MOOSE, and relies on its multiphysics capabilities.

MOOSE provides a framework for solving PDEs based on the finite element method. It has a highly modular, object-oriented architecture, and provides a set of interfaces that allow developers to easily extend it to solve new physics equations or include new models for material behavior. Code modules based on MOOSE have ready access to all solution variables, which makes it straightforward to develop models that depend on multiple physics. This is the case for ASR simulations, where models depend on humidity, temperature, and stress. Using the pluggable interfaces provided by MOOSE, code modules for all of the terms in the PDEs for heat and moisture transport and mechanical deformation have been implemented in Grizzly, including a comprehensive set of models for the material properties in those equations.

MOOSE employs a preconditioned Jacobian-free Newton Krylov solution scheme to solve the full set of equations in a tightly coupled manner. This scheme does not require the full Jacobian matrix to be formed, but uses a finite-difference approximation of it within a Krylov method to compute the iterative update to the solution vector within a Newton method. An important benefit of this technique is that it does not explicitly require the application developer to provide the off-diagonal entries in the Jacobian matrix corresponding to coupling of physics, which can be a major challenge.

Validation

A limited set of validation problems has been developed, and is documented in [4]. This includes a problem on coupled heat/moisture transfer, as well as a set of laboratory problems with prescribed heat and moisture environment and a variety of mechanical constraint conditions that permit a comparison of predicted ASR expansion with experimentally measured values. Grizzly predictions in these cases were generally quite good, but a much larger set of validation problems is needed to provide a capability that can be confidently applied to large-scale structural analysis. Work is underway at the University of Tennessee, Knoxville on large-scale experiments intended to validate this model, as described in [10].

Example Application

A model of a structure representative of those found in a nuclear power plant was constructed to demonstrate the coupled ASR model described here. This model is of a portion of a thick-walled cylindrical concrete structure, modeled here using a 2D axisymmetric representation. The cylinder has an inner radius of 19.0 m, and a wall thickness of 1.5 m. A 10 m tall section of this structure is modeled here. Only a portion of the structure in the vertical direction is modeled, and the part modeled is intended to represent the behavior in the region at ground level, so the lower portion of this section is assumed to be below ground level, while the upper portion is above ground level.

Figure 2 shows the finite element mesh used to represent this structure. It is important to note that there are two very important simplifications made in this model: it does not contain reinforcing bars, and concrete is modeled using an elastic material model, so there is no provision to model cracking or nonlinear behavior under compression. These are both very important for a realistic simulation, but are features that are not yet available in Grizzly. Because of this, this simulation is intended only as a demonstration of current Grizzly capabilities, and not as an analysis of any real structure.

This structure is assumed to have a liner that would act as a moisture barrier on the inner surface, so there are no-flux boundary conditions for moisture transport on the left surface, as well as the top and bottom surfaces, which are continuous with the rest of the structure. On the outer surface, the lower half of the structure has a prescribed relative humidity of 1.0, which linearly ramps down to 0.5 between the mid-height and top of the structure, to represent the transition from conditions in the soil to atmospheric conditions. The temperature on the inner surface is prescribed at 26.6 °C. On the outside, the temperature is 5 °C below the mid-height, and increases linearly up to 10 °C at the top of the model. As for moisture, the top and bottom surfaces are insulated. Mechanically, the bottom surface is restrained against vertical displacement, and the top surface is free to move in the vertical direction, but

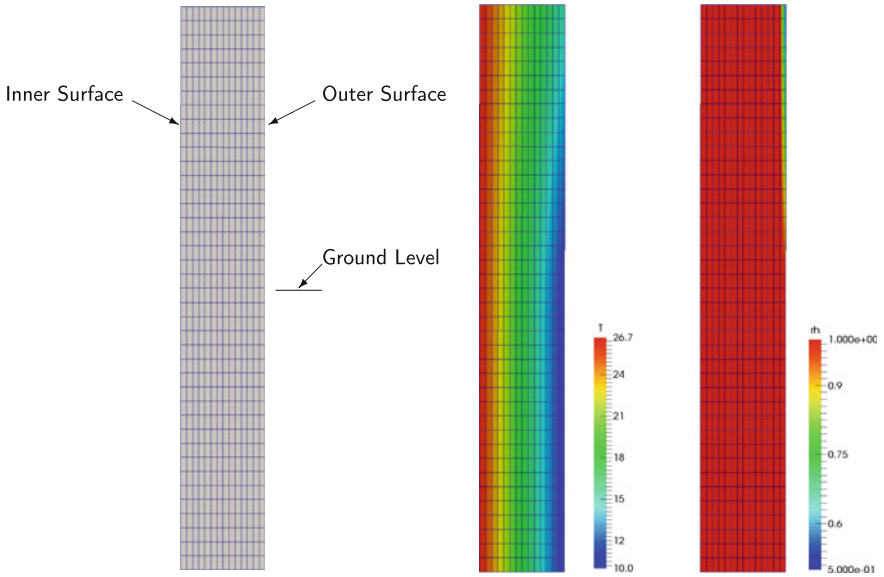

Fig. 2 Cylindrical structure model with results after 10 years. (left) Finite element mesh, (center) Temperature (K), (right) Relative Humidity (fraction)

all nodes on that surface are constrained to have the same vertical displacement, so that surface remains horizontal. Body forces are applied for gravity loading, and a dead load due to 20 m of additional cylindrical structure above this structure is applied to the top surface.

Multiple options are available for the moisture diffusivity model. The Bažant model [5] was used in this case. Constant values of $k = 3W/(m\,^{\circ}\mathrm{C})$ and $C = 1100.0\,\mathrm{J/(kg\,^{\circ}C)}$ were used in the heat conduction model. The following parameters governing the ASR kinetics and resulting strains were used here: $\theta_0 = 37.85\,^{\circ}\mathrm{C}$, $U_L = 9400\,K$, $U_C = 5400\,K$, $\tau_C(\theta_0) = 80.0$, $\tau_L(\theta_0) = 300.0$, and $\varepsilon^{\infty} = 0.00262$. These parameters are highly dependent on the reactivity of the specific concrete being considered, and have a strong influence on the mechanical behavior. It is important to emphasize that these do not represent the behavior of any specific concrete mixture, and are only used for demonstration purposes.

This model was subjected to the boundary conditions described above for 10 years, and Figs. 2 and 3 show some key solution fields obtained from this tightly coupled simulation. The temperature varies nearly linearly across the section, and the relative humidity decreases over a small zone near the outer surface at the top where the humidity is decreased, as shown in Fig. 2. Because of the sharp gradient in the relative humidity field near that surface, a more refined mesh may be necessary to capture that gradient for some applications. In Grizzly's tightly coupled physics simulation strategy, the same mesh must be used for all solution fields, but it is possible to use a separate mesh for fields with different refinement needs, and transfer solutions between them using a staggered solution strategy.

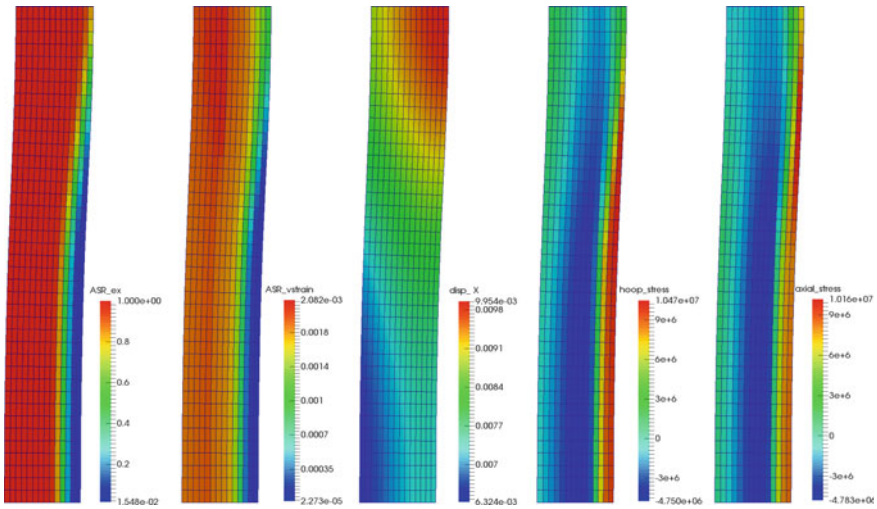

Fig. 3 Mechanical response parameters for cylindrical structure after 10 years (displacements magnified 100×). From left to right: ASR reaction extent, ASR volumetric strain, x-component of displacement (m), hoop stress (Pa), axial stress (Pa). Tensile stresses are positive

The fields relating to mechanical response are shown in Fig. 3, and the displacements are shown magnified 100× in those results. After 10 years, the inner portion of the wall has experienced full ASR reaction because the reaction is highly temperature sensitive, and the temperature is higher in that region. The volumetric strains from ASR are also higher in that region, as would be expected. Because the temperature is higher in the upper portion of the structure, ASR reaction and strains are higher, and the radial displacement is also higher. The radial displacement of this structure ranges from about 6 to 10 mm. Because this model does not include cracking, there are high tensile hoop stresses near the outer surface. In reality, those would be significantly decreased due to cracking. Including that is the subject of ongoing work. There are significant axial stresses induced by the nonuniform behavior in this model. Often, the most damaging effects of ASR are due to stresses induced by local nonuniformities in the extent of the ASR reaction and accompanying volumetric strains. Although it is still missing some important features, this simulation demonstrates that Grizzly is capable of simulating some key aspects of ASR behavior.

Summary

ASR is one of a number of mechanisms that can degrade concrete structures over time. A tool that can be used to predict future progression of these degradation mechanisms and assess their effects on a structure in its current state can be very

useful for making safety and economic decisions regarding long term operation of nuclear power plants. This paper summarizes the current state of capabilities in Grizzly for solving coupled physics models of heat and moisture transport and mechanical deformation induced by ASR. It also demonstrates an application of these capabilities to a prototypical structure. Development is underway to extend Grizzly to include models for concrete cracking and other nonlinear mechanical behavior, and to include models of reinforcement, both of which are essential for realistic models of ASR-affected structures. In addition, work is underway to include models for radiation-induced volumetric expansion in Grizzly. In addition to this model development, additional work is also needed to develop validation data for the parameters used the ASR models shown here.

References

1. B. Spencer, M. Backman, P. Chakraborty, W. Hoffman, Reactor pressure vessel fracture analysis capabilities in Grizzly. Technical Report INL/EXT-15-34736, Idaho National Laboratory, Idaho Falls, ID, March 2015
2. H. Graves, Y. Le Pape, D. Naus, J. Rashid, V. Saouma, A. Sheikh, J. Wall, Expanded Materials Degradation Assessment (EMDA) Volume 4: Aging of Concrete and Civil Structures. Technical Report NUREG/CR-7153, Vol. 4, ORNL/TM-2013/532, Oak Ridge National Laboratory, Oak Ridge, TN, October 2014
3. V. Saouma, M. Hariri-Ardebili, W. Puatatsananon, Y. Le Pape, Structural significance of alkali-silica reaction in massive reinforced concrete structures. Technical Report ORNL/TM-2014/489, Oak Ridge National Laboratory, 2014
4. H. Huang, B.W. Spencer, G. Cai. Grizzly model of multi-species reactive diffusion, moisture/heat transfer and alkali-silica reaction in concrete. Technical Report INL/EXT-15-36425, Idaho National Laboratory, Idaho Falls, ID, September 2015
5. P. Zdeněk, Bažant, Jenn-Chuan Chern, and Werapol Thonguthai. Finite element program for moisture and heat transfer in heated concrete. Nucl. Eng. Des. **68**(1), 61–70 (1982)
6. Victor Saouma and Luigi Perotti. Constitutive model for alkali-aggregate reactions. ACI Mater. J. **103**(3), 2006
7. Franz-Josef Ulm, Olivier Coussy, Li Kefei, Catherine Larive, Thermo-chemo-mechanics of asr expansion in concrete structures. J. Eng. Mech. **126**(3), 233–242 (2000)
8. S. Multon, F. Toutlemonde, Effect of applied stresses on alkali–silica reaction-induced expansions. Cem. Concr. Res. **36**(5), 912–920 (2006)
9. D.R. Gaston, C.J. Permann, J.W. Peterson, A.E. Slaughter, D. Andrš, Y. Wang, M.P. Short, D.M. Perez, M.R. Tonks, J. Ortensi, L. Zou, R.C. Martineau, Physics-based multiscale coupling for full core nuclear reactor simulation. Ann. Nucl. Energy **84**, 45–54 (2015)
10. A.B. Giorla. Simulation of concrete members affected by alkali-silica reaction with grizzly. Technical Report ORNL/TM-2016/523, Oak Ridge National Laboratory, Oak Ridge, TN, September 2016

Overview of EPRI Long Term Operations Work on Nuclear Power Plant Concrete Structures

Joe Wall and Sam Johnson

Abstract The Electric Power Research Institute (EPRI) has been engaged in collaborative research and development activities related to concrete in nuclear applications over the past several years in concert with the nuclear generation industry, foreign and domestic national laboratories and regulatory bodies and universities. The EPRI Long Term Operations program is focused on performing research activities that will help the industry extend operation beyond the first period of license renewal, which for US plants means operation beyond 60 years. In this overview talk, three subjects will be addressed—radiation damage in boiling and pressurized water reactor concrete biological shields, boric acid attack of pressurized water reactor spent fuel pool concrete substructures and alkali-silica reaction degradation of concrete structures. The results of these and other studies are expected to support utilities as they demonstrate technical bases to regulatory bodies for long term operation of commercial nuclear plants.

Keywords Concrete irradiation damage · Spent fuel pool leakage · Alkali silica reaction · Concrete degradation

Introduction

Long-term operation of the existing fleet of commercial power reactors in the United States is critical to any realistic energy portfolio. The original licenses for commercial nuclear reactors were for a period of 40 years. The US Nuclear Regulatory Commission (NRC) has already granted operating license extensions to 60 years for numerous US operating nuclear plants. It is anticipated that extension to 80 years operation and perhaps longer may be economically viable and

J. Wall (✉) · S. Johnson
Nuclear Sector, Electric Power Research Institute, Charlotte, NC 28262, USA
e-mail: jwall@epri.com

J. Wall
G.W. Woodruff School of Mechanical Engineering, Georgia Institute of Technology, Atlanta, GA 30332, USA

J.H. Jackson et al. (eds.), *Proceedings of the 18th International Conference on Environmental Degradation of Materials in Nuclear Power Systems – Water Reactors*, The Minerals, Metals & Materials Series, https://doi.org/10.1007/978-3-319-68454-3_13

technically achievable for most currently operating plants. Sound technical bases will be required to support utility decision making and any subsequent licensing requests and approvals for further extended nuclear plant operation.

The Electric Power Research Institute (EPRI) Long-Term Operation (LTO) and U.S. DOE Light Water Reactor Sustainability (LWRS) programs are engaged in collaborative research on materials aging in order to allow the safe, reliable, and economical operation of commercial nuclear power reactors beyond 60 years. One of the primary focus areas of this research is potential issues with aging-related degradation of reinforced concrete structures. Recently, at the request of the U.S. Nuclear Regulatory Commission (NRC), a prioritization of R&D topics for LTO of concrete structures in nuclear applications was performed by representatives from industry, U.S. national laboratories, and academia. The result of this exercise, the so-called Expanded Materials Degradation Assessment (EMDA) [1], identified potential issues for LTO of concrete nuclear structures. Irradiation damage of reactor cavity concrete was identified as a high-priority issue, primarily due to a general lack of knowledge about the effects of radiation on concrete properties and microstructure as well as potential consequence of failure of the reactor vessel support structures. The EMDA also identified degradation of pressurized water reactor (PWR) spent fuel pool concrete due to leakage of borated water coming into contact with the concrete substructure as a potential issue affecting LTO, primarily because the degradation rate was largely unknown. In addition, the document identified alkali-silica reaction (ASR) as a potential issue for LTO based primarily on recent operating experience at a plant in the US.

In response to these potentially life limiting issues, the EPRI LTO Program funded three separate studies in the areas of irradiation effects on concrete, spent fuel pool aging management and risk screening and structural effects of ASR. The concrete irradiation damage project was done via coordination with fundamental studies performed at Oak Ridge National Laboratory (ORNL). The PWR spent fuel pool concrete degradation work was done at MPR Associates and Commissariat l'Energie Atomique (CEA) in France. The ASR project is being done in concert with ongoing research funded by the US NRC at University of Texas—Austin and the National Institute of Standards and Technology (NIST).

Epri Research

Irradiation Damage in Concrete Biological Shielding

When neutrons of sufficient energy from a light water reactor core exit the reactor vessel, they collide with atoms in the concrete biological shield and cause point defects in the aggregates. These defects can agglomerate, causing macroscopic swelling at higher fluences. As a consequence, as demonstrated by Hilsdorf [2] and later Field et al. [3], neutron radiation causes a degradation of mechanical properties

in concrete after some nominal fluence damage threshold at around 1×10^{19} n/cm^2 (E > 0.1 meV) and that macroscopic swelling occurs. LePape et al. [4] showed that concrete swelling and resultant microcracking and the change in mechanical properties are correlated. A 2014 EPRI report by Esselman et al. [5] examined the different biological shield designs for PWRs and boiling water reactors (BWRs) and estimated accumulated neutron fluence at 80 years of operation using neutron fluxes measured at the inner diameter of the biological shield at the core mid plane for each operating reactor in the US fleet. It was found that the entire fleet of BWRs will be near or below 1×10^{19} n/cm^2 after 80 years. The fluence for PWRs ranges from 1×10^{19} n/cm^2 to 6.1×10^{19} n/cm^2, with the highest expected fluence for 2-loop and 3-loop PWRs (4-loop units have a thicker reactor vessel, hence the accumulated fast neutron fluence is lower).

An EPRI report was published in 2016 examining radiation damage in the US BWR fleet [6]. BWRs in the US fleet are supported from beneath by the so-called reactor vessel pedestal, which is heavily reinforced concrete and is part of the biological shield. Using a simplified, conservative analysis, which applied a distance correction to the beltline fluence using dimensions taken from an operating unit, it was demonstrated that radiation damage in BWRs will not likely affect the structural bearing capacity of the reactor vessel pedestals because the 80 year fluence at the pedestals is well below the threshold for damage published in the US Nuclear Regulatory Commission in their Standard Review Plan for Subsequent License Renewal (1×10^{19} n/cm^2) [7].

Another EPRI report was published in 2016 regarding gamma heating in PWR biological shielding due to neutron capture gamma rays [8]. Gamma rays interact with atoms in the concrete, transmitting their energy to them and causing heating. Gamma rays produced inside the reactor vessel are for the most part blocked by the steel of the reactor vessel. As such, the fission produced gamma dose in the concrete biological shielding is relatively low. However, neutrons, which are relatively transparent to steel, can be absorbed by certain atomic species in the concrete, creating neutron capture gamma rays. As such, the focus was on 2-loop and 3-loop PWRs since they have the highest neutron flux. A number of Monte Carlo n-Particle (MCNP) simulations of an operating 2-loop PWR biological shield were run to examine the factors that contribute to gamma heating in the concrete biological shields. The model was constructed in a way such that heat loads as a function of depth into the biological shield were output and fed into a finite element model that calculated the temperature as a function of depth into the biological shield. Several parameters were varied to determine sensitivity of variables. The results of the analyses indicated that the maximum temperature in the biological shield was 16 cm into the concrete and for the base case (likely operating conditions) was estimated at 175.3 °C and is expected to exceed American Concrete Institute (ACI) recommendations for localized areas [9].

As mentioned previously, neutron radiation is known to change the mechanical properties of concrete and cause macroscopic swelling. A 2016 EPRI report examines these phenomena in the context of the effects on structural margin using a simplified finite element analysis [10]. Drawings were obtained from a recently shut

down 2-loop PWR with a Westinghouse Type 1 reactor vessel support [10], which was determined to be the most susceptible design to radiation effects as is briefly discussed in [11], and used to construct the 3-D finite element model of the biological shield (60 degree section), which included the dead load of the reactor vessel and unsupported primary loop piping. The finite element model mesh is illustrated in Fig. 1. Although the model was simplified and thus has a relatively high degree of uncertainty, for example it did not consider moisture transport and temperature effects and used a relatively coarse finite element mesh, it showed that safety factors greater than 20 are expected in the five failure modes defined in the model. The model also indicated, that neutron radiation, which attenuates quickly in concrete as a function of depth, is not expected to have a significant effect on the overall load bearing capacity of the biological shield. Assigning lower bounds to several

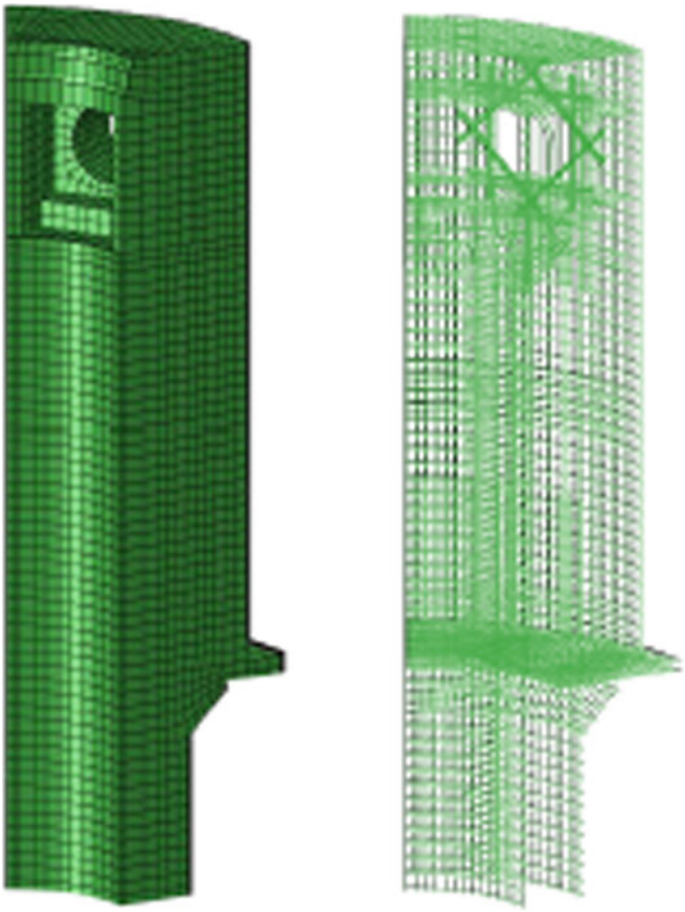

Fig. 1 Concrete brick elements and rebar truss elements used for the finite element structural model

variables such as concrete and steel strength and a statistical analysis of safety factors yielded a lower bound safety factor of ~10, which is well within the realm of safe operation. Follow up modeling efforts are underway at EPRI and ORNL currently. Follow up modeling (currently unpublished) has shown that raising the neutron fluence to the bounding value identified in [5] show a decrease in structural capacity though the margin remains relatively high (safety factor on the order of 10).

Spent Fuel Pool Concrete Degradation

PWR spent fuel pools, which act as interim storage of used fuel from a reactor, contain water poisoned with typically ~2300 ppm boric acid. Most spent fuel pools have a stainless steel liner that was seam welded together from plates that acts as the primary moisture barrier. A schematic of a PWR spent fuel pool is shown in Fig. 2. Many of these pools are leaking due to cracks in seam and plug welds into a drainage collection system. As a result, the spent fuel pool water containing aqueous boric acid can come into contact with the concrete substructure. In this case, the boric acid reacts with the constituents of the concrete. Operating experience at one plant indicated that minerals can be leached from the concrete due to pooling between the substructure and liner and be concentrated and redeposited in the leakage collection channels and obstruct them, potentially creating a groundwater contamination issue. Based on this and other operating experience, EPRI published a report on the aging management of leaking PWR spent fuel pools in 2016 [12]. The report reviews operating experience at a number of plants,

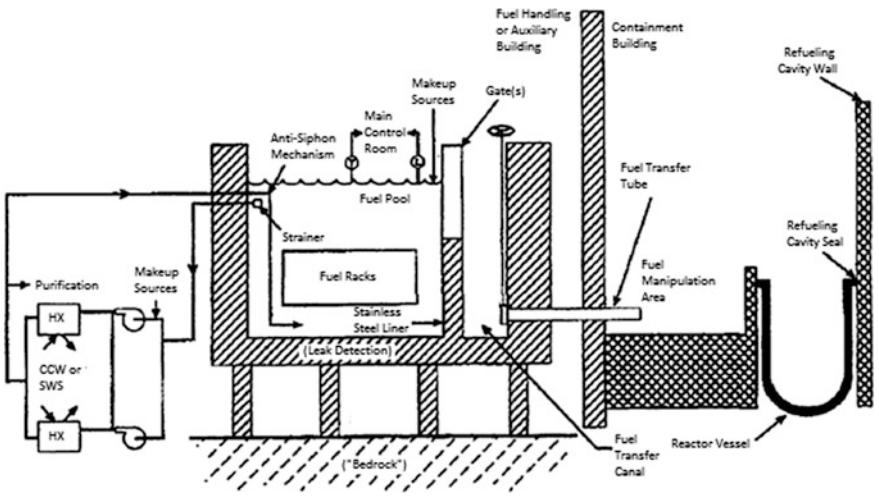

Fig. 2 Typical PWR spent fuel pool configuration

references several experimental studies on characterization of degradation of concrete due to aqueous boric acid and presents a framework for development of site-specific aging management programs. The experimental studies, one funded by EPRI performed at CEA in Saclay, France, one funded by a US utility conducted by MPR Associates and one conducted at Sandia National Laboratory, indicated that degradation generally follows classical diffusion behavior and that the kinetics of chemical degradation is sufficiently sluggish that the cover concrete is not likely to be eroded during operation to 80 years ($\sim 1.4''$ at 80 y). The CEA study found that reactive aggregate (limestone, dolomitic limestone) actually retarded the kinetics of degradation as opposed to non-reactive aggregate (granite). As such, the body of the report focuses on how to manage leakage as a full repair or replacement of the liner is not practical.

Alkali-Silica Reaction

The EMDA [1] identified alkali-silica reaction as a potential issue for long term operations of nuclear power plants and a concrete degradation mechanism that needed further research and understanding to provide proper aging management. Alkali-silica reaction (ASR) is a concrete degradation mechanism that occurs when reactive silica found in the aggregate reacts with hydroxyl ions and alkali ions in the pore solution. The reaction causes a gel, which expands in the presence of water, to form around the aggregate inducing tensile stresses on the surrounding concrete and resulting in microcracking. If the expansion and resulting tensile stresses are sufficient enough, pattern cracking of the concrete can occur.

Over the past few years, EPRI has been conducting research to provide the nuclear industry the technical basis needed to provide proper aging management for ASR affected structures. In 2015, EPRI published a report on tools for early detection of ASR [13]. This report outlines the options and steps utilities should take to assess the susceptibility of structures to ASR (reactive aggregate types), identify the symptoms of ASR (pattern cracking, warping of structures), and confirm the presence of ASR (petrography). In 2016, EPRI started to focus research efforts to providing the technical basis for aging management once ASR is confirmed at a nuclear power plant. The technical basis comes from previous research and ongoing research on ASR affected structures, guidance from other industries, and operating experience from nuclear power plants that have identified ASR. To date, EPRI has published two reports on expansion measurements and monitoring [14] and on structural deformations due to ASR [15]. Both of these reports provide guidance on what utilities should incorporate into an aging management program for extended operations, for example tracking the cracking index or monitoring strain accumulation in susceptible components. Ongoing research is looking to cover topics related to ASR such as material degradation impacts on structural performance, monitoring strategies, and repair and mitigation efforts.

Conclusion

The EPRI LTO Program is committed to supporting the nuclear industry as lead plants prepare to submit second license extensions to 80 years of operation. Proactive research has been performed by EPRI and others in anticipation of regulatory hurdles imposed by US and international regulatory bodies. Recent EPRI research in the areas of concrete degradation due to stressors such as irradiation, boric acid attack and ASR was done in anticipation of lead plant second license renewal submittals. The recent publication of the US NRC Standard Review Plan for Subsequent License Renewal [7], outlines regulatory guidance on second license renewal submittals, which is consistent with the goals of this research and potential issues as identified in the EMDA. Summaries of EPRI research on these three topics were presented within the context of LTO.

References

1. H. Graves, Y. LePape, D.J. Naus, J. Rashid, V. Saouma, A. Sheikh, J.J. Wall, Expanded Materials Degradation Assessment–Volume 4: Aging of Concrete and Civil Structures, NUREG/CR-7153(2014)
2. H. Hilsdorf, J. Kropp and H. Koch, "The Effects of Nuclear Radiation on the Mechanical Properties of Concrete", American Concrete Institute Report SP-55-10 223–254 (1978)
3. K. Field, I. Remec, Y. LePape, Radiation effects in concrete for nuclear power plants – Part I: Quantification of radiation exposure and radiation effects. Nucl. Eng. Des. **282**, 126–143 (2015)
4. Y. LePape, K. Field, I. Remec, Radiation Effects in Concrete for Nuclear Power Plants – Part II: Perspective from Micromechanical Modeling. Nucl. Eng. Des. **282**, 144–157 (2015)
5. Expected Condition of Reactor Cavity Concrete after 80 Years of Radiation Exposure, EPRI Report 3002002676 (2014)
6. Structural Disposition of Neutron Radiation Exposure in BWR Vessel Support Pedestals, EPRI Report 3002008128 (2016)
7. US Nuclear Regulatory Commission, "Standard Review Plan for Review of Subsequent License Renewal Applications for Nuclear Power Plants", NUREG-2192 (2016)
8. Long Term Operations: Impact of Radiation Heating on PWR Biological Shield Concrete, EPRI Report 3002008129 (2016)
9. American Concrete Institute, "Code Requirements for Nuclear Safety-Related Concrete Structures and Commentary", ACI 349-13 (2014)
10. Structural Model for PWR Reactor Pressure Vessel Supports—Effects of Chronic Radiation Exposure on Margin, EPRI Report 3002007347 (2016)
11. W. S. Lapay, C.Y. Yang, C. Kim, "License Renewal Evaluation: Aging Management for Reactor Coolant System Supports", Westinghouse Report WCAP-14422 (2000)
12. Aging Management for Leaking Spent Fuel Pools", EPRI Report 3002007348 (2016)
13. Tools for Early Detection of ASR in Concrete Structures EPRI Report 3002005389 (2015)
14. Long-Term Operations: Cracking-Index Criteria for Alkali Silica-Reaction Affected Structure EPRI Report 3002008117 (2016)
15. Structural Deformation as a Result of Expansion from Alkali Silica Reaction EPRI Report 3002007595 (2016)

The Effects of Neutron Irradiation on the Mechanical Properties of Mineral Analogues of Concrete Aggregates

Thomas M. Rosseel, Maxim N. Gussev and Luis F. Mora

Abstract Plans for extended operation of US nuclear power plants (NPPs) beyond 60 years have resulted in a renewed focus on the long-term aging of materials in NPPs, and specifically on reactor cavity concrete. To better understand the effects of neutron irradiation on reactor cavity concrete, a select group of mineral analogues of concrete aggregates were irradiated at the Oak Ridge National Laboratory High Flux Isotope Reactor at three different fluence levels and at two temperatures. The purpose was to investigate the degradation of mechanical properties at neutron doses above the levels expected in US NPPs under extended operation. Preliminary findings using nanoindentation clearly show that changes in the mechanical properties of these minerals can be observed and correlated to the neutron-induced damage. Scanning electron microscopy reveals changes in deformation and fracture mechanisms in the irradiated mineral analogies. Results for the nanohardness as a function of dose and temperature are presented and discussed for quartz, calcite, and dolomite.

Keywords Mineral analogues · Aggregates · Neutron irradiation · Concrete degradation · Nanohardness

T.M. Rosseel (✉) · M.N. Gussev · L.F. Mora
Oak Ridge National Laboratory, Oak Ridge, TN 37831, USA
e-mail: rosseeltm@ornl.gov

M.N. Gussev
e-mail: gussevmn@ornl.gov

L.F. Mora
e-mail: moralf@ornl.gov

J.H. Jackson et al. (eds.), *Proceedings of the 18th International Conference on Environmental Degradation of Materials in Nuclear Power Systems – Water Reactors*, The Minerals, Metals & Materials Series, https://doi.org/10.1007/978-3-319-68454-3_14

Introduction

Extending the operating lifetimes of current nuclear power plants (NPPs) beyond 60 years and making additional improvements in their productivity is essential to meeting future US national energy needs. Although much of the early research has focused on the performance and possible degradation mechanisms of metals affected by increased periods of exposure to time to temperatures, stresses, coolants, and radiation fields, other materials, such as concrete are also critical to the long-term NPP operation. To address these extended lifetimes effects, Oak Ridge National Laboratory (ORNL), through the support of the US Department of Energy (DOE), Light Water Reactor Sustainability (LWRS) Program, has established a research plan to investigate the aging and degradation processes associated with concrete used in NPPs [1, 2]. The basis for the plan arose in part from the Expanded Materials Degradation Analysis (EMDA) report *on* "*The Aging of Concrete and Civil Structures*", an effort jointly supported by DOE and the US Nuclear Regulatory Commission and performed by expert panels from US national laboratories, industry, academia, and international organizations. A key finding of the panel of experts on concrete was that there is an urgent need to develop a consistent knowledge base on radiation damage in reactor cavity concrete [3].

Over the last decade, data on the mechanical degradation of concrete due to long-term irradiation were thought to be quite limited. Moreover, recent studies have suggested that many of the data compiled in the 1978 Hilsdorf Curve [4] were not representative of concrete mixtures and radiation fields seen in LWRs [5, 6]. The reasons for these seemingly contradictory interpretations are two-fold. For many of the older experiments, important pieces of information such as the cutoff energy of the neutron fluence, composition of the concrete, irradiation temperature, and gamma-ray dose are limited or missing. Consequently, the applicability to NPP concrete may be uncertain. Furthermore, critical data may not have been in the public domain when Hilsdorf's report was completed; and fundamental studies following the publication of the Hilsdorf paper had not been compiled into a single source.

A comprehensive review of the literature by Field et al. [6] has greatly expanded the database and confirmed the predominant role of radiation-induced volumetric expansion (RIVE). Although the revised data set also has limitations, it suggests a decrease in compressive strength above a neutron dose of 2.0×10^{19} n/cm^2, with an average loss of strength of about 50% of the initial strength at 1.0×10^{20} n/cm^2. Similar trends are observed for tensile strength and elastic modulus data, with average losses of, respectively, about 60 and 30% of the initial strength at 1.0×10^{20} n/cm^2. Moreover, the development of a specifically targeted micromechanical model using the available data from literature confirms the predominant role of aggregates in the macroscopic expansion of irradiated concrete [7].

Based on these reevaluations of the accelerated irradiated concrete data found in the literature—and the confirmation of the predominant role of aggregates in the macroscopic expansion of irradiated concrete, due to the development of internal

Table 1 The fluence, flux, sample and load matrix for the SVMA experiment

Capsule ID	Fluence, n/cm^2	Flux (E > 0.1 meV), $n/cm^2/s$	Irradiation temperature, °C	Capsule type	Capsule location	Samples
C100S	5.04×10^{18}	8.4×10^{14}	~95	Sealed	HT-4 (int)	Quartz [SiO_2] Dolomite [$CaMg(CO_3)_2$] Calcite [$CaCO_3$]
C800S	4.03×10^{19}					
C4000S	2.02×10^{20}					
C100P	4.92×10^{18}	8.2×10^{14}	~52	Perforated	HT-6 (int)	
C800P	3.94×10^{19}					
C4000P	1.97×10^{20}					

damage in the aggregates—well-defined experiments that reduce uncertainty are desirable. It is also clear that accelerated irradiation experiments require considerably higher neutron and gamma fluxes than those observed in the NPP biological shields; the needed fluxes are anticipated to be higher by a factor of 50–100. Analysis of the temperatures of the samples will also be necessary, and additional cooling of concrete samples may be required. Moreover, the effects of dose rate have not been fully evaluated.

Using Seeberger and Hilsdorf [8] as a guide, three common minerals found in concrete aggregates—α-quartz (SiO_2), dolomite ($CaMg(CO_3)_2$), and calcite ($CaCO_3$)—were selected for the study based on the observation that silicates exhibit large expansion, whereas carbonates exhibit limited expansion [6]. The nominal neutron fluences selected for this study were 0.5, 4.0, and 20.0×10^{19} n/cm^2 (E > 0.1 meV) (See Table 1 for details).

Investigated Materials and Experimental Methods

Plans were developed for studying the effects of irradiation on mineral analogues of aggregate swelling in concrete using the hydraulic tube (HT) sample positions at the ORNL High Flux Isotope Reactor (HFIR) (Fig. 1a, b). Specifically, a series of short-term, high-flux irradiations of minerals at different fluence levels were performed at two temperatures. The purpose was to investigate the evolution of aggregate and mineral amorphization past typical neutron fluences seen in NPP concrete. The potential for complete amorphization can thereby be evaluated in the mineral analogues. Furthermore, the HT irradiation positions at HFIR offered several advantages over other options at HFIR. These include:

1. The ability to perform short-duration experiments because of the higher flux simplified the task of irradiating the samples at a series of neutron fluences below swelling through metamictization (amorphization).
2. A variety of capsule designs previously approved for use in HFIR were available.

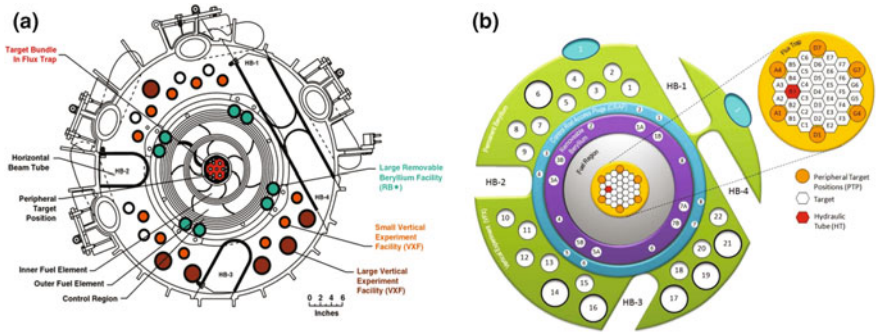

Fig. 1 **a** Schematic of the ORNL HFIR showing irradiation positions, including the flux trap; **b** reactor core assembly showing flux trap positions, including the hydraulic tube (B3). (Figures courtesy of the High Flux Isotope Reactor)

3. The ability to simultaneously irradiate two capsules with similar flux and therefore fluence.
4. The ability to irradiate sealed capsules and perforated capsules. Sealed capsules duplicated the conditions, including elevated temperature, of many of the experiments found in the literature. A perforated capsule provided an option to irradiate the samples at ~50–55 °C (coolant temperature), which was similar to the temperature of the biological shield.

The matrix of temperature, flux, fluence, and capsule load plan is described in Table 1.

Single-crystal quartz (X- and Y- cut) boules and natural calcite and dolomite crystals were cut using a Buehler IsoMet slow-speed saw. An MTI diamond wire saw was used to prepare additional samples for unirradiated baseline measurements. The quartz samples were cut so that the X and Y directions were the along the C-axis of the parent crystal. The maximum dimensions of specimens were determined by the capsule geometries, the estimated maximum swelling [6, 8], and the loading of four specimens of each mineral at the same horizontal position within each of the six capsules. Each sample was engraved or marked with a unique identification to ensure proper tracking.

The irradiated samples were mounted in epoxy and prepared using standard metallographic procedures; the final polishing step was performed using colloidal silica. Nanoindentation experiments were performed on unirradiated and irradiated single-crystal quartz, calcite, and dolomite using the Agilent Technology Inc. G200 Nanoindenter. The system provides a displacement resolution of 0.01 nm (or better) and a force resolution of 50 nN (0.05 μN). The measurements were performed using a Berkovich diamond indenter. Each experiment consisted of load, hold, and unload segments, with the unloading segment used to calculate the nanohardness and indentation modulus. The loading rate was 200 μN/s. Hold time at peak load

was 10 s, and unloading rate was 200 μN/s. Indentations were made to a maximum depth of 1000 nm (1 μm); and the maximum load value varied from ~50 to ~180 mN, depending on the material. The depth and load values were chosen based on the results of preliminary tests; it was important to ensure that the indentation depth was significantly larger than the surface features (mainly surface roughness, ~10 nm) and that the sampled volume would encompass a homogeneous representation of the material properties. At the same time, the depth value was limited to 1000 nm to avoid excess cracking and fracture of the material; this aspect was especially important for quartz.

Nano-indentation tests were performed 25 times per specimen (except unirradiated quartz specimens, for which 9–16 indentations were performed), and the average nanohardness values were calculated. The data were processed using NanoSuite software v.6.10.331 (Agilent Technology), allowing for the calculation of the nanohardness and necessary statistic parameters. The tested specimens were analyzed using an optical microscope, as well as a scanning electron microscope (SEM) equipped with a backscattered electron detector. Before the SEM analysis, the samples were coated with a thin layer of carbon to eliminate charging effects.

Experimental Results and Discussion

As shown in Fig. 2, an initial set of nanohardness values were measured for unirradiated single-crystal specimens of quartz, dolomite, and calcite. All materials revealed crack formation around the indentations. Cracking was more severe in quartz, whereas calcite and dolomite exhibited pronounced surface relief around the

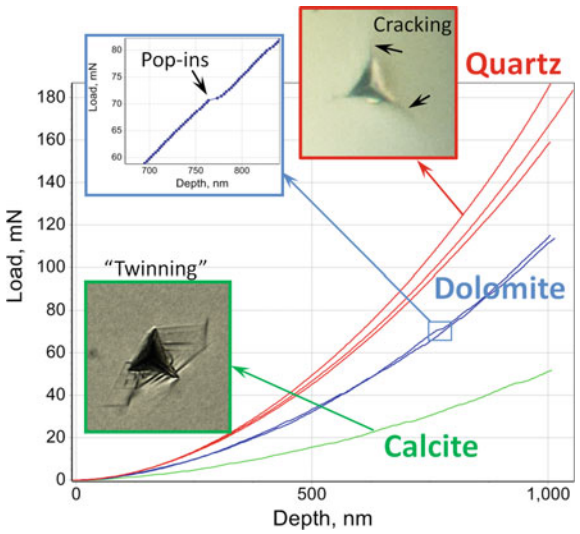

Fig. 2 Representative "load versus depth" curves for 1000 nm indentations for unirradiated quartz, dolomite, and calcite. Insertions show indentation appearance for calcite and quartz (optical microscopy) and illustrate a pop-in event for dolomite

indentation, probably caused by twinning. Nano-indentation load-depth curves contained specific pop-in events (steps or discontinuities), most likely due to cracking and twinning. These discontinuities were more pronounced in calcite and dolomite samples compared with quartz.

Nanohardness measurements of irradiated and unirradiated quartz: In most cases, the indentation curves for unirradiated and irradiated quartz specimens were smooth and without visible pop-in events. For the few exceptions with pronounced pop-in events, the pop-ins were connected to inclusions or defects at the surface. Interestingly, crack formation around the indentations did not lead to the appearance of any specific details on the indentation curves. Data scattering was small, and the indentation curves demonstrated very good reproducibility. For example, curves for the same sample were, in most cases, practically identical.

As shown in Fig. 3, irradiation did not change the appearance of the load-displacement curves. Although the slope decreased as a function of dose, the curves were smooth and without any specific features for all analyzed samples. Moreover, as seen in Fig. 4, nanohardness values exhibit a decrease above a dose of $\sim 1.5 \times 10^{19}$ n/cm^2 that is similar to the loss of strength seen in previous studies [5, 6, 8]. Interestingly, the error and scattering reach a maximum at $\sim 4 \times 10^{19}$ n/cm^2. Finally, there is no pronounced difference between specimens irradiated at 52 and at 95 °C. At a dose of 2×10^{20} n/cm^2, at which the sample should be nearly amorphized, the decrease in nanohardness was $\sim 35\%$.

Nanohardness measurements of irradiated and unirradiated calcite and dolomite: Pronounced slip lines and possibly deformation-induced twins were often observed around nano-indentations in unirradiated calcite samples; however, fractures and cracks were rarely found before irradiation. After irradiation, twin-like formations often coexisted with cracks and brittle cleavage areas, as shown in

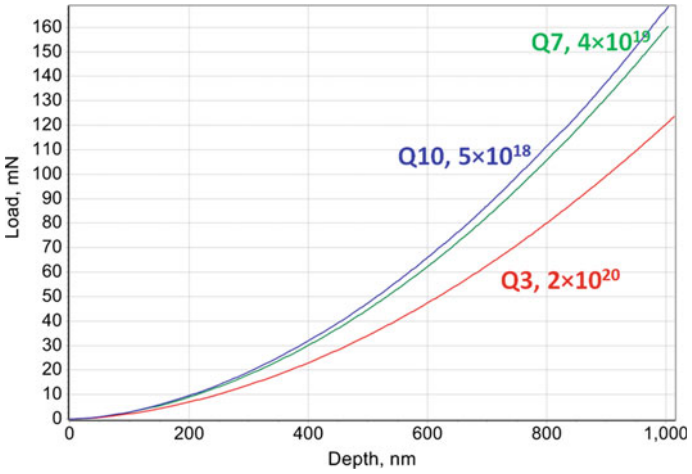

Fig. 3 Representative "load versus depth" curves for irradiated quartz

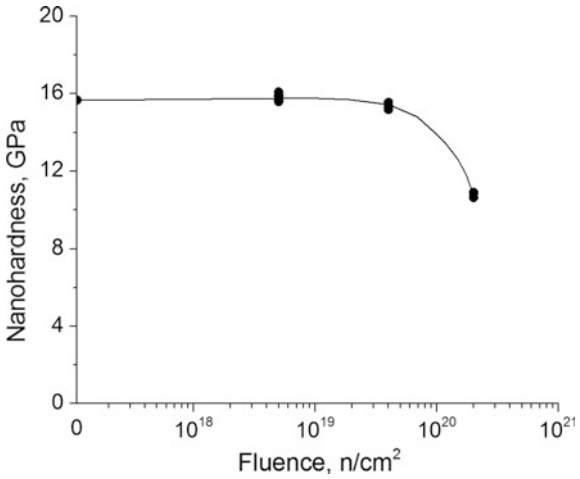

Fig. 4 Effect of irradiation on nanohardness of quartz

Fig. 5. Cracks most often formed if the indentation was performed close to the specimen edge (Fig. 6). Cleavage spots appeared regardless of the indentation location and depth. The effect of fluence was weak, with no clear differences observed for specimens irradiated at different fluences or at different temperatures (Figs. 5 and 7). As in calcite, cleavage fracture and cracks appeared in almost all irradiated dolomite samples. As shown in Fig. 7, the fracture pattern appears to depend upon crystal orientation and surface quality.

As shown in Fig. 8, the nanohardness values decrease with increasing fluence for dolomite; however, the nanohardness decreases sharply at a lower fluence before slowing at doses >1 $\times$ 10^{19} n/cm^2. Nanohardness values for calcite specimens, however, demonstrate a weak tendency to increase with dose, which may be caused by radiation-induced hardening. As in the irradiated quartz samples, there is no pronounced difference between specimens irradiated at 52 and at 95 °C. Although the effect of irradiation temperature was weak, higher irradiation temperatures tended to produce a softer material at fluences above 4 $\times$ 10^{19} n/cm^2.

Conclusions

To better understand the effects of neutron irradiation on reactor cavity concrete, a select group of mineral analogues of concrete aggregates were irradiated at ORNL's HFIR at three fluence levels and two temperatures. Neutron irradiation experiments and post-irradiation evaluation were performed on single crystals of quartz, calcite, and dolomite. Nanohardness measurements for quartz and dolomite showed a sharp change in the mechanical properties as a function of neutron fluence, which was correlated to neutron-induced damage. The change in calcite hardness with fluence

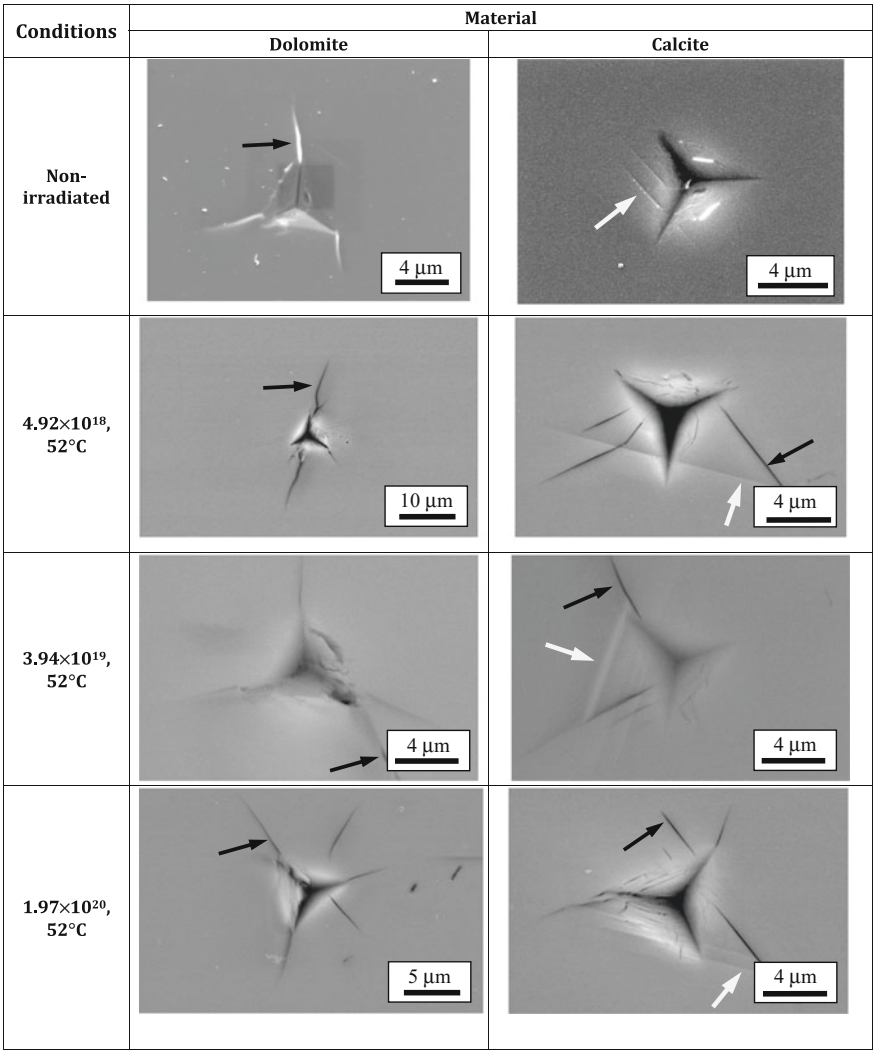

Fig. 5 SEM images of nano-indentations in dolomite and calcite. Black arrows point to cracks, and white arrows show slip lines or deformation twins. After irradiation, twin-like formations were often found to coexist with cracks and brittle cleavage areas

was small, which is in agreement with previous mechanical property studies, but the calcite samples showed much less scatter than previous studies [4, 6, 8]. SEM also revealed changes in deformation and fracture mechanisms in the irradiated mineral analogues.

Specifically, nanohardness in quartz exhibited a decrease above a dose of $\sim 1.5 \times 10^{19}$ n/cm^2 that was similar to the decrease seen in the loss of strength [4, 6, 8]. Interestingly, the error and scattering (presented as one standard deviation)

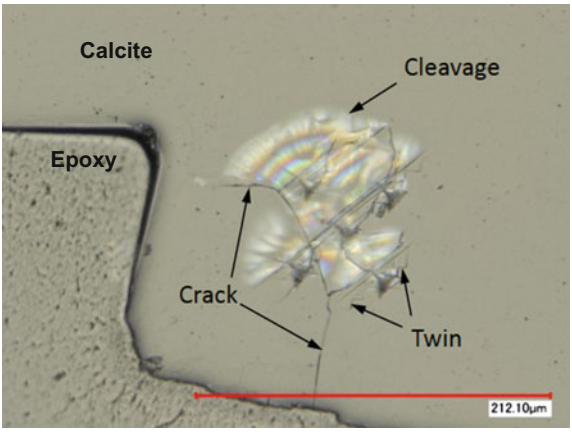

Fig. 6 Cracks, cleavage fractures, and twins around the calibration indentations (5 µm depth, in contrast to the 1 µm test indentations) in neutron-irradiated calcite. Note the specific rainbow-like halo around the indentations, suggesting the formation of under-surface cracks. Optical images are shown to illustrate sub-surface cracks

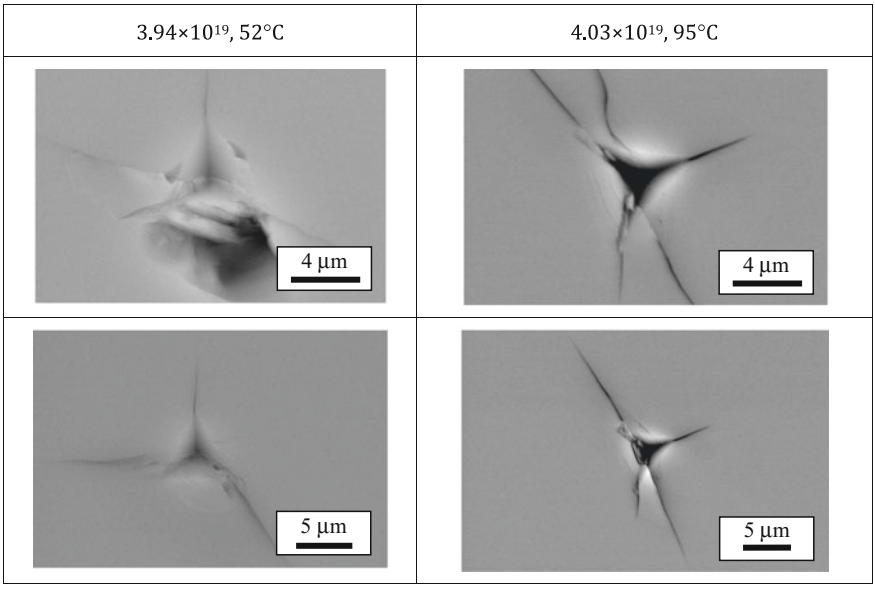

Fig. 7 SEM images of nano-indentations in dolomite irradiated at different temperatures

were much smaller than was seen in previous bulk mechanical property studies [4, 6, 8] and reached a maximum at $\sim 4 \times 10^{19}$ n/cm^2. Finally, there was no pronounced difference between quartz specimens irradiated at 52 and at 95 °C. At a

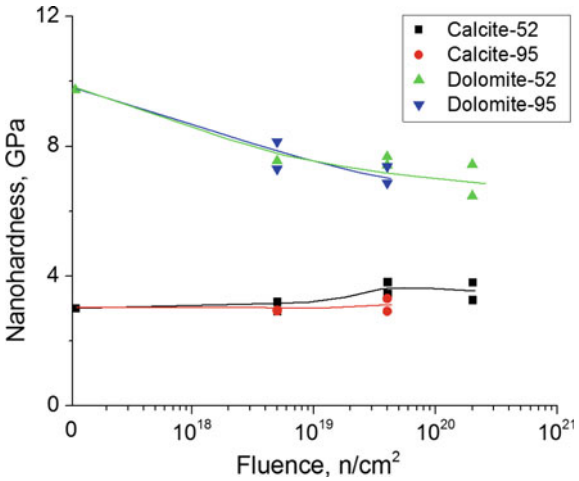

Fig. 8 The effects of neutron fluence and irradiation temperature on the nanohardness of dolomite and calcite. Error bars (1 standard deviation value, STD) are not shown because the STD for most specimens was fairly small, <0.2–0.3 GPa

dose of 2×10^{20} n/cm^2, at which the sample should be nearly amorphized, the decrease in nanohardness was ~35%.

Nanohardness values for dolomite decreased with increasing fluence; however, those values decreased more sharply at lower fluence before the decrease slowed at doses $>1 \times 10^{19}$ n/cm^2. The nanohardness of calcite specimens demonstrated a weak tendency to increase with dose, which may have been caused by radiation-induced hardening. As in the irradiated quartz samples, there was no pronounced difference between specimens irradiated at 52 and at 95 °C. Although the effects of irradiation temperature were weak for calcite and dolomite, at fluences above 4×10^{19} n/cm^2, higher irradiation temperatures tended to produce softer materials.

Acknowledgements This research was sponsored by the US Department of Energy, Office of Nuclear Energy, LWRS Program. The authors gratefully acknowledge that the irradiation of the mineral analogues of concrete aggregates was conducted at the HFIR, a DOE Office of Science User Facility operated by ORNL. The authors wish to thank Dr. Keith Leonard for his support and Tom Geer for his guidance on polishing the mineral analogue samples.

References

1. T.M. Rosseel, J.J. Wall, K.G. Field, Y. Le Pape, D.J. Naus, I. Remec, J.T. Busby, P. Bruck, Dommages d'irradiation dans les cavites en beton des reacteurs aux Etats-Unis. *La Revue Generale Nucleaire, Janvier-Fevrier* N#1, 21–27 (2015). (Radiation Damage in Reactor Cavity Concrete, in Fontevraud 8—Contribution of Materials Investigations and Operating Experience to LWRs' Safety, Performance and Reliability, Avignon, France, September 14–18, 2014)
2. T.M. Rosseel, I. Maruyama, Y. Le Pape, O. Kontani, A.B. Giorla, I. Remec, J.J. Wall, M. Sircar, C. Andrade, M. Ordonez, Review of the current state of knowledge on the effects of radiation on concrete. J. Adv. Conc. Tech. **14**, 368–383 (2016)

3. H. Graves, Y. Le Pape, D. Naus, J. Rashid, V. Saouma, A. Sheikh, and J. Wall, Expanded material degradation assessment (EMDA), Volume 4: Aging of concrete, NUREG/CR-7153, ORNL/TM-2011/545, US Nuclear Regulatory Commission (2014)
4. H. Hilsdorf, J. Kropp, H. Koch, The effects of nuclear radiation on the mechanical properties of concrete. Spec. Publ. Am. Concr. Inst. **55**, 223–254 (1978)
5. O. Kontani, Y. Ichikawa, A. Ishizawa, M. Takizawa, O. Sato, Irradiation effects on concrete structure. International Symposium on the Ageing Management and Maintenance of Nuclear Power Plants, Mitsubishi Research Institute, 173–182 (2010)
6. K.G. Field, I. Remec, Y. Le Pape, Perspective on radiation effects in concrete for nuclear power plants—Part I: Quantification of radiation exposure and radiation effects. Nucl. Eng. Des. **282**, 126–143 (2015)
7. Y. Le Pape, K.G. Field, I. Remec, Perspective on radiation effects in concrete for nuclear power plants—Part II: Perspective from micromechanical modelling. Nucl. Eng. Des. **282**, 144–157 (2015)
8. J. Seeberger, H. Hilsdorf, Einfluß von radioactiver Strahlung auf die Festogkeit and Struktur von Beton (Institut für Massivbau and Baustofftechnologie, Universität Karlsruhe, 1982)

Part III
Accident Tolerant Fuel Cladding

Accident Tolerant FeCrAl Fuel Cladding: Current Status Towards Commercialization

Kevin G. Field, Yukinori Yamamoto, Bruce A. Pint, Maxim N. Gussev and Kurt A. Terrani

Abstract FeCrAl alloys are rapidly becoming mature candidate alloys for accident tolerant fuel applications. The FeCrAl material class has shown excellent oxidation resistance in high-temperature steam environments, a key aspect of any accident tolerant cladding concept, while also being corrosion resistant, stress corrosion cracking (SCC) resistant, irradiation-induced swelling resistant, weldable, and formable. Current research efforts are focused on design, development and commercial scaling of advanced FeCrAl alloys including large-scale, thin-walled seamless tube production followed by a broad spectrum of degradation evaluations in both normal and off-normal conditions. Included in this discussion is the theoretical analysis of the alloying principles and rules, alloy composition design, and overview of the most recent empirical database on possible degradation phenomena for FeCrAl alloys. The results are derived from extensive in-pile and out-of-pile experiments and form the basis for near-term deployment of a lead-test rod and/or assembly within a commercially operating nuclear power plant.

Keywords FeCrAl · Accident tolerance · Commercialization

Introduction

The 2011 light water reactor (LWR) Fukushima Daiichi incident spawned research programs focused on the development of materials-based technologies which offered increased accident tolerance during off-normal conditions in LWRs. Key performance indicators for these new materials technologies included improved

K.G. Field (✉) · Y. Yamamoto · B.A. Pint
Materials Science and Technology Division, Oak Ridge National Laboratory, Oak Ridge, TN 37831, USA
e-mail: fieldkg@ornl.gov

M.N. Gussev · K.A. Terrani
Fusion and Materials for Nuclear Systems Division, Oak Ridge National Laboratory, Oak Ridge, TN 37831, USA

J.H. Jackson et al. (eds.), *Proceedings of the 18th International Conference on Environmental Degradation of Materials in Nuclear Power Systems – Water Reactors*, The Minerals, Metals & Materials Series, https://doi.org/10.1007/978-3-319-68454-3_15

reaction kinetics with steam, reduced hydrogen production, increased cladding and/or fuel properties, and improved fission product retention while still having acceptable performance during normal operation. Several different technologies have been proposed including monolithic cladding replacements, cladding coatings, novel fuel forms or any combination of the proposed.

Iron-chromium-aluminum (FeCrAl) alloys are currently under investigation as an option for monolithic accident tolerant fuel (ATF) cladding in light water reactors (LWRs). FeCrAl alloys represent a family of advanced oxidation resistant alloys with typical Cr contents between 10 and 22 wt% and Al contents between 4 and 8 wt% [1–3]. The Cr and Al contents are primarily within this range as these compositions are known to exhibit enhanced oxidation resistance in elevated temperature steam when compared to Zr-based alloys [1, 4–8]. These fully ferritic, body-centered-cubic alloys have been investigated as part of a multiyear, multifaceted alloy development effort to establish a working materials database to enable full commercialization of FeCrAl alloys for ATF cladding deployment in LWRs [9].

The overall research and development (R&D) effort is broad with focuses on accident scenario testing, irradiation materials screening tests, safety/economic analysis, fabrication studies, vendor (commercial) interface, and integral testing such as water loop testing. These activities enable a robust and vast material database to be developed which in-turn provides a fundamental scientific basis for alloy selection and production for commercial deployment. In the case of the R&D effort, the goal is to deploy the selected alloy(s) as part of a Lead Fuel Rod(s) (LFR) in a Lead Test Assembly (LTA). Within this effort, the primary focus is on the development and maturation of the clad. The fuel remains unchanged from the typical commercial standard and hence will remain conventional UO_2.

An overview of the general structure of the R&D program, Fig. 1, shows the tiered approach where basic testing, such as oxidation testing, materials irradiation, and neutronics evaluations are used to define the working compositions for viable FeCrAl alloys as ATF cladding. This foundation is then used to develop more robust alloys that are closer in approximation of a commercially produced alloy and used in integral testing such ATF-2 and IFA-796 which are both neutron irradiation water loop tests in materials test reactors. This tiered approach resulted in a multi-phase development program where lower tiered examinations were completed on simple FeCrAl alloys deemed “Generation I” FeCrAl alloys. These alloys typically only contained Fe, Cr, Al, and Y (for enhanced oxidation resistance) and were not fully optimized for nuclear power applications. An overview of the R&D activities related to this generation of alloys can be found in multiple references [9, 10]. Testing on Generation I alloys has given way to more complicated testing on more advanced alloys that closely approximate the expected composition and microstructure of the alloy(s) to be deployed within a lead fuel assembly (LFA). These alloys are deemed “Generation II” alloys.

Generation II alloys are easily distinguishable from Generation I alloys as the Generation II alloys have near-optimized microstructures and chemistries. Generation II alloys fall within the “lean-alloy” chemistry class of the FeCrAl family. Typically, Generation II alloys have Cr contents between 10 and 13 wt%

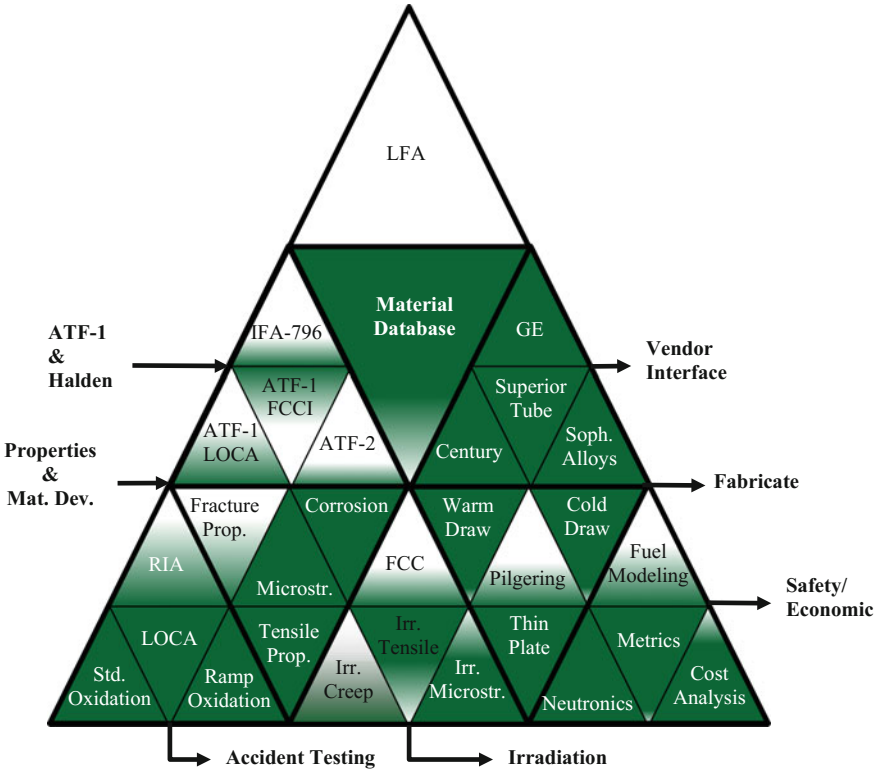

Fig. 1 R&D program design strategy. Filled polygons represent a qualitative assessment on the extent of testing completed regarding the specified topic. Definitions: Std: standard; LOCA: loss of coolant accident; RIA: reactivity insertion accident; Irr.: irradiation; Microstr.: microstructure; FCCI: fuel-cladding chemical interaction; Soph.: Sophisticated; LTR: lead test rod; GE: General Electric Corporation

and Al contents between 5 and 6 wt%. The lean-alloy composition space was selected for the Generation II alloys due to the known miscibility gap in the high-Cr (>9–10 wt% Cr) FeCr and FeCrAl phase diagrams at temperatures below 500 °C [11–22]. Additionally, Generation II alloys include minor alloying additions such as niobium and molybdenum. These minor alloying additions are added to increase the alloy strength at typical cladding operation temperatures [10]. Higher strengths provide the ability for designers to reduce the cladding thickness thereby reducing the overall neutronic penalty of FeCrAl alloys compared to Zr-based alloys [23]. Additionally, heat treatment procedures have been developed to introduce a fine grain size which also promotes increased strength, increased radiation tolerance, and increased workability. All Generation II alloys are produced using traditional wrought fabrication techniques to minimize production costs and enable rapid interface with commercial vendors such as nuclear fuel vendors as well as seamless tube production vendors.

Figure 1 also provides a qualitative representation of the extent of testing completed regarding a specific topic of interest based on the currently available literature. For example, the irradiation tensile topic within the "Irradiation" group is partially filled at nearly 50%. This assessment is based on the wealth of irradiated mechanical properties for Generation I FeCrAl alloys [24] but only limited low dose [<2 displacements per atom (dpa)] data for Generation II FeCrAl alloys [25]. Another example is from the more complicated integral testing such as the Accident Tolerant Fuel (ATF)-2 test. The ATF-2 test is currently in the design stage and therefore does not show significant progress within Fig. 1. The most important aspect is the material database shown in Fig. 1. Significant progress has been made within the R&D effort resulting in a large degree of data on Generation I, Generation II, and commercially available FeCrAl alloys. The reminder of this discussion is orientated to providing an overview of the current materials database for FeCrAl alloys.

Overview of Materials Database

The current understanding of Cr and Al on different material properties and conditions for FeCrAl alloys as well as the wealth of data for a specific topic of interest for ATF cladding is depicted schematically in Fig. 2. It should be noted that the topics listed in Fig. 2 are not the sole topics/focus areas currently under investigation to enable deployment of a LFA. The topics listed are only a representative cross section of focus areas that were or are under investigation. Additionally, Fig. 2 also lists Generation I, Generation II, and commercial alloys. Investigations on all three FeCrAl classes has enabled the understanding of composition effects for a given topic/property. Only a brief discussion on the current materials database and discussion on future directions for the database is discussed as a handbook on material properties which discusses in great detail the topics represented (and not represented) in Fig. 2 is forth coming [26].

Figure 2 shows the inherent complexity in designing FeCrAl alloys for ATF cladding applications. For example, it has been shown that large amounts of Al and to a lesser degree, Cr, has significant impacts on the fabrication and especially joining of FeCrAl alloys. High Al and Cr content FeCrAl alloys have been shown to be susceptible to weld-induced cracking [27–29] as well as have stronger propensity for work hardenability leading to cracking during typical compressive tube-drawing activities [30–32]. Additionally, high Cr additions (>10–12 wt%) in Generation I FeCrAl alloys are susceptible to α' formation, leading to significant radiation-hardening and potential embrittlement near end of life irradiation doses [21, 24, 33–35]. On the other hand, Cr and Al additions, at concentrations where α' is expected to form and weld-induced cracking is an issue, are needed to form a dense passivating α-Al_2O_3 layer during elevated steam exposure [1, 4–8]. In this respect, many of the material properties require a delicate balancing act to optimize the chemistry (and the microstructure) to ensure successful operation of FeCrAl

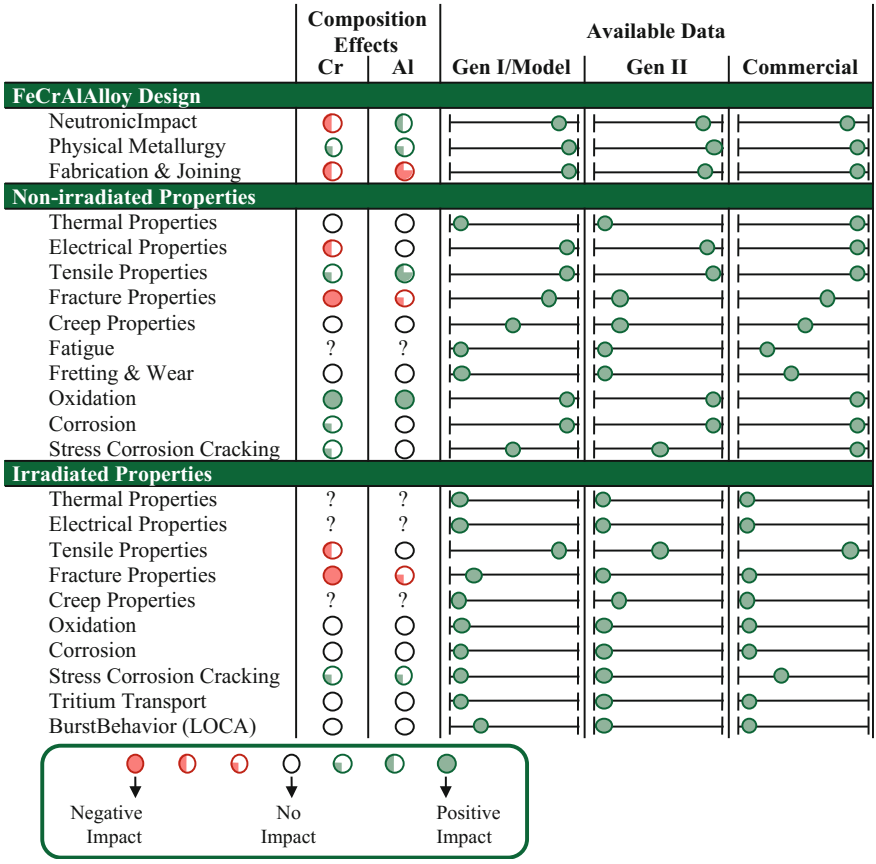

Fig. 2 Summary of the materials database on FeCrAl alloys for accident tolerant fuel cladding applications. The amount of symbol fill in the Cr and Al columns is a qualitative representation on the degree of severity on the impact of a property/topic of interest. "?" denotes areas with unknown effects, if any. Available data columns represent degree of data; left: limited data set(s), right: complete data set(s)

cladding during normal and off-normal operation within a LWR. Given this, other materials properties, as shown in Fig. 2, are rather insensitive to starting composition such an aqueous corrosion, at least within the composition range currently under investigation.

The complex interplay between different material properties is a primary driving factor for the limited studies conducted on more complex material behavior such as stress corrosion cracking and fuel-clad behavior in the presence of an irradiation field, Figs. 1 and 2. These integral tests (IFA-796, ATF-1 FCCI, ATF-1, and ATF-2—Fig. 1) require complex designs leading to long experimental development times (on the order of 1–2 years) and due to limited in-core materials testing reactor core space only a limited dataset of alloys can be investigated. Hence, several

FeCrAl alloy down-selections have occurred prior to the start of these complicated experiments.

The most significant down selection was within the transition from Generation I to Generation II FeCrAl studies. As noted prior, the Cr content was down selected to only include alloys with 10, 12, or 13 wt% Cr and Al contents of either 5 or 6 wt%. This narrow composition band represents alloys predicted to have the best optimization of materials properties and hence are those proposed for use in the advanced, integral tests. The result is future development within the material database, especially for oxidation, corrosion, stress corrosion cracking, and LOCA behavior of irradiated cladding will be completed within this refined alloy space on Generation II alloys. Additionally, the current materials database is established primarily on thin-plate material; thin-walled tubing evaluations remain limited within the materials database.

Currently, thin-walled seamless tube production using commercial drawing processes is being pursued to increase the data availability within the materials database. Production of seamless tube will also be needed for deployment within a LFA/LTA. Finally, large quantity (on the order of thousands of meters) thin-walled seamless tube production will demonstrate feasibility for scalable, commercial production of ATF FeCrAl cladding. Three different thin-wall tube fabrication approaches have been identified and pursued; cold-drawing, warm-drawing, and cold-pilgering. All three approaches are being pursued by independent commercial entities. No significant advantage has been identified between the warm and cold-drawing processes; hence, cold-drawing production has seen the largest focus to-date. Cold-drawing within the dimensional requirements for both pressurized water reactor (PWR) and boiling water reactor (BWR) cladding configurations has been completed on Generation II FeCrAl. To meet these requirements, and limit cracking, careful balancing between the area reduction per pass and a proper inter-pass annealing is needed. Current production using cold-drawing has been limited to <150 meters per alloy, but total production is anticipated to increase significantly to enable a LFA/LTA insertion within US fiscal year 2018. Additionally, cold-pilgering has been pursued and seen initial success, but scalable production has not been demonstrated to-date.

In the terms of a LFA/LTA, a Generation II FeCrAl alloy will be deployed as the cladding. Therefore, the advanced testing on the thin-walled tubing currently being produced will be directly applicable towards the understanding of the performance of the LFA within a commercial LWR. Finally, it should be noted that insertion of a LFA/LTA only represents the first steps to a fully adopted, commercially deployed ATF FeCrAl cladding for today's current LWR fleet. Zr-based alloys have seen decades of refinement based on lab-scale experimentation and modeling as well as based on operational knowledge. FeCrAl alloys are anticipated to be no different, and the knowledge gained from the first series of LFA(s) within a LWR will enable further refinement of the Generation II alloy class and eventually enable a nuclear fuel vendor to provide an inherently accident tolerant fuel cladding within today's commercial LWRs.

Summary

An extensive R&D program focused on the development of ATF FeCrAl cladding for commercial LWRs that will enhance the inherent safety of nuclear power generation in the United States and abroad is on-going. The focus of the program is identifying FeCrAl alloy(s) that perform well in both normal and off-normal operation. To accomplish this task, a tiered program-structure was developed with focuses on accident testing, irradiation testing, safety/economic analysis, fabrication studies, integral testing, and commercialization efforts. This tiered approach has led to a vast materials database on three classes of FeCrAl alloys: Generation I, Generation II, and commercial FeCrAl alloys. Generation II FeCrAl alloys represent the alloys which closely resemble the expected chemistry and microstructure of a commercially deployable ATF FeCrAl cladding. Generation II alloys were developed based on the fundamental studies completed on Generation I and commercial FeCrAl alloys. A significant milestone lays ahead for FeCrAl alloys with the deployment of a LFA within a LTA in a commercial LWR and the established materials database for all three alloy classes is one of the primary enabling factors to meet this milestone.

Acknowledgements This research was funded by the U.S. Department of Energy's Office of Nuclear Energy, Advanced Fuel Campaign of the Fuel Cycle R&D program and the U.S. Department of Energy, Office of Nuclear Energy, for the Nuclear Energy Enabling Technologies (NEET) program for the Reactor Materials effort. This manuscript has been authored by UT-Battelle, LLC under Contract No. DE-AC05-00OR22725 with the U.S. Department of Energy. The United States Government retains and the publisher, by accepting the article for publication, acknowledges that the United States Government retains a non-exclusive, paid-up, irrevocable, world-wide license to publish or reproduce the published form of this manuscript, or allow others to do so, for United States Government purposes. The Department of Energy will provide public access to these results of federally sponsored research in accordance with the DOE Public Access Plan (http://energy.gov/downloads/doe-public-access-plan).

References

1. K.A. Terrani, S.J. Zinkle, L.L. Snead, Advanced oxidation-resistant iron-based alloys for LWR fuel cladding. J. Nucl. Mater. **448**, 420–435 (2013). doi:10.1016/j.jnucmat.2013.06.041
2. Z. Duan, H. Yang, Y. Satoh, K. Murakami, S. Kano, Z. Zhao et al., Current status of materials development of nuclear fuel cladding tubes for light water reactors. Nucl. Eng. Des. **316**, 131–150 (2017). doi:10.1016/j.nucengdes.2017.02.031
3. S.J. Zinkle, K.A. Terrani, J.C. Gehin, L.J. Ott, L.L. Snead, Accident tolerant fuels for LWRs: A perspective. J. Nucl. Mater. **448**, 374–379 (2014). doi:10.1016/j.jnucmat.2013.12.005
4. B.A. Pint, K.A. Terrani, Y. Yamamoto, L.L. Snead, Material Selection for Accident Tolerant Fuel Cladding. Metall. Mater. Trans. E. **2**, 190–196 (2015)
5. B.A. Pint, K.A. Terrani, M.P. Brady, T. Cheng, J.R. Keiser, High temperature oxidation of fuel cladding candidate materials in steam–hydrogen environments. J. Nucl. Mater. **440**, 420–427 (2013). doi:10.1016/j.jnucmat.2013.05.047

6. K.A. Unocic, Y. Yamamoto, B.A. Pint, Effect of Al and Cr Content on Air and Steam Oxidation of FeCrAl Alloys and Commercial APMT Alloy. Oxid. Met. **87**, 431–441 (2017). doi:10.1007/s11085-017-9745-1
7. D.J. Park, H.G. Kim, J.Y. Park, Y. Il Jung, J.H. Park, Y.H. Koo, A study of the oxidation of FeCrAl alloy in pressurized water and high-temperature steam environment. Corros. Sci. **94**, 459–465 (2015). doi:10.1016/j.corsci.2015.02.027
8. R.B. Rebak, R.J. Blair, P.J. Martiniano, F. Wagenbaugh, E.J. Dolley, Resistance of Advanced Steels to Reaction with High Temperature Steam as Accident Tolerant Fuel Cladding Materials, (n.d.). https://www.researchgate.net/profile/Raul_Rebak/publication/288720128_Resistance_of_advanced_steels_to_reaction_with_high_temperature_steam_as_accident_tolerant_fuel_cladding_materials/links/56a639be08aeca0fddcb4a0f.pdf (Accessed 21 June 2017)
9. M. Snead, L.L. Snead, K.A. Terrani, K.G. Field, A. Worrall, K.R. Robb et al., *Technology Implementation Plan ATF FeCrAl Cladding for LWR Application* (Oak Ridge National Laboratory, Oak Ridge, TN, 2014)
10. Y. Yamamoto, B.A. Pint, K.A. Terrani, K.G. Field, Y. Yang, L.L. Snead, Development and property evaluation of nuclear grade wrought FeCrAl fuel cladding for light water reactors. J. Nucl. Mater. **467**, 703–716 (2015). doi:10.1016/j.jnucmat.2015.10.019
11. H.G. Read, H. Murakami, Microstructural influences on the decomposition of an Al-containing ferritic stainless steel. Appl. Surf. Sci. **94**, 334–342 (1996)
12. H.G. Read, H. Murakami, K. Hono, Al partioning in MA 956, An ODS ferritic stainless steel. Scr. Mater. **36**, 355–361 (1997)
13. C. Capdevila, M.K. Miller, J. Chao, Phase separation kinetics in a Fe–Cr–Al alloy. Acta Mater. **60**, 4673–4684 (2012). doi:10.1016/j.actamat.2012.05.022
14. M. Pinkas, Z. Foxman, N. Froumin, P. Hähner, L. Meshi, Sensitivity of thermo-electric power measurements to α–α' phase separation in Cr-rich oxide dispersion strengthened steels. J. Mater. Sci. **50**, 4629–4635 (2015). doi:10.1007/s10853-015-9014-0
15. Z. Száraz, G. Török, V. Kršjak, P. Hähner, SANS investigation of microstructure evolution in high chromium ODS steels after thermal ageing. J. Nucl. Mater. **435**, 56–62 (2013). doi:10.1016/j.jnucmat.2012.12.016
16. G. Electric, 630A Mark V Maritime Nuclear Steam Generator Design Studies Summary, GEMP-359. (1965)
17. P.J. Grobner, The 885F (475C) embrittlement of ferritic stainless steels. Metall. Trans. **4**, 251–260 (1973)
18. R.O. Williams, Further studies of the iron-chromum system. Trans. Met. Soc. AIME. **212**, 497–502 (1958)
19. G. Bonny, D. Terentyev, L. Malerba, On the α–α' miscibility gap of Fe–Cr alloys. Scr. Mater. **59**, 1193–1196 (2008). doi:10.1016/j.scriptamat.2008.08.008
20. C.S. Wukusick, *The physical metallurgy and oxidation behavior of Fe-Cr-Al-Y alloys* (Cincinnati, Ohio, 1966)
21. S. Kobayashi, T. Takasugi, Mapping of 475 °C embrittlement in ferritic Fe–Cr–Al alloys. Scr. Mater. **63**, 1104–1107 (2010). doi:10.1016/j.scriptamat.2010.08.015
22. J. Ejenstam, M. Thuvander, P. Olsson, F. Rave, P. Szakalos, Microstructural stability of Fe-Cr-Al alloys at 450–550 °C. J. Nucl. Mater. (2014). doi:10.1016/j.jnucmat.2014.11.101
23. N.M. George, K. Terrani, J. Powers, A. Worrall, I. Maldonado, Neutronic analysis of candidate accident-tolerant cladding concepts in pressurized water reactors. Ann. Nucl. Energy **75**, 703–712 (2015). doi:10.1016/j.anucene.2014.09.005
24. K.G. Field, S.A. Briggs, K. Sridharan, R.H. Howard, Y. Yamamoto, Mechanical Properties of Neutron-Irradaited Model and Commercial FeCrAl Alloys. J. Nucl. Mater. **489**, 118–128 (2017)
25. K.G. Field, S.A. Briggs, P.D. Edmondson, J.C. Haley, R.H. Howard, X. Hu, et al., Database on Performance of Neutron Irradiated FeCrAl Alloys, ORNL/TM-2016/335. (2016)

26. K.G. Field, M. Snead, Y. Yamamoto, B.A. Pint, K.A. Terrani, Materials properties of FeCrAl alloys for nuclear power production applications, ORNL/TM-2017/186. (2017)
27. J.R. Regina, J.N. Dupont, A.R. Marder, The effect of chromium on the weldability and microstructure of Fe-Cr-Al weld cladding. Weld. J. **86**, 170–178 (2007)
28. M.N. Gussev, K.G. Field, Y. Yamamoto, Design, Properties, and Weldability of Advanced Oxidation-Resistant FeCrAl Alloys. Mater. Des. **129**, 227–238 (2017)
29. J.N. Dupont, J.R. Regina, K. Adams, Improving the weldability of fecral weld overlay coatings, Foss. Energy Mater. Conf. 131–137 (2007)
30. Y. Yamamoto, Development and Quality Assessments of Commercial Heat Production of ATF FeCrAl Tubes (2015)
31. Y. Yamamoto, M.N. Gussev, B.A. Pint, K.A. Terrani, Examination of Compressive Deformation Routes for Production of ATF FeCrAl Tubes, ORNL/TM-2016/509. (2016)
32. W. Chubb, S. Alfant, A.A. Bauer, E.J. Jablonowski, F.R. Shober, R.F. Dickerson, Constitution, metallurgy, and oxidation resistance of iron-chromium-aluminum alloys: BMI-1298, (1958)
33. K.G. Field, X. Hu, K.C. Littrell, Y. Yamamoto, L.L. Snead, Radiation tolerance of neutron-irradiated model Fe–Cr–Al alloys. J. Nucl. Mater. **465**, 746–755 (2015). doi:10.1016/j.jnucmat.2015.06.023
34. S.A. Briggs, P.D. Edmondson, Y. Yamamoto, C. Littrell, R.H. Howard, C.R. Daily et al., A combined APT and SANS investigation of alpha prime phase precipitation in neutron-irradiated model FeCrAl alloys. Acta Mater. **129**, 217–228 (2016)
35. P.D. Edmondson, S.A. Briggs, Y. Yamamoto, R.H. Howard, K. Sridharan, K.A. Terrani et al., Irradiation-enhanced α' precipitation in model FeCrAl alloys. Scr. Mater. **116**, 112–116 (2016). doi:10.1016/j.scriptamat.2016.02.002

Interdiffusion Behavior of FeCrAl with U_3Si_2

Rita E. Hoggan, Lingfeng He and Jason M. Harp

Abstract Advanced steels, including FeCrAl are being considered as an alternative to the standard light water fuel (LWR) cladding, Zircalloy. FeCrAl has superior mechanical and thermal properties and oxidation resistance relative to the Zircalloy standard. Uranium Silicide (U_3Si_2) is a candidate to replace uranium oxide (UO_2) as LWR fuel because of its higher thermal conductivity and higher fissile density relative to the current standard, UO_2. The interdiffusion behavior between FeCrAl and U_3Si_2 is investigated in this study. Commercially available FeCrAl, along with pellets fabricated at the Idaho National Laboratory were placed in diffusion couples. Individual tests have been run at temperatures ranging from 500 °C to 1000 °C for 30 h and 100 h. The interdiffusion is analyzed with an optical microscope and scanning electron microscope (SEM). Uniform and planar diffusion regions along the material interface are illustrated with backscatter electron micrographs and energy-dispersive X-ray spectroscopy (EDS).

Keywords Accident tolerant fuels · U_3Si_2 · FeCrAl · Cladding

Introduction

Safe, reliable and economic operation of the current nuclear power reactor fleet is a top priority for the nuclear industry. After the events at Fukushima in 2011, resulting from the Great East Japan Earthquake, emphasis has been placed on enhancing the accident tolerance of LWRs. This work is part of an Accident

R.E. Hoggan (✉) · L. He · J.M. Harp
Idaho National Laboratory, MS6188, PO Box 1625, Idaho Falls ID 83415-6188, USA
e-mail: Rita.Hoggan@inl.gov

L. He
e-mail: Lingfeng.He@inl.gov

J.M. Harp
e-mail: Jason.Harp@inl.gov

J.H. Jackson et al. (eds.), *Proceedings of the 18th International Conference on Environmental Degradation of Materials in Nuclear Power Systems – Water Reactors*, The Minerals, Metals & Materials Series, https://doi.org/10.1007/978-3-319-68454-3_16

Tolerant Fuel (ATF) Development program initiated by the Department of Energy. In addition to safety, reliability and economy are important considerations for this new fuel system to be adopted by the current commercial nuclear fuel users. An ATF system would tolerate loss of cooling in the reactor core or other beyond design basis events while maintaining or improving the fuel performance, relative to the current system during normal operation [1]. Any candidate for ATF must perform as good as or better than UO_2–Zr in all three areas to be considered as a viable replacement. The UO_2–Zr system has performed adequately for many years, but we know it can be improved upon not only for safety reasons, but for economic reasons as well.

FeCrAl alloy is a candidate cladding material to replace zirconium alloy. FeCrAl has outstanding high-temperature mechanical strength and oxidation resistance under accident conditions. [2] Uranium Silicide (U_3Si_2) is in use as a dispersion plate fuel in test reactors, but has not been fully tested in conditions. U_3Si_2 pellets have been fabricated for use in commercial LWRs as part of an ATF system [3]. U_3Si_2 has higher uranium loading density as well as a higher thermal conductivity relative to UO_2. Figure 1 compares the thermal conductivity of UO_2, Zr, U_3Si_2, and FeCrAl [4–6]. The U_3Si_2–FeCrAl system is expected to provide more than double the amount of time from a control rod insertion until failure criteria for the reactor is met, as well as producing roughly half the amount of hydrogen gas in the event of a loss of coolant accident (LOCA) [7].

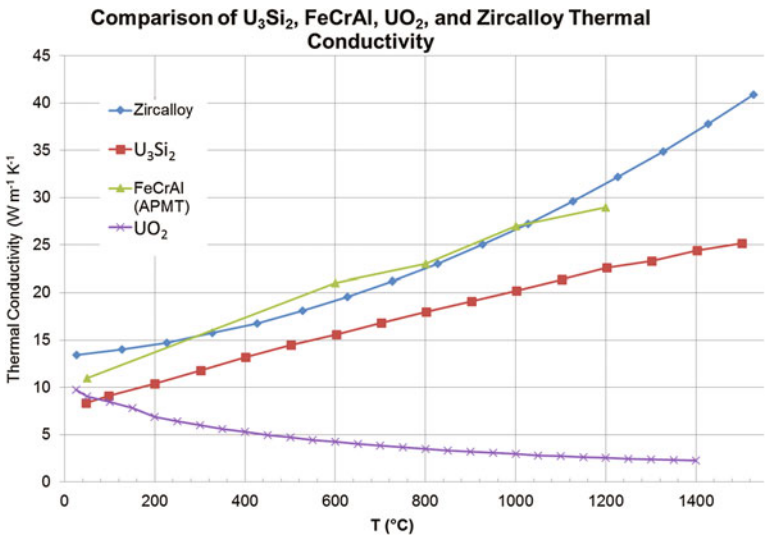

Fig. 1 Literature values for thermal conductivity of U_3Si_2 [4], FeCrAl [5], UO_2 and Zircalloy [6]

An economic assessment by George et al. reported an increase in fuel cost per cladding design of about twenty percent for FeCrAl relative to Zry, based on the use of UO_2 fuel and the higher U-235 enrichment requirement due to the neurotic penalty associated with FeCrAl [8]. The thermal neutron absorption cross section of FeCrAl is 2.43 barns, while that of Zr is 0.20 barns. George et al. also found the yield stress of FeCrAl to be approximately four times higher than for Zircaloy-2. Because FeCrAl is mechanically stronger than Zr, its cladding wall thickness can be made thinner than Zr, reducing the material area for neuron absorption as well as increasing the area available for fuel. The higher uranium density of the U_3Si_2 fuel may also offset the neutronic penalty of the FeCrAl cladding.

An analysis of the benefits during a BWR station black out event showed that the substitution of Zr with FeCrAl delayed accident progression and decreased the amount of gases generated. These analyses were done ignoring possible eutectics between FeCrAl and other core components because there is not enough data available [9].

Fuel clad chemical interaction, and the chemical compatibility between the fuel and clad material is of prime importance because of the formation of low melting eutectics which may often limit the life of the fuel pin in a reactor. The temperature of the eutectic reaction between the fuel and the cladding is considered as a critical parameter for the design of the metallic fuel pin. The integrity of the cladding is of fundamental concern for designers since it provides the primary barrier to the release of radionuclides [10].

Uranium and iron have well known eutectics, as seen in the U-Fe phase binary phase diagram, Fig. 2 [11], that enhance diffusion in the U_3Si_2/FeCrAl fuel system. The interaction of iron with molten uranium has been investigated. In the U-Fe system, UFe_2, which melts congruently at 1236 °C, forms a eutectic with iron that melts at 1078 °C and has a composition of U-77at.% Fe. UFe_2 also forms a eutectic with U_6Fe that melts at 719 °C and has a composition of U-33at.% Fe [12] Normal LWR operating temperatures for U_3Si_2 fuel is expected to be around 300–400 °C. The eutectic reactions in a Fe-U system would nominally only be of concern in accident scenarios.

Experimental

The polycrystalline depleted U_3Si_2 sample pellets used in the present work were sintered at Idaho National Laboratory following the procedure given in [3]. The density of sintered U_3Si_2 pellets is 11.8 g/cm^3, which is 96.9% of the theoretical density. XRD of sintered pellets showed roughly 84–88 wt% U_3Si_2, 8–13 wt% USi and 2–4 wt% UO_2 determined by X-ray diffraction. [3].

A rod of Kanthal APMT FeCrAl, commercially available, was obtained and machined down to the approximate diameter of the U_3Si_2 pellets, about 8 mm. The approximate composition of the FeCrAl is 70 wt% Fe, 22.2 wt% Cr, 4.75 wt% Al, and 3.09 wt% Mo. The FeCrAl was sectioned and polished in a similar manner to

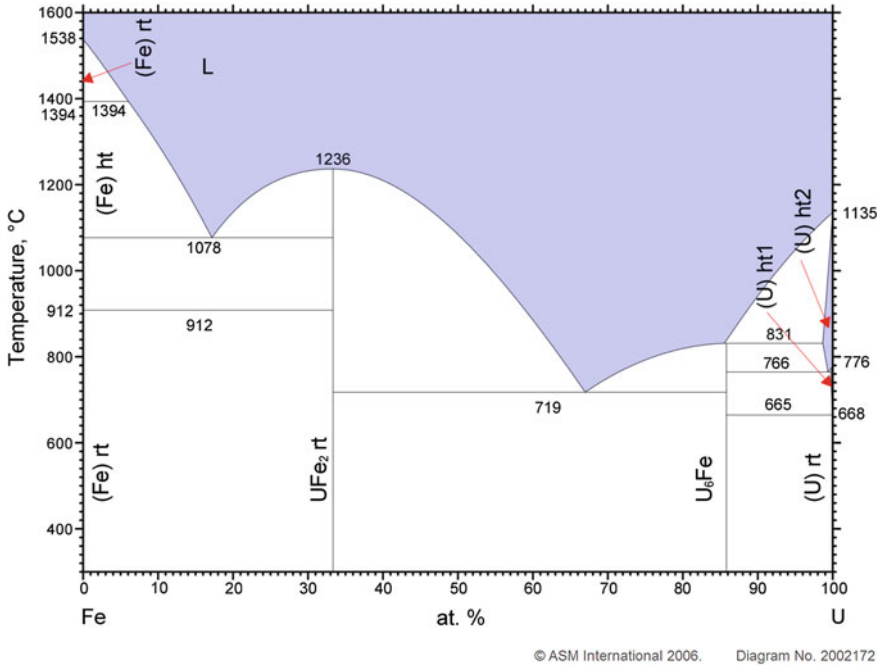

Fig. 2 Phase diagram of the iron-uranium binary system [5]

the U_3Si_2 (described below) in preparation for placement in diffusion couples. Figure 3 shows the FeCrAl rod once polished and prepared for the diffusion couple.

The U_3Si_2 pellets were sectioned into ~2 mm thick disks with a Struers high speed precision saw, Accutom-50, using a cylindrical jig and SiC cut-off wheel, 10S15 in a radiological hood. Both sides of the disks were polished to a mirror finish with a Beuhler EcoMet 250 grinder/polisher prior to diffusion tests. Polishing

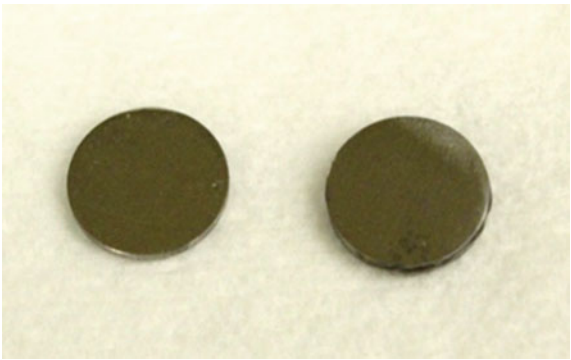

Fig. 3 FeCrAl rod sectioned and polished prior to placement in diffusion couple

was done to maximize the surface area of the material interface, and ensure a good contact between the materials in the diffusion couple.

The diffusion couple, composed of a U_3Si_2 disk surrounded by two FeCrAl disks surrounded in Ta foil, were fixed in an Invar alloy jig, shown in Fig. 4. The material composing the diffusion couple was forced together (hand tightened) in the jig to replicate the mechanical interaction that would be experienced after time in a reactor do to swelling and creep. Tantalum foils were used to eliminate diffusion between the diffusion couple and jig, and also to absorb any excess O_2 in the heating process. The diffusion tests were conducted in a RD Webb "Red Devil" vacuum furnace for 30 h and 100 h at several different temperatures, summarized in Table 1. Higher temperatures than are expected during normal operation conditions were chosen for these tests (fuel cladding temperatures of 300–400 °C are nominally expected). This was done both to accelerate any possible diffusion and also to simulate conditions that might occur during a LOCA. Neutron irradiation, and creation of fission products may also accelerate interdiffusion, as some phases of uranium and silicon may become amorphous under irradiation [13]. Thus, it is necessary to test the un-irradiated system at more extreme conditions than expected in operation.

It was found that many of the samples had a very weak bond or possibly no bonding at all. In an effort to maintain the contact area the annealed diffusion couple, remaining in the jig, was surrounded in epoxy for stabilization before sectioning. The diffusion couples were cut down the center providing two separate

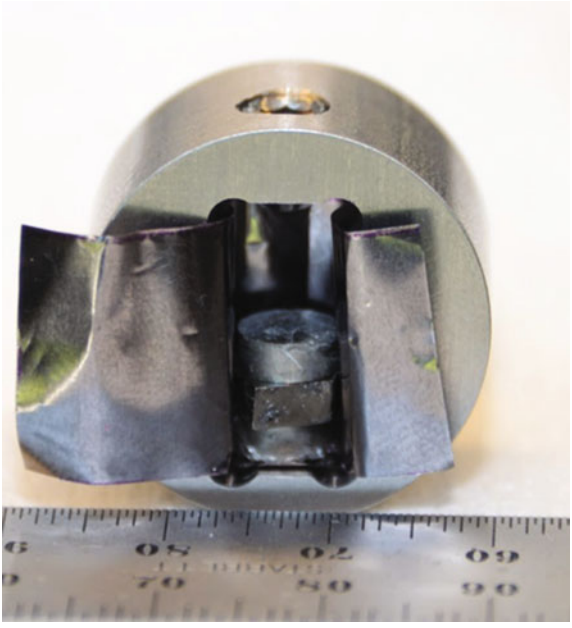

Fig. 4 Diffusion couple test set up composed of a U_3Si_2 disk surrounded by two FeCrAl disks surrounded in Ta foil inside an Invar alloy jig

Table 1 Diffusion test parameters and subsequent reaction layer width

	Temperature (°C)	Time (hours)	Width of reaction layer (μm)
1.	500	30	0 (no interaction)
2.	500	100	0
3.	600	100	2.6
4.	800	30	12
5.	800	100	1–6 (de-bonded)
6.	1000	30	65
7.	1000	100	96

cross section faces for examination. The cross sections were polished using a combination of SiC and diamond abrasive to ensure a flat surface between the softer FeCrAl material relative to the more brittle U_3Si_2 material.

The microstructure of the samples after diffusion tests was examined by, scanning electron microscopy (SEM). Surface morphologies were evaluated using a JEOL 7600 field emission SEM equipped with energy-dispersive spectrometer (EDS) and a Phenom XL with EDS detector. Standardless semi-quantitative EDS equipped on the SEM was applied to obtain a semi quantitative chemical composition of each phase, a concentration profile across the interface, and elemental mapping.

Results and Discussion

No diffusion upon examination via SEM was detected in the diffusion couple heated at 500 °C for 30 h, illustrated in Fig. 5. Figure 5 has a backscattered electron micrograph of the material interface with a line indicating where an EDS line scan

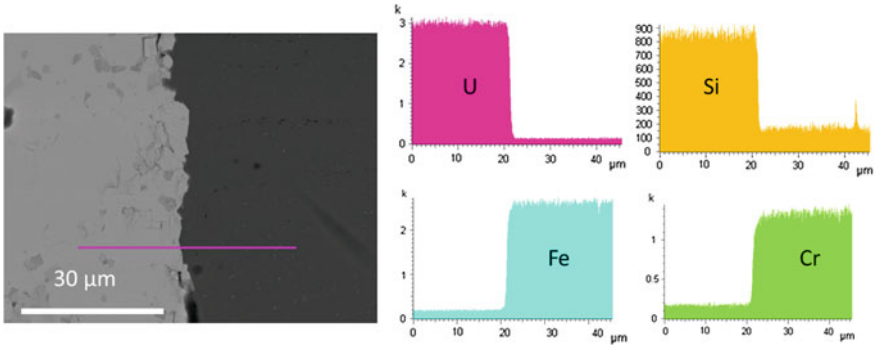

Fig. 5 SEM backscattered electron micrograph of the diffusion couple heated at 500 °C for 30 h with a line across the material interface where and EDS line scan was taken. The corresponding major element (U, Si, Fe, and Cr) concentrations, in terms of EDS signal, provide a qualitative composition of the elements present

was taken along with corresponding major element concentration in terms of EDS signal, giving qualitative composition across the interface. The slight composition slope at the interface is likely an artifact of the EDS spot size and volume interaction at the interface. The diffusion couple test heated at 500 °C for 100 h showed some indication of interaction, as EDS indicated a slight amount of Fe diffused into the fuel. There were, however, no discernable diffusion layers, as were seen in all tests at 600 °C and above. The average thicknesses for the total interaction zone at each diffusion test are listed in Table 1. This measurement was obtained by averaging multiple point-to-point distances on a backscattered electron micrograph with the SEM software. The test at 800 °C for 100 h likely de-bonded during the experiment causing a smaller than expected interaction layer.

Microstructural analysis of the diffusion couple heated at 1000 °C for 100 h, shown in Fig. 6, revealed an excellent bond formation at the interface. This diffusion zone was also visible with an optical microscope at 200x magnification. The thickness and interface between two of the interaction layers are mostly uniform and planar, respectively, as illustrated with EDS concentration intensity mapping, Fig. 6b–h. The diffusion couple, also heated at 1000 °C but for only 30 h, shows a similar diffusion pattern as the 100 h test with slightly thinner reaction zones. Average thicknesses and compositions of interaction layers of this diffusion couple are reported in Table 2. The composition, reported in weight percent, was gained from non-standardized EDS. The results are an average of a semi-quantitative EDS line point spectra taken on this diffusion couple parallel to the material interface

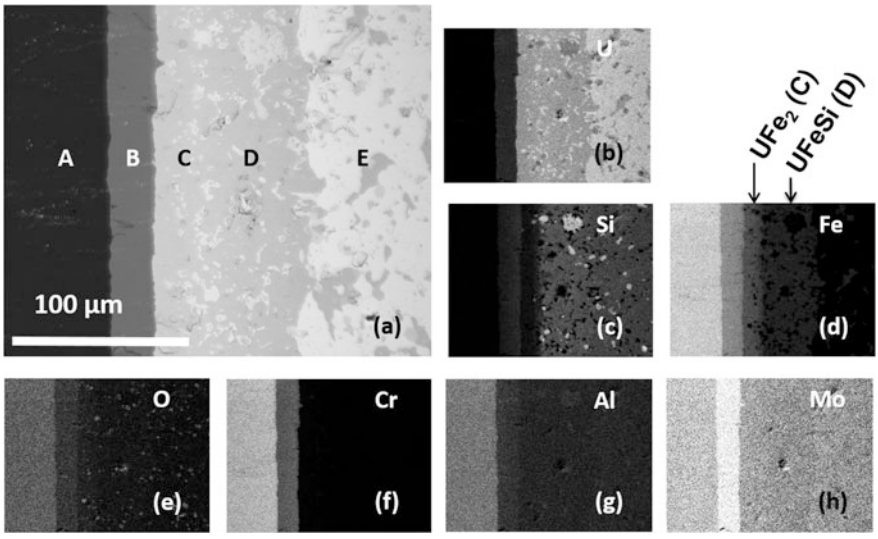

Fig. 6 **a** SEM backscattered electron micrograph of a diffusion couple heated at 1000 °C for 100 h labeled A-E with the A layer the FeCrAl side of the diffusion couple and the E layer the U_3Si_2 side of the diffusion couple. **b-h** are the elemental composition intensity maps for each of the major constituents with whiter hue indicating higher concentration and blacker hue indicating lower composition

Table 2 Elemental compositions, gained from EDS, and width of individual reaction layers A–E, labeled in Fig. 6a

	FeCrAl (section A)	B	C	D	U_3Si_2 (section E)
Width (μm)		20.3	10	66.8	
U	0	8.3	31.5	39.9	53.7
Fe	60.1	51.9	51.0	25.7	0
Cr	26.8	20.8	7.4	2.04	0
Mo	1.9	3.7	0	0	0
Al	11.2	3.7	0	0	0
Si	0	11.6	12.2	39.9	46.3

within each interaction layer with roughly 50 points per interaction layer. Layer A is the FeCrAl side of the diffusion couple, and Layer E, the U_3Si_2, is on the opposite side, with the interaction layers labeled B, C, and D in the middle. The B and C layers are basically homogenous while the D layer exhibits a more characteristic diffusion composition that changes with respect to position.

EDS mapping shows an intensity concentration of each major constituent element, Fig. 6b–h. The map for iron, Fig. 6d, shows the presence of the C layer most obviously, as this layer is very subtle in the rest of the maps and images. The C layer is likely UFe_2. The implications of this reaction layer are discussed below. The iron map also shows iron rich phases penetrating further back into the fuel matrix. EDS quantification confirms the composition of the iron rich phase to be UFeSi. The D layer contains UFeSi phases along with other U-Fe–Si phases and OU_2 impurities from the original composition of the U_3Si_2. The uranium map, Fig. 6b, shows some penetration of U into the FeCrAl. This map, Fig. 6b, along with the Cr and Al maps, Fig. 6f and 6g respectively, and the backscatter micrograph, Fig. 6a, give a good indication the original material interface was likely between the B and C layers. The silicon map, Fig. 6c, shows Si rich phases within the U_3Si_2, as expected from the original fuel composition. The Si map shows the C layer void of Si, and Si migration into the B layer. This is also shown in the concentrations listed in Table 2. The molybdenum map, Fig. 6h, shows an elevated concentration of Mo in the B layer. This shows a higher composition in the interaction zone than for the original material, indicating Mo diffusion towards the U_3Si_2. Both Fig. 6h, g show Mo and Al, respectively, across the entire area which is an artifact of the small signal reading making their results somewhat unreliable.

EDS spectra gathered near the center of the U_3Si_2 disk, the point farthest away from the FeCrAl, showed an iron rich phase, likely UFeSi, permeated the fuel. This was observed via SEM in all diffusion couple tests down to the 600 °C with the percent Fe in the fuel matrix for each test increasing with increasing heating temperatures, as expected. In tests heated to 800 °C and higher U rich spots are visible, as seen in the FeCrAl section, layer A, and also slightly visible in section B of Fig. 6a. An average of several semi-quantitative EDS spectra indicate the spots are UFe_6, which makes sense considering that UFe_6 is liquid down to 719 °C according to the U-Fe binary phase diagram, Fig. 2.

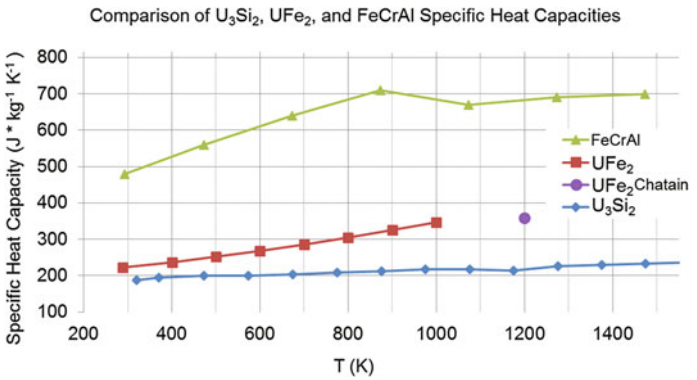

Fig. 7 Literature values for specific heat of U_3Si_2 [4], UFe_2 [11, 14] and FeCrAl [5]

The overall performance of the FeCrAl–U_3Si_2 system may not be greatly affected by the presence of different phases in the interaction region. A comparison of U_3Si_2, UFe_2 and FeCrAl's experimentally measured specific heat capacities, found in literature, is given in Fig. 7 [4, 5, 11, 14]. While the measured heat capacity values for UFe_2 are higher than that of U_3Si_2, they are well below the reported values for FeCrAl. The melting point of the overall system is, however, reduced by the presence of the U-Fe eutectic phases. The U-Fe system has been well investigated, but much less is known about the U–Fe–Si system. Thermal properties measurements on the interaction layers and/or the phases identified would help elucidate how these interaction phases affect the fuel/clad performance.

Conclusion

In a non-irradiated U_3Si_2–FeCrAl fuel system, annealing at temperatures greater than 500 °C with direct contact, causes chemical diffusion. Well known iron–uranium eutectics contribute to the formations of Fe–U rich interactions layers. At higher annealing temperatures (800–1000 °C) three distinct interaction layers are observed with an SEM back scatter electron detector. These layers are similar to those formed in a binary U-Fe system. U travels into the matrix of the FeCrAl as UFe_6 forming circular/spherical uniform spots while iron travels far into the matrix of the U_3Si_2 forming irregular shaped UFeSi phase, similar in composition to that of layer D, the interaction layer closest to the U_3Si_2 matrix, that becomes smaller further away from the material interface. It is unknown how the presence of interaction layers will affect fuel performance. The data gathered in this study will help to inform modeling of accident scenarios to further elucidate implications of interaction regions at higher than normal operating temperatures.

Other candidate cladding materials have been planned for similar analysis. A study on the interaction of U_3Si_2 with Zircaloy—4 has been done in parallel with this study. [5] An irradiation, including diffusion couple systems pairing U_3Si_2 with three potential cladding candidates: FeCrAl, Zircaloy—4, and SiC, to study material interaction under reactor conditions, is planned. These tests will help to inform modeling and ultimately determine the attractiveness and acceptability of the U_3Si_2–FeCrAl fuel system.

Acknowledgements The authors gratefully acknowledge the work of INL electron microscopy staff Tammy Trowbridge and James Madden, as well as Michael Heiss and Michael Chapple for their help in design and fabrication of the diffusion couple holders.

References

1. S.B. Sitton et al., Advanced Fuels Campaign Light Water Reactor Accident Tolerant Fuel Performance Metrics," (Prepared for U.S. Department of Energy Advanced Fuels Campaign, INL/EXT-13-29957 FCRD-FUEL-2013-000264, 2014) (https://nuclearfuel.inl.gov/atf/Reports/ATF%20Metrics%20Report%20Feb%202014.pdf)
2. B.A. Pint et al., High temperature oxidation of fuel cladding candidate materials in steam-hydrogen environments. J. Nucl. Mater. **440**(1), 420–427 (2013)
3. J.M. Harp, P.A. Lessing, R.E. Hoggan, Uranium silicide pellet fabrication by powder metallurgy for accident tolerant fuel evaluation and irradiation. J. Nucl. Mater. **466**, 728–738 (2015)
4. J.T. White, A.T. Nelson, J.T. Dunwoody, D.J. Safarik, K.J. McClellan, Corrigendum to Thermophysical Properties of U_3Si_2 to 1773 K [J. Nucl. Mater. 464 (2015) 275–280]. J. Nucl. Mater. **484** 386–387 (2017)
5. Kanthol.com, Kanthol APMT (Tube) Datasheet, updated 2012 08 16. (http://www.kanthal.com/en/products/material-datasheets/tube/kanthal-apmt/)
6. Nuclear Power Technology Development Section, Thermophysical Properties Database of Materials for Light Water Reactors and Heavy Water Reactors, (Report IAEA-TECDOC-1496, International Atomic Energy Agency, Vienna, 2006), 91 and 253
7. X. Wu et al., Preliminary safety analysis of the PWR with accident-tolerant fuels during severe accident Conditions. Ann. Nucl. Energy **80**, 1–13 (2015)
8. N.M. George, K. Terrani, J. Powers, Neutronic Analysis of Candidate Accident-Tolerant Iron Alloy Cladding Concepts. (Technical Report ORNL/TM-2013/121, Oak Ridge National Laboratory, 2013
9. K.R. Robb, Analysis of the FeCrAl Accident Tolerant Fuel Concept Benefits during BWR Station Blackout Accidents. (Paper presented at the 16th International Topical Meeting on Nuclear Reactor Thermal Hydraulics, Chicago, IL, USA, 01 January 2015)
10. Sudhir Mishra et al., Compatibility Study between U-UO_2 Cermet Fuel and T91 Cladding. J. Nucl. Mater. **481**, 1–12 (2016)
11. S. Chatain, C. Guéneau, D. Labroche, J. Rogez, O. Dugne, Thermodynamic assessment of the Fe-U binary system. J. Phase Equilib. **24**(2), 122–131 (2003)
12. C.M. Walter, L.R. Kelman, The interaction of iron with molten Uranium. J. Nucl. Mater. **20** (3), 314–322 (1966)
13. M.R. Finlay, G.L. Hofman, J.L. Snelgrove, Irradiation behavior of Uranium Silicide compounds. J. Nucl. Mater. **325**(2), 118–128 (2004)
14. G. Campbell, The Thermodynamic Properties of UFe_2: agreement with the Campbell correlation of laves phase compounds. Metall. Trans. A **8A**, 1493 (1977)

Mechanical Behavior of FeCrAl and Other Alloys Following Exposure to LOCA Conditions Plus Quenching

Evan J. Dolley, Michael Schuster, Cole Crawford and Raul B. Rebak

Abstract The US Department of Energy is working with commercial fuel vendors to develop advanced technology or accident tolerant fuels (ATF) for the current fleet of light water power reactors. General Electric and Oak Ridge National Laboratory are evaluating the concept of using iron-chrome-aluminum (FeCrAl) alloys as cladding for the current fuel of uranium dioxide pellets. In the case of a loss of coolant accident, the reactor may need to be flooded with fresh water when the cladding could be in the temperature range above 1000 °C. It is important to determine the integrity of the cladding material after being quenched in water. Tests were performed for six alloys of interest which were exposed for 2 h at 1200 °C in air, argon or steam and then quenched in ambient temperature water. The resulting mechanical properties were evaluated and compared with the mechanical properties of the as received material. The FeCrAl alloy retains its yield strength after the high temperature excursions, with minimal oxidation but with some loss of ductility.

Keywords FeCrAl cladding · Accident tolerant · Thermal shock · Mechanical properties

Introduction

The March 2011 earthquake and tsunami in Japan devastated large areas of land and displaced thousand of persons. The Fukushima nuclear power reactors were damaged during this disaster and continue to have an affect on the surrounding area. During this event, the lack of coolant in the reactor core and in the used fuel storage pools caused the zirconium cladding to react with water and steam to produce combustible hydrogen gas and excessive heat.

Finding a fuel configuration that can better tolerate the loss of coolant than traditional zirconium alloy and uranium dioxide pellets has become an important

E.J. Dolley · M. Schuster · C. Crawford · R.B. Rebak (✉)
GE Global Research, 1 Research Circle, Schenectady, NY 12309, USA
e-mail: rebak@ge.com

J.H. Jackson et al. (eds.), *Proceedings of the 18th International Conference on Environmental Degradation of Materials in Nuclear Power Systems – Water Reactors*, The Minerals, Metals & Materials Series, https://doi.org/10.1007/978-3-319-68454-3_17

task for the international community. The U.S. Department of Energy Office of Nuclear Energy has guided efforts in the U.S. to develop an accident tolerant fuel (ATF) to enhance the safety and performance of current and future nuclear fuel plants [1]. The vision of the DOE-NE is to have a collaborative effort with the industry, universities and national laboratories to create a fleet of reactors with enhanced accident tolerance which will provide clean electricity [2]. The US DOE identified five areas of study that needed to be addressed to reach the milestone of developing a successful concept for an accident tolerant fuel (Fig. 1) [3]. Each concept of ATF should be evaluated in each area of assessment according to the metrics provided by the DOE [3, 4].

As part of the alloy characterization for cladding application, it should be demonstrated that the cladding will survive quenching or thermal shock measures. In the case of a lack of coolant accident, fresh water may need to be pumped into the reactor core to flood or quench the overheated fuel rods [5, 6]. It is important that the candidate cladding would resist the ingress of fresh water without disintegrating or without releasing the radionuclides to the water. Cladding integrity is crucial upon quenching. It has been known for decades that a family of alloys iron-chrome-aluminum (FeCrAl) was resistant to attack by oxygen and steam up to their melting points. The FeCrAl alloys develop protection against steam by the initial formation of a chromium oxide layer on the surface which protects the alloy up to approximately 1100 °C. This chromium oxide film allows for the formation of an alpha alumina layer between the chromium oxide and the metal. As the temperature increases above 1200 °C, the chromium oxide volatilizes in the presence of water molecules, leaving behind the compact and adherent alumina layer on the surface as a protection from further attack by the environment. APMT is one of the

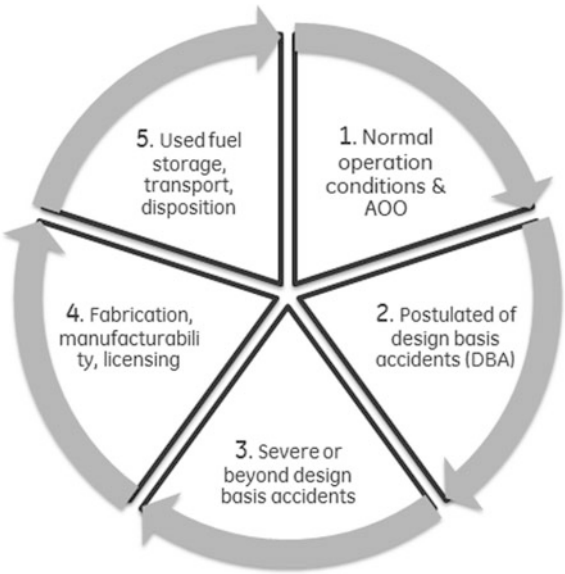

Fig. 1 US DOE identified areas of assessment for ATF

current FeCrAl alloy under consideration for cladding applications, which is produced by Kanthal via powder metallurgy [7].

Extensive steam oxidation studies of APMT at Oak Ridge National Laboratory, Los Alamos National Laboratory and GE Global Research showed that APMT had always the lowest oxidation rate in superheated steam of all the tested metallic alloys. [8–10] The oxidation rate of APMT in steam at 1200 °C is ~1000 times lower than for zirconium alloys. [8–10] Currently ORNL is exploring the manufacturing and tube fabrication of optimized FeCrAl (C26 M) by traditional methods for the cladding application [11].

Experimental Setup and Procedures

To test the relative performance of FeCrAl alloy APMT, five other nuclear materials were tested along with APMT. The alloy selection, compositions and test conditions are in Table 1. To assess the mechanical capability of these alloys in accident condition, each alloy was exposed to 1200 °C temperatures for 2 h before being rapidly quenched in water. To gain a greater understanding on the effect of oxidation and quench, three separate environments were used: argon, air and steam along with a baseline as-received condition where the alloys were not exposed to a high temperature environment. A button head tensile test was used to compare the mechanical properties of each alloy post quench while a witness coupon was exposed alongside the mechanical specimen to study the alloy chemistry effect (Figs. 2 and 3).

A test setup was purposely built at GE Global Research to simulate a accident condition using a 50-mm diameter and 1-m long quartz tube mounted in a vertical resistive tube furnace (Fig. 2). Water-cooled stainless steel end caps with high temperature O-rings were used to seal the tube at both ends (Fig. 2). The lower end cap featured a hinged door and gas inlet while the upper end cap exhausted the gases to a condenser and airlock. For air and argon testing, the gas was regulated and metered through the quartz tube to maintain a consistent flow for all the tests. For steam tests, a small resistive heating tube furnace was fed with distilled water via a peristaltic pump to produce dry steam.

Table 1 Alloy selection and compositions. Two specimens were tested for each condition

Alloys	Nominal composition	RT, AR	1200 °C, 2 h in steam	1200 °C, 2 h in argon	1200 °C, 2 h in air
Zirc-2	>99% Zr	2	2	2	2
600	Ni + 16Cr + 9Fe	2	2	2	2
APMT	Fe + 22Cr + 5Al + 3Mo	2	2	2	2
T91	Fe + 9Cr + 1Mo	2	2	2	2
4C54	Fe + 26.5Cr + 0.2 N	2	2	2	2
304SS	Fe + 19Cr + 10Ni	2	2	2	2

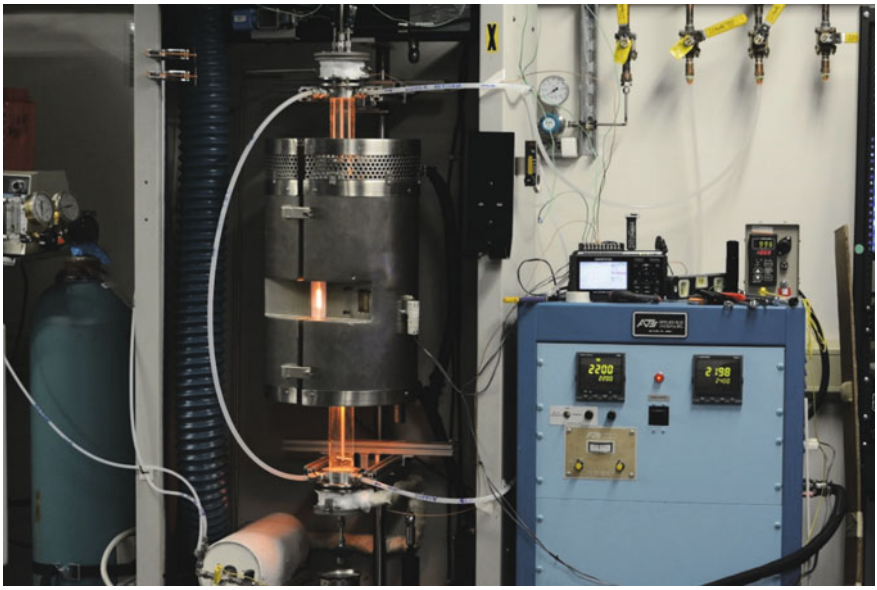

Fig. 2 High temperature test setup constructed at GE global research

Fig. 3 Alumina specimen hanger with integrated thermocouple. The tensile specimen is exposed with a witness coupon

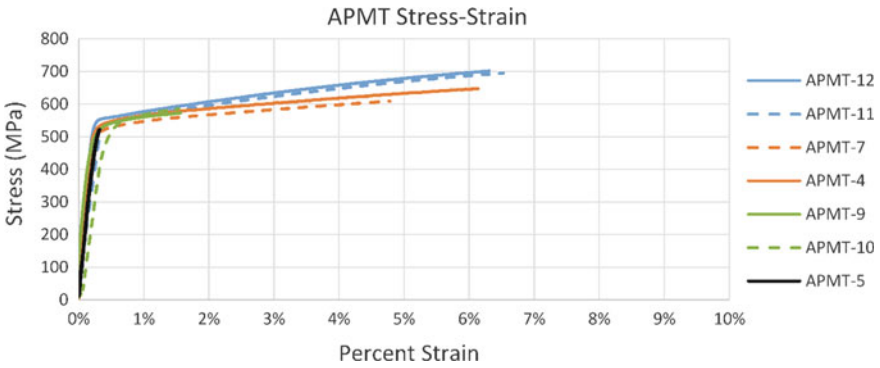

Fig. 4 Stress-strain curve for APMT after water quenching. Blue lines are baseline (non-pre-exposed). Orange Lines are pre-exposed in air at 1200 °C for 2 h and then water quenched, green lines are pre-exposed in argon and black lines are pre-exposed in steam

Achieving the correct thermal conditions within the furnace was critical to these experiments so temperatures were painstakingly measured throughout the system. Locations of thermocouple attachment included test furnace control outside of the quartz tube, steam generator furnace, steam tubing, upper and lower flanges. The upper end cap had ports for 2 alumina sheathed thermocouples to drop in above and below the location where the specimen would sit during the 2-hour exposure. The top flange also had a port for an alumina rod that was used to hang the specimens from with platinum wire. This alumina rod could be raised and lower to the desired locations during the exposure and subsequent quench. It also contained a length of TC wire that was attached to a small piece of APMT that acted as an instantaneous temperature measurement wherever the specimens were located within the furnace. This allows for a high degree of confidence in the specimen temperature while not directly affecting each specimen.

Existing mechanical test setups were utilized at GE Global Research to generate tensile stress-strain curves. An Instron hydraulic test frame was equipped with clamshell-style button head tension grips. An MTS Model 632.53 extensometer with a 25-mm gage section and alumina v-notch rods was used to collect strain data.

All tensile and witness coupons were machined in GE Global Research Fabrication shop. Witness coupons were polished, weighed and photographed before testing for oxide mass measurements. Tensile specimens were machined into 57 mm long button head specimens with a 19-mm gage length and 4 mm gage diameter. The specimens were attached to the alumina rod with platinum wire. The Zircaloy-2 coupons required molybdenum wire during argon tests due to a reaction between platinum and zirconium in the absence of oxygen at 1200 °C. The specimens were raised on the alumina rod to the pre-test location just inside of the hinged door and the flange sealed with a silicone gasket. Air or argon flows were then started at 1.5 L/min calibrated to air. The specimens remained below 200 °C at this location for the furnace temperature ramp and soak. For steam tests, argon flow

was used during the furnace ramp to flush oxygen from the system and then steam flow started at 8 mg/cm^2/s once the test furnace reached temperature. After roughly 30 min had elapsed and the temperatures and flows stabilized, the alumina rod was pulled up through the top flange, raising the specimens into the hot zone where they remained for the duration of the environmental exposure.

To quench the specimens after the exposure, the above process was simply reversed. A separate stainless steel beaker was filled with distilled water for the witness and tensile coupon and was placed below the bottom flange. The flange door was opened and the alumina rod lowered until the specimens entered the quench beakers. This process took less than 30 s and temperatures were continually monitored from the specimen TC to ensure quenches occurred above 800 °C.

After quenching, the witness specimen beaker was filtered to collect any spalled material. This was set out to dry along with the tensile specimen, photographed and weighed after a 24-hour period. The tensile specimen diameter was re-measured to account for any change due to oxide formation and put on frame to test within an hour. The specimens were pulled (strained) at 0.5 mm/min until final failure and the post-test minimum diameter recorded to measure percent reduction in area. This metric is a good measure of ductility that introduces less error than manual measurements of percent elongation.

Mechanical Behavior

Each alloy of interest was mechanically tested in an as as-received condition as well as after a 2 h 1200 °C exposure to either air, argon or steam followed by a quench in water. Two specimens were tested for each condition (Table 1). In the stress-strain plots in Figs. 4, 5, 6, 7, 8 and 9 below, blue curves denote the

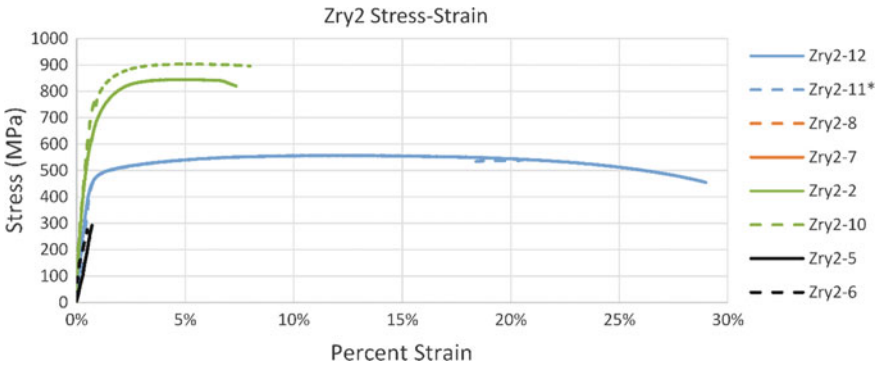

Fig. 5 Stress-Strain Curve for Zircaloy-2 after water quenching. Blue lines are baseline (non-pre-exposed). Orange Lines are pre-exposed in air at 1200 °C for 2 h and then water quenched, green lines are pre-exposed in argon and black lines are pre-exposed in steam. The asterisk denotes the removal of an elongation clip during the straining test

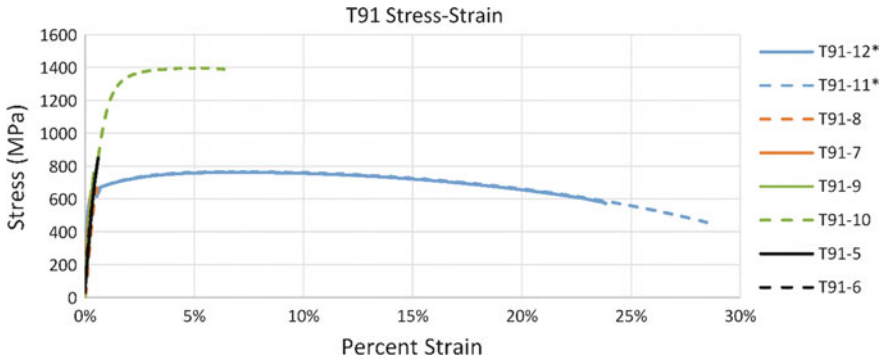

Fig. 6 Stress-Strain Curve for T91 after water quenching. Blue lines are baseline (non-pre-exposed). Orange Lines are pre-exposed in air at 1200 °C for 2 h and then water quenched, green lines are pre-exposed in argon and black lines are pre-exposed in steam. The asterisk denotes the removal of an elongation clip during the straining test

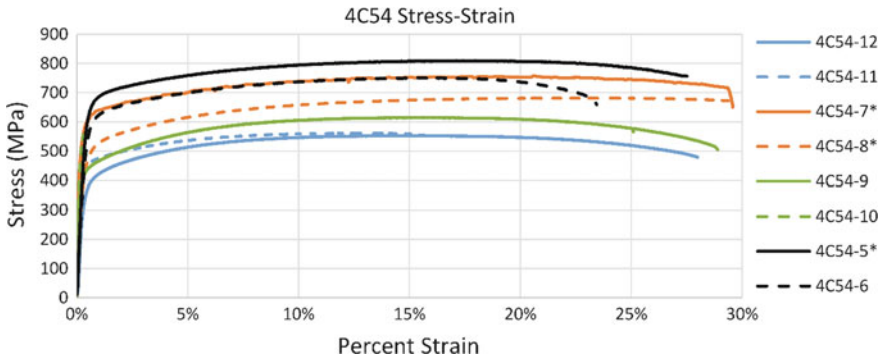

Fig. 7 Stress-Strain Curve for 4C54 after water quenching. Blue lines are baseline (non-pre-exposed). Orange Lines are pre-exposed in air at 1200 °C for 2 h and then water quenched, green lines are pre-exposed in argon and black lines are pre-exposed in steam. The asterisk denotes the removal of an elongation clip during the straining test

as-received condition, green the argon condition, orange the air condition and black lines in the steam condition. The extensometer required removal near its operational limit of 20% strain and tests are noted with an asterisk next to their specimen number to indicate that the final failure was not captured in strain.

In Fig. 4 above, APMT showed consistent mechanical behavior in each condition tested. The results for APMT in steam represent the data of one test only since the other two tested specimens did not fail in the gauge. More tests are being conducted using a different heat of material. In general, APMT showed the lowest strain to failure of all the alloys. The tested APMT material originated from a square billet (heat Melt 241975) which did not have uniform grain size and particularly many stringers. The results for APMT are currently being repeated using a rod with

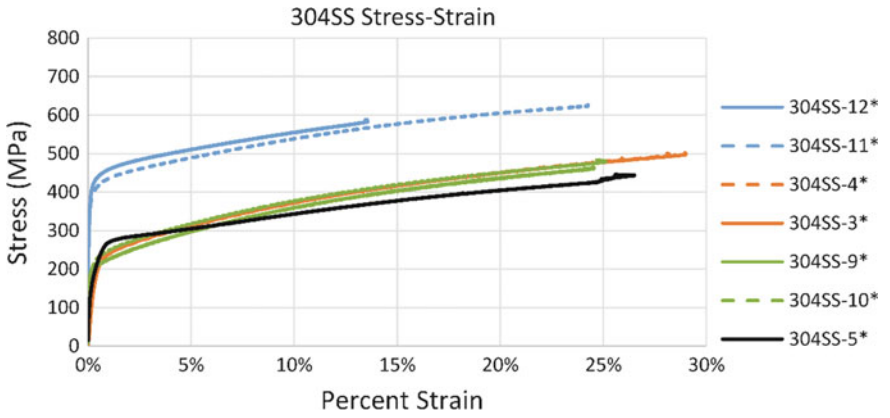

Fig. 8 Stress-Strain Curve for 304SS after water quenching. Blue lines are baseline (non-pre-exposed). Orange Lines are pre-exposed in air at 1200 °C for 2 h and then water quenched, green lines are pre-exposed in argon and black lines are pre-exposed in steam. The asterisk denotes the removal of an elongation clip during the straining test

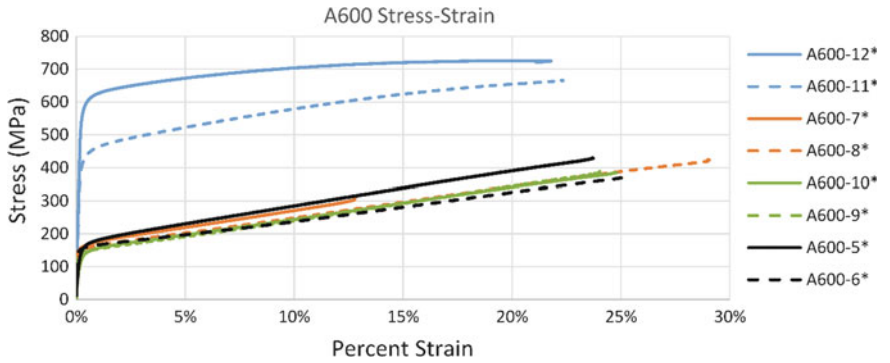

Fig. 9 Stress-Strain Curve for Alloy 600 after water quenching. Blue lines are baseline (non-pre-exposed). Orange Lines are pre-exposed in air at 1200 °C for 2 h and then water quenched, green lines are pre-exposed in argon and black lines are pre-exposed in steam. The asterisk denotes the removal of an elongation clip during the straining test

better microstructure. Zircaloy-2 showed high ductility in the as-received condition however, it significantly reduced after exposure to the LOCA environment. In fact, the air test specimens could not even be fit into the test frame due to the severe oxidation and distortion of the specimen. Even Zircaloy-2 specimens pre-exposed in argon showed significant embrittlement and small strains to failure with little plasticity. T91 performed like Zircaloy-2, showing a definite reduction in ductility after 1200 °C exposure. Greater ductility was observed for 304SS, Alloy 600 and 4C54 however 304SS and A600 had a reduction in yield strengths for the high temperature pre-exposed conditions. The ductility of 4C54 remained high after

quenching except for a few tests that exhibited low strain failures. Figures 10 and 11 show comparisons of yield strengths and percent reduction in area, respectively. The same color scheme used in the stress-strain plots above is employed for the bar charts below. Figure 10 shows that the ferritic materials (T91, 4C54 and APMT) in general retained a high yield strength after exposure to 1200 °C for 2 h in air, argon or steam and then water quenched. The results for APMT in steam (black column) represent the data of one test only since the other two specimens did not fail in the gauge. More tests are being conducted using a different heat of material.

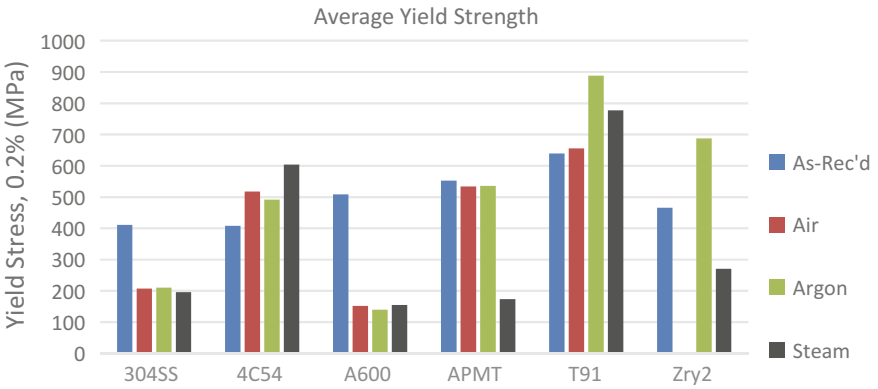

Fig. 10 Average yield strength of each alloy and environment. Before mechanical testing, each specimen was pre-exposed to air, argon or steam for 2 h at 1200 °C and then water quenched

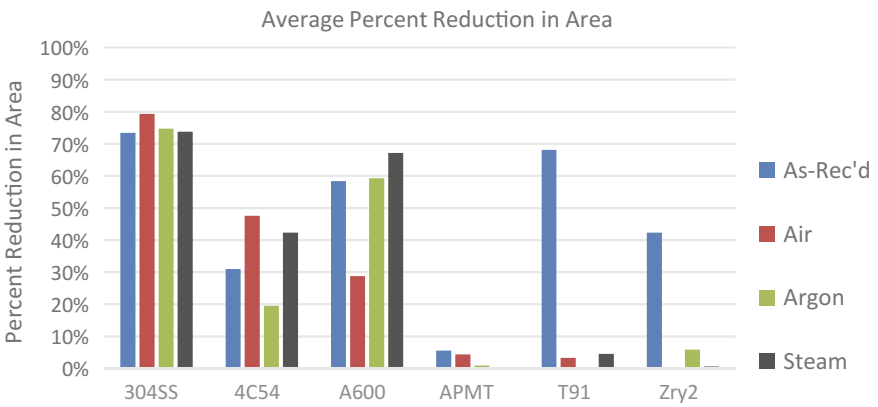

Fig. 11 Average percent reduction in area of each alloy and environment. Before mechanical testing, each specimen was pre-exposed to air, argon or steam for 2 h at 1200 °C and then water quenched

Characterization of Surface Oxides

When the tensile specimens were pre-exposed in air, argon or steam for 2 h and when water quenched, a witness coupon of each material was used to evaluate the oxidation characteristics in the three environments (Figs. 3 and 12). Figures 13, 14 and 15 show the characteristics of the oxides formed on the witness coupons of the six tested alloys in argon, air and steam, respectively. For coupons exposed at 1200 °C in argon for 2 h, very little oxidation was observed (Fig. 13). It is possible that some oxidation could occur when the specimens leave the furnace before entering the quench beaker as well as during the quench although the time over which this could occur is very short (tens of seconds). The clean surfaces in Fig. 13 also indicate the quality of test environment. Interestingly, Zircaloy-2 shows some oxide as well as a potential phase change possibly due to oxygen diffusion from the environment into the metal near the surface. For 304SS and A600, there was a distinct softening while maintaining their ductility as measured by percent reduction in area (Figs. 10 and 11). It should be noted that both T91 specimens experienced failures at the button head because of their increased hardness.

Figure 14 shows the metallographic cross-sections of each of the six alloy witness coupons that were exposed in air at 1200 °C for 2 h and then water quenched. The degree of oxidation varied from material to material. For example,

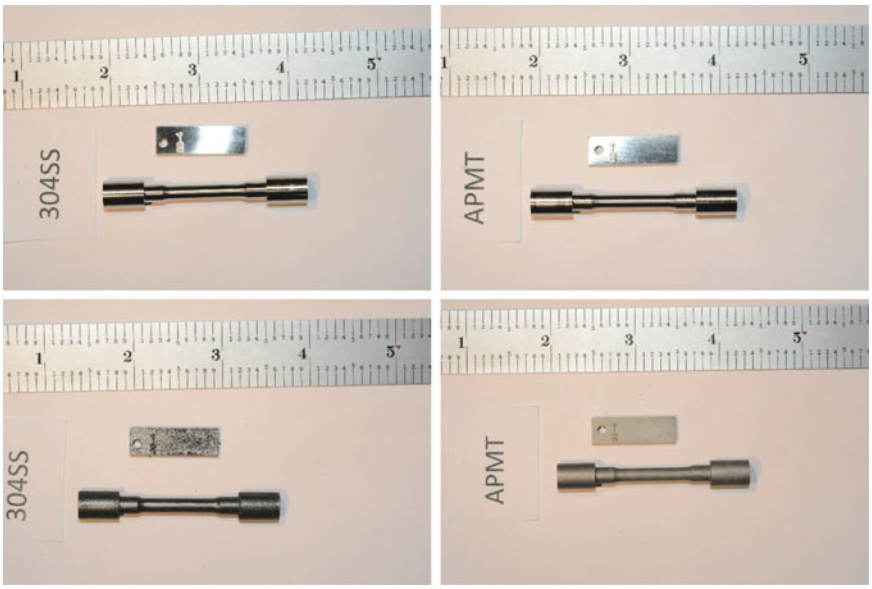

304SS, before test (top) and after exposure to air at 1200°C for 2h + Water Quench.

APMT, before test (top) and after exposure to air at 1200°C for 2h + Water Quench.

Fig. 12 Example of tensile specimen and witness coupons before and after environmental exposure for 2 h at 1200 °C

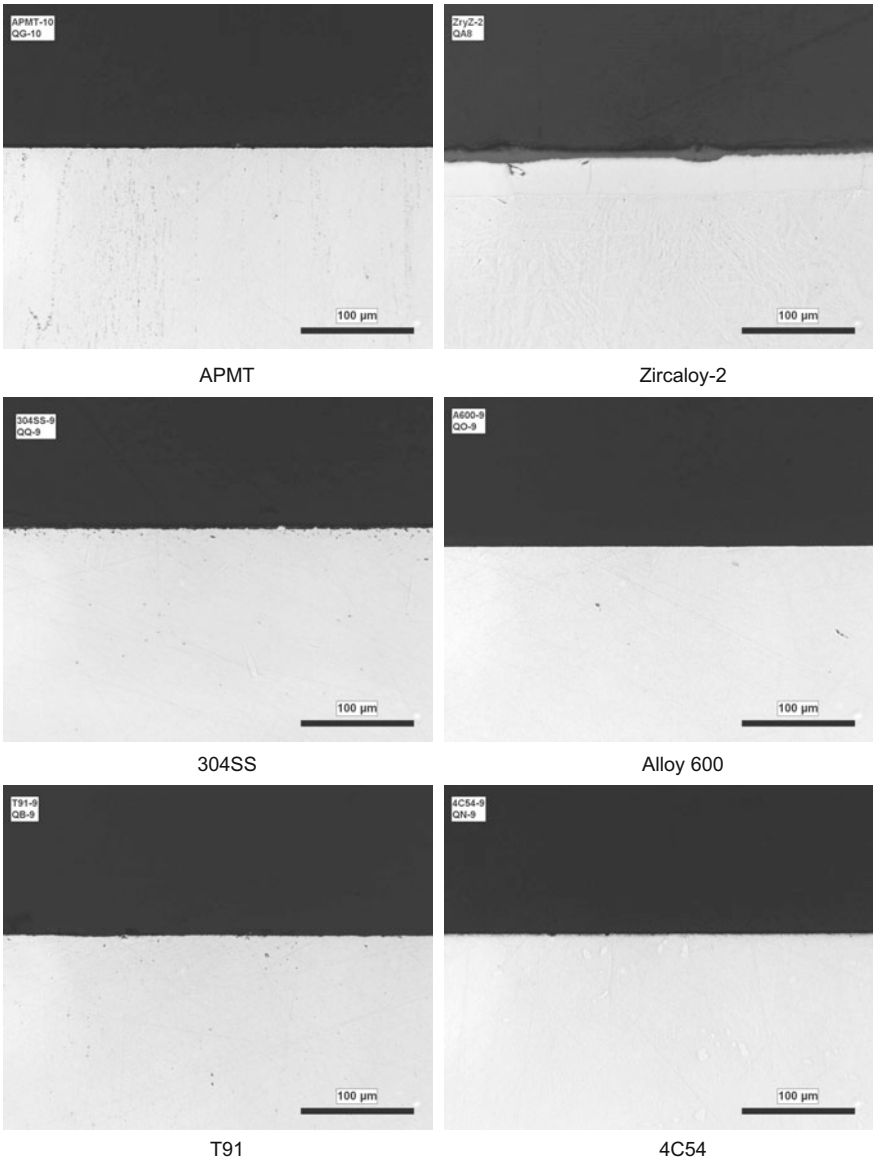

Fig. 13 Micrographs of cross sections of alloy coupons exposed to argon at 1200 °C for 2 h and the water quenched. The largest oxidation was for Zirc-2, which also showed phase transformation in the external section

the Zircaloy-2 coupon was completely consumed while APMT showed little oxidation. X-ray diffraction was performed on these materials to identify the phases present in each of the specimens. APMT developed a thin alumina layer as

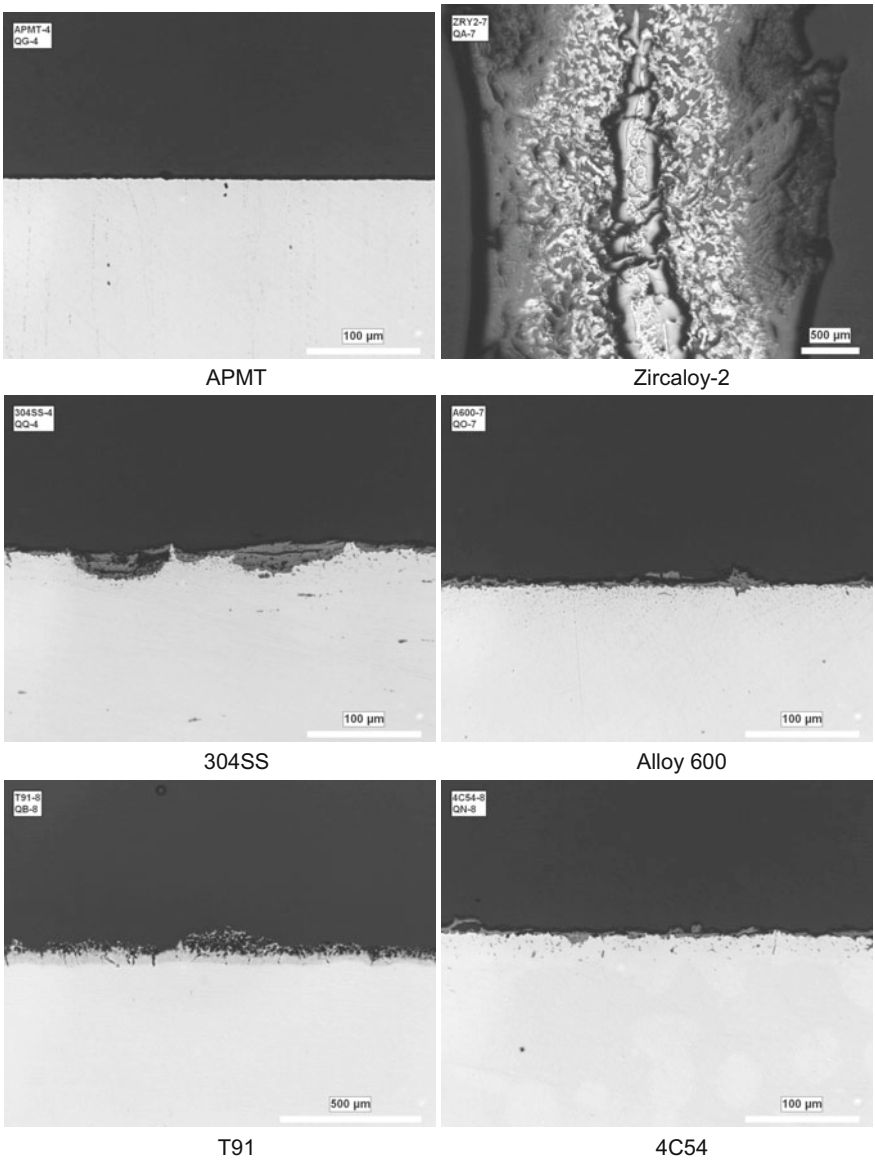

Fig. 14 Micrographs of cross sections of alloy coupons exposed to air at 1200 °C for 2 h and the water quenched. The largest oxidation was for Zirc-2, which also showed phase transformation in the external section

expected, which is barely visible at the shown scale. Zircaloy-2 on the other hand was nearly consumed in the formation of zirconium oxide. T91 also formed a significant oxide layer composed of several common forms of iron oxide. For air

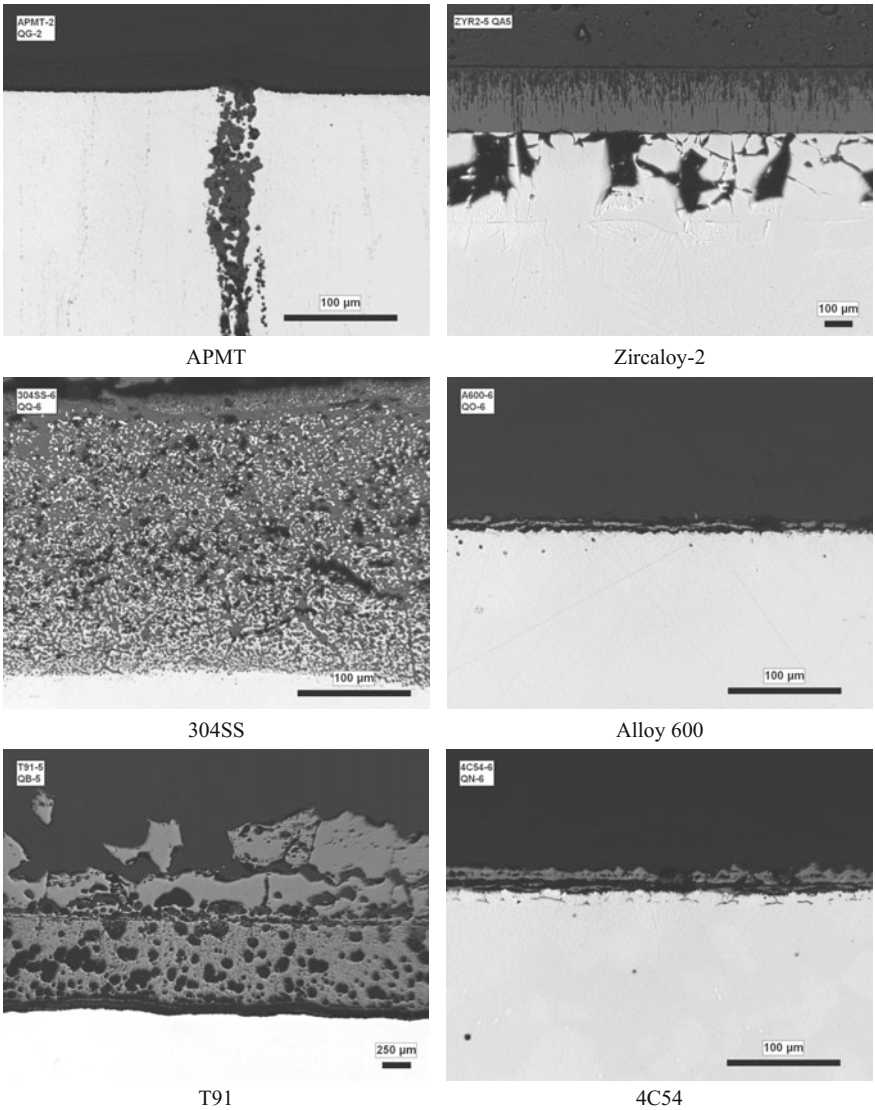

Fig. 15 Micrographs of cross sections of alloy coupons exposed to steam at 1200 °C for 2 h and the water quenched. APMT showed little or no oxidation from the surface but had some stringer associated failure

tests, the oxide layer in T91 flaked off and revealed a reduced diameter. Subsequently, under straining, it failed in a brittle fashion with very low reduction in area. Other alloys show modest oxide growth containing chromium and iron oxides that did not vary their yield strength compared to argon tests but did affect their ductility.

Figure 15 shows the metallographic cross-sections of each of the six alloy witness coupons that were exposed in steam at 1200 °C for 2 h and then water quenched. The degree of oxidation varied from material to material. For example, Alloy 600 and 4C54 had a generally good performance. For steam tests, the oxide layer in T91 flaked off and revealed a reduced diameter. APMT had little or no oxidation attack however, the image in Fig. 15 show a "separation" due to the presence or stringers that met the surface. These tests will be repeated using APMT with a more uniform microstructure. Figure 16 shows scanning electron microscopy (SEM) images of the same APMT coupon in Fig. 16, with details of the stringers that intersect the surface. Figure 16 also shows the second phase particles in APMT and the protective alumina layer on the surface. The Zircaloy-2 coupon had two levels of penetration, a thick oxide and then a phase transformation layer with voids. In general, Zircaloy-2 was more resistant to attack in steam than in air at the same temperature. Figure 16 shows SEM images of the oxide formed on Zircaloy-2. There are three layers of attack since the oxide has two layers separated with a string of second phase particles. Figure 16 also shows in higher magnification the boundary between the oxide and the non-oxidized metal, with stringers of second phase particles left unoxidized in the oxide layer.

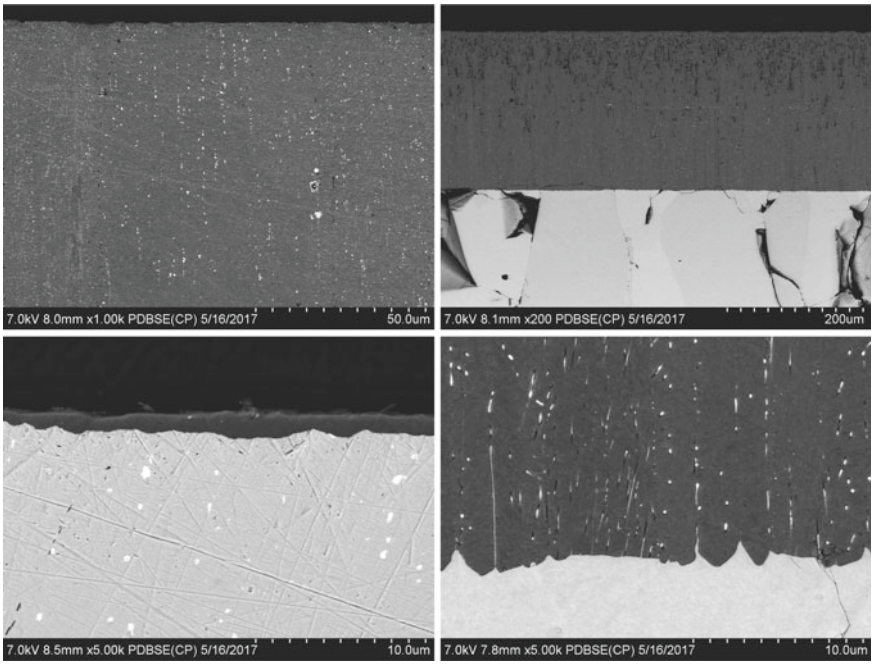

APMT QG-6 Coupon exposed to steam at 1200°C for 2 h and then water quenched.

Zircaloy-2 QA-5 Coupon exposed to steam at 1200°C for 2 h and then water quenched.

Fig. 16 Scanning Electron of cross section of witness coupons

Summary and Conclusions

The goal of the U.S. Department of Energy Accident Tolerant Fuel Program for Light Water Reactors is to identify alternative fuel technologies that enhance the safety, competitiveness and economics of nuclear power. Accident tolerant fuels will endure loss of cooling in the reactor core for longer period than the current generation of fuel. At a minimum, these new technologies should maintain the performance during standard operations, if not improve upon them.

The ATF design concept proposed by General Electric utilizes an FeCrAl alloy (such as APMT) for fuel rod cladding in combination with the current generation uranium dioxide fuel pellets.

Currently six alloys were exposed for 2 h at 1200 °C in three environments (argon, air and steam) and then quenched in water. All the tested materials showed in general a superior behavior than the zirconium based alloy. APMT showed a high resistance to oxidation and retained its mechanical properties following the quench procedure. More studies are in progress to determine that APMT can accept the presence of fresh water without suffering embrittlement.

Acknowledgements The authors would like to thank the characterization lab at GE Global Research, including Mike Larsen, Jae-Hyuk Her and Ian Spinelli. Great thanks to Lisa Sciubba at Lucideon (Schenectady, NY) for metallographic cross sections. The funding support from GE Hitachi is gratefully acknowledged. This material is based upon work supported by the Dept. of Energy [National Nuclear Security Administration] under Award Number DE-NE0008221. This report was prepared as an account of work sponsored by an agency of the United States Government. Neither the United States Government nor any agency thereof, nor any of their employees makes any warranty, express or implied, or assumes any legal liability or responsibility for the accuracy, completeness, or usefulness of any information, apparatus, product, or process disclosed, or represents that its use would not infringe privately owned rights. Reference herein to any specific commercial product, process or service by trade name, trademark, manufacturer, or otherwise does not necessarily constitute or imply its endorsement, recommendation, or favoring by the United States Government or any agency thereof. The views and opinions of authors expressed herein do not necessarily state or reflect those of the United States Government or any agency thereof.

References

1. J. Kotek, Fukushima: Looking Back, Looking Ahead. energy.gov/ne/articles. (Retrieved 2016 04 19)
2. US Department of Energy, Development of Light Water Reactor Fuels with Enhanced Accident Tolerance, Report to Congress, June 2015
3. S. Bragg-Sitton et al. (10 more names), Advanced Fuels Campaign LWR Accident Tolerant Fuel Performance Metrics, Idaho National Laboratory, Advanced Fuels Campaign, FCRD-FUEL-2013-000264, INL/EXT-13-30226 (February 2014)
4. J. Carmack, F. Goldner, Forward for special JNM issue on accident tolerant fuels for LWRs. J. Nuclear Mater. **448** (1–32014), 373 (2014)

5. V.K. Dhir, R.B. Duffey, I. Cation, Quenching Studies on a Zircaloy Rod Bundle. J. Heat Transfer **103**(1981), 293–299 (1981)
6. F.S. Gunnerson, T.R. Yackle, Quenching and rewetting of nuclear fuel rods. Nucl. Technol. **54**(1), 113–117 (1981)
7. R.B. Rebak, Alloy selection for accident tolerant fuel cladding in commercial light water reactors. Metallurg. Mater. Trans. E **2E**, 197–207 (2015)
8. K.A. Terrani, S.J. Zinkle, L.L. Snead, Advanced oxidation-resistant iron-based alloys for LWR fuel cladding. J. Nucl. Mater. **448**(1–3), 420–435 (2014)
9. R.E. Stachowski1, R.B. Rebak, W.P. Gassmann, J. Williams, Progress of GE Development of Accident Tolerant Fuel FeCrAl Cladding. Top Fuel 2016, Boise Idaho, September 2016
10. B.A. Pint, K.A. Terrani, Y. Yamamoto, L.L. Snead, Material selection for accident tolerant fuel cladding. Met. Mater. Trans. E **2E**, 190 (2015)
11. K.A. Terrani, B.A. Pint, Y.-J. Kim, K.A. Unocic, Y. Yang, C.M. Silva, H.M. Meyer III, R.B. Rebak, Uniform corrosion of FeCrAl alloys in LWR coolant environments. J. Nucl. Mater. **479**, 36–47 (2016)

Mechanical Behavior and Structure of Advanced Fe-Cr-Al Alloy Weldments

M.N. Gussev, K.G. Field, E. Cakmak and Y. Yamamoto

Abstract FeCrAl alloys are promising for developing accident tolerant nuclear fuel claddings. These alloys showed good environmental compatibility and oxidation resistance in elevated-temperature water and steam, as well as low radiation-induced swelling. However, FeCrAl alloys may suffer from several degradation mechanisms, one of which may be a susceptibility to cracking during welding. Here, a set of advanced modified FeCrAl alloys were designed and produced by varying Al-content and employing additions of Nb and TiC. Strength, ductility, and deformation hardening behavior of the advanced FeCrAl alloys and their weldments are discussed.

Keywords FeCrAl alloys · Laser-beam welding · EBSD · Digital image correlation

Introduction

The designs for electrical power plants call for materials that can withstand harsh and extreme environments, including elevated temperature, high mechanical stresses, acute and chronic corrosive media attack, to name a few. Many applications also

M.N. Gussev (✉) · K.G. Field · E. Cakmak · Y. Yamamoto
Oak Ridge National Laboratory, One Bethel Valley Road MS-6151, P.O. Box 2008, Oak Ridge, TN 37831, USA
e-mail: gussevmn@ornl.gov

J.H. Jackson et al. (eds.), *Proceedings of the 18th International Conference on Environmental Degradation of Materials in Nuclear Power Systems – Water Reactors*, The Minerals, Metals & Materials Series, https://doi.org/10.1007/978-3-319-68454-3_18

require materials with good weldability [1], where the welds are also repairable [2]. In the case of nuclear power plants, radiation tolerance and the ability to survive normal and off-normal conditions (e.g., loss-of-coolant accidents [LOCA]) [3] are also important material-performance metrics. Iron-chromium-aluminum (FeCrAl) alloys are one class of materials showing initial promise as robust materials for use in power production applications. These alloys have shown excellent environmental compatibility, including a resistance to aqueous corrosion [4, 5], compatibility with heavy metal [6], and a resistance to oxidation in the high-temperature air [7] and steam [3, 8]. It is worth noting that these FeCrAl alloys also exhibit low radiation-induced swelling [9, 10] and are tolerant to LOCA conditions [3]. This aggregate of beneficial properties makes the FeCrAl alloy class promising for further optimization through additional composition and processing refinements [11].

The FeCrAl alloys containing less than about 12 wt% aluminum can be processed using several techniques, including traditional wrought processing and more modern powder metallurgy [12]. Even though good weldability was demonstrated for some FeCrAl alloy compositions using laser beam welding [11], the loss of ductility and grain coarsening in the weldment [1] remains one of the major concerns. Several reports have indicated that many FeCrAl alloy compositions are susceptible to welding-induced cracking. For example, Regina et al. [13] and Dupont et al. [14] have shown that FeCrAl weld overlays, performed using gas tungsten arc welding (GTAW) and gas metal arc welding (GMAW), have a higher susceptibility to welding-induced cracking when high-chromium and high-aluminum variants are used. Such poor performance during welding may be a limiting factor in the design and technological deployment of FeCrAl alloys in electrical power plants.

Typically, advanced and custom-designed modern materials have highly-tailored microstructures and microchemistry that enhance their performance. The high-heat input from welding leads to the localized melting of the material and inevitably the destruction or, at a minimum, degradation of the tailored microstructure and microchemistry at and near the weld. Processes in the welding pool may be very complicated [15, 16], leading to element segregation, evaporation, etc. [16]. Even in regions outside the fusion zone, localized heating can be at or above critical temperatures (e.g., the critical temperature for recrystallization), leading to additional changes in microstructure. These regions are typically referred to as heat-affected zones (HAZs) and often experience increased stresses and strains from shrinking during weldment cooling [17].

Therefore, regardless of the performance and promises of advanced oxidation-resistant FeCrAl alloys, their weldability and weldment performance should be examined in detail. In particular, the cracking susceptibility, resulting microstructure, and post-welding mechanical properties should be studied and determined. The present work analyzes the impact of laser-beam welding on the properties and structure of advanced oxidation-resistant FeCrAl alloys with composition and processing refinements.

Investigated Materials and Experimental Methods

The present work focuses on the role of alloying, including the role of several modified FeCrAl alloys, on weldability and the performance of the weldments. Early alloys, including Generation I FeCrAl alloys [11], demonstrated good weldability but had high chromium content ($\leq 17\%$) and low aluminum content ($\leq 4.42\%$) and suffered from significant hardening due to the α'-phase formation during aging or irradiation [18–22]. Additionally, the weldment yield strength (~ 360 MPa) compared to the bulk properties, left significant room for improvement.

To overcome these issues, Generation II FeCrAl alloys based on the alloy designated as C35M were developed. Since the same alloys are being used by several programs [11, 18, 20, 23], it is appropriate to use the internal alloy identifiers (ID) (like C35M) within the present work. One alloy was developed to explore the effects of aluminum on weld-induced cracking. For example, Regina et al. [13] has indicated a composition-based cracking boundary for FeCrAl alloys where high aluminum and/or high chromium content FeCrAl alloys are more susceptible to weld-induced cracking. Another group of alloys were designed to explore the role of secondary phases on the weldability of alloys. Two secondary phases were studied, the first was Fe_2Nb-type Laves phase precipitates introduced through alloying of molybdenum and niobium and the second the TiC phase. Both precipitate dispersions are hypothesized to be benign hydrogen trapping sites with the benefit of acting as grain boundary pinning sites during solidification and recrystallization. The specific alloy designations and their chemistry are provided in Table 1. Within Table 1, bolded and underlined compositions represent variations in nominal chemistries from the reference C35M FeCrAl material. Details on the fabrication routes including thin plate production and the autogenous, bean-on-plate welding technique used in this study for each alloy can be found in previous studies [21].

Electron back scattered diffraction (EBSD) analysis was conducted using a JEOL JSM 6500F SEM with a field emission gun equipped with an EDAX EBSD system to determine the grain size, texture (orientation), and grain shape of the alloy prior to and after welding. All samples investigated were carefully polished using standard metallography procedures to produce a defect-free, mirror-like surface. The accelerating voltage for the investigations was 20 kV, and the working distance was 12–17 mm. The step size of the EBSD maps varied between 0.5 and 3.0 μm depending on the resolution needed for microstructural assessment. The camera operated in a 2×2 binning mode at around 90–100 frames per second.

Tensile specimens were produced from the welded plates using an electric discharge machine (EDM). The fusion zone was in the center of the welded specimen gauge. After EDM cutting, the 1-mm thick specimen blanks were mechanically ground to fit the thickness dimension of the SS-J tensile specimen.

Tensile tests were performed on an MTS Insight 2-52 one-column tensile screw machine with a 2 kN load cell. All tensile specimens (3–5 per alloy and condition) were shoulder loaded and tested at room temperature. Before the tensile tests,

Table 1 Composition (wt%) of the investigated second-generation FeCrAl alloys

Alloy ID	Short composition notation	Fe	Cr	Al	Y	Si	Nb	C	O	N	P	Ti
C35M	Fe-13Cr-5Al	79.43	13.06	5.31	0.053	0.13	<0.01	0.001	0.0012	0.0003	0.007	<0.01
C37M	Fe-13Cr-7Al	77.49	13.01	**7.22**	0.081	0.19	<0.01	0.001	0.0026	0.0002	0.004	<0.01
C35MN	Fe-13Cr-5Al-1Nb	78.7	13	5.11	0.044	0.18	**0.96**	0.005	0.0014	0.0002	<0.002	–
C35M01TC	Fe-13Cr-5Al-0.1TiC	79.51	13	5.2	0.04	0.15	<0.01	**0.024**	0.0009	0.0004	0.002	**0.08**
C35M03TC	Fe-13Cr-5Al-0.3TiC	79.34	13.03	5.17	0.04	0.15	<0.01	**0.058**	0.0009	0.0003	0.003	**0.22**
C35M10TC	Fe-13Cr-5Al-1TiC	78.82	12.95	5.14	0.01	0.2	<0.01	**0.18**	0.0012	0.0007	<0.002	**0.71**

In all alloys, Mo is 2%. All other elements (Zr, B, Hf, V, W, Ce, Co, Cu, La, Mn, and Ni) measured to be at or below <0.01. S < 0.0003

specimens were painted with a random speckle pattern. The surface speckle pattern allows for optical, non-contact strain measurements using a digital image correlation (DIC) approach [24]. This method is now a common research tool employed by many research teams [25–27] for strain measurements, visualization of deformation bands, necking analysis, etc. In terms of weldment performance analysis, DIC enables the investigator to measure local yield stress (LYS) and retrieve local deformation values [17, 27, 28]. The features and limitations of DIC are widely described in the literature [24] and will not be discussed here. High-resolution Allied Vision GT6600 and GX3300 cameras were used in the experiments; the lenses provided a resolution of around 5 μm per pixel. Strain fields and true stress–true strain curves were calculated using VIC-2D commercial software and another custom software application.

Experimental Results

Figure 1 shows typical microstructures of the investigated alloys. SEM-EBSD maps, not optical images, are presented because SEM-EBSD also provides information on texturing and internal misorientation gradients in the microstructure. All alloys showed a microstructure consistent with warm-rolled material conditions, with a mix of deformed (non-recrystallized) and recrystallized grains.

The recrystallized grains often formed elongated chains in the rolling direction. An alternating mix of recrystallized and non-recrystallized grains sometimes resulted in a band-like microstructure, most pronounced in the C35M alloy. All alloys exhibited strong texturing near the [101] corner of the unit triangle (with respect to the warm-rolling direction, which was also the tensile direction). Recrystallized grains, as a rule, had a close-to-random texture, with the C37M alloy being the best example. However, sometimes the chains of recrystallized grains had a similar orientation (color in IPF map). This orientation could, potentially, lead to the decreased mechanical performance. Such a case, with detrimental texturing and

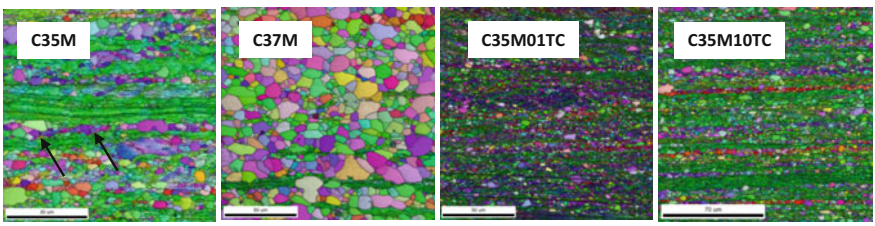

Fig. 1 Typical EBSD IPF maps for the investigated materials. The C35M03TC alloy was omitted as its structure was close to that of the C35M10TC. C35MN was close to that of C35M. IPFs are colored with respect to the tensile direction. Black arrows point to the chains of closely-oriented grains ("streams" in terms of [29])

ridging due to the presence of coarse-grain chains ("streams"), was discussed by Patra et al. [29] for a ferritic steel with an 11 wt% of chromium.

Unlike the nominally-identical processing routes, recrystallization degree varied for the investigated materials. The C35M (Fig. 1) and C35MN (not shown) alloys experienced moderate recrystallization, whereas C37M demonstrated an almost fully (>90%) recrystallized structure with well-shaped grains and just a few remaining non-recrystallized areas (Fig. 1). Recrystallization was less pronounced in the C35M01TC, C35M03TC, and C35M10TC alloys with the TiC-additions. The size of the recrystallized grains was significantly smaller in these alloys compared to C35M and C37M, suggesting a positive effect that TiC has on grain refinement. It appears that small variations in the composition may lead to significant changes in the recrystallization kinetics [30] and final grain size of these alloys (e.g., C35M vs. C37M as shown in Fig. 1).

Figure 2 shows the structure of the investigated alloys' weldments. For most alloys (C35M, C37M, C35M01TC, and C35M03TC), welding led to the formation of relatively large grains of irregular shapes near the weldment centerline. This feature was complemented by elongated or columnar grains which appeared roughly 200–300 μm away from the centerline. The width of the columnar-grain area was around 300 μm. Distinct areas of coarse, round-shaped grains were observed nearly 600 μm away from the centerline. It is believed this is a region of the HAZ where melting did not occur, but the specimen temperature was well above the recrystallization temperature for the investigated materials. Interestingly, alloys with niobium and TiC additions demonstrated smaller grain growth in this region.

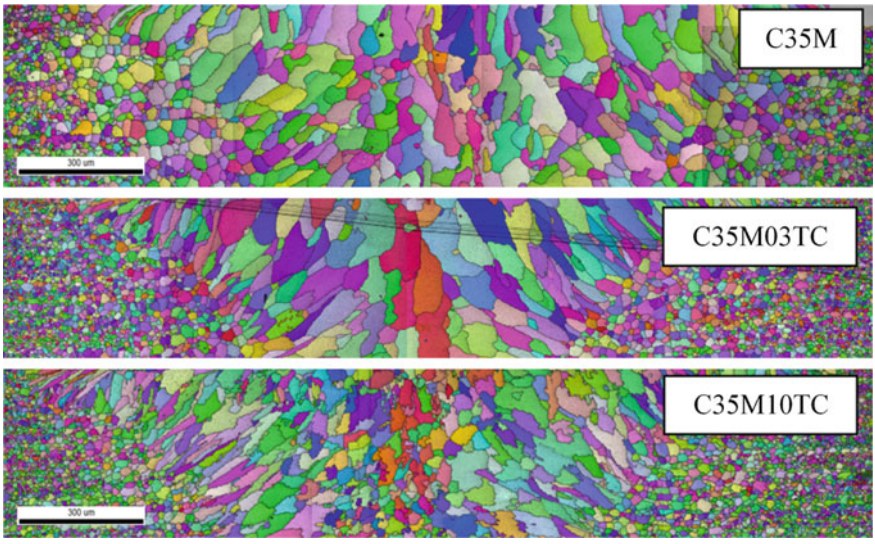

Fig. 2 Stitched EBSD IPF maps showing weldment structure for several alloys. Images for other alloys were omitted since the structure was very close to that of the C35M alloy weldment

The C35M10TC alloy had a distinctly different microstructure in the fusion zone compared to other materials. The grain size of the fusion zone was significantly reduced and was on the order of 3–5× smaller. The grains near the weldment center had specific morphology with torturous boundaries. The columnar-grain area was also smaller and appeared more elongated. Based on the observed microstructures in Fig. 2, the 1% addition of TiC appeared to increase the fraction of grain boundaries pinned during the melt and solidification processes. The grain boundary pinning limited the grain growth and resulted in the reduced grain size in this alloy, as shown in Fig. 2. The grain boundary pinning and grain refinement were most pronounced in the fusion zone, where base metal melting occurred. In the elongated grain region, the TiC-effect was much weaker. In the grain-growth area and the HAZ, TiC addition played a critical role in preventing significant grain growth.

Table 2 shows the engineering and mechanical properties of the investigated alloys in as-received (AR) condition and after-welding (AW) condition. Among the as-received materials, the highest strength was observed in the C35MN alloy, which included a niobium addition; the high strength can, most likely, be attributed to the presence of the Laves phases, which could delay or slow down recrystallization. Also, even in solid solution, niobium might have provided some additional solid solution hardening compared to the rest of the alloys. Yield stress for the rest of the as-received materials was within a 10% margin with respect to the reference C35M alloy.

Ductility of the as-received materials showed a close grouping of around 20% for total elongation and 5% for uniform elongation, demonstrating the weak role of alloying on the ductility values; the only exception was the C35MN alloy, which had lower elongation values compared to the reference. Tensile curves (Fig. 3) were also similar (except for C35MN), with a pronounced descending component in the plastic regime that corresponded to necking. Pronounced necking (the difference between full and uniform elongations) suggests high local ductility for the studied materials.

Welding led to some softening for all materials; yield stress dropped to around 500–560 MPa. Fractures in the welded specimens always occurred in the weldment. The estimated fracture location was close to the weldment's center line. The C35MN alloy had largest yield stress value in a weldment at 569 MPa.

The softening degree (the ratio of yield stress change after welding to the initial yield stress value, $\Delta\sigma_{02}/\sigma_{02-AR}$, %) varied slightly for the investigated materials. The largest softening degree (34%) was observed for the C35MN alloy, which had the highest yield stress prior to welding. Most likely, welding led to the dissolution of the hardening precipitation phases, which survived annealing but dissolved, at least partially, during welding. The smallest softening degree (11%) was observed for alloys with 0.3 and 1% TiC; this value is small enough and easy to compensate for using local design variations (thickening).

While yield strength of the welded specimens varied slightly among the investigated materials, the ductility response demonstrated more pronounced changes. As shown in the mechanical test results (Fig. 3), the C37M alloy specimens showed unexpected, early fracture without neck formation and with low

Table 2 Mechanical properties of the modified alloys after welding

Alloy	Conditions	Yield stress, σ_{02} (MPa)	Ultimate stress (MPa)	Uniform elongation (%)	Total elongation (%)	Softening degree (%)	Sudden fracture events	Fracture type
C35M	AR	627.4 ± 13.8 (4)[a]	717.2 ± 15	12.5 ± 0.3	20.9 ± 0.4	18	–	Ductile
	AW	515.5	601.6	4.7	11.4		–	Ductile
C37M	AR	587.2	720.9	10.8	20.4	12	–	Ductile
	AW	514.0	629.05	4.5	4.5		All tests (4)[b]	Cleavage
C35MN	AR	863.1	933.6	6.3	10.9	34	–	Ductile
	AW	569.0	631.3	2.3	5.4		50% (4)[b]	Cleavage
C35M01TC	AR	674.4	755.2	10.7	17.8	19	–	Ductile
	AW	545.8	623.8	4.9	12.6		–	D: 30%, C: 70%[c]
C35M03TC	AR	595.3	701.8	13.2	22.5	11	–	no data
	AW	528.9	650.9	5.6	9.1		–	Cleavage
C35M10TC	AR	581.6	707.5	14.6	23.0	11	–	D: 30%, C: 70%[c]
	AW	518.8	683.4	6.8	12.0		–	D: 50%, C: 50%[c]

[a]One standard deviation value is shown for one alloy to illustrate the result scattering

[b]Value in brackets indicates the number of tested specimens

[c]"D" is the ductile fracture percentage and "C" is the cleavage fracture percentage

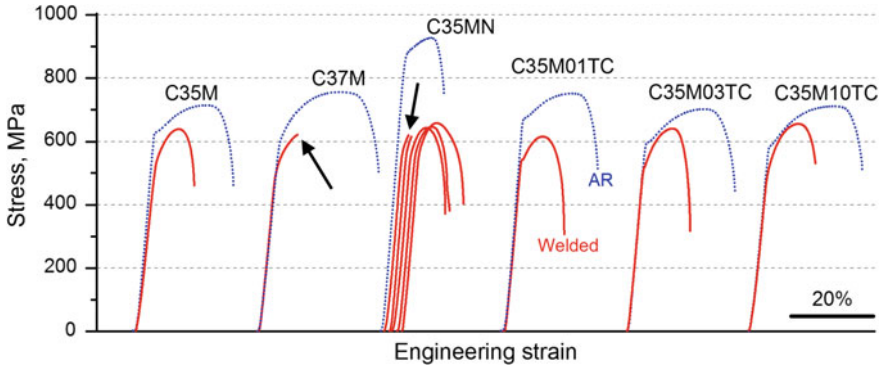

Fig. 3 Representative tensile curves for the investigated materials in the as-received conditions (dotted blue curves) and after welding (solid red lines). Several curves are shown for the C35MN alloy to illustrate the brittle fracture cases. Black arrows point to sudden fracture events

overall ductility (Table 1). Only one curve is given in Fig. 3; however, sudden fractures happened for all the welded specimens of C37M alloy tested here. Additionally, about half of the welded C35MN alloy specimens fractured unexpectedly, at small strains, after welding. These fractures may be caused by pre-existing defects like, for example, undetected voids and cracks. Although not observed during the weldment evaluation, tiny cracks or voids even at low number densities could become critical defects and initiate the fracture. Compared to the as-received C35M alloy, materials with the TiC addition (Table 1) demonstrated very weak changes in the yield and ultimate stress levels after welding. No sudden fracture events were observed in the welded specimens of these alloys.

After welding, the C35M alloy demonstrated mostly ductile fracturing; the dimple height tended to decrease compared to the material in as-received condition, but no cleavage spots were observed. In contrast, after welding, the C37M alloy had completely-brittle fractures; only cleavage surfaces were observed; no signs of ductile dimples were detected. Additions of niobium and 0.1% TiC also led to the dominating cleavage fracture, and very few ductile fracture regions were found. These observations are summarized in Table 2 under the "Fracture type" heading.

The behavior of alloys with TiC changed depending on the TiC content. With an increased TiC content, the fracture mechanism in the weldment shifted from dominating cleavage ($\sim$70% in C35M01TC) to a mixed ($\sim$50%) fracture. Interestingly, the cleavage fracture mechanism did not interfere with high local ductility and neck development in the modified alloys. Most likely, fractures occurred only after reaching some stress-level threshold, below which, the material behavior may be considered ductile. In other words, below some critical stress level, the material should remain structurally sound. Additional tests focusing on fracture processes and resistance to crack propagation are needed to gain additional understanding.

To investigate weldment behavior, which can occur in a complex, gradient manner, the local mechanical behavior was analyzed using DIC data for the welded and as-received specimens. True stress-strain curves were calculated using common approaches [27] to ascertain the real material behavior prior to and after welding. This type of curve has no ultimate stress point or uniform elongation limit, and the true curves end with the specimen fracturing at some critical strain/stress value. During the experiment, the maximum strain value is limited by some degree because of the limitation of the experimental method used to retrieve the true curves. For instance, with the DIC approach as the main tool, the inaccuracy increases when necking begins or when a complex stress state forms [28]. Detailed analysis of the true curves usually includes some constitutive equations [31] or modern approaches based on the physics of plasticity [32], but this aspect was out of the present work scope.

Figure 4 shows true local stress–true strain curves representing the behavior of the as-received materials and their fusion zones (~300 μm central areas of the weldments). As shown in Fig. 4, the weldments demonstrated significant local ductility; true strains reached around 0.25–0.3 or more for all investigated alloys, except C37M. This value was sufficient to accept some cold working, as necessary. Even welded C37M alloy with low engineering ductility (total elongation, TE < 5%) demonstrated some local true strains (~0.1–0.15) in the weldment.

For the reference material (C35M) and ME-branch alloys (C37M and C35MN), the true curves for the weldments were shifted to the smaller stresses and appeared to have smaller deformation hardening rates. This observation reflects the recrystallization and grain growth processes, which eliminated the controlled microstructure introduced by the manufacturing process and formed large grains in the weldment (Fig. 2). A grain size increase usually leads to a reduction in the strain hardening parameters for metallic systems [31].

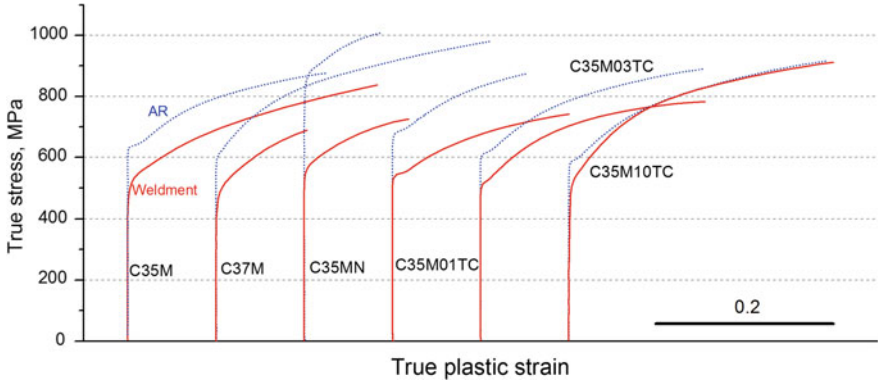

Fig. 4 Representative "true stress, MPa—true plastic strain" curves for the as-received materials (dashed-blue lines) and for the weldments (solid-red lines)

Interestingly, for materials with a TiC addition, the deformation hardening rate appears to increase for the weldments as the TiC content increased. In the alloy containing 1% TiC (C35M10TC), the stress level in the weldment is close to the as-received material starting at a true strain level of around 0.1–0.15 (Fig. 4). It may be explained, in the first iteration, by grain refinement in the C35M10TC alloy weldment.

Discussion of Alloying and Weldment Performance

The present work, in addition to previous research [11, 13, 14], has indicated that alloying plays a significant role in weld performance—and on weld-induced cracking and yield strength in particular. For example, weldments of the Generation I alloys [11] had a yield stress of around 340–360 MPa (Fig. 5). These alloys, which did not have a significant solid-solution strengthening, spanned a wide composition range for aluminum and chromium. Moving towards higher aluminum and lower chromium content in these alloys minimized the impact of being within the α′-regime area [18, 20]. Additionally, an increase in yield stress in the weldments became obvious with the increasing aluminum content. In this study, weldments of the improved C35M alloy had a yield stress of around 515 MPa, which is about 155 MPa higher than the yield stress of Generation I alloys. The C35M alloy had good weldability with crack-free weldments and ductile fracture mechanisms in the weldments. However, if the assumed alloying scheme seeks additional refinement using only aluminum and chromium additions—and additional solid-solution strengthening from the molybdenum additions in the C35M alloy—this yield stress value is likely an upper limit. As shown in the results, further increasing the aluminum content, with a static molybdenum content, did not further strengthen the weldment (C35M vs. C37M) but instead led to embrittlement at the weldment (Table 2).

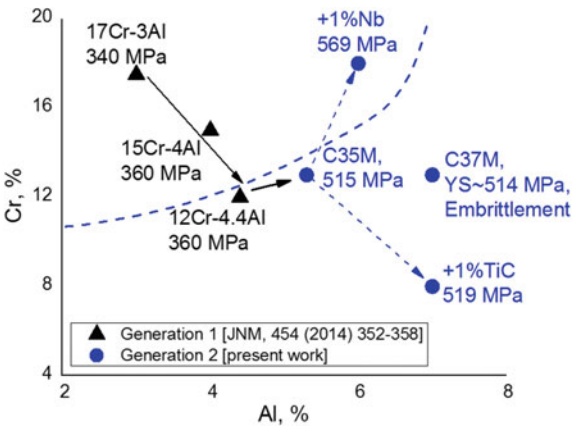

Fig. 5 Role of alloying in the weldment yield stress. The plot summarizes previous data on Generation I alloys [11] and results from the present work. Dashed-blue line shows the α'-embrittlement regime (after [36]). Note: the alloys with niobium and TiC do not follow the aluminum-chromium coordinates

The observed transition—as aluminum content in the alloy is increased—from good ductility to cleavage fracture supports previous conclusions [13, 14] that increasing aluminum content is detrimental to the weld performance of FeCrAl alloys. Although cracking of the weldments was not observed here, which is in direct disagreement with [13], the decreased ductility and cleavage fracture suggests the low performance of the C37M-alloy weldments. It should be noted that many differences exist between this study and the cited work [13]; for instance, the welding technique and the weld geometry differ between the cited work and the experiment described here. This disagreement suggests the need for a more robust weldability map that takes these variations into account, but such a large-scale systematic study was not within the scope of the present work.

At first glance, the alloy with a 1% TiC addition did not seem to demonstrate a huge advantage over the reference material (the yield stress value was comparable to that of C35M); however, the grain size in the weldment was reduced significantly, and welding-induced softening in the HAZ was less pronounced. Additionally, the strain hardening rate in the weldment was higher compared to the reference C35M alloy. Also, one may speculate that better results may be achieved if more complex welding techniques are used (e.g., employing filler wires as described in [33] or modifying the shielding gas [34, 35]). The C35MN alloy, as a base metal with a high strength level, may be combined with the C35M10TC alloy wires to provide grain refinement and ductility in the weldment.

Conclusion

Six new compositions of advanced FeCrAl alloys—variants with +2% aluminum, +1% niobium, and 0.1, 0.3, and 1% TiC additions over the reference alloy [Fe-13% Cr-5%Al (in wt%)]—were produced and tested to investigate weldability, structure, and mechanical properties of the parent alloys and their weldments. Tensile tests using a DIC approach and EBSD scanning were performed to characterize the microstructure, mechanical strength, and deformation hardening behavior of the weldments, HAZs, and parent materials. The results showed that all investigated alloys demonstrated yield stress in the weldment over 500 MPa; no welding-induced cracking was observed in the present work.

Increasing the aluminum content to over 5% was found to be detrimental to the alloy and led to embrittlement and decreased ductility in the weldment; all welded specimens fractured in a brittle fashion after reaching limited plastic strain in the weldment ($\sim$0.1–0.15).

The niobium addition was beneficial for preventing grain growth, reducing local softening in the weldment, and decreasing HAZ dimensions. The TiC addition was also beneficial and effectively refined grain structure in the weldments; the fracture mechanism of the alloys with a TiC addition moved from completely brittle to mixed ($\sim$50 to 50%), and the weldments demonstrated high local ductility (up to $\sim$0.25–0.3 in true stress terms).

Acknowledgements This research was sponsored by the U.S. Department of Energy, Office of Nuclear Energy, for the Nuclear Energy Enabling Technologies (NEET) program for the Reactor Materials effort. This report was authored by UT-Battelle, LLC under Contract No. DE-AC05-00OR22725 with the U.S. Department of Energy. Authors would like to thank Dr. L. Tan (ORNL) for fruitful discussion of the results and S. Crawford (ORNL) for valuable help in manuscript preparation.

References

1. M.O.H. Amuda, S. Mridha, Comparative evaluation of grain refinement in AISI 430 FSS welds by elemental metal powder addition and cryogenic cooling. Mater. Des. **35**, 609–618 (2012)
2. I. AghaAli, M. Farzam, M.A. Golozar, I. Danaee, The effect of repeated repair welding on mechanical and corrosion properties of stainless steel 316L, in *Materials & Design (1980–2015)*, vol. 54 (2014), pp. 331–341
3. S.J. Zinkle, K.A. Terrani, J.C. Gehin, L.J. Ott, L.L. Snead, Accident tolerant fuels for LWRs: a perspective. J. Nucl. Mater. **448**, 374–379 (2014)
4. J. Lim, I.S. Hwang, J.H. Kim, Design of alumina forming FeCrAl steels for lead or lead–bismuth cooled fast reactors. J. Nucl. Mater. **441**, 650–660 (2013)
5. B.A. Pint, K.A. Terrani, Y. Yamamoto, L.L. Snead, Material selection for accident tolerant fuel cladding. Metall Mater Trans E **2**, 190–196 (2015)
6. J. Lim, H.O. Nam, I.S. Hwang, J.H. Kim, A study of early corrosion behaviors of FeCrAl alloys in liquid lead–bismuth eutectic environments. J. Nucl. Mater. **407**, 205–210 (2010)
7. J. Engkvist, U. Bexell, M. Grehk, M. Olsson, High temperature oxidation of FeCrAl-alloys–influence of Al-concentration on oxide layer characteristics. Mater. Corros. **60**, 876–881 (2009)
8. B.A. Pint, K.A. Unocic, K.A. Terrani, Effect of steam on high temperature oxidation behaviour of alumina-forming alloys. Mater. High Temp. **32**, 28–35 (2015)
9. R. Kögler, W. Anwand, A. Richter, M. Butterling, X. Ou, A. Wagner, C.-L. Chen, Nanocavity formation and hardness increase by dual ion beam irradiation of oxide dispersion strengthened FeCrAl alloy. J. Nucl. Mater. **427**, 133–139 (2012)
10. E. Little, D. Stow, Void-swelling in irons and ferritic steels: II. An experimental survey of materials irradiated in a fast reactor. J. Nucl. Mater. **87**, 25–39 (1979)
11. K.G. Field, M.N. Gussev, Y. Yamamoto, L.L. Snead, Deformation behavior of laser welds in high temperature oxidation resistant Fe–Cr–Al alloys for fuel cladding applications. J. Nucl. Mater. **454**, 352–358 (2014)
12. W. Chubb, S. Alfant, A.A. Bauer, E. Jablonowski, F. Shober, R.F. Dickerson, *Constitution, Metallurgy, and Oxidation Resistance of Iron-Chromium-Aluminum Alloys* (Battelle Memorial Inst, Columbus, OH, 1958)
13. J. Regina, J. Dupont, A. Marder, The effect of chromium on the weldability and microstructure of Fe-Cr-Al weld cladding. Weld J New York **86**, 170 (2007)
14. J. DuPont, J. Regina, K. Adams, Improving the weldability of fecral weld overlay coatings, in *Annual Conference on Fossil Energy Materials*. Citeseer, p. 132 (2007)
15. R. Trivedi, S. David, M. Eshelman, J. Vitek, S. Babu, T. Hong, T. DebRoy, In situ observations of weld pool solidification using transparent metal-analog systems. J. Appl. Phys. **93**, 4885–4895 (2003)
16. T. Zacharia, J. Vitek, J. Goldak, T. DebRoy, M. Rappaz, H. Bhadeshia, Modeling of fundamental phenomena in welds. Modell. Simul. Mater. Sci. Eng. **3**, 265 (1995)
17. M. Turski, M. Smith, P. Bouchard, L. Edwards, P. Withers, Spatially resolved materials property data from a uniaxial cross-weld tensile test. J. Press. Vessel Technol. **131**, 061406 (2009)

18. P.D. Edmondson, S.A. Briggs, Y. Yamamoto, R.H. Howard, K. Sridharan, K.A. Terrani, K. G. Field, Irradiation-enhanced α′ precipitation in model FeCrAl alloys. Scripta Mater. **116**, 112–116 (2016)
19. J. Ejenstam, M. Thuvander, P. Olsson, F. Rave, P. Szakalos, Microstructural stability of Fe–Cr–Al alloys at 450–550 °C. J. Nucl. Mater. **457**, 291–297 (2015)
20. K.G. Field, X. Hu, K.C. Littrell, Y. Yamamoto, L.L. Snead, Radiation tolerance of neutron-irradiated model Fe–Cr–Al alloys. J. Nucl. Mater. **465**, 746–755 (2015)
21. K.G. Field, M.N. Gussev, R. Howard, First Annual Progress Report on Radiation Tolerance of Controlled Fusion Welds in High Temperature Oxidation Resistant FeCrAl Alloys, *ORNL/TM-2015/770* (2015)
22. D. Naumenko, J. Le-Coze, E. Wessel, W. Fischer, W.J. Quadakkers, Ultra-high purity metals. II. Effect of trace amounts of carbon and nitrogen on the high temperature oxidation resistance of high purity FeCrAl alloys. Mater. Trans. **43**, 168–172 (2002)
23. B. Pint, Experimental observations in support of the dynamic-segregation theory to explain the reactive-element effect. Oxid. Met. **45**, 1–37 (1996)
24. M.A. Sutton, J.J. Orteu, H. Schreier, *Image Correlation for Shape, Motion and Deformation Measurements: Basic Concepts, Theory and Applications*. Springer Science & Business Media (2009)
25. Y.B. Das, A.N. Forsey, T.H. Simm, K.M. Perkins, M.E. Fitzpatrick, S. Gungor, R.J. Moat, In situ observation of strain and phase transformation in plastically deformed 301 austenitic stainless steel. Mater. Des. **112**, 107–116 (2016)
26. L. Huynh, J. Rotella, M.D. Sangid, Fatigue behavior of IN718 microtrusses produced via additive manufacturing. Mater. Des. **105**, 278–289 (2016)
27. C. Leitão, I. Galvão, R. Leal, D. Rodrigues, Determination of local constitutive properties of aluminium friction stir welds using digital image correlation. Mater. Des. **33**, 69–74 (2012)
28. M.O. Acar, S. Gungor, Experimental and numerical study of strength mismatch in cross-weld tensile testing. J. Strain Anal. Eng. Des., p. 0309324715593699 (2015)
29. S. Patra, A. Ghosh, J. Sood, L.K. Singhal, A.S. Podder, D. Chakrabarti, Effect of coarse grain band on the ridging severity of 409L ferritic stainless steel. Mater. Des. **106**, 336–348 (2016)
30. S. Dziaszyk, E.J. Payton, F. Friedel, V. Marx, G. Eggeler, On the characterization of recrystallized fraction using electron backscatter diffraction: a direct comparison to local hardness in an IF steel using nanoindentation. Mater. Sci. Eng. A **527**, 7854–7864 (2010)
31. M. Gussev, T. Byun, J. Busby, Description of strain hardening behavior in neutron-irradiated fcc metals. J. Nucl. Mater. **427**, 62–68 (2012)
32. A. Patra, D.L. McDowell, Crystal plasticity investigation of the microstructural factors influencing dislocation channeling in a model irradiated bcc material. Acta Mater. **110**, 364–376 (2016)
33. V. Villaret, F. Deschaux-Beaume, C. Bordreuil, G. Fras, C. Chovet, B. Petit, L. Faivre, Characterization of Gas Metal Arc Welding welds obtained with new high Cr–Mo ferritic stainless steel filler wires. Mater. Des. **51**, 474–483 (2013)
34. H. Li, W. Xing, X. Yu, W. Zuo, L. Ma, P. Dong, W. Wang, G. Fan, J. Lian, M. Ding, Dramatically enhanced impact toughness in welded ultra-ferritic stainless steel by additional nitrogen gas in Ar-based shielding gas. J. Mater. Res. **31**, 3610–3618 (2016)
35. Y. Zheng, Y. Wang, H. Li, W. Xing, X. Yu, P. Dong, W. Wang, G. Fan, J. Lian, M. Ding, An experimental study of nitrogen gas influence on the 443 ferritic stainless steel joints by double-shielded welding. Int. J. Adv. Manuf. Technol., 1–9 (2016)
36. S. Kobayashi, T. Takasugi, Mapping of 475 °C embrittlement in ferritic Fe–Cr–Al alloys. Scripta Mater. **63**, 1104–1107 (2010)

Investigating Potential Accident Tolerant Fuel Cladding Materials and Coatings

K. Daub, S.Y. Persaud, R.B. Rebak, R. Van Nieuwenhove, S. Ramamurthy and H. Nordin

Abstract Thermal energy release and hydrogen generation due to breakaway oxidation of Zr fuel cladding materials are of concern in accident scenarios involving extreme temperature increase (up to 1200 °C). As a result, potential accident tolerant fuel cladding (ATFC) materials and coatings are being investigated. Physical vapor deposited CrN coatings are considered as possible protective barrier materials for Zircaloys. In addition, Fe–Cr-Al alloys are considered potential candidate materials for ATFC due the formation of protective alumina at high temperatures which maintains resistance by preventing oxide breakdown. Both CrN-coated Zircaloys and a Fe–Cr-Al model alloy were exposed to 300 °C water and steam environments up to 1200 °C to evaluate their resistance to corrosion under normal reactor operating conditions and to high temperature steam oxidation. Surface analytical techniques are used to evaluate the effectiveness of oxides and/or coatings over the 300 °C water to 1000 °C steam temperature regime.

Keywords Fuel cladding · Coatings · Fe–Cr-Al · Corrosion · Steam

Introduction

During a loss of coolant accident scenario, temperatures up to 1200 °C can be reached, resulting in enhanced oxidation of the zirconium-based alloy fuel cladding, subsequently resulting in increased hydrogen generation. This scenario is known to

K. Daub (✉) · S.Y. Persaud · H. Nordin
Canadian Nuclear Laboratories, 286 Plant Road, Chalk River, ON K0J 1J0, Canada
e-mail: kevin.daub@cnl.ca

R.B. Rebak
GE Global Research, 1 Research Circle, Schenectady, NY 12309, USA

R. Van Nieuwenhove
Institutt for Energiteknikk, Halden, Norway

S. Ramamurthy
Surface Science Western, Western University, London, ON, Canada

J.H. Jackson et al. (eds.), *Proceedings of the 18th International Conference on Environmental Degradation of Materials in Nuclear Power Systems – Water Reactors*, The Minerals, Metals & Materials Series, https://doi.org/10.1007/978-3-319-68454-3_19

have occurred during the Fukushima-Daichii accident. Therefore, development of accident tolerant fuel cladding (ATFC), which could have lower oxidation kinetics and hydrogen generation, is of high interest. This paper analyzes two possible routes of developing ATFC. The first is analyzing a new oxidation resistant alloy, specifically a Fe–Cr-Al alloy, and the second method is to analyze the effect of an additional barrier material on the Zircaloy cladding, specifically a vapour-deposited CrN coating.

To add a barrier material through a coating method, there are several methods, including: vapour deposition, sol-gel, spray coating, electrodeposition, and hot dipping. In 2011, a number of commercially available ceramic coatings, applied by physical vapour deposition (PVD), were proposed by Van Nieuwenhove [1] to improve the performance of cladding materials. Vapour–deposited coatings are essentially pore-free and dense provided a thick enough layer is applied. This type of coating results in a reduction in the amount of moisture or gas that can penetrate through the film. Therefore, this type of film would be ideal to reduce corrosion of materials. It has been proposed that coatings applied by PVD could be suited to reduce corrosion in a nuclear environment. This applies to normal operating conditions of present-day reactors, potential operating conditions of future reactor designs, and for an additional barrier for ATFC. Numerous researchers have examined the effects of chromium- and nitride-based coatings on various materials [2–10]. In general, results have suggested that when the coatings are free of pores and other defects they are able to increase the corrosion resistance of materials in various corrosive environments. Coating tests by R. Van Nieuwenhove on small samples were investigated in out-pile and in-pile experiments in the Halden reactor in the period 2011–2012. From these tests, it was found that CrN coatings remained intact both in BWR and PWR conditions. Based on the very promising results with CrN coatings on small Inconel 600 samples in the Halden reactor, a follow-up test with a CrN coated fuel rod was performed in the Halden reactor under pressurized water reactor (PWR) conditions. The results of these investigations (irradiation performed from March to November 2014) [11] and more recent tests, have demonstrated that a CrN coating provides a combination of corrosion protection in PWR conditions, corrosion protection in steam environments, a hard surface resistant to damage, and a barrier to prevent hydrogen ingress.

Fe–Cr-Al alloys are advanced steels under consideration as candidate materials for ATFC [12–22]. The alloys are considered oxidation resistant in steam to temperatures up to 1200 °C [14, 15, 22, 23]. Several authors have demonstrated the better oxidation resistance of Fe–Cr-Al alloys in high temperature steam environments compared to conventional Zr fuel cladding alloys. The formation of a highly stable and protective Al_2O_3 oxide scale is credited for the exemplary performance of Fe–Cr-Al alloys in high temperature environments; the kinetics of oxide formation (i.e. Al and O diffusion) are relatively slow in high temperature steam [22–24]. Binary Fe–Al alloys containing high concentrations of Al, to allow for formation of Al_2O_3, are known to be brittle. As a result, the addition of Cr is critical as the combination of the two reactive elements (Al, Cr) is required to form protective scales from 300 to 1200 °C through the “third element effect”, which is not yet well

understood [12, 15, 25, 26]. To explore the oxidation resistance of Fe–Cr-Al alloys, a model alloy, APMT (Fe-21Cr-5Al), is tested in the present study.

After detailed characterization of the Fe–Cr-Al alloy and prepared CrN-coated Zr-2 samples, a range of tests were performed to identify if the chosen candidate materials showed promise in increasing corrosion resistance, in either aqueous environments at 300 °C or under a steam environment up to 1000 °C.

Experimental

For the experimental processes discussed below, IFE-Halden organized the preparation of the CrN-coated Zr-2 samples through a commercial supplier and performed steam exposure tests, while Canadian Nuclear Laboratories (CNL) performed the long–term aqueous exposure tests and detailed surface analysis. The Fe–Cr-Al APMT model alloy was prepared by GE Global Research and a section of the material was shipped to CNL. APMT sample preparation and 300 °C water exposures were performed at CNL. Following this, APMT steam exposures were performed using the atmospheric pressure gas reactor at Surface Science Western, Western University.

Material Preparation

Plates of Zr-2 (30 mm × 10 mm × 1 mm) with a single mounting hole (3 mm diameter) were prepared and sent to a commercial PVD coating company. To apply a CrN coating, the PVD mounting technique resulted in one face being coated, followed by flipping the samples and coating the back face. This resulted in a CrN thickness of 4 μm on the two large faces and a double layer of coating applied to the four thin edge faces. Additionally, this coating procedure results in no CrN layer being applied to the circumferential face of the mounting hole. After coating, a selection of samples were scratched in four locations (two scratches across each large face), to simulate possible damage to the coating layer. A selection of the scratched coupons were analyzed by laser profilometry. The scratches were seen to be consistent in width and depth across the full length of an individual scratch, and across all scratches measured the depth was relatively uniform (40 ± 9 μm).

Flat coupons (10 mm × 5 mm × 2 mm) of APMT, Zr-2, Zr-4, and 304L stainless steel were prepared for Fe–Cr-Al experiments in 300 °C water and high temperature steam. The latter three alloys were included in experiments to provide relevant comparisons with currently used fuel cladding material and other proposed alternative alloys. Flat coupons were ground using SiC paper. Following this, step-wise fine polishing was done using diamond paste and alumina suspension to a 0.05 μm finish. Samples were ultrasonically cleaned in de-ionized water during polishing stages.

300 °C Water Corrosion Tests

The corrosion resistance of the proposed ATFC materials were studied using two tests. Both tests exposed the materials to environments simulating primary coolant in a CANDU reactor.

For the CrN-coated sample exposures, multiple samples, which had been weighed and dimensioned, were loaded on a sample tree and placed into an autoclave vessel. A prepared solution of heavy water, adjusted to a $pH_{a25\ °C}$ of 10.4 using LiOH, was added to the autoclave. After solution addition, the system was purged with Ar for 4 h to remove oxygen. The system was then completely sealed, heated to 300 °C, and left at 300°C for 30 days. At the end of 30 days, the system was cooled to room temperature, samples were removed and washed with deionized water and dried under an Ar gas line. Samples were further weighed and dimensioned. Some samples were kept for further surface analysis, while the remaining samples were loaded for an additional 30-day test. Testing over 30-day increments of exposure to 300 °C and $pH_{a25\ °C}$ 10.4 lasted up to 120 days.

Fe–Cr-Al experiments were carried out in the H5 loop at CNL. The H5 loop is primarily constructed using 304SS and has been used to simulate primary coolant in a CANDU reactor ($pH_{25\ °C}$ 10.4) successfully at temperatures up to 305 °C; in the current work, temperature is maintained at 300 ± 5 °C. Key components of the loop include a 200 L feed tank, positive displacement pumps and a full-flow ion exchange system, which operate at near ambient pressure and temperature. The ½ inch 304SS tube containing 16 flat coupons (4 each of Fe–Cr-Al APMT, Zr-2, Zr-4, and 304L SS) is attached to the test section area in the H5 loop. Pumps are used to pressurize the test solution and maintain flow in the loop. Following pressurization, the solution is heated using electric heaters and pumped through the test section. The test section is housed within a custom-made electric oven for accurate temperature control. The loop is equipped with on-line monitors for dissolved oxygen content and hydrogen concentration, ionic conductivity, pH, flow rate and temperature. Hydrogen content was maintained at approximately 7 cm^3 H_2/kg H_2O. Exposures were carried out for 600 h. Data were recorded using custom-made data acquisition software. Upon completion of experiments, samples were stored in a desiccator until exposures in high temperature steam.

Steam Corrosion Tests

For the CrN-coated samples, steam exposure tests were performed at IFE-Halden using a modified HGA-S-CX1300 High Temperature Steam System from Micropyretics Heaters International Inc. This system allows steam testing up to 1300 °C. During testing, the injection pump was set to add distilled water with a constant flow of about 10 ml/min. The water was converted to vapor inside a steam generator and lead into the furnace where the test samples were placed in a sample

holder. The test temperature was measured using 3 thermocouples attached to the sample holder. The furnace in the experimental set-up had a rather narrow temperature profile. The temperature drop was estimated to be approximately 40–60 °C from its center compared to 15 mm off-center. During testing the sample holder was positioned so that one thermocouple was placed at the hottest position in the center of the furnace. Two additional thermocouples, both located ~15 mm off-centre, experienced more or less the same test temperature. The specified test temperature was aimed to be achieved at the center of the furnace.

Fe–Cr-Al high temperature steam experiments were carried out in an atmospheric pressure gas reactor at Surface Science Western, London, ON, Canada. Three 24 h experiments were performed with four samples (one each of Fe–Cr-Al APMT, Zr-2, Zr-4, and 304L stainless steel) exposed in each test; the water-formed oxide was present on the samples and the temperatures used for exposures were 500, 750 and 1000 °C. The heart of the system is a tube reactor enclosed in a furnace. The furnace is unable to encase the ends of the tube and heating tapes were used to heat exposed areas. Argon gas was used to purge the system of air prior to experiments. Steam was continuously refreshed using de-ionized water that was pumped into the system using a peristaltic pump. Water was initially fed into a stainless steel block at 300 °C where it was vaporized prior to entering the reactor. Upon exit from the reactor, the steam was condensed and the water was disposed of. Upon completion of the experiments, the heating and pump were turned off with only argon gas being fed to the reactor during cooldown. The samples were then removed and shipped to CNL for analysis using high resolution electron microscopy techniques.

A summary of all test conditions and materials is shown in Table 1.

Surface Characterization

Multiple surface science and electron microscopy techniques were used to characterize the corrosion resistance behaviour of the coated Zr-2 samples and Fe–Cr-Al alloys.

Surface imaging was performed with a Zeiss Supra-55 WDS-VP scanning electron microscope (SEM) using an electron beam voltage of 10 kV. The SEM was equipped with an Oxford Instruments X-act energy dispersive X-ray (EDX) spectrometer, operated using the Inca software package.

Table 1 Summary of experimental tests performed

Material(s)	Aqueous corrosion test conditions	Steam corrosion test conditions
CrN-coated Zr-2	300 °C, $pH_{a25\ °C}$ 10.4 D_2O (LiOH added), Ar-purged, up to 120 days	500 °C, 750 °C, 1000 °C, aerated distilled water, up to 1 h
Fe–Cr-Al, Zr-2, Zr-4, SS304L	300 °C, $pH_{25\ °C}$ 10.4, H_2O (LiOH added), 7 cm^3 H_2/kg H_2O, up to 600 h	500 °C, 750 °C, 1000 °C, Ar-purged steam, up to 24 h

Transmission electron microscopy (TEM) specimens were fabricated from pieces of the coated substrate using a Zeiss NVision 40 focused ion beam (FIB) system that uses a focused beam of Ga ions for site–specific milling and for viewing [27, 28]. The FIB specimens were examined in an FEI Titan 80 TEM operating at 300 kV at McMaster University. The EDX analysis was performed in high-angle annular dark field scanning transmission electron microscopy (HAADF STEM) mode using an Oxford Instruments INCA acquisition system. Electron energy loss spectrometry (EELS) was conducted on the specimens using a collection semi–angle β of 15.4 mrad, a convergence semi–angle (α) of 6 mrad, and with a nominal electron probe size of 1 nm.

EDX elemental maps were done on a FEI Technai Osiris TEM operating at 200 keV in ChemiSTEM mode at Queen's University, Kingston, ON, Canada. It is equipped with four Super-X silicon drift detectors which enables much quicker elemental mapping on a selected area compared to other conventional TEM EDX mapping methods. High angle annular dark field (HAADF) images were first obtained in STEM mode at the area of interest, and then quantitative elemental maps (Q-map) were generated using Bruker ESPRIT software.

Structural characteristics of the coatings were made using a rotating anode 9 kW Rigaku Smartlab X-ray diffractometer with parallel beam optics and a diffracted beam monochromator.

All secondary ion mass spectrometry (SIMS) analyses were carried out using a CAMECA IMS 6f ion microanalyzer equipped with an electrostatic analyzer, followed by a magnetic-sector mass spectrometer and a channel-electron multiplier detector. All SIMS analysis was completed using a 10 keV Cs^+ primary ion beam rastered over a 250 μm × 250 μm area. To avoid edge effects during the collection of the depth profiles, secondary ions were sampled from a 100 μm^2 area centred over the 250 μm × 250 μm sputter area. A sample accelerating voltage (SAV) of 4925 V was used to collect the mass spectra and the depth profiles.

Results and Discussion

As-Prepared Samples

To characterize the prepared CrN-coated samples, SEM imaging was performed at varying magnifications to look for consistency across the coatings and to observe any locations of obvious defects. Coupled with SEM, EDX analysis was used to determine the elemental composition of the coatings over all analysis areas. For all coated samples, the surfaces were uniform and consistent across the areas examined, with no visible defects. Higher magnification images showed the presence of droplets, which were believed to be from the target source used to deposit the coatings on the Zr-2 samples [3]. Cross-section STEM imaging showed the presence of droplets at various depths within the coating structure. The droplets, up to approximately 1 μm in diameter, created regions of voids and deformation around

them. Previous research has shown that these droplets can be detrimental to the overall protectiveness of a chromium and nitride based coating [2, 3, 6, 9]. For example, if the droplets increase in number and are present near the coating/substrate interface, porous channels can develop into which solution is able to reach the underlying substrate, resulting in high localized corrosion rates. Some researchers have examined the effect of a post-coating treatment to remove some of the droplets and seal some of the pores, which was found to increase the corrosion resistance performance [3]. Additionally, careful control and calibration of the magnetron sputtering time to apply the coating can control and limit the formation of droplets. Of the limited TEM foils examined to date, the droplets have only been observed in the upper half of the coating and not at the coating/substrate interface.

The STEM imaging also showed that the CrN coatings consisted of columnar, nanocrystalline grains. The columnar grains formed a sharp interface with the substrate. Aside from a few droplet areas, the coatings appeared to be dense as pores were not noticeable at the column boundaries or at the sharp interface with the substrate. These observations are consistent with other TEM examinations of coatings [29–31]. A summary of STEM and EELS images are presented in Fig. 1.

The EELS analysis indicated that the CrN coating was uniform in composition. The N-K energy loss near edge structure (ELNES) observed in the CrN coating is typical for cubic transition metal nitrides that have near stoichiometric nitrogen content [32, 33].

Analysis by XRD showed the coatings to have some shifts in d-space when compared to library spectra of CrN. A shift in d-space could be explained by the relative thin nature of the coatings (4 μm) and likely internal stresses, or by the coatings not being directly stoichiometric. Another note from the XRD is that thin zones of structural variance near the substrate/coating interface have been observed on Zircaloy coated samples.

The composition of the Fe–Cr-Al APMT alloy used in experiments is provided in Table 2. Optical micrographs revealing the microstructure of the Fe–Cr-Al APMT alloy are shown in Fig. 2 at low (a) and high (b) resolution. A long and flat

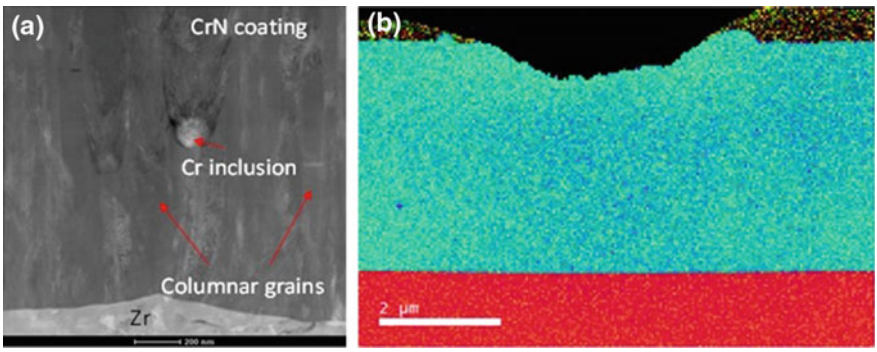

Fig. 1 **a** STEM cross-section of as-prepared CrN PVD coated Zr-2 sample and **b** EELS colour map (Cr = blue, N = green, Zr = red)

Table 2 Composition (wt%) of Fe–Cr-Al APMT used for experiments in the present study

Element	Fe	Cr	Al	C	Cu	Mn	Mo	P	S	Si
Composition	Bal.	21.5	4.9	0.04	0.02	0.2	3.2	0.009	0.0004	0.4

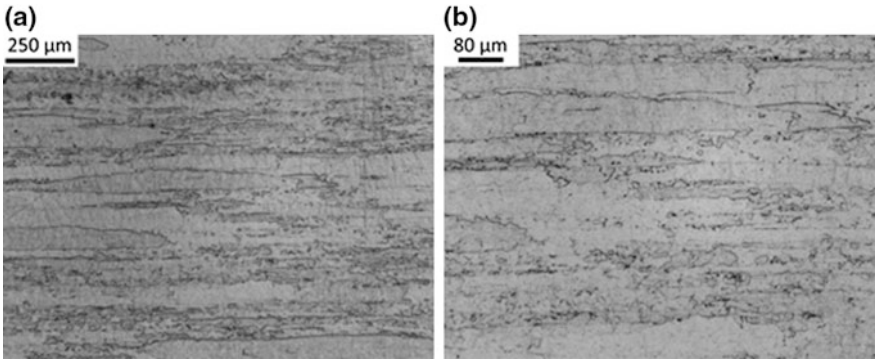

Fig. 2 Optical micrographs showing the microstructure of Fe–Cr-Al APMT material. A long and flat grain structure is apparent with fine precipitates distributed throughout the material

grain structure is present with length or width measuring a few hundred microns in some cases. Also, precipitates are visible in the material; the particle dispersion helps to strengthen the alloy.

Fe–Cr-Al alloys generally have good formability, excellent oxidation resistance, and high strength which make them ideal for use as ATFC materials. During exposure to normal operating conditions, APMT forms a protective Cr-rich oxide which is generally thought to prevent environmental degradation [34, 35]. In the event of an accident scenario where temperatures may reach up to 1200 °C, the corrosion resistance of APMT is exemplary, largely due to the transition to thermodynamically favourable alumina, formed at the chromia-metal interface [12–22]; the thin alumina layer is inert, non-porous, and adherent. The presence of 5% Al and 22% Cr in the alloy leads to the "third element effect" [12, 15, 25, 26] whereby the presence of one reactive element aids in the outward diffusion and stable oxide formation of the other; this phenomenon has been known for some time in the high temperature oxidation community but is not yet well understood.

Aqueous Corrosion Results

After 30-day increment exposure cycles, the CrN-coated Zr-2 samples showed very little visual change, however, darkened regions around the mounting holes were observed on some samples. Also, one coated sample had a darkened region in the middle of one face. With repeated 30-day exposure the regions darkened further. Upon removal, CrN-coated Zr-2 samples were sectioned in half lengthwise and

cross sections of the coatings were analyzed by SEM, Figs. 3 and 4. For the coated sample, the bulk of the coating remained intact, dense, and well adhered to the surface, however, near the mounting hole, in the visually darkened region, the coating was thinned to under 1 μm. For the coated and scratched sample, the coating remained intact, dense, and well adhered to the surface. For these samples, damage done to the coating due to the scratching process resulted in coating fracture and a pathway for solution diffusion. These damaged regions resulted in some oxide formation at the base of the fracture, however, no further damage or loss of adhesion of the coating near these oxides appears to have occurred.

Depth profiling with SIMS showed the coatings to remain uniform with depth and only a minor amount of surface oxide present, occurring also with the presence of surface adventitious carbon, Fig. 5. For all spectra, the vertical red lines

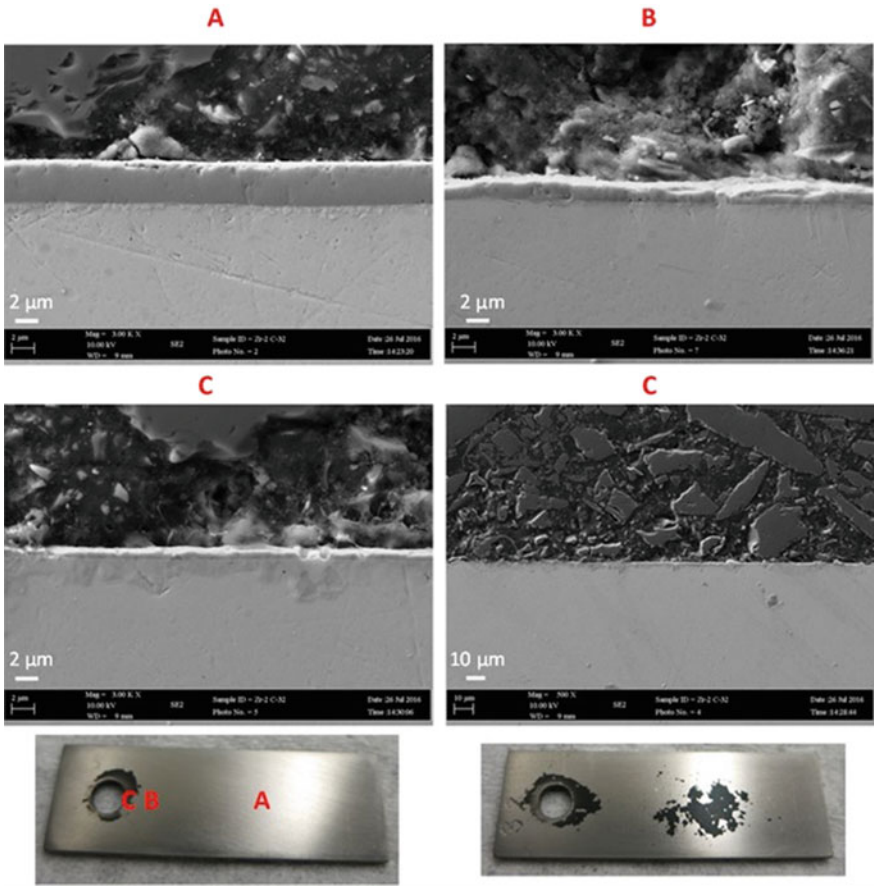

Fig. 3 SEM cross-section images of CrN-coated Zr-2 after 120 days of exposure to $pH_{a25\ °C}$ 10.4 solution at 300 °C. The top and middle images are the cross-section samples prepared from locations A, B, and C. The bottom right image is the opposite face of the sample

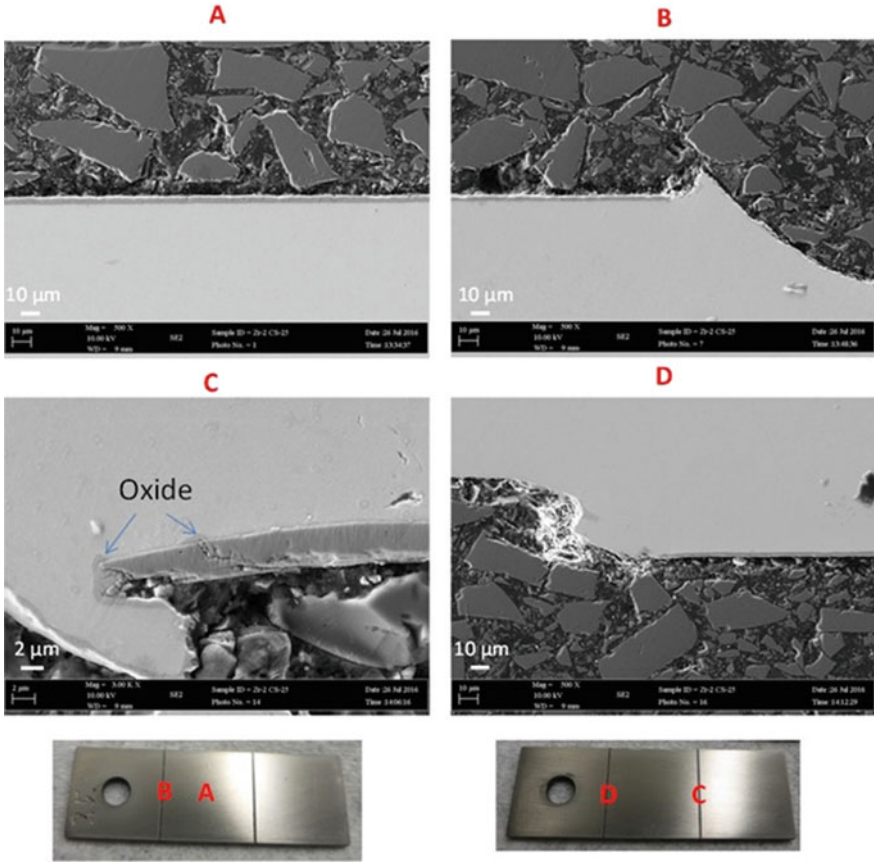

Fig. 4 SEM cross-section images of CrN-coated & scratched Zr-2 after 120 days of exposure to $pH_{a25\ °C}$ 10.4 solution at 300 °C. The top and middle images are the cross-section samples prepared from locations A, B, C, and D

represents an approximation of coating and substrate interface. The line indicates the approximate median, 50% of the chosen negative secondary ion intensity differences between its steady-state coating and metal levels. For all spectra, there was no appreciable evidence of substrate (Zr) species diffusing out through the coating; however, there was some detectable oxygen ($^{16}O^-$) as the coating was sputtered. The profile of the $^{16}O^-$ matched the behaviour with depth of the $^{52}Cr^{16}O^-$ profile. It is likely that the detected oxygen was associated with chromium. The $^{16}O^-$ profile decreased in intensity from the outer surface towards the substrate. The 100 μm spot size and ppm level detection limit for $^{16}O^-$ in SIMS, are the likely reasons why it is detectable in the SIMS profile as compared to the averaged narrow TEM windows analyzed. Additionally, as was seen in the SEM cross section images, a relative difference in coating thickness, seen with the relative difference in sputter time, was observed at regions near and away from the mounting hole.

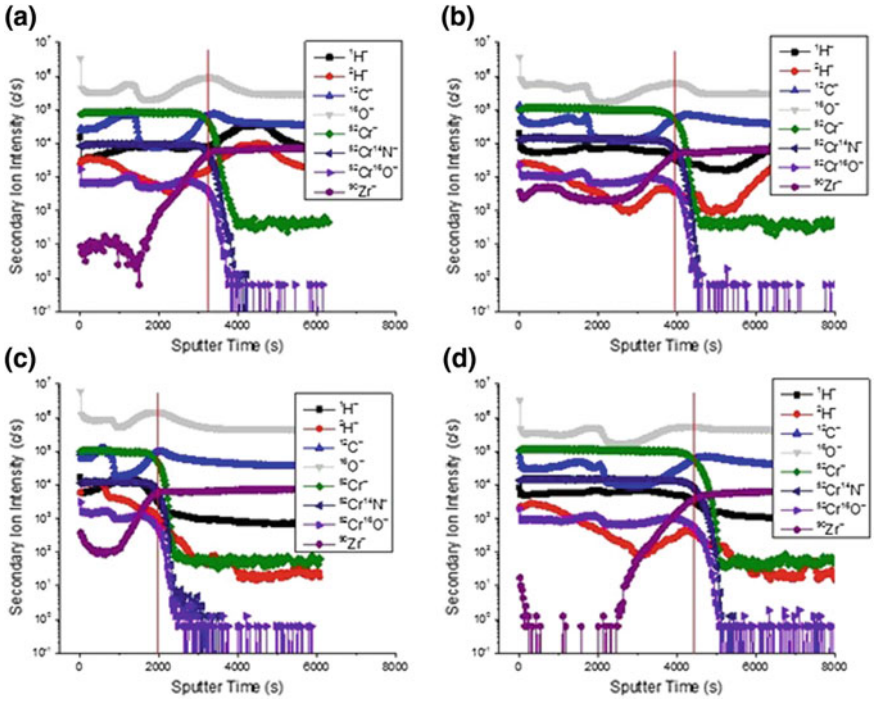

Fig. 5 SIMS depth profiles of **a**, **b** coated and **c**, **d** coated & scratched CrN-coated Zr-2 samples after 120 days of exposure to $pH_{a25\ °C}$ 10.5 solution at 300 °C. Spots **a** and **c** were analyzed near the mounting hole, while spots **b** and **d** are analyzed in the middle of one face

All coated samples, both scratched and not scratched, appeared to show a general trend of an increasing weight loss as a function of exposure time. After 120 days, the weight loss for coated samples was 22.70 mg/dm^2, while the weight loss for coated and scratched samples was 44.29 mg/dm^2. The thickness of CrN on all samples was approximately 4 μm, and therefore, using the density of CrN (5.9 g/cm^3) it can be calculated that a complete loss of CrN would correspond to a weight loss of 236 mg/dm^2. Therefore, the observed weight losses suggest a partial coating loss, either the result of uniform thinning of the coating across the samples, or variable regions of complete coating loss and thinning in adjacent areas.

A portion of the Zr-2 coated samples removed at various increments of exposure were analyzed by hot vacuum extraction mass spectrometry (HVEMS) in order to determine the deuterium ingress, from the heavy water solution, to then determine the effectiveness of a complete CrN coating or a damaged CrN coating on reducing deuterium ingress, Table 3.

The HVEMS measurements show that the CrN-coated Zr-2 reduced the deuterium concentration by approximately 2–3 times that of non-coated Zr-2. This result is consistent with previous results obtained on CrN-coated tube Zircaloy samples [36]. Additionally for the coated sample, there was no change in deuterium

Table 3 Deuterium concentration measurements of CrN-coated Zr-2 samples exposed to a $pH_{a25\ °C}$ heavy water at 300 °C

Sample type	Days of exposure	Deuterium concentration (ppm)	Deuterium ingress (mg/dm^2)
Coated	30	9.3 ± 0.4	0.26
Coated	60	9.8 ± 0.5	0.27
Coated	120	10.1 ± 0.8	0.28
Coated & scratched	30	15.7 ± 0.8	0.44
Coated & scratched	60	14.0 ± 0.7	0.39
Coated & scratched	120	28 ± 1	0.78
Non-coated	30	37 ± 2	1.0
Non-coated	90	26 ± 1	0.73
Non-coated	120	29 ± 1	0.81

concentration between 30 and 120 days of exposure, suggesting even the thinning coating layer near the mounting hole has maintained barrier properties. The results for the coated and scratched samples showed deuterium concentrations approximately 2 times less than those for non-coated Zr-2, however the sample removed after 120 days of exposure had a much larger deuterium concentration, similar in value to those of the non-coated Zr-2. The higher deuterium concentrations than the fully coated material suggest that the scratches likely provided a deuterium ingress route, while the increase at 120 days may suggest, although not observed in SEM cross-section, a coating or oxide breakdown event had occurred between 90 and 120 days of exposure.

In order to better characterize phenomena that might be occurring to the CrN coating properties, especially as a function of distance from a damaged/uncoated region, a selection of exposed samples are scheduled to be further analyzed by TEM.

Following water exposures, Fe–Cr-Al APMT, Zr-2, Zr-4 and 304L stainless steel samples were characterized using analytical TEM techniques. TEM sample preparation was done using a conventional FIB lift-out from the surface of samples; TEM lamella are shown in Fig. 6. As expected, oxide was present on the surface of all samples. The oxide on Zr alloys, in Fig. 6a, b, was thickest at 500 nm to 1 μm, probably depending on grain orientation. The 304L stainless steel sample, in Fig. 6c, had an oxide thickness of approximately 400 nm with penetration of oxide reaching greater depths at grain boundaries; the latter intergranular oxidation is well known in stainless steels and is suggested to have an effect on stress corrosion cracking of the material [37–39], but further investigation is beyond the scope of this work. Fe–Cr-Al APMT oxide thickness, in Fig. 6d, was significantly more shallow at approximately 10–20 nm. Further chemical composition analysis using EELS or EDX was performed, depending on which technique was deemed most appropriate for a given alloy.

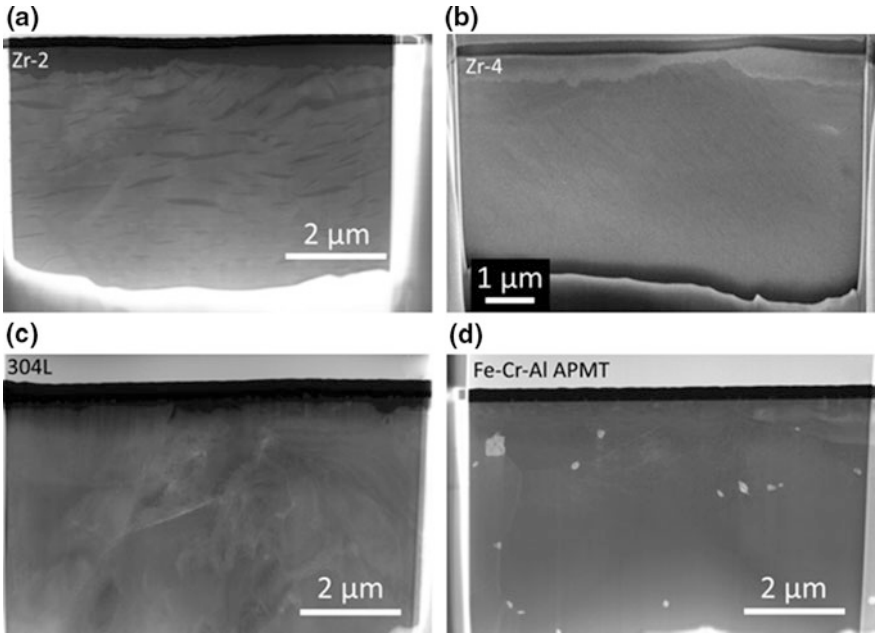

Fig. 6 TEM or FIB-SEM images of a water-exposed TEM sample from **a** Zr-2, **b** Zr-4, **c** 304L stainless steel and **d** Fe–Cr-Al APMT. The wide variation in oxide thickness/behaviour is evident among the samples

EDX elemental maps for the oxide formed on a Fe–Cr-Al APMT sample are provided in Fig. 7. Particles present on the top surface of the material are shown to be a combination of Ni and Zn oxides. Beneath the oxide particles, relatively continuous 10–20 nm Al- and Cr-rich oxide(s) are formed. Initial results suggested that a greater concentration of the Al oxide was formed closer to the metal matrix, but this is yet to be confirmed. The oxide composition and thickness are generally in accordance with the findings of other studies [12–22]. The inert, non-porous, and adherent benefits of the Al oxide formed on Fe–Cr-Al APMT in high temperature water are clearly evident when compared to the oxide thicknesses of the other materials tested. In addition to the surface oxide, several particle inclusions were captured in the TEM sample shown in Fig. 6d. The various elements detected in these inclusions are identified in the EDX maps shown in Fig. 8; the composition is complex with Mo, Cu, Si, Ti, Zn, and Ni detected across all inclusions characterized using EDX. Carbon and nitrogen were also detected in inclusions using EELS, but is not shown.

For comparison with APMT, the oxides formed on 304L stainless steel, Zr-2, and Zr-4 samples were also characterized using EDX and EELS. EDX elemental maps for the oxide formed on a 304L stainless steel sample are shown in Fig. 9. The oxide is primarily Cr-rich with Ni-enrichment present at the oxide-metal interface. In addition, a network of Ni is present in some regions throughout the

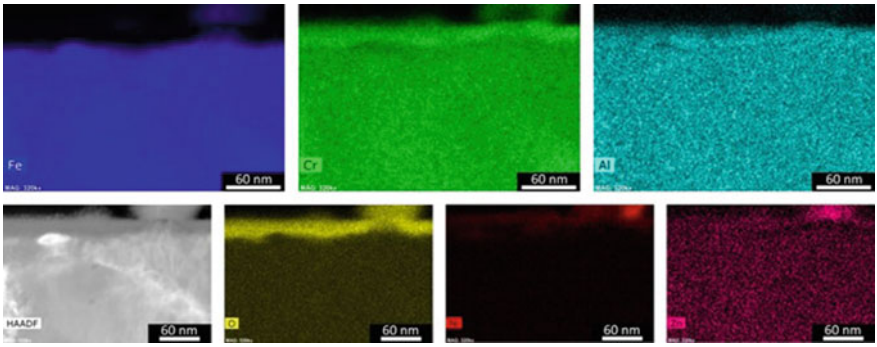

Fig. 7 EDX elemental maps for the oxide formed on the Fe–Cr-Al APMT TEM sample, in Fig. 6d. Oxide particles are present on the top surface, composed of Ni and Zn. A relatively continuous oxide spans the entire surface which is primarily enriched in Cr and Al

oxide. In general, the oxide structure conforms with the results reported elsewhere for stainless steel in high temperature primary water conditions [37–39]. EELS elemental maps showing the oxide formed on the Zr-4 sample, in Fig. 6b, are shown in Fig. 10; in this case, EELS was used for characterization rather than EDX due to the well known electron loss near edge structures associated with Zr metal, oxides, and hydrides. The oxide is comprised of primarily ZrO_2 with ZrO and Zr(O) formed at the oxide-metal interface. The oxide structure and composition on Zr-2 was identical to observations in Zr-4. Overall, the oxides formed on Zr-2, Zr-4 and 304L stainless steel can be regarded as less protective, in terms of adherence, porosity, and inertness, when compared to the oxide formed on the Fe–Cr-Al APMT sample; however, all four alloys are likely reliable under normal operating conditions.

Steam Corrosion Results

To date, steam exposure tests of the CrN-coated Zr-2 samples have been performed at 500, 750, and 1000 °C, for up to one hour. Light optical microscope images of non-coated Zr-2 and coated & scratched Zr-2 exposed to the most extreme test conditions to date (1000 °C for one hour), are shown in Fig. 11. For a non-coated Zr-2 sample exposed to 1000 °C steam, a uniform oxide is formed across the entire surface, while for the coated & scratched sample, oxide formation is largely limited to non-coated areas (scratched grooves) or the short edges of the sample. These results appear to show that the CrN coating can act at least as a temporary barrier to corrosion under steam environments. While the coatings did largely stay adhered, occasional areas of local oxide growth were observed on coated and coated & scratched samples. Also, oxide formation on the short edge faces was observed at all test temperatures for coated and coated & scratched samples. The oxidation of

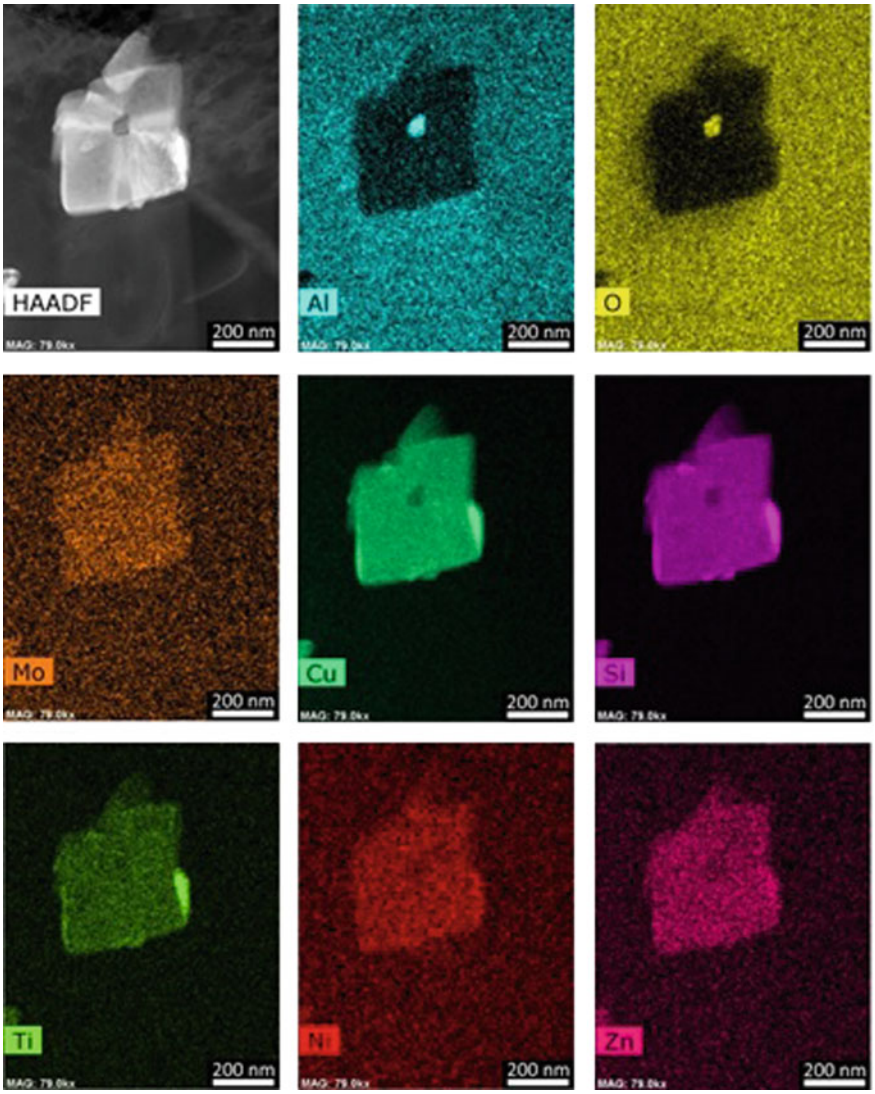

Fig. 8 EDX elemental maps for a large inclusion present in the Fe–Cr-Al APMT sample, in Fig. 6d. The inclusion is composed of several elements. In addition, carbon and nitrogen were identified in the inclusion using EELS

the short edges may have resulted from the coating procedure of the plate samples and initiation of oxidation through coating damage at sharp edges. Also of note, simultaneous tests, not shown, were performed on CrN-coated 316L stainless steel samples, which also showed oxidation on the short edge faces, however, the amount of localized oxide spots on the long faces of the coated and coated & scratched samples were less than those seen on Zr-2. The reason for this is not

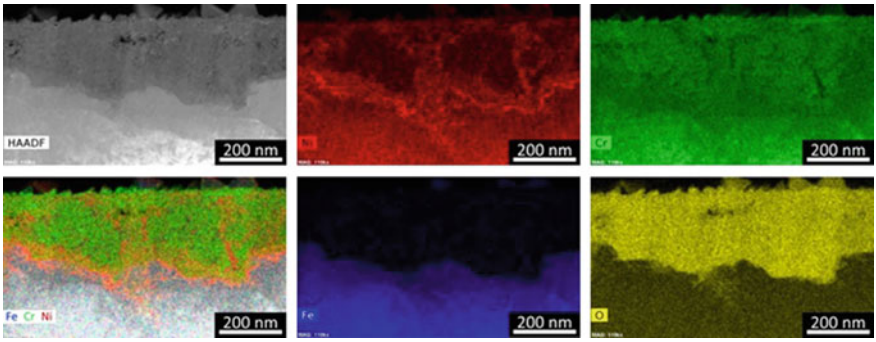

Fig. 9 EDX elemental maps showing the oxide formed on a 304L stainless steel sample, in Fig. 6c. The oxide is primarily Cr-rich. Also, Ni is detected at the oxide-metal interface and forms a network through the oxide, in some areas, that is connected to the surface of the sample

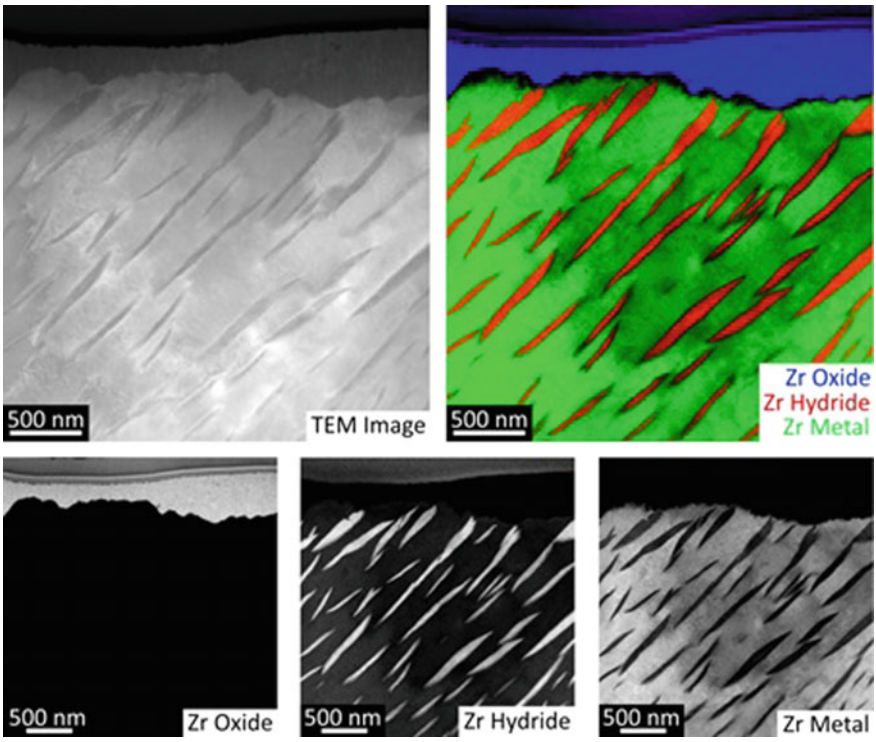

Fig. 10 Low-loss EELS elemental maps for an area of the TEM sample in Fig. 6b. The oxide is primarily ZrO_2 with ZrO and Zr(O) identified at the oxide-metal interface. Zr Hydrides are present throughout the sample

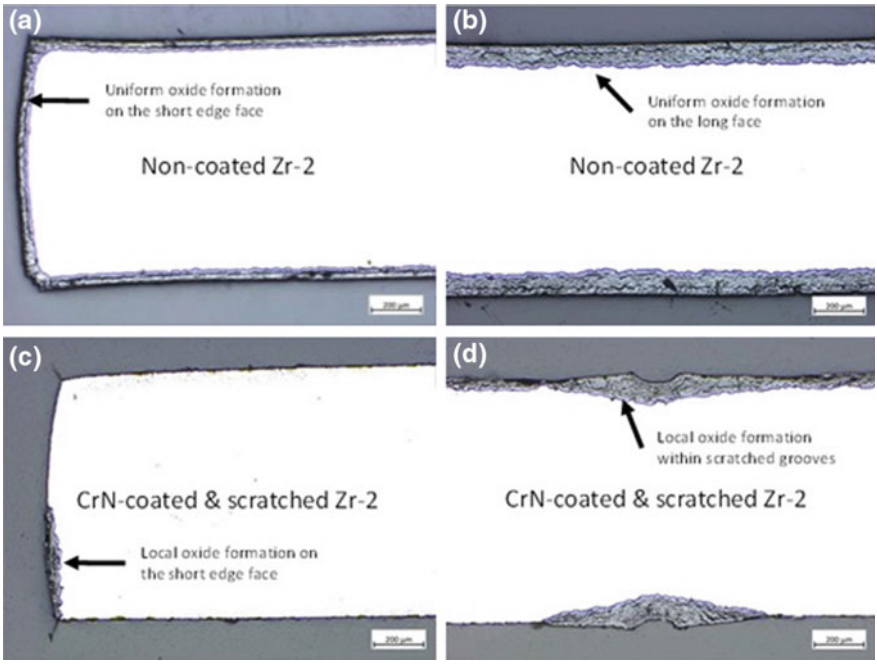

Fig. 11 Light optical microscopy cross-section images of **a**, **b** non-coated Zr-2 and **c**, **d** CrN-coated & scratched Zr-2 exposed to 1000 °C steam for one hour

completely certain, however it is believed that this may result from an improved adhesion between CrN and 316L versus Zr-2, which may be due to the differing air-formed oxides formed on the surfaces between polish and coating. Future coated samples are being designed to limit the amount of short and sharp edges and to have limited surface oxide before the coating procedure, in an attempt to maximize the CrN adhesion.

Steam exposure tests for the Fe–Cr-Al alloys have also been performed at 500, 750, and 1000 °C, but for an exposure time of 24 h at each temperature. Optical images of Fe–Cr-Al plus 304L stainless steel and Zr-2 and Zr-4 after an exposure to 1000 °C for 24 h are shown in Fig. 12. Significant corrosion, with the formation of thick spalling oxides was observed on the stainless steel and Zircaloy samples, while the Fe–Cr-Al showed relatively minimal oxidation. Similar observations were observed at the other two test temperatures.

Further detailed analysis of steam exposed CrN-coated Zr-2 and Fe–Cr-Al, including TEM/EELS analysis, is scheduled to be performed in the near future.

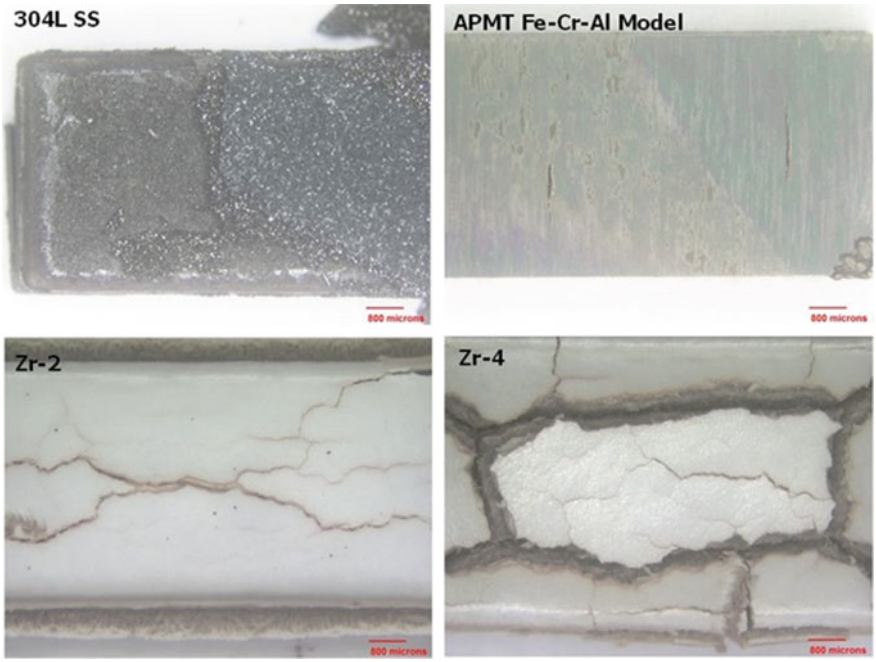

Fig. 12 Optical images of the sample surface after steam oxidation treatment at 1000 °C for 24 h

Conclusions

A range of corrosion tests were performed on CrN-coated Zr-2 and Fe–Cr-Al samples in aqueous conditions at 300 °C and steam environments up to 1000 °C. CrN has been shown to be a barrier to corrosion and deuterium ingress under aqueous corrosion conditions and to act at least as a temporary barrier to corrosion under steam conditions. The Fe–Cr-Al alloy studied has shown much lower corrosion rates as compared to stainless steel and Zircaloy, most strikingly under 1000 °C conditions. Both examples studied have shown promise as potential routes for ATFC material design by showing an overall lowering of oxidation rates, as compared to standard Zircaloy.

Future work will include longer duration steam exposure tests of the CrN-coated Zr-2, TEM/EELS analysis of aqueous corrosion scratched CrN coatings as a function of distance from a damaged/uncoated region, and more detailed TEM/EELS analysis of steam exposed CrN-coated Zr-2 and Fe–Cr-Al.

References

1. R. Van Nieuwenhove, Application of coatings and plasma treatments for nuclear applications, EHPG-Meeting, Sandefjord, 3–7 Oct 2011, Halden Reactor Project Report HWR-1028, declassified
2. G.-H. Song, X.-P. Yang, G.-L. Xiong, Z. Lou, L.-J. Chen, The corrosive behaviour of Cr/CrN multilayer coatings with different modulation periods. Vacuum **89**, 136–141 (2013)
3. S.B. Abusuilik, K. Inoue, Effects of intermediate surface treatments on corrosion resistance of cathodic arc PVD hard coatings. Surf. Coat. Technol. **237**, 421–428 (2013)
4. B. Kilinc, S. Demirkiran, U. Sen, S. Sen, Corrosion behavior of nitride and Cr-Al-N coatings formed on AISI D2 steel. Acta Phys. Pol., A **123**, 268–270 (2013)
5. A. Basu, J. Dutta Majumdar, I. Manna, Structure and properties of Cr_xN coating. Surf. Eng. **28**, 199–204 (2012)
6. F. Cai, Q. Yang, X. Huang, R. Wei, Microstructure and corrosion behavior of CrN and CrSiCN coatings. J. Mater. Eng. Perform. **19**, 721–727
7. S. Kaciulis, A. Mezzi, G. Montesperelli, F. Lamastra, M. Rapone, F. Casadei, T. Valente, G. Gusmano, Multi-technique study of corrosion resistant CrN/Cr/CrN and CrN: C coatings. Surf. Coat. Technol. **201**, 313–319 (2006)
8. U. Bardi, S.P. Chenakin, F. Ghezzi, C. Giolli, A. Goruppa, A. Lavacchi, E. Miorin, C. Pagura, A. Tolstogouzov, High-temperature oxidation of CrN/AlN multilayer coatings. Appl. Surf. Sci. **252**, 1339–1349 (2005)
9. H.-P. Feng, C.-H. Hsu, J.-K. Lu, Y.-H. Shy, Effects of PVD sputtered coatings on the corrosion resistance of AISI 304 stainless steel. Mater. Sci. Eng., A **347**, 123–129 (2003)
10. C. Liu, Q. Bi, A. Leyland, A. Matthews, An electrochemical impedance spectroscopy study of corrosion behaviour of PVD coated steels in 0.5 N NaCl aqueous solution: Part II. EIS interpretation of corrosion behaviour. Corros. Sci. **45**, 1257–1273 (2003)
11. R. Van Nieuwenhove, V. Andersson, J. Balak, B. Oberländer, In-pile testing of CrN, TiAlN and AlCrN Coatings on Zircaloy cladding in the Halden Reactor, 18th International Symposium on Zirconium in the Nuclear Industry, Hilton Head, USA, 2016,, STP1597 ASTM International's STP: Selected Technical Papers on 18th International Symposium on Zirconium in the Nuclear Industry (2017)
12. E. Airiskallio, E. Nurmi, M.H. Heinonen, I.J. Väyrynen, K. Kokko, M. Ropo et al., High temperature oxidation of Fe–Al and Fe–Cr–Al alloys: the role of Cr as a chemically active element. Corros. Sci. **52**, 3394–3404 (2010)
13. J.K. Bunn, R.L. Fang, M.R. Albing, A. Mehta, M.J. Kramer, M.F. Besser et al., A high-throughput investigation of Fe-Cr-Al as a novel high-temperature coating for nuclear cladding materials. Nanotechnology **26**, 1–9 (2015)
14. J. Ejenstam, M. Thuvander, P. Olsson, F. Rave, P. Szakalos, Microstructural stability of Fe–Cr–Al alloys at 450–550°C. J. Nucl. Mater. **457**, 291–297 (2015)
15. M.H. Heinonen, K. Kokko, M.P.J. Punkkinen, E. Nurmi, J. Kollár, L. Vitos, Initial Oxidation of Fe–Al and Fe–Cr–Al alloys: Cr as an alumina booster. Oxid. Met. **76**, 331–346 (2011)
16. D.J. Park, H.G. Kim, J.Y. Park, Y.I. Jung, J.H. Park, Y.H. Koo, A study of the oxidation of FeCrAl alloy in pressurized water and high-temperature steam environment. Corros. Sci. **94**, 459–465 (2015)
17. B.A. Pint, K.A. Terrani, M.P. Brady, T. Cheng, J.R. Keiser, High temperature oxidation of fuel cladding candidate materials in steam–hydrogen environments. J. Nucl. Mater. **440**, 420–427 (2013)
18. R.B. Rebak, R.J. Blair, P.J. Martiniano, F. Wagenbaugh, E.J. Dolley, Resistance of Advanced Steels to Reaction with High Temperature Steam as Accident Tolerant Fuel Cladding Materials, presented at the NACE Corrosion 2014, San Antonio, TX (2014)
19. K.A. Terrani, S.J. Zinkle, L.L. Snead, Advanced oxidation-resistant iron-based alloys for LWR fuel cladding. J. Nucl. Mater. **448**, 420–435 (2014)

20. S.J. Zinkle, K.A. Terrani, J.C. Gehin, L.J. Ott, L.L. Snead, Accident tolerant fuels for LWRs: a perspective. J. Nucl. Mater. **448**, 374–379 (2014)
21. F. Liu, M. Halvarsson, K. Hellström, J.-E. Svensson, L.-G. Johansson, First three-dimensional atomic resolution investigation of thermally grown oxide on a FeCrAl alloy. Oxid. Met. **83**, 441–451 (2015)
22. T. Cheng, J.R. Keiser, M.P. Brady, K.A. Terrani, B.A. Pint, Oxidation of fuel cladding candidate materials in steam environments at high temperature and pressure. J. Nucl. Mater. **427**, 396–400 (2012)
23. B.A. Pint, S. Dryepondt, K.A. Unocic, D.T. Hoelzer, Development of ODS FeCrAl for compatibility in fusion and fission energy applications. J. Miner. Met. Mater. Soc. (TMS) **66**, 2458–2466 (2014)
24. H. Hindam, D.P. Whittle, Microstructure, adhesion, and growth kinetics of protective scales on metals and alloys. Oxid. Met. **18**, 245–284 (1982)
25. S.W. Guan, W.W. Smeltzer, Oxygen solubility and a criterion for the transition from internal to external oxidation of ternary alloys. Oxid. Met. **42**, 375–391 (1994)
26. Y. Niu, S. Wang, F. Gao, Z.G. Zhang, F. Gesmundo, The nature of the third-element effect in the oxidation of Fe–xCr–3at.% Al alloys in 1 atm O_2 at 1000°C. Corros. Sci. **50**, 345–356 (2008)
27. In-Situ Lift-Out Preparation of TEM Lamellas, Carl Zeiss SMT – Nano Technology Systems Division Application Note, www.smt.zeiss.com/nts
28. L.A. Giannuzzi, F.A. Stevie, *Introduction to Focused Ion Beams Instrumentation, Theory, Techniques and Practice* (Springer Science and Business Media Inc, USA, 2005)
29. M. Nordin, M. Larsson, S. Hogmark, Mechanical and tribological properties of multilayered PVD TiN/CrN, TiN/MoN, TiN/NbN and TiN/TaN coatings on cemented carbide. Surf. Coat. Technol. **106**, 234–241 (1998)
30. M. Nordin, F. Ericson, Growth characteristics of multilayered physical vapour deposited TiN/TaN_x on high speed steel substrate. Thin Solid Films **385**, 174–181 (2001)
31. H. Era, Y. Ide, A. Nino, K. Kishitake, TEM study on chromium nitride coatings deposited by reactive sputter method. Surf. Coat. Technol. **194**, 265–270 (2005)
32. Q. Luo, Z. Zhou, W.M. Rainforth, PEh Hovsepian, TEM-EELS of low-friction superlattice TiAlN/VN coating: the wear mechanisms. Tribol. Lett. **24**, 171–178 (2006)
33. C. Mitterbauer, C. Hebert, G. Kothleitner, F. Hofer, P. Schattschneider, H.W. Zandbergen, Electron energy loss-near edge structure as a fingerprint for identifying chromium nitrides. Solid State Commun. **130**, 209–213 (2004)
34. G. Berthomé, E. N'Dah, Y. Wouters, A. Galerie, Temperature dependence of metastable alumina formation during thermal oxidation of FeCrAl foils. Mater. Corros. **56**, 389–392 (2005)
35. H. Josefsson, F. Liu, J.E. Svensson, M. Halvarsson, L.G. Johansson, Oxidation of FeCrAl alloys at 500-900°C in dry O_2. Mater. Corros. **56**, 801–805 (2005)
36. K. Daub, R. Van Nieuwenhove, H. Nordin, Investigation of the impact of coatings on the corrosion of nuclear components. J. Nucl. Mater. **467**, 260–270 (2015)
37. Y.Z. Huang, S. Lozano-Perez, R.M. Langford, J.M. Titchmarsh, M.L. Jenkins, Preparation of transmission electron microscopy cross-section specimens of crack tips using focused ion beam milling. J. Microsc. **207**, 129–136 (2002)
38. Y.Z. Huang, J.M. Titchmarsh, TEM investigation of intergranular stress corrosion cracking for 316 stainless steel in PWR environment. Acta Mater. **54**, 635–641 (2006)
39. S. Lozano-Perez, J.M. Titchmarsh, TEM Investigations of intergranular stress corrosion cracking in austenitic alloys in PWR environmental conditions. Mater. High Temp. **20**, 573–579 (2003)

Steam Oxidation Behavior of FeCrAl Cladding

B.A. Pint, K.A. Terrani and R.B. Rebak

Abstract In order to better understand the high temperature steam oxidation behavior of FeCrAl alloys, this study addressed two topics. The first is continuing to evaluate the effect of alloy composition on performance of commercial and laboratory-made candidate FeCrAl alloys. For a few optimized compositions, this includes the performance of commercially-made tubing where it is clear that dropping the Cr content from 20% to 10–13% reduces the maximum operating temperature in steam by ~50 °C. The second addresses more realistic accident conditions. Model FeCrAl compositions that were exposed in ~300 °C water for 1 year were subsequently "ramp" tested in steam at 5 °C/min to 1500 °C to assess the effect of the Fe-rich oxide formed in water on the subsequent steam oxidation resistance. For Fe-18Cr-3Al+Y, the 1 year exposures in three different LWR water chemistries did not affect the ability to form alumina to 1500 °C. However, for marginal alloys Fe-13Cr-4Al and Fe-10Cr-5Al, some specimens began forming voluminous Fe-rich oxide at lower temperatures.

Keywords Fuel cladding · High temperature oxidation · Steam · FeCrAl · Al_2O_3

B.A. Pint (✉) · K.A. Terrani
Oak Ridge National Laboratory, P. O. Box 2008, Oak Ridge, TN 37831-6156, USA
e-mail: pintba@ornl.gov

K.A. Terrani
e-mail: terranika@ornl.gov

R.B. Rebak
GE Global Research, 1 Research Circle, Schenectady, NY 12309, USA
e-mail: rebak@ge.com

J.H. Jackson et al. (eds.), *Proceedings of the 18th International Conference on Environmental Degradation of Materials in Nuclear Power Systems – Water Reactors*, The Minerals, Metals & Materials Series, https://doi.org/10.1007/978-3-319-68454-3_20

Introduction

For high temperature alloy oxidation resistance, there are only three protective oxide scales: Cr_2O_3, Al_2O_3 and SiO_2. [1]. Engineering alloys typically do not contain enough Si to form an exclusive silica scale as is found on $MoSi_2$ or SiC [2]. For the highest temperature applications, Al_2O_3 is much more stable and slow-growing than Cr_2O_3, which is more widely used at lower temperatures, i.e. <900 °C. Thus, it is not surprising that when candidate alloys were screened for accident tolerant (or advanced technology) fuel (ATF) cladding that alumina-forming FeCrAl alloys were selected [3–10]. Conventional Zr-based fuel cladding with UO_2 fuel has dominated light water reactors (LWR) for decades, however, the beyond design basis accident (BDBA) in three units at the Fukushima Daiichi power plant in March 2011 [11, 12] has spawned a search for materials that can provide larger safety margins and potentially avoid severe core degradation [5, 13]. Nickel is undesirable from a neutronics perspective and chromia-forming Fe–Cr alloys require very high (~25%) Cr contents for steam oxidation resistance at 1200 °C [14, 15]. An extensive effort has been conducted to evaluate FeCrAl alloy properties [16–22] and develop an optimized composition for the ATF application [23]. While the initial work screened candidates to 1200–1350 °C [3, 4], more recent studies have pushed the maximum temperature to 1400–1700 °C [7–10], well above the typical FeCrAl solidus temperature of ~1520 °C. However, this is the information needed to model behavior over various accident scenarios. Not surprisingly, these conditions have not been previously investigated and a number of questions still remain about the high temperature oxidation behavior.

The current work addressed two topics related to the high temperature steam oxidation performance of FeCrAl in accident conditions: (1) the effect of composition on performance, by adding additional commercial and laboratory FeCrAl compositions to the existing 1200–1500 °C database and (2) better simulating an accident scenario by first growing an oxide in LWR operation conditions for 1 year followed by steam oxidation testing in a "ramp" test to 1500 °C.

Experimental Procedure

Specimens for this work have evolved from ~10 × 20 × 1–2 mm coupons with a 600 grit polish to commercially fabricated tubing, typically ~12.5 mm lengths of ~9.5 mm diameter tubing with 0.3–0.7 mm wall thickness and 6–9 cm^2 surface area. Table 1 provides alloy compositions discussed in this study. New compositions were initially vacuum cast, rolled and annealed at Oak Ridge National Laboratory [23], while tube material was commercially fabricated using traditional wrought alloy techniques for seamless tube production to facilitate commercialization. Oxidation exposures were conducted in two systems: (1) a high temperature (1700 °C) test rig consisting of a vertical alumina tube with two resistively heated

Table 1 Alloy compositions (mass% and ppmw) determined by inductively coupled plasma and combustion techniques

Alloy	Fe	Cr	Al	Mn	Si	Zr	Y ppm	S ppm	Other
OP	76.6	18.1	4.5	0.2	0.2	0.04	590	< 3	0.04Hf
OQ	72.9	20.2	6.0	0.2	0.3	0.04	550	< 3	0.04Hf
OR	79.7	14.3	4.6	0.3	0.3	0.16	10	3	
APM	73.3	20.4	5.5	0.1	0.2	0.10		10	0.05O, 0.03Ti
APMT	69.8	21.2	4.8	0.1	0.5	0.11	2100	< 3	2.8Mo, 0.17Hf
B106Y	84.0	10.1	5.9	<	<	<	30	28	0.004C, 0.012O
B136Y	80.8	13.0	6.2	<	<	<	300	10	< 0.01C
B108Y	82.2	10.0	7.8	<	<	<	190	6	0.002C, 0.002O
B183Y	79.3	17.5	3.0	<	0.01	<	190	11	0.2W, 0.003C, 0.002O
B134Y	83.0	13.0	3.9	<	<	<	70	15	0.006C, 0.001O
B105Y	85.2	10.0	4.8	<	<	<	380	13	0.005C, 0.002O
C135M	79.4	13.1	5.3	<	0.1	<	530	< 3	2.0Mo, 0.001C

< denotes less than 0.01%

furnaces; and (2) a magnetic suspension thermal gravimetric analysis (TGA) using a Rubotherm DynTHERM LP-HT-II instrument where the alumina test chamber with 100% steam was fully isolated from the weighing mechanism at up to 1500 °C [2]. In the first system, steam entered the bottom of the reaction tube and was preheated to 1000–1300 °C by the first furnace. Tube specimens were held in the second furnace in an alumina holder [10] designed to catch any oxidation debris for exposures up to 1700 °C but still allow steam to impinge on the tube outer diameter (OD).

The specimen was ramped to high temperature using a variety of scenarios. In one case, the specimens were heated for 1.5 h (10–19 °C/min) and held for 1 min at temperature before cooling to room temperature in flowing argon. Initially, Ar (500 cc/min) was used to purge the system while it was heated to 600 °C at 20 °C/min, then steam was introduced. In a second scenario, a similar procedure was used to heat the specimen to 600 °C and begin steam flow. The tube sample was then ramped to 1200°C at 12°C/min, held for 50 min at 1200 °C followed by ramping at 11.1 °C/min to a final temperature of between 1400–1500°C. Similar to the other scenario, after a 1 min hold, the specimen was cooled to room temperature in flowing argon. In the TGA experiments, the specimen was suspended with a Pt–Rh wire, which experienced little evaporation in steam. In this system, the specimens were ramped at 5 °C/min and similarly, the steam was introduced at 600 °C after an Ar purge. With the TGA monitoring mass gain, the ramp was stopped if the total mass gain exceeded ~10 mg or the temperature reached 1500 °C. The water

used to generate steam in both rigs was deionized but not Ar-bubbled or filtered as is typically done for ~600 °C steam testing [7]. The gas velocity in the TGA experiments was typically 1 cm/s while the steam velocity was 50–60 cm/s (~200 ml/h) in the high temperature furnace. The mass change of all specimens was measured using a Mettler Toledo model XP205 balance with ± 0.04 mg or <0.01 mg/cm^2 accuracy. After exposure, specimens were metallographically sectioned and examined by light microscopy. In some cases, the specimens were Cu-plated prior to mounting to protect the surface reaction product.

Results and Discussion

Effect of Alloy Composition on the Steam Oxidation Behavior of FeCrAl Alloys

A range of FeCrAl compositions are commercially available for a variety of heat resistant applications including heating elements, automotive catalyst supports and heat shields [1]. The most typical compositions for the highest temperature applications have 19–21 wt%Cr and 5–6%Al. A variety of "leaner" compositions are marketed with 12–14%Cr and 3–4%Al as they are easier to fabricate (e.g. rolling, joining) but can still form a protective alumina scale over a range of conditions. For the fuel cladding application, there is concern about the formation of Cr-rich α' under irradiation and the associated embrittlement [18, 21]. Thus, there has been an effort to minimize the Cr content in an optimized cladding composition [23]. Early in the evaluation process it was discovered that dropping the Cr content reduced the steam oxidation resistance at 1200 °C in both model and commercial alloys [4, 7, 8, 14]. Figure 1a shows how at ~20%Cr, Al contents from 3–6%Al form a protective alumina scale at 1200 °C in steam. However, at 10–15%Cr, >4%Al was needed for protective behavior and most alloys under development contain 5–6%Al [10, 23]. Three additional commercial alloys were recently evaluated for this application, designated OP, OQ and OR for this study. The measured compositions are shown in Table 1. Based on the composition, all three appeared to be potential cladding compositions with OR having the leanest composition, near to the protective-non protective border in Fig. 1a. Steam oxidation test results for 4 h at 1200 °C for the three alloys are shown in Fig. 1b. The TGA mass gain results are shown versus the square root of time to show the expected solid-state diffusion limited parabolic relationship [1]. While the OP and OQ specimens showed very similar parabolic behavior, the OR specimen initially showed a similar low mass gain but could not maintain the low rate during the 4 h isothermal exposure. Macroscopically, one corner of the coupon started to form an obvious Fe-rich oxide nodule. However, in cross-section near the middle of the specimen, the oxide looked similar to that formed on the other two alloys (OP and OQ), Fig. 2. An occasional imperfection was observed, such as the small nodule in Fig. 2a. Nevertheless, OR is listed as being non-protective at 1200 °C in Fig. 1a.

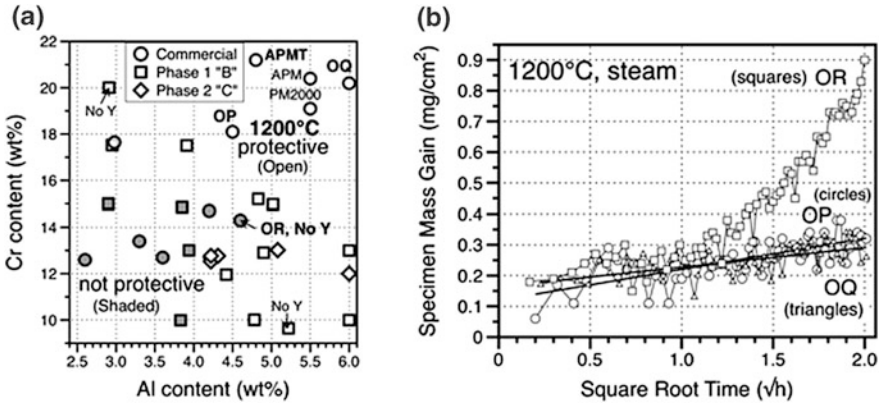

Fig. 1 **a** Effect of alloy Cr and Al content in commercial and laboratory FeCrAl alloys on oxidation resistance at 1200 °C in steam and **b** specimen mass gain in 1200 °C steam plotted versus the square root of time. The phase 1 alloys are ternary FeCrAl±Y alloys and phase 2 are FeCrAlY+Mo, Si

In addition to the lower Cr and Al contents relative to the other commercial alloys, OR also contained much less Y and no Hf but a higher Zr content, Table 1. It is difficult to say if this difference contributed to the failure. These "reactive" elements (RE) are known to have beneficial effects on high temperature oxidation resistance of all alumina-forming alloys [24–26] with Y being effective alone but combinations of Y and Hf providing an optimum benefit for FeCrAl in terms of slowing the alumina scale growth rate and improving scale adhesion [25, 26]. Early versions of alloy APM contained only Zr but showed good behavior [27]. For comparison, Fig. 2d shows a model Fe-10Cr-6Al+Y alloy (B106Y). The slightly thicker protective scale formed on this alloy is attributed to the low Y content (30 ppm), Table 1. This alloy experienced scale spallation problems at higher temperatures.

While Fig. 1a provides a snapshot of 1200 °C behavior, BDBA scenarios involve increasingly higher temperatures. Initial screenings were performed isothermally at 1200 °C (Fig. 1a) and 1400 °C for 4 h. Particularly in the high steam flow rate in the

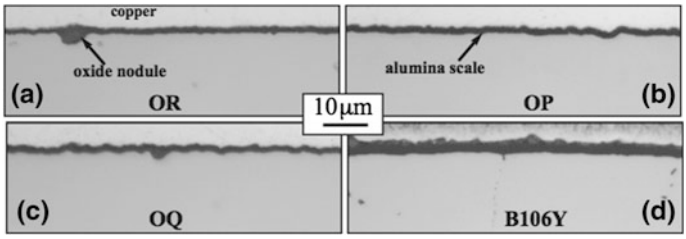

Fig. 2 Light microscopy of polished cross-sections of the scale formed after 4 h at 1200 °C in steam on **a** OR, **b** OP, **c** OQ and **d** B106Y (Fe-10Cr-6Al+Y)

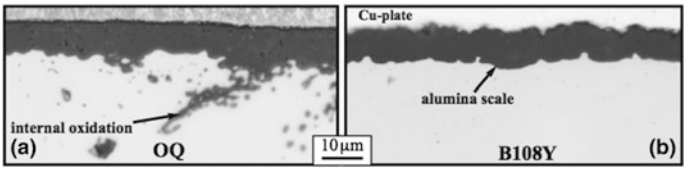

Fig. 3 Light microscopy of polished cross-sections of the scale formed after oxidation for 4 h at 1400 °C **a** OQ and **b** B108Y (Fe-10Cr-8Al+Y)

HTF, it was discovered that many FeCrAlY compositions could not survive a fast heating in argon followed by steam exposure for 4 h. Among these alloys, only the OQ alloy with the highest Cr and Al contents survived this exposure. The thicker scale with significant internal oxidation of the Y, Hf and Zr is shown in Fig. 3a. The other alloy specimens were completed consumed. Among the low Cr model alloys, only a composition with B108Y (10Cr-8Al) survived this condition. In this case, the alloy had a relatively low RE addition of 190 ppm Y and no internal oxidation was observed, Fig. 3b. While this alloy illustrated that even higher Al contents were needed with 10%Cr, it was found to have low ductility and was not recommended for tube production.

The steam oxidation evaluations have evolved to include ramp testing after the initial 4 h screening test at 1200 °C [8, 28]. Consistent with prior results for alloys in this composition range, the OP and OQ specimens survived ramp testing to 1500 °C (5 °C/min heating rate). The OR specimen gained 2 mg/cm^2 by 1335 °C and was stopped before 1400 °C. This behavior is consistent with a composition that struggled to form alumina at 1200 °C.

As compositions have been down-selected for tube production, the ramp testing has continued on tube samples with additional ramp scenarios being performed to support various BDBA models. In these scenarios, one metric is the maximum temperature where alumina formation can be maintained. Figure 4 shows the behavior of B136Y tube specimens ramped at 11.1 °C/min after a 50 min hold at 1200 °C. The mass gain results indicate that the tube specimens ramped to 1400 and 1450 °C were able to maintain an alumina scale while specimens ramped to 1475 and 1500 °C were not with the high mass gains indicating complete oxidation of the thin-walled (~390 μm) tube specimen. This result was consistent with other indications that lower Cr content compositions sometimes could not reach 1500 °C, like high-Cr content compositions like Kanthal APMT® (Advanced Powder Metallurgy Tube) [29] and APM [10]. Figure 4 shows that the APMT tube specimen formed a protective scale even for ramping to 1500 °C as evidenced by the low mass gain (0.6 mg/cm^2).

Steam Oxidation Testing of Model FeCrAl Alloys After Exposure to Hydrothermal Corrosion

While FeCrAl alloys perform extremely well in steam at high temperature, there was some concern about their behavior in normal operating conditions in ~300 °C water.

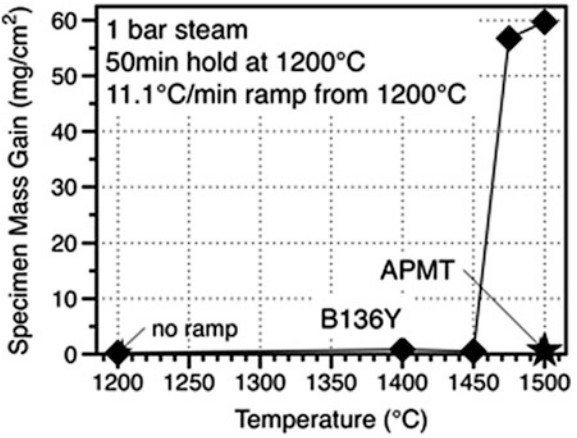

Fig. 4 Specimen mass gain after holding for 50 min at 1200°C followed by ramping to temperatures above 1200°C at 11.1°C/min

A recently published study indicated that this was not a concern either [22]. However, a remaining issue was whether the Fe-rich oxide formed in water (characterized previously [22]) would disrupt or inhibit alumina formation during a subsequent BDBA. Thus, three sets of model FeCrAlY specimens from the 1 year hydrothermal corrosion study were ramp tested to 1500 °C. Each alloy was ramp tested in the as-fabricated state and after 1 year exposures in (1) pressurized water reactor (PWR) conditions of 3.57 ppm H_2, 330 °C, 7.2 pH and 15 MPa, where these alloys formed predominantly magnetite with some hematite on B183Y, (2) boiling water reactor, hydrogen water chemistry (BWR-HWC) conditions of 0.3 ppm H_2 290 °C, 5.6 pH and 7 MPa, where these alloys formed magnetite scales and (3) boiling water reactor, normal water chemistry (BWR-NWC) conditions of 1.0 ppm O_2 290 °C, 5.6 pH and 7 MPa, where they formed a very thin layer (<0.5 μm) of hematite with some wüstite [22]. Example ramp tests results are shown for the Fe-18Cr-3Al+Y (B183Y) specimens in Fig. 5a. All of the specimens survived to 1500 °C with low mass gains. Considering Fig. 1a, this alloy and B105Y both have reasonable steam oxidation resistance. However, B134Y was not protective at 1200 °C in steam. Figure 5b summarizes the mass change for all of the specimens tested. Three of the four B134Y specimens formed Fe-rich oxide during the exposure and the as-fabricated specimen reached 2 mg/cm^2 in the ramp test by 1285 °C. For the B105Y specimens, only the specimen exposed in BWR-NWC did not reach 1500 °C, it began to show increasing mass gain at 1375 °C. There did not appear to be any correlation between the starting oxide phase formed in the LWR conditions (e.g. hematite, magnetite and/or wüstite) and the subsequent formation of a protective alumina scale. All of the specimens exposed to the PWR conditions formed a protective alumina scale in ramp testing. However, B134Y formed a similar 2–3 μm thick, magnetite-rich scale in PWR and BWR-HWC and yet did not survive ramp testing after the latter exposure [22].

Images of all of the specimens are shown in Fig. 6. Figure 7 shows cross-sections of the B183Y specimens. The oxide thicknesses are consistent with the post-test specimen mass change data in Fig. 5. After exposure to 1500 °C, the alumina scale is relatively thick but protective. For the B183Y specimen exposed to BWR-HWC, remnants of the thicker Fe-rich magnetite scale formed in this environment are present as an outer oxide

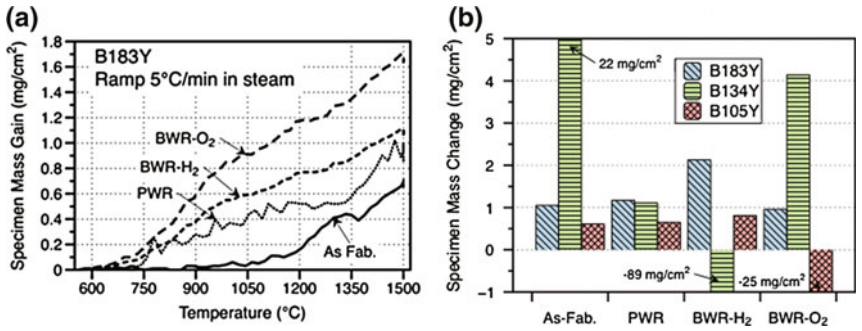

Fig. 5 **a** Specimen mass gain during ramp testing in 1 bar steam to 1500 °C for B183Y (Fe-18Cr-3Al+Y) specimens with and without 1-year exposure to different LWR conditions, **b** specimen mass change after ramp testing for three different FeCrAl compositions

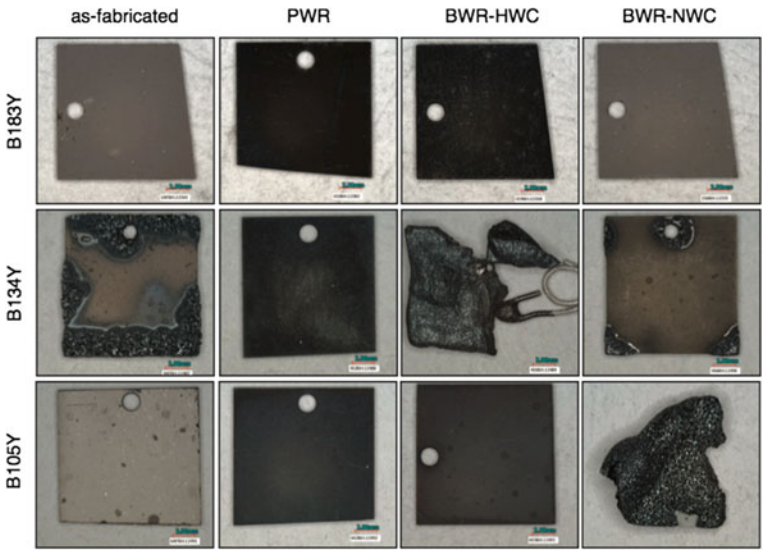

Fig. 6 Images of the FeCrAlY specimens after ramp testing in steam at 5 °C/min

layer, Fig. 7c. Additional characterization of these specimens is in progress to clearly identify the location of any Fe-rich oxide after ramp testing.

Summary

Three additional FeCrAl commercial compositions were evaluated in steam oxidation at 1200–1500 °C for fuel cladding more resistant to a BDBA scenario. The three alloys were consistent with prior results where dropping the Cr requires higher

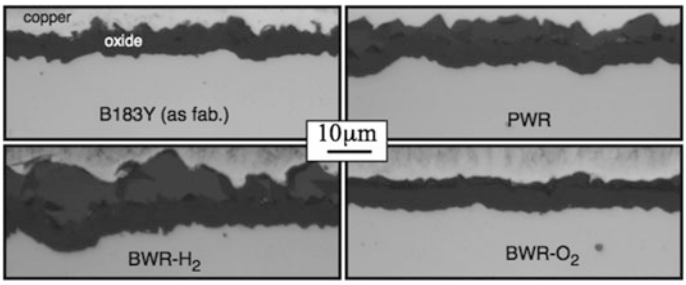

Fig. 7 Light microscopy of B183Y (Fe-18Cr-3Al+Y) specimens after ramp testing to 1500 °C in 1 bar steam on **a** as fabricated specimen and after a 1-year exposure in **b** PWR, **c** BWR H_2 environment and **d** BWR O_2 environment

Al contents for protective behavior, particularly at 1400–1500 °C. Only the high Cr alloys are found to be protective during isothermal testing at 1400 °C and ramp testing to 1500 °C. Dropping the Cr content from 20% to 10–13% reduced the maximum operating temperature by ~50 °C. To more accurately assess the accident scenario, model FeCrAlY samples were exposed in ~300 °C water for 1 year and then ramp tested to 1500 °C in steam. For marginal alloys Fe-13Cr-4Al and Fe-10Cr-5Al, some specimens were not able to reach 1500 °C. However, for Fe-18Cr-3Al+Y, the 1 year exposures in three different LWR water chemistries did not affect the ability to form alumina to 1500 °C.

Acknowledgements The experimental work was conducted by M. Howell, T. Lowe and T. Jordan. S. S. Raiman provided useful comments on the manuscript. This research was funded by the U.S. Department of Energy's Office of Nuclear Energy, Advanced Fuel Campaign of the Fuel Cycle R&D program.

References

1. D.J. Young, *High temperature oxidation and corrosion of metals*, 2nd edn. (Elsevier, Oxford, 2016)
2. K.A. Terrani et al., Silicon carbide oxidation in steam up to 2 MPa. J. Am. Ceram. Soc. **97**, 2331–2352 (2014)
3. T. Cheng et al., Oxidation of fuel cladding candidate materials in steam environments at high temperature and pressure. J. Nucl. Mater. **427**, 396–400 (2012)

4. B.A. Pint et al., High temperature oxidation of fuel cladding candidate materials in steam-hydrogen environments. J. Nucl. Mater. **440**, 420–427 (2013)
5. K.A. Terrani, S.J. Zinkle, L.L. Snead, Advanced oxidation-resistant iron-based alloys for LWR fuel cladding. J. Nucl. Mater. **448**, 420–435 (2014)
6. R.B. Rebak, Alloy selection for accident tolerant fuel cladding in commercial light water reactors. Metal. Mater. Trans. E **2**, 197–207 (2015)
7. B.A. Pint et al., Material selection for accident tolerant fuel cladding. Metal. Mater. Trans. E **2**, 190–196 (2015)
8. B.A. Pint, K.A. Unocic, K.A. Terrani, The effect of steam on the high temperature oxidation behavior of alumina-forming alloys. Mater. High Temp. **32**, 28–35 (2015)
9. K.A. Unocic, Y. Yamamoto, B.A. Pint, Effect of Al and Cr content on air and steam oxidation of FeCrAl alloys and commercial APMT alloy. Oxid. Met. **87**, 431–441 (2017)
10. B.A. Pint, Performance of FeCrAl for Accident Tolerant Fuel Cladding in High Temperature Steam. *Corrosion Reviews* **35**(3), 167–175 (2017) doi:10.1515/corrrev-2016-0067
11. R. Gauntt, et al., Fukushima Daiichi Accident Study (Status as of April 2012). Sandia National Laboratory Report, SAND2012-6173, Albuquerque, NM, (2012)
12. K.R. Robb, M.W. Francis, L.J. Ott, Insight from Fukushima Daiichi Unit 3 investigations using MELCOR. Nucl. Technol. **186**, 145–160 (2014)
13. S.J. Zinkle et al., Accident tolerant fuels for LWRs: a perspective. J. Nucl. Mater. **448**, 374–379 (2014)
14. B.A. Pint, et al., Material selection for fuel cladding resistant to severe accident scenarios. NACE paper ED2013-3083, Houston, TX, presented at the 16th Environmental Degradation conference, Asheville, NC, August 2013
15. B.A. Pint, K.A. Unocic, Evaluation of Fe-Cr alloys for accident tolerant fuel cladding. Oxid. Met. **87**, 515–526 (2017)
16. Y. Yan et al., Post-quench ductility evaluation of Zircaloy-4 and select iron alloys under design basis and extended LOCA conditions. J. Nucl. Mater. **448**, 436–440 (2014)
17. K.G. Field et al., Deformation behavior of laser welds in high temperature oxidation resistant Fe-Cr-Al alloys for fuel cladding applications. J. Nucl. Mater. **454**, 352–358 (2014)
18. K.G. Field et al., Radiation tolerance of neutron-irradiated model Fe-Cr-Al alloys. J. Nucl. Mater. **465**, 746–755 (2015)
19. X.X. Hu et al., Hydrogen permeation in FeCrAl alloys for LWR cladding application. J. Nucl. Mater. **461**, 282–291 (2015)
20. C.P. Massey et al., Cladding burst behavior of Fe-based alloys under LOCA. J. Nucl. Mater. **470**, 128–138 (2016)
21. P.D. Edmondson et al., Irradiation-enhanced α' precipitation in model FeCrAl alloys. Scripta Mater. **116**, 112–116 (2016)
22. K.A. Terrani et al., Uniform corrosion of FeCrAl alloys in LWR coolant environments. J. Nucl. Mater. **479**, 36–47 (2016)
23. Y. Yamamoto et al., Development and property evaluation of nuclear grade wrought FeCrAl fuel cladding for light water reactors. J. Nucl. Mater. **467**, 703–716 (2015)
24. B.A. Pint, Experimental observations in support of the dynamic segregation theory to explain the reactive element effect. Oxid. Met. **45**, 1–37 (1996)
25. B.A. Pint, Optimization of reactive element additions to improve oxidation performance of alumina-forming alloys. J. Am. Ceram. Soc. **86**, 686–695 (2003)
26. D. Naumenko, B.A. Pint, W.J. Quadakkers, Current thoughts on reactive element effects in alumina-forming systems—in memory of John Stringer. Oxid. Met. **86**, 1–43 (2016)
27. B.A. Pint, A.J. Garratt-Reed, L.W. Hobbs, The reactive element effect in commercial ODS FeCrAl alloys. Mater. High Temp. **13**, 3–16 (1995)
28. B.A. Pint et al., Development of ODS FeCrAl for compatibility in fusion and fission applications. JOM **66**, 2458–2466 (2014)
29. B. Jönsson et al., High temperature properties of a new powder metallurgical FeCrAl alloy. Mater. Sci. Forum **461–464**, 455–462 (2004)

In-Situ Proton Irradiation-Corrosion Study of ATF Candidate Alloys in Simulated PWR Primary Water

Peng Wang and Gary S. Was

Abstract Irradiation enhanced corrosion behavior of Accident Tolerant Fuel candidate alloys T91 and Fe15Cr4Al were evaluated using in-situ proton irradiation-corrosion experiments in hydrogenated pure water (at 320 °C, 3 wppm H_2) with a 5.4 MeV proton beam. The thin sample acted as a "window" to allow protons to fully penetrate the sample while maintaining system pressure. The area of the samples exposed to the proton beam experienced effects from displacement damage and radiolysis products. The aim of the study was to characterize the effect of radiation on the kinetics and character of oxidation caused by accelerated waterside corrosion under irradiation. Samples irradiated with protons for total displacement damage of ~0.1 dpa (dose rate in water, 400 kGy/s) at an exposure time of 24 h were compared. Oxide morphology, phase structure, and composition of the oxide, metal and the metal/oxide interface were investigated using TEM and EDS and are related to the test conditions. The oxidation rate or resulting oxide thickness is dependent on the alloy Cr content; the oxidation rate increased as the Cr content decreased. The resulting oxide consists of an inner layer of Cr-rich spinel oxide and outer magnetite crystals in the unirradiated region; while the irradiated region consists of Cr-rich inner oxide spinel that was partially dissolved and coverage of outer non-faceted hematite precipitates.

Keywords Accident tolerant fuel · Irradiation · Proton · Corrosion

P. Wang (✉) · G.S. Was
Nuclear Engineering and Radiological Science, University of Michigan,
2355 Bonisteel Blvd, Ann Arbor, MI 48109, USA
e-mail: wpf@umich.edu

G.S. Was
e-mail: gsw@umich.edu

J.H. Jackson et al. (eds.), *Proceedings of the 18th International Conference on Environmental Degradation of Materials in Nuclear Power Systems – Water Reactors*, The Minerals, Metals & Materials Series, https://doi.org/10.1007/978-3-319-68454-3_21

Introduction

Following the high oxidation rate of fuel rods during the Fukushima Daiichi nuclear accident in 2011, the emphasis for nuclear fuel R&D activities has shifted from fuel reliability and waste minimization to enhancing the accident tolerance of LWR fuel. Hence, accident tolerance fuel (ATF) became the focus for nuclear fuel research since 2011. By definition, accident tolerant fuel can tolerate a loss of active cooling in the core for a considerably longer period compared with the current zirconium-UO_2 system. Furthermore, the ATF fuel/cladding system should maintain or improve the fuel performance during normal operations, operational transients, as well we in the event of an accident.

One of the approaches is to replace zirconium cladding with an alternative oxidation resistance high-performance cladding. Even though much experimental research and system simulation under accident conditions have been done, only a few detailed evaluations of the impact of advanced cladding at normal operation conditions is available in the literature. GE Global Research had conducted research to demonstrate that advanced steels such as ferritic-martensitic alloys and iron-chromium-aluminum (FeCrAl) alloys could be used as ATF cladding material in commercial light water reactors [1, 2]. These alloys are proposed to improve behavior under severe accident scenarios due to the addition of aluminum, which forms a dense protective oxide and prevents further oxidation at very high temperature. A substantial neutron penalty is identified when these advanced steels were used as monolithic cladding for current oxide fuel. To compensate for the decrease in reactivity, oxide fuel must be enriched, or cladding thickness has to be reduced [3].

Fuel vendors have also investigated their ATF concepts as well, AREVA and Westinghouse had developed a strategy to reduce the corrosion rate under accident condition by coating the Zr cladding, creating a hydride cladding. Several of these hydride cladding systems have been evaluated that may be more practical based on an economics evaluation during the transition from the current UO_2/Zr to ATF system. However, a few issues remain to be resolved, such as coating spallation, and inter-diffusion with zirconium [4].

Each of the approaches would substantially increase the fuel and electricity costs. However, the advanced steels have more advantage over the coated Zr cladding system due to its monolithic structure, since defects can be introduced during the manufacturing process of coated Zr cladding. Furthermore, the coated cladding tube can lose all its benefit if ballooning and rupturing of the tube occurred during accident.

Ferritic-martensitic (FM) steels are utilized in steam boilers and piping. T91 was developed in 1970s for the liquid metal fast breeder reactor and was characterize by improved thermal and mechanical properties at high temperatures and pressure compared to other ferritic steels, and in some cases even to austenitic stainless steels. FM steels also exhibit low swelling and activation under irradiation, higher thermal conductivity and lower thermal expansion than austenitic steels, low

susceptibility to stress corrosion cracking and modest corrosion resistance [5, 6]. For the above advantages, FM steels have been considered as promising candidate materials for ATF cladding materials [7]. However, the existing data on the corrosion of T91 in a water environment corresponding to light water reactor (LWR) environment is scarce; therefore, further investigation is necessary. FeCrAl alloys have also been considered as strong candidate materials for ATF cladding application. Studies of corrosion behavior of FeCrAl in high-temperature water have been conducted in the past. The general understanding of FeCrAl in high-temperature water system was that the formation of an alumina film at the surface under normal operating temperature (i.e. 280–340 °C) was not expected and passive protection was attributed to the presence of a chromia containing film [3]. However, a study of SS316L under irradiation-corrosion condition also indicated that oxide dissolution could occur during simultaneous proton irradiation, due to the formation of water-soluble hexavalent Cr ions in high potential water environment [8]. These advanced steels have similar or lower Cr content compared to SS316L and could suffer from the same oxide dissolution problem under irradiation conditions.

This study focused on the characterization of the oxide film formed on T91 and FeCrAl that has been exposed to the PWR primary water environment (without B and Li addition) during proton irradiation. During the proton irradiation study, the material experienced the combined effects of displacement damage, radiolysis product of water and possibly exciton production.

Experiments

A set of in-situ corrosion-irradiation experiments was conducted at the Michigan Ion Beam Laboratory (MIBL), at the University of Michigan. The experiments were designed to investigate the effects of displacement damage and water radiolysis products on corrosion.

Materials

Based on the available literature information, two steels were chosen for evaluation for the ATF cladding application. A ferritic FeCrAl alloy (Fe15Cr4Al) and a ferritic-martensitic alloy (T91) were investigated. The average lath size in T91 was about 1 μm. The ferritic steel Fe15Cr4Al has relatively larger equiaxed grains of size 30–50 μm. Chemical composition of the alloys in this study are shown in Table 1.

Irradiation

A 3 MV Pelletron accelerator at MIBL was used to produce the proton beam with an energy of 5.4 MeV. The proton beam was raster-scanned over an area of 8 mm × 8 mm on the slits system, which has a 6 mm × 6 mm opening to allow the beam to pass through. The beam current was also monitored and recorded on each slit to ensure beam position was maintained on each slit. After passing through the slits, the beam size was further reduced by a 1.2 mm diameter circular aperture on the back of the sample mount to define the exposed area of the sample.

The sample was designed to allow protons to fully pass through the sample while simultaneously being exposed to high-temperature high-pressure water (∼14 MPa) on one side and a high vacuum (10^{-12} MPa or 10^{-8} torr) on the other. At 5.4 MeV, proton range in these advanced steels were calculated as ∼95 μm using TRIM 2013 in simple Kichin-Pease mode [9]. As shown in Fig. 1, an 80 μm final sample thickness was chosen to ensure full penetration of the proton and minimize variation of damage profile across the sample thickness.

The displacement damage (expressed in displacement per atom, dpa) can be calculated from its direct relationship with the beam current incident on the target material [9]. Under normal irradiation conditions, and using displacement energies of 40 eV for Fe and Cr, and 25 eV for Al [10] the damage rate for the proton irradiation was about 2.2 × 10^{-7} dpa/s.

Disks with a diameter of 7.6 mm with a thickness of 500 μm were made from the alloys under investigation using electric discharge machining (EDM). The disks were then lapped to a thickness of ∼85 μm using abrasive paper (grit 400-1200) and 0.05-μm colloidal silica suspension to ensure that the two surfaces of the disks are flat and parallel. After final polishing, further reduce the thickness to ∼80 μm,

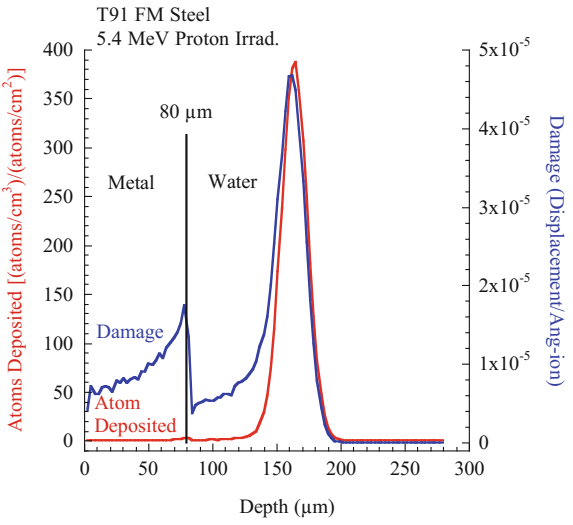

Fig. 1 Damage and ion range plots for 5.4 MeV proton in T91 as calculated by TRIM 2013 in K-P mode

the disk was sandwiched between a type 316 stainless steel washer and a 316 sample housing that were then welded using an Orion pulse arc welder to add structural rigidity and support to the sample.

A miniature autoclave made of 316 stainless steel was used in this study. All proton irradiation experiments were carried out at 320 °C. A more elaborate description of the experimental design and setup can be found elsewhere [11]. Deionized water bubbled with hydrogen gas was used to simulate the 3 ppmw H_2 PWR water chemistry without the Li and B addition. Dissolved oxygen (DO) and water conductivity were recorded on both the inlet and outlet of the corrosion cell during the experiment.

Post Irradiation Characterization

Focused ion beam (FIB) milling was used to prepare lamellas for transmission electron microscopy (TEM) analysis on a FEI Helios 650 Nanolab SEM/FIB. Both irradiated region (IR) and unirradiated region (UR) from the same sample were examined for oxide thicknesses. The oxide microstructure was characterized in bright field (BF) and high angle annular dark field (HAADF) mode using a JEOL 3100R05 STEM. Chemical composition studies were carried out in JEOL 2100 STEM using energy dispersive X-ray spectroscopy (EDS). Raman spectra were also recorded using a Renishaw inVia microscope with a RenCam CCD detector. The spectra were collected using a 633 nm wavelength laser, at a typical laser power of 50 mW, during a total of 900 s.

Results

Characterization of the sample was focused on the resulting IR and UR oxide morphology, oxide microstructure, oxide thickness.

Oxide Morphology

After 24 h of in-situ irradiation-corrosion exposure in primary water condition, T91 and Fe15Cr4Al showed a dark matte gray appearance. For both alloys, the UR region had a greater coverage of oxides with different morphology compared to those in the IR region as shown in Fig. 2. Noticeably, there is also a very sharp boundary between the IR and UR region indicating the proton beam has minimal divergence when passing through the sample. At high magnification, the outer particles were clearly faceted in the UR region. The original metal surface was covered by a layer of oxide visible through the gaps in the outer precipitates as

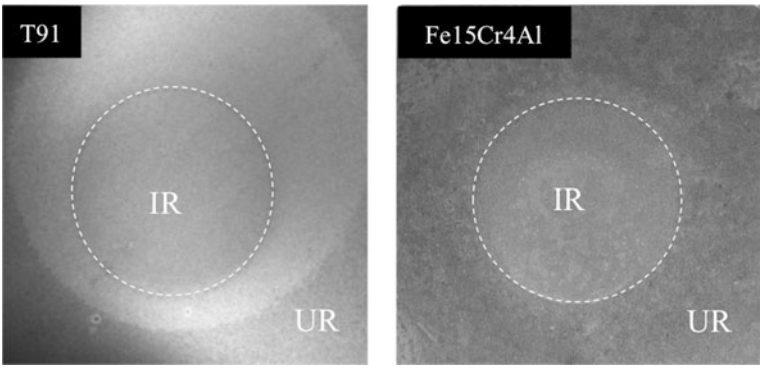

Fig. 2 SEM image of the sample surface after in-situ irradiation-corrosion experiment, the irradiated regions (IR) and unirradiated regions (UR) are highlighted

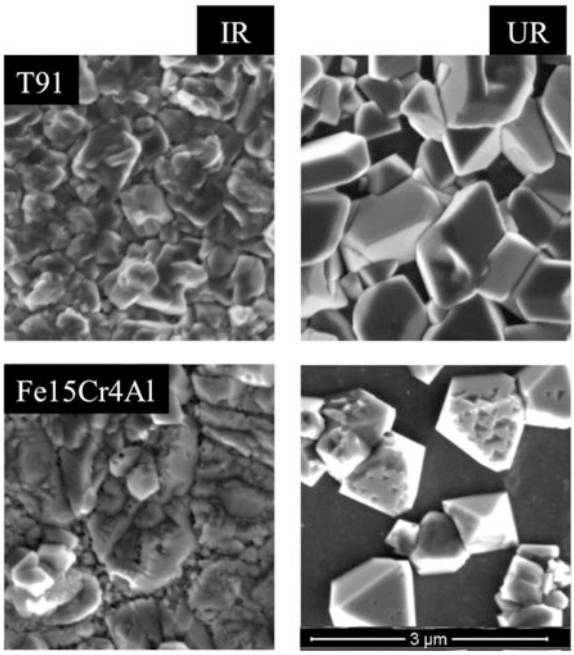

Fig. 3 High magnification SEM image of the IR and UR regions of the irradiated sample T91 and Fe15Cr4Al

shown in Fig. 3. On the contrary, in the IR region, the particle density of the outer precipitates was much higher, and the particles usually had irregular shapes. Furthermore, the IR region has complete oxide coverage such that the inner oxide layer was not visible under the SEM.

Oxide Species Found in IR/UR Regions

The oxide species found on the sample surface were identified by Raman spectroscopy. Three individual Raman spectra were taken in each region for data consistency check.

As shown in Fig. 4, the Raman shifts related to α-Fe_2O_3 were observed in the IR regions on all samples. This observation indicated that when the sample surface was in contact with the radiolysis products of water (OH and O radicals and H_2O_2), the corrosion potential was high enough to form hematite. The increase in potential is likely due to radiolysis products, comprised of short-lived highly oxidizing free radical species, such as OH radical and the much longer lived hydrogen peroxide molecules [12, 13]. The short-lived radiolysis products, e.g. OH radicals, cannot escape the IR region. However, the long-lived specie H_2O_2 can be carried away from the IR region into the UR region by convection flow of the heated water. However, hematite formation was not observed in the UR region where convection flow of the heated water took place. This indicated that H_2O_2 was not directly affecting the oxide species in the UR region. The UR regions showed a typical Raman spectrum of magnetite (Fe_3O_4). In primary water chemistry (PWC), the only stable iron oxide is magnetite which was observed in the UR region only. However, the Fe_3O_4 peaks at 531 and 665 cm^{-1} overlapped with $FeCr_2O_4$ peak at 535 and 678 cm^{-1} making the Raman spectra for the UR region difficult to interpret. Possible dissolution of Cr^{3+} could have occurred in the inner layer and substitution of Cr with Fe would result in an oxide that it is close to Fe_3O_4, which could be the reason for the appearance of the 665 cm^{-1} Fe_3O_4 peak.

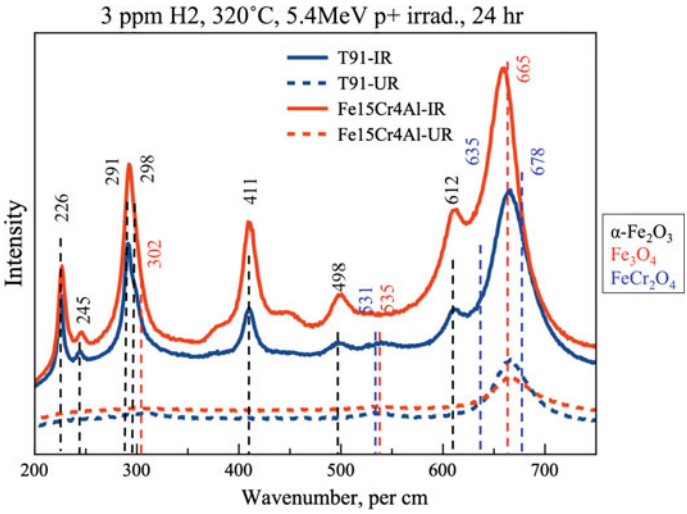

Fig. 4 Raman spectra collected from IR and UR regions on the irradiated sample T91 and Fe15Cr4Al

Microstructure Observations

TEM analysis was conducted to obtain more detailed microstructural information on the oxide layers. The HAADF images shown in Fig. 5 were collected for oxide thickness and microstructure analysis. Under HAADF imaging conditions, the oxides have a dark contrast compared to the metal substrate or platinum protective coating. Moreover, the contrast between different oxide constituents was slightly different. However, due to the complex shape of the interface, it was difficult to differentiate the inner oxide from the outer oxide, especially in the IR case of Fe15Cr4Al, where the inner oxide was thin.

T91 had the thickest oxides between the two alloys after the 24 h exposure. From the STEM image shown in Fig. 5, the IR oxide layer formed in the IR region on T91 consisted of large outer densely packed precipitates with continuous porous inner oxide. This porosity could be caused by the selective dissolution of Cr ions during corrosion. In the IR region where water radiolysis products can significantly increase the corrosion potential, resulting in the formation of hexavalent Cr ions, hence leaving the remaining oxide with a porous structure deficient of Cr. The UR region of the T91 sample has a similar oxide structure, with less porosity observed for the inner oxide, and the overall oxide thickness was much thicker compared to IR region (Table 2).

In the UR region of sample Fe15Cr4Al, the large outer precipitates were isolated, and the inner oxide was continuous and preserved the original metal surface as seen as a flat interface. In the UR case, the inner oxide was slightly

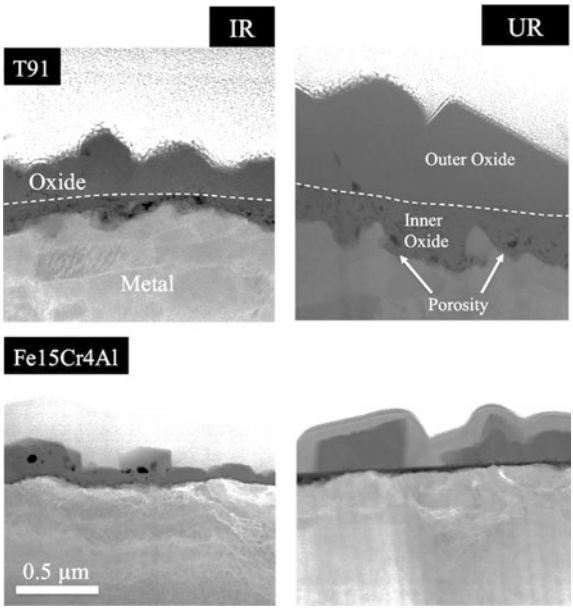

Fig. 5 HAADF-STEM images of the FIB lemella taken from T91 and Fe15Cr4Al

Table 1 The chemical composition of the alloys in this study

	Fe	Cr	Al	Mo	Y	V
T91	Bal.	9	–	1	–	0.2
Fe15Cr4Al	Bal.	15	4	–	0.12	–

Table 2 Individual inner and outer oxide layer thicknesses on T91 and Fe15Cr4Al

	Irradiated region (IR)		Unirradiated region (UR)	
	Inner oxide (nm)	Outer oxide (nm)	Inner oxide (nm)	Outer oxide (nm)
T91	118 ± 35	239 ± 30	253 ± 75	585 ± 80
Fe15Cr4Al	15 ± 8	142 ± 42	62 ± 30	86 ± 52

thicker compared to the IR region. On the Fe15Cr4Al sample, the IR region has a continuous outer oxide layer. A thin discontinuous layer of inner oxide with a darker contrast was observed underneath the precipitates at the metal/oxide interface. The oxide thickness data are listed in Table 2. The individual inner and outer layer thickness is shown in Fig. 6.

Oxide Composition Analysis

Figures 7 and 8 showed the chemical composition of the oxide from EDS line scan profiles of the oxide/metal interfaces for both IR and UR region on samples T91

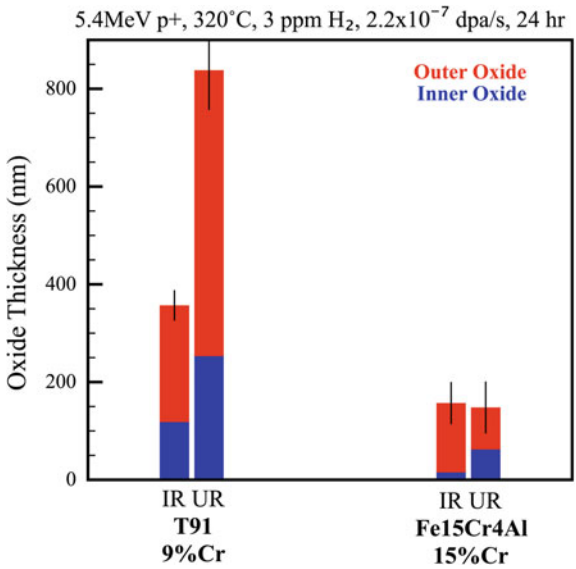

Fig. 6 The inner, outer and overall oxide thickness plot as a function of Cr content for both IR and UR regions on T91 and Fe15Cr4Al

and Fe15Cr4Al. In all IR cases, the outer oxide has a composition of ~40 at.% Fe and 60 at.% O, which indicates that the outer oxide precipitates were Fe_2O_3. Raman spectroscopy results of the IR region oxide species also suggested the present of Fe_2O_3. In Fig. 7, the composition of the inner oxide on T91 IR sample consists of ~25 at.% Fe, 15 at.% Cr and 60 at.% O, which was slightly different from the theoretical values of the $FeCr_2O_4$—spinel phase (14.3 at.% of Fe—28.5 at.% of Cr—57.2 at.% of O). The lower Cr content can be attributed to possible Cr dissolution under such irradiated conditions.

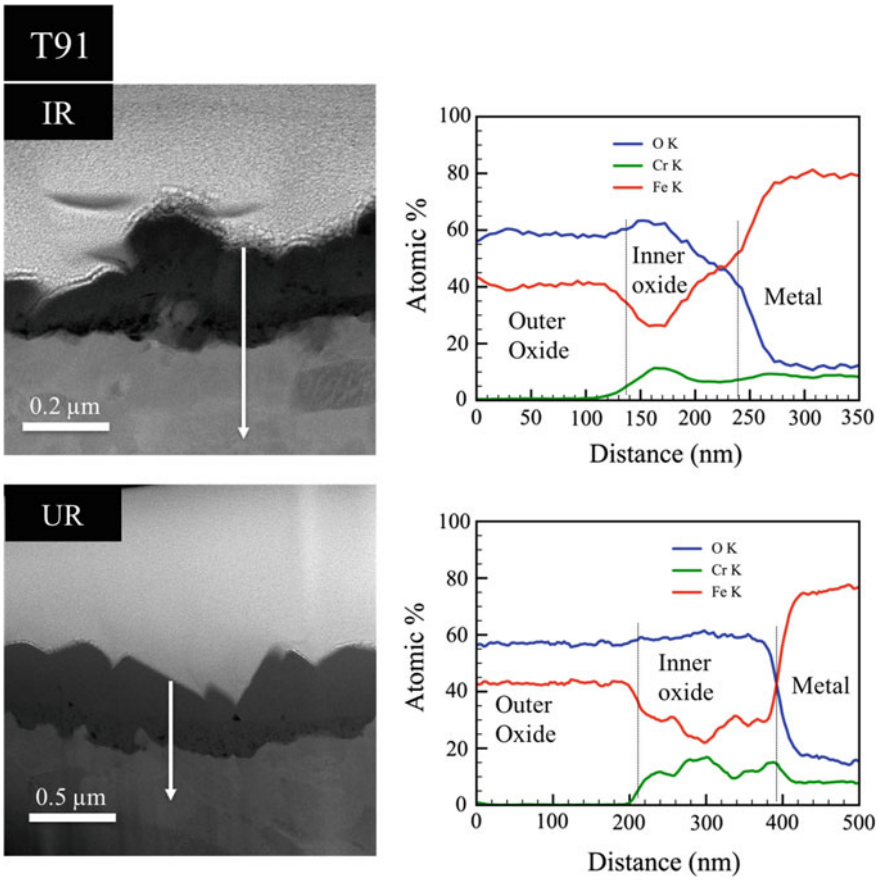

Fig. 7 EDS line scans across oxides formed at both IR and UR region on sample T91

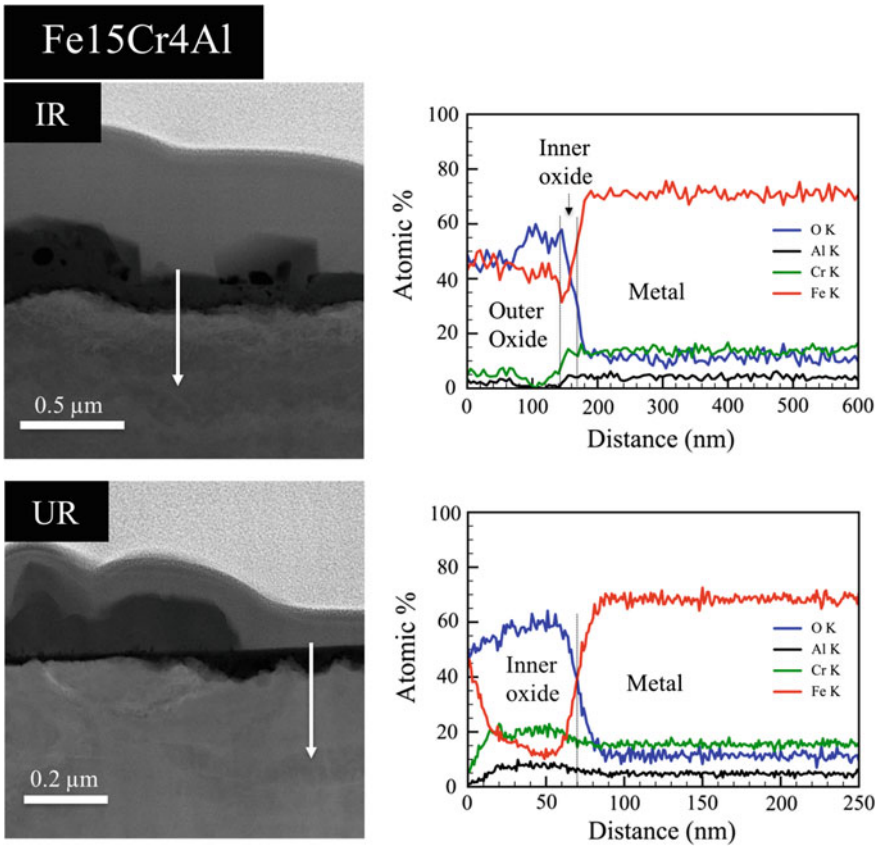

Fig. 8 EDS line scans across oxides formed at both IR and UR region on sample Fe15Cr4Al

Discussion

Corrosion Mechanism

From the oxide morphology and TEM observations, the selected alloys under study form a duplex oxide film on the surface of the steels. Under normal corrosion conditions with irradiation, this duplex film consists of a uniform Cr-rich spinel layer adjacent to the metal and magnetite crystals on top of that layer. The growth of the outer oxide was facilitated via outward diffusion of Fe ions towards the oxide/solution interface, whereas the inner oxide growth was governed via inward diffusion of the oxidizing species, e.g. oxygen ions. In primary water, the formation of magnetite (Fe_3O_4) and chromite ($FeCr_2O_4$) was predicted by Terrani et al., using a Pourbaix diagram of a Fe-10Cr system at typical PWR operating temperature (330 °C) and water pressure (15 MPa) [2]. Fe ions have faster diffusing rates than

Cr ions in the spinel lattice, diffusion coefficient of Fe is orders of magnitude higher than Cr with the same oxygen activities [14]. Although both cations enter the developing oxide scale, Fe ions tend to segregate to the outer scale regions, whereas Cr-rich regions are normally found near the oxide/metal interface. The magnetite outer oxides were precipitated from the ions released due to the selective rejection of rapidly diffusing species from the steel into the solution. In the experimental setup of this study, deionized water was continually fed into the autoclave that was subsequently filtered. Therefore, the influence of bulk water Fe-ion concentration was expected to be negligible. It is reasonable to assume that water near the solution/oxide interface was saturated with Fe ions, the magnetite particles were precipitated out from the saturated solution. Hence, the outer oxide growth was mainly supplied by the Fe rejection from the metal during inner oxide formation. This was evidenced by the porosity left in the inner oxide on T91. As the inner oxide thickens, the rate of rejection of Fe towards the surface is postulated to be proportional to the growth rate of the inner oxide, which is oxygen diffusion limited.

Oxide Dissolution

From the STEM examination of the resulting oxide layer at both IR and UR regions, there was a trend of decreasing oxide thickness as the Cr content increased from 9–15% as shown in Fig. 6. It is known, during air exposure, in temperature range 700–1000 °C, that the oxide scale composition varies with Cr concentration, and the oxidation resistance increases with increasing Cr content [15]. The observation on T91 suggests that the oxide consists of magnetite accompanied by internal oxide precipitates of $FeCr_2O_4$ spinel. At high corrosion potential, which was expected in the IR region during the in-situ irradiation-corrosion experiment, chromium dissolution in a form of releasing hexavalent $HCrO_4^-$ ions is also expected. The amount of radiolysis products at a dose rate of 400 kGy/s will result in an increase of ECP at the oxide/water interface, from −700 mV to almost +350 mV, this ECP shift was enough to oxidize Fe^{2+} ions to the more stable Fe^{3+} ions, which lead the transition of Fe_3O_4 to Fe_2O_3 [8]. This transition process started with ferrous and hydroxide interaction and formation of soluble ferrous hydroxide ions which then further oxidized into Fe^{3+} and precipitate out as hematite [16]. This inner oxide dissolution process can be evidenced by the rough inner/outer oxide interface in the IR region.

Regarding the inner oxide microstructure, the differences between T91 and Fe15Cr4Al may be influenced by their Cr content, hence the ability to form a continuous Cr-rich spinel layer. The 9% Cr content in T91 could be insufficient to form a continuous chromite spinel layer. Instead, a mixture of precipitates of $FeCr_2O_4$ and Fe_3O_4 maybe formed. However, in Fe15Cr4Al, the Cr content maybe sufficient to form a continuous $Fe(Cr, Al)_2O_4$ layer, since Cr and Al can both be trivalent ions in the spinel structure. Under irradiation, both the inner oxide layer

showed a Fe depletion and Cr enrichment near the inner/outer oxide interface. On the contrary, under normal conditions, both the inner oxide showed a Fe enrichment and Cr depletion at the inner/outer oxide interface.

Conclusion

The following conclusion can be drawn:

- The two alloys under investigation formed a Cr-rich spinel oxide (inner layer) that was covered with magnetite crystals (outer particles) in the unirradiated condition in hydrogenated water chemistry autoclave environment (3 ppm dissolved H_2). In the irradiated condition, the Cr-rich inner oxide spinel partially dissolves and coverage of outer precipitates is enhanced.
- The oxidation rate or resulting oxide thickness is dependent on the alloy Cr content; the oxidation rate increased as the Cr content decreased. Hence, the FM steel T91 has higher corrosion rate than Fe15Cr4Al under both IR and UR conditions.
- The inner oxide microstructure may be influenced by the Cr content, below a critical level of Cr content, the protective Cr-rich inner protective oxide may be partially formed and discontinuous.

Acknowledgements This research was supported by Department of Energy (DOE), Nuclear Energy University Programs (NEUP), Grant No. DE-NE0008272. The authors also acknowledge the MIBL facilities and the MIBL staff who helped with the irradiations.

References

1. R.B. Rebak, Ferritic alloys as accident tolerant fuel cladding material for light water reactors, DE-NE0000568, Final Report Phase 1A FY2013-2014, General Electric
2. K.A. Terrani et al., Uniform corrosion of FeCrAl alloys in LWR coolant environments. J. Nucl. Mat. **479**, 36–47 (2016)
3. K.A. Terrani, S.J. Zinkle, L.L. Snead, Advanced oxidation-resistant iron-based alloys for LWR fuel cladding. J. Nucl. Mat. **448**, 420–435 (2014)
4. S. Bragg-Sitton, Overview of international activities in accident tolerant fuel development for light water reactors. Presentation given at the IAEA technical working group on fuel performance and technology, Vienna, Austria, 24–25 April 2014
5. P. Ampornrat, G.S. Was, Oxidation of ferritic-martensitic alloys T91, HCM12A, and HT-9 in supercritical water. J. Nucl. Mat. **371**, 1–17 (2007)
6. R.L. Klueh, K. Ehrlich, F. Abe, Ferritic/martensitic steels: promises and problems. J. Nucl. Mate. **191–194**, 116–124 (1992)
7. R.B. Rebak, in *Advanced Steels for Accident Tolerant Fuel Cladding in Commercial Nuclear Reactors*, ed by T. Ohji, J. Matyáš, N.J. Manjooran, G. Pickrell, A. Jitianu. Advances in Materials Science for Environmental and Energy Technologies III. The American Ceramic Society, published 2014 by Wiley

8. S. Raiman, Irradiation accelerated corrosion of 316L stainless steel in simulated primary water, Ph.D. thesis, University of Michigan, 2016
9. J.F. Ziegler, The stopping and range of ions in matter (SRIM) 2013. Available from http://www.srim.org
10. ASTM E521. Standard practice for neutron radiation damage simulation by charged-particle irradiation (American Society for Testing and Materials, Philadelphia, 1996)
11. S. Raiman, A. Flick, O. Toader, P. Wang, N.A. Samad, Z. Jiao, G.S. Was, A facility for studying irradiation accelerated corrosion in high-temperature water. J. Nucl. Mater. **451** (1–3), 40 (2014)
12. S. Le Caër, Water radiolysis: influence of oxide surfaces on H22 production under ionizing radiation. Water **3**, 235–253 (2011)
13. R. Springell et al., Water corrosion of spent nuclear fuel: radiolysis driven dissolution at the UO_2 water interface. Faraday Discuss. **180**, 301–311 (2015)
14. J. Töpfer, S. Aggarwal, R. Dieckmann, Point defects and cation tracer diffusion in (CrxFe1-x) 3-δO4 spinels. Solid State Ionic **81**, 251–266 (1995)
15. L. Singheiser et al., High temperature corrosion issues for metallic materials in solid oxide fuel cells. Shreir's Corrosion **1**, 482–517 (2010). Elsevier
16. B.J. Lewis, E.N. Onder, A.A. Prudil, *Fundamentals of Nuclear Engineering* (Wiley, Hoboken, 2017)

Hydrothermal Corrosion of SiC Materials for Accident Tolerant Fuel Cladding with and Without Mitigation Coatings

Stephen S. Raiman, Caen Ang, Peter Doyle and Kurt A. Terrani

Abstract As a candidate material for accident-tolerant fuel cladding for light water reactors (LWR), SiC_f–SiC composite materials possess many attractive properties. However, prior work has shown that SiC is susceptible to aqueous dissolution in LWR coolant environments. To address this issue, candidate coatings have been developed to inhibit dissolution. For this study, CVD SiC samples were prepared with Cr, CrN, TiN, ZrN, NiCr, and Ni coatings. Uncoated SiC and SiC_f–SiC samples were also prepared. The samples were exposed for 400 h in 288 °C water with 2 wppm DO in a constantly-refreshing autoclave to simulate BWR–NWC. Cr and Ni coated samples lost less mass than the uncoated SiC sample, indicating an improvement in performance. The CrN coating resisted oxidation, but some of the coating was lost due to poor adhesion. The TiN coated sample gained significant mass due to oxidation of the coating. ZrN and NiCr coatings showed significant corrosion attack. SiC_f–SiC ceramic matrix composite materials dissolved much faster than the CVD SiC sample, demonstrating the need for mitigation coatings if CMCs are to be used in LWRs. This work demonstrates the promise of Cr, Ni and CrN coatings for corrosion mitigation in LWRs, and shows that NiCr and ZrN are not promising coating materials.

Keywords Silicon carbide · Accident-tolerant fuel · Coatings · Corrosion · BWR–NWC

S.S. Raiman (✉) · C. Ang · P. Doyle · K.A. Terrani
Oak Ridge National Laboratory, 1 Bethel Valley Drive, Oak Ridge, TN 37830, USA
e-mail: raimanss@ornl.gov

J.H. Jackson et al. (eds.), *Proceedings of the 18th International Conference on Environmental Degradation of Materials in Nuclear Power Systems – Water Reactors*, The Minerals, Metals & Materials Series, https://doi.org/10.1007/978-3-319-68454-3_22

Introduction

The development of accident tolerant fuel cladding has been a subject of great interest since the Fukushima incident in 2011. Among the cladding materials being considered to replace Zircaloy tubing, silicon carbide (SiC) has emerged as a leading candidate material [1, 2]. To overcome the brittleness of the material, ceramic matrix composite (CMC) materials have been developed in which silicon carbide is deposited onto a woven layer of silicon carbide fibers (SiC_f–SiC). Despite possessing favorable mechanical properties, high-temperature corrosion resistance [3, 4], and excellent neutronics [5], SiC_f–SiC has been found to dissolve during light water reactor (LWR) normal operating conditions [6].

To improve material compatibility, corrosion resistant coatings are being considered as a method for mitigating hydrothermal corrosion of CMC SiC during LWR normal operating conditions. Several studies have already examined corrosion mitigation coatings on Zircaloy [7–9]. Cr, CrN, and TiN were found to have favorable compatibility in LWR water when compared to uncoated Zircaloy.

The objective of this work is to test several candidate coatings for use on SiC cladding. Cr, CrN, and TiN coatings, which performed well as coatings on Zircaloy, were chosen for this work. Additionally, samples with Ni and NiCr coatings were tested for comparison. Additionally, ZrN was chosen as a coating to study the effect of oxidation on the adherence of the coating. The results of experiments in which coated SiC specimens are exposed to 288 °C water with 2 wppm dissolved oxygen (DO) to simulate boiling water reactor normal water chemistry (BWR–NWC) are reported, to show the effectiveness of the candidate coatings. BWR–NWC was chosen as an initial test due to its aggressiveness when compared to hydrogen water chemistry (HWC). Future work will present more in-depth characterization of the samples shown in this work, along with the results of the same materials exposed to BWR–HWC and pressurized water reactor (PWR) primary water.

Experiment

Samples Prepared

For this work, coated and uncoated samples were exposed to BWR–NWC conditions (288 °C, 3 wppm DO) for up to 400 h. Coated coupons were prepared by applying candidate coatings to high purity, stoichiometric CVD SiC from Rohm and Haas (now Dow Chemical Company, PA). Coatings were applied by two methods. The first method was cathodic arc physical vapor deposition (PVD), in which the coating was deposited by an industrial vendor which used cathodic arc evaporation of metallic targets. The second was an electrochemical method in which a thin electroless Ni coating was applied to SiC substrates. In the case of the NiCr sample, the Ni coating was only a very thin compatibility layer, on which a

conventional electroplated coating of Ni-3% Cr was applied. CVD SiC was chosen as a substrate for these preliminary tests due to the difficulty of obtaining SiC_f–SiC. It is expected that in later works, SiC_f–SiC will be used as a substrate for the coating candidates which perform best. One uncoated CVD SiC sample was also exposed for comparison. The coupons measured 25 × 6 × 1 mm with a 2 mm hole, from which the coupons were hung.

Also tested were two SiC_f–SiC matrix-composite coupons. One was a previous generation of composite using Hi-Nicalon Type-S 0.5 K SiC fiber (CMC-N). The other was a contemporary composite using Tyranno SA-3 fiber (CMC-T). Both composites used a proprietary CVI/D SiC from Hypertherm (now Rolls-Royce, Ltd) for both matrix and overcoat. The major difference between the two composites was the lower density of the older generation of composites.

Table 1 shows the processing, process temperature, deposit thickness, compatibility coat and top coats by phase composition in the coatings. The phase composition of the specimens was characterized by X-ray diffraction (XRD). The sample was rotated at 10 rpm with a 2θ scan range from 10° to 130° under Cu Kα radiation using a Bruker D2 Phaser X-ray diffractometer (30 kV, 30 mA) equipped with a LynxEye detector. The data was analyzed by PANalytical HighScorePlus for phase identification using Powder Diffraction File (PDF) database and profile fitting conducted by Rietveld analysis. Instrumental broadening was calculated by a NIST 660 LaB6 and the samples were spiked with a NIST 640d Si standard.

Experimental Procedure

Exposures were conducted using a controlled chemistry water loop at the Hydrothermal Corrosion Laboratory (HCL) at Oak Ridge National Laboratory. A schematic of the water loop is shown in Fig. 1. Samples were hung from zirconia

Table 1 Details of the samples used for this work, including coated samples of SiC substrates, uncoated SiC_f–SiC samples, and solid samples for purposes of comparison

Sample ID	Substrate	Coating	Process	Coating thickness (μm)	Phases
SiC	SiC	none	CVD	–	99.9% SiC
CMC-N	SiC_f	SiC	CVI/D	–	>99% SiC
CMC-T	SiC_f	SiC	CVI/D	–	99.9% SiC
Solid Cr	Cr	none	Cast	–	Not measured
Solid TiN	TiN	none	Hot pressed	–	TiN
Ni–SiC	CVD SiC	Ni	Electrochemical	30	Ni
NiCr–SiC	CVD SiC	NiCr	Electrochemical	40	Ni, Ni-3%Cr
Cr–SiC	CVD SiC	Cr	PVD	20	Cr
CrN–SiC	CVD SiC	CrN	PVD	30	$CrN_{(1-x)}$/Cr
TiN–SiC	CVD SiC	TiN	PVD	5	$TiN_{(1-x)}$/Ti
ZrN–SiC	CVD SiC	ZrN	PVD	5	$ZrN_{(1-x)}$/Zr

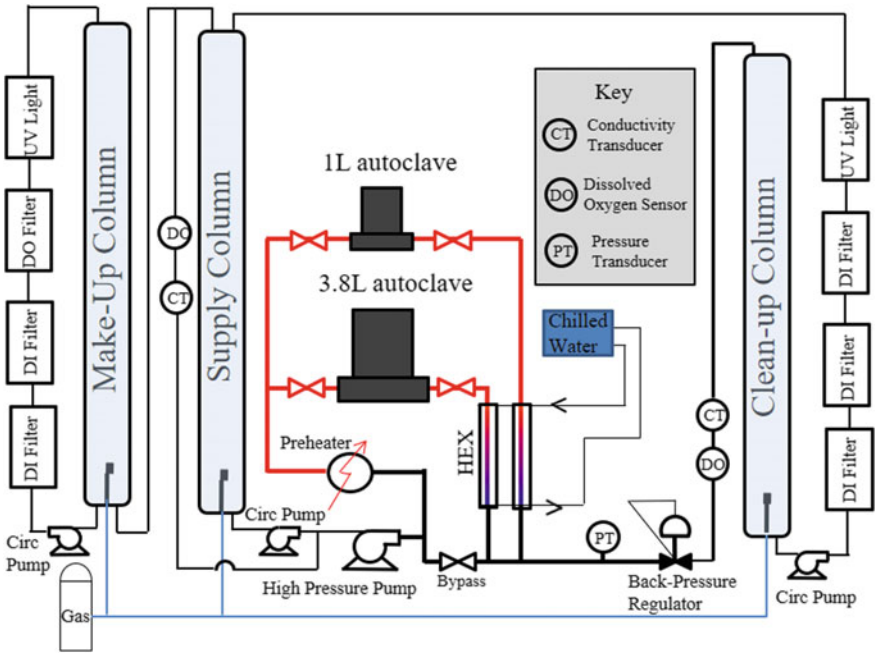

Fig. 1 Schematic drawing of the controlled chemistry water loop at the hydrothermal corrosion laboratory at ORNL

rods in the 3.8 L Hastelloy 276 autoclave. A gas blend of 95% argon and 5% oxygen was bubbled through the main column to maintain a dissolved oxygen (DO) concentration of ~2 wppm. Water from the column was fed to a Pulsafeeder high-pressure pump which maintained a pressure of 1900 psi. Water was heated by a pre-heater and a heating band over ~3–4 h to 288 °C and maintained for 200 h before cooling to room temperature. Water flowing from the autoclave was chilled and depressurized before flowing into a clean-up column where it was collected, and then run through a series of DI filters and a UV light before recirculating into the supply column.

Samples we exposed for 2 cycles of 200 h. They were characterized using light microscopy and scanning electron microscopy (SEM), and were weighed to determine mass change.

Results

To measure mass change, samples were weighed before exposure, after 200 h, and after 400 h, and the results are shown in Fig. 2.

Both the solid TiN coupon and the TiN-coated coupon gained mass during the exposures, suggesting the growth of an adherent oxide film.

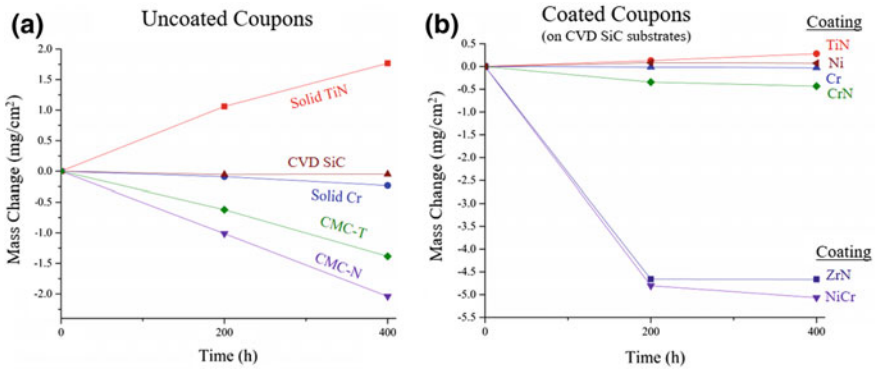

Fig. 2 Mass change of **a** coated and **b** uncoated coupons. Values are graphed as the change in mass relative to the coupon mass before exposure

The SiC_f–SiC coupons both lost significant mass at a linear rate, while the uncoated CVD SiC sample lost a small amount of mass. Terrani et al. [6] reported a similar mass loss for a CVD-SiC sample exposed to NWC, but reported a mass *gain* for a sample of Tyranno SiC_f–SiC during the first month of exposure, which disagrees with the mass loss observed after 400 h in this work. The reason for this discrepancy is not clear

The solid Cr coupon and the Cr-coated coupon both lost mass at a relatively slow, and relatively linear rate. The solid Cr coupon was cut from a drop-cast with large visible pores, and it is hypothesized that this porosity accounts for the higher rate of mass loss seen in the solid Cr coupon (0.23 mg/cm^2 after 400 h) compared to the mass loss of the Cr coated coupon (0.026 mg/cm^2 after 400 h). The CrN coated sample lost mass at a higher rate during the first 200 h exposure, and the rate of mass loss slowed during the second exposure. The partial spallation visible on the CrN coated coupon (Fig. 3) is the likely reason for the higher rate of initial mass loss, and the slower rate of mass loss after 200 h suggests that CrN may still be a viable mitigation coating. Future characterization of the coating will aid in this determination. The Ni coated sample gained a slight amount of weight during exposure, likely due to oxidation of the Ni coating to form NiO, which will be determined with future work. NiCr and ZrN coated samples lost mass rapidly during the first 200 h exposure, but the rate of mass loss slowed or stopped during the second exposure.

Light micrographs of the coated coupons before exposure, after 200 h of exposure, and after 400 h of exposure are shown in Fig. 3. Significant spallation of the CrN and NiCr coatings is visible in the images, and it appears the majority was lost during the first 200 h exposure. Aside from the spalled areas, the CrN coating shows little sign of corrosive attack where the coating remained adherent. The Cr coated coupon shows little sign of corrosion or spallation. The TiN and ZrN coupons show significant signs of corrosive attack. This is most easily seen by observing the difference in surface color and finish between the center regions of

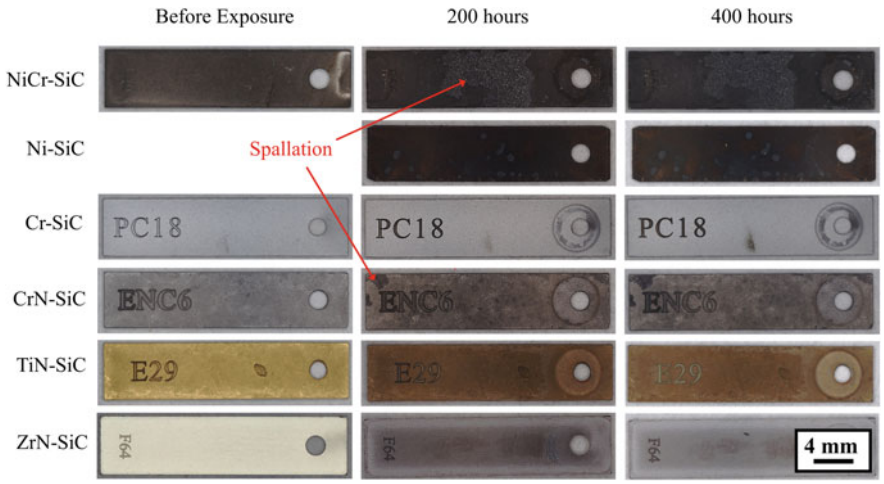

Fig. 3 Light micrographs of coated coupons imaged before exposure, after 200 h, and after 400 h of exposure. Six different coupons are shown, each with a different coating applied to a SiC substrate. The Ni coated sample was not imaged prior to exposure

the coupons and the edges. Further characterization is planned for the future to better understand the nature of the corrosive attack.

The ZrN coupon's rapid weight loss appears to be the result of this attack, as no spallation is visible on the sample. The rapid weight loss of the NiCr coupon during the initial 200 h exposure, however, was likely due to large area from which the coating spalled, shown in Fig. 3. The sample continued to lose mass during the second exposure, suggesting the coating is not a good candidate, even if it were to adhere to the substrate. The ZrN coupon did not lose mass during the second exposure, after a rapid mass loss during the first exposure. The images in Fig. 3 do not show any spallation, so it is likely that the initial weight loss is due to corrosive attack, and the lack of weight change during the second exposure is possibly due to the growth of an adherent film concurrent with corrosive dissolution. Due to the rapid corrosive attack, ZrN is not a good candidate as a mitigation coating.

Light micrographs of the uncoated SiC, SiC_f–SiC, and solid coupons before exposure, after 200 h of exposure, and after 400 h of exposure are shown in Fig. 4. Some signs of attack are visible on the SiC_f–SiC samples, but very little change is visible on the uncoated SiC sample. The solid Cr and TiN samples show some signs of a surface oxide. The irregular shape of the TiN coupon is due to difficulty machining the material.

SEM–EDS images of the Ni-3Cr coated sample are shown in Fig. 5. The Si signal indicates areas where the coating spalled, and the SiC substrate is visible. The coating has oxidized, as shown by the oxygen signal on the areas where the NiCr coating remains.

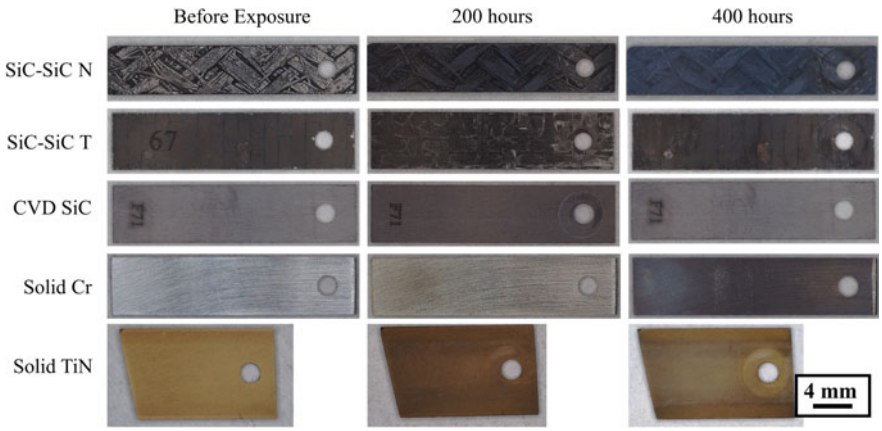

Fig. 4 Light micrographs of uncoated SiC, SiC_f–SiC, and solid coupons before exposure, after 200 h, and after 400 h of exposure

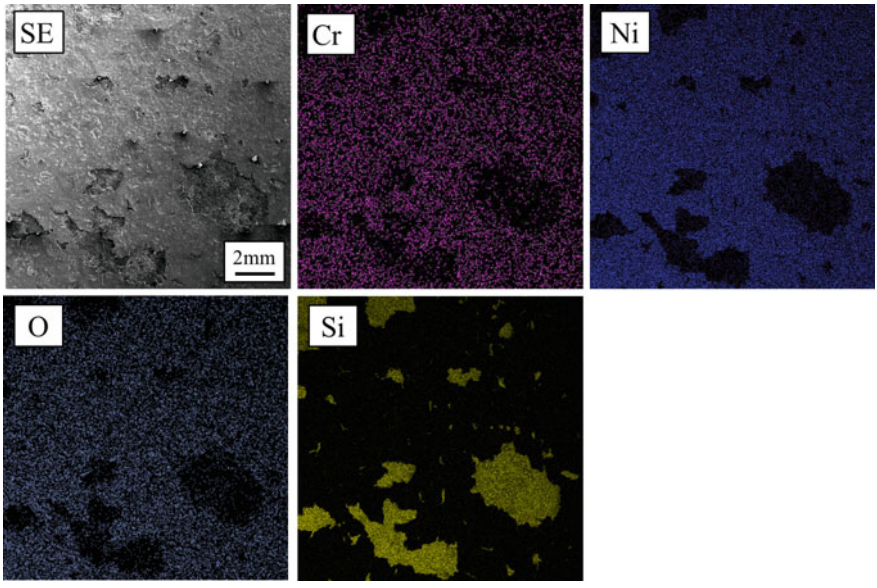

Fig. 5 SEM–EDS images of the NiCr coated sample

SEM–EDS images of the CrN coated sample are shown in Fig. 6. As with the NiCr sample, the area on which spallation occurred is visible by the strong Si signal. The much weaker oxygen signal indicates that the CrN coating did not oxidize as much as the NiCr coating.

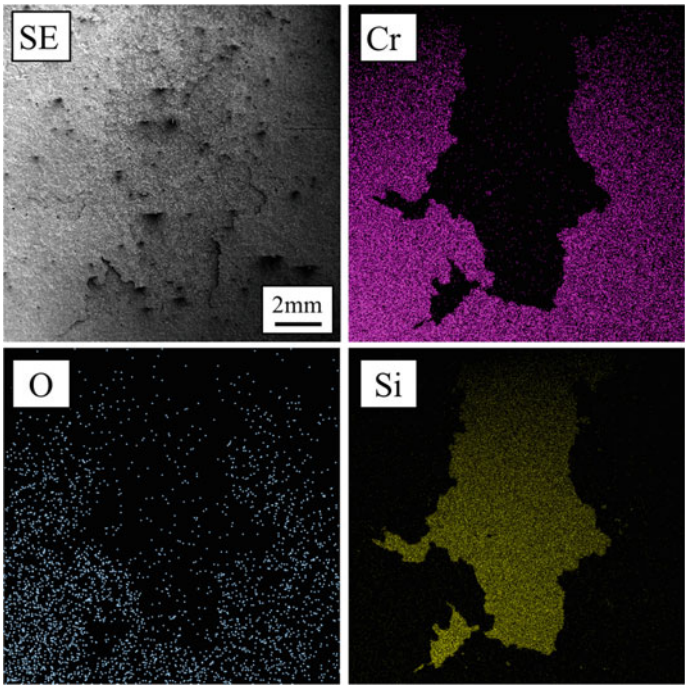

Fig. 6 SEM–EDS images of the CrN coated sample

Conclusions

After 400 h of autoclave exposure, the Ni and Cr coatings exhibited the least amount of mass change. The CrN coupon lost more mass than the Cr coupon, but examination of the coupons showed little oxidation, so it appears that the coating may perform acceptably, and the mass loss can be attributed to poor adhesion of the coating to the substrate. The TiN coated coupon gained significant mass, consistent with the even greater mass gain shown by the solid TiN coupon, both attributable to oxidation of the coating material. The ZrN and NiCr coated coupons lost the most mass, and showed significant signs of corrosive attack. The preliminary results shown in this work will be supplemented with additional characterization in the future to better determine the nature of corrosive attack and coating adherence. Based on the results shown in the present work, Ni, Cr, and CrN show the most promise for future study as a coating material on SiC_f–SiC ceramic matrix composite cladding.

Acknowledgements The authors acknowledge the valuable assistance of Adam Willoughby and Tracie Lowe. This research was funded by U.S. Department of Energy's Office of Nuclear Energy, Advanced Fuel Campaign.

References

1. D.M. Carpenter, *An Assessment of Silicon Carbide as a Cladding Material for Light Water Reactors*, PhD Thesis, MIT (2010)
2. S.J. Zinkle, K.A. Terrani, J.C. Gehin, L.J. Ott, L.L. Snead, Accident tolerant fuels for LWRs: a perspective. J. Nucl. Mater. **448**(1), 374–379 (2014)
3. K.A. Terrani, B.A. Pint, C.M. Parish, C.M. Silva, L.L. Snead, Y. Katoh, Silicon Carbide Oxidation in steam up to 2 MPa. J. Am. Ceram. Soc. **97**(8), 2331–2352 (2014)
4. T. Cheng, J.R. Keiser, M.P. Brady, K.A. Terrani, B.A. Pint, Oxidation of fuel cladding candidate materials in steam environments at high temperature and pressure. J. Nucl. Mater. **427**, 396–400 (2012)
5. L.J. Ott, K.R. Robb, D. Wang, Preliminary assessment of accident-tolerant fuels on LWR performance during normal operation and under DB and BDB accident conditions. J. Nucl. Mater. **448**(1), 520–533 (2014)
6. K.A. Terrani, Y. Yang, Y.-J. Kim, R. Rebak, H.M. Meyer, T.J. Gerczak, Hydrothermal corrosion of SiC in LWR coolant environments in the absence of irradiation. J. Nucl. Mater. **465**, 488–498 (2015)
7. I. Younker, M. Fratoni, Neutronic evaluation of coating and cladding materials for accident tolerant fuels. Prog. Nucl. Energy **88**, 10–18 (2016)
8. J.-H. Park, H.-G. Kim, J. Park, Y.-I. Jung, D.-J. Park, Y.-H. Koo, High temperature steam-oxidation behavior of arc ion plated Cr coatings for accident tolerant fuel claddings. Surf. Coatings Technol. **280**, 256–259 (2015)
9. E. Alat, A.T. Motta, R.J. Comstock, J.M. Partezana, D.E. Wolfe, Multilayer (TiN, TiAlN) ceramic coatings for nuclear fuel cladding. J. Nucl. Mater. **478**, 236–244 (2016)

Characterization of the Hydrothermal Corrosion Behavior of Ceramics for Accident Tolerant Fuel Cladding

Peter J. Doyle, Stephen S. Raiman, R. Rebak and Kurt A. Terrani

Abstract Accident-tolerant fuel (ATF) is an increasingly important research topic for the nuclear industry, and ceramics such as SiC are strong contenders for deployment as ATF cladding. The hydrothermal corrosion characteristics of SiC and Al_2O_3 were investigated via constantly-refreshing autoclave corrosion and post exposure characterization. Four different types of chemical vapor deposited (CVD) SiC specimens were examined (two with high electrical resistance, one with low electrical resistance, and a single crystal 4H structural variant). Al_2O_3 specimens were prepared in single crystal and polycrystalline states. PWR primary water, BWR–HWC, and BWR–NWC environments were maintained throughout the experiments. Characterization conducted using SEM and EDS was used to determine factors affecting corrosion rates and susceptibility to grain boundary attack in each water chemistry condition. Raman spectroscopy was also used to determine chemical variation of the surface with corrosion. Grain boundary attack was found to be significant for both alumina and SiC polycrystalline variants.

Keywords Accident-tolerant fuel · ATF · SiC · Al_2O_3 · Hydrothermal corrosion

P.J. Doyle (✉) · S.S. Raiman · K.A. Terrani
Oak Ridge National Laboratory, Oak Ridge, TN 37831, USA
e-mail: pdoyle3@vols.utk.edu

R. Rebak
GE Global Research Center, Schenectady, NY 12309, USA

J.H. Jackson et al. (eds.), *Proceedings of the 18th International Conference on Environmental Degradation of Materials in Nuclear Power Systems – Water Reactors*, The Minerals, Metals & Materials Series, https://doi.org/10.1007/978-3-319-68454-3_23

Background

The use of SiC [1] in the nuclear industry has been driven by factors including possible uses in fusion power plants, Generation IV reactor concepts, and, for light water reactors (LWRs), the limitations of zirconium-based fuel claddings. While zirconium-based alloys have been used as fuel cladding for LWRs since the beginning of nuclear power, there is substantial concern over its continued use [2, 3]. Reasons for this include the desire to go to higher fuel burnups and the safety issues raised by the 2011 Fukushima-Daiichi nuclear plant accident where Zircaloy oxidation led to a buildup of hydrogen gas and an explosion. While many cladding alternatives have been explored for such accident-tolerant fuels (ATF), SiC's radiation resistance and physical properties and lack of runaway oxidation under LOCA makes it one of the most attractive clad alternatives [4, 5].

However, under normal operating conditions there is some indication that SiC corrodes at a significant, possibly unacceptable rate, especially under irradiation conditions [6, 7]. There has also been some indication that grain boundary attack is an important cause of the high corrosion rate [8–10]. Moreover, it has been established that reasonable corrosion rates can be determined from the reactions of SiC with O_2 or H_2O [7, 10]. In the reaction with water, SiO_2 is formed as an intermediate step with accompanying CH_4, CO, and CO_2 (see Section "SiC Corrosion Characteristics"). At low temperatures this forms a mildly protective film through which water or O_2 must pass to cause corrosion. However, at high temperatures in either steam or liquid water, this film is stripped away quickly re-exposing the substrate [7, 9]. Thus mass loss is reaction-limited and should have a simple linear relationship with time. If extensive grain boundary attack exists, grain fallout will lead to a super-linear (faster than linear) kinetics. The goal of this study was to evaluate how changes in the physical properties of SiC affects its corrosion characteristics, while also examining Al_2O_3 as a common, typically stable reference material in followup to [7]. To this end, four different variants of CVD SiC, fused SiO_2, single crystal Si, and two variants of Al_2O_3 were exposed to PWR, BWR–NWC, and BWR–HWC conditions for up to 3 months, and the resulting microstructures were characterized.

Experimental

SiC variants consisted of high resistance (HR) and low resistance (LR) SiC from Coorstek (Oak Ridge, TN), a high resistance equivalent (HHT) from Rohm and Haas (Deer Park, TX), and 4H single crystal from University Wafer (South Boston, MA). The HR variant is high purity SiC, while LR is achieved by addition of nitrogen.Fused SiO_2 and single crystal Si were both from University Wafer. Alumina variants, single and polycrystalline, were from University Wafer and Coorstek, respectively. Samples were cut into 20 mm $\times$ 5 mm rectangular coupons and tested in the as-received surface condition.

Table 1 Specific water chemistry conditions for PWR, BWR–NWC, BWR–HWC simulation tests

Condition designation	Gas conc. (ppm)	Temperature (°C)	pH	Pressure (MPa)
PWR	3.57 H_2	330	5.8	15
BWR–HWC	0.3 H_2	290	5.6	7.5
BWR–NWC	1.0 O_2	290	5.6	7.5

Coupons were exposed in a 3.8 L type 316 stainless steel autoclave with constantly-refreshing water at GE Global Research Center (Schenectady, NY). Water chemistries simulated PWR, BWR–HWC, and BWR–NWC conditions, see Table 1. No boric acid or lithium hydroxide were added to the PWR system. One sample was used per exposure condition, per sample type. Samples were exposed for three months, and were removed at the end of each month to measure mass loss. Mass loss on each sample was reported as the average of three measurements. Each measurement had an accuracy of 0.001 mg with an average precision of 0.02 mg.

Samples were ultrasonically cleaned after exposure for 5 min in acetone, 5 min in methanol, and 3 min in ethanol followed by examination using a Hitachi S4800 FEG-type microscope at Oak Ridge National Laboratory (ORNL). Energy dispersive spectroscopy (EDS) was performed on the S4800 microscope at 20.0 kV with EDAX's TSL OIM Analysis 7 software. A LabRAM HR Evolution Raman Spectrometer by Horiba Scientific was used to obtain Raman spectra of the samples. Spectra were taken from all samples and from their un-corroded references. All spectra were taken using a 532 nm laser.

Results and Discussion

All SiO_2 samples dissolved completely within the first month and only one Si sample survived the first month. The remaining sample, which was exposed to BWR–NWC conditions had lost 33% of its initial weight. It completely dissolved in the second month. The obvious rapidity of the corrosion of Si and SiO_2 confirms previous results [7] and together with the chemical equations in Section "SiC Corrosion Characteristics" suggests SiC reactions with water is the rate-limiting step in its corrosion. If SiO_2 dissolved at a similar rate to SiC, then the rate limiting step would be the dissolution of SiO_2 after the SiC reacts with water. The corrosion properties of Al_2O_3 and SiC are discussed in separate sections below.

Alumina Corrosion Characteristics

Weight measurements are shown in Fig. 1 and indicate that single crystal dissolution is slower than for the polycrystalline materials. This suggests a pronounced

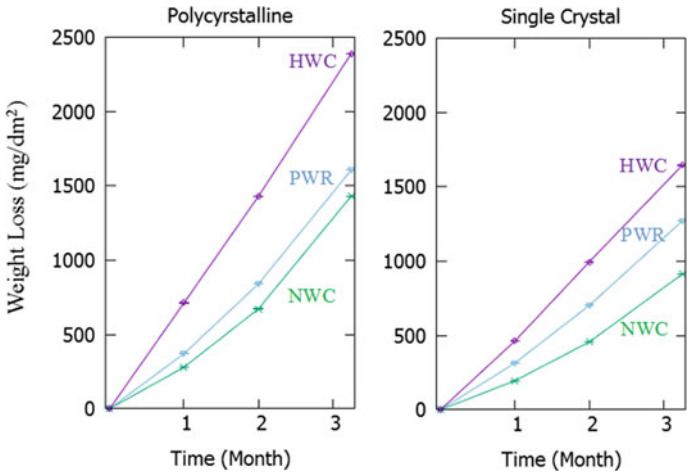

Fig. 1 Alumina mass loss data for both **a** polycrystalline and **b** single crystalline microstructures over 3 months in PWR, BWR–HWC, and BWR–NWC chemistry conditions. The chemistry conditions are labeled on the graphs

effect of grain boundaries on the dissolution. Figure 1a shows polycrystalline Al_2O_3 corrodes at rates such that BWR–HWC > PWR > BWR–NWC conditions. Figure 1b shows the single crystalline variety corroding with the same trend, but at noticeably lower rates than Fig. 1a. This behavior can be explained by some of the surface features in Figs. 2 and 3.

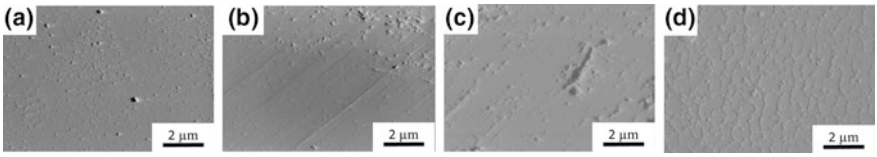

Fig. 2 SEM-SE (secondary electron) photographs of single crystal alumina. **a** is a reference sample that was un-corroded and after exposre for 3 months in **b** PWR, **c** BWR–HWC, and **d** BWR–NWC

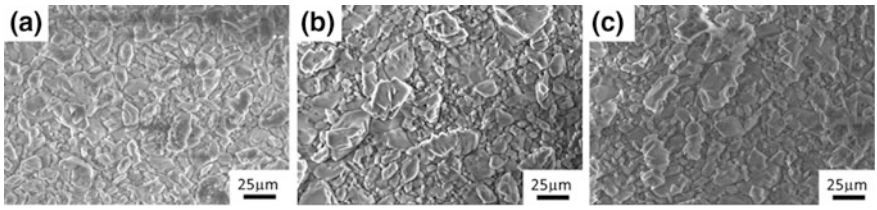

Fig. 3 SEM–SE images of polycrystalline alumina corroded under **a** BWR–HWC **b** PWR **c** BWR–NWC at low (× 1.00 k) magnification

Figure 2 compares SEM micrographs for single crystal samples from each condition. The images are indistinguishable with no indication of localized corrosion. Any deviations from uniform corrosion would be caused by localized chemistry, which typically is exacerbated by rough surfaces, crevices, etc., none of which are apparent in these images.

Figure 3 shows low magnification images of polycrystalline alumina exposed to each of the three water chemistries. These are also indistinguishable and each sample shows clearly protruding regions of alumina that appear to be individual grains. It is suggested that uniform corrosion of grain surfaces is combined with selective attack of grain boundaries leading to grain fallout. The observation that polycrystalline samples corroded significantly faster than the single crystal samples agrees with this hypothesis. Whether this additional material loss leads to super-linear behavior requires more data points to quantify.

Figure 4 shows Raman spectra of the same samples with corresponding peak identifications. Several Al_2O_3 (corundum) peaks were present in the polycrystalline case, Fig. 4a, but were not seen in the single crystal spectrum, Fig. 4b. Fundamental αAl_2O_3 peaks from the single crystal case are at 417, 450, 576, and 750 cm^{-1}. These images are in agreement with previously observed corundum spectra [11]. The polycrystalline spectra add in additional αAl_2O_3 peaks at 645 and 378 cm^{-1}. These peaks are also seen in reference [10] and seem to be unique to the polycrystalline case. This may be caused by grain boundary stresses altering the chemical environment of the Al_2O_3 in the vicinity of those boundaries.

The additional peaks are only present in the NWC-exposed sample and represent diaspore, AlO(OH), having peaks at 287, 330, 447, 498, 792 cm^{-1} (see [12, 13] for comparison of aluminum oxide/hydroxide mineral spectra). No choice of locations on the sample showed diaspore peaks in HWC or PWR samples and different locations on NWC samples gave varying spectra. Some results showed only corundum peaks, while others showed almost only diaspore peaks, with the rest having mixtures of the two. The presented spectrum for the NWC polycrystalline case is representative of a mixed-species spectrum. Because both species exist in

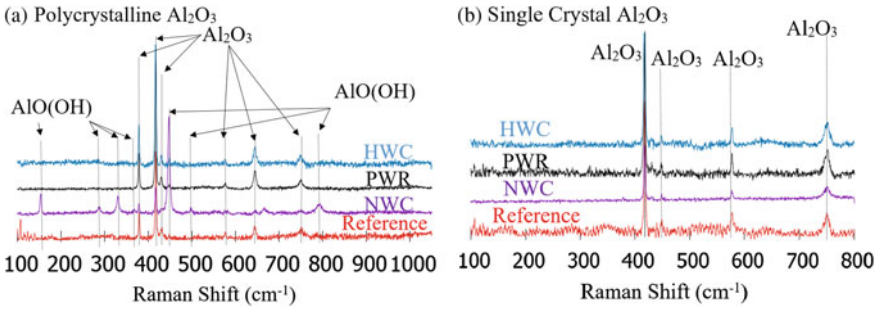

Fig. 4 Raman spectra of Alumina in reference and corroded states. The first graph compares each corroded specimen to the reference for the polycrystalline crystal case. The second graph gives the same comparison for the single crystal case. Peak designations for Diaspore (AlO(OH)) and Corundum (Al_2O_3) can be found in [11, 12]

various amounts there is either some mineral-to-mineral transformation under these conditions, or some dissolving Al_2O_3 subsequently redeposits as AlO(OH). Of these the latter is the most likely since AlO(OH) has been shown to have a significantly lower equilibrium constant for dissolution than Al_2O_3 and AlO(OH) typically transforms into Al_2O_3 slowly over time, rather than the reverse due to significant differences in the Gibb's free energy of formation [14, 15]. However, this makes the deposition of AlO(OH) surprising due to its greater thermodynamic instability. It may be that the flowrate of water through the system may be slow enough that sufficient Al^{3+} builds up to precipitate out AlO(OH), whereas not enough builds up to deposit Al_2O_3. This may account, in part, for the low corrosion rate of the NWC condition, and possibly PWR, relative to the HWC condition. However, this explanation would lead to the expectation of AlO(OH) on the single crystal specimens as well, which was not observed. This implies that there is faster loss of Al_2O_3 in the NWC specimen than PWR and HWC, but less overall mass loss due to diaspore buildup, possibly in sample crevices.

As a rough kinetics analysis, Al_2O_3 was assumed to dissolve by the following equation and rate constant, neglecting re-deposition. For this simplistic analysis, linear kinetics were also assumed, despite the above discussion.

$$Al_2O_3 + 2H_2O \rightarrow 2AlO_2^- + 4H^+; \quad \frac{d(Al_2O_3)}{dt} = Ka_{Al_2O_3}a_{H_2O}^2 \tag{1}$$

While there are many other possible equations of dissolution, this was assumed to be dominant due to the relative abundance of water compared to its self-ions. Assuming unit activities of water and the alumina specimen, the rate is simply equal to rate constant, K with units of mg/dm^2-s. For polycrystalline specimens, $K_{NWC,P} = 1.5 \times 10^{-4}, K_{HWC,P} = 2.8 \times 10^{-4}, K_{PWR,P} = 1.8 \times 10^{-4}$. For the single crystalline specimens,$K_{NWC,S} = 1.0 \times 10^{-4}, K_{HWC,S} = 2.0 \times 10^{-4}, K_{PWR,S} = 1.5 \times 10^{-4}$.

SiC Corrosion Characteristics

Figure 5a–c shows the mass losses for NWC, PWR, and HWC, respectively. In the following comparisons, it should be noted that the mass-loss-per-area numbers reported were obtained for extremely low true mass losses (on the order of hundredths to tenths of a mg for most samples and up to a few mg for the most corroded (LR, NWC) sample). Coupled with the fact that only one sample was used for each condition, these trends should be seen as approximate trends rather than exact kinetic representations. Generally, losses are such that NWC > PWR > HWC. Except for the LR sample exposed to NWC, there is little difference among specimen types.

Under NWC conditions, the LR material corroded in a clearly super-linear fashion ($w(t) \approx 21t^{1.34}, R^2 = 0.91$). In the HWC condition, the rate was significantly smaller

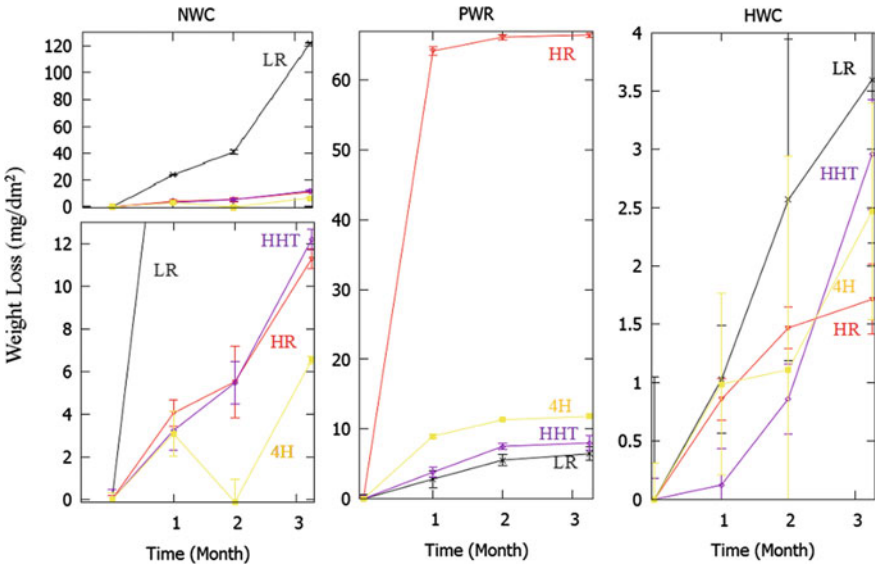

Fig. 5 Mass loss data for all four SiC variants over time in NWC, PWR, and HWC conditions, respectively, moving from left to right. The lower graph under "NWC" expands the upper graph to show the other three variant trends. Note that each graph has a different scale as labeled above

$(w(t) \approx 1.2t, R^2 = 0.92)$. In both conditions, the LR variant had the highest rate, although there was little significance in the differences seen among the different variants for the HWC condition, which corrode similarly with high measurement error due to the low mass change. It is significant that the HR and HHT specimens had virtually identical kinetics and also appeared to be super-linear for NWC-exposed specimens $(w(t) \approx 3t^{1.1}, R^2 = 0.95)$, while being closer to linear or parabolic for the HWC-exposed specimens with dramatically less mass loss. In fact, the coupon mass loss for these samples was on the order of 0.01 mg. Noting that both of these materials are high resistance variants (one from Coorstek (HR), and one from Rohm and Haas (HHT)), they should corrode similarly. Comparison of the trends in the 4H-SiC samples from these cases is not very useful because of the apparent measurement error in the LR case at 2 months. Considering error in the measurement, the 4H samples appear to corrode at essentially the same rates in each condition.

In primary water, all variants corrode parabolically. The HR variant had the largest total mass loss, but after the large mass loss following 1 month, it corroded at a similar rate to the others. Since none of the materials were polished prior to exposure, it is possible that the initial, rapid loss of material may simply be the removal of the deformed region on the surface of the material due to machining, followed by essentially steady corrosion afterwards. This also would account for the observation that the 4H single crystal variant appears to corrode slightly faster than either the LR or HHT, whereas under oxygenated conditions, some have observed that grain fallout is prevalent on the surface of 3C-SiC (cubic SiC) [7, 8], implying that the polycrystalline variants should corrode more quickly.

Except for the LR variant, primary water appears to corrode SiC at about half the rate of the NWC condition. Both of these are more corrosive than the HWC condition by 2–6 times (again, except for the LR case in the NWC condition). The largest difference is that the PWR chemistry seems to have parabolic growth, while the NWC condition trends toward super-linearity, and the HWC condition is indeterminate. The similarity of corrosion rates is possibly due to the competing effects of oxygen (NWC), and higher temperature (PWR), both of which accelerate corrosion of SiC [7, 10].

In Fig. 6, the LR variant is compared across the three chemistries to the starting morphology. In Figs. 6d and 6h significant grain-fallout was observed for NWC-exposed samples where several grain surfaces appear to be corroding uniformly, while large valleys are created between them, presumably by grain removal. The PWR micrographs show significant roughening and possible grain fallout, but not on the order of the NWC-exposed sample. The HWC-exposed sample does not seem to have any substantial grain removal, but does show some roughening. Figure 7 shows a boring, yet expected, result from the 4H samples, where there is no distinction between the various corrosion conditions, or even from the reference, indicating that mass loss is uniform, except, perhaps, at the corners of the sample The HR variant, Fig. 8, shows a greater discrepancy where the reference is most

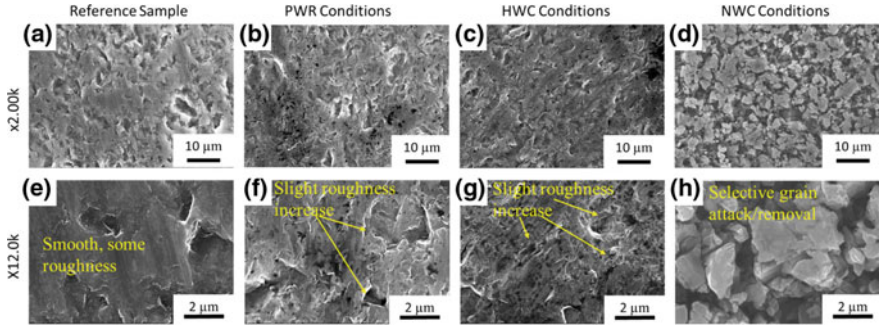

Fig. 6 SEM micrographs of samples belonging to the SiC-LR variant at × 2.00 k magnification, **a–d**, and × 12.0 k magnification, **e–h**. Samples **a** and **e**, **b** and **f**, **c** and **g**, and **d** and **h** correspond to the reference sample, and the samples exposed to PWR, HWC, and NWC conditions, respectively. The labels on each row/column reflect this designation

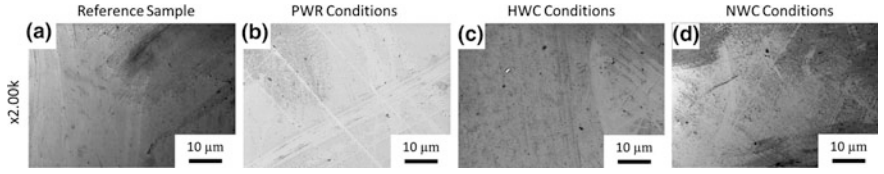

Fig. 7 SEM-SE micrographs of samples belonging to the SiC-4H variant at × 2.00 k magnification, **a–d**. **a** is the reference sample with **b**, **c**, and **d** corresponding to PWR, HWC, and NWC exposed samples. The labels on each row/column reflect this designation

similar to the samples from the HWC condition while the PWR-exposed specimen reveals mostly uniform corrosion but suggests limited grain removal. The NWC condition shows the most extensive grain attack/removal. Figure 9 provides the best evidence for grain boundary attack, showing regions where grain boundaries are clearly selectively attacked. Significantly, regions of this sort were not found in samples from the PWR or HWC conditions, indicating that grain attack is less prominent or not existent.

Raman spectra for each of the variants across all chemistries were compared to their references in Fig. 10. The only conclusion from this figure is that only SiC is found on the surface of the samples, indicating immediate dissolution of SiO_2 when it forms. In Fig. 10d for the NWC case, the unmarked peaks do not align with any Si, SiO_2, or SiC peaks and thus are likely to be from metal oxide contaminants that deposited on the surface of the specimen.

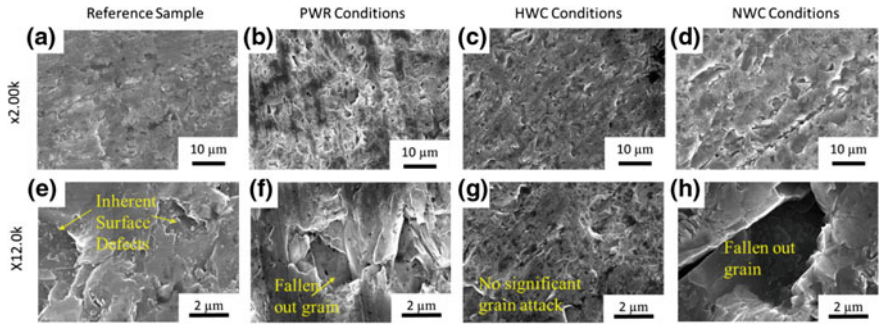

Fig. 8 SEM-SE micrographs of samples belonging to the SiC-HR variant at × 2.00 k magnification, **a**–**d**, and × 12.0 k magnification, **e**–**h**. Samples **a** and **e**, **b** and **f**, **c** and **g**, and **d** and **h** correspond to the reference sample, and the samples exposed to PWR, HWC, and NWC conditions, respectively. The labels on each row/column reflect this designation

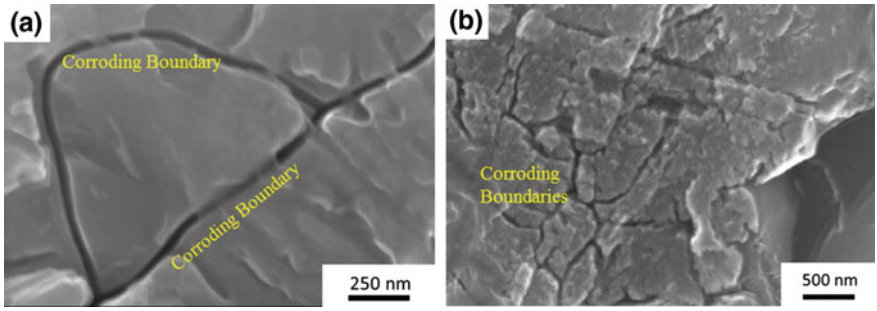

Fig. 9 High magnification SEM-SE images of **a** HR-NWC and **b** HHT–NWC revealing grain boundary attack

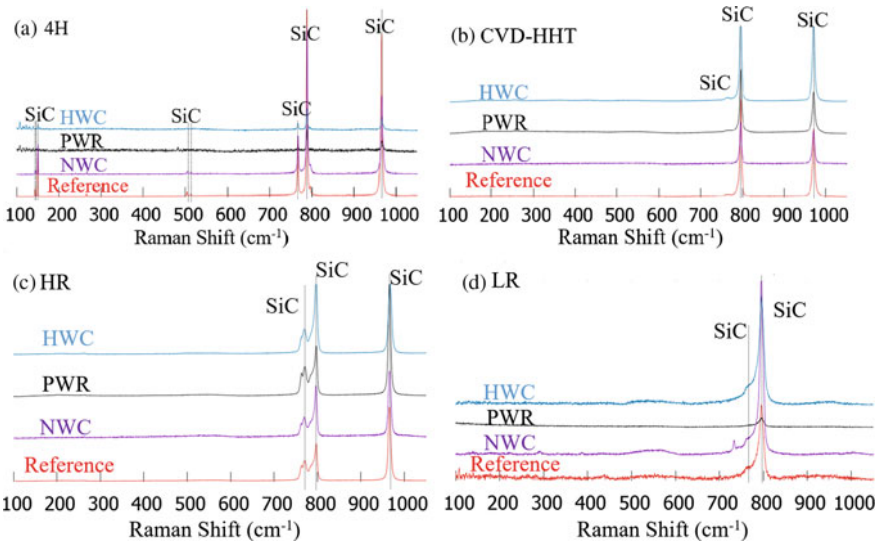

Fig. 10 Comparison of the Raman spectra for each SiC variant. Sample types are compared to their reference for **a** 4H, **b** Rohm and Hass (HHT), **c** HR, and **d** LR

While the above discussion expects the corrosion rate is not necessarily linear, as a first-order approximation, rate constants for linear kinetics were determined based on the following reactions [7].

$$SiC + 2H_2O \rightarrow SiO_2 + CH_4 \quad (2)$$

$$SiC + O_2 \rightarrow SiO_2 + C; \quad (3)$$

$$SiC + 1.5O_2 \rightarrow SiO_2 + CO\ ; \quad (4)$$

$$SiC + 2O_2 \rightarrow SiO_2 + CO_2 \quad (5)$$

Equation (2) is one of several possibilities for SiC corrosion in the absence of oxygen. However, since none of the gaseous products of this reaction are present in the reactor, and the activities of water and SiC are unity, the overall dissolution rate constant will not change by considering alternative equations. Eqs. (3), (4) and (5) are obviously only relevant to NWC conditions. All the rate constants below have units of mg/(dm^2-s). For the HWC samples, the rates reflect the reaction with water only. $K_{HWC,4H} = 2.7x10^{-7}, K_{HWC,HR} = 1.3x10^{-7}, K_{HWC,HHT} = 2.8x10^{-7}$, $K_{HWC,LR} = 4.2x10^{-7}$. These rates were subtracted from the observed rate in the NWC condition and the remaining corrosion rate was attributed to the activity of the oxygen. For the general equation $\frac{d(SiC)}{dt} = K_{O_2} a_{SiC} a_{O_2}^2$ where the choice of reaction (5) is to compare with previous data and the activity is taken as the partial pressure of O_2, the rate constants are found to be $K_{O_2,4H} = 9.1x10^5, K_{O_2,HR} = 1.0x10^6$,

$K_{O_2,HHT} = 1.0x10^6, K_{O_2,LR} = 1.2x10^7$. The PWR rate constants were determined to be the following from reaction (2). The first data point was ignored for each data set, per the above discussion about the PWR results. $K_{PWR,4H} = 5.3x10^{-7}, K_{PWR,HR} = 4.6x10^{-7}, K_{PWR,HHT} = 8.3x10^{-7}, K_{PWR,LR} = 6.8x10^{-7}$. From [7], CVD-SiC has been found to corrode with a similar rate constant of about $K_{O_2} = 1.3x10^6$, with the exception of the LR sample exposed to NWC conditions. The reaction (2) data from [7] also agrees at $K_{HWC} = 7.2x10^{-7}$; $K_{PWR} = 9.5x10^{-7}$, despite being a little higher than the present estimation. Considering the number of data points and the errors considered earlier, the degree of agreement is reasonable. Since the PWR and HWC conditions are essentially the same except for temperature, the activation energy for dissolution can be roughly estimated and the results are $E_{a,4H} \approx 19kJ/mol; E_{a,HHT} \approx 32kJ/mol; E_{a,HR} = 20kJ/mol; E_{a,LR} \approx 14kJ/mol$. A similar estimation for CVD-SiC from [7] yielded $E_a \approx 18kJ/mol$.

Conclusions

This study examined the corrosion susceptibility of SiO_2, single crystal Si, four variants of SiC, and polycrystalline and single crystal Al_2O_3 variants under simulated PWR primary water, BWR–HWC, and BWR–NWC conditions. The alumina samples corroded quickly in the BWR–HWC condition, more slowly in PWR, and slowest in NWC. SEM images suggest that grain fallout may account for a significant portion of the measured weight loss. Additionally, it appeared that some diaspore forms during the corrosion in NWC conditions, which may account for reduced corrosion rates due to lower solubility of diaspore in water and possible re-deposition of Al^{3+} as diaspore slowing overall corrosion.

The SiO_2 and Si specimens dissolved too quickly to obtain data, confirming that corrosion rates of SiC are limited by reaction with the water rather than removal of the product or diffusion of corroding species through the product (similarly to passive films on many steels). The single crystal 4H SiC microstructure showed uniform corrosion with possible shallow pitting whereas the other three polycrystalline variants exhibited grain boundary attack. Overall, this attack was greatest for the BWR–NWC condition, less for the PWR condition, and not significant in the BWR–HWC condition. This result agreed with mass loss trends, which were super-linear for the NWC condition. The PWR rates appeared parabolic, which may be the result of the surfaces not being polished before testing. The BWR–HWC condition showed the lowest corrosion rates for all samples, for which trends were not clear because of the low mass loss/high measurement error. One of the most important conclusions is that, in general, the effect of grain fallout is less significant than expected and is only actually significant for the LR sample in the NWC condition, and possibly all NWC conditions. The SiC kinetics are consisted with previous results. Further, as expected [16] both Al_2O_3 variants corroded orders of magnitude faster than SiC, indicating that SiC is more corrosion resistant under LWR conditions.

Acknowledgements This research was funded by U.S. Department of Energy's Office of Nuclear Energy, Advanced Fuel Campaign of the Fuel Cycle R&D Program.

References

1. Y. Katoh, L.L. Snead, I. Szlufarska, W.J. Weber, Radiation effects in SiC for nuclear structural applications. Curr. Opin. Solid State Mater. Sci. **16**, 143–152 (2012). doi:10.1016/j.cossms.2012.03.005
2. S.K. Ghosal, G.C. Palit, P.K. De, Corrosion of zirconium alloys in nuclear applications—A review. Miner. Process. Extr. Metall. Rev. **22**, 519–546 (2002). doi:10.1080/08827500208547428
3. T.R. Allen, R.J.M. Konings, A.T. Motta, *Corrosion of Zirconium Alloys* (Elsevier Inc., 2012). doi:10.1016/B978-0-08-056033-5.00063-X
4. C.P. Deck, G.M. Jacobsen, J. Sheeder, O. Gutierrez, J. Zhang, J. Stone, H.E. Khalifa, C.A. Back, Characterization of SiC-SiC composites for accident tolerant fuel cladding. J. Nucl. Mater. **466**, 1–15 (2015). doi:10.1016/j.jnucmat.2015.08.020
5. T. Cheng, J.R. Keiser, M.P. Brady, K.A. Terrani, B.A. Pint, Oxidation of fuel cladding candidate materials in steam environments at high temperature and pressure. J. Nucl. Mater. **427**, 396–400 (2012). doi:10.1016/j.jnucmat.2012.05.007
6. S. Kondo, S. Mouri, Y. Hyodo, T. Hinoki, F. Kano, Role of irradiation-induced defects on SiC dissolution in hot water. Corros. Sci. **112**, 402–407 (2016). doi:10.1016/j.corsci.2016.08.007
7. K.A. Terrani, Y. Yang, Y.-J. Kim, R. Rebak, H.M. Meyer, T.J. Gerczak, Hydrothermal corrosion of SiC in LWR coolant environments in the absence of irradiation. J. Nucl. Mater. **465**, 488–498 (2015). doi:10.1016/j.jnucmat.2015.06.019
8. S. Kondo, M. Lee, T. Hinoki, Y. Hyodo, F. Kano, Effect of irradiation damage on hydrothermal corrosion of SiC. J. Nucl. Mater. **464**, 36–42 (2015). doi:10.1016/j.jnucmat.2015.04.034
9. E. Barringer, Z. Faiztompkins, H. Feinroth, T. Allen, M. Lance, H. Meyer, L. Walker, E. Lara-Curzio, Corrosion of CVD silicon carbide in 500 degrees C supercritical water. J. Am. Ceram. Soc. **90**, 315–318 (2007). doi:10.1111/j.1551-2916.2006.01401.x
10. H. Hirayama, T. Kawakubo, A. Goto, T. Kaneko, Corrosion Behavior of Silicon Carbide in 290 °C Water. J. Am. Ceram. Soc. **72**, 2049–2053 (1989). doi:10.1111/j.1151-2916.1989.tb06029.x
11. University of Arizona Mineral Museum, Corundum R040096, (n.d.). http://www.rruff.info/Corundum/R040096. Accessed 1 Jan 2017
12. R.Sh. 62047-42, Diaspore X050055, (n.d.). http://www.rruff.info/Diaspore/X050055. Accessed 1 Jan 2017
13. H.D. Ruan, R.L. Frost, J.T. Kloprogge, Comparison of Raman spectra in characterizing gibbsite, bayerite, diaspore and boehmite. J. Raman Spectrosc. **32**, 745–750 (2001). doi:10.1002/jrs.736
14. A.H. Carim, G.S. Rohrer, N.R. Dando, S.-Y. Tzeng, C.L. Rohrer, A.J. Perrotta, Conversion of diaspore to corundum: a new α-Alumina transformation sequence. J. Am. Ceram. Soc. **80**, 2677–2680 (1997). doi:10.1111/j.1151-2916.1997.tb03171.x
15. F.J. Peryea, J.A. Kittrick, Relative solubility of corundum, gibbsite, boehmite, and diaspore at standard state conditions. Clays Clay Miner. **36**, 391–396, (1988) http://www.clays.org/journal/archive/volume36/36-5-391.pdf. Accessed 6 Mar 2017
16. T. Sato, S. Sato, A. Okuwaki, S.-I. Tanaka, corrosion behavior of alumina ceramics in caustic alkaline solutions at high temperatures. J. Am. Ceram. Soc. **74,** 3081–3084 (1991) http://www.onlinelibrary.wiley.com/doi/10.1111/j.1151-2916.1991.tb04304.x/abstract

Corrosion of Multilayer Ceramic-Coated ZIRLO Exposed to High Temperature Water

Kiran K. Mandapaka and Gary S. Was

Abstract The corrosion behavior of ceramic coated ZIRLO tubing was evaluated in supercritical water to determine its behavior in high temperature water. The coating architecture consisted of a 4 bilayer TiAlN/TiN coating with Ti bond coat on Zirlo tubes using cathodic arc physical vapor deposition (CA-PVD) technique. On exposure to deaerated supercritical water at 542 °C for 48 h coated tubes exhibited significantly higher weight gain compared to uncoated Zirlo. Examination revealed formation of a uniform ZrO_2 layer beneath the coating and of a thickness similar to that on the uncoated tube inner surface. The defects generated during the coating process acted as preferential paths for diffusion of oxygen resulting in the oxidation of substrate Zirlo. However, there was no delamination of the coating.

Keywords Zirlo · Multilayer coating · Supercritical water · Corrosion · Coating defects

Introduction

Zirconium-based alloys have been in use as fuel cladding in water cooled nuclear reactors by virtue of their low neutron absorption cross section, resistance to oxidation at high temperature, adequate mechanical strength and resistance to irradiation damage such as void swelling [1–3]. Zr-based alloys have performed satisfactorily in terms of oxidation and hydrogen pick-up behavior during reactor operating conditions, however, a major drawback lies in their performance during a loss of coolant accident (LOCA) scenario. During a LOCA, high temperatures of

K.K. Mandapaka
Materials Processing and Corrosion Engineering Division, Bhabha Atomic Research Centre, Trombay, Mumbai 400 085, India

G.S. Was (✉)
Nuclear Engineering & Radiological Sciences, University of Michigan, 2355 Bonisteel Boulevard, Ann Arbor, MI 48109, USA
e-mail: gsw@umich.edu

J.H. Jackson et al. (eds.), *Proceedings of the 18th International Conference on Environmental Degradation of Materials in Nuclear Power Systems – Water Reactors*, The Minerals, Metals & Materials Series, https://doi.org/10.1007/978-3-319-68454-3_24

the order ~1200 °C are reached and result in an enhancement in oxidation kinetics and consequent hydrogen generation leading to hydrogen gas release and clad failure due to brittle hydrides [4–7]. Post LOCA quenching tends to produce dense hydride rings over the clad outer surface leading to considerable degradation in mechanical properties [8]. Hydrogen generation through autocatalytic clad oxidation was a major problem in the Fukushima-Daichii accident [9] in Japan in 2011.

Though research has been conducted to develop accident tolerant fuel (ATF) cladding to replace Zr alloys, work has accelerated since the Fukushima-Daichii accident. There are two major approaches to ATF clad development; the identification and optimization of new, more oxidation resistant alloys [10, 11], and the development of oxidation resistant coatings on Zr alloy cladding [12–15]. While the former may necessitate major changes in the reactor core design, implementation of the later may be more seamless considering the advantage of utilizing the Zr alloy experience base. Several types of coatings have been proposed such as FeCrAl, TiN, and TiAlN [12–15].

The research presented here was conducted as a part of a program to develop multilayer ceramic coatings of TiN/TiAlN on Zirlo cladding and to assess the corrosion behavior. The coatings were deposited using the cathodic arc physical vapor deposition (CA-PVD) technique. On one hand, CA-PVD is more advantageous over other deposition techniques in terms of a higher kinetic energy of depositing species resulting in compressive residual stresses helpful for crack termination and better control of interfaces in multilayers. However, a major drawback of the process lies in the creation of macro-particles incorporated within the coating during the deposition process. Such particles can either be molten droplets of low melting materials like Al or of solid particles due to incomplete ionization and resulting in potential stress concentration or crack initiation sites, or thickness/composition variation across the film [16].

The basic idea behind development of multilayer coatings is to provide for enhanced hardness and strength over either TiN or TiAlN due to an increased number of interfaces [17, 18]. At high temperature, the Al in TiAlN reacts with oxygen to form a thin layer of Al_2O_3 that considerably reduces further oxidation by restricting oxygen diffusion [14]. The advantage of having a TiN outer layer is to prevent Al diffusion to the outer surface to form a detrimental boehemite (AlOOH) phase [12, 14]. The disadvantage is that it will inhibit alumina formation. These coatings have been studied for their oxidation behavior in operating environments and have performed satisfactorily [12, 14]. An exposure to water at 360 °C and 18.7 MPa exhibited about 6 times smaller weight gain compared to uncoated Zirlo [14].

This study addresses the corrosion behavior of multilayer TiAlN/TiN and coated Zirlo tubes in supercritical water (SCW) environment at 542 °C and 24.5 MPa. The environment was selected to represent a more extreme condition than normal operating temperature. The coatings were deposited using a CA-PVD technique and the corrosion behavior of coated Zirlo tubes in a SCW environment was assessed.

Experiment

Materials

The nominal chemical composition of the Zirlo tube used in this study is 1% Nb, 1% Sn, 300–600 wt. ppm Fe and balance Zr. The Zirlo tubes, 40 mm in length, 19.2 mm OD and 0.6 mm wall thickness, were deposited with a coating consisting of 4 bilayers of TiAlN/TiN with a Ti bond coat. The thickness of each layer was approximately 1 μm for a total coating thickness of about 9 μm. The coating was deposited using the cathodic arc physical vapor deposition (CA-PVD) technique. The cathodes used in the CA-PVD were, (a) 99.999% elemental Ti for bond coat/TiN layer and (b) TiAl (33 at.% Ti—67 at.% Al) for the TiAlN deposition. Further details of deposition process and parameters are explained in another publication [14].

Corrosion Experiment

Zirlo tube samples, both coated and uncoated, were exposed in pure supercritical water at a temperature 542 °C and pressure 24.5 MPa for a duration of 48 h. The experiment was conducted in a 2-liter autoclave made of Inconel 625 attached to a recirculation loop while maintaining a flow rate of ~40 ml/min. The dissolved oxygen (DO) level was maintained at <10 ppb by purging with high purity argon gas. The conductivity remained at <0.1 μS/cm inlet and <2 μS/cm outlet throughout the duration of the experiment. The tubes were suspended in a custom made sample tree (made of Inconel 625) at the center of the autoclave. The base of the tubes rested on a hollow ceramic washer, and a Ni wire with ceramic sheaths through the tube was used to suspend it from the branch. The thermocouple was positioned to read temperature at the middle branch of the sample tree. It should be noted that the variation of temperature between branches of the sample tree from top to bottom was less than 0.5 °C.

Characterization

The weights of the tube samples before and after exposure to SCW were measured using a digital balance with an accuracy of 0.01 mg. An average of three weight gain readings were taken and weight gain is reported per unit surface area in mg/dm^2.

Scanning electron microscopes (SEM); a Philips XL30 field emission gun (FEG), a JEOLJSM-6480 and FEI Helios 650 nanolab, all equipped with x-ray energy dispersive spectroscopy (EDS) were used for characterization of the coating

morphology on the surface and cross section. Elemental mapping across the coating layers before and after oxidation and composition along defects was achieved using energy dispersive x-ray spectrometry. The cross sections were prepared by mounting in epoxy resin followed by grinding and polishing and subsequently sputter depositing a thin gold layer to increase surface conductivity. TEAM Basic EDAX software was used for EDS mapping and line scans. The top TiO_2 layer post oxidation of coated tubes was measured after fibbing a cross section using the Helios nanolab. The oxide thickness for ZrO_2 on the tube outer diameter (OD) underneath the coating and on the inner diameter (ID) was measured using SEM images. The ZrO_2 and TiO_2 thicknesses measured from SEM images were then converted to equivalent weight gain in mg/dm^2 using densities of 5.68 and 4.23 g/cm^3, respectively. Laser Raman spectroscopy with a 532 nm laser was used to establish the surface oxide structure after exposure.

Results and Discussion

Weight Gain Post SCW Exposure

The OD of the tubes were coated with 4 bilayers of TiAlN/TiN and were exposed to the SCW environment at a temperature of 542 °C and pressure 24.5 MPa for duration of 48 h. Uncoated Zirlo tubes were also included in the exposure as control specimens. Figure 1 summarizes the oxidation weight gain data after exposure. An important observation from the figure is that the coated tubes exhibited significantly

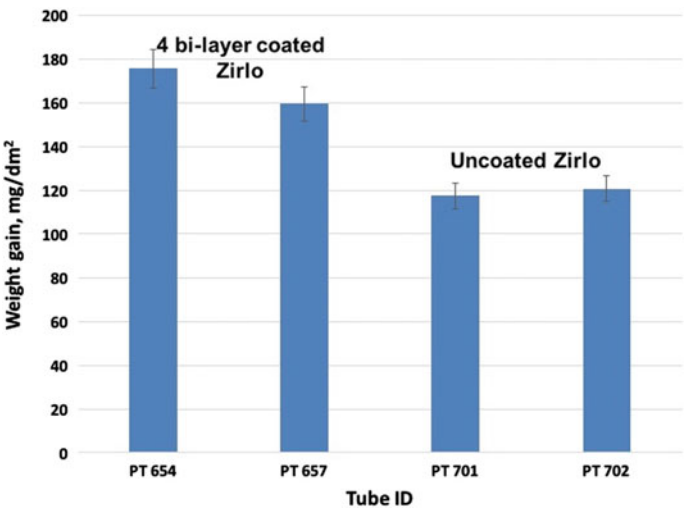

Fig. 1 Weight gain values for uncoated and coated Zirlo after exposure in 542 °C SCW environment for 48 h

higher weight gain than the uncoated Zirlo tubes. The next section will present observations on morphologies and composition of surface and cross sections before and after exposure and oxide thicknesses.

Characterization of Coating Architecture

The surface of the coated tube and the architecture of coating layers deposited by CA-PVD technique for four bilayers of TiAlN/TiN are shown in Fig. 2. Figure 2a presents the surface morphology of the as-coated tube; while Fig. 2b–d show the individual layers in the cross sectional micrographs. The as-coated tube was found to contain numerous macro-particles on the surface (Fig. 2a). The number density of these macro-particles was calculated from multiple SEM images over the tube surfaces. The resulting number density was 3176 mm^{-2}, yielding an average inter-particle distance of ~18 μm. Figure 2b shows a representative cross section of the layers describing the coating architecture in which the four alternate bilayers of TiAlN/TiN, bond coat of Ti, and the top layer TiN layer are clearly visible. The

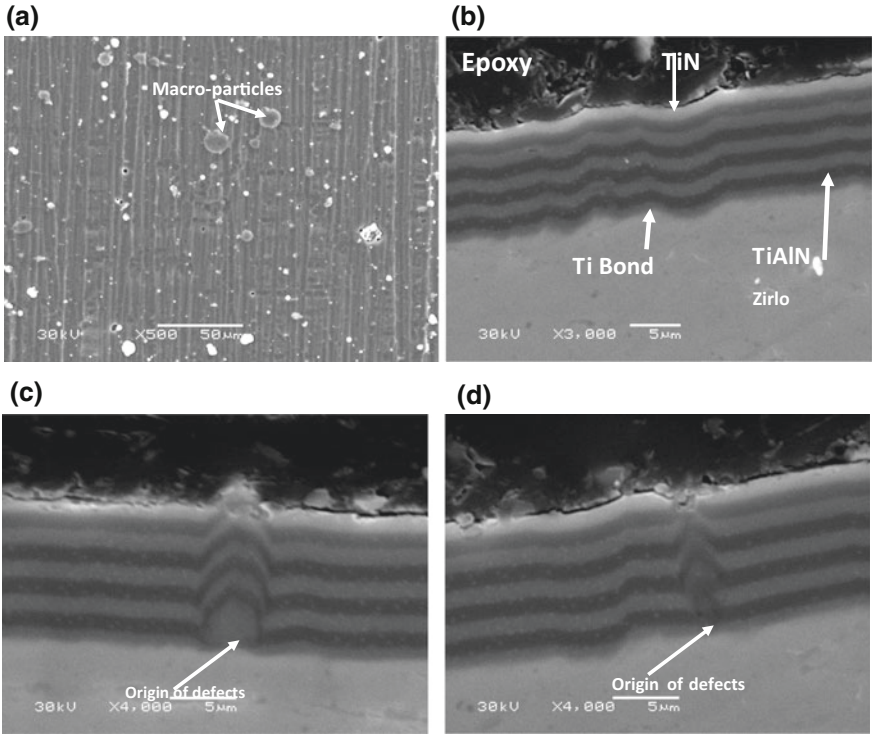

Fig. 2 Surface morphology of the as-coated tube PT 653 (**a**), and cross-sections of the 4 bilayer coating morphology (**b**)–(**d**)

macro-particles observed in Fig. 2a are located on the Zirlo surface. There are also particles in the bond coat as shown in Fig. 2c, d. These particles cause a distortion of subsequent layers that propagates to the surface. The particles likely originate from release of chunks of Al (Fig. 2d) or Ti (Fig. 2c) during sputtering to form the bond coat or the first TiAlN layer in the CA-PVD process. Elemental composition maps presented in subsequent sections demonstrate these origins better.

Coating Morphology Post Oxidation

The surface morphology of the four bilayer coating after exposure to SCW is shown in Fig. 3a, b. The macro-particles are apparent after exposure, albeit oxidized, as shown in Fig. 3a. The average inter-particle distance, size of these particles and overall morphology remains similar to that before exposure. In addition to the macro-particles, there is also evidence of cracks on the oxidized surface as shown in Fig. 3b. The coefficient of thermal expansion (CTE) for TiAlN has been reported to be 7.5×10^{-6} while that for TiN is 9.4×10^{-6} [12–14]. The mismatch of CTE for

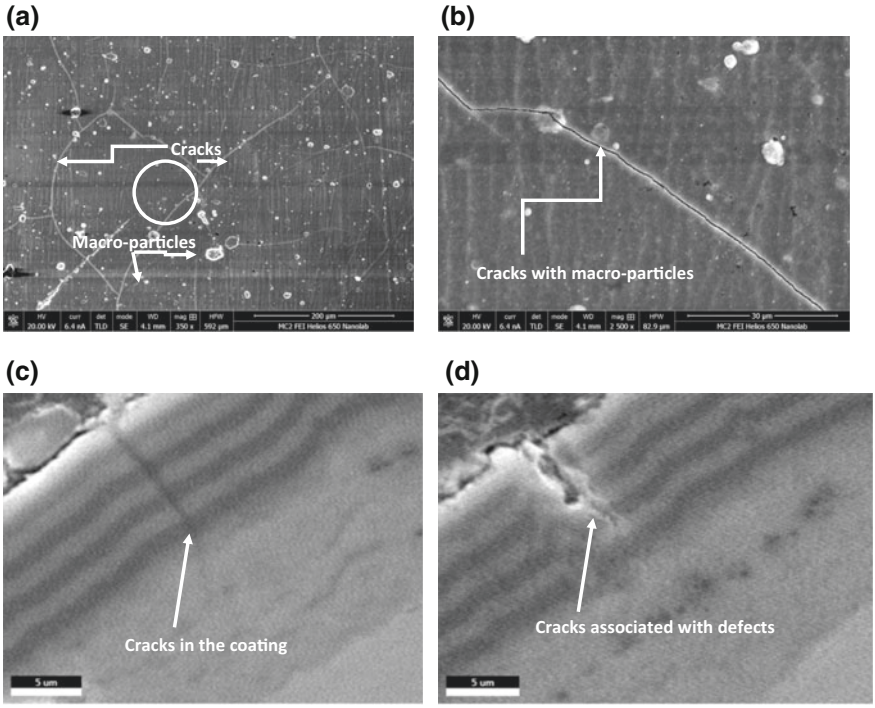

Fig. 3 The morphology post exposure in SCW for tube PT 655 showing the oxidized macro-particles and presence of cracks on the surface (**a**) and (**b**), and through the coating (**c**) and (**d**)

the alternate layers of TiAlN and TiN might have contributed to the formation of cracks while cooling from the autoclave temperature of 542 °C. The CTE for Zirlo (6.3×10^{-6}) is significantly lower than that for either TiN or TiAlN and would contribute to additional tensile stresses in the layers upon cooling. Both the macro-particles and cracks are observed to extend through all the layers down to the bond coat. Figure 3c is an example of a crack extending all the way to the bond layer. Some particles have cracks associated with them as shown in Fig. 3d.

Elemental mapping of the oxidized multilayer coated tube around the macro-particles in tube PT 655 is shown in Figs. 4 and 5. Figure 4 is an example of an Al-rich (Ti-deficient) macro-particle originating at the coating-substrate interface. Conversely, Fig. 5 shows an example of a Ti-rich (Al-deficient) macro-particle originating from a thicker Ti bond coat.

The top surface of the coated tubes consisted of a thin layer of titanium oxide as shown in Fig. 6. Figure 6a shows the cross section of a multilayer coated tube after oxidation. Figure 6b shows the corresponding Raman spectrum on the top oxide surface. The spectra clearly reveal both rutile and anatase phases of TiO_2. The surface oxide formed over the coating is about 0.5 μm thick and is uniform.

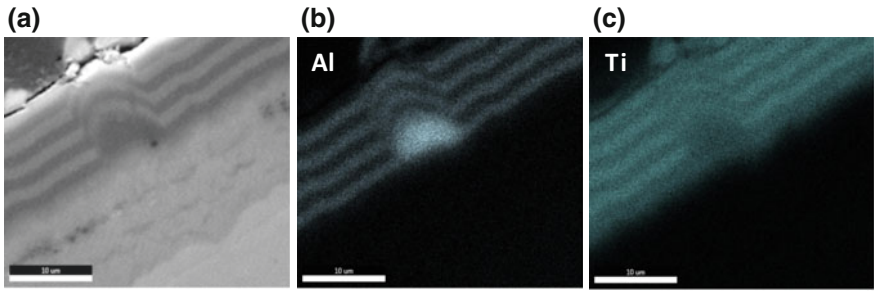

Fig. 4 Elemental mapping of 4 bilayer TiAlN/TiN coated Zirlo tube PT 655 after exposure to SCW environment at 542 °C for 48 h. The distortion in the layers is caused by deposition of a chunk of Al; **a** secondary electron image, **b** Al map and **c** Ti map

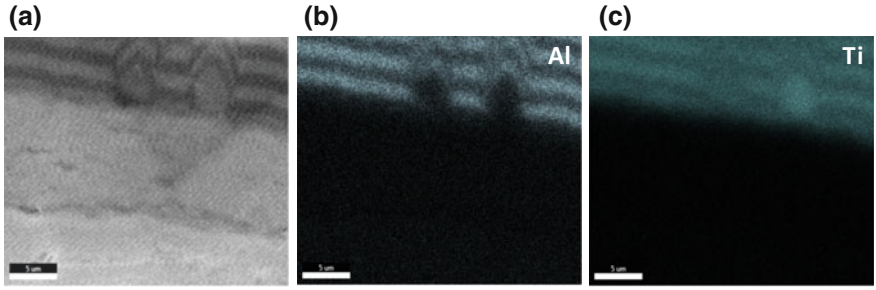

Fig. 5 Elemental mapping of 4 bilayer TiAlN/TiN coated Zirlo tube PT 655 after exposure to SCW environment at 542 °C for 48 h. The distortion in the layers is caused by deposition of a chunk of Ti; **a** secondary electron image, **b** Al map and **c** Ti map

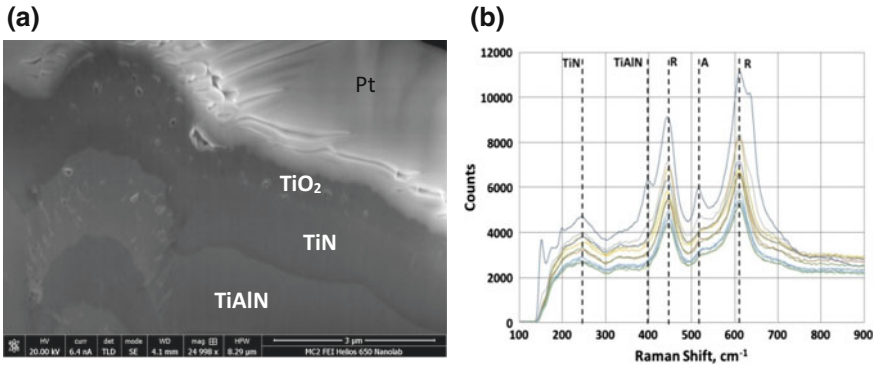

Fig. 6 The cross section of **a** 4 bilayer coated Zirlo tube PT 655, and **b** Raman spectra of the oxidized surface

Oxidation of Tube OD Beneath the Coating

The data in Fig. 1 show that the weight gain of the coated tubes was greater than that of the uncoated tubes. Except for the thin titanium oxide layer on the TiN top layer, the coating should have prevented oxidation of the outer Zirlo surface, yielding a weight gain of approximately half that of the uncoated tube. Cross sections of the multilayer coating and underlying Zirlo, Fig. 7, show that, in fact, significant oxidation of the Zirlo occurred beneath the multilayer coating. Figures 7a shows the oxide layer below the multilayer coating, and Fig. 7b shows the oxide on the uncoated tube ID.

A summary of the thickness data and the weight gains measured and weight gain values calculated from thickness values along with the stoichiometry of oxides is given in Table 1. The estimated weight gain values from thicknesses are slightly

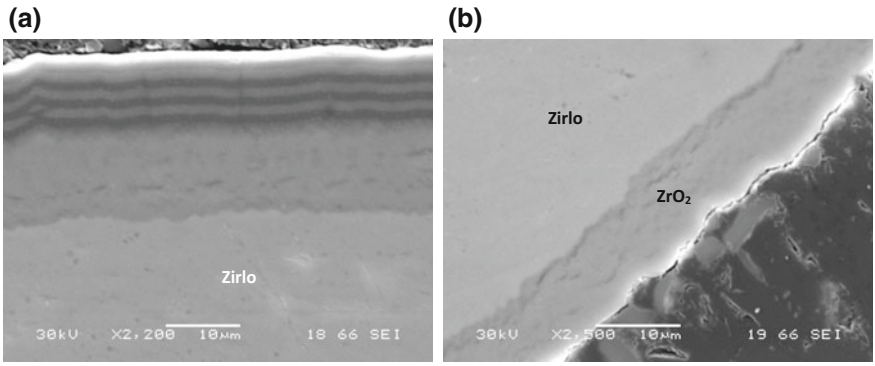

Fig. 7 The morphology of ZrO_2 layer **a** on the tube OD beneath the multilayer coating, and **b** on the uncoated tube ID

Table 1 Summary of oxidation behavior of uncoated and coated Zirlo tubes following exposure in SCW environment at 542 °C for 48 h

Tube ID/description	Weight gain, mg/dm^2 (measured)	Oxide thickness (μm)			Oxide composition (at.%)			Weight gain, mg/dm^2 (from thickness)
		OD ZrO_2	ID ZrO_2	Top TiO_2	OD Zr:O	ID Zr:O	Top Ti:O	
PT 701/uncoated Zirlo	117	8.0 ± 0.015	7.9 ± 0.015	NA	32:68	32:68	NA	117
PT 655/coated 4 bilayer TiAlN/TiN	173	10.4 ± 0.078	9.3 ± 0.028	0.56 ± 0.01	44:56	43:57	43:57	156

lower compared to the values measured following autoclave exposure, but fall in the same order as the thickness. Note that the thickness of the ZrO_2 layer beneath the coating is as thick as that on the ID of the tubes. Furthermore, the oxide layer beneath the coating was of uniform thickness, indicating that the coatings provided essentially no protection of the underlying Zirlo from the environment. This could only be possible if the coating was highly defective. The defects are likely the macro-particles that resulted in distortion of the layers and cracking in the perturbed regions.

EDS line profiles of oxygen were taken across the region above the particles and one such profile is shown in Fig. 8. The profile clearly demonstrates enhanced oxygen levels around the particles as compared to the flat region of the coating layers. These macro-particles can be considered to be preferential sites for oxygen access to the substrate. The diffusion coefficient for oxygen in zirconium oxide has been reported to be about 10^{-11} cm^2/s at 542 °C and 10^{-13} cm^2/s at 360 °C [19]. For a diffusion coefficient of 10^{-11} cm^2/s, an exposure of 48 h would result in a diffusion length of oxygen of about 13 μm assuming parabolic oxidation kinetics. Thus, the thickness of the observed oxide layer beneath the coating is consistent with rapid penetration of oxygen through the coating and growth of the zirconium oxide by solid state oxidation. For a macro-particle spacing of 18 μm, each particle has an associated area of radius 9 μm if uniformly distributed. That this effective "diffusion length" corresponds with the range of oxide thickness may explain why the oxide underneath the coating is so uniform in thickness. That is, the defect spacing is small enough that oxide formed at the base of the defects merges to form a continuous layer. Similar observations were made on magnetron sputtered multilayer coating at lower temperatures (360 °C). In this case, the substrate oxidation was localized to the sites of these macro-particle forming oxides that emerged from the point of the defect to a depth of ~2 μm while the rest of the Zirlo was

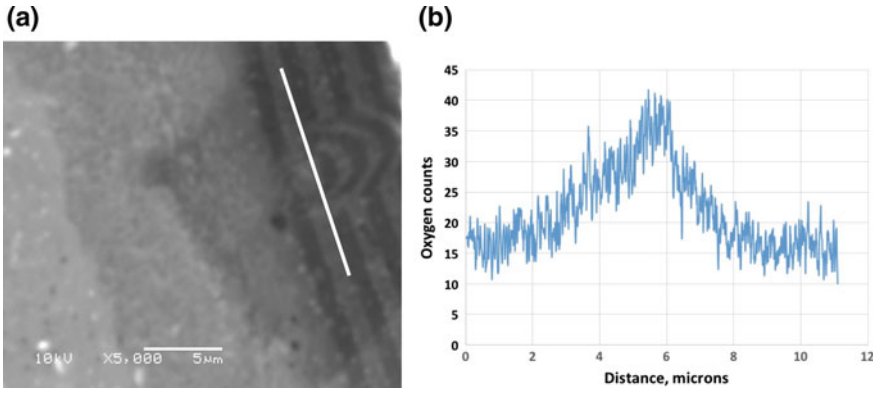

Fig. 8 Oxygen concentration profile using SEM-EDS along a macro-particle in oxidized 4 bilayer coated Zirlo tube PT 655; **a** secondary electron image, and **b** EDS profile for oxygen along the defect shown in (**a**)

unoxidized [20]. These results are consistent with a diffusion coefficient that is two orders of magnitude less than that at 542 °C. For the CA-PVD multilayer coated Zirlo, the substrate was not shown to oxidize in 360 °C water resulting in much lower weight gain [12–14].

Conclusions

The corrosion behavior of a multilayer ceramic coated Zirlo tube exposed to supercritical water at 542 °C was studied to evaluate the efficacy of the coating as a potential accident tolerant fuel cladding concept. Zirlo tubes were coated with 4 bilayers of TiAlN/TiN on top of a Ti bond layer. The PA-CVD process resulted in the formation of Al- or Ti-rich macro-particles originating at the Zirlo surface and causing a distortion of subsequent layers that propagates to the surface, sometimes accompanied by cracks. These distortions and cracks provided a pathway for rapid access of oxygen to the underlying Zirlo. Their density was such that the oxide layer formed beneath the coatings was of uniform thickness by the time it grew to $\sim$10 μm thick. The underlying oxide thickness is consistent with a mechanism of rapid oxygen access to the underlying Zirlo followed by solid state oxidation at a rate that was similar to uncoated Zirlo, rendering the coating ineffective.

Acknowledgements The authors acknowledge research grant by Office of Nuclear Energy, NEUP program with contract # A13-0708-S001. The CA-PVD coating of multilayer TiN/TiAlN was performed at Penn State University. Authors thank Dr. D. E. Wolfe and group for providing the coated samples for this research. The Zirlo material was provided by Westinghouse. Authors acknowledge help from Alexander Flick during SCW exposure experiment.

References

1. IAEA TECDOC-996, “Waterside corrosion of zirconium alloys in nuclear power plants”, International Atomic Energy Agency Technical Document 996 (1998)
2. C. Lemaignan, A.T. Motta, Zirconium alloys in nuclear applications, in ed. by B.R.T. Frost (Ed.), Mater. Sci. Technol. A Comp. Treat. 10B, New York: VCH (1994) 1–51
3. K.K. Mandapaka, S. Aggarwal, V. Kain, T. Saario, M. Bojinov, Nucl. Eng. Des. **240**, 985–994 (2010)
4. V. Swan, Proc. ANS ILL (1994) 303–308
5. C. Lemaignan, J. Nucl. Mater. **187**, 122–130 (1992)
6. R.A. Perkins, R.A. Busch, ASTM STP-1132, 595–612 (1991)
7. N. Ramasubramanian, ASTM STP-1132 613–627 (1991)
8. M. Grosse, J. Stuckert, M. Steinbrück, A. Kaestner, J. Nucl. Mater. **420**, 575–582 (2012)
9. N.P. Neureiter, B.J. Garrick, R.A. Bari, J. Beard, M. Percy, M.Q. Brewster, M.L. Corradini, Lessons learned from the Fukushima nuclear accident for improving safety of U.S. Nuclear Plants. Natl. Acad. Sci. (2014)
10. K.A. Terrani, S.J. Zinkle, L.L. Snead, J. Nucl. Mater. **448**, 420–435 (2014)
11. P. Ahmedabadi, G.S. Was, Corrosion **72**(1), 66–77 (2016)

12. E. Alat, A.T. Motta, R.J. Comstock, J.M. Partezana, D.E. Wolfe, Surf. Coat. Technol. **281**, 133–143 (2015)
13. Y. Liu, I. Bhamji, P.J. Withers, D.E. Wolfe, A.T. Motta, M. Preuss, J. Nucl. Mater. **466**, 718–727 (2015)
14. E. Alat, A.T. Motta, R.J. Comstock, P. M Jonna, D.E Wolfe. J. Nucl. Mater. (2016)
15. W. Zhong, P.A. Mouche, X. Han, B.J. Heuser, K.K. Mandapaka, G.S. Was, J. Nucl. Mater. **470**, 327–338 (2016)
16. D. Mattox, *Handbook of Physical Vapour Deposition (PVD) Processing: Film Formation, Surface Preparation and Contamination Control* (Noyes Publications, Adhesion, 1998)
17. L. Chen, D. Yong, F. Yin, J. Li, Int. J. Refract. Met. Hard Mater. **25**, 72–76 (2007)
18. H.G. Prengel, P.C. Jindal, K.H. Wendt, A.T. Santhanam, P.L. Hegde, R.M. Penich, Surf. Coat. Technol. **139**, 25–34 (2001)
19. C. Anghel, Doctoral thesis on "Modified oxygen and hydrogen transport in Zr-based oxide", KTH Industrial Engineering and Management (2006)
20. M. Patel, K. Sickafus, "Multilayer ceramic coating architectures on Zirlo", presented at CARAT 2016

Part IV
General SCC and SCC Modeling

Calibration of the Local IGSCC Engineering Model for Alloy 600

Thierry Couvant, Jacqueline Caballero, Cécilie Duhamel, Jérôme Crépin and Takaharu Maeguchi

Abstract Many Stress Corrosion Cracking (SCC) models have been developed so far. Quantitative empirical models, trying to predict initiation and crack growth rate of nickel alloys exposed to pressurized water reactor primary water do not describe physical mechanism and suffer a lack of accuracy. By contrast, models describing the possible involved physical mechanisms responsible for degradation (selective oxidation of grain boundaries in the case of Alloy 600 exposed to PWR primary water) are usually qualitative. In the current paper, a 'local' model is proposed to better predict SCC. In order to succeed, behaviors assumed to be involved in the SCC process were calibrated and coupled: intergranular oxidation rate, intergranular stresses, resistance to cracking of oxidized grain boundaries. The output of the model is the time to reach a given crack depth. This paper introduces the first calibration of parameters for Alloy 600 exposed to primary water.

Keywords Intergranular stress corrosion cracking · Alloy 600 · Primary water · Intergranular oxidation · Crystal plasticity · Fracture of oxidized grain boundaries · Local model · Initiation · Crack growth

Background

To date, EDF has predicted Stress Corrosion Cracking (SCC) of nickel alloys in Pressurized Water Reactor (PWR) primary water by chaining two isolated stages of cracking: initiation (involving the slow crack growth regime) and fast crack growth.

T. Couvant (✉) · J. Caballero
EDF R&D, Avenue des Renardières, 77250 Moret-sur-Loing, France
e-mail: thierry.couvant@edf.fr

C. Duhamel · J. Crépin
MINES ParisTech, PSL—Research University, MAT—Centre des matériaux, CNRS UMR 7633, BP 87, 91003 Evry, France

T. Maeguchi
MHI, Takasago R&D Center, Tokyo, Japan

J.H. Jackson et al. (eds.), *Proceedings of the 18th International Conference on Environmental Degradation of Materials in Nuclear Power Systems – Water Reactors*, The Minerals, Metals & Materials Series, https://doi.org/10.1007/978-3-319-68454-3_25

In the case of initiation, an 'index' model was proposed for Alloy 600 [1] where the time to initiation t_i (Eq. 1) depends on a material index i_m defining the intrinsic susceptibility to SCC of the material depending on manufacturing [2], on a temperature index i_T (Eq. 2) expressing the dependency to temperature with an activation energy Q_i, and on a stress index i_σ (Eq. 3), where the stress σ is higher than yield stress.

$$t_i = \frac{10,000}{i_m \times i_\sigma \times i_T} \tag{1}$$

$$i_T = 9.49 \times 10^{15} \times \exp\left(\frac{-Q_i}{RT}\right) \tag{2}$$

$$i_\sigma = 2.44 \times 10^{-11} \times \sigma^4 \tag{3}$$

where t_i is in h, T is in K, σ is in MPa, $R = 8.314$ J mol^{-1} K^{-1} and $Q_i = 183{,}000$ J mol^{-1}.

The crack growth rate (CGR) was modeled (Eq. 4) [3–5] assuming a threshold K_{ISCC} in stress intensity factor K for crack growth, a dependency to temperature (with an activation energy Q_c) and a dependency f_{CW} to cold work (CW).

$$\mathrm{Max}(CGR) = C_1(K - K_{ISCC})^{C_2} \times f_{CW} \times \exp\left(\frac{-Q_c}{RT}\right) \tag{4}$$

where CGR is in µm h^{-1}, K and K_{ISCC} are in MPa m$^{1/2}$, C_1 and C_2 are constant depending on the heat ([3–5] proposes parameters for some Alloy 600 bars).

The main limitations of such an approach are:

- The absence of crack depth associated to the predicted time to initiation. As a consequence, the chaining between initiation and fast crack growth is only possible if the time to initiation is assumed to be the time to reach K_{ISCC}.
- The difficulty to incorporate new influencing parameters in the prediction of initiation (dissolved hydrogen, CW, strain path).
- The absence of underlying mechanism for incubation, initiation and crack growth. In particular, parameters used to predict initiation are macroscopic parameters, while SCC is a local phenomenon.

The goal of the current study is to propose an alternative modeling approach to reduce previous limitations, using the local model already proposed for Alloy 182 [6].

The 'Local Model'

Assumptions

The proposed model relies on a cracking scenario and local parameters. While no crack is present (incubation, initiation), 'local' refers to grain boundaries (GB), where the degradation happens. As soon as cracking occurs, 'local' refers to the intergranular crack tip. The modeled scenario is the following:

- **Incubation**: the model predicts the time to reach a critical oxidation depth. It is assumed that exposure to primary water allows oxidation of emerging GBs and that oxidation strongly decreases the stress to fail them as soon as the critical oxidation depth is reached. Regarding nickel alloys 600 and 182, the intergranular oxidation rate mainly depends on temperature, grain boundary coverage with chromium carbides and dissolved hydrogen in primary water [7–9]. However, additional dependencies may be considered in the future, such as plastic strain, stress, hydrogen (in the metal).
- **Initiation**: the model predicts the probability to reach the critical stress to fail a sufficiently oxidized grain boundary.
- **Crack extension**: the crack extension is described by a sigmoid function of K, in order to reach a slow CGR (crack extension and implicit progressive coalescence of initiated cracks) then a transition into a fast CGR (crack extension of a single dominating crack).

Intergranular Oxidation Rate

The intergranular oxidation rate is assumed to be the combination of the oxidation rate of three phases:

- A 'nom' chromium-nominal phase (average level of the material, typically 16% in the following).
- A 'carb' chromium-rich phase (chromium carbides). This phase is usually quantified by the grain boundary coverage (GBC) with chromium carbides.
- A 'depl'chromium-depleted phase (due to chromium carbide precipitation [10]).

In a first approach, for each phase i, the maximal oxidation depth p_i (in nm) is assumed to have a logarithmic dependency to the time t (in h) of exposure to primary water (Eq. 5).

$$p_i = a_i + \frac{1}{b_i}\mathrm{Ln}(1 + c_i \times t) \times f(\Delta EcP) \times g(T) \tag{5}$$

In addition, p_i depends (Eq. 6) on dissolved hydrogen DH content in primary water (in ml kg^{-1} water), via $f(\Delta EcP)$, with ΔEcP (in mV), the potential difference of the electrochemical potential of the alloy, EcP, and the potential of the Ni/NiO transition, $EcP_{Ni/NiO}$ (Eq. 7) [11]. Last, p_i depends on temperature (Eq. 8), via $g(T)$, depending on the activation energy Q_{ox} (in J mol^{-1})

$$f(\Delta EcP) = H_1 + H_2 \times \exp(-H_3 \times \Delta EcP) \tag{6}$$

with

$$\Delta EcP = EcP_{Ni/NiO} - EcP \tag{7}$$

$$g(T) = g_T \times \exp\left(\frac{-Q_{ox}}{RT}\right) \tag{8}$$

where H_1, H_2, H_3 and g_T are constant.

The oxidation rate of a GB is calculated as follow:

1. Random sampling of the 3 phases satisfying given GB properties: GBC, mean size ($2 \times r_c$) of chromium carbides, mean length (z_{Cr}) of chromium depletion associated with each chromium carbide.
2. Discretization (1 nm in the current paper) of the total GB length (1 mm).
3. Incremental calculation of the time to oxidize the discretized GB with the following rules:
   a. The time to oxidize a GB portion composed of a given phase is estimated using oxidation kinetics of the same phase.
   b. When a new phase is reached by the oxidation front at a depth p (transition from phase i to phase j), the new oxidation rate is the oxidation rate of phase j for p, assuming that formed oxides are similar whatever the phase where they grow. In other words, a transition in oxidation rate corresponds to the shift in time at p of the new oxidation law to reach the time and depth of the transition.
   c. A direct transition between kinetics is assumed as soon as the oxide front meets a new phase.

Figure 1 illustrates the simulated oxidation process: kinetics of oxidation following nominal Cr phase, Cr carbide phase and Cr depleted phase are given in blue, green and red on the left. The random grain boundary, including one Cr carbide and two associated depleted areas is shown on the right. The simulated oxidation rate along the grain boundary is the dark curve: it matches first with the oxide growth rate of the nominal Cr phase. Then, a short increase in oxidation rate is experienced when the oxidation reaches the chromium-depleted zone, until the oxide front reaches the Cr carbide. This last transition is followed by a large decrease in oxidation rate.

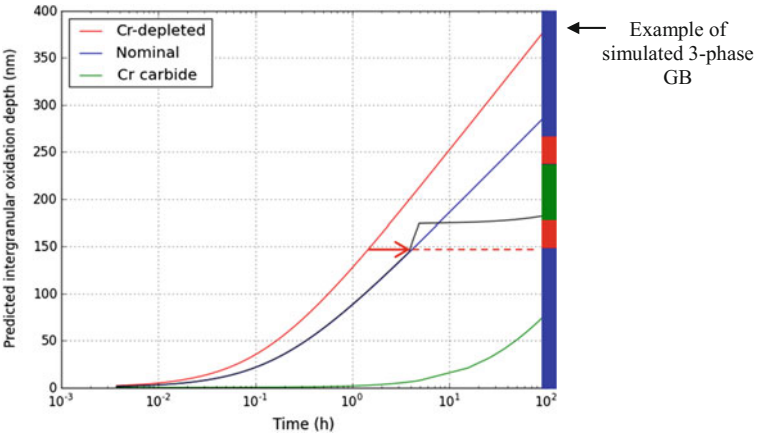

Fig. 1 Simulated oxide growth (dark curve) along a grain boundary (on the right) with Cr carbide (green portion) surrounded with two Cr-depleted zones (red portions). The blue portions correspond to a nominal Cr content. The red arrow illustrates the change in oxidation rate as soon as the intergranular oxidation front reaches the first interface (nominal/depleted). The change corresponds to the simple shift in time of the oxidation kinetics along the depleted phase up to the current time. Oxidation rates given at 320 °C with DH = 30 ml kg^{-1} water (Color figure online)

Stress Concentration at Grain Boundaries

Crystal plasticity modeling is an appropriate approach to evaluate the stress concentrations at the grain boundaries of a polycrystalline aggregate, taking into account activation of slip systems. In the frame of small deformation assumption the strain rate $\dot{\varepsilon}$ can be decomposed into elastic $\overset{\sim}{\dot{\varepsilon}}^{e}$ and plastic $\overset{\sim}{\dot{\varepsilon}}^{p}$ parts (Eq. 9).

$$\overset{\sim}{\dot{\varepsilon}} = \overset{\sim}{\dot{\varepsilon}}^{e} + \overset{\sim}{\dot{\varepsilon}}^{p} \tag{9}$$

Considering that intragranular deformation is the main contribution, the plastic strain rate $\overset{\sim}{\dot{\varepsilon}}^{p}$ in a grain is the sum of elementary shear rates $\dot{\gamma}^{s}$ extending over all active slip systems s (Eq. 10):

$$\overset{\sim}{\dot{\varepsilon}}^{p} = \sum_{s} \dot{\gamma}^{s} \, \widetilde{m}^{s} \tag{10}$$

where $\widetilde{m}^{s}$ is the orientation tensor (Eq. 11).

$$\widetilde{m}^{s} = \frac{1}{2}\left(\bar{l}^{s} \otimes \bar{n}^{s} + \bar{n}^{s} \otimes \bar{l}^{s}\right) \tag{11}$$

where $\bar{n}^s$ is the normal vector to the slip plane and $\bar{l}^s$ is a vector corresponding to slip direction and $\otimes$ is the tensor product. Crystal plasticity models rely on the assumption that plastic deformation between room temperature and 360 °C occurs by crystallographic slip following Schmidt's law. The shear rate $\dot{\gamma}^s$ is linked to the motion of dislocations in active slip systems. The flow rule $\dot{\gamma}^s$ can be described by a phenomenological relation involving ingredients of interest: viscosity, isotropic and kinematic hardening. The resolved shear stress τ^s on a given slip system s is the projection (Eq. 12) of the local stress tensor on $\widetilde{m}^s$.

$$\tau^s = \widetilde{\sigma} : \widetilde{m}^s \tag{12}$$

After computation on a polycrystalline aggregate, in a first approach, the standard deviation (SD) of calculated local stresses σ can be correlated to the average stress $mean(\sigma)$ in the polycrystal (Eq. 13), assuming a Gaussian distribution of local stresses.

$$SD(\sigma) = S \times mean(\sigma) \tag{13}$$

The parameter S is estimated thanks to finite element computations on a polycrystalline aggregate. Last, the largest stress levels are usually observed at grain boundaries (based on finite element modeling). As a consequence, in the 'local' model, the tail of the assumed Gaussian stress distribution is assumed to be responsible for initiation.

Initiation

Initiation is defined as the failure of an oxidized grain boundary. Such a failure is assumed to be possible as soon as both of the following conditions are satisfied:

1. A grain boundary is sufficiently oxidized: the oxidation depth is deeper than a critical value (p_c).
2. The local stress experienced by the grain boundary is higher than the critical opening stress (σ_c) to fail an oxidized GB.

Crack Growth

The sigmoid crack extension law (upper bound) is given in Eq. 14. It depends on K (*in* MPa $m^{1/2}$), T (*in* K) and ΔEcP (in V) via f_H. Q_g is the activation energy for crack growth CGR (in µm h^{-1}).

$$\max(CGR) = g_1 \times \frac{K^{g_2}}{1 + \exp[-g_3 \times (K - g_4)]} \times f_H \times \exp\left(\frac{-Q_g}{RT}\right) \quad (14)$$

where g_1 to g_4 are constant. f_H depends on ΔEcP, as shown in Eq. 15.

$$f_H = 1 + f_1 \times \exp\left[-\frac{1}{2}\left(\frac{\Delta EcP + f_2}{f_3}\right)^2\right] \quad (15)$$

where f_1–f_3 are constant.

SCC Computation

The local model was integrated to Code_Coriolis, the EDF numerical tool allowing to simulate SCC which make use of finite element modeling (FEM) post analysis [12].

Calibration of the Model Parameters

Materials

Chemical compositions and mechanical properties of several Alloy 600 heats or heat treatment conditions are given in Tables 1 and 2 respectively. They meet RCC-M French requirements. Microstructures are as follow:

- **RND-M-B-369** and **RND-M-B-356** hot rolled bars are from the same heat. The bar registered as RND-M-B-369 was heat treated 1 h at 820 °C. The ASTM grain size (G) is 8 and the grain boundary coverage (GBC) with chromium carbides is 33%. A lot of intragranular carbides can be found (banded along the axis of the bar). The bar registered as RND-M-B-356 was heat treated 1 h at 720 °C, G = 11 and GBC = 58%.
- **RND-M-U-510** hot rolled bar was heat treated at 820 °C. The GBC is 40% and the grain size (G = 10) is the largest of studied hot rolled bars.
- **RND-M-U-589** hot forged (1100–1200 °C) bar experienced a final 2 h-heat treatment at 820 °C. Many intragranular carbides are observed, revealing the location of the grain boundaries before recrystallization. By contrast, only a limited number of chromium carbides are observed on current grain boundaries (GBC = 15%). The grain size is G = 10.

Table 1 Chemical composition (%wt.) of studied materials

Material	C (%)	Mn (%)	Si (%)	S (%)	P (%)	Ni (%)	Cr (%)	Cu (%)	Co (%)	Al (%)	Ti (%)	Fe (%)
RND-M-B-369 RND-M-B-356	0.049	0.87	0.30	<0.001	0.0045	72.49	16.15	0.02	<0.01	0.41		9.70
RND-M-U-510	0.033	0.65	0.27	<0.001	0.008	74.31	14.40	0.04	0.02	0.13	0.17	10.0
RND-M-U-589	0.058	0.81	0.45	<0.001	0.007	73.20	16.05	0.02	0.04	0.24	0.29	8.8
RCC-M 4102	<0.10	<1.0	<0.5	<0.015	<0.025	>72.0	14–17	<0.5	–	0.2–0.8	0.65–1.15	6–10

Table 2 Tensile properties of studied materials

Material	Temperature (°C)	$YS_{0.2}$ (MPa)	UTS (MPa)	El. (%)
RND-M-B-369	20	536	736	37
	325	484	694	34
RND-M-U-510	20	481	688	36.8
	360	474	684	35.6
RND-M-U-589	20	468	729	33.0
	360	430	462	30.0
RCC-M 4103	20	>40	>550	>30.0
	325	>190	–	–

Intergranular Oxidation Kinetics

Calculations were performed considering a set of 100 GBs, satisfying grain boundary properties (GBC, r_c, z_{cr}) of the different materials.

As shown in Fig. 2, after 100 h at 325 °C, the maximum intergranular oxidation depth decreases when ΔEcP increases (when the dissolved hydrogen content increases from 3 to 60 ml kg^{-1}). ΔEcP (in V) was calculated as follow [13]:

$$\Delta EcP = 1000 \times \frac{RT}{2F} \times Ln\left(\frac{[H_2]_{test}}{[H_2]_{Ni/NiO}}\right) \tag{16}$$

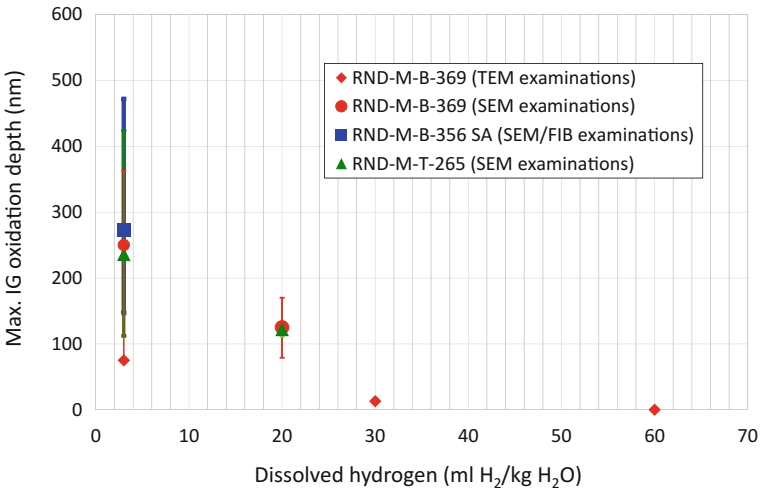

Fig. 2 Maximal intergranular oxide penetration at 320–325 °C observed in different Alloy 600, as a function of dissolved hydrogen. Examinations on grain boundaries without any chromium carbides emerging at the surface

where F = 96,500 C mol^{-1}, T is the temperature (in K), $[H_2]_{test}$ and $[H_2]_{Ni/NiO}$ are respectively the hydrogen concentrations (in ml kg^{-1}) during testing and at the Ni/NiO equilibrium (at a given T). In other words, intergranular oxidation is enhanced when NiO stability increases.

In addition, the increase in temperature, for a given dissolved hydrogen content, is accompanied by a significant increase in intergranular oxidation (Fig. 3). For 20 ml kg^{-1} H_2O, intergranular oxidation in Alloy 600 registered RND-M-B-356 is multiplied by 2 when temperature increases from 320 to 360 °C and is divided by 2 when the temperature decreases from 320 °C down to 290 °C.

No chromium depletion was noticed (after transmission electron microscopy) in studied materials. Therefore the extension of the Cr-depletion (z_{Cr}) was assigned to 0 nm, while the typical carbide length ($2 \times r_c$) was assigned to 100 nm (after TEM examinations). Based on these values, random representative boundaries were simulated, with a spatial resolution of 1 nm.

Parameters of the oxidation law (Table 3) were calibrated based on TEM and SEM/Tomography examinations which provided the required input parameters (grain boundary length, GBC, maximum oxidation depth, environmental conditions…). Figure 4 compares observed intergranular oxidation depths with predicted ones. Current parameters overestimate short oxidation depths (<200 nm) but a good fit is reached within the range 200 nm–2 µm. Therefore, the use of current oxidation parameters to predict SCC initiation may lead to overconservative times to initiation if IG oxidation is limited.

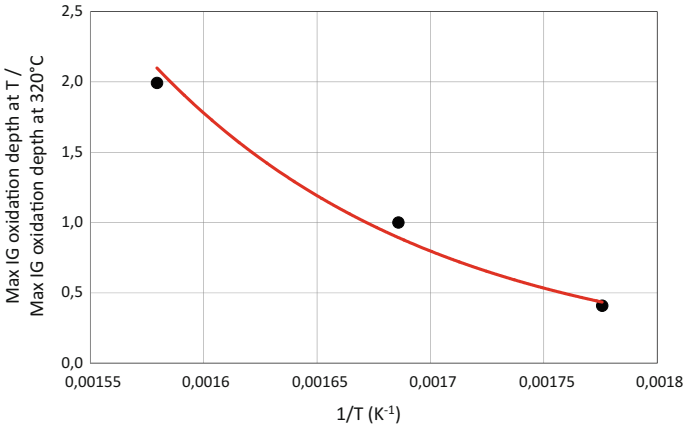

Fig. 3 Effect of temperature on the maximum intergranular oxidation depth observed on alloy 600 registered as RND-M-B-369 after 1000 h-oxidation tests in primary water with 20 ml H_2 kg^{-1} H_2O

Table 3 Parameters of the oxidation rate model (Eqs. 5–8) for the three materials (only the GBC differs)

a_{nom} a_{carb} a_{depl} (nm)	b_{nom} (nm^{-1})	c_{nom} (h^{-1})	b_{carb} (nm^{-1})	c_{carb} (h^{-1})	b_{depl} (nm^{-1})	c_{depl} (h^{-1})	H_1	H_2	H_3 (mV^{-1})	g_T	Q_{ox} (J/mol)	r_c (nm)	z_{Cr} (nm)
0	1.37×10^{-15}	3.3519	1.72×10^{-14}	7.58	1.37×10^{-15}	3.3519	0.27	0.65	0.018	8×10^{12}	139,000	50	0

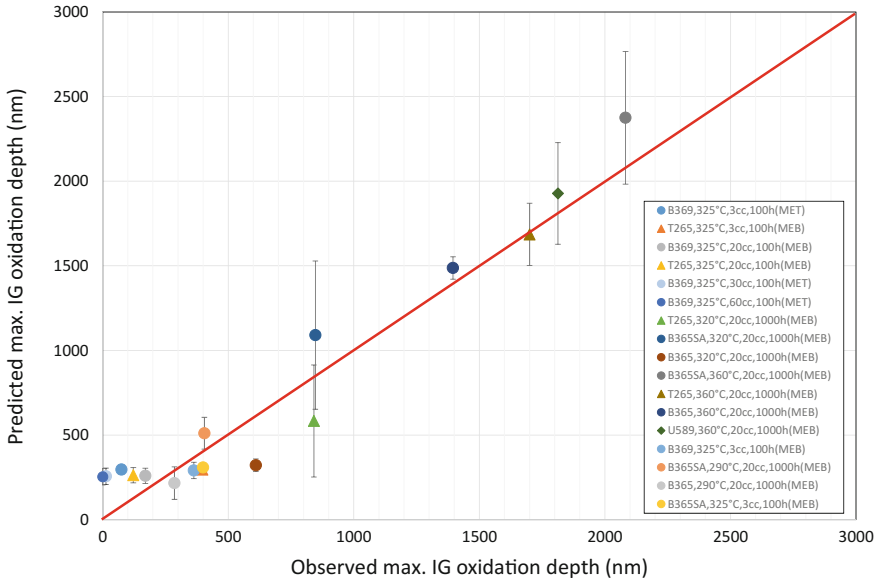

Fig. 4 Comparison between predicted and observed maximal intergranular oxidation depth. The comparison covers large ranges of temperature (290–360 °C), DH (3–60 ml kg^{-1}), GBC (0–58%) and times (100–1000 h)

Stress Concentration at Grain Boundaries

The microstructure was simulated with a polycrystal involving 172 grains. The aggregate was meshed with tetrahedral elements (150,000 nodes). Hardening behavior (Eq. 17) was calibrated on stress-strain curves and cyclic tension-compression curves (only for RND-M-B-369 material), assuming a Norton-like viscoplastic relation, where K_s is the viscosity constant and n_s is the stress sensitivity:

$$\dot{\gamma}^s = \left\langle \frac{|\tau^s - x^s| - \tau_c^s}{K_s} \right\rangle^{n_s} \frac{(\tau^s - x^s)}{|\tau^s - x^s|} \tag{17}$$

where x^s is the kinematic hardening, proportional to α^s (Eqs. 18 and 19):

$$X^s = c\,\alpha^s \tag{18}$$

$$\dot{\alpha}^s = \dot{\gamma}^s - d\alpha^s|\dot{\gamma}^s| \tag{19}$$

where c is a constant. τ_c^s is the isotropic hardening, depending on the cumulated strain γ_{cum}^r (Eqs. 20 and 21):

$$\tau_c^s = \tau_0 + Q \sum_r h_{rs} \left(1 - \exp(-b\gamma_{cum}^r)\right) \tag{20}$$

$$\gamma_{cum}^r = \int_t |\dot{\gamma}^r| dt \tag{21}$$

where h is the interaction matrix, describing the self-hardening (diagonal components) and the latent hardening (non-diagonal components) of the crystal slip systems. All components h_{rs} of h were normalized by the self-hardening components. Only five interaction coefficients h_{rs} exist in face cubic centered structures such as austenitic materials. When strain hardening is isotropic, h is independent of the active slip system. Therefore, in this situation $h_{rs} = 1$. Usually, self-hardening components are lower than latent components. Both isotropic and kinematic hardenings were considered to model the behavior of the material. However, in a first approach [14], it is assumed that $h_{rs} = 1$. Calculations were performed using EDF finite element modeling Code_Aster [15]. Parameters are given in Table 4. Computations were done with an isotropic elasticity (see moduli of elasticity E and Poisson's ratio v in Table 4). Last, lattice rotation was considered, in order to update the orientation of the normal to the slip planes at each step of the computation. Values of mean (σ) and S (Eq. 13) are given in Table 5.

Table 4 Parameters of the crystalline behaviors (elasticity, plastic hardening defined in Eqs. 17–20)

Material registration	Temperature (°C)	E (MPa)	ν	n_s	K_s	c	τ_0 (MPa)	b	Q (MPa)	h_{rs}	d
RND-M-B-369 RND-M-B-356	20	203	0.33	4	10	600	199	2.30	106	1	19.9
	325	210	0.33	4	10	600	177	1.40	165	1	21.1
RND-M-U-589	20	203	0.33	4	10	600	200	1.71	133	1	18.8
	325	203	0.33	4	10	600	140	4.43	84	1	35.8
RND-M-U-510	20	240	0.33	4	10	600	164	2.14	119	1	21.1
	325	203	0.33	4	10	600	141	1.72	125	1	22.3

Table 5 Results of calculations on the 172-grain aggregate

Specimen	Material	Imposed el. (%)	Final mean(σ_{zz}) (MPa)	Final SD(σ_{zz}) (MPa)	S
1866–90	RND-M-U-589	15.0	774	984	1.27
1866–91	RND-M-U-589	2.5	467	316	0.68
1866–98	RND-M-B-369	10.0	767	849	1.11

Initiation Criterion

The initiation is supposed to be possible as soon as a critical depth of intergranular oxidation is reached. The model assumes that initiation is possible as soon as a critical depth of intergranular oxidation is reached together with a critical stress to oxide failure. The critical stress to fail oxidized grain boundaries was evaluated combining the experimental results of a tensile test with results of FEM on the polycrystalline aggregate. The procedure involved the following steps.

Oxidation of a Non-stressed Tensile Specimens
Tensile specimens were cut (L orientation) by electro-discharge machining in RND-M-B-356 and RND-M-U-589 bars, then mechanically polished down to 1 μm and finally polished with colloidal silica for 30–40 min under a load of 20 N. Prior to the oxidation test, the specimen was ultrasonically cleaned in ethanol then in distilled water. The specimen was insulated from the Hastelloy (C-276) autoclave by oxidized Zircaloy to avoid galvanic coupling. Oxidation was conducted in a loop under open circuit conditions during 1000 h. The environment simulated a PWR primary water (1000 ppm B as boric acid, 2 ppm Li as lithium hydroxide, 20 ml H_2 kg^{-1} water) at 360 °C.

Tensile Test Under Vacuum at 360 °C
The oxidized specimen was pulled using in-situ SEM tensile machine MTEST5000 W model (5 kN). The tensile test was stopped every 1% elongation for detailed inspection of the surface of the specimen. The test was definitely stopped as soon as clearly defined intergranular cracks were observed (Fig. 5). SEM examinations on cross sections showed that cracking occurred either within the intergranular oxide or at the metal/oxide interface (Fig. 6).

Fraction of Cracked Grain Boundaries
After tensile test on the oxidized specimen, the fraction F_{CGB} of cracked grain boundaries was estimated by dividing the total number of cracked grain boundaries by the total number of grain boundaries observed on a cross section. The estimated F_{CGB} are given in Table 6. In the following, results collected on specimen 1866–90 will not be considered: a more accurate estimation of the stress to fail oxidized grain boundaries is expected using results reached on specimen 1866–91, cut from the same bar, but that experienced a lower elongation (leading to a lower F_{CGB}).

Cracking Criterion for Oxidized Grain Boundaries
The local stresses σ in the microstructure were fitted by Gaussian distributions (see Figs. 7, 8 and 9). For example, for a mean stress of 531 MPa in the RND-M-U-589 aggregate, the standard deviation of the local stresses was estimated to be 361 MPa using Eq. 13 with S = 0.68.

Stresses usually exhibit wider distributions close to GBs. Therefore, it was assumed that sufficiently oxidized grain boundaries that failed were those subjected to the highest stress. Using quantile functions, the stress representing 35% of the highest loaded GBs, would statistically correspond to about 670 MPa in alloy

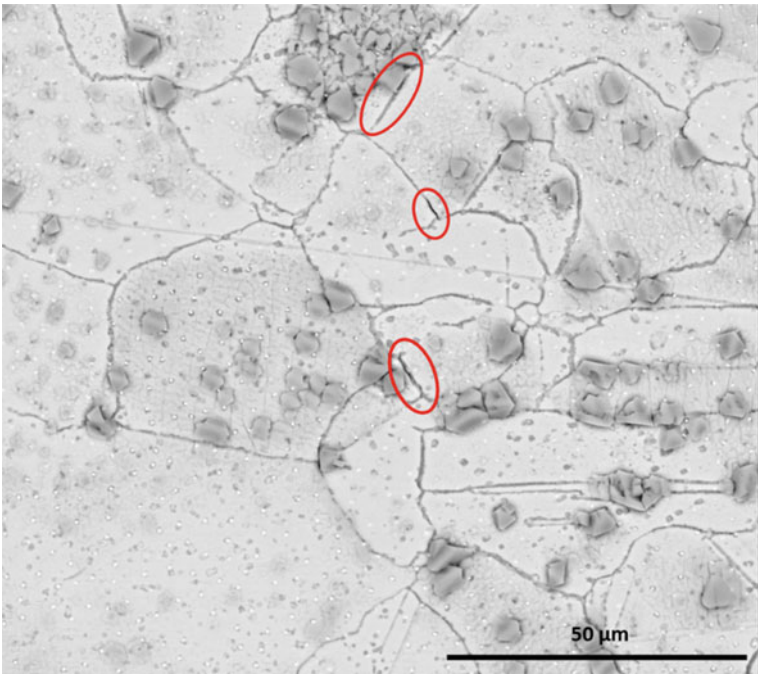

Fig. 5 SEM observation of cracked GBs after 2.5% el. at 360 °C of the specimen registered 1866–91 (RND-M-U-589)

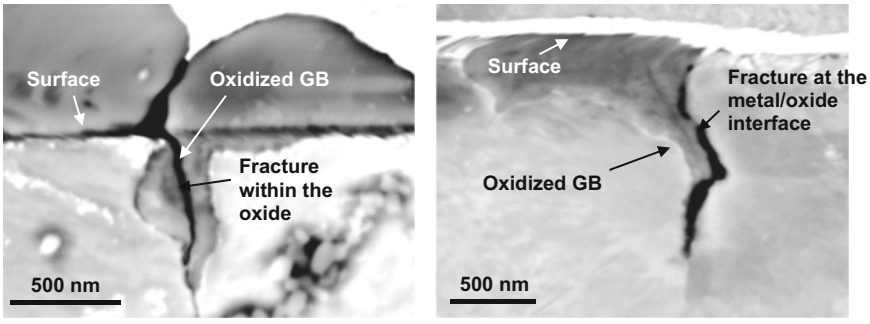

Fig. 6 Intergranular cracking within the oxide (left) and at the metal/oxide interface (right), observed on the RND-M-U-589 bar (1866–91) after 2.5% el. in vacuum at 360 °C

Table 6 Results of tensile tests on oxidized specimens

Material	Specimen	F_{CGB} (%)	Final stress (MPa)	Final el. (%)	Average IG oxidation depth (nm)	IG oxidation depth (nm) required to observe cracking	IG oxidation depth (nm) leading to systematic cracking
RND-M-U-589	1866–90	73	704	15.0	786 ± 405	200	1400
RND-M-U-589	1866–91	35	531	2.5	999 ± 412	300	2400
RND-M-B-356	1866–98	42	734	10.0	954 ± 393	400	1700

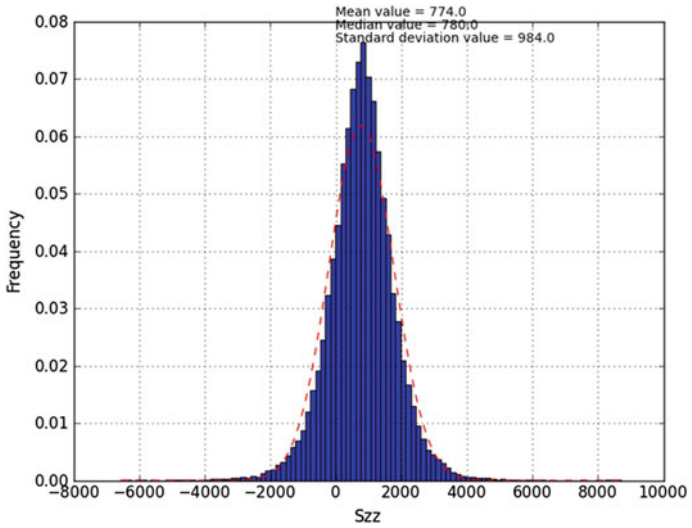

Fig. 7 Histogram of σ_{zz} stress after 15% el. of the aggregate (RND-M-U-589) along z-axis

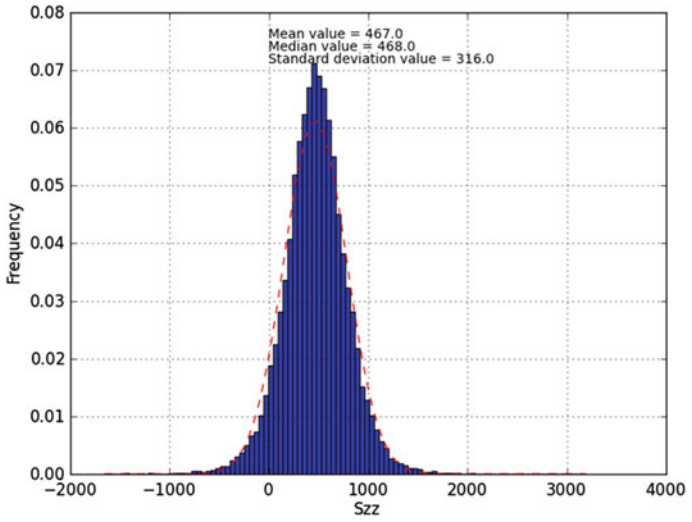

Fig. 8 Histogram of σ_{zz} stress after 2.5% el. of the aggregate (RND-M-U-589) along z-axis

RND-M-U-589. The stress representing 42% of the highest loaded GBs, would statistically correspond to about 900 MPa in alloy registered RND-M-B-356. Details are given in Tables 7 and 8. Note that a deeper critical oxidation depth was observed for the second material (leading to a lower susceptibility to SCC initiation).

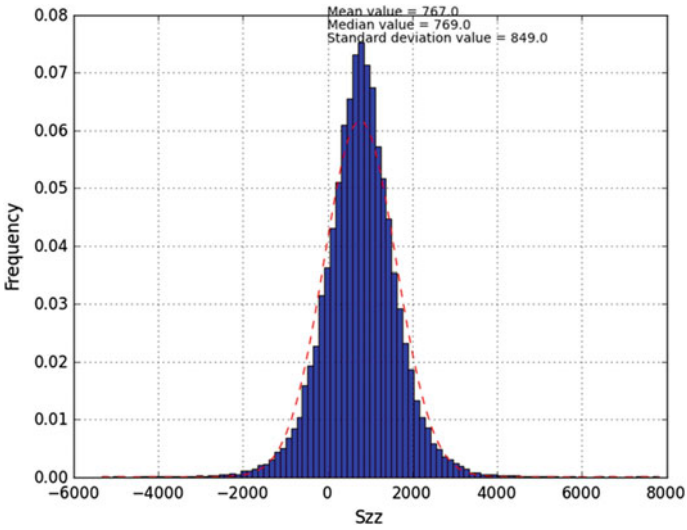

Fig. 9 Histogram of σ_{zz} stress after 10% el. of the aggregate (RND-M-B-369 and RND-M-B-356) along z-axis

Table 7 Calculated stress to fail at 360 °C oxidized grain boundaries

Specimen	Material	*Mean* (σ_{zz}) (MPa)	*S*	*SD* (σ_{zz}) (MPa)	F_{CGB} (%)	Estimated stress (MPa) to fail oxidized grain boundaries
1866–91	RND-M-U-589	531	0.68	361	35	670
1866–98	RND-M-B-356	734	1.11	815	42	900

Table 8 Cracking criteria to fail at 360 °C oxidized grain boundaries

Material	Critical oxidation depth (nm)	Estimated stress (MPa) to fail oxidized grain boundaries
RND-M-U-589	300	670
RND-M-B-356	400	900

In a first approach, the initiation criterion at 360 °C for Alloy 600 was assumed to be the critical stress of 670 MPa applied on a GB oxidized deeper than 300 nm (most severe criterion). This criterion corresponds to the heat RND-M-U-589, recognized for its high susceptibility to SCC.

Crack Growth

The transition to the slow crack growth regime is supposed to occur as soon as initiation happened, at a depth corresponding to the critical depth of intergranular oxidation (300 nm for the heat RND-M-U-589).

The f_H dependency to dissolved hydrogen concentration and associated ΔEcP (Eq. 15) is based on parameters proposed by Young [16]. Parameters for the fast crack growth regime and K transition from slow to fast crack growth regime are shown in Table 9 and in agreement with the original CGR law (obtained from fatigue pre-cracked Compact Tension specimens) [5]. Parameters of the slow crack extension regime were fitted in a different study [12].

K was calculated with Eqs. 22–25. These equations were fitted using FEM calculations on Open C-ring specimens with different crack depths.

$$K = Aa^2 + Ba + C \tag{22}$$

where K is in MPa $m^{0.5}$. A, B and C are functions depending on the stress σ_i at the initiation site, perpendicular to the crack extension:

$$A = \min\{-0.07672\sigma_i + 5.579, 1.6300\sigma_i + 967.9\} \tag{23}$$

$$B = \max\{0.1252\sigma_i - 7.274,\ 1.7281\sigma_i - 995.76\} \tag{24}$$

$$C = \max\{0.009652\sigma_i + 1.829, 0.2642\sigma_i - 160.38\} \tag{25}$$

Results

SCC predictions are detailed in Table 10 and illustrated in Fig. 10. Regarding the hot rolled bar registered RND-M-B-369, in four cases, stresses to initiation are lower than 350 MPa. Strains at initiation sites are always lower than 0.08. Therefore, even if strain was not taken into account in the initiation stage in the current model, it may be supposed that it has no major consequence on the predictions. Final K are always lower than 25 MPa $m^{0.5}$. In fact, a detailed study of K

Table 9 Parameters of the sigmoid crack growth law (CR orientation)

Material	g_1	g_2	g_3	g_4	Q_g (J/mol)	f_1	f_2	f_3
RND-M-B-369	8.61×10^9	0.48	0.4	12	130,000	3.604	11.33	43.36
RND-M-U-589	1.80×10^{10}	0.50	0.8	12				
RND-M-U-510	8.61×10^9	0.48	0.4	12				

Table 10 Cracking depth predicted with FEM post analyses, chaining the local model and the sigmoid crack growth behavior of the material

Specimen	Material	Observed		Calculated				
		Cumulated time (h)	SCC depth (μm)	Stress (MPa)	Strain (MPa)	Final K (MPa $m^{1/2}$)	Final time (h)	Final depth (μm)
1650–06	RND-M-B-369	6010	1290	318	0.006	17.7	8011	1118
1650–08	RND-M-B-369	3000	140	346	0.076	9.0	1500	140
1650–09	RND-M-B-369	2000	1290	408	0.048	19.8	1754	1221
1650–10	RND-M-B-369	2000	1100	474	0.030	25.3	1272	1110
1650-14	RND-M-B-369	8705	1150	402	0.006	18.0	6971	1151
1650–20	RND-M-B-369	8705	10	435	0.044	1.0	200	10
1650-38	RND-M-B-369	6010	1260	336	0.006	16.8	6607	1261
1650–42	RND-M-B-369	2005	913	425	0.041	25.1	1446	967
1650–43	RND-M-B-369	2005	1226	324	0.006	16.5	7556	1250
1650–44	RND-M-B-369	2005	1187	444	0.033	22.2	1436	1240
1650–45	RND-M-B-369	2005	1240	448	0.034	22.2	1386	1250
1650–46	RND-M-B-369	1000	323	465	0.025	18.9	1095	302
1650–49	RND-M-U-589	1000	63	348	0.031	12.5	2036	232
1650–59	RND-M-U-510	4010	720	318	0.030	18.6	769	712

Opening stress and strain (calculated by 3D FEM) at the initiation site, as predicted by FEM post analyses

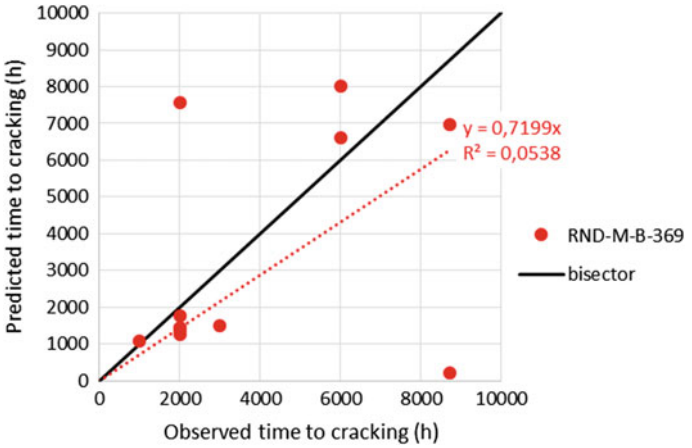

Fig. 10 Predicted times to reach observed crack depth versus times to observed crack depth. Calculated with FEM post analyses, chaining the local model with a sigmoid crack growth law. The largest deviation between observed and predicted time to cracking correspond to the shortest crack depth (10 μm)

values along the crack growth path clearly indicates that estimated crack growth rates are probably not highly accurate in the current predictions, due to a lack of experimental data at low K. Finally, all predicted times to initiation are very brief (lower than 100 h). This is due to the lack of accuracy of the intergranular oxidation rate in the earliest times to oxidation: the current oxidation model overestimates the maximum oxide depth in the first hundreds of nanometers.

Nevertheless, as shown in Fig. 11, in average on the current database (RND-M-B-369 bar, TT820 °C), the prediction of the local model is closer to observations than the predictions based on the model index approach for initiation, despite the fact that the parameters of the slow crack growth regime were optimized using the index model (not the local model). The local model simulation of the test on specimen 1650–49 cut in the bar RND-M-U-589 is in good agreement with the observation. Indeed, this material has a low GBC, leading to a fast intergranular oxidation rate, which is well predicted by the oxidation model. Regarding specimen 1650–59 cut from RND-M-U-510 bar, with a quite high GBC (40%), the prediction of the local model chained with the crack growth behavior of the heat RND-M-B-369 is too conservative. Nevertheless, the prediction of the model could be improved after the calibration of the actual crack growth behavior of the bar RND-M-U-510. The same initiation parameters were used for every heat (the most severe). Future work could considered heat to heat parameters when additional data will be collected. It may help to be reach a better fit in the case of the heat RND-M-B-369, increasing the time to initiation.

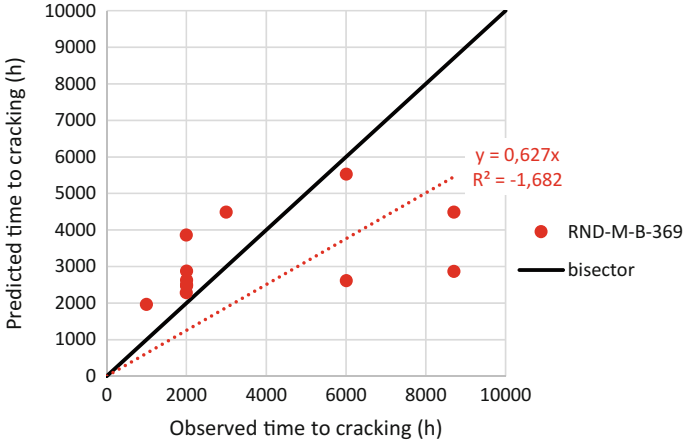

Fig. 11 Predicted times to reach observed crack depth versus time to observed crack depth in the RND-M-B-369 bar. Calculated with FEM post analyses, chaining the index model (with average i_m) with a sigmoid crack growth law. The largest deviation between observed and predicted time to cracking correspond to the shortest crack depth (10 μm)

Discussion

Comparison of the Models
The index model delivers a time to initiation without associated crack depth, contrary to the local model. The model index is a purely empirical model whereas the local model relies on a simple cracking mechanism, but which is believed to be consistent with current mechanistic understanding.
The 'local' model is based on a progressive weakening of GBs due to oxidation (incubation) leading to initiation by the mechanical failure of the highest stressed GB, followed by a slow then fast crack extension. The reliability of such a scenario still has to be proved.

Initiation is always possible according to the index model, even if an extremely long time is predicted, whereas the local model can predict that initiation is impossible under some circumstances (if the critical oxidation depth or the stress to fail grain boundaries are never reached).

The calibration of the parameters of the index model requires IGSCC results. For highly IGSCC resistant materials, the model calibration is a challenge and a long term action. By contrast, the calibration of the local model is based on a fit of more simple behaviors (IG oxidation, failure of oxidized GBs) which are capable of estimation using suitable testing or calculation. Therefore, the local model can be calibrated in the short term and validated in the long term (for highly resistant materials).

Benefits of the Local Model The model relies on a cracking scenario and physical mechanisms. Therefore, it is easier to extrapolate, to incorporate additional effects (dissolved hydrogen or zinc) or to upgrade current behavior predictions. The incubation period is explicitly modeled.

The probability to initiate IGSCC relies on the behavior of a population of grain boundaries emerging at the surface exposed to the primary water. Therefore, the probability to initiate will increase with the density of (susceptible) grain boundaries suffering from oxidation.

Benefits of the Simulation of SCC Tests
FEM post analysis allows to better evaluate IGSCC models and better fit model parameters, chaining available initiation with crack growth at large scales (from microns to millimeters). Analyses are no more restricted to a single stage of the degradation. Thus, a global view of the degradation is systematically delivered.

The methodology allows reducing/clarifying some classical assumptions (stress, chaining between IGSCC stages).

Current Main Limitations
The main limitations of the current model are:

- The lack of accuracy of the cracking kinetics in the slow crack growth regime.
- The non-simulation of the influence of the surface finish (residual stress and strain gradients at the surface) of specimens.

- The lack of accuracy of the cracking criteria of oxidized GBs.

In addition, a physically based oxidation model could be preferred to the proposed empirical model. Finally, regarding the mechanical behavior, it will be necessary to validate the prediction of stress at the grain boundaries. Indeed, opening stresses play a major role in initiation. Furthermore, kinematic hardening and viscosity have to be improved: the same set of parameters cannot predict properly strain-stress cycles of low and large strain amplitudes and stress relaxation has to be well predicted.

Conclusions

The proposed model relies on the description of a cracking scenario involving successive stages: incubation, crack initiation, slow crack extension then fast crack extension. Each stage of the model is controlled by a local parameter, recognized to play a role in the mechanism according to the current knowledge. Oxidation and stress at grain boundaries are statistically coupled to predict initiation. The major benefit of the proposed model is to deliver a time-depth couple at each stage of the degradation (from incubation to fast crack growth).

The 'local' approach allows bridging scales: results of TEM examinations are used to calibrate the model developed to predict SCC kinetics at a large scale.

Last, the model could be calibrated for different materials and environment such as Alloy 600 exposed to secondary side, stainless steels and high strength materials exposed to primary water.

In the future, the challenge will be (1) to better correlate local parameters to macroscopic parameters and (2) to correlate macroscopic parameters to manufacturing conditions (which influence surface finish and hence SCC initiation) and (3) to validate SCC predictions at the scale of the component [12].

References

1. S. Le Hong, C. Amzallag, A. Gelpi, Modelling of stress corrosion crack initiation on alloy 600 in primary water of PWRs, in *9th International Conference on Environmental Degradation of Materials in Nuclear Systems-Water Reactors*, Newport Beach (California), (1999)
2. J.M. Boursier, Y. Rouillon, S. Le Hong, Relationship between microstructure and PWSCC susceptibility in wrought alloy 600. Eurocorr', (2000)
3. F. Vaillant et al., Crack growth rates on vessel penetrations in alloy 600 in primary water. Fontevraud 4, (1998)
4. F. Vaillant et al., Crack growth rates in thick materials of alloy 600 and weld metals of alloy 182 in laboratory primary water. Comparison with field experience. Fontevraud 5, (2002)
5. T. Couvant, F. Vaillant, E. Lemaire, 'Stress corrosion crack growth rate in rolled alloy 600 exposed to primary PWR environment', in *14th International Conference on Environmental*

Degradation of Materials in Nuclear Power Systems-Water Reactor, Virginia Beach (Virginia), 2009
6. T. Couvant, M. Wehbi, C. Duhamel, J. Crépin, R. Munier, 'Development of a local model to predict SCC: preliminary calibration of parameters for nickel alloys exposed to primary water', in *17th International Conference on Environmental Degradation of Materials in Nuclear Systems-Water Reactors*, Ottawa (Canada), 2015
7. M. Wehbi, T. Couvant, C. Duhamel, J. Crépin, Oxidation of nickel-base welds 182 and 82 in simulated primary water of pressurised water reactors. Mater. High Temp. **32**(1–2) (2015)
8. C. Duhamel, M. Wehbi, T. Couvant, J. Crepin, Grain Boundary Oxidation of Nickel Base Welds 182/82 in Simulated PWR Primary Water, in *17th International Conference on Environmental Degradation of Materials in Nuclear Systems-Water Reactors*, Ottawa (Canada), 2015
9. J. Caballero, J. Crépin, T. Couvant, C. Duhamel, Intergranular oxidation of alloy 600 exposed to simulated PWR primary water. Eurocorr, Pisa (Italy), 2014
10. L. Thomas, M. Olszta, B. Johnson, S. Bruemmer, Microstructural characterization of primary water stress-corrosion cracks in Alloy 182 welds from PWR components and laboratory tests, in *14th International Conference on Environmental Degradation of Materials in Nuclear Power Systems-Water Reactors*, Virginia Beach (Virginia), 2009
11. S. Attanasio, D. Morton, Measurement of the Nickel/Nickel Oxide Transition in Ni-Cr-Fe Alloys and Updated Data and Correlations to Quantify the Effect of Aqueous Hydrogen on Primary Water SCC, in *11th International Conference on Environmental Degradation of Materials in Nuclear Power Systems-Water Reactors*, Stevenson (Washington), 2003
12. T. Couvant, Prediction of IGSCC as a FEM post analysis, in *18th International Conference on Environmental Degradation of Materials in Nuclear Systems-Water Reactors*, Portland (Oregon), 2017
13. D. Morton, S. Attanasio, G. Young, Primary water SCC understanding and characterization through fundamental testing in the vicinity of the nickel/nickel oxide phase transition, in *10th International Conference on Environmental Degradation of Materials in Nuclear Power Systems-Water Reactors*, Lake Tahoe (California), 2001
14. G. Cailletaud, A micromechanical approach to inelastic behaviour of metals. Int. J. Plast **8**(1), 55–73 (1992)
15. www.code-aster.org
16. G. Young, W. Wilkening, D. Morton, E. Richey, N. Lewis, The mechanism and modeling of intergranular stress corrosion cracking of nickel-chromium-iron alloys exposed to high purity water, in *12th International Conference on Environmental Degradation of Materials in Nuclear Power Systems-Water Reactor*, 2005

Prediction of IGSCC as a Finite Element Modeling Post-analysis

Thierry Couvant

Abstract A numerical approach was developed to predict Stress Corrosion Cracking (SCC) kinetics and location, in 3D. The calculation is a fast post finite element modeling analysis chaining IGSCC initiation and crack growth models. Firstly, the proposed methodology offers the possibility to optimize the calibration of models, when SCC tests are simulated. Secondly, calibrated models can be used to predict SCC in large structures. In the proposed paper, benefits and limitations of the methodology will be introduced.

Keywords SCC · Alloy 600 · Intergranular oxidation · Crystal plasticity · Fracture of oxidized grain boundaries · Local model · Initiation · Sigmoid crack growth · Code_Coriolis

Background

As a consequence of the operational experience on Alloy 600, EDF needs to understand observed in-service cracking. It is also necessary to evaluate possible mitigating methods in operating Pressurized Water reactors (PWRs): changes in water chemistry (increasing dissolved hydrogen, zinc injection), improvement of surface finishes (introducing compressive stresses), replacement of materials (increasing chromium content) or changes in design (reducing stress concentrations). Such mitigations aim at extend the lifetime of components.

To date, EDF predicts Intergranular Stress Corrosion Cracking (IGSCC) of Alloy 600 based on two isolated stages of cracking: initiation (involving incubation and the slow crack growth regime) and fast crack growth.

Thus, an 'index' model was proposed for Alloy 600 [1, 2] where the time to initiation t_i (Eq. 1) depends on a material index i_m defining the intrinsic susceptibility to IGSCC of the material [3], on a temperature index i_T (Eq. 2) expressing the

T. Couvant (✉)
EDF R&D, Avenue des Renardières, 77250 Moret-sur-Loing, France
e-mail: thierry.couvant@edf.fr

J.H. Jackson et al. (eds.), *Proceedings of the 18th International Conference on Environmental Degradation of Materials in Nuclear Power Systems – Water Reactors*, The Minerals, Metals & Materials Series, https://doi.org/10.1007/978-3-319-68454-3_26

dependency to an activation energy Q_i, and on a stress index i_σ (Eq. 3), where the stress σ is higher than yield stress.

$$t_i = \frac{10,000}{i_m \times i_\sigma \times i_T} \tag{1}$$

$$i_T = 9.45 \times 10^{15} \times \exp\left(\frac{-Q_i}{RT}\right) \tag{2}$$

$$i_\sigma = 2.44 \times 10^{-11} \times \sigma^4 \tag{3}$$

where R = 8.314 J mol^{-1} K^{-1} and Q_i = 180 kJ mol^{-1}.

The crack growth rate (CGR) was modeled (Eq. 4) for Alloy 600 [4–6] assuming a threshold K_{ISCC} in *K for crack growth*, a dependency on temperature (with an activation energy Q_c) and a dependency f_{CW} on cold work (CW).

$$\text{Max}(CGR) = C_1(K - K_{ISCC})^{C_2} \times f_{CW} \times \exp\left(\frac{-Q_c}{RT}\right) \tag{4}$$

where C_1 and C_2 are constant depending on manufacturing parameters (rolling versus forging, for example). For Alloy 600, it was assumed that Q_c = 130 kJ mol^{-1}.

The main limitations of such an approach are:

- The absence of crack depth associated with the predicted time to initiation. As a consequence, the chaining between initiation and fast crack growth is only possible if the time to initiation is assumed to be the time to reach K_{ISCC}.
- The difficulty to incorporate in predictions, with relevance, new controlling parameters (dissolved hydrogen, zinc injection, cold work, strain path).
- The absence of underlying mechanism (incubation, initiation, crack growth). In particular, parameters used to predict an initiation are macroscopic parameters, while IGSCC is a local phenomenon.

In this context, recent EDF Researches aimed at improving the prediction of IGSCC, upgrading and developing new models implemented in a dedicated software (Code_Coriolis) to evaluate the IGSCC susceptibility of components, such as reactor vessel nozzles, bolts, pins, etc.

New IGSCC Models

The assumed IGSCC scenario relies on local parameters. While no crack is present (incubation, initiation), 'local' refers to grain boundaries (GB), where the degradation happens. As soon as cracking occurs, 'local' refers to the intergranular crack tip. The modeled scenario is the following:

- **Incubation**: time to reach a critical oxidation depth. It is assumed that exposure to primary water allows oxidation of emerging GBs and that oxidation strongly decreases the stress to fail them as soon as the critical oxidation depth is reached. Regarding nickel alloys 600 and 182, the intergranular oxidation rate mainly depends on temperature, grain boundary coverage (GBC) with chromium carbides and dissolved hydrogen in primary water [7–9].
- **Initiation**: probability to reach the critical stress to fail a sufficiently oxidized grain boundary.
- **Crack extension**: successive cracking of intergranular oxide extensions ahead of the crack tip.

Although the reliability of such a simple scenario still has to be proved, the local model starts to offer relevant predictions.

Parameters of the oxidation law were calibrated for Alloy 600 [10] and Alloy 182 [11] thanks to transmission electron microscope (TEM) and Scanning Electron Microscope/Focused Ion Beam (SEM/FIB) examinations. Indeed, these observations provided the required input parameters (grain boundary length, GBC, maximum oxidation depth, environmental conditions…). Figure 1 compares observed intergranular oxidation depths with predicted ones for Alloy 600. Current fitted parameters slightly overestimate oxidation depths (<2 μm). A similar trend is observed for Alloy 182. Therefore, the use of current oxidation parameters to predict IGSCC initiation leads to conservative times to initiation. A better

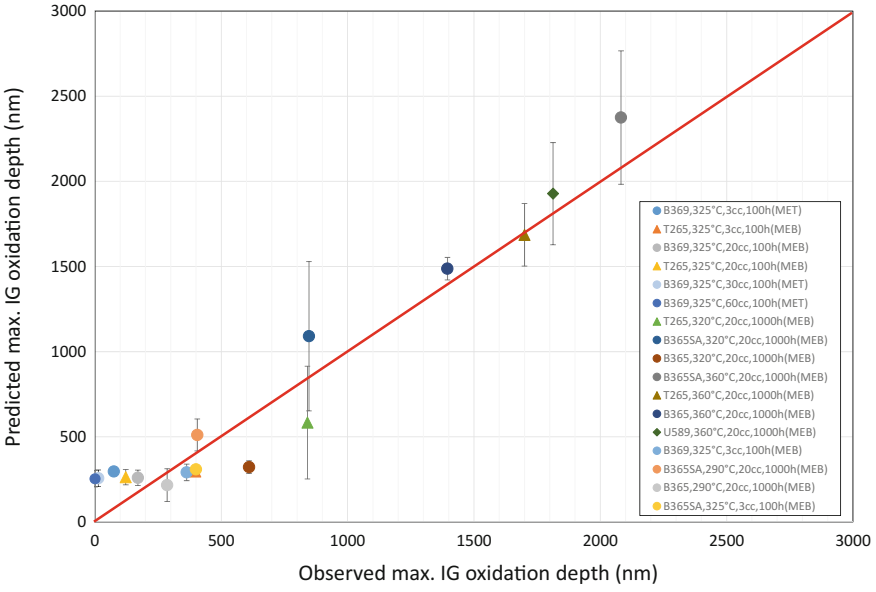

Fig. 1 Comparison between predicted and observed maximal intergranular oxidation depth in Alloy 600 [10]. The comparison covers large ranges of temperature (290–360 °C), DH (3–60 ml kg^{-1}), GBC (0–58%) and times (100–1000 h)

prediction of the short oxidation length will be necessary in the short term, considering for example the effects of stress and plastic strain. The logarithmic dependency on time could also be revised.

In order to guarantee a simple chaining between initiation and growth regime, the crack growth rate was assumed to have a sigmoid dependency to K. Indeed, such a dependency allows to consider both the slow and fast crack growth regimes. The crack extension law (upper bound) is given in Eq. 5. It depends on K (in MPa $m^{1/2}$) and T (in K). Q_g is the activation energy for crack growth CGR (in $\mu m\ h^{-1}$).

$$\max(CGR) = g_1 \times \frac{K^{g_2}}{1 + \exp[-g_3 \times (K - g_4)]} \times h(DH) \times f(\varepsilon) \times \exp\left(\frac{-Q_g}{RT}\right) \quad (5)$$

where g_1 to g_4 are constants, $h(DH)$ is the dependency on dissolved hydrogen (DH) and $f(\varepsilon)$ is the dependency on plastic deformation (ε). Crack growth parameters were calibrated for different materials in other studies [10, 11].

Methodology to Predict SCC

In parallel with the improvement of existing Stress Corrosion Cracking (SCC) models and the development of the new 'local' model, a methodology was selected to easily apply it on specimens and PWR components. The proposed Finite Element Modeling (FEM) post analysis (Fig. 3), named Code_Coriolis, offers a 3D study, closer to the actual situation than traditional 1D or 2D approaches. Kinetics and crack growth paths are predicted. Statistics on initiation time and cracking locations are possible. FEM post analysis allows to better evaluate the relevance of SCC models and to better fit model parameters, chaining initiation with crack growth at large scales (from nanometers to centimeters). Thus, analyses are not restricted to a single stage of the degradation and a global view of the degradation is systematically delivered (Fig. 2).

As illustrated in Fig. 3, a model is first meshed using the GEOM and SMESH modules of the Salomé_Méca numerical platform [12]. Second, stresses and strain are calculated in the model based on Code_Aster FEM code [12]. The SCC computation uses as an input the mesh and the associated stress/strain fields. In addition, environmental conditions and SCC initiation and crack growth models have to be selected. The computation is performed following the algorithm given in Fig. 4. If the local model is selected to predict initiation, a grain boundary sampling is required to feed the initiation model (involving an incubation model). A more detailed algorithm for the use of the local model was introduced in a previous paper [11]. After SCC computation, it is possible to visualize sites for SCC initiation and the path followed by the main crack tip within the model.

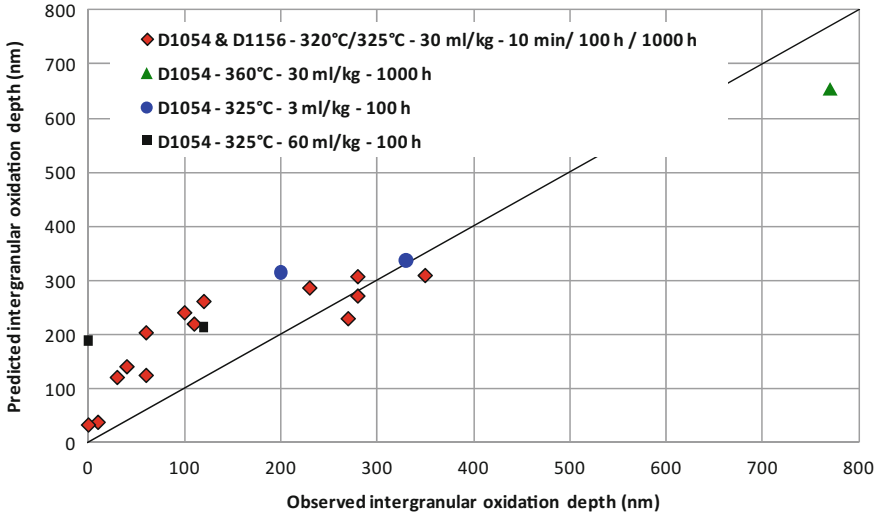

Fig. 2 Comparison between predicted and observed intergranular oxidation depths in Alloy 182 [11]

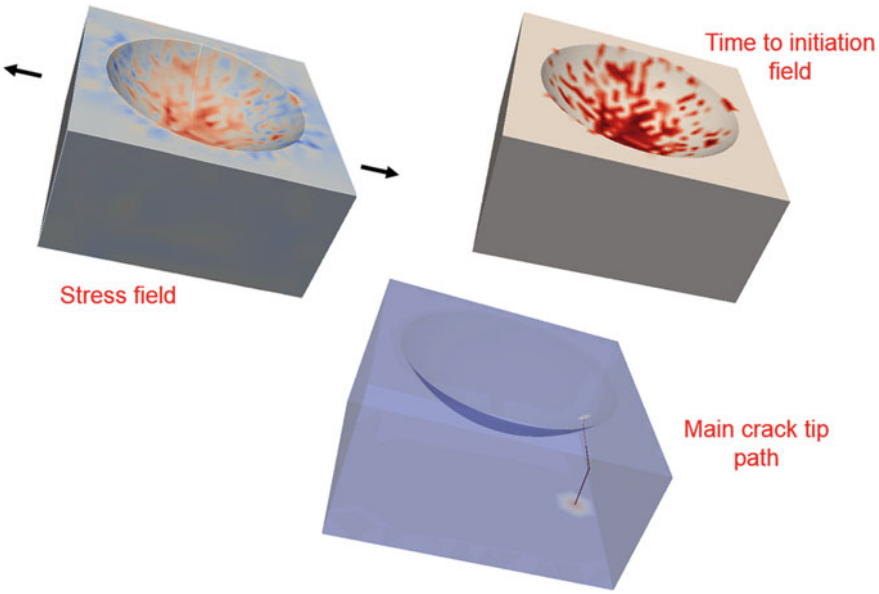

Fig. 3 Main input/outputs of the SCC prediction as a post analysis (with Code_Coriolis) of FEM computation (with Salomé_Méca)

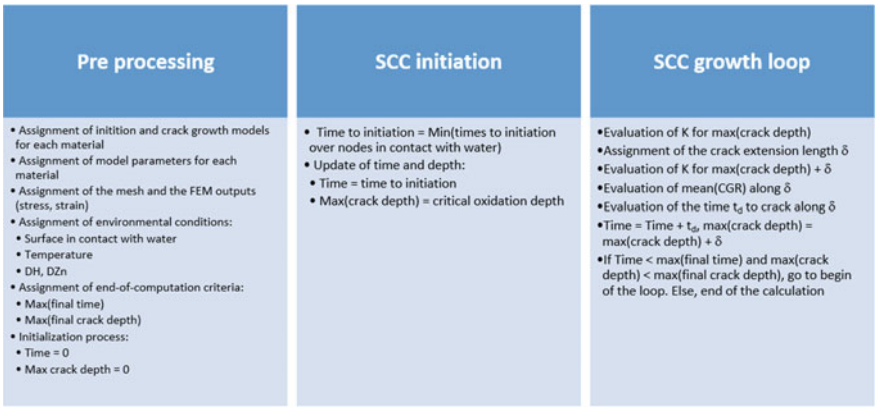

Fig. 4 General algorithm for the SCC computation (with Code_Coriolis)

Simulating SCC Laboratory Tests

The simulation of laboratory IGSCC tests ('initiation') is an efficient way to better calibrate models. In the following, the simulation of an initiation test on Open C-Ring (OCR) specimen designated as 1650–42 (Fig. 5) cut in Alloy 600 designated as RND-M-B-369 [10] is illustrated. First, stresses at the testing temperature (360 °C) were calculated (Fig. 6), taking into account the prior loading at room temperature. Second, SCC behaviors were selected:

- Local model with parameters fitted for Alloy 600 designated as RND-M-B-369 (TT820 °C).
- CGR sigmoid law with parameters fitted for Alloy 600 (TT820 °C) designated as RND-M-B-369.

Third, environmental conditions were assigned at the surface: 360 °C, 30 ml of dissolved hydrogen per kg water. Finally, the function allowing to properly calculate the stress intensity factor K in such a specimen [10], as a function of crack depth, was selected. After SCC computation, different results were extracted:

- The map of the predicted times to initiation at the surface of the specimen (Fig. 7).
- The histogram of the predicted times to initiation at the surface of the specimen (Fig. 8).
- The cumulated fraction of initiation sites (nodes of the mesh) as a function of time, at the surface of the specimen (Fig. 9).
- The SCC kinetics and the observed final SCC depth, reported for comparison (Fig. 10). Parameters of the models (initiation, crack growth, K) can be tuned to guarantee that predictions will match with observations.
- The stress intensity factor (K) and crack growth rate (CGR) along the main crack tip as a function of crack depth (Fig. 11). Thanks to the specific function

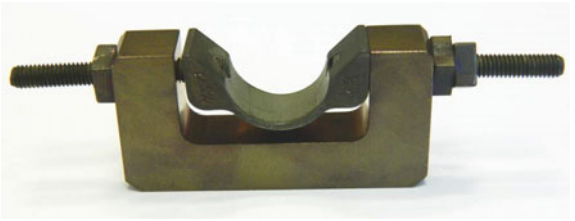

Fig. 5 Open C-ring loading

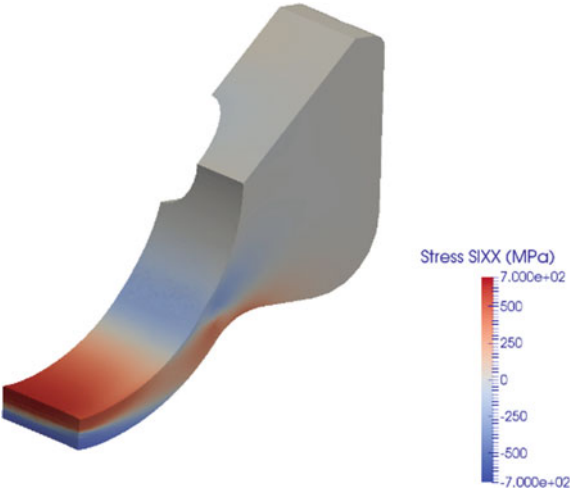

Fig. 6 Stress field at the end of the final loading of the OCR designated as 1650–42

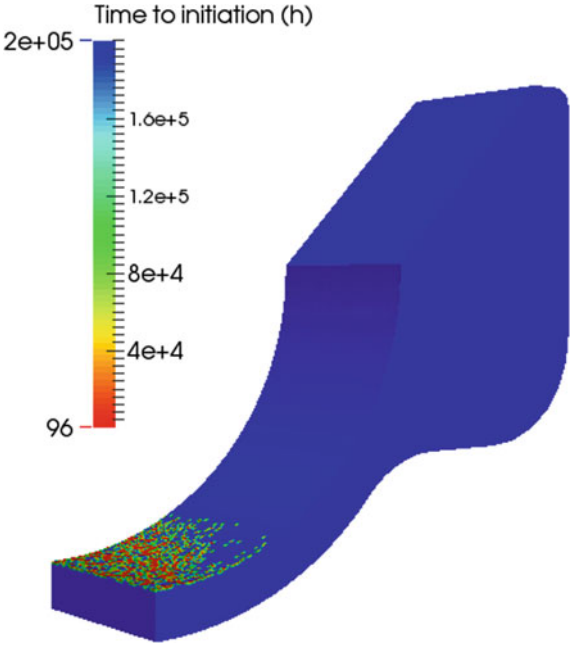

Fig. 7 Map of the predicted times to initiation (with the local model) at the surface of the specimen designated 1650–42 (Alloy 600)

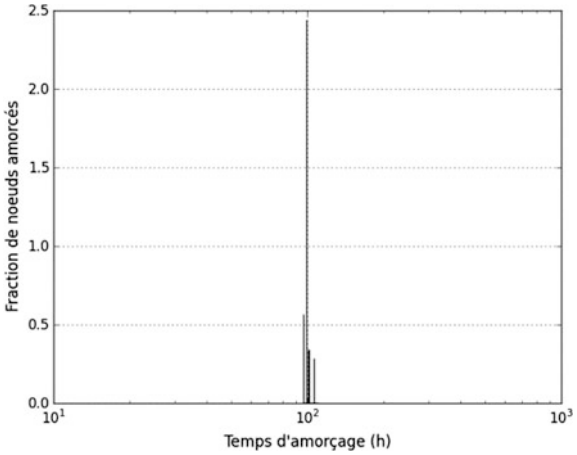

Fig. 8 Histogram of the predicted times to initiation (with the local model) at the surface of the specimen designated 1650–42 (Alloy 600)

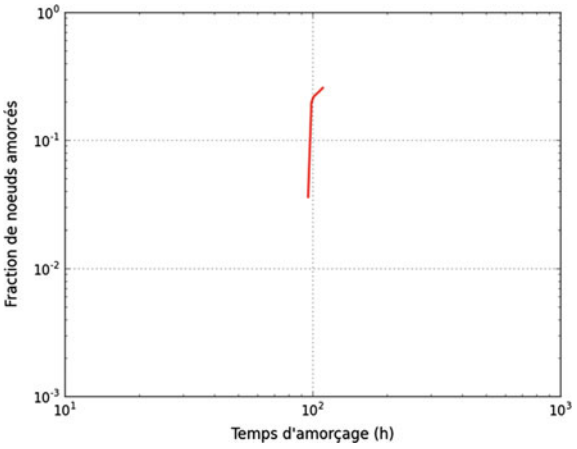

Fig. 9 Predicted (with the local model) cumulated fraction of initiation sites (nodes of the mesh) as a function of time, at the surface of the specimen designated 1650–42 (Alloy 600)

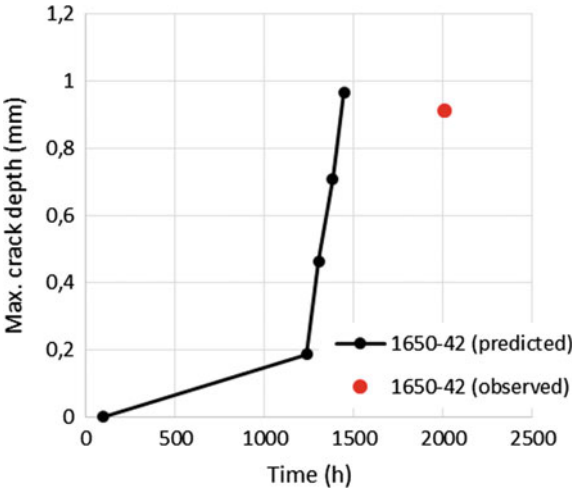

Fig. 10 Predicted (with the local model) SCC kinetics of the specimen designated 1650–42 (Alloy 600). The observed final SCC depth is reported for comparison

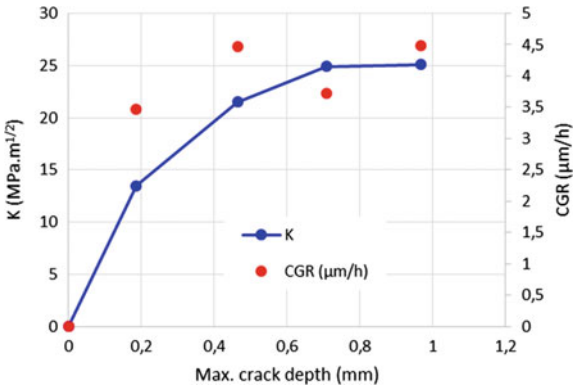

Fig. 11 Predicted stress intensity factor (K) and crack growth rate (CGR) along the main crack tip as a function of crack depth. Specimen designated 1650–42 (Alloy 600)

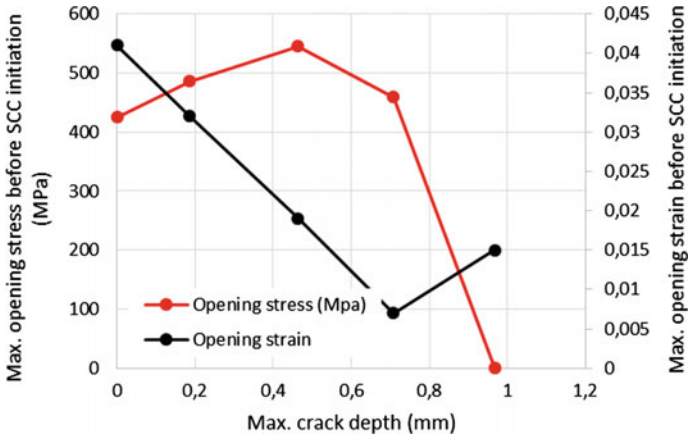

Fig. 12 Predicted opening stress and strain before SCC initiation along the main crack tip as a function of crack depth. Specimen designated 1650–42 (Alloy 600)

calibrated for OCRs a realistic prediction of K was performed, given the initial compressive stress present in some areas of the specimen (Fig. 6).

- The opening stress and strain before SCC initiation along the main crack tip as a function of crack depth (Fig. 12).

Such post-test analyses allow a fast and quantitative comparison of models. For example, in the following, results obtained with the local model are compared with those observed with the index initiation model:

- **Times to initiation** are more continuously distributed at the surface of the specimen (Fig. 13) when the index model is preferred to the local model (Fig. 7). As a consequence, a substantially wider range of times to initiation is

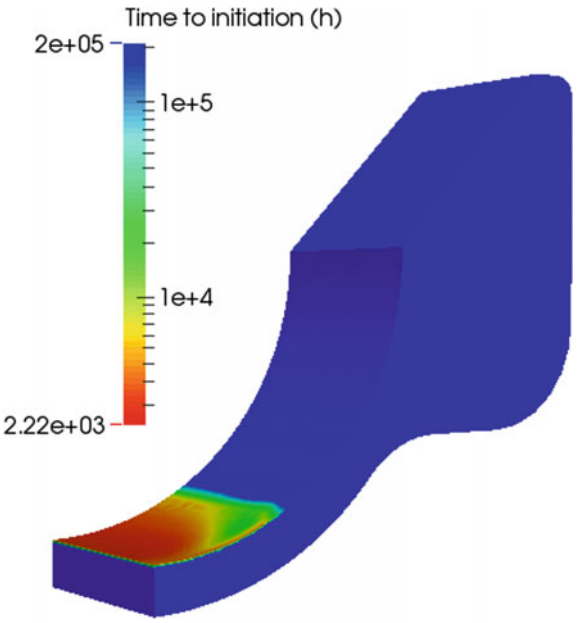

Fig. 13 Map of the predicted times to initiation at the surface of the specimen designated 1650–42 (Alloy 600)

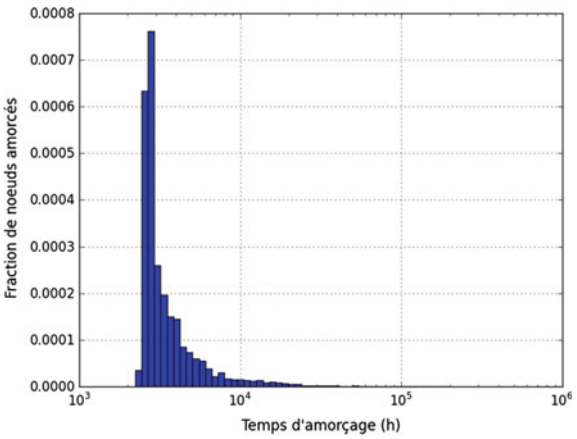

Fig. 14 Histogram of the predicted times to initiation at the surface of the specimen designated 1650–42 (Alloy 600)

observed with the index model (Fig. 14) compared to the local model (Fig. 8) where a more limited number of initiation sites is observed. This is confirmed by the comparison of the asymptote of the cumulated number of initiation sites over time: less than 30% of the nodes of the mesh in the analyzed area for the local model (Fig. 9), compared to more than 80% for the index model (Fig. 15).

- **Global SCC kinetics** are not conservative (Fig. 16) when the index model replaced the local model (Fig. 10). The only difference between the two

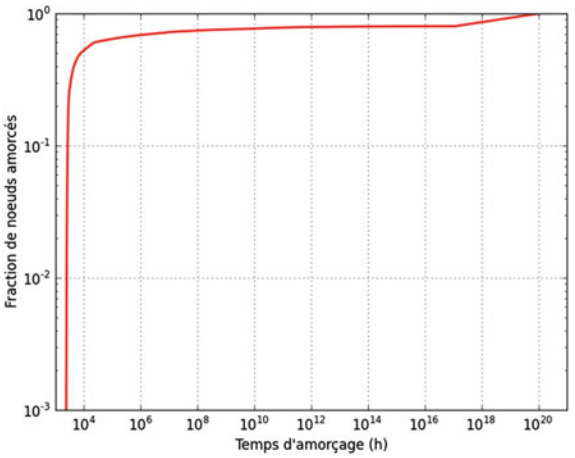

Fig. 15 Predicted cumulated fraction of initiation sites (nodes of the mesh) as a function of time, at the surface of the specimen designated 1650–42 (Alloy 600)

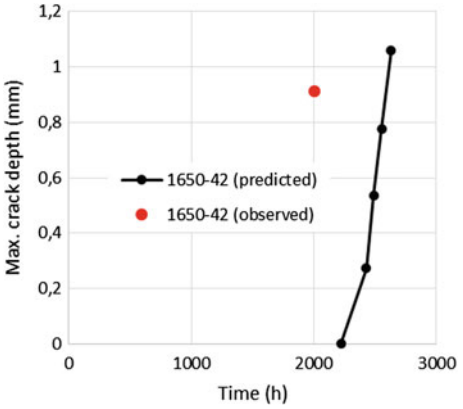

Fig. 16 Predicted SCC kinetics of the specimen designated 1650–42 (Alloy 600). The observed final SCC depth is reported for comparison

simulations is the initiation model: very short initiation (200 nm deep) time for the local model, too long for the index model (longer than the observed time to failure involving a crack growth of 1 mm).

Simulating SCC of Components

The same methodology used for SCC specimens can be directly used at a larger scale to simulate SCC of components. It may be useful:

- To support examinations on retired components.
- To perform parametric studies to evaluate the benefits of mitigations: changes in water chemistry (hydrogen, zinc), surface finish (residual stresses after peening), replacement of materials, or design changes for example.

Figure 17 shows preliminary simulations on a simplified nozzle (index model for the prediction of initiation). The predicted site of initiation is located on an axial defect emerging at the inner surface of the tube (Alloy 600) in front of the weld (Alloy 182). In the current simulation, SCC was only induced by welding residual stresses. Table 1 illustrates a parametric study performed on another simplified nozzle without emerging axial defect. SCC parameters correspond to laboratory materials (Alloys 182 and 600) with a high susceptibility to SCC. Preliminary computations led to the following observations:

- When SCC initiates in the weld, then due to inappropriate meshing, no growth is predicted after initiation when the CGR law is a classical $(K - K_{ISCC})^n$ function. Similar observations were usually reached when laboratory SCC initiation tests were simulated. By contrast, a CGR law with a sigmoid dependency on K guaranties to avoid such artefacts due to meshing.
- When a stress relief heat treatment was simulated, the time to initiation in the weld was multiplied by 19, and the total time to reach 10 mm in depth was multiplied by 27.
- According to the index model, SCC initiates in the base metal (at the inner diameter, in front of the weld), whereas replacing this model by the local model leads to the absence of initiation (up to 10^{20} h). The absence of initiation predicted by the local model is probably mainly due to the very low probability to reach the stress to fail oxidized grain boundaries in a component operating at 290 °C (compared to a specimen usually quite highly loaded at 360 °C).

Figure 18 introduces an example of stress calculation in a bolt made of 316L stainless steel. A stress concentration is observed at the head/shank junction, promoting SCC initiation. As shown in Fig. 19 predicted SCC kinetics decrease when the level of cold work (CW) decreases. In addition, SCC kinetics are higher if the bolt is made of A-286 instead of 25%CW 316L stainless steel (Fig. 20).

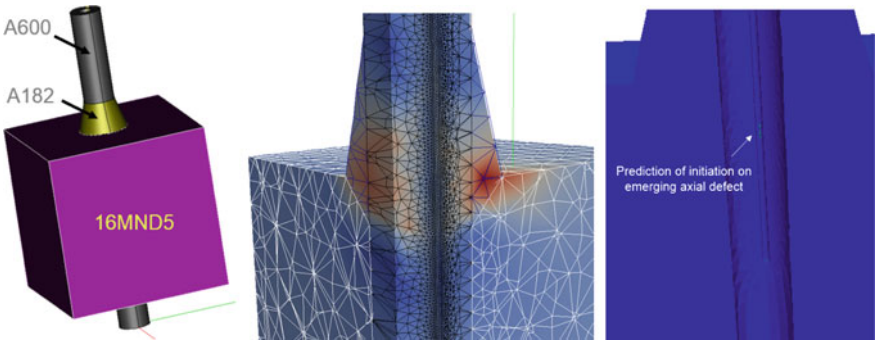

Fig. 17 Predicted site of initiation in a BMI nozzle where an axial defect emerges at the inner surface of the tube (Alloy 600) in front of the weld (Alloy 182). In the current simulation, SCC was only induced by welding residual stresses

Table 1 Preliminary parametric study on the susceptibility to SCC of a simplified nozzle. SCC parameters correspond to laboratory materials with a high susceptibility to SCC

Cracking location	Selected SCC models	Time to initiation (h)	Time to reach 10 mm (h)	Time to initiation relative to the reference	Time to reach 10 mm relative to the reference	Surface stress to initiation (MPa)
A182-AW	Index + K_{th}	29,000	No growth	1	No growth	562
A182-AW	Index + $K_{sigmoid}$	29,000	38,000	1	1	562
A182-SR	Index + $K_{sigmoid}$	554,000	769,000	19	27	366
A600 (TT720 °C)	Index + $K_{sigmoid}$	567,000	628,000	1	1	318
A600 (TT720 °C)	Local + $K_{sigmoid}$	$>10^{20}$	No SCC	$>10^{14}$	No SCC	No SCC

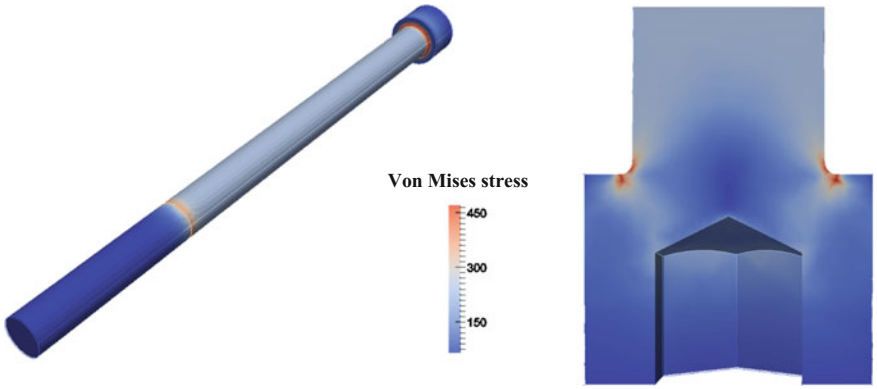

Fig. 18 Predicted stress in a simplified bolt made of 316L stainless steel

Discussion

The methodology allows reducing/clarifying some classical assumptions (stress, chaining between IGSCC stages). It becomes easier to **identify the weak points** of the modeling:

- For **specimens** tested in the laboratory, where the stress level is usually high, the main weak point is the prediction of the slow crack growth regime. This is due to the lack of data to fit parameters of the crack growth low for low K and low strain rate values. As soon as imposed stress is low, a second important weak point emerges: the absence of modeling of the stress and strain fields at the surface (surface finish).

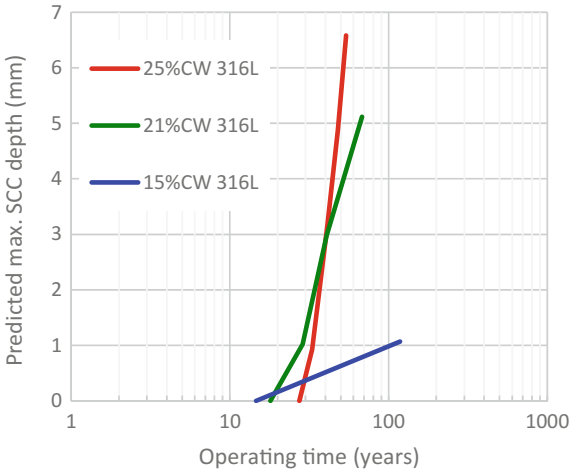

Fig. 19 Predicted SCC kinetics in a simplified bolt made of cold worked (CW) 316L stainless steel

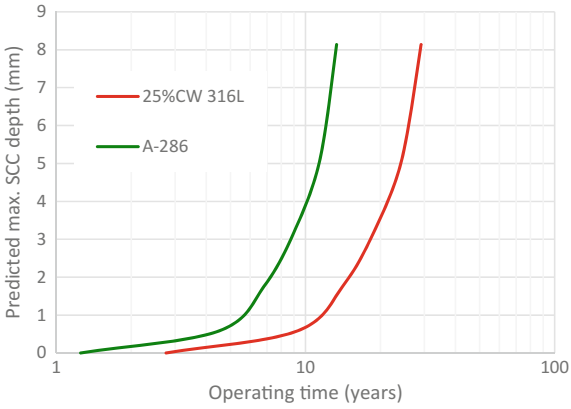

Fig. 20 Predicted SCC kinetics in a simplified bolt made of 25%CW 316L or A-286 stainless steels

- For **components**, where the stress level is low and surface finishes are complex, the weak point is definitely the ability to simulate relevant stress fields, especially in weld metals and heat affected zones. It may be also difficult to predict relevant stress and strain fields in presence of small defects.

In both situations, after initiation, the lifetime strongly depends on K. Therefore, a proper evaluation of K is necessary, taking into account the fact that crack extensions modify the original stress field, allowing crack growth in areas where stress was in compression before cracking. Since the FEM post-analysis delivers the crack growth path, it is possible to validate or calibrate a relevant K function with an explicit modeling of the crack.

The current main limitations are:

- The lack of accuracy of the cracking kinetics in the slow crack growth regime.
- The non-simulation of the surface finish (residual stress and strain gradients at the surface) of specimens.
- The lack of accuracy of the cracking criteria of oxidized GBs.

Conclusions

A new framework was proposed to improve IGSCC modeling feeding, step by step, using predictive engineering models with physical ingredients (intergranular oxidation kinetics, stress to fail in PWR environment oxidized grain boundaries).

A new model was proposed, relying on local parameters, explicitly describing the different stages of cracking (incubation, initiation, slow then fast crack growth). Predictions of the local model are promising but it could be improved:

- The assumed logarithmic dependency of the oxide growth on time may be revised. The effect of dissolved zinc may be introduced in the oxide growth model and/or in the stress to fail oxidized grain boundaries.
- Stress concentration at grain boundaries may be better predicted, taking into account the effect of changes in strain path (expected to increase opening stresses). The prediction may be improved with a more physical description of strain mechanisms in the vicinity of grain boundaries (use of a crystal plasticity law relying on dislocation densities). Creep may be better considered in the near future.
- The current crack growth laws are empirical and the slow crack growth rates are poorly calibrated.

In parallel, a significant increase in data analysis was achieved in the current work, thanks to a new FEM post analysis named Code_Coriolis. It offers the possibility to better calibrate and validate models with a global 3D view. In the near future, the same tool may be used for the evaluation of SCC of components as a support to examinations on retired components or for parametric studies.

First computations demonstrated that SCC can be simulated at the scale of a 'large' component thanks to a physically-based model relying on local observations (SEM, TEM) and small scale simulations (crystal plasticity).

In the near future, efforts will address the validation of the developed methodology (based on mockup characterizations and operational experience).

References

1. S. Le Hong, 'Modélisation de l'amorçage de la fissuration sous contrainte de l'alliage 600 en milieu primaire REP', EDF-EMA, HT-44/98/004/B
2. S. Le Hong, C. Amzallag, A. Gelpi, Modelling of stress corrosion crack initiation on alloy 600 in primary water of PWRs, in *9th International Conference on Environmental*

Degradation of Materials in Nuclear Systems-Water Reactors, Newport Beach (California), 1999
3. J.M. Boursier, Y. Rouillon, S. Le Hong, Relationship between microstructure and PWSCC susceptibility in wrought alloy 600. Eurocorr', 2000
4. F. Vaillant et al., Crack growth rates on vessel penetrations in alloy 600 in primary water. Fontevraud 4 (1998)
5. F. Vaillant et al., Crack growth rates in thick materials of alloy 600 and weld metals of alloy 182 in laboratory primary water. Comparison with field experience. Fontevraud 5 (2002)
6. T. Couvant, F. Vaillant, E. Lemaire, Stress corrosion crack growth rate in rolled alloy 600 exposed to primary PWR environment, in *14th International Conference on Environmental Degradation of Materials in Nuclear Power Systems-Water Reactor*, Virginia Beach (Virginia), 2009
7. M. Wehbi, T. Couvant, C. Duhamel, J. Crépin, Oxidation of nickel-base welds 182 and 82 in simulated primary water of pressurised water reactors. Mater. High Temp. **32**(1–2) (2015)
8. C. Duhamel, M. Wehbi, T. Couvant, J. Crepin, Grain boundary oxidation of nickel base welds 182/82 in simulated PWR primary water, in *17th International Conference on Environmental Degradation of Materials in Nuclear Systems-Water Reactors*, Ottawa (Canada), 2015
9. J. Caballero, J. Crépin, T. Couvant, C. Duhamel, Intergranular oxidation of Alloy 600 exposed to simulated PWR primary water. Eurocorr, Pisa (Italy) (2014)
10. T. Couvant, J. Caballero, C. Duhamel, J. Crépin, T. Maeguchi,' Calibration of the local IGSCC engineering model for alloy 600, in *18th International Conference on Environmental Degradation of Materials in Nuclear Systems-Water Reactors*, Portland (Oregon), 2017
11. T. Couvant, M. Wehbi, C. Duhamel, J. Crépin, R. Munier, Development of a local model to predict SCC: preliminary calibration of parameters for nickel alloys exposed to primary water, in *17th International Conference on Environmental Degradation of Materials in Nuclear Systems-Water Reactors*, Ottawa (Canada), 2015
12. http://code-aster.org/

Monte Carlo Simulation Based on SCC Test Results in Hydrogenated Steam Environment for Alloy 600

Yohei Sakakibara, Ippei Shinozaki, Gen Nakayama, Takashi Nan-Nichi, Tomoyuki Fujii, Yoshinobu Shimamura and Keiichiro Tohgo

Abstract We investigated the applicability of a stress corrosion cracking (SCC) engineering model and simulation method developed on the basis of the SCC of sensitized 304 stainless steel in a simulated BWR environment to the primary water stress corrosion cracking (PWSCC). We conducted a uniaxial constant loading test on Alloy 600 in a 400 °C hydrogenated steam environment and found that the number of cracks observed on a specimen surface after every passage of 450 h could be approximated to Poisson distribution, indicating that a Poisson random process model is applicable to the SCC in this system. By applying the engineering model, we statistically processed experimental data by assuming that the time distribution of occurrence of microcracks follows exponential distribution, and then obtained input data for the SCC simulation. Using coalescence coefficient, k, as a fitting parameter to obtain a reasonable k-value, it was found that the best agreement between the experimental and simulation results for the number of microcracks and the maximum crack length at k = 0.15. This is about one third the k-value of 0.5 found in sensitized 304 stainless steel in the BWR environment, indicating that coalescence is more subdued in PWSCC than in SCC in the BWR environment.

Keywords PWSCC · Nickel base alloy · Hydrogenated steam · UCL · Monte-Carlo simulation · Exponential distribution · Initiation · Coalescence

Y. Sakakibara (✉) · I. Shinozaki · G. Nakayama
IHI Corporation Research Laboratory,
1, Shin-Nakahara-Cho, Isogo-Ku, Yokohama 235-8501, Japan
e-mail: yohei_sakakibara@ihi.co.jp

T. Nan-Nichi
IHI Corporation Nuclear Power Operations,
1, Shin-Nakahara-Cho, Isogo-Ku, Yokohama 235-8501, Japan

T. Fujii · Y. Shimamura · K. Tohgo
Department of Mechanical Engineering, Shizuoka University,
3-5-1, Johoku, Naka-Ku, Hamamatsu 432-8561, Japan

J.H. Jackson et al. (eds.), *Proceedings of the 18th International Conference on Environmental Degradation of Materials in Nuclear Power Systems – Water Reactors*, The Minerals, Metals & Materials Series, https://doi.org/10.1007/978-3-319-68454-3_27

Introduction

The behavior of occurrence of stress corrosion cracking (SCC) is recently drawing attention in the study of primary water stress corrosion cracking (PWSCC) in pressurized water reactors (PWR). In such studies, Alloy 600 is used as a reference material, in which susceptibility to PWSCC is observed in both laboratory-based and field-based studies, with the purpose of determining the factor of improvement (FOI) for Alloy 690, which is currently used in plants, relative to Alloy 600 [1–3]. FOI is determined by

$$\mathrm{FOI} = t_A / t_R \tag{1}$$

where t_A is the time of PWSCC occurrence in an alternative material, and t_R is that in a reference material.

Alloy 690 is highly resistant to PWSCC; it has been reported that no failure occurred when a constant-load test was conducted over 100,000 h in a simulated PWR primary system environment [4]. Therefore, the direct-current potential drop (DCPD) method has been used recently to detect the occurrence of microcracks during a constant-load test. It is expected that this method will allow us to determine the time of occurrence of microcracks.

However, the FOI for the time of occurrence of microcracks ($\mathrm{FOI_{MC}}$) is different from that for the time of occurrence of "engineering cracks" ($\mathrm{FOI_{EC}}$) found in actual plants. Here, engineering cracks are defined as cracks that have a depth of 2 mm or more and can be detected by nondestructive inspection such as UT (ultrasonic testing). Through the direct observation of specimens of sensitized 304 stainless steel after SCC testing in a boiling water reactor (BWR) environment, we statistically processed the microcrack data obtained and fit the time distribution of occurrence of microcracks to exponential distribution [5–7]. In a study conducted in cooperation with Togo et al., we used these data as input data for a Monte Carlo simulation and successfully reproduced the occurrence of SCC in laboratory-tested specimens [8]. According to this simulation, adding 10 times the number of $\mathrm{FOI_{MC}}$ only resulted in increasing $\mathrm{FOI_{EC}}$ to two times. Therefore, mistaking $\mathrm{FOI_{MC}}$ to be obtained in the future for $\mathrm{FOI_{EC}}$ in the PWSCC of Alloy 690 will lead to a non-conservative prediction of PWSCC occurrence in actual plants.

Besides our research group, S. Fyfitch and the Electric Power Research Institute (EPRI) have developed a simulation program called xLPR [9]. Their module for SCC occurrence is designed to generate engineering cracks at certain times, and therefore has a risk of providing a non-conservative prediction as mentioned above. T. Couvant is focusing on the physical phenomena of SCC occurrence to develop a simulation method based on grain boundary oxidation and stress localization [10, 11]. Because this requires a large-scale computation to determine $\mathrm{FOI_{EC}}$, it is still difficult to predict the occurrence of engineering cracks. In our simulation, we use laboratory data to predict the occurrence of engineering cracks, which cause problems in actual plants. In the future, our simulation may play an intermediate

role of connecting between the above two simulation approaches. Against this backdrop, this study investigates the applicability of the Monte Carlo simulation method developed on the basis of SCC in a BWR to PWSCC.

Stastical Interperetation of PWSCC Data

Figure 1 shows a flowchart of SCC simulation that we have developed. The most important input data for the simulation is the time distribution of microcrack occurrence. Our simulation, based on the Poisson random process model proposed by Akashi [5–7], assumes that the time distribution of microcrack occurrence follows exponential distribution. Given that the distribution of the number of microcracks after a given time of a test follows Poisson distribution, it has been deductively demonstrated that the occurrence of microcracks follows exponential

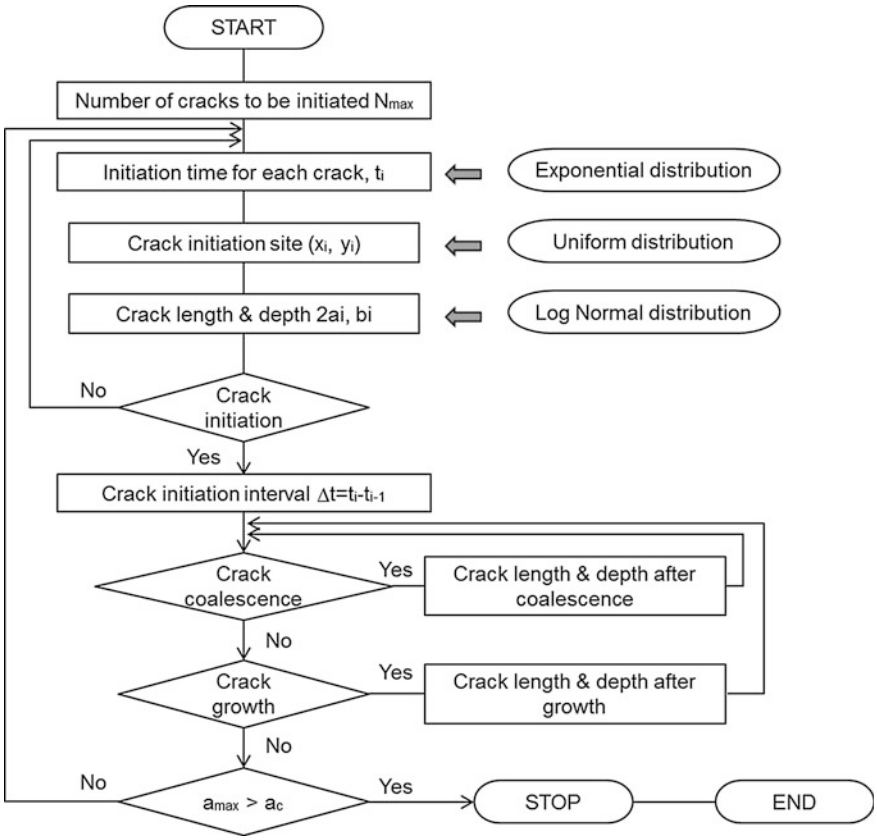

Fig. 1 Flowchart of simulation

distribution. We therefore investigated whether the distribution of the number of microcracks in PWSCC follows Poisson distribution.

We conducted accelerated PWSCC tests in a hydrogenated steam environment [12, 13]. In this paper, we use the results of a uniaxial constant load (UCL) test on Alloy 600 MA (Mill annealed) conducted in a 400 °C hydrogenated steam environment. The material has small carbides on the grain boundaries. Table 1 shows the chemical composition and mechanical property of Alloy 600 used in this study. The material was in the mill-annealed state. Figure 2 shows the specimen used in this study. One side of the specimen was finished with emery paper #600–#2000 before the test. The test was conducted at 400 °C, total pressure of 200 MPa, partial hydrogen pressure of 200 kPa, and applied stress of 500 MPa. See our previous paper for other settings of the test [12, 13]. The test was halted every 450 h to observe the specimen surface under a scanning electron microscope (SEM). After passage of 900 h, a lot of intergranular stress corrosion cracking (IGSCC) was observed along grain boundaries as shown in Fig. 3. At each time of observation, we obtained a panoramic view on a parallel part of the specimen at a magnification of 500 or 300 to measure the length and number of microcracks. Although the occurrence of microcracks was observed in a 90° orientation, no significant differences were found, and therefore the occurrence of microcracks was tracked in a particular orientation (in 0° orientation). The UCL test was conducted repeatedly up to a duration of 1800 h. Figure 4 shows a histogram of crack length for different test durations. We used these data to investigate whether the number of cracks can be approximated to the Poisson distribution. The number of cracks within a field of view was grouped into 9 classes, and then the numbers of cracks in 80 SEM images were classified accordingly to create a histogram. Figure 4 is based on 240 images (=80 images × 3). The Poisson distribution, $p(m')$, is given by the following Eq. (2).

$$p(m') = \frac{\lambda^{m'}}{m'!}\exp(-\lambda) \quad \mathrm{m} = 0, 1, 2\ldots \tag{2}$$

Here, λ is hazard rate, and class m' is a rank (starting from 0) obtained by adequately classifying the numbers of cracks within the field of view. For the purpose of comparison with histograms, $p(m')$ was multiplied by the number of views (n = 80) to obtain $A(m')$. Figure 5 shows histograms and $A(m')$ values when classification is made according to the number of cracks, Nc. The good agreement between the histogram and $A(m')$ indicates that the experimentally obtained number

Table 1 Chemical composition and mechanical properties of materials

Chemical composition/ mass%							Tensile property at room temperature		
C	Si	Mn	S	Ni	Cr	Fe	Yield strength/MPa	Tensile strength/MPa	Elongation/ %
0.03	0.2	0.2	0.001	Bal.	15.6	8.9	310	622	45

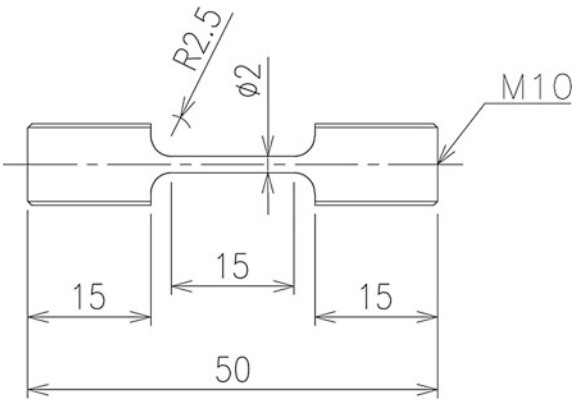

Fig. 2 Configuration of UCL specimen

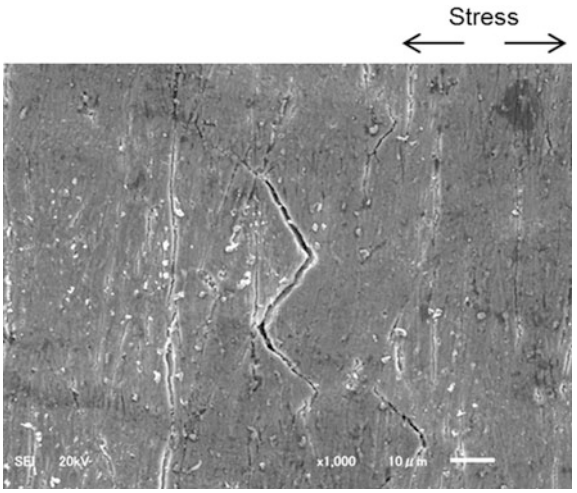

Fig. 3 An SEM image on UCL specimen after 900 h

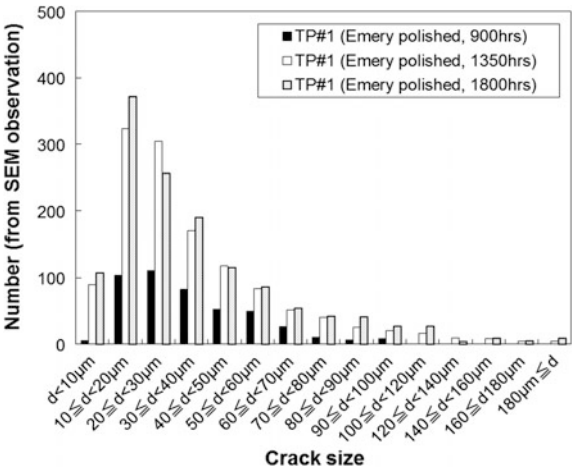

Fig. 4 Histograms of crack size on the specimen at the various test time

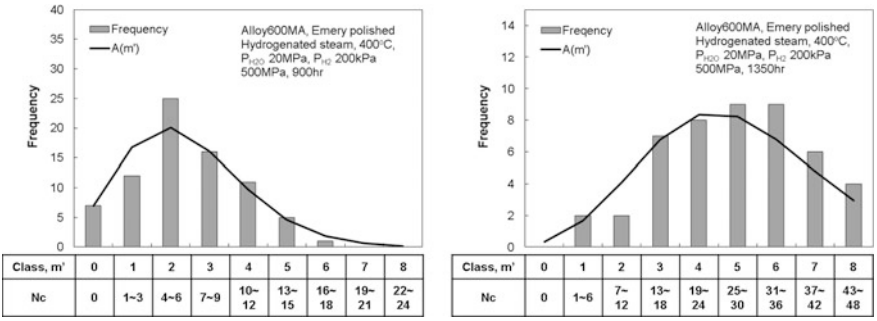

Fig. 5 Classification of crack number in each SEM image region and Poisson distribution. (Left; after 900 h, Right; 1350 h)

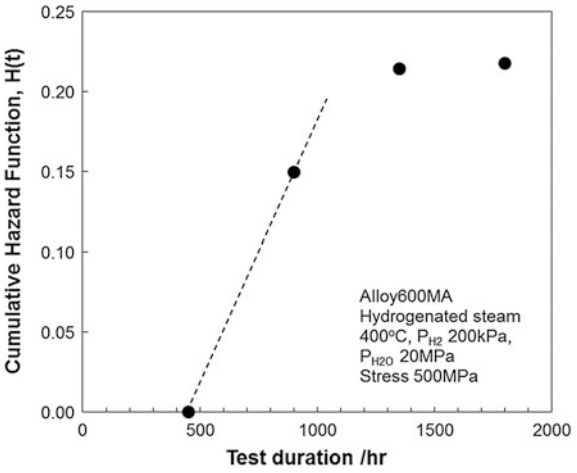

Fig. 6 Cumulative hazard function as a function of test duration

of cracks fits well to the Poisson distribution. It is therefore possible to approximate the time distribution of the occurrence of microcracks to exponential distribution, as noted at the beginning of this chapter. In the case of exponential distribution, cumulative failure rate, $H(t)$, is given by Eq. (3).

$$\begin{aligned} H(t) &= (t-a)/\theta \quad t \geqq a \\ &= 0 \qquad\qquad a < t \end{aligned} \tag{3}$$

Here, a is a location parameter indicating the minimum lifetime, t is test duration, and θ is a scale parameter. As the cumulative failure rate is obtained by dividing the number of microcracks by the number of grain boundaries that can be generated, it is possible to create a graph showing changes in cumulative failure rate with time (Fig. 6) from the data given in Fig. 4. The cumulative failure rate increased linearly during the time period from 450 h to 1350 h and ceased to increase at 1800 h. Given that the number of cracks observed may decrease due to

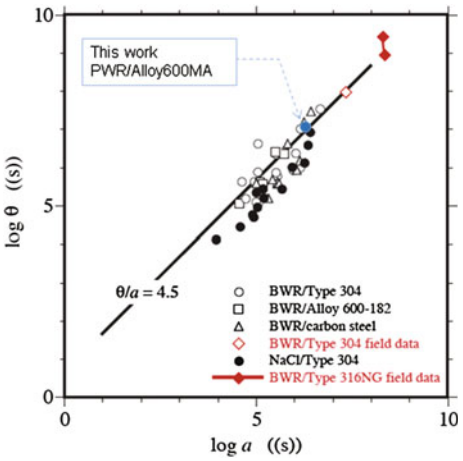

Fig. 7 Relationship between a and θ of the various types of SCC. The plot in this paper is located on the tendency

coalescence, we used the numbers of cracks at 450–900 h to obtain a linear line, which was used as input data for the SCC simulation. As a result, we obtained a = 1.62 Ms and θ = 8.4 Ms. The x-intercept and the slope of the line respectively correspond to a and 1/θ in Eq. (2). Akashi argued that the behavior of SCC occurrence in accelerated laboratory tests including those in a simulated BWR environment and a neutral chloride environment can be explained by the Poisson random process model [5–7]. The a/θ values obtained in such tests are reported to be constant, and the a and θ values in our study, together with data from other studies [7], are plotted in Fig. 7.

Reproduction of the Behavior of SCC Occurrence in Hydrogenated Steam by SCC Simulation

As shown in Fig. 1, information is required on the size, aspect ratio, and growth rate of microcracks initially generated, as well as the a and θ parameters of exponential distribution. The size of microcracks, which is assumed to depend on grain diameter, was given in the form of grain size distribution. Figure 8 shows a grain size distribution and a specimen viewed under an optical microscope. As the Alloy 600 plates used for the current study partly showed inhomogeneous grain growth, we used exponential normal distribution; although, a referenced study used normal distribution [8]. The rate of crack growth in the studied material was measured in a hydrogenated steam environment [12], and the rate was assumed to be proportional to the n-th power of stress intensity factor, K, based on the MRP-55 equation proposed by EPRI [14]. Table 2 summarizes the input data used for the SCC simulation. As reported previously, coalescence coefficient, k, was used as a fitting parameter. This coefficient is used in Eq. (4) to define the critical radius of coalescence, r_c.

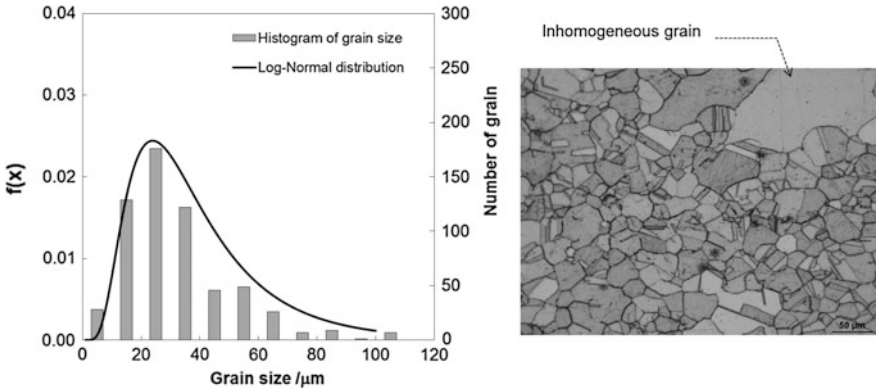

Fig. 8 Log-normal distribution of grain size (left) and an optical microscope image including inhomogeneous grain (right)

Table 2 Parameters for SCC simulation

Parameter	Value
a (Ms)	1.62
q (Ms)	10.8
Yield strength (MPa)	240
Applied stress (MPa)	500
Average grain size (μm)	35
Standard deviation of grain size (μm)	21
Area of simulation (mm)	3.5 × 3.5
Crack growth rate, da/dt (m/s) [14]	$da/dt = \exp\left[-\frac{Q}{R}\left(\frac{1}{673}-\frac{1}{598}\right)\right] \times 5 \times 10^{-14}(K - K_{th})^2$
Threshold stress intensity factor, $K_{I,\,scc}$ (MPa $\sqrt{m}$)	2
Activation energy, Q (kJ/mol) [14]	130
Gas constant, R (J/K•mol)	8.314

$$r_c = \frac{k}{\pi}\left(\frac{K_{IA}}{\sigma_y}\right)^2_{crack1} + \frac{k}{\pi}\left(\frac{K_{IA}}{\sigma_y}\right)^2_{crack2} \tag{4}$$

Here, σ_y is 0.2% yield strength. In the simulation, we calculate the K_{IA} value at microcrack ends and the distance between crack ends, r; if the distance is less than the critical radius of coalescence, r_c, the microcracks will be coalesced in the next calculation step.

Figure 9 shows the experimental and simulation results of changes in the number of cracks with time. They are in good agreement when coalescence coefficient, k, is 0.15. Figure 9 also shows much smaller crack density when k is 0.5. Similarly, Fig. 10 shows the experimental and simulation results of the maximum crack length at $k = 0.15$. They also show generally good agreement, suggesting the adequacy of input data and the k-value. According to a previous study, a k-value of

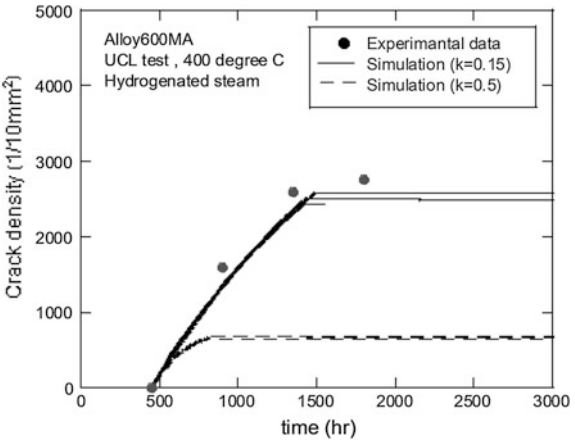

Fig. 9 Comparison in crack density between the simulation results and the experimental data

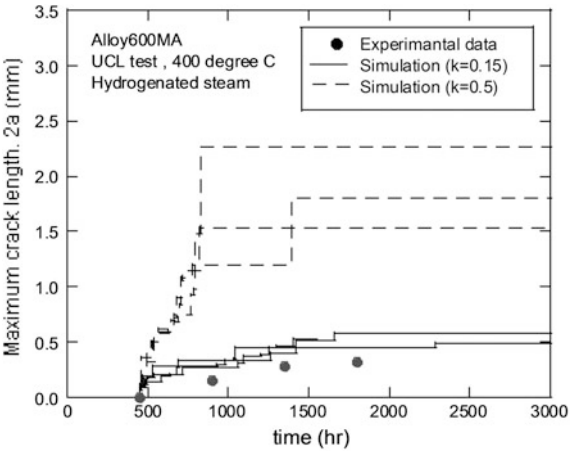

Fig. 10 Comparison in maximum crack length on the surface between the simulation results and the experimental data

0.5 is adequate for sensitized 304 stainless steel in a BWR environment. The *k*-value suggested in our study for the SCC of Alloy 600 in a hydrogenated steam environment is about one third that suggested for the BWR environment. This means that coalescence is less likely to occur in the SCC of Alloy 600 in a hydrogenated steam environment; either the occurrence of cracks or the growth of cracks that have occurred is dominant, and they do not develop into engineering cracks. The hydrogenated steam environment used in this study had a redox potential comparable to that in a PWR environment, and the generated surface oxide film was thinner than that generated in a BWR environment. Terachi studied the influence of dissolved hydrogen (DH) on oxide film on Alloy 600. He reported that NiO outer layer was observed when DH was 0, on the other hand, thin Cr-rich oxide and Ni-Cr-Fe spinel was observed with higher DH [15]. It means that high potential in BWR provides thicker NiO layer. It is expected that the condition of

coalescence is influenced by the formation rate of oxide film and the level of stress required for failure.

Conclusions

UCL test was conducted for Alloy 600 in hydrogenated steam and microcrack data was interpreted by statistically. It showed that SCC occurrence behavior in steam can be approximated to the Poisson random process model as well as SCC in the other environment. SCC occurrence was reproducible by SCC simulation based on the engineering model. Using coalescence coefficient, k, as a fitting parameter to obtain a reasonable k-value, it was found that the best agreement between the experimental and simulation results for the number of microcracks and the maximum crack length at k = 0.15. This is about one third the k-value of 0.5 found in sensitized 304 stainless steel in the BWR environment, indicating that coalescence is more subdued in PWSCC than in SCC in the BWR environment.

References

1. M.B. Toloczko, M.J. Olszta, Z Zhai, S.M. Bruemmer, *in Proceedings. of 17th International Conference on Environmental Degradation of Materials in Nuclear Power Systems–Water Reactors*, August 9–13. Stress Corrosion Crack Initiation Measurements Of Alloy 600 in Pwr Primary Water, (Ottawa, ON, Canada, 2015)
2. T Moss, G S. Was, *in Proceedings. of 17th International Conference on Environmental Degradation of Materials in Nuclear Power Systems–Water Reactors*, August 9–13. Factor Of Improvement in Resistance Of Stress Corrosion Crack Initiation Of Alloy 690 Over Alloy 600, (Ottawa, ON, Canada, 2015)
3. Materials Reliability Program, *Technical Basis for Reexamination Interval Extension for Alloy 690 PWR Reactor Vessel Top Head Penetration Nozzles (MRP-375)* (Palo Alto, CA, 2014)
4. K. Sakima, T. Maeguchi, K. Sato, K. Fujimoto, Y. Nagoshi, M. Nakano, *In Proceedings of 17th International Conference on Environmental Degradation of Materials in Nuclear Power Systems—Water Reactors*, August 9–13. An Update On Alloys 690/52/152 Pwscc Initiation Testing, (Ottawa, ON, Canada, 2015)
5. M. Akashi, An Exponential Distribution Model for Assessing the Stress-Corrosion Cracking Lifetime of BWR Component Materials, In Life Prediction of Corrodible Structures, R.N. Parkins, (eds.), NACE International, Houston, No. 94–067148, Vol. II, (1994), pp. 1040–1049
6. M. Akashi, G. Nakayama, *In Proceedings Inter. Symp. on Plant Aging and Life Prediction of Corrodible Structures, T. Shoji, T. Shibata, (eds.), Jap. Soc. Corros. Eng, NACE International*, Stress-Corrosion Crack Initiation Process Model for BWR Plant Materials, (1997), pp. 99–106
7. M. Akashi, The poisson random-process model for initiation of the stress-corrosion crack propagation. Paper presented at workshop on detection, avoidance, mechanisms, modeling, and prediction of scc initiation in water cooled nuclear reactor plants, J. Gorman, R. Staehle, (eds.), Paper No. 12–1 (2009)

8. Keiichiro Tohgo, Hiromitsu Suzuki, Yoshinobu Shimamura, Guen Nakayama, Takashi Hirano, Monte Carlo simulation of stress corrosion cracking on a smooth surface of sensitized stainless steel type 304. Corros. Sci. **51**, 2208–2217 (2009)
9. S. Fyfitch, C. Harrington, *In Proceedings of 16th International Conference on Environmental Degradation of Materials in Nuclear Power Systems –Water Reactors,* August 11–15. PWSCC Initiation Modeling For The Extremely Low Probability Of Rupture (Xlpr) Code, (Asheville, NC, USA, 2013)
10. T. Couvant, M. Wehbi, C. Duhamel, J. Crépin, R. Munier, *In Proceedings of 17th International Conference on Environmental Degradation of Materials in Nuclear Power Systems—Water Reactors*, August 9–13. Development of a 'Local' Model to Predict Igscc: Preliminary Calibration of Parameters for Nickel Alloys Exposed to Primary Water, (Ottawa, ON, Canada, 2015)
11. T. Couvant, D. Haboussa, S. Meunier, G. Nicolas, E. Julan, K. Sato, F. Delabrouille, *In Proceedings. of 17th International Conference on Environmental Degradation of Materials in Nuclear Power Systems—Water* Reactors, August 9–13. A Simulation of Igscc of Austenitic Stainless Steels Exposed to Primary Water, (Ottawa, ON, Canada, 2015)
12. Y. Sakakibara, I. Shinozaki, G, Nakayama, T. Sato, T. Hirano, *In Proceedings of 17th International Conference on Environmental Degradation of Materials in Nuclear Power Systems –Water Reactors*, August 9–13. Acoustic Emission Monitoring of Scc Behavior In Superheated Hydrogenated Steam For Ni-Base Alloys, (Ottawa, ON, Canada, 2015)
13. Y. Sakakibara, I. Shinozaki, G. Nakayama, Surface Finishing Effect on Stress Corrosion Cracking Test Results of Alloy 600 by Uni-Axial Constant Load Test in Hydrogenated Steam Environment, Zairyo-to-Kankyo, 66 (2017) pp. 136–141 (Jpn.)
14. Materials Reliability Program Crack Growth Rates for Evaluating Primary Water Stress Corrosion Cracking of Thick-wall Alloy 600 Materials, MPR-55, Revision 1, Nov 2002
15. T. Terachi, N. Totsuka, T. Yamada, T. Nakagawa, H. Deguchi, M. Horiuchi, M. Oshitani, Influence of dissolved hydrogen on structure of oxide film on alloy 600 formed in primary water of pressurized water reactors. J. Nucl. Sci. Technol. **40**, 509–516 (2003)

Protection of the Steel Used for Dry Cask Storage System from Atmospheric Corrosion by Tio_2 Coating

Jing-Ru Yang, Mei-Ya Wang, Tsung-Kuang Yeh and Peter Chen

Abstract Austenitic 304 stainless steels (SS) and carbon steels (CS) are widely used as structural materials for components and pipe assemblies in nuclear power plants. Steels also act as the important canister materials in the dry storage of spent nuclear fuels. However, it is well known that stainless steels and carbon steels are susceptible to stress corrosion cracking (SCC) in certain environments induced by sea salt particles and chlorides. It is known that the TiO_2 coating acts as a non-sacrificial anode and protects the steel cathodically under UV illumination. In this study, the photoelectrochemical behavior of the steel with TiO_2 coating by sol-gel method was investigated to mitigate atmospheric SCC. In addition, the slow decline of photovoltage of the samples coated with TiO_2 after UV illumination have been studied. These results indicate that the TiO_2 treatment with or after UV illumination would effectively reduce the steel corrosion rate in atmospheric environments.

Keywords Carbon steel · TiO_2 · Electrochemical corrosion potential · Photoelectrochemical behavior

Nomenclature

CS Carbon steel
ITO Indium-doping Tin oxide glasses

J.-R. Yang · T.-K. Yeh
Department. of Engineering and System Science, National Tsing Hua University, 300 Hsinchu City, Taiwan

M.-Y. Wang (✉)
Nuclear Science and Technology Development Center, National Tsing Hua University, 300 Hsinchu City, Taiwan
e-mail: meywang@mx.nthu.edu.tw

T.-K. Yeh
Institute of Nuclear Engineering and Science, National Tsing Hua University, 300 Hsinchu City, Taiwan

P. Chen
Berlin Co., Ltd, 812 Kaohsiung City, Taiwan

J.H. Jackson et al. (eds.), *Proceedings of the 18th International Conference on Environmental Degradation of Materials in Nuclear Power Systems – Water Reactors*, The Minerals, Metals & Materials Series, https://doi.org/10.1007/978-3-319-68454-3_28

Introduction

For nuclear power plant, steels are widely used as canisters for dry storage for spent nuclear fuel. TiO_2 acts as an inhibitor to reduce the corrosion of metal substrates. When exposed to ultraviolet light or radiation, TiO_2 coating acts a non-sacrificial anode and protects the substrates, causing lower electrochemical corrosion potential. To demonstrate the cathodic protection of metal substrate by ceramic or semiconductor coating under UV illumination, the photoelectrochemical behavior of carbon steel coated with TiO_2 by sol-gel method has been studied recently. TiO_2 can be provided by methods such as sputtering and chemical vapor deposition etc. However, it is difficult and expensive to deposit the uniform TiO_2 coating coverage on the substrate. The advantages of sol-gel method, are such as conducting the procedure at room temperature and independent of substrate shape etc. Nevertheless, after stopping UV illumination, the electrochemical corrosion potential will recover to original electrochemical corrosion potential rapidly. Tsujikawa et al. [1] proposed a concept, called Memory effect, to study the interaction between TiO_2 coating and iron oxide, the appropriate condition will cause the slower recombination of electron which is produced by UV illumination. Thus, the mechanism will retard the photovoltage recover to original state and decrease the corrosion rate of substrate. Therefore, the main objective of this research is to investigate the appropriate heat treatment conditions for the formation of an oxide layer of carbon steel as well as those used following TiO_2 coating, the photovoltage will remain at lower value even after stopping UV illumination. The interaction between TiO_2 coating and iron oxide significantly affects the photoelectrochemical behavior; the relationship between the photovoltage and oxide layer of carbon steel are discussed briefly.

Experimental

Preparation of Substrate

The carbon steel sheets with thickness of 1 mm were prepared for substrates. The substrates were cut into the size of 20×20 mm^2. The testing side of samples were ground with 180 to 800 abrasive paper and were cleaned in acetone. To form oxide layer on the carbon steel substrates, the samples were heated at different temperatures for 30 min under oxygen atmosphere. For removing any unexpected effect of the carbon steel substrates on the TiO_2 coating, Indium-doping Tin oxide (ITO) glasses with the same size as carbon steel were used as reference substrates.

Preparation of TiO_2 Coating

TiO_2 sol-gel solution was obtained from 29.3 g titanium isopropoxide with the dropwise addition of 8 g ethanol. The sol-gel solution was kept stirring at room temperature, whilst mixing with 2 g acetic acid. After stirring for 5 min, 24 g ethanol were added [2]. The TiO_2 coatings formed on the carbon steel and ITO substrates were prepared by dip-coating method in the prepared sol-gel solution. The withdrawal speed was controlled at the constant speed of 0.15 mm/s. The dip-coating samples were dried at room temperature, and heated in furnace for different temperature and time. After heat treatment, the TiO_2 coating on the substrates were obtained.

Characterization

Raman spectra were recorded at room temperature using a LABRAM HR 800 UV Spectroscope with a 632.8 nm He–Ne laser. The beam power at the sample surface was 17 mW. The depth profile analysis of TiO_2/carbon steel samples were carried out by Electron Spectroscopy for Chemical Analysis (ESCA). The surface of samples was sputtered by Ar ion gun. The relative atomic concentration were calculated from the areas of the elements.

Photoelectrochemical Measurements

The photoelectrochemical measurement were conducted under illumination of a UV spot light source (HAMAMATSU, LC8-02, 4500 mW/cm^2). The measurements were carried out in air with the electrolyte of 0.05 M $NaHCO_3$. The electrode potential was referred to a saturated calomel electrode (SCE). The photoelectrochemical measurements were conducted at room temperature.

Results and Discussion

Effect of Heat Treatment Temperature on the Photovoltage of TiO_2 Coated on ITO

Figure 1 shows the electrochemical corrosion potential of TiO_2 coated on ITO samples heated at different temperature for 1 h under argon atmosphere. It was

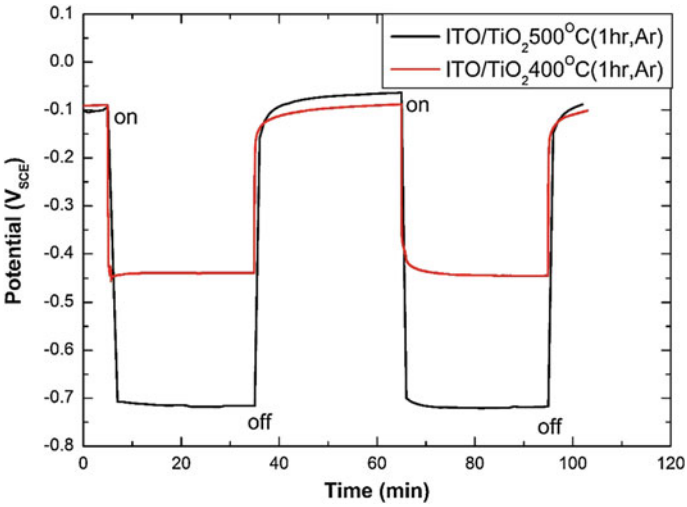

Fig. 1 Electrochemical corrosion potential of TiO_2-coated ITO samples for different heat treatment condition for TiO_2 coating for 1 h in argon

found that the photocatalytic effect would significantly influenced by heat treatment temperature. The potential difference between dark potential and photovoltage for the samples heated at 400 °C and 500 °C are respectively 350 mV and 600 mV. The main result of these two samples was the different phase of TiO_2. For the lower heat treatment temperature sample, the TiO_2 was amorphous combined with an anatase crystalline phase, whereas the higher temperature produced just an anatase phase. The photocatalytic effect was less for the lower heat treatment [3].

Behaviour of Oxide Layer on Carbon Steels Under Different Heat Treatment Condition

Before TiO_2 coating of the carbon steel samples, the oxide structure of carbon steel was characterized by Raman analysis. Figure 2 shows the results of Raman spectra of carbon steel samples under different heat treatment condition.

The Raman wavenumber of iron oxide of Fe_2O_3 and Fe_3O_4 are listed in Table 1, [4]. The 227, 293 and 414 Raman shift peak can be registered as Fe_2O_3, and the 616 and 663 peak can be registered as Fe_3O_4. It was found that the higher temperature results in a higher intensity corresponding to the Raman peak of Fe_2O_3.

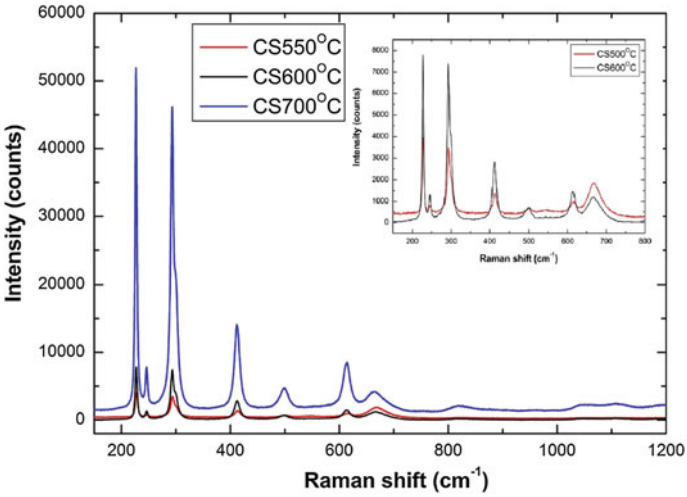

Fig. 2 Raman spectra of carbon steels for different oxidation temperature

Table 1 Raman wavenumber for iron oxide of carbon steel [4]

Oxides	Wave number (cm^{-1})
α-Fe_2O_3	227, 245, 293, 414, 501
Fe_3O_4	616, 663

Effect of Heat Treatment Temperature on the Photovoltage of TiO_2 Coated on Carbon Steel for Different Oxidation Condition

Figure 3 shows the electrochemical corrosion potential of carbon steel samples for which the oxide layer was formed at 600 °C, with heat treatment after TiO_2 coating at 500 °C. It was indicated that the potential difference between dark potential and photovoltage was about 400 mV. In contrast to the ITO samples, after stopping UV illumination, the potential still remained at the lower value.

Figure 4 shows the electrochemical corrosion potential of carbon steel samples with the oxide layer formed at 550 °C and heat treated at 500 °C after TiO_2 coating. It was found that the potential difference was 150 mV. In this case, the sample showed a slow decline of photovoltage after stopping UV illumination for 1.5 h.

Trying lower heat treatment temperature for TiO_2, the electrochemical corrosion potential behaviour is shown in Fig. 5. It was demonstrated that the potential difference was about 150 ~ 200 mV. The electrochemical corrosion potential of carbon steel samples which formed oxide layer at 700 °C and heat treated at 500 °C for TiO_2 is shown in Fig. 6. It was clear that the potential difference between dark and photo potential was about 100 mV in early stage. The potential difference increased with the increasing of UV illumination. After total illumination time for 4 h, the potential drop reached to 150 mV.

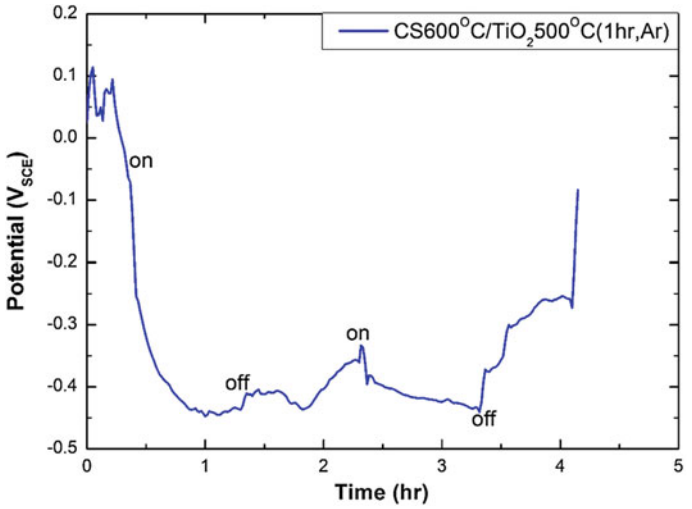

Fig. 3 Electrochemical corrosion potential of TiO_2-coated carbon steel. The steel was oxidized at 600 °C for 30 min in oxygen. Heat treatment condition for TiO_2 coating was 500 °C for 1 h in argon

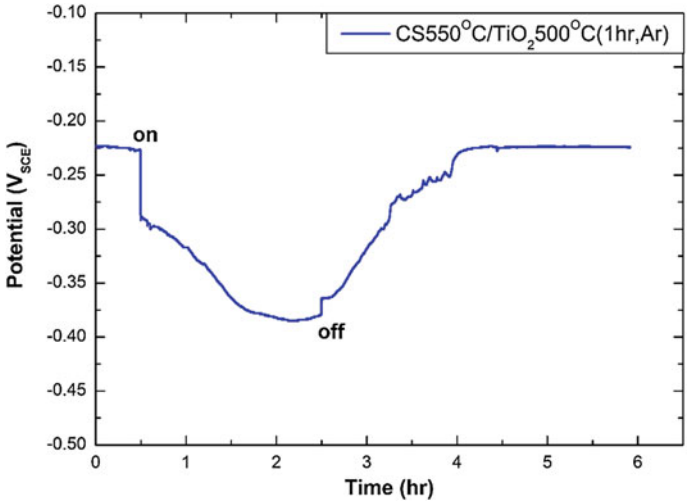

Fig. 4 Electrochemical corrosion potential of TiO_2-coated carbon steel. The steel was oxidized at 550 °C for 30 min in oxygen. Heat treatment condition for TiO_2 coating was 500 °C for 1 h in argon

Figures 3, 4, 5 and 6 show the electrochemical corrosion potential of TiO_2 coated on carbon steel samples for each oxidation condition of oxide layer and different heat treatment temperature for TiO_2. It is clear that the electrochemical behaviour between samples was different, depending on the temperature for both

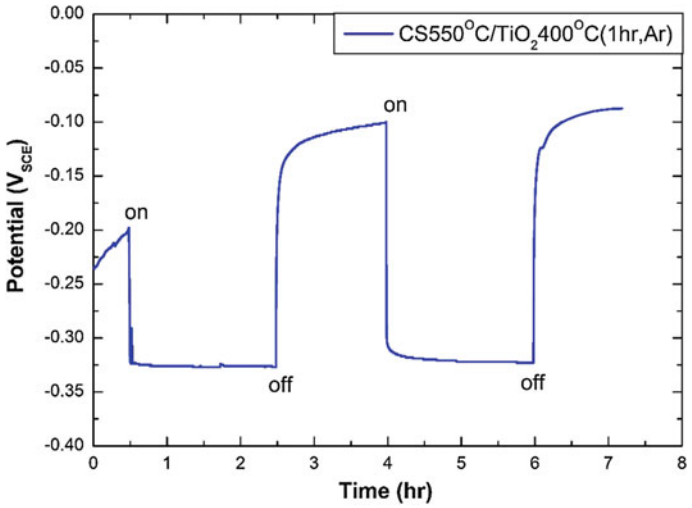

Fig. 5 Electrochemical corrosion potential of TiO_2-coated carbon steel. The steel was oxidized at 550 °C for 30 min in oxygen. Heat treatment condition for TiO_2 coating was 400 °C for 1 h in argon

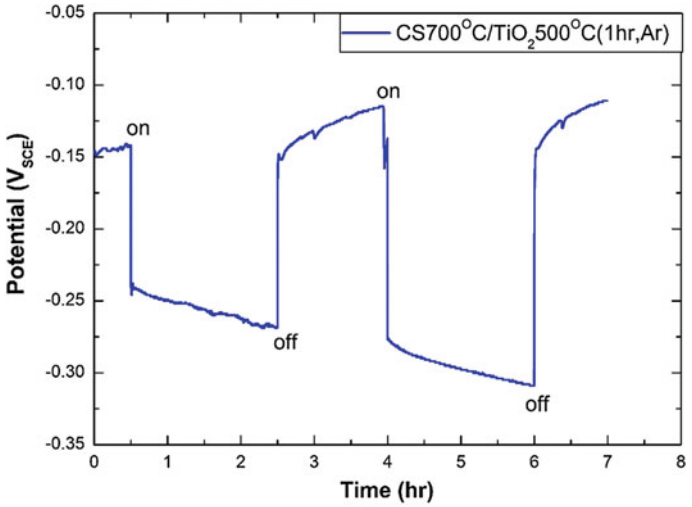

Fig. 6 Electrochemical corrosion potential of TiO_2-coated carbon steel. The steel was oxidized at 700 °C for 30 min in oxygen. Heat treatment condition for TiO_2 coating was 500 °C for 1 h in argon

oxidation and heat treatment after coating. Previous studies indicated that a higher proportion of Fe_2O_3 in oxide layer produces the better photocatalytic effect [5, 6]. The results may be attributed to the reason that each oxide layer condition has a significant impact on the electrochemical corrosion potential behaviours. The depth

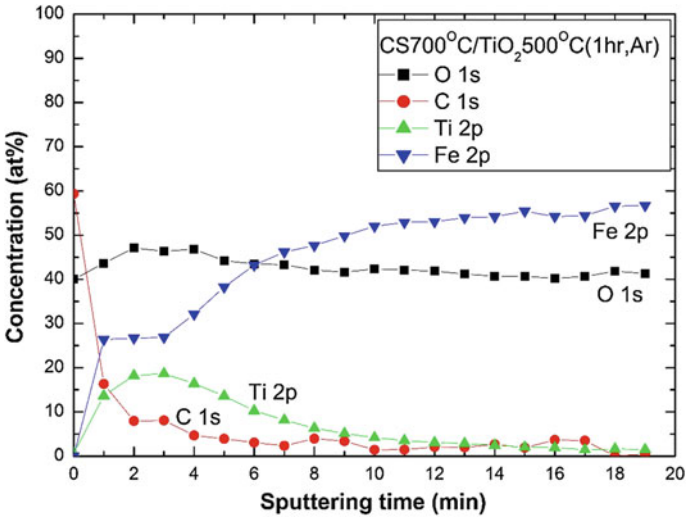

Fig. 7 ESCA depth profile of TiO_2/carbon steel. The carbon steel was oxidized at 700 °C for 30 min in oxygen. Heat treatment condition for TiO_2 coating was 500 °C for 1 h in argon

profile for the 700 °C oxidation +500 °C TiO_2 coating condition is shown in Fig. 7. As we can see, the structure of the specimen is the thicker oxide layer on the substrate, and thinner coating layer on the oxide layer. According to analysis, this demonstrated that there is large amount of Fe particles diffusing into coating layers. Because the coating layer contaminated by Fe, the photocatalytic effect of TiO_2 would decrease. Thus, the potential difference of carbon steel specimens was lower compare with the ITO specimens. Therefore, the heat treatment condition would influence the Fe diffusion [7].

Conclusions

The sol-gel method of TiO_2 coating of carbon steel and ITO samples were investigated in this paper as a possible means of mitigating atmospheric SCC of cabon steels by reducing the local electrochemical potential during and, to some extent, after UV irradiation. For the TiO_2 coated ITO samples, a heat treatment at 500 °C produced a great potential difference than at 400 °C. The potential increased rapidly when the UV illumination was removed. These results indicated that the TiO_2 by sol-gel method presents the better photocatalytic property when the coating heat treatment was at 500 °C. For carbon steel, there is evidence that, for appropriate heat treatments, the low potential is sustained for a period after removing the UV illumination which indicates a potential benefit in practice. Our research also provides the evidence that the photoelectrochemical behaviors shows a great

correlation to properties of oxide layer. With UV illumination, it is expected that the atmospheric SCC would be mitigated due to the decreasing of the electrochemical corrosion potential. After stopping illumination, the photovoltage remained at a lower value or slowly declined for samples with appropriate heat treatment condition.

References

1. T. Konishi, S. Tsujikawa, Slow Decline of Photovoltage After Illumination, Presented at The Electrochemical Society, Paris, 1997
2. J. Huang, T. Konishi, T. Shinohara, S. Tsujikawa, Sol-gel derived Ti-Fe oxide coating for photoelectrochemical cathodic protection of carbon steel. Zairyo-to-Kankyo **47**(3), 193–199 (1998)
3. J. Yuan, S. Tsujikawa, Characterization of Sol-Gel-Derived TiO_2 Coatings and Their Photoeffects on Copper Substrates. J. Electrochem. Soc. **142**(10), 3444–3450 (1995)
4. S.J. Oh, D.C. Cook, H.E. Townsend, Characterization of iron oxides commonly formed as corrosion products on steel. Hyperfine Interac. J. Art. **112**(1), 59–66 (1998)
5. J. Huang, T. Shinohara, S. Tsujikawa, Effects of interfacial iron oxides on corrosion protection of carbon steel by TiO_2 coating under illumination. Zairyo-to-Kankyo **46**(10), 651–661 (1997)
6. J.C. Yu, W. Ho, J. Lin, H. Yip, P.K. Wong, Photocatalytic activity, antibacterial effect, and photoinduced hydrophilicity of TiO_2 films coated on a stainless steel substrate. Environ. Sci. Technol. **37**(10), 2296–2301 (2003)
7. J. Yuan, S. Tsujikawa, Photo-effects of sol-gel derived TiO_2 coating on carbon steel in alkaline solution. Zairyo-to-Kankyo **44**(10), 534–542 (1995)

Predictive Modeling of Baffle-Former Bolt Failures in Pressurized Water Reactors

Gregory A. Banyay, Matthew H. Kelley, Joshua K. McKinley, Matthew J. Palamara, Scott E. Sidener and Clarence L. Worrell

Abstract Baffle-former bolt failures have been observed in recent inspections of pressurized water reactors (PWRs). These failures are understood to be primarily caused by irradiation-assisted stress corrosion cracking (IASCC). A prognostic method has been developed for simulating the degradation of baffle-former bolts due to IASCC. The method characterizes the evolution of stress in a reactor environment, as well as the redistribution of stress amidst neighboring bolt failures. Empirically-validated Weibull parameters are utilized in a stochastic framework, and the model is exercised as a Monte Carlo simulation to evaluate a range of plausible scenarios from which trends of bolt failure rates and patterns can be

18th International Conference on Environmental Degradation of Materials in Nuclear Power Systems.

G.A. Banyay · M.H. Kelley · J.K. McKinley · M.J. Palamara (✉)
S.E. Sidener · C.L. Worrell
Westinghouse Electric Company LLC, 1000 Westinghouse Drive,
Cranberry Township, PA 16066, USA
e-mail: palamamj@westinghouse.com

G.A. Banyay
e-mail: banyayga@westinghouse.com

M.H. Kelley
e-mail: kelleymh@westinghouse.com

J.K. McKinley
e-mail: mckinljk@westinghouse.com

S.E. Sidener
e-mail: sidenese@westinghouse.com

C.L. Worrell
e-mail: worrelcl@westinghouse.com

J.H. Jackson et al. (eds.), *Proceedings of the 18th International Conference on Environmental Degradation of Materials in Nuclear Power Systems – Water Reactors*, The Minerals, Metals & Materials Series, https://doi.org/10.1007/978-3-319-68454-3_29

determined. This semi-empirical methodology is informed by both operating experience and a more detailed, predictive finite element analysis model that encompasses the full range of phenomenological effects common to the operating environment within a PWR.

Keywords Baffle-former bolt · Stochastic · Semi-empirical · Reliability

Introduction

Greater-than-expected numbers of baffle-former bolt failures were observed during recent visual and ultrasonic inspections at several pressurized water reactors in the United States [1]. For example, the Salem Unit 1 inspection in the spring of 2016 identified that almost one-quarter of the total baffle-former bolt population installed in the reactor exhibited inspection indications, and over 75% of those indications were localized to one quadrant. Spatial clustering of degraded bolts like this can be associated with, separated bolt heads and lock bars, instances of fuel rod leakage, or gaps opening between the baffle plates.

The baffle-former bolts are located in the reactor vessel internals (RVI) assembly. Figure 1 depicts the interior of the lower internals, without fuel assemblies. The baffle plates are vertically oriented and adjacent to the fuel when the core is in place. The baffle-former bolts are depicted as small dots in Fig. 1. These bolts attach the baffle plates to the former plates. The function of the baffle-former assembly is to maintain the fuel assembly structural integrity to ensure that the control rods insert, maintain a coolable core geometry, and ensure a core configuration that supports long-term reactor shutdown.

The primary operational concern with the baffle-former bolts is the potential for failed bolts to impact fuel integrity. This could occur due to a number of effects from a failed bolt, including a loose bolt head directly damaging the fuel rods or high-pressure baffle jetting through gaps opened between the baffle plates or through open bolt holes. Under the extreme condition where all bolts for a given plate have failed, shifting of the plate could interfere with coolant flow. Nuclear Safety Advisory Letter (NSAL)–16–1 [1] summarized a systematic evaluation of the issue and concluded that bolt degradation does not present a "Substantial Safety Hazard" as defined by regulation. The letter provides recommendations for inspection, analysis, and bolt replacement where warranted.

While the nuclear safety concern has been evaluated, the economic impact of baffle-former bolt degradation can be significant for a plant. Some bolt failure patterns could preclude continued operation of a given plant within its design basis. Plant shutdown, or extended refueling outages when bolt failures are discovered, can be very costly. Inspection and replacement activities also increase radiological dose received by plant workers and elevate the industrial safety hazard for those workers, given that the bolts are located in the higher radiation area within the reactor vessel.

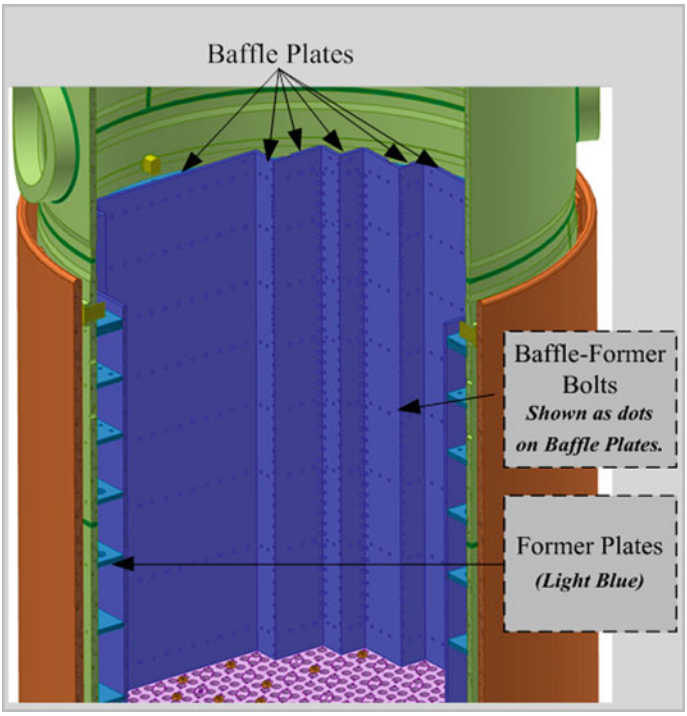

Fig. 1 Depiction of baffle plates, baffle formers, and baffle-former bolts inside the reactor vessel

The observed bolt failures (e.g., Spring 2016 and similar outage seasons) may largely be the result of a two-stage process. In the first stage as the plant operates with all bolts intact, the bolts accumulate IASCC damage over time, and IASCC begins to initiate at essentially random locations across the baffle plates. Given the steady and oscillatory pressure loading within the baffle-former region of a reactor, the cracking is expected to propagate across the bolt shanks relatively rapidly once initiated. In the second stage, these failed or degraded bolts "offload" forces to adjacent unfailed bolts. IASCC initiation and growth are both strongly dependent on the applied stress, so when this re-distribution of forces from failed bolts increases the stress in the adjacent bolts, the rate of degradation in the adjacent bolts increases. Over time, this causes clustered patterns of bolt failures, as observed in the recent operating experience.

Other contributing factors include the design of the baffle-former assembly, the flow configuration of the plant, and the bolt design and material properties. When considering the baffle-former assembly design, the baffle plates in two- and three-loop PWRs typically have more bolts per square inch than those in four-loop reactors, resulting in lower forces imposed onto each bolt. For the flow configuration, there are downflow plants which have more differential pressure across the baffle plates than plants with an upflow design, leading to higher applied bolt

stresses and elevated IASCC risk. Regarding bolt design, the combination of material type (e.g., Type 316 or 347 stainless steel), head design (e.g., internal vs. external hexagon), and head-to-shank radius appear to influence the susceptibility to IASCC-induced failures. These postulations are supported by the operating experience, where the greatest extent of clustered failures was observed in four-loop downflow plants with susceptible bolt designs.

Predictive Methodology Development

Given the potential consequences of baffle-former bolt degradation, a verified and validated method to estimate baffle bolt reliability and to inform inspection and replacement activities is needed to support the operating PWRs. Westinghouse has developed a baffle-former bolt predictive methodology that can be applied before, during, or after a plant outage as summarized in Table 1.

The methodology includes a mix of stochastic and deterministic variables, and applies those variables through both a mechanistic and empirical understanding of how IASCC initiation in baffle-former bolts occurs. The stochastic elements are applied where there is significant uncertainty or randomness, for example with selecting bolt failure locations at each time step. Deterministic elements are used where well-established phenomenological models are available, for example when calculating the distribution of stresses across the baffle-former plate being transferred to intact bolts. The mechanistic understanding of IASCC initiation was drawn from an evaluation of available laboratory data to determine the effects of stress and dose on initiation rate. Finally, the empirical data from baffle-former bolt inspection operating experience were used to calibrate the Weibull parameters used to model bolt reliability.

The model elements are implemented in an overall probabilistic Monte Carlo framework, in the form of a network model using the Analytica software by Lumina Decisions Systems, Inc, which is described in [2]. A probabilistic network model takes a graphical format where variables are represented as nodes and interactions are defined by links between the nodes. A network model can capture complex sets

Table 1 Guidance offered by the baffle-former bolt predictive methodology

Period	Guidance
Pre-outage	Provide guidance for contingency planning and general outage preparation (crew and equipment reservations, number of replacement bolts to order, inspection and replacement timing, etc.)
Outage	Provide real-time recommendations for bolt replacement patterns during the plant outage including replacement of bolts with indications and bolts without indications for additional margin
Post-outage	Use the inspection results to recommend a re-inspection frequency, coverage area, and type of inspection and also determine if and when a plant should be prepared for future replacements

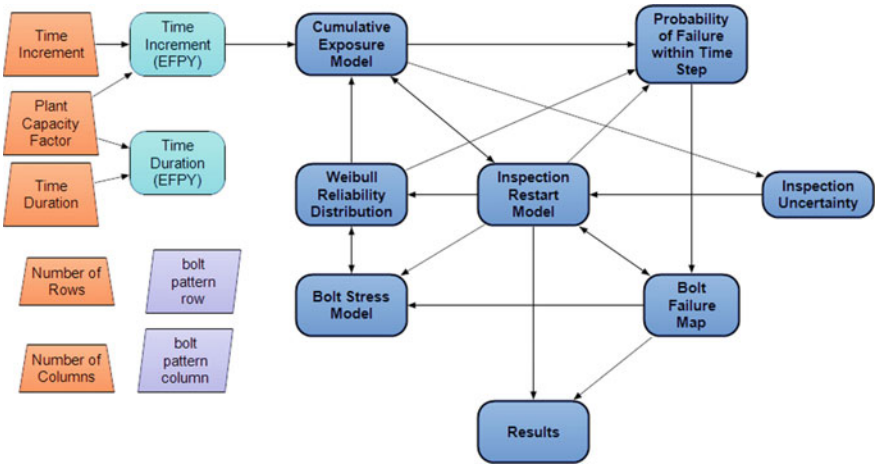

Fig. 2 Predictive model influence diagram

of interdependencies between nodes while maintaining a graphical, intuitive structure, as described in [3]. Figure 2 depicts a high-level influence diagram of the baffle-former bolt model structure.

In Fig. 2, the user-defined inputs are on the left, and the variables and sub-models are in the center and right side of the figure. The various sub-models contain inputs, calculations, other sub-models, and output nodes. The full baffle-former bolt model contains over 200 individual nodes. Each of the major model elements are discussed in the following sections.

At a high level, the simulation starts with a newly fueled reactor that has not yet been operated, with all baffle-former bolts intact. At each subsequent time increment of full reactor power, the model tracks accumulated radiological exposure of the bolts in displacements per atom (dpa) and the changes in total stress on the bolts due to irradiation-induced stress relaxation. The conditional probability of bolt failure is determined using a Weibull distribution and the status (failed or intact) of every individual bolt is tested using a Bernoulli distribution. At the end of each time increment, if additional bolts have failed, the new stress on each bolt is calculated using a finite element analysis of the baffle-former assembly. This provides the redistribution of stress from failed bolts to their neighbors. The results of any inspections or bolt replacements are incorporated into the simulation once those time steps are reached. The simulation continues until the user-specified end point is reached, for example to the end of the current operating license for the plant. The calculations are made using effective full power years (EFPY) but may be presented in terms of calendar years by using the plant capacity factor. The primary output is a baffle-former bolt map that shows the evolution of bolt failures as a function of time.

Additional details are provided in the following sections to describe several of the more critical sub-models used:

1. Weibull reliability model—models the aging of the bolts and provides the probabilistic inputs to the analysis
2. Bolt stress model—evaluates stress and stress redistribution at each bolt location during each time step
3. Cumulative exposure model—used to track the accumulation of damage by each bolt
4. Bolt Failure Probability Model—calculates the conditional probability of failure at each time step
5. Bolt Failure Map—tracks the locations of failed bolts and displays the accumulated probability of failure
6. Inspection restart model—incorporates the results of inspections and replacements performed at the plant.

Weibull Reliability Model

The 'Weibull Reliability Distribution' module models the bolt reliability using the Weibull distribution. The Weibull distribution is used widely for component reliability and in life analyses, and it provides as probability of failure as a function of time, or age [4]. The two-parameter version of the distribution is used for the baffle bolt model and is described by the following probability density and cumulative density functions:

$$\text{Weibull Probability Density} : f(t;k,\lambda) = \frac{k}{\lambda^k} t^{k-1} e^{-\left(\frac{t}{\lambda}\right)^k}$$

$$\text{Weibull Cumulative Density} : F(t;k,\lambda) = 1 - e^{-\left(\frac{t}{\lambda}\right)^k}$$

where t is the time, k is the Weibull shape parameter, λ is the Weibull scale factor, and e is the natural number. Note that the Weibull scale λ is in units of time, consistent with the units of t. Figure 3 illustrates the effect that varying the shape and scale parameters has on the distribution. The Weibull formula reduces to an exponential distribution for $k = 1$, models early life failures for $k < 1$, and models late life failure acceleration or "wear out" failures for $k > 1$. Increasing the scale parameter broadens and shifts the density to the right.

For the baffle bolts, the likelihood of failure due to IASCC is expected to increase with time. Early life failures are unlikely under normal plant operating and bolt stress conditions. This is supported by the plant operating experience, which shows that plants have operated for many years before observed baffle-former bolt degradation. Therefore, the Weibull shape parameter is expected to be greater than 1 and the scale parameter is expected to be relatively large.

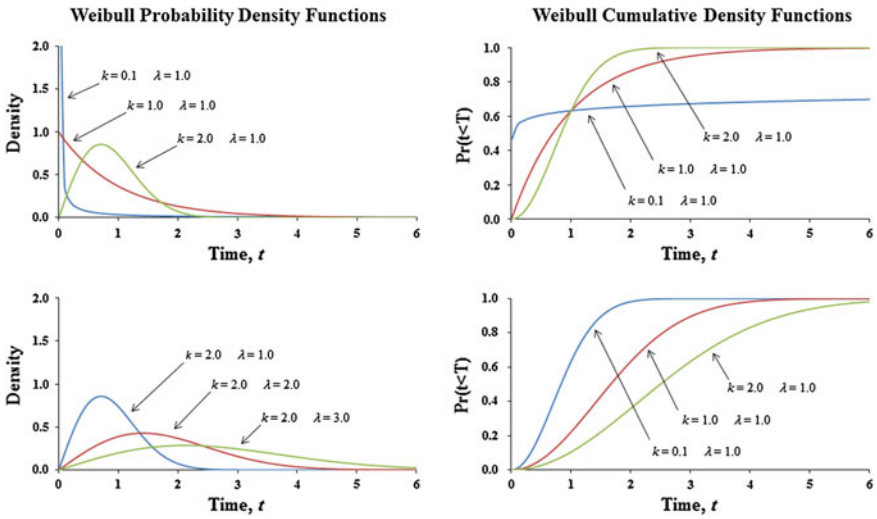

Fig. 3 Two-parameter Weibull distribution for various shape and scale parameters

Inspection results from approximately 20 plants were tabulated, and since several of these plants underwent multiple re-inspections, the compiled data include a total of nearly 40 inspections. Some inspections were partial, and some include all baffle-former bolts, yielding inspection history for over 17,000 bolts. The majority of these inspections used Ultrasonic (UT) volumetric evaluation of the bolt. Thus, the Weibull parameters developed here are primarily based on UT indications with some input from visual observation of completely failed bolts.

A parametric distribution analysis using arbitrary (left and right) censoring was performed to develop a Weibull distribution fitted to the operating experience. Left censoring was applied to cases where the inspection detected an indication, since the inspection result only shows that the bolt developed an indication prior to the inspection and not the exact failure date. Right censoring was applied to cases where the inspection did not detect an indication and the bolt was considered intact and functional.

Note that an attempt was made to filter out bolts involved in clustered failures, such that the resulting Weibull distribution would represent independent failures occurring prior to cluster formation. This, however, was unsuccessful due to relatively limited set of data. It is possible that future re-inspection will provide the data necessary to perform this analysis. In the meantime, the fitted distribution using all data is judged acceptably conservative due to its inclusion of clustered failures and how it is used in the predictive methodology. Data from IASCC initiation laboratory tests were also gathered and analyzed with arbitrary censoring in a similar fashion.

The Weibull shape parameter was developed from the combined evaluation of the plant inspection and laboratory initiation data. The form of the scale parameter was also developed based on both sets of data. The accelerated laboratory testing provided the form of the scale parameter. A non-linear regression was performed on

the laboratory data to develop the following estimation of the scale parameter at time step i:

$$\lambda_i = \frac{e^a}{\left(\frac{\sigma_i}{S_y}\right)^b} \Bigg/ 1 - e^{-\left(\frac{t_i \times dpa}{d_0}\right)^c}$$

In this expression, σ_i is the applied stress at time step i, S_y is the irradiated yield strength of the material, dpa is the radiation dose in displacements per atom, t_i is the time of the predictive evaluation at time step i, and d_0 is an adjustment factor used to tune the effect that dose has on scale based on laboratory testing. Note that σ_i is dependent upon the finite element based stress redistribution model and corresponding pressure loading as well as the accumulated dose and associated impact on preload stress.

Exponents a and b are based on a non-linear regression fit in which exponent a is used to tune the effective scale based on the observed operating experience. Similarly, exponent c is used to accommodate the effect that dose has on the effective scale. Thus, the scale is first established based on the laboratory data and then validated based on the operating experience.

Figure 4 illustrates the effect of stress on the estimated Weibull scale parameter (i.e., characteristic life based on material and environment). This plot includes the Weibull scale parameter for multiple example bolt locations. The scale parameter increases when the stress decreases, indicating that the rate of bolt degradation has decreased, and decreases when the stress increases, indicating a shorter life. The increases in bolt stress/decreases in scale parameter correspond to locations where adjacent bolts fail at some point, increasing (re-distributing) the stress to which the unfailed bolt is exposed. Note that in Figs. 4, 5, 7, and 8 the line colors pertain to a particular circumferential bolt location amongst a row of bolts at a given elevation.

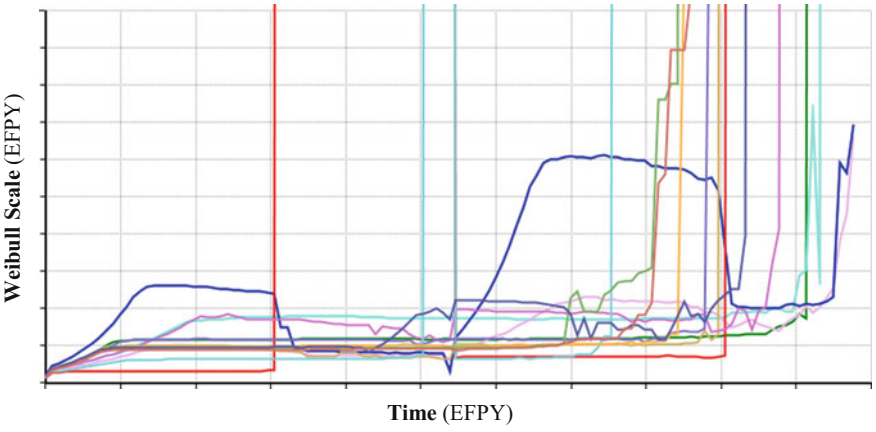

Fig. 4 Stress effect on Weibull scale parameter (typical)

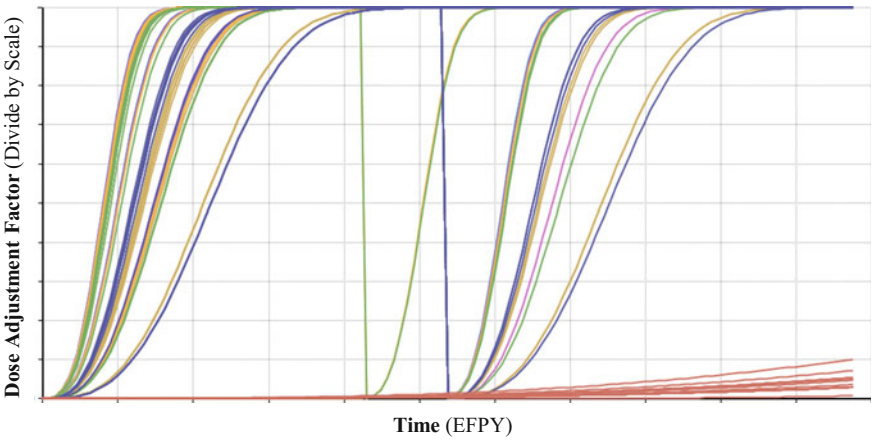

Fig. 5 Dose effect on Weibull scale parameter (typical)

Figure 5 illustrates the effect of radiological dose exposure on the estimated bolt Weibull scale parameter. The scale parameter is adjusted upward with increasing dose exposure by dividing by this factor. This adjustment to the scale parameter addresses the fact that IASCC does not occur at zero dose.

Bolt Stress Model

The applied stress on each baffle-former bolt is a critical input to the predictive methodology to determine the likelihood of IASCC initiation. The bolt stress model in the methodology estimates the stress at each individual bolt location for each time step in the simulation. The model includes the initial bolt stress (prior to plant startup) and the effect of stress relaxation as the bolts are exposed to the operating reactor environment over time. These initial input stress parameters are obtained from the baffle-former bolt stress models used in developing acceptable bolting patterns per the Nuclear Regulatory Commission-approved methodology in [5].

This module also includes a finite element analysis model that runs at each time step to estimate the redistribution of stresses when bolts fail during that time step. The finite element analysis model uses the ANSYS software and is specific to the reactor under study (Fig. 6).

When bolts begin to fail as the simulation progresses through time, the stress re-distributes such that surviving bolts carry higher stresses. As described in Section "Bolt Stress Model", the higher stresses reduce the effective Weibull scale which then results in a higher conditional probability of bolt failure in subsequent time steps. An example of the evolution of bolt stress versus simulation time is shown in Fig. 7.

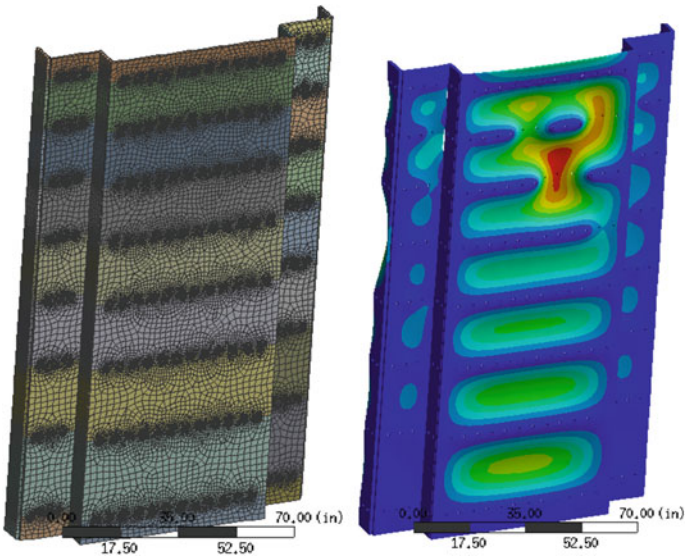

Fig. 6 Stress re-distribution finite element analysis model mesh and example displacement contour

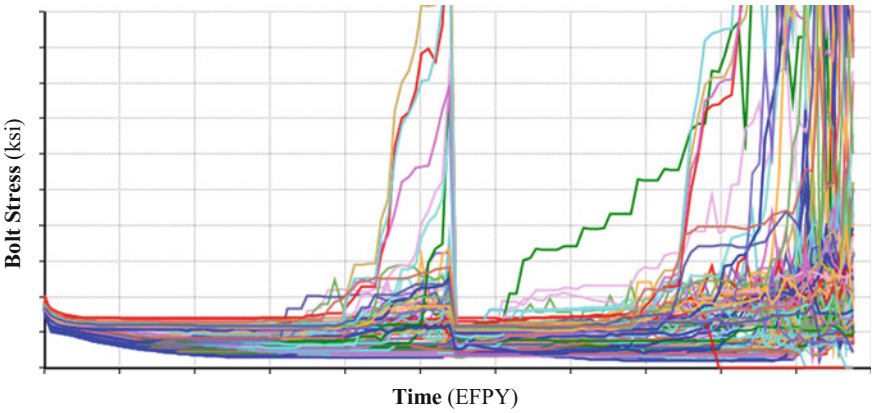

Fig. 7 Bolt stress versus time (typical)

Cumulative Exposure Model

The 'Time Increment', 'Plant Capacity Factor', and 'Time Increment (EFPY)' nodes are inputs used in the 'Cumulative Exposure Model'. As the simulation progresses from initial plant startup through the prediction time of interest, the 'Cumulative Exposure Model' tracks the duration to which the baffle bolts have

been exposed to full reactor power and calculates the cumulative exposure consistent with well-accepted reliability analysis techniques described in [6]. At each time increment, Δt_i, using the Weibull scale λ_i in a manner analogous to fatigue usage, an incremental exposure is determined as:

$$\epsilon_i = \frac{\Delta t_i}{\lambda_i}$$

This incremental exposure is summed over time to determine a cumulative exposure at each time step:

$$\sum \epsilon(t_i) = \sum_{i=t_{start}}^{t_i} e_i$$

Bolt Failure Probability Model

The probability of failure at each time step is calculated as a conditional probability given that the subject bolt survived to the beginning of the time step. This is computed with the following expression, where k is the Weibull shape parameter:

$$P(t_i) = 1 - e^{-\left(\sum \epsilon(t_i)^k - \sum \epsilon(t_{i-1})^k\right)}$$

Figure 8 illustrates this conditional probability as a function of time, for a typical row of baffle-former bolts. Note that this figure includes a model re-start

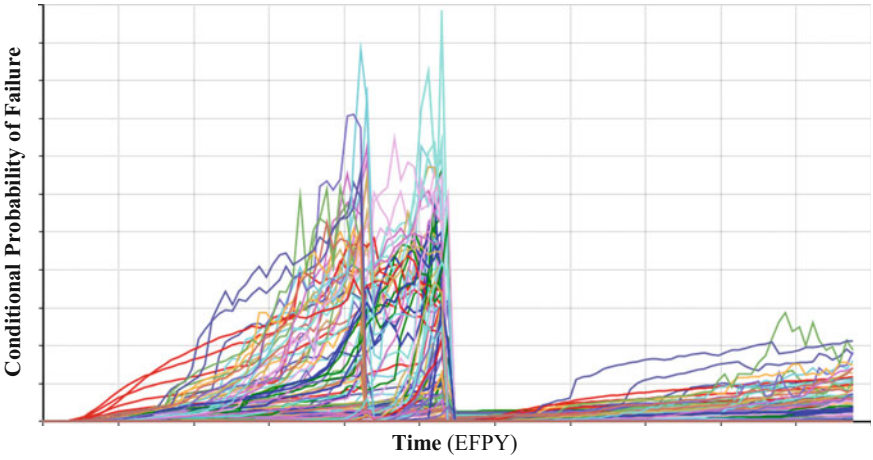

Fig. 8 Conditional probability of failure for a row of baffle-former bolts (typical)

representing an inspection and replacement program after which the probability of bolt failure is very low due to the replacements.

This conditional probability is then compared to a random number between zero and one generated by a Bernoulli distribution. If the probability is less than the random number then the bolt survives that time step. Conversely, if the probability is greater than the random number then the bolt fails during that time step. This module simulates the stochastic nature of IASCC initiation in baffle-former bolts.

Bolt Failure Map

The bolt failure map module tracks the status (failed or intact) of each bolt as a function of time throughout the simulation. During the simulation, this information is used by calculations in the subsequent time step, and at the end of the simulation the bolt failure map provides the final evaluation results. An example of the bolt failure map, colored by probability of failure, is shown in Fig. 9. Red indicates higher probability of degradation, and green indicates lower probability of degradation.

Inspection Restart Model

As shown in Fig. 8, the predictive evaluation model is capable of simulating an inspection or a replacement of the baffle-former bolts. This feature is contained in the "Inspection Restart Model" module of Fig. 2. It incorporates the results of one or more inspections conducted on the baffle-former bolts by updating the knowledge of the bolts with and without inspection indications, or accommodating inconclusive inspection results, thus effectively calibrating the simulation and its predicted bolt maps (from the module described in Section "Bolt Failure Map") to the actual inspection results. It addresses the effect of bolt replacements through resetting the individual bolt damage accumulation accounted for through the modules described in Sections "Cumulative Exposure Model" and "Bolt Failure Probability Model", effectively resetting the IASCC damage on those bolts, and also resetting the irradiation-induced stress relaxation. The replacement of the bolts also has an impact on the stress redistribution model, since the replaced bolts prevent the distribution of high stresses to the bolts adjacent to failed clusters.

Fig. 9 Illustration of probability of bolt failure heat map

Accounting for these various effects results in changes to the bolt stress and condition probability as shown in Figs. 7 and 8. This decrease in redistributed stress and the conditional bolt failure probability is consistent with the expected reduction in bolt degradation rate after a replacement campaign.

Predictive Evaluation Results and Discussion

Figure 10 illustrates one of the key outputs of this predictive methodology. This shows the effect of a predictive evaluation restart following an inspection, including three different replacement bolt options. It may be seen that the predictive methodology described in this paper is able to project the proportion of failed bolts following an inspection and replacement program, based on which particular bolts are replaced. Each of these lines represents a median estimate of the proportion of failed bolts with time.

The blue solid line represents what would happen if the bolts were inspected but no replacements were conducted before continuing operation. This case assumed that the inspection discovered the same number of degraded bolts as the model predicted. The evaluation predicts continued and accelerating degradation for the bolts.

The other two cases represent what would happen if the degraded bolts were replaced (red dashed line) and if the degraded bolts plus some additional "anti-clustering" bolts were replaced (green dotted line). These reduce the number of failed bolts after the replacement to zero. However, the accumulated degradation on the bolts continues to cause further degradation and clustering. The anti-clustering bolts are chosen to limit the amount of future clustering that can

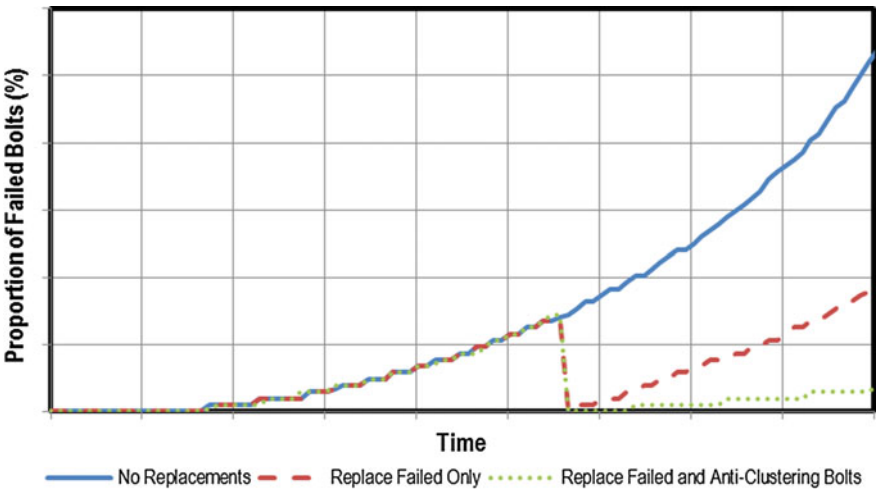

Fig. 10 Proportion of failed bolts versus time with different replacement bolt cases

occur, which causes a substantial long-term difference in the future degradation predicted for these two cases.

In each of these cases, the plausible bolt patterns determined by the Monte Carlo simulation are evaluated with respect to the acceptability of a given bolting pattern under various design-basis conditions (e.g., [5]). As such, a percentage of the projected bolt degradation patterns which show acceptability may be determined. Thus, this permits the replacement bolting patterns to be informed by the projected future outlook of potential clustered BFB degradation. Note that this assessment is done without lengthy finite element analysis.

Benchmarking Through Finite Element Modeling

To benchmark the behavior of the predictive methodology, an alternative method to predict baffle-former bolt degradation was developed based on the probabilistic methods described here and an existing, more detailed finite element model (FEM) of a 3-loop downflow PWR. This finite element analysis (FEA) addresses changes that occur in the RVI materials due to irradiation effects such as irradiation embrittlement, stress relaxation and creep, and void swelling, through use of a material module. The material module, which is based on a constitutive model for irradiated austenitic stainless steels developed in [7] and published by the Electrical Power Research Institute's Material Reliability Program in support of MRP-227-A [8], has been previously used to assess aging effects on baffle-former assemblies [9]. The effects from the materials module are applied to the stainless steel internals, which generates stresses due to the elastic-plastic interactions, creep, and void swelling that are expected to occur as the internals age. The module also addresses the effects of dose accumulation and heat generation from the fuel.

This more detailed FEM with its material module was combined with the statistical predictive analysis described in Section "Weibull Reliability Model". The more detailed FEM and material module incorporate expected aging effects that are not directly addressed by the predictive methodology described in the rest of this paper, and provide an additional way to benchmark it. Like the predictive methodology already described herein, this benchmarking analysis is stochastic in nature, in that it includes the ability to independently "fail" bolts when the probability of failure exceeds a randomly generated number. Upon failure of a bolt, stresses in the baffle-former assembly redistribute and the effects are accounted for when the bolt-by-bolt probabilities of failure are calculated in the next time step of the analysis. The FEA solution follows this process through a 60-year plant life, resulting in a predicted outcome which includes detailed maps of the bolt failures, which can then be summarized in terms of a percentage of failed bolts over time. This process was repeated a number of times to develop a statistical model of baffle-former bolt patterns in 3-loop downflow PWRs.

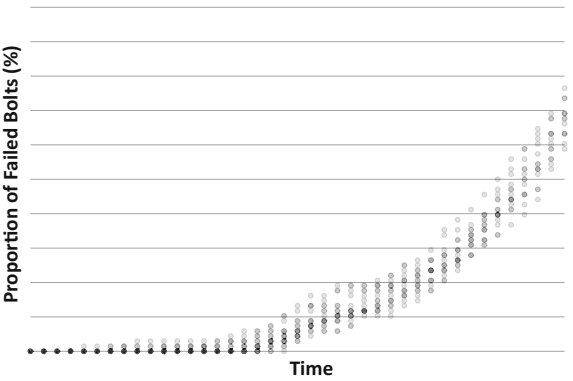

Fig. 11 Baffle-former bolt FEM predictive evaluation results

Figure 11 presents an example of the collective results from the predictive FEM in a plot of percentage of baffle-former bolt failures versus time. Such results were used to compare to the results of the semi-empirical model, in order to validate its behavior.

Conclusions

In conclusion, the Westinghouse baffle-former bolt predictive reliability methodology integrates known empirical and phenomenological considerations within the context of a probabilistic network model. This methodology has been verified and validated through experimental results, plant operating experience, and an independent finite element model. The predictions provided by the methodology are useful in supporting operating PWRs in making decisions about baffle-former bolt inspections, replacements, and other aging management.

References

1. Westinghouse Nuclear Safety Advisory Letter, NSAL-16-1, Revision 1, "Baffle-Former Bolts," August 1, 2016
2. M.G. Morgan, M. Henrion, M. Small, *Uncertainty: A Guide to Dealing with Uncertainty in Quantitative Risk and Policy Analysis* (Cambridge University Press, Cambridge, 1992)
3. U.B. Kjaerulff, A.L. Madsen, *Bayesian Networks and Influence Diagrams: A Guide to Construction and Analysis*, 2nd edn. (Springer, Heidelberg, 2013)
4. R.B. Abernethy, *The New Weibull Handbook*, 4th edn. (Robert B. Abernethy, North Palm Beach, FL, 2000)
5. Westinghouse Report WCAP-15030-NP-A, *Westinghouse Methodology for Evaluating the Acceptability of Baffle-Former-Barrel Bolting Distributions Under Faulted Load Conditions*, January 1999
6. K.C. Kapur, L.R. Lamberson, *Reliability in Engineering Design* (Wiley, Hoboken, 1977)

7. *Materials Reliability Program: Development of Material Constitutive Model for Irradiated Austenitic Stainless Steels (MRP-135-Rev. 1)*. EPRI, Palo Alto, CA: 2010. 1020958
8. *Materials Reliability Program: Pressurized Water Reactor Internals Inspection and Evaluation Guidelines (MRP-227-A)*. EPRI, Palo Alto, CA: 2011. 1022863
9. F.J. Marx, R.G. Lott, C.L. Boggess, A. Dema, ICONE17-75788: Aging Management of Nuclear Power Plant Reactor Internals, in *Proceedings of 17th International Conference on Nuclear Engineering*, ICONE-17 2009, July 2009

Technical Basis and SCC Growth Rate Data to Develop an SCC Disposition Curve for Alloy 82 in BWR Environments

Katsuhiko Kumagai, Yusuke Sakai and Takayuki Kaminaga

Abstract Alloy 82 weld metal shows higher Stress Corrosion Cracking (SCC) resistance in BWR environments than Alloys 182 and 132. To define the relative factor of improvement in SCC resistance and its impact on plant management properly, it is appropriate to establish a SCC growth rate disposition curve for Alloy 82 in BWR environments. In this study, several factors that influence SCC growth behavior of Alloy 82 are evaluated based on the latest Crack Growth Rate (CGR) data collected in Japan BWR Owners Group projects. The goal is to provide a technical basis on which the validity of the data will be evaluated prior to proposing a new disposition curve. The factors evaluated include effects of type of Alloy 82 weld, specimen size, post weld heat treatment (PWHT) and sulfate addition on SCC growth rate.

Keywords Stress corrosion cracking · Ni base alloy · BWR · Crack growth rate · Disposition curve · Weld type · Size effect

Introduction

Ni base Alloy 182, 132 and 82 weld metals are widely used in dissimilar weld joints between the Reactor Pressure Vessel (RPV) made of ferritic low alloy steel (LAS) and core internal structures made of austenitic stainless steels. Alloys 182 and 132 proved to be quite susceptible to SCC in BWR environment, and Alloy 82 with higher Cr content and automated welding applicability is now used.

Although Alloy 82 has shown higher SCC resistance in both BWR plant operational experience and in laboratory tests, the relative factor of improvement

K. Kumagai (✉) · Y. Sakai
R&D Center, Tokyo Electric Power Company Holdings (TEPCO), 4-1 Egasaki-Cho, Tsurumi-Ku, Yokohama 230-8510, Japan
e-mail: kumagai.k@tepco.co.jp

T. Kaminaga
Nuclear Asset Management Department, TEPCO, 1-1-3 Uchisaiwai-Cho, Chiyoda-Ku, Tokyo 100-8560, Japan

J.H. Jackson et al. (eds.), *Proceedings of the 18th International Conference on Environmental Degradation of Materials in Nuclear Power Systems – Water Reactors*, The Minerals, Metals & Materials Series, https://doi.org/10.1007/978-3-319-68454-3_30

(FOI) versus Alloys 182 and 132 has not been credited in plant management, partly because an SCC growth rate disposition curve for Alloy 82 in BWR environment has not been established in Japanese and US codes and standards.

Efsing et al. proposed a disposition curve (Swedish curve) based on SCC growth rate data at a stress intensity factor (K) range of 14–50 MPa$\sqrt{m}$ and concluded that the relative FOI versus Alloy 182 is 2.9 [1]. This FOI is consistent with the FOI of 2.6 for PWSCC growth rate of Alloy 82 versus Alloys 182 and 132 [2].

The majority of the data used to develop the Swedish curve are, however, obtained with periodic partial unloading (PPU) cycles with hold times at K_{max} of >9000 s. Applying PPU cycles is reasonable way to obtain a conservative estimate within a limited test time, especially for resistant materials such as Alloy 82. However, PPU always biases the lower CGR data more, and thus the FOI could be even higher if the disposition curve were established based on SCC growth rate data under static loading conditions such as constant K or constant load.

In establishing a disposition curve for Alloy 82, data at a higher K (>50 MPa$\sqrt{m}$) are also needed because the threshold K for stress corrosion cracking propagation from a Ni-base alloy to LAS is estimated to be about 60 MPa$\sqrt{m}$ [3].

In this study, several influential factors on SCC growth behavior of Alloy 82 are evaluated as a part of data collection activities in Japan BWR Owners Group (JBOG) projects to provide technical basis for data screening procedure that should precedes the disposition curve development.

Test Materials

RPVs are clad with austenitic stainless steel to minimize general corrosion. In Japanese BWRs, Alloy 82 clad is also employed adjacent to the dissimilar weld joint with core internals such as core shroud support legs and control rod drive stub tubes. Figure 1 shows a typical configuration of a dissimilar weld joint between an RPV and a core shroud support leg (H11 weld) in Japanese BWRs. Strip clad welding techniques by submerge arc welding (SAW) or electro slag welding (ESW) are used for both stainless steel and Alloy 82. In some units, attachment pads of Alloy 82 are placed onto the cladding by metal inert gas (MIG) welding followed by a PWHT. Core shroud support legs are then attached with Alloy 182 (shielded metal arc welding, SMAW) or Alloy 82 (gas tungsten arc welding, GTAW), that receives no PWHT.

The test materials used in this study were taken from a mockup block of H11 weld, shown in Fig. 2a. Three layers of Alloy 82 cladding by SAW and weld buildup by Alloy 82 MIG with 50 mm thickness were deposited on a LAS plate (SQV2A, equivalent to A533B) of 100 mm thickness. To evaluate multiple factors of the weld type on SCC behavior properly, the fabrication procedures of an H11 weld of an actual unit were simulated, as summarized in Table 1.

CT specimens of three different sizes, 0.5 inch (0.5TCT), 1 inch (1TCT) and 1.5 inch (1.5TCT) in thickness, were machined from the weld mockup as shown in Fig. 2a.

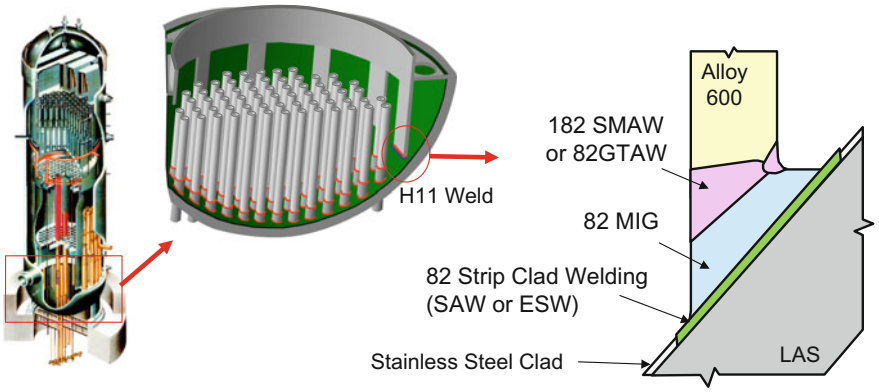

Fig. 1 Weld configuration and weld types used at a dissimilar weld joint between RPV and core shroud support leg (H11 weld)

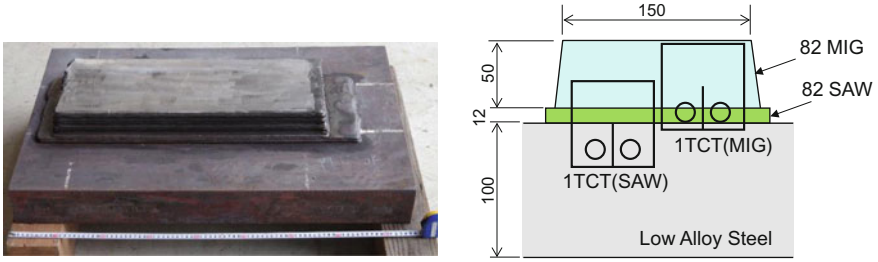

(a) H11 weld mockup block used for Alloy 82 MIG and SAW samples tested at GE-GRC and TEPCO.

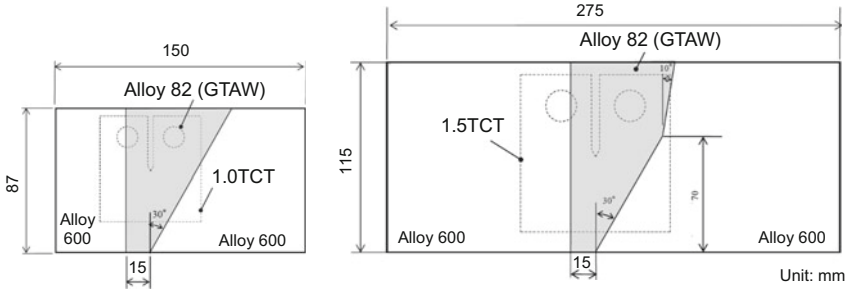

(b) Examples of butt weld block for Alloy 82 GTAW samples tested at Toshiba and Hitachi-GE in JBOG project.

Fig. 2 Schematics of test materials and the CT sample orientation/location.

Table 1 Fabrication procedure of H11 weld mockup

	Process	Note
1	Strip Clad welding by SAW	3 layers with 9 passes in total Strip Electrode: 0.4 mm × 75 mm Preheating & Interpass Temp: 116–162 °C
2	PWHT 1	615 °C × 2.5 h
3	Weld Buildup by MIG	18 layers with 352 passes in total Rod Diameter: 1.2 mm Preheating & Interpass Temp: 6–67 °C
4	PWHT 2	615 °C × 18 h

Table 2 Chemical composition of filler metals for different types of Alloy 82 weld (wt%)

		C	Si	Mn	P	S	Ni	Cu	Cr	Fe	Nb + Ta	Ti
SAW		0.005	0.07	3.28	0.004	0.001	71.6	0.01	20.97	0.82	2.61	0.52
MIG		0.031	0.06	2.81	0.004	0.001	71.0	0.03	20.75	1.74	2.93	0.48
GTAW A		0.030	0.12	2.94	0.005	0.001	70.4	0.02	20.94	2.05	2.94	0.45
GTAW B		0.011	0.22	3.06	0.005	0.001	70.76	0.02	20.45	2.09	2.71	0.53
Spec.	min	–	–	2.5	–	–	67.0	–	18.0	–	2.0	–
	max	0.1	0.5	3.5	0.030	0.015	–	0.50	22.0	3.0	3.0	0.75

Table 3 Mechanical properties of different types of Alloy 82 weld materials at 288 °C

		Yield stress (MPa)	Relative yield stress versus SAW	Tensile strength (MPa)	Flow stress (MPa)	Elongation (%)
SAW		302	1.0	524	413	44
MIG		393	1.30	594	494	34
GTAW A	PWHT	421	1.39	593	507	30
	As Weld	431	1.43	589	510	30
GTAW B		435	1.44	639	537	34

Butt weld blocks consisting of Alloys 600/82/600 were also evaluated in a JBOG project (Fig. 2b). GTAW was used for all the blocks using two different heats of Alloy 82 filler metal A and B, mainly focusing on the effect of carbon content on the SCC growth rate.

The chemical composition and mechanical properties of test material are summarized in Tables 2 and 3, respectively.

Experimental Procedures

CT specimens with 5% side grooves on each side were machined from the H11 mockup weld and were installed in a stainless steel autoclave equipped with Interactive Instruments model 5K or 10K servo loading systems or Instron Model 8862 servo-electric testing machines. The crack length (a) of the specimens was monitored using a reversed DC potential drop (DCPD) technique. Both the loading systems and the DCPD equipment were controlled by single PC program, which controls constant K or dK/da as the crack advances. SCC growth rate measurements of H11 mockup materials were conducted at constant K (dK/da = 0) by reducing the applied load based on the measured crack extension.

When two CT specimens were installed in one autoclave in tandem, each specimen was fatigue pre-cracked in air prior to the in situ transitioning in the test environment. To achieve a gradual transition of the crack morphology from transgranular to inter-dendritic (ID) cracking, the loading frequency was decreased stepwise to 0.1, 0.01 and 0.001 Hz, while maintaining a load ratio R = 0.4–0.7. Before transitioning to a fully static load condition, trapezoidal wave loading steps with hold times at K_{max} of 3000–85,400 s were introduced. Some tests used 10 ppb sulfate (as H_2SO_4) during in situ pre-cracking to achieve higher ID crack engagement along the crack front. Actual pre-crack procedures were determined based on the crack behavior of each specimen, therefore, applied R ratio and hold times differ specimen to specimen.

The tests of the H11 mockup material were conducted in 288 °C water containing 2 ppm dissolved oxygen (DO) in separate laboratories at GE Global Research Center (GE-GRC) and TEPCO. Influent water was kept at 0.055–0.057 μS/cm unless sulfate was injection. Effluent water was generally ~0.06 μS/cm at GE-GRC and ~0.09 μS/cm at TEPCO. The difference is mainly caused by the chromate ion released from the hot stainless steel tubing used at TEPCO; Ti tubing is used at GE-GRC.

After the test, the CT specimens were fatigued apart for fractography examination. The correction of DCPD measurement was then made by comparing the crack length measured by DCPD versus crack length based on fractography that was determined by dividing the ID crack area by the total width of the ID crack regions. The crack growth rate data were considered to be inappropriate and were screened out when the ID crack engagement (width of ID crack area/specimen thickness) was less than 50% [2].

Results and Discussion

The test results of H11 mockup material are summarized in Table 4. The crack growth rate data of the GTAW butt weld material in the JBOG project are tentative values and are shown only in CGR versus K plots (Figs. 3, 7 and 8) since they are

Table 4 Test results of Alloy 82 MIG and SAW specimen taken from H11 mockup block tested at GE-GRC (indicated by ID starts with C) and TEPCO (ID starts with S)

Sample ID	Sample size	Weld type	SO_4^{2-} injection (ppb)	Applied K (MPa$\sqrt{m}$)	CGR (mm/s)
S002	0.5TCT	SAW	–	39	4.70E-09
S001	0.5TCT	SAW	–	41	1.98E-08
C764	0.5TCT	SAW	–	41	3.00E-09
C764	0.5TCT	SAW	–	42	1.40E-08
C761	1.0TCT	SAW	–	54	5.00E-09
C759	1.0TCT	SAW	–	55	6.00E-08
C759	1.0TCT	SAW	–	55	1.30E-07
C759	1.0TCT	SAW	–	55	4.20E-08
C761	1.0TCT	SAW	–	72	3.90E-09
C759	1.0TCT	SAW	–	77	6.50E-09
S005	0.5TCT	MIG	–	39	7.16E-09
S006	0.5TCT	MIG	–	42	3.68E-08
C765	0.5TCT	MIG	–	71	1.40E-07
C760	1.0TCT	MIG	–	55	6.00E-08
C760	1.0TCT	MIG	–	55	1.10E-07
C760	1.0TCT	MIG	–	55	3.00E-08
C760	1.0TCT	MIG	–	80	7.00E-09
C760	1.0TCT	MIG	–	80	4.00E-09
S008	1.0TCT	MIG	–	90	4.11E-08
S010	1.0TCT	MIG	–	117	3.28E-07
S019	1.0TCT	MIG	–	118	3.58E-07
S023	1.5TCT	MIG	–	100	8.84E-08
S002	0.5TCT	SAW	10	39	3.57E-09
S001	0.5TCT	SAW	10	41	2.50E-08
C764	0.5TCT	SAW	10	43	1.30E-08
C764	0.5TCT	SAW	10	43	2.00E-09
S013	0.5TCT	SAW	10	55	2.86E-08
S014	0.5TCT	SAW	10	55	4.77E-08
S007	1.0TCT	SAW	30	45	3.55E-08
S007	1.0TCT	SAW	10	45	3.53E-08
C759	1.0TCT	SAW	10	55	2.00E-07
C761	1.0TCT	SAW	10	55	1.40E-07
S005	0.5TCT	MIG	10	39	1.25E-08
S006	0.5TCT	MIG	10	42	6.14E-08
C765	0.5TCT	MIG	10	51	7.00E-08
C760	1.0TCT	MIG	10	55	4.50E-07
S020	1.0TCT	MIG	10	123	7.89E-07

still under evaluation by the JBOG members in the on-going project. All of the data will undergo an intensive review and screening, likely by international experts, before a final disposition curve is proposed.

Effect of Weld Type

As shown in Table 3, yield stress of Alloy 82 SAW material is significantly lower than MIG and GTAW materials, probably due to the higher weld heat input. It is well known that an increase in yield stress of a material, e.g. by plastic deformation or neutron irradiation, tends to increase the SCC growth rate. A comparison of the CGR in SAW and MIG materials is shown in Fig. 3. Figure 4 shows typical examples of the macrograph of the fracture surface of SAW and MIG specimens (0.5TCT).

As shown in Fig. 3, both MIG and SAW data have significant scatter with some very low growth rates that are 10 times lower than other specimens tested at the same K level. The scatter in the SAW and MIG data substantially overlap. There seems to be some tendency, however, that the ID crack area of the low CGR specimens (including that formed during in situ transitioning) is smaller in the SAW specimens than in the MIG specimens. In other words, in some MIG specimens, a certain amount of ID crack developed during transitioning but slowed down significantly as the loading condition became closer to static load, whereas the crack

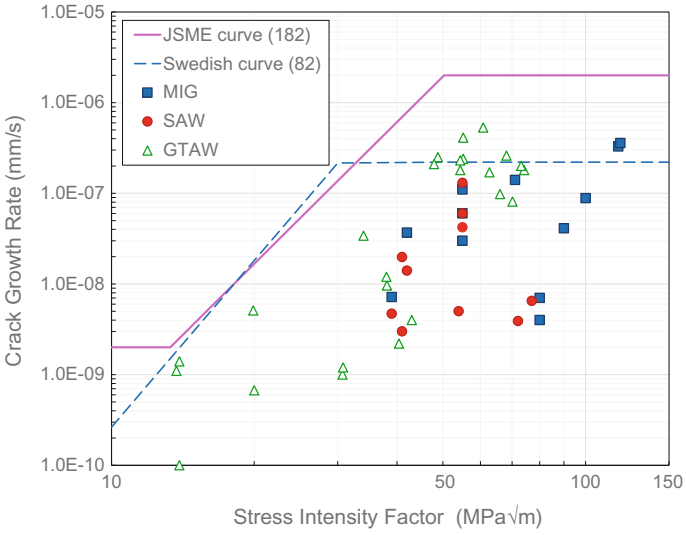

Fig. 3 Crack growth rate versus stress intensity factor plot focusing on the possible difference in CGR between different weld types of Alloy 82

Fig. 4 Macro photographs of 0.5TCT Alloy 82 SAW specimen c764 (left) and 0.5TCT Alloy 82 MIG specimen c765 (right)

growth rates of some SAW specimen were low from the beginning even during transitioning.

This suggests a somewhat lower SCC susceptibility of Alloy 82 SAW than MIG. However, once a steady crack growth is achieved, no significant difference in CGR is expected between MIG and SAW since the maximum CGRs at each K level in Fig. 3 is quite similar.

The data for the GTAW material (plotted using open symbols in Fig. 3) also show little difference in maximum growth rate and falls in the scatter band. At least in terms of disposition curve development, it can be concluded that no discrimination of weld types is needed for Alloy 82.

Sample Size Effect

As discussed in the prior section, crack growth rate data of Alloy 82 at elevated K levels of >50 MPa$\sqrt{\text{m}}$ may be necessary, depending on the weld configuration and on the residual stress profile of the dissimilar weld joint at the RPV bottom. To accumulate enough data at elevated K region, it is preferable to use of smaller specimens, which can be justified by evaluating sample size effect of Alloy 82, rather than testing with larger specimens of a "valid" size for the higher K value.

Sample size criteria for fracture toughness testing (ASTM E1820) or fatigue testing (ASTM E647) are often referred in SCC crack growth evaluations. In those standards, the allowable K is:

$$\text{E1820}: K < \sigma_y \sqrt{(B_{\text{eff}}/2.5)} \tag{1}$$

$$\text{E647}: K < \sigma_y \sqrt{(\pi L/4)} \tag{2}$$

where,

σ_y Yield stress at test temperature
B_{eff} Effective specimen thickness
L Remaining Ligament

The ASTM E647 indicates that when the tensile strength σ_u exceeds $1.3\sigma_y$, σ_y in Eq. (2) can be replaced by the flow stress $\sigma_f = (\sigma_u + \sigma_y)/2$

Richey et al. conducted an extensive study of sample size effects on SCC growth rate of Alloy 600 in PWR primary water environment [4]. They concluded that it is not necessary to meet the validity criteria in ASTM E1820 or E647, and proposed a different criterion:

$$\text{Richey}: K < \sigma_y \sqrt{(2B_{\text{eff}})} \tag{3}$$

The allowable K values for different sizes of Alloy 82 MIG specimens based on the criteria above are summarized in Table 5. How much higher K can be used than indicated by the validity criteria for a given specimen size remains controversial.

In this study, therefore, higher K values than the validity criteria were applied in some tests that used 1.0T and 0.5TCT specimens. Figure 5 shows the crack growth behavior of Alloy 82 MIG, 1.0TCT specimen (sample ID: s019) tested at a K of 120 MPa$\sqrt{\text{m}}$. A sudden increase in PDM signal was observed at 966 h in the test, after 400 h of steady crack growth at a constant K condition. The specimen was automatically unloaded immediately and the test temperature was left unchanged for 20+ hours after the jump. The crack turned out to be yawed open with significant plastic deformation at the un-cracked ligament. The crack extension associated with the jump in PDM signal could easily be identified by the color of the fracture surface due to the thin oxide film formed during the 20+ hours (Fig. 6). SEM observation clearly showed that the failure was due to the ductile fracture caused by the plastic instability.

Table 5 Allowable K maximum for different sized alloy 82 (MIG) CT specimens evaluated based on various validity criteria (MPa$\sqrt{\text{m}}$)

	ASTM E1820 (Thickness)	ASTM E647 (Ligament)	Richey [4] (Thickness)
Parameter	σ_y	σ_f	σ_y
0.5TCT	27.3	51.7	61.0
1.0TCT	38.6	73.1	86.3
1.5TCT	47.3	89.5	106
2.0TCT	54.6	103.4	122

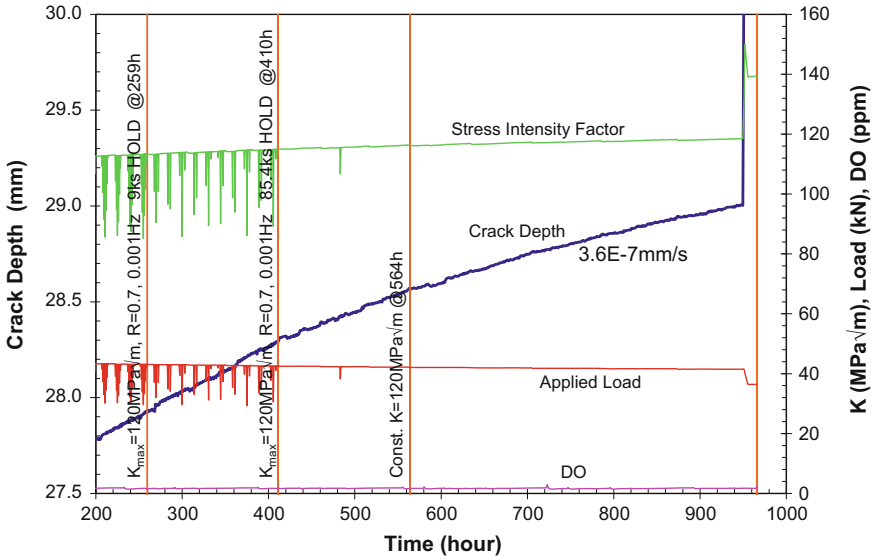

Fig. 5 Crack depth versus time for 1TCT specimen s019 of Alloy 82 MIG tested at elevated K level of 120 MPa$\sqrt{\text{m}}$ (288 °C, 2 ppm DO with no impurity addition)

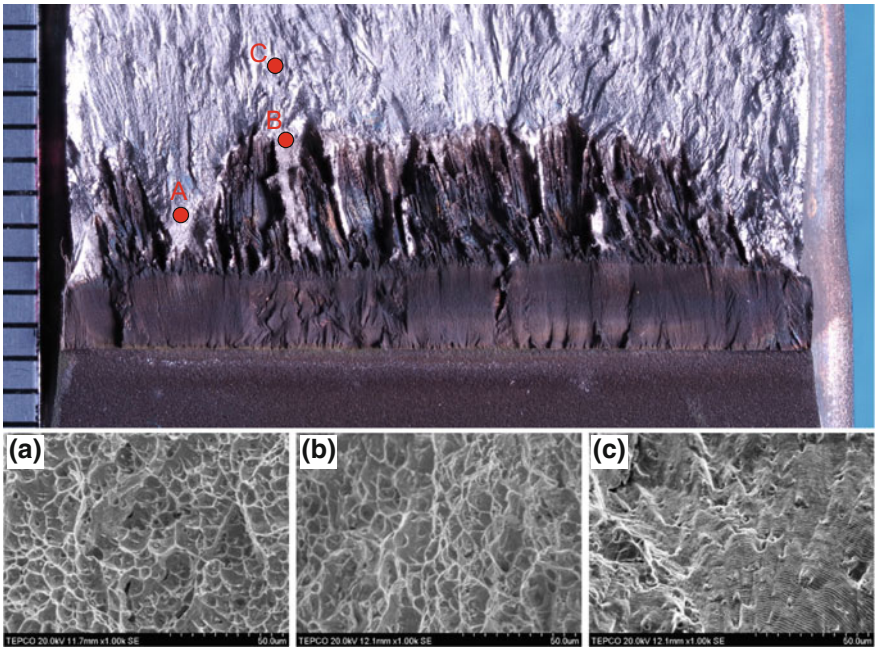

Fig. 6 Fracture surface of 1TCT Alloy 82 MIG specimen s019 tested at elevated K level of 120 MPa$\sqrt{\text{m}}$ where rapid ductile fracture occurred after a period of steady SCC growth

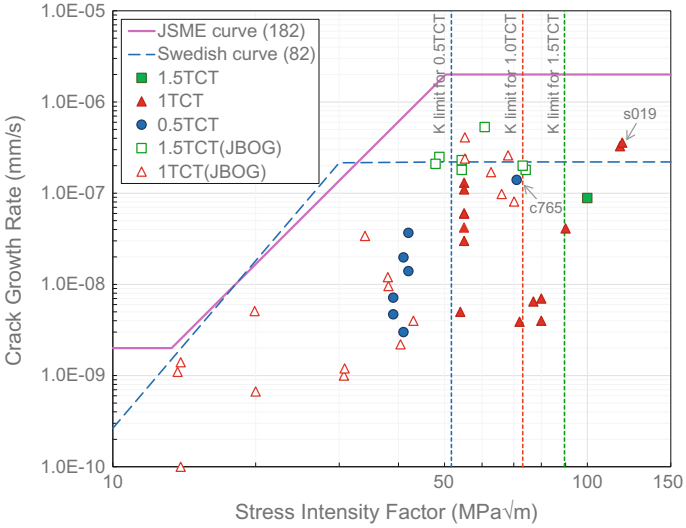

Fig. 7 Crack growth rate versus stress intensity factor plot of Alloy 82 SAW, MIG and GTAW highlighting the effect of specimen size and CGR at elevated K levels beyond the validity criterion in Eq. (3)

Three 1TCT specimens in total were subjected to tests at the same K level, and similar rapid ductile fracture after several hundred hours of steady SCC growth was observed in all cases. This indicates that 120 MPa$\sqrt{m}$ is close to the upper limit that can be applied to 1TCT specimen. As shown in Fig. 7, however, SCC growth rate data measured during the static loading prior to the rapid fracture are fairly close to those obtained at lower K level of 50–100 MPa$\sqrt{m}$. Similarly, SCC growth rate at 70 MPa$\sqrt{m}$ using 0.5TCT specimen (Sample ID: c765) shows no excessive acceleration in comparison with other data obtained using different size CT specimens at the same K level.

More data should be collected to draw definitive conclusions; however, it suggests that even the criterion in Eq. (3) is conservative and that SCC growth rate testing up to $\sim$100 MPa$\sqrt{m}$ can be conducted using 1TCT specimens at least in the case of Alloy 82 weld metal in BWR water.

Effect of PWHT

Le Hong et al. suggested that CGRs of stress relieved specimens of Alloy 182 in primary water of PWR are lower by half compared to as-received specimens [5]. Since as-welded Alloy 82 exists in some Japanese BWRs, CGR measurements on as-welded specimens were also conducted in the JBOG program. As shown in

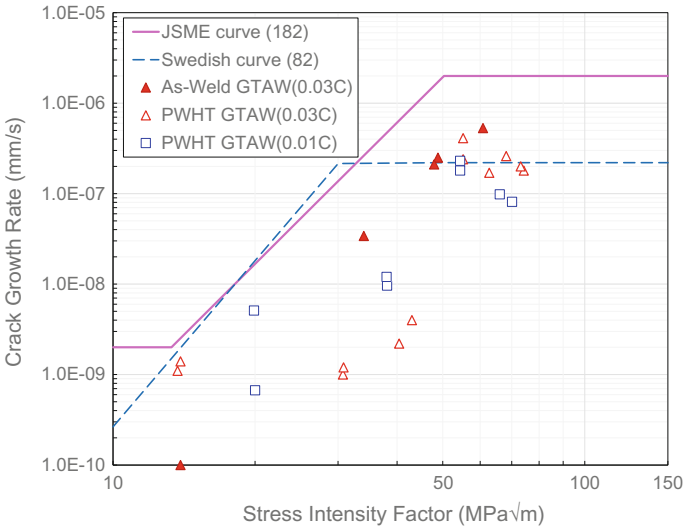

Fig. 8 Crack growth rate versus stress intensity factor for Alloy 82 GTAW A and B with different carbon contents, highlighting the effect of PWHT

Fig. 8, data from as-welded specimens are located at the upper end of the wide scatter of the entire data set.

Amzallag et al. suggested that the effect of the PWHT on the PWSCC growth rate of Alloy 182 is larger when the carbon content is higher [6]. The current dataset in this study is inconclusive, and PWHT effect should also be evaluated using materials of different carbon content. However, this result suggests that some beneficial effect of PWHT in lowering SCC growth rate may also exist in BWR NWC environments.

Effect of Sulfate Injection

Multiple SCC growth rate data of Alloy 82 are reported in oxygenated high temperature water with 10–30 ppb of sulfate added [7]. For materials with higher SCC resistance, such as Alloy 82, sulfate injection helps achieve a steady SCC growth with higher ID crack engagement, which is vital to properly evaluating the effect of influential parameters such as K or ECP.

To utilize such data in an SCC disposition curve development, however, it is important to quantitatively understand how much acceleration of SCC growth rate is expected by injecting $\sim$30 ppb of sulfate to the test environment.

In this study, some CGR data were measured at constant K with 10 ppb of sulfate to reinforce the same study concluding the sulfate effect is "$\sim$2–3X" [7].

Figure 9 highlights the comparison between CGR in pure water and 10 ppb sulfate environment. By comparing the maximum crack growth rate at each *K* level, the acceleration by 10 ppb sulfate was evaluated to be "1.7–4.4X".

Remaining Tasks in Alloy 82 Disposition Curve Development

EPRI organized an Expert Panel consists of international experts to develop SCC disposition curves for Alloys 82, 182 and 132 in PWR primary water. The report of the extensive discussions has been published as a Technical Report of the PWR Materials Reliability Program [2].

Figure 10 shows an example of data screening by the experts. Almost 70% of the available data (101 out of 144) were screened out because of the insufficient data quality. The data summarized in Table 4 and JBOG project should also undertake intensive review and screening, preferably from International Experts, and at an early stage so that the proposed disposition curve will be more reliable and credible.

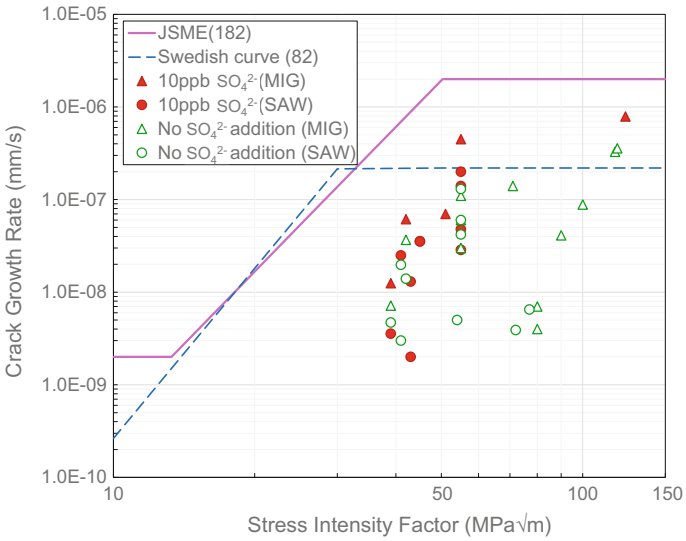

Fig. 9 Crack growth rate versus stress intensity factor for Alloy 82 MIG and SAW, highlighting the effect 10 ppb sulfate in the test environment

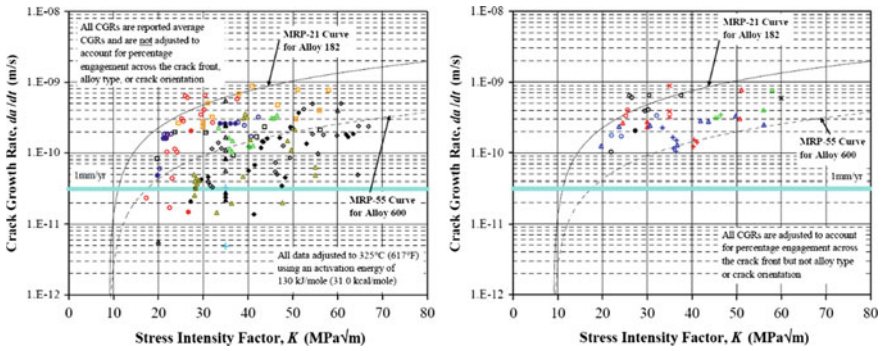

Fig. 10 An example of data screening of PWSCC growth rate data for Alloy 600 conducted in MRP-115 where 144 available data in total (left) were reduced to only 31 (right) by the screening procedure

Conclusions

- No significant difference in SCC growth rate of Alloy 82 was observed between different weld types despite a 30–40% difference in yield strength.
- SCC growth rate tests using 1TCT specimen of Alloy 82 at an elevated K level of $\sim$100 MPa$\sqrt{\text{m}}$ suggest that the validity criterion of $K < \sigma_f\sqrt{(2B_{eff})}$ can be applicable to Alloy 82 in BWR NWC environments.
- The SCC growth rate of Alloy 82 after PWHT is somewhat lower than in as-welded specimens, although more CGR data and metallurgical evaluations are necessary.
- Injection of $\sim$10 ppb of sulfate can accelerate the SCC growth rate by 2–4 times.
- Undertaking intensive data quality review and screening procedure are important prior to the developing a disposition curve that is credible and reliable.

Acknowledgements GTAW data were collected in a co-operative research program between Japan BWR Owners Group (The Chugoku Electric Power Co., Tohoku Electric Power Co., Tokyo Electric Power Company Holdings, Chubu Electric Power Co., Hokuriku Electric Power Company, The Japan Atomic Power Company, Electric Power Development Co., Toshiba Corporation and Hitachi-GE Nuclear Energy. Some of the MIG/SAW tests were performed at the GE Global Research Center. Those valuable data and many discussions are gratefully acknowledged.

References

1. P. Efsing et al., IGSCC disposition curve for Alloy 82 in BWR normal water chemistry, in *13th International Conference on Environmental Degradation of Materials in Nuclear Power Systems* (2007)

2. Materials Reliability Program, *Crack Growth Rates for Evaluating Primary Water Stress Corrosion Cracking (PWSCC) of Alloy 82, 182, and 132 Welds (MRP-115)*, EPRI, Palo Alto, CA: 2004, 1006696
3. K. Kumagai et al., Effects of K and Impurity Concentration on Crack Growth Kinetics At Alloy 182/A533B Weld Overlay Boundaries in BWRs, in *14th International Conference on Environmental Degradation of Materials in Nuclear Power Systems* (2009)
4. E. Richey, D. Morton, W. Moshier, Influence of specimen size on the SCC growth rate of Ni-alloys exposed to high temperature water, in *Proceedings of Corrosion 2006*, Paper 06513, NACE (2006)
5. S. Hong et al., Measurements of stress corrosion cracking growth rates in Weld Alloy 182 in primary water of PWR, in *10th International Conference on Environmental Degradation of Materials in Nuclear Power Systems* (2002)
6. C. Amzallag et al., Stress corrosion life assessment of 182 and 82 welds used in PWR components, in *10th International Conference on Environmental Degradation of Materials in Nuclear Power Systems* (2002)
7. P. Andresen, SCC of Alloy 182 and 82 weld metals in BWR water, in *Proceedings of Corrosion 2010*, Paper 10284, NACE (2010)

Part V
BWR SCC and Water Chemistry

SCC and Fracture Toughness of XM-19

Peter Andresen, Martin Morra and Robert Carter

Abstract The effect of stress intensity factor, cold work, corrosion potential and water purity on the stress corrosion crack (SCC) growth rate behavior of as-received and as-received plus 19.3% cold worked XM-19 was investigated in 288 °C BWR water. For 19.3% cold rolled XM-19, high to very high crack growth rates were consistently observed at high corrosion potential, largely independent of heat or orientation. As received XM-19 exhibited SCC growth rates ~5–10X slower than cold worked XM-19, but these rates are still considered high. For all materials and conditions, low corrosion potential conditions reduced the growth rates by about an order of magnitude, and somewhat more if impurities were present in the water. The SCC growth rates for both conditions of XM-19 were somewhat higher than the equivalent conditions of 18-8 stainless steels, such as Types 304/304L and 316/316L. Higher growth rates tend to be observed at higher yield strength, and XM-19 has an elevated yield strength from nitrogen-strengthening; incomplete annealing in the as-received material can also increase the yield strength. The J-R fracture resistance of 19.3% cold rolled XM-19 and as-received XM-19 in multiple orientations and with replicates was evaluated in 288 °C air. The data show a significant effect of crack orientation in the plate (the rolling plane coincides with the plane of the plate), consistent with the inhomogeneous nature of the microstructure. The fracture resistance of as-received XM-19 was good, but the 19.3% cold rolled XM-19 specimens exhibited low toughness, to the extent that many tests were invalid. Fracture resistance in 80–288 °C water environments was not evaluated, but is relevant to LWR components. Irradiation of this heat of XM-19 is in progress at the Idaho National Laboratory Advanced Test Reactor.

P. Andresen (✉)
Andresen Consulting, 12204 Wildwood Park Place, Bakersfield, CA 93311, USA
e-mail: PLAndresen@gmail.com

M. Morra
GE Global Research Center, One Research Circle, Schenectady, NY 12309, USA

R. Carter
Electric Power Research Institute, 1300 West W.T. Harris Blvd., Charlotte, NC 28262, USA

J.H. Jackson et al. (eds.), *Proceedings of the 18th International Conference on Environmental Degradation of Materials in Nuclear Power Systems – Water Reactors*, The Minerals, Metals & Materials Series, https://doi.org/10.1007/978-3-319-68454-3_31

Keywords Stress corrosion cracking · Crack growth rate · Cold work · J-R fracture resistance · Boiling water reactor · XM-19 stainless steel · Water chemistry

Introduction

Many structural materials used in boiling water reactors (BWRs) and pressurized water reactors (PWRs) have exhibited stress corrosion cracking (SCC). While the crack growth behavior of various grades of stainless steel, Alloy 600 (UNS N06600), Alloy 182 weld metal, and low alloy and carbon steels have been extensively investigated [1–13], until recently there was only limited stress corrosion crack growth rate data on XM-19 (UNS S20910) in high temperature, pure water [14], especially in processing forms and heat treatments relevant to plant components. XM-19 is attractive because of its higher yield strength, and because the somewhat higher Cr content is perceived as beneficial to SCC resistance.

These studies focused on BWR environments, but are also relevant to PWR environments, given that the crack tip is deaerated and at low potential (with the increasing adoption of NobleChem™ in BWRs, even the surface corrosion potential is low). Thus, the crack tip conditions in BWR and PWR-primary systems are closely related [2–4, 11–13], differing primarily in temperature (most BWR components operate at 274 °C vs. 290–343 °C in PWRs), H_2 fugacity (10–150 ppb in BWRs vs. ≈3000 ppb in PWRs) and coolant additives that shift the pH at temperature from 5.6 in BWRs to 6.8–7.4 in PWRs.

The role of retained deformation is important because there are many instances of incomplete annealing, straightening, welding and other processes that can induce bulk deformation. Weld residual strains in particular peak near the fusion line and the weld root, and often peak in the range of 20–30% (Fig. 1). SCC growth rates in

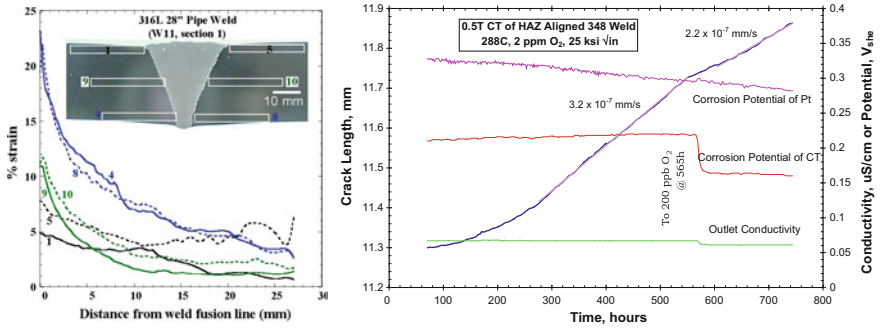

Fig. 1 Left: Equivalent room temperature tensile strain in the heat affected zone adjacent to the weld fusion line determined from electron backscattered diffraction [15–17]. The peak strain always occurs near the fusion line and at the root of the weld, with values of 20–30% being common both in stainless steel and Alloy 600. Right: SCC response for a Nb-stabilized, high N-bar stainless steel specimen aligned along the weld HAZ

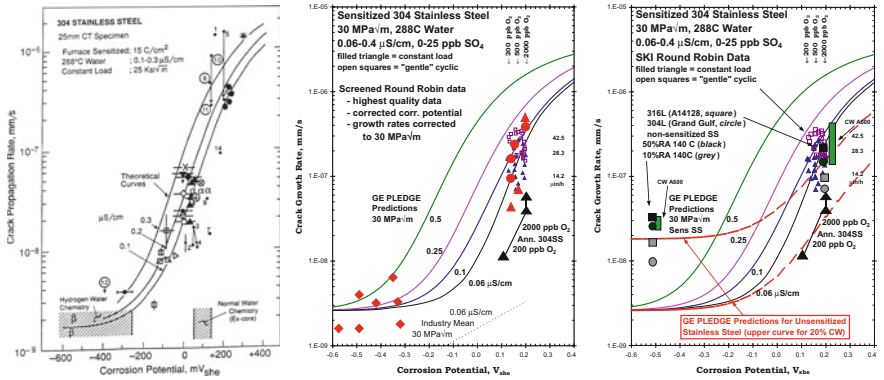

Fig. 2 SCC growth rate versus corrosion potential for stainless steels tested in 288 °C high purity water containing 2000 ppb O_2 and 95–3000 ppb H_2. [5–10]

the heat affected zone (HAZ) of stainless steel are *high*, and often as high as ~20% bulk cold worked material (Fig. 2) [15–17].

Experimental Procedures

SCC growth rate tests were also performed in 288 °C water on 19.3% cold rolled XM-19 (specimens c530 and c531) and as-received XM-19 (specimens c743 and c744). The composition of heat A17509 of XM-19 (UNS S20910, also known as Nitronic 50) is 20.8 Cr, 12.7 Ni, 4.5 Mn, 2.07 Mo, 0.42 Si, 0.3 N, 0.19 V, 0.18 Nb, 0.033 C, 0.028 P, 0.03 Co, 0.003 S, bal F. Macro etched sections of this heat showed coarse grain regions from abnormal grain growth (AGG) or critical grain growth (CGG), a result of subcritical plastic strain during rolling. AGG areas tend to have somewhat lower yield strength, but their most significant effect is to impair ultrasonic inspectability. Optical microscopy (Fig. 3) and SEM-EDS the grain size and carbide banding, along with many multiphase stringers composed of coarse NbC carbides and MnS. The mechanical properties are negatively impacted by the banding, with the yield strength, elongation, and reduction in area (%RA) significantly reduced in the transverse orientation. The average of six 25 °C yield strength measurements was 405 MPa (longitudinal) and 350 MPa (transverse). The average %RA was 73% (longitudinal) and 39% (transverse). The transverse fractures were flat and showed none of the ductile cup and cone morphology of the longitudinal specimens. Additional characterization details are presented elsewhere [18].

The four specimens were tested in the S-L orientation relative to both the plate microstructure and deformation (rolling plane). A prior test (c218) was performed on another heat of XM-19 in 2002 [14] that was cold forged by 21%. The CT specimens were instrumented with platinum current and potential probe leads for dc potential drop (DCPD) measurements of crack length. In this technique, current

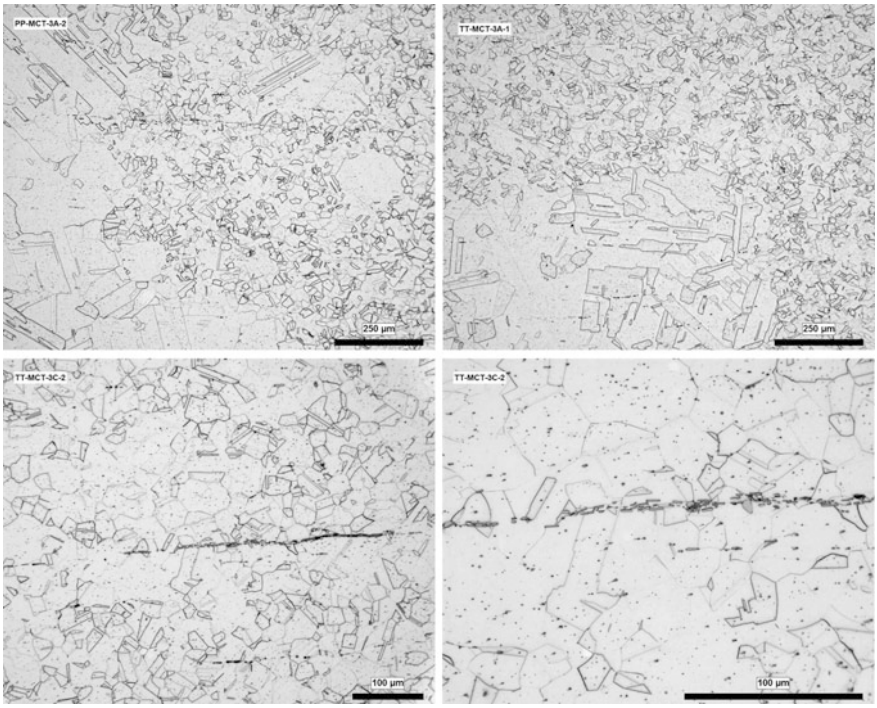

Fig. 3 Optical micrographs from regions identified as coarse grain in macro-etched sections. The coarse grain region is due to abnormal or critical grain growth from subcritical plastic strain during the rolling operation (low thickness reduction passes)

flow through the sample is reversed about once per second primarily to reduce measurement errors associated with thermocouple effects. An integrating nanovoltmeter is used to measure the ~ 100 μV potentials on the CT specimen, and can resolve ~ 1 nV. Key elements include very stable current, low thermal offset reed relay multiplexer, very stable (room and autoclave) temperature, shielded and twisted pair wiring, voltmeter integration over ≥ 1 power line cycle, very stable attachment points on the CT specimens, etc. Integration of the DCPD system with the servo loading system permitted constant K conditions to be maintained, and automated changes in loading conditions to be made a pre-defined crack lengths.

Deaerated, demineralized water was drawn through another demineralizer and submicron filter to ensure ultra-high purity (0.055 μS/cm) and then into a glass column (6.4-cm diameter by 183 cm long). A low pressure pump provided positive pressure to the high pressure pump, and drew water from and recirculated excess water (water that did not go into the high pressure pump) back into the glass column. The autoclave effluent was back-pressure regulated, then measured for conductivity. The dissolved oxygen or hydrogen concentration was controlled by bubbling gas mixtures through the water. Impurities were added to the glass column using a metering pump which was controlled by the conductivity meter. Tests were

performed in 4 liter stainless steel autoclaves at 288 °C, typically at 10.3 MPa (1500 psi). A zirconia membrane reference electrode [19] was employed for continuous measurement of the corrosion potential of the CT specimen.

J-R tests were performed in 288 °C air in a 250 kN Instron servohydraulic testing machine. Specimens were fatigue pre-cracked, then tested using a fixed actuator displacement rate of 10^{-4} mm/s (10^{-5} mm/s for some of the as-received XM-19), and actuator displacement, load and crack length (by DC potential drop) were monitored. Careful calibration of the system permitted an accurate conversion from actuator displacement to crack mouth opening displacement at the CT specimen. After testing, the J-R analysis diagram was constructed and evaluated.

Results and Discussion—SCC Growth Rate

Detailed crack length versus time graphs associated with each test are provided in reference [20], including a test overview graph, and detailed graphs associated with fatigue precracking and each test segment and transition in the test. Tests were performed first on XM-19 with 19.3% cold rolling (specimens c530 and c531), and later on as-received XM-19 (specimens c743 and c744).

Specimens c530 and c531 of 19.3% cold rolled XM-19 were fatigue precracked in air to the same a/W, then tested in tandem (series) loading in the same autoclave. Figures 4, 5, 6 and 7 show the growth rates of specimens c530 and c531 in 10 ppb sulfate as a function of corrosion potential and stress intensity factor.

These data are similar to the data obtained in 2002 [14] on another heat of 21% cold forged XM-19 (Fig. 8), although the older data are perhaps 2X lower, which may be related to the use of pure water in these older data and/or the use of T-L orientation versus S-L orientation in specimens c530 and c531.

The SCC growth rate data are remarkably consistent in every regard, and show that cold worked XM-19 has significant susceptibility to SCC. While 20% cold work is not expected in terms of the bulk processing of the alloy, it is a common level of cold work in the heat affected zone of structural welds in stainless steels (Fig. 1).

Specimens c743 and c744 of as-received XM-19 were fatigue precracked in air to the same a/W, then tested in tandem (series) loading in the same autoclave. Figures 9, 10, 11 and 12 show the growth rates of the two specimens in 10 ppb sulfate and in pure water as a function of corrosion potential. While the growth rates are lower than the 19.3% cold rolled XM-19, they nonetheless fall into the high range, and may reflect some residual deformation in the as-received material, or perhaps just the elevated yield strength inherent in this nitrogen-strengthened stainless steel—all other things being equal, increased yield strength increases SCC growth rates [5–10]. A typical yield strength for 304L/316L stainless steel at 288 °C is ~175 MPa, whereas this heat of as-received XM-19 has a 288 °C yield strength of ~250 MPa, and the 19.3% cold worked XM-19 has a 288 °C yield strength of about 700 MPa.

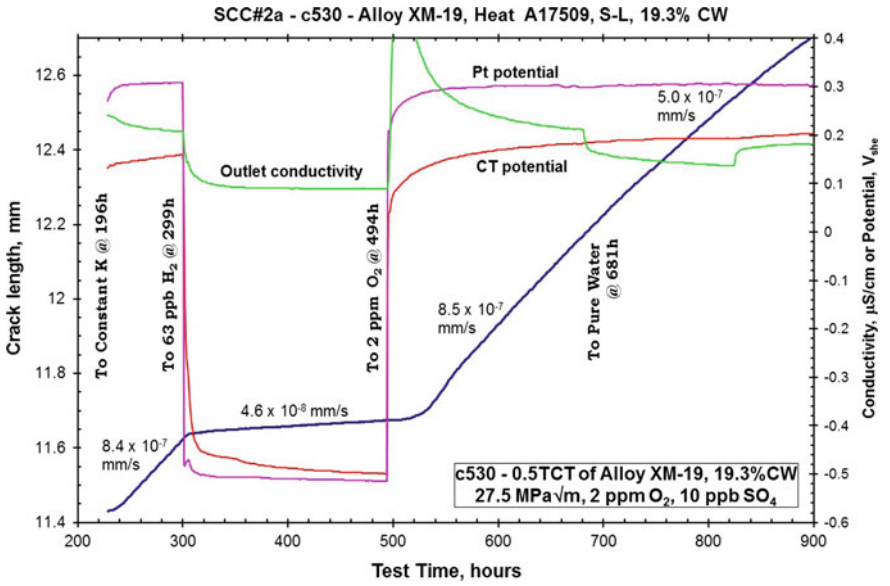

Fig. 4 SCC growth rate in 288 °C water of specimen c530 of heat A-17509, 19.3% cold rolled XM-19 in the S-L orientation

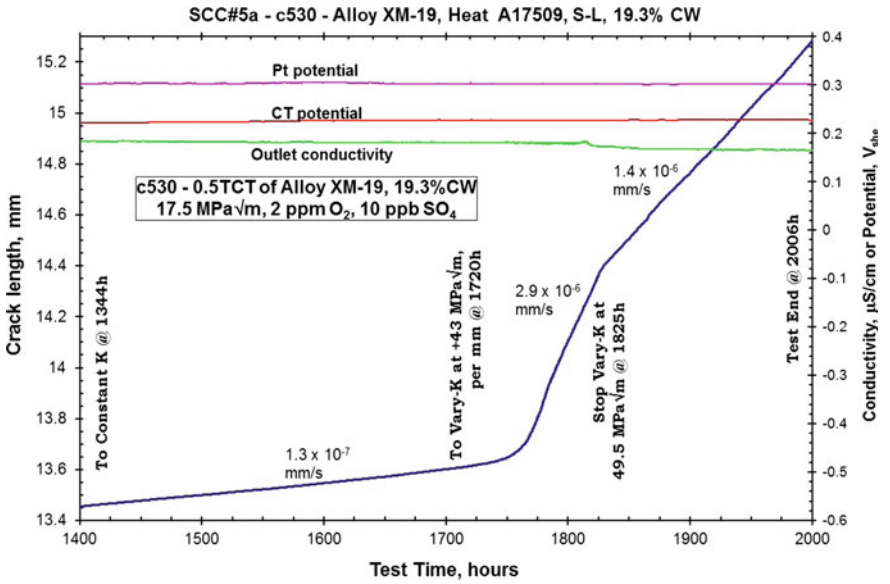

Fig. 5 SCC growth rate in 288 °C water of specimen c530 of heat A-17509, 19.3% cold rolled XM-19 in the S-L orientation

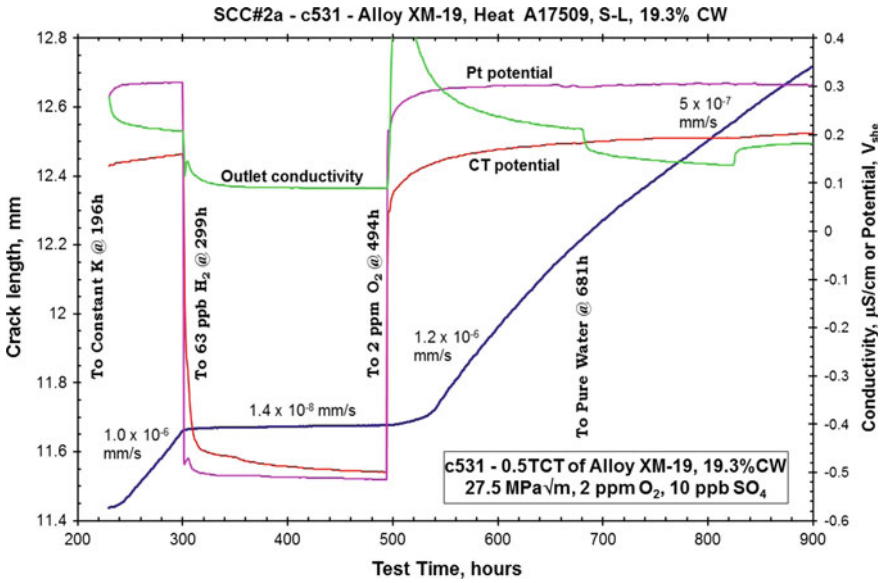

Fig. 6 SCC growth rate in 288 °C water of specimen c531 of heat A-17509, 19.3% cold rolled XM-19 in the S-L orientation

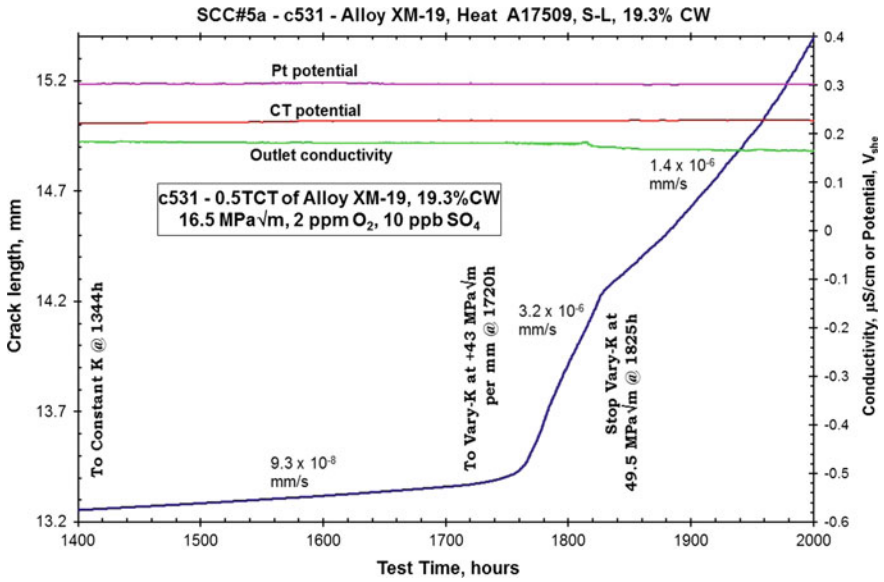

Fig. 7 SCC growth rate in 288 °C water of specimen c531 of heat A-17509, 19.3% cold rolled XM-19 in the S-L orientation

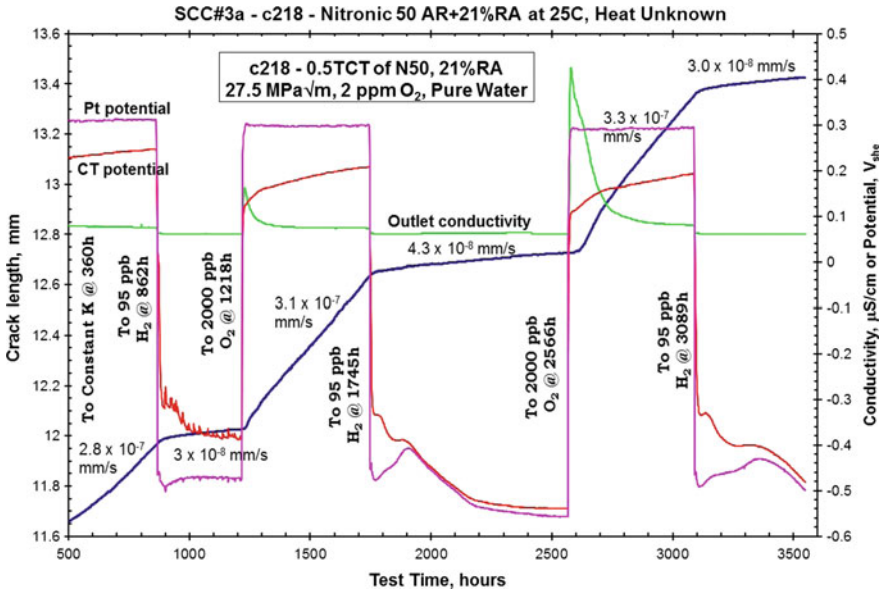

Fig. 8 SCC growth rate in 288 °C water of specimen c218, 21% cold rolled XM-19

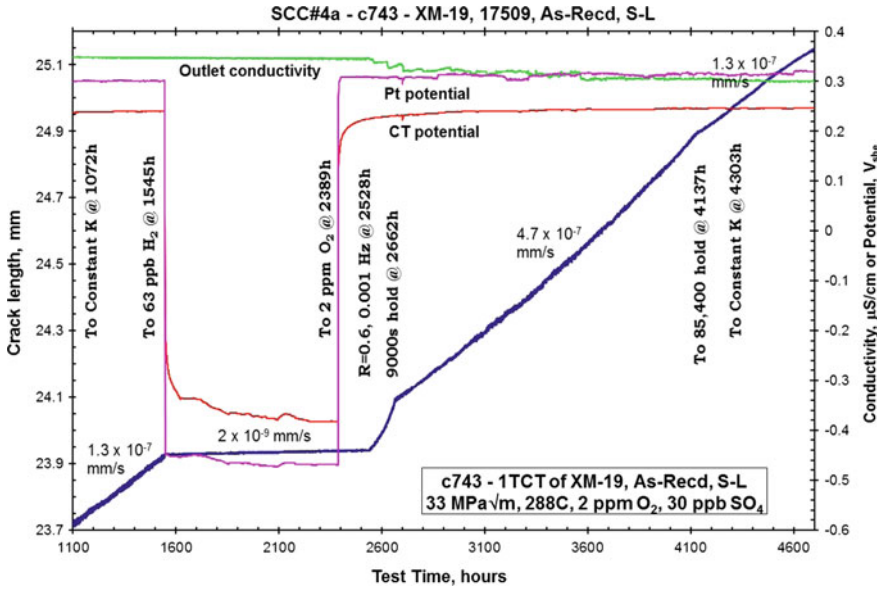

Fig. 9 SCC growth rate in 288 °C water of specimen c743 of heat A-17509 of as-received XM-19 in the S-L orientation

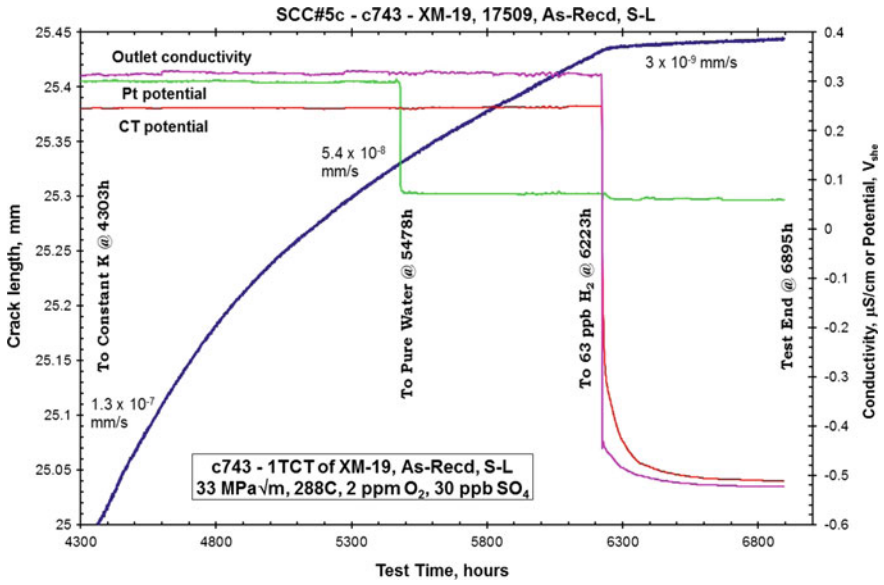

Fig. 10 SCC growth rate in 288 °C water of specimen c743 of heat A-17509 of as-received XM-19 in the S-L orientation

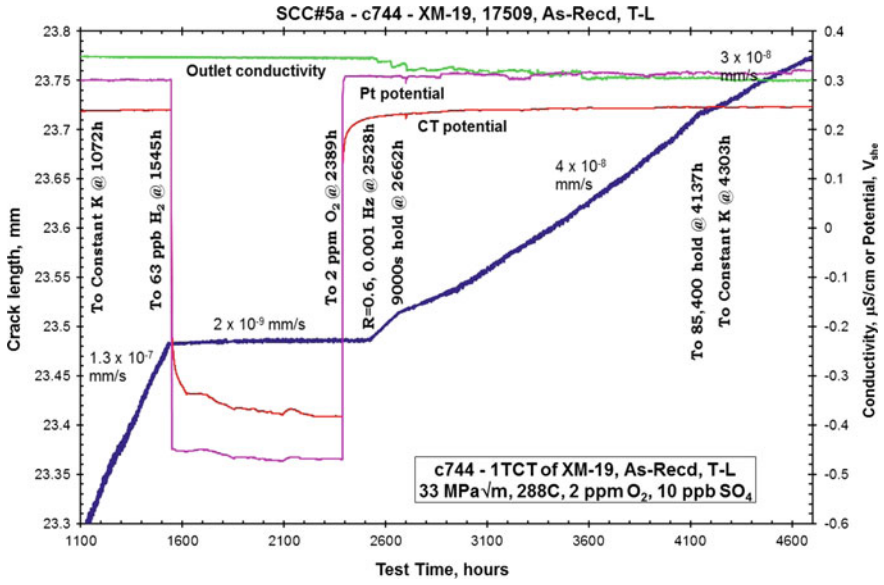

Fig. 11 SCC growth rate in 288 °C water of specimen c744 of heat A-17509 of as-received XM-19 in the S-L orientation

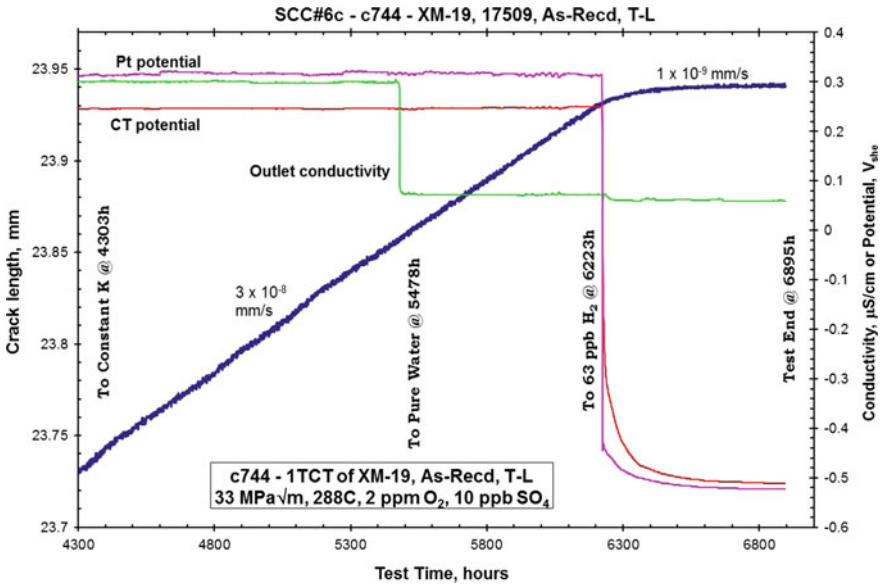

Fig. 12 SCC growth rate in 288 °C water of specimen c744 of heat A-17509 of as-received XM-19 in the S-L orientation

A general categorization of SCC growth rates has evolved in which very long structural component lifetimes are expected for growth rates below $\sim 5 \times 10^{-9}$ mm/s, which is therefore considered *low*. A *medium* growth rate corresponds to a growth rate above *low* and below 5×10^{-8} mm/s, broadly consistent with possibility of cracking over a period of ~10–50 years. A *high* growth extends from *medium* to 3×10^{-7} mm/s, with higher growth rates considered *very high*. Obviously, many specific aspects of a given component—the material condition and homogeneity, cold work, welding, temperature, water chemistry, stressing—will have a huge effect on when cracking might develop, but avoiding conditions that yield *medium, high* and *very high* growth rates is crucial to extended plant lifetime. With reference to Fig. 2, the growth rate of annealed 304/316/L stainless steels generally falls below $\sim 3 \times 10^{-8}$ mm/s at high corrosion potential, while ~20% cold work or sensitization increases the growth rate by ~10X. The growth rate of ~20% cold worked XM-19 is well above that of ~20% cold worked 304/316/L stainless steels, and the growth rate of as-received XM-19 is broadly similar to 20% cold worked 304/316/L stainless steels. This is consistent with the higher yield strength of XM-19 associated primarily with its addition of nitrogen.

The effect of corrosion potential on the SCC growth rates of all conditions of XM-19 is shown in Fig. 13, which represents a change in growth rate on changing corrosion potential in "on-the-fly" changes, where nothing else is changed in adjacent segments of the test. The factor-of-improvement on changing to low corrosion potential is ~13X in pure water, and higher when sulfate is present.

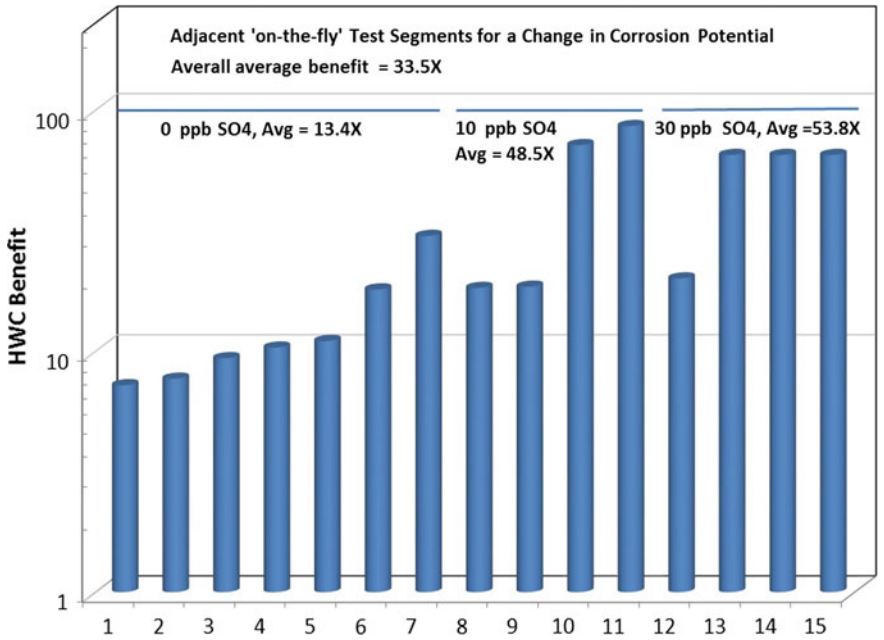

Fig. 13 Effect on the SCC growth rate in 288 °C water of XM-19 of on-the-fly changes in corrosion potential where all other factors remain constant in the test, including both ~20% cold worked and as-received XM-19. The bars represent individual on-the-fly observations

The effect of 10 or 30 ppb sulfate on the SCC growth rate of all conditions of XM-19 for the same, adjacent, "on-the-fly" changes is shown in Fig. 14, and average 1.5X. The effect on SCC growth rates of 19.3% cold rolled XM-19 of changes in stress intensity factor is shown in Fig. 15, where a dependency of $\sim K^2$ to $K^{2.3}$ is evident.

Results and Discussion—Fracture Toughness

J-R fracture resistance tests were performed in 288 °C air on five specimens 19% cold worked XM-19, and four specimens of as-received XM-19, all from heat A17509. Material availability limited specimen size to 0.5T CT specimens for the 19.3% cold rolled XM-19. Each specimen was fatigue precracked in 288 °C air at a K_{max} of 30 MPa$\sqrt{m}$ and R = 0.5 from an a/W of ~0.40 to ~0.50 (for 1T CT specimens) or to ~0.43 (for 0.5T CT specimens). J-R tests were performed 288 °C air in displacement control starting at the maximum load at the end of fatigue precracking. Most tests were performed at 1×10^{-4} mm/s.

The 19.3% cold worked XM-19 exhibited low or no tearing (Fig. 16, Table 1), and thus for four of five specimens no formal toughness determination is possible.

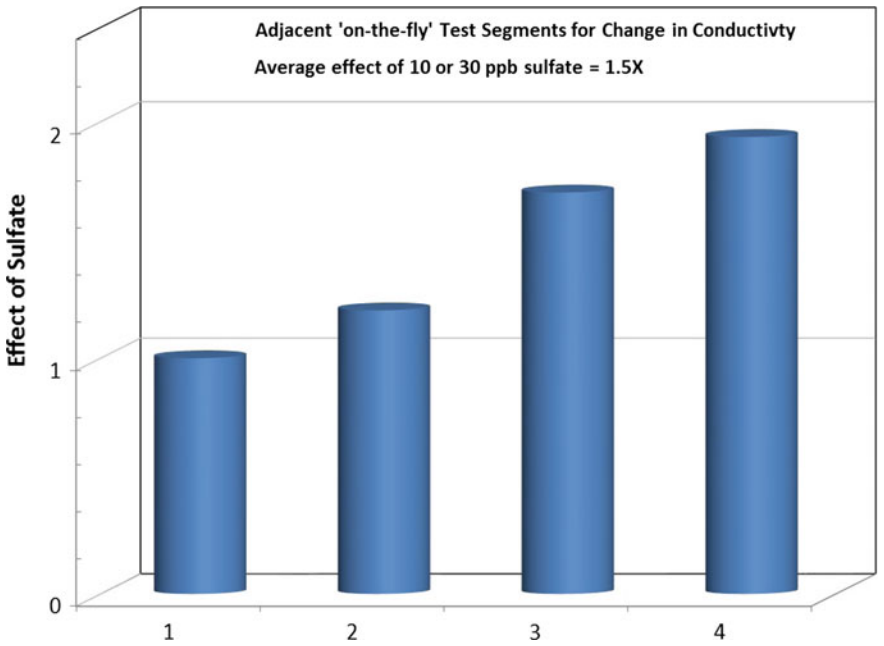

Fig. 14 Effect on the SCC growth rate of XM-19 in 288 °C water of on-the-fly changes to zero sulfate where all other factors remain constant in the test. The bars represent individual on-the-fly observations between 10 or 30 ppb sulfate and pure water

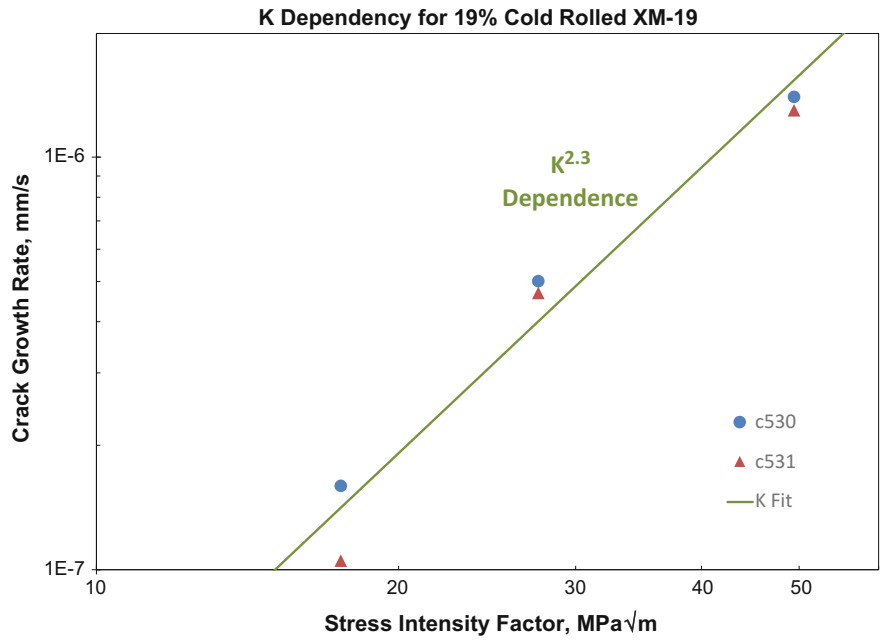

Fig. 15 Effect of stress intensity factor (K) on the SCC growth rate in 288 °C water of specimens c530 and c531 of heat A-17509 of 19.3% cold rolled XM-19 in the S-L orientation

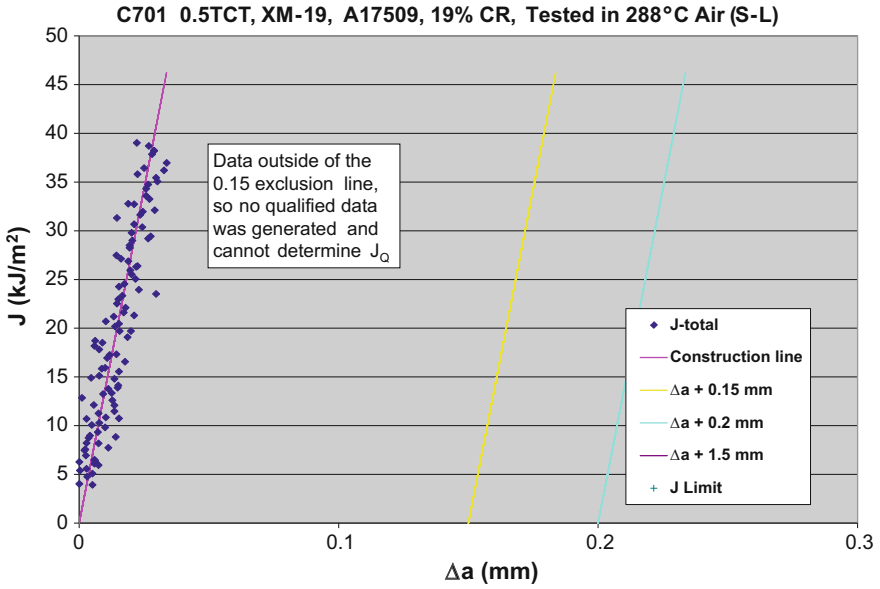

Fig. 16 Analyzed results of the J-R testing in 288 °C air of specimen c701 of XM-19, heat A17509, 19% cold rolled, S-L orientation. No tearing was observed, as was the case for most cold rolled tests

Table 1 Summary of J-R fracture resistance results on XM-19, heat A17509

Specimen	Condition	Specimen size	Orientation	Valid?	J_Q (kJ/m^2)	K_{IC} (MPa$\sqrt{m}$)	J_{IC} (kJ/m^2)
C700	19.3% Cold Rolled	0.5TCT	S-L	[a]1	33	86	33
C701	19.3% Cold Rolled	0.5TCT	S-L	No			
			Average=		**33**	**86**	**33**
C702	19.3% Cold Rolled	0.5TCT	T-L	No			
C705	19.3% Cold Rolled	0.5TCT	T-L	No			
			Average=		–	–	–
C706	19.3% Cold Rolled	0.5TCT	L-T	No			
			Average=		–	–	–
C747	As-Received	1TCT	L-T	Yes	388	296	388
C748	As-Received	1TCT	L-T	Yes	354	283	354
			Average=		**371.0**	**289.5**	**371.0**
C749	As-Received	1TCT	S-L	Yes	288	255	288
C750	As-Received	1TCT	S-L	Yes	220	223	220
			Average=		**254.0**	**239.0**	**254.0**

[a]1—insufficient data to determine J_{IC}

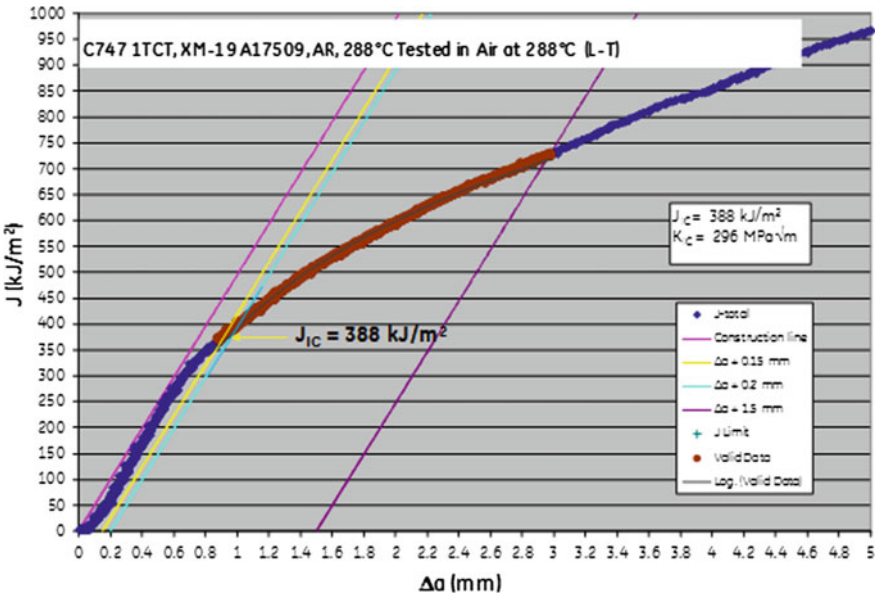

Fig. 17 Analyzed results of the J-R testing in 288 °C air of specimen c706 of XM-19, heat A17509, as-received, L-T orientation. Excellent data were obtained on all as-received specimens

However, the toughness is clearly low, as corroborated by the one specimen (c700) that did provide some valid data. In most cases, stainless steels, even stainless steels with >20% cold work, have very high toughness. For example, in the same time frame as these tests, both annealed and ~30% cold worked 316L stainless steel 0.5TCT specimens exhibited very high toughness of K_{IC} = 400–650 MPa$\sqrt{m}$ and J_{IC} = 815 kJ/m^2. The challenges with data validity were all related to excessive plasticity, unlike the XM-19 tested in this study.

The J-R testing on the 1T CT specimens of as-received XM-19 was well behaved, and fracture toughness determinations were possible (Fig. 17, Table 1). The replicate tests are in good agreement, with average values of J_{IC} = 371 kJ/m^2 and K_{IC} = 290 MPa$\sqrt{m}$ for the L-T orientation, and somewhat lower values for the S-L orientation: J_{IC} = 254 kJ/m^2 and K_{IC} = 239 MPa$\sqrt{m}$, consistent with the banded microstructure.

Conclusions

The SCC growth rate response of XM-19 qualifies as high in pure water at high corrosion potential, somewhat higher than common grades of austenitic stainless steel, such as Types 304, 304L, 316, and 316L in an equivalent condition, such as as-received or with 20% reduction in thickness. While XM-19 has slightly higher

Cr content, it also has a higher yield strength, primarily from additions of N. If used in a well-annealed condition, the growth rates are ~10X lower than if there is retained deformation. XM-19 exhibits a similar K dependency ($\sim K^2$) as common grades of austenitic stainless steel, and shows a similar and strong effect of corrosion potential.

The J-R fracture resistance data depends strongly on retained deformation and microstructure. The XM-19 plate exhibited significant grain size and carbide banding, and suffered from abnormal or critical grain growth because of insufficient plastic strain during production (low thickness reduction passes). The 19.3% cold rolled material showed little plasticity and thus most of the J-R data obtained was invalid. As-received XM-19 showed moderate plasticity, but the J-R data was considerably lower in the S-L (vs. T-L) orientation, where banding plays a role.

References

1. *Proceedings of the 1st through 17th International Symposium on Environmental Degradation of Materials in Nuclear Power Systems—Water Reactors*, NACE/ANS/TMS, (1983–2015)
2. F.P. Ford, P.L. Andresen, Corrosion in nuclear systems: environmentally assisted cracking in light water reactors, in *Corrosion Mechanisms*, ed. by P. Marcus, J. Ouder (Marcel Dekker, 1994), pp. 501–546
3. P.L. Andresen, F.P. Ford, Life prediction by mechanistic modelling and system monitoring of environmental cracking of Fe and Ni alloys in aqueous systems. Mater. Sci. Eng. A **103**, 167–183 (1988)
4. F.P. Ford, D.F. Taylor, P.L. Andresen, R.G. Ballinger, *Corrosion Assisted Cracking of Stainless and Low Alloy Steels in LWR Environments*, EPRI RP2006-6, Report NP5064M (1987)
5. P.L. Andresen, L.M. Young, W.R. Catlin, R.M. Horn, *Stress Corrosion Crack Growth Rate Behavior of Various Grades of Cold Worked Stainless Steel in High Temperature Water*, Corrosion/02, Paper 02511 (NACE, 2002)
6. P.L. Andresen, T.M. Angeliu, L.M. Young, W.R. Catlin, R.M. Horn, Mechanisms and kinetics of SCC in stainless steels, in *Proceedings of the 10th International Symposium on Environmental Degradation of Materials in Nuclear Power Systems—Water Reactors*, NACE (2002)
7. P.L. Andresen, T.M. Angeliu, W.R. Catlin, L.M. Young, R.M. Horn, *Effect of Deformation on SCC of Unsensitized Stainless Steel*, Corrosion/2000, Paper 00203 (NACE, 2000)
8. P.L. Andresen, P.W. Emigh, M.M. Morra, R.M. Horn, Effects of yield strength, corrosion potential, stress intensity factor, silicon and grain boundary character on the SCC of stainless steels, in *Proceedings of 11th International Symposium on Environmental Degradation of Materials in Nuclear Power Systems—Water Reactors*, ANS (2003)
9. P.L. Andresen, Stress corrosion cracking in austenitic stainless steels, in book "*Understanding and Mitigating Ageing in Nuclear Power Plants*", ed. by P.G. Tipping (Woodhead Publishing, 2010)
10. P.L. Andresen, M.M. Morra, SCC of stainless steels and Ni alloys in high temperature water. Corrosion **64**, 15–29 (2008)
11. P.L. Andresen, *Conceptual Similarities and Common Predictive Approaches for SCC in High Temperature Water Systems*, Paper 96258, Corrosion/96 (NACE, 1996)
12. P.L. Andresen, F.P. Ford, S.M. Murphy, J.M. Perks, State of knowledge of radiation effects on environmental cracking in light water reactor core materials, in *Proceedings of 4th*

International Symposium on Environmental Degradation of Materials in Nuclear Power Systems—Water Reactors (NACE, 1990), pp. 1–83 to 1–121
13. P.L. Andresen, L.M. Young, Characterization of the roles of electrochemistry, convection and crack chemistry in stress corrosion cracking, in *Proceedings of 7th International Symposium on Environmental Degradation of Materials in Nuclear Power Systems—Water Reactors* (NACE, 1995), pp. 579–596
14. P.L. Andresen, *Factors Influencing SCC and IASCC of Stainless Steels in High Temperature Water*, PVP, vol. 479, (ASME, 2004)
15. T.M. Angeliu, P.L. Andresen, J.A. Sutliff, R.M. Horn, Intergranular stress corrosion cracking of unsensitized stainless steels in BWR environments, in *Proceedings of 9th International Symposium on Environmental Degradation of Materials in Nuclear Power Systems—Water Reactors* (AIME, 1999), pp. 311–318
16. T.M. Angeliu, P.L. Andresen, E. Hall, J.A. Sutliff, S. Sitzman, *Strain and Microstructure Characterization of Austenitic Stainless Steel Weld HAZs*, Paper 00186, Corr/2000 (NACE, 2000)
17. P.L. Andresen, *Similarity of Cold Work and Radiation Hardening in Enhancing Yield Strength and SCC Growth of Stainless Steel in Hot Water*, Corrosion/02, Paper 02509 (NACE, 2002)
18. M.M. Morra, *BWRVIP- 240: BWR Vessel and Internals Project, Metallurgical Analyses and Macro and Microstructural Mapping of Alloy X-750 and Alloy XM-19 Plates*, EPRI Report 1021003, August 2010
19. L.W. Niedrach, A new membrane type pH sensor for use in high temperature high pressure water. J. Electrochem. Soc. **127**, 2122 (1980)
20. P.L. Andresen, M.M. Morra, *Microstructure, SCC and J-R fracture resistance of alloy X-750 and XM-19* (Final Report, EPRI, Palo Alto, 2017)

On the Effect of Preoxidation of Nickel Alloy X-750

Silvia Tuzi, Kenneth Göransson, Fang Liu, Mattias Thuvander and Krystyna Stiller

Abstract Nickel Alloy X-750 is a Ni-Cr–Fe alloy with good corrosion properties and high strength at elevated temperature. It is commonly used for spacer grids in Boiling Water Reactors (BWR). In this environment, the material can suffer from significant corrosion, leading to weight loss by metal dissolution. To further improve the characteristics of this material, a process called preoxidation is often performed. This results in the formation of strengthening γ'-Ni_3(Ti, Al) precipitates and a thin oxide on the surface. In this paper, preoxidized and non-preoxidized specimens are compared with respect to their oxidation properties. We report about microstructural studies made on specimens exposed in simulated BWR environment for 24 h and 840 h. Electron microscopy techniques have been used to investigate the oxide microstructures. A comparison between these specimens shows the complexity of the corrosion process and the impact of preoxidation. Preoxidized specimens show thinner and more homogenous oxides than non-preoxidized ones. They lose less mass and build thinner oxides. The preoxidation layer consists of a bilayer oxide of $NiFe_2O_4$ and Cr_2O_3 that is preserved during the long exposure. $NiFe_2O_4$ spinel crystals are present on the surface of all exposed specimens, a result of re-precipitation of dissolved metal ions.

Keywords High temperature water · X-750 · Corrosion · $NiFe_2O_4$ · Oxide formation · BWR · Nickel based alloys

S. Tuzi (✉) · F. Liu · M. Thuvander · K. Stiller
Chalmers University of Technology, 412 96 Göteborg, Sweden
e-mail: silvia.tuzi@chalmers.se

K. Göransson
Westinghouse Electric Sweden AB, 721 63 Västerås, Sweden

J.H. Jackson et al. (eds.), *Proceedings of the 18th International Conference on Environmental Degradation of Materials in Nuclear Power Systems – Water Reactors*, The Minerals, Metals & Materials Series, https://doi.org/10.1007/978-3-319-68454-3_32

Introduction

Nuclear reactors possess an aggressive environment, with highly oxidizing water and corrosive conditions. High demands are put on the materials that have to perform in this environment. Ni Alloy X-750 has been used in Boiling Water Reactors (BWRs) for more than 30 years [1, 2], and it has generally shown good corrosion resistance. The alloy is used for many purpose as springs, bolts, guide pins and spacer grid to hold the fuel rods in position. X-750 is a Ni-Cr–Fe precipitation hardened alloy. When it undergoes the preoxidation treatment γ'-Ni_3(Ti, Al) precipitates are developed [3], and contribute to the high strength at elevated temperature. The preoxidation results also in a 200 nm thick oxide formed on the specimen surface consisting of three layers. Ni- and Fe-rich oxide in the outer part of the scale, Cr- and Ti-rich oxide in the middle layer and Si- and Al-rich oxide nanoparticles at the innermost layer [4]. In this paper, in order to understand the effect of preoxidation on the corrosion resistance of the alloy in BWR, the microstructure of specimens that have received preoxidation and those that have not, have been investigated.

The specimens have been exposed in a simulated BWR environment for two different exposure times; 24 and 840 h. A layer of $NiFe_2O_4$ is expected to form during exposure, as this oxide is stable in BWR [5, 6]. Furthermore, from our previous studies [7], it is found that the specimens lose mass, indicating dissolution of metal into the water.

Experimental

The effect of preoxidation of Ni Alloy X-750 on its corrosion properties in BWR environment has been studied using high resolution electron microscopy techniques. The chemical composition of the alloy is shown in Table 1. Alloy X-750 was solution annealed for 1–3 min in inert atmosphere at 1050–1100 °C. The investigated specimens have received a mechanical polishing and a pickling (a chemical etching). The pickling procedure removes up to 2 μm of the material, eliminating possible composition gradients formed through manufacturing, oxide residues and cold worked material. Two batches, one that has undergone a preoxidation treatment and the other that has not, have been studied. The preoxidation process consists of a heat treatment performed for 20 h at 700 °C in controlled moist air. The result is not only the formation of γ' precipitates but also the creation of a thin oxide layer on the surface.

Table 1 Chemical composition of investigated X-750 material (wt%)

Fe	Ni	Cr	C	Si	Mn	Ti	Nb	Al	N
8.3	70.8	16.0	0.02	0.35	0.57	2.4	0.81	0.59	0.01

The specimens have been exposed in an autoclave that simulates the BWR conditions. The system is the same as in our previous work [4, 7]. The radiolysis condition of the real reactor is simulated by continuously adding 500 ppb of H_2O_2 to the water, which impinges on the samples as a water jet. The operating conditions are 287 °C and 80 bar. Test coupons of 20 × 20 × 0.3 mm^3 were placed in the autoclave and were exposed for 24 and 840 h. The coupons were weighed before and after the exposure. A focused ion beam (FIB) combined with FEI Versa 3D scanning electron microscope (SEM) has been used to make lift-out specimens for FEI Titan 80–300 transmission electron microscope (TEM)/scanning transmission electron microscope (STEM). The morphology of the specimens has been studied with a Zeiss LEO Ultra 55 FEG/SEM.

Results

The results from the weighing are shown in Fig. 1. From the plot, it is visible that the specimens lose mass, as expected. This effect is much more evident on non-preoxidized specimens. However, no material shows signs of visible spallation after the autoclave exposure, which means that material is being dissolved into the water.

After 24 h, a morphology investigation by SEM (Fig. 2) shows that the non-preoxidized specimen has blocky crystals of size 0.5 μm on the surface, which correspond to non-stoichiometric (with respect to the Fe/Ni ratio) $NiFe_2O_4$. The coverage of this structure is only about 30% of the surface. The specimen that has received preoxidation shows a more homogeneous surface oxide. Using a higher magnification, it is possible to observe blocky structures of 50–100 nm covering the whole surface.

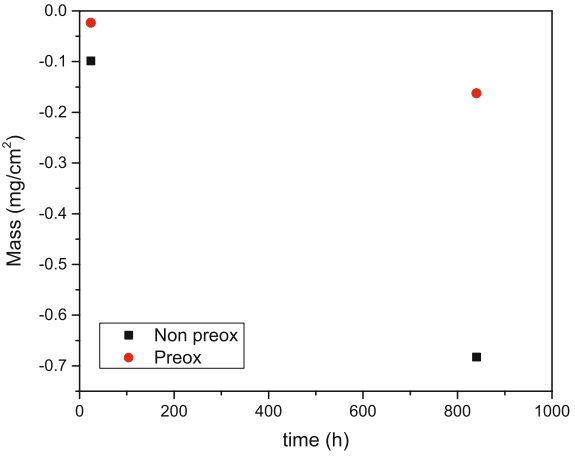

Fig. 1 Mass as function of the exposure time

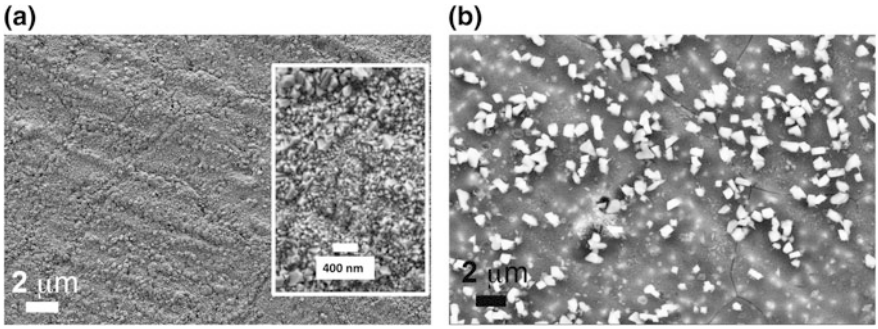

Fig. 2 SEM top view images of specimens exposed 24 h **a** preoxidized with an inset at higher magnification and **b** the non-preoxidized specimen

High angle annular dark field scanning transmission electron microscopy (HAADF-STEM) images, Fig. 3, of specimens exposed for 24 h, show a quite striking difference in microstructure. The preoxidized specimen displays a uniform 250 nm oxide layer adherent to the surface (Fig. 3a), while the non-preoxidized specimen shows a bilayer structure with a top layer of big blocky structures and underneath an inner fine-grained oxide (Fig. 3b).

In Fig. 4, it is marked where an energy dispersive x-ray (EDX) line scan was performed on the preoxidized material. Figure 5 shows the compositional profiles. From the profiles, it is possible to discern the chemical composition of the oxide scale. It consists of a top layer enriched in Ni and Fe and a bottom layer rich in Cr and with some inclusion of Ti.

The results of the EDX line scan on the 24 h non-preoxidized specimen shows that the blocky structure is a $NiFe_2O_4$, with a significant amount of Ti (about 5%) while the inner fine-grained structure seems to be a mixture of Ni- and Cr-rich oxides (Figs. 6 and 7).

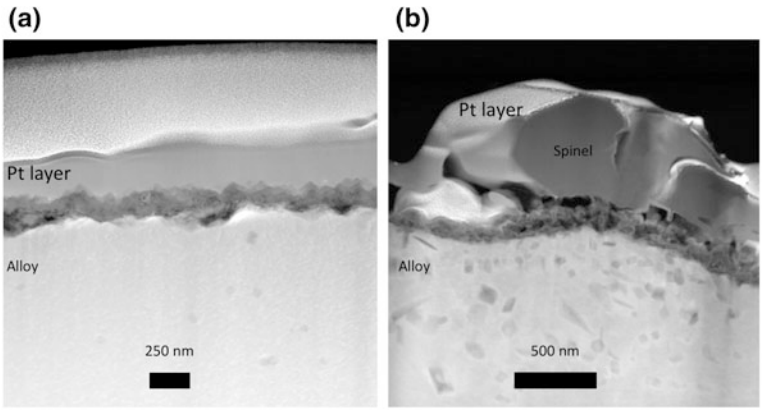

Fig. 3 HAADF STEM images of 24 h exposed **a** preoxidized specimen and **b** non-preoxidized specimen

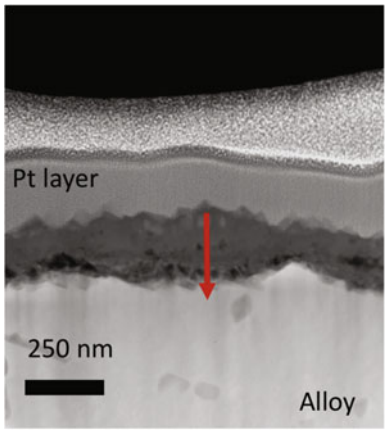

Fig. 4 HAADF STEM image of preoxidized specimen exposed 24 h. The arrow marks where the EDX line scan presented in Fig. 5 was acquired

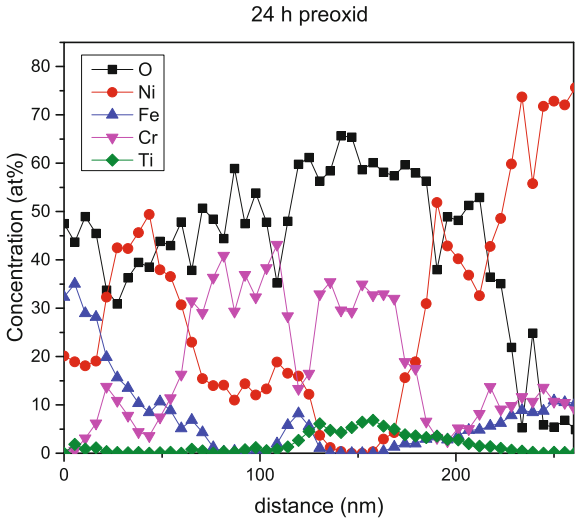

Fig. 5 EDX line scan along the arrow in Fig. 4. The starting point (0 nm) is at the tail and the head is at 265 nm

After 840 h, the morphology of the specimens has changed as shown in Fig. 8. Now the preoxidized specimen shows big blocky structures on the surface of the alloy. The coverage of this structure is about 50% and the size of the crystals varies from 1 μm and down to a few tens of nm. On the non-preoxidized specimen instead, there is an oxide made of blocky structures that cover the entire surface. These blocky crystals are of size 1–1.5 μm.

Figure 9 shows STEM images of the specimens exposed for 840 h. The preoxidized specimen shows a microstructure different from the non-preoxidized specimen. In the first case a thin oxide is present on the surface and on top of this it is possible to spot some blocky structures. In the latter case a 4-layer structure is observed. The oxide scale below the blocky crystals appears to be porous. From the STEM EDX line profiles shown in Figs. 10, 11, 12 and 13, we can compare the two oxides.

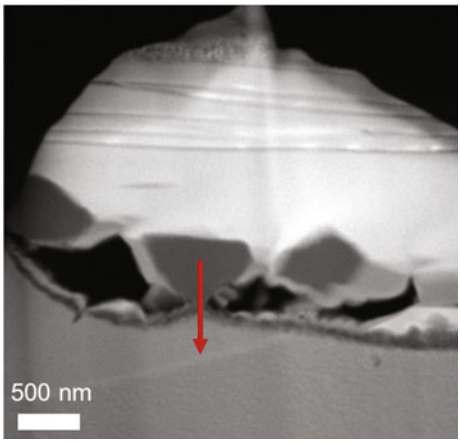

Fig. 6 HAADF STEM image of non preoxidized specimen exposed 24 h. The arrow marks where the EDX line scan presented in Fig. 7 was acquired

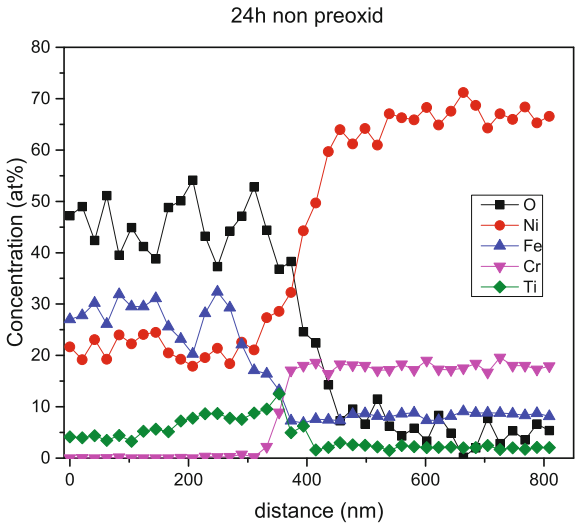

Fig. 7 EDX line scan along the arrow in Fig. 6. The starting point (0 nm) is at the tail and the head is at 810 nm

For the preoxidized specimen, Figs. 10 and 11, the chemical composition shows that there are $NiFe_2O_4$ on the top surface, underneath a layer made of Ni and Cr is present with some Ti inclusion. The non-preoxidized specimen, Figs. 12 and 13, shows a 4-layer structure: $NiFe_2O_4$, NiO, and oxidized base alloy consisting of two distinct layers; an outer which is enriched in Cr and Ti, and an inner that matches the composition of the alloy.

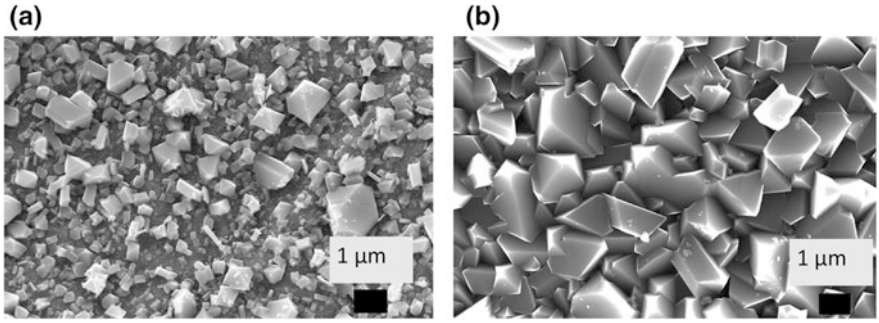

Fig. 8 SEM top view images of specimens exposed 840 h, **a** preoxidized and **b** non-preoxidized

Discussion

After 24 h exposure in water, the oxide thickness on the preoxidized sample is about 250 nm and has a bilayered structure (Figs. 3a, 4 and 5). Ni and Fe containing oxide in the outer part and Cr and Ti containing oxide in the inner part. The thickness of the Ni- and Fe-rich layer is 60 nm, while the Cr-rich layer is 190 nm thick. This is in good agreement with our previous studies [6] where the oxide scale formed after preoxidation is a 200 nm thick oxide and that consists of three layers. Ni- and Fe-rich oxide in the outer part of the scale, Cr- and Ti-rich oxide in the middle layer and Si- and Al-rich oxide nanoparticles at the innermost layer. We will refer to the Ni- and Fe-rich layer of the preoxidized as a primary spinel.

After 840 h the total thickness of the scale is 680 nm, where the spinel part is 300 nm thick and 220 nm is the Cr-rich layer, 160 nm is the Ni rich inner layer (Figs. 9a, 10 and 11) [4].

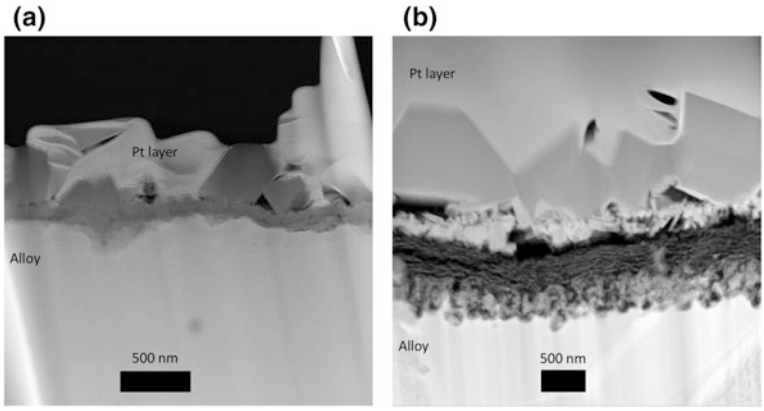

Fig. 9 HAADF STEM images of specimen exposed for 840 h, **a** preoxidized and **b** non-preoxidized

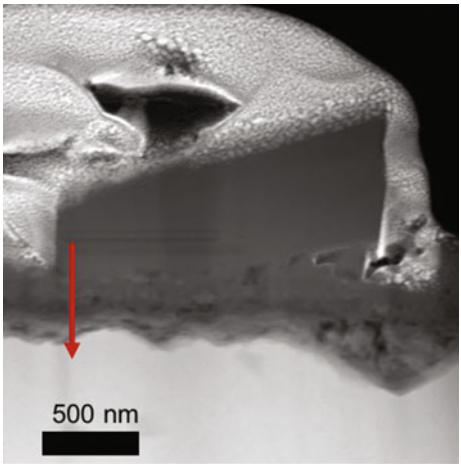

Fig. 10 HAADF STEM image of preoxidized specimen exposed 840 h. The arrow marks where the EDX line scan presented in Fig. 11 was acquired

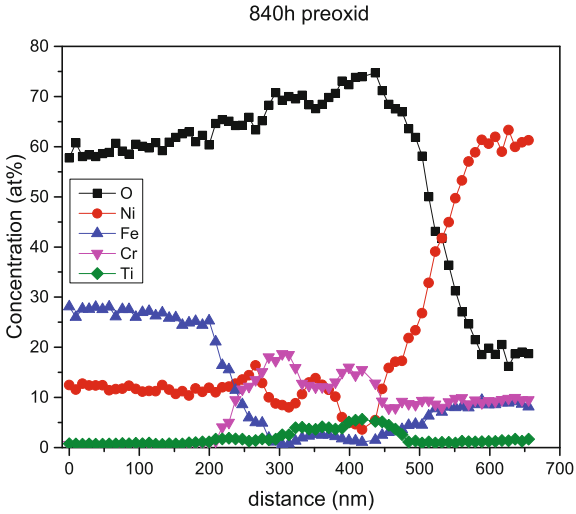

Fig. 11 EDX line scan along the arrow in Fig. 10. The starting point (0 nm) is at the tail and the head is at 660 nm

The specimen that has not received the preoxidation shows a different oxide growth. After 24 h the oxide consists of a bilayer with spinel crystals on the top, and beneath an oxide depleted in Fe but rich in Ni and Cr (Figs. 3b, 6 and 7). After 840 h, the spinel layer has grown to fully cover the surface of the specimen (Fig. 2b). The oxide structure is different than in case of the non preoxidized specimen (Figs. 9b, 12 and 13). Four layers are now present in contrast with a three-layer oxide on the preoxidized sample. The total oxide is also thicker, 2 μm compared to 680 nm for the preoxidized specimen.

From Fig. 1, where the mass loss data is plotted, it is clear that the preoxidized specimens have lost less mass than the non-preoxidized specimens. Both types of specimens dissolve in water, even if the scale is growing and includes oxygen ions.

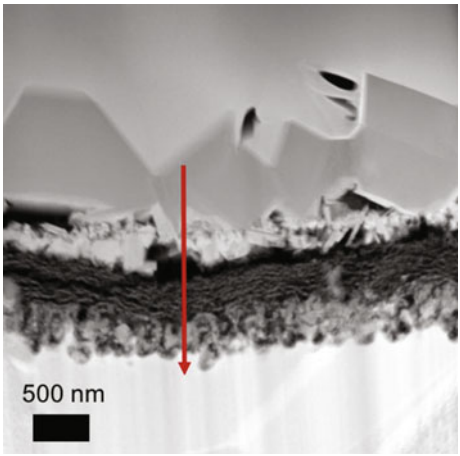

Fig. 12 HAADF STEM image of non preoxidized specimen exposed 840 h. The arrow marks where the EDX line scan presented in Fig. 13 was acquired

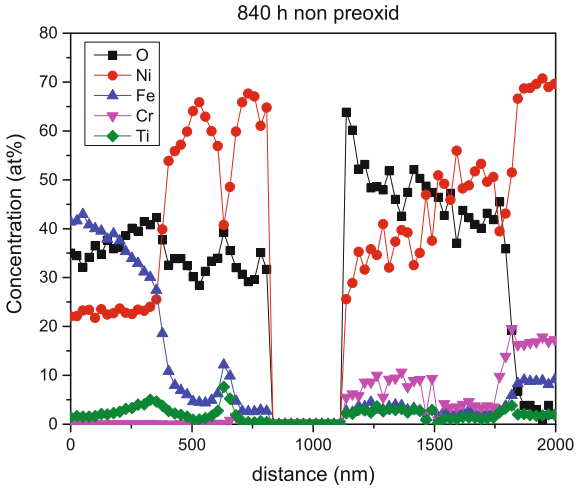

Fig. 13 EDX line scan along the arrow in Fig. 12. The starting point (0 nm) is at the tail and the head is at 2000 nm

The preoxidized specimens have a different behavior thanks to the additional oxide layer created by the pretreatment. This layer, that consists of Ni-Fe rich layer on the top and Cr–Ti rich underneath, helps to protect the material, reducing the mass loss [4, 7].

During the preoxidation, a primary spinel is formed and allows a Cr-rich layer (we will refer to it as chromia) to grow continuously underneath. Chromia is not stable in high temperature reactor water, so if the primary spinel is not built, there will be a slight enrichment of Cr and Ni on the surface, as in the case of the non-preoxidized specimen. The lack of a well adherent chromia layer will make the mass loss more severe. This is due to the fact that as seen from the specimen exposed 840 h another layer of spinels is formed. To form this layer, Ni and Fe have to diffuse and then dissolve into the water. But in the case of the preoxidized

specimen, a thin layer is built up. Instead for the non-preoxidized specimen a very dense layer of spinels is formed on the surface. Since here there isn't any oxide on the surface (lack of preoxidation) it is easier for the Ni and Fe to move towards the water and then dissolve. Eventually, Ni and Fe will re-precipitate to form the blocky spinels. When the chromia layer is dense, as in the preoxidized specimens, it causes a limited flux of ions in both direction [4]. The poor flux gives rise to a thin secondary blocky spinel layer, since the amount of Ni and Fe in the water is less than in the non-preoxidized case.

Conclusion

In this paper a study of Alloy X750 was carried out. We have investigated the impact of preoxidation on the alloy corrosion using electron microscopy techniques. The major findings are:

- Preoxidized material shows better corrosion properties due to the fact that it builds a thin and protective oxide scale, consisting of both of $NiFe_2O_4$ and Cr_2O_3, that restrains the mass loss.
- Non-preoxidized specimen grows a porous oxide scale, consisting of four layers: $NiFe_2O_4$, NiO, Cr-Ni rich layer and inner oxidized alloy, that allows ingress of the water into the material with subsequence dissolution of the alloy.

References

1. E. Calota, L. Hallstadius, M. Dahlback, C. Onneby, B. Helmersson, Spacer Grid. United States Patent Application Publication, (2011)
2. K. Göransson, L. Hallstadius, C. Gustafsson, H. Lai, S. Tuzi, M. Thuvander, K. Stiller, A. Kucuk, B. Josefsson, Corrosion behaviour of alloy X-750 in BWR fuel at high flow rates, in Conference Proceeding Top Fuel 2015, Zurich 13–17 September 2015, n.d
3. Gaylord D. Smith, Brian A. Baker, *Mechanical Engineers Handbook: Materials and Mechanical Design*. Chapter 6 Nickel and Its Alloys, (2006)
4. S. Tuzi, H. Lai, K. Göransson, M. Thuvander, K. Stiller, Corrosion of pre-oxidized nickel alloy X-750 in simulated BWR environment. J. Nucl. Mater. **486**, 350–360 (2017). doi:10.1016/j.jnucmat.2017.01.051
5. N.I.Y. Hemmi, Y. Uruma, General corrosion of materials under simulated bwr primary water conditions. J. Nucl. Sci. Technol. **455**, 443–455 (1994). doi:10.1080/18811248.1994.9735174
6. Y. Hemmi, N. Ichikawa, Protective oxide film on alloy X750 formed in air at 973 K. J. Nucl. Sci. Technol. **31**, 552–561 (1994). doi:10.1080/18811248.1994.9735190
7. S. Tuzi, K. Göransson, S.M.H. Rahman, S.G. Eriksson, F. Liu, M. Thuvander, K. Stiller, Oxide evolution on Alloy X-750 in simulated BWR environment. J. Nucl. Mater. **482**, 19–27 (2016). doi:10.1016/j.jnucmat.2016.09.026

Microstructures of Oxide Films Formed in Alloy 182 BWR Core Shroud Support Leg Cracks

Jiaxin Chen, Daniel Jädernäs, Fredrik Lindberg, Henrik Pettersson, Martin Bjurman, Kwadwo Kese, Anders Jenssen, Massimo Cocco and Hanna Johansson

Abstract This paper contributes to a TEM examination on the oxide films formed at three locations along a crack path in Alloy 182 weld from a BWR core shroud support leg, namely, the crack mouth, the midway between the mouth and the crack tip, and the crack tip. In the crack mouth the oxide film was approximately 1.6 μm in thickness and consisted of relatively pure NiO. The midway oxide film was mainly a nickel chromium oxide with a film thickness of 0.3 μm. At the crack tip the oxide film was a nickel chromium iron oxide with a film thickness of 30 nm. In all studied locations the main oxides had the similar rocksalt structure and the cracks were much wider than the thicknesses of the oxide films. It probably suggests that the corroded metal was largely dissolved into the coolant. The different dissolution rates of nickel, chromium and iron cations in the oxide films are clearly displayed with the compositions of the residual oxides. The oxide stability under different redox potentials along the crack path is briefly discussed.

Keywords Crack · Oxide microstructure · BWR · Core shroud · Support leg · TEM · FIB · SEM

J. Chen (✉) · D. Jädernäs · M. Bjurman · K. Kese · A. Jenssen
Studsvik Nuclear AB, Nyköping, Sweden
e-mail: jiaxin.chen@studsvik.se

F. Lindberg
Swerea KIMAB, Kista, Sweden

H. Pettersson
Department of Physics, Chalmers University of Technology, Gothenburg, Sweden

M. Cocco · H. Johansson
Forsmark Kraftgrupp AB, Forsmark, Sweden

J.H. Jackson et al. (eds.), *Proceedings of the 18th International Conference on Environmental Degradation of Materials in Nuclear Power Systems – Water Reactors*, The Minerals, Metals & Materials Series, https://doi.org/10.1007/978-3-319-68454-3_33

Introduction

During the outage of 2011, cracks were found in core shroud support legs in Forsmark BWR Unit 1. In order to remove the cracks and to obtain samples for failure analysis, boat samples were extracted by electro discharge machining (EDM). Figure 1 shows a photograph of the crack and its relative location in one core shroud support leg. The surface crack had a length of 16 mm which was confined only to the buttering. The long crack started at the wetted surface, extended 20 mm in depth and appeared to end at approximately 0.5 mm from the boat keel and did not contain the interface between RPV steel and Alloy 182. The crack has been examined by using various advanced analytical techniques, including Stereo Light Optical Microscopy (LOM), Focused Ion Beam (FIB), Electron Backscatter Diffraction (EBSD), Micro/Nano-Indentation, Scanning Electron Microscopy (SEM) and Analytical Transmission Electron Microscopy (ATEM). Some of these analyses are reported separately in another paper [1] and a TEM examination on the oxide film microstructures in the crack mouth was reported elsewhere [2]. In this paper the microstructures of the oxide films formed in the crack mouth, the midway between the mouth and the crack tip, and the crack tip are summarized and compared to shed some light on the evolution of oxide film microstructure along the deep crack path where the redox environment changed rapidly from oxidizing to reducing conditions.

Experimental

Material and Examined Locations

The boat sample was a weld material of Alloy 182. Figure 2 shows a schematic drawing of the boat sample in-half that was sectioned into seven parallel pieces

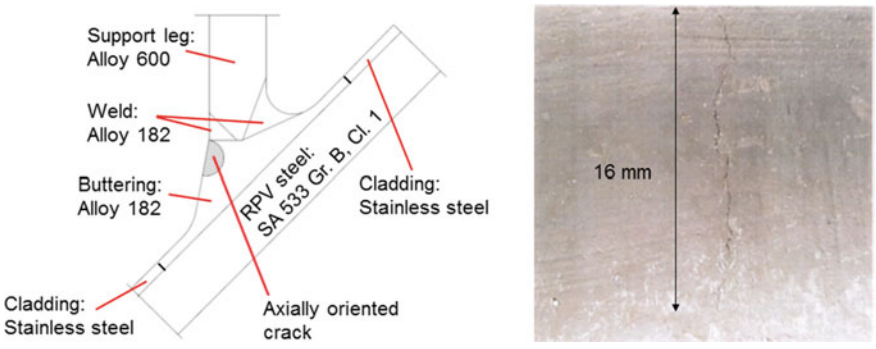

Fig. 1 Photograph and schematic drawing of the crack and its location in one core shroud support leg examined in this study

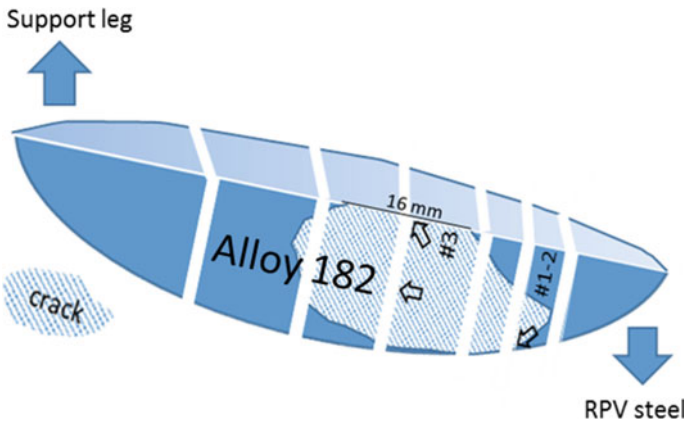

Fig. 2 The crack area and the examined locations in the boat sample in-half

including two pieces, marked #3 and #1–2 in the drawing, that are examined in this paper. The three examined locations are marked with hollow arrows. The examination on the sample piece #3 included two locations, namely, the crack mouth and the midway between the mouth and the boat keel. The examination on crack tips was made on the sample piece #1–2 where the crack tip locations were close to the boat keel. The approximate crack area inside the boat sample is illustrated based on the cross section LOM images obtained [1].

TEM Lamella Liftout with FIB/SEM

A Zeiss Auriga Cross-Beam FIB/SEM was used to fabricate the TEM-lamellas. In the crack mouth and the midway, the oxide films included on one side of the crack were selected for FIB liftout and made into TEM-lamellas. To prepare TEM-lamellas from the crack tip region, the boat keel was ground and polished in some angle, as schematically illustrated in Fig. 3, to reveal the active crack tip from which the TEM-lamellas were prepared. After a successful TEM-lamella liftout operation, a second TEM lamella was similarly prepared from the active crack tip region by re-polishing the same side.

The interested sample surface area was first protected by depositing Pt layers in situ in the FIB/SEM. The FIB technique employed focused high energy (1–30 kV acceleration voltage) gallium ions (mainly Ga^+) impinging on the sample surfaces. A high acceleration voltage and ion current were applied initially for achieving higher milling rates, which were gradually reduced when the lamellas became thin. At the final milling stage the acceleration voltage was decreased to 3 kV to remove the layers affected by the Ga ions on each side of the lamellas.

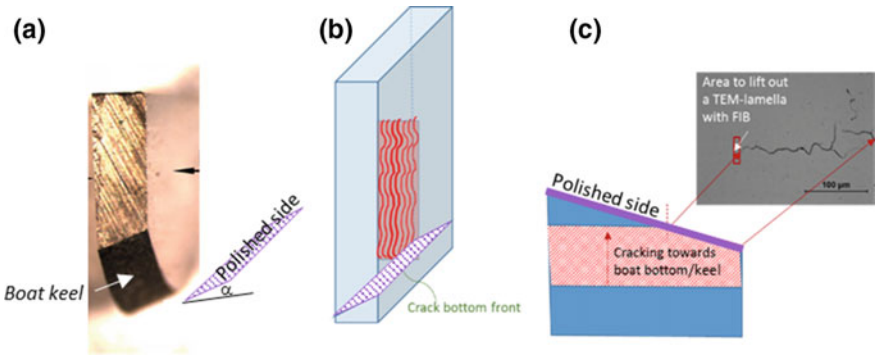

Fig. 3 Photo of the sample piece #1–2 (**a**), a schematic illustration of the polished side relative to the boat keel and crack area (the central patterned area) inside the sample piece (**b**), and the location for lamella lift-out on the polished side (**c**)

TEM Instrumentation

A field emission type TEM (JEOL, model JEM-2100F) was used to examine the first three TEM-lamellas as reported in this paper. Operated at 200 kV, the microscope was equipped with Energy Dispersive X-ray Spectroscopy (EDS) detectors (Oxford Instruments—X-Max^N 80 TLE), Electron Energy-Loss Spectroscopy (EELS) detectors, and bright and dark field scanning transmission electron microscopy detectors for compositional analysis and imaging. A combined analysis with Selected Area Electron Diffraction (SAED) and EDS was performed to identify phase compositions of some selected oxide grains, or some regions of interest with typical compositions. The TEM-lamella as last reported in this paper, which included a crack tip, was examined with another field emission type TEM (FEI, model TITAN 80–300) which operated at 300 kV.

Results

Microstructures of Oxide Films in the Crack Mouth

The oxide film microstructures in the crack mouth were reported elsewhere [2]. The oxide film was mainly composed of nickel oxide. More detailed examinations revealed the presence of two separate nickel oxide phases of slightly different compositions (one phase was columnar and surrounded by the other phase). The oxide film was fine polycrystalline and approximately 1.6 μm in thickness measured on one side of the crack. In the oxide/metal interface regions there was a thin amorphous oxide layer. Small pores were found in the oxide film and at the oxide/metal interface regions.

Microstructures of Oxide Films in the Midway Between the Crack Mouth and Tip

Figure 4 shows STEM bright field (BF) and dark field (DF) cross section images from the midway. Generally the oxide film was uneven in thickness (up to 0.3 μm), and contained some distinct oxide species. In Table 1 the elemental compositions of

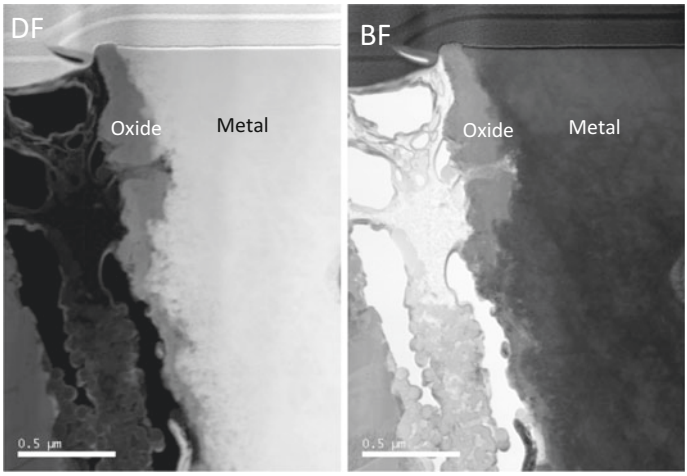

Fig. 4 STEM BF and DF cross section images of a midway location

Table 1 Elemental compositions (in at%) of some oxide film locations indicated in Fig. 5

Location	O	Si	Cr	Mn	Fe	Ni
"Mean"	55.5	1.7	14.6	2.5	5.2	18.5
#1	2.0	0.9	13.7	7.3	8.1	68.1
#2	28.0	0.6	1.6	0.9	39.9	29.0
#3	28.3	0.8	1.9	0.4	40.2	28.4
#4	3.3	0.7	15.7	5.6	9.6	65.1
#5	47.1	49.3	0.4	0.3	0.9	2.1
#6	44.7	49.8	0.8	0.2	1.1	3.4
#7	44.3	39.2	3.2	1.0	3.1	9.2
#8	25.9	0.3	5.5	0.2	32.8	35.3
#9	16.9	1.3	21.1	4.9	6.9	48.9
#10	43.1	42.1	1.7	0.3	3.7	9.1
#11	47.1	49.4	0.5	0.2	0.8	1.9
#12	42.7	51.4	0.8	0.2	1.3	3.5
#13	9.4	1.0	18.8	5.4	8.0	57.4
#14	14.3	1.2	21.2	4.5	8.0	50.9
#15	12.5	1.0	20.1	5.3	7.3	53.7
#16	4.0	0.8	16.2	7.7	7.7	63.6

the oxide films at some locations are presented. In particular, the "mean" composition in the table was for the thick oxide film marked in Fig. 5a, which contained mainly a nickel chromium oxide with a nominal composition of $(Ni_{0.55}Cr_{0.45})O$. In Fig. 5b the points #1, #4 and #16 were likely base metal, and the points #5–7 and #10–12 were probably SiO_2. In some oxide film locations, such as the points #2–3, #8–9 and #14–15, very low oxygen contents were detected, some of which might be due to that the locations were mixtures of metal and oxide, some might be underestimation by the instrument. If it is the latter case, the ratios of metal elements may sometimes provide good hints about oxide stoichiometry. For example, the point #3 may be iron nickel oxide that is often identified as $Ni_xFe_{3-x}O_4$ ($x < 1$).

In Figs. 6 and 7 a part of the oxide film was selected for performing EDS mapping and for point analysis. Generally, the selected oxide film had largely even element concentrations except for the oxide/water interface region where the ratio of nickel to chromium, or nickel to iron, was about doubled. The SAED pattern taken in the oxide region near metal/oxide interface region can be indexed with NiO of the rocksalt structure (Fig. 8). A tilt experiment was performed in three diffraction angles to verify the oxide crystal structure. The results are summarized in Tables 2 and 3. The results could exclude the possibility of presence of either $NiCrO_3$ (corundum structure) or $NiCr_2O_4$ (cubic structure). In Fig. 9 two high resolution TEM images are shown, one from the oxide/metal interface region and another from the outer part of the oxide film, respectively. As can be seen in the corresponding fast Fourier transform (FFT) images both parts of the oxide film have a similar crystal orientation, suggesting the epitaxial growth of the thin oxide film.

Microstructures of Active Crack Tips

Two TEM-lamellas were prepared from crack tips in the sample piece #1–2 in this study. In Fig. 10 STEM DF and BF images of two regions of a crack tip are shown.

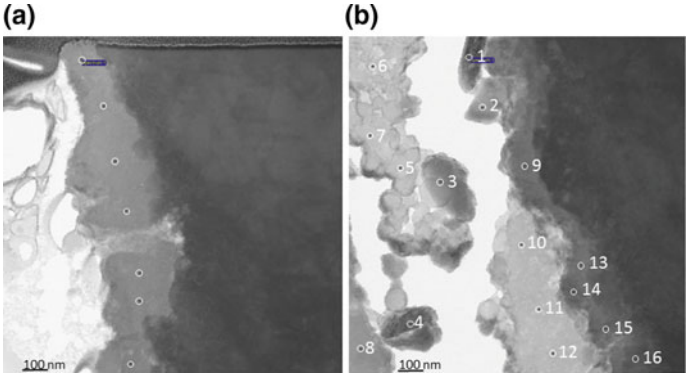

Fig. 5 STEM BF cross section images of two midway locations where EDS point analyses were made (see Table 1)

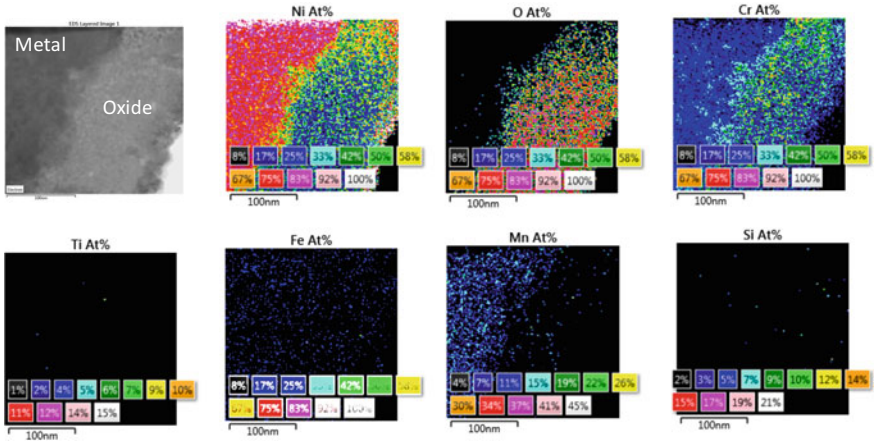

Fig. 6 Elemental composition maps in a selected area of oxide film. Top-left is a STEM BF image

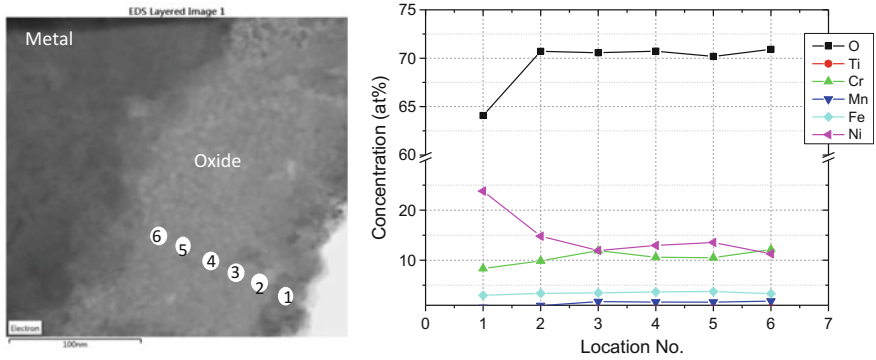

Fig. 7 Element compositional profiles across an oxide layer with a different outer oxide layer marked ①. The image to the left is the same image as shown in Fig. 6

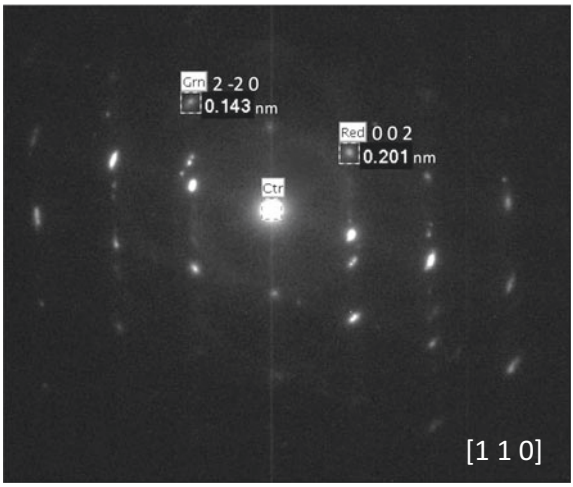

Fig. 8 Electron diffraction pattern of an oxide area. Indexed with cubic NiO

Table 2 Measured *d*-values and corresponding crystal planes of different oxides

$d_{meas.}$ (Å)	(*h k l*) in *NiO*	(*h k l*) in $NiCrO_3$	(*h k l*) in $NiCr_2O_4$
2.0-2.1	(0 0 2)	(2 0 2)[a]	(4 0 0)[b]
1.43	(2 2 0)	(3 0 0)[a] or (2 1 4)[a]	(4 4 0)[b]
0.93	(2 4 0)	Not in table	Not in table
0.58	(4 6 2)	Not in table	(7 5 1)

[a]Not possible because 202 and 300 alternatively 202 and 214 need to be in the same zone axis pattern with 90° angle
[b]Not possible because 400 and 440 need to be in the same zone axis pattern with 90° angle

Table 3 Tilt experiments according to cubic NiO

From [*h k l*]	To [*h k l*]	Tilt angle measured (°)	Theoretical angles (°)
[1 1 0]	[3 2 0]	11.7	11.3
[3 2 0]	[2 1 0]	4.7	7.3
[2 1 0]	[1 0 0]	27	26.5

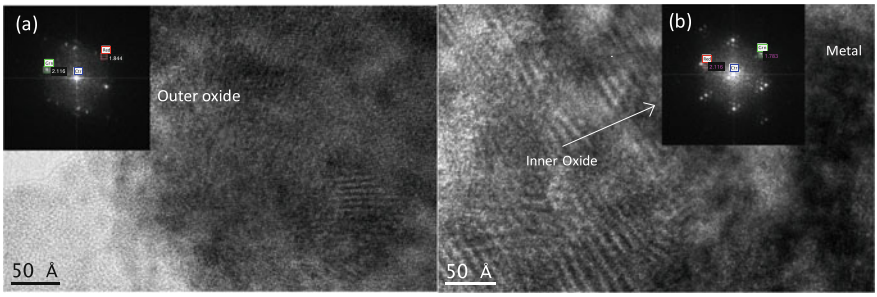

Fig. 9 High resolution TEM images with FFT image insets from (**a**) an outer oxide layer and (**b**) an inner oxide layer of a selected part of oxide film

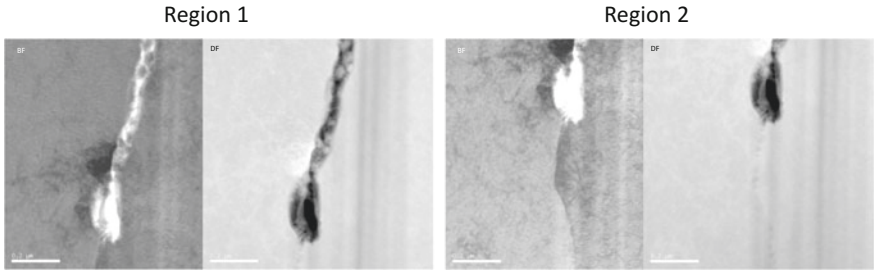

Fig. 10 STEM BF and DF images showing two regions of a crack tip

In the narrow crack path one can see some oxides and voids. In the crack tip there is a relatively large void of oval shape. At a high magnification one can see a thin oxide film covering the metal grains (see Fig. 11). According to the EDS measurements (Table 4), the oxide film mainly consisted of a nickel chromium iron oxide with a nominal composition of $(Ni_{0.56}Cr_{0.26}Fe_{0.18})O$. EDS X-ray mapping performed in the metal/metal grain boundary region ahead of the crack tip reveals the presence of some Cr-rich grains but no oxygen (Fig. 12). As further revealed by the high resolution TEM imaging and FFT analysis, the thin oxide film near the crack tip is polycrystalline (Fig. 13).

Figure 14 shows STEM cross section images of the crack tip region of the second TEM-lamella. As the crack tip is in contact with the deposited Pt layer, the active crack tip might not have been included in this TEM-lamella. The crack is intergranular along the ~2 μm long path in which a large grain of precipitate, probably (Nb,Ti)C, is present (Fig. 15 for the EDS X-ray mapping result). Along the crack path oxide films of up to ~50 nm in thickness can be seen. Two oxide locations marked in Fig. 16 were measured with EDS and the results are presented

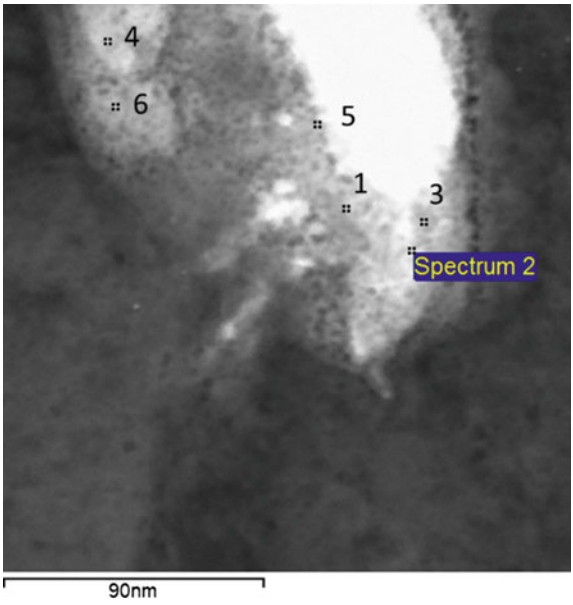

Fig. 11 STEM BF image of the crack tip region and the points measured with EDS

Table 4 Elemental compositions (in at%) of oxides in the crack tip region (see Fig. 11)

Location	O	Si	Ti	Cr	Mn	Fe	Ni
#1	49.4	3.7	12.9	15.0	1.2	3.0	14.8
#2	51.0	2.3	0.2	10.9	3.3	8.7	23.7
#3	38.3	1.8	0.2	10.2	2.8	9.7	36.9
#4	53.5	3.3	0.2	5.1	3.3	7.2	27.4
#6	59.2	1.9	0.4	4.1	2.5	6.0	26.0

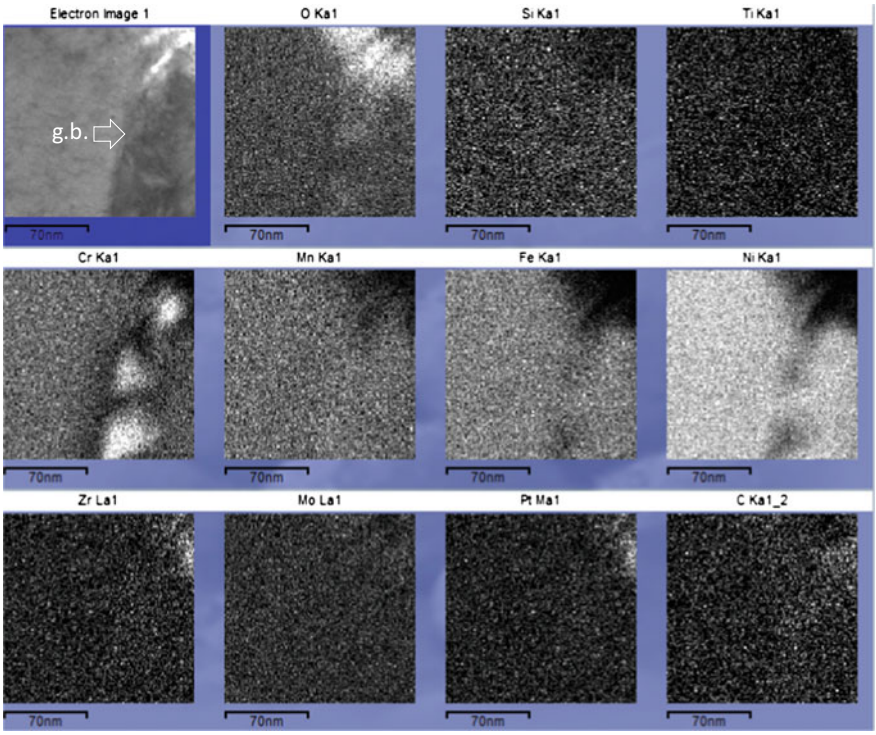

Fig. 12 EDS element X-ray mapping in the metal/metal grain boundary region ahead of the crack tip

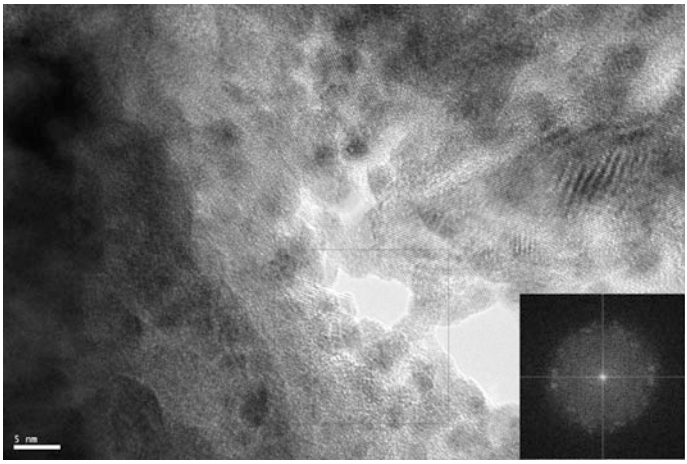

Fig. 13 High resolution TEM image of the crack tip region. The inset is a FFT image from the rectangular area marked

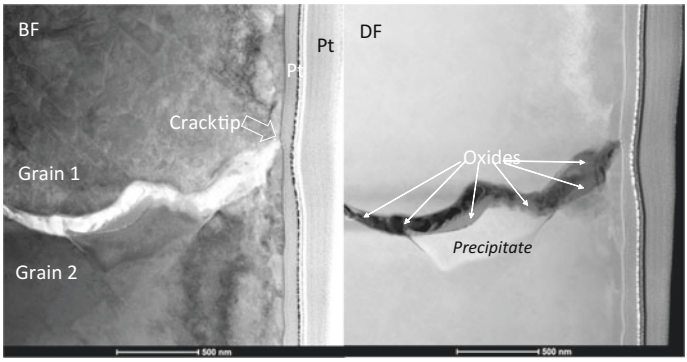

Fig. 14 STEM bright field and dark field cross section images showing the crack tip region

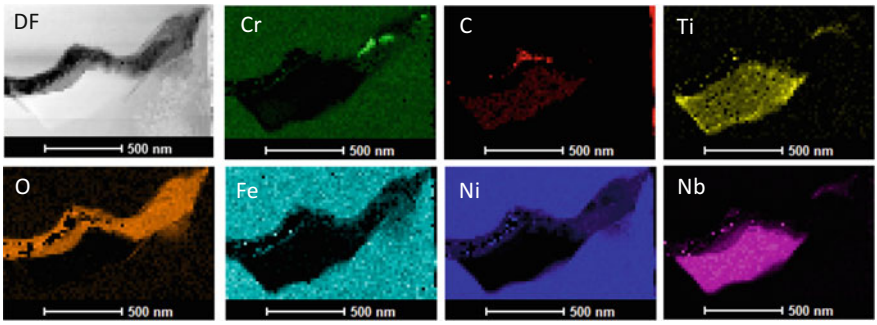

Fig. 15 EDS element X-ray mapping in the crack tip region

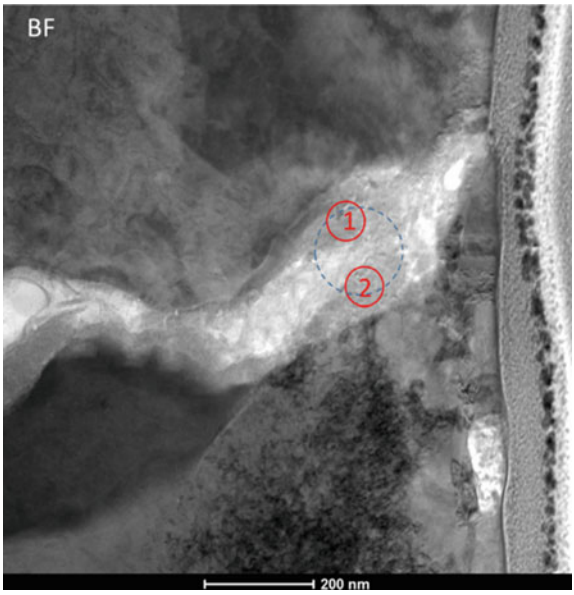

Fig. 16 STEM BF image showing the crack tip region and two oxide locations ① and ② for EDS measurement as well as one location (dotted blue circle) for electron diffraction (Color online figure)

in Table 5. The point #1 is mainly a nickel niobium oxide while the point #2 a nickel chromium iron oxide with a nominal composition of $(Ni_{0.56}Cr_{0.26}Fe_{0.18})O$. The electron diffraction pattern from the oxide region shows a few broken rings that could be indexed with either NiO or $NiFe_2O_4$ structure (Fig. 17 and Table 6). Because of the high Ni fraction in the oxide, the possible presence of $NiFe_2O_4$ structure is excluded. A rocksalt structure is therefore suggested. A high resolution TEM image of the crack tip is shown in Fig. 18.

Table 5 Element compositions (in at%) of two oxide locations in Fig. 16

Location	O	Ti	Cr	Mn	Fe	Ni	Nb
#1	62.4	2.9	1.9	0.7	1.1	17.6	12.7
#2	56.6	0.4	10.7	1.0	5.5	25.2	0.5

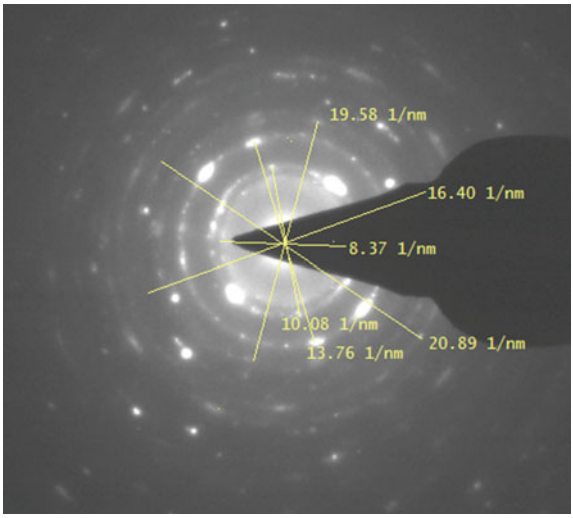

Fig. 17 Electron diffraction pattern obtained from the oxide region marked with dotted blue circle in Fig. 16 (Color online figure)

Table 6 Measured *d*-values for the diffraction rings in Fig. 17 and reference powder diffraction data for cubic NiO and $NiFe_2O_4$

Ring no.	d_{meas} (Å)	NiO		$NiFe_2O_4$	
		d_{ref} (Å)	*h k l*	d_{ref} (Å)	*h k l*
1	2.39	2.412	1 1 1	2.408	2 2 2
2	1.98	2.089	2 0 0	2.0850	4 0 0
3	1.45	1.4768	2 2 0	1.4760	4 4 0
4	1.22	1.2594	3 1 1	1.2036	4 4 4
5	1.02	1.044	4 0 0	1.0424	8 0 0
6	0.96	0.934	4 2 0	0.9630	7 5 1

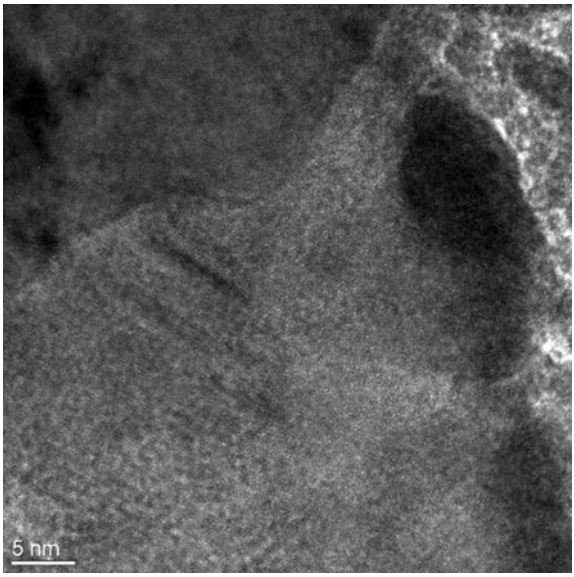

Fig. 18 High resolution TEM image of the crack tip region

Discussion

The corrosion behavior of Alloy 182 material in reactor coolant conditions may be generally explained with the PDM model [3] as such that during corrosion the barrier oxide film would refresh its constituents with the outward diffusing metal cations and other defects (e.g. cation interstitials and oxygen vacancies) that are formed at the metal/oxide interface. At the barrier oxide/water interface, the metal cations of the oxide film react with water and release into coolant. The release results in oxide film thinning and elevation of metal impurity level in BWR coolant, while the oxygen anions of water fill the oxygen vacancies at the oxide/water interface, leading to oxide film growth. The competitive processes in sustaining the presence of the oxide film are reflected in the following mass balance equation:

$$W_m = \Delta W + W_{ox} \tag{1}$$

where W_m is the weight of corroded metal of a sample; ΔW the weight loss of the sample; W_{ox} the weight of oxide films. One can see that the amount of corroded metal, W_m, depends on both the oxide film thickness, a measure of W_{ox}, and weight loss of the sample, ΔW. As different oxide films may have different dissolution rates in a corrosive environment or an oxide film may have different dissolution rates in different environments, oxide film thickness alone cannot be used to judge how much metal is corroded.

In Table 7 the characteristics of the oxide films formed in the crack mouth, at the crack tip and in the midway between the crack mouth and tip are summarized. Let us assume the width of the crack path is solely caused by metal corrosion removal.

Table 7 Summary of oxide film microstructures along the crack path

Crack location	Crack width (μm)	Oxide structure	Nominal compositions[a]	Max. oxide film thickness (μm)
Mouth	50	Rocksalt	NiO	1.6
Midway	25	Rocksalt	$(Ni_{0.55}Cr_{0.45})O$	0.3
Tip	0.1 ~ 0.2	Rocksalt	$(Ni_{0.56}Cr_{0.26}Fe_{0.18})O$	0.03

[a] The constituents of <5 at % are not included

As $W_m \gg W_{ox}$, $\Delta W > 0$. That is, the corrosion would be a weight loss process and the metal constituents in the oxide films would come from only a very small fraction of the corroded metal. A majority of corroded metal would therefore be dissolved into the coolant. This hypothesis has been partly confirmed by corrosion kinetic studies on some nickel base alloys including Alloy 182 under the BWR NWC coolant conditions [4, 5].

Among the three crack locations examined, the coolant condition around the crack mouth resembles the bulk coolant condition in terms of oxygen and hydrogen peroxide concentrations. The oxide film in the crack mouth region is basically a single layer of nickel oxide, unlike the duplex-layer structure (i.e. an outer $NiFe_2O_4$ grains and a porous inner NiO layer) observed on a similar material surface after short corrosion exposure. Recall that NiO is thermodynamically unstable in the BWR NWC condition. The presence of porous NiO layer but absence of the outer $NiFe_2O_4$ grains in the crack mouth may be due to two reasons. One was that the redox condition in the crack mouth region dropped sufficiently low so that NiO became a thermodynamically stable phase. Another was that the redox condition in the crack mouth region remained high but the underlying porous NiO layer had poor physical contact with the outer $NiFe_2O_4$ grains so that these outer grains were lost during corrosion or TEM-lamella preparation.

When the crack propagated deep into the weld, the redox condition may change from oxidizing to reducing. Thermodynamically, such a change would favor the formation of chromium oxide and nickel oxide. If such a nickel chromium oxide film is more protective, the corrosion rate may be further decreased. More studies are needed to verify such a hypothesis.

In the crack tip regions the oxide films mainly contain nickel, chromium and iron. In Table 8 the atomic ratios of the main metal elements in the base metal and in the oxide in the crack tip are compared. One may see that [Ni]/[Cr] and [Ni]/[Fe] in the oxide are about half of that in the base metal or less. In other words, a considerable fraction of corroded nickel did not form oxide but dissolved into the coolant. Similarly, a larger fraction of the corroded chromium than the corroded iron also dissolve into the coolant.

Table 8 Atomic ratios* of metals in the base metal and the oxide in the crack tip

	Base metal	Oxide
[Ni]/[Cr]	4.2	2.2
[Ni]/[Fe]	8.2	3.1
[Cr]/[Fe]	1.9	1.4

* As determined with EDS/TEM

Oxide film morphology, compositions and crystal structure are closely related to the physical and chemical characteristics of base metal, local corrosion environment and exposure duration. After more such knowledge is obtained one may be able to tell, based on the oxide film microstructures in a crack tip region, the actual crack growth rate in the crack tip.

Conclusions

In the present study, the microstructures of the oxide films formed in a crack mouth, crack tip and midway between the mouth and tip from a cracked core shroud support leg have been examined. In the crack mouth a relatively thick but porous nickel oxide layer was formed. In the midway point there was a thin nickel chromium oxide film. In the crack tip region intergranular cracking could also be clearly identified. The cracked metal grain surfaces were covered by a very thin layer of nickel chromium iron oxide. In all locations the main oxides had a similar rocksalt crystal structure. In all studied locations the cracks were much wider than the thicknesses of the oxide films, for which a possible explanation was that the corroded metal had been largely dissolved into the coolant. The different dissolution rates of nickel, chromium and iron cations in oxide films were clearly displayed for the oxide films formed.

Acknowledgements The authors wish to express their sincere gratitude to Mr. Roger Lundström and Mr. Michael Jakobsson at Studsvik Nuclear AB who performed light optical microscopy work, and to Dr. J. Öijerholm at Studsvik Nuclear AB for his technical and administrative support.

References

1. M. Bjurman et al., Root cause analysis of cracking in Alloy 182 BWR core shroud support leg cracks. Paper to be presented at the 2017 environment degradation conference, Portland, OR
2. J. Chen et al., TEM Examination of Oxide Films Formed in the Crack Opening of Alloy 182 Weld Metal under BWR Normal Water Chemistry Conditions. Paper presented at the 20th international conference on water chemistry of nuclear reactor systems, October 2–7 2016. Brighton, UK.)
3. D.D. Macdonald, Some personal adventures in passivity—a review of the point defect models for film growth. Russ. J. Electrochem. **48**(3), 235–258 (2012)
4. C. Gustafsson et al., Corrosion Kinetics of Nickel-Base Alloys in Simulated BWR Conditions under High Flow Velocity Paper presented at the 16th lnternational conference on environmental degradation of materials in nuclear power system—water reactors, August 11–15, 2013, Asheville, NC, USA
5. C. Chen et al., Corrosion Kinetics of Nickel-Base Alloys with High Chromium Contents under Simulated BWR Normal Water Chemistry Conditions and High Flow Velocity. Paper presented at the 17th international conference on environmental degradation of materials in nuclear power systems—water reactors. August 9–13, 2015. Ottawa, Canada

Effect of Chloride Transients on Crack Growth Rates in Low Alloy Steels in BWR Environments

Xiaoyuan Lou and Raj Pathania

Abstract The objective of this study was to quantify the effect of chloride transients on stress corrosion cracking of pressure vessel low alloy steels. Two heats of reactor pressure vessel steel were evaluated at various chloride concentrations in both NWC and HWC environments. The tests showed that low alloy steels can exhibit a delayed cracking response during a chloride transient. The delayed response is attributed to the concentrating and dilution processes of anionic impurities inside the crack. The crack can maintain its original growth rate for a certain period after the chemistry change. The effects of chloride concentration, stress intensity factor (K) and periodic load cycling on the crack incubation and growth in low alloy steel will be discussed. The results from this work will provide a direct input to development of a crack growth model for low alloy steels, water chemistry guidelines and effects of chloride transients on crack growth.

Keywords Pressure vessel low alloy steel · Stress corrosion cracking · Chloride · Boiling water reactor · Crack growth · Memory effect

Introduction

Due to the importance of reactor pressure vessel (RPV) as the key pressure boundary component in boiling water reactors (BWRs), stress corrosion cracking (SCC) of pressure vessel low alloy steel (LAS) in high temperature water has been widely studied since 1970s [1–3]. 40 years' lab and field experience has demonstrated that good practice of water chemistry in reactor can significantly reduce stress corrosion cracking susceptibility of the structural materials used in the reactor. Three chemistry action levels have been established in EPRI boiling water

X. Lou (✉)
GE Global Research, One Research Circle, Niskayuna, NY 12309, USA
e-mail: xiaoyuanlou@gmail.com

R. Pathania
Electric Power Research Institute, 3420 Hillview Ave, Palo Alto, CA 94304, USA

J.H. Jackson et al. (eds.), *Proceedings of the 18th International Conference on Environmental Degradation of Materials in Nuclear Power Systems – Water Reactors*, The Minerals, Metals & Materials Series, https://doi.org/10.1007/978-3-319-68454-3_34

reactor water chemistry guideline [4] with increasing order of severity. Action levels were determined based on quantitative analysis on the effects of the chemistry variables on the corrosion behavior of reactor materials, fuel performance and radiation field buildup. For chloride transient in primary cooling water, Table 1 shows the 2014 guideline for chloride levels. The lowest action level of chloride was ≥ 5 ppb for both NWC and HWC in the 2014 guideline.

However, independent work conducted in Paul Scherrer Institute (PSI) and GE confirmed a very pronounced effect of chloride, at levels as low as 3 ppb, in initiating and sustaining rapid crack growth in low alloy steel [5–9]. Therefore, based on the results of these studies BWRVIP issued an Interim Guidance in 2016 revising the chloride action limit to ≥ 3 ppb.

The new observations of SCC susceptibility of pressure vessel steel at <5 ppb chloride raised a concern for the current fleet of boiling water reactors. Chloride can be introduced into the reactor cooling system during periods of significant condenser in-leakage or other incidents. To determine the impact of this period on the existing flaws on pressure vessel steel, it is critical to obtain the crack growth rate data of the steel in chloride containing environments and understand how long the fast growth rate can sustain after the clean-up. GE has observed that low alloy steels can exhibit a delayed cracking response under the transient of chloride. There is an incubation time before the crack growth rate starts to increase after chloride is added. Similarly, there is a delay time or so called "memory" effect after chloride is removed before the crack growth rate starts to decrease. These observations raised concerns in regard of the evaluation of crack growth rates in the primary pressure boundary components after the chloride transient. The adequacy of the current BWRVIP-60-A stress corrosion cracking (SCC) disposition lines (DLs) need to be re-evaluated for chloride transient conditions.

The main purpose of this research was to generate data to support the possible revision of BWRVIP-60-A LAS SCC disposition lines for chloride transient. Quantitative analysis of memory effects is also conducted to determine impact of chemical transient and operation practice during the transient. Two different heats of pressure vessel steel from the actual reactor pressure vessels (RPV) were evaluated under both periodic partial unloading (PPU) condition and constant load/K condition without unloading. A wide range of chloride levels (5, 20, 100, 500 ppb for NWC, and 5, 50, 200, 500 ppb for HWC) were evaluated to provide adequate data to all three action levels and possible severe condition beyond the action level 3. Effects of electrochemical potential (ECP), stress intensity factor (K), and heat-to-heat difference were also studied in detail.

Table 1 EPRI boiling water reactor water chemistry control guideline for NWC, HWC and HWC + NMCA or OLNC (data from [4])

	Action Level 1	Action Level 2	Action Level 3
Chloride	≥ 5 ppb	>20 ppb	>100 ppb
Sulfate	>5 ppb	>20 ppb	>100 ppb

Experimental Procedures

Two different heats of high sulfur low alloy steels were tested in this study. Table 2 shows the chemical compositions of the steels. Both heats were studied in the previous EPRI-GE program for evaluating the impact of < 5 ppb chloride on SCC of LAS in high temperature water [7]. SWRI heat is A533 Grade B Class 1 LAS from the reactor pressure vessel head of a canceled plant. Figure 1 shows the orientation of the material relative to the vessel heat plate. This heat has been used in EPRI's RPV boric acid corrosion testing program. 1bG heat is also A533B grade LAS, and this specific heat was used in a previous BWRVIP test program. Both materials were tested along T-S orientation in this study to simulate through-wall crack propagation in the reactor vessel.

Since all the materials received were from the actual reactor vessels, they were tested in as-received condition with no additional treatment. The crack growth rate tests were performed using 1-inch (1T) compact tension (CT) specimens with 5% side grooves on each side. The tests were conducted in 288 °C BWR water. A close-loop system with demineralizer was used to purify the outlet water from the autoclave back to above 18 MΩ-cm. Chloride concentration in the autoclave was maintained by injecting the dilute HCl solution and controlling the water inlet conductivity to a pre-calculated constant value. The study was conducted in both, low corrosion potential hydrogenated water (63 ppb H_2 in water) and high corrosion potential oxygenated water (2 ppm O_2). The CT specimens were instrumented

Table 2 Chemical compositions of the steels tested (wt%)

	S	C	Al	Co	Cr	Cu	Mn	Mo	Ni	Si	P	V
SWRI	0.015	0.2	0.021	0.018	0.066	0.07	1.25	0.55	0.58	0.23	0.01	0.0015
1bG	0.013	0.19	0.028	0.017	0.078	0.099	1.25	0.53	0.62	0.25	0.01	0.003

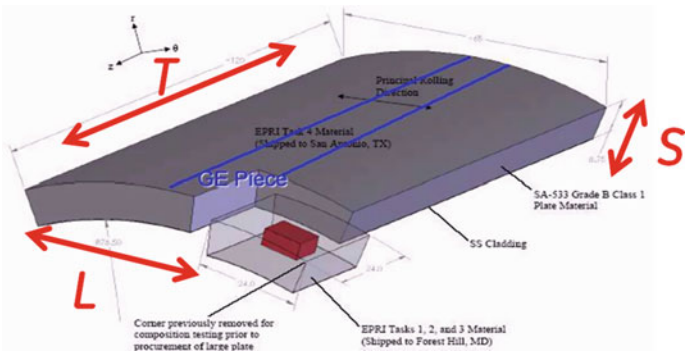

Fig. 1 Specimen orientation relative to the vessel plate sent to GE (re-plotted based on reference [13])

with platinum current and potential leads for dc potential drop (DCPD) measurements of crack length. Current flow through the specimen was reversed about once per second to reduce the measurement errors associated with thermocouple effects and amplifier offsets. A DCPD correction factor must be accurately estimated to ensure little or no rise in K during the exposure period. The final crack growth rate was also calculated based on the fracture micrograph performed after the test. The computer controlled current reversal, data acquisition, data averaging, the calculation of crack length from the potential, and the auto-control of constant stress intensity factor (K). [10, 11] The specimen was electrically insulated from the loading rig by zirconia sleeve and washer. Within the autoclave a zirconia washer also isolated the upper pull rod from the internal load frame. The lower pull rod was electrically isolated from the autoclave using a pressure seal and an insulating washer. Fatigue pre-cracking was performed at the beginning of each test at $\sim$1 Hz and an increasing load ratio (K_{min}/K_{max}) R = 0.2, 0.4, and 0.6. Subsequent pre-crack steps to transition the crack to intergranular type were performed by decreasing the frequency to 0.001 Hz, then by introducing a hold time, and finally to a fully constant K test with no cycling. The corrosion potentials of the CT specimen and a Pt coupon were measured relative to a zirconia membrane Cu/CuO reference electrode [12].

The main focus was generating stress corrosion crack growth rate data to re-evaluate the SCC behaviors of low alloy steel at different chloride transient conditions. SCC memory effects was quantified by evaluating the delayed time of the cracking response to a change in chloride concentration (both chloride increase and decrease). Figure 2 shows the schematic of both time-to-activation and time-to-arrest of a stress corrosion cracking during a chloride transient. Time-to-activation defines the incubation time before the crack growth rate starts to increase after chloride is added, while time-to-arrest defines a so called "memory" effect after chloride is removed before the crack growth rate starts to decrease.

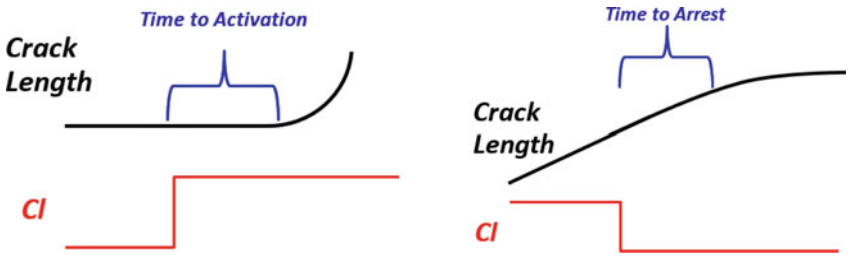

(a) Time to activation after chloride increase (b) Time to arrest after chloride decrease

Fig. 2 Schematic of the definition of stress corrosion crack memory in this report

Results

Crack Growth Rate Under Constant Load in Normal Water Chemistry

Figure 3 shows a summary of crack growth rate data from both SWRI and 1bG heats under constant load/K condition and different chloride levels. The data are plotted against EPRI BWRVIP-60-A LAS SCC disposition line, also to GE low and high sulfur lines. In all these tests, the loading conditions did not exceed the K/size criteria by ASTM E399. Those SCC growth tests which did not show sustained crack growth were not included in this plot. It should be kept in mind that there were still data showing no crack growth that are not included in Fig. 3. The data at <5 ppb chloride condition was obtained from earlier research [7] and tested in higher oxygen conditions (8 ppb). With the chloride transient at 5–100 ppb, most stress corrosion cracks exhibited growth rate higher than GE low sulfur line. But all the cracks were still bounded by GE high sulfur line. Generally speaking, stress corrosion crack growth rate in low alloy steel increases as K and chloride increase. The only data showing the crack growth rate above high sulfur line was during the chloride transient of 500 ppb. But when the chloride level is above 100 ppb, the chemistry reaches action level 3 (Table 1) and the reactor should be shut down. With SWRI heat and 1bG heat, there were few data showing high crack growth rate when the chloride was below 5 ppb. But according to our previous research [7], on a more susceptible heat of low alloy steel from a plant (PSI heat), 3–5 ppb chloride can activate an arrested crack and sustain the high crack growth rate when the corrosion potential is very high.

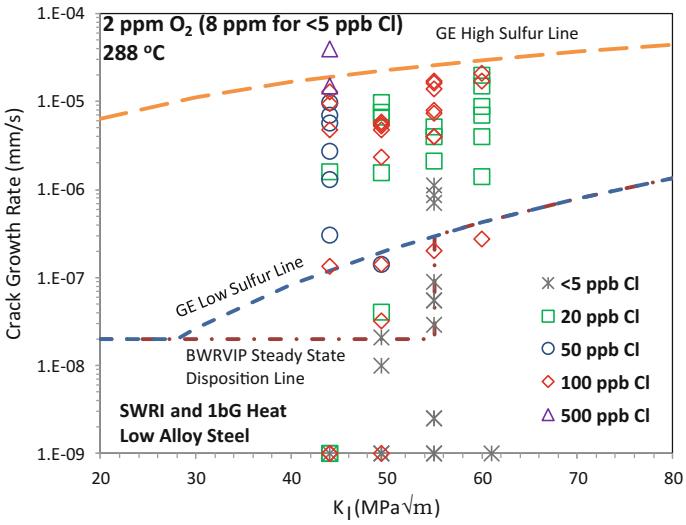

Fig. 3 Summary of the crack growth rates measured under constant load/K condition in this program compared with BWRVIP/GE disposition lines

Crack Growth Rate Under Constant Load in Hydrogen Water Chemistry

Figure 4 shows a summary of SCC crack growth rate of both SWRI and 1bG steels in hydrogenated water containing 63 ppb H_2. The chloride levels used in this study were 5 ppb, 50, 200, and 500 ppb. It should be noted that a chloride concentration of 50 ppb exceeds Action Level 2 and 200–500 ppb chloride exceeds Action Level 3. The purpose of testing at these high concentrations was to evaluate the effect of severe chloride transients on crack growth rates, Such transients can occur in plants because of condenser tube failures. Under constant load/K condition where K is in a range of 49.5–55 MPa$\sqrt{m}$, stress corrosion cracks in both heats show no growth in hydrogenated water. Under cyclic load condition at R = 0.6 and Frequency = 0.001 Hz, cracks can sustain the growth. However, no chloride effect was observed in all the tests in HWC at the chloride level up to 500 ppb. Therefore, in HWC, low alloy steel shows no SCC risk during a chloride transient up to 500 ppb in this research.

Heat-to-Heat Comparison

Figures 5 and 6 show the comparison of crack growth rate of two different LAS heats tested in this program in two different chloride conditions (20 and

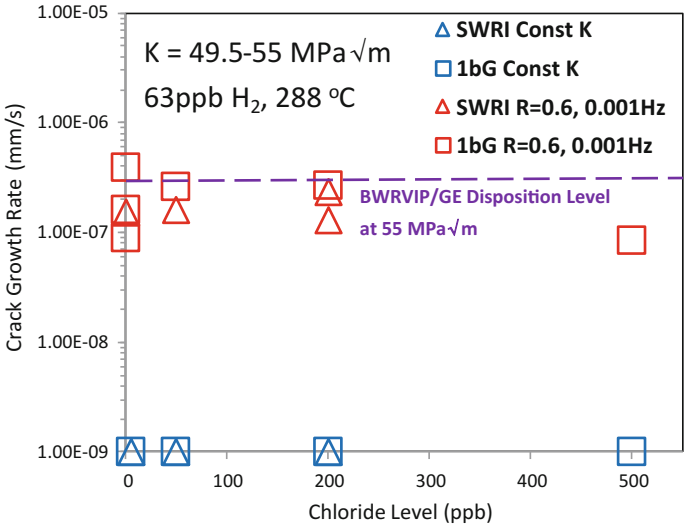

Fig. 4 Summary of CGRs in 63 ppb hydrogenated water at K = 49.5–55 MPa$\sqrt{m}$ under both constant load and cyclic load conditions

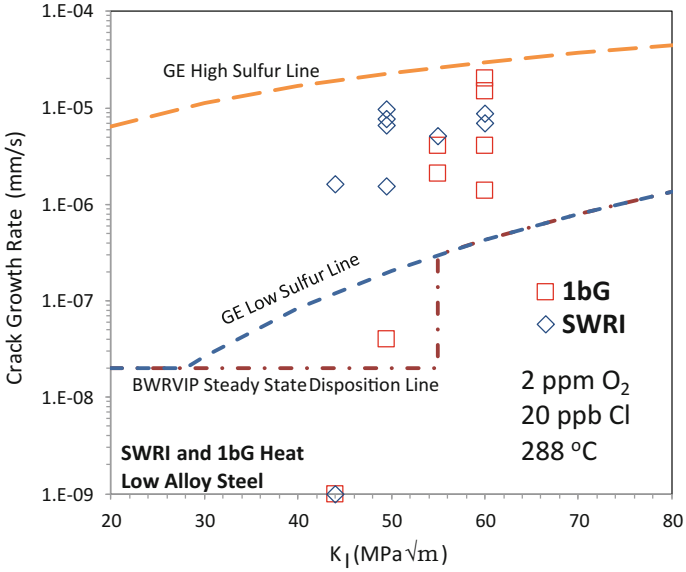

Fig. 5 Comparison of crack growth rate of two different heats at 2 ppm O_2 and 20 ppb Cl

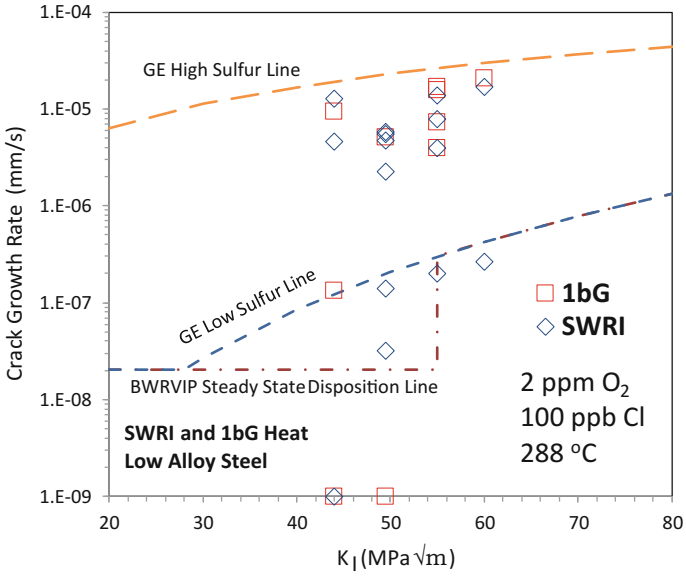

Fig. 6 Comparison of crack growth rate of two different heats at 2 ppm O_2 and 100 ppb Cl

100 ppb Cl). The tests showed that there was no apparent difference in SCC growth rate in these two heats of pressure vessel steels in BWR normal water chemistry. Though some cracks exhibited slow crack growth rates in the plots, most cracks showed high growth rates and the data from two heats overlapped on each other. SCC susceptibility of both heats increases as K and chloride increases. Earlier work on these two heats has shown that SWRI and 1bG heats have similar chemical composition, sulfide distribution, and grain structure. This result is consistent with the earlier observations [7].

Chloride Memory Effect on Stress Corrosion Crack of Low Alloy Steel

Figure 7 shows how a stress corrosion crack in low alloy steel responds to chloride incubation and memory effect during and after the chloride transient. The behavior of a stress corrosion crack can be described in 4 different steps during a chloride transient period, as listed below:

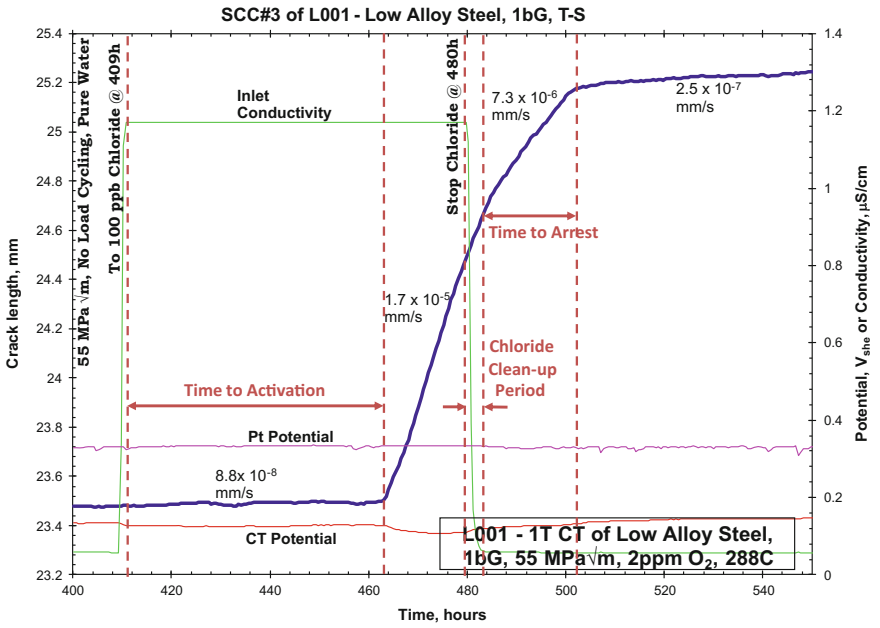

Fig. 7 A typical example of chloride memory effect in low alloy steel

(1) Time-to-activation: the time period that is needed to re-activate an arrested crack. This delayed response may be attributed to the transport of the anions through the crack and oxide to the crack tip.
(2) Crack growth period: fast crack growth in chloride containing environment after the crack activation.
(3) Chloride clean-up period: the time that is taken to clean the reactor water.
(4) Time-to-arrest: the time that is needed to arrest the growing crack in pure water.

This paper defines the starting time of time-to-activation by the time when the reactor water reaches the targeted chloride level. In the same way, the starting time of time-to-arrest is defined by the moment when the reactor water reaches <1 ppb Cl. The ending time of time-to-arrest in this research is defined by the moment when the crack growth rate is below 3×10^{-7} mm/s.

With the 4-liter autoclave set-up in GE lab, the water clean-up usually takes about 4 h. Most of the data obtained in this program show that the crack generally does not slow down during the chloride clean-up period. It is reasonable to treat the crack during the clean-up period with the same growth rate as it does in chloride containing water. However, after the clean-up period, the crack can keep the same fast growth rate for a while. It should be noted that the fast momentum of the crack generally does not take long. Although it can take very long time to fully arrest a crack from chloride transient, the advance of a crack in low alloy steel is in general slow for the most of the time.

Figure 8 shows the summary of time-to-activate when the chloride level in reactor increases to the action level. The plot only includes the crack that could be

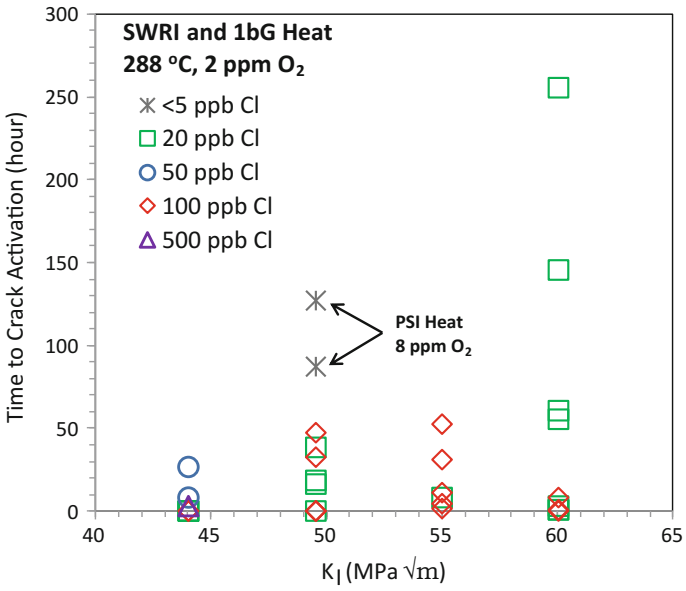

Fig. 8 Summary of time-to-activation during the chloride transient

activated in the test. There were many cases where the arrested crack could not be re-activated within 300–500 h of testing time in this study. The data in <5 ppb chloride from the earlier research program (different heat and 8 ppm O_2 condition) is also included for comparison. From these data, it is not so clear to conclude how the time-to-activation during a chloride transient is related to both chloride level and K level. The large variation in time-to-activation may be due to the variation in the starting status of a crack (crack length, crack front evenness, oxide inside crack, crack tip bluntness, etc.) The maximum time-to-activation was around 250 h, which does not include those cracks that could not be activated. Though there were a few cracks that required very long time to activate, most cracks could be activated within 70 h.

Figure 9 summarizes how long it takes to arrest an actively growing crack after the chloride contamination was cleaned from the reactor cooling water. The time-to-arrest in the paper only counts the time when the crack growth rate was higher than 3×10^{-7} mm/s. It is true that cracks may take long time to be fully arrested (crack growth rate is equal to zero). But we should not take too much consideration of the period when the crack grew slowly due to the following reasons: (1) the crack advance in length during this period was generally very small even though the time was long; (2) there can be huge variations if counting the arrest time of a slowly growing crack, which can provide misleading conclusions on how the arresting crack will impact the reactor pressure vessel. In most cases, such information tends to overestimate the damage to the reactor vessel. Though the data were scattered, the plot still shows the trend that time-to-arrest of a growing crack

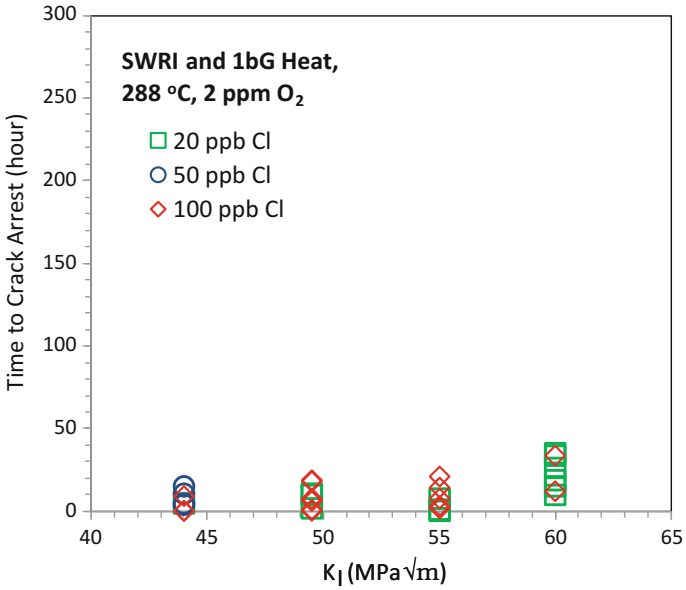

Fig. 9 Summary of time-to-arrest after the chloride clean-up

after chloride clean-up increased as the chloride level and K increased. The maximum time-to-activation was around 50 h. By comparing Fig. 9 with Fig. 8, it can be concluded that the time-to-arrest was generally less than the time-to-activation in all tested K and chloride levels. Based on the data in this study, it may not be necessary to have a penalty on the vessel life assessment because of the memory effect of the chloride clean-up because it will be balanced by the time to crack activation.

While the delayed time can provide some insights to how to quantify chloride memory, it is also important to understand how deep the crack can actually grow during this period so people can better assess the actual damage created by the memory effect after the chloride clean-up. Figure 10 shows the summary of the crack advance length measured from CT specimens after the chloride clean-up. Different from time-to-arrest, those data were obtained by calculating the time between the moment when water reached zero chloride condition and the moment when the crack was fully arrested (no growth). In all the tested heats and conditions, there was only one crack that grew for around 0.62 mm before it fully stopped. Most data show the crack extension after the water clean-up was below 0.3–0.4 mm in NWC. It is interesting to note that no clear correlation was observed between the actual crack extension and the chloride/K levels. All the arresting cracks in different chloride and K conditions grew similar distances after the chloride clean-up.

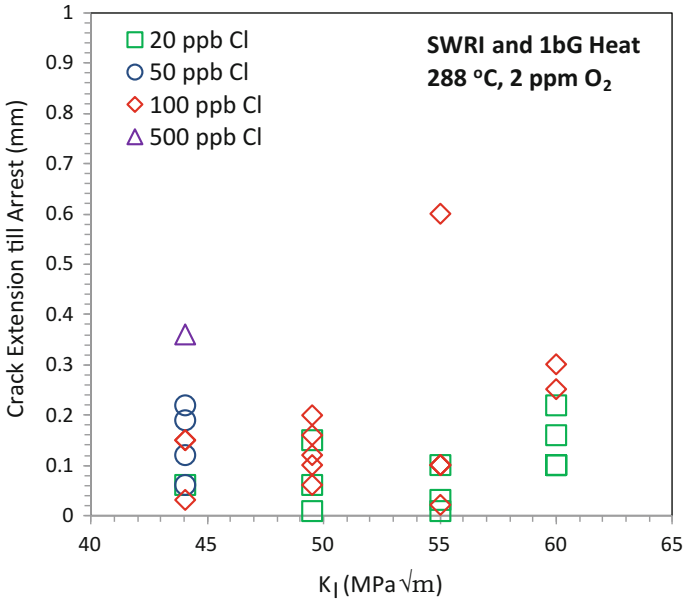

Fig. 10 Crack extension after the chloride clean-up [data was obtained by calculating the time between the moment when water reached zero chloride condition and the moment when the crack was fully arrested (no growth)]

Conclusions

SCC crack growth rates of pressure vessel low alloy steel were evaluated at 288 °C with 5, 20, 100, and 500 ppb chloride for normal water chemistry (NWC) and 5, 50, 200, and 500 ppb chloride for hydrogen water chemistry (HWC). The study also quantitatively evaluates the impact from the delayed cracking response during chloride transient (so-called memory effect) to the existing flaw in the pressure vessel steel. In NWC, higher chloride level increases the crack growth rate of LAS. GE low sulfur line cannot bound the crack growth rate data at >3 ppb chloride. However, GE high sulfur line is still a good bound for all the tested CGRs up to action level 3 (100 ppb chloride). In hydrogen water chemistry, no chloride effect or chloride memory effect was observed in all the tested heats and chloride/K conditions in this study. The crack arrest generally takes less time than crack activation during chloride transient period in all tested K and chloride levels. Based on the data analysis in this study, it may not be necessary to put a penalty on the vessel life assessment due to the impact from the memory effect of the chloride clean-up because it will be balanced by the effect of time to crack activation.

Acknowledgements This research is sponsored by Boiling Water Reactor Vessel and Internals Program, Electric Power Research Institute. Authors thank Dr. Peter Andresen for many helpful discussion.

References

1. P.L. Andresen, L.M. Young, Crack tip microsampling and growth rate measurements in low alloy steel in high temperature water. Corrosion **51**, 223 (1995)
2. F.P. Ford, P.L. Andresen, *Stress corrosion cracking of low alloy steels in 288C water* (NACE, New Orleans, 1989)
3. F.P. Ford, D.F. Taylor, P.L. Andresen, R.G. Ballinger, environmentally-controlled cracking of stainless and low-alloy steels in light-water reactor environments, 2006
4. EPRI, BWRVIP-190 Revision 1: BWR Vessel and Internals Project, Volume 1: BWR Water Chemistry Guidelines—Mandatory, Needed, and Good Practice Guidance, EPRI, Palo Alto, CA, 2014
5. H.P. Seifert, S. Ritter, *Research and service experience with environmentally-assisted cracking of carbon and low-alloy steels in high-temperature water* (Stockholm, Sweden, 2006)
6. H.P. Seifert, S. Ritter, The influence of ppb levels of chloride impurities on the stress corrosion crack growth behaviour of low-alloy steels under simulated boiling water reactor conditions. Corros. Sci. **108**, 134–147 (2016)
7. X.Y. Lou, P.L. Andresen, *BWRVIP-292: Effects of Low Level Chloride on Stress Corrosion Cracking of Low Alloy Pressure Vessel Steels in BWR Environments, 3002005622* (EPRI, Palo Alto, CA, USA, 2015)
8. X.Y. Lou, P.L. Andresen, T.G. Lian, R. Pathania, *Effect of ppb Levels of Chloride on the Stress Corrosion Cracking of Pressure Vessel Steel* (Canadian Nuclear Society, Ottawa, Ontario, Canada, 2015)
9. H.P. Seifert, S. Ritter, Stress corrosion cracking of low-alloy reactor pressure vessel steels under boiling water reactor conditions. J. Nucl. Mater. **372**, 114–131 (2008)

10. P.L. Andresen, C.L. Briant, Environmentally assisted cracking of types 304L/316L/316NG stainless steel in 288C water. Corrosion **45**, 448–463 (1989)
11. P.L. Andresen, Environmentally assisted growth rate response of nonsensitized AISI 316 grade stainless steels in high temperature water. Corrosion **44**, 450 (1988)
12. L.W. Niedrach, A new membrane type pH sensor for use in high temperature high pressure water. J. Electrochem. Soc. **127**, 2122 (1980)
13. C. Marks, D. Macdonald, W. Coulson, *Materials Reliability Program Reactor Vessel Head Boric Acid Corrosion Testing (MRP-165)* (Electric Power Research Institute, Palo Alta, 2005)

Electrochemical Behavior of Platinum Treated Type 304 Stainless Steels in Simulated BWR Environments Under Startup Conditions

Chu-Yung Yuan, Tsung-Kuang Yeh and Mei-Ya Wang

Abstract As reactor startup begins, the ECP is initially high in the oxygenated water environment established during a cold shutdown. Consequently, the components would exhibit the higher crack initiation and propagation rates of IGSCC during startup period than in the remainder of the cycle. The corrosion current density response of stainless steel exposed to H_2O_2 was larger than that of those exposed to O_2, and it remained at a higher value even at the low level of several ppb. As noble metal was applied in the BWRs to catalyze the chemical reactions of H_2O_2 and O_2, this study evaluated the corrosion behaviors of both oxidants on the components of stainless steel. The corrosion potentials and corrosion current densities of 304SS with Pt coating were investigated in pure water with dissolved oxygen or hydrogen peroxide concentrations at various temperatures.

Keywords Stress corrosion cracking · Reactor startup · 304 stainless steel · Pt · Normal water chemistry

Introduction

As the boiling water reactors (BWRs) age, incidents of intergranular stress corrosion cracking (IGSCC) and irradiation-assisted stress corrosion cracking (IASCC) are more readily seen in the vessel internals. In order to mitigate the problem of

C.-Y. Yuan · T.-K. Yeh
Department of Engineering and System Science,
National Tsing Hua University, Hsinchu, Taiwan

T.-K. Yeh
Institute of Nuclear Engineering and Science,
National Tsing Hua University, Hsinchu, Taiwan

M.-Y. Wang (✉)
Nuclear Science Technology and Development Center,
National Tsing Hua University, Hsinchu, Taiwan
e-mail: meywang@mx.nthu.edu.tw

J.H. Jackson et al. (eds.), *Proceedings of the 18th International Conference on Environmental Degradation of Materials in Nuclear Power Systems – Water Reactors*, The Minerals, Metals & Materials Series, https://doi.org/10.1007/978-3-319-68454-3_35

stress corrosion cracking (SCC) in the structural components, the technology of hydrogen water chemistry (HWC) [1] or low HWC combined with noble metal chemical application (NMCA) or On-line NobleChemTM (OLNC) has been widely adopted in BWRs around the world. The oxidizing chemistry environment of BWR reactor water is the key factor promoting IGSCC of stainless steel and nickel-based alloys in the reactor coolant system piping and vessel internals. The major oxidant determined in BWR coolant is hydrogen peroxide (H_2O_2), which is directly generated by water radiolysis. The electrochemical corrosion potential (ECP) response of stainless steel exposed to H_2O_2 was larger than that of those exposed to O_2, even at the low level of several ppb. H_2O_2 has the ability to gain or lose electrons, which acts as both an oxidizing agent and a reducing agent. As noble metal was applied in the BWRs to catalyzethe chemical reactions of H_2O2 and O_2, this study evaluated the corrosion behaviors of both oxidants on the components of stainless steel.

Due to the unique operating conditions of a BWR, the required feedwater hydrogen concentration ($[H_2]_{FW}$) needed to reduce the ECP below the critical corrosion potential for IGSCC (E_{IGSCC}) of −0.23 V_{SHE} varies from plant-to-plant and from region-to-region within a given plant. The ECP in the primary coolant circuit (PCC) of a BWR is in fact a mixed potential reflecting the amounts of major redox species (i.e. hydrogen, oxygen, and hydrogen peroxide) present in the reactor coolant. The major shortcoming of HWC is that a higher dissolved H_2 level ($[H_2]_{FW} > 0.5$ ppm) tends to increase the radiation field in a BWR plant [2]. Due to the adverse effects of HWC in raising the operational and shutdown dose rates in a BWR, the technique of noble metal treatment was proposed to enhance the effectiveness of HWC in lowering hydrogen consumption and increasing protection areas. At present, more than thirty BWRs have been treated with noble metal and are being operated under low-level HWC worldwide.

At early stages, hydrogen injection is not placed into service until the reactor power exceeds 30% of the rated power during the actual practice of HWC. Recently the power levels at which U.S. BWRs start hydrogen injection was 10% power or lower. The reactor coolant, which usually contains high levels of dissolved oxygen due to intrusion of atmospheric air in the cold shutdown period, could remain relatively oxidizing during a startup operation. As a matter of fact, some laboratory data have already demonstrated that under normal water chemistry (NWC) conditions the rates of IGSCC at intermediate temperatures during reactor startup periods were actually higher than those at operating temperatures [3]. Several plants have implemented design changes to begin injecting hydrogen into the feedwater at low power (>5%) during startup operations to suppress IGSCC during these periods. A trial HWC during a reactor startup was adopted to evaluate the suppression of SCC initiation at some commercial plants [4, 5]. Furthermore, a program sponsored by Electric Power Research Institute (EPRI) was initiated to conduct feasibility studies on effectively lowering the ECP of noble metal treated stainless steel (SS) by injecting sufficient hydrogen at startup temperatures. This process, named early hydrogen water chemistry (EHWC), was first performed at Exelon's Peach Bottom 3 nuclear power plant in 2011 [6]. For BWR plants that have adopted the technology of noble metal treatment but without EHWC, it is important to

understand whether noble metal would cause any detrimental impact on the corrosion of stainless steel components during startup operations.

The aim of this study is to investigate the effect of H_2O_2 and O_2 on the components of austenitic 304SS with NMCA in pure water environments under plant startup conditions. The corrosion potentials and corrosion current densities of 304SS were investigated in 288, 250 and 200 °C pure water with dissolved oxygen and hydrogen peroxide concentrations. In addition, the specimens with Pt coating were also conducted via electrochemical polarization experiment under the same water chemistry condition. Finally, the corrosion behaviors of H_2O_2 and O_2 on the components of stainless steel with noble metal chemical addition were investigated in this study.

Experimental

The alloy used in this study was Type 304 SS, and the chemical composition of this material is shown in Table 1. Samples in the shape of square plate ($20 \times 20 \times 1$ mm^3) were prepared. All samples were thermally sensitized at 650 °C for 24 h, polished with 800 grit emery paper, and cleaned with acetone and deionized water in an ultrasonic bath. The samples were then pre-oxidized in pure water with a $[O_2]_{dis}$ of 1 ppm at 288 °C for 14 days. During the pre-oxidization process, the ECP response of the sample was continuously monitored to assure that a stabilized ECP value was reached at the end of pre-oxidization, and a balance between the growth and the dissolution of the oxide film was also attained. Some of the pre-oxidized samples were further treated with platinum via hydrothermal deposition. The platinum treating process was conducted at 280 °C for 7 days in a dynamic loop that contained pure water and 1 ppm $Na_2Pt(OH)_6$. Each sample was thoroughly cleansed with acetone in an ultrasonic bath prior to the Pt treatment. After the deposition process, the surfaces of Pt treated samples were examined by scanning electron microscopy (SEM) and energy dispersive X-ray spectroscopy (EDX) to confirm the presence of Pt.

ECP measurements and electrochemical polarization analyses were conducted in a Type 316 SS autoclave in serial connection with a pure water circulation loop, which is schematically shown in Fig. 1. The coolant temperature was maintained at 288 °C in the autoclave, and the coolant conductivity monitored at the autoclave outlet was less than 0.15 μS/cm. The coolant conductivity was measured by a GLI conductivity meter. The water chemistry in the loop could be controlled by properly adjusting the injection rates of O_2, H_2, and Ar gases into the reservoir tank. The flow rate of the coolant in the loop was 50 ml/min. On the other hand, since H_2O_2 is

Table 1 Chemical composition of Type 304 stainless steel used in this study (wt %)

Element	Fe	C	Si	Mn	P	S	Cr	Ni	N	Cu
Mass%	71.0	0.042	0.606	1.14	0.0397	0.003	17.8	8.20	0.026	0.205

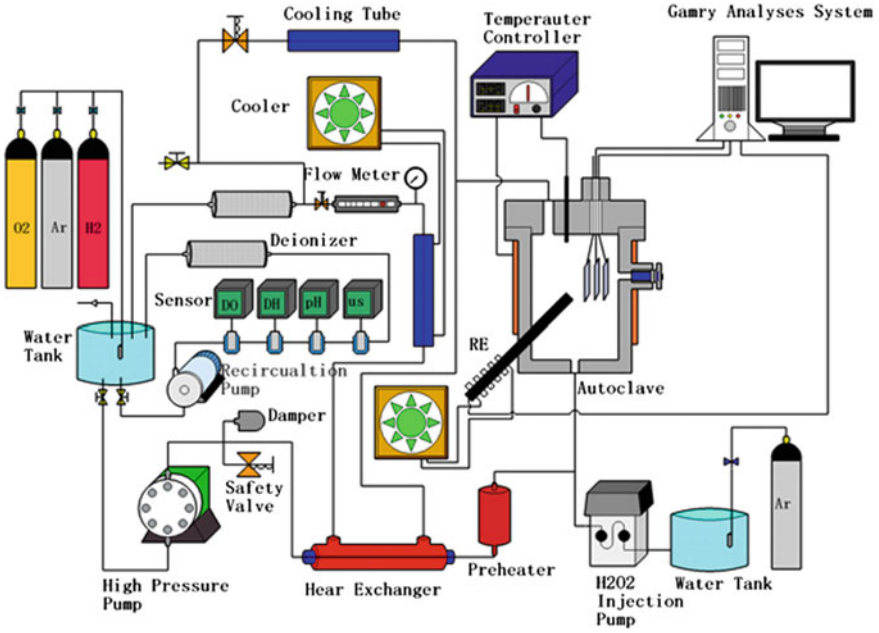

Fig. 1 Schematic of the high temperature water circulation loop

unstable in high temperature water due to its easy decomposition into O_2 and water, bulk H_2O_2 solution preserved in a dark glass tank was directly injected into the autoclave through a Teflon-lined tube by a high pressure metering pump. The H_2O_2 concentration in the autoclave was determined by the mixing ratio of the injected H_2O_2 and the circulating coolant. A three-electrode cell, consisting of a Zr/ZrO_2 reference electrode, a platinum counter electrode, and either an untreated or a Pt-treated sample as the working electrode, was used in this study. Heat-shrinkable PTFE tubes were used for electrical insulation. The electrodes were then mounted in a CONAX fitting secured at the top lid of the autoclave and inserted into the autoclave. The Zr/ZrO_2 electrode was installed in parallel with the platinum electrode and the samples. The measured ECPs were converted to the standard hydrogen electrode (SHE) scale. A Gamry PC4/300 electrochemical analyzer was used to perform the polarization analyses. A steady ECP for each sample at the designated $[O_2]_{dis}$ or $[H_2O_2]$ was obtained prior to each polarization test. The potential increment or decrement was set at 15 mV for every 6 min. The cathodic polarization range was from the E_{corr} to 0.3 V below the E_{corr}, and the anodic polarization range was from the E_{corr} to 0.3 V above the E_{corr}. The positive-feedback loops built in the electrochemical analyzer were activated to compensate for the ohmic resistance experienced by the testing system.

Results and Discussion

The surface morphologies of the untreated pre-oxidized and platinum-treated 304 SS samples are shown in Fig. 2. The oxide particles were uniformly distributed on the surface of the sample, and the oxide particle size ranged from 0.5 to 1 μm in diameter. It was also observed that the surface oxides exhibited a two-layer structure. The SEM images show that the Pt nanoparticles were deposited on the oxide surfaces in an uneven and discontinuous manner. The EDX analyses confirmed that the particles included Pt. The amounts of platinum deposited on the oxide surfaces after the platinum treating process are 3.18 μg/cm^2 by the ICP-MS loading measurements.

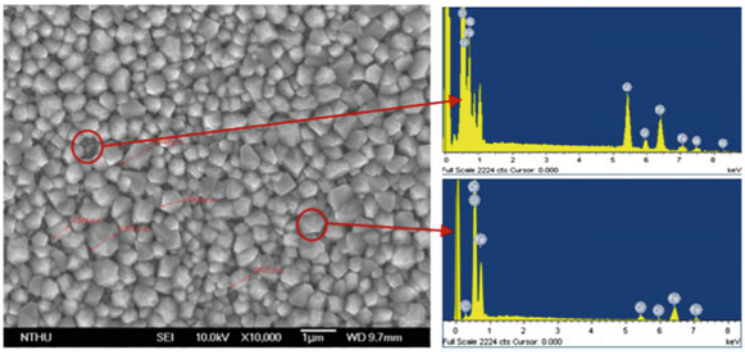

(a) Pre-oxidized 304 SS sample

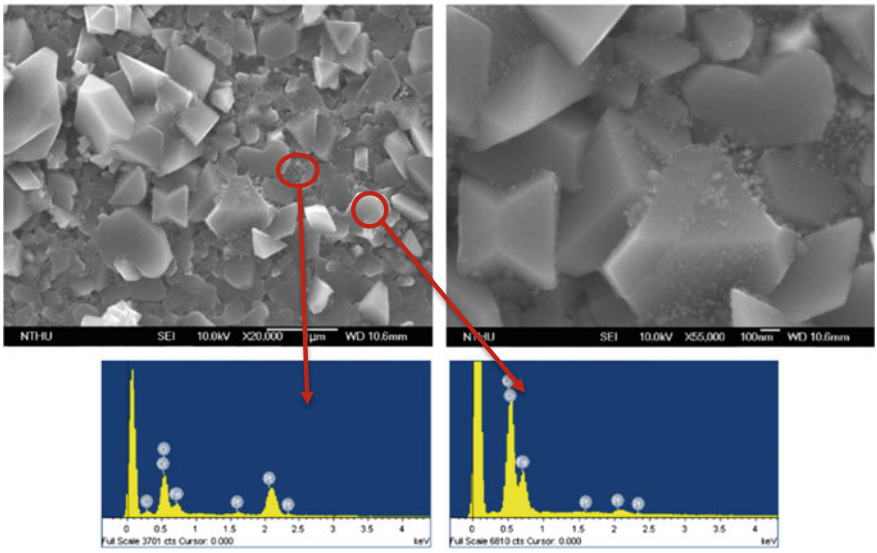

(b) Pt-treated 304 SS sample

Fig. 2 SEM micrographs and EDX mapping results of the untreated pre-oxidized and Pt-treated 304 SS samples

It should be noted that prior to each single polarization test the sample was immersed in the test environment for a period of time for the ECP to stabilize. Figures 3 and 4 show the polarization curves of the untreated pre-oxidized and

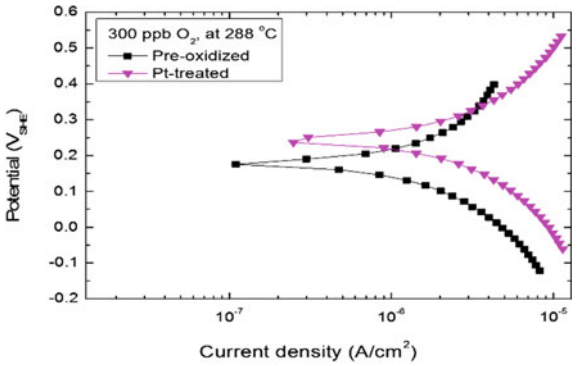

(a) 288 °C

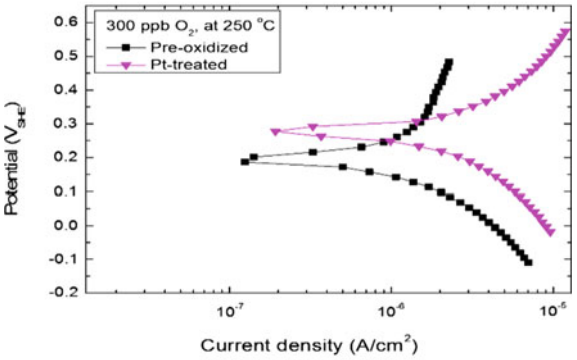

(b) 250 °C

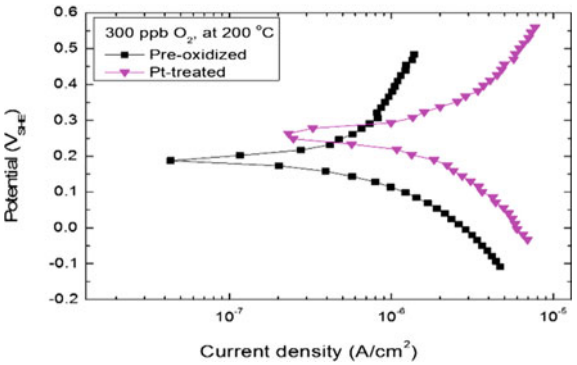

(c) 200 °C

Fig. 3 Polarization curves of the pre-oxidized and Pt-treated samples in high temperature pure water at a $[O_2]_{dis}$ of 300 ppb

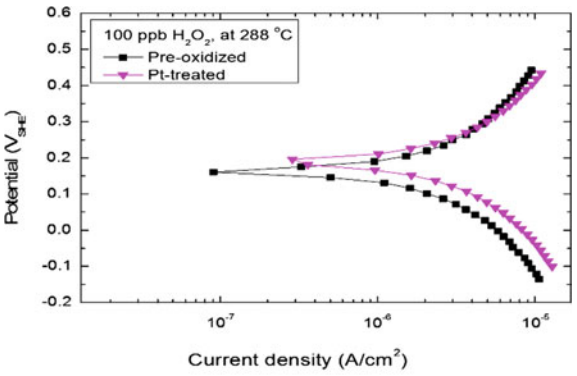

(a) 288 °C

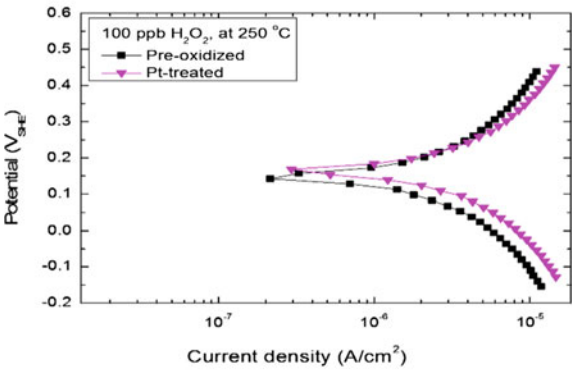

(b) 250 °C

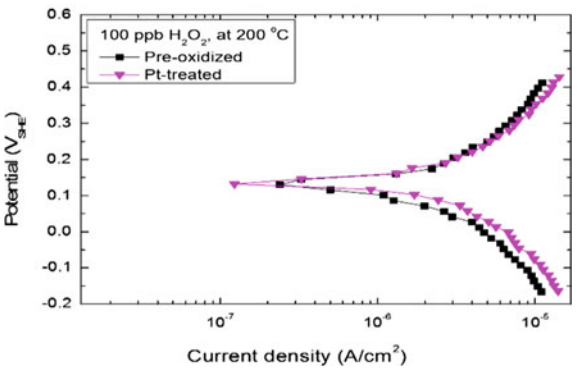

(c) 200 °C

Fig. 4 Polarization curves of the pre-oxidized and Pt-treated samples in high temperature pure water at a [H_2O_2] of 100 ppb

Pt-treated samples in a pure water containing 300 ppb O_2 and 100 ppb H_2O_2 at various temperatures (200, 250 and 288 °C), respectively. The ECP and i_{corr} data are summarized in Tables 2 and 3.

For the untreated sample, the ECPs at the designated $[O_2]_{dis}$ of 300 ppb were 188, 187, 174 mV_{SHE} at the temperatures of 200, 250 and 288 °C, respectively. The i_{corr} of 0.365 μA/cm^2 at 200 °C was lower than those of 0.689 and 0.655 μA/cm^2 at 250 and 288 °C. For the Pt-treated sample, the ECP at 288 °C was lower than those at 200 and 250 °C at the same water chemistry condition, and a relatively large difference in i_{corr} (0.598 μA/cm^2 at 200 °C, 1.017 μA/cm^2 at 250 °C and 1.344 μA/cm^2 at 288 °C). In the meantime, the ECP and the i_{corr} of the Pt-treated sample were both higher than those of the untreated one at the same testing temperature.

Table 2 ECPs and i_{corr}s of the Pre-oxidized and Pt-treated 304 SS samples at a $[O_2]_{dis}$ of 300 ppb

Temperature	Samples	ECP (V_{SHE})	i_{corr} (μA/cm^2)	β_c (V/decade)	$E_{0,O}$ (V_{SHE})	$i_{0,O}$ (nA/cm^2)
200 °C	Pre-oxidized sample	0.188	0.365	−0.172	0.502	5.4
	Pt-treated sample	0.263	0.598	−0.161		19.7
250 °C	Pre-oxidized sample	0.187	0.689	−0.193	0.400	53.7
	Pt-treated sample	0.278	1.017	−0.190		230.1
288 °C	Pre-oxidized sample	0.174	0.655	−0.175	0.316	101.4
	Pt-treated sample	0.236	1.344	−0.203		542.3

Table 3 ECPs and i_{corr}s of the Pre-oxidized and Pt-treated 304 SS samples at a $[H_2O_2]$ of 100 ppb

Temperature	Samples	ECP (V_{SHE})	i_{corr} (μA/cm^2)	β_c (V/decade)	$E_{0,O}$ (V_{SHE})	$i_{0,O}$ (nA/cm^2)
200 °C	Pre-oxidized sample	0.130	0.499	−0.162	0.868	0.01
	Pt-treated sample	0.132	0.841	−0.162		0.15
250 °C	Pre-oxidized sample	0.142	0.722	−0.174	0.766	0.25
	Pt-treated sample	0.168	0.805	−0.181		0.65
288 °C	Pre-oxidized sample	0.160	0.812	−0.162	0.678	0.59
	Pt-treated sample	0.196	0.816	−0.185		2.02

Figure 3 also shows that the cathodic current density of 300 ppb O_2 on the Pt-treated sample was distinctly larger than that on the untreated one. Accordingly, the exchange current density (ECD) for the O_2 reduction reaction on the Pt-treated sample was found five times greater than that on the untreated one at three test temperatures.

Electrochemical polarization analyses on both untreated and the Pt-treated sample were performed under the water chemistry condition of 100 ppb [H_2O_2]. The Untreated and Pt-treated samples did not show any significant difference at 250 and 288 °C temperatures in terms of i_{corr}, but a relatively large difference at 200 °C. In the meantime, the ECD for the H_2O_2 reduction reaction on the Pt-treated sample was found fifteen times greater than that on the untreated one at 200 °C. The ECD for the H_2O_2 reduction reaction only three times at 250 and 288 °C with Pt treatment.

The difference in testing temperature distinctly influenced the Pt efficiency on catalyzing the cathodic reaction and hence led to the significant variations in both i_{corr} of the Pt-treated sample and ECD of the O_2 or H_2O_2 reduction reaction on this sample at the three temperatures. In summary, the Pt treatment was shown to have a negative impact on the corrosion behavior of the treated Type 304 SS at the three testing temperatures, rendering the technology of EHWC a remedial measure for corrosion mitigation during plant startup operations.

Conclusions

In a pure water environment with a $[O_2]_{dis}$ of 300 ppb or [H_2O_2] of 100 ppb, the Pt treatment could pose a detrimental impact on the corrosion of treated Type 304 SS. The ECP and the i_{corr} of the Pt-treated sample were shown higher than those of the untreated one at the same testing temperature. A lower temperature of 200 °C would deter the Pt efficiency on catalyzing the cathodic reaction and hence led to smaller increases in both i_{corr} of the Pt-treated sample and ECD of the O_2 reduction reaction on this sample. For the H_2O_2 reduction reaction on the Pt-treated sample, the Pt efficiency on catalyzing the cathodic reaction was higher at lower temperature although the i_{corr} and ECD values were lower.

References

1. S. Hettiarachchi, BWR SCC Mitigation experiences with hydrogen water chemistry, in *Proceedings of the 12th International Symposium on Environmental Degradation of Materials in Nuclear Power Systems—Water Reactors*, (TMS The Minerals, Metals & Materials Society, Salt Lake City, UT, U.S.A., August 14–18, 2005), pp. 685–699
2. R.L. Cowan, The mitigation of IGSCC of BWR internals with hydrogen water chemistry, in *Water Chemistry of Nuclear Reactor Systems 7* (BNES, Bournemouth, England, 13–17 October 1996), p. 196

3. S.E. Garcia et al., Effect of hydrazine, carbohydrazide and hydrogen injection on noble metal treated stainless steel ECP and IGSCC mitigation during BWR startups, in *2010 International Conference on Water Chemistry of Nuclear Reactor Systems* (Quebec City, Canada, 3–7 October 2010), 3.09P
4. A. Abe et al., Mitigation of SCC initiation on BWR core internals by means of hydrogen water chemistry during start-up. Nucl. Sci. Eng. **149**, 312 (2005)
5. K. Ishida et al., Applying hydrogen water chemistry to boiling water reactor during normal operation and start-up to mitigate stress corrosion cracking at shimane nuclear power station's unit 2, in *2008 International Conference on Water Chemistry of Nuclear Reactor Systems* (Berlin, Germany, 14–18 September 2008), L04-3
6. S.E. Garcia, A.D. Odell, J.F. Giannelli, Early hydrogen water chemistry in the boiling water reactor: industry-first demonstration, in *2012 International Conference on Water Chemistry of Nuclear Reactor Systems* (Paris, France, 23–27 September 2012), P2-64-82

Investigations of the Dual Benefits of Zinc Injection on Cobalt-60 Uptake and Oxide Film Formation Under Boiling Water Reactor Conditions

Samuel Holdsworth, Fabio Scenini, M. Grace Burke, Tsuyoshi Ito, Yoichi Wada, Hideyuki Hosokawa, Nobuyuki Ota and Makoto Nagase

Abstract Zinc injection in reactor feed water is a well-known mitigation strategy for prevention of radioactive ^{60}Co deposition in both Boiling and Pressurised water reactors. Furthermore, zinc leads to the formation of a thinner, more stable oxides arising from the thermodynamically driven replacement of Ni and Fe in the characteristic spinel type oxide formed on stainless steel. However, the interaction of zinc with the oxide formation under different water chemistries is not fully understood. Oxidation tests on type 316 stainless steel were performed under two hydrogen water chemistry conditions (HWC), with and without zinc injection and the resultant oxides analysed using analytical electron microscopy (AEM), field emission gun scanning electron microscopy (FEG-SEM), and energy dispersive X-ray spectroscopy (EDXS). The present work identifies and quantifies the positive microstructural changes that Zn has on the oxide formation on a #600 grit surface and an OPS polished 316 SS surface under boiling water reactor (BWR) conditions.

Keywords Hydrogen water chemistry · Normal water chemistry · Analytical electron microscopy · Scanning electron microscopy · Energy dispersive X-ray · Zinc injection · Oxide characterisation

Introduction

After several decades of operation, many boiling water reactors (BWR) experienced incidences of stress corrosion cracking (SCC) [1, 2]. This brought about the development and introduction to water chemistry changes known as hydrogen water chemistry (HWC) whereby hydrogen is injected into the feed water to reduce

S. Holdsworth (✉) · F. Scenini · M. Grace Burke
T. Ito · Y. Wada · H. Hosokawa · N. Ota · M. Nagase
University of Manchester, Manchester, UK
e-mail: samuel.holdsworth@manchester.ac.uk

J.H. Jackson et al. (eds.), *Proceedings of the 18th International Conference on Environmental Degradation of Materials in Nuclear Power Systems – Water Reactors*, The Minerals, Metals & Materials Series, https://doi.org/10.1007/978-3-319-68454-3_36

the radiolytic yield of oxidising agents such as hydrogen peroxide [1]. This lowered the electrochemical corrosion potential (ECP) on stainless steel internals thus reducing susceptibility to SCC. However, many plants switching to the reducing conditions of HWC from the oxidising conditions of the previously used normal water chemistry (NWC), saw increases in out-of-core radiation fields which in turn increased plant personnel dose [3]. The radiation fields are mainly attributed to the gamma emitting ^{60}Co ion which is activated on the fuel assembly and released into the coolant before being transported around the circuit and absorbed into the characteristic oxide that forms on the reactor internals.

The nature and composition of the oxide generated, controls the Co uptake rates. However, the formation of a duplex oxide layer has been well documented for high temperature aqueous conditions [4]. The inner layer consists of a thin, dense, fine-grained Cr-rich spinel layer (chromite) followed by a coarse-grained Fe-rich outer layer (ferrite) [5]. The Cr remains within the inner layer and occupies the octahedral sites within the spinel which then forces the Ni/Fe cations diffusing up from the matrix to occupy the tetrahedral sites [4]. However, any Co ions within the coolant can be sorbed onto the oxide surface and due to its higher tetrahedral site preference energy it can replace the Ni and/or Fe at tetrahedral sites [6].

Under NWC the oxidising conditions give rise to a more haematite based oxide (α-Fe_2O_3) moreover α-Fe_2O_3 belongs to the rhombohedral lattice system, therefore, uptake of Co into the oxide is less favourable [5]. On the other hand under the reducing conditions of HWC, the oxide consists of a chromite ($Fe/NiCr_2O_4$) inner layer and ferrite ($Fe_3O_4/NiFe_2O_4$) outer layer. The Gibbs free energy for the substitution of Co into the chromite inner and ferrite outer layer is lower resulting in higher uptake rates [6]. The increase in radiation fields at plants switching from NWC to HWC was therefore attributed to a larger proportion of oxide more prone to Co uptake.

Many strategies to reduce personnel dose rates were developed; the most significant development in dose reduction through water chemistry control was Zn injection whereby Zn ions are introduced in low concentrations (<50 ppb) into the reactor feed water. The Zn incorporates into the oxide using same mechanism as Co. However, it forms a very stable Zn-chromite based inner layer, which prevents the uptake of ^{60}Co due to its high stability over Co-chromite.

Furthermore, the positive effects of Zn on oxide formation can also be seen through the increased corrosion resistance of oxides generated under Zn-injection due to the formation of the more stable Zn chromite [6]. The oxide yielded under Zn injection is generally thinner and more protective. The formation of Zn-chromite gives a reduction in unit cell lattice parameter ($FeCr_2O_4$ a = 8.379 Å and $ZnCr_2O_4$ a = 8.328 Å), which increases the resistance to both electronic and ionic mobility (diffusion) within the oxide thus reducing cation release rates and oxide growth [7]. Furthermore, Henshaw et al., 2016 [8] indirectly modelled the effects of Zn pickup and found that the solid phase diffusion constant on ex- core surfaces fell by 60% after one cycle of Zn injection.

In this paper, we present quantitative data on the Zn uptake under Hydrogen water chemistry conditions as a function of surface finish. Furthermore, the detailed microstructural characterisation results obtained from post-test specimens provide new insight concerning the corrosion rates on deformed and polished surfaces.

Materials and Methods

Sample Preparation and Oxidation

The experiments were performed on Type 316 SS the composition of which is reported in Table 1. Two sets of samples was prepared for oxidation; the first set were mechanically ground to a 600-grit surface using SiC paper whilst the second set was mechanically polished to an oxide polishing silica (OPS) finish using standard metallographic preparation techniques. The sample geometries used were $15 \times 8 \times 1.5$ mm^3 coupons and were ultrasonically cleaned immersed in iso-propyl alcohol to remove contaminants prior to oxidation.

The oxidation experiments were conducted for 500 h in a modified recirculating flow loop autoclave constructed of Type 316 SS. The autoclave was modified to simulate both the oxidising conditions of NWC and also the reducing conditions of HWC. Direct control of water chemistry conditions including specific metal ion concentrations was accomplished using two high performance liquid chromatography (HPLC) pumps supplied by separate PTFE storage tanks. The metal ion solutions were injected through PTFE capillary tubing directly into the high temperature/pressure region of the autoclave. The metal ion concentrations in the high pressure and temperature circuit were monitored using inductively couple plasma mass spectrometry (ICP-MS).

Water returning from the high temperature/pressure region was then passed through a separate low pressure loop. The low pressure loop contained the dissolved oxygen, hydrogen, conductivity and pH sensors (in series configuration) and the demineraliser (nuclear grade mixed bed ion exchange resins). Water returning from the demineraliser was then fed into the 200 litre feedtank where the water chemistry was controlled by bubbling H_2, O_2 and N_2 to the test specific requirements. The full water chemistry conditions of the tests conducted are summarised in Table 2.

Table 1 Chemical composition (wt%) of the 316 SS test specimens

Elements	C	Si	Mn	P	S	Co	Ni	Cr	Mo	Fe
wt%	0.04	0.63	0.93	0.031	0.001	0.14	10.22	16.81	2.06	Balance

Table 2 Water chemistry conditions for the HWC oxidation tests with/without Zn injection on a mechanically polished and #600 grit surface

	ECP vs. SHE	DH	DO	Co	Zn
HWC (#600 grit/mechanically polished)	−400 mV	50 ppb	<5 ppb	0.05 ppb	0 ppb
HWC + Zn (#600 grit/mechanically polished)	−400 mV	50 ppb	<5 ppb	0.05 ppb	5.0 ppb

Microstructural Characterisation

The oxide film generated under each water chemistry condition was investigated at the macro and microscopic scale using techniques, including scanning electron microscopy (SEM), focused ion beam (FIB)—and AEM. The morphological analysis of the oxide was performed using a Zeiss Sigma field emission gun (FEG)-SEM equipped with an Oxford Instruments X-Max 150 Silicon Drift Detector (SDD) for EDXS microanalysis and an AZTEC analysis system. Compositional information on the oxide was obtained via discrete spot STEM-EDX analyses and EDX spectrum imaging. Digital image analysis of the SEM microstructural data was perfomed to assess oxide morphology.

The nanometre-scale STEM-EDX microanalysis was performed on electron-transparent cross-section samples prepared using a Helios NanoLab™ 660 DualBeam focused ion beam (FIB) microscope. These thin cross-section TEM specimens were characterised using the FEI Talos F200X FEG Analytical TEM with Super X (4 SDDs) operated at 200 kV. Data analysis was performed using Gatan Digital Micrograph™ and the Velox™ software.

Results

Machined Surface (#600 Grit)

Figure 1a, b shows a secondary electron (SE) image of the oxides generated on Type 316 SS after 500 h exposure under HWC conditions with and without a 5.0 ppb Zn injection.

Upon oxidation without Zn injection, the outer oxide crystallites shown in Fig. 1a were evenly distributed across the surface and octahedral in morphology with an average diameter of $\sim$1.04 μm. The oxide crystallites generated under HWC with 5.0 ppb Zn injection were considerably finer (Fig. 1b). The outer layer crystallites had a higher packing density, however, the average crystallite size was $\sim$0.35 μm.

Further characterisation performed using AEM techniques and selected area diffraction (SAD) was completed for both samples to identify the composition and crystal structure of the inner and outer oxides. The STEM-high angle annular dark-field (HAADF) image and corresponding 2D elemental maps extracted from the STEM-EDX spectrum image dataset of the oxide (Fig. 2a), discrete spot analyses and SAD pattern (SADP) analysis indicated that the oxide generated under HWC with no Zn injection on a machined surface had the following characteristics:

(1) Coarse octahedral single crystals of non-stoichiometric Fe_3O_4 and $NiFe_2O_4$ were present as the outer layer crystallites (Fig. 2a).

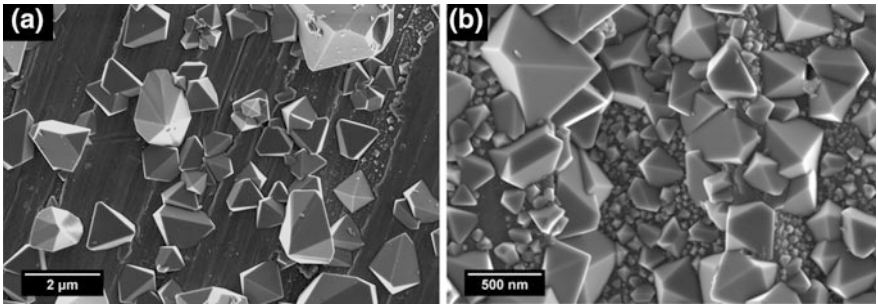

Fig. 1 **a** Secondary electron (SE) images of the oxide formed after a 500 h exposure to HWC; **b** HWC with a continuous 5.0 ppb Zn injection. The Type 316 SS surface was ground #600 grit SiC paper prior to exposure

(2) The inner layer oxide was a continuous ~210 nm thick polycrystalline Cr-rich spinel structure, whose SADP indexed as $FeCr_2O_4$. The inner layer contained very fine pores (Fig. 2b).
(3) An enrichment of metallic Ni (up to 50 wt%) at the inner oxide/metal interface caused by the depletion of Cr was observed (Fig. 2 a).
(4) The presence of a deformed and nano-grained region under the oxide layer was observed (Fig. 2b).

The AEM characterisations of the Zn-injection sample revealed the following:

(1) Finer octahedral discrete oxides, which indexed as Fe_3O_4 from SADP analysis, were observed on the outer surface of the specimen (Fig. 3).
(2) A continuous Zn-enrichment was detected at the inner oxide—water interface, which had a negative concentration gradient through the thickness of the oxide (Fig. 3). STEM-EDX discrete spot analyses of this region revealed an enrichment of ~10 wt% at the inner oxide—water interface that decreased to <0.2 wt% at ~175 nm into the oxide.
(3) SADP analysis confirmed that the inner oxide layer was $ZnCr_2O_4$ with spinel-type structure (Fig. 3).

OPS-Polished Surface

Figure 4a, b shows the SE images of the oxides formed after 500 h exposure under HWC conditions with and without a 5.0 ppb Zn injection on OPS-polished Type 316 SS.

The outer oxide dimensions measured for the non-Zn treated, and Zn-treated specimens were markedly different. The non-Zn treated sample had coarse outer

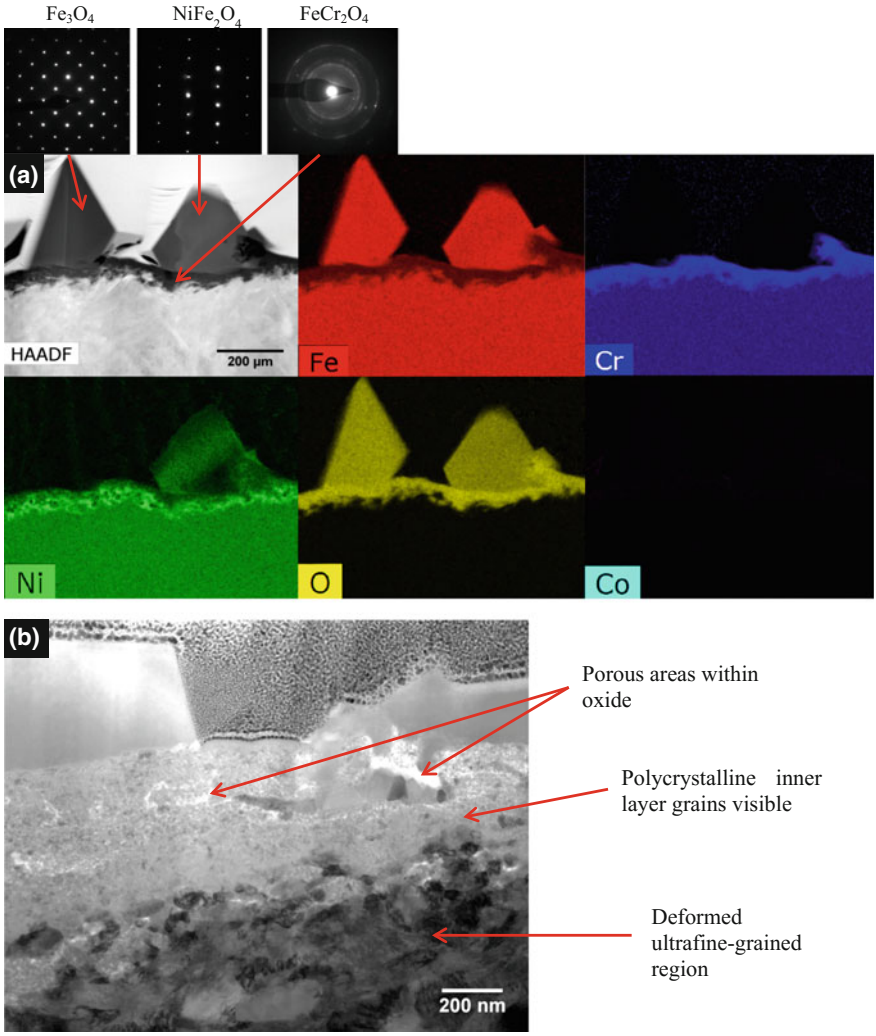

Fig. 2 **a** STEM-HAADF image and corresponding elemental maps extracted from the STEM-EDX spectrum image dataset of the oxide formed under HWC after 500 h. The presence of a Cr-enriched inner layer, a Ni-rich layer beneath the inner layer oxide and the presence of both Fe_3O_4 and $NiFe_2O_4$ in the outer specimen surface was detected. **b** Bright-field (BF) STEM image showing the oxide porosity within the inner layer and the deformed ultrafine-grained region in the Type 316 near-surface region

layer oxide crystallites with an average diameter of ~1.5 µm and a surface coverage of 55%. In contrast, the Zn-treated sample was characterised by much finer oxides with an average diameter of ~26 nm with ~20% coverage.

AEM characterisation of the FIB-prepared cross-section specimens revealed that the inner layer oxide thicknesses varied significantly between the non-Zn (Fig. 5a)

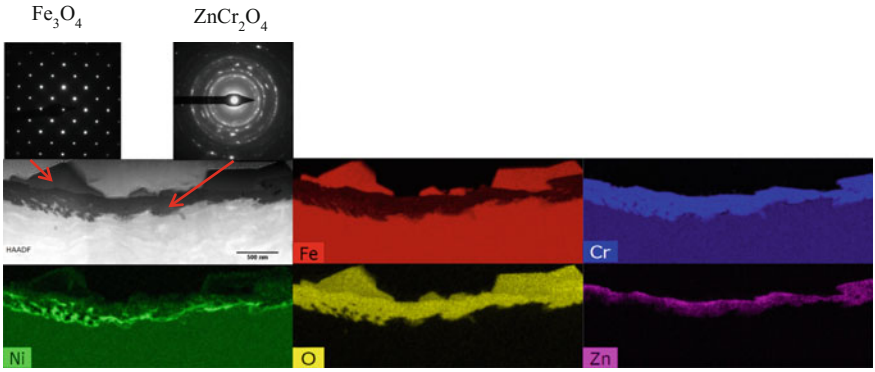

Fig. 3 STEM-HAADF image and corresponding elemental maps extracted from the STEM-EDX spectrum image dataset of the oxide formed under HWC after 500 h. The presence of a Cr-enriched inner oxide layer with a Ni-rich layer beneath the inner layer oxide was observed. Both Fe_3O_4 and $NiFe_2O_4$ were identified as the outermost oxides

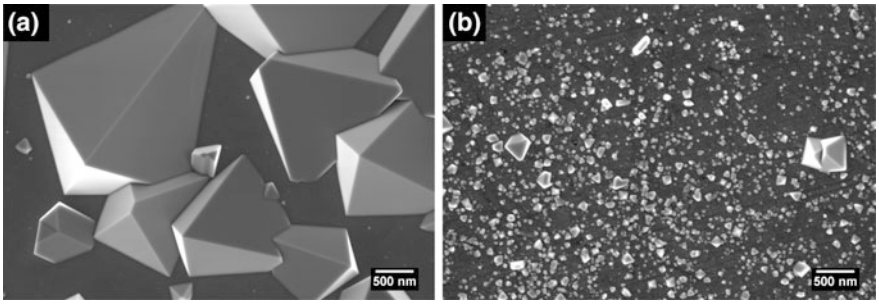

Fig. 4 SE images of the oxide formed after a 500 h exposure to: **a** HWC; and **b** HWC with a continuous 5.0 ppb Zn injection. The Type 316 SS surface was mechanically polished to an OPS finish

and Zn-treated (Fig. 6) samples. The inner layer oxide thickness of the OPS-polished but non-Zn treated sample was ~550 nm. In contrast, the OPS-polished and Zn-treated sample was characterised by a much thinner (~45 nm) inner layer (more than an order of magnitude thinner). The 2D elemental maps from the STEM-EDX spectrum image dataset for the non Zn-treated sample show that the polished surface generated a considerably thicker Cr-rich inner layer. The outer layer oxide crystallites shown in Fig. 5 had a composition close to $NiFe_2O_4$.

The 2D elemental maps from the STEM-EDX spectrum image dataset for the OPS-polished and Zn-treated sample (Fig. 6) shows the Zn localisation to the inner layer oxide as a consistent continuous layer. Using STEM-EDX discrete spot analyses revealed an enrichment of up to ~11 wt% of Zn within the inner layer oxide.

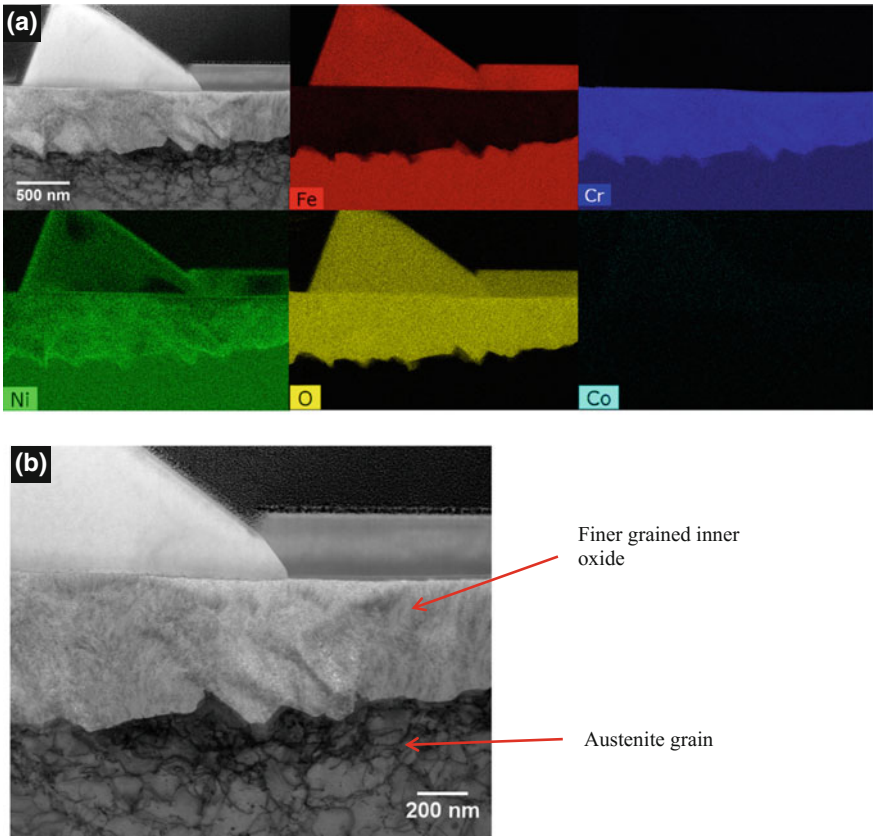

Fig. 5 **a** BF-STEM image and corresponding elemental maps from the STEM-EDX spectrum image dataset of the oxide formed under HWC after 500 h on a polished surface. **b** BF-STEM image showing the fine-grained inner oxide layer of the inner oxide with no apparent porosity

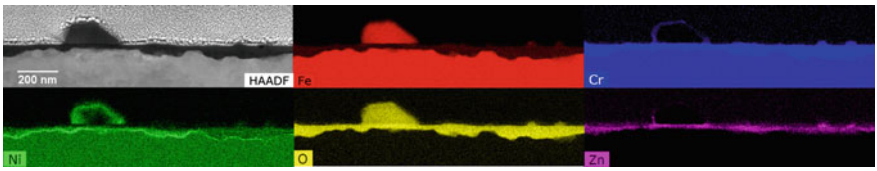

Fig. 6 STEM-HAADF image and corresponding elemental maps extracted from the STEM-EDX spectrum image dataset of the oxide formed on the polished surface under HWC with Zn-injection after 500 h exposure

Discussion

The oxides formed on the surface of Type 316 SS after subsequent oxidation in HWC with and without Zn-injection have been characterised. The effects of Zn-injection on the oxide formation have been documented along with the effects of surface preparation on the oxide formation.

Machined Surface (#600 Grit)

The effect of Zn injection on oxide formation on the #600 grit-prepared surface showed a reduction in inner layer oxide thickness of ~34 nm (210 nm to 176 nm). This can be explained by considering the accepted model for oxide growth under high temperature aqueous conditions. In 1991 J.Robertson [4] stated that the outer layer forms by reprecipitation of ions at the oxide-solution interface caused by local supersaturation. The inner layer growth is controlled by diffusion of species between the metal- oxide interface and the oxide-solution interface. However, the diffusion of species can occur via several mechanisms: solid-state diffusion through the inner oxide, diffusion of species through pores in the oxide, and diffusion along inner oxide grain boundaries [9]. In the present study, SADP analysis (Figs. 2 and 3) confirmed the Zn-incorporation into the tetrahedral sites of the oxide resulting in the change from $FeCr_2O_4$ to $ZnCr_2O_4$, which has an associated reduction in spinel lattice parameter. The change in lattice parameter retards solid-state diffusion through the oxide, hence, reducing cation release rates and oxide growth. The reduction of cation release rate is then consistent with the sequential reduction in outer oxide crystallite size since rate control will reside in the inner oxide. Furthermore, the STEM-EDX discrete spot analyses indicated a maximum Zn enrichment of ~10 wt%, significantly less than the maximum allowable 36 wt% Zn to reach stoichiometric $ZnCr_2O_4$.

OPS-Polished Surface

The inner oxide film formed on the OPS-polished surface after 500 h oxidation under HWC conditions was considerably thicker (~550 nm) than the oxide formed on the #600 grit surface (~210 nm).

The sample with a #600 grit surface had significant subsurface deformation (Fig. 2b), which would permit faster diffusion of Cr into the oxide because the high dislocation density coupled with the ultrafine-grained structure provide short circuit paths for diffusion [4, 9]. The oxide also contained very fine porosity, (not previously observed under these conditions) within the inner oxide layer (Fig. 2b) that would increase diffusion of species from the solution through the pores. The oxide

layer formed on the OPS-polished sample (Fig. 5b) appeared dense and no micro-porosity detected. This suggests that the oxide is more protective and therefore thinner, however, the oxide formed on the OPS-polished surface was considerably thicker than the oxide formed on #600 grit surface. Similar results have previously been seen under simulated PWR conditions [9].

It is therefore proposed that the oxide formed on #600 grit surface has reached steady-state conditions and the dissolution rate is equal to the oxide growth rate. The OPS-polished sample with the thicker, less porous oxide is thicker because the dissolution rate is lower. The results suggest a relationship between porosity and dissolution rates.

The effect of Zn-injection on the OPS-polished surface oxide film was substantially larger than the #600 grit surface as the inner layer oxide thickness was reduced from ~550 to 44 nm, or a factor of 10. Significantly, work completed under simulated PWR conditions on a mechanically-polished surface with a 10 ppb Zn injection yielded a factor of 5 reduction in oxide thickness [10]. Furthermore, no porosity was observed in the inner oxide layer, suggesting that the effect of Zn reducing oxide layer thickness is based solely on the reduction of solid-state diffusion through the inner oxide lattice.

Conclusions

The exposed sample with a #600 grit surface had a significantly thinner inner oxide film compared to the OPS-polished sample. Very fine oxide porosity was observed within the inner oxide layer, whereas no porosity was apparent in the OPS-polished sample. These results suggest that the oxide formed on the #600 grit surface samples which contained the fine porosity, was more friable compared to the polished sample.

The polished and #600 grit finished samples both exhibited a maximum Zn enrichment of up to ~10 wt%. The Zn injection for the OPS-polished and #600 grit surfaces promoted reductions in the inner and outer oxide thickness, with the polished sample exhibiting a reduction in inner oxide thickness of over a factor of 10.

References

1. H. Takiguchi, M. Sekiguchi, A. Abe, K. Akamine, M. Sakai, Y. Wada, S. Uchida, Evaluation of Effectiveness of Hydrogen Water Chemistry for Different Types of Boiling Water Reactors. J. Nucl. Sci. Technol. **36**(2), 179–188 (1999)
2. F.P. Ford, B.M. Gordon, R.M. Horn, *Intergranular Stress Corrosion Cracking (IGSCC) in Boiling Water Reactors (BWRs)*, (Woodhead Publishing Limited, Sawston, 2012)
3. C.C. Lin, F.R. Smith, R.L. Cowan, Effects of hydrogen water chemistry on radiation field buildup in BWRs. Nucl. Eng. Des. **166**(1), 31–36 (1996)

4. J. Robertson, The Mechansim Of High Temperature Aqueous Corrosion Of Stainless Steel. Corros. Sci. **32**(4), 443–465 (1991)
5. C.C. Lin, A review of corrosion product transport and radiation field buildup in boiling water reactors. Prog. Nucl. Energy **51**(2), 207–224 (2009)
6. A. Navrotsky, O.J. Kleppa, The thermodynamics of cation distributions in simple spinels. J. Inorg. Nucl. Chem. **29**(11), 2701–2714 (1967)
7. S.E.E. Ziemniak, M. Hanson, Zinc treatment effects on corrosion behavior of 304 stainless steel in high temperature, hydrogenated water. Corros. Sci. **48**(10), 2525–2546 (2002)
8. J. Henshaw, S. Bowskill, S. Dickinson, M. Redmond, J. Glover, Material and Activity Transport Modelling in BWRs Paper. Nucl. Plant Chem. Conf. (2016)
9. S. Cissé, L. Laffont, B. Tanguy, M.C. Lafont, E. Andrieu, Effect of surface preparation on the corrosion of austenitic stainless steel 304L in high temperature steam and simulated PWR primary water. Corros. Sci. **56**, 209–216 (2012)
10. X. Liu, X. Wu, E.H. Han, Influence of Zn injection on characteristics of oxide film on 304 stainless steel in borated and lithiated high temperature water. Corros. Sci. **53**(10), 3337–3345 (2011)

SCC Mitigation in Boiling Water Reactors: Platinum Deposition and Durability on Structural Materials

Pascal V. Grundler, Stefan Ritter and Lyubomira Veleva

Abstract Noble metal injection is widely used to mitigate stress corrosion cracking (SCC) of reactor components. Despite its wide use, there are still open questions regarding the parameters affecting the application process and possible improvements to it. Laboratory experiments in a high-temperature water loop at PSI were complemented by exposure of specimens in the mitigation monitoring system (MMS) at KKL. The influence of parameters such as flow conditions, structural material composition, surface roughness and geometry on the deposition behavior of the platinum (Pt) nanoparticles was investigated. Furthermore, the long-term stability of the coverage of surfaces by Pt particles was analyzed. The composition of the underlying alloy was found to have an effect on the deposition behavior, whereas surface roughness has no measurable impact. Pt showed a limited durability on steel surfaces and, after the end of the application, the remobilized Pt seems to re-deposit only minimally on nearby surfaces.

Keywords SCC mitigation · BWR · Noble metal · Platinum · Nanoparticles · NobleChem™

Introduction

In boiling water reactors (BWRs), the radiolysis of water with subsequent partitioning of the hydrogen into the steam, leaving an excess of H_2O_2 and O_2 in the liquid phase, is at the origin of highly oxidizing conditions. This corrosive environment coupled to sensitive materials leads to stress corrosion cracking (SCC) of reactor internals and recirculation pipes, a well-known issue in BWRs [1, 2]. At first mitigation was attempted by injecting hydrogen into the feed water, a method termed hydrogen water chemistry (HWC) [3]. Although hydrogen injection reduces

P.V. Grundler (✉) · S. Ritter · L. Veleva
Nuclear Energy and Safety Research Division, Paul Scherrer Institut (PSI),
5232 Villigen PSI, Switzerland
e-mail: pascal.grundler@psi.ch

J.H. Jackson et al. (eds.), *Proceedings of the 18th International Conference on Environmental Degradation of Materials in Nuclear Power Systems – Water Reactors*, The Minerals, Metals & Materials Series, https://doi.org/10.1007/978-3-319-68454-3_37

the electrochemical corrosion potential (ECP), and therefore lowers the SCC susceptibility, it comes at the cost of a problematic side-effect. The high hydrogen content favors the partitioning of reduced ^{16}N species into the steam and thus significantly increases the steam line dose rates.

The high hydrogen levels are a consequence of the relatively low turnover of the reaction between the reactive oxygen species and the added hydrogen. A further development has been to add a catalyst to improve this chemical reaction [4]. Consequently the amount of hydrogen needed could be reduced, which in turn substantially decreased the amount of ^{16}N in the steam. This catalytic technology, developed by General Electric (nowadays General Electric-Hitachi Nuclear Energy) to mitigate SCC, uses noble metals (Pt, Rh) as catalysts. Currently, the most widely used application procedure consist in injecting $Na_2Pt(OH)_6$ into the reactor feed water during operation at full power ("Online NobleChem^{TM}", OLNC) [5, 6]. Under the influence of the elevated temperature, the injected Pt complex breaks down and produces very fine metallic particles (nanoparticles) which can deposit on the water-wetted surfaces where they stay electrocatalytic over extended periods, thus providing SCC mitigation if sufficient H_2 is present [7]. More detailed information on the use of this technology can be found in a review [8].

Despite the fact that OLNC is widely used there are still open questions regarding ways to optimize the procedure and assess its efficiency. Aspects regarding formation and transport of Pt nanoparticles in BWRs have been presented in earlier papers [9–13]. Here the aim is to understand the possible effect of the substrate on the deposition and retention of Pt nanoparticles. The surface roughness, the chemical nature of substrate and the redistribution of Pt after the OLNC application has ended are investigated.

This work has been performed in the frame of a joint research project between the Paul Scherrer Institut (PSI) and the Swiss Federal Nuclear Safety Inspectorate (ENSI), as well as the Swiss nuclear power plants of Leibstadt (KKL) and Mühleberg (KKM).

Materials and Methods

Materials

Specimens consisted of coupons with the dimensions 13 × 10 × 4 mm. Three different structural materials, commonly used in BWR systems, were used: AISI 304L stainless steel, Ni-base alloy Inconel 182 and low-alloy reactor pressure vessel steel SA533 B Cl.1. Chemical compositions of these materials are listed in Table 1. Surface finish was "*N5*" (R_a = 0.4 µm, *DIN EN ISO 1302*) with exception of the roughened specimens (only AISI 304L). These were made by transverse grinding of standard specimens with *P40* emery paper. Final roughness of these specimens was in average R_a = 2.1 µm. Some of the stainless steel specimens were

Table 1 Chemical composition of the alloys used for the specimens

Components (wt%)	Stainless steel AISI 304L	Low-alloy steel SA 533 B Cl.1	Ni-base alloy Inconel 182
Fe	69.5	>96.5	5.19
C	0.024	0.250	0.034
Si	0.35	0.240	0.561
Mn	1.49	1.420	6.21
P	0.026	0.006	0.002
S	0.005	0.018	0.005
Ni	10.00	0.620	69.4
Cr	17.9	0.120	16.0
Mo	0.247	0.540	0.178
V	–	0.007	0.022
Cu	0.305	0.150	0.0068
Co	0.088	–	0.0134
Al	–	0.030	0.0241
Nb	0.001	–	2.325
Ti	0.001	–	0.0722
N_{tot} (ppm)	590	60	240
O_{tot} (ppm)		20	

pre-oxidized (PO) for two weeks in simulated BWR-HWC environment before being used for the Pt deposition tests; all other specimens were used in the as-received (AR) state.

The Pt source was an aqueous solution of $Na_2Pt(OH)_6$ made from a commercial 1% solution (courtesy of KKM) by dilution (Pt concentration in feed solution: 94–107 ppb) with high-purity water. The diluted solution was used for injection into the high-temperature water during the Pt deposition experiments.

Experimental Set-Up and Procedures

Figure 1 shows a schematic of the sophisticated high-temperature water loop in use at PSI to reproduce the water chemistry of a BWR. The water chemistry can be precisely adjusted (H_2, O_2 and Pt dosing) and closely monitored (dissolved H_2 and O_2 concentrations, conductivity, ECP, flow, temperature and pressure). Specimens were either exposed to the high-temperature water in the autoclave or placed in specimens holders located in series after the autoclave. In these specimens holders the high-temperature water flows across the specimen surface in rectangular ducts. The precise geometry (Fig. 2) ensures well-defined flow conditions [12, 14]. To increase flow velocity on one side of the specimens, the duct on the opposite side can be obstructed.

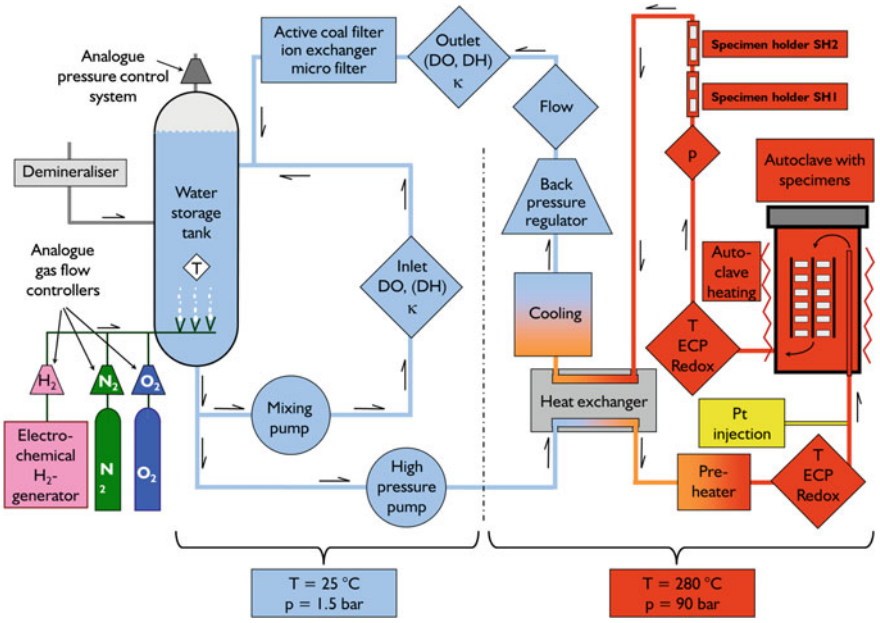

Fig. 1 Schematic of the PSI high-temperature loop as used for the Pt deposition experiments

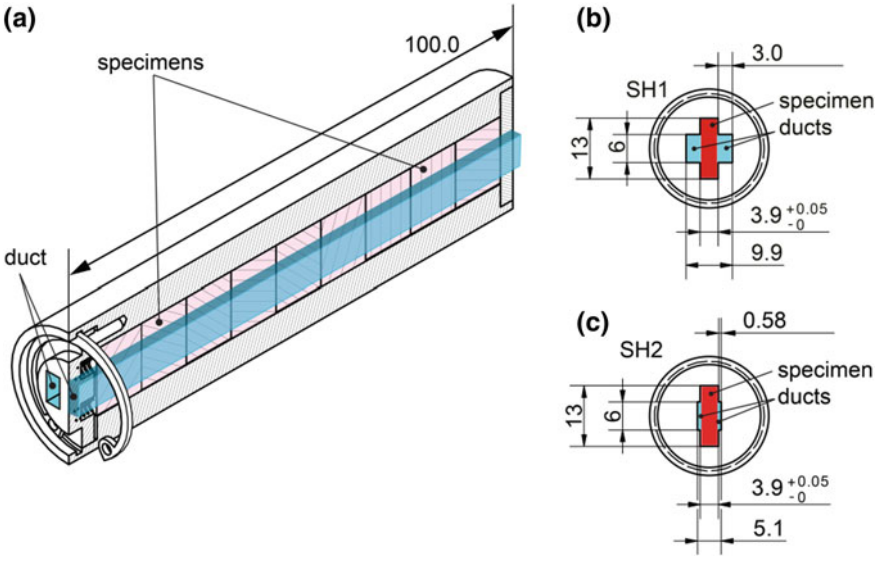

Fig. 2 Drawing of specimen holders, **a** cut-away view of assembly (the larger ducts of SH1 are depicted for clarity) and **b**, **c** cross sections of SH1 and SH2, respectively. All dimensions in millimeters

The specimens were pre-conditioned in the loop for one week before the start of the Pt application. The Pt solution was then injected into the feed-water stream of the autoclave with a dosing pump. The Pt concentration in the loop water is calculated on the basis of the Pt concentration in the injected solution, the injection flow rate and the fluid flow rate in the autoclave feed water stream. This represents the maximal concentration, as deposition along the flow path will reduce it. Nevertheless enough Pt remains in the fluid to allow the deposition of adequate loadings in the last specimen holder. At the end of the Pt injection period, the system is kept under the same BWR-HWC conditions for three more days before shut down and removal of the specimens from the loop. Detailed parameters for the tests are listed in Tables 2 and 5.

Specimens are then examined by Scanning Electron Microscopy (SEM) to document the appearance of the oxide film and determine the particle size distribution of the Pt particles. Quantitative determination of the Pt surface loading is performed by Laser Ablation—Inductively Coupled Plasma—Mass Spectrometry (LA-ICP-MS) [15].

Results and Discussion

Effect of Surface Roughness

In four tests stainless steel coupons with higher surface roughness experienced an OLNC application under simulated BWR conditions. The results were compared to coupons with the lower roughness. Particle size analysis shows no clear difference

Table 2 Experimental parameters for the tests with the different materials

Experiment designation	Test I	Test II
Pressure (bar)	90	91
T autoclave (°C)	280	281
Water mass flow (kg/h)	10	10
Bulk flow velocity in SH1 (m/s)	0.10	0.20
Bulk flow velocity in SH2 (m/s)	0.52	1.04
Water chemistry Molar ratio (H_2/O_2) DH in/out (ppb) DO in/out (ppb) Conductivity in/out (µS/cm)	 4.0/- 75/30 300/0 0.054/0.090	 4.2/- 75/30 285/0 0.054/0.083
Pt injection period (h)	167	255
Pt conc. of injection sol. (ppb)	99	100
Pt injection rate (µg/h)	3.92	2.09
Nom. Pt conc. in water (ppt)	392	209
Total Pt injected (µg)	656	533

on the average particle size. Also the Pt surface loading measurements by LA-ICP-MS revealed no clear effect of the surface roughness. To conclude, the results obtained here show that there is no major effect of the roughness, in the range investigated here (0.1–3.5 μm), on the deposition behavior. Chemical nature of the oxide film or geometrical factors affecting the flow condition, have a much more important effect.

Effect of Alloy Composition

Although many components of reactor systems are made out of stainless steel, some other types of alloys are also in contact with the hot reactor water and should therefore also be protected against SCC, thus be evenly covered with Pt nanoparticles from the OLNC process. In this context, knowledge of the Pt deposition behavior on these other materials is also of interest for an assessment of this SCC mitigation technology. Testing all materials present in a reactor system is beyond the capabilities of the present project and therefore the focus was on two additional representative materials: a Ni-base alloy, commonly used for (dissimilar metal) weldments and a low-alloy steel, as it is used for reactor pressure vessels, to complement the results obtained with the 304L stainless steel.

Chemical compositions of the materials used are listed in Table 1. The coupon specimens made of these materials, together with stainless steels coupons to be used as references, were exposed in the autoclave and in the specimen holders during Tests I and II. In the latter, one side of the specimen holders was obstructed to double the flow velocity on the remaining side. Another significant difference between the two tests is the change in the Pt injection rate which was almost halved. Experimental parameters are summarized in Table 2.

Already observation by the "naked eye" after removal of the specimens from the loop at the end of Test I, revealed a difference in oxidation behavior of the different materials as is documented in Fig. 3, the Ni-base alloy showing the most distinctive appearance. Investigations by electron microscopy confirmed notable differences in the appearance of the oxide film on the different materials (Fig. 4). On the low-alloy steel a compact oxide film of large and complex euhedral crystals is present. In strong contrast, the Ni-base alloy has only sparsely distributed, mainly octahedral crystals constituting its outer oxide layer. The appearance of the stainless steel is in-between these two extremes. Pt particles are found on all three types of materials. However, the Ni-base alloy has a distinctively homogenous coverage by an abundance of small particles (Fig. 4d). The spatial distribution is much more scattered on the low-alloy steel. Again the stainless steel fits in-between. Particle size distributions were determined for all materials and are displayed in Fig. 5. Stainless steel and low-alloy steel carry Pt particle with very similar mean sizes whereas Ni-base alloy has clearly smaller particles. The chemical nature and/or the morphology of the oxide film seem to have a noticeable influence on the Pt deposition behavior.

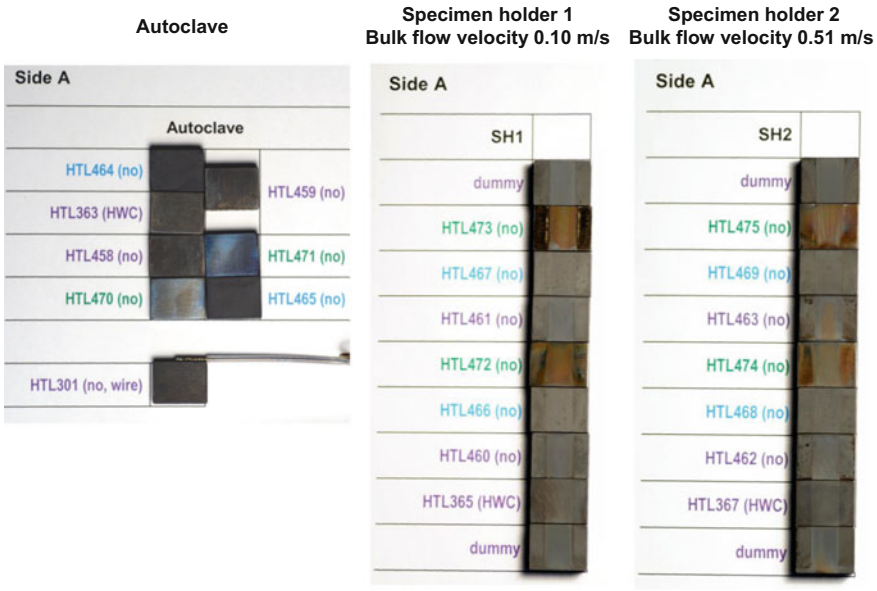

Fig. 3 Specimens from Test I after the Pt application, low-alloy steel (464–468), Ni-base alloy (470–475), the remainder are stainless steel coupons

The Pt loadings measured by LA-ICP-MS are listed in Table 3. The low-alloy steel always has the lowest Pt loading of the three materials within the same test. There also seems to be a small difference between the Ni-base alloy and the stainless steel but there is no clear trend. Despite having smaller Pt particles at its surface, the Ni-base alloy has a comparatively high Pt loading. This combination points towards a very even and dense Pt coverage, thus confirming the impression given by the SEM pictures of this material (Fig. 4d). All investigated materials seem to have Pt loadings sufficient to make their surface catalytically active and thus be at a low ECP if sufficient H_2 is present.

The results from these tests may actually give an insight into fundamental aspects of the Pt deposition mechanism. At the molecular level, the surface of the metal oxide in contact with the water is not constituted of an alternation of metallic cations and O^{2-} anions but is constituted of a layer of OH groups. In this way the coordination sphere of the metallic cations at the interface is complete and the O^{2-} anions are interacting with the solvent molecules via hydrogen bonds. Depending on the pH of the solution, the amount of H^+ that is present at the interface will vary and thus affect the surface charge of the metal oxide. At a certain pH the overall surface charge will be zero; this is the so called isoelectric point. Isoelectric points have been reported for many oxides and other materials [16, 17]. The reported values often show some variation due to factors such as grain size, oxidation state (for multivalent metals), impurities and mode of preparation but also measurement method and solution composition play a role. However, when studying this data,

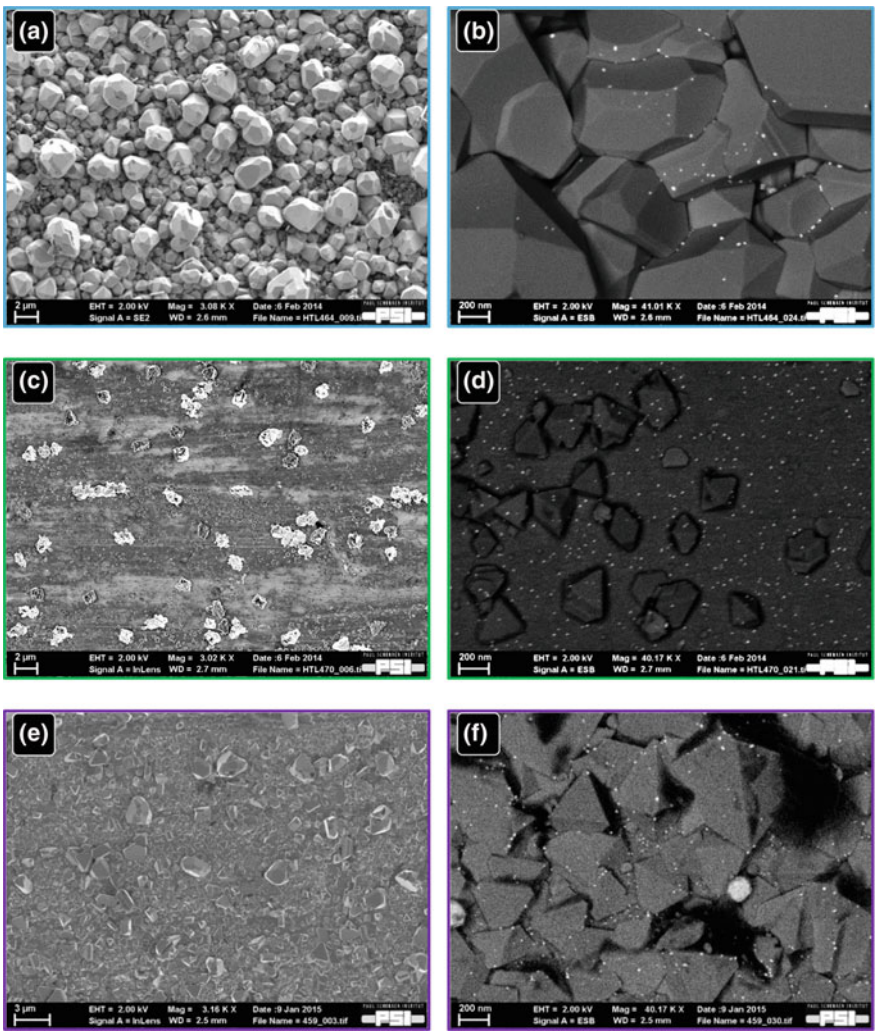

Fig. 4 SEM micrographs of the surfaces of **a**, **b** low-alloy steel, **c**, **d** Ni-base alloy and **e**, **f** stainless steel after testing. The white dots in pictures **b**, **d** and **f** represent Pt particles

one will notice that nickel oxide has generally a much higher isoelectric point than the oxides of iron or chromium under similar conditions (Table 4). The difference between nickel and the two other metals also affects the isoelectric points of the mixed oxides, where the ones containing nickel also have a comparatively higher isoelectric point. Therefore in pure water, under neutral pH, the surface of the Ni-rich oxides will have a more positive charge than the surface of the Fe–Cr oxides. On the other hand the isoelectric point of bulk Pt is low compared to all these oxides [18] which means that when placed in the same environment the Pt

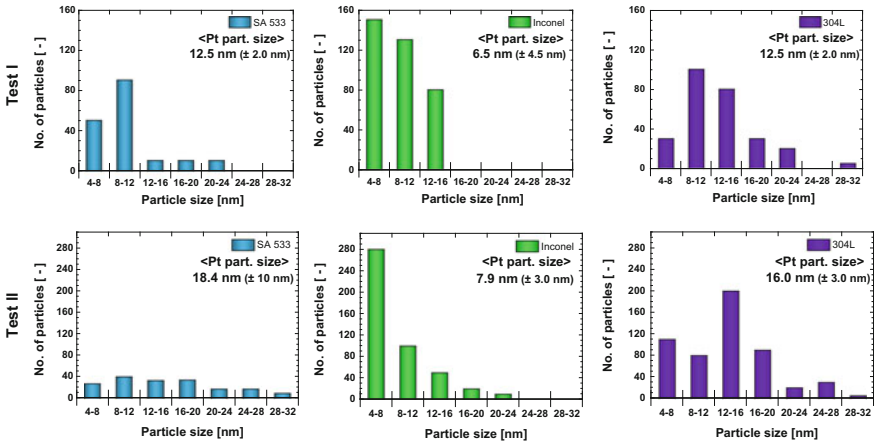

Fig. 5 Pt particle size distribution on the three different materials for the two tests

Table 3 Pt loadings on three different structural materials

Material	Low-alloy steel SA 533 B Cl.1		Ni-base alloy Inconel 182		Stainless steel AISI 304L	
Test	Test I	Test II	Test I	Test II	Test I	Test II
Flow vel. autocl. [m/s]	>0.005	>0.005	>0.005	>0.005	>0.005	>0.005
Pt loading autocl. [ng/cm^2]	120 ± 20	149 ± 13	440 ± 100	166 ± 10	160 ± 30	144 ± 10
Flow vel. SH1 [m/s]	0.10	0.20	0.10	0.20	0.10	0.20
Pt loading SH1 [ng/cm^2]	20 ± 10	47 ± 3	90 ± 20	50 ± 3	70 ± 30	102 ± 11
Flow vel. SH2 [m/s]	0.52	1.04	0.52	1.04	0.52	1.04
Pt loading SH2 [ng/cm^2]	60 ± 20	32 ± 1	210 ± 40	103 ± 12	180 ± 50	175 ± 26

Table 4 Isoelectric points for selected oxides and Pt (RT: room temperature)

Material	Isoelectric point	Reference
Pt 120 mesh (~120 μm)	3.3 (20 °C)	[18]
Pt 3–5 nm	2.8 (RT)	[19]
NiO	7–11 (RT)	[23]
Cr_2O_3	6–7 (RT)	[23]
$FeFe_2O_4$	6.5 (25 °C)	[24]
$NiFe_2O_4$	7.7 (25 °C)	[24]
$FeCr_2O_4$	6 (RT)	[25]
ZrO_2	6–7 (RT)	[23]

will have a more negative charge than the oxides. Recently the isoelectric point of ligand free Pt nanoparticles has been determined [19] which behave in the same manner as the metal. Therefore a coulombic attractive force between the Pt particles and the oxide surface exists, and will be stronger with Ni-rich oxides thus explaining the trend towards more Pt particles on the Ni-base alloy than on the iron rich alloys. If the trend between isoelectric point and particle size is real for Pt (first two entries in Table 4), then it could also explain to some extend why the mean particle size on the Ni-base alloy is smaller than on the two steels. This discussion is based on data from room temperature studies. Quantitative data for the materials at high temperature is unfortunately limited. The surface charge of magnetite ($FeFe_2O_4$) up to 290 °C has been determined [20] and some predictive models developed [21] which show that the trend seems to be maintained to some extend at higher temperatures. Dedicated studies would be needed to confirm this.

Post-application Pt Redistribution

Evaluation of specimens from the mitigation monitoring system (MMS) at KKL showed that Pt is lost from the surface during the post-OLNC application time [22]. Preliminary short term tests with the loop at PSI didn't provide conclusive results so a longer term test was undertaken. Pt was applied to a set of specimens with a "standard" testing procedure consisting in a Pt injection rate of 2 µg/h for 250 h under BWR-HWC conditions. Approximatively three days after the end of the application the loop was cooled down to remove a subset of specimens and replace them by fresh ones. The loop was then restarted and run under HWC conditions for further ~5.5 weeks, when again a subset was removed before restarting the loop a last time for another ~7.5 weeks. Full details are given in Table 5. Particle size distribution obtained from the SEM investigations of the specimens are summarized in Table 6 and displayed in Fig. 6. They show a slight trend towards mean size increase for autoclave specimens and some specimens exposed in the specimen holders. Generally, even after 92 days after Pt application the specimens give the impression of having a good coverage with Pt particles.

More quantitative data was obtained from the LA-ICP-MS measurements. Results are displayed in Fig. 7. The plots show that in some cases there is a significant scatter in the measured Pt loadings which also reflects in the standard deviations of the mean loadings. In the case of the AR specimen taken from the autoclave shortly after the end of the Pt applications, one extreme loading outlier was measured. This may be due to a transient problem with the LA-ICP-MS instrument but could also indicate an exceptional clustering of Pt on the surface. Such an extreme value influences the regression slope and thus the calculated erosion rate. In this case the value of the slope, with and without this outlier has

Table 5 Experimental parameters for initial Pt application runs and two subsequent run without Pt application

Experiment designation	Test III-0	Test III-1	Test III-2
Pressure (bar)	89	90	90
T autoclave (°C)	280	280	280
Water mass flow (kg/h)	10	10	10
Time at temperature (h; days)	502.7; 20.9	884.7; 36.9	1245; 51.9
Water chemistry Molar ratio (H_2/O_2) DH in/out (ppb) DO in/out (ppb) Conductivity in/out (µS/cm)	 4.4 82/45 300/0 0.054/0.086	 4.6 85/45 293/0 0.054/0.085	 4.5 83/46 295/0 0.054/0.080
Pt injection period (h)	253.5	n/a	n/a
Post-injection time (h; days)	81.5; 3.4	966.2; 40.3	2211; 92.1
Pt conc. of injection sol. (ppb)	107	n/a	n/a
Pt injection rate (µg/h)	2.26	n/a	n/a
Nom. Pt conc. in water (ppt)	226	n/a	n/a
Total Pt injected (µg)	571.5	n/a	n/a

been calculated, see Fig. 7. An analysis of variance shows that the slopes are only significantly different from zero for half of the sets namely ACL-PO, SH1-AR and SH2-PO. This is due to scatter in the measured loadings and indicates that the variation within one population, e.g. one specimen, is larger than the variation between the populations (specimens).

Excluding the one slightly positive slope (ACL-PO) and taking the slope obtained by excluding the extreme outlier (ACL-AR), an over-five-sets averaged Pt erosion rate of ~ 0.2 ng cm^{-2} day^{-1} is obtained. This rate is close to the value reported for the MMS specimens from KKL (~ 0.5 ng cm^{-2} day^{-1}) [22].

The other question is: how much of the Pt which leaves the surface of the specimens actually redeposits on nearby surfaces? To investigate this Pt redistribution, Pt-free specimens were inserted 3.4 days after the end of the application and then left in the loop for 89 days. Examination by SEM showed no visible Pt particles, but LA-ICP-MS analyses could detect a Pt loading (Fig. 8), albeit with a significant scatter. Therefore the slopes have a high standard error and the analysis of variance indicates again that they are not significantly different from zero. However, this does not change the fact that Pt is present on these surfaces and that the re-deposition rate is estimated to be in the range of ~ 0.2 ng cm^{-2} day^{-1}, a value similar to that of the erosion rate.

Finally it has to be stated that, as the statistical evaluation shows, the methods used here are getting to their limits when trying to quantify these small changes.

Table 6 Comparison of mean Pt particle sizes at three locations for AR/PO specimens exposed during Test III

Location U_b (m/s)		3.4 days after end of Pt injection			40 days after end of Pt injection			92 days after end of Pt injection		
Initial condition of specimen		<arithmetic> ± 1 SD (nm)	<geometric> */1 SD (nm)	mode (nm)	<arithmetic> ± 1 SD (nm)	<geometric> */1 SD (nm)	mode (nm)	<arithmetic> ± 1 SD (nm)	<geometric> */1 SD (nm)	mode (nm)
ACL	AR	14.7 ±6.6	13.4 */1.57	10.9	15.2 ±6.9	13.5 */1.66	10.5	16.1 ±7.1	14.6 */1.60	11.7
	PO	11.4 ±5.8	10.1 */1.64	7.9	n/a	n/a	n/a	17.5 ±6.8	16.1 */1.54	13.4
SH1 0.51	AR	6.7 ±2.4	6.4 */1.40	5.7	11.8 ±6.6	9.9 */1.83	6.9	8.5 ±5.2	7.3 */1.70	5.5
	PO	9.6 ±3.9	8.8 */1.51	7.5	n/a	n/a	n/a	9.4 ±3.3	8.8 */1.43	7.7
SH2 1.02	AR	n/a	n/a	n/a	8.3 ±4.9	7.3 */1.64	5.7	8.5 ±4.7	7.5 */1.61	6.0
	PO	9.4 ±3.3	8.8 */1.40	7.9	n/a	n/a	n/a	8.9 ±3.1	8.3 */1.44	7.3

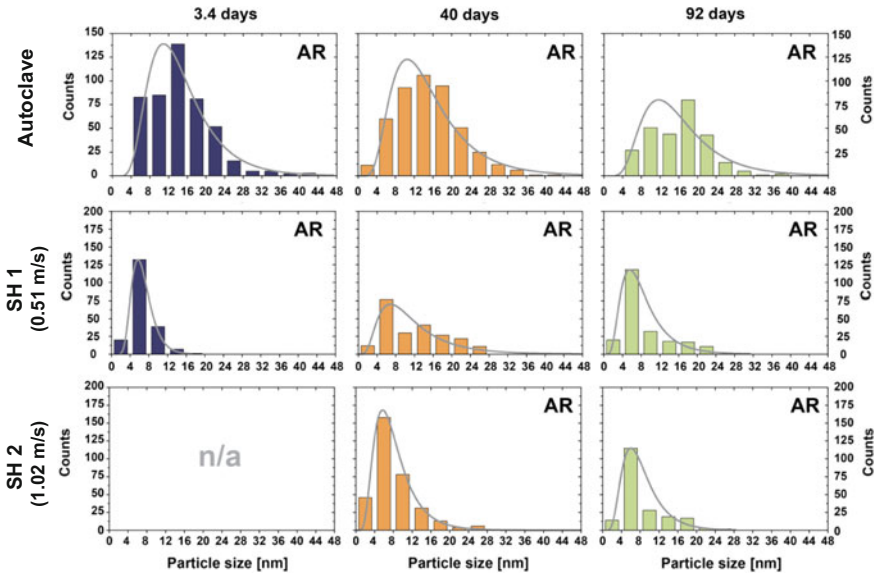

Fig. 6 Histograms showing the evolution of the Pt particle size distribution as a function of the number of days post-Pt-application for specimens in as-received condition (AR) during Tests III-0 to -2 (SH = specimen holder)

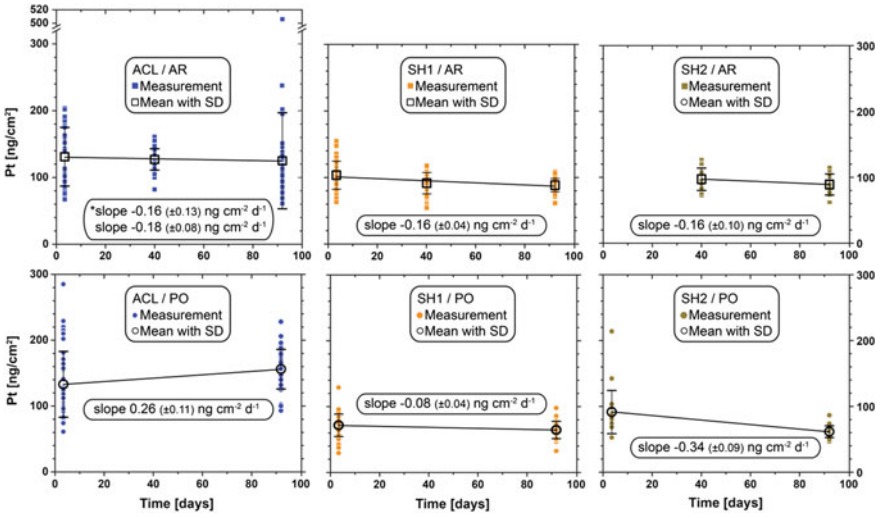

Fig. 7 Plot showing the Pt loadings as a function of the time elapsed after the Pt injection has ended, as a function of location and specimens' initial condition. Straight lines represent linear regressions (corresponding slopes are given with standard error). Bulk flow velocity: in SH1 0.51 m/s, in SH2 1.02 m/s. (ACL = autoclave, SH = specimen holder). *Including outlier at 500 ng/cm^2

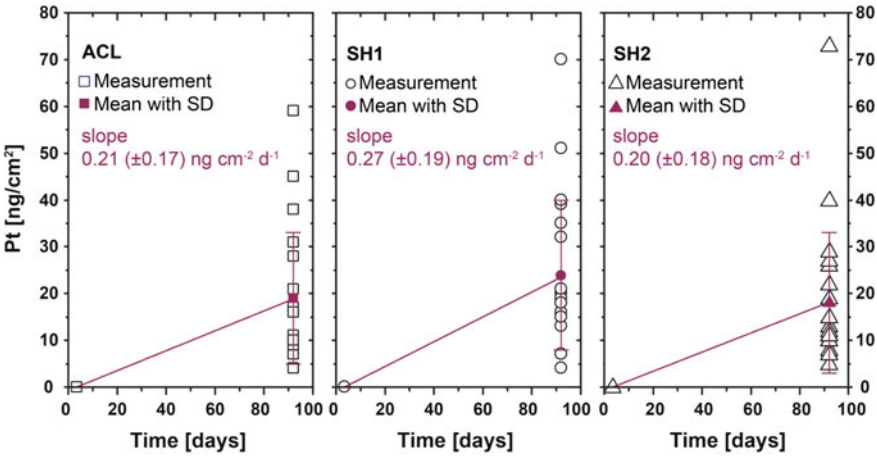

Fig. 8 Plots showing the amount of Pt redistributed after the end of the Pt application for three different locations of the loop. Bulk flow velocity: in SH1 0.51 m/s, in SH2 1.02 m/s. Straight lines represent linear regressions. The scatter in the measurements may be related to the presence of clustered Pt particles

Conclusions

The present investigations on the OLNC technology have shown that surface roughness does not play a significant role in the deposition of Pt particles. In contrast, the chemical composition of the support material has an impact on Pt deposition. Although the surface morphology of the oxide film could also play a role, it is more likely that the chemical properties (surface charge) of the oxide film are the reason for this behavior. Further dedicated investigation would be needed to confirm this. Finally, it has been shown that the Pt surface loading decreases slowly with time. Re-deposition of Pt on virgin surfaces is only minimal and insufficient to provide the low ECP needed for SCC mitigation. Therefore one cannot expect to achieve protection from SCC by post-application redistribution alone. To compensate for the loss, recurring reapplications are needed. In case of the PSI loop, 50% of the Pt would be lost in about 250 days assuming a linear decrease.

Acknowledgements The financial support by the Swiss Federal Nuclear Safety Inspectorate (ENSI) is gratefully acknowledged. We are also indebted to the Swiss nuclear power plants KKL and KKM for their precious in-kind contributions to the project. Beat Baumgartner and Pia Reichel (both PSI) are thanked for their experimental contribution.

References

1. R. Kilian, A. Roth, Corrosion behaviour of reactor coolant system materials in nuclear power plants. Mater. Corros. **53**, 727–739 (2002)
2. C.J. Wood, Water chemistry control in LWRs, in *Comprehensive Nuclear Materials* ed. by R. J.M. Konings (Elsevier, Oxford, 2012), pp. 17–47
3. R.L. Cowan, C.C. Lin, W.J. Marble, C.P. Ruiz, Hydrogen water chemistry in BWRs, *5th International Symposium on Environmental Degradation of Materials in Nuclear Power Systems—Water Reactors* (pp. 50–58) (1991)
4. S. Hettiarachchi, R.L. Cowan, T.P. Diaz, R.J. Law, S.E. Garcia, Noble Metal Chemical Addition… from Development to Commercial Application, *7th International Conference on Nuclear Engineering* (1999)
5. L. Oliver, B. Helmersson, G. Ledergerber, W. Kaufmann, G. Wikmark, B. Cheng, A. Kucuk, Review of Water Chemistry and Corrosion Products in a NWC Plant Transitioned to Hydrogen Injection and OLNC, *Nuclear Plant Chemistry (NPC) Conference* (2010)
6. S. Hettiarachchi, C. Weber, Water Chemistry Improvements in an Operating Boiling Water Reactor (BWR) and Associated Benefits, *Nuclear Plant Chemistry (NPC) Conference* Paper No. 2.04 (2010)
7. Y.-J. Kim, P.L. Andresen, S. Hettiarachchi, T.P. Diaz, Hydrothermal formation and distribution of noble metal particles on type 304 SS in high temperature water, *CORROSION 2007*, Paper 07604 (2007)
8. P.V. Grundler, S. Ritter, Noble Metal Chemical Addition for Mitigation of Stress Corrosion Cracking: Theoretical Insights and Applications. PowerPlant Chem. **16**(2), 76–93 (2014)
9. P.V. Grundler, A. Ramar, V. Karastoyanov, S. Abolhassani-Dadras, I. Guenther-Leopold, N. Kivel, S. Ritter, Effect of injection rate on Platinum deposition behaviour on stainless steel under simulated BWR conditions, *Nuclear Plant Chemistry (NPC) Conference*, Paper 117 Poster 1–46 (2012)
10. A. Ramar, P.V. Grundler, V. Karastoyanov, I. Günther-Leopold, S. Abolhassani-Dadras, N. Kivel, S. Ritter, Effect of Pt injection rate on corrosion potential and Pt distribution on stainless steel under simulated boiling water reactor conditions. Corros. Eng., Sci. Technol. **47** (7), 489–497 (2012)
11. A. Ramar, P.V. Grundler, V. Karastoyanov, I. Günther-Leopold, S. Abolhassani-Dadras, N. Kivel, S. Ritter, Platinum deposition behaviour on stainless steel under varying water chemistry in simulated BWR conditions, *Nuclear Plant Chemistry (NPC) Conference*, Paper 116 Poster 1–45 (2012)
12. P.V. Grundler, A. Ramar, L. Veleva, S. Ritter, Effect of flow conditions on the deposition of platinum nanoparticles on stainless steel surfaces. Corrosion **71**(1), 101–113 (2015)
13. P.V. Grundler, L. Veleva, H. Gu, S. Allner, B. Niceno, S. Ritter, Noble metal applications for SCC mitigation in BWRs: Platinum nanoparticle penetration into crevices and cracks under controlled flow conditions, *17th International Conference on Environmental Degradation of Materials in Nuclear Systems—Water Reactors* 16 (2015)
14. H. F. Gu, B. Niceno, P. V. Grundler, M. Sharabi, L. Veleva, S. Ritter, Computational study of platinum nanoparticle deposition on the surfaces of crevices, Nucl. Eng. Des. **304**, 84–99 (2016)
15. D. Günther, B. Hattendorf, Solid sample analysis using laser ablation inductively coupled plasma mass spectrometry. Trends Anal. Chem. **24**(3), 255–265 (2005)
16. G.A. Parks, The isoelectric points of solid oxides, solid hydroxides, and aqueous hydroxo complex systems. Chem. Rev. **65**(2), 177–198 (1965)
17. M. Kosmulski, *Surface charging and points of zero charge* (CRC Press, Boca Raton, FL, 2009)
18. N. Kallay, Z. Torbic, M. Golic, E. Matijevic, Determination of the isoelectric points of several metals by an adhesion method. J. Phys. Chem. **95**(18), 7028–7032 (1991)

19. G. Marzun, C. Streich, S. Jendrzej, S. Barcikowski, P. Wagener, Adsorption of colloidal platinum nanoparticles to supports: charge transfer and effects of electrostatic and steric interactions. Langmuir **30**(40), 11928–11936 (2014)
20. D.J. Wesolowski, M.L. Machesky, D.A. Palmer, L.M. Anovitz, Magnetite surface charge studies to 290°C from in situ pH titrations. Chem. Geol. **167**(1–2), 193–229 (2000)
21. M.A.A. Schoonen, Calculation of the point of zero charge of metal oxides between 0 and 350° C. Geochim. Cosmochim. Acta **58**(13), 2845–2851 (1994)
22. S. Ritter, P.V. Grundler, L. Veleva, G. Ledergerber, Platinum deposition behaviour on stainless steel surfaces in a boiling water reactor plant, *EUROCORR 2015*, 870 (2015)
23. M. Kosmulski, Compilation of PZC and IEP of sparingly soluble metal oxides and hydroxides from literature. Adv. Coll. Interface. Sci. **152**(1–2), 14–25 (2009)
24. M. Barale, G. Lefèvre, F. Carrette, H. Catalette, M. Fédoroff, G. Cote, Effect of the adsorption of lithium and borate species on the zeta potential of particles of cobalt ferrite, nickel ferrite, and magnetite. J. Colloid Interface Sci. **328**(1), 34–40 (2008)
25. Y. Wang, R.J. Pugh, E. Forssberg, The influence of interparticle surface forces on the coagulation of weakly magnetic mineral ultrafines in a magnetic field. Colloids Surf., A **90**(2–3), 117–133 (1994)

Confirmation of On-Line NobleChem™ (OLNC) Mitigation Effectiveness in Operating Boiling Water Reactors (BWRs)

Joe Kopcash, Juan Varela, Hubert Huie and G. Depta

Abstract The development and implementation of On-Line NobleChem™ (OLNC) has now occurred for many years with almost the entire US BWR fleet, including Mexico, and some European BWRs using this process to achieve mitigation of IGSCC. The data confirming the effectiveness of OLNC has indirectly shown significant reductions in incidences of crack initiation as well as the suppression of growth of any previously existing cracks. However, the robustness of the process and its ability to protect all core and lower plenum regions requires on-going confirmation of the presence of nanometer sized platinum particles as well as verifying the adequacy of the coverage on surfaces of the core structural materials. Efforts by GE Hitachi Nuclear Energy (GEH) have continued in cooperation with the BWR utilities to both properly inject the platinum solution into the coolant as well as to monitor the surface characteristics of actual core components. This paper will show the results of on-going efforts to confirm platinum coverage of stainless steel surfaces using Field Emission Scanning Electron Microscopy (FE-SEM) methods. Additional efforts to tie all the process methods together to establish and confirm OLNC performance will also be presented. Finally, the paper will review continuing plans moving forward to validate OLNC performance across the BWR fleet.

Keywords On-Line NobleChem (OLNC) · Platinum (Pt) · FE-SEM · Deposition · MMS · Coupons

Introduction

The OLNC application process is performed worldwide to mitigate Intergranular Stress Corrosion Cracking (IGSCC) of piping and Reactor Pressure Vessel (RPV) internal components in the presence of excess hydrogen (hydrogen to oxidant molar ratio greater than two). Currently, the OLNC process is performed at

J. Kopcash (✉) · J. Varela · H. Huie · G. Depta
GE-Hitachi Nuclear Energy LLC and EPRI, Wilmington, USA
e-mail: joe.kopcash@ge.com

J.H. Jackson et al. (eds.), *Proceedings of the 18th International Conference on Environmental Degradation of Materials in Nuclear Power Systems – Water Reactors*, The Minerals, Metals & Materials Series, https://doi.org/10.1007/978-3-319-68454-3_38

thirty-six (36) BWRs worldwide. An OLNC application is routinely performed on an average of one application per year or two applications per fuel cycle. This application strategy may vary depending on the plant's fuel cycle of twelve (12) months, eighteen (18) months, or twenty-four (24) months. In addition to being able to perform OLNC applications during full power operation, a key benefit of OLNC is the ionic Pt injected forms finer particles when injected into higher temperature water than the original classic NobleChem™ (NMCA) process, which was performed at ~135 °C. Laboratory evidence shows about a 10X smaller Pt particle size with the size-distribution often centered below 5 nm for OLNC, but can have a range of 2–15 nm as seen in Fig. 1. Even with this range, OLNC has a much finer Pt particle size than the 50 nm average for NMCA [1]. A 10X decrease in particle size yields 1000× more particles for a given weight of Pt injected. However, the type of nucleation that takes place in a plant can affect the actual size and distribution of the Pt particles on the surfaces and the corresponding catalytic effectiveness. The purpose of this effort was therefore directed toward evaluating the actual Pt particle characteristics on Mitigation Monitoring System (MMS) coupons and RPV artifacts from actual BWRs following OLNC treatment. Since these specimens were irradiated and contaminated, GEH developed FE-SEM capabilities at Vallecitos Nuclear Center (VNC) to perform these critical assessments. The results and interpretation of these plant specimens are the subject of this paper.

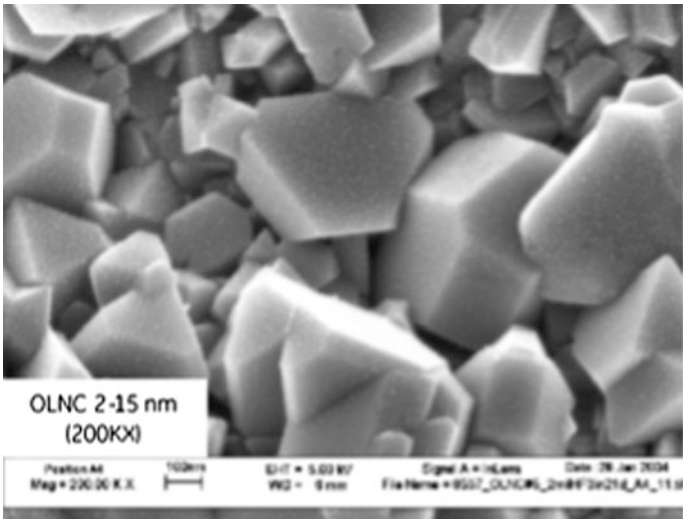

Fig. 1 GEGRC laboratory image of OLNC Pt particle size

Experimental Methods and Plant Specimen History

GEH along with EPRI developed a program to characterize Pt deposition on RPV internals treated with OLNC. The overall program included reviewing the assessment of Pt loading values using wet chemistry to serve as the baseline evaluation and to be used for comparison with the detailed SEM surface assessments. The analyses of the specimens were limited to nine (9) MMS coupons and four (4) types of RPV internal components available after removal from selected plants. For the detailed characterization effort, a Hitachi SU8220 FE-SEM was used to create high resolution magnified images of the MMS coupons and artifact surfaces. The next section details the methodology for the surface evaluation of the specimens. The selection criteria of RPV artifacts was based on three major factors: locations of interest, number of OLNC applications performed, and availability. A list of all plant artifacts and locations was reviewed and then used in the process of selecting various artifacts for analysis.

The majority of the specimens were MMS coupons which are external from the RPV and were more readily available to be retrieved by the fleet. These coupons were initially designed to be used to monitor Pt loading once an OLNC application has been performed. Four different types of in-plant artifacts were chosen for the evaluation. These specimens, of higher interest since they were retrieved form the reactor internal region, were the primary focus of the study. First, an Alloy X-750 tie rod latch was selected due to the availability from a BWR-2 and the location in the downcomer region near the recirculation suction nozzle. The second artifact, a jet pump auxiliary wedge constructed using both type 316L SS and Alloy X-750, was selected due to the availability from a BWR-5. Its location was also the downcomer region since it was designed to prevent vibration in the jet pump assembly. The third type of artifact, bottom head drain line (BHDL) ECP probes, were selected due to the availability and their installation location. This area is comparable to the lower plenum region of the RPV which is extremely difficult for the utilities to inspect during a refueling outage. The final type of artifact, a fuel channel fastener, was selected due to the near-term availability from a BWR-4 and its location at the top of the fuel bundle of the inner core bypass region near the top guide plate. This artifact is of particular interest due to its location in an area where water exiting the fuel channels is saturated with steam and whether or not Pt particles reach this area. It also presents a component that could be retrieved easily from many different plants and potentially used for continuing surveillance.

Surface Characterization Results

The purpose for this effort was to confirm Pt particles were deposited on the reactor internal surfaces after an OLNC application(s) as reported in laboratory specimens. These analyses provided images of Pt particles deposited on the surface of each

MMS coupon or plant artifact. These images were also used to provide the number of Pt particles in a known area, the average Pt particle size (measured diameter of a Pt particle) in each image, and the Pt particle density which is the number of Pt particles per total area represented in each image. Each sample surface was imaged at four random locations unless otherwise specified using the Secondary Electron (SE(U)) and Yttrium Alumina Garnet Backscatter Secondary Electron (YAGBSE) detectors. Each location was imaged at three different magnifications: 10,000×, 100,000×, and 250,000×. The Energy-Dispersive Spectroscopy (EDS) detector was only used in one location to verify the existence of elemental Pt particles. Using the YAGBSE image, areas were selected containing the bright white particles. The EDS detector was then used to verify the particles were Pt. Once this has been determined, it was assumed that all such particles were Pt particles.

Once all imaging was completed, Clemex Vision software was used on the YAGBSE images to calculate the amount of Pt particles deposited on the surface, the size of the Pt particles, the Pt particle density on the surface, and to gather all the statistical data generated. The software selected the platinum particles based on the contrast within the image. Once the Pt particles were recognized by the software, all statistical data was calculated.

MMS Coupons

The results of the FE-SEM analyses are presented in Table 1. Given these specimens were far away from the reactor internals regions requiring mitigation, these data established a conservative bound for the Pt particle characteristics.

All nine (9) MMS coupons had an average Pt particle size less than fifteen (15) nanometers which matches with the GEGRC results reported in Fig. 1. Out of the nine (9) MMS coupons studied, only five (5) MMS coupons were exposed to one (1) OLNC application. Out of those five (5) MMS coupons, only two (2),

Table 1 FE-SEM data of MMS coupons

Plant type	Serial number	OLNC application(s)	Average Pt particle size (nm)	100 k average (Particle/μm^2)	250 k average (Particle/μm^2)
BWR-4	2010-088	1	5–6	269	379
BWR-4	2009-194	3	3–7	25	76
BWR-3	2009-376	4	4–6	297	380
BWR-3	2009-385	1	3–7	39	57
BWR-3	2009-498	1	3–5	316	478
BWR-4	00689-15	4 + 1[a]	4–9	178	680
	2009-466	1	9 –13	89	322
BWR-6	2009-409	1	10–11	5	18
	2009-410	2	11–14	21	53

[a]Four (4) OLNC applications and one (1) NMCA application

coupon 2010-088 and coupon 2009-498, showed similar results. The other three coupons exposed to a single OLNC application had Pt particle densities much lower. When reviewing the data of all nine (9) MMS coupons, a correlation between OLNC application(s) and Pt particle densities cannot be made.

Reactor Internal Component Artifacts

These artifacts were the focus of the program. Table 2 presents the results of the artifacts analyzed which are discussed in more detail.

Tie Rod Latch

The first plant artifact evaluated in this program was a tie rod latch from a BWR-2. The tie rod latch was installed in 2005 and removed in April 2013. During this time, a total of seven (7) OLNC applications were performed.

The average Pt particle size was 13–14 nm and the Pt particle density was 623 particles/μm^2 for 100,000× magnification and 692 particles/μm^2 for 250,000× magnification.

The tie rod latch was manufactured using Alloy X-750. The oxide layer which developed on the surface of the artifact is vastly different than the oxide layer observed on MMS coupons. The oxide layer was also observed to contain a high amount of crud particles deposited onto the surface. Due to the exposure of seven (7) OLNC applications and the artifact's location in the downcomer region, the images of highly distributed Pt particles on the oxide layer of the tie rod latch was

Table 2 FE-SEM data of RPV artifacts

Plant type	RPV component	OLNC application (s)	Average Pt particle size (nm)	100 k average (Particle/μm^2)	250 k average (Particle/μm^2)
BWR-2	Tie rod latch	7	13–14	623	692
BWR-5	Jet pump auxiliary wedge (X-750)	5	13	285	322
	Jet pump auxiliary wedge (316L SS)	5	18–19	199	221
BWR-4	Bottom head drain line platinum ECP probe	4 + 1[a]	11–12	170	434
	Bottom head drain line iron/iron oxide ECP probe	4 + 1[a]	11–13	253	371
BWR-4	Fuel channel fastener	2	11–18	118	379

[a]Four OLNC applications and one NMCA application

expected. The average Pt particle size of 13–14 nm is on the higher end when comparing to particle sizes generated in GE Global Research Center (GEGRC) laboratory tests, see Fig. 2. The Pt particle densities were the highest among all MMS coupons and plant artifacts analyzed

Jet Pump Auxiliary Wedge

The second plant artifact studied was a jet pump auxiliary wedge obtained from a BWR-5. The jet pump auxiliary wedge was installed in 2004 and removed in April 2012, and during this time, five (5) OLNC applications were performed. The jet pump auxiliary wedge is comprised of two (2) types of material, Alloy X-750 and Type 316L SS. Both materials were examined by FE-SEM.

The Alloy X-750 had an average Pt particle size of 13 nm and the Pt particle density was 285 particles/μm^2 for 100,000× magnification and 322 particles/μm^2 for 250,000× magnification. The Type 316L SS had an average Pt particle size of 18–19 nm and the Pt particle density was 199 particles/μm^2 for 100,000× magnification and 221 particles/μm^2 for 250,000× magnification. See Figs. 3 and 4.

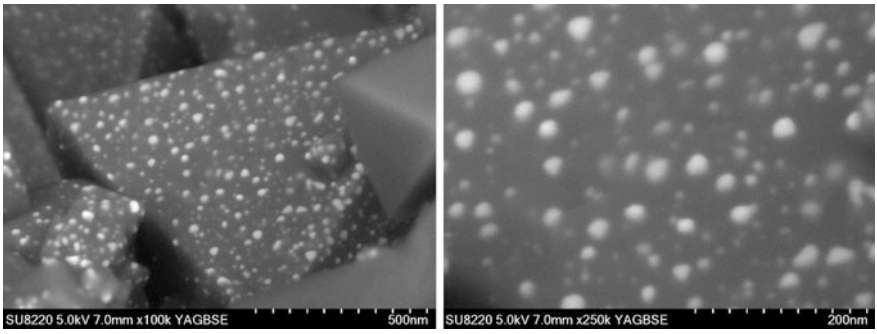

Fig. 2 Tie rod latch, 100 K magnification (L) and 250 K magnification (R)

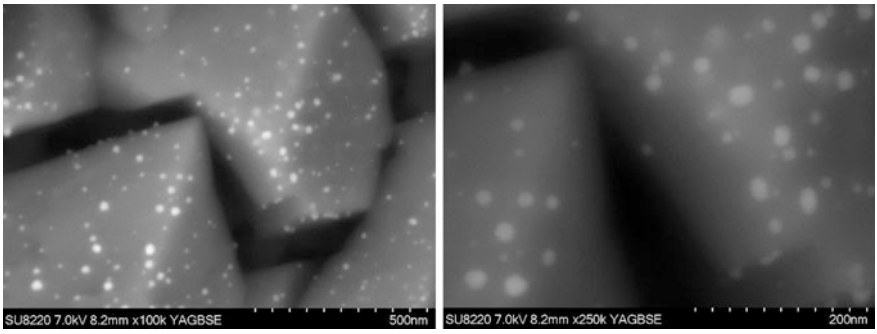

Fig. 3 Jet pump auxiliary wedge, 316L SS, 100 K magnification (L) and 250 K magnification (R)

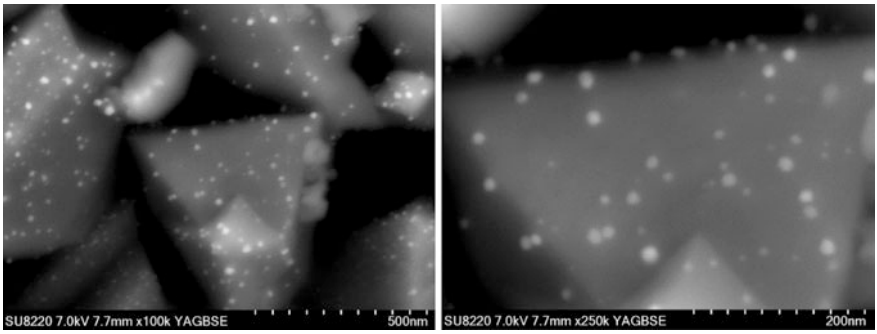

Fig. 4 Jet pump auxiliary wedge, Alloy X-750, 100 K magnification (L) and 250 K magnification (R)

While the Type 316L SS section of the jet pump auxiliary wedge had the largest particle size range compared to all MMS coupons and plant artifacts studied, this particle size range was slightly larger than the particle size range reported in GEGRC laboratory tests in Fig. 1.

Bottom Head Drain Line ECP Probes

The third type of artifact studied in this program are four ECP probes from the bottom head drain line of a BWR-4. The BHDL ECP probes consist of two iron/iron oxide ECP probes and two platinum ECP probes. All four probes were installed in March 2000 and removed in February 2015. While the ECP probes were installed, one (1) NMCA application and four (4) OLNC applications were performed.

The SS housing on the Pt ECP probes had an average Pt particle size range of 11–12 nm and the Pt particle density was 170 particles/μm^2 for 100,000× magnification and 434 particles/μm^2 for 250,000× magnification.

The SS housing on the iron/iron oxide ECP probes had an average Pt particle size range of 11–13 nm and the Pt particle density was 253 particles/μm^2 for 100,000× magnification and 371 particles/μm^2 for 250,000× magnification.

All four probes were installed into a flange assembly where each ECP probe was inserted into a guide tube. The Pt ECP probes were long enough to allow the probe tip and part of the Type 304 SS housing to be exposed to flow. The iron/iron oxide ECP probes were long enough to allow for the probe tip and braze material section to be exposed to flow, but the Type 304 SS housing was covered by the guide tube. See Figs. 5 and 6. This can explain the difference in Pt particle densities between the two types of ECP probes.

For both types of ECP probes, large deposits of crud covered the oxide surface. For the Pt ECP probes, Pt particles were distributed on both the crud particles and the oxide crystals. For the iron/iron oxide ECP probe, the Pt particles were mainly

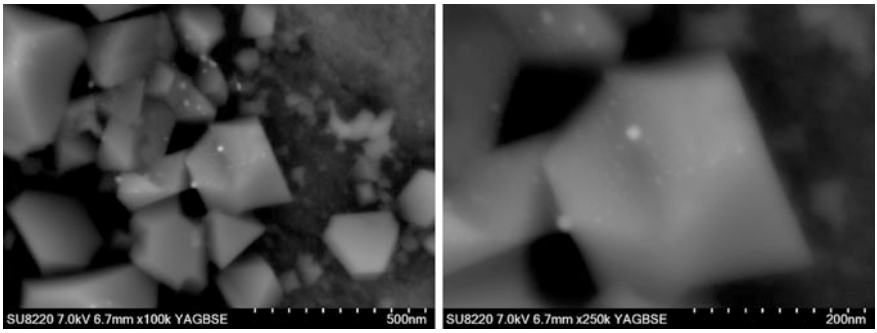

Fig. 5 BHDL iron/iron oxide ECP probe, 304 SS housing, 100 K magnification (L) and 250 K magnification (R)

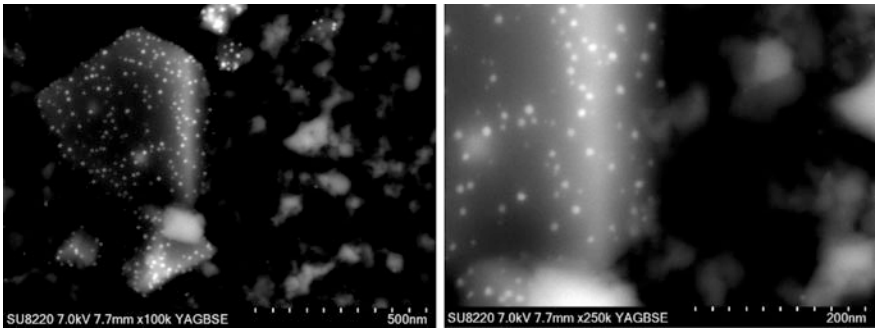

Fig. 6 BHDL platinum ECP probe, 304 SS housing, 100 K magnification (L) and 250 K magnification (R)

deposited onto the oxide crystals. Since the SS housing on the iron/iron oxide ECP probe was contained inside the guide tube, this proves Pt particles can migrate into crevices even if there is little to no flow in the region.

The particle size averages are in the range of GEGRC laboratory testing, but there was a non-homogenous distribution of Pt particles deposited onto the surfaces of the SS housing which was not observed in the GEGRC laboratory tests seen in Fig. 1.

Fuel Channel Fastener

The fourth type of artifact included in this study was a fuel channel fastener from a BWR-4. The fuel channel fastener was installed for a single fuel cycle in February 2012 and removed in February 2014. This channel fastener was exposed to two (2) OLNC applications during its installation period.

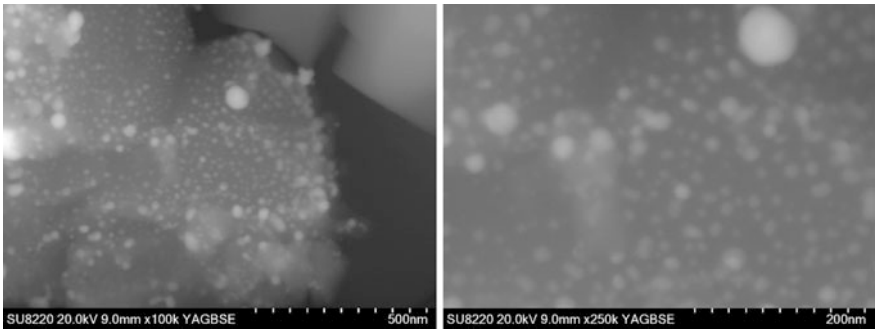

Fig. 7 Fuel channel fastener, stainless steel, 100 K magnification (L) and 250 K magnification (R)

The SS channel fastener had an average Pt particle size range of 11–18 nm and the Pt particle density was 118 particles/μm^2 for 100,000× magnification and 379 particles/μm^2 for 250,000× magnification. See Fig. 7.

While less crud was observed on the channel fastener surface compared to other plant artifacts, the oxide surface contained multiple layers of oxide crystals. During the sample cutting process, the oxide surface was observed to be less adherent to the channel fastener when comparing it to MMS coupons or other plant artifacts.

The fuel channel fastener showed a mixture of results with respect to Pt particle deposition. In some locations platinum particles were deposited on the surface in a non-homogenous fashion. In other locations Pt particles were found deposited within the multi layers of oxide crystals. Other than the Pt particle size, visually, the Pt distribution and particle density were much lower than the laboratory results.

Summary of Results

Currently, this program has analyzed a total of nine (9) MMS coupons from seven (7) different plants and four (4) different types of RPV artifacts retrieved from four (4) different plants.

While Pt loading has been one of the accepted methods for determining the success of Pt deposition when applying OLNC, through FE-SEM imaging this program has shown this may not be the only source of information needed. As an example, the MMS coupon, 2009-385, had a loading value of 0.13 $\mu g/cm^2$ after its initial OLNC application. Once the sample was imaged, large Pt particle clusters were observed on the oxide surface, see Fig. 8, and did not show the homogenous nanometer size Pt particles deposited on the oxide surface like the laboratory testing performed by GEGRC. Since Pt loading incorporates all the Pt deposited on the surface along with any Pt that may have been buried beneath crud or individual oxide layers, this establishes the need for FE-SEM imaging to be done in conjunction with Pt loading analysis to determine if the Pt was deposited in a homogenous manner demonstrated previously by GEGRC.

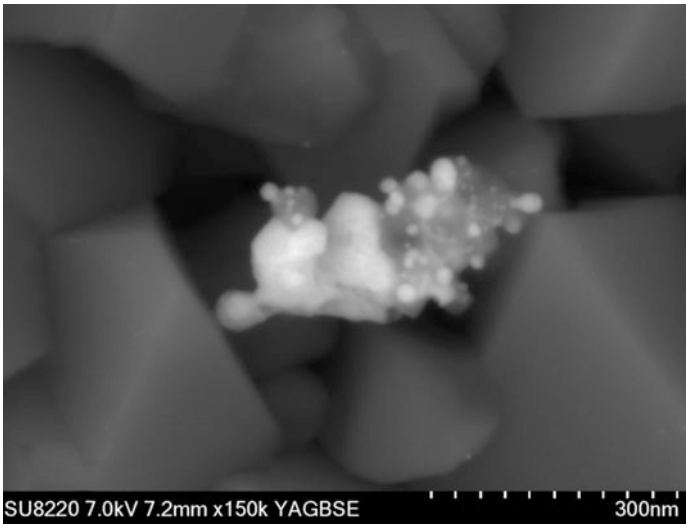

Fig. 8 Pt particle cluster on MMS coupon 2009-385

With the FE-SEM, a process of choosing four (4) random positions on the sample surface and taking images at three different levels of magnification, 10,000×, 100,000×, and 250,000×, has been established. With the 10,000× magnification, the oxide layer can be examined to help determine if the surface has been disturbed in any way, how much crud has been deposited on to the surface, or if any anomalies exist on the oxide surface. As the magnification was increased from 10,000× to 100,000×, Pt particles began to appear on the oxide surface allowing for Pt particles to be measured and the Pt particle density to be calculated. The Pt particle size was established by measuring the diameter of the particle in nanometers and the Pt particle density is referenced as Pt particles per micron squared (part/μm^2). As the magnification was increased from 100,000× to 250,000×, additional Pt particles less than five (5) nanometers became more visible. Since more Pt particles became visible and a smaller surface area was analyzed, all Pt particle densities calculated for 250,000× magnification increased in value when compared to the 100,000× magnification. This is demonstrated in Tables 1 and 2.

In Table 1, each MMS coupon varied in results. All the particle size ranges were slightly elevated compared to the laboratory range of 2–15 nm, reported in Reference 1. Out of the nine (9) MMS coupons analyzed, five (5) coupons were exposed to a single OLNC application, and out of those five (5) coupons, only 2010-088 and 2009-498 had comparable results from a single OLNC application. All other coupons were much lower. A direct correlation between the number of OLNC applications performed versus the Pt particle densities cannot be made at this time.

In Table 2, each RPV artifact also varied in results. The average Pt particle size range was generally higher when comparing to the MMS coupons Pt particle size range. Only the jet pump auxiliary wedge Type 316L SS portion and the fuel channel fastener had particle size ranges slightly larger than the range of 2–15 nm reported in Fig. 1. As the number of OLNC applications increased, so did the Pt particle densities which was not the case for the MMS coupons. For the RPV artifacts, this may have more to do with the location of the artifact within the reactor, distance between the injection point and the artifact, and flow rates observed at the location of the artifact. With the current selection of RPV artifacts, there is definitive proof Pt particles are being deposited in the downcomer region, bottom head drain line, and the inner by-pass flow of the reactor during an OLNC application.

Conclusions and Future Work

Currently, based on the data obtained from this project, a direct correlation between the amount of OLNC applications and Pt particle densities from MMS coupons cannot be made. The variation between each MMS coupon in Table 1 supports this statement. Due to the conservative nature of the MMS coupons, the results from the RPV artifact analyses is a more substantial representation on how the Pt particles are depositing onto the RPV internals. Depending on a location of interest, the area is best represented by an available artifact pulled from the same region instead of drawing a correlation from the results obtained from an MMS coupon. Since an MMS coupon can be removed while the reactor is operating, a MMS coupon can be used to determine if Pt particles were deposited on the internal surfaces of the reactor after an OLNC application, but an examination of a RPV artifact would be better suited to understand the Pt particle sizes deposited, whether the Pt particles were deposited homogenously, and the Pt particle density.

In the near future, this program has an additional MMS coupon from the BWR-2 in which the tie rod latch was removed. This MMS coupon will be used to help determine if a correlation can be established between the tie rod latch and the MMS coupons, which were installed during the same period of time as the tie rod latch was installed. An additional fuel channel fastener from the same BWR-4 the first channel fastener was removed from will be analyzed. This channel fastener was exposed to two (2) fuel cycles and will have a total of four (4) OLNC applications applied to it. A comparison study will be completed on both channel fasteners to determine if the Pt particle density increased on the second fuel channel fastener, the Pt particle size range is the same on both fasteners, and if there is any difference in the way the Pt particles deposited onto the surfaces. This work will entail the continual use of the FE-SEM to gather data and to help further understand how Pt particles are depositing onto the surface of RPV internals during an OLNC application.

GEH is in the developmental stages of measuring an Electrochemical Corrosion Potential (ECP) value on Pt deposited surfaces of all MMS coupons and plant RPV internal artifacts. This requires additional laboratory testing using a high temperature/high pressure test loop simulating BWR water chemistry. This data can help establish a baseline Pt loading value necessary to obtain a ECP value of < -230 mV SHE, which is the value recognized by the industry as the threshold for mitigation.

Acknowledgements Significant technical contributions to this program were made by Sharik Cochinwala, Laura Beale, Ron Horn, Kimberly Sbrocchi, and Dora Tien from GEH as well as Raj Pathania and Susan Garcia from EPRI.

Reference

1. P.L. Andresen, PLM 004N0759, Theoretical and Practical Considerations for OLNC (Jan. 2017)

Development of the Fundamental Multiphysics Analysis Model for Crevice Corrosion Using a Finite Element Method

Masahiko Tachibana, Yoichi Wada, Takayuki Arakawa, Yoshiharu Kikuchi and Takehiro Seto

Abstract It is necessary to study crevice structures which can mitigate crevice corrosion as the origin of SCC of materials used in BWR core region. A fundamental crevice corrosion simulation model has been developed to design corrosion control structures for these materials. Effects of the width and the depth on the corrosive environment in a crevice were studied based on that model. Calculated pH in the crevice decreased with time for all crevice geometries. The lowest pH was found at the deepest position in the crevice for all the cases. It seemed there was only a negligible difference in pH where the crevice depth was deeper than the specific depth which depended on the crevice width.

Keywords BWR · Crevice corrosion · Stress corrosion cracking · Control rod · Electrochemical corrosion potential · Stainless steel

Introduction

Small-sized cracks have been observed on some metals of boiling water reactor (BWR) components including some types of control rods (CR) [1]. The cracks were observed on sheaths and tie-rods made of 316L stainless steel (SS) which were equipped as one of the structural component of CR. There are several factors that contribute to IASCC such as water chemistry, stress conditions and material degradation by irradiation. Crevice corrosion act as an initiation site of stress corrosion cracking (SCC) in BWR environment [2]. The cracks observed on CR were thought to be due to irradiation assisted stress corrosion cracking (IASCC) due

M. Tachibana (✉) · Y. Wada
Center for Technology Innovation, Hitachi, Ltd.,
7-2-1, Omika-cho, Hitachi, Ibaraki 319-1221, Japan
e-mail: masahiko.tachibana.kh@hitachi.com

T. Arakawa · Y. Kikuchi · T. Seto
Hitachi-GE Nuclear Energy, Ltd.,
5-2-2 Omika-cho, Hitachi, Ibaraki 319-1221, Japan

J.H. Jackson et al. (eds.), *Proceedings of the 18th International Conference on Environmental Degradation of Materials in Nuclear Power Systems – Water Reactors*, The Minerals, Metals & Materials Series, https://doi.org/10.1007/978-3-319-68454-3_39

to crevice corrosion [1]. Therefore, such cracks can be prevented by mitigating crevice corrosion. Consequently, evaluating the possibilities of crevice corrosion generation is important. Additionally, the crevice corrosion-resistant design is also important. Crevice corrosion-resistant structures should be specified to mitigate IASCC.

Some example cases in which raw water intrusion occurred in reactor coolant systems caused by condenser tube leaks were reported in some BWR plants [3–5]. In such cases, crevice corrosion resulted from impurities such as chloride and sulfate ions in raw water. Especially, chloride is known that it has an adverse effect for crevice corrosion even in high temperature water [6]. Although the instance of raw water intrusion into the coolant is relatively infrequent, evaluating both the possibilities of crevice corrosion generation and the crevice corrosion-resistant design is also important.

However, evaluating all the equipment by disassembling is impractical because the whole cooling system consists of several tens of thousands of parts, and there is also an issue of worker exposure if the inspection is not completely done remotely. Additionally, conditions inside crevices are invisible and inaccessible. Thus, observation of conditions inside a crevice is very difficult especially in a high temperature water environment.

Therefore, a crevice corrosion simulation model was developed by using multiphysics finite element method (FEM) to assess the in-crevice environment, and to determine crevice corrosion-resistant structures. Although the final modeling objective is to evaluate the corrosion environment dependence for the variously shaped crevices, the purpose of this investigation is to confirm feasibility of the multiphysics FEM modeling.

Developing the fundamental crevice corrosion simulation model, as a first step, crevice corrosion phenomena in seawater under atmospheric pressure and room temperature was simulated by a 2-dimensional multiphysics FEM model to precede simulations in high temperature-high purity water. Seawater was chosen as the target solution because a lot of studies have been done and many results have been reported. Although the study mentioned above was incomplete without verification experiments, the result of the feasibility study was described. Although the completed model has yet to be reached, features of the constructed model are reported below to clarify some problems and issues for crevice corrosion simulation model.

Overview of Simulation

The effects of crevice geometry (crevice width and depth) for five corrosive environment parameters (oxygen concentration, electrochemical corrosion potential (ECP), anodic current density, metal ion concentration and pH) in the crevice were evaluated by using the FEM software COMSOL multiphysics (version 4.4). Dependence of each parameter on elapsed time was calculated for up to 100 h.

Generally, crevice corrosion is attributed to a lack of oxidant in a crevice [2]. Common mechanisms of crevice corrosion are listed below.

(1) Dissolved oxygen concentration inside the crevice decreases compared with the outside because oxygen is consumed by a reduction reaction on the crevice inside surface.
(2) An "oxygen concentration cell" is formed between the surfaces inside and outside the crevice.
(3) ECP at the surface inside the crevice decreases, depending on oxygen concentration in the crevice.
(4) A metal dissolution (anodic) site occurs only on the surface inside the crevice. The surface outside the crevice still remains as oxygen reduction reaction (cathodic) site.
(5) Dissolved metal ions are hydrolyzed to form hydroxide and H^+ which lowers the pH in the crevice.

Crevice corrosion is known to occur or propagate when an unstable passivation film forms. A passivation film will be unstable under the condition of a specific low pH inside a crevice due to hydrolysis of the metal ions. This specific low pH is called the depassivation pH. pH inside the crevice is determined by the hydrolysis rate. The hydrolysis rate is mainly determined by the dissolution rate of metal on the surface in the crevice. The metal dissolution rate is determined by the anodic current. The anodic current is determined by the ECP that depends on an anodic polarization curve (Fig. 1). Accordingly, the model was aimed at calculating pH inside a crevice because crevice corrosion generation can be identified by comparing the pH with the depassivation pH of the target material.

The defined shape of the model is shown in Fig. 2. The shape of a solution in the crevice was mainly modeled. Additionally, a 10 × 10 mm square shaped bulk solution part connected with the crevice part was modeled. Crevice geometry was simply defined by two parameters: width w (10, 100, 1000 μm) and depth L (10, 30, 50 mm). Initial conditions of water quality are shown in Table 1. Concentrations of

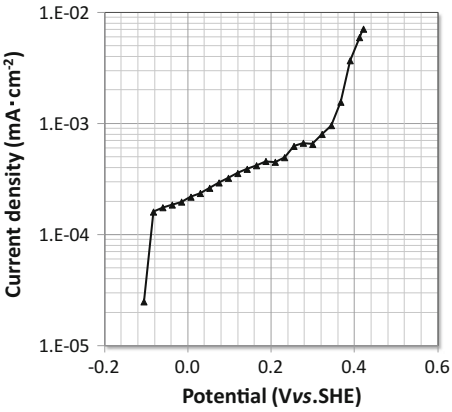

Fig. 1 Anodic polarization curve of type 304 stainless steel measured at 50 °C in diluted simulated seawater as input data

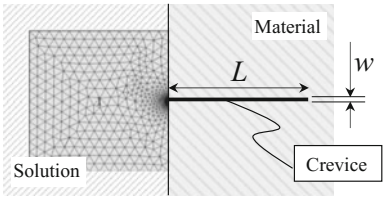

Fig. 2 Defined shape of crevice

Table 1 Initial conditions of water quality

Chemical parameters	Set values	
	Inside the crevice	Outside the crevice
Oxygen concentration (ppm)	8	8
Cl^- concentration ($mol \cdot m^{-3}$)	0	1
Na^+ concentration ($mol \cdot m^{-3}$)	0	1
Fe^{2+} concentration (ppm)	0	0
$Fe(OH)^+$ concentration (ppm)	0	0
H + concentration (M)	10^{-7}	10^{-7}
OH- concentration (M)	10^{-7}	10^{-7}

Cl^-, Na^+ and oxygen on the edges of the solution domain were set at constant 1 mol/kg Na^+, 1 mol/kg Cl^- and 0.031 mol/kg O_2. And, concentrations of H^+ and OH^- on the edges were set at 10^{-7} mol/kg. Since the main purpose of this work was to develop the fundamental model to solve the crevice corrosion problem, those values do not correlate well with any actual facilities.

In order to calculate the decreasing behavior of pH that evolves from lack of oxygen in a crevice, a multiphysics calculation was conducted that included three components of physical phenomena: (1) mass transfer; (2) electrochemical reactions; and (3) chemical reactions. Diffusion and migration were included in the model as component (1). The anodic polarization curve of 304 SS and the cathodic polarization curves of some reduction reaction were used for modeling component (2). Hydrolysis of Fe^{2+} ion was included as component (3).

The pH calculation procedure is explained briefly in the following.

(1) Mass transfer is governed by the Nernst-Plank equation (Eq. 1) and mobility (Eq. 2). In Eq. 1, on the right-hand side, the first term is diffusion, the second term is migration and third term is convection. However, in this work, the third convection term was not included in the model to simulate stagnant condition which is conservative for crevice corrosion due to restrict mass transport.

$$\mathbf{N}_i = -D\nabla c_i - z_i u_{m,i} F c_i \nabla \phi_l + c_i \mathbf{u} \tag{1}$$

$$u_{m,i} = \frac{D_i}{RT} \tag{2}$$

where:

- $\mathbf{N_i}$, flux vector of species i in solution
- D, diffusion coefficient of species
- i; c_i, concentration of species i
- z_i, valence of ion i
- $u_{m,i}$, mobility of species
- i; F, Faraday constant
- $_l$, potential in solution l
- $\mathbf{u}$, velocity vector

(2) The electrochemical characteristics on the boundary between metal and solution are allocated. Cathodic electrochemical reactions of two species (Eqs. 3 and 4) are governed by the Butler-Volmer equation (Eq. 5) and the over potential relationship (Eq. 6). Applied electrochemical constants of reduction reactions are shown in Table 2 [7]. The anodic reaction is defined by the measured anodic polarization curve of 304 SS. In this work, all of anodic current was assumed as Fe dissolution reaction (Eq. 7). Total current density is calculated from the intersecting point of the anodic polarization curve and the total cathodic polarization curve which is evaluated from Eqs. 5 and 6.

$$O_2 + 2H_2O + 4e^- \rightarrow 4OH^- \tag{3}$$

$$2H^+ + 2e^- \rightarrow H_2 \tag{4}$$

$$i = i_0 \left[\frac{c_a}{c_b} \exp\left(\frac{\alpha_a F}{RT} \eta \right) - \frac{c_c}{c_b} \exp\left(-\frac{\alpha_c F}{RT} \eta \right) \right] \tag{5}$$

$$\eta = \phi_M - \phi_l - E_{eq} \tag{6}$$

$$Fe \rightarrow 2Fe^{2+} + 2e^- \tag{7}$$

Table 2 Electrochemical constants of reduction reactions [3]

Electrochemical parameters	Oxygen reduction reaction	Hydrogen ion reduction reaction
Equilibrium potential E_{eq} (V*vs*.SHE)	0.814	−1.03
Exchange current density i_0 (A•m^{-2})	1×10^{-7}	1.1×10^{-2}
Tafel constant b (V•decade^{-1})	−0.13	−0.15
Limiting current Density i_L(A•m^{-2})	2.54×10^{-1}	1930×10^{-pH}

where:

- i_0, exchange current density
- $c_a/c_b/c_c$, concentration of redox species
- α_a/α_c, mass transfer coefficient
- R, gas constant; T, temperature
- η, over potential
- E_{eq}, equilibrium potential
- ϕ_M, potential of metal phase
- ϕ_l, potential of liquid phase

(3) Hydrolysis of metal ion (Eq. 8) is evaluated by the method of Walton et al. [8]. All current is consumed in Fe^{2+} dissolution based on Faraday's law (Eq. 9). H^+ concentration is calculated by assuming the equilibrium constant K_1 is 1.63×10^{-7}. pH is calculated from $[H^+]$ by Eq. 10.

$$Fe^{2+} + H_2O \rightarrow Fe(OH)^+ + H^+ \tag{8}$$

$$M_{dis} = i_{corr} \cdot (z \cdot F)^{-1} \tag{9}$$

$$pH = -\log([H^+]) \tag{10}$$

In addition to the above, the current conservation law, the species conservation law and the Laplace equation are considered. The three components (1), (2) and (3) of the phenomena are included in the multiphysics calculation as mentioned above. All variables are calculated compatibly at all nodes.

Results and Discussion

The pH dependence on elapsed time was calculated for all the combinations of crevice depth L and width w. Representative calculation examples of each parameter on the surface in the crevice at w = 10 um, L = 50 mm are shown in Fig. 3a–e. The horizontal axis indicates the distance toward the depth direction from the crevice mouth. Oxygen concentration decreased as time lapsed. No large difference of oxygen concentration dependence on location was observed. ECP also declined in conjunction with the decrease in oxygen concentration. Anodic current density which was determined by the anodic polarization curve and cathodic current rise from the oxygen reduction reaction was very low after 1000 s had elapsed. The Fe^{2+} concentration gradually increased with the lapse of time. The pH decreased as more Fe^{2+} generated in the solution. After 100 s had elapsed, pH had decreased in the entire crevice.

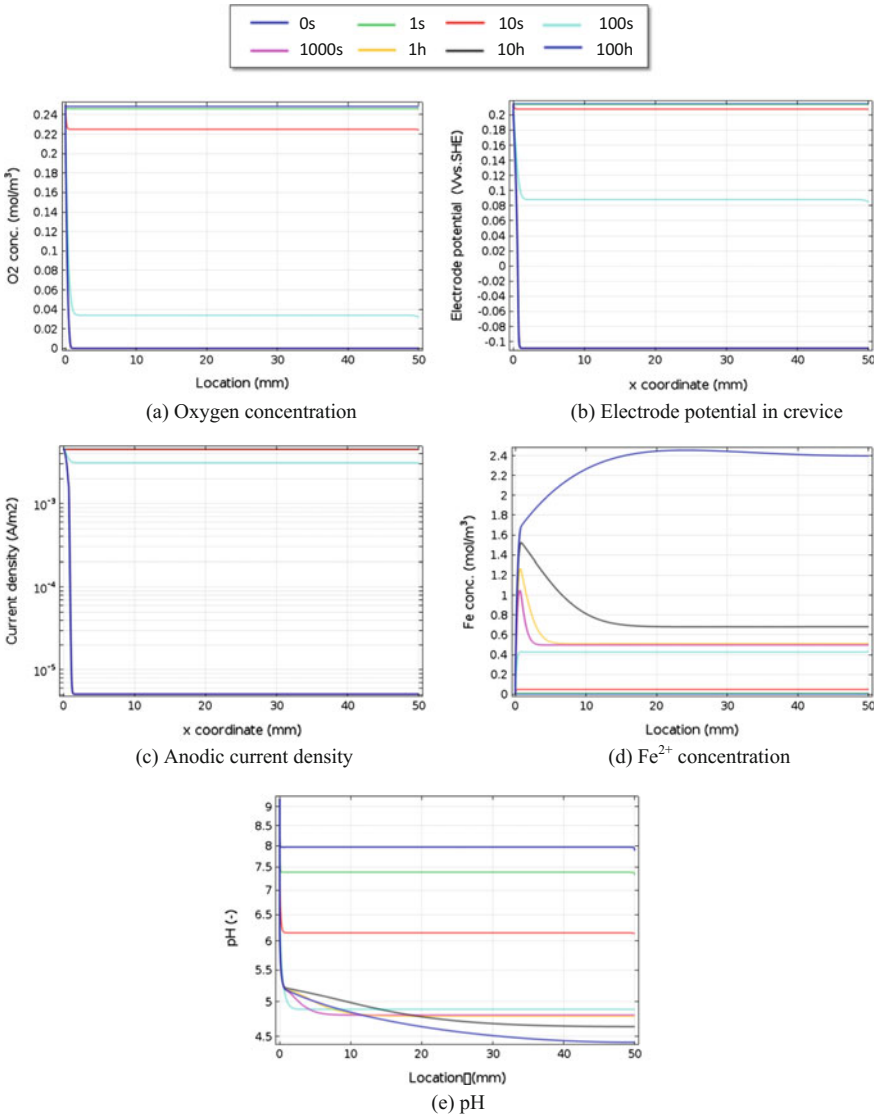

(a) Oxygen concentration

(b) Electrode potential in crevice

(c) Anodic current density

(d) Fe^{2+} concentration

(e) pH

Fig. 3 Calculation examples of each parameter on the surface in a crevice at w = 10 μm, L = 50 mm

Likewise, all calculated pH values in the crevice decreased with time for all crevice geometries (crevice depth L = 10–50 mm and crevice width w = 0.01–1 mm) (Fig. 4a–i). The lowest pH was found at the deepest position in the crevice for all cases. It seemed there was only a negligible difference in pH where the depth L was longer than the specific depth which was dependent on w. pH values had their

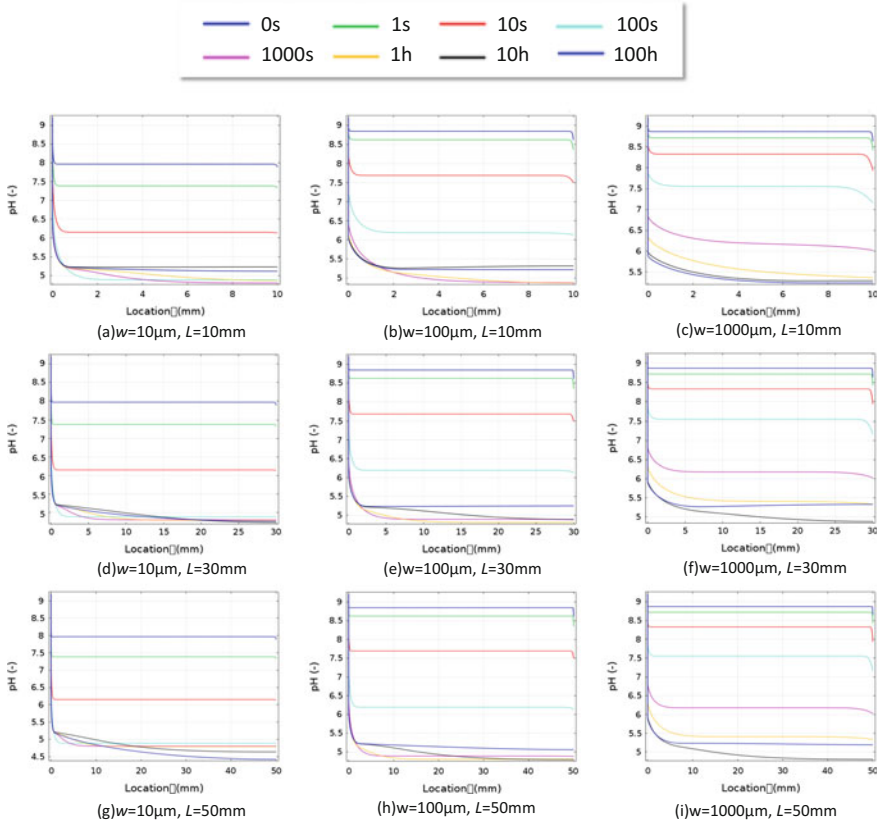

Fig. 4 Calculated pH values against elapsed time for each geometries

lowest value at the point of approximately 10 mm away from the outer edge (crevice mouth) for the same crevice width, *w*.

It was confirmed that the pH decreasing behavior in the crevice was able to be predicted quantitatively by use of the multiphysics FEM model. However, the decrease in the pH value was insufficient compared with some literature data which were obtained experimentally. Experimental studies for pH in crevices have been conducted since the 1970s using an atypical electrochemical cell which was separated into the anodic chamber and the cathodic chamber via a porous glass membrane. The solution in the anodic chamber (anolyte) was analyzed chemically after electrolyzing stainless steel [9]. In recent years, in situ measurement of pH in the crevice was performed using a sensing plate which varied in color tone with the pH change [10]. Adachi et al. [11] measured some anolytes after electrolyzing a 304 SS electrode in 5% NaCl solution. The pH decreased from pH 5.5 to pH 3 after electrolyzing the electrode at 353 K for 480 h, and it decreased from pH 5.5 to pH 2.5 after electrolyzing it at 313 K for 10 days.

The pH in the crevice varied with application of an electric charge. The pH of anolyte (for a quasi-crevice solution) decreased from pH 5 to pH 2 after applying a charge of 10 C/cm^3 to a 304 SS electrode in 0.28 N NaCl solution [12]. In addition, the pH in a crevice formed by 316L SS and asbestos decreased to pH 1.56 in 0.5 N NaCl solution at 303 K [9].

The conditions of all the literature studies differed from those of this work in terms of applying a potential to a stainless steel electrode, and all pH values in crevices mentioned above were considerably lower than the calculated pH in this work (minimum pH 4.4). Crevice corrosion occurred when the pH in the crevice deteriorated below the specific depassivation pH (pH_{dp}) which depends on material and solution. pH_{dp} of 304 SS was reported as pH 1.5 in 3% NaCl solution [13]. pH_{dp} was also reported to be a function of Cr and Mo concentrations for Fe-Cr (11–20%)-Mo(0–2%) alloy (Eq. 11) [14].

$$pH_{dp} = 4.98 - 0.13[Cr] - 0.43[Mo]. \tag{11}$$

304 SS contains 18–20%Cr and 0%Mo; then, pH_{dp} of 304 SS was calculated to be 2.6–3.4 by Eq. 11. The calculated pH in this work was inadequate to reach pH_{dp}. It seemed that the multiple-stage hydrolysis reaction and hydrolysis reaction of Cr shown below are also required.

$$Fe^{3+} + H_2O = Fe(OH)^{2+} + H^+ \tag{12}$$

$$Fe(OH)^{2+} + H_2O = Fe(OH)_2^+ + H^+ \tag{13}$$

$$Fe(OH)_2^+ + H_2O = Fe(OH)_3 + H^+ \tag{14}$$

$$Cr^{3+} + H_2O = CrOH^{2+} + H^+ \,(\text{at pH} > 4) \tag{15}$$

$$Cr^{3+} + 3H_2O = Cr(OH)_3 + 3H^+ \,(\text{at pH} < 4) \tag{16}$$

The results can be summarized as follows. The drop of pH values in the crevice was confirmed by the concentration of H^+ which was generated by the hydrolysis reaction along with corrosion of metal. However, the calculated pH in the crevice did not correspond to the pH_{dp} values of 304 SS (approximately pH 2) reported in some literature [9–13]. It was concluded that the multiple-stage hydrolysis reaction of Fe and the hydrolysis reaction of Cr were also needed. More specifically, in order to increase H^+ by hydrolysis of Fe ion, it may be that the activated (high current density) anodic polarization curve which was measured in the lower pH solution was also used as electrochemical input data. These options need to be considered in future work.

Conclusions

The fundamental crevice corrosion simulation model using FEM was developed to enhance corrosion control design for BWR in-reactor materials such as control rods. Crevice geometries which had mitigated crevice corrosion as the cause of cracking were studied. An assessment technique by corrosion simulation modeling was considered. The final objective of the modeling will be to evaluate the pH in variously shaped crevices as a representative factor of corrosive environment of crevice corrosion.

The multiphysics FEM model which include electrochemical reactions on the surface, mass transfer and hydrolysis of corroded Fe ion was employed. The time-dependent pH distributions in the crevice with various crevice widths, w (w = 10–1000 μm) and crevice depths, L (L = 10–50 mm) were determined. The target material was 304 SS, and the target environment was air saturated seawater (as $[Cl^-]$ = 1 N, $[O_2]$ = 8 ppm). This allowed comparison with literature data.

Calculated pH in the crevice decreased with time for all crevice geometries. It was confirmed that the fundamental crevice corrosion simulation model could qualitatively reproduce the actual corrosion phenomena at the point of pH decline to pH 4.4 by hydrolysis of Fe ion. The lowest pH was found at the deepest position in the crevice for all cases. However, the positions L where pH sharply decreased were at a shallow region within a few millimeters from the crevice mouth. The variation of pH values was less in the deep region than in the shallow region. It seemed there was only a negligible difference in pH where the depth, L was longer than the specific depth which depended on w. The larger w was, the more gradual the pH in the deep direction decreased. Additionally, the larger w was, the less the pH decreased. However, predicted pH decrease amounts were insufficient compared with the pH values which had been reported in some experiments that had measured in-crevice pH of 304 SS (pH $\sim$2). The multiple-stage hydrolysis reaction of Fe and Cr were also needed. In other words, in order to increase H^+ by hydrolysis of Fe ion, the activated anodic polarization curve which was measured in a lower pH solution might also be needed.

References

1. S. Ooki, et al., The investigation of the damages of irradiated 316L stainless steel used for the hafnium plate type of control rods in BWR plants, Proceedings of 14th International Conference on Environmental Degradation of Materials in Nuclear Power Systems, Virginia Beach, VA, 23–27 August 2009, p. 1259
2. A. Watanabe et al., Effects of local radiolysis and geometric parameters on intergranular attack caused by crevice corrosion. J. Nucl. Sci. and Technol. **52**, 651 (2015)
3. B.M. Gordon, S.E. Garcia, Effect of two impurities and zinc on stress corrosion cracking, Nuclear Plant Chemistry Conference, CNS, October 4–7, 2010, Quebec City, Canada (2010)
4. B. Cheng, Chemistry Monitoring and Control for Fuel Reliability, EPRI technical report #1009731 (2004)

5. Y. Wada et al., Effects of seawater components on radiolysis of water at elevated temperature and subsequent integrity of fuel materials. J. of Nucl. Sci. and Technol. **53**, 809 (2016)
6. M. Tachibana et al., Effects of gamma-ray irradiation on crevice corrosion repassivation potential of stainless steel in high temperature diluted simulated seawater. J. of Nucl. Sci. and Technol. **53**, 981 (2016)
7. Q&A on Metallic Corrosion Electrochemistry, Edited by Japan Society of Corrosion Engineering, Maruzen (2002). [in Japanese]
8. J.C. Walton et al., A numerical model of crevice corrosion for passive and active metals. Corros. Sci. **38**, 7 (1996)
9. M. Yamabe, et al., Influence of ion permselective property of gasket material on crevice corrosion of stainless steel. Boshoku-Gijutsu (Corros. Eng.), **23**, 85 (1974). [in Japanese]
10. T. Kaji et al., Visualization of pH and pCl distributions: initiation and propagation criteria for crevice corrosion of stainless steel. J. Electrochem. Soc. **159**, C289 (2012)
11. T. Adachi et al., The charge of pH in crevice due to crevice corrosion of stainless steels. Iron Steel Inst. Jpn **63**, 614 (1977). [in Japanese]
12. M. Onoyama, et al., Concentration and corrosiveness of anolyte within crevice of stainless steels in hot water environment. Boshoku-Gijutsu (Corros. Eng.), **28**, 532 (1979). [in Japanese]
13. N. Sato, Fundamental of Corrosion and Anticorrosion—Electrochemistry on Metal Surface—(IV). Proc. Jpn Inst. Met. Mater. **20**, 935 (1981). [in Japanese]
14. M. Onoyama, M. Tsuji, K. Shitani, Concentration and corrosiveness of anolyte within crevice of stainless steels in hot water environment, Boshoku-Gijutsu (Corros. Eng.), **28**, 532 (1979). [in Japanese]

In Situ Electrochemical Study on Crevice Environment of Stainless Steel in High Temperature Water

Y. Soma, C. Kato and F. Ueno

Abstract In situ electrochemical impedance spectroscopy measurement within crevice of stainless steel in 288 °C water has been conducted to analyze crevice water chemistry. Small sensors ($\varphi \sim 250\,\mu m$) measured local solution electrical conductivity κ_{crev}, polarization resistance and electrochemical corrosion potential. Real-time response of the κ_{crev} as functions of bulk water conductivity and dissolved oxygen (DO) concentration has been quantitatively analyzed. The κ_{crev} differ more than an order of magnitude depending on the oxygen potential inside the crevice. The κ_{crev} increased with addition of small amount of bulk DO (e.g. 30 ppb). The maximum κ_{crev} was observed with DO of 32,000 ppb and became more than 100 times higher than that of bulk water. The effect of geometrical factors on the crevice environment was also found to play an important role in the water chemistry inside.

Keywords High temperature water · BWR · Stainless steel · Crevice water chemistry · In situ measurement

Introduction

Effect of bulk water properties such as dissolved oxygen (DO) concentration and impurities on stress corrosion cracking (SCC) behavior of stainless steels (SS) have been widely studied [1–8]. Trace amounts of DO and anionic impurities in the bulk water affect can significantly affect the crack growth [2, 3, 5, 8]. Such behaviors are conventionally explained in terms of "crack/crevice chemistry" as reviewed in the

18th International Conference on Environmental Degradation of Materials in Nuclear Power Systems—Water Reactors, August 13–17, 2017, Marriott Portland Downtown Waterfront Portland, Oregon, USA.

Y. Soma (✉) · C. Kato · F. Ueno
Japan Atomic Energy Agency (JAEA), Tokai-Mura, Naka-Gun, Ibaraki-Ken, Japan
e-mail: soma.yasutaka@jaea.go.jp

J.H. Jackson et al. (eds.), *Proceedings of the 18th International Conference on Environmental Degradation of Materials in Nuclear Power Systems – Water Reactors*, The Minerals, Metals & Materials Series, https://doi.org/10.1007/978-3-319-68454-3_40

literature [4, 9]. However, relatively limited data is available on the relationship between water chemistry in bulk environment and that of the occluded region.

In the present study, in situ electrochemical measurements were carried out inside three different types of crevice of SS316 specimens to characterize the effect of bulk water chemistry and geometrical factors on the crevice water chemistry.

Experimental

Preparation of Crevice Specimen with Sensors

Type-316L austenitic stainless steel (solution annealed at 1050 °C for 30 min, water-quenched) was used for this study. The chemical composition of the specimen material is shown in Table 1.

Figure 1 illustrates crevice specimens with sensors for the electrochemical measurement. Three types of specimens were prepared for the measurement. All specimens were composed of a couple of the SS plates with the electrochemical sensors. Each specimen has their own features as follows:

Type I: This specimen has a rectangular shaped crevice opening to bulk water at one end. This geometry enables us to investigate the crevice chemistry with quasi-one-dimensional diffusion behavior. The sensors (I-A, I-B, I-C) are positioned at 3, 12, and 21 mm (in the example shown in Fig. 6) or 2, 5, and 8 mm (in the example shown in Fig. 11) from the crevice mouth. The crevice gap was 16 μm under all sensors.

Type II: This specimen has a wedge-like shaped crevice composed of two SS plates with a 100 μm thick SS spacer inserted between the two plates at one end. Three sensors (II-A, II-B, II-C) are positioned at 11, 14, and 17 mm from the end where the two plates are in contact. The crevice gap at the location of each sensor was approximately 4.4, 9.1, and 25 μm for II-A, II-B, and II-C, respectively. These values were determined by post-test measurements on the cross section of the assembly imbedded in resin. This geometry is expected to enhance accumulation of impurities at the crevice tip.

Type III: This specimen is composed of a couple of symmetrical plate with the electrochemical sensor. The sensor faces each other with a distance of 200 μm by inserting 200 μm-thick SS plates at both ends of the specimen plate. Our previous study showed that crevice gap of 200 μm would not show remarkable crevice effect [10] so we used this setting to analyze the bulk water chemistry.

Table 1 Chemical composition of specimen material (wt%)

C	Si	Mn	P	S	Ni	Cr	Mo	Fe
0.008	0.043	0.083	0.023	0.001	12.55	17.54	2.11	Bal.

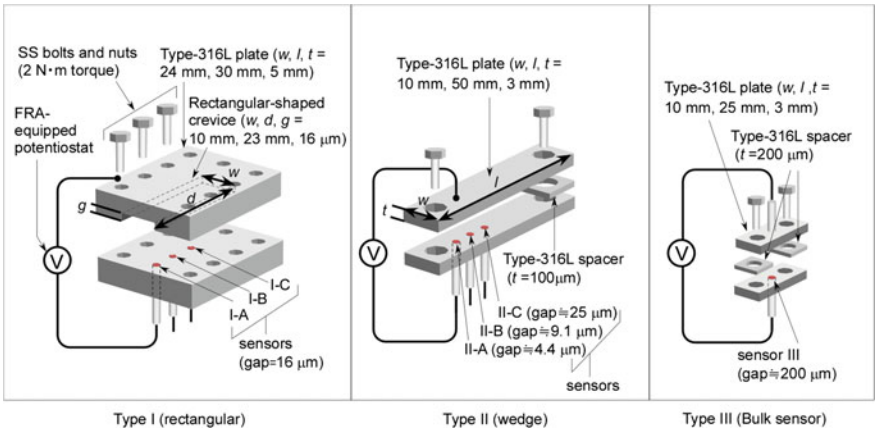

Fig. 1 Crevice specimens with sensors for the electrochemical measurement

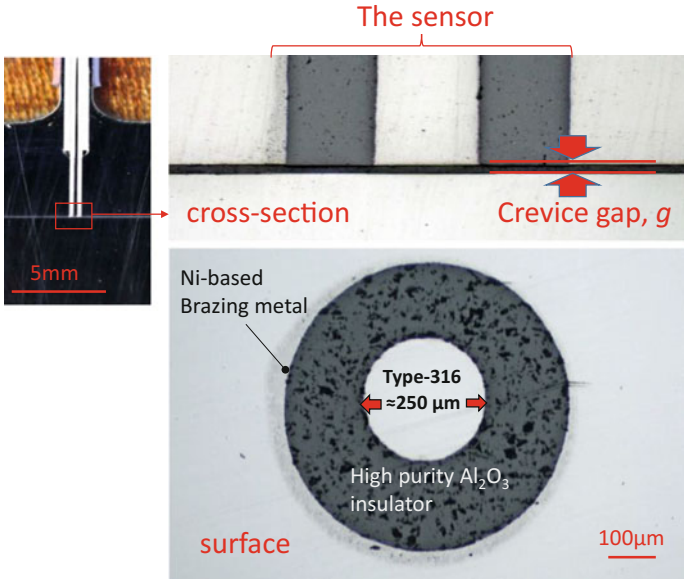

Fig. 2 Optical images of the cross-section and the surface of the sensor used for the in-situ electrochemical measurement

Figure 2 shows the optical images of the cross-section and the surface of the sensor. The sensor is composed of a Type 316 SS core electrode. The surrounding alumina insulator was imbedded into the crevice specimen by means of brazing using a Ni-based filler material. The sensor surface was polished with 1 μm diamond paste to achieve flat and fine surface finish of the crevice as shown in Fig. 2. Details of the sensor were described in a previous paper [10].

Electrochemical Measurement

Alternating current (AC) was applied between the sensor electrode-specimen plate (for Type-I and II) or sensor electrode-sensor electrode (for Type-III) in the specimens. The impedance spectrum was obtained by two electrode modes with a AC amplitude of 20 mV (peak-to-peak) and a frequency range of 10^{-2}–10^{5} Hz. Measurements were carried out every hour. When the impedance measurement was off, the potential was measured by using an electrometer and an external pressure balanced reference electrode (Ag/AgCl, 0.01 M KCl). The raw potential values were converted into Standard hydrogen electrode (SHE) values at 288 °C. Unless otherwise stated, potentials in this study will be given with respect to the SHE scale.

Exposure Test to High-Temperature Water

The crevice specimens were immersed in water at 288 °C and 8 MPa. High temperature water loop system equipped with autoclave (Material: Type-316 SS, Capacity: 1.8 L, Flow rate: 5 L h^{-1}) was used. To purify the water in the loop, a coupled ion-exchange resin and a microfilter were used and the conductivity of the feed water was maintained at 0.060 ± 0.001 μS cm^{-1} throughout the test. Reagent grade Na_2SO_4 dissolved into high purity water was injected to the water conditioning tank to increase the water conductivity in the loop level when needed. To control DO concentration of the feed water, high purity N_2, O_2, and their mixture were injected into the water conditioning tank.

Analysis of Surface Oxide

Surface oxide was analyzed using laser Raman spectroscopy with a beam diameter of approximately 30 μm. The specimens were then imbedded into resin, cut, and polished with #4000 silicon carbide paper to observe the cross section of the surface oxide using scanning electron microscopy (SEM, JEOL JSM-7000F). Due to the resolution of the SEM, measured oxide thickness contains error of several tens of nm.

Results and Discussion

Surface and Electrochemical Analysis with DO of 32 Ppm

Figure 3a shows Type-I crevice specimen after 100 h exposure in the 288 °C pure water (inlet conductivity was 0.060 μS·cm^{-1}) with 32 ppm of DO. Figure 3b shows

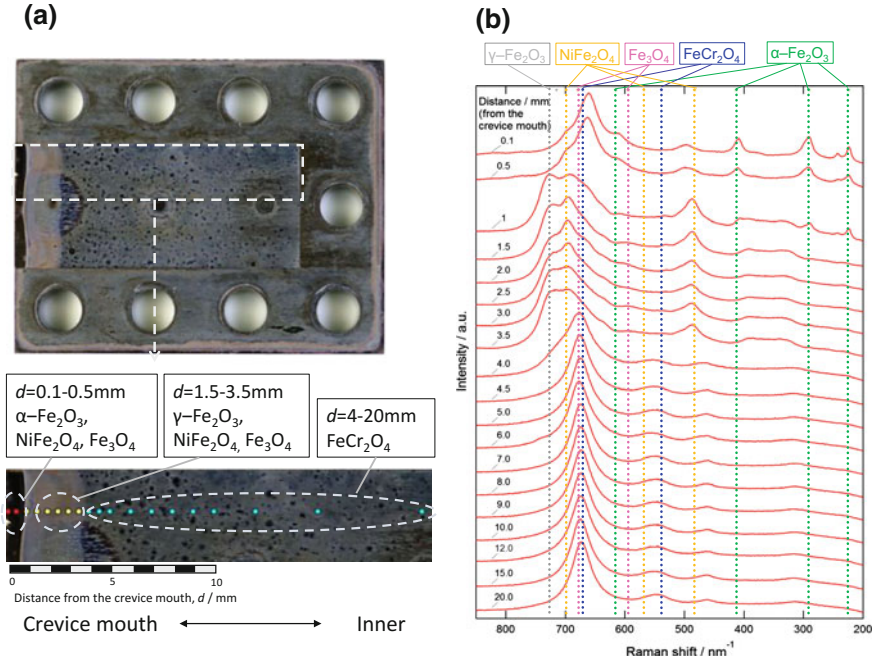

Fig. 3 **a** The crevice specimen (Type-I) after 100 h immersion in 288 °C pure water with DO concentration of 32 ppm. **b** Raman spectra of the surface oxide

Raman spectra measured at different *d* (distance from the crevice mouth) positions. In the figure, reference peaks of α-Fe_2O_3, Fe_3O_4, $NiFe_2O_4$, $FeCr_2O_4$ [11] and γ-Fe_2O_3 [12] were referred to the literature. At d = 0.1–0.5 mm, $NiFe_2O_4$, Fe_3O_4, and α-Fe_2O_3 were detected and this was almost the same as to the bulk surface. At d = 1.5–3.5 mm, $NiFe_2O_4$ and Fe_3O_4 were still detected but α-Fe_2O_3 disappeared and was replaced by γ-Fe_2O_3. At d > 4.0 mm, only a broad peak estimated to be Fe_3O_4 or $FeCr_2O_4$ was observed. Referring to the previous study [13], the oxide was determined as $FeCr_2O_4$. Iron oxides are known for being very sensitive to oxygen potential [14]. γ-Fe_2O_3 does not form in reductive condition (cf. N_2–4% H_2) and began to form when DO is more than 4 ppb. α-Fe_2O_3 starts to occur only after DO reaches 8 ppb [14]. As a result, the findings in this experiment suggest that oxygen potential decreases with increasing distance from the crevice mouth.

Figure 4 shows the result of cross-sectional analysis of surface oxide along the longitudinal direction of the same Type-I specimen discussed above. The surface oxide layer exhibit double-layer appearance with a relatively compact inner layer and an outer layer of precipitated oxide as reported elsewhere [15]. As shown in the figure, the inner oxide layer was approximately 100 nm thick and almost independent of *d* while the outer layer of precipitated oxide only appears in the range of

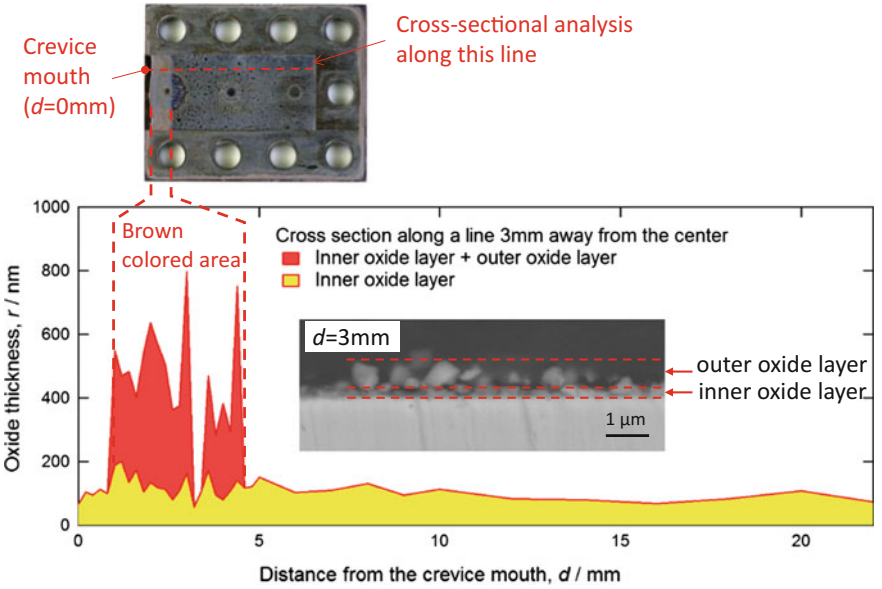

Fig. 4 Thickness of the oxide layer on the Type-I specimen (also shown in Figs. 2 and 3)

$1 < d < 4$ mm. This region was consistent with the brown colored area shown in the embedded photo.

Figure 5 shows the typical impedance spectra of sensors I-A, I-B, and I-C after 80 h of immersion in 288 °C water with DO of 32 ppm. While the impedance $|Z|$ differs significantly between the sensors, they all showed resistor-capacitor type impedance spectra. In this study, we defined electrical conductivity of crevice solution, κ_{crev}, [16] and polarization resistance, R_p by Eqs. (1) and (2), respectively.

$$\kappa_{crev} = \left(|Z_{10^3 Hz}| * A\right)/g)^{-1} \quad (1)$$

$$R_p = |Z_{10^{-2} Hz}| * A \quad (2)$$

A Surface area (cm)
g Crevice gap (cm)

Figure 6 shows the change in κ_{crev} and R_p in Type-I crevice as a function of time. From the beginning of the exposure to ca. 50 h, all three sensors showed similar κ_{crev} values of 600 ~ 1000 μS·cm^{-1}. After 50 h, only the κ_{crev} of the sensor I-A began to decrease and became ca. 20 μS·cm^{-1} at 100 h. The R_p of all sensors decreased as time elapsed till 70 h after which only the R_p of the sensor I-A drastically increased from 1.1 (at 72 h) to 372 Ω·cm^2 (at 100 h). As shown in the inserted photo (sensor equipped specimen after the test), brown colored area which suggest γ-Fe_2O_3 containing precipitation (see Fig. 3) has slightly crossed the sensor

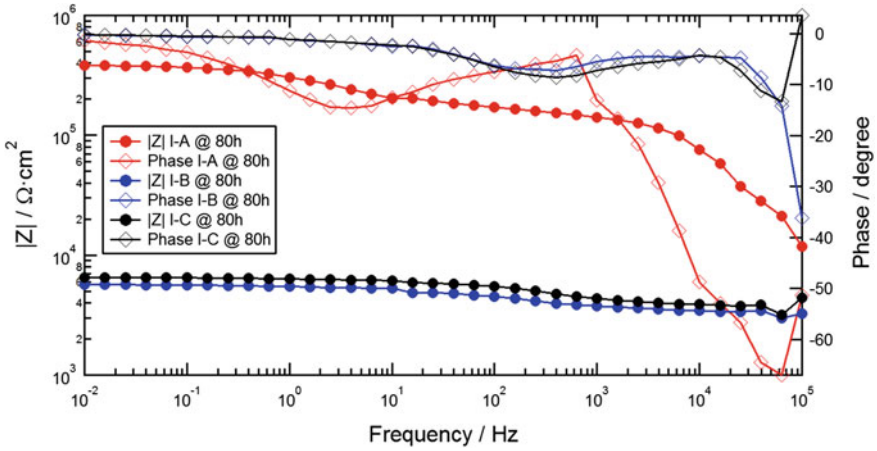

Fig. 5 Typical impedance spectra of the sensors in Type-I crevice specimen after 80 h immersion in 288 °C pure water with DO of 32 ppm

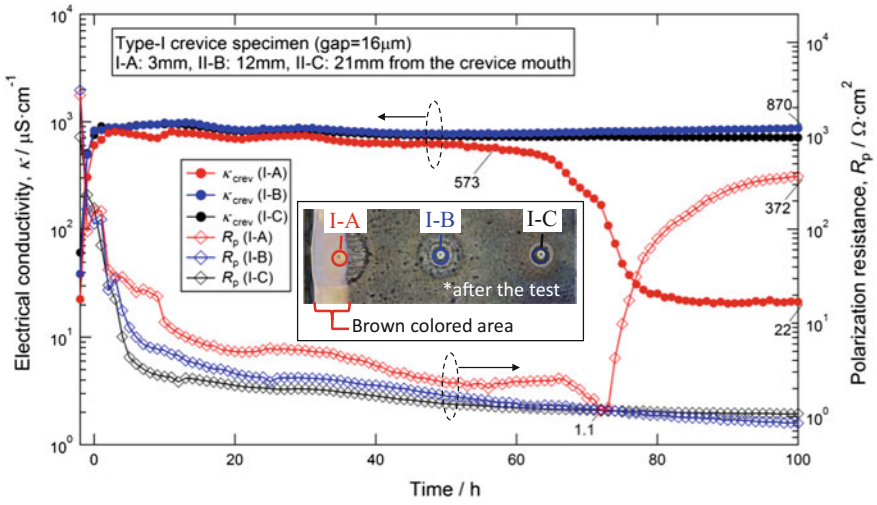

Fig. 6 Change in κ_{crev} and R_p as a function of time within the Type-I crevice immersed in 288 °C pure water with DO concentration of 32 ppm

I-A. This indicates that ingression of oxygen enlarged the brown colored area and reduced the solution conductivity. This behavior can be explained from the thermodynamic viewpoint as follows. Hydrolysis reaction of Fe^{2+} and equilibrium concentration of Fe^{2+} can be given by Eqs. (3) and (4), respectively [15].

$$3Fe^{2+} + 4H_2O = Fe_3O_4 + 8H^+ + 2e \quad (3)$$

$$\log(C_{Fe^{2+}}) = 4.51 - 5.99\,E - 2.66\,pH \quad (4)$$

$C_{Fe^{2+}}$ Equilibrium concentration of Fe^{2+} ($mol \cdot kg^{-1}$)
E Potential (V)

Equation (4) suggests that $C_{Fe^{2+}}$ decrease exponentially with increasing potential. The oxygen intrusion caused potential increase followed by precipitation of Fe^{2+} as oxide. The decrease of Fe^{2+} resulted in low κ_{crev}. On the other hand, quantitative interpretation of R_p is difficult because of the following reason: R_p can be related to corrosion current, I_{corr}, by Eq. (5).

$$I_{corr} = B/R_p \quad (5)$$

Provided that B [constant (V)] being 0.26 V [17], the R_p of the sensor I-A of 1.1 $\Omega \cdot cm^2$ at 72 h corresponds to I_{corr} of 0.23 $A \cdot cm^{-2}$. If we regard thickness of the inner oxide layer in Fig. 4 as corrosion loss, the oxide growth rate (100 nm 100 h^{-1}) corresponds to approximately 1 $\mu A \cdot cm^{-2}$ (using faraday's law assuming that substrate is Fe) in corrosion current. The I_{corr} calculated by the Eq. (5) was far higher than that of oxide growth. Therefore, R_p is considered to partly reflect electrochemical reaction (e.g. oxidation/reduction reaction of surface oxide) but deviate from actual corrosion/oxidation rate of the substrate [18].

Figure 7 summarize the result of surface analysis and the electrochemical measurement. Crevice environment can be divided into three regions. Region i (near the crevice mouth) featuring α-Fe_2O_3 containing surface oxide similar to bulk surface oxide and low conductivity of <10 $\mu S \cdot cm^{-1}$ (will be discussed in Section "Influence of Na_2SO_4 and DO Transients"). Region ii exhibited moderate conductivity and precipitated outer oxides containing γ-Fe_2O_3, and can be regarded as the transition region. Region iii showed relatively high conductivity due to low potential and high solubility of Fe^{2+}. Absence of Fe_2O_3 indicates that this region is oxygen-depleted.

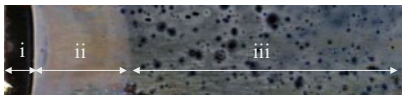

Region	i	ii	iii
κ_{crev} ($\mu S \cdot cm^{-1}$)	<10	moderate	>100
Surface oxide	α-Fe_2O_3, $NiFe_2O_4$, Fe_3O_4	γ-Fe_2O_3, $NiFe_2O_4$, Fe_3O_4	$FeCr_2O_4$

Fig. 7 Summary of K_{crev} and surface oxide within the Type-I crevice specimen after 100 h immersion to 288 °C pure water with DO concentration of 32 ppm

As shown above, no localized corrosion have occurred in the Type-I crevice while the same environment caused intergranular corrosion in the Type-II crevice [10]. This fact suggest that reducing the crevice gap ($\partial g/\partial d < 0$) has a strong effect on the crevice environment.

Influence of DO Transients

Figure 8 shows κ_{crev} and potential response as a function of increasing DO levels in the Type-II crevice immersed in 288 °C pure water (inlet water conductivity was fixed at 0.060 μS·cm^{-1}). κ_{crev} was relatively high at the initial few hours then all sensors stabilized at 50 ~ 75 μS·cm^{-1} under the deoxygenated operation for the first 48 h. Changing the DO level from 2 ~ 3 to 50 ppb increased the potential and κ_{crev}. κ_{crev} (II-A) peaked at ~120 h while κ_{crev} (II-C) showed a delayed response. From 120 to 155 h, the three sensors showed almost the same κ_{crev}, but κ_{crev} (II-C) began to decrease at 156 h followed by κ_{crev} (II-B) at 160 h. On the contrary, κ_{crev} (II-A) showed the maximum value of 1550 μS·cm^{-1} at 178 h and maintained >1000 μS·cm^{-1} during the highest DO operation. At 190 h N_2 injection was started. This caused a decrease in κ_{crev} (II-A) while that of II-B and II-C showed the opposite behavior. The increase in κ_{crev} with increasing DO is consistent with the conventional theory. Different response between the sensors II-A and II-C suggest that deeper crevice with smaller gap can produce strong crevice effect. It was difficult to associate the potential shift with those of κ_{crev} because the sensor II-A

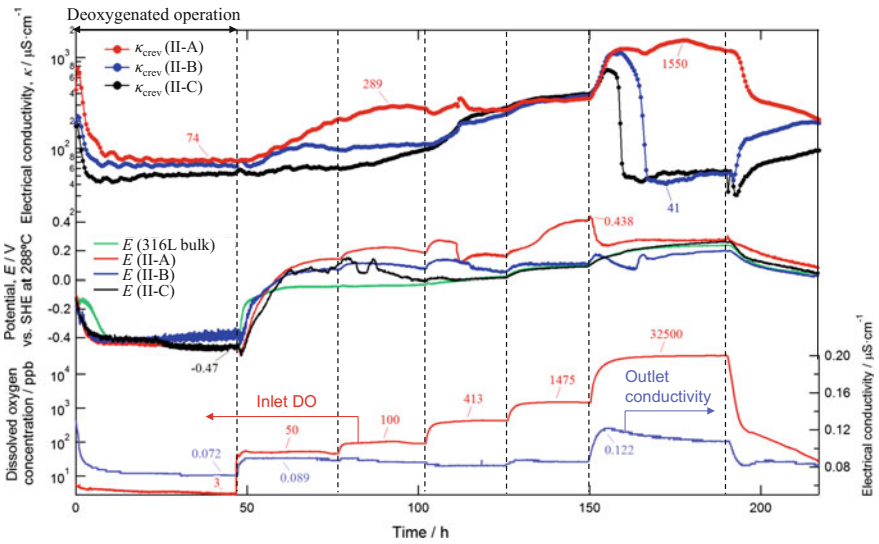

Fig. 8 The κ_{crev} and potential response (Type-II crevice) under stepwise increase of DO concentration in 288 °C water (inlet conductivity was fixed at 0.06 μS·cm^{-1})

locate in the deepest position inside the crevice showed highest value under the existence of oxygen. This result contradicts to the conventional "crack chemistry" mechanism in which anions migrate to the inside of the crevice under a decreasing potential gradient. Even the sensors II-B and C showed somewhat higher potentials compared to that of the Type-316L plate exposed to the bulk water. In addition, the highest value of potential found on the sensor II-A cannot be achieved in normal BWR operation condition and is inconsistent with the experimental facts shown by Andresen [4]. The potential value measured in this method seemed to include significant error.

Influence of Na_2SO_4 and DO Transients

Figure 9 shows κ_{crev} response with changing bulk water conductivity (by addition of Na_2SO_4) and DO levels in the Type-II crevice.

Figure 10 shows the electrical conductivity of solution as a function of Na_2SO_4 concentration calculated by a simulation software [19]. In Fig. 9, at the initial deaerated stage, κ_{crev} (II-A) was relatively low (30 ~ 40 μS·cm^{-1}) and that of κ_{crev} (III) was 5 ~ 6 μS·cm^{-1}. When Na_2SO_4 was injected at 70 h, both the outlet conductivity and κ_{crev} (III) responded with minor delay. As shown in Fig. 10, κ_{crev} (III) before (5 ~ 6 μS·cm^{-1}) and after (23 ~ 24 μS·cm^{-1}) the addition of Na_2SO_4 was similar to that of the bulk water at 288 °C estimated using the simulation software. It is therefore assumed that the sensor III worked as bulk water sensor. On

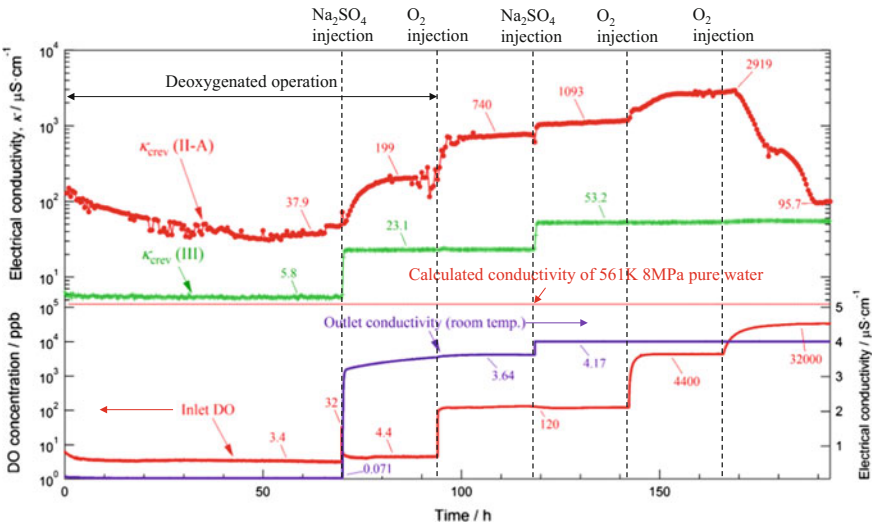

Fig. 9 The κ_{crev} response (Type-II and III crevices) with injection of Na_2SO_4 and O_2 in 288 °C water

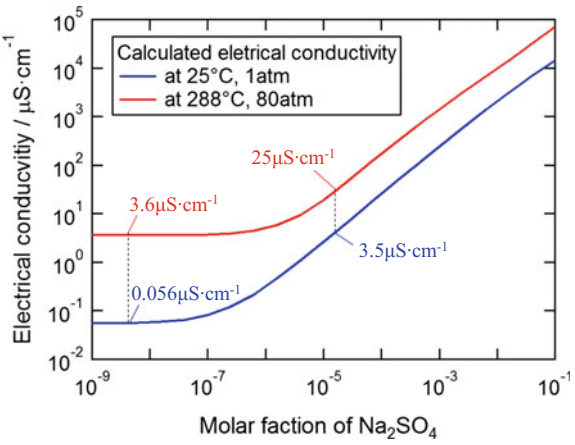

Fig. 10 Electrical conductivity versus Na_2SO_4 concentration (calculated by a simulation software)

the other hand, after the first addition of Na_2SO_4, κ_{crev} (II-A) gradually increased and took around 13 h to become saturated at 200 $\mu S \cdot cm^{-1}$. The addition of Na_2SO_4 caused slight increase in DO (maximum 32 ppb in a moment) and might have affected the κ_{crev} increase as will be discussed later. O_2 level was increased from 4.4 to 120 ppb at 94 h. This caused an increase in κ_{crev} (II-A) from 200 to 740 $\mu S \cdot cm^{-1}$ but κ_{crev} (III) was unchanged. The different response of κ_{crev} (II-A) and κ_{crev} (III) to the addition of O_2 clearly shows that only the crevice geometry of sensor II-A is under the "crevice effect". This result also supports that gradient of oxygen potential attribute to accumulation of anionic impurities inside the crevice. Similar trend was shown following the cycle of injection of Na_2SO_4 and increase in DO level. The highest DO of 32,000 ppb caused drop of κ_{crev} (II-A) similar to the previous cases.

Figure 11 shows κ_{crev} response with changing bulk water conductivity and DO levels in Type-I crevice. In this case, the sensors I-A, I-B, and I-C were positioned at 2, 5, and 8 mm from the crevice opening, respectively. In the figure, data in the first 24 h was lost due to system error and the recording began at 24 h. There are some unknown oscillations in all curves. During the first deoxygenated operation, $\log(\kappa_{crev})$ of all sensors decreased almost linearly with time and the Na_2SO_4 injection at 48 h caused no change in κ_{crev}. This suggest that in the deoxygenated stage, initially dissolved Fe ions flow out as no force exist to accumulate impurities. At 72 h, increasing the DO level to 30 ppb caused an increase in κ_{crev} on all sensors. No remarkable difference of response time was found among the sensors. The following response of the κ_{crev} to Na_2SO_4 and O_2 injection showed similar trend to that of the Type-II specimen but in this case, the increase in κ_{crev} became saturated after the DO level reached 300 ppb. In addition, the DO-assisted increase in κ_{crev} occurred at the location of the sensor I-A just 2 mm from the crevice opening to the sensor I-C located 8 mm away. Along with the findings in the Type-II specimen, the results suggest that narrow crevice effectively suppress oxygen ingress while migration assisted accumulation of impurities is relatively fast and affects deep inside the crevice [4].

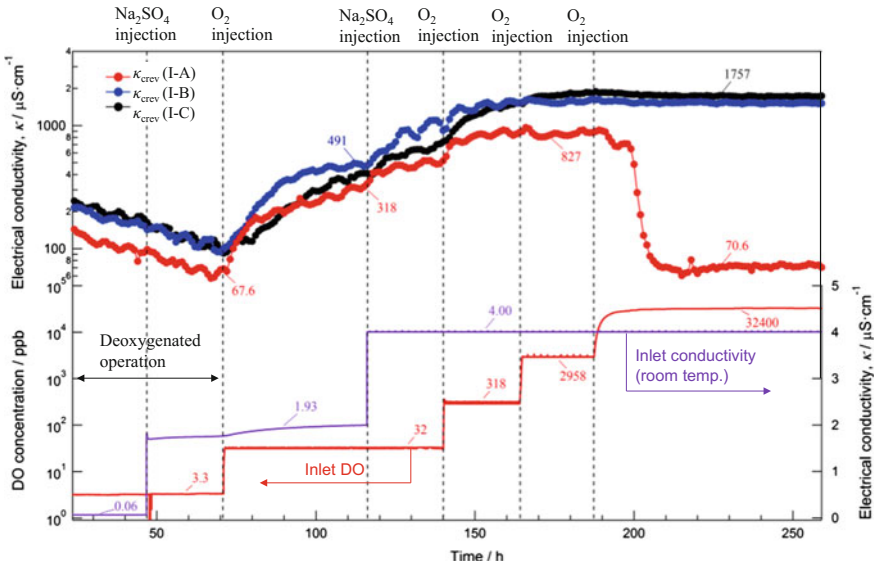

Fig. 11 The κ_{crev} response (Type-I crevice) with injection of Na_2SO_4 and O_2 in 288 °C water

Conclusions

Water chemistry in fine crevices (gap <100 μm) of stainless steel in 288 °C water was quantitatively studied by using electrical conductivity of the crevice solution, κ_{crev}, as the major index describing the crevice environment. The following conclusions were obtained:

(1) Within the crevice immersed in the solution with 32 ppm of DO, gradient of oxygen potential was formed. The κ_{crev} (and also R_p) responded to the change in oxygen potential which indicates oxygen ingress into the crevice can be detected by the sensor.
(2) The κ_{crev} under the initially deaerated condition increased by addition of relatively low DO of 30 ppb in Type-I crevice.
(3) The maximum DO assisted κ_{crev} in bulk pure water was 1.5×10^3 μS·cm^{-1} and was attained at 32,000 ppb of DO concentration in the wedge-shaped crevice. This is a factor of >100 times higher than that of the bulk water.
(4) Crevice geometry significantly affected the response of κ_{crev} to the change in the bulk conductivity and DO level.

Acknowledgements This study includes the result of collaborative research with Chubu Electric Power Co.

References

1. P.L. Andresen, M.E. Indig, Effects of impurities and supporting electrolytes on SCC of 304 stainless steel in high temperature aqueous environments. Corrosion **38**, 531–541 (1982)
2. P.S. Maiya, W.J. Shack, Stress corrosion cracking susceptibility of AISI 316NG and 316 stainless steel in an impurity environment. Corrosion **41**, 630–634 (1985)
3. L.G. Ljungberg, D. Cubicciotti, M. Trolle, Effects of impurities on the IGSCC of stainless steel in high-temperature water. Corrosion **44**, 66–72 (1988)
4. P.L. Andresen, L.M. Young, Characterization of the Roles of Electrochemistry, Convection and Crack Chemistry in Stress Corrosion Cracking, in *Proceeding 7th International Conference on Environmental Degradation of Materials in Nuclear Power System Reactors* (Breckenridge, Colorado, 1995)
5. P. Lidar, Influence of Sulfate Transients on Crack Growth in Type 304 Stainless Steel in Water at 288 °C, in *Proceeding 7th International Conference on Environmental Degradation of Materials in Nuclear Power System Reactors* (Breckenridge, Colorado, 1995)
6. H.P. Hermansson. K. Gott, Mechanism for The Effect of Sulfate on SCC in BWRs, in *Proceeding 8th International Conference on Environmental Degradation of Materials in Nuclear Power System Reactors* (Amelia lsland Plantation, Fernandina Beach, FA, 1997)
7. M. König, K. Gott, P. Efsing, The Effect of Sulfate Impurities on the Stress Corrosion Cracking of Nickel Alloys in High Temperature Primary Water, in *Proceeding 14th International Conference on Environmental Degradation of Materials in Nuclear Power System Reactors* (Virginia, 2009)
8. D. Morton, SCC Growth Rate Testing of Stainless Steel in Aerated Water With and Without Anion Impurities, in *Proceeding 16th International Conference on Environmental Degradation of Materials in Nuclear Power System Reactors* (Asheville, NC, 2013)
9. P. Aaltonen et al., Facts and views on the role of anionic impurities, crack tip chemistry and oxide films in environmentally assisted cracking, VTT Research notes 2148 (2002)
10. Y. Soma, C. Kato, F. Ueno, In-situ Measurement of Solution Electrical Conductivity within Crevice of Stainless Steels in High Temperature Water, in *Proceeding 17th Asian Pacific Corrosion Control Conference*, APCCC paper No. 17007 (Mumbai, India, 2016)
11. T. Miyazawa, T. Terachi, S. Uchida, T. Satoh, T. Tsukada, Y. Satoh, Y. Wada, H. Hosokawa, Effects of hydrogen peroxide on corrosion of stainless steel, (V) characterization of oxide film with multilateral surface analyses. J. Nucl. Sci. Technol. **43**, 884–895 (2006)
12. M. Hanesch, Raman spectroscopy of iron oxides and (Oxy) hydroxides at low laser power and possible applications in environmental magnetic studies. Geophys. J. Int. **177**, 941–948 (2009)
13. Y. Soma, C. Kato, M. Yamamoto, Multilayered surface oxide within crevices of Type 316L stainless steels in high-temperature pure water. Corrosion **70**, 366–374 (2014)
14. C.S. Kumai, T.M. Devine, Influence of oxygen concentration of 288 °C water and alloy composition on the films formed on Fe–Ni–Cr alloys. Corrosion **63**, 1101–1113 (2007)
15. Y. Soma, C. Kato, M. Yamamoto, Surface oxide layers on 316L stainless steel formed in 561 K pure water at different potentials. J. Electrochem. Soc. **159**, C334–C340 (2012)
16. D.D. Macdonald, H. Song, M. Makela, K. Yoshida, Corrosion potential measurements on Type 304SS and Alloy 182 in simulated BWR environments. Corrosion **49**, 8–16 (1993)
17. R. Grauer, P.J. Moreland, G. Pini, Report prepared for the European Federation of Corrosion Working Party, (1982) NACE
18. M.E. Indig, Technology transfer: aqueous electrochemical measurements room temperature to 290 °C. Corrosion **46**, 680–686 (1990)
19. OLI Analyzer Studio 3.1., http://www.olisystems.com/index.shtml

Part VI
Zirconium and Fuel Cladding

Corrosion Fatigue Crack Initiation in Zr-2.5Nb

H.M. Nordin, A.J. Phillion, T.M. Karlsen and S. Persaud

ABSTRACT In-service inspections of Zr-2.5Nb pressure tubes may reveal blunt flaws such as fretting wear or crevice corrosion marks. These flaws pose no immediate threat to the integrity of the pressure tube but may be potential fatigue crack initiation sites. An understanding of the effect of the coolant environment, specifically on fatigue crack initiation, is important in this context. Tests were conducted on notched transverse tensile specimens at 275 and 300 °C with a load rise time between 50 and 3600 s. Current tests investigated the effects of applied loading frequency and hydrogen on fatigue crack initiation. Results have indicated that long rise time and a water environment reduce the time to fatigue crack initiation in non-hydrided and pre-hydrided specimens as compared to tests conducted in air. If enough hydrogen is able to diffuse to the notch during the test, it may also be possible to reach conditions where there is an interaction between corrosion, fatigue and hydride cracking.

Keywords Corrosion · Fatigue · Zr-2.5nb · Hydrogen · Crack initiation · DCPD

Introduction

Zr-2.5Nb is used for fabricating pressure tubes in CANDU power reactor. This material was selected because of its strength relative to Zircaloy, high corrosion resistance, good creep resistance and small neutron capture cross-section. Pressure tubes form the primary pressure boundary in the core. As the reactor is subjected to pressure and temperature cycles under normal operation for the tubes lifetime of at least 25 years, knowledge of the fatigue properties is important. As part of the

H.M. Nordin (✉) · A.J. Phillion · S. Persaud
Canadian Nuclear Laboratories, Chalk River Laboratories,
Chalk River, ON K0J 1J0, Canada
e-mail: heidi.nordin@cnl.ca

T.M. Karlsen
Institute for Energy Technology, OECD Halden Reactor Project, Halden, Norway

J.H. Jackson et al. (eds.), *Proceedings of the 18th International Conference on Environmental Degradation of Materials in Nuclear Power Systems – Water Reactors*, The Minerals, Metals & Materials Series, https://doi.org/10.1007/978-3-319-68454-3_41

Canadian Standards Association (CSA) fitness-for-service requirements for pressure tubes [1], flaws or stress risers that potentially lead to cracks cannot exist in pressure tubes in operating reactors. Flaws may include: fuel bundle scratches, crevice corrosion marks, fuel bundle bearing pad fretting flaws and debris fretting flaws. These flaws may be a precursor to cracking and must be mitigated or the tube removed if the flaw cannot be suitably dispositioned. This provides protection against pressure tube failure from crack initiation and delayed hydride cracking.

A limited amount of fatigue data exists for zirconium alloys. The data in the literature concentrate on fatigue life [2–7] or crack growth rate tests [7–14]. Often the effects of environment (such as irradiation and hydrogen content) during these tests are unclear.

This paper presents the results from a fatigue crack initiation test program on Zr-2.5Nb specimens conducted in heavy water at high temperatures representative of pressurized water reactor operating conditions. The tests investigated the effects of applied loading frequency and hydrides on fatigue crack initiation.

Experimental Procedure

Specimens

Transverse tensile specimens (Fig. 1) were machined from as-received[1] and pre-hydrided Zr-2.5Nb pressure tube material. In the remainder of the paper the as-received specimens will be referred to as non-hydrided specimens.

To pre-hydride the pressure tube material, a ring of the pressure tube ($\sim$3 cm long ring with the same thickness and diameter of the pressure tube) was electrolytically hydrided in a solution of 1% H_2SO_4 in H_2O for 72 h. The temperature of the solution was maintained at approximately 70 °C during the day and was reduced to 50 °C overnight to reduce evaporation of the electrolyte. The cathodic voltage was approximately 7 V and the current was on average 15 A. The rings were then diffusion annealed at 300 °C for 72 h to obtain a uniform distribution of hydrides throughout the ring. The total hydrogen concentration in each ring was determined by hot vacuum extraction mass spectrometry (HVEMS [15]) to be approximately 55–58 μg/g.

Each specimen had a 45° notch perpendicular to the gauge length across the entire width of the specimen, to initiate a crack in the radial direction. The notch was made by applying multiple passes with a broaching tool to achieve a 15 ($\pm$2) μm root radius notch of the desired depth (0.8 μm)

[1]As-received pressure tube material was extruded at 815 °C, cold worked 27% and steam autoclaved at 400 °C for 24 h.

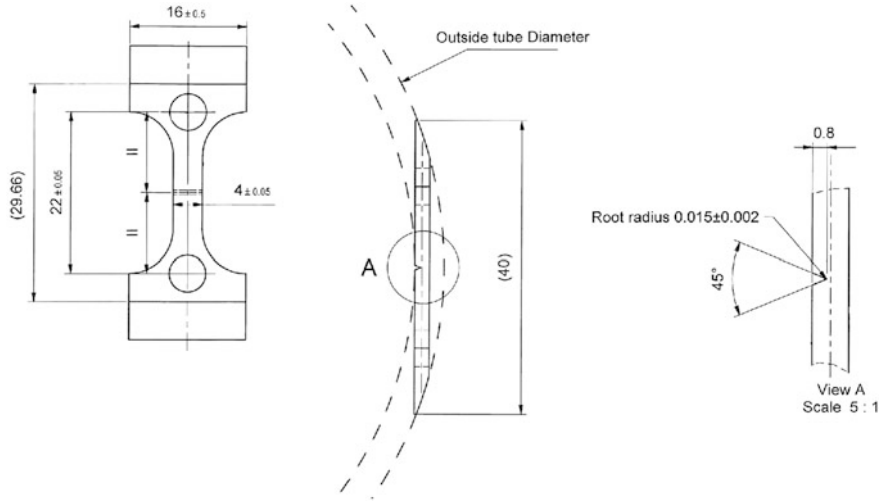

Fig. 1 Notched transverse tensile specimen geometry

Fatigue Tests

Corrosion fatigue crack initiation tests were conducted in the autoclave facilities at the Institute for Energy Technology, Halden reactor site, at 275 and 300 °C in heavy water with water chemistry specifications as listed in Table 1. The test loop, gas pressurized bellows loading units and crack initiation detection technique are explained in more detail elsewhere [16]. A reversing direct current potential drop (DCPD) technique was used to determine crack initiation in situ. Crack initiation was defined when a 15 μm long crack, averaged over the specimen width, was detected by the PD system.

Six corrosion fatigue tests were conducted (three on non-hydrided and three on pre-hydrided specimens). Each test run consisted of eight specimens tested at two temperatures (four at 275 °C and four at 300 °C). Three specimens in each autoclave were instrumented with DCPD leads to measure crack initiation. The fourth specimen in each autoclave was not instrumented but was loaded in the same manner as the other specimens. Loading continued on this specimen until crack initiation was detected in all specimens in the same autoclave. The fourth specimen acted as a control specimen to determine the amount of hydrogen[2] ingress that would occur just by being tested in the environment and to ensure potential drop leads were not contributing to hydrogen ingress as was seen in previous tests [16]. In all tests, a saw tooth wave form was applied with a maximum load of 750 N and

[2]Hydrogen and hydrides refer to all isotopes of hydrogen and all solids precipitated once solubility has been exceeded, respectively. In these tests, hydrogen ingress refers to deuterium ingress and hydrides to deuterides.

Table 1 Coolant chemistry specification

Parameter	Specification
Lithium content (in water phase)	1.1 μg/g
pH value (at 25 °C)	10.7
Chloride	<0.1 mg/kg D_2O
Oxygen content (O_2)	<5 ppb
Deuterium content (D_2)	7 Nml/kg D_2O
Water conductivity (D_2O at 20 °C)	5–15 μS/cm
Suspended particles	<0.1 mg/kg D_2O

the ratio of the minimum to maximum load was R = 0.2. Although the maximum load for each test run was the same, the time required to reach maximum load was varied. The loading rise times selected were: 50, 1800 and 3600 s.

A limited number of fatigue tests were also conducted on non-hydrided and pre-hydrided specimens in an air environment at 275 or 300 °C. Loading was done using computer controlled single access load frames. The same load conditions and loading rates as for the corrosion fatigue tests were used. Crack initiation was also monitored using DCPD.

Characterization

Following the corrosion fatigue tests and the fatigue tests conducted in air, selected specimens were broken apart by applying a quick tensile pull in air at room temperature to examine the fracture surfaces. The fracture surfaces were examined in a JEOL JSM-6100 scanning electron microscope (SEM). The crack area was determined from the images so that the crack length could be compared with the value determined by DCPD.

For specimens that were not broken open, the gauge length was mounted in cross-section and polished so the crack length could be measured. The samples were also etched to reveal any hydrides that were present.

HVEMS analysis was completed on most specimens to determine hydrogen ingress during the test. This also helped to confirm that the DCPD test leads did not add an excess of hydrogen to the specimens during the test.

For two samples, focused ion beam (FIB) samples were prepared from the fatigue crack tip using a Zeiss NVision 40 FIB-SEM with a Ga^+ ion beam (30 kV accelerating voltage). Final polishing was carried out at 10 kV with a current of 80 pA. Transmission electron microscope (TEM) images and electron energy loss spectroscopy (EELS) were acquired using an FEI Titan cubed TEM, operated at 300 kV. The dwell time for each pixel was 0.01 s, with an entrance aperture of 5 mm, a collection semi-angle of approximately 40 mrad, and a convergence semi-angle of 19 mrad.

Results and Discussion

In all tests, fatigue crack initiation was observed to initiate in each sample soon after cyclic loading was started. Figure 2 provides an example of the DCPD signal for a corrosion fatigue test conducted at 275 °C on three samples.

The results of the corrosion fatigue tests are shown in Fig. 3a for non-hydrided and Fig. 3b for pre-hydrided specimens. For comparison purposes, the graphs include data available from tests conducted in air at 275 and 300 °C. To put the results into context with previous results, two curves are also shown on the graphs. These curves are based on crack growth rate tests conducted on hydrided Zr-2.5Nb material in air at 300 °C (Lepik curve) [8] and on irradiated, hydrided Zircaloy-2 in steam generated heavy water reactor environment conditions at 260 °C (Pickles and Picker curve) [9, 10]. The curves show the number of cycles to grow a 15 μm long crack. The curve from Lepik [8] is based on Paris law. The data from Pickles and Picker [9, 10] form the technical basis of the CSA standard [1] for evaluating flaws in pressure tubes.

Figure 3a shows that in air a long rise time reduced the number of cycles before crack initiation occurred. This effect of rise time in air is likely related to strain ageing and creep mechanisms. At temperatures consistent with the test conditions for this work, the ultimate tensile strength, the yield stress and the strain-hardening index are all strain-rate dependent [17–20]. This strain rate dependence would account for the rise time effect seen in the current fatigue tests. An effect of rise time was also observed with the tests conducted in water. The effect of environment can also be seen as specimens tested in water have a reduced number of cycles to crack initiation when compared to the tests conducted in air. An environmental effect, consistent with these results, has been observed in crack growth rate tests [7–12].

For the pre-hydrided materials in air (Fig. 3b), a long rise reduced the number of cycles before crack initiation occurred similar to what was observed for the non-hydrided specimens. The effect of rise time is also seen on the tests conducted in water at 300 °C going from 1800 to 3600 s rise times. At 275 °C, the effect of rise

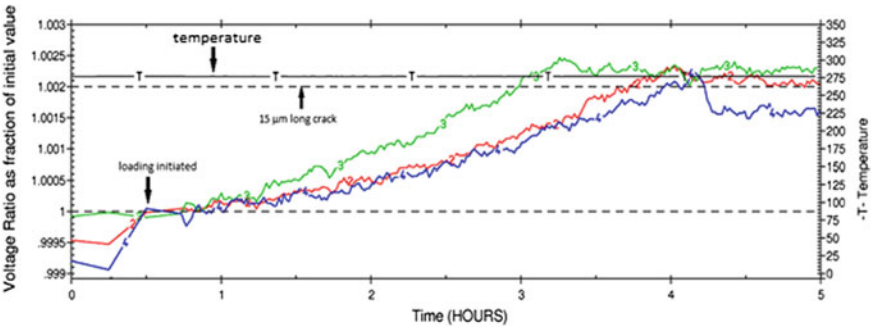

Fig. 2 DCPD signals showing the voltage ratio versus time for 3 specimens tested at 275 °C with a 50 s rise time. DCPD signals appear similar for all specimens tested

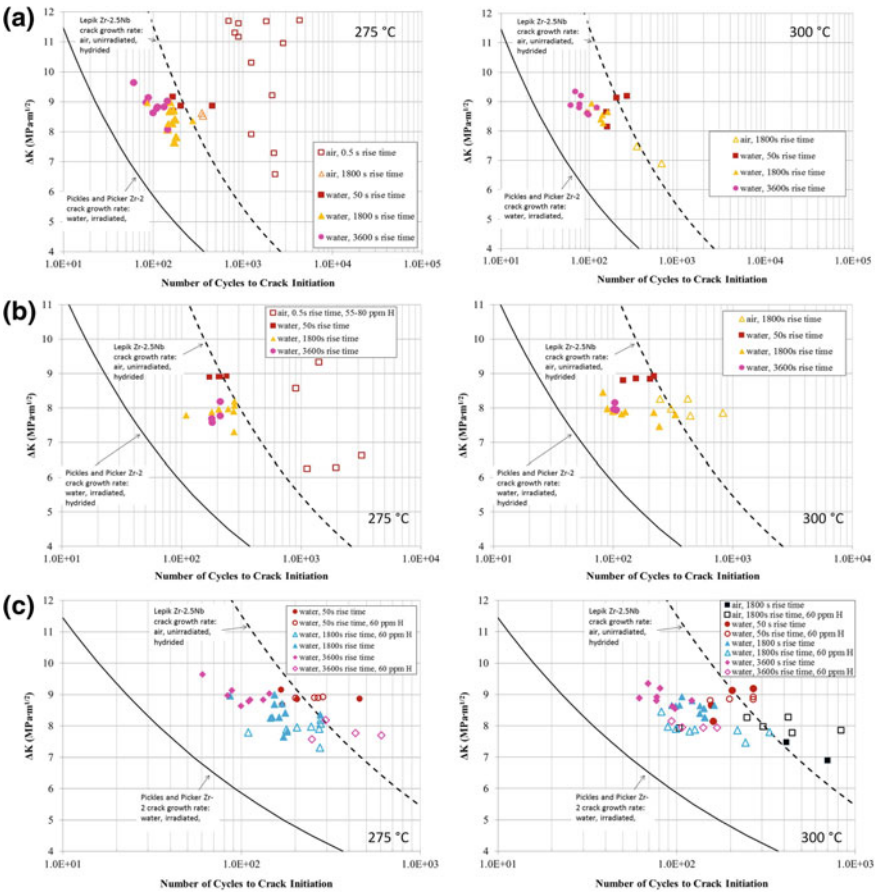

Fig. 3 Stress intensity versus the number of cycles to crack initiation (15 μm long crack) for **a** as–received specimens, **b** pre-hydrided specimens and **c** as-received and pre-hydrided specimens at 300 °C. The plot also shows crack growth rate curves obtained from tests on unirradiated Zr-2.5Nb in air at 300 °C [8] and on irradiated Zircaloy-2 in steam generating heavy water reactor environment conditions at 260 °C [9, 10]

time on the pre-hydrided specimens in water isn't as clear due to the limited amount of data available. The effect of environment is also seen in pre-hydrided specimens with the tests conducted in water having a reduced number of cycles to crack initiation when compared to tests conducted in air. For the pre-hydrided material, the environmental effect at 300 °C with an 1800 s rise time is very small. However, there are very few data points and a large degree of scatter in the air data which skews the average number of cycles to crack initiation in air at these test conditions that was used to calculate the ratio. The effect of environment is consistent with observations from crack growth rate tests [7, 8] however, the magnitude of the effect appears to be reduced at longer rise times under the loading conditions applied.

Table 2 Ratios of the average number of cycles to crack initiation to indicate the impact of environment

Ratio	**No H**	**H**
275 °C air (50 s rise time)/275 °C water (50 s rise time)	7.2	8.3
275 °C air (1800 s rise time)/275 °C water (1800 s rise time)	2.1	–
300 °C air (1800 s rise time)/300 °C water (1800 s rise time)	4.4	2.4

The ratios of the average number of cycles to crack initiation in air to the average number of cycles in water are given in Table 2. These ratios indicate that although the magnitude of the effect changes with rise time and temperature, the environment has an effect on reducing the time to crack initiation.

Figure 3c compares the data from the as-received and pre-hydrided material. In air at 300 °C, crack initiation seemed to be similar in non-hydrided material and pre-hydrided material. This result is consistent with the findings on crack growth rate [12]. The pre-hydrided specimens tested in water with an 1800 s rise time and a 3600 s rise time seemed to have an increased number of cycles to crack initiation than non-hydrided specimens. However, a direct comparison between the as-received and pre-hydrided specimens is difficult to make as the stress intensity for the pre-hydrided samples tended to be less than for the as-received samples due to variations in the notch geometry[3] that occurred as the different batches of specimens were machined.

For the current tests conducted in water, the results fall between the results from the Leipik [8] tests conducted in air and the Pickles and Picker [9, 10] tests conducted on irradiated, hydrided Zircaloy-2 in water. This is as expected as fatigue crack initiation in water has been demonstrated to occur sooner than in air and the Pickles and Picker test is believed to be done under the most aggressive test conditions as it included both irradiation and a water environment. The Zr-2.5Nb specimens tested in water require a greater number of cycles to fatigue crack initiation than the irradiated Zircaloy-2 tested in water. The effect of irradiation on fatigue crack initiation of Zr-2.5Nb in a water environment is unknown.

Figure 4 shows a cross-sectional view of the cracks formed at the notch and a fracture face for specimens tested at 300 °C with an 1800 s rise time. In the as-received specimens, the cross-sectional view (Fig. 4a) shows small hydrides distributed throughout the specimen. The deuterium concentration measured with HVEMS was 0.34 μg/g. This is a low concentration that could be a consequence of the oxidation process or a small amount of ingress from the DCPD leads. In the pre-hydrided specimens, the cross-sectional view (Fig. 4b) shows numerous large hydrides distributed around the notch. The hydrides are aligned circumferentially. It

[3]Although nominally the notches have a root radius of 15 ± 2 μm and a notch depth of 0.8 μm, the pre-hydrided specimens tended to have a shallower notch depth than the non-hydrided specimens.

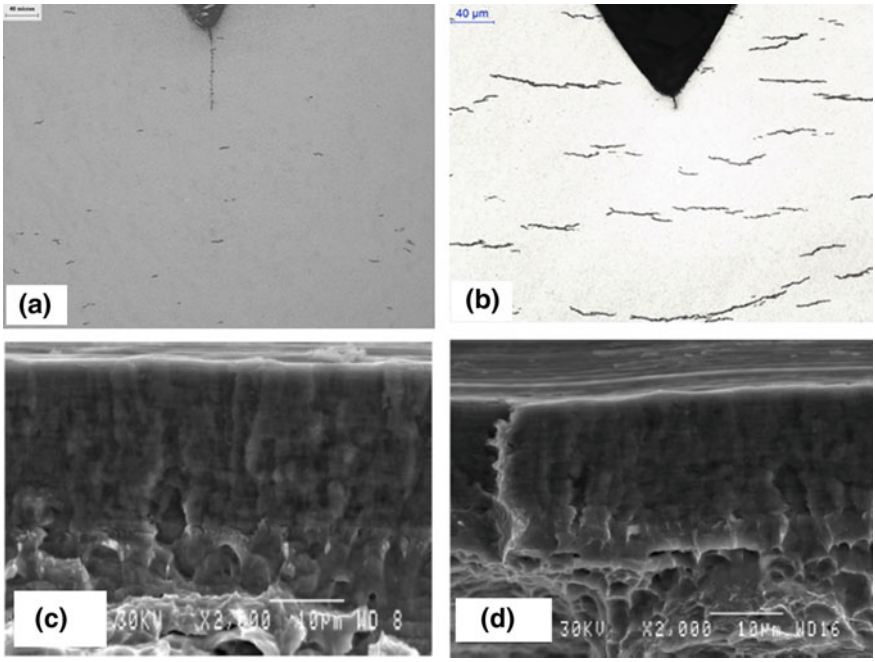

Fig. 4 Cross-sectional image of **a** an as-received specimen and **b** a pre-hydrided specimen and fracture faces from **c** an as-received specimen and **d** a pre-hydrided specimen. All specimens were fatigue tested at 300 °C with an 1800 s rise time

was expected that during the test the hydrides would start to reorient to align perpendicular to the tensile stress as is observed with the delayed hydride cracking mechanism in zirconium alloys [21–25]. The load was removed from the specimen once a 15 µm long crack was formed but the specimen remained in the autoclave at temperature until cracks had initiated in all specimens. As the hydrogen concentration was below the solubility limit ($[H]_{eq} \sim 60$ µg/g at 300 °C), hydrogen would be able to diffuse away from the notch and be uniformly distributed through the sample. The fracture surfaces (Fig. 4c, d) indicate a flat fatigue fracture front with striations and dimple-fracture in the ductile region that was produced following the test when a tensile load was applied to break the specimen open in air. As both fracture surfaces appear similar, hydride cracking did not occur in the pre-hydrided specimens. Although differences in the fatigue striation height and spacing have been observed between 304 stainless steel pre-charged with hydrogen and uncharged [26], differences cannot be readily detected in the fracture surfaces between non-hydrided and pre-hydrided Zr-2.5Nb tested in a water environment. This is likely due to the fine details of the fracture surfaces of the samples tested in water being obscured by an oxide film.

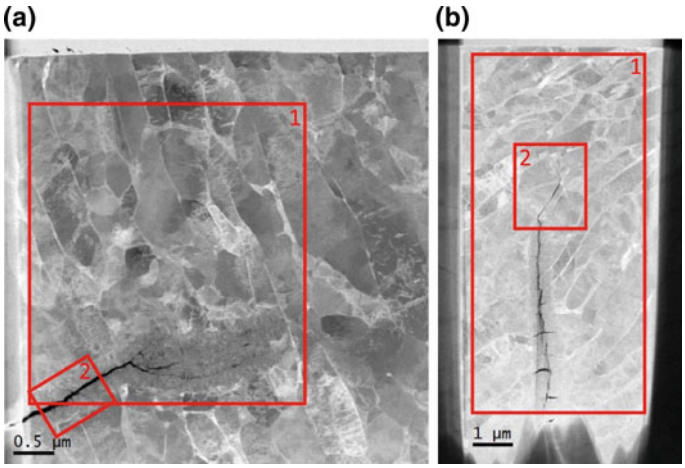

Fig. 5 TEM image of a fatigue crack formed in **a** a pre-hydrided specimen tested at 300 °C with 50 s rise time and **b** a non-hydrided specimen tested at 300 °C with 3600 s rise time but high ingress into the specimen occurred during the test. The boxes indicate where the EELS spectra were acquired (Figs. 6 and 7 for the pre-hydrided specimen and Figs. 8 and 9 for the as-received specimen) (Color figure online)

Zr-2.5Nb pressure tube material consists of elongated grains of hcp α-Zr, partially surrounded by a thin network of filaments of bcc β-Zr. TEM examination of FIB samples prepared from the cracks formed in two samples that were corrosion fatigue tested show that the fatigue crack is transgranular, crossing numerous α-Zr and β-Zr grains (Fig. 5). No hydrides are observed in the TEM images even though the sample in Fig. 5a was pre-hydrided to ~60 µg/g prior to fatigue testing and although the sample in Fig. 5b was originally non-hydrided, high levels of hydrogen ingress were observed as the DCPD leads used on this specimen were a nickel alloy which were previously shown to act as windows for hydrogen ingress into zirconium alloys [16]. The lack of hydrides observed in the TEM images may just be due to the imaging conditions used. Tilting the sample to more favorable diffraction conditions may have allowed the hydrides to be more apparent.

Figures 6 and 7 show the low-loss EELS elemental maps for the specimen that was pre-hydrided to ~60 µg/g and then corrosion fatigue tested at 300 °C with a 50 s rise time. A relatively thick oxide comprised mostly of ZrO_2 fills the crack. Hydride platelets ~40 nm thick and 200 nm long are observed with low-loss EELS. The hydrides form both at the α/β grain boundaries and within the α-grains. Although the optical images didn't show hydride reorientation, on the microscopic scale there appears to be a limited amount of reorientation of the hydrides along the crack and perpendicular to the applied tensile stress (i.e., circumferential hydrides reorient to the radial direction due to the applied tensile stress). Hydride reorientation and accumulation at a stress riser is an important aspect for DHC [21–25].

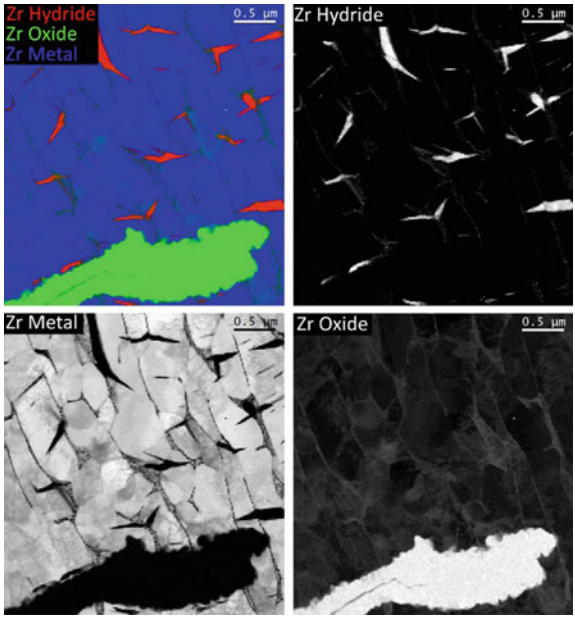

Fig. 6 Low-loss EELS elemental map for area 1 from the TEM image shown in Fig. 5a. Although hydrides were not observed in the TEM image, the EELS maps indicate that hydrides are present

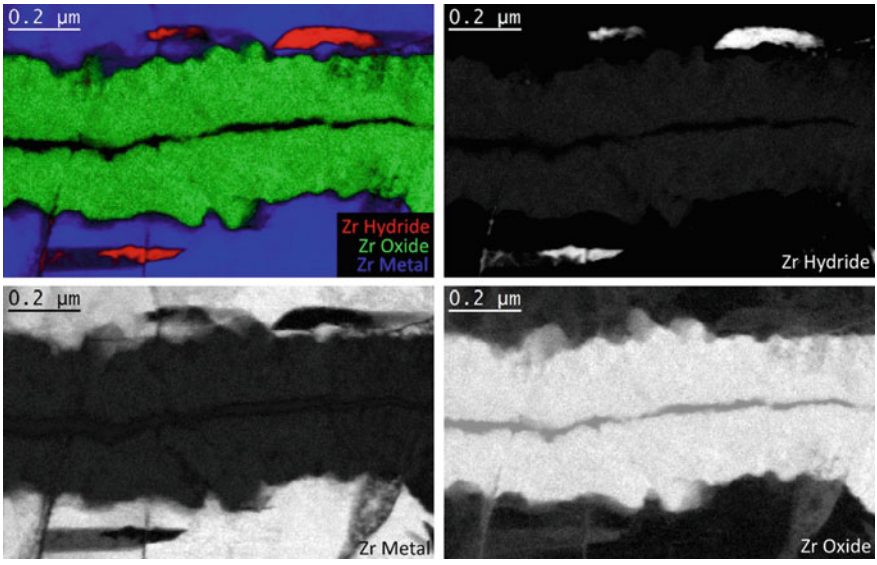

Fig. 7 Low-loss EELS elemental map for area 2 from the TEM image shown in Fig. 5a. Small hydrides have aligned along the sides of the crack

The diffusion of hydrogen to the crack tip and precipitation of hydrides is expected to play a role in the fatigue crack initiation and growth mechanism. As the samples remained at temperature without load applied once the target crack length was reached, hydrogen in solution would have been able to diffuse away from the crack tip and the observed distribution of hydrides may not be the distribution that existed during loading.

Figures 8 and 9 show the low-loss EELS elemental maps for the as-received specimen corrosion fatigue tested at 300 °C with a 3600 s rise time. Figure 9 also shows the EDX map for Nb which is overlayed with the EELS maps. Although this specimen was as-received, a large concentration of hydrogen was absorbed by the sample during the test due to the DCPD leads [16]. Although TEM was performed on this sample, it was not included with the fatigue data shown in Fig. 3 as the final hydrogen equivalent concentration was approximately 100 μg/g making it difficult to directly compare with the fatigue data obtained for non-hydrided specimens and those pre-hydrided to ~60 μg/g. With a hydrogen equivalent concentration of 100 μg/g, the terminal solid solubility (TSS) of hydrogen was exceeded and solid hydrides would have been present at the test temperature. For the specimens pre-hydrided to ~60 μg/g, TSS would not have been exceeded at 300 °C meaning all hydrogen was in solution. The EELS images indicate that the crack that formed appeared very similar to that in the pre-hydrided specimen shown in Fig. 6. A thick oxide comprised mostly of ZrO_2 formed along either side of the crack. Figure 9 shows that the oxide (and the crack) extends for about 1 micron beyond the base of the thick oxide that formed around the crack. This is likely a relatively recent extension of the crack and it may be influenced by hydrogen diffusing to the crack tip. Figure 9 clearly shows that the hydrides form both at the α/β grain boundaries

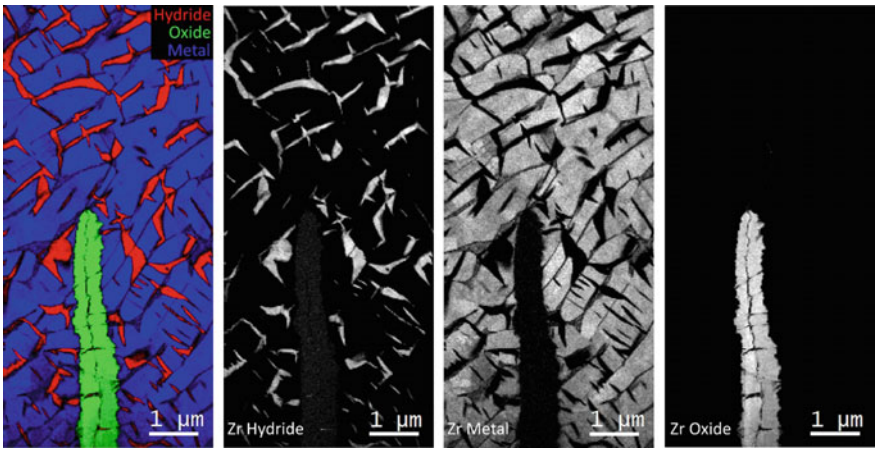

Fig. 8 Low-loss EELS elemental map for area 1 from the TEM image shown in Fig. 5b

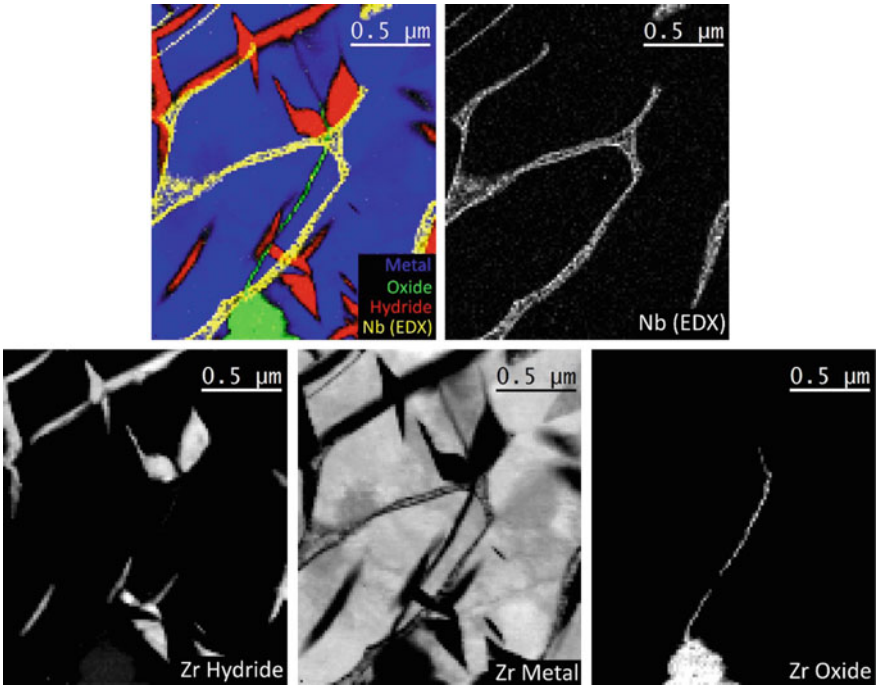

Fig. 9 Low-loss EELS elemental map and Nb EDX map for area 2 from the TEM image shown in Fig. 5b

and within the α-grains. There appears to be a limited amount of reorientation of the hydrides along the crack and perpendicular to the applied tensile. The amount of reorientation of hydrides appears to be greater than seen in Fig. 6. The β-phase does not seem to affect the cracking mechanism as the crack just extends straight through this phase. The narrow crack extension seen in Fig. 9 does seem to change direction after crossing the β-phase. The cause of this directional change is unknown but may be due to dislocation structures in that area, grain orientation or the presence of hydrides.

The available literature on mechanisms of corrosion fatigue crack initiation suggests that the mechanism is a complex synergy between mechanical, chemical and metallurgical factors [27]. Several mechanisms have been proposed, all of which have contradictions and as such have difficulties fully explaining the experimental results [27]. For the case of corrosion fatigue in Zr-2.5Nb, the mechanism of surface film rupture seems to provide the best explanation of the experimental data. This mechanism is shown schematically in Fig. 10. As part of the corrosion process a protective oxide film forms on the surface of the specimen. When subjected to a mechanical stress the oxide film ruptures causing fresh metal

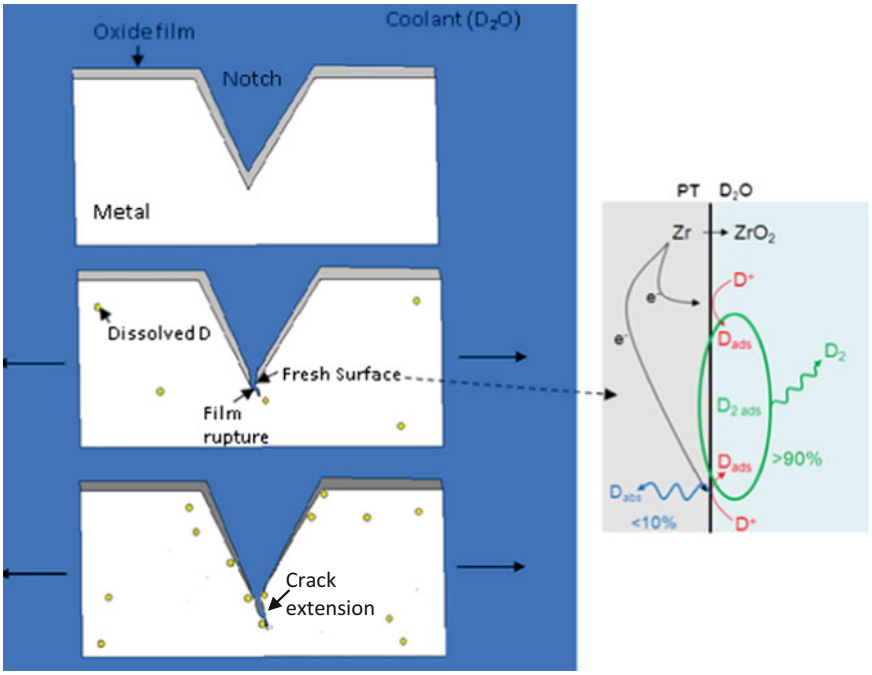

Fig. 10 Schematic diagram showing oxide film rupture corrosion fatigue mechanism Schematic diagram showing the oxide film rupture mechanism and the effect of hydrogen on corrosion fatigue crack initiation. Prior to testing, a uniform oxide forms on the specimen surfaces. When the load is applied, the oxide film ruptures leaving fresh surfaces to oxidize. As part of the corrosion process a small fraction of deuterium is absorbed into the metal. With continued cycling, the process continues with the crack extension increasing as the oxide film ruptures leaving fresh oxidizing surfaces

to be exposed. With successive fatigue cycles the crack extends into the metal. As oxidation would occur more quickly in water than in an air environment, this could help explain why there is less variability in the results for tests conducted in water. For the pre-hydrided specimens, the mechanism is more complicated as in addition to the oxide film rupture, diffusion of hydrogen and hydride precipitation also play a role. This is shown schematically in Fig. 11. The TEM images and EELS data do indicate that there is hydrogen near the notch and along the sides of the crack. In steels, it was found that without hydrogen the plastic zone around the crack is broad and crack tip blunting occurs [26]. In the presence of hydrogen, the plastic zone is shallower. With decreased frequency of loading a large amount of hydrogen concentrates near the crack tip which enhances crack opening and the crack continues to grow and the crack front does not become blunt [26]. There may be evidence of this occurring in Fig. 10 in the specimen where hydrogen exceeded TSS as the crack tip does not appear to be as blunt as for the pre-hydrided specimens below TSS and there is a narrow crack extension beyond the base of the thick oxide observed.

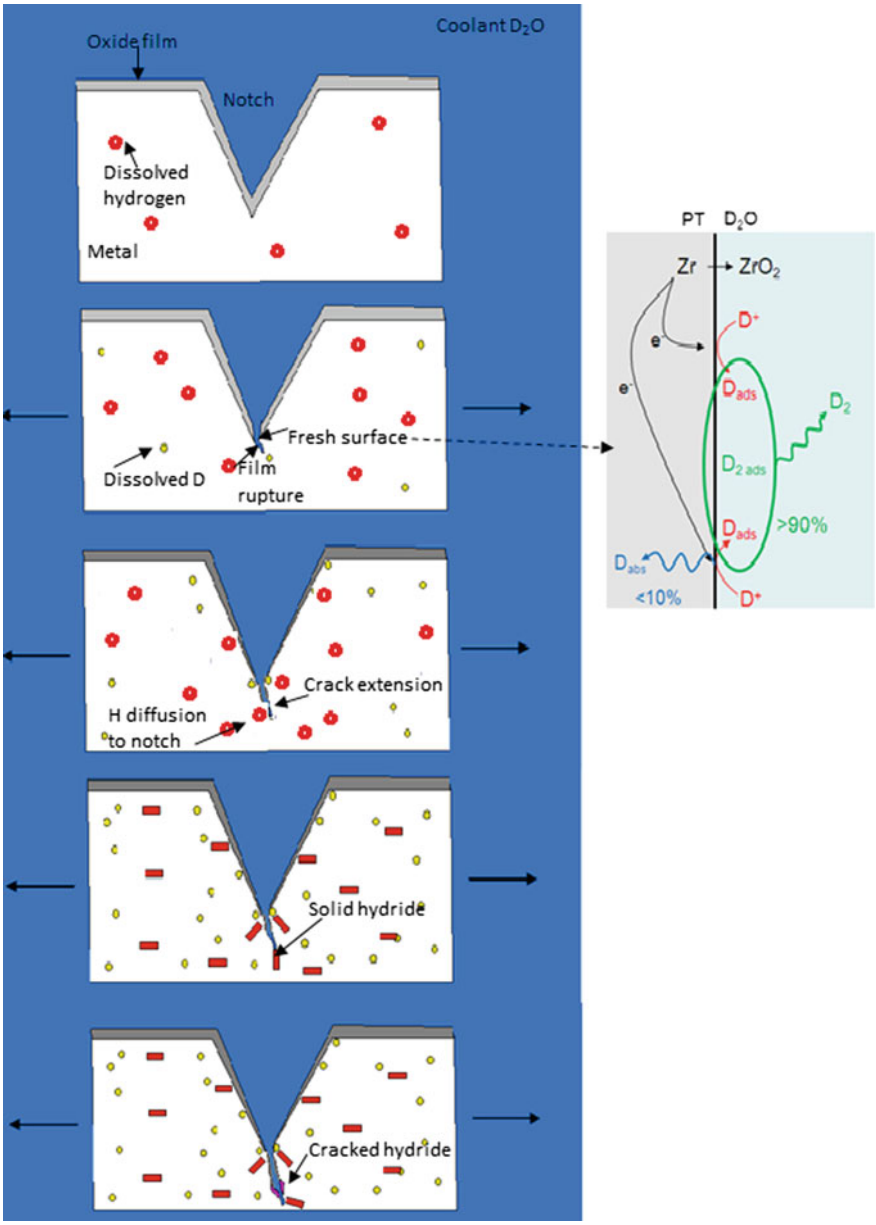
Coolant D_2O
Oxide film
Notch
Dissolved hydrogen
Metal
Fresh surface
Dissolved D
Film rupture
Crack extension
H diffusion to notch
Solid hydride
Cracked hydride
PT
D_2O
Zr
ZrO_2
D^+
e
D_{ads}
D_2
$D_{2\ ads}$
>90%
<10%

◂**Fig. 11** Schematic diagram showing the oxide film rupture mechanism and the effect of hydrogen on corrosion fatigue crack initiation. Prior to testing, a uniform oxide forms on the specimen surface. Provided the hydrogen concentration is below TSS the hydrogen is uniformly distributed in solution. When the load is applied, the oxide film ruptures leaving fresh surfaces to oxidize. As part of the corrosion process a small fraction of deuterium is absorbed into the metal. With continued cycling, the process continues with the crack extension increasing as the oxide film ruptures leaving fresh oxidizing surfaces. Hydrogen will diffuse to the notch where it will precipitate forming solid hydrides once TSS is exceeded. If the hydrides are aligned at the crack extension the brittle hydrides will crack causing a more rapid extension of the crack. The model shown in Fig. 10 would start exhibiting the same mechanisms as shown in this figure if the ingress from the corrosion process is high (or over long time periods) and TSS is exceeded

Summary

Fatigue crack initiation experiments were conducted on Zr-2.5Nb in air and in water at 275 and 300 °C. The main findings are:

1. In air, a long rise time reduced the number of cycles to fatigue crack initiation in both non-hydrided and pre-hydrided specimens.
2. In water, a long rise time also reduced the number of cycles to fatigue crack initiation in both non-hydrided and pre-hydrided specimens.
3. Exposure to a water environment also reduced the number of cycles to fatigue crack initiation in both non-hydrided and pre-hydrided specimens in comparison with tests conducted in air. The magnitude of the effect seems to decrease with an increased rise time.
4. TEM and EELS analysis indicated transgranular cracks formed with hydrides forming both at α/β boundaries and within α-Zr grains. There appears to be a limited amount of hydride reorientation along the crack and perpendicular to the tensile stress particularly for the specimen with a hydrogen content in excess of the terminal solid solubility (TSS). Further investigation is needed to elucidate the fatigue crack initiation mechanism.

Acknowledgements The authors acknowledge: J. Liverud, P.A. Wiig, C. Hartmann, K.L. Moum, V. Andersson, P-M. Harlem, V. Staal, I. Thoresen, and F.H. Lilleborgen from IFE for test setup, autoclave facility operation and SEM analysis. M. Seguin, A. Briton and R. MacLeod from CNL for performing the metallography and HVEMS analysis.

References

1. *Technical Requirements for In-Service Evaluation of Zirconium Alloy Pressure Tubes in CANDU Reactors*, CSA-N285.8-05 (Canadian Standards Association, 2005)
2. D. Lee, The role of plastic anisotropy in the fatigue behavior of zircaloy. Metall. Trans. **3**, 315–322 (1972)
3. W.J. O'Donenell, B.F. Langer, Fatigue design basis for zircaloy components. Nucl. Sci. Eng. **20**, 1–12 (1964)

4. C.K. Chow, C.E. Coleman, M.H. Koike, A.R. Causey, C.E. Ells, R.R. Hosbons, S. Sagat, V. F. Urbanic, D.K. Rodgers, Properties of an Irradiated Heat-Treated Zr–2.5Nb Pressure Tube Removed from the NPD Reactor. in *Zirconium in the Nuclear Industry: Eleventh International Symposium*, ASTM STP 1295, ed. by E.R. Bradley, G.P. Sabol (ASTM International, West Conshohocken, PA, USA, 1996), pp. 469–491
5. M. Nakatsuka, T. Kubo, Y. Hayashi, Fatigue Behavior of Neutron Irradiated Zircaloy-2 Fuel Cladding Tubes. in *Zirconium in the Nuclear Industry: Ninth International Symposium*, ASTM STP 1132, ed. by C.M. Eucken, A.M. Garde (ASTM International, West Conshohocken, PA, USA, 1991), pp. 230–245
6. J. Tan, S. Ying, C. Li, C. Sun, Effect of zirconium hydrides on cyclic deformation behavior of Zr–Sn–Nb alloy. Scr. Mayerialia **55**, 513–516 (2006)
7. S.B. Wisner, M.B. Reynolds, R.B. Adamson, Fatigue Behavior of Irradiated and Unirradiated Zircaloy and Zirconium. in *Zirconium in the Nuclear Industry: Tenth International Symposium*, ASTM STP 1245, ed. by A.M. Garde and E.R. Bradley (ASTM International, West Conshohocken, PA, USA, 1994), pp. 499–520
8. O.E. Lepik, D.M. McCluskey, Fatigue Crack Growth Behaviour of Zr-2.5Nb in a CANDU Reactor Water Environment. in *Proceedings of SMiRT-12*, Paper FG14/4 (Stuttgart, Germany, 1993 August)
9. B.W. Pickles, C. Picker, The Effects of Environment and Neutron Irradiation on the Fatigue Crack Growth Behaviour of Zircaloy-2. in *Proceedings of SMiRT-6*, vol C, Paper F6/4 (Paris, France, 1981 August)
10. C. Picker, B.W. Pickles, The Enhancement of Fatigue Crack Growth Rates in Zirconium Alloys in a Reactor Environment. in *Proceedings of the International Conference on Dimensional Stability and Mechanical Behaviour of Irradiated Metals and Alloys* (Brighton, UK, 1983), pp. 179–182
11. C.F. Gee, Fatigue Properties of Zircaloy-2 in a PWR Water Environment. in *First International Symposium on Environmental Degradation of Materials in Nuclear Power Systems—Water Reactors* (NACE, Myrtle Beach, South Carolina, 1984 August), pp. 687–700
12. C.F. Gee, P.M. Scott, A.E. Truswell, Factors Affecting Fatigue Crack Growth Rates in Zircaloy Components in Reactor Water Environments. in *Fourth International Symposium on Environmental Degradation of Materials in Nuclear Power Systems—Water Reactors* (NACE, Jekyll Island, Georgia, 1989 August), pp. 10.47–10.58
13. L.A. James, Environmentally aggravated fatigue cracking of Zircaloy-2. Nucl. Appl. Technol. **9**, 260–267 (1970)
14. P.J. Pankaskie, Fatigue Crack Growth and Propagation in 2.5Nb Zirconium Alloy Pressure Tubing. in *Applications Related Phenomena for Zirconium and its Alloys*, ASTM STP 458, (American Society for Testing and Materials, 1969), pp. 129–140
15. G.A. Bickle, L.W. Green, M.W.D. James, T.G. Lamarche, P.K. Leeson, H. Michel, The determination of hydrogen and deuterium in Zr-2.5Nb material by hot vacuum extraction mass spectrometry. J. Nucl. Mater. **306**, 21–29 (2002)
16. H.M. Nordin, M. Lundgren, A.J. Phillion, M.D. Wright, A. Douchant, Fatigue Crack Intitiation Tests on Zr-2.5Nb in a Heavy Water Reactor Environment. in *17th International Conference on Environmental Degradation of Materials in Nuclear Power Systems—Water Reactors* (Ottawa, Ontario, Canada, 2015 August)
17. S. Graff, Viscoplastic Behavior of Zirconium Alloys in the Temperatures Range 20C-400C Characterization and Modeling of Strain Ageing Phenomena, Mechanics [physics.med-ph] (École Nationale Supérieure des Mines de Paris, 2006)
18. V.J. Farron, Effects of Microstructure and Strain Ageing on Toughness of Nuclear PWR Reactor Weld Metals. in *A thesis submitted to the Faculty of Engineering of the University of Birmingham for the Degree of Doctor of Philosophy* (School of Metallurgy and Materials, The University of Birmingham, 2009)
19. K. Kapoor, K. Murlidharan, K.M. Sreedharan, High-Temperature Mechanical Behavior of Cold-Worked Stress-Relieved Zr-2.5Nb. J. Mater. Eng. Perform. **4**, 610–616 (1995)

20. A.K. Bind, R.N. Singh, H.K. Khandelwal, S. Sunil, G. Avinash, J.K. Chakravartty, P. Ståhle, Influence of loading rate and hydrogen content on fracture toughness of Zr-2.5Nb pressure tube material. J. Nucl. Mater. **465**, 177–188 (2015)
21. A. Sawatzky, C.E. Ells, Understanding Hydrogen in Zirconium, in *Zirconium in the Nuclear Industry: Twelfth International Symposium*. ASTM STP 1354, ed. by G.P. Sabol, G.D. Moan (ASTM International, West Conshohocken, PA, USA, 2000), pp. 32–48
22. R.N. Singh, N. Kumar, R. Kishore, S. Roychaudhury, T.K. Sinha, B.P. Kashyap, Delayed hydride cracking in Zr-2.5Nb pressure tube material. J. Nucl. Mater. **304**, 189–203 (2002)
23. B.A. Cheadle, C.E. Coleman, J.F.R. Ambler, Prevention of Delayed Hydride Cracking in Zirconium Alloys. in *Zirconium in the Nuclear Industry: Seventh International Symposium*, ASTM STP 939, ed. by R.B. Adamson, L.F.P. Van Swam (ASTM International, West Conshohocken, PA, USA, 1987), pp. 224–240
24. D. Weinstein, F.C. Holtz, Susceptibility of zirconium and zirconium alloys to delayed failure hydrogen embrittlement. Trans. ASM. **57**, 284–293 (1964)
25. C.J. Simpson, C.E. Ells, Delayed hydrogen embrittlement of Zr-2.5 wt% Nb. J. Nucl. Mater. **52**, 289–295 (1974)
26. Y. Murakami, S. Matsuoka, Effect of hydrogen on fatigue crack growth of metals. Eng. Fract. Mech. **77**, 1926–1940 (2010)
27. T.S. Srivatsan, T.S. Sudarshan, Mechanisms of fatigue crack initiation in metals: role of aqueous envirronments. J. Mater. Sci. **23**, 1521–1533 (1988)

Cluster Dynamics Model for the Hydride Precipitation Kinetics in Zirconium Cladding

Donghua Xu and Hang Xiao

Abstract Hydride precipitation in zirconium cladding is known to cause severe loss of toughness and greatly increase the risk of mechanical failure and fuel leakage. Modeling hydride formation kinetics is critical to the safety assessment of the fuel-cladding system and the entire reactor system. Existing reduced order models do not provide such details as number density and size distribution of hydride precipitates. We have recently developed a cross-scale cluster dynamics model with increased physical details and enhanced predictive capability for the hydride formation kinetics in zirconium. Our model takes information from atomistic simulations, such as migration energy of interstitial hydrogen and formation/binding energy of hydride embryos/clusters, as input, and establishes and solves a system of rate equations that describe the evolution of concentrations of freely migrating hydrogen as well as sessile hydride clusters of all different sizes. Used here to simulate an in situ hydride growth experiment on a TEM, our model is able to reproduce the linear growth behavior of pre-existing hydrides under hydrogen ion implantation and provide possible explanations for the estimated growth rate.

Keywords Precipitation kinetics · Cluster dynamics modeling · Zirconium cladding · Hydrogen

D. Xu (✉)
School of Mechanical, Industrial and Manufacturing Engineering,
Oregon State University, Corvallis, OR 97331, USA
e-mail: donghua.xu@oregonstate.edu

H. Xiao
Department of Nuclear Engineering, University of Tennessee,
Knoxville, TN 37996, USA

J.H. Jackson et al. (eds.), *Proceedings of the 18th International Conference on Environmental Degradation of Materials in Nuclear Power Systems – Water Reactors*, The Minerals, Metals & Materials Series, DOI 10.1007/978-3-319-68454-3_42

Introduction

As a consequence of hydrogen pick-up from the coolant water, thermal diffusion of hydrogen into the zirconium matrix and the limited solubility of hydrogen in zirconium, hydride precipitation and growth takes place in zirconium cladding used in light water reactors (LWRs) during normal operation of nuclear power plants. Accumulation of hydrides significantly reduces the ductility of the cladding and increases the risk of its mechanical failure. Hence, detailed information about hydrides, such as the time-dependent number density, the size and size-distribution and the spatial distribution, is highly desired for accurate mechanics modeling and safety assessment of the fuel-cladding system and even the entire reactor. Existing models [1–4] for the hydrogen transport and hydride formation kinetics are of reduced order and only provide the hydrogen partition, i.e., the total hydrogen concentration in the metal matrix (solid solution form) and in all hydrides, not able to untangle the number density and the size information of the hydrides. As the first attempt of its nature, we have recently developed a high resolution microscopic model for this problem using diffusion-reaction rate theory based cluster dynamics [5]. Cluster dynamics is a computational approach that has been used extensively to model kinetic processes, e.g. defect clustering and helium bubble formation, in irradiated materials [6–10].

Applying the cluster dynamics approach to the hydrogen diffusion and precipitation kinetics, our microscopic model, in its general form, is represented by the following system of differential equations:

$$\begin{cases} \frac{\partial C_1(x,t)}{\partial t} = -\frac{\partial}{\partial x}J + 2\times k_2^- C_2 + \sum_{n>2} k_n^- C_n - 2\times k_1^+ C_1^2 - \sum_{n>1} k_n^+ C_1 C_n \\ \left.\frac{\partial C_n(x,t)}{\partial t}\right|_{n>1} = k_{n-1}^+ C_1 C_{n-1} + k_{n+1}^- C_{n+1} - k_n^+ C_1 C_n - k_n^- C_n \end{cases} \tag{1}$$

where C stands for the concentration (nm^{-3}), k_n^+ and k_n^- are the reaction rate constants for a cluster (hydride) containing n-H atoms to capture and emit a H-atom, respectively, and J is the diffusion flux of the free hydrogen monomers in the zirconium matrix which may be driven by concentration and/or temperature gradient. The capturing and emission rate constants are related to each other as $k_n^- = k_n^+ C_0 \exp\left(-\frac{E_{b,n}}{k_B T}\right)$ according to detailed balance required by thermodynamics, where C_0 is the atomic number density of the zirconium matrix, and $E_{b,n}$ is the binding energy of a hydrogen atom to the hydride containing n- hydrogen atoms. In this current model, the hydrides are assumed to have a fixed stoichiometry (e.g., $\delta-$ hydride often observed) and hence the H-number is sufficient to represent a hydride cluster. It is also assumed that a hydride cluster contains at least two H-atoms (hence C_1 refers to the concentration of hydrogen in the metal matrix) and that the influence of the zirconium atoms, which are readily available from the matrix, on the rate of the hydride formation kinetics is negligible.

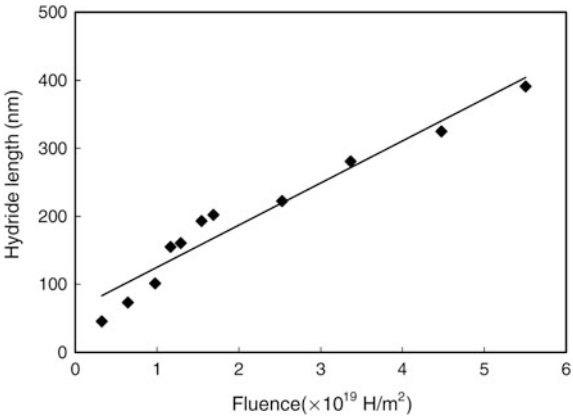

Fig. 1 Experimental data for the growth of the pre-existing hydride under in situ 20 keV hydrogen ion implantation at a flux of 5.5×10^{15} H/(m^2 s) at 25 °C. (reproduced from [11])

In a recent publication [5], we incorporated into this model some realistic, or relatively well known, fuel cladding parameters in LWRs, namely, wall thickness, temperature, temperature gradient, Soret effect constant and hydrogen pickup rate at the waterside (as a boundary condition), and demonstrated the capability of this model to predict the long term dynamic evolution of concentrations of freely migrating H-monomers and hydride clusters of all different sizes at different positions across the entire cladding thickness. However, as pointed in that paper, the model and its certain fundamental physical parameters, such as the binding energy of all different-sized hydride clusters, need to be thoroughly validated through relevant experiments.

Here we report our recent validation effort using an in situ TEM (transmission electron microscopy) experiment in the literature [11]. Specifically, we are referring to the dynamic growth of a pre-existing hydride observed in situ during hydrogen ion implantation on an electron microscope, as depicted in the Figs. 3a–d and 9 ("un-irradiated" case, reproduced here as Fig. 1) in [11]. An apparently near-spherical pre-existing hydride with a diameter of about 40 nm was formed prior to the ion implantation as a result of electrochemical polishing in TEM sample preparation. Upon in situ hydrogen ion implantation at room temperature (25 °C) using an ion energy of 20 keV and a flux of 5.5×10^{15} H/(m^2 s), the hydride exhibited one dimensional growth at a rate of $\sim$0.03 nm/s (estimated from Fig. 1).

Model Setup

Unlike the in-reactor condition where hydrogen is introduced into zirconium matrix predominantly from one side (water side), hydrogen in the referenced in situ experiment was introduced by implantation throughout the thickness ($\sim$100 nm) of the TEM foil. Figure 2 shows the depth-dependent stopping probability of 20 keV hydrogen in a 100 nm zirconium foil, calculated using the SRIM (Stopping and Range of Ions in

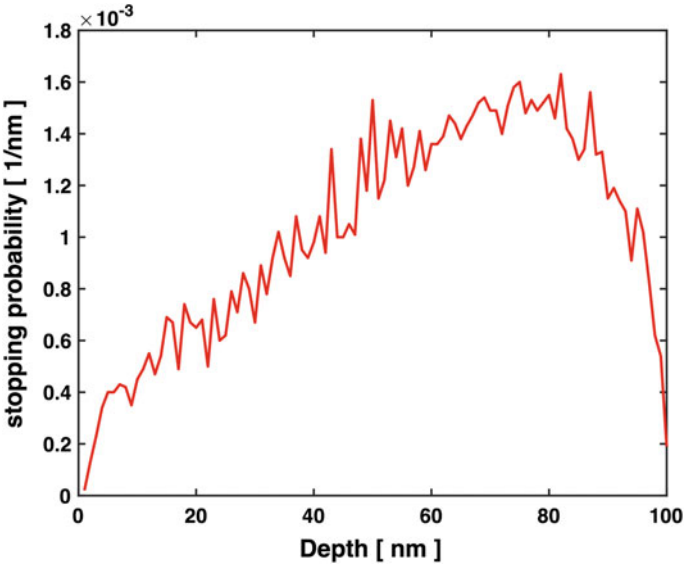

Fig. 2 SRIM calculated stopping probability of 20 keV hydrogen ions in 100 nm thick Zr foil using a displacement threshold of 40 eV

Matter) program [12] with a Zr-displacement threshold of 40 eV. The integrated stopping probability across the foil thickness is 0.1, indicating that 90% of implanted ions penetrate the thin foil or are back scattered (very small portion). Averaging the stopping probability across the 100 nm, the mean hydrogen production rate inside the foil is estimated to be 5.5×10^{21} H/(m^3 s). The referenced paper reported a somewhat lower value, 4×10^{21} H/(m^3 s) which we will use first in this work.

To simulate the referenced experiment, the generic form [Eq. (1)] of our model is modified as follows:

$$\begin{cases} \frac{dC_1(t)}{dt} = P + 2 \times k_2^- C_2 + \sum_{n>2} k_n^- C_n - 2 \times k_1^+ C_1^2 - \sum_{n>1} k_n^+ C_1 C_n \\ \left.\frac{dC_n(t)}{dt}\right|_{n>1} = k_{n-1}^+ C_1 C_{n-1} + k_{n+1}^- C_{n+1} - k_n^+ C_1 C_n - k_n^- C_n \end{cases} \quad (2)$$

where P is the production rate of hydrogen monomers. The initial condition for this problem is a nonzero concentration of the pre-existing hydride ($\sim$40 nm diameter) and zero concentrations for all other species including the hydrogen monomer. Considering the apparent shape change of the hydride before and after the implantation induced growth, we treat any hydrides smaller than 40 nm diameter (initially not existing but potentially to be formed during implantation) as spherical and those bigger than the 40 nm diameter as a capsule, as shown in Fig. 3. For the spherical hydrides, the radius is related to the number of hydrogen monomers contained in the hydride as $r = n^{1/3} \times 0.15$ (n > 1, r in nm), where 0.15 is obtained from the ab initio calculated lattice constant and the number of hydrogen atoms in one unit cell of δ

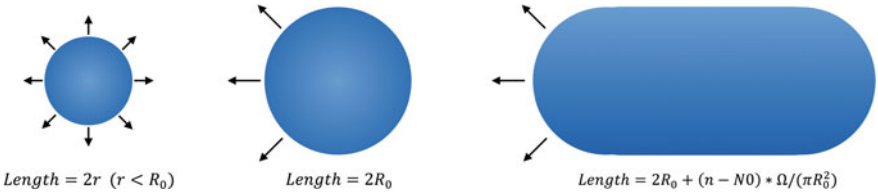

Fig. 3 Geometric considerations for different sized hydrides in the model

hydride [13]. For these hydrides, the size (or, "length") is simply the diameter. The 40 nm diameter, i.e., the initial size of the near-spherical pre-existing hydride, corresponds to 2370371 hydrogen monomers. For the capsular hydrides, the length is linearly dependent on the number of hydrogen monomers contained as $l = 40 + (n - 2370371) \times \Omega/(\pi \times 20^2)$ (in nm), where $\Omega = 4\pi \times 0.15^3/3$.

The capturing rate of hydrogen monomers by different-sized hydrides is also treated differently according to the size of the hydrides, as indicated by the arrows in Fig. 3. For the spherical hydrides smaller than 40 nm diameter, the common expression in the diffusion–reaction rate theory, $k_n^+ = 4\pi(r_1 + r_n)(D_1 + D_n)$, is used, where $r_1 = 0.053$ nm is the radius of the hydrogen monomer in the matrix and D is diffusivity. Here we only consider hydrogen monomer in the zirconium matrix to be mobile with a migration energy of 0.47 eV and a pre-factor of 7×10^{-3} $cm^2\ s^{-1}$ [14], consistent with the literature. For the capsular hydrides, hydrogen monomers are considered to be absorbed only from one side of the surface, i.e., $k_n^+ = 2\pi(r_1 + 20nm)D_1$, and independent of the increasing length of the capsule.

The binding energy of a hydrogen monomer to a hydride cluster is estimated based on the commonly used capillary law as $E_{b,n} = G_{dissl} - 0.44\left[n^{2/3} - (n-1)^{2/3}\right]$ (in eV) where G_{dissl} is the dissolution energy of hydrogen in Zr, and $0.44 = 4\pi \times 0.15^2 \times 1.56$ is based on an assumed interfacial energy of 1.56 eV/nm^2 (0.25 J/m^2). To the best of our knowledge, there has not been a dedicated study on the interfacial energy between $\delta-$ hydride and zirconium matrix either through computation or specially designed experiments. In general, interfacial energy between a precipitate and a matrix is on the order of 0.1–1 J/m^2. For the hydrogen dissolution energy, we use $G_{dissl} = k_B[5130 - Tln(29.79)]$ formulated from a recent ab initio study [13]. It is noted that with increasing n, the interfacial energy term in the binding energy formulation vanishes and the binding energy saturates quickly to the G_{dissl} and becomes independent of the hydride size.

Results and Discussion

With the above model setup and the hydrogen monomer production rate of 4×10^{-6} H/(nm^3 s) and the initial number density of the pre-existing hydrides, 9×10^{-8} nm^{-3}, provided in [11], our model is used to calculate the time-dependent

concentrations of hydrogen monomer in the matrix and hydride clusters containing from 2 to ~10,000,000 hydrogen atoms. To solve this large system of differential equations, we employ our high-efficiency cluster dynamics code PARASPACE which supports sparse matrix and OpenMP parallelism (for multi-core shared memory system) and utilizes high performance ILUPACK [15] linear algebra solver and METIS ordering library [16], as detailed in our previous publication [9].

Figure 4 presents the total number density and Fig. 5 presents the average length of the hydrides equal to or greater than the 40 nm initial size as a function of time. It can be seen in Fig. 4 that the total number density remains constant, indicating that no new hydrides are formed that reach this pre-existing hydride size regime, although very small hydride clusters with a handful number of hydrogen monomers that are certainly beyond the TEM resolution are indeed found in the simulation. Figure 5 shows a linear growth behavior of the pre-existing hydrides, which agrees qualitatively with the experimental trend shown in Fig. 1. However, the growth rate in Fig. 5 is only 5×10^{-4} nm/s, lower than the 0.03 nm/s in Fig. 1.

The apparently higher 0.03 nm/s hydride growth rate in Fig. 1 (the referenced experiment) is not completely understood but several factors may have contributed, as detailed below.

We first note that this growth rate may not be representative of all the pre-existing hydrides at the reported number density (9×10^{-8} nm^{-3}) and the initial size of ~40 nm in [11], since that would require a hydrogen production rate of 2.4×10^{-4} H/(nm^3 s), much greater than the 4×10^{-6} H/(nm^3 s) reported. It appears more likely that the high growth rate is only for one particular hydride. Several TEM micrographs in [11] indicated a significant fluctuation in the local

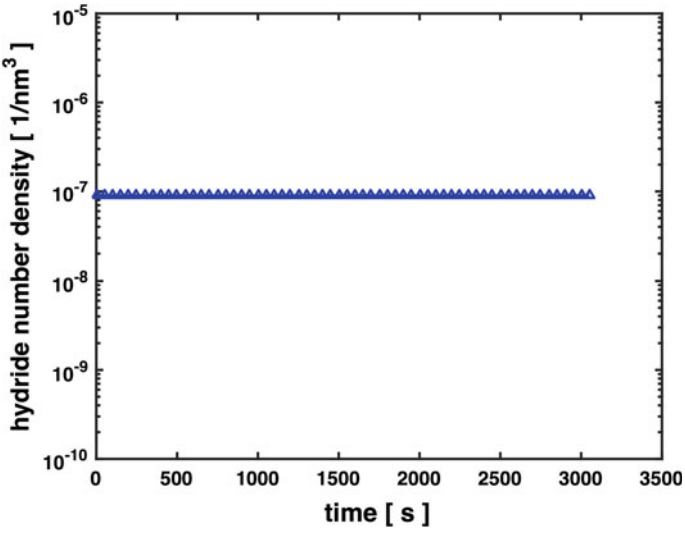

Fig. 4 Total number density of hydrides equal to or greater than the initial 40 nm size as a function of time, predicted by the model for the in situ 20 keV hydrogen ion implantation at a flux of 5.5×10^{15} H/(m^2 s) at 25 °C

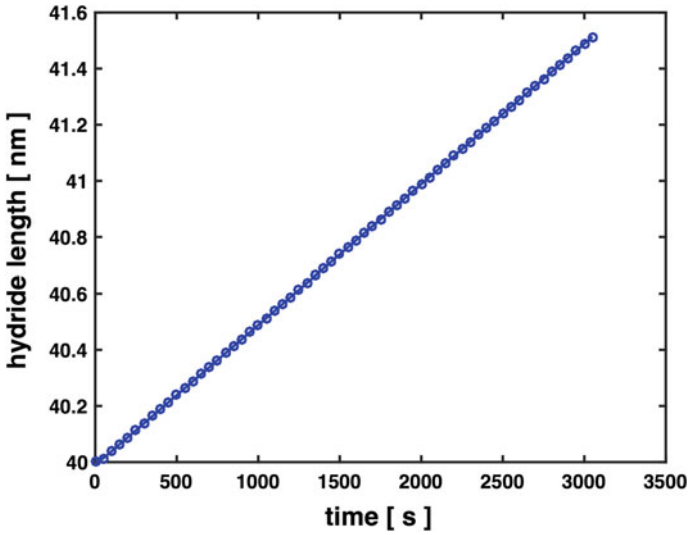

Fig. 5 Averaged length of hydrides equal to or greater than the initial 40 nm size as a function of time, predicted by the model for the in situ 20 keV hydrogen ion implantation at a flux of 5.5×10^{15} H/(m^2 s) at 25 °C

number density of the pre-existing hydrides, although no clear discussion was made therein.

Hence, our model is employed to perform a parametric study on the effect of the initial hydride number density on the growth rate. Figure 6 presents the model predicted growth curve using an initial number density of 1.5×10^{-9} nm^{-3}. It shows a short "incubation" period and then a transition into a linear growth stage. The "incubation" period is understood as the adjustment of the background hydrogen monomer concentration due to mutual clustering of the newly introduced hydrogen. The linear growth rate calculated based on the range between 1500 and 2500 s is 0.028 nm/s, very close to the 0.03 nm/s in Fig. 1.

The 1.5×10^{-9} nm^{-3} local number density of pre-existing hydrides used in Fig. 6 may appear too low in comparison with the reported 9×10^{-8} nm^{-3} in [11]. However, other factors may have simultaneously contributed to the apparently high growth rate of a particular pre-existing hydride, which then does not require such a low number density of pre-existing hydrides.

As mentioned in the previous Model Setup section, our SRIM calculation for 20 keV hydrogen in a 100 nm zirconium foil suggested a somewhat higher depth-averaged hydrogen production rate, 5.5×10^{-6} H/(nm^3 s), than the reported 4×10^{-6} H/(nm^3 s) in [11]. Moreover, there is a depth dependence of the hydrogen stopping probability, as revealed in Fig. 2. At the peak stopping position, the local hydrogen monomer production rate can be as high as 8.3×10^{-6} H/(nm^3 s). Hence, our model is also used to study the effect of uncertainty in the local hydrogen monomer production rate on the growth rate, fixing the number density of

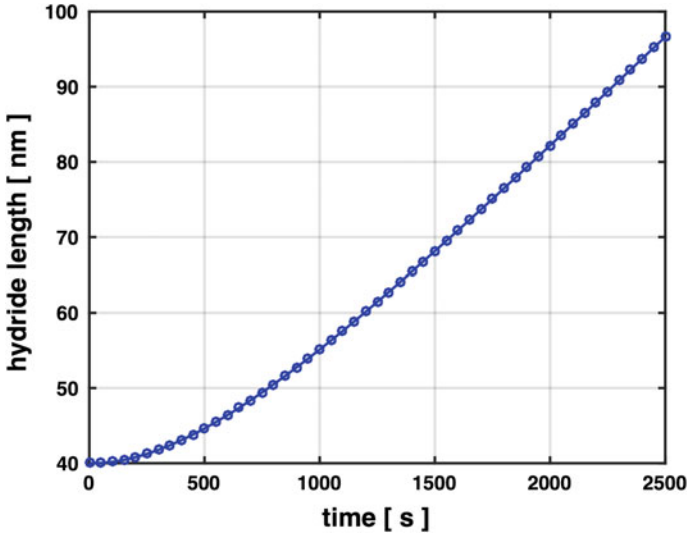

Fig. 6 Hydride growth curve predicted by the model with a lower initial hydride number density for the in situ 20 keV hydrogen ion implantation at a flux of 5.5×10^{15} H/(m^2 s) at 25 °C

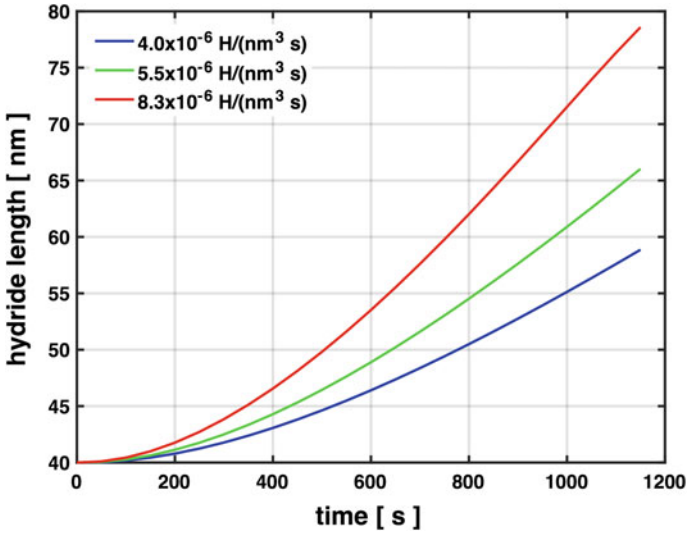

Fig. 7 Effect of uncertainty in local hydrogen production rate on the growth rate of pre-existing hydrides, predicted by the model for the in situ 20 keV hydrogen ion implantation at a flux of 5.5×10^{15} H/(m^2 s) at 25 °C

pre-existing hydrides to be 1.5×10^{-9} nm^{-3}. As shown in Fig. 7, an increase in the local hydrogen monomer production rate from 4×10^{-6} H/(nm^3 s) to 5.5×10^{-6} H/(nm^3 s) or to 8.3×10^{-6} H/(nm^3 s) clearly increases the apparent growth rate of

the pre-existing hydride. The linear growth rate estimated for the highest hydrogen production rate in Fig. 7 is 0.047 nm/s, higher than the 0.03 nm/s from Fig. 1. Figures 6 and 7 together suggest that moderate fluctuations in the local number density of the pre-existing hydrides and in the local hydrogen monomer production rate may be a plausible explanation for the observed 0.03 nm/s growth rate of the pre-existing hydride in Fig. 1.

There are yet other factors that may have played a role in determining the actual growth rate, such as the non-uniform sizes of the pre-existing hydrides and the non-ideal geometries of the pre-existing hydrides and the grown hydrides. Hence, it is our plan to continue to test and validate our microscopic model for the hydride precipitation and growth kinetics in Zr with a broader set of suitable experiments in the future.

Conclusions

We have recently developed a new microscopic model for the hydride precipitation and growth kinetics in zirconium using diffusion-reaction rate theory based cluster dynamics approach. This paper has been focused on comparing our model with an in situ TEM experiment in the literature. Our model correctly reproduces the linear growth behavior of the pre-existing hydrides under 20 keV hydrogen ion implantation. By considering possible fluctuations in the local number density of the pre-existing hydrides and in the local hydrogen monomer production rate, our model also provides a possible explanation for the relatively high growth rate of 0.03 nm/s reported in the referenced experiment. More thorough validation of our model will be conducted in the future.

Acknowledgements D. Xu acknowledges support from the DoE CASL (Consortium for Advanced Simulation of Light water reactors) program under the subcontracts UT-B 4000139375 and UT-B 4000154162 and new faculty startup fund from Oregon State University.

References

1. G.P. Marino, Nucl. Sci. Eng. **49**, 93 (1972)
2. C.F. Bilsby, J. Nucl. Mater. **68**, 1 (1977)
3. B.F. Kammenzind, D.G. Franklin, H.R. Peters, W.J. Duffin, in *The Nuclear Industry: 11th International Symposium*, ed. by E.R. Bradley, G.P. Sabol, ASTM STP 1295, (American Society for Testing and Materials, 1996), p. 338
4. M.S. Veshchunov, V.E. Shestak, V.D. Ozrin, J. Nucl. Mater. **472**, 65 (2016)
5. A. Aryanfar, J. Thomas, A. Van Der Ven, D.H. Xu, M. Youssef, J. Yang, B. Yildiz, J. Marian, JOM **68**, 2900 (2016)
6. D.H. Xu, A. Certain, H.J.L. Voigt, T. Allen, B.D. Wirth, J. Chem. Phys. **145**, 104704 (2016)
7. D.H. Xu, G. VanCoevering, B.D. Wirth, Comput. Mater. Sci. **114**, 47 (2016)
8. D.H. Xu, B.D. Wirth, M.M. Li, M.A. Kirk, Appl. Phys. Lett. **101**, 101905 (2012)

9. D.H. Xu, B.D. Wirth, M.M. Li, M.A. Kirk, Acta Mater. **60**, 4286 (2012)
10. D.H. Xu, B.D. Wirth, J. Nucl. Mater. **403**, 184 (2010)
11. Y. Shinohara, H. Abe, T. Iwai, N. Sekimura, T. Kido, H. Yamamoto, T. Taguchi, J. Nucl. Sci. Tech. **46**, 564 (2009)
12. J.F. Ziegler, J.P. Biersack, U. Littmark, *The Stopping and Range of Ions in Matter* (Pergamon, New York, 1984)
13. M. Christensen, W. Wolf, C. Freeman et al., J. Phys.: Condens. Matter **27**, 025402 (2015)
14. D. R. Olander, *Fundamental Aspects of Nuclear Reactor Fuel Elements* (ERDA, 1976)
15. A. Rafiei, M. Bollhofer, Numer. Math. **118**, 247 (2011)
16. G. Karypis, V. Kumar, SIAM J. Sci. Comput. **20**, 359 (1999)

Modeling Corrosion Kinetics of Zirconium Alloys in Loss-of-Coolant Accident (LOCA)

Léo Borrel and Adrien Couet

Abstract Correctly predicting the mechanical behavior of zirconium fuel cladding during a LOCA transient is critical for nuclear safety analysis as the fuel rod needs to maintain its coolable geometry throughout the LOCA sequence. A physically-based zirconium alloy corrosion model called the Coupled Current Charge Compensation (C4) is developed. The model calculates the coupling of oxygen, electron and hydrogen currents and predicts the oxide, oxygen-stabilized α-Zr and prior-β-Zr layers kinetics as well as the oxygen concentration profiles during a LOCA scenario. The results obtained during isothermal conditions are compared to experimental data for validation. Future developments of the C4 model include an implementation into the nuclear performance code BISON, which currently does not provide a physical description of the oxygen and hydrogen concentration profiles in the cladding. Thanks to the C4 implementation into BISON, structural integrity of the fuel cladding following a LOCA event can be assessed.

Keywords Zirconium corrosion · Oxidation model · Oxygen diffusion · LOCA

Introduction

The corrosion of zirconium alloy fuel cladding is a life-limiting degradation mechanism in Light Water Reactors (LWRs). Indeed, the growth of a brittle ZrO_2 protective oxide and associated hydrogen ingress embrittle the cladding [1, 2]. During a hypothetical Loss-of-Coolant Accident (LOCA) scenario, the high temperature corrosion, coupled with oxygen ingress in the metal, leads to a more complex mechanism and an overall higher oxidation rate.

L. Borrel (✉) · A. Couet
Department of Engineering Physics, University of Wisconsin-Madison, Madison, WI, USA
e-mail: borrel@wisc.edu

A. Couet
e-mail: couet@wisc.edu

J.H. Jackson et al. (eds.), *Proceedings of the 18th International Conference on Environmental Degradation of Materials in Nuclear Power Systems – Water Reactors*, The Minerals, Metals & Materials Series, https://doi.org/10.1007/978-3-319-68454-3_43

A Loss-of-Coolant accident (LOCA) is a designed accidental scenario in which the fuel cladding is subjected to a rapid temperature transient from 360 to 1200 °C, because of the loss of coolant. The high temperature regime lasts hundreds of seconds and is followed by a quench to room temperature. Figure 1 illustrates a LOCA event and the behavior of zirconium cladding during this temperature transient.

At high temperature, the oxidation kinetics is greatly increased compared to normal conditions. Furthermore, zirconium alloys undergo a phase change around 815 °C from an HCP α-Zr phase to a BCC β-Zr phase. In addition, oxygen diffusion in the metal ahead of the oxide creates an oxygen-stabilized α-Zr phase between the oxide layer and the β-Zr phase. After the quench, the oxide and the α-Zr layers are brittle, and thus the remaining cladding ductility is only due to the prior-β-Zr layer and is highly dependent on oxygen and hydrogen content in this phase [3, 4].

The oxidation of zirconium alloys is usually described by a power law: $\delta(t) = kt^n$ where δ is the oxide thickness and t is the exposure time. At normal operating conditions (T = 320 °C), n goes from 0.2 for ZrCu to 0.5 for ZrNb, depending on the alloy, with $n = 1/2$ corresponding to the eletroneutral case (parabolic oxidation) derived by Hauffe and Wagner [5, 6]. This power law fitting is valid for pre-transition regime (until $\delta \approx 3$ μm). The transition is defined as the time when the oxide layer become unprotective and leads to the growth of a new protective oxide layer following the same power law (illustrated in Fig. 4).

The physically-based model that is being developed, called the Coupled Current Charge Compensation (C4) model, is meant to provide oxide, oxygen-stabilized α-Zr layer and prior-β-Zr layer kinetics as well as oxygen and hydrogen concentration profiles. Both low *and* high temperature isotherms as well as temperature

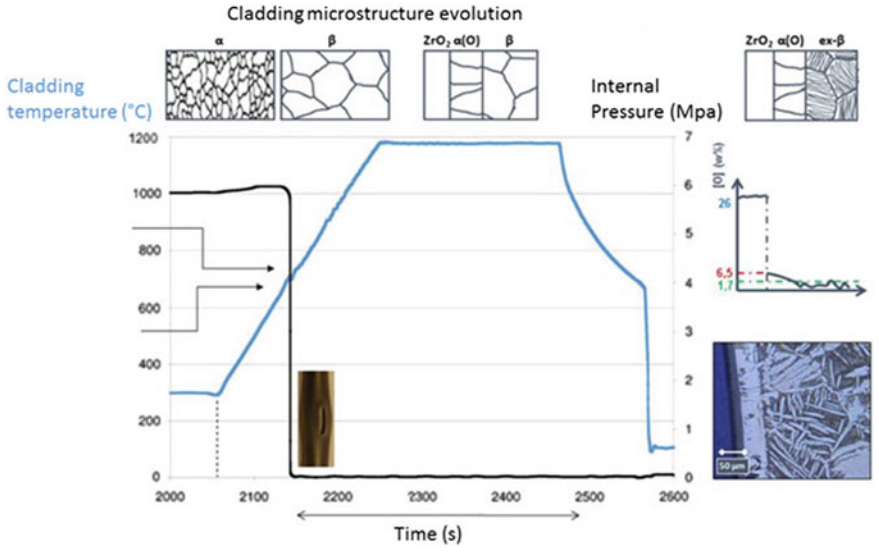

Fig. 1 Schematic of a LOCA transient and the resulting zirconium alloy behavior

transients such as LOCA can be correctly modeled for different zirconium-niobium alloys with this single model, making it unique and versatile in its use. This paper focuses on parabolic oxidation (because this is the regime observed at high temperature for all the different alloys), but an enhanced model is also under development for sub-parabolic oxidation at low temperature [7]. This paper will describe the C4 model and compare it to experimental data for validation.

Coupled Current Charge Compensation (C4) model

Assumptions

A detailed description of the C4 model with justification of the assumptions is available in [8]. A brief summary of the main features of the C4 model is provided below:

- The doubly-charged oxygen vacancies $V_{\ddot{O}}$ and electrons e^- fluxes are modeled through the oxide, along with oxygen atoms ingress into the metal. Hydrogen can be implemented as well, but the addition of the hydrogen flux and diffusion is beyond the scope of this paper.
- The effect of the electric field on the mobility of the charged diffusing species is also taken into account explicitly in addition to the chemical driving force (i.e. the electrochemical potential is modeled).
- Steady state hypothesis: the concentration of species and electric fields adjustments upon the formation of an oxide monolayer are much faster than the growth of one oxide monolayer.
- The concentration of species at the interfaces are constant with regards to time (i.e. the reactions at the interfaces are at equilibrium).
- The rate-limiting step for the oxidation reaction is the diffusion-migration of species across the oxide (which correlates with an oxidation rate depending on the thickness of the oxide).
- All species are in solid solution and the delayed oxidation of precipitates is not modeled. The solubility limit of Nb in α-Zr is around 0.6% [3], thus the Zr-1.0Nb alloy used in this study has been annealed at 720 °C (in the α-Zr + β-Zr dual phase) and quenched to remove all the Nb rich β-Nb precipitates [9].
- The oxide-water and oxide-metal interfaces are considered planar.
- No macroscopic net current is observed through the oxide during the corrosion process. This means that the coupled-current equation of net zero charge transport through the protective oxide is imposed: $\sum_{s}^{diffusingspecies} Z_s e J_s = 2J_{V_{\ddot{O}}} - J_{e^-}$. As the mobility of vacancies and electrons are not the same, their local concentrations are different, which creates a difference of charge concentration locally. To account for this difference, two mechanisms can be assumed: (i) a local electric field can result from the mobility difference; (ii) oxidized aliovalent ions (which are not migrating) can compensate to some extent the charge difference [2, 6–8, 10].
- A hydrogen pickup fraction of 15% is assumed for high temperature corrosion.

Moving Boundary Diffusion Model

Figure 2 is a scheme describing our system during high temperature corrosion. The two arrows at the top ($v_{\ddot{O}}$ and $O_O^{\times}$) are two different forms to depict the flux of doubly-charged vacancies. The two driving forces are represented: the concentration gradient and the electric field. As the oxide grows, the α-Zr/β-Zr and α-Zr/ZrO_2 interfaces advance inside the metal (toward the left on the scheme), whereas the ZrO_2/H_2O interface progresses towards the electrolyte (on the right on the scheme) because of oxide volume expansion.

For low temperature, the scheme is similar, with two main discrepancies: the oxide dissolution is negligible compared to oxide growth, and the metal is a single homogeneous α-Zr phase.

The oxygen balance at the α-Zr/ZrO_2 interface results in the well known moving interface equation:

$$\frac{d\xi_1}{dt} = \frac{J_O - J_{v_{\ddot{O}}}}{PBR\, C^O_{ox-\alpha} - C^O_{\alpha-ox}} \tag{1}$$

where ξ_1 is the position of the α-Zr/ZrO_2 interface (in cm); J_O [respectively $J_{v_{\ddot{O}}}$] is the flux of atomic oxygen in the metal [respectively the flux of vacancies in the oxide] (in $cm^{-2}s^{-1}$); $PBR = \frac{V_{oxide}}{V_{metal}} = 1.55$ (for zirconium) is the Pilling-Bedworth ratio describing the difference of molar volume between the oxide and the pure metal (unitless); $C^O_{ox-\alpha}$ [respectively $C^O_{\alpha-ox}$] is the concentration of oxygen in the oxide [respectively in the α phase] at the α-Zr/ZrO_2 interface (in cm^{-3}).

The flux of the vacancies $J_{v_{\ddot{O}}}$ is determined by the C4 model (see [8] for the derivation of the expression), whereas the flux of oxygen J_O follows Fick's law of diffusion into the metal: $J = -D\frac{dC}{dx}$ with D the diffusion coefficient of the species in

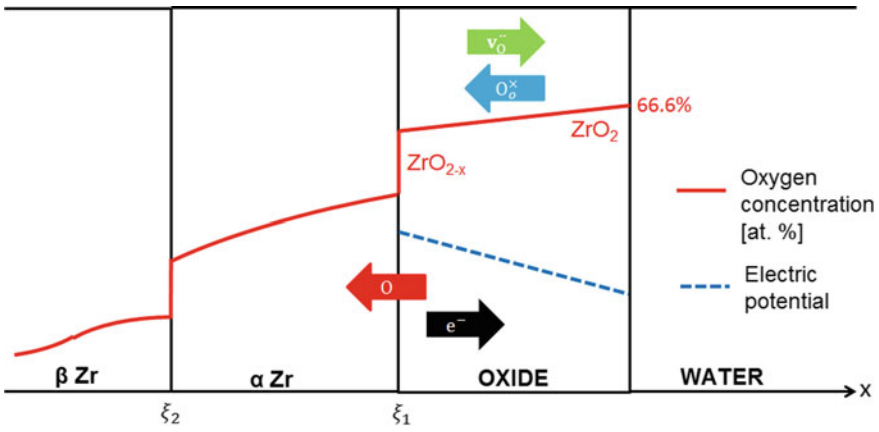

Fig. 2 Schematic diagram of the fluxes involved in the oxidation of Zirconium alloy at high temperature

the material and C their concentration. As expected, Eq. (1) shows that when oxide growth is greater than oxide dissolution, the interface advances into the metal.

A similar expression using the oxygen balance at the α-Zr/β-Zr interface can be derived for the moving a-Zr/b-Zr interface:

$$\frac{d\xi_2}{dt} = \frac{J_{\beta\to\alpha} - J_{\alpha\to\beta}}{C^O_{\alpha-\beta} - C^O_{\beta-\alpha}} \tag{2}$$

where ξ_2 is the position of the α-Zr/β-Zr interface (in cm); $J_{\beta\to\alpha}$ [respectively $J_{\alpha\to\beta}$] is the oxygen flux from the β-Zr to the α-Zr phase [respectively from the α-Zr to the β-Zr phase] (in $cm^{-2}s^{-1}$); $C^O_{\alpha-\beta}$ [respectively $C^O_{\beta-\alpha}$] is the oxygen concentration in the α-Zr phase [respectively in the β-Zr phase] at the α-Zr/β-Zr interface (in cm^{-3}) [3, 11].

Results and Discussion

In this section, first a comparison between the C4 model and experimental data for the oxidation kinetics at 360 °C during 240 days in pressurized pure water autoclave of zirconium with 1.0% of niobium (Zr-1.0Nb) is presented. Then, a comparison between the C4 model and experimental data for Zircaloy-4 oxidized at 1100 and 1200 °C in steam for different exposure times is discussed. In the latter, oxide thickness, α-Zr phase thickness and oxygen concentration profile in the metal are studied. The composition of Zircaloy-4 is given in Table 1 (the experimental conditions can be found in [9]).

Parameters Used

The alloy-dependent parameters are listed in Table 2 while the temperature-dependent parameters are listed in Table 3. These parameters are used throughout this study.

The electron and vacancy migration energies of the alloys describe the mobility of each species and are used as fitting parameters to differentiate the oxidation kinetics of different alloys. An extensive study has been performed in [8] deriving the different combination of migration energies allowed. Furthermore, the electric field and space charge effects on the oxidation kinetics is decreasing as temperature increases, so at high temperature all different alloys have close to parabolic kinetics.

Table 1 Composition of Zircaloy-4 (in wt%) [3]

Sn	Fe	Cr	O	Zr
1.3	0.2	0.1	0.13	Bal.

Table 2 Alloy-dependent parameters

Alloy	Zr-1.0Nb	Zry-4
Electron untrapping energy ($E_m^{e^-}$) [eV]	1.35	1.00
Vacancy migration energy ($E_m^{V_O^{\cdot\cdot}}$) [eV]	1.43	1.43

Table 3 Temperature-dependent parameters

Temperature	360 °C	1100 °C	1200 °C
Alloy	Zr-1.0Nb	Zry-4	Zry-4
Concentration of oxygen in the oxide at the α-Zr/ZrO_2 interface ($C_{ox-\alpha}^O$) [atomic fraction] [3]	66.17% ($ZrO_{1.985}$)	65.19% ($ZrO_{1.9558}$)	65.08% ($ZrO_{1.9525}$)
Concentration of vacancies at the oxide-water interface ($C_{ox-w}^{V_O^{\cdot\cdot}}$) [particles/$cm^3$] [8]	10^{17}	10^{17}	10^{17}
Concentration of electrons at the oxide-water interface ($C_{ox-w}^{e^-}$) [particles/cm^3] [8]	10^{17}	10^{17}	10^{17}
Concentration of vacancies at the oxide-metal interface ($C_{ox-\alpha}^{V_O^{\cdot\cdot}}$) [particles/$cm^3$] [3]	4.2×10^{20}	1.23×10^{21}	1.32×10^{21}
Concentration of electrons at the oxide-metal interface ($C_{ox-\alpha}^{e^-}$) [particles/cm^3] [3]	8.4×10^{20}	2.46×10^{21}	2.64×10^{21}
Concentration of oxygen in the α-Zr phase at the α-Zr/ZrO_2 interface ($C_{\alpha-ox}^O$) [atomic fraction] [11]		29.53%	29.98%
Concentration of oxygen in the α-Zr phase at the α-Zr/β-Zr interface ($C_{\alpha-\beta}^O$) [atomic fraction] [11]		8.59%	10.86%
Concentration of oxygen in the β-Zr phase at the α-Zr/β-Zr interface ($C_{\beta-\alpha}^O$) [atomic fraction] [11]		1.74%	2.79%
Nominal concentration of oxygen in the β-Zr phase in Zircaloy-4 (C_{nom}^O) [atomic fraction] [11]		0.74%	0.74%
Oxygen diffusion coefficient in α-Zr phase (D_α) (cm^2/s) [11]		2.48×10^{-8}	8.50×10^{-8}
Oxygen diffusion coefficient in β-Zr phase (D_β) (cm^2/s) [11]		8.44×10^{-7}	1.55×10^{-6}

The first part of the Table 3 contains the parameters for the migration of electrons and vacancies in the oxide, used both at low and high temperatures, whereas the second part contains parameters for the diffusion of oxygen in the metal used only at high temperature.

The concentration of vacancies and electrons at the oxide-water interface is assumed to be negligible compared to their concentration at the α-Zr/ZrO_2 interface [8]. The concentration of vacancies at the oxide-metal interface is determined by using the Zr–O phase diagram [3, 12]. The electron concentration is then chosen to compensate the charge at the interface, and so is equal to twice the value of the doubly-charged vacancies [8].

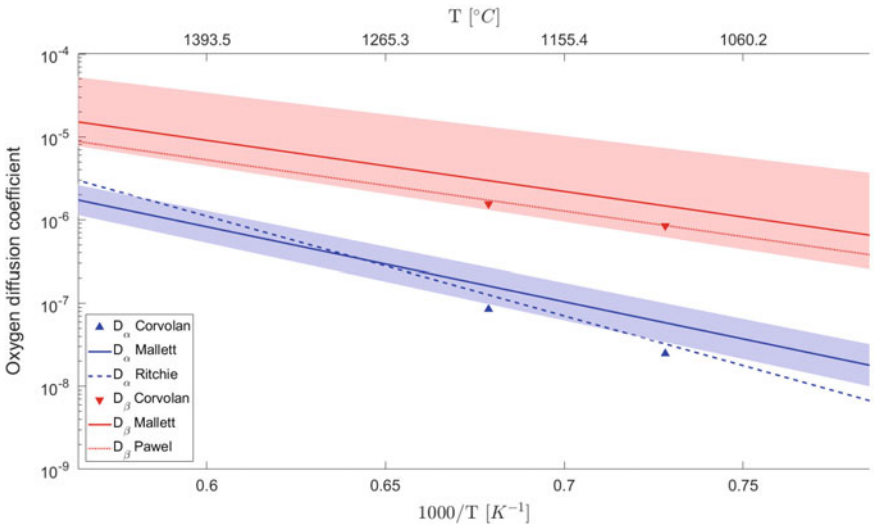

Fig. 3 Comparison of oxygen diffusion coefficient with literature values [11, 14–16]. The colored zones correspond to the uncertainty given by the authors (Color figure online)

The other oxygen concentrations and the oxygen diffusion coefficient in the α-Zr and β-Zr phases are taken from [11]. These parameters either come from literature [12] or from zircaloy thermodynamic databases [13], except for the diffusion coefficient of oxygen in the α-Zr phase which is used as a fitting parameter at high temperature. Resulting oxygen diffusion coefficients in α-Zr and β-Zr phases are compared to other literature values [14–16] in Fig. 3.

Low Temperature Oxidation (360 °C)

Figure 4 shows a comparison between the C4 model and experimental data for oxidation kinetics of Zr-1.0Nb oxidized in water at 360 °C during 240 days.

The oxide thickness at transition is determined empirically since the model does not take into account the stresses responsible for transition. The values obtained with the model are matching the experimental values very well.

Oxide and α-Zr Phase Growth Kinetic at High Temperature

This study focuses on validating the model with experimental data for high temperature isotherm oxidation. First, Table 4 presents a comparison of oxide and α-Zr phase thicknesses, and weight gain between the model and experimental data [1].

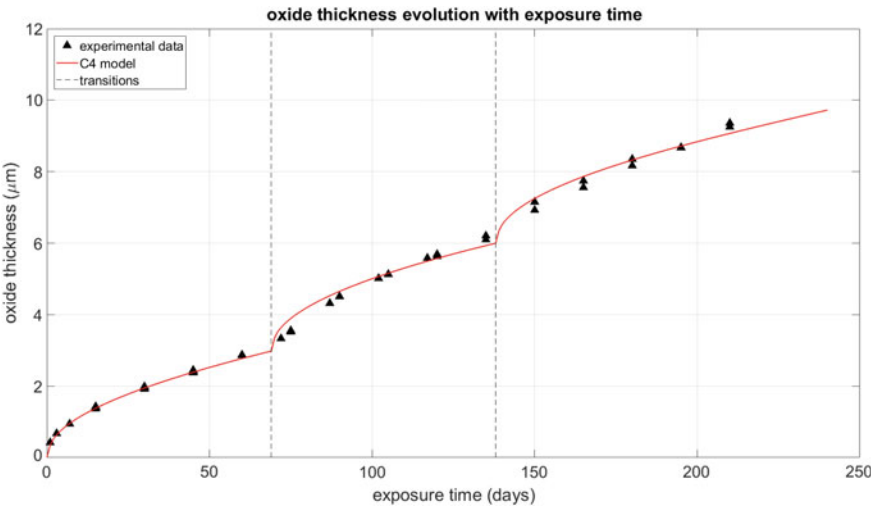

Fig. 4 Oxide thickness of Zr-1.0Nb annealed (oxidized in water at 360 °C during 240 days) as function of exposure time

The weight gain is defined as the mass difference between the oxidized and unoxidized sample divided by the surface area subject to corrosion.

The results at 1100 °C are very accurate for oxide layer thickness, with less than 1% of difference between the model and the experiment. The model is underpredicting the weight gain by around 10%.

For 1200 °C, the results are less accurate with a difference between experiment and model around 10% for the oxide and α-Zr phase thickness (except for the α-Zr thickness at 166 s of oxidation).

The experimental weight gain obtained at 1200 °C is not representative because it has not been determined experimentally but computed using the Cathcart-Pawel empirical model [17].

Overall, the data obtained with the C4 model are in good agreement with the experimental data, using the same parameters as at low temperature, but the model is still underpredicting weight gain. A possible explanation for the difference between the model and the experimental data is that the experiment is done on samples subject to double-side corrosion, whereas the model simulates only single-side corrosion. Thus, depending on the thickness of the sample and the diffusion of oxygen in the metal, the impact of the other oxidized side can be significant, changing both the weight gain and the thickness of the different layers. The effect is more visible at higher temperature because the diffusion is faster. An updated version of the model is under development to take into account double-sided corrosion.

Table 4 Comparison of the properties of Zircaloy-4 generated by the C4 model and by experiment [1]

Parameter	Experiment	C4 model	Percentage difference
Temperature (°C)	1100	1100	11.6%
Oxidation time (s)	1065	1065	
Weight gain (mg/cm^2)	13.2	11.7	
Oxide layer thickness (μm)	69	68.8	0.34%
Temperature (°C)	1200	1200	20.6%
Oxidation time (s)	400	400	
Weight gain (mg/cm^2)	13.5[a]	10.71	
Oxide layer thickness (μm)	67	58.8	12.3%
Temperature (°C)	1200	1200	18.4%
Oxidation time (s)	166	166	8.6%
Weight gain (mg/cm^2)	8.35[a]	6.8	41.2%
Oxide layer thickness (μm)	41.5	37.9	
α-Zr layer thickness (μm)	34	48.0	

[a]obtained with Cathcart-Pawel empirical model

Oxygen Concentration Profile at High Temperature

Using the same parameters (see Tables 2 and 3), the oxygen concentration profiles in the metal are compared to empirical data obtained by electron probe micro analysis (EPMA) available in the literature [11, 18]. Figures 5 and 6 show the oxygen concentration profiles in the α-Zr and β-Zr phases for Zircaloy-4 respectively oxidized at 1100 and 1200 °C.

The profiles obtained with the C4 model are globally very close to the experimental data. They are particularly close at 1100 °C both in the α-Zr phase and the β-Zr phase, as well as at 1200 °C for low oxidation times. For oxidation at 1200 °C during 520 s, the oxygen content deep inside the prior-β-Zr phase is not decreasing as the model predicts. The reasons for that discrepancy are not known at the moment and additional samples will be analyzed in our facilities for further investigation.

Thus, preliminary comparison of the C4 model with high temperature corrosion data of zirconium alloys (weight gain, oxide and α-Zr phase thickness, oxygen concentration profiles) using physically-based parameters are extremely promising. The model is currently being tested against more extensive data set including temperature transient scenario.

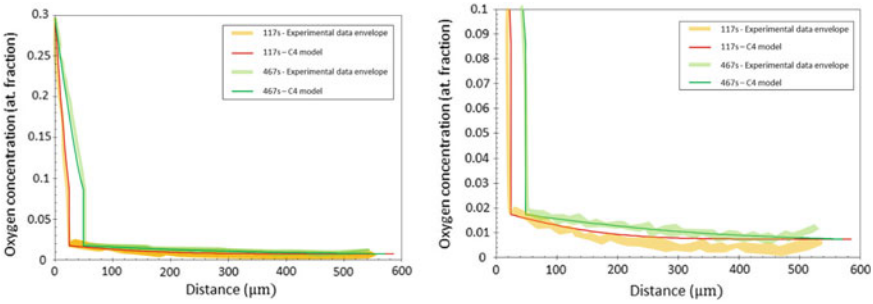

(a) α and β phases (b) zoom on the β phase

Fig. 5 Oxygen concentration profile for Zircaloy-4 oxidized at 1100 °C

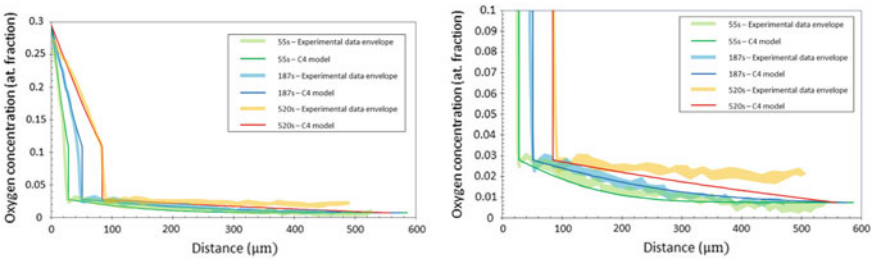

(a) α and β phases (b) zoom on the β phase

Fig. 6 Oxygen concentration profile for Zircaloy-4 oxidized at 1200 °C

Conclusion

A model for zirconium alloy corrosion at low and high temperature has been developed to predict oxidation kinetics and the oxygen concentration profiles in the metal. The Coupled Current Charge Compensation model is based on first principles and physical parameters. Its main asset is its good corrosion prediction at low and high temperature with different alloys at different temperature using the same set of parameters.

The model is still under development and several features are currently being added:

- Enable the model to be used for temperature transient with dynamic phase change;
- Enable the growth of a pre-oxide prior to a high temperature transient in order to simulate LOCA event occurring after a long exposure in reactor;
- Implement the model in BISON, a finite-element based fuel performance code developed by Idaho National Laboratory [19].

Acknowledgements Funding for this project was provided by CASL (Consortium for Advanced Simulation of Light Water Reactors).

References

1. M. Billone, Y. Yan, T. Burtseva, R. Daum, Cladding embrittlement during postulated loss-of-coolant accidents. Off. Nucl. Regul. Res., NUREG/CR-6967, 386 (2008)
2. A. Motta, A. Couet, R.J. Comstock, Corrosion of zirconium alloys used for nuclear fuel cladding. Ann. Rev. Mater. Res. **45**, 311–343 (2015)
3. X. Ma, C. Toffolon-Masclet, T. Guilbert, D. Hamon, J.C. Brachet, Oxidation kinetics and oxygen diffusion in low-tin zircaloy-4 up to 1523 K. J. Nucl. Mater. **377**(2), 359–369 (2008)
4. K. Petterson, M. Billone et al., Nuclear fuel behaviour in loss-of-coolant accident (loca) conditions, Report 6846, OECD (Organisation for Economic Co-operation and Development), January 2009
5. K. Hauffe, *Oxidation of Metals* (Springer, Berlin, 1995)
6. C. Wagner, W. Schottky, Theory of controlled mixed phases. Z. Physik. Chem. **B11**, 163 (1930)
7. A. Couet, A. Motta, R.J. Comstock, A. Ambard, Hydrogen pick-up mechanism in zirconium alloys, in *ASTM STP: Selected Technical Papers* (2016)
8. A. Couet, A. Motta, A. Ambard, The coupled current charge compensation model for zirconium alloy fuel cladding oxidation: I. parabolic oxidation of zirconium alloys. Corros. Sci. **100**, 73–84 (2015)
9. J. Romero, J. Partezana, R.J. Comstock, L. Hallstadius, A. Motta, A. Couet, Evolution of hydrogen pickup fraction with oxidation rate on zirconium alloys, in *Proceeding of Top Fuel Reactor Fuel Performance 2015*, p. 630, 13–17 September 2015
10. A.T. Fromhold, Parabolic oxidation of metals. Phys. Lett. A **29**(3), 157–158 (1969)
11. C. Corvalan-Moya, C. Desgranges, C. Toffolon-Masclet, C. Servant, J.C. Brachet, Numerical modeling of oxygen diffusion in the wall thickness of low-tin zircaloy-4 fuel cladding tube during high temperature (1100–1250 °C) steam oxidation. J. Nucl. Mater. **400**(3), 196–204 (2010)
12. H.M. Chung, T.F. Kassner, Pseudobinary zircaloy-oxygen phase diagram. J. Nucl. Mater. **84** (1), 327–339 (1979)
13. N. Dupin, I. Ansara, C. Servant, C. Toffolon, C. Lemaignan, J.C. Brachet, A thermodynamic database for zirconium alloys. J. Nucl. Mater. **275**(3), 287–295 (1999)
14. M.W. Mallett, M.W. Albrecht, P.R. Wilson, The diffusion of oxygen in alpha and beta zircaloy 2 and zircaloy 3 at high temperatures. J. Electrochem. Soc. **106**(3), 181–184 (1959)
15. I.G. Ritchie, A. Atrens, The diffusion of oxygen in alpha-zirconium. J. Nucl. Mater. **67**(3), 254–264 (1977)
16. R.E. Pawel, R. Perkins, R.A. McKee, J.V. Cathcart, G. Yurek, R. Druschel, Diffusion of oxygen in beta-zircaloy and the high temperature zircaloy-steam reaction. Zirconium Nucl. Ind., 119–133 (1977)
17. R.E. Pawel, J.V. Cathcart, R.A. McKee, The kinetics of oxidation of zircaloy-4 in steam at high temperatures. J. Electrochem. Soc. **126**(7), 1105–1111 (1979)
18. J.C. Brachet, V. Vandenberghe-Maillot, L. Portier, D. Gilbon, A. Lesbros, N. Waeckel, J.-P. Mardon, Hydrogen content, preoxidation and cooling scenario effects on post-quench microstructure and mechanical properties of zircaloy-4 and M5 alloys in LOCA conditions. J. ASTM Int. **5**(5), 91–118 (2008)
19. R.L. Williamson, J.D. Hales, S.R. Novascone, M.R. Tonks, D.R. Gaston, C.J. Permann, D. Andrs, R.C. Martineau, Multidimensional multiphysics simulation of nuclear fuel behavior. J. Nucl. Mater. **423**(13), 149–163 (2012)

Progressing Zirconium-Alloy Corrosion Models Using Synchrotron XANES

Michael Moorehead, Adrien Couet, Jing Hu and Zhonghou Cai

Abstract The corrosion and hydrogen pickup of in-reactor zirconium-based cladding is currently limiting the maximum fuel burnup in light-water reactors. Since the oxidation rate and hydrogen pickup fraction of zirconium alloys vary significantly as a function of exposure time, burnup, and alloy composition, it is critical to better understand the underlying mechanisms to model and predict corrosion behavior. Following the analysis of ~500 autoclave coupons, a physically based zirconium-alloy corrosion model founded on first principles, named "Coupled Current Charge Compensation (C4)", has been developed. The model reproduces the differences in oxidation kinetics and hydrogen pickup between different zirconium alloys, such as Zr-Nb and Zircaloy-4. Since oxidized solute elements affect the corrosion process through a space-charge compensation mechanism, synchrotron nano-beam X-ray Absorption Near-Edge Spectroscopy has been performed on multiple oxidized Zr-Nb alloys to determine the oxidation-state profile of niobium in the oxide layer. The results inform the C4 model and the associated hydrogen pickup fraction.

Keywords XANES · C4 Model · Zirconium corrosion

Introduction

In light-water reactors, corrosion of zirconium-based cladding, and the associated hydrogen pickup, imposes limitations on the maximum allowable burnup and the maximum in-reactor lifetime for a fuel rod. To increase these durations, and thereby

M. Moorehead (✉) · A. Couet
Department of Engineering Physics, University of Wisconsin-Madison, Madison, WI 53706, USA
e-mail: moorehead2@wisc.edu

J. Hu
Department of Materials, University of Oxford, Oxford OX1 3PH, UK

Z. Cai
Advanced Photon Source, Argonne National Laboratory, Lemont, IL 60439, USA

J.H. Jackson et al. (eds.), *Proceedings of the 18th International Conference on Environmental Degradation of Materials in Nuclear Power Systems – Water Reactors*, The Minerals, Metals & Materials Series, https://doi.org/10.1007/978-3-319-68454-3_44

the efficiency of reactors, fuel cladding alloy compositions must be tailored to minimize the oxidation rate and the hydrogen pickup fraction. To achieve this goal, a comprehensive understanding of the effects of alloying elements on the corrosion mechanics of reactor materials is needed.

It has been shown that zirconium alloys can produce vastly differing oxidation kinetics given only minimal variations in alloying elements [1–3]. For example, oxidation at 360 °C in pure water of Zr-1.0 Nb alloy annealed at 720 °C follows a power law with an exponent of n = 0.5 whereas Zircaloy-4 under the same conditions has an exponent of n = 0.3 [1]. Parabolic kinetics, as observed in Zr-1.0 Nb alloy annealed at 720 °C, indicate electroneutrality and uniform stress throughout the oxide whereas sub-parabolic kinetics, such as those of Zircaloy-4, suggest the presence of a stress gradient, a grain-size gradient, and/or the existence of space charge within the oxide [4–7]. Since it is unlikely that small variations in alloying elements from alloy to alloy would lead to a significant stress or grain-size gradient, as the oxidation kinetics would otherwise necessitate, it is thought that the primary cause of the difference in oxidation kinetics between zirconium alloys is the effect of solute trapping on the space charge within the oxide.

To better describe the oxidation of zirconium alloys, the Coupled Current Charge Compensation model (C4 model) was developed to account for space charges and their compensation mechanisms within the oxide layer [7]. The C4 model functions on the principle that the fluxes of charged species through the oxide must be equal and opposite (coupled current), as there can be no net current through the oxide. However, since the migration energy of oxygen vacancies and electrons are not necessarily equal, a difference in local concentrations of these species within the oxide arises. For instance, if the migration energy of electrons is lower than that of oxygen vacancies in ZrO_2 [7], the C4 model predicts a higher number of oxygen vacancies locally compared to the amount needed to neutralize the local charge of the diffusing electrons. This results in a net positive charge and thus a local electric field. The electric field produced by this space charge further slows the diffusion of oxygen vacancies thus leading to sub-parabolic kinetics. An example of a C4 model fit of parabolic oxidation kinetics can be seen in Fig. 1.

One mechanism to compensate the electric field produced by this space charge, and thus to obtain parabolic kinetics, would be by the presence of aliovalent ions within the oxide. These additional charges would be electronegative in comparison to zirconium cations. Indeed, one of the C4 model results is to predict the amount of these aliovalent species needed to compensate such an electric field, and to obtain parabolic kinetics, based on their oxidation state relative to the matrix cation.

The purpose of this study is to further inform the C4 model by determining the oxidation-state profile of niobium in Zr-Nb alloys showing different oxidation kinetics, with different compositions and microstructures, namely Zr-0.5Nb and Zr-1.0Nb, using synchrotron nano-beam X-ray Absorption Near-Edge Spectroscopy (XANES). The Zr-1.0Nb alloy system is divided into two alloys, one annealed at 720 °C, in the α-Zr + β-Zr region, and the other at 580 °C (referred to hereinafter as Zr-1.0Nb (720 °C) and Zr-1.0Nb (580 °C), respectively). These alloys were chosen as representatives of the Zr-Nb alloys currently used in industry

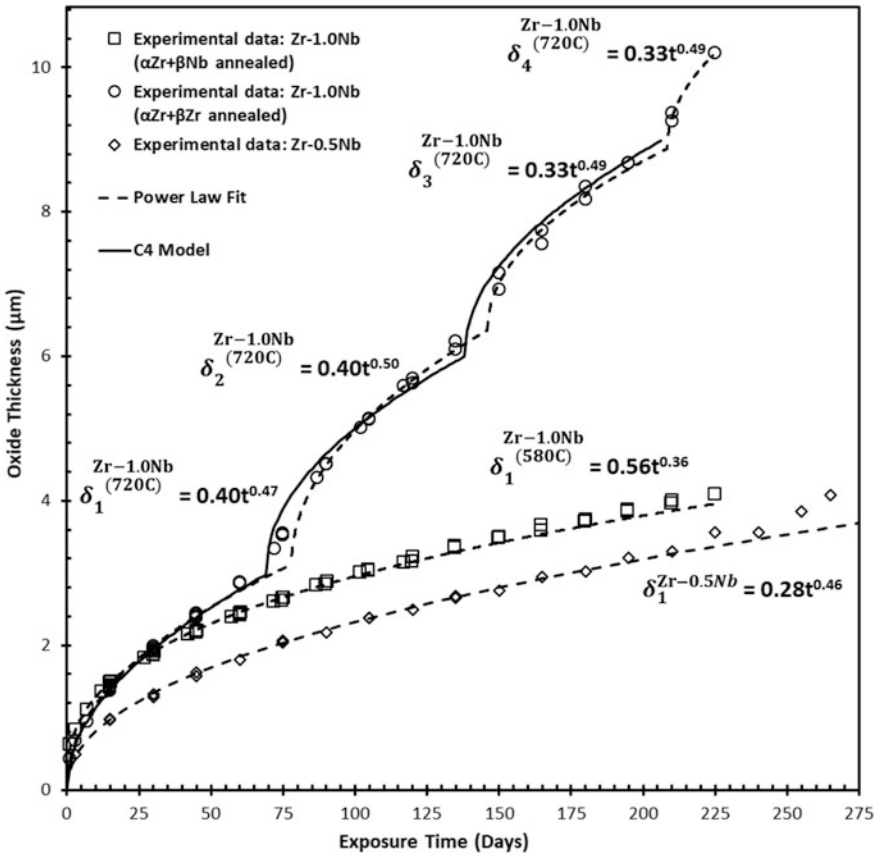

Fig. 1 Experimental weight gain of Zr-0.5Nb, Zr-1.0 (580 °C), and Zr-1.0Nb (720 °C) oxidized in 360 °C pressurized (18 MPa) pure water including C4 model fit for Zr-1.0Nb (720 °C)

for fuel claddings and for their different distributions of Nb which gives rise to greatly different oxidation kinetics. Using XANES the behavior of the niobium in these oxides is compared. This analysis will provide insight into the distribution of the niobium oxidation states across different microstructures and the effect of niobium on the oxidation kinetics of the selected Zr-Nb alloys.

Experimental Procedures

For this experiment, nano-beam XANES was performed at the Advanced Photon Source at Argonne National Laboratory. To perform XANES, a monochromatic X-ray beam is directed onto the area of interest on the sample, and the energy of the beam is varied across the K-edge of the element being investigated. Doing so

generates an absorption spectrum which encompasses the K-edge of the target element. Since the energy to remove a K-shell electron is greater when the target element is oxidized, akin to the increasing trend of ionization energies, an oxidized element will have a K-shell absorption edge at higher energy than its metallic counterpart. More generally, an element that has a higher oxidation state will have a K-edge centered around a higher energy that the same element with a lower oxidation state; thus, by generating an absorption spectrum using XANES, one is able to gain information about the oxidation state of the target element based on the shift in its K-edge energy.

The Zr-0.5Nb, Zr-1.0Nb (580 °C), and Zr-1.0Nb (720 °C) samples were provided by Westinghouse, and oxidized in 360 °C, pressurized (18 MPa), pure water in a stainless-steel autoclave at different exposure times. No additional gases were added to the autoclave and the water during the corrosion testing was static. Samples used from this experiment were produced as part of the Mechanistic Understanding of Zirconium Corrosion (MUZIC) consortium and their characterizations were made in collaboration with Oxford University (UK).

To determine the change in oxidation state and relative oxidized fraction of alloying elements in the oxide, samples of different oxide thicknesses were probed using nano-beam XANES at a series of locations crossing the oxide/metal interface and continuing into the oxide. X-ray absorption spectrums were fit against a series of standards using the program ATHENA [8]. A more detailed description of the XANES procedure, standard acquisition, and fitting with ATHENA can be found in a previous paper by Couet et al [9].

Though oxidized fraction was previously used to assess the state of alloying elements in the zirconium oxide layer [9], more rigorous computational modeling requires knowledge of the oxidation state of each element with respect to space for computing the net electric field in the oxide. Not only is the oxidation-state profile desirable to this end, but its close correlation to the oxidation-fraction profile may allow future work to be done in converting data from oxidized fractions to oxidation states thereby enabling previously collected data to be used to validate newer models. To produce these oxidation-state profiles in this experiment and discriminate between Nb^{2+}, Nb^{4+}, and Nb^{5+}, improvements were needed to increase the counts of the niobium X-ray signal collected during XANES and thus improve the statistical significance of the curve fitting performed using ATHENA. To do this, the X-ray detector was moved closer to the sample, though this alone would not increase counting efficiency due to the increase in dead time by the saturation of the detector from the zirconium X-ray signal. To preferentially filter out the zirconium X-rays, an aluminum attenuator was added to the detector which was able to exploit the energy difference between the Zr K_α and the Nb K_α to better attenuate the lower-energy Zr K_α signal. Addition of the attenuator and placement of the detector increased the Nb/Zr signal ratio by a factor of four compared to previous results [9].

Results

Oxidation-state and oxidized-fraction profiles were generated for the three alloys featured in this experiment. The location of the oxide/metal interface was determined using X-ray Fluorescence (XRF) and the beam-spot location during XANES was confirmed by comparing the Zr signal generated during XANES and the XRF map. In Fig. 2, the Nb average oxidation-state and Nb oxidized-fraction profiles are shown for Zr-1.0Nb (720 °C) as function of distance from the oxide/metal interface; the total oxide thickness for this post-transition sample is 6.3 μm with a protective oxide thickness of 3 μm, as determined by weight gain analysis and verified through Scanning Electron Microscopy (SEM). Both profiles appear to follow a similar trend, beginning with a rapid increase after the oxide/metal interface and a flattening out beginning at about half the protective oxide thickness. It is important to note that the average oxidation state of niobium gradually increases as a function of distance away from the oxide/metal interface. Additionally, it can be seen that a significant fraction of the oxide features an average niobium oxidation state less than 4^+, which plays an important role for space-charge compensation discussed later. This lower oxidation state of niobium in the oxide has already been reported [9–11]. Consequently, close to the oxide/metal interface, niobium plays the role of an acceptor rather than a donor center.

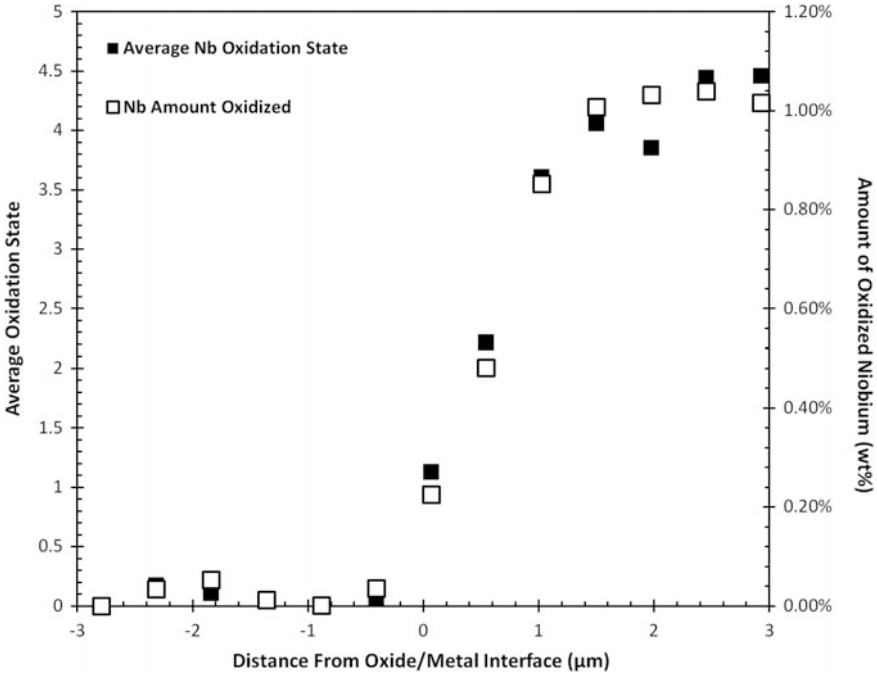

Fig. 2 Comparison of oxidation-state and oxidized-amount profiles of Zr-1.0Nb (720 °C), oxidized for 135 days. 3 μm represents the protective oxide thickness determined from weight gain

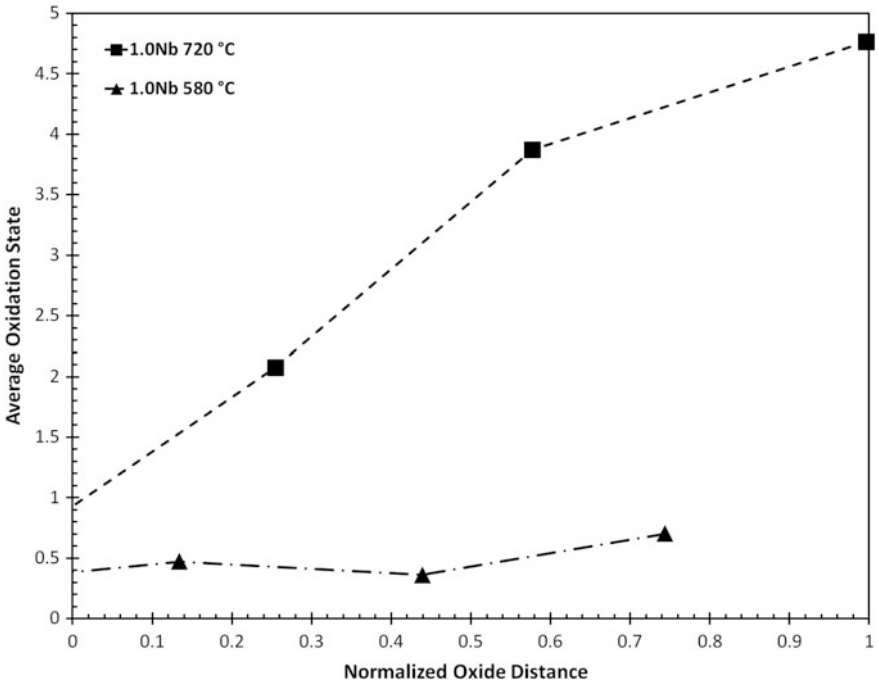

Fig. 3 Oxidation-state profiles of Zr-1.0Nb (720 °C) and Zr-1.0Nb (580 °C) each oxidized for 7 days. The origin represents the oxide/metal interface

In comparing the different annealing temperatures of Zr-1.0Nb, significant differences in the oxidation behavior of niobium are found between the two alloys. Figure 3 compares the oxidation-state profiles of two Zr-1.0Nb samples, one annealed at 720 °C the other at 580 °C and both oxidized for 7 days. It can be seen that for similar relatively thin oxide layers (both <1 μm), Zr-1.0Nb (580 °C) shows significantly slower oxidation of niobium than its counterpart annealed at 720 °C. A detailed discussion of this behavior can be found later in Section "Zr-1.0Nb (580 °C)".

Discussion

Comparison with C4 Model

One of the assumptions of the C4 model is that all of the alloying elements are in solid solution within the matrix. This is necessary as all uniform corrosion models assume a 1-dimensional system, which is all but incompatible if precipitates are present. Though the solubility limit of Nb in Zr is nominally 0.6%, some β-Nb precipitates have been seen in Zr-0.5Nb [12], however, for the purpose of fitting Zr-0.5Nb to the C4 model it is assumed the contribution of these precipitates is negligible in comparison to the amount of niobium in solid solution.

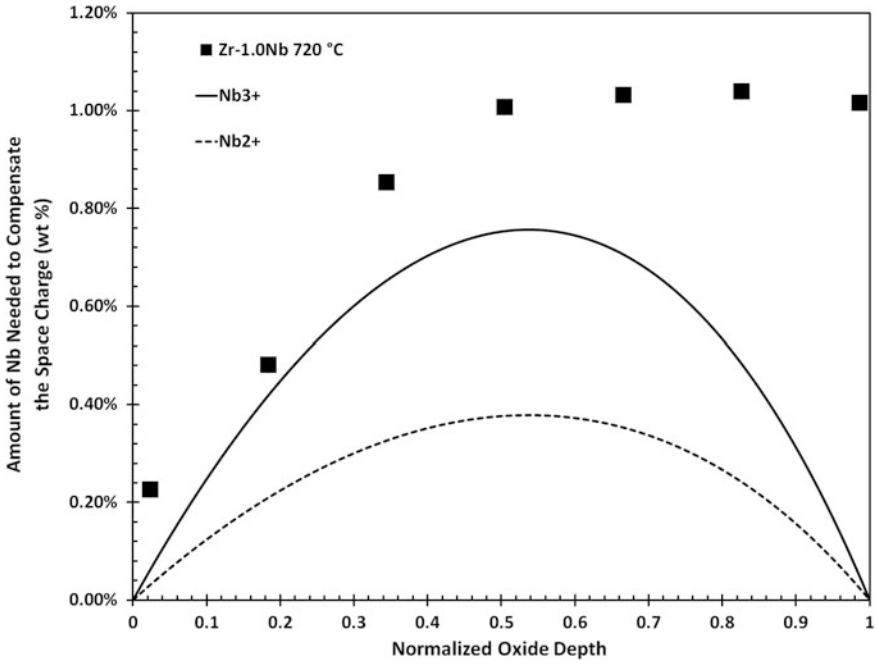

Fig. 4 XANES oxidized fraction data compared with C4 model predictions of oxidized Nb necessary to compensate space charge in Zr-1.0Nb (720 °C). The origin represents the oxide/metal interface

Figures 4 and 5 below show the amount of oxidized niobium needed to compensate the electric field generated by the difference in local concentrations of diffusing oxygen vacancies and electrons, as calculated by the C4 model, compared to the oxidized fraction of niobium of each alloy determined using XANES. The Nb^{3+} and Nb^{2+} curves produced by the C4 model are generated from the oxidation kinetics modeling [7]. In Fig. 4, it can be seen that Zr-1.0Nb (720 °C) has a sufficient amount of oxidized niobium in solid solution to compensate the space charge in the oxide, as indicated by the XANES data points falling above both the Nb^{3+} and Nb^{2+} lines. This agrees well with experimental weight gain data that shows Zr-1.0Nb (720 °C) follows parabolic oxidation kinetics (n = 0.50, see Fig. 1). In comparison, Fig. 5 shows that for Zr-0.5Nb annealed at 580 °C there is enough oxidized niobium present initially, however by the center of the oxide the amount of oxidized niobium is insufficient to completely compensate the space-charge induced electric field which would be necessary for parabolic kinetics. Indeed, as one would expect from partially compensating the electric field, the exponent for the weight-gain fit of Zr-0.5Nb is near but slightly below parabolic (n = 0.46, see Fig. 1), supporting the results from the C4 model [13].

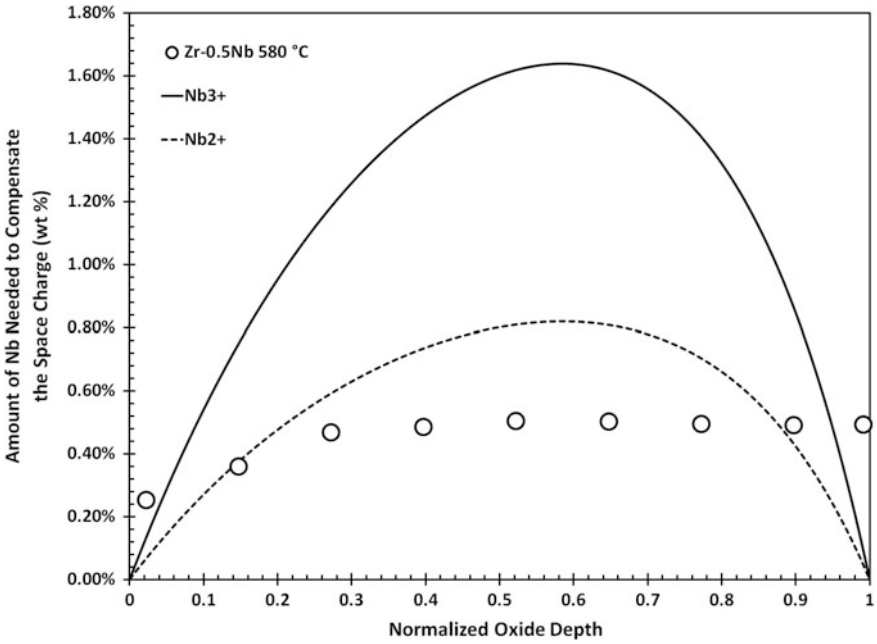

Fig. 5 XANES oxidized fraction data compared with C4 model predictions of oxidized Nb necessary to compensate space charge in Zr-0.5Nb annealed at 580 °C. The origin represents the oxide/metal interface

Zr-1.0Nb (580 °C)

As seen from Fig. 3, the oxidation behavior of Zr-1.0Nb is greatly dependent on the temperature at which the alloy was annealed and thus greatly dependent on the microstructure of the alloy. The microstructure of this alloy has been characterized by Transmission Electron Microscopy (TEM) at Oxford University [14].The microstructure of Zr-1.0Nb (720 °C) features α-Zr grains with large β-Zr precipitates at the grain boundaries, as seen in Fig. 6, in contrast to the microstructure of Zr-1.0Nb (580 °C) which features α-Zr grains with small β-Nb precipitates found distributed intragranularly as well as at the grain boundaries [14]. Through EDX mapping, the concentration of niobium in β-Zr and β-Nb has been measured to be approximately 20% and 80% respectively [14].

Previous XANES analysis has shown that niobium experiences delayed oxidation in comparison to zirconium [9], and the results from this experiment suggest that niobium oxidizes more slowly in β-Nb than in β-Zr. As β-Nb precipitates oxidize, it has been shown that they slowly become amorphous [2, 14], illustrated through EDX mapping in Fig. 7 of Zr-1.0Nb (580C) from the Mechanistic Understanding of Zirconium Corrosion (MUZIC-2) program [14]. In Fig. 7, it can be seen that the β-Nb precipitates remain intact well past the oxide/metal interface in Zr-1.0Nb (580 °C). In contrast, it has been shown through EDX that the concentration of Nb in β-Zr is decreased in these

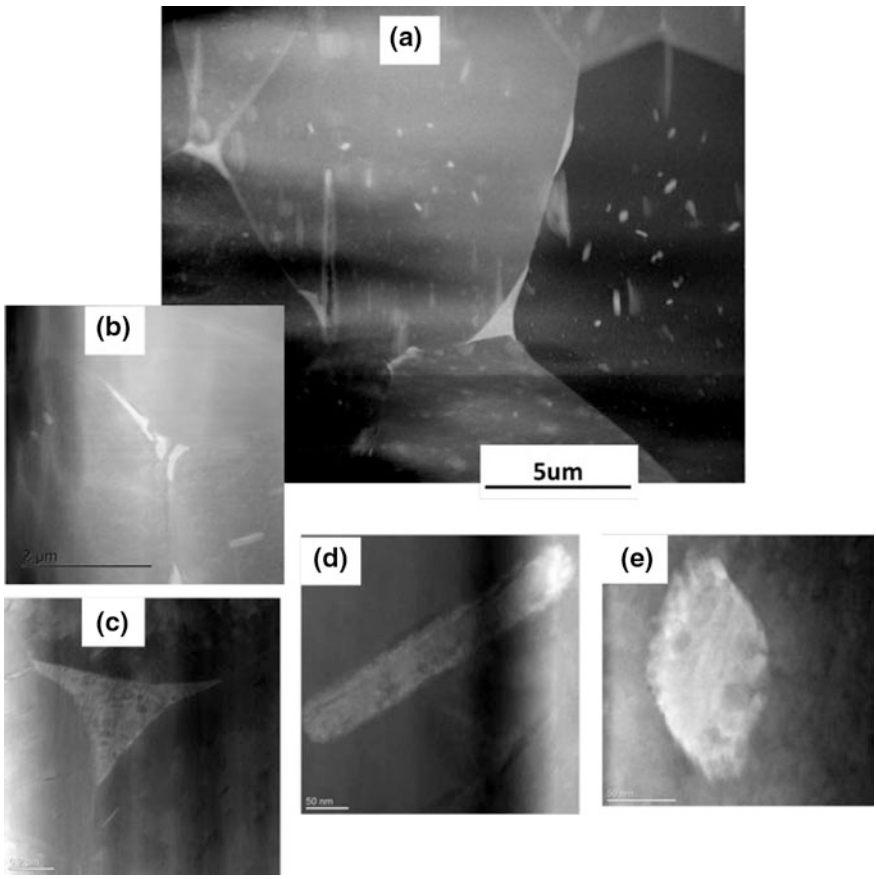

Fig. 6 Series of Scanning Transmission Electron Microscope (STEM) micrographs taken of Zr-1.0Nb (720 °C); **a** is an overview image, **b** and **c** depict large β-Zr precipitates forming at the grain boundaries of α-Zr, and **d** and **e** show intragranular β-Zr precipitates within α-Zr grains [14]

precipitates found inside the oxide, starting very near to the oxide/metal interface, suggesting that Nb may begin diffusing out of β-Zr at the onset of oxidation.

In the context of space-charge compensation, the phase in which niobium is present appears to play an important role in the overall oxidation kinetics of the alloy. If the niobium content of an alloy is found predominately in β-Nb, where it is more localized in comparison to β-Zr or to solid solution, it would not participate in the macroscopic compensation of the space-charge-induced electric field. This would explain the sub-parabolic kinetics of Zr-1.0Nb (580 °C) in comparison to the parabolic kinetics of Zr-1.0Nb (720 °C).

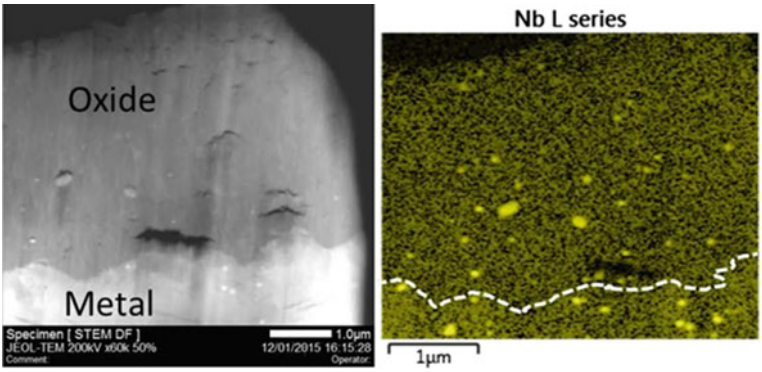

Fig. 7 EDX mapping of oxide layer of Zr-1.0Nb (580 °C) [14]

Metallic Depth Analysis

In order to compare the results of the XANES analysis from samples of varying oxide thicknesses, points of interest in the oxide are normalized to the sample oxide thickness. As has been done in previous work, the point in the oxide in which at least 50% of the niobium remains metallic is chosen and declared the metallic depth (δ_{met}), which allows one to track a point of constant oxidized-niobium fraction across a broad range of samples. In Fig. 8, normalized δ_{met} is plotted against the protective oxide thickness, δ_p, for the three alloys investigated. Error bars for Fig. 8 are a result of the 200 nm beam spot size relative to the thickness of the oxide, as well as interpolation between select points.

Observing Fig. 8, it can be seen that δ_{met} of Zr-1.0Nb annealed 720 °C remains relatively invariant with respect to oxide thickness. If the gradient of oxygen across the oxide layer is fixed at the interfaces and independent of oxide thickness, which it is thought to be within δ_p, then the invariance of normalized δ_{met} would indicate the niobium oxidizing at the same partial pressure of oxygen regardless of oxide thickness. This is in contrast to Zr-1.0Nb (580 °C), where it can be seen that normalized δ_{met} is appreciably larger at smaller oxide thicknesses, indicating a further delay in the niobium oxidation of β-Nb over niobium found in solid solution or β-Zr. Additionally, the decrease in δ_{met} for Zr-1.0Nb (580 °C) with oxide thickness suggests the oxidation of β-Nb precipitates is not dependent solely on the partial pressure of oxygen and is perhaps kinetically limited by the diffusion of oxygen into the precipitate.

Considering Zr-0.5Nb in Fig. 8, it can be seen that normalized δ_{met} has a slight dependence on oxide thickness as well, which would not be expected if all of the niobium were in solid solution. This may be caused by some of the small β-Nb precipitates reported in Zr-0.5Nb, causing the alloy's behavior to fall between the two Zr-1.0Nb alloys. However, the scatter of the data does not provide as much confidence for this trend in comparison to the trends discussed for the Zr-1.0Nb alloys.

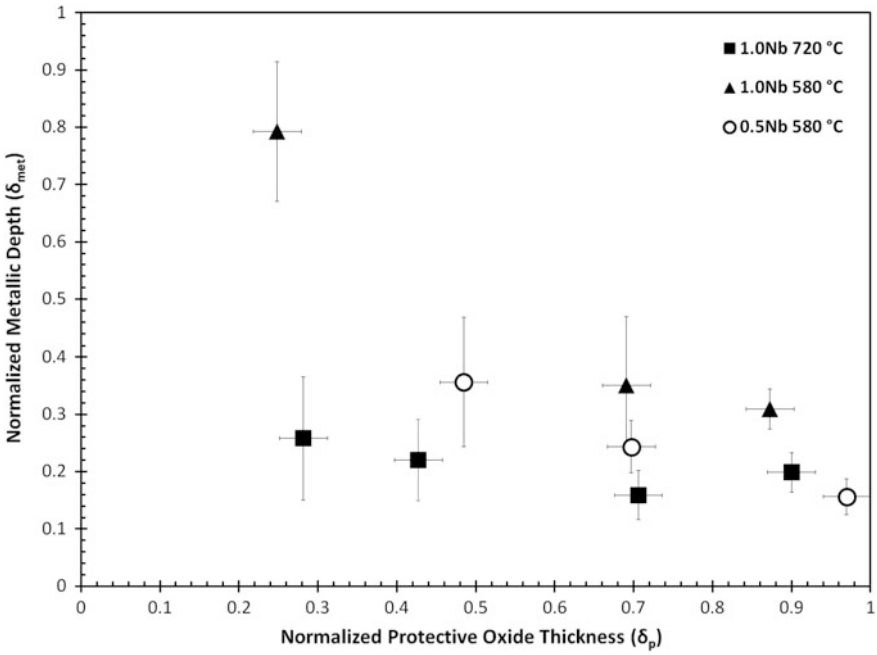

Fig. 8 Plot of metallic versus protective oxide thickness of Zr-0.5Nb annealed at 580 °C, Zr-1.0Nb (580 °C), and Zr-1.0Nb (720 °C)

Conclusion

The oxidation of niobium in one Zr-0.5Nb alloy annealed at 580 °C and two Zr-1.0Nb alloys, one annealed at 580 °C and the other at 720 °C, was analyzed using synchrotron nano-beam XANES. This experiment enabled the generation of oxidation-state and oxidation-fraction profiles for each alloy, allowing further comparison and validation of the C4 model. The results show:

- Zr-1.0Nb (720 °C), with a microstructure containing α-Zr and β-Zr, has enough niobium in solid solution to completely compensate the space-charge-induced electric field and achieve parabolic oxidation kinetics.
- Zr-0.5Nb annealed at 580 °C has been shown to have nearly enough niobium in solid solution to compensate the space-charge-induced electric field, leading to slightly sub-parabolic kinetics.
- While not being able to compare Zr-1.0Nb (580 °C) to the C4 model, as a significant portion of the niobium is found in β-Nb precipitates, the XANES analysis reinforces previous work showing the delayed oxidation of β-Nb in comparison to niobium in solid solution.

Further development of the C4 model will seek to include the effects of precipitates and other microstructural anisotropies known to affect oxidation kinetics

and likely the space charge. Additional work may be done on refining the standards used in the fitting process by using XANES standards generated computationally. Being able to computationally generate XANES standards would not only eliminate the noise seen in experimentally generated profiles, but also allow for standards to be created which simulate different bonding environments for niobium.

Acknowledgements The authors would like to thank those at Westinghouse for providing the samples used in this experiment as well as those at Oxford University and in the MUZIC community. This research used resources of the Advanced Photon Source, a U.S. Department of Energy (DOE) Office of Science User Facility operated for the DOE Office of Science by Argonne National Laboratory under Contract No. DE-AC02-06CH11357.

References

1. J.P.J. Romero, R.J. Comstock, L. Hallstadius, A. Motta, A. Couet, Evolution of hydrogen pickup fraction with oxidation rate on zirconium alloys, in *Top Fuel Reactor Fuel Performance* Zurich, Switzerland (2015)
2. H.-G. Kim, B.-K. Choi, J.-Y. Park, H.-D. Cho, Y.-H. Jeong, Analysis of oxidation behavior of the β-Nb phase formed in Zr–1.5Nb alloy by using the HVEM. J. Alloys Compd. **481**, 867–871 (2009)
3. B. De Gabory, A.T. Motta, K. Wang, Transmission electron microscopy characterization of Zircaloy-4 and ZIRLO oxide layers. J. Nucl. Mater. **456**, 272–280 (2015)
4. G.P. Sabol, S.B. Dalgaard, The origin of the cubic rate law in zirconium alloy oxidation. J. Electrochem. Soc. **122**, 316–317 (1975)
5. X.-M. Bai, Y. Zhang, M.R. Tonks, Strain effects on oxygen transport in tetragonal zirconium dioxide. Phys. Chem. Chem. Phys. **15**, 19438–19449 (2013)
6. G.A. Eloff, C.J. Greyling, P.E. Viljoen, The role of space charge in the oxidation of Zircaloy-4 between 350 and 450 °C in air. J. Nucl. Mater. **199**, 285–288 (1993)
7. A. Couet, A.T. Motta, A. Ambard, The coupled current charge compensation model for zirconium alloy fuel cladding oxidation: I. Parabolic oxidation of zirconium alloys. Corros. Sci. **100**, 73–84 (2015)
8. B. Ravel, M. Newville, ATHENA, ARTEMIS, HEPHAESTUS: data analysis for X-ray absorption spectroscopy using IFEFFIT. J. Synchrotron Radiat. **12**, 537–541 (2005)
9. A.T.M. Adrien, Couet, Benoit de Gabory, Zhonghou Cai, microbeam X-ray absorption near-edge spectroscopy study of the oxidation of Fe and Nb in zirconium alloy oxide layers. J. Nucl. Mater. **452**, 614–627 (2014)
10. A. Froideval, C. Degueldre, C.U. Segre, M.A. Pouchon, D. Grolimund, Niobium speciation at the metal/oxide interface of corroded niobium-doped Zircaloys: a X-ray absorption near-edge structure study. Corros. Sci. **50**, 1313–1320 (2008)
11. K. Sakamoto, K. Une, M. Aomi, T. Otsuka, K. Hashizume, Change of chemical states of niobium in the oxide layer of zirconium-niobium alloys with oxide growth. J. Nucl. Sci. Technol. **52**, 1259–1264 (2015)
12. Y.H. Jeong, H.G. Kim, D.J. Kim, B.K. Choi, J.H. Kim, Influence of Nb concentration in the α-matrix on the corrosion behavior of Zr–xNb binary alloys. J. Nucl. Mater. **323**, 72–80 (2003)
13. A.M. Adrien Couet, R. Comstock, Hydrogen pickup mechanism in zirconium alloys, in *18th International Symposium on Zirconium in the Nuclear Industry*, Hilton Head Island, SC (2016)
14. J. Hu, High resolution characterisation of corrosion and hydrogen pickup of Zr-Nb cladding alloys, in Department of Materials, University of Oxford, p. 249 (2016)

Advanced Characterization of Hydrides in Zirconium Alloys

S.M. Hanlon, S.Y. Persaud, F. Long and M.R. Daymond

Abstract The mechanical properties of zirconium alloys are affected by the presence of hydrides. The strain fields around hydrides, which are affected by the size, orientation, and hydride phase, are believed to influence the apparent hysteresis between solubility limits on heating and cooling. TEM characterization of dislocation fields near hydrides in Zircaloy-4 specimens, which were exposed to 300 °C primary-water conditions for 600 h, was performed both before and after a heating and cooling cycle. In addition, EELS characterization is provided before heating. In situ TEM imaging/recording and nano-diffraction allowed monitoring of the morphology of dissolving hydrides throughout the temperature cycling. No dislocations in the matrix surrounding the hydrides were visible prior to heating; however, when the hydrides dissolved, dislocations were visible in the space the hydrides had previously occupied, providing a map of the original hydride distribution. These dislocation 'nests' are likely the preferential sites for subsequent hydride precipitation and elucidate the so-called 'memory effect'. Advancing the understanding of hydride formation kinetics, hydride morphology, and hydrogen solid solubility limits can help to reduce uncertainties and conservatism when addressing the risks of hydrogen embrittlement and hydride cracking in zirconium components.

Keywords Zirconium · Hydrides · Hydrogen embrittlement · Oxidation · Transmission electron microscopy · Electron energy loss spectroscopy · Focused ion beam

S.M. Hanlon (✉) · S.Y. Persaud
Canadian Nuclear Laboratories, 286 Plant Road, Chalk River, ON K0J 1J0, Canada
e-mail: sean.hanlon@cnl.ca

F. Long · M.R. Daymond
Nuclear Materials Group, Department of Mechanical and Materials Engineering,
Queen's University, Kingston, ON K7L 3N6, Canada

J.H. Jackson et al. (eds.), *Proceedings of the 18th International Conference on Environmental Degradation of Materials in Nuclear Power Systems – Water Reactors*, The Minerals, Metals & Materials Series, https://doi.org/10.1007/978-3-319-68454-3_45

Introduction

The ingress of hydrogen and subsequent nucleation and growth of hydrides in zirconium alloys can limit the service life of nuclear components such as CANDU®[1] reactor pressure tubes. Hydrides are generally considered brittle and have a deleterious effect on mechanical and cracking properties, depending on their orientation [1]. There are several possible sources of hydrogen ingress, including corrosion and diffusion through interfaces with other components [2]. When the solubility limit is exceeded, hydride nucleation usually occurs heterogeneously at dislocations or grain boundaries, while growth rates and the hydride phase formed depend on cooling rate; high cooling rates promote precipitation of needle-like γ hydride, while slow cooling rates encourage precipitation of plate-like δ hydride [3]. There are other possible hydride phases [4], however, they are usually only considered significant when hydrogen concentrations exceed 1000 ppm [5]. Some hydride related studies assume that only δ phase is present, which may confound results under certain conditions. Hydrogen induced cracking, or delayed hydride cracking (DHC), occurs in zirconium alloys when repeated hydride nucleation and growth is followed by fracture [6]; presumably the differences in crystal structure, morphology, and solubility limits between δ and γ hydrides will affect fracture toughness, DHC growth rates, and other mechanical properties.

The presence of dislocation fields around hydrides characterized by transmission electron microscopy (TEM) [3, 7, 8] suggest that hydride growth is a non-equilibrium process due to the plastic strain and surface energy associated with their formation. When hydrides form with small interhydride spacing their strain fields may overlap, which causes further changes to resultant mechanical properties [9–11]. The presence of multiple phases, including β phase in Zr-2.5Nb, and changes of phase with temperature or radiation damage further complicates the predicted effect of interhydride spacing. The apparent hysteresis between hydride precipitation and dissolution curves is a result of these factors as well as slow kinetics [12]. Several studies have shown a mix of δ and γ hydrides in the α matrix under certain conditions, using tools and techniques such as; metallography, time-temperature-transformation (TTT) diagrams, TEM, and X-Ray diffraction (XRD) [13–17]. The co-existence of multiple hydride phases in the Zr–H system and the presence of multiple apparent solvus lines violate the equilibrium phase rule and further suggest a non-equilibrium formation process [18].

Dislocations formed during hydride precipitation may remain after hydride dissolution upon heating, depending on the maximum temperature and hold time. The ‘memory effect’ occurs when these remnant dislocations provide nucleation sites for hydrides during subsequent cooling [19]. An example of a thermo-mechanical ‘memory-effect’ cycle is the full dissolution of stress-reoriented radial hydrides in pressure tube material with a short hold below 400 °C, followed by cooling with no stress applied. This treatment results in some re-precipitation of

[1]CANDU® is a registered trademark of Atomic Energy of Canada Limited.

the less favorable radial hydride orientation rather than the expected circumferential hydrides that would have resulted had the initial stress-reorientation cycle not been performed; this 'natural' orientation is determined by the microstructure and texture. The tendency to re-precipitate with the previous orientation is due to the dislocation structures formed during the preceding cycle [19]. If nucleation is facilitated by remnant dislocation networks, then the measured precipitation temperature should be higher when they are present; it has been suggested that this phenomenon is the cause of the wide variation in precipitation solvi quoted in the literature [20]. The stability and structure of the dislocation networks are also affected by yield strength, cold work, and irradiation. For example, 1 MeV electron irradiation to a dose less than 0.1 dpa had a significant immobilization effect on the dislocations generated during hydride formation [8]. Other work suggests that stress-induced hydride growth causes re-orientation of the α matrix by twinning in a thin plastic deformation zone around a hydride, which provides a means for a re-oriented hydride to precipitate in its normal habit plane [21].

The relative stability of γ and δ hydrides at low temperatures has not been conclusively determined. Many studies conclude that γ hydride is metastable [13, 22–24] however, others predict that gamma is stable at low temperatures [20, 25–27]. These previous studies used a variety of zirconium alloys, hydriding techniques, and thermo-mechanical cycles, which makes direct comparisons difficult. It is possible that a stable γ hydride requires either a low strength matrix (high purity Zr) or the presence of β phase, such as in Zr-2.5Nb [28]; perhaps the formation of gamma hydride requires an initial transformation of α to β, which is conceivable due to the strong β stabilizing effect of hydrogen [29]. The presence of oxygen both strengthens the matrix and stabilizes α and thus has been shown to promote the formation of δ hydride [5], which agrees with the β transformation prediction. The presence of impurities, such as oxygen, might also favour dislocation slip on different planes and change the hydride-matrix orientation relationship. This effect has been shown with aluminum impurity in titanium alloys, which is a system similar to zirconium [5]. Other work predicts a core-shell hydride model, where a layer of γ hydride forms a shell around δ hydride [15, 16]. One core-shell model predicts a metastable γ phase which precipitates first due to faster kinetics, grows, and eventually transforms to thermodynamically stable δ phase [16]. Another core-shell model predicts that stable δ will precipitate above 180 °C, while below this threshold stable γ precipitates. During long holds below 180 °C the δ will slowly transform to the more stable γ hydride at the interface, forming a shell [26]. A study using XRD characterization of DHC showed a change in the hydride phase present on the DHC fracture surface just below 180 °C, from δ dominant above to γ dominant below, though no conclusions on stability were made [30]. Another possible formation mechanism is that stable γ hydride precipitation occurs through a martensitic (invariant plane strain) type transformation involving a metastable gamma hydride precursor [23, 31]. Regardless of the formation mechanism or the thermodynamic stability, the tendency to form γ hydride below a threshold temperature or above a threshold cooling rate could likely correspond to a change in functional form of the solubility curve below the transition; stepwise continuous solubility curves have been proposed previously [25, 32].

As described above, there are several opposing views on the stability of zirconium hydrides, reasons for the solubility limit hysteresis, and the hydride formation mechanisms, which are confounded by the use of a variety of materials, different thermo-mechanical cycling, and different characterization techniques. Hydriding technique is another source of variation, as hydrogen is usually artificially added to specimens at elevated temperature. Specimen preparation, annealing temperature, time, and final concentration will have an effect on the resulting hydride morphology [5, 33, 34]. Adding hydrogen using pressure, temperature, and chemistry as similar as possible to in-service conditions would likely provide a more representative hydride distribution. Previous studies have focussed primarily on characterization using neutron diffraction, XRD, and/or TEM. Recent work on zirconium oxide has demonstrated some advantages of using electron energy loss spectroscopy (EELS) characterization as a complimentary technique [35, 36]. Further observation of hydride morphology and dislocation structures before and after thermal cycles using a representative sample and using multiple techniques could help substantiate the proposed correlations between dislocations (memory effect), solid solubility hysteresis, and the kinetics and thermodynamics of hydride formation.

Experimental

The material used in this study was Zircaloy-4 strip. The strip was intended for use as CANDU® calandria tubes; this material has been previously summarized [37]. The initial hydrogen concentration was less than 5 ppm. Coupons from the Zr-4 strip (10 mm × 5 mm × 2 mm) were prepared by grinding using SiC paper followed by step-wise fine polishing using diamond paste and alumina suspension to a 0.05 μm finish. Samples were ultrasonically cleaned in de-ionized water between polishing stages.

There were three material conditions used in this report: as-received, exposed, and quenched. The as-received samples received no further processing after polishing. The exposures were performed in 300 °C water in the H5 loop at CNL. The H5 loop is primarily constructed using 304SS and has been successfully used to simulate primary coolant in CANDU® reactors at temperatures up to 305 °C. In this case, the temperature was maintained at 300 ± 5 °C for a duration of 600 h. Key components of the loop include a 200 L feed tank, positive displacement pumps and a full-flow ion exchange system, which operate at near ambient pressure and temperature. The ½ inch 304SS tube containing four flat coupons is attached to the test section area in the H5 loop. The loop is equipped with on-line monitors for dissolved oxygen content and hydrogen concentration, ionic conductivity, pH, flow rate and temperature. Hydrogen content was maintained at approximately 7 cm^3 H_2/kg H_2O. Upon completion of experiments, the exposed samples were stored in a desiccator. Differential Scanning Calorimetry (DSC) analysis of the exposed samples provided a hydrogen concentration result of about 10 ppm.

The quenched sample condition was achieved by heating one of the exposed samples to 400 °C in a furnace for five minutes, then dropping it into a room temperature brine, which provides a very rapid quench [38]. The purpose of the fast quench was to encourage the formation of γ hydrides to allow for comparisons with δ hydrides in the slow cooled exposed specimens using several characterization tools, including EELS and TEM.

TEM specimens were prepared from each of the three specimen conditions with a Zeiss NVision 40 focused ion beam (FIB) system using a conventional lift-out technique. The NVision system was capable of depositing tungsten in situ using the Ga^+ ion beam. Final polishing was carried out at 10 kV with a current of 80 pA to achieve a thickness of approximately 40 nm. After FIB foil preparation, EELS characterization was performed using two TEM systems: a FEI Titan 80 TEM and a FEI Titan cubed TEM, both operating at 300 kV. Both microscopes were equipped with a Gatan Image Filter (GIF). On the FEI Titan 80 TEM, the collection semi-angle was 15 mrad, and the convergence semi-angle (α) was 8 mrad. On the FEI Titan cubed TEM, the collection semi-angle was approximately 40 mrad and convergence semi-angle was 19 mrad. The resulting EELS spectra were aligned in energy using Gatan Digital Micrograph 3.0. EELS analysis is useful for identification of low Z elements and detecting changes in local bonding. In the present study, low loss EELS spectra, which exhibit changes due to plasmon interactions from oscillations in valence electrons, are used to characterize changes in microstructure associated with Zr hydrides, Zr metal, and Zr oxide(s); reference low loss EELS spectra for Zr and related compounds of interest were available in literature [39–42]. Conventional core loss EELS edge spectra for Zr and O, from inner electron shell ionization of specific elements, were also collected but are not discussed.

Diffraction, high resolution TEM (HRTEM), and in situ heating of the FIB foils were carried out with a FEI Tecnai Osiris S/TEM, operated at 200 kV. The FIB foils were loaded into a double tilt Gatan 652 heating stage, which has a tantalum specimen cup with heating capability up 1000 °C. Prior to heating, the hydride morphology, phase, and orientation relationship with the surrounding matrix were studied by performing diffraction down several zone axes. The TEM was also used in scanning microprobe mode for diffraction pattern (DP) acquisition of selected areas with nano-beam electron diffraction (NBED). This technique uses a small C2 aperture (10 μm diameter), which makes the beam nearly parallel; DPs can be obtained from a nano-sized (<5 nm) area. HRTEM images were also acquired in TEM mode to observe the atomic structure of hydrides, the surrounding α-matrix and the interface structure. During heating, the samples were tilted to two beam conditions from the zone axis for better image contrast. To avoid significant thermal drift, the samples were allowed to stabilize at hold temperatures for approximately five minutes prior to imaging. The temperature was controlled manually by ramping up in 10 °C steps. A maximum temperature of 500 °C was reached.

Results

FIB

As expected, the as-received specimen had no remarkable features besides the usual distribution of intermetallic particles, and is not shown. A secondary electron image of a TEM sample prepared from a Zr-4 sample after exposure to 300 °C water is shown in Fig. 1a; two grain boundaries and three grains were captured in the specimen. An oxide film is present on the sample surface which ranges in thickness from 200 to 700 nm across three grains. The difference in oxide thickness across the grains can likely be attributed to changes in grain orientation [43]. A STEM-HAADF image of a TEM sample extracted from a quenched Zr-4 specimen is shown in Fig. 1b. A distribution of elongated structures of darker contrast are visible in both exposed samples; these structures and surface oxides are characterized further using low loss EELS in the following section.

EELS

EELS characterization was performed to complement selected area electron diffraction (SAED) results. Low loss EELS spectra from areas of interest were extracted from exposed and quenched FIB-prepared TEM samples; Fig. 2 shows the low loss EELS spectra for α-Zr, δ-hydride, and the α/δ interface. The extracted spectra for the α and δ phases agree with prior spectra collected by other authors [39–42]. The α-Zr phase exhibits a plasmon peak at approximately 16.9 eV while the δ-Zr hydride phase exhibits a similar low loss EELS spectra with the plasmon peak shifted to approximately 19.2 eV. Woo et al. [39] have reported that the γ-Zr hydride phase exhibits a similar EELS low loss spectrum as α-Zr and δ-Zr hydride, but the plasmon peak is shifted to 18.3 ± 0.2 eV. This γ spectrum corresponds closely to the interface spectrum shown in Fig. 2, which has an approximate thickness of 20 nm. EELS maps for a region in the Zr-4 exposed TEM sample in Fig. 1a are shown in Fig. 3. The surface oxide is predominantly composed of ZrO_2, where the low loss Zr oxide edge spectrum attributed to the ZrO_2 phase agrees well with reference spectra available in literature [42]. Other Zr oxide phases were also detected at the oxide-metal interface in TEM samples characterized, however, discussion related to Zr oxidation/corrosion is beyond the scope of the present study. Characterization of oxidation of Zr using high resolution electron microscopy and surface science techniques has been studied at length by others [44–46].

As expected, δ-hydrides are present throughout the alloy matrix of the exposed sample and appear to have a preferred orientation, which was confirmed by TEM. Most of these hydrides have an interface structure similar to that shown in Fig. 2, although it is difficult to resolve the thin interface at lower magnification.

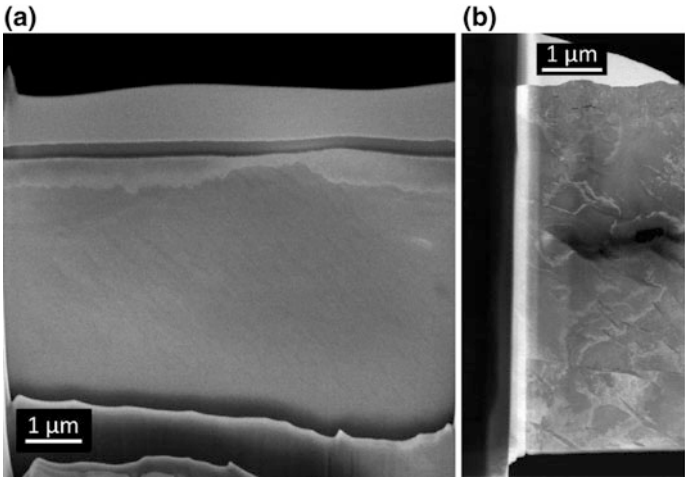

Fig. 1 TEM samples extracted from Zr-4 specimens after exposure to 300 °C water for 600 h (**a**) and after an additional high temperature quench (**b**)

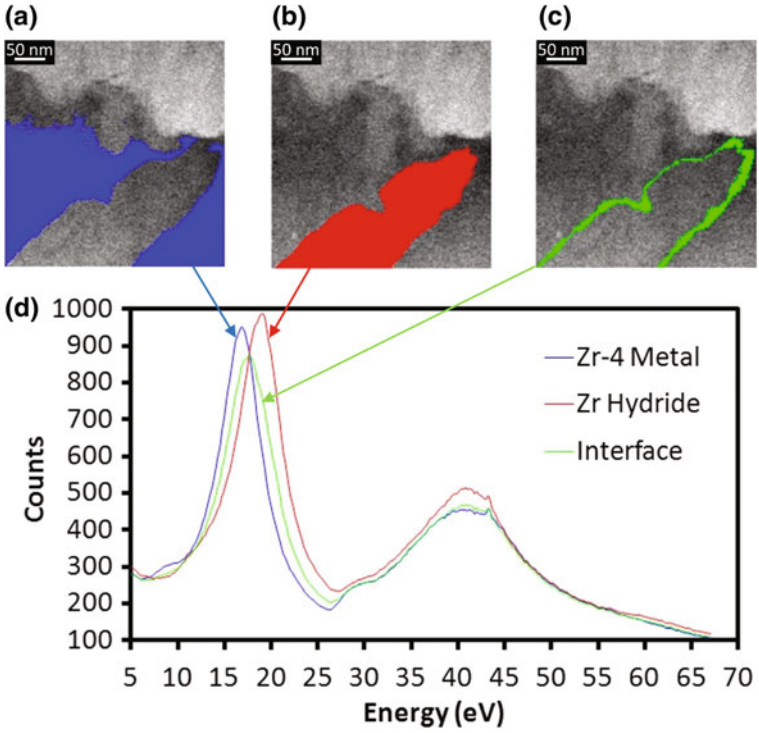

Fig. 2 Low loss EELS spectra for α-Zr (**a**), δ-Zr hydride (**b**), and the α/δ interface region (**c**) extracted from TEM specimens in Fig. 1. The spectra (**d**) are in accordance with reference spectra available in literature for these phases [39]

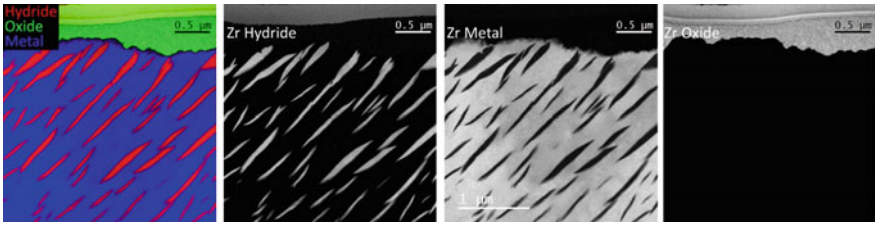

Fig. 3 Zr hydride, Zr metal, and Zr oxide EELS maps for a section of the Zr-4 TEM sample extracted from a Zr-4 specimen exposed to 300 °C water

A second set of EELS maps for a region in the Zr-4 exposed TEM sample are provided in Fig. 4. The section characterized contains two grains, each having the preferred hydride-matrix orientation relationship. A large intergranular hydride was observed near the center of the image, with some extension into the adjacent grains. Overall, the general features highlighted in Figs. 3 and 4 agree with SAED results in Section "TEM".

EELS maps taken from a region in the quenched Zr-4 TEM sample, in Fig. 1b, are provided in Fig. 5. Contrary to expectation, all hydrides in the quenched sample have a low loss EELS edge spectra suggesting a δ hydride phase; there was no evidence for a shift in the EELS spectra associated with γ hydride.

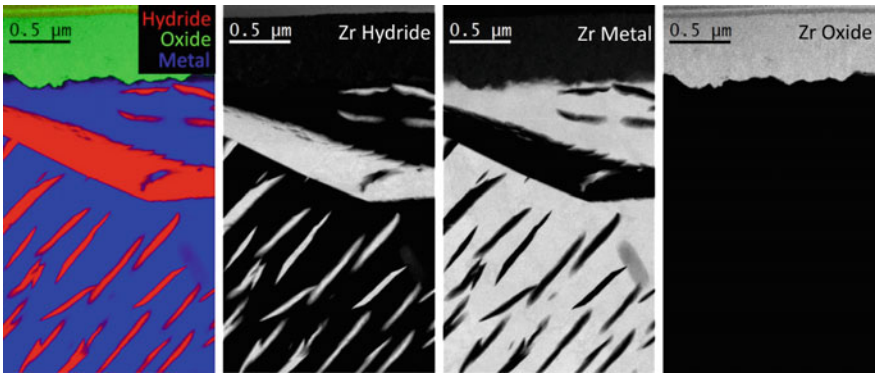

Fig. 4 Zr hydride, Zr metal, and Zr oxide EELS maps for a section of the Zr-4 TEM sample extracted from a Zr-4 specimen exposed to 300 °C water. A large hydride is observed to precipitate on the grain boundary. Also, hydrides exhibit planar alignment, differing depending on grain orientation

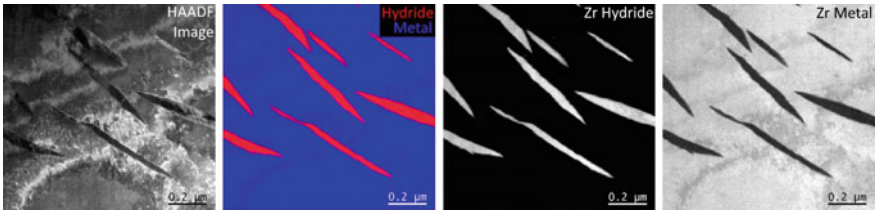

Fig. 5 Zr hydride and Zr metal EELS maps for a section of the Zr-4 TEM sample in Fig. 1b, extracted from a Zr-4 specimen that was quenched from high temperature in an attempt to precipitate γ-hydrides. However, the maps revealed that the FIB-prepared TEM specimen only contained δ-hydrides

TEM

As shown in Fig. 6a, a significant number of δ-hydride platelets have formed in the as-exposed alloy. No hydrides were visible in the as-received specimen. The orientation relationship between the formed δ-hydride and surrounding matrix in the exposed sample was determined by using the NBED technique. Although the hydride platelets have a thickness of only about 50 nm, well defined diffraction patterns can still be obtained on multiple zone axes. To determine the orientation relationship between the formed hydride and the parent α-phase, the foil was first tilted to the $\left[11\bar{2}0\right]_{\alpha}$ zone axis of the α-matrix, as shown in Fig. 6b. Corresponding

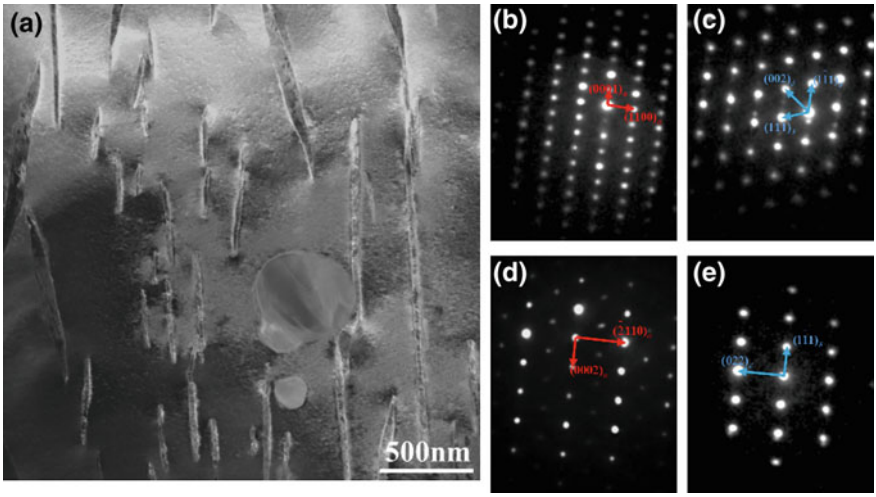

Fig. 6 **a** HAADF image of hydride platelets formed in the as-exposed alloys. **b**, **c** DP of matrix and hydride acquired on $\left[11\bar{2}0\right]_{\alpha}$ zone axis, following the $(0001)_{\alpha}//(111)_{\delta}$, $\left(11\bar{2}0\right)_{\alpha}//\left(1\bar{1}0\right)_{\delta}$ orientation relationship, **d**, **e** DP of matrix and hydride acquired on $\left[10\bar{1}0\right]_{\alpha}$ zone axis, along which the δ/α orientation relationship becomes $(0001)_{\alpha}//\left(1\bar{1}1\right)_{\delta}$, $\left[01\bar{1}0\right]_{\alpha}//\left[21\bar{1}\right]_{\delta}$

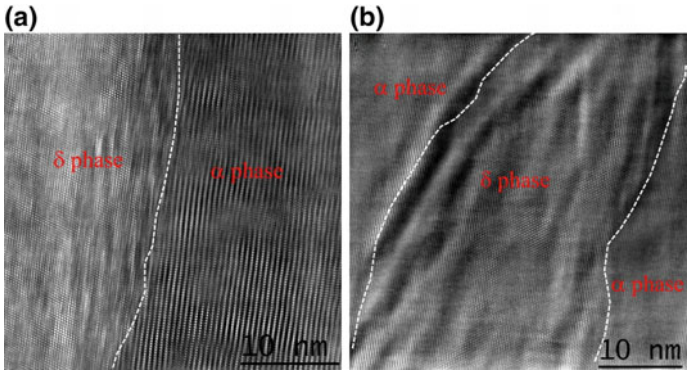

Fig. 7 HRTEM of α and δ phase: **a** along $[11\bar{2}0]_\alpha$ zone axis and **b** along $[01\bar{1}0]_\alpha$ zone axis

DPs were acquired from individual hydrides at the same beam angle, which were indexed to the $[110]_\delta$ zone axis, as shown in Fig. 6c. The expected orientation relationship between α and δ phases is $(0001)_\alpha // (111)_\delta$, $(11\bar{2}0)_\alpha // (1\bar{1}0)_\delta$ and was confirmed by NBED. Figure 6d is the DP of the α-matrix tilted to the $[01\bar{1}0]_\alpha$ zone axis, and Fig. 6e is the corresponding hydride zone axis, which was determined to be the $[21\bar{1}]$ direction. Indexing the DPs with this beam angle provides further evidence that the $(0001)_\alpha$ plane is parallel to the $(1\bar{1}1)_\delta$ plane. Furthermore, the $(\bar{2}110)_\alpha$ plane is found to be parallel to the $(022)_\delta$ plane.

Figure 7a, b are HRTEM images at the $[11\bar{2}0]_\alpha$ and $[01\bar{1}0]_\alpha$ zone axes, respectively, with phase interfaces outlined by white lines. The different atomic arrangement in the hydride and matrix is visible across the phase interface in each zone axis, with the $[11\bar{2}0]_\alpha$ zone axis image having a more defined interface than the $[01\bar{1}0]_\alpha$ zone axis. Given the lattice constants of a = 3.232 Å, c = 5.148 Å for HCP α phase, and a = 4.778 Å for FCC δ phase, the d-spacings of lattice planes were calculated and are shown in Table 1. The d-spacings of parallel planes $(\bar{2}110)_\alpha$ and $(022)_\delta$ along the $[01\bar{1}0]_\alpha$ zone axis are similar and thus α and δ appear similar under this imaging condition, while the d-spacing of the parallel planes $(10\bar{1}0)_\alpha$ and $(002)_\delta$ along the $[11\bar{2}0]_\alpha$ zone axis are quite different. This difference makes the phase interface more distinguishable along the $[11\bar{2}0]_\alpha$ zone axis.

Table 1 d-spacing of lattice planes on the $[01\bar{1}0]_\alpha/[21\bar{1}]_\delta$ and $[11\bar{2}0]_\alpha/[1\bar{1}0]_\delta$ zone axes

Zone axis	$[01\bar{1}0]_\alpha$		$[21\bar{1}]_\delta$		$[11\bar{2}0]_\alpha$		$[1\bar{1}0]_\delta$	
	$(0002)_\alpha$	$(\bar{2}110)_\alpha$	$(1\bar{1}1)_\delta$	$(022)_\delta$	$(0002)_\alpha$	$(10\bar{1}0)_\alpha$	$(1\bar{1}1)_\delta$	$(002)_\delta$
d spacing (Å)	2.573	1.616	2.759	1.689	2.573	2.798	2.759	2.389

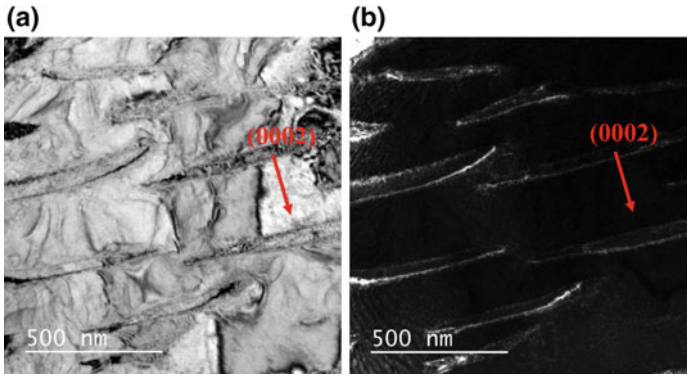

Fig. 8 TEM (**a**): BF, (**b**): DF image of the formed δ hydride platelets, captured with $(0002)_\alpha$ reflection along $[11\bar{2}0]_\alpha$ zone axis

BF/DF images were then taken with the $(0002)_\alpha$ reflection along the $[11\bar{2}0]_\alpha$ zone axis. As shown in Fig. 8a, b the α/δ interface has a strong contrast in both the BF and DF images. This may imply the existence of c-component interfacial dislocations, as a-type dislocations are invisible with the $(0001)_\alpha$ imaging reflection. Figure 9 shows the DF images in the center (a) and tip (b) of a δ-hydride at high magnification, obtained with the $(\bar{1}011)_\alpha$ reflection on the $[11\bar{2}0]_\alpha$ zone axis. It appears that tight layers of interfacial dislocations are present within a 20 nm width of the α/δ phase boundary. According to the HRTEM image shown in Fig. 9c, the existence of such dense dislocations at the interface resulted in an irregular atomic structure.

A similar hydride and dislocation analysis was performed for the quenched sample. Diffraction results agreed with the EELS spectra for the quenched samples; the hydrides present were δ phase. A small fraction of the hydrides present in the

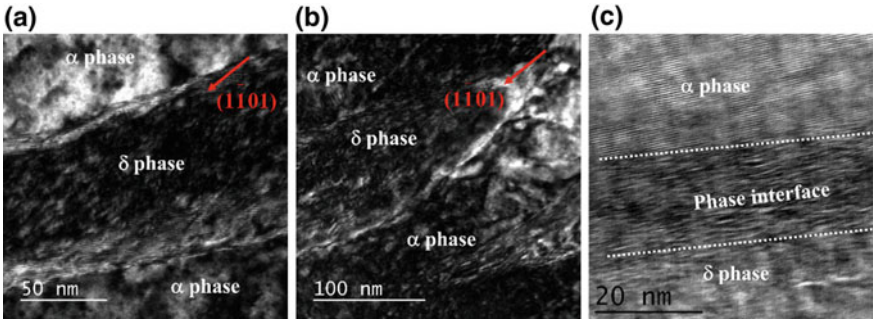

Fig. 9 **a**, **b** TEM DF images showing high density of interfacial dislocations on the α/δ phase interface, imaged with $(1\bar{1}01)_\alpha$ reflection along $[11\bar{2}0]_\alpha$ zone axis, **c** HRTEM image showing the phase interface

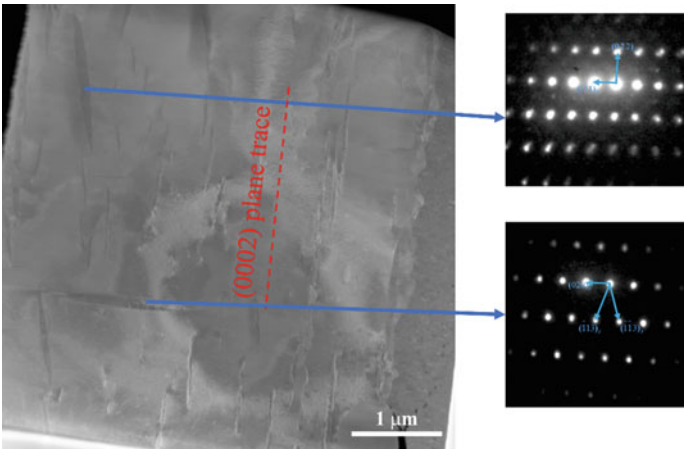

Fig. 10 **a** HAADF image showing distribution of hydrides in the FIB foil lifted out of the brine quenched sample. Most hydrides followed the common α/δ orientation relationship, evidenced by the δ-hydride DP in (**b**) acquired along the $\left[10\bar{1}0\right]_{\alpha}$ zone axis. **c** DP of the hydride orientated differently, showing a $\left(10\bar{1}0\right)_{\alpha}//(301)_{\delta}$,$\left(2\bar{1}\bar{1}0\right)_{\alpha}//(101)_{\delta}$,$(0002)_{\alpha}//(020)_{\delta}$ orientation relationship

quenched sample had an alternate orientation relationship with the matrix: $\left(10\bar{1}0\right)_{\alpha}//(301)_{\delta}$,$\left(2\bar{1}\bar{1}0\right)_{\alpha}//(101)_{\delta}$,$(0002)_{\alpha}//(020)_{\delta}$ [47], as shown in Fig. 10. Dislocation analysis of the quenched sample, shown in Fig. 11, showed evidence of c-component dislocations in the matrix as well as at the α/δ interface.

Two exposed samples were subjected to in situ heating and cooling runs to determine the hydride and dislocation evolution with changing temperature. The HAADF images in Fig. 12 were acquired at different temperatures during the heating and cooling process. By comparing Fig. 12a, b, upon heating to 400 °C it

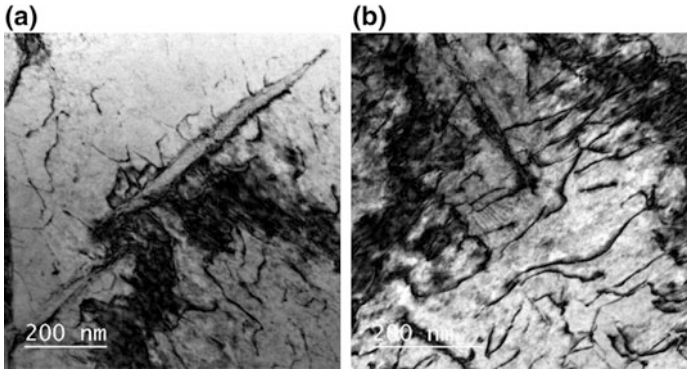

Fig. 11 **a**, **b** many c-component dislocations are found around δ-hydrides in a FIB foil extracted from a quenched sample

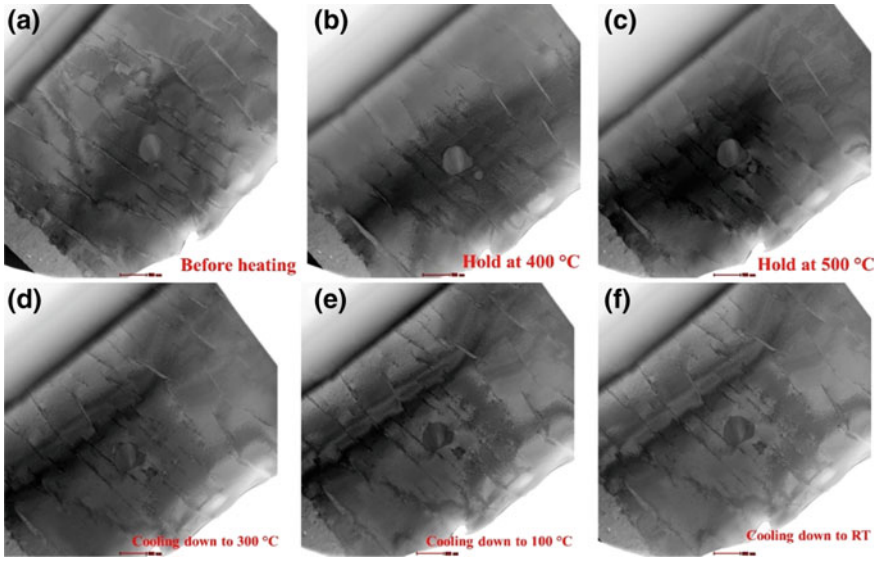

Fig. 12 HAADF images showing morphology evolution of hydrides in as-exposed sample during in situ heating and cooling. The hydrides generally became thinner and shorter as temperature increased, but did not regain their previous size on cool-down

can be seen that most of the hydrides in the foil have dissolved or became smaller in both thickness and length. HRTEM images in Fig. 13 provide a comparison of hydride morphology before and after heating. Figure 13a shows a hydride before heating with a ~50 nm thick δ core surrounded by a less than 10 nm thick interface. Figure 13b, c show examples of how the interface has moved to both reduce the length (b) and thickness (c) of the hydrides. The thickness of the interface during dissolution (c) is much larger than prior to heating (a). At 500 °C most hydrides had completely dissolved, however, features which appear to be c-component dislocations remain at the locations of the previous hydride-matrix interfaces. DPs taken near these interfacial features show no evidence of any remaining FCC structure. However, some of the larger hydrides remained even after holding at 500 °C for 30 min. The FIB foil was then cooled down in an attempt to precipitate hydrides and determine whether they preferentially nucleate at the remnant c-component dislocations formed by the previous hydrides. However, as shown in Fig. 12d–f, no hydride precipitation or growth occurred on cooling.

Figure 14a, b are the BF and DF image of the dislocations remaining after hydride dissolution, acquired with (0002) imaging reflection after the heating experiment. These dislocations were already visible at the interface (Figs. 8 and 11). The black/white diffraction contrast in Fig. 14 provides further evidence for the existence of interfacial features in the location of the previous hydrides that remain after heating to 500 °C.

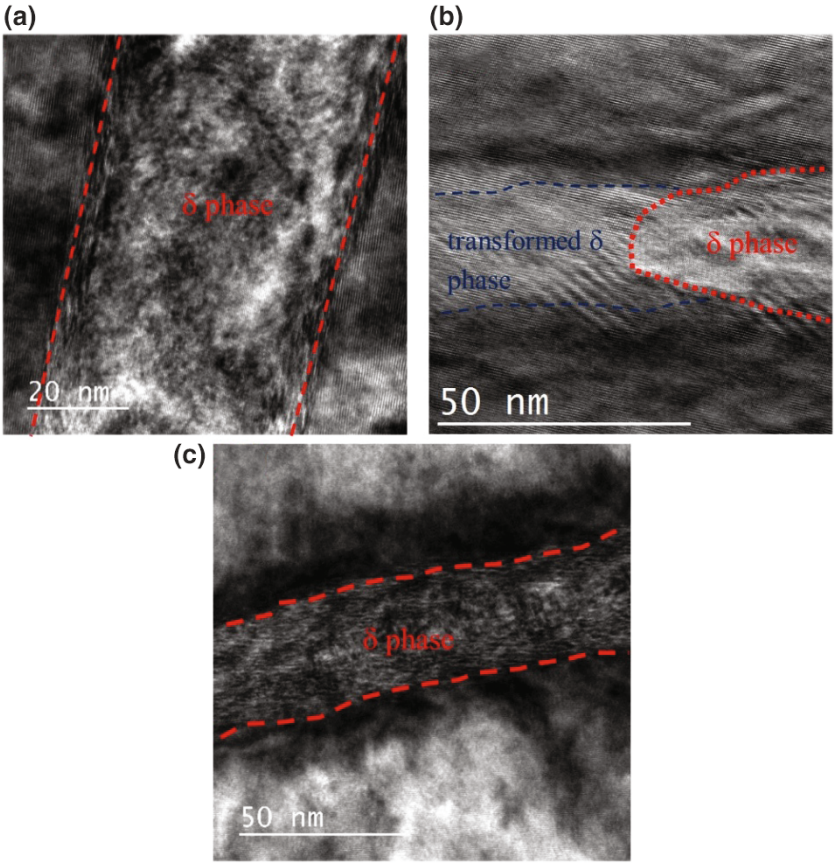

Fig. 13 **a** Hydrides before heating, **b** hydride dissolved from one end after heating, **c** hydride dissolved by reducing thickness after heating of as-exposed sample

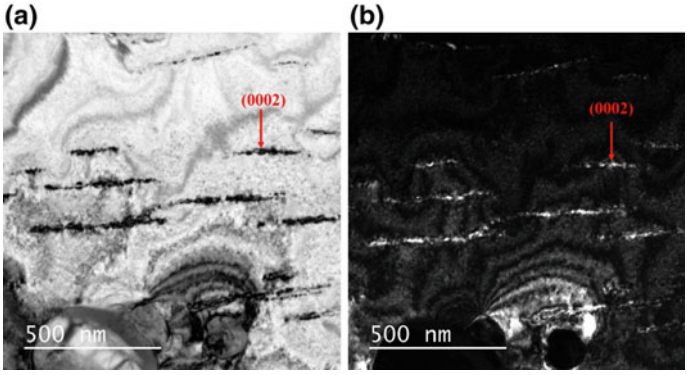

Fig. 14 BF and DF images showing c-component dislocations remained at the original phase boundary after hydride has been dissolved during heating of as-exposed sample

While the average H content in the exposed sample was 10 wppm, it is apparent from the microstructure that there is substantially more than 10 wppm (approx. 0.1 vol.%) in the region near the oxide interface from which the FIB foil was cut. A hydrogen solubility equation for Zircaloy [48] suggests that 10 wppm of H corresponds to a dissolution temperature of just under 200 °C. The presence of hydrides at 500 °C implies a hydrogen concentration of at least 350 wppm (approx. 5 vol.%), assuming equilibrium has been reached; such a volume fraction is reasonable based on the microstructure observed by EELS and TEM. The presence of significant gradients in hydride populations near the oxidised surface of zirconium alloys has been previously reported [49].

The heating experiment was repeated on another FIB foil extracted from the as exposed sample to confirm the hydride distribution was representative. Again, some hydrides were still present after heating, as indicated by white arrows in the HAADF image in Fig. 15a. EDX elemental mapping was carried out on the area containing the remnant hydrides to confirm they were not oxide. Figure 15b–d are the HAADF and corresponding elemental maps; no oxygen accumulation is visible. To unambiguously determine the crystal structure of the remnant phase, HRTEM images were obtained along three different zone axes and fast Fourier transforms (FFT) were performed on each image to determine crystal structure. As shown in Fig. 16a, b, c the remnant phase was indexed as FCC δ-hydride down three zone axes and obeyed the typical δ/α orientation relationship outlined previously.

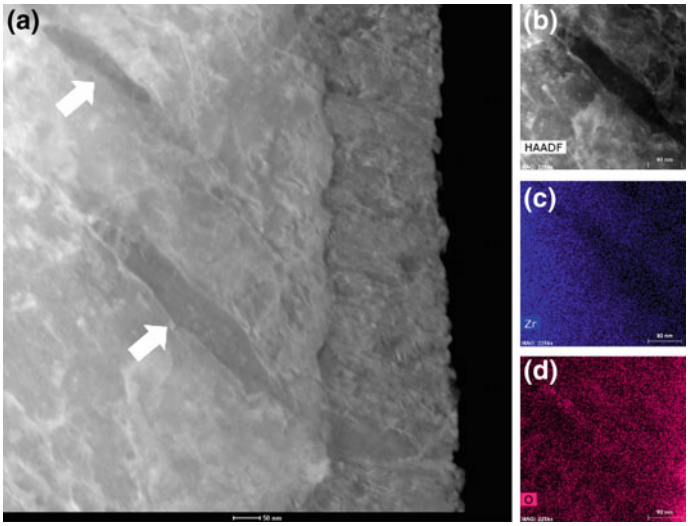

Fig. 15 TEM HAADF image showing remnant phases below the oxide layer after heating an as-exposed sample. **b–d** EDX mapping on one of the remnant phase showing no oxygen concentration difference between it and the surrounding alloy matrix

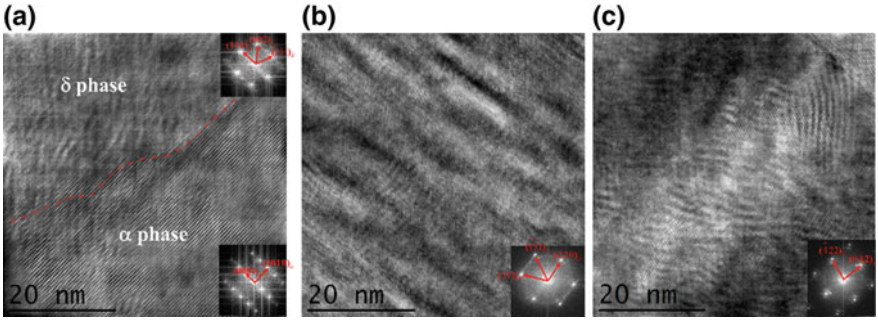

Fig. 16 HRTEM images of the remnant phase along different zone axes, which has been determined to be undissolved δ-hydride. **a** $[111]_{\delta}$ zone axis, the inserted FFT of the α and δ phase indicate the common orientation relationship. **b** $[114]_{\delta}$ zone axis, **c** $[324]_{\delta}$ zone axis

Discussion

Observation of hydride morphology and dislocation structures using EELS and NBED both before and after heating cycles, specifically at the hydride-matrix interface, was completed to determine what inferences could be made regarding formation kinetics and thermodynamics of hydride formation, the dislocation memory effect, and solubility hysteresis.

Given the relatively low bulk hydrogen concentration measurement of 10 ppm in the exposed material, the appearance of a larger than expected number of hydrides in the FIB foils might at first sight be considered to be an artefact of specimen preparation. However, as-received (unexposed) samples from the same material prepared in the same way did not contain any visible hydrides and it seems unlikely that there could have been significant hydrogen ingress during the polishing, FIB preparation, or EELS analysis. An increased concentration of hydride near the surface of water-oxidised zirconium alloys has been previously reported, with such an increased concentration extending several micrometers into the sample [50, 51]. This gradient can be partially attributed to the tensile stress generated by the oxide layer in the Zircaloy matrix near the oxide interface of the exposed sample (since H migrates towards tensile stresses), but mostly to the complex chemical potential and thermodynamics occurring at the interface during the oxidation process [49].

Based on the many studies of γ hydride outlined earlier, it was expected that a brine quench from 400 °C, well above the bulk dissolution temperature determined by DSC, would result in γ phase precipitation. Although 400 °C was not hot enough to dissolve all the hydrides near the oxide interface where the FIB samples were taken (at least 350 wppm as outlined in Section "TEM"), a large fraction of hydrogen in solution at 400 °C (about 160 ppm) was nevertheless expected to precipitate as γ hydrides. However, the quenched samples had only δ hydrides. Given that the previous results in literature were obtained by electropolishing the

samples, it appears that the FIB preparation could induce a phase transformation; this type of transformation has been shown previously in stainless steel [34]. Local heating and Ga^+ ion implantation could induce a phase transformation; high temperatures favour δ hydride while the high energy ion beam induces a damage layer which increases yield strength and introduces an impurity element to the matrix. More direct comparisons between FIB and electropolished samples are required to confirm this observation.

EELS results showed a clear contrast between hydride and matrix and also revealed an interface structure as shown in Fig. 2. The thickness of the interface structure was between 10 and 20 nm, which agreed well with the interface thickness determined via HRTEM in Figs. 9 and 13. The plasmon peak in the low loss EELS edge spectrum of the interface structure is between that of α and δ and thus could be interpreted as a mixture of phases, an artefact of the dislocation structure at the interface (dampening of the electron beam), or an artefact of plasmon interaction at an interface. It is also possible that this interface is a γ hydride shell surrounding a δ core, given that its spectral peak agrees with that of γ hydride reported in literature [39]. Dislocation analysis with TEM revealed the presence of c-dislocations in the interface region while HRTEM showed a difference in atomic structure at the interface. Diffraction analyses could only identify the δ and α phases. If there was γ phase present, the dislocations structures in the interface region may have confounded the diffraction results such that conclusive identification of γ hydride was not possible.

Diffraction results showed evidence of c-component dislocations at the α/δ interface both before and after heating. The exposed samples showed no evidence of matrix loops pinned to the ends of the hydride, sometimes called 'butterfly dislocations', as shown by Carpenter et al. [8] using single crystal Zr with low oxygen. The material used in this study was polycrystalline Zr-4 and thus the dislocations formed likely had a higher critical resolved shear stress which may have prevented significant loop formation in the matrix. The c-component dislocations at the hydride-matrix interface remained at temperatures up to 500 °C. These dislocations are predicted to be responsible for the memory effect described in the literature [19]. An example of the memory effect is the repeated heating and cooling cycles (called ratcheting) of bulk samples that occurs during DSC analysis. The first heating and cooling cycles are usually disregarded, since dissolution and precipitation temperatures are slightly different than subsequent runs. The hydride size and distribution is affected by cooling rate and the nucleation sites present during the previous cycle(s), thus it takes one cycle to 'normalize' the hydrides to the new heating/cooling rates, after which the hydrides will 'remember' their previous distribution through nucleation at c-component dislocations where the α/δ boundary had been during the previous cycle. In this study, hydrides did not precipitate on cooling in the FIB foils. The foils were welded to a copper TEM holder on one edge, which may have affected the hydrogen distribution at higher temperatures. The first exposed FIB sample had a thicker frame around the central electron transparent region that may have provided a sink for hydrogen in solution during the high temperature anneal. The second sample only had a thick frame on

the side that was welded to the holder, yet no precipitation occurred. Temperature and stress gradients (gradients in chemical potential) are driving forces for hydrogen diffusion [52, 53]; stresses at the weld and diffusion of hydrogen into the copper holder could have acted as hydrogen sinks. Another possibility is that a significant portion of the hydrogen went to the gas phase, given the partial pressure curves established by Singh et al. [54]. The predicted partial pressure at 500 °C is about 10^{-2} torr; given the high surface area to volume ratio it's likely that the rate of hydrogen loss per volume is orders of magnitude faster for a FIB sample than a bulk sample with a thick oxide layer.

The strength of the memory effect should be largely dependent on whether there are other dislocation structures present that provide good hydride nucleation sites. In the quenched samples there were many c-type dislocations in the matrix due to large thermal stresses during cooling. Some of these matrix dislocations intersected the α/δ interface. They provide alternate hydride nucleation sites and likely explain why some hydrides in the quenched sample formed with an alternate orientation relationship [47].

Although most of the hydrides completely dissolved at the maximum heating temperature of 500 °C, well above the nominal dissolution temperature, a few of the initially large hydrides remained. These remnant hydrides were generally located near the oxide film and were most likely stabilized by residual stress resulting from the oxide layer formation, or perhaps as a result of the FIB milling process.

Conclusions

1. The 'memory effect' of hydride precipitation in zirconium alloys can be explained by the presence of c-type dislocations at the hydride-matrix interface that were not removed after complete hydride dissolution and provide nucleation sites for subsequent precipitation.
2. The δ/α interface has the EELS spectra of γ hydride, although its structure could not be confirmed.
3. During heating, the δ/α interface appears to grow as the δ hydride dissolves; a γ hydride shell may grow at the expense of a δ hydride core.
4. FIB preparation of quenched samples results in a distribution of δ hydrides rather than the expected γ hydride phase; the FIB may induce a hydride phase transformation.
5. Some hydrides in the FIB foils were stable to temperatures well above the bulk sample dissolution temperature, due to a significantly higher hydride content near the oxide layer.

References

1. B.A. Cheadle, *The Physical Metallurgy of Zirconium Alloys* (No. CRNL–1208, Atomic Energy of Canada Limited, 1975)
2. V.F. Urbanic, M. Griffiths, Microstructural aspects of corrosion and hydrogen ingress in Zr-2.5 Nb, in *Zirconium in the Nuclear Industry: Twelfth International Symposium*. ASTM International (2000)
3. J.E. Bailey, Electron microscope observations on the precipitation of zirconium hydride in zirconium. Acta Metall. **11**(4), 267–280 (1963)
4. M. Christensen et al., Effect of hydrogen on dimensional changes of zirconium and the influence of alloying elements: first-principles and classical simulations of point defects, dislocation loops, and hydrides, in *Zirconium in the Nuclear Industry: 17th Volume*. ASTM International (2015)
5. C.D. Cann et al., The effect of metallurgical factors on hydride phases in zirconium. J. Nucl. Mater. **126**(3), 197–205 (1984)
6. C.E. Coleman, J.F.R. Ambler, Delayed hydrogen cracking in Zr-2.5 wt% Nb alloy. Rev. Coat. Corros. **111**(2 & 3), 105–157 (1979)
7. G.J.C. Carpenter, J.F. Watters, R.W. Gilbert, Dislocations generated by zirconium hydride precipitates in zirconium and some of its alloys. J. Nucl. Mater. **48**(3), 267–276 (1973)
8. G.J.C. Carpenter, The precipitation of γ-zirconium hydride in zirconium. Acta Metall. **26**(8), 1225–1235 (1978)
9. C.E. Coleman, D. Hardie, The hydrogen embrittlement of α-zirconium—A review. J. Less Common Met. **11**(3), 168–185 (1966)
10. D.O. Northwood, U. Kosasih, Hydrides and delayed hydrogen cracking in zirconium and its alloys. Int. Met. Rev. **28**(1), 92–121 (1983)
11. R. Daum, S. Majumdar, M. Billone, Experimental and analytical investigation of the mechanical behavior of high-burnup Zircaloy-4 fuel cladding, in *Zirconium in the Nuclear Industry: 15th International Symposium*, ASTM International (2009)
12. O. Zanellato et al., Synchrotron diffraction study of dissolution and precipitation kinetics of hydrides in Zircaloy-4. J. Nucl. Mater. **420**(1), 537–547 (2012)
13. B. Nath, G.W. Lorimer, N. Ridley, The relationship between gamma and delta hydrides in zirconium-hydrogen alloys of low hydrogen concentration. J. Nucl. Mater. **49**(3), 262–280 (1974)
14. R.W.L. Fong, S. Spooner, Investigation of zirconium hydrides and hydrogen solubility limit in Zr-2.5 Nb alloy by small angle neutron scattering. Scr. Metall. Mater. **30**(5), 649–654 (1994)
15. J.H. Root et al., Kinetics of the δ to γ zirconium hydride transformation in Zr-2.5 Nb. Acta Mater. **51**(7), 2041–2053 (2003)
16. A.T.W. Barrow, A. Korinek, M.R. Daymond, Evaluating zirconium–zirconium hydride interfacial strains by nano-beam electron diffraction. J. Nucl. Mater. **432**(1), 366–370 (2013)
17. Anton Pshenichnikov, Juri Stuckert, Mario Walter, Microstructure and mechanical properties of Zircaloy-4 cladding hydrogenated at temperatures typical for loss-of-coolant accident (LOCA) conditions. Nucl. Eng. Des. **283**, 33–39 (2015)
18. Josiah Willard Gibbs, On the equilibrium of heterogeneous substances. Am. J. Sci. **96**, 441–458 (1878)
19. D.J. Cameron, R.G. Duncan, On the existence of a memory effect in hydride precipitation in cold-worked Zr-2.5% Nb. J. Nucl. Mater. **68**(3), 340–344 (1977)
20. J.H. Root, R.W.L. Fong, Neutron diffraction study of the precipitation and dissolution of hydrides in Zr-2.5 Nb pressure tube material. J. Nucl. Mater. **232**(1), 75–85 (1996)
21. Y.S. Kim et al., Precipitation of reoriented hydrides and textural change of α-zirconium grains during delayed hydride cracking of Zr–2.5% Nb pressure tube. J. Nucl. Mater. **297**(3), 292–302 (2001)

22. B. Nath, G.W. Lorimer, N. Ridley, Effect of hydrogen concentration and cooling rate on hydride precipitation in α-zirconium. J. Nucl. Mater. **58**(2), 153–162 (1975)
23. G.C. Weatherly, The precipitation of γ-hydride plates in zirconium. Acta Metall. **29**(3), 501–512 (1981)
24. E. Zuzek et al., The H-Zr (hydrogen-zirconium) system. J. Phase Equilib. **11**(4), 385–395 (1990)
25. S. Mishra, K.S. Sivaramakrihnan, M.K. Asundi, Formation of the gamma phase by a peritectoid reaction in the zirconium-hydrogen system. J. Nucl. Mater. **45**(3), 235–244 (1972)
26. J.H. Root et al., Kinetics of the δ to γ zirconium hydride transformation in Zr-2.5 Nb. Acta Mater. **51**(7), 2041–2053 (2003)
27. T. Maimaitiyili et al., In situ observation of γ-ZrH formation by X-ray diffraction. J. Alloy. Compd. **695**, 3124–3130 (2017)
28. L. Lanzani, M. Ruch, Comments on the stability of zirconium hydride phases in Zircaloy. J. Nucl. Mater. **324**(2), 165–176 (2004)
29. G.K. Dey, S. Banerjee, P. Mukhopadhyay, Formation of gamma hydride in alpha and beta zirconium alloys. Le J. de Phys. Colloques **43**(C4), C4–C327 (1982)
30. S. Hanlon et al., Stopping DHC by heating. Poster presented at: ASTM Zirconium in the Nuclear Industry—Eighteenth International Symposium, Hilton Head, SC, 15th–19th May 2016
31. P. Vizcaíno et al., Effect of crystallite orientation and external stress on hydride precipitation and dissolution in Zr2. 5% Nb. J. Nucl. Mater. **447**(1), 82–93 (2014)
32. A. McMinn, E.C. Darby, J.S. Schofield, The terminal solid solubility of hydrogen in zirconium alloys, in *Zirconium in the Nuclear Industry: Twelfth International Symposium*. ASTM International (2000)
33. C.D. Cann, A. Atrens, A metallographic study of the terminal solubility of hydrogen in zirconium at low hydrogen concentrations. J. Nucl. Mater. **88**(1), 42–50 (1980)
34. R.Prasath Babu et al., Nature of gallium focused ion beam induced phase transformation in 316L austenitic stainless steel. Acta Mater. **120**, 391–402 (2016)
35. N. Ni, S. Lozano-Perez, J. Sykes, C. Grovenor, Multi-scale characterisation of oxide on zirconium alloys. Mater. High Temp. **29**, 166–170 (2014)
36. J. Hu, A. Garner, N. Ni, A. Gholinia, R.J. Nicholls, S. Lozano-Perez et al., Identifying suboxide grains at the metal-oxide interface of a corroded Zr-1.0%Nb alloy using (S)TEM, transmission-EBSD and EELS. Micron **69**, 35–42 (2015)
37. M.P. Puls, R.L. Tapping, Z.H. Walker, ACR-700 advances in materials. Phys. Can. **60**(6), 369–381 (2004)
38. G.E. Totten, C.E. Bates, N.A. Clinton, *Handbook of Quenchants and Quenching Technology* (ASM International, 1993), p. 307
39. O.T. Woo, G.J.C. Carpenter, Identification of zirconium hydrides by electron energy loss spectroscopy. Scr. Metall. **20**, 423–426 (1986)
40. N. Ni, S. Lozano-Perez, J. Sykes, C. Grovenor, Quantitative EELS analysis of zirconium alloy metal/oxide interfaces. Ultramicroscopy **111**, 123–130 (2011)
41. B. de Gabory, Y. Dong, A.T. Motta, E.A. Marquis, EELS and atom probe tomography study of the evolution of the metal/oxide interface during zirconium alloy oxidation. J. Nucl. Mater. **462**, 304–309 (2015)
42. K.J. Annand, I. MacLaren, M. Gass, Utilising DualEELS to probe the nanoscale mechanisms of the corrosion of Zircaloy-4 in 350 °C pressurised water. J. Nucl. Mater. **465**, 390–399 (2015)
43. H.G. Kim, T.H. Kim, Y.H. Jeong, Oxidation characteristics of basal (0002) plane and prism (1120) plane in HCP Zr. J. Nucl. Mater. **306**(1), 44–53 (2002)
44. M. Preuss, P. Frankel, S. Lozano-Perez, D. Hudson, E. Polatidis, N. Ni et al., Studies regarding corrosion mechanisms in zirconium alloys. J. ASTM Int. **8**, 1–23 (2011)
45. S.S. Yardley, K.L. Moore, N. Ni, J.F. Wei, S. Lyon, M. Preuss et al., An investigation of the oxidation behaviour of zirconium alloys using isotopic tracers and high resolution SIMS. J. Nucl. Mater. **443**, 436–443 (2013)

46. A.T. Motta, A. Couet, R.J. Comstock, Corrosion of zirconium alloys used for nuclear fuel cladding. Ann. Rev. Mater. Res. **45**, 311–343 (2015)
47. F. Long et al., Microstructure characterization of a hydride blister in Zircaloy-4 by EBSD and TEM. Acta Mater. **129**, 450–461 (2017)
48. Canadian Standards Association, Technical requirements for inservice evaluation of zirconium alloy pressure tubes in CANDU reactors, N285.8-05 (2005)
49. M.S. Veshchunov, V.E. Shestak, V.D. Ozrin, A new model of hydrogen redistribution in Zr alloy claddings during waterside corrosion in a temperature gradient. J. Nucl. Mater. **472**, 65–75 (2016)
50. A.M. Garde, Enhancement of aqueous corrosion of zircaloy-4 due to hydride precipitation at the metal-oxide interface, in *Zirconium in the Nuclear Industry: Ninth International Symposium*. ASTM International (1991)
51. S.-J. Kim et al., The effect of hydride on the corrosion of Zircaloy-4 in aqueous LiOH solution. J. Nucl. Mater. **256**(2), 114–123 (1998)
52. S. Sagat et al., Delayed hydride cracking in zirconium alloys in a temperature gradient. J. Nucl. Mater. **279**(1), 107–117 (2000)
53. G.A. McRae, C.E. Coleman, B.W. Leitch, The first step for delayed hydride cracking in zirconium alloys. J. Nucl. Mater. **396**(1), 130–143 (2010)
54. R.N. Singh et al., Hydrogen charging, hydrogen content analysis and metallographic examination of hydride in Zirconium alloys, BARC report No. BARC/2003/E/034 (2003)

Influence of Alloying Elements and Effect of Stress on Anisotropic Hydrogen Diffusion in Zr-Based Alloys Predicted by Accelerated Kinetic Monte Carlo Simulations

Jianguo Yu, Chao Jiang and Yongfeng Zhang

Abstract The presence of hydrogen (H) can detrimentally affect the mechanical properties of many metals and alloys. To mitigate these detrimental effects requires fundamental understanding of the thermodynamics and kinetics governing H pickup and hydride formation. In this work, we focus on H diffusion in Zr-based alloys by studying the effects of alloying elements and stress, factors that have been shown to strongly affect H pickup and hydride formation in nuclear fuel claddings. A recently developed accelerated kinetic Monte Carlo method is used for the study. It is found that for the alloys considered here, H diffusivity depends weakly on composition, with negligible effect at high temperatures in the range of 600–1200 K. Therefore, the small variation in H diffusivity caused by variations in compositions of these alloys is likely not a major cause of the very different H pickup rates. In contrast, stress strongly affects H diffusivity. This effect needs to be considered for studying hydride formation and delayed hydride cracking.

Keywords Hydrogen diffusion · Zirconium alloys · Accelerated kinetic monte carlo

J. Yu (✉) · C. Jiang · Y. Zhang
Fuels Modeling and Simulation, Idaho National Laboratory,
Idaho Falls, ID 83415, USA
e-mail: jianguo.yu@inl.gov

C. Jiang
e-mail: chao.jiang@inl.gov

Y. Zhang
e-mail: yongfeng.zhang@inl.gov

J.H. Jackson et al. (eds.), *Proceedings of the 18th International Conference on Environmental Degradation of Materials in Nuclear Power Systems – Water Reactors*, The Minerals, Metals & Materials Series, https://doi.org/10.1007/978-3-319-68454-3_46

Introduction

Zirconium (Zr) alloys are extensively used as fuel cladding tubes in nuclear reactors owing to their low capture cross section to thermal neutron, good mechanical properties, and good corrosion resistance in various environmental conditions [1–3]. Most of current claddings are made of two Zr-based alloys [Zircaloy-2 (Zr2) and Zircaloy-4 (Zr4)]. Zr4 is mainly used in pressurized water reactors (PWRs) and Zr2 in boiling water reactors (BWRs). Significant effort has led to the development of modern Zr-based alloys with improved corrosion resistance and mechanical properties to meet the demands of higher fuel duty. For example, ZIRLO® and M5™ are more resistant to corrosion and hydrogen (H) pickup compared to Zr2 and Zr4, and they are used to replace Zr4 in PWRs. In addition, some other modern Zr-based alloys such as J-alloys and AXIOM™ have also been shown to not have enhanced corrosion at high burnups [1].

An interesting feature of these Zr-based claddings is that the addition or variation of a very small amount of alloying elements (typically less than 0.5% in concentration or weight) may be sufficient to dramatically change the corrosion behavior as well as H pickup fraction [1, 2] under operating conditions. For instance, with higher Fe content substituted for Ni, Zr4 (Zr-1.5Sn-0.2Fe-0.1Cr in wt%) was developed with significantly lower H pickup fraction compared to that exhibited by Zr-2 (with an approximate composition of Zr-1.5Sn-0.14Fe-0.10Cr-0.06Ni in wt%). For H to accumulate in the metal matrix of claddings, it needs to be produced during oxidation, and then transport over the oxide layer and eventually in the metal matrix. Therefore, the very different H pickup rates in various Zr-based alloys could be caused by (1) different oxidation kinetics and thus H production rates, (2) different transport speeds over the oxide layers [1] which have generally been regarded as an effective barrier to the absorption of hydrogen [3] and (3) different diffusion speeds in the metal matrix. However, it is not clear how the alloying elements will affect H diffusion, which is one of focuses in this study.

Another factor that may strongly affect H diffusion is stress. For instance, during hydride formation, stress may be induced by the mismatch between hydrides and the Zr matrix [3]. Upon cyclic thermal and mechanical loadings, hydrides can dissolve and reorient; this process involves H diffusion with the presence of stress. Meanwhile, stress may also be concentrated at crack tips during delayed-hydride-cracking (DHC). Zr-based alloy cladding tubes used in the nuclear industry are highly susceptible to DHC, which occurs when dissolved H atoms diffuse along the stress gradient towards the tensile stress concentration region at the crack tip, followed by reformation of hydrides at the crack tip and subsequent fracture [3, 4]. DHC may take place at stress levels much lower than the yielding stress and has remained a concern for cladding integrity during used fuel storage. A more comprehensive understanding on hydride reorientation and DHC requires a fundamental understanding of the stress state effect on the H diffusion.

In the past, a plethora of investigations on understanding of H diffusion in α-Zr and Zr alloys has been reported in the literature. However, most investigations

relied on experimental measurements [5–9]. It has been commonly accepted that H diffuses in Zr alloys via the same mechanism as in α-Zr, with additional trapping caused by alloying elements and impurities. Due to the hexagonal symmetry of α-Zr, the diffusivity of H along <c> usually differs from that along <a> (in a plane parallel to <a> and normal to <c>), with the former suggested to be higher than the latter with D_c/D_a >1, but not exceeding 2, at temperatures above 600 K by Kearns et al. [8]. In addition to these experiments, atomic scale studies such as density functional theory (DFT) calculations have also been applied to H diffusion in α-Zr [10–12].

H diffusion in α-Zr involves multiple hopping paths coupled with each other for long-range diffusion. The hopping rates obtained from DFT calculations need to be incorporated into either analytical theories or other modeling methods such as kinetic Monte Carlo (KMC) to predict diffusivity. One challenge to apply KMC to H diffusion in hcp metals is that the potential energy surface contains an energy basin formed by neighboring tetrahedral sites, which strongly limits the efficiency of KMC at low temperatures due to basin trapping. Since accurate H diffusivity is highly desired at low temperatures [4] to predict the kinetics of DHC, which is active in the temperature range of about 150 to 300 °C, acceleration of KMC is needed. Although guidance for general acceleration approaches already exists in the literature [13], analytical solutions that directly apply to interstitial diffusion in hcp crystals are yet to be derived. Recently an accelerated KMC method was developed for H diffusion in hcp metals by co-authors of this study [14]. Parameterized by DFT calculations, the accelerated KMC method is capable of efficiently calculating H diffusivity in a variety of Zr alloys, without altering the kinetics of long-range diffusion. Using this accelerated KMC method, this article is aimed at modeling H diffusion in Zr-based alloys under the influence of both alloying elements and stress.

Methods

DFT Calculations

To obtain the migration barriers for H diffusion as well as the binding energies between alloying elements (Sn, Fe, Cr, Ni, Nb) and H, we performed ab initio calculations using the all-electron projector augmented wave method within the generalized gradient approximation of Perdew, Burke, and Ernzerhof (PBE-GGA) [15], as implemented in VASP [16]. 96-atom supercells, which can be constructed from a 4 × 4 × 3 extension of the 2-atom hcp Zr unit cell, are used. Spin-polarized calculations are performed for Fe, Cr and Ni. A plane-wave cut-off energy of 500 eV and a 5 × 5 × 5 Monkhorst–Pack *k*-point mesh are used to ensure high numerical accuracy for total energy calculations. All internal atomic positions are fully optimized using a conjugate gradient method until forces are less than

0.01 eV/Å. Further relaxations of supercell volumes have been found to have negligible effect on the final results. To study the stress effect on H diffusion, the 96-atom hcp Zr supercell is hydrostatically strained by −2, −1, 0, +1 and +2%, respectively. The corresponding hydrostatic stress is 6.2, 2.9, 0, −2.7 and −5.1 GPa, respectively. Such stress levels can be reached at crack tips and at hydride/matrix interfaces. More computational details can be found in Ref. [14].

Accelerated Lattice Kinetic Monte Carlo

The accelerated KMC method recently developed by co-authors [14] is used in this article. For acceleration, the KMC events in basins are replaced using the solutions detailed in Ref. [14]. The calculations are performed from 300 to 1200 K, one data point every 100 K, covering the temperature range used in previous experiments. To minimize stochastic scattering, at each temperature 100,000 KMC simulations are carried out, each lasting until 100,000 basin exits are detected for sufficient statistics. The averaged mean-square-displacements (MSD) display the expected linear relationship with time, with the slope proportional to diffusivity.

Results and Discussion

Results from DFT Calculations

The calculated binding energies between H and alloying elements are listed in Table 1. For Sn, Fe, Cr, and Ni, the results have been previously reported in Ref. [14]. As mentioned in Ref. [14], there exist three different interactions between H and an impurity within the first nearest neighbor (1NN) distance. A binding energy of E_b^O represents octahedral (O) H trapped by one impurity site within 1NN distance, $E_b^{T_c}$ is for tetrahedral (T) H interstitials trapped by one impurity site within 1NN distance along <c> and $E_b^{T_a}$ denotes tetrahedral H interstitials trapped by one impurity site within 1NN distance in the basal plane. As shown in Table 1, Fe, Cr and Ni are attractive to H while Sn is repulsive to H. However, the binding energies between H and Nb are unusual. Specifically, the interaction is weakly repulsive when H occupies the tetrahedral sites, but attractive when H is at the octahedral site. As will be shown later by KMC simulations, such unusual feature of the binding energies between H and Nb can lead to lower anisotropic ratio of H diffusivity in Zr alloy system containing Nb element.

The activation barriers versus strain predicted by DFT calculations are given in Table 2 and plotted in Fig. 1a. Under compressive stress, the activation barriers for all four hopping paths increase. Under tensile stress, the activation barriers for all four hopping paths decrease. It is also shown that, although the activation barriers

Table 1 Binding energies [eV] between H and alloying elements from DFT calculations. Positive (negative) binding energy means attractive (repulsive) interaction. Results for Sn, Fe, Cr, and Ni are from Ref. [14]

Element	$E_b^{T_c}$	$E_b^{T_a}$	E_b^{O}
Sn	Not stable [14]	Not stable [14]	−0.037 [14]
Fe	0.094 [14]	0.069 [14]	0.106 [14]
Cr	0.089 [14]	0.065 [14]	0.085 [14]
Ni	0.212 [14]	0.153 [14]	0.165 [14]
Nb	−0.0024	−0.0007	0.042

Table 2 H migration barriers [eV] versus applied hydrostatic strains and the corresponding stresses [GPa] for 1NN jumps from DFT calculations

Pressure [GPa]	T-T	T-O	O-T	O-O	Strain %
6.247	0.14592	0.42383	0.45171	0.52806	−2.0
2.942	0.13576	0.41658	0.3984	0.46177	−1.0
0	0.12952	0.40612	0.34574	0.39849	0.0
−2.71	0.1251	0.39299	0.29653	0.33965	1.0
−5.134	0.12328	0.37747	0.24796	0.28139	2.0

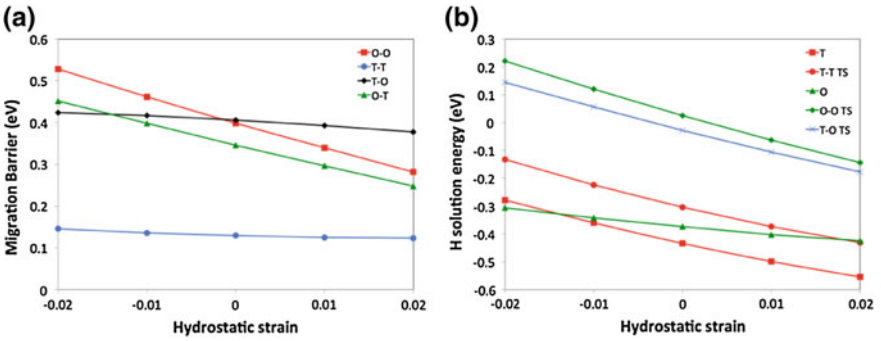

Fig. 1 DFT calculated H migration barrier (**a**) and H solution energy (**b**) in hcp Zr as a function of hydrostatic strain

for all four hopping paths depend nearly linearly on the applied stress, the activation barriers for the O-T and O-O jumps are much more significantly modified by the applied stress compared with T-T and T-O jumps. This can be understood since the O site is significantly larger than the T site and the transition states (TSs) volumetrically. Therefore, the solution energy of a H atom at the O site will exhibit much weaker pressure dependence compared with a H at the TS for either O-T or O-O jump (see Fig. 1b). Conversely, as shown in Fig. 1b, H atom at a T site exhibits very similar pressure-dependent behavior as the H atom at the TS for either T-T or T-O jump. The migration barrier, which is the energy difference between TS and T, therefore shows weak pressure dependence for T-T and T-O jumps. It is also

interesting to note that, under compressive stress, the O site can become more favorable than T site for H occupation. This is due to the fact that H energy at T site increases much faster with pressure than at O site.

Hydrogen Diffusion in Zr Alloys

KMC simulations are carried out to study the effect of alloy elements on H transport in Zr alloys. The corresponding approximate concentrations of the alloying elements of Zr alloys used in the KMC simulations are listed in Table 3. J3 (Zr-2.5Nb in wt%) alloy in the J-Alloys family (used extensively in pressure tubes in Canada Deuterium Uranium (CANDU) nuclear reactors [4]) is considered in this study. The results for the three-dimensional H diffusivity and the anisotropic diffusivity ratio in a variety of Zr alloys calculated are plotted in Fig. 2. As shown in Fig. 2 (a), at high temperatures in the range of 600–1200 K, the variation of H diffusivity in the Zr alloys studied here is very small. This indicates that the addition of alloying elements slightly reduces H diffusivity, with negligible effect at high temperatures. This observation is also in line with previous experiments, which found similar H diffusivity in α-Zr, Zr2, and Zr4 [8]. Using $D = D_0 \exp(-E_m/K_B T)$ with D_0 being the prefactor and E_m the effective migration barrier, fitted parameters for D_0 and E_m using the KMC results are listed in Table 4. The fitted results agree nicely with previously KMC values of 1.08×10^{-6} m^2/s and 0.46 eV shown in Fig. 2 (a) [14] and the averaged values of 7.0×10^{-7} m^2/s and 0.46 eV for α-Zr and Zircaloy from experiments [8]. At room temperature, the diffusivity of H in Zr2 is significantly lower than those of other alloys, presumably due to its higher concentration

Table 3 Approximate concentrations c_i (atomic fraction) of Sn, Fe, Cr, Ni and Nb in a variety of Zr alloys

Alloy	Sn	Fe	Cr	Ni	Nb
Zircaloy-2	0.011526	0.002287	0.001754	0.000932	0
Zircaloy-4	0.009990	0.003267	0.001754	0	0
ZIRLO®	0.007684	0.001633	0	0	0.009819
Optimized ZIRLO™	0.005149	0.001633	0	0	0.009819
J-Alloys					
J1	0	0	0	0	0.017674
J2	0	0	0.001754	0	0.015710
J3	0	0	0	0	0.024547
AXIOM™ alloys					
X2	0	0.000980	0	0	0.009819
X5	0.002305	0.005717	0.004386	0.000777	0.006873
X5A	0.003458	0.005717	0.004386	0	0.002946

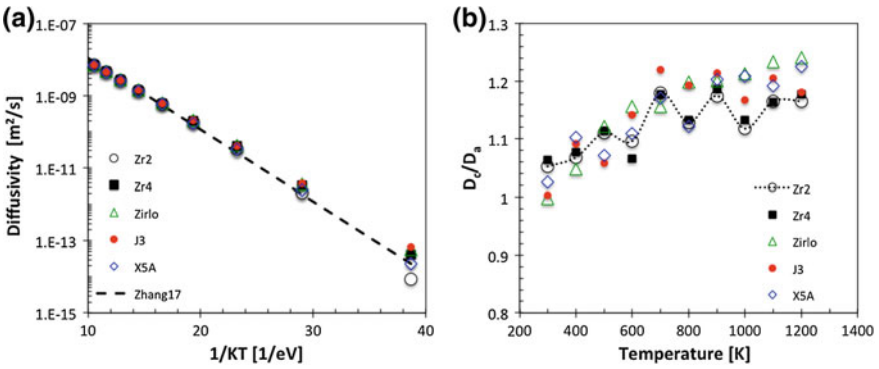

Fig. 2 **a** H diffusivity in Zr alloys of Zr2, Zr4, Zirlo, J3 and X5A as a function of inverse temperature, 1/KT; **b** D_c/D_a ratio from 300 to 1200 K

Table 4 Fitting of the KMC results using $D = D_0 \exp(-E_m/K_B T)$

	D_0 [m^2/s]	E_m [eV]
Zhang17 [14]	1.08×10^{-6}	0.46
Zr2	1.08×10^{-6}	0.457
Zr4, ZIRLO, J3	7.0×10^{-7}	0.425
X5A	9.0×10^{-7}	0.448

of Ni that strongly traps H atoms. Intriguingly, the lower H diffusivity in Zr2 than in Zr4 is in contrast with the lower H pickup in the latter. Therefore, the present results suggest that H diffusion in the metal matrix may not be the reason for the very different H pickup in various cladding alloys.

As shown in Fig. 2b, the diffusivity of H is anisotropic, which is in line with previous experiments [8] and KMC results [14]. In particular, the ratio of $D_c/D_a > 1$ is observed at temperatures above 400 K. The addition of alloying elements is found to have little effect on the anisotropy. For all alloys studied here, the ratio of D_c/D_a is about 1 at room temperature and increases with increasing temperature. A plateau at about 1.2 is reached at high temperatures, similar to the behavior of H in pure Zr [4]. Some stochastic effect is also noticed in the KMC results shown in Fig. 2b.

Stress Effect on Hydrogen Diffusion

To explore the effect of stress, the diffusivity of H in a variety of Zr alloys with 5 different applied hydrostatic stresses (6.2, 2.9, 0, −2.7 and −5.1 GPa, respectively) have been studied. The KMC simulation results for the stress effect on H diffusivity for Zr2, Zr4, Zirlo, J3 and X5A alloys are plotted in Figs. 3, 4, 5, 6 and 7, respectively. As expected, the H diffusivity is reduced under compressive stress and

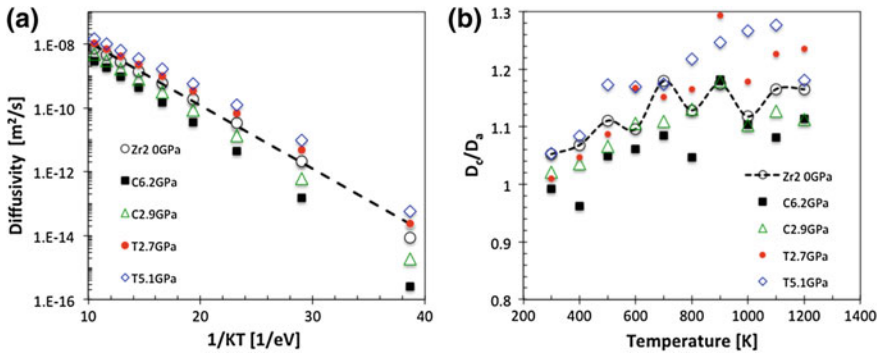

Fig. 3 Effect of stress on (**a**) H diffusivity in Zr2 alloy as a function of inverse temperature, 1/KT; (**b**) D_c/D_a ratio from 300 to 1200 K

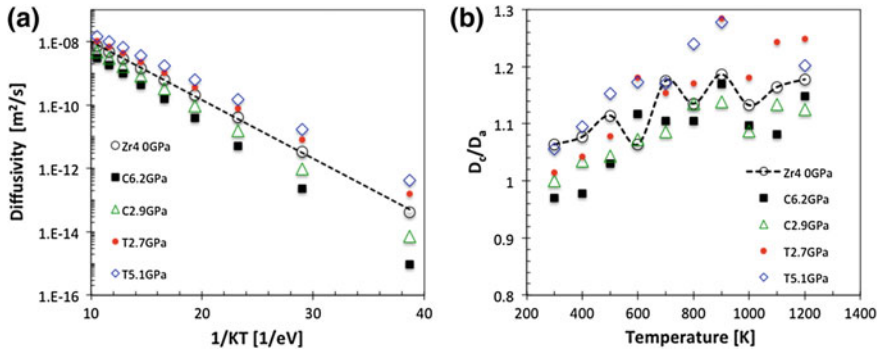

Fig. 4 Effect of stress on (**a**) H diffusivity in Zr4 as a function of inverse temperature, 1/KT; (**b**) D_c/D_a ratio from 300 to 1200 K

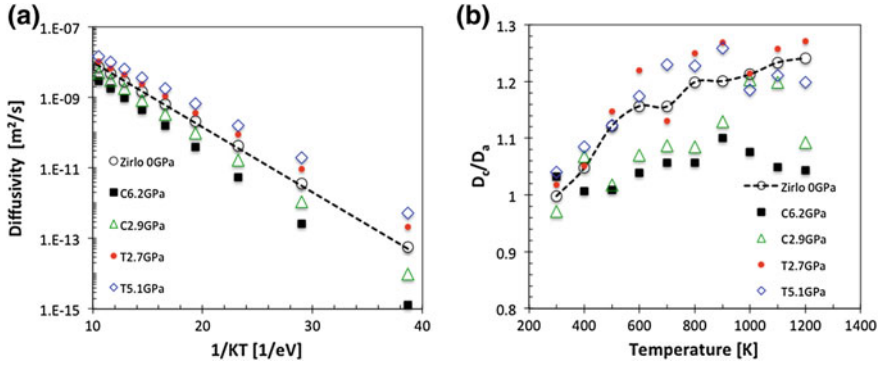

Fig. 5 Effect of stress on (**a**) H diffusivity in Zirlo as a function of inverse temperature 1/KT; (**b**) D_c/D_a ratio from 300 to 1200 K

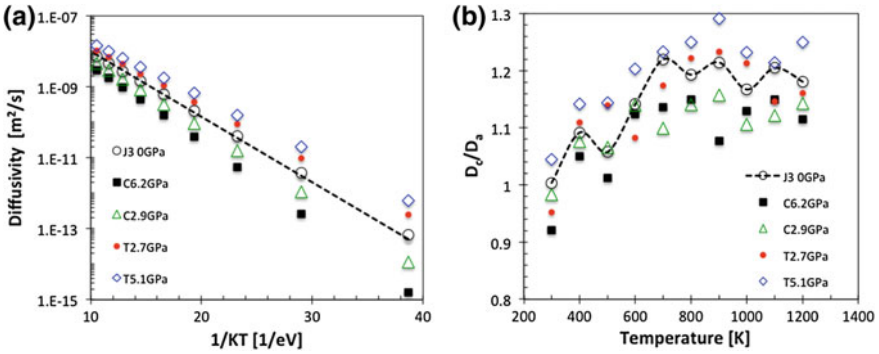

Fig. 6 Effect of stress on (**a**) H diffusivity in J3 as a function of inverse temperature, 1/KT; (**b**) D_c/D_a ratio from 300 to 1200 K

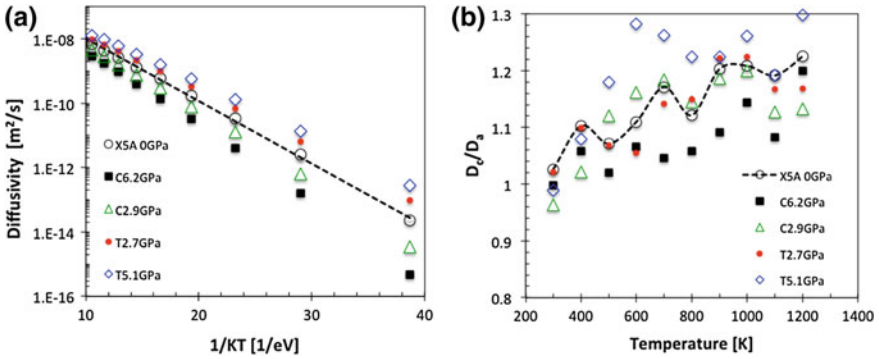

Fig. 7 Effect of stress on (**a**) H diffusivity in X5A as a function of inverse temperature, 1/KT; (**b**) D_c/D_a ratio from 300 to 1200 K

increased under tensile stress. Furthermore, the ratio D_c/D_a depends on both temperature and pressure. In all five Zr alloys considered, a general trend can be seen that both temperature and tensile stress will increase the D_c/D_a ratio and thus promote the anisotropy. At room temperature and under compressive stress, the ratio D_c/D_a can also become less than 1.

Elastic Dipole Tensor

It is also desired to have analytical descriptions for the dependence of migration barriers on elastic strain. Based on the theory of linear elasticity, the interaction energy between an external strain field ε_{ij} and a point defect can be calculated from its elastic dipole tensor P_{ij} as [17]:

Table 5 Elastic dipole tensors P_{ij} for H at various interstitial sites and transition states in hcp Zr

Site	P_{11} (eV)	P_{22} (eV)	P_{33} (eV)
T	1.999	1.999	3.265
O	0.779	0.779	1.313
T-T TS	3.404	3.404	1.174
O-O TS	3.105	3.105	3.801

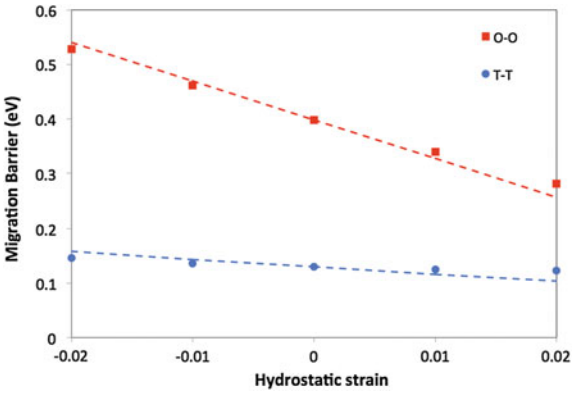

Fig. 8 Migration barriers for O-O and T-T paths in hcp Zr as a function of applied hydrostatic strain. Solid symbols are from the present DFT calculations. Solid lines represent results from elastic calculations

$$\Delta E = -\sum_{ij} P_{ij}\varepsilon_{ij} \tag{1}$$

In this study, we have calculated the elastic dipole tensors for H at O, T, and TS positions in hcp Zr using DFT. The results are reported in Table 5 and plotted in Fig. 8. The computational details can be found in Ref. [17]. Due to its low symmetry, the elastic dipole tensor of the TS for the T-O jump is not calculated here. As shown in Fig. 8, results from elastic theory calculations agree quantitatively with direct DFT calculations. Such a good agreement suggests that Eq. (1) can be used to accurately describe H diffusion behavior under an elastic stress field (e.g. around a crack tip) in hcp Zr. It also indicats that the effect of stress on H diffusion is most likely dominated by the elastic interaction.

Conclusion

In this work, an accelerated KMC method is used to reveal the influence of alloying elements and the effect of applied stress on H diffusivity in hcp Zr alloys. It is found that at very low temperature around ambient, H diffusivity might depend on the addition of alloying elements. However, at high temperatures in the range of 600-1200 K, the discrepancy of H diffusivity in the Zr alloys studied here is very

small. This indicates that the addition of alloying elements has negligible effect at high temperatures on H diffusivity, and this is likely not the reason for the very different H pickup in various cladding alloys. Applied stress is found to have a stronger effect on H diffusion than alloying elements. H diffusivity decreases under compressive and increases under tensile stress. Such change in H diffusion needs to be considered at stress fields induced by crack tips or hydrides.

Acknowledgements We gratefully acknowledge the support of the Department of Energy (DOE) Nuclear Energy Advanced Modeling and Simulation (NEAMS) program. This manuscript has been authored by Battelle Energy Alliance, LLC under Contract No. DE-AC07-05ID14517 with the U.S. Department of Energy. The United States Government retains and the publisher, by accepting the article for publication, acknowledges that the United States Government retains a nonexclusive, paid-up, irrevocable, world-wide license to publish or reproduce the published form of this manuscript, or allow others to do so, for United States Government purposes.

References

1. A.T. Motta, A. Couet, R.J. Comstock, Corrosion of zirconium alloys used for nuclear fuel cladding. Annu. Rev. Mater. Res. **45**, 311–343 (2015)
2. S.J. Zinkle, K.A. Terrani, L.L. Snead, Motivation for utilizing new high-performance advanced materials in nuclear energy systems. Curr. Opin. Solid State Mater. Sci. **20**, 401–410 (2016)
3. T. Allen, R. Konings, A. Motta, Corrosion of zirconium alloys. Compreh. Nuclear Mater. **5**, 49–68 (2012)
4. K.S. Chan, An assessment of delayed hydride cracking in zirconium alloy cladding tubes under stress transients. Int. Mater. Rev. **58**, 349–373 (2013)
5. A. Sawatzky, The diffusion and solubility of hydrogen in the alpha-phase of zircaloy-2. J. Nucl. Mater. **2**, 62–68 (1960)
6. C.M. Schwartz, M.W. Mallett, Observations on the behavior of hydrogen in zirconium. Trans. Am. Soc. Metals **46**, 640–654 (1954)
7. J.J. Kearns, Terminal solubility and partitioning of hydrogen in alpha phase of zirconium zircaloy-2 and zircaloy-4. J. Nucl. Mater. **22**, 292–303 (1967)
8. J.J. Kearns, Diffusion coefficient of hydrogen in α-Zr, Zircaloy2 and Zircaloy4. J. Nucl. Mater. **43**, 330–338 (1972)
9. C.S. Zhang, B. Li, P.R. Norton, The study of hydrogen segregation on Zr (0001) and Zr(10(1) over-bar0) surfaces by static secondary ion mass spectroscopy, work function, Auger electron spectroscopy and nuclear reaction analysis. J. Alloy. Compd. **231**, 354–363 (1995)
10. D.S. Sholl, Using density functional theory to study hydrogen diffusion in metals: a brief overview. J. Alloy. Compd. **446**, 462–468 (2007)
11. M. Christensen, W. Wolf, C. Freeman, E. Wimmer, R.B. Adamson, L. Hallstadius, P.E. Cantonwine, E.V. Mader, H in alpha-Zr and in zirconium hydrides: solubility, effect on dimensional changes, and the role of defects. J. Phys.-Conden. Matter **27**, 025402 (2015)
12. C. Domain, R. Besson, A. Legris, Atomic-scale Ab-initio study of the Zr-H system: i bulk properties. Acta. Materialia. **50**, 3513–3526 (2002)
13. B. Puchala, M.L. Falk, K. Garikipati, An energy basin finding algorithm for kinetic Monte Carlo acceleration. J. Chem. Phys. **132**, 134104 (2010)
14. Y.F. Zhang, C. Jiang, X.M. Bai, Anisotropic hydrogen diffusion in alpha-Zr and Zircaloy predicted by accelerated kinetic Monte Carlo simulations. Sci. Rep. **7**, 41033 (2017)

15. J.P. Perdew, K. Burke, M. Ernzerhof, Generalized gradient approximation made simple. Phys. Rev. Lett. **77**, 3865–3868 (1996)
16. G. Kresse, J. Furthmuller, Efficient iterative schemes for ab initio total-energy calculations using a plane-wave basis set. Phys. Rev. B **54**, 11169–11186 (1996)
17. R. Agarwal, D.R. Trinkle, Light-element diffusion in Mg using first-principles calculations: Anisotropy and elastodiffusion. Phys. Rev. B **94**, 054106 (2016)

Part VII
Stainless Steel Aging and CASS

Influence of δ-Ferrite Content on Thermal Aging Induced Mechanical Property Degradation in Cast Stainless Steels

Thak Sang Byun, Timothy G. Lach, Ying Yang and Changheui Jang

Abstract Thermal degradation of cast stainless steels was studied to provide an extensive knowledgebase for the assessment of structural integrity during extended operations of reactor coolant systems. The CF3 and CF8 series cast stainless steels with relatively low (5–12%) δ-ferrite contents were thermally aged at 290–400 °C for up to 10,000 h and tested to measure changes in tensile and impact properties. The aging treatments caused significant reduction of tensile ductility, but only slight softening or negligible strength change. The thermal aging also caused significant reduction of upper shelf energy and large shift of ductile-brittle transition temperature (ΔDBTT). The most influential factor in thermal degradation was ferrite content because of the major degradation mechanism occurring in the phase, while the nitrogen and carbon contents caused only weak effects. An integrated model is being developed to correlate the mechanical property changes with microstructural and compositional parameters.

Keywords Cast austenitic stainless steels · Thermal aging · Mechanical properties

Introduction

Cast austenitic stainless steels (CASSs) are highly corrosion-resistant Fe–Cr–Ni alloys with 300 series stainless steel compositions and mostly austenite (γ)–ferrite (δ) duplex structures, which are produced by various casting processes [1–10]. The CASS materials are extensively used for various large components of light water reactor (LWR) primary coolant systems, including coolant piping, valve

T.S. Byun (✉) · T.G. Lach
Pacific Northwest National Laboratory, 902 Battelle Blvd., Richland, WA 99352, USA
e-mail: thaksang.byun@pnnl.gov

Y. Yang
Oak Ridge National Laboratory, 1 Bethel Valley Road, Oak Ridge, TN 37831, USA

C. Jang
Korea Advanced Institute of Science & Technology, Daejeon 34141, Republic of Korea

J.H. Jackson et al. (eds.), *Proceedings of the 18th International Conference on Environmental Degradation of Materials in Nuclear Power Systems – Water Reactors*, The Minerals, Metals & Materials Series, https://doi.org/10.1007/978-3-319-68454-3_47

bodies, pump casings, and piping elbows [1, 2]. Many of these components are operated in complex and persistently damaging environments, such as elevated temperature coolant, high stress, and radiation, for long periods of time. Any significant degradation in mechanical properties (cracking resistance, in particular) that affects the structural integrity of the large CASS components would raise serious concern on the performance of the entire nuclear power plant.

Although the commonly used static and centrifugal casting processes enable fabrication of massive components with proper resistance to environmental attack, local alloying and microstructural conditions are not highly controllable in actual fabrication routes. In the corrosion-resistant Fe–Cr–Ni alloy system, therefore, the minor phase (i.e., the δ-ferrite phase) is inevitably introduced during the casting process, and is a non-equilibrium phase subjected to detrimental changes during exposure to elevated temperature and/or radiation. It has been well-known that thermal aging, as well as neutron irradiation, can cause degradation of static and dynamic fracture toughness in cast stainless steels [3–5]. In general, the relative amount of δ-ferrite is the most influential microstructural parameter in thermal degradation behavior of CASS materials since the high temperature ferrite (δ) phase decomposes into ferrite (α) and martensite (α′) through spinodal decomposition [11–15].

In the past a variety of cast stainless steels with different chemical compositions and δ-ferrite contents have been used in nuclear power plants and accordingly, a wide range of degradation behaviors have been measured among the steels [3–10]. The CASS alloys are typically graded by their chemical compositions and microstructural constituents, and the most common CF family of CASS alloys used in nuclear power plants have duplex structures of austenitic (γ) and ferritic (δ) phases. The CF family cast grades, including CF3, CF3M, CF8, CF8M, and their variants, have 17–22% Cr, 8–12% Ni, <1.5% Mn and <1.5% Si. The Mo-containing CASS alloys such as CF3M and CF8M contain up to 2.5% Mo. In the casting process, the main alloy elements, such as Fe, Cr, Ni, Mo, Mn, Si and C, and the cooling rate ultimately determine the final microstructure, in particular, the volume fractions and compositions of δ-ferrite and austenite phases. The CASS alloys contain 3–40% δ-ferrite in austenite matrix, depending on chemistry and cooling route. As shown in Fig. 1, the different casting processes can produce very different amounts of δ-ferrite, which is mainly due to different cooling rates. This study aims at elucidating the influence of δ-ferrite content on thermal aging degradation of mechanical properties [10, 16] in the CASS alloys with relatively low δ-ferrite contents.

Experiment and Analysis

Four (4) model CASS alloys (i.e., CF3, CF3M, CF8, and CF8M) have been produced for a systematic study on thermal aging effects [16, 17]. Although a large variety of cast stainless steels have been used in nuclear power plants as the reactor

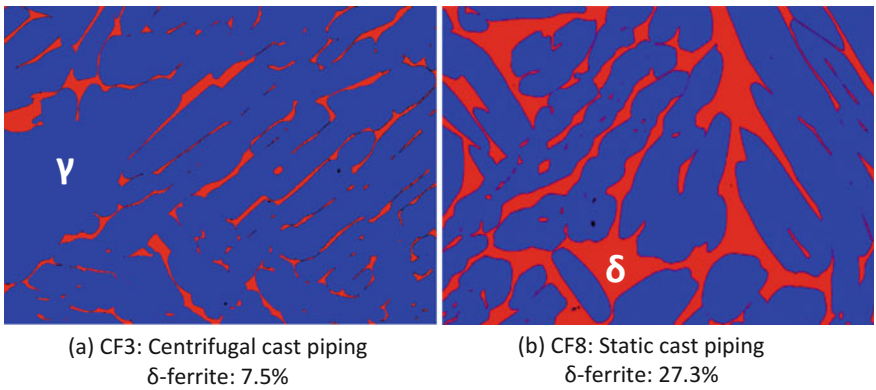

Fig. 1 Duplex austenitic (γ) and ferritic (δ) structures observed in **a** centrifugal cast CF3 piping and **b** static cast CF8 piping [16]

models and alloy selections have evolved with the year of construction, the most commonly used CASS alloys include the four alloys and their variants such as CF3A, CF8A, and CPF8M [3–10] (note: A-anneal, M-molybdenum, and P-piping). It is thought, therefore, that those four CASS grades (i.e., CF3, CF3M, CF8, and CF8M) can represent the vast majority of CASS alloys used in LWR power plants. Tables 1 and 2 list, respectively, chemical composition and δ-ferrite volume fraction data obtained for the model alloys. Note that the average ferrite volume fractions in Table 2 are relatively low (5–12%), which is due to the relatively high cooling rate during the small volume production of the model alloys.

To measure any thermal aging effects on the strength and ductility, tensile tests were carried out at room temperature (RT) to 400 °C for the four model alloys aged at 290, 330, 360, and 400 °C for 1500 and 10,000 h. The tensile specimens were SS-3 dog-bone type flat specimens with the gage section dimensions of 7.62 × 0.76 × 1.52 mm, and were tested at a displacement rate of 0.5 mm/min. Strength and ductility parameters were determined using the engineering stress-strain curves constructed from the load-displacement raw data and initial gage section dimensions.

Standard impact toughness testing was performed to evaluate the effect of thermal aging on the transition behavior of impact toughness or absorbed energy. Standard Charpy specimens (i.e., 10 × 10 × 55 mm bend bar with a 2 mm deep 45° notch) of aged and non-aged materials were tested in a Tinius-Olsen 300 J capacity Charpy impact testing machine. For each alloy and aging condition, 12–13 tests were performed to construct a complete impact energy transition curve and curve-fitting analysis on the impact energy dataset was performed to determine the transition curve parameters using a four-parameter hyperbolic tangent function [18, 19]:

Table 1 Chemical Compositions of the model CASS alloys in wt% or in ppm (for C, S, O and N)

Grade[a]	Fe	Cr	Ni	Mn	Mo	Si	Cu	Co	V	P	C	S	O	N
CF3 (304L)	Bal.	19.17	8.11	1.44	0.34	0.99	0.41	0.18	0.07	0.029	262	324	204	1020
CF3M (316L)	Bal.	19.28	9.81	1.14	2.30	1.22	0.28	0.15	0.05	0.033	284	253	224	838
CF8 (304)	Bal.	18.72	8.91	1.10	0.29	1.27	0.29	0.15	0.05	0.026	665	376	161	606
CF8M (316)	Bal.	18.52	10.38	0.65	2.33	1.02	0.33	0.17	0.06	0.031	433	243	207	1020

[a]CASS grade (closest equivalent wrought alloy). Data produced by Dirats Laboratories in Westfield, MA

Table 2 The volume fractions of δ-ferrite in the model CASS alloys (in %). The volume fractions have been measured by the line intercept method

CASS Grade	SEM-1	SEM-2	SEM-3	Optical-1	Average	Stand. Dev.
CF3	11.8	5.1	8.2	11.8	**9.2**	3.23
CF3M	15.0	17.5	7.2	7.9	**11.9**	5.13
CF8	5.6	3.7	6.0	6.7	**5.5**	1.28
CF8M	5.9	7	7.2	11.6	**7.9**	2.52

$$E(T) = A + B \times \tanh\left(\frac{T - D}{C}\right) \tag{1}$$

where A is the vertical position of the inflection point, B is the vertical distance between point A and the upper and lower shelves, C is one-half the width of the transition region, and D is the horizontal position of the inflection point. Key transition curve parameters can be defined using these parameters: the value $A + B$ is defined as the upper shelf energy (USE), and $A-B$ is defined as the lower shelf energy (LSE). The parameter D becomes the ductile-brittle transition temperature (DBTT), which is the midpoint temperature in the transition region. The best fit curves can be found using an ordinary least squares (OLS) regression technique or similar regression methods. In practical analysis the two parameters, LSE and USE, can be determined by plotting measured absorbed energy data, and therefore the DBTT value is used as an iteration parameter. The LSE can be set at 20 J for stainless steels.

Effect of Aging on Strength and Ductility

In Fig. 2, the yield strength (YS) values before and after thermal aging are plotted against test temperature. A general temperature dependence of strength observed in the model alloys before aging was that YS decreased with test temperature up to 290 °C and showed little change in the aging temperature range of 290–400 °C. Comparing the YS data of the as-cast alloys indicates that the 1500 and 10,000 h aging treatments have caused similar levels of softening but with large scatters. Such reduced strengths might indicate that some softening mechanisms have over-compensated the hardening amount by various precipitations. This relatively aging-insensitive aspect found in strength is clearly contrary to the impact energy behavior to be described in the next sections.

It is also commonly observed in all alloys that the thermal aging has not changed the temperature dependence of strength, which may indicate that the strengthening mechanisms being operated in the test temperature range remain unchanged. This strength behavior without evident dependence on aging temperature might indicate

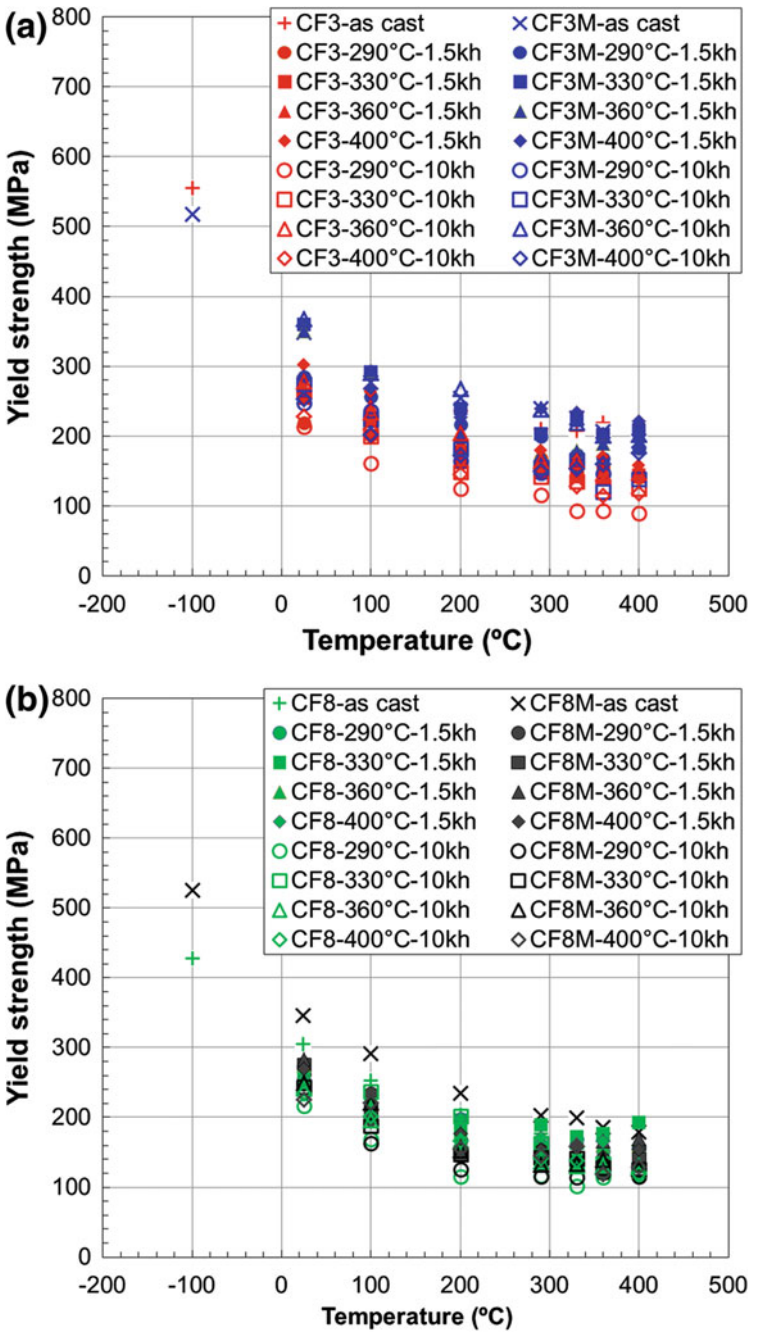

Fig. 2 Effect of thermal aging on YS in **a** CF3 and CF3M and **b** CF8 and CF8M alloys

that the microstructural mechanisms inducing strength change during aging in 290–400 °C range are either negligible or remained complementing each other.

The total elongation (TE) data displayed in Fig. 3 indicates a significant and complex degradation behavior in the ductility of model alloys. It is commonly found in the datasets for all non-aged alloys that the elongation decreases with test temperature before they become nearly temperature independent in the aging temperature region (290–400 °C). This test temperature dependence of ductility is very similar to that of strength although the large scattering in elongation data seems to be too large to discern any occurrence of aging-temperature dependence within the aging temperature range. The ductility datasets for aged alloys show that such temperature dependence has been retained after aging; however, it has become less steep in the lower temperature region up to 200 °C, which resulted in relatively large reduction in ductility in the lower temperature region and relatively muted temperature dependence in the test temperature range of 200–400 °C.

A comparison between the TE data of aged and non-aged alloys also shows that the ductility at or above room temperature is significantly reduced after aging. A few elongation data after aging present more than 50% reduction at room temperature, while the ductility reduction is typically 20–30% in the 290–400 °C region. Although the ductility data display significant scattering and thus the ranges of elongation datasets for 1500 and 10,000 h treatments are generally not discernable, it is evident that the CF3, CF8, CF8M alloys show a significant recovery of ductility after aging at the relatively low temperatures of 290 and 330 °C. These materials have relatively low (<10%) δ-ferrite contents and the ductility recovery should be due to the softening effect from precipitation and coarsening in the austenite phase. Such a softening effect might not be dominant in the CF3M alloy, where the δ-ferrite content is highest among the model alloys and the ductility reduction due to the spinodal decomposition in δ-ferrite has a larger influence. It is also observed that the 400 °C aging does not induce such ductility recovery, which indicates that the spinodal decomposition in δ-ferrite, the main embrittlement mechanism in the cast stainless steels, is actively progressed at the highest aging temperature. In any aging conditions, however, the model alloys retain high uniform ductility > ~20% over the whole test temperature range.

It is also observed that a higher percent reduction in ductility occurs at lower test temperatures, the majority of which occurred in uniform ductility. Further, as observed in the strength and ductility data in Figs. 2 and 3, the thermal aging treatments have resulted in a simultaneous reduction of strength and ductility. These phenomena might be explained by the characteristic deformation mechanism in austenitic stainless steels: a highly linear dislocation slip occurs in the model alloys, in particular, at lower temperatures [20] and the slip might become less linear after thermal aging due to an increase of precipitates, which leads to loss of ductility.

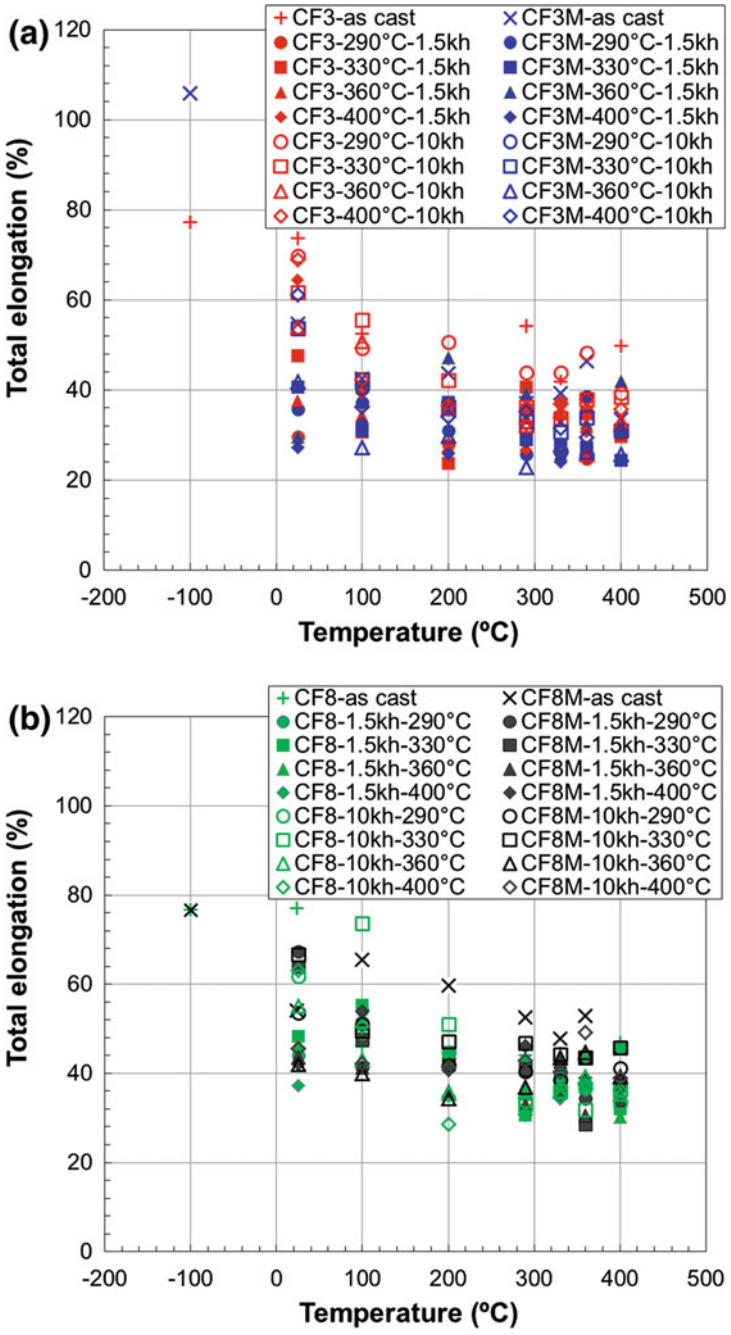

Fig. 3 Effect of thermal aging on TE in **a** CF3 and CF3M and **b** CF8 and CF8M alloys

Effect of Aging on Impact Toughness

The experimental USE data used in the transition curve analysis are compared altogether in Fig. 4, where the columns with a red border are those of the non-aged CASS alloys. The impact energy transition behaviors indicate that the effects of thermal aging on different parameters in the CASS alloys do not occur in a uniform manner: the average reduction of USE is the most substantial in CF3, and the smallest in CF8. In each of these alloys, however, the different aging times (i.e., 1500 and 10,000 h) have resulted in similar amounts of USE reduction. Interestingly, the USE data of the CF3 and CF8M alloys after 10,000 h aging indicate slight recovery when compared to those after 1500 h aging. Further, the USE data after aging display the least dependence on aging temperature in CF3 but much clearer temperature dependence in the Mo-containing CF3M and CF8M alloys. Despite significant reductions in USE for all aged model alloys, no alloy showed embrittlement in the upper shelf region, which is near or above room temperature. The lowest USE after aging, which was measured in CF3M, was still as high as 94 J.

It was predicted that the USE after aging at the highest aging temperature of 400 °C would be the lowest for each alloy. Before aging the USE was relatively high for non-aged CF3 and CF8 alloys (∼240 J), and slightly lower for CF3M and CF8M alloys (182 and 198 J, respectively). The USE measurements for all model

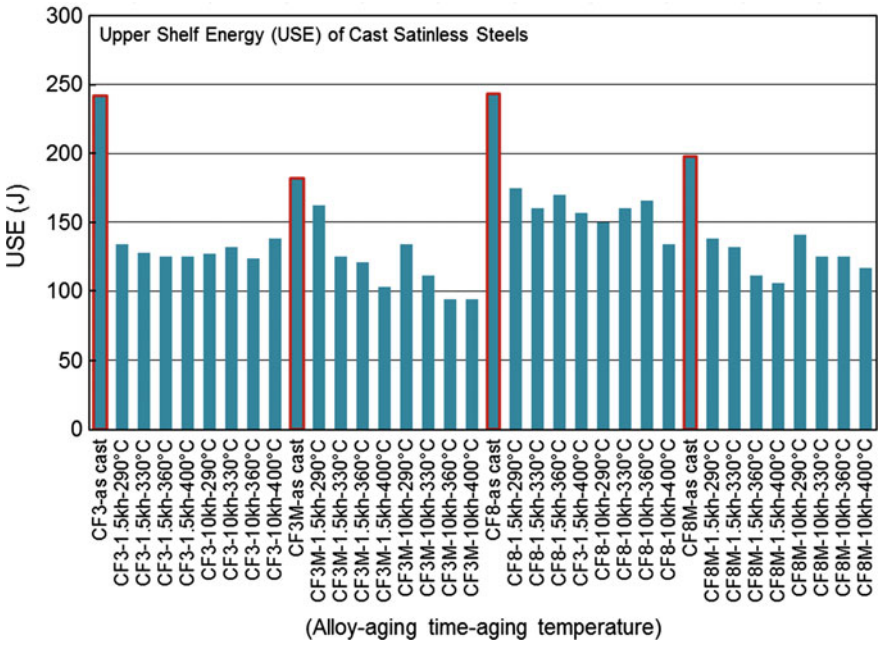

Fig. 4 Reduction of USE after 1500 and 10,000 h aging

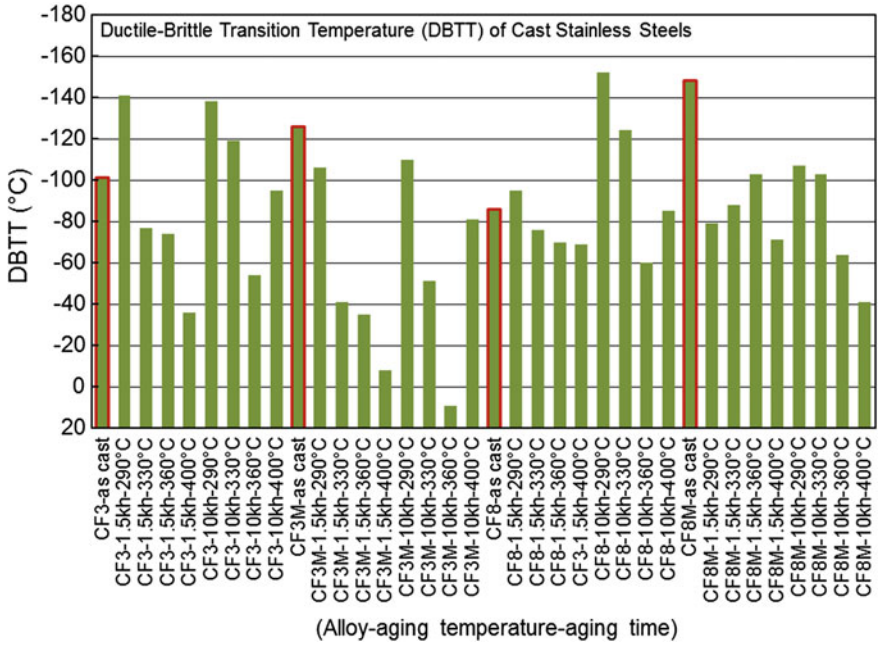

Fig. 5 Effect of 1500 and 10,000 h aging on DBTT

alloys were reduced by 40–50% after the severest aging (i.e., 10,000 h at 400 °C). Overall, the CF8 alloy retained the highest USE during aging, which may be due to the lowest δ-ferrite content (5.5%) among the model alloys. This is consistent with the smallest shift in transition temperature, as discussed below.

Figure 5 compares the DBTT data measured from the four model alloys before and after aging for 1500 and 10,000 h. The most substantial and gradual shift of DBTT is observed in CF3M: The DBTT of −126 °C in the as-cast condition changed to −106, −41, −35, and −8 °C after 1500 h aging at 290, 330, 360, and 400 °C, respectively. The DBTT of CF3M has changed to −110, −51, +9, and −81 °C after 10,000 h aging at the same aging temperatures. Among the four model alloys, the CF8 alloy seems to show the highest resilience to the DBTT shift, as the DBTT change in CF8 was relatively moderate and the maximum ΔDBTT was only +26 °C after aging at 360 °C for 10,000 h. Meanwhile, the DBTT data of CF8M show that thermal aging has shifted DBTT by relatively larger amounts of 45–107 °C. Overall, the DBTT shift is dependent on alloy and aging temperature. Relatively stronger aging-temperature dependence is found in the CF3 and CF3M alloys, compared to the CF8 and CF8M alloys.

An inverse aging effect was also observed for some cases: the decrease of DBTT in CF3M from −8 to −81 °C at 400 °C aging between 1500 and 10,000 h might be due to overaging. Such a behavior of overaging or decrease of DBTT was also observed in CF3 and CF8 after the 10,000 h aging. The maximum shift of DBTT

(ΔDBTT) measured among the datasets was +135 °C, which was observed in CF3M alloy after aging at 360 °C for 10,000 h. It is believed that such negative DBTT shifts found at the lower aging temperatures are associated with the mathematical definition of DBTT. That is, the USE after aging was significantly reduced at the lower aging temperatures (i.e., 290 and 330 °C), and such a large USE reduction with a small shift of the transition region sometimes resulted in the negative shift of DBTT. For a scientific discussion, therefore, it is recommended to use the transition temperature at a fixed energy, e.g., the transition temperature at 41 J or T_{41J}.

Concluding Remarks

This paper provides the mechanical test results obtained for aged and non-aged model CASS alloys with relatively low δ-ferrite contents. Uniaxial tensile and Charpy impact test data comprise the key datasets used to display the effect of thermal aging. The discussion focused on the degree of aging degradation and on possible influential factors in those model alloys: (a) Short-term (1500 h) aging treatment resulted in significant reduction of absorbed energy and shift of ductile-brittle transition temperature (ΔDBTT). The longer-term (10,000 h) aging treatment resulted in only a mild further reduction of absorbed energy. (b) Aging degradation was less significant in tensile properties than in impact toughness. Loss of ductility was significant only at relatively low test temperatures. (c) Overaging recovery was observed in tensile and impact properties after 10,000 h. (d) The aging degradation was dependent predominantly on the initial volume fraction of δ-ferrite and molybdenum content.

Acknowledgements This research was sponsored by U.S. Department of Energy/Office of Nuclear Energy through Light Water Reactor Sustainability R&D Program and International Nuclear Energy Research Initiative (I-NERI) Program. Pacific Northwest National Laboratory is operated by Battelle Memorial Institute for the U.S. Department of Energy under Contract No. DEAC05-76RL01830.

References

1. J.T. Busby, P.G. Oberson, C.E. Carpenter, M. Srinivasan, *Expanded Materials Degradation Assessment (EMDA)-Vol. 2: Aging of Core Internals and Piping Systems*, NUREG/CR-7153, Vol. 2, ORNL/TM-2013/532, October 2014
2. R. Dyle, *Materials Degradation Matrix and Issue Management Tables Overview-LTO Update* (The 2nd Workshop on U.S. Nuclear Power Plant Life Extension, Washington, D.C, 2011)
3. O.K. Chopra, A. Sather, *Initial Assessment of the Mechanisms and Significance of Low-T Embrittlement of Cast Stainless Steels in LWR Systems* (NUREG/CR–5385, 1990)

4. O.K. Chopra, *Effects of Thermal Aging and Neutron Irradiation on Crack Growth Rate and Fracture Toughness of Cast Stainless Steels and Austenitic Stainless Steel Welds* (NUREG/CR-7185, 2014)
5. O.K. Chopra, *Estimation of Fracture Toughness of Cast Stainless Steels during Thermal Aging in LWR Systems* (NUREG/CR-4513, 1991)
6. W.F. Michaud, P.T. Toben, W.K. Soppet, O.K. Chopra, *Tensile-Property Characterization of Thermally Aged Cast Stainless Steels* (NUREG/CR-6142, 1994)
7. H.M. Chung, T.R. Leax, Mater. Sci. Technol. **6**, 249–262 (1990)
8. H.M. Chung, *Evaluation of Aging of Cast Stainless Steel Components* (Presented at ASME Pressure Vessel & Piping Conference, San Diego, CA, 1991)
9. H.M. Chung, *Presented at the American Society for Mechanical Engineers-Material Properties Council Symposium on Plant Life Extension for Nuclear Components* (Honolulu, Hawaii, 1989)
10. T.S. Byun, Y. Yang, N.R. Overman, J.T. Busby, Thermal aging phenomena in cast duplex stainless steels. JOM **68**(2), 507–526 (2016)
11. M. Murayama, Y. Katayama, K. Hono, Metall. Mater. Trans. A **30A**, 345 (1999)
12. T. Sourmail, Mater. Sci. Tech. **17**, 1 (2001)
13. L.P. Stoter, J. Mater. Sci. **16**, 1039 (1981)
14. B. Weiss, R. Stickler, Metal Trans. **3**, 851 (1972)
15. J.E. Spruiell, J.A. Scott, C.S. Ary, R.L. Hardin, Metal Trans. **4**, 1533 (1973)
16. T.S. Byun, N.R. Overman, T.G. Lach, *Mechanical Properties of Model Cast Austenitic Stainless Steels after Thermal Aging for 1500 h, LWRS Report, PNNL-25377*, April 2016
17. T.G. Lach, T.S. Byun, *Microstructural Evolution of Cast Austenitic Stainless Steels under Accelerated Thermal Aging, 18th International Conference on Environmental Degradation of Materials in Nuclear Power Systems—Water Reactors*, Portland, Oregon, USA, Aug 13–17, 2017
18. W. Oldfield, Curve fitting impact test data: a statistical procedure. ASTM Standardization News **3**(11), 24–29 (1975)
19. K. Yeager, *Nonlinear curve fitting and the Charpy impact test: statistical, mathematical, and physical considerations* (https://www.uakron.edu/dotAsset/2116623.pdf)
20. T.S. Byun, N. Hashimoto, K. Farrell, Acta Mater. **52**, 3889–3899 (2004)

Microstructure and Deformation Behavior of Thermally Aged Cast Austenitic Stainless Steels

Y. Chen, C. Xu, X. Zhang, W.-Y. Chen, J.-S. Park, J. Almer, M. Li, Z. Li, Y. Yang, A.S. Rao, B. Alexandreanu and K. Natesan

Abstract Cast austenitic stainless steels (CASS) consist of a dual-phase microstructure of delta ferrite and austenite. The ferrite phase is critical for the service performance of CASS alloys, but can also undergo significant microstructural changes at elevated temperatures, leading to severe embrittlement. To understand thermal aging embrittlement, fracture toughness J-R curve tests were performed on unaged and aged CF8 specimens at 315 °C. The microstructure of CF8 was also examined before and after thermal aging with transmission electron microscopy and atom probe tomography. While no microstructural change was observed in the austenite after thermal aging, a high density of G-phase precipitates and a phase separation of alpha/alpha prime were detected in ferrite. To study the deformation behavior, tensile tests were performed at room temperature with in situ wide-angle X-ray scattering measurements. The differences in lattice strains between ferrite and austenite were much higher in the aged than in the unaged samples, suggesting a higher degree of incompatible deformation between ferrite and austenite in the aged samples.

Keywords Cast austenitic stainless steels · Thermal aging embrittlement · Fracture toughness · Microstructural characterization · Wide-angle X-ray scattering

Y. Chen (✉) · X. Zhang · W.-Y. Chen · J.-S. Park · J. Almer · M. Li · B. Alexandreanu · K. Natesan
Argonne National Laboratory, 9700 S. Cass Ave., Lemont, IL 60439, USA
e-mail: yiren_chen@anl.gov

C. Xu · Z. Li · Y. Yang
University of Florida, Gainesville, FL 32611, USA

A.S. Rao
US Nuclear Regulatory Commission, 11545, Rockville Pike, Rockville, MD 20852, USA

J.H. Jackson et al. (eds.), *Proceedings of the 18th International Conference on Environmental Degradation of Materials in Nuclear Power Systems – Water Reactors*, The Minerals, Metals & Materials Series, https://doi.org/10.1007/978-3-319-68454-3_48

Introduction

Cast austenitic stainless steels (CASSs) are used widely in light water reactors (LWRs) thanks to their excellent mechanical properties and corrosion resistance. Most reactor components exposed to high-temperature coolants are made of 300-series stainless steels (SSs) and their cast equivalents. The ASME SA-351 CF3, CF8, CF3 M and CF8 M are the most common cast grades found in LWRs [1]. The CF grades are resistant to corrosion in a variety of acids and aqueous environments [2], and retain high strength and ductility at reactor operating temperatures [3, 4]. As a near-net shape manufacture method, stainless steel castings also offer tremendous advantages for fabricating large and complex-shaped components, such as valve body, pump casing, elbow, pipe, support column etc. These reactor components are not only critical for the structural integrity of primary pressure boundaries, but also important for supporting and maintaining the configuration of fuel assemblies inside the reactor core. Because of their critical role in the safety and reliability of reactor operation, the long-term service performance of CASS alloys is an important issue for aging management and license renewal of LWRs.

The CF grades normally consist of a dual-phase microstructure of delta ferrite and austenite. This unique microstructure is a result of cast solidification, which has a profound impact on the performance of CASS alloys. The delta ferrite is a primary phase forming first from liquid during casting. The nucleation and growth of austenite follows as a secondary phase at the liquid/solid interface. With further cooling, the Cr/Ni ratio under which the ferritic phase is stable varies, creating a driving force for solid-state transformation from ferrite to austenite [5]. Consequently, the austenite becomes the dominant phase in casting, leaving behind 5–20% delta ferrite in the CF grades used in LWRs. Depending on the alloy's composition, solidification condition, and cooling rate, the retained ferrite normally shows a vermicular or lacy morphology in its final casting microstructure [6].

Although delta ferrite is a minor phase in CASS alloys, it is crucial for the properties and service performance of CASS alloys. Delta ferrite is critical for the soundness of castings, and a minimum amount of delta ferrite is often required in foundry and welding practices to avoid solidification cracking or "hot cracking". This is because delta ferrite has a relatively higher solubility for impurities and can help reduce the tendency of segregation and cracking during solidification [7]. In addition, as a secondary phase surrounded by austenitic matrix, the retained ferrite is also critical for the strength of CASS alloys. The yield stresses of CASS alloys are found to be proportional to their ferrite contents up to 40% [8]. For the coarse grain structure of CASS alloys, phase boundaries provide an effective strengthening mechanism for the soft austenite matrix. Furthermore, delta ferrite is beneficial for corrosion resistance and stress corrosion cracking (SCC) performance. Previous studies have shown that CASS alloys are more resistant to sensitization and SCC in simulated LWR environments [9] [10]. These beneficial effects of delta ferrite are critical for the successful applications of CASS alloys in LWRs.

In addition to the favorable effects of delta ferrite, it also has some negative impacts on CASS alloys. Ferrite reduces low-temperature ductility and is vulnerable to thermal aging embrittlement [11]. Delta ferrite is unstable at elevated temperatures, and precipitations and phase separation can occur between 300–500 °C [12, 13]. Significant hardening can be observed after thermal aging, and both ductility and impact energy are reduced after prolonged exposures at elevated temperatures [14, 15]. To understand this thermally induced embrittlement behavior, a CF8 alloy was characterized before and after thermal aging with transmission electron microscopy (TEM) and atom probe tomography (APT). Fracture toughness J-R curve tests were performed on the unaged and aged samples to assess the extent of embrittlement. In this study, in situ tensile tests were also performed with wide-angle X-ray scattering (WAXS) technique to analyze the deformation behavior of CASS samples.

Experimental

Material and Specimens

A CF8 alloy with 23% ferrite was selected for the microstructural and deformation study. The alloy was obtained from a previous research program and was cut from a large statically cast slab of 610 × 610 × 76 mm. The chemical composition and ferrite content of the slab are given in Table 1. The ferrite content was measured with a ferroscope on the cast slab. Some of the as-received (i.e., unaged) material was thermally aged at 400 °C for 10,000 h. A previous study on the kinetics of thermal aging embrittlement [4] showed that this thermal aging condition is equivalent to a service exposure to reactor coolant at ~320 °C for 40 years.

Figure 1 shows the optical images of the CF8 alloy before and after thermal aging. The samples were polished with SiC papers up to 1200 grit. After a final finish with 3-μm diamond slurry, the polished surfaces were etched with ferric chloride. A vermicular morphology of ferrite can be seen in the unaged and aged specimens. The thermal aging treatment at 400 °C does not alter the quantity or morphology of ferrite.

Table 1 Chemical composition and ferrite content of CF8 used in the study

Heat ID	Delta ferrite	Composition (wt%)								
		Mn	Si	P	S	Mo	Cr	Ni	N	C
68	23%	0.64	1.07	0.021	0.014	0.31	20.46	8.08	0.062	0.063

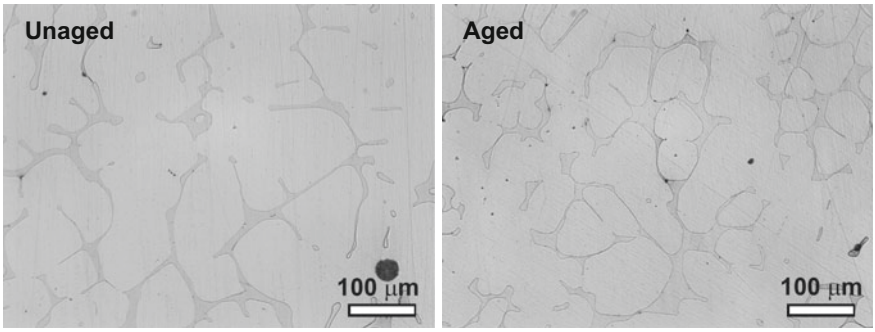

Fig. 1 Optical images of the CF8 with 23% ferrite before and after thermal aging at 400 °C for 10,000 h. Note that darker gray is delta ferrite in the images

Fracture Toughness J-R Curve Tests

Compact-tension (CT) specimens were used for the fracture toughness J-R curve test in this study. A schematic of the CT sample is shown in Fig. 2. The sample has a nominal width of 12 mm, a thickness of 6.5 mm (1/4T-CT), and an initial notch size of 6 mm. To ensure an in-plane crack growth, a side groove approximately 5% of the thickness was machined on each side of the sample, giving rise to a net thickness of 5.85 mm. Prior to each J-R curve test, the sample was tested in high-purity water with low dissolved oxygen (DO, <10 ppb) for corrosion-fatigue and stress corrosion (SCC) cracking performances. Crack growth rates (CGRs) were measured on the sample under cyclic and static loads, and the results will be reported elsewhere. After the CGR test, a J-R curve test was performed on the same sample in the same test environment. So, the starter crack for the J-R curve test was a SCC crack resulting from a previous CGR test.

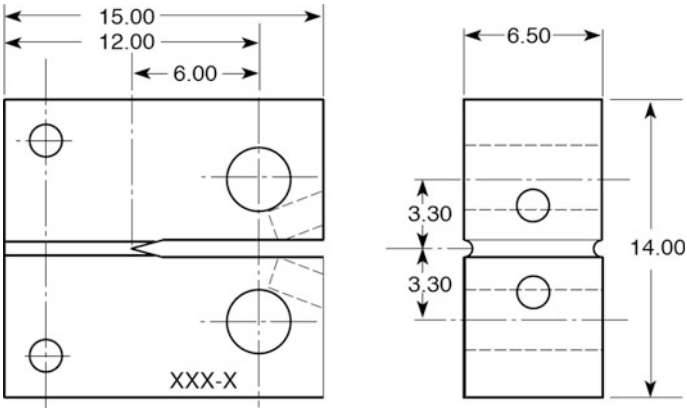

Fig. 2 1/4T-CT sample used for J-R curve test (dimensions in mm)

The J-R curve tests were performed to the ASTM standard E1820-15. For each test, the sample was loaded in tension at a constant cross-head displacement rate of 0.43 μm/s. A load versus load-line displacement curve was recorded during the test. At a regular interval, the loading was paused and the crack length was measured with direct current potential drop (DCPD) method. After the test, a J-integral value was calculated at each crack extension along the load vs. load-line displacement curve, and a J-resistance curve was obtained by plotting the J values as a function of crack length.

Microstructural Characterization

Three-mm TEM disks were cut from the unaged and aged materials and thinned mechanically to 100–150 μm. The TEM disks were electrochemically polished with a twin-jet polisher at −35 °C in an electrolyte of 5% perchloric acid and methanol until perforation. The obtained TEM thin foils were examined with a Hitachi-H9000 TEM at the Intermediate Voltage Electron Microscopy (IVEM) facility at ANL. Dislocation and precipitate microstructures were imaged with diffraction contrast under two-beam bright-field or dark-field conditions in both austenite and ferrite.

The specimens were also examined with APT at the Center for Nanophase Materials Sciences of the Oak Ridge National Laboratory. The APT samples were fabricated from the ferrite phase of the CASS specimens using focused ion beam (FEI Nova 200 dual beam FIB). The APT data were collected with CAMECA Instruments Inc. LEAP 4000X HP local electrode atom probe. The data acquisition was conducted in a laser-pulsed mode with a sample base temperature of 30 K. Ultraviolet laser pulses at a frequency of 200 kHz with a laser energy of 100 pJ were used to field evaporate the surface ions. Data reconstruction and analysis were performed with CAMECA's Interactive Visualization Software (IVAS 3.6.6).

Wide-Angle X-Ray Scattering (WAXS) with In Situ Tensile

To understand the deformation behavior of CASS alloys, two tensile tests were performed on unaged and aged specimens with in situ WAXS measurements. These tests were conducted with a recently developed experimental module at Beamline 1-ID of the Advanced Photon Source (APS). This experimental module can be connected to a servo-hydraulic test system located in the X-ray beamline, enabling a wide range of diffraction and tomographic measurements with high-energy synchrotron X-rays during mechanical tests. More details about the experimental setup and its capabilities can be found in references [16–18].

Figure 3 shows the flat tensile sample used in the in situ tests. Both the unaged and aged samples were tested in air at room temperature. For each specimen, a low

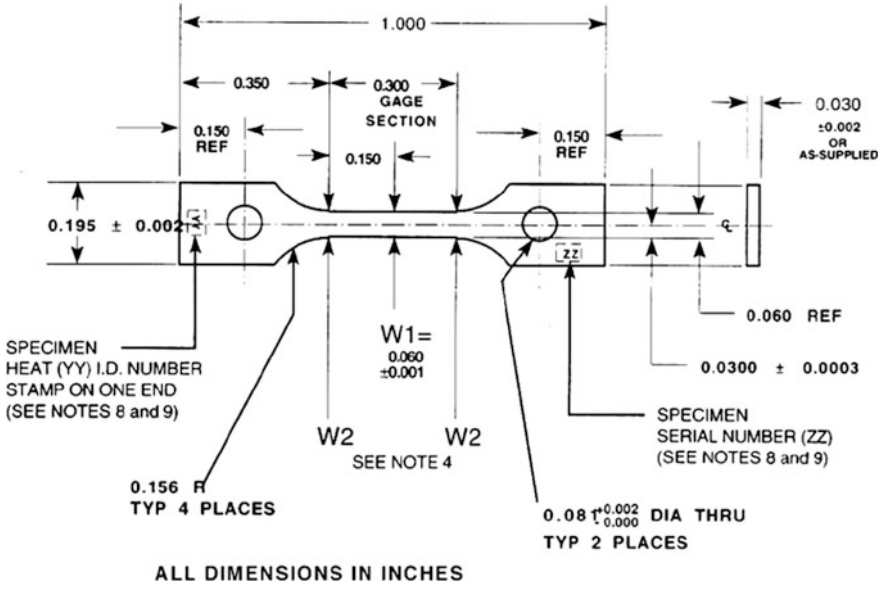

Fig. 3 Tensile sample used in this study. Note that all dimensions are in inch

strain rate of 5×10^{-5} 1/s was used at the beginning of the test. The strain rate was later increased to about 1×10^{-4} 1/s and kept at this rate until failure. For the unaged test, the X-ray energy used was 123 keV and the incident beam size was 0.25×0.25 mm^2. For the aged test, the X-ray energy and beam size were 71.68 keV and 0.5×0.5 mm^2, respectively. In the X-ray beam, the sample was translated along its loading axis for a range of 7 mm with a step-size between 0.5 and 1 mm during the test. WAXS data were collected continuously from the sub-volume illuminated by the incident beam within the sample gauge section (Fig. 4). A four-panel WAXS area detector was used in both tests. The sample-to-detector distance was 2630 and 1760 mm, respectively, for the unaged and aged tests, and was calibrated with CeO_2 and LaB_6 powder samples.

The coarse grain structure of the CASS alloys was a major challenge for the WAXS measurement. To obtain powder-like diffraction patterns, the sample was rotated ±30° about the incident beam with an angular step-size of 1° during the test. As the sample was rotated and deformed, a series of diffraction images were containing 120–200 exposures were recorded. The diffraction images at a given strain are integrated over ±15° azimuthal angle in the directions parallel and orthogonal to the loading axis to obtain diffraction spectra for those directions. Figure 5 shows a 2D diffraction pattern at ~ 40% engineering strain, and a series of spectra along the loading axis at different applied strain levels. Diffraction peaks on each spectrum were fit with pseudo-Voigt functions to obtain lattice d-spacings for different {hkl} planes.

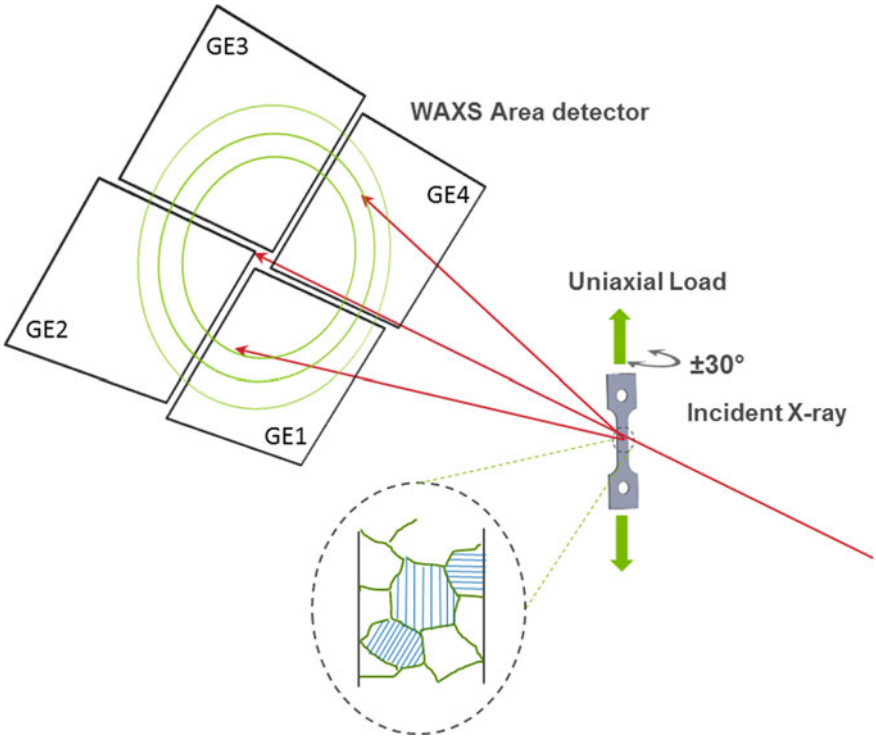

Fig. 4 Schematic for in situ tensile test with WAXS measurement at beamline 1-ID-E of the Advanced Photon Source. GE1-4 are four panels of GE amorphous Si area detectors

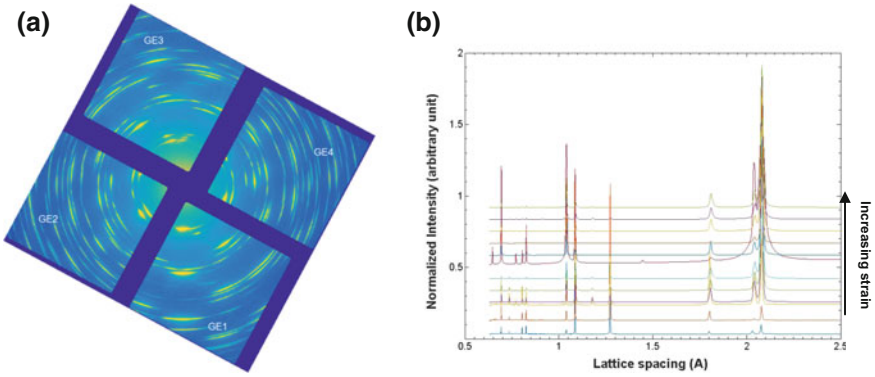

Fig. 5 **a** A 2D diffraction pattern obtained at ~40% strain, and **b** a series of 1D diffraction profiles from GE1 panel integrated over ±15° azimuthal angle about the loading axis at different deformation levels

Results and Discussion

J-R Curve Tests

Before testing the CT samples, we performed tensile tests on the unaged and aged specimens to determine their flow stresses at 315 °C. This information is needed for the J-R curve analysis. The tensile tests were conducted in air with a strain rate of 1×10^{-3} s^{-1}. The results are shown in Fig. 6 and Table 2. Both yield stress (YS) and ultimate tensile strength (UTS) are higher for the aged than unaged samples. The flow stresses are 286 and 333 MPa, respectively, for the unaged and age samples. While the work-hardening rate remains high after thermal aging, the uniform elongation is much shorter for the aged sample. It is clear that the applied thermal aging treatment increases the strength and reduces the ductility of CF8.

Figure 7 shows the J-R curve results of the unaged and aged specimens. As recommended by Mills [3] for ductile materials exhibiting high strain-hardening rates, a blunting line of 4X the flow stress was used for each J-R curve test. Data points obtained between the 0.15- and 1.5-mm exclusion lines were fitted to a power-law relationship for each test, and the results are shown in Table 3. Note that, the $J_{0.2\text{-mm}}$ values estimated from the J-R curves cannot be validated for J_{1c} per ASTM standard, and should not be considered as size-independent material properties. This is because the sample used in this study is too small to maintain the necessary constraint at the crack front required for in-plane crack extension.

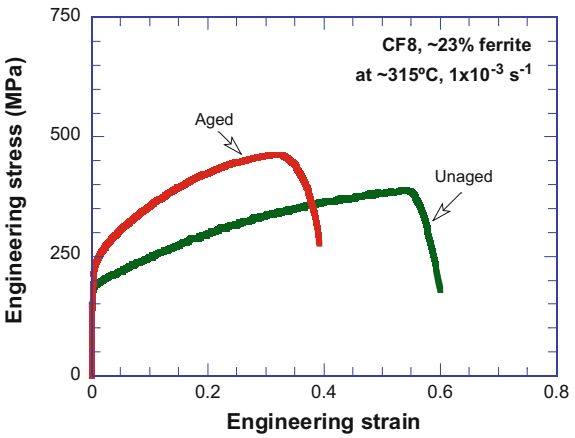

Fig. 6 Tensile tests of unaged and aged CF8 with 23% ferrite at ~315 °C

Table 2 Tensile tests on CF8 specimens at 315 °C

Aging condition	Yield stress (MPa)	Ultimate tensile strength (MPa)	Uniform elongation
Unaged	183	389	0.54
10,000 h at 400 °C	204	462	0.32

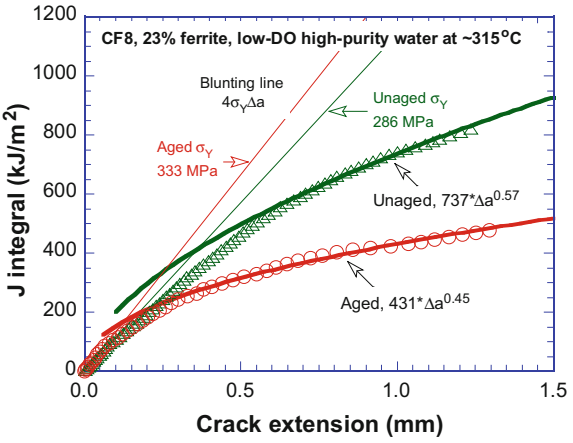

Fig. 7 J-R curves for the unaged and aged specimens tested at ~315 °C

Table 3 J-R curve tests on unaged and aged specimens at 315 °C

Aging condition	C	n	$J_{0.2\text{-mm}}$ (kJ/m^2)	$J^{a}_{2.5\text{-mm}}$ (kJ/m^2)
Unaged	737	0.57	623	1600
10,000 h at 400 °C	431	0.45	291	710

[a]Estimated value at the 2.5-mm offset line

Nonetheless, the J-R curves obtained from similar samples can be compared and used for assessing their relative resistance to crack extension. As shown in Fig. 7, the J integral (i.e., strain energy release rate) required for a certain crack extension is much less for the aged than unaged samples. Both the power-law pre-factor (C) and exponent (n) decrease after thermal aging, indicating a declined resistance to crack growth in the aged sample.

Microstructural Characterization

The microstructure of the unaged and aged CF8 is examined with the TEM to reveal its microstructural changes resulting from thermal aging. In the unaged sample, both austenite and ferrite show very low dislocation densities and are mostly free of second-phase precipitates. Some carbide particles are observed at the austenite/ferrite boundaries but the overall population is low. Thermal aging at 400 °C does not affect the austenite, and its microstructure remains unchanged after 10,000 h (as shown in Fig. 8). For the ferrite however, a high-density of precipitates are observed after thermal aging as shown in Fig. 9. With the diffraction patterns of aged ferrite, the precipitates are identified as G-phase, a nickel-silicide with face centered cubic (fcc) crystal structure and a lattice constant of 4X that of ferrite [19]. The average size of the G-phase precipitates is about ~3 nm, and the

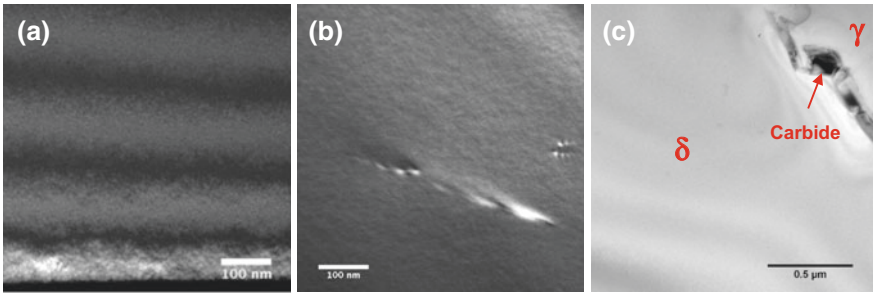

Fig. 8 Austenite microstructure of CF8, dark-field images **a** before and **b** after thermal aging, and **c** carbides at austenite/ferrite boundary (before aging)

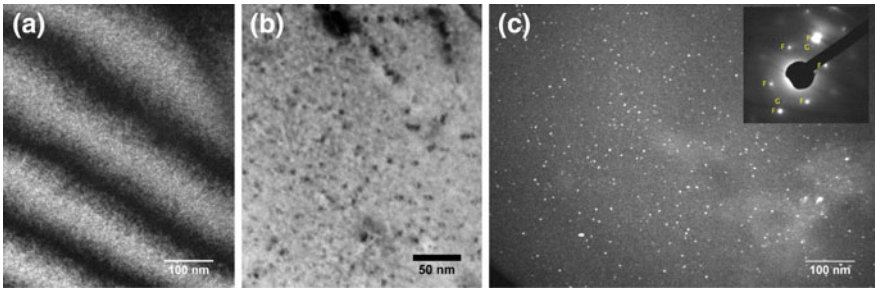

Fig. 9 Ferrite microstructure of CF8, **a** before aging, featureless background with thickness fringes, after aging **b** bright-field, and **c** dark-field imaged with G-phase reflection

density is on the order of 10^{22} m^{-3}. In another TEM study by Chen et al. [20], the distribution of G-phase precipitates is found to be dependent on the distance from the phase boundaries and the presence of carbides nearby. The reported density in CF8 varies from 10^{22} to 10^{23} m^{-3}.

The presence of G-phase precipitates in the aged ferrite is also confirmed with APT. As shown in Fig. 10, Ni-Si rich clusters are visible in both unaged and aged samples, suggesting a non-uniform distribution of Ni and Si even under the unaged condition. The clusters defined by the concentration iso-surface of 7 at% Ni + Si are obviously much larger after thermal aging, and the size distribution of the clusters are also changed by thermal aging. It is possible that the small Ni-Si rich clusters observed by APT in the unaged sample have not developed into a well-defined G-phase crystal structure. Therefore, their strain contrast is too weak to be imaged with diffraction techniques using TEM. This is consistent with a detailed study on stainless steel welds by Matsukawa et al. [21]. They found that a critical composition and size are required for Ni-Si–Mn solute-enriched clusters to develop into G-phase precipitates.

In addition to G-phase precipitates, the APT analysis was also used to investigate the phase separation of Fe-rich α and Cr-rich α' in CF8. Chromium concentration

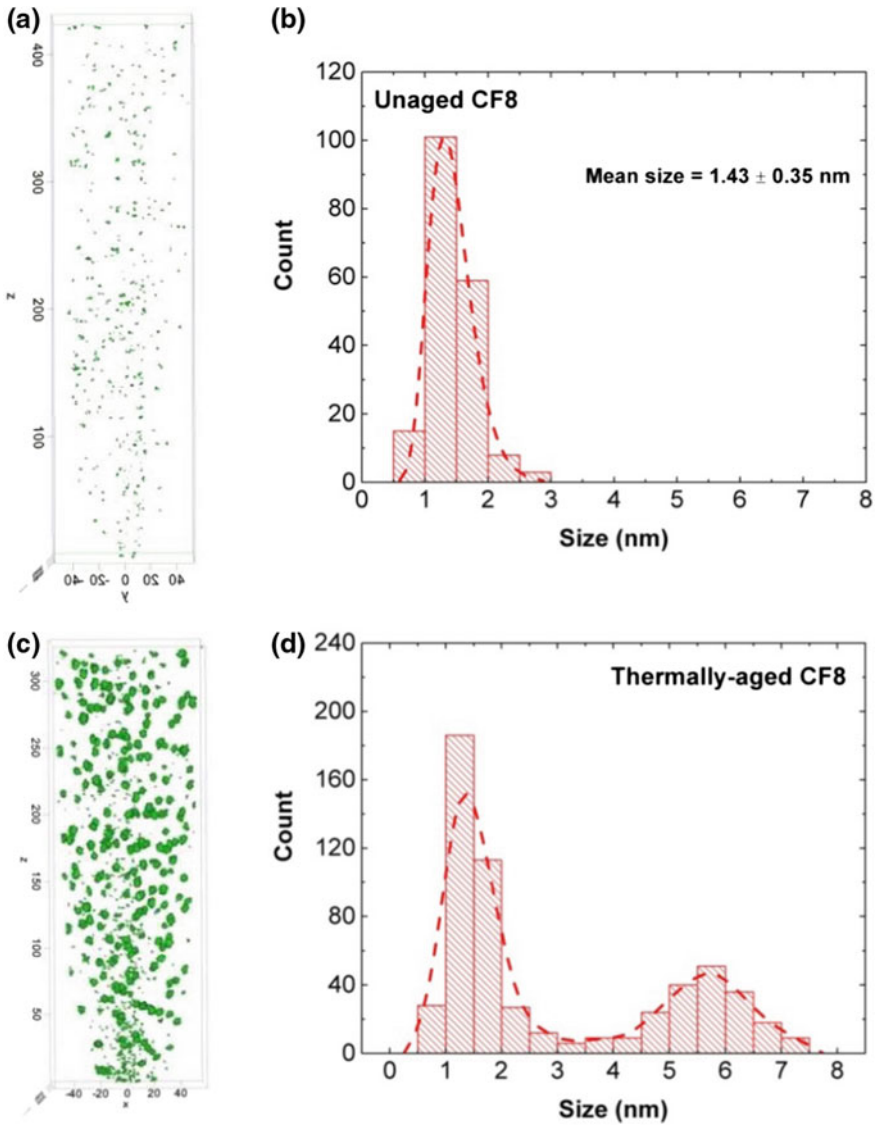

Fig. 10 Atom probe tomography results of NiSi clusters in ferrite, **a** and **c** are the concentration iso-surfaces of 7at% NiSi for the unaged and aged specimens, **b** and **d** are their corresponding size distributions

distributions in the unaged and aged ferrite were measured, and analyzed with the Langer, Bar-on, Miller (LBM) model [22]. With the LBM model, the obtained Cr concentration distribution was fitted with two Gaussian functions centered about μ1 and μ2, for the α and α' phases, respectively. Figure 11 shows the results of LBM analysis on the unaged and aged CF8. The shift of μ2 value from below 29% in the

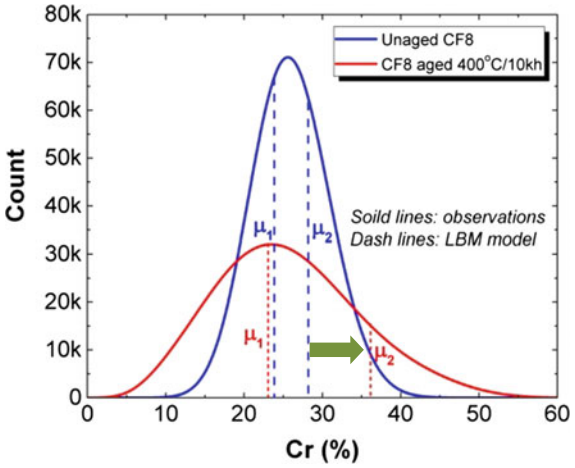

Fig. 11 Cr concentration distributions in the unaged and aged ferrite

unaged sample to above 36% in the aged sample is a clear indication of α/α' spinodal decomposition. It is evident that both G-phase precipitation and spinodal decomposition occurred in ferrite during thermal aging at 400 °C for 10,000 h. The resulting microstructure is a mixture of nm-size precipitates and spinodal decomposition of α/α'. Since the microstructural changes (G-phase precipitate and α/α' decomposition) are only observed within ferrite, the hardening and embrittlement induced by thermal aging are expected to affect merely ferrite.

In Situ Tensile Tests

Two tensile tests were performed at room temperature on unaged and aged CF8 specimens with in situ WAXS measurements. The lattice strains along the loading axis were analyzed and the results are plotted against engineering strain in Fig. 12. Because of the samples' coarse casting structure, diffraction patterns are quite "spotty" (i.e., incomplete Debye rings) in these tests. For this reason, some data points are missing in the WAXS results, particularly at the early stage of deformation. Several overlaps between austenite and ferrite peaks also make some {hkl}s unusable, and they are not included in the figure. The large data scatter shown in Fig. 12 is mostly due to the coarse casting structure and load variation during sample rotation. In addition, since the sample gauge was scanned continuously along its loading axis, the sub-volume illuminated by X-ray constantly changed during the test. This scanning motion also contributes to the fluctuations of lattice strains shown in the figure.

The WAXS results show all lattice strains along the loading direction increase during the in situ tests. The different {hkl}s respond differently to the applied strain. The initial increases in lattice strains are quite rapid, corresponding to the elastic

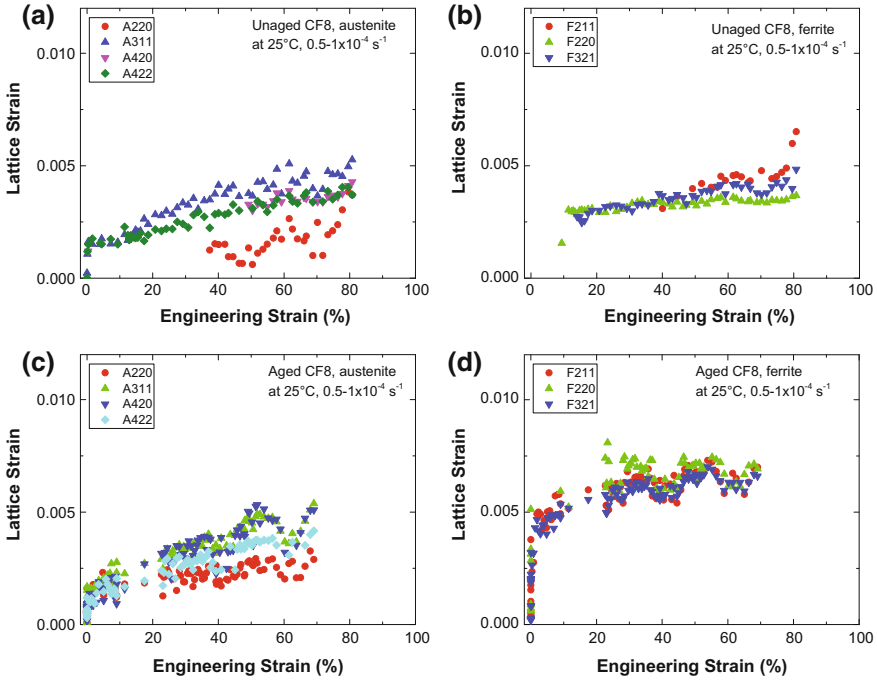

Fig. 12 Lattice strains of different {hkl} planes in **a** unaged austenite, **b** unaged ferrite, **c** aged austenite, and **d** aged ferrite

portion of the macroscopic tensile curve. After the sample yields, the lattice strains continue to increase with much shallower increasing rates, corresponding to the work hardening stage of plastic deformation. While the transitions from the elastic to plastic deformation occur at different lattice strains for different {hkl}s, a general trend can be seen between the austenite and ferrite. The austenite {hkl}s break from linearity (or "yield") at lower lattice strains than that of ferrite, indicating a lower strength of austenite compared to ferrite. The differences between the austenite and ferrite become more evident after thermal aging. The aged ferrite yields at much higher lattice strains compared to its unaged counterpart (Fig. 12b vs. d). The transitions from elastic to plastic deformation occur at similar levels for the unaged and aged austenite (Fig. 12a vs. c).

To understand the stress states of the two phases in CF8, austenite {311} and ferrite {321} are used to represent their "bulk" responses during deformation. Figure 13 shows the evolution of phase-specific lattice strains during the tests. For the austenite, the lattice strain of {311} is nearly identical before and after thermal aging. For the ferrite however, the lattice strain of {321} is increased by $\sim$0.002 after thermal aging. If we assume the elastic modulus of ferrite is about 210 GPa,

the increased stress in the aged ferrite phase of the sample is 420 MPa. With an overall volume fraction of ~23%, the hardening of ferrite should produce an increase of ~97 MPa on the flow stress of the aged sample. This estimate agrees very well with that observed from the tensile curves as shown in Fig. 13c. This result is also consistent with the microstructural observation, suggesting that thermal aging-induced hardening occurs only in the ferrite and the austenite is unaffected.

The observed hardening in ferrite should be attributed to both G-phase precipitates and α/α' phase separation. With a dispersed barrier hardening mode, the contribution of G-phase precipitates can be estimated by:

$$\Delta\sigma = M\alpha\mu b(Nd)^{1/2},$$

where M is the Tayler factor (taken as 3), α is the barrier strength, μ is the shear modulus, b is the unit of the Burgers vector, N is the number density, and d is the average size of the particles. For the aged sample, the mean size and average density of G-phase precipitates visible under TEM are 3.1 nm and $1.9\text{x}10^{22}$ m^{-3}, respectively. By assuming a barrier strength of 0.5 and shear modulus of 82 GPa,

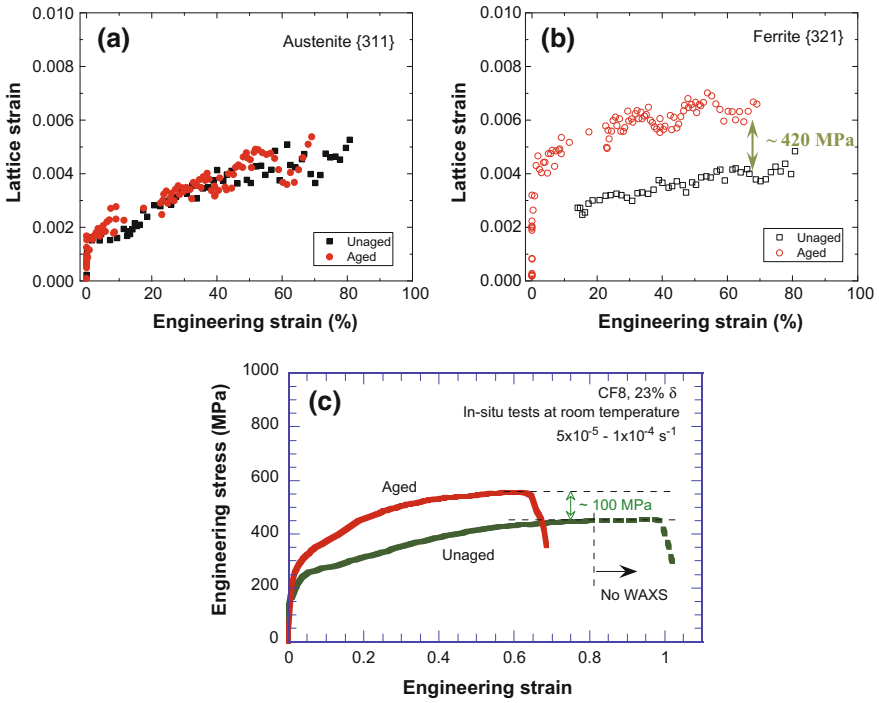

Fig. 13 Comparisons of phase-specific lattice strains closely resemble the "bulk" stress conditions in **a** austenite, and **b** ferrite, and the in situ tensile curves

the increase in yield stress by G-phase precipitates is about ~235 MPa. If the contributions of G-phase and α/α' separation to hardening are linearly additive, the magnitude of strengthening resulting from α/α' should be about 185 MPa. More information about the amplitude of phase compositions and wave length is needed to further assess the hardening effect of α/α' phase separation.

With a hardened ferrite phase, the load partitions between the two phases must be different between the unaged and aged samples. Figure 14 shows the ratio of lattice strains between ferrite {321} and austenite {311} as a function of plastic strain. Again, the stress conditions on these two planes are used to represent the bulk responses of their corresponding phases. At the beginning of the test, the load is rapidly shifted from austenite to ferrite, and the stress in the aged ferrite can be significantly higher than that of austenite. With the increase of plastic strain, the ratio gradually reduces in both unaged and aged samples. Nonetheless, the ratio is always higher in the aged than unaged samples, and the difference between them remains constant until the end of the tests. This suggests that incompatible strains developed between the austenite and ferrite are always higher in the aged than unaged samples. Consequently, higher internal stresses between the two phases are expected in the aged sample, leading to stress concentration at the phase boundaries. This embrittlement mechanism seems consistent with previous results on Charpy impact specimens where cleavage of ferrite or fracture of phase boundaries was often observed among room temperature tests [4]. In the aged sample, the higher incompatible strain between austenite and ferrite provides stress concentrations at phase boundaries, which may help in reaching the critical cleavage stress of ferrite locally, leading to premature fracture or embrittlement.

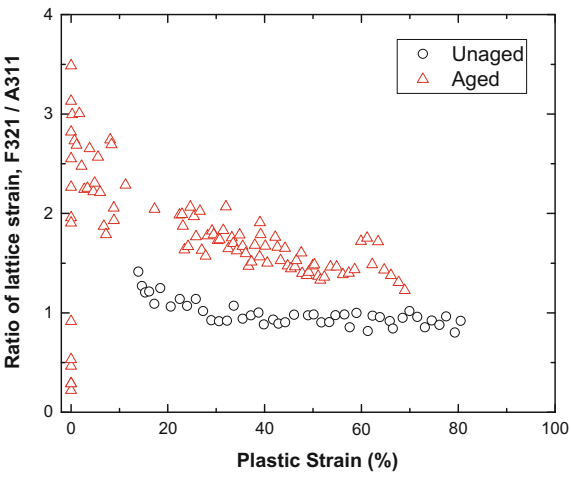

Fig. 14 Ratio of lattice strains between ferrite {321} and austenite {311}

Conclusions

Fracture toughness J-R curve tests were performed on unaged and aged CF8 specimens with 23% ferrite. Significant embrittlement can be observed after thermal aging at 400 °C for 10,000 h. The microstructures of the unaged and aged samples were examined with TEM and APT. While the austenite phase remained unchanged after thermal aging, G-phase precipitates and α/α' phase separation were observed in ferrite. In situ tensile tests were performed at room temperature with WAXS measurements to provide the information on phase-specific lattice strains. Much higher lattice strains were observed in ferrite for the aged sample, and the observed hardening in the aged ferrite can account for the overall increase in flow stress in the tensile tests. This confirms that thermal aging can only harden the ferrite, and the austenite is not affected. The in situ tensile tests also showed that the differences in lattice strains between ferrite and austenite were much higher in the aged than unaged samples, suggesting a higher degree of incompatible strain between ferrite and austenite. The high incompatible strain provides stress concentration at phase boundaries, and may be responsible for the thermal-aging embrittlement of CASS alloys at room temperature.

Acknowledgements This work is sponsored by the U.S. Nuclear Regulatory Commission, under Job Code V6380, and by the U.S. Department of Energy, under contract # DE-AC02-06CH11357. The work at the IVEM and CAES was supported by the U.S. Department of Energy, Office of Nuclear Energy under DOE Idaho Operations Office Contract DE-AC07-051D14517. This research used resources of the Advanced Photon Source, a U.S. Department of Energy (DOE) Office of Science User Facility operated for the DOE Office of Science by Argonne National Laboratory under Contract No. DE-AC02-06CH11357.

References

1. U.S. NRC, Expert Panel Report on Proactive Materials Degradation Assessment, NUREG/CR-6923 (2006)
2. M. Blair, T.L. Stevens, Corrosion-resistant high alloy steels, in Steel Castings Handbook, 6th Edition, Steel Founders' Society of America and ASM International, (1995)
3. W.J. Mills, Int. Mater. Rev. **4**(2), 45 (1997)
4. O.K. Chopra, A. Sather, Initial assessment of the mechanisms and significance of low-temperature embrittlement of cast stainless steels in LWR systems, NUREG/CR-5385, ANL-89/17 (1990)
5. G.L. Leone, H.W. Kerr, Weld. J. **61**, 13s (1982)
6. J.W. Elmer, S.M. Allen, T.W. Eagar, Mater. Trans. A, 20A (1989) 2117
7. J.C. Borland, Br. Weld. J. **7**(8), 508 (1960)
8. F.H. Beck, E.A. Schoefer, J.W. Flowers, M.G. Fontana, New Cast High-Strength Alloy Grades by Structure Control, in *Advances in the Technology of Stainless Steels and Related Alloys*, ASTM STP 369, 1965
9. F.H. Beck, J. Juppenlatz, P.F. Wieser, Effects of Ferrite and Sensitization on Intergranular and Stress Corrosion Behavior of Cast Stainless Steels, in *Stress Corrosion—New Approaches*, ed. by H.L. Craig, Jr. ASTM STP 610, 1976

10. N.R. Hughes, W. L. Clarke, D. E. Delwiche, Intergranular stress-corrosion cracking resistance of austenitic stainless steel castings, in *Stainless Steel Castings*, eds. V.G. Behal, A.S. Melilli, ASTM STP 756, 1982
11. H.D. Solomon, T.M. Devine Jr., Duplex stainless steels—a tale of two phases, in *Duplex Stainless Steels*, ed. by R.A. Lula (Metals Park, ASM, 1983), pp. 693–756
12. T.J. Nichol, A. Datta, G. Aggen, Metall. Mater. Trans. A, **11**(4), 573–585 (1980)
13. H.M. Chung, T. R. Leax, Mater. Sci. Technol. **6**, 249 (1990)
14. W.F. Michaud, P.T. Toben, W.K. Soppet, O.K. Chopra, Tensile-property Characterization of Thermally aged Cast Stainless Steels, NUREG/CR-6142, ANL-93/35, 1994
15. O.K. Chopra, Long-term embrittlement of Cast Duplex Stainless Steels in LWR Systems, NUREG/CR-4744, **6**(1), ANL-91/22, 1991
16. X. Zhang, C. Xu, L. Wang, Y. Chen, M. Li, J.D. Almer, E. Benda, P. Kenesei, A. Mashayekhi, J. S. Park, F. J. Westferro, Rev. Sci. Instrum. **88**(1), 015111 (2017)
17. L. Wang, M. Li, J. Almer, Acta. Mater. **62**, 239–249 (2014)
18. X. Zhang, M. Li, J.S. Park, P. Kenesei, J. Almer, C. Xu, J.F. Stubbins, Acta. Mater. **126**, 67–76 (2017)
19. J.M. Vitek, Metall. Trans. A **18,** 154 (1987)
20. W-Y. Chen, M. Li, X. Zhang, M.A. Kirk, P.M. Baldo, T. Lian, J. Nucl. Mater. **464,** 185 (2015)
21. Y. Matsukawa, T. Takeuchi, Y. Kakubo, T. Suzudo, H. Watanabe, H. Abe, T. Toyama, Y. Nagai, Acta. Mater. **116**, 104–113 (2016)
22. J.S. Langer, M. Bar-on, H.D. Miller, Phys. Rev. A **11**, 1417 (1975)

Microstructural Evolution of Cast Austenitic Stainless Steels Under Accelerated Thermal Aging

Timothy G. Lach and Thak Sang Byun

Abstract Thermal aging degradation of cast austenitic stainless steels (CASS) was studied by electron microscopy to understand the mechanisms for thermal embrittlement potentially experienced during extended operations of light water reactor coolant systems. Four CASS alloys—CF3, CF3M, CF8, and CF8M—were thermally aged up 1500 h at 330 and 400 °C, and the microstructural evolution of the material was characterized by analytical aberration-corrected scanning transmission electron microscopy. The primary microstructural and compositional changes during thermal aging were spinodal decomposition of the δ-ferrite into α/α′, precipitation of G-phase in the δ-ferrite, segregation of solute to the austenite/ferrite interphase boundary, and growth of $M_{23}C_6$ carbides on the austenite/ferrite interphase boundary. These changes were shown to be highly dependent on aging temperature and chemical composition, particularly the amount of C and Mo. A comprehensive model is being developed to correlate the microstructural evolution with mechanical behavior and simulation.

Keywords Thermal aging degradation · Duplex stainless steel · Spinodal decomposition · Solute segregation · G-phase precipitation

Introduction

Cast austenitic stainless steels (CASS), with a duplex austenite (γ)–ferrite (δ) phase structure, are often used in structural applications due to their high corrosion resistance combined with relatively high strength, ductility, and toughness [1–4]. Thus, they are widely used for various large components within light water reactor (LWR) primary coolant systems, such as piping and pump casings [5–7]. These components are used in persistently extreme and damaging environments including

T.G. Lach (✉) · T.S. Byun
Nuclear Sciences Division, Energy and Environment Directorate,
Pacific Northwest National Laboratory, 902 Battelle Blvd., Richland, WA 99352, USA
e-mail: timothy.lach@pnnl.gov

J.H. Jackson et al. (eds.), *Proceedings of the 18th International Conference on Environmental Degradation of Materials in Nuclear Power Systems – Water Reactors*, The Minerals, Metals & Materials Series, DOI 10.1007/978-3-319-68454-3_49

high temperature and high pressure coolant water and low dose radiation for extended periods of time. The principal susceptibility of these materials under these conditions is thermal aging degradation and embrittlement. For LWR applications, the degree and mechanisms of thermal aging degradation must be understood to make conclusive predictions about the lifetime of LWRs and these components during service conditions [8]. Thus, advanced characterization along with mechanical properties testing has been carried out on these materials before and after being subjected to accelerated thermal aging [9, 10].

Previous researches have determined the primary mechanism for the microstructural evolution of duplex stainless steels under thermal aging to be spinodal decomposition of the non-equilibrium δ-ferrite phase that was formed during the casting process [11–15]. Spinodal decomposition is the spontaneous separation of the δ-ferrite into two phases—Fe-rich α-ferrite and Cr-rich α′-martensite—with feature sizes on the order of nanometers. This makes the original ferrite grains much harder leading to embrittlement of the whole material. Other microstructural changes may also exist such as the precipitation of G-phase particles in the ferrite matrix and carbides at the austenite/ferrite interphase interface.

In this ongoing study, accelerated thermal aging to 1500 h of four common CASS alloys (CF3, CF3M, CF8, and CF8M) has been completed; these alloys are the cast equivalents of 304L, 316L, 304, and 316 wrought stainless steels, respectively. The primary differences among these alloys are the C concentration, as denoted by the number—3 means under 300 wt ppm and 8 means under 800 wt ppm—and the Mo concentration—M means addition of Mo up to 2.5 wt%. This study takes a comprehensive look at the thermal aging degradation mechanisms using aberration-corrected scanning/transmission electron microscopy (STEM), energy dispersive spectroscopy (EDS), and atom probe tomography (APT) to determine the dependence of these mechanisms on microstructure, chemical composition, aging temperature, and in future studies, aging time. Together with mechanical and fracture behavior analysis and computer simulation, the goal is to make predictive models for thermal aging degradation in duplex stainless steels.

Methods

Materials and Thermal Aging

In this long-term study in conjunction with mechanical behavior evaluations [16], four sets of CASS alloys are being evaluated for thermal aging degradation mechanisms. The compositions are presented in Table 1 as determined by Dirats Laboratories using inductively coupled plasma—mass spectroscopy (ICP-MS). The compositions of all four alloys are within the ASTM specifications for these grades. The ferrite contents of each alloy, which are relatively low, were determined by SEM and optical microscopy imaging of several large areas of material.

Table 1 Composition of four cast alloys (noted with their wrought equivalents)—ferrite in vol.%, most elements in wt%, and C, S, O, N in wt ppm

Grade	Ferrite	Fe	Cr	Ni	Mn	Mo	Si	Cu	Co	Ti	Al	V	Nb	W	B	P	Se	C	S	O	N
CF3 (304L)	9.2 ± 3.2	Bal	19.17	8.11	1.44	0.34	0.99	0.41	0.18		0.01	0.07	0.01	0.04	0.001	0.029	0.01	262	324	204	1020
CF3M (316L)	11.9 ± 5.1	Bal	19.28	9.81	1.14	2.30	1.22	0.28	0.15	0.01		0.05		0.02	0.001	0.033	0.01	284	253	224	838
CF8 (304)	5.5 ± 1.3	Bal	18.72	8.91	1.10	0.29	1.27	0.29	0.15			0.05		0.03	0.001	0.026		665	376	161	606
CF8M (316)	7.9 ± 2.5	Bal	18.52	10.38	0.65	2.33	1.02	0.33	0.17	0.01		0.06		0.04	0.001	0.031	0.04	433	243	207	1020

The alloys have been aged at four different temperatures in four large muffle furnaces (MTI Co. Model KSL-1200X-L). The chamber temperatures are controlled by UDIAN programmable controllers at an accuracy of $< \pm 1$ °C using K-type thermocouples; spatial variation within chamber is ±5 °C. Aging temperatures were set at 290, 330, 360, and 400 °C. At this point in the long-term study, sets of material have been retrieved from the furnaces after 1500 h of aging. In this current part of the study, characterization was carried out on the as-cast, 330 °C, and 400 °C conditions.

Microstructural and Elemental Characterization

Aberration-corrected TEM and STEM were the primary means of studying the changes the materials underwent when subjected to thermal aging using a probe aberration-corrected JEOL ARM200F TEM/STEM. Bright field (BF) and high angle annular dark field (HAADF) micrographs were obtained in STEM mode in conjunction with EDS for chemical analysis. BF and DF TEM micrographs, along with selected area electron diffraction (SAED) patterns, imaged the microstructural changes and diffraction contrast among different phases.

Cross-sectional areas were obtained using a dual beam focused ion beam/scanning electron microscope (FIB/SEM) (FEI Helios NanoLab 660 or FEI Quanta) and conventional TEM lift-out methods to a thickness of about 500 nm at operating voltage of 30 kV on gold half-grids [17]. Further thinning was performed by a custom fabricated assembly to electrochemically polish the samples with 5% perchloric acid at −50 °C and 11 V. This was done to minimize gallium-ion damage that may appear similar to microstructural changes during thermal aging when observed in TEM/STEM.

APT was performed on a Cameca LEAP 4000X using voltage mode with a pulse fraction of 20% at 250 kHz at a temperature of 40 K. APT tips were sharpened using the FIB/SEM annular milling technique on 6 × 6 Si microtip arrays [18]. Ga-ion damage is minimized using low kV final sharpening.

Results and Discussion

Thermal aging results show that after 1500 h of aging there appear to be four primary microstructural feature changes: spinodal decomposition, G-phase precipitation, segregation of solute, and precipitation of carbides. The first two take place within the ferrite phase while the latter two take place at the ferrite/austenite interphase boundary. There is a large dependence of these feature changes on chemical composition and aging temperature, as they are all diffusional processes.

Spinodal decomposition of the ferrite phase into Fe-rich α and Cr-rich α' is a well-known characteristic of the microstructural evolution of ferrite during thermal

aging. However, the degree to which these microstructural changes are affected by aging conditions (time and temperature) and chemical composition are not as well understood. Figure 1 shows STEM-BF images of all four alloys after 1500 h of aging at either 330 °C or 400 °C in regions that are several hundreds of nanometers from any interface or grain boundary. The same features were also observed in STEM-HAADF, but the contrast is better in the STEM-BF images. Spinodal decomposition and/or G-phase precipitation is observed in all the alloys at a temperature of 400 °C; however it is not noticeable within STEM-HAADF or BF imaging in the as-cast condition or aging at 330 °C. It is also clear, though to a lesser extent, that there is a difference between the low Mo steels and the Mo-bearing steels at 400 °C; the features are much more pronounced in their contrast, and the feature size is slightly larger in the Mo-bearing steels—about 3 nm in size compared to 2 nm in size. Neither spinodal decomposition nor G-phase precipitation was observed in the as-cast materials or in the materials aged at 330 °C for 1500 h using STEM-HAADF/BF imaging.

Through STEM-HAADF/BF imaging and EDS mapping, it is difficult to distinguish spinodal decomposition and G-phase decomposition; thus other characterization methods are being utilized to determine their extent. Preliminary data from atom probe tomography (APT) of the ferrite in a CF8M aged for 1500 h at 400 °C shows that the feature size of both is approximately the same and both are finely dispersed, see Fig. 2. The APT data clearly show decomposition of Fe and Cr into two separate regions, while Ni, Si, Cu, and P cluster together, and Mo tends to segregate to the Cr-rich regions and the Ni/Si-rich clusters. The Ni/Si-rich clusters are the G-phase while the Fe and Cr-rich regions are α and α′, respectively. Other researchers have shown that there is a small degree of spinodal decomposition even

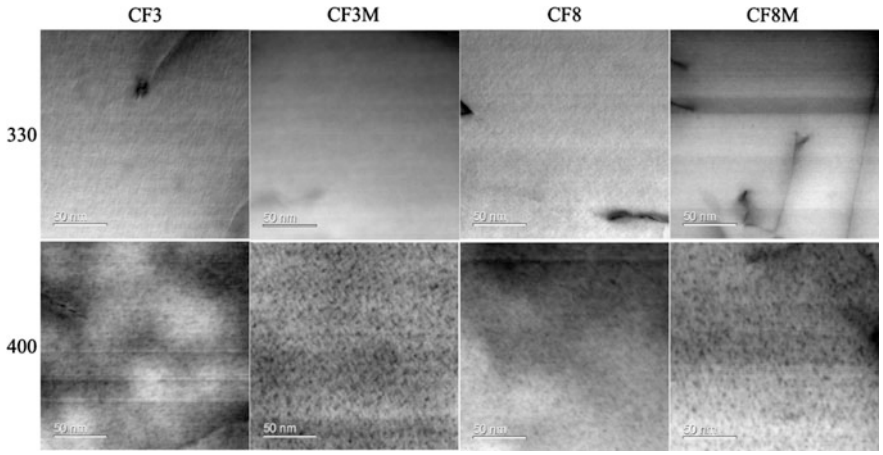

Fig. 1 STEM-BF images of spinodal decomposition after 1500 h of aging at 330 and 400 °C in CF3, CF3M, CF8, and CF8M alloys

in the as-cast condition, though it is small in both feature size and in amplitude of concentration—much smaller than in the 400 °C aged sample in Fig. 2.

While decomposition and G-phase precipitation take place internally in the ferrite phase, there are also important microstructural and elemental changes occurring on the austenite-ferrite interphase boundary, particularly in the higher C and higher Mo steels. The lower Mo, lower C CF3 steel has the least change in this way with little segregation observed at the phase boundary based on STEM-EDS mapping seen in Fig. 3. In CF3, as is the case in the other steels as well, Fe and Ni are preferentially in austenite, while Cr and Si are preferentially in the ferrite, with a minor amount of enrichment of Cr and depletion of Fe at the interphase boundary.

The higher C, lower Mo alloy CF8 is similar to the CF3 alloy in regions where the interphase interface is clean, but in many places, carbides have formed at the interphase interface; see Fig. 4. These carbides are observed in a limited extent in the as-cast condition but are much more prevalent in the aged materials, both at 330

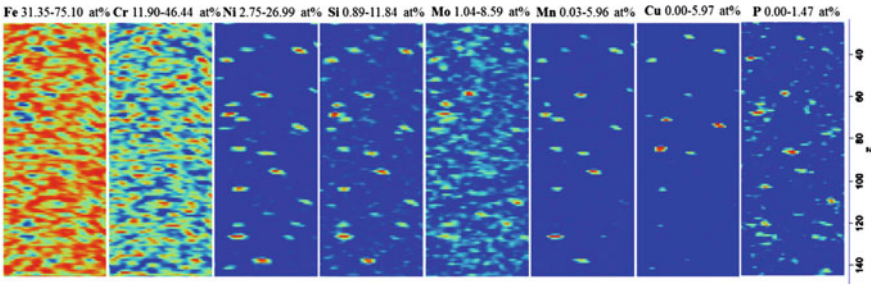

Fig. 2 APT concentration maps with 1 nm^3 voxels for ferrite in a CF8M steel aged for 1500 h at 400 °C. Area is 50 nm × 120 nm and sampled 1 nm in depth. Blue represents lower concentration and red represents higher concentration of each element. Concentration range is noted above each one

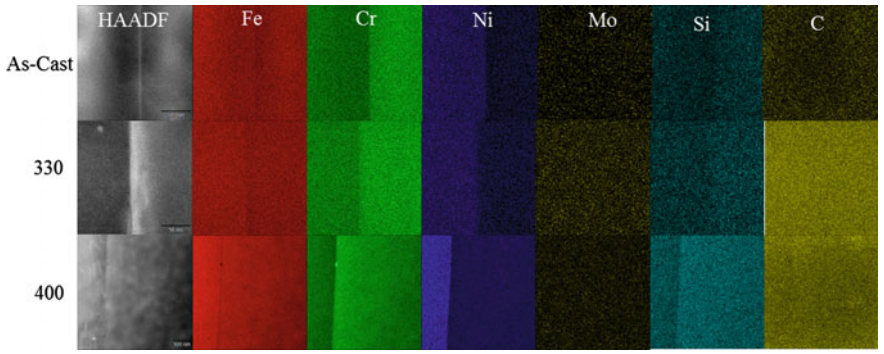

Fig. 3 STEM-EDS mapping of segregation at phase boundary in CF3 alloy in the As-Cast condition and after aging for 1500 h at 330 and 400 °C

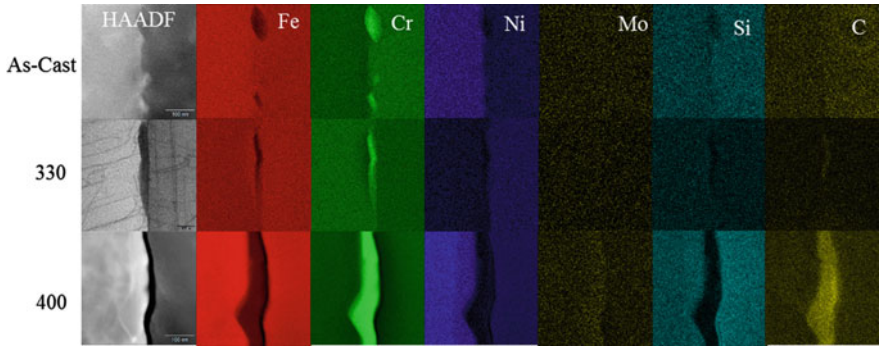

Fig. 4 STEM-EDS mapping of segregation and carbide growth at phase boundary in CF8 alloy in the As-Cast condition and after aging for 1500 h at 330 and 400 °C

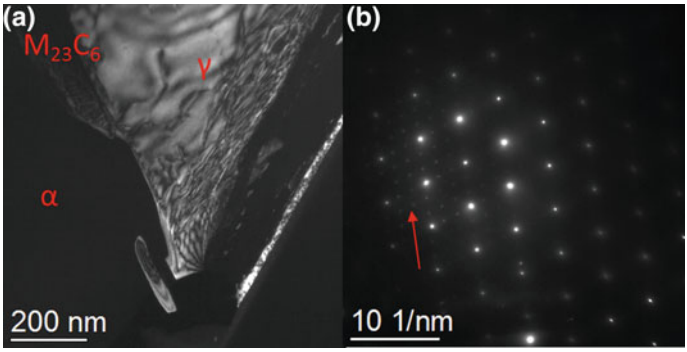

Fig. 5 **a** TEM DF image using (011)γ reflection and **b** SAED at (011)γ zone axis of a carbide at the interphase interface in a CF8 alloy aged at 330 °C for 1500 h. Faint reflections, indicated by red arrow, that are 1/3 the d-spacing of the strong γ reflections are from the $M_{23}C_6$

and 400 °C. They tend to be rich in Cr and slightly enriched in Mo with depletion in Fe, Ni, and Si. Based on the as-cast condition where C is not enriched in the clusters shown, it appears that at least in some cases the Cr segregates into clusters along the interphase boundary before absorbing C during aging to form a carbide. In the DF TEM image and SAED pattern of a CF8 alloy aged at 330 °C for 1500 h in Fig. 5, it is seen that the Cr-rich carbides, which have the $M_{23}C_6$ structure, form cube-on-cube on the austenite side of the boundary and grow into the ferrite, where the Cr-content is higher in ferrite and the diffusivity of Cr is higher in the ferrite and in the phase boundary [11]. Further evidence pointing to the carbides growing into the ferrite phase is shown in the STEM-EDS line scans across the Cr-rich regions (carbides in the aged samples) in Fig. 6, where there is a depletion of Cr near the carbide in the ferrite but not so in the austenite. This depletion region is approximately 50 nm from the carbide/ferrite interface, consistent with research on aging

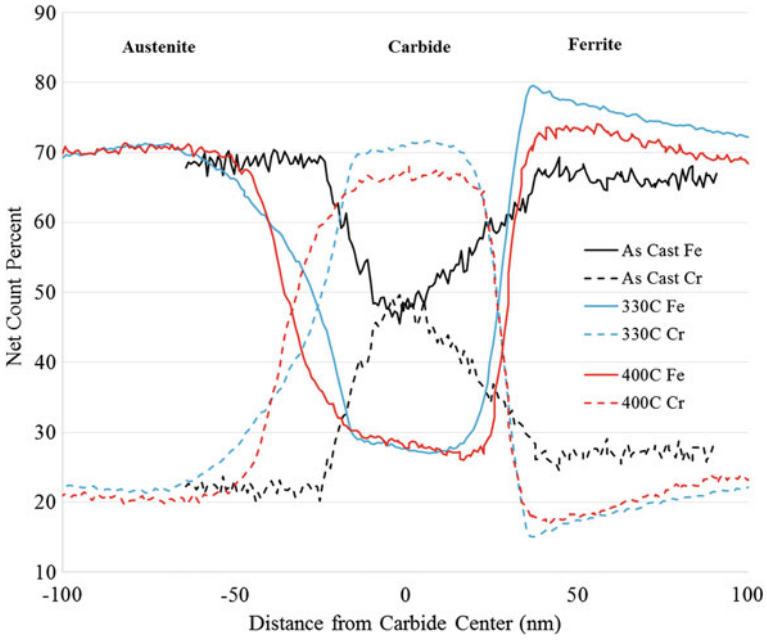

Fig. 6 STEM-EDS line scan of carbide at phase boundary in CF8 alloy in the As-Cast condition (black) and after aging for 1500 h at 330 °C (blue) and 400 °C (red)

of CF8 steels, though taking place at a much shorter aging time than the 4300 h reported elsewhere [11]; as the carbide consumes local solute from the ferrite due to the higher diffusivity in the ferrite. Possibly a dynamic equilibrium is reached at a distance of 50 nm from the interface when near stoichiometry of the $M_{23}C_6$ carbide is reached; thus the reason for the same depletion distance at 1500 and 4300 h [11]. Concentration profiles in longer-term aged samples in subsequent studies may help prove this.

The lack of C in the CF3 and CF3 M steels explains why there are no observable carbides in that material, but it does not account for no observed carbides in the CF8 M alloys after 330 °C or 400 °C aging for 1500 h. Another mechanism, influenced by the larger concentration of Mo, must be at play, where Mo atoms interact and segregate at the phase boundary with other solute elements, in particular Si [19]. Indeed, as evidenced by STEM-EDS maps in Fig. 7, Mo and Cr both segregate to the interphase boundary, even in the as-cast condition. After thermal aging, Si and to a smaller extent C also segregate to the interphase boundary. It is unknown at this time why the degree of segregation is much greater in the 330 °C sample than in the 400 °C sample. It is clear, though, that the interaction of Mo, Si, Cr, and C at the boundary changes reduces the tendency to form any carbide phases at the boundary. This segregation is also seen in the CF3M alloy but to a lesser extent than in the CF8M alloy possibly due to the lack of C at the interface prompting less segregation of Mo and Si to the interface.

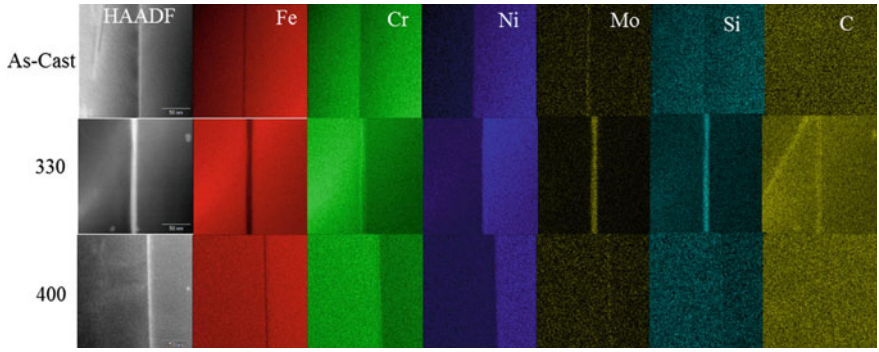

Fig. 7 STEM-EDS mapping of segregation at phase boundary in CF8M alloy in the As-Cast condition and after aging for 1500 h at 330 and 400 °C

Conclusion

This study presents characterization results by TEM/STEM, EDS, and APT of the microstructural evolution of four CASS alloys aged for 1500 h at 330 and 400 °C. These alloys were primarily distinguished by their C and Mo concentration, ranging from low C/low Mo to high C/high Mo. There were four primary changes in the microstructure as a result of thermal aging, the extent of which strongly depended on composition and aging temperature: spinodal decomposition of ferrite, G-phase precipitation, carbide formation on the interphase interface, and segregation of solute to the interphase interface.

It is clearly evident that both C and Mo content play a domineering role in the thermal aging behavior of these CASS alloys, particularly in their interaction with Cr. All four alloys experience spinodal decomposition or G-phase precipitation, but it is the high Mo alloys, CF3M and CF8M, that undergo this to the greatest extent, as Mo has a preferential interaction with Cr relative to Fe. Also, it is the high C and high Mo alloys that experience higher segregation to the interphase interface boundary as Mo segregates to the interphase boundary bringing with it Cr and Si. In the low Mo/high C CF8 alloy, Cr-rich $M_{23}C_6$ carbides form on the austenite side of the boundary and grow into the ferrite, resulting in a depletion of Cr on the ferrite side of the carbide. These microstructural changes and processes have a large dependence on composition and aging temperature.

Acknowledgements This research was sponsored by U.S. Department of Energy/Office of Nuclear Energy through Light Water Reactor Sustainability R&D Program and International Nuclear Energy Research Initiative (I-NERI) Program. Pacific Northwest National Laboratory is operated by Battelle Memorial Institute for the U.S. Department of Energy under Contract No. DEAC05-76RL01830. APT and FIB/SEM were performed at PNNL's Environmental Molecular Sciences Laboratory, a Department of Energy—Office of Biological & Environmental Research national scientific user facility.

References

1. O.K. Chopra, Effects of Thermal Aging and Neutron Irradiation on Crack Growth Rate and Fracture Toughness of Cast Stainless Steels and Austenitic Stainless Steel Welds (NUREG/CR-7185, 2014)
2. J.D. Tucker, M.K. Miller, G.A. Young, Assessment of thermal embrittlement in duplex stainless steels 2003 and 2205 for nuclear power applications. Acta Mater. **87**, 15 (2015)
3. Y.H. Yao, J.F. Wei, Z.P. Wang, Effect of long-term thermal aging on the mechanical properties of cast duplex stainless steels. Mater. Sci. Eng., A **551**, 116 (2012)
4. R.P. Kolli et al., Characterization of element partitioning at the austenite/ferrite interface of as cast CF-3 and CF-8 duplex stainless steels. Microsc. Microanal. **21**, 365 (2015)
5. J.T. Busby, P.G. Oberson, C.E. Carpenter, M. Srinivasan, Expanded materials degradation assessment (EMDA)-Vol. 2: aging of core internals and piping systems, NUREG/CR-7153, Vol. 2, ORNL/TM-2013/532, Oct 2014
6. R. Dyle, Materials degradation matrix and issue management tables overview-LTO update (The 2nd Workshop on U.S. Nuclear Power Plant Life Extension, Washington, D.C, 2011)
7. O.K. Chopra, A. Sather, Initial assessment of the mechanisms and significance of low-T embrittlement of cast stainless steels in LWR systems. NUREG/CR–5385 (1990)
8. T.S. Byun, J.T. Busby, Cast Stainless Steel Aging Research Plan. ORNL/LTR-2012/440
9. T.S. Byun, Y. Yang, N.R. Overman, J.T. Busby, Thermal aging phenomena in cast duplex stainless steels. J. Met. **68**, 507 (2016)
10. T.S. Byun, N.R. Overman, T.G. Lach, Mechanical properties of model cast austenitic stainless steels after thermal aging for 1500 h. LWRS Report, PNNL-25377, Apr 2016
11. S. Mburu et al., Effect of aging temperature on phase decomposition and mechanical properties in cast duplex stainless steels. Mater. Sci. Eng., A **690**, 365 (2017)
12. C. Pareige et al., Kinetics of G-phase precipitation and spinodal decomposition in very long aged ferrite of a Mo-free duplex stainless steel. J. Nucl. Mater. **465**, 383 (2015)
13. W. Liu et al., Phase-field simulation of the separation kinetics of a nanoscale phase in a Fe-Cr alloy. J. Mater. Eng. Perform. **25**, 1924 (2016)
14. N. Pettersson et al., Nanostructure evolution and mechanical property changes during aging of a super duplex stainless steel at 300C. Mater. Sci. Eng., A **647**, 241 (2015)
15. J. Zhou et al., Concurrent phase separation and clustering in the ferrite phase during low temperature stress aging of duplex stainless steel weldments. Acta Mater. **60**, 5818 (2012)
16. T.S. Byun, T.G. Lach, Y. Yang, C. Jang, Influence of δ-ferrite content on thermal aging induced mechanical property degradation in cast stainless steels, in *Proceedings of the 18th International Conference on Environmental Degradation of Materials in Nuclear Power Systems—Water Reactors* (2017) Submitted
17. B. Myers, TEM sample preparation with the FIB/SEM. NUANCE Center. Northwestern University (2009)
18. A. Devaraj, et al., Three-dimensional nanoscale characterization of materials by atom probe tomography. Int Mater Rev 1 (2017)
19. N. Shigenaka, T. Hashimoto, M. Fuse, Effects of alloying elements (Mo, Si) in an austenitic stainless steel on dislocation loop nucleation under ion irradiation. J. Nucl. Mater. **207**, 46 (1993)

Electrochemical Characteristics of Delta Ferrite in Thermally Aged Austenitic Stainless Steel Weld

Gokul Obulan Subramanian, Sunghoon Hong, Ho Jung Lee, Byeong Seo Kong, Kyoung-Soo Lee, Thak Sang Byun and Changheui Jang

Abstract An austenitic stainless steel Type 316L weld was thermally aged for 20,000 h at 400 °C and electrochemical characterization was performed to measure corrosion resistance in δ–ferrite phase. It is well known that a severe thermal aging causes decrease of fracture resistance and increase of the hardness of δ–ferrite, which was related to the spinodal decomposition. After thermal aging, the DL-EPR response of 316L weld was dominated by parent austenite matrix without reactivation peak. To characterize the δ–ferrite only, austenite phase was selectively dissolved from the matrix by electrochemical etching method. The double–loop electrochemical potentiokinetic reactivation (DL-EPR) analysis of the δ–ferrite phase showed degradation in corrosion resistance after thermal aging with the appearance of a cathodic loop and reactivation peak during the reverse scan. The degradation in corrosion resistance of δ–ferrite phase could be attributed to the localized Cr-depletion due to spinodal decomposition and precipitation of intermetallic phases during thermal aging.

G.O. Subramanian · S. Hong · H.J. Lee · B.S. Kong · C. Jang (✉)
Department of Nuclear and Quantum Engineering, KAIST,
Daejeon, Republic of Korea
e-mail: chjang@kaist.ac.kr

G.O. Subramanian
e-mail: gokul@kaist.ac.kr

S. Hong
e-mail: acehongsam@kaist.ac.kr

H.J. Lee
e-mail: leehojung@kaist.ac.kr

B.S. Kong
e-mail: assaultpc@kaist.ac.kr

K.-S. Lee
Central Research Institute, KHNP, Daejeon, Republic of Korea
e-mail: leekys1003@khnp.co.kr

T.S. Byun
Pacific Northwest National Laboratory, Richland, WA, USA
e-mail: thaksang.byun@pnnl.gov

J.H. Jackson et al. (eds.), *Proceedings of the 18th International Conference on Environmental Degradation of Materials in Nuclear Power Systems – Water Reactors*, The Minerals, Metals & Materials Series, https://doi.org/10.1007/978-3-319-68454-3_50

Keywords DL-EPR analysis · Stainless steel weld · Thermal aging · Corrosion · Delta ferrite

Introduction

Austenitic stainless steels welds (ASSWs) are extensively used in light water reactor (LWR) as joints in primary recirculation piping, pressurizer surge line, and in–core components for its excellent mechanical properties, corrosion resistance and weldability [1]. In typical ASSWs, 5–20% residual δ–ferrite is present to avoid hot cracking in the weld fusion zone during welding. However, these ASSWs show thermal embrittlement problems after being aged for long operation periods. Extensive analysis by various researchers have reported the appearance of Cr–rich α' phase, Ni– and Si–rich G–phase and $M_{23}C_6$ carbides in the δ–ferrite region and ferrite/austenite phase boundary due to thermal aging [2–5]. The evolution of several embrittling phases in δ–ferrite has been known to increase the strength and hardness, while reducing the ductility and fracture toughness of ASSWs.

The spinodal decomposition is primarily attributed to the thermal embrittlement degradation along with the precipitation of other secondary phases [3, 4]. Also the corrosion resistance decreases after thermal aging, which was attributed to the formation of Cr–depleted regions due to spinodal decomposition and precipitation of other phases [1]. The electrochemical response from δ–ferrite alone would be directly associated with the localized Cr–depletion and the corresponding mechanical behaviour changes after thermal aging. However, much of the electrochemical responses had been from the parent austenite matrix, since the δ–ferrite phase content was around 10 wt.% only. In this regard, the purpose of this study is to isolate the δ–ferrite phase from the austenite matrix and to investigate the electrochemical behaviour of the δ–ferrite phase before and after thermal aging. The degree of decrease in corrosion resistance after thermal aging are then discussed with the observed localized Cr-depletion.

Materials and Experimental

A test block of 316L ASSW was fabricated by building–up layers of weld deposits on 316L plates using gas tungsten arc welding (GTAW) method. The δ–ferrite content in the finished weld deposit was found to be around 11% by FERITSCOPE® FMP30. The chemical composition of the 316L ASSW was determined by inductively coupled plasma–atomic emission spectroscopy (ICP–AES) analysis and the result is shown in Table 1. Then the fabricated welds were cut into small pieces and subjected to the accelerated thermal aging at 400 °C for 20,000 h in air environment.

Table 1 Chemical composition of as–welded 316L ASSW in wt.%

Fe	Cr	Ni	C	Si	Mn	Mo
Bal.	18.4	11.0	0.008	0.4	1.74	2.56

Specimens with 3 mm by 2 mm were prepared from both as–welded and thermally aged weld blocks. Then the specimens were spot welded with electrode wires and cold–mounted with epoxy resin in such a way to expose the area along the transverse-longitudinal (TL) direction. Then the specimens were polished down to #4000 emery grit paper and cleaned ultrasonically. To selectively dissolve the austenite phase for obtaining δ–ferrite phase, an anodic dissolution technique [6] was applied. For the selective austenite etching, a three electrode setup was used with a standard calomel reference electrode and graphite rod counter electrode in a solution of non–deaerated 3.6 N H_2SO_4 + 0.1 N NH_4SCN solution. The specimens were maintained at −120 mV_{SCE} for 300 s, taken out, washed in ethanol and dried.

The ASSW specimens after the selective austenite dissolution were analysed by X–ray diffraction (XRD, Rigaku D/MAX–2500) and scanning electron microscope (SEM, Magellan400). Further, electrochemical analysis was performed for the as–welded and thermally aged specimens before and after the selective austenite etching. The open spaces left behind from the dissolved parent austenite phase were filled by an epoxy resin, therefore exposing only δ–ferrite phase for the electrochemical analysis. Again, another three electrode system was employed for the electrochemical analysis with the double–loop electrochemical potentiokinetic reactivation (DL–EPR) technique, with standard calomel reference electrode and graphite rod counter electrode in a solution of non–deaerated 1 M H_2SO_4 + 0.1 M KSCN solution with the masked δ–ferrite containing specimen as the working electrode. Before the analysis, the specimen was held potentiostatically at −500 mV_{SCE} for 60 s to remove any surface oxide films. Then the specimen was scanned anodically from the open circuit potential to +300 mV_{SCE} and reversed back to open circuit potential at a scan rate of 1.67 mV/s.

Results and Discussion

Electrochemical Analysis of 316L ASSW

From the TEM analysis of 316L ASSW after thermally aged at 400 °C for 20,000 h (Fig. 1), spinodal decomposition showing fluctuation of Cr content was observed in the δ–ferrite phase. A fluctuation of Cr content and simultaneously varying Fe and Ni content was observed from HR–TEM/EDS analysis. The extent of the Cr content fluctuation was roughly around 5–12 nm in width. Meanwhile, $M_{23}C_6$ carbide precipitation was not observed after thermal aging, that could be attributed to the lower C content in the 316L ASSW used in the study.

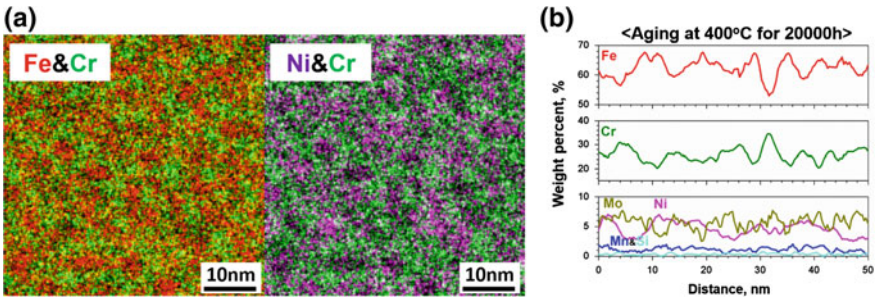

Fig. 1 HR-TEM/EDS analysis showing **a** elemental mapping and **b** line scan of δ-ferrite in 316L ASSW aged at 400 °C for 20,000 h

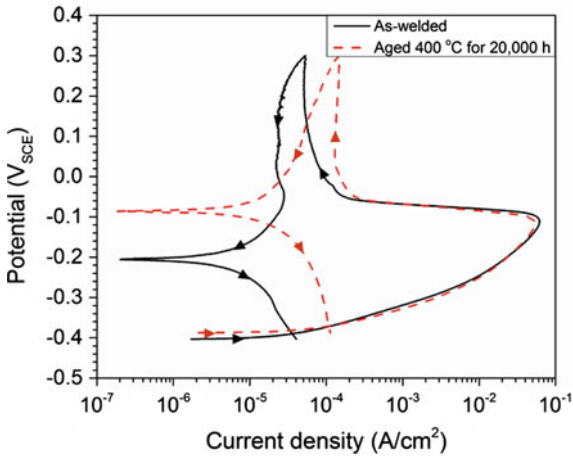

Fig. 2 DL–EPR analysis of the as–welded and aged (at 400 °C for 20,000 h) 316L ASSW before selective austenite dissolution process

The electrochemical analysis results by DL–EPR technique for the as–welded and thermally aged 316L ASSW are shown in Fig. 2. It can be observed from Fig. 2 that the activation peak current density was similar for both conditions. However, there was an increased passive current density observed for aged specimens, indicating a degradation in the passive film. Although no reactivation peak was observed during the reverse scan, the cathodic current density of aged specimen was higher. It indicates that additional reduction of passive film also occurs during the cathodic polarization, indicating the passive film formed was somewhat unstable. However, no quantitative drop in corrosion resistance for the aged specimens can be derived from the analysis due to the absence of reactivation peak current density.

Since the electrochemical analysis was done on the specimens comprising both austenite and δ–ferrite phases, much of the electrochemical response was that from the austenite phase, resulting in only a fraction of change in the corrosion resistance. Meanwhile, in a similar study [1], the reactivation peak current density was

clearly observed. It should be noted that the width of δ–ferrite in that study was quite large, around 8 μm, which is much larger than the 1 μm wide δ–ferrite existing in our case, enabled to receive strong electrochemical response from a continuous δ–ferrite region. Nonetheless, it is essential to have the electrochemical response from the δ–ferrite phase only to associate it with the extent of Cr content fluctuation in δ–ferrite region.

Selective Austenite Etching

Duplex stainless steels exhibit different anodic polarization peaks upon anodic polarization [6, 8]. Generally, the individual austenite phase show noble corrosion potentials in which the ferrite phase corrodes at lower potential. Thus the combined behaviour of individual phases is observed during the anodic polarization of duplex stainless steels. This behaviour is attributed to the difference in corrosion resistance due to dissimilar contents of alloying elements in them. Therefore, at sufficiently higher anodic potentials, it facilitates a preferential dissolution of austenite phase at which the less noble ferrite phase exists in the passivation regime. In this study, an anodic potential of −120 mV_{SCE} in potentiostatic mode was optimized for dissolving austenite phase without attacking the δ–ferrite phase. On potentiostatically dissolving the austenite phase for longer duration, it was observed that the δ–ferrite tend to get detached from the matrix surface into the solution, therefore the duration was limited to 300 s to minimize the loss of δ–ferrite phase.

Figure 3 shows the results of the glancing angle XRD analysis for 316L ASSW before and after selective austenite etching. The diffraction peaks were predominantly those from δ–ferrite after selective austenite etching, confirming the effective removal of austenite matrix. The SEM image of the δ–ferrite microstructure after selective austenite etching is shown in Fig. 4a. The δ–ferrites were continuously distributed showing a honeycomb structure. To eliminate the electrolyte penetration through the vacant pores, the vacant area was masked by cold–setting epoxy resin with doctor blade technique and dried, showing only δ–ferrite phase for the electrochemical analysis as shown in Fig. 4b. After the masking process, the δ–ferrite matrix was not as continuous as before as a fraction of δ–ferrite matrix was detached or covered during the masking process.

Electrochemical Analysis of δ–Ferrite Phase

The results of electrochemical analysis by DL–EPR technique of δ–ferrite phase after masking the vacant region is shown in Fig. 5. The abscissa axis indicating the current was not normalized since the surface area exposed after selective austenite etching was not accurately known for now, though would be quiet similar for both specimens. However, quantitative values of corrosion resistance could be extracted

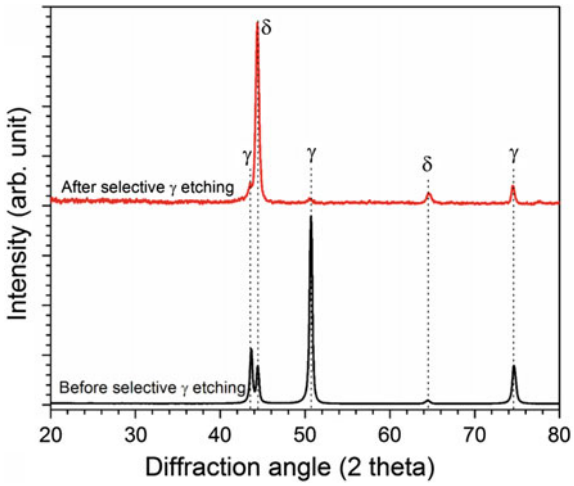

Fig. 3 XRD result of the as–welded 316L ASSW before and after selective austenite etching at −120 mV_{SCE} for 300 s

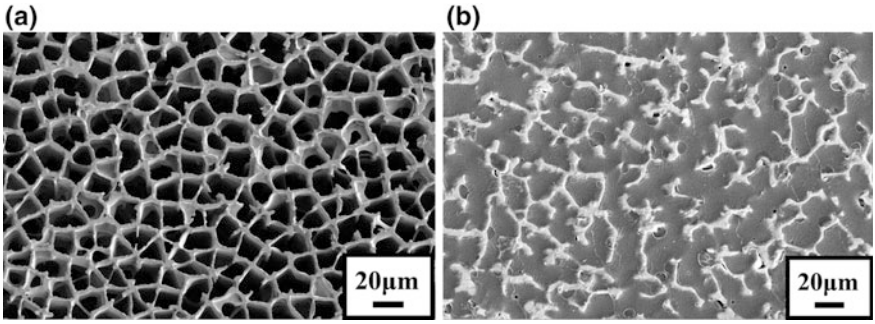

Fig. 4 SEM analysis of the as–welded 316L ASSW **a** after selective austenite etching at −120 mV_{SCE} for 300 s and **b** followed by dried cold–setting epoxy resin

from similar DL–EPR curves provided the reactivation to activation peak current ratio multiplied by 100, known as DL–EPR value [1].

It can be observed from Fig. 5 that the aged specimen showed higher anodic corrosion peak current and passivation current than the as–welded specimens, assuming similar exposed area of δ–ferrite. No reactivation peak current was observed for the as–welded specimen which showed a hydrogen reduction reaction present in the cathodic polarization similar to Fig. 2. Meanwhile, a cathodic loop (denoted by C) was observed for the aged specimen representing dissolution of passive film by reduction [9], without any hydrogren reduction behaviour. This was followed by an anodic reactivation peak (denoted by A) at lower potentials,

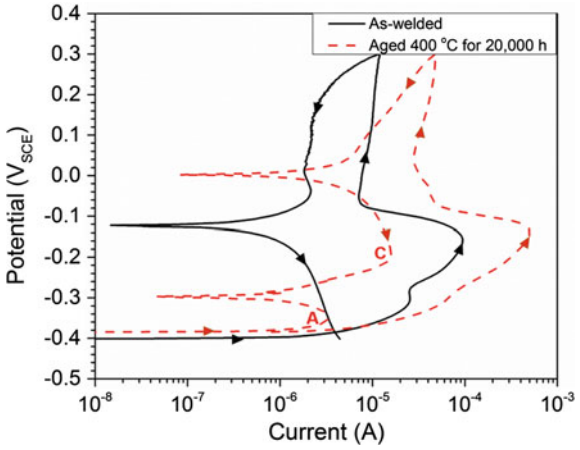

Fig. 5 DL–EPR analysis of the as–welded and aged (at 400 °C for 20,000 h) 316L ASSW after selective austenite etching and subsequent masking

indicating anodic dissolution at the δ–ferrite phase in aged specimen. Thus, the passive film formed in the aged specimen reduced upon cathodic polarization, indicating deterioration in the corrosion resistance compared to the as–welded specimen. The degradation in corrosion resistance cannot be solely associated with the localized Cr depletion in δ–ferrite alone. On the other hand, the intermetallic phases such as G–phase that tend to precipitate in δ–ferrite during thermal aging would also have significant influence on the corrosion resistance, which should be studied in detail.

Thus, this electrochemical investigation can evaluate the corrosion performance of δ–ferrite phase after thermal aging, given continuously attached matrix of δ–ferrite in the austenitic material. However, in materials containing lower quantity of δ–ferrite without continuous attachment, it would be recommended to evaluate by micro–electrochemical techniques [10, 11], requiring sophisticated equipment with a microcapillary tip of 1–1000 μm diameter.

The effect of thermal aging on the corrosion performance during in–service condition was not studied extensively as compared to the mechanical behaviour. The Cr–segregation in δ–ferrite after thermal aging would also affect the corrosion performance in pressurized water reactor (PWR) operating conditions as degradation in passive film is observed in this study. Also, further deterioration in corrosion resistance could be expected in off–normal PWR primary water chemistry with the presence of dissolved oxygen, aggressive chloride and sulphate anions.

The heat affected zone (HAZ) of 316L weld material had previously exhibited stress corrosion cracking (SCC) susceptibility in PWR environment [12]. Similar to Cr–segregation during thermal aging, the sensitization along the grain boundaries during thermal treatment of austenitic stainless steels is known to compromise the corrosion resistance, further leading to SCC development along the grain boundaries. Though SCC is not a concern in ferritic phase, it still influences the SCC crack growth behaviour in austenitic stainless steels [13, 14]. For instance, it was reported that δ–ferrite retards SCC crack growth because of its high Cr content and

higher corrosion resistance [15]. Thus, the Cr–segregation after thermal aging would affect the local corrosion behaviour at the SCC crack tip in δ–ferrite phase therefore influencing SCC growth in the ASSWs, should be further evaluated.

Summary

The DL–EPR analysis of the aged specimen did not exhibit any reactivation current density peak. To study the separate electrochemical response of δ–ferrite, the austenite phase was selectively etched to isolate δ–ferrite dendrites in the matrix. The DL–EPR analysis of the masked δ–ferrite phase after selective austenite etching indicated degradation in corrosion resistance with the cathodic reduction of passive film and anodic dissolution of δ–ferrite. Further study needs to be conducted to identify the extent of corrosion resistance degradation by spinodal decomposition and G–phase precipitation.

Acknowledgements This study is mainly supported by the Korea Hydro and Nuclear Power Co., Ltd. as the Proactive Material Aging Management Project. Part of the funding is provided as Nuclear R&D Program (2015M2A8A2074798) of the MSIP/NRF of Rep. of Korea. Financial support for three of the authors is provided by the BK-Plus Program of the MSIP of Rep. of Korea.

References

1. K. Chandra, V. Kain, V.S. Raja, R. Tewari, G.K. Dey, Low temperature thermal ageing embrittlement of austenitic stainless steel welds and its electrochemical assessment. Corros. Sci. **54**, 278–290 (2012)
2. D.J. Alexander, K.B. Alexander, M.K. Miller, R.K. Nanstad, Y.A. Davidov, The effect of aging at 343 °C in the microstructure and mechanical properties of type 308 stainless steel weldments" (Report NUREG/CR-6628, Oak Ridge National Laboratory, 2000)
3. O.K. Chopra, Estimation of fracture toughness of cast stainless steels during thermal aging in LWR systems (Report NUREG/CR-4513, Argonne National Laboratory, 1994)
4. O.K. Chopra, W.J. Shack, "Mechanical properties of thermally aged cast stainless steels from Shippingport reactor components" (Report NUREG/CR-6275, Argonne National Laboratory, 1995)
5. S.A. David, J.M. Vitek, D.J. Alexander, Embrittlement of austenitic stainless steel welds. J. Nondestr. Eval. **15**, 129–136 (1996)
6. T.P.S. Gill, J.B. Gnanamoorthy, A method for quantitative analysis of delta–ferrite, sigma and $M_{23}C_6$ carbide phases in heat treated Type 316 stainless steel weldments. J. Mater. Sci. **17**, 1513–1518 (1982)
7. S. Hong, H. Kim, B.S. Kong, C. Jang, I.H. Shin, J.-S. Yang, K.-S. Lee, Evaluation of the thermal ageing of austenitic stainless steel welds with 10% of δ–ferrites, Int. J. Press. Vessels Pip. (2017) (In press)
8. J.-S. Lee, K. Fushimi, T. Nakanishi, Y. Hasegawa, Y.-S. Park, Corrosion behaviour of ferrite and austenite phases on super duplex stainless steel in a modified green–death solution, Corros. Sci. **89**, 111–117 (2014)

9. I. Chattoraj, S.K. Das, S. Jana, S.P. Chakraborty, A.K. Bhattamishra, Passivity breakdown due to discontinuous precipitation during ageing of 21Cr–10Mn–5Ni stainless steel. J. Mater. Sci. **30**, 5313–5320 (1995)
10. H. Böhni, T. Suter, F. Assi, Micro-electrochemical techniques for studies of localized processes on metal surfaces in the nanometer range. Surf. Coat. Technol. **130**, 80–86 (2000)
11. C.J. Park, H.S. Kwon, M.M. Lohrengel, Micro-electrochemical polarization study on 25% Cr duplex stainless steel. Mater. Sci. Eng., A **372**, 180–185 (2004)
12. L. Dong, Q. Peng, E. Han, W. Ke, L. Wang, Stress corrosion cracking in the heat affected zone of a stainless steel 308L-316L weld joint in primary water. Corros. Sci. **107**, 172–181 (2016)
13. D.J. Edwards, L.E. Thomas, K. Asano, S. Ooki, S.M. Bruemmer, Microstructure, microchemistry and stress corrosion crack characteristics in a BWR 316L SS core shroud weld (Paper presented at the 13th International Conference on Environmental Degradation of Materials in Nuclear Power Systems—Water Reactors, 2007)
14. K.N. Krishnan, K.P. Rao, Effect of microstructure on stress corrosion cracking behaviour of austenitic stainless steel weld metals. Mater. Sci. Eng., A **142**, 79–85 (1991)
15. H. Abe, Y. Watanabe, Role of δ-ferrite in stress corrosion cracking retardation near fusion boundary of 316NG welds. J. Nucl. Mater. **424**, 57–61 (2012)

Effect of Long-Term Thermal Aging on SCC Initiation Susceptibility in Low Carbon Austenitic Stainless Steels

So Aoki, Keietsu Kondo, Yoshiyuki Kaji and Masahiro Yamamoto

Abstract The objective of this study was to clarify the effect of long-term thermal aging on SCC initiation susceptibility in low carbon austenitic stainless steels. Specimens used were Type 304L and 316L austenitic stainless steels. Both steels were cold worked to 20% thickness reduction (CW) followed by long-term thermal aging at 288 °C for 14,000 h (LTA). Creviced Bent Beam (CBB) testing was carried out to estimate the SCC initiation susceptibility under BWR simulated water condition at high temperature. The results of the CBB tests showed that Type 304L specimens with CW and LTA treatment exhibited no SCC susceptibility. In contrast, the SCC initiation susceptibility of Type 316L increased by the combination of cold work and long-term thermal aging. To understand these results, evaluations on the changes of microchemistry, microstructure and mechanical properties induced by the CW and LTA treatment have been performed, and their correlation with the SCC initiation susceptibility was discussed.

Keywords Low-carbon austenitic stainless steel · Stress corrosion cracking · Long-term thermal aging · Cold work · Creviced bent beam (CBB) test

Introduction

With the increasing interest in the life time extension of components in light water reactor (LWR) with maintaining the safe and reliable operation, countermeasure to Stress Corrosion Cracking (SCC) on austenitic stainless steels is one of the most important subjects among aging degradations [1]. In recent years, intergranular SCC (IGSCC) incidents have been reported in low carbon austenitic stainless steels used in commercial BWR components operating for more than 10 years, where the neutron irradiation damage was negligibly small [2, 3].

S. Aoki (✉) · K. Kondo · Y. Kaji · M. Yamamoto
Japan Atomic Energy Agency, Nuclear Science and Engineering Center,
2-4 Shirakata, Tokai-Mura, Naka-Gun, Ibaraki 319-1195, Japan
e-mail: aoki.so@jaea.go.jp

J.H. Jackson et al. (eds.), *Proceedings of the 18th International Conference on Environmental Degradation of Materials in Nuclear Power Systems – Water Reactors*, The Minerals, Metals & Materials Series, https://doi.org/10.1007/978-3-319-68454-3_51

Transmission Electron Microscope (TEM) examination on the core shroud sample of low carbon stainless steel extracted from where the IGSCC occurred during the reactor operation did not show Cr depletion in the vicinity of its grain boundaries [2, 4]. Fundamental experimental studies have been also conducted in order to analyze SCC factors. Those researches were carried out by simulating the materials heat history in weld heat-affected zone (HAZ), i.e., the sensitization heat treatment expected to induce the degradation of corrosion resistance in the vicinity of grain boundaries and the cold rolling process in order to achieve relatively high levels of hardness and residual stress [5–7]. And it was reported that the heat treatment above 500 °C for the relatively short term such as several hours would not cause the drastic Cr depletion around grain boundaries of low carbon stainless steel [4]. On the other hand, Tsubota et al. focused on the mechanical properties on SCC susceptibility, and reported that the specified correlative relation was confirmed between Vickers hardness of materials and SCC initiation susceptibility [8]. In spite of extensive studies on SCC in low carbon stainless steels, however, that mechanism has not been fully understood yet. Those issues have led us to the idea that the long-term, such as several years, exposure of materials at the LWR operation temperature, at which the reduction of hardness in the HAZ is suppressed compared to sensitization heat treatment, has a possibility to cause changes in microstructure and microchemistry at the grain boundaries which induce the increase in the SCC susceptibility.

The objective of this study was to clarify the effect of long-term thermal aging on SCC initiation susceptibility in low carbon austenitic stainless steels.

Experimental Procedure

Specimens

Specimens used in this study were low carbon austenitic stainless steels (SSs), Types 304L and 316L. Their chemical compositions are shown in Table 1. Both steels were solution annealed (SA) at 1030 °C for 30 min. After the solution annealing, specimens were cold worked to 20% thickness reduction (20% CW) to simulate the mechanical properties of HAZ of the weld process. Long-term thermal aging (LTA) treatment at 288 °C of BWR operating temperature was conducted for 14,000 h on SA and CW specimens, expressed in LTA and CW + LTA, respectively.

Table 1 Chemical composition of the specimen (mass%)

Steel	C	Si	Mn	P	S	Cr	Ni	Mo	N
304L	0.009	0.58	0.85	0.020	0.001	18.43	9.78	–	0.04
316L	0.008	0.43	0.83	0.023	0.001	17.54	12.55	2.11	0.03

Specimens were fabricated in a form of plate with dimensions of 50 mm long, 10 mm wide and 2 mm thick for the SCC tests. The final surface preparations were mechanical polishing using a 0.06 μm colloidal silica suspension followed by electro-polishing using an electrolyte solution of phosphoric acid, sulfuric acid and methanol. The aim of this preparation was to clearly observe SCC initiation and any deformed microstructure around the cracks after the SCC test.

Creviced Bent Beam (CBB) Test

Creviced Bent Beam (CBB) testing was carried out to estimate the SCC initiation susceptibility under simulated BWR water conditions at 288 °C for 1000 h. The CBB test technique has been developed by Akashi et al., and used for estimating the SCC initiation susceptibility comprehensively in a relatively short time. More information of CBB test can be found in ref [9, 10].

Types 304L and 316L plate specimens with conditions SA, LTA, CW and CW + LTA were CBB-tested. The specimen was set up in the CBB test jig by bolts to give the specimen about 1% strain. Graphite fiber wool was also set as a crevice former between the specimen and the CBB test jig. Dissolved oxygen in the test water was 8 ppm. Electric conductivity of the test water was 0.067 μS/cm in inlet and below 0.2 μS/cm in outlet. After the test, the surface examination was carried out by means of Scanning Electron Microscope (SEM).

Hardness Measurement

Hardness measurements were carried out using a Vickers hardness tester to investigate the effect of LTA treatment on the mechanical strength of the stainless steels. The final surface treatment of specimens for the hardness test was electro-polished. The test force applied was 9.807 N and retention time in each measurement was 15 s.

TEM Observation and EDX Chemical Composition Analysis Around Grain Boundaries

Transmission Electron Microscope (TEM) observation and Energy Dispersive X-ray spectroscopy (EDX) analysis were carried out to investigate the effect of LTA treatment on microstructure and microchemistry. Specimen thickness was thinned down to about 0.2 mm by mechanical polishing. After that, a disk specimen with a diameter of 3 mm was made by a disk punch system, and then the disk specimen was electro-polished with A8 electrolyte using a twin jet system.

Experimental Results

CBB Test

The number of SCC cracks observed on the specimen after the CBB test for 1000 h is shown in Table 2. The results of the CBB tests showed that Type 304L exhibited no SCC susceptibility after any treatment (SA, CW, LTA, and CW + LTA). No SCC crack was observed on Type 316L SA, CW, and LTA, while 20 SCC cracks were observed on Type 316L CW + LTA. The SCC initiation susceptibility of Type 316L SS increased clearly by the combination of the cold work and the long-term thermal aging, however, such synergistic effect was not observed in Type 304L SS.

Hardness Measurement

The Vickers hardness (HV) data of the SS specimens are shown in Fig. 1. The number of SCC cracks is also shown above each bar in Fig. 1. The hardness data of

Table 2 Number of SCC cracks observed on the specimen after the CBB test

	Specimen	CBB results Number of SCC cracks
304L	LTA	0
	CW	0
	LTA + CW	0
316L	LTA	0
	CW	0
	LTA + CW	20

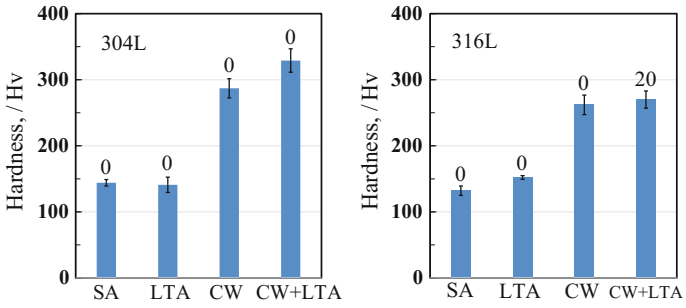

Fig. 1 Vickers hardness of the specimen. [Number of SCC cracks is given above each bar.]

Types 304L SA and 316L SA were 144 Hv and 132 Hv, respectively. The hardness of the steels did not increase by LTA, but significantly increased by CW. The hardness of the CW specimens was almost twice that of the SA specimens (i.e., Type 304L CW: 287 Hv, Type 316L CW: 262 Hv). The hardness of Type 316L CW + LTA, which exhibited the SCC initiation susceptibility in the CBB test, was 270 Hv, which is on the same level as that of Type 316L CW. No significant increase in hardness occurred by the combination of CW and LTA. Therefore, It can be concluded that there is no influence of LTA on the hardness of these stainless steels.

TEM Observation and EDX Chemical Composition Analysis Around Grain Boundaries

TEM observation photograph around a grain boundary in Type 316L LTA is shown in Fig. 2 as a representative microstructure with the long term ageing effect. The result of EDX line analysis of chemical composition across the grain boundary along the line indicated in Fig. 2 is shown in Fig. 3. Neither Cr depletion nor enrichment of other elements was observed in this analysis. Furthermore, no precipitate such as carbides was observed in Type 316L CW + LTA, which exhibited the SCC initiation susceptibility in the CBB test.

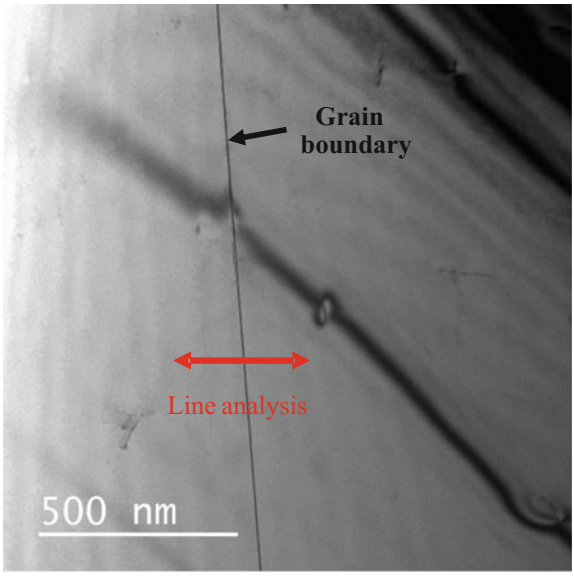

Fig. 2 TEM observation photograph around the grain boundary

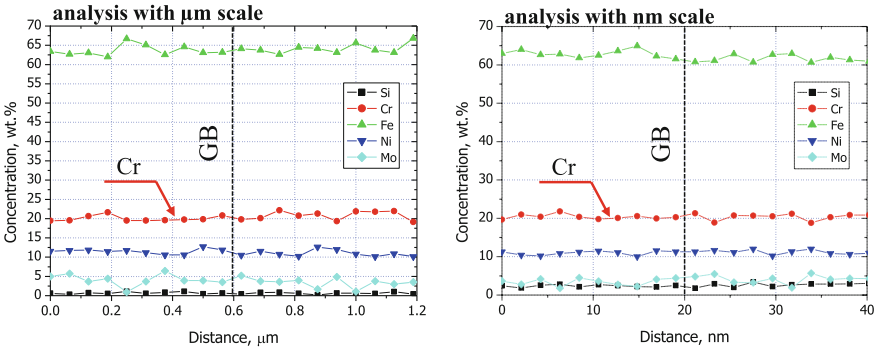

Fig. 3 EDX line analysis of chemical composition across the grain boundary

Surface Examination of CBB-Tested Specimens by Means of SEM

SEM observation photograph of a typical SCC crack in this CBB test (Type 316L CW + LTA) is shown in Fig. 4. The SCC cracking typically initiated and propagated perpendicular to the bending tensile stress of the CBB test. The middle region of the observed SCC crack seemed to be cracked in brittle manner, because no slip trace was observed in neighbor grains. On the other hand, lots of slip plane traces were observed in grains around the crack tip. It is, therefore, speculated that the crack initiated in the middle region of the observed crack, and propagated with plastic deformation in neighboring grains due to the stress concentrations at around the crack tip. It could be also suggested that the crack initiation was induced elastically under the material condition with higher yield stress by the cold work process.

Figure 5 shows the typical surface morphology of CW and CW + LTA specimens after the CBB test observed by means of SEM. As the specimen surface treatment was finished by electro-polishing prior to the CBB test started, surface features such as the slip line pattern resulting from the emergence of moving dislocations could be observed after the CBB test. The character of surface slip traces of Type 304L CW was fine and wavy. This type of plastic deformation could be considered to be homogeneous. A similar surface feature was observed in Type 304L CW + LTA. This observation result suggests that LTA treatment did not cause the change in deformation microstructure of Type 304L. Both grains with fine wavy slip and course planar slip coexisted in the surface of the CBB-tested Type 316L CW. On the other hand, the slip line pattern of Type 316L CW + LTA, which was the only material exhibited the SCC susceptibility in this study, was mainly characterized by coarse and planar. That result could suggest that the deformation microstructure in Type 316L was changed after the LTA treatment. However, the further observation is ongoing to confirm the representativeness of those observation results.

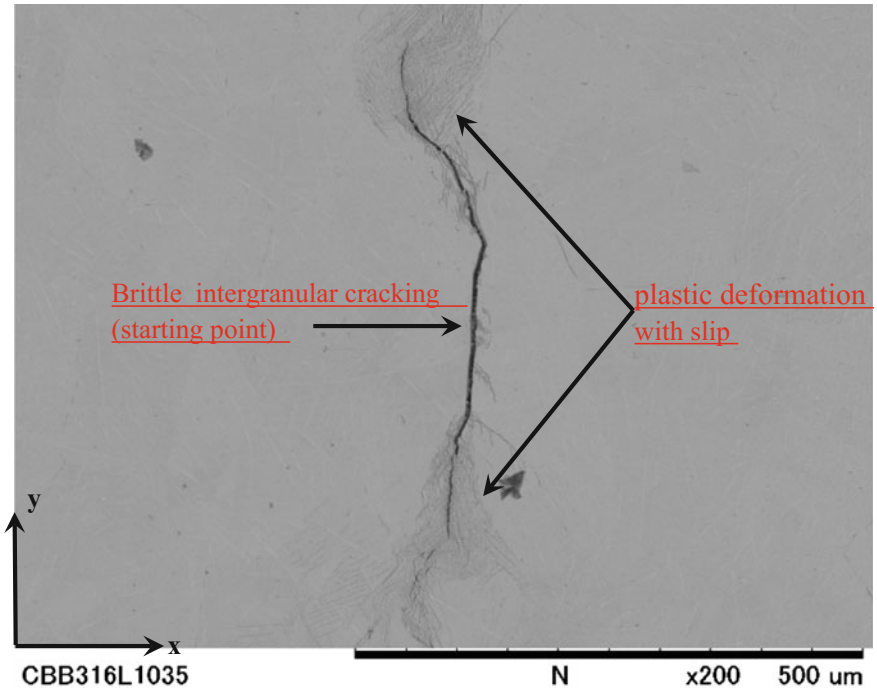

Fig. 4 SEM observation photograph of a typical SCC crack in this CBB test (316L CW + LTA). [x axis direction: the bending tensile direction]

Discussion

No SCC crack was observed in Types 304L LTA and 316L LTA. This result suggests that the SCC initiation susceptibility was not increased by the long-term thermal aging treatment only. In contrast, some 20 SCC cracks were observed in Type 316L CW + LTA. It is considered that a synergistic effect of cold work and long-term thermal aging induced the SCC initiation susceptibility in the specimens, especially in Type 316L SS.

The hardness of Type 316L CW + LTA, which exhibited the SCC initiation susceptibility in the CBB test, was on the same level as that of Types 304L CW and 316L CW. Tsubota et al. reported that SCC initiation susceptibility increased with materials hardness [8]. In this study, however, it is difficult to confirm the SCC initiation susceptibility with respect to the hardness of specimens, considering that the type 304L CW + LTA, which was harder than type 316L CW + LTA, exhibited no SCC susceptibility.

In this present TEM/EDX examination on Type 316L CW + LTA, neither Cr depletion nor precipitation of any other elements was observed. This result indicates

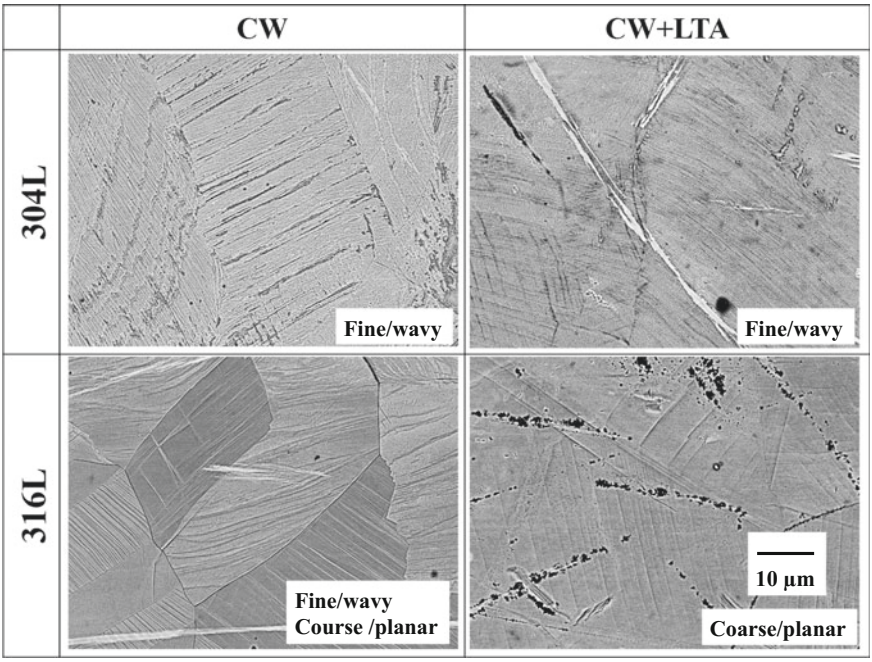

Fig. 5 SEM observation photographs of typical surface morphology of CW and CW + LTA specimens after the CBB test

that the cause of increase of SCC initiation susceptibility could not be explained by the LTA sensitization. Sahlaoui et al. examined the precipitation behavior of 316L SS after long term thermal treatment above 500 °C for up to 80000 h, and revealed the thermal treatment at 500 °C didn't cause the formation of intermetallic phase such as Laves phase, although the Cr carbide precipitation at grain boundaries was induced [11]. In this study, neither Cr carbide precipitate nor solute segregation was confirmed at grain boundaries of Type 316L LTA at 288 °C. It could be concluded, therefore, the drastic degradation of corrosion resistance near grain boundaries was not induced by the LTA treatment. Further investigation, however, would be necessary on the grain boundary segregations of Mo and minor elements such as P and S with atomic resolution by Three Dimensional Atom Probe (3DAP), in order to assess the cause of the grain boundary crack in Type 316L CW + LTA.

Focusing on the deformation microstructure of cold worked Type 316L SS before and after LTA, the slip line pattern on the surface of the CBB-tested Type 316L CW + LTA specimen, which exhibited the SCC initiation susceptibility in this study, was characterized to be coarse and planar. Whereas, fine and wavy slip traces were observed in Types 304L CW, 304L CW + LTA and 316L CW, even though some grains of Type 316L CW exhibited the coarse planar slip traces. It was reported by some researchers [12] that the stacking fault energy (SFE) of Type 304L SS is lower than that of Type 316L SS, and that planar slip was enhanced in

304L SS compared to 316L SS. However, that is discrepant with the result of surface observation after CBB test, that is, wavy slip was dominant in 304L SS. Morphology of surface slip pattern (wavy or planar) might be influenced by not only SFE but also other factors that control the multiple slip and consequent crystal lattice distortion. Murayama et al. reported that Mo and N addition to stainless steels lead to the planar dislocation microstructure during the plastic deformation [13]. In this study, coarse planar slip was observed in both Types 316L CW and 316L CW + LTA, and it seemed that such surface slip pattern was more enhanced in CW + LTA specimen. Generally, it is suggested that such coarse and planar slip causes the localization of the strain and promotes the brittle failure. It could be derived from the experimental results obtained in this study that one of the possible reasons for the high SCC initiation susceptibility of Type 316L CW + LTA was the enhancement of coarse planar slip after LTA treatment on Type 316L CW. Further investigation on the correlation between SCC susceptibility and enhancement of planar slip after LTA treatment is necessary to confirm the hypothesis mentioned above.

Conclusions

To clarify the effect of long-term thermal aging on SCC initiation susceptibility in low carbon austenitic stainless steels, CBB tests using Types 304L and 316L SSs treated with the long-term thermal aging at 288 °C for 14,000 h was carried out. In addition, the material properties and microstructure of the specimen were analyzed. The results are summarized as follows.

1. The long-term thermal aging or 20% cold working alone did not increase SCC initiation susceptibility of the test materials. On the other hand, the SCC initiation susceptibility of Type 316L SS increased clearly by the combination of cold work and long-term thermal aging, however, such synergistic effect was not observed in Type 304L SS.
2. Neither Cr depletion nor enrichment of other elements was observed around the grain boundaries in this analysis. Furthermore, no precipitate such as carbide was observed in Type 316L CW + LTA, which exhibited SCC initiation susceptibility in the CBB test. This result indicates that the LTA treatment did not induce drastic degradation of corrosion resistance near grain boundaries.
3. The hardness of Type 316L CW + LTA, which exhibited the SCC initiation susceptibility in the CBB test, was on the same level as that of Type 316L CW. No increase in hardness occurred by the combination of CW and LTA. It is difficult to confirm the SCC initiation susceptibility with respect to the hardness of specimens, considering that Type 304L CW + LTA, which was harder than Type 316L CW + LTA, exhibited no SCC susceptibility.
4. The middle region of a SCC crack seemed to be cracked in a brittle manner, while lots of slip plane traces were observed in grains around the crack tip. It is,

therefore, speculated that the crack initiated in the middle region of the observed crack, and propagated with plastic deformation in neighboring grains due to the stress concentrations at around the crack tip.

5. The characteristics of surface slip traces in Type 304L CW and CW + LTA was fine and wavy in the surfaces of CBB-tested specimens. The slip line pattern of Type 316L CW + LTA, which was the only material that exhibited SCC susceptibility in this study, was mainly characterized to be coarse and planar. It could be derived from these experimental results obtained in this study that one of the possible reasons of the high SCC initiation susceptibility of Type 316L CW + LTA was the enhancement of coarse planar slip after LTA treatment.

References

1. K.J. Leonard, T.M. Rosseel, and J.T. Busby, Light water reactor sustainability program materials aging and degradation pathway technical program plan. (Report ORNL/LTR-2012/327 Revision 5, Oak Ridge National Laboratory, 2016)
2. T. Tsukada et al., Report of examination of the samples from core shroud (2F3-H6a) at Fukushima Dai-ni nuclear power station unit-3. (Report JAERI-Tech 2004-044, Japan Atomic Energy Research Institute (currently, Japan Atomic Energy Agency), 2004)
3. Y. Okamura et al., Structural integrity evaluation for core shroud and PLR piping with SCC. J. High Press. Inst. Jpn. **43**, 4–14 (2005)
4. T.M. Angeliu et al., in *The IGSSCC behavior of L-grade stainless steel in 288 °C water*. Proceeding of the 8th International Symposium on Environmental Degradation of Materials in Nuclear Power System Water Reactors, no. 8 (1997), pp. 649–662
5. J. Kuniya et al., Stress corrosion cracking susceptibility of various austenitic stainless steel pipe welds in high temperature oxygenated water. Boshoku-Gijutsu **31**, 261–267 (1982)
6. R.M. Horn et al., Experience and assessment of stress corrosion cracking in L-grade stainless steel BWR internals. Nucl. Eng. Des. **174**, 313–325 (1997)
7. V. Kain et al., Effect of cold work on low-temperature sensitization behavior of austenitic stainless steels. J. Nucl. Mater. **334**, 115–132 (2004)
8. M. Tsubota, Y. Kanazawa, H. Inoue, in *The Effect of Cold Work on SCC Susceptibility of Austenitic Stainless Steel*. Proceeding of the 7th International Symposium on Environmental Degradation of Materials in Nuclear Power Systems Water Reactors, no. 7 (1995), pp. 519–527
9. M. Akashi, T. Kawamoto, The effect of molybdenum addition on SCC susceptibility of stainless steel in oxygenated high temperature water. Boshoku-Gijutsu **27**, 165–171 (1978)
10. M. Akashi et al., Metallurgical factors influencing the susceptibility of non-sensitized stainless steel to intergranular stress-corrosion cracking in high-temperature, high-purity water environments. Paper presented at corrosion 99, San Antonio, Texas, 25 April 1999, 451
11. H. Sahlaoui et al., Effect of ageing condition on the precipitates evolution, chromium depletion and intergranular corrosion susceptibility of AISI 316L: experimental and modeling results. Mater. Sci. Eng., A **372**, 98–108 (2004)
12. G. Mereic de bellefon, J.C. van Duysen, Tailoring plasticity of austenitic stainless steels for nuclear applications: review of mechanisms controlling plasticity of austenitic steels below 400 °C. J. Nucl. Mater. **475**, 168–191 (2016)
13. M. Murayama et al., The combined effect of molybdenum and nitrogen on the fatigued microstructure of 316 type austenitic stainless steel. Scripta Mater. **41**, 467–473 (1999)

Crack Growth Rate and Fracture Toughness of CF3 Cast Stainless Steels at ~3 DPA

Y. Chen, W.-Y. Chen, B. Alexandreanu, K. Natesan and A.S. Rao

Abstract Cast austenitic stainless steels (CASS) used in reactor core internals are subject to high-temperature coolant and energetic neutron irradiation during power operations. Due to both thermal aging and irradiation embrittlement, the long-term performance of CASS materials is of concern. To assess the cracking behavior of irradiated CASS alloys, crack growth rate (CGR) and fracture toughness J-R curve tests were performed on two CF3 alloys. Miniature compact tension specimens were irradiated to ~3 dpa, and were tested at ~315 °C in simulated LWR coolant environments with low corrosion potentials. No elevated cracking susceptibility was observed at this dose in the test environments. The power exponents of the 3 dpa J-R curves were much lower than that of unirradiated or irradiated specimens at lower doses, indicating a significant decline in fracture resistance. A preliminary microstructural study revealed irradiation-induced microstructural changes in both austenite and ferrite, suggesting an embrittlement mechanism involving both phases at this dose level.

Keywords Cast austenitic stainless steels · Neutron irradiation · Stress corrosion cracking · Thermal aging · Irradiation embrittlement · Microstructural characterizations

Introduction

The main structural materials of the cooling system and reactor core of light water reactors (LWRs) are austenitic stainless steels (SSs). Many reactor components with complex shapes at the primary pressure-boundary and inside the reactor vessel are made of stainless steel castings [1, 2]. The most common cast austenitic stainless

Y. Chen (✉) · W.-Y. Chen · B. Alexandreanu · K. Natesan
Argonne National Laboratory, 9700 S. CASS Ave., Darien, IL 60439, USA
e-mail: yiren_chen@anl.gov

A.S. Rao
US Nuclear Regulatory Commission, 11545 Rockville Pike, Rockville, MD 20852, USA

J.H. Jackson et al. (eds.), *Proceedings of the 18th International Conference on Environmental Degradation of Materials in Nuclear Power Systems – Water Reactors*, The Minerals, Metals & Materials Series, https://doi.org/10.1007/978-3-319-68454-3_52

steels (CASSs) used in LWRs are the corrosion-resistant CF8 and CF3 grades, which are the cast equivalents of Type 304 and 304L SSs, respectively. Molybdenum-bearing CF3M and CF8M alloys can also be found in some LWRs. With high chromium and nickel contents, CASS alloys possess excellent corrosion resistance and mechanical properties. CASS alloys are found to be more resistant than their wrought SS counterparts to sensitization at elevated temperatures and stress corrosion cracking (SCC) in aqueous environments [3]. The strength and fracture toughness of CASS alloys are also comparable to those of wrought SSs [4, 5]. Thanks to their good compatibility with wrought SSs, CASS alloys have been used extensively in LWRs.

The CF-grades of CASS alloys have a unique solidification microstructure consisting of delta ferrite and austenite. While the austenite is the dominant phase, the CF-grades also contain $\sim$5–25% delta ferrite [6]. The exact ratio between the ferrite and austenite in the microstructure depends on the alloy composition, casting and cooling rate [7]. In CASS alloys, delta ferrite forms directly from the liquid phase and is very important for the soundness of castings. A minimum amount of delta ferrite is often required in steel castings to avoid "hot cracking" during solidification. In the final microstructure of castings, the retained ferrite also plays a crucial role in strengthening the austenite matrix and improving the resistance to sensitization and stress corrosion cracking (SCC). These beneficial effects of delta ferrite contribute to the successful applications of CASS alloys in LWRs.

The ferritic phase in CASS alloys can also have a negative impact on fracture toughness. Exposed to elevated temperatures and neutron irradiations, CASS alloys can experience hardening and embrittlement. It is well accepted that the ferrite is vulnerable to thermal aging embrittlement due to its inherent instability [8, 9]. An increased tensile strength and reduced ductility can be observed after long-term exposure at 300–500 °C. The upper-shelf impact energies of ferritic materials can be reduced, and their ductile-to-brittle transition temperatures are increased after thermal aging [10]. In addition, irradiation embrittlement is also a concern for CASS alloys used in reactor core internals. Fast neutron irradiations can induce displacement damages and various irradiation effects, leading to deteriorated ductility and fracture toughness of CASS alloys [11]. The possible interplay between the two degradation processes, i.e., thermal aging and neutron irradiation, needs to be evaluated carefully. A previous study on CASS alloys irradiated to a low dose showed that the degree of embrittlement may be higher than expected for the irradiated and thermally aged CASS materials, suggesting a combined effect of thermal aging and irradiation embrittlement [12]. At present, the cracking behavior of CASS alloys have not been studied extensively at intermediate or high doses, and a dose dependence of fracture toughness is lacking. As the LWR ages, the long-term service performance of CASS alloys is of concern for aging management and extended license renewal. In this paper, we report a recent study on the crack growth behavior and fracture resistance of CASS alloys in low-corrosion-potential environments. The effect of neutron irradiation, with or without prior thermal aging, on the embrittlement of CASS alloys will be evaluated at an intermediate dose with mechanical tests and microstructural examinations.

Experimental Details

Materials and Specimens

Two CF3 heats of static castings were tested in this study. Table 1 shows their chemical compositions and ferrite contents. The heat with 24% ferrite was a large slab of 610 × 610 × 76 mm in dimension. The heat with 14% ferrite was a keel block approximately 180 mm long and 120 mm high with a tapered thickness from 30 to 90 mm. The ferrite contents of these heats were measured with a ferroscope from the castings. Rectangular bars about 150 mm long with and 10 × 10-mm cross-section were cut from the slab and keel block. A sample blank of 50 × 50 × 25 mm in size were also cut from the slab. Several of the rectangular bars and the sample blank were thermally aged to simulate the service condition during power operation, and the aging conditions are also reported in Table 1. Metallographic examinations showed that the morphology and quantity of the delta ferrite was not affected by the thermal aging, and the dual-phase structure remained unchanged after thermal aging. These unaged and aged materials were used in fabricating the specimens for mechanical tests and microstructural examinations.

Compact tension (CT) specimens were used for the crack growth rate and fracture toughness J-R curve tests. The sample has a nominal width of 12 mm and a thickness of 6.5 mm (i.e., ~1/4T-CT). The initial notch size is 6 mm. To ensure an in-plane crack growth, side-grooves approximately 5% of the sample thickness were machined on both sides of the specimen, giving a typical net thickness of 5.85 mm. Figure 1 shows a sketch of the CT sample used in this study.

Transmission electron microscopy (TEM) disk samples (3 mm in diameter) were punched from thin coupons cut from the rectangular bars and sample blank. The TEM disks were mechanically ground to 0.1–0.2 mm thick prior to irradiation. After irradiation, the TEM disks were electrochemically polished with a twin-jet polisher until perforation. A 5% perchloric acid and methanol solution was used and the polishing condition was 28 V at −40 °C. The obtained thin foils were examined with a Hitachi-H9000 TEM at 200 keV.

Table 1 Chemical compositions of the CF3 alloys used in this study

Heat ID	Delta ferrite (%)	Composition (wt%)									Aging condition
		Mn	Si	P	S	Mo	Cr	Ni	N	C	
69	24	0.63	1.13	0.015	0.005	0.34	20.18	8.59	0.028	0.023	Unaged
											10,000 h, 400 °C
52	14	0.57	0.92	0.012	0.005	0.35	19.49	9.40	0.052	0.009	Unaged
											55,000 h, 320 °C

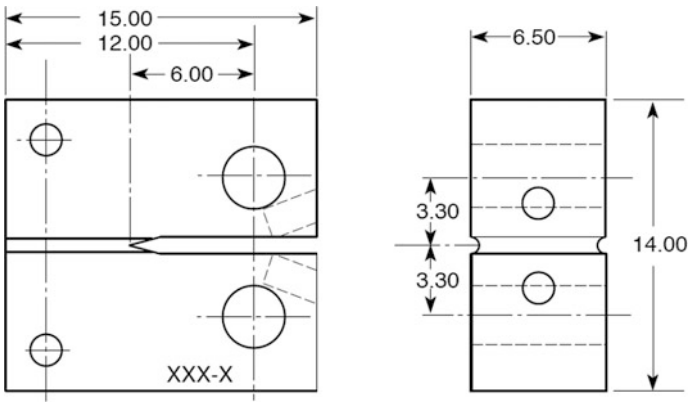

Fig. 1 Schematic of 1/4T-CT specimen used in this study

Irradiation

All CT and TEM samples were irradiated in a helium-filled capsule in the Halden reactor operated by the Institute for Energy Technology in Norway. The irradiation capsule was equipped with two sets of melting alloy assembly to monitor the capsule's temperature during the irradiation. Outside the irradiation capsule, multiple Fe-Ni-Al/Co alloy wires were attached to the capsule to record the fast and thermal neutron fluence received by the samples.

The irradiation experiment was conducted during a period of four years with three loading cycles. The fast neutron ($E > 1$ meV) fluence received by the capsule was 1.91×10^{21} n/cm^2, corresponding to a displacement damage dose of 2.9 dpa. The irradiation temperature varied with reactor operational cycles, and a post-irradiation analysis on the melting alloy assemblies showed an average temperature of $\sim$307 °C, and the peak temperature was below 311 °C. After the irradiation, the samples were discharged from the irradiation capsules and transferred to Argonne National Laboratory (ANL) for testing.

Crack Growth Rate and J-R Curve Tests

Crack growth rate (CGR) and fracture toughness J-R curve tests were conducted in hot cells in a radiation-controlled laboratory at ANL. The exposure rates of these irradiated specimens were quite high despite their small dimensions. The dose rate of a CT sample is typically around 10 R/hr at 30 cm. The tests were performed either in simulated pressurized water reactor (PWR) water or in high-purity water with low dissolved-oxygen (DO). Both environments have low corrosion potentials, and are known to reduce the sensitivity of SSs to stress corrosion cracking (SCC)

[13]. The simulated PWR water contained approximately 2 ppm lithium, 1000 ppm boron, and 2 ppm hydrogen. The conductivity was approximately 20 μS/cm. The low-DO high-purity water contained less than 10 ppb DO, and was covered with a gas mixture of nitrogen with 4% hydrogen. The conductivity was kept below 0.07 μS/cm. During the test, water was circulated at a constant rate of 20–30 mL/min through the autoclave. The temperature and pressure of the autoclaves were kept at ~315 °C and ~1800 psig, respectively.

The CGR test was started with cyclic loading at a load ratio of 0.2 and a frequency of 1 Hz. The maximum stress intensity factor (K_{max}) was kept between 14 and 15 MPa $m^{1/2}$. The crack length was monitored continuously during the test with a direct current potential drop (DCPD) method. After the sample was pre-cracked in water, environmentally-enhanced cracking was induced by a series of cyclic loading steps with gradually increased rise time and load ratio. Once environmentally-enhanced cracking was stabilized, a SCC test was performed, and SCC CGRs were recorded at several stress intensity factors with or without periodical partial unloading (PPU). As the crack propagated during the test, a near constant-K condition was maintained at the crack tip by load shedding.

After the CGR test, a fracture toughness J-R curve test was conducted with the SCC starter crack in the same test environment. A few gentle loading cycles (less than 10 cycles) were applied on the sample prior to the start of the J-R test to break any unbroken ligaments resulting from the SCC test. During the test, the sample was loaded in tension at a constant displacement rate of 0.43 μm/s, and the load and sample extension were recorded. The loading was also interrupted at a regular interval during the test to measure the crack extension by DCPD. With the load vs. load-line displacement curve, J-integral values were calculated and plotted against the crack extension. The obtained J-resistance data were fitted to a power-law correlation per ASTM E 1820-15a. After the J-R test, the specimen was fractured with cyclic loading in air at room temperature. The fracture surface of the tested sample was examined with replicas in a scanning electron microscope (SEM). The final crack size was determined with SEM images, and the CGR and J-R curve results were corrected proportionally to match the measured crack length.

Results

Cyclic and SCC Crack Growth Rates

Four CGR tests were conducted on 2.9 dpa CF3 samples with and without prior thermal aging. The samples with 24% ferrite were tested in high-purity water with low-DO, and the samples with 14% ferrite were tested in simulated PWR water environment. All specimens were pre-cracked with cyclic loading in the test environments. Once the crack initiated, environmentally-enhanced cracking was encouraged with gradually increased load ratio and rise time. The measured cyclic

CGRs were compared with the anticipated fatigue CGRs in air under the same loading conditions. The difference between the CGR in water and the CGR in air, i.e., the acceleration due to environment, is used to assess the extent of environmental enhancement. Figure 2 shows the cyclic CGRs measured during these tests. A corrosion-fatigue curve developed for SSs in low-DO water (<0.2 ppm DO) [14] is also included as a reference. Environmentally-enhanced cracking can be seen among these tests, and the differences between the aged and unaged samples are too small to be statistically significant. Although the samples had been irradiated to 2.9 dpa, it was difficult to establish elevated growth rates in the low-corrosion-potential environments with cyclic loading. The corrosion-fatigue responses of these irradiated samples were sluggish regardless of their prior thermal aging treatment or ferrite contents. The crack growth was often stalled at high load ratios, and repeated attempts were required to re-activate a stalled crack and to stabilize an elevated CGR. It is evident that the beneficial effect of low-corrosion-potential environments remains effective for CASS alloys at 2.9 dpa.

Following the cyclic CGR tests, constant-load CGR tests were conducted with and without PPU every 2 h at one or two stress intensity factors (K). The measured SCC CGRs are plotted against K in Fig. 3, along with a disposition curve that bounds SCC CGRs of sensitized SSs in high-purity water taken from NUREG-0313 [15]. While moderate CGRs up to $\sim 2 \times 10^{-11}$ m/s were measured with PPU, the constant-load CGRs without PPU were below the detectable limit of the DCPD system. All data points with PPU were fitted to a K-dependent relationship with a power exponent of 2.16. The result is about one order of magnitude lower than the NUREG-0313 curve as shown in Fig. 3. Obviously, the SCC susceptibility of the 2.9 dpa CASS specimens was not elevated in the test environments.

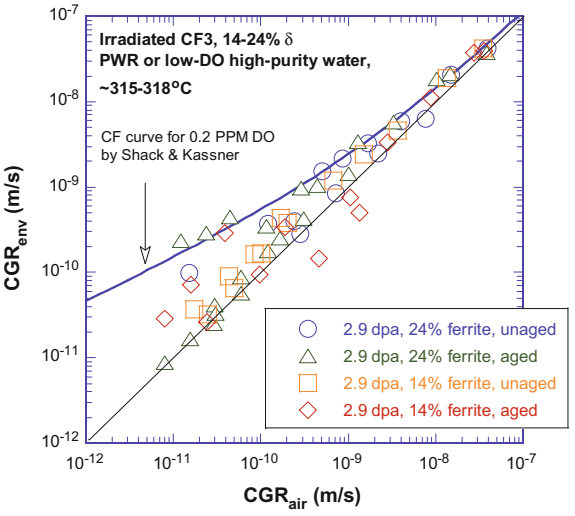

Fig. 2 Cyclic CGRs of CF3 irradiated to 2.9 dpa

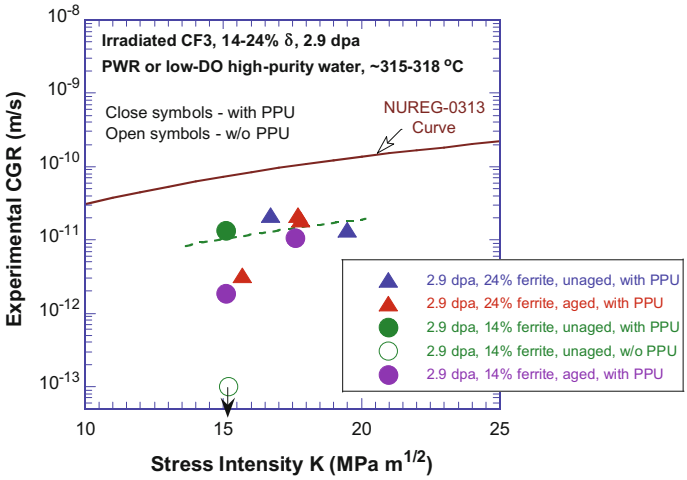

Fig. 3 SCC CGRs of CF3 irradiated to 2.9 dpa

Fracture Toughness

Figure 4 shows the J-R curves obtained from the four CF3 specimens irradiated to 2.9 dpa. A blunting line with a slope of 4X the flow stress and an estimated value of flow stress at 2.9 dpa were used for each J-R curve analysis. The power-law fitting results are summarized in Table 2. Note that the $J_{0.2\text{-mm}}$ values obtained in these tests cannot be validated rigorously to J_{1C} per ASTM 1820-15a. Although most of the constraint requirements defining the measurement capacity can be readily satisfied with these irradiated specimens, the requirements on the straightness of final cracks are sometime violated in these tests.

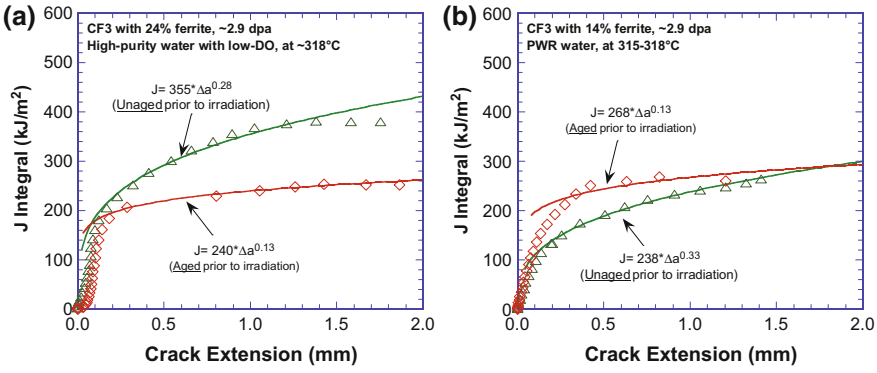

Fig. 4 J-R curves at ~315 °C for CF3 irradiated to 2.9 dpa, **a** with 24% ferrite, and **b** with 14% ferrite

Table 2 J-R curve tests on 2.9 dpa CF3 specimens at 315 °C

Ferrite content (%)	Aging condition	Water environment	C	n	$J_{0.2\text{-mm}}$ (kJ/m^2)	$J^1_{2.5\text{-mm}}$ (kJ/m^2)
24	Unaged	Low-DO, high-purity	355	0.28	250	467
24	10,000 h at 400 °C	Low-DO, high-purity	240	0.13	202	272
14	Unaged	PWR	238	0.33	151	327
14	55,000 h at 320 °C	PWR	268	0.13	225	303

[1]Estimated value at the 2.5-mm offset line

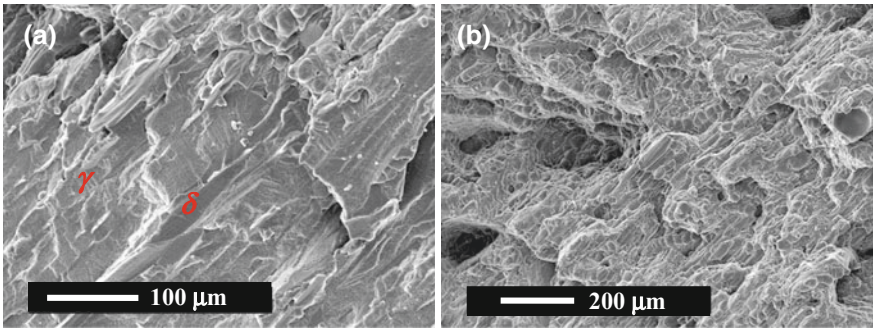

Fig. 5 Fracture morphology of **a** CGR and **b** J-R test regions of the aged CF3 with 24% ferrite irradiated to 2.9 dpa. Crack growth direction is from the bottom to top in the pictures

For the CF3 with 24% ferrite, the J-R curve of the aged sample is below that of the unaged specimen as shown in Fig. 4. The pre-factor (C) and power exponent (n) are both lower for the aged than the unaged specimens. For the CF3 with 14% ferrite however, the pre-factors of the unaged and aged samples are similar, and the unaged one is slightly lower. Nonetheless, the power exponent of the aged CF3 with 14% ferrite is much lower than that of its unaged counterpart, consistent with that observed with the 24%-ferrite specimens. In general, all specimens tested in this study show rather shallow J-R curves, suggesting a reduced resistance to crack extension.

All the specimens tested in this study show transgranular cracking during their CGR tests. Depending on their ferrite contents, ferrite islands are recognizable at the end of the CGR test where subcritical crack growth took place. Figure 5a is an example of such cracking morphology in the aged CF3 with 24% ferrite. On the other hand, the J-R curve test regions are covered with small dimples as shown in Fig. 5b. The contrast between the CGR and J-R test regions is evident. Despite their low J-R responses, significant plasticity remains in the CASS alloys at 2.9 dpa, and the dominant fracture mode is still ductile. Occasionally, small areas of cleavage-like morphology can be seen on the fracture surface, suggesting a critical role of delta ferrite in the fracture resistance of irradiated CASS alloys.

Irradiated Microstructure

The unaged and aged CF3 specimens were examined with a TEM to characterize their irradiated microstructures at 2.9 dpa. Both austenite and ferrite were observed with diffraction contrast imaging techniques. Figure 6 shows the results of the unaged specimen. As expected, faulted dislocation loops are the main microstructural feature in austenite (Fig. 6a–c). No extended dislocation microstructure can be seen at this dose level. Using rel-rod images (Fig. 6c, the inset is the rel-rod reflection used), the size and density of the faulted loops were determined. The loop size varies from a few to 20 nm with an average value of 7.2 nm. The loop density is on the order of 10^{22} m^{-3}. In addition, a low density of precipitates may be present in the austenite (revealed by a diffraction pattern that is not shown in the figure). The nature of the precipitates is unknown and additional analyses are needed to characterize them. In ferrite, a high density of microstructural features can be seen in bright-field and weak-beam dark-field images (as shown in Fig. 6d, e). These irradiation-induced features are presumably dislocation loops and G-phase precipitates which cannot be readily distinguished with their diffraction contrast. Their average size is less than 2 nm, and their density is above 10^{23} m^{-3}. The dark-field image formed with G-phase reflection (Fig. 6f) reveals that a large fraction of these irradiation-induced features are in fact G-phase precipitates.

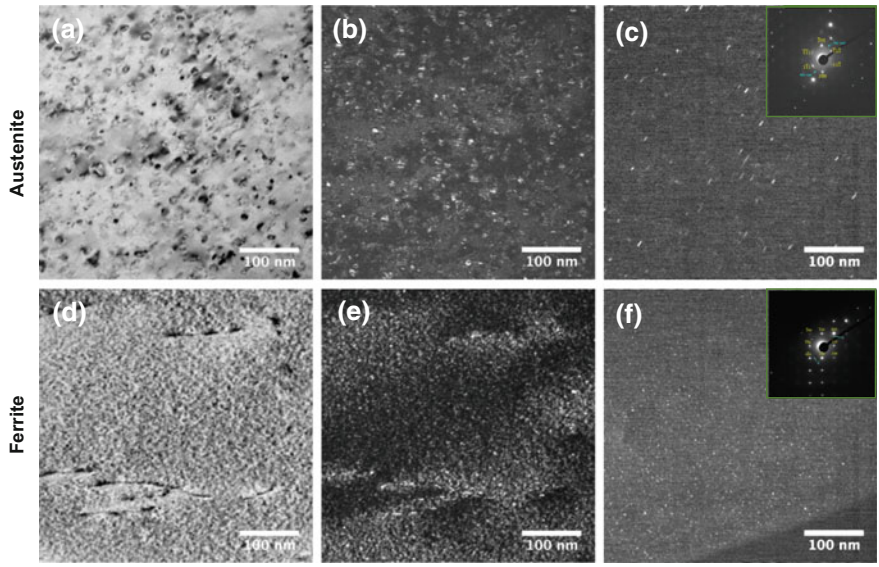

Fig. 6 Unaged CF3 at 2.9 dpa. Irradiated microstructure of austenite imaged with **a** bright-field, **b** weak-beam dark-field (g = −200), and **c** rel-rod dark-field images; and irradiated microstructure of ferrite imaged with **d** bright-field, **e** weak-beam dark-field (g = 110, g5 g), and **f** irradiation-induced precipitates with G-phase reflection in ferrite (inset shows the G-phase reflections)

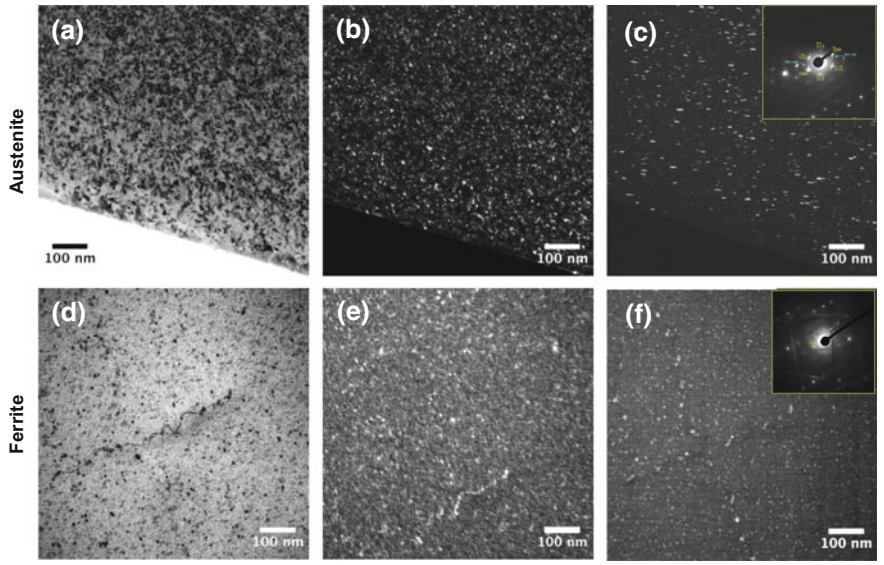

Fig. 7 Aged CF3 at 2.9 dpa. Irradiated microstructure of austenite imaged with **a** bright-field, **b** weak-beam dark-filed (g = −200), and **c** rel-rod dark-field images; and irradiated microstructure of ferrite imaged with **d** bright-field, **e** dark-field (g = 110), and **f** precipitates with G-phase reflection in ferrite (inset shows the G-phase reflections)

Figure 7 shows the TEM results of the aged CF3 specimen. Again, faulted dislocation loops dominate the irradiated microstructure in austenite as shown by the bright-field and dark-field images. The rel-rod image was used for quantitative measurements. The average loop size is similar but slightly lower than that of the unaged CF3. The density however is much higher, on the order of 10^{23} m^{-3}. Similar to the unaged austenite, some precipitates may also be present in the aged sample with a lower density. In ferrite, both dislocation loops and G-phase precipitates were observed as shown in Fig. 7d–f. The density of the irradiation-induced features is quite high. Compared with the unaged specimen, G-phase precipitates appear larger in the aged sample.

Discussion

No elevated cyclic or SCC CGRs were observed in the 2.9 dpa CF3 samples tested in the low-corrosion-potential environments. Thermal aging prior to neutron irradiation did not have a significant impact on the crack growth behavior of the CF3. In all tests performed on the 2.9 dpa specimens, environmental enhancement was difficult to establish with cyclic loading in the test environments, and SCC CGRs were barely detectable without PPU. This good corrosion-fatigue and SCC

performance are consistent with our previous observations on unirradiated and low-dose (~0.08 dpa) CASS samples [16, 17]. To compare the SCC responses at different doses, the SCC CGRs of the CF3 specimens obtained with PPU are plotted in Fig. 8. We do not distinguish thermal aging history or ferrite content in this figure. It is clear that neutron irradiation up to 2.9 dpa does not affect the cracking behavior of CF3 alloys. Between 15 and 25 MPa $m^{1/2}$, the SCC CGRs of the unirradiated and irradiated specimens are comparable and show a similar K-dependence at different doses. The low cracking susceptibility observed in these CF3 alloys may be attributed to the low-corrosion-potential environments and the beneficial effect of delta ferrite.

While the crack growth behavior was not affected at 2.9 dpa, the fracture resistance of CASS alloys was influenced strongly by neutron irradiation. Figure 9 shows the fitting curves of J-R data for all CF3 specimens at different doses. With an increasing dose, the power-law exponent of the J-R curve decreases considerably and the J-R curves become much shallower. This implies a declined strain energy release rate for crack extension in irradiated materials. This effect of irradiation embrittlement is more evident in the unaged samples (Fig. 9a, c) where much steeper J-R curves can be seen before irradiation. On the other hand, the effects of neutron irradiation and thermal aging are very similar at the low-dose (0.08 dpa), leading to comparable J-R curve responses (see the blue and green curves in Fig. 9b, d). Additional irradiation up to 2.9 dpa decreases the fracture resistance further, demonstrating a significant impact of irradiation on top of thermal aging embrittlement. The J values at 2.5-mm crack extension can be reduced to about 1/2 of their aged values. For the CF3 alloys, the difference between high- and low-ferrite contents is not obvious. This lack of sensitivity to ferrite content may be related to the different thermal aging conditions applied to the two heats. Additional

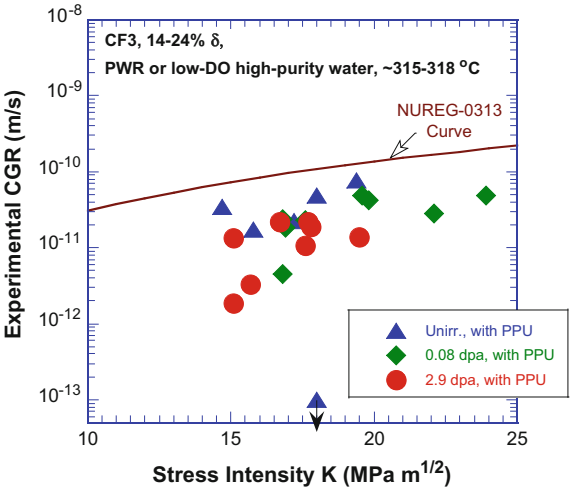

Fig. 8 SCC CGRs of CF3 in low-corrosion-potential environments at different doses

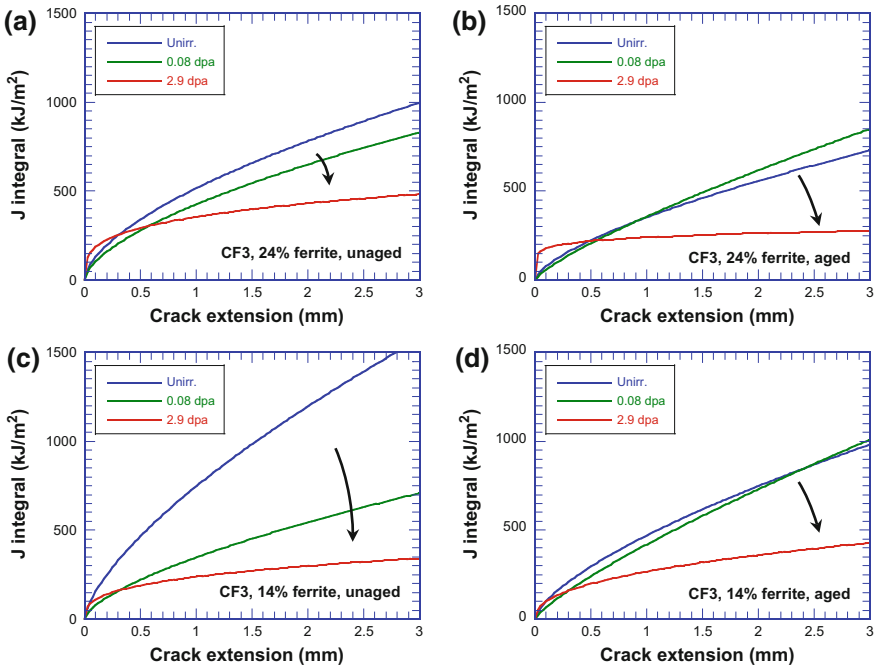

Fig. 9 Comparisons of the J-R curves at ~315 °C for different doses, **a** unaged and **b** aged CF3 with 24% ferrite, and **c** unaged and **d** aged CF3 with 14% ferrite. Arrows point to the direction of increasing dose

effort is needed to further explore the influence of ferrite content on irradiation embrittlement.

Defect and precipitate microstructures resulting from the neutron irradiation and thermal aging are responsible for the deteriorated fracture resistance observed in the CASS materials. Previous studies have shown that, while no microstructural change was visible under TEM in austenite after low-dose neutron irradiation, α/α' phase separation and G-phase precipitation were observed after either thermal aging or low-dose neutron irradiation [18, 19]. The current TEM result at 2.9 dpa further confirms that G-phase precipitation can indeed take place in irradiated ferrite regardless of its prior thermal aging history. Since G-phase precipitation is closely correlated with α/α' phase separation [18], α/α' decomposition should also be anticipated to some extent in the 2.9 dpa samples. Future atom probe tomography on the 2.9 dpa samples can help clarify this assumption. Nonetheless, it is clear that the neutron irradiation conducted in this study can enable or facilitate the precipitation or phase separation that would otherwise occur too slowly in ferrite under thermal aging at the irradiation temperature. Thus, the two degradation processes (i.e., thermal aging and neutron irradiation) are coupled and contribute coordinately to the embrittlement in CASS alloys.

With the increase in irradiation dose, the role of irradiation defects (i.e., dislocation loops and defect clusters) should become more important. Due to their difference in crystal structures, the evolution of irradiation defects with dose is expected to be different in ferrite and austenite. Without pre-existing microstructure, the development of irradiation defects in austenite is relatively simple. As shown in Fig. 10a–d, no visible irradiation-induced defect can be seen at 0.08 dpa. At 2.9 dpa, however, a high density of dislocation loops developed in both unaged and aged austenite. These faulted loops can affect dislocation motion strongly, leading to hardening and embrittlement. Since the prior thermal aging does not affect the austenite phase, the dose-dependent behavior of hardening and embrittlement is expected to be the same for the unaged or aged austenite. For the ferrite phase however, the evolution of irradiation microstructure is more complex (Fig. 10e–h). A relatively open structure of bcc crystal and pre-existing precipitation microstructure resulting from thermal aging or low-dose irradiation could play an important role in the kinetics of defect production and evolution. Additional effort is still needed for a quantitative analysis and detailed understanding of the dose-dependent defect evolution in ferrite. Nonetheless, since both austenite and ferrite are affected by neutron irradiation at higher doses, the embrittlement mechanism must involve both phases and their interactions will be crucial for the assessment of long-term performance of CASS components in reactor core internals.

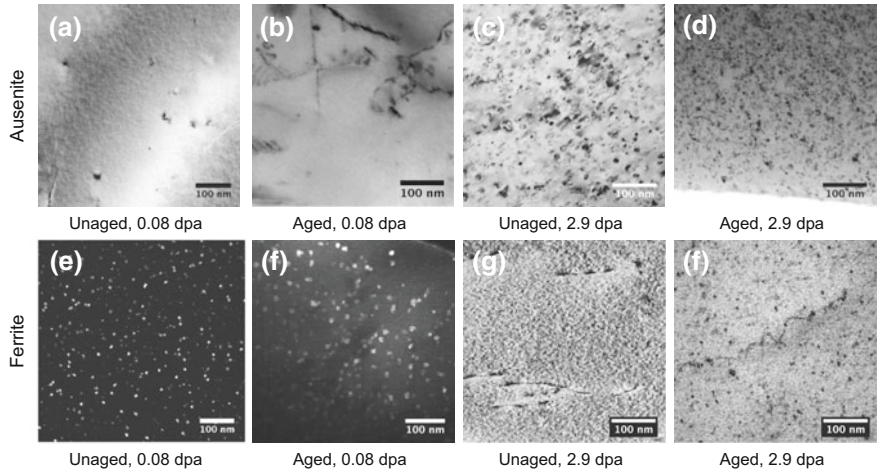

Fig. 10 Microstructure evolution, in austenite **a–b** unaged and aged samples at 0.08 dpa, and **c–d** unaged and aged samples at 2.9 dpa; in ferrite **e–f** unaged and aged samples at 0.08 dpa, and **g–h** unaged and aged samples at 2.9 dpa. (Note that *e* and *f* are dark-field images formed with G-phase reflections)

Conclusions

Crack growth rate and fracture toughness J-R curve tests have been performed in low-corrosion-potential environments on 2.9 dpa CF3 alloys with 14 and 24% ferrite. Both unaged and aged specimens are included to evaluate the impact of combined degradations of thermal aging and irradiation embrittlement. No elevated cracking susceptibility has been observed at 2.9 dpa in the test environments for either unaged or aged samples. The cyclic and SCC responses of the 2.9 dpa samples are similar to those before irradiation or at 0.08 dpa. Meanwhile, the fracture behavior of the 2.9 dpa CF3 specimens is quite different from those without irradiation or at lower doses. The J-R curves at 2.9 dpa are much shallower than those at 0.08 dpa and without irradiation, indicating a significant decline in fracture resistance. This irradiation-induced embrittlement is more evident in the samples without prior thermal aging. Some preliminary microstructural results show that irradiation-induced microstructural changes are present in both austenite and ferrite, suggesting an embrittlement mechanism involving both phases in CASS alloys. While dislocation loops are the dominant defects in austenite, both dislocation loops and G-phase precipitates can be seen in ferrite. Also, irradiation-induced G-phase precipitates are observed in both unaged and aged samples with a slightly larger average size in the aged sample. This observation further confirms that neutron irradiation and thermal aging are related deterioration mechanisms and their combined effect should be evaluated carefully when both forms of degradation are present.

Acknowledgements The authors would like to thank Ms. T. M. Karlsen, OECD Halden Reactor Project, Halden, for her help with the irradiation experiment and specimen transfer. Chi Xu and Loren Knoblich are acknowledged for their contributions to the experimental effort. The TEM work was performed at the IVEM-Tandem Facility funded by the US Department of Energy Office of Nuclear Energy. This work is sponsored by the U.S. Nuclear Regulatory Commission, under Project V6380, and by the U.S. Department of Energy, under contract # DE-AC02-06CH11357.

References

1. U.S. NRC, Expert panel report on proactive materials degradation assessment, NUREG/CR-6923, 2006
2. T. Meyer, C. Boggess, S. Byrne, R. Schwirian, F. Gift, R. Gold, Materials reliability program: screening, categorization, and ranking of reactor internals components for westinghouse and combustion engineering PWR design (MRP-191), EPRI Technical Report, Project Manager H. T. Tang, Nov 2006
3. F.H. Beck, J. Juppenlatz, P.F. Wieser, in *Stress Corrosion—New Approaches*, ed. by H.L. Craig, Jr. Effects of Ferrite and Sensitization on Intergranular and Stress Corrosion Behavior of Cast Stainless Steels (ASTM STP 610, 1976)
4. S. Floreen, H.W. Hayden, The influence of austenite and ferrite on the mechanical properties of two-phase stainless steels having microduplex structures. ASM Trans. Q. **61**(3), 489–499 (1968)

5. W.J. Mills, Fracture toughness of type 304 and 316 stainless steels and their welds. Int. Mater. Rev. **4**(2), 45 (1997)
6. N.R. Hughes, W.L. Clarke, D.E. Delwiche, in *Stainless Steel Castings*, ed. by V.G. Behal, A. S. Melilli. Intergranular Stress-Corrosion Cracking Resistance of Austenitic Stainless Steel Castings (ASTM STP 756, 1982)
7. L.S. Aubry, P.F. Wieser, W.J. Pollard, E.A. Schoefer, in *Stainless Steel Castings*, ed. by V.G. Behal, A.S. Melilli Ferrite Measurement and Control in Cast Duplex Stainless Steels (ASTM STP 756, American Society for Testing and Materials, 1982), pp. 126–164
8. S.S. Brener, M.K. Miller, W.A. Soffa, Scr. Metall. **16**, 831(1982)
9. P.J. Grobner, Metall. Trans. **4**, 251 (1973)
10. O.K. Chopra, A. Sather, Initial assessment of the mechanisms and significance of low-temperature embrittlement of cast stainless steels in LWR systems (NUREG/CR-5385, ANL-89/17, 1990)
11. O.K. Chopra, W.J. Shack, Crack growth rates and fracture toughness of irradiated austenitic stainless steels in BWR environments (NUREG/CR-6960, ANL-06/58, 2008)
12. Y. Chen, B. Alexandreanu, W.-Y. Chen, K. Natesan, Z. Li, Y. Yang, A.S. Rao, J. Nucl. Mater. **466**, 560–568 (2015)
13. P.L. Andresen, F.P. Ford, S.M. Murphy, J.M. Perks, in *State of Knowledge of Radiation Effects on Environmental Cracking in Light Water Reactor Core Materials*. Proceedings of 4th International Symposium on Environmental Degradation of Materials in Nuclear Power Systems—Water Reactors (NACE, Houston, TX, 1990), pp. 1.83–1.121
14. J.W. Shack, T.F. Kassner, Review of environmental effects on fatigue crack growth of austenitic stainless steels (NUREG/CR-6176, 1994)
15. W.S. Hazelton, W.H. Koo, technical report on material selection and processing guidelines for BWR coolant pressure boundary piping (NUREG-0313, Rev. 2, 1988)
16. Y. Chen, B. Alexandreanu, W. Chen, Z. Li, Y. Yang, K. Natesan, and A.S. Rao, *Crack Growth Rate and Fracture Toughness J-R Curve Tests on Irradiated Cast Austenitic Stainless Steels*. 17th International Conference on Environmental Degradation of Materials in Nuclear Power Systems—Water Reactors, Ottawa, Ontario, Canada, 9–13 August 2015
17. Y. Chen, B. Alexandreanu, K. Natesan, Crack growth rate and fracture toughness tests on irradiated cast stainless steels (NUREG/CR-7184, ANL-12/56, 2015)
18. Z. Li, W.-Y. Lo, Y. Chen, J. Pakarinen, Y. Wu, T. Allen, Y. Yang, J. Nucl. Mater. **466**, 201 (2015)
19. Y. Chen, B. Alexandreanu, W.-Y. Chen, K. Natesan, Z. Li, Y. Yang, A.S. Rao, J. Nucl. Mater. **466**, 560–568 (2015)

Effects of Thermal Aging and Low Dose Neutron Irradiation on the Ferrite Phase in a 308L Weld

Z. Li, Y. Chen, A.S. Rao and Y. Yang

Abstract The integrity of reactor internal components made of austenitic stainless steel welds with a duplex structure can potentially be affected by thermal aging and/or neutron irradiation induced embrittlement. There have not been sufficient studies on the long-term service performance of SS welds in light water reactors. In this study, thermal aging was performed at 400 °C for up to 2220 h on a 308L weld, and the irradiation was conducted in the Halden reactor at ~315 °C to 0.08 dpa (5.6×10^{19} n/cm^2, E > 1 meV). The microstructural evolution of the ferrite phase was characterized using atom probe tomography (APT) and auxiliary transmission electron microscope studies. Spinodal decomposition and Ni-Mn-Si solute clusters were observed in both the thermally aged and neutron irradiated 308L welds. As compared with thermal aging, low dose neutron irradiation induced similar spinodal decomposition with slightly larger concentration wavelength and amplitude. The solute clusters in irradiated ferrite phase also show a larger mean size, a wider size distribution, but a lower number density as compared with those in thermally aged ferrite phase. In addition, the neutron irradiation significantly promotes segregation of trace elements, particularly phosphorus, at the Ni-Mn-Si solute clusters.

Keywords Thermal aging · Neutron irradiation · Austenitic stainless steel weld

Z. Li · Y. Yang (✉)
Department of Materials Science and Engineering, Nuclear Engineering Program, University of Florida, Gainesville, FL 32611, USA
e-mail: yongyang@ufl.edu

Y. Chen
Nuclear Engineering Division, Argonne National Laboratory, Lemont IL 60439, USA

A.S. Rao
US Nuclear Regulatory Commission, 11545 Rockville Pike, Rockville MD 20852, USA

J.H. Jackson et al. (eds.), *Proceedings of the 18th International Conference on Environmental Degradation of Materials in Nuclear Power Systems – Water Reactors*, The Minerals, Metals & Materials Series, https://doi.org/10.1007/978-3-319-68454-3_53

Introduction

Austenitic stainless steels are extensively used as structural alloys for the internal components in light water reactors (LWR) because of their excellent mechanical properties, corrosion resistance, and formability. Type 308/308L weld metals are often used for welding the austenitic steel parts, e.g. circumferential and vertical welds in BWR core shroud, in-vessel weld for the core control drives, and the jet pump assembly welds. These weld alloys are also used in the overlay cladding of the reactor pressure vessels. To prevent hot cracking, stainless steel (SS) welds normally contain a small amount of δ-ferrite up to 10% in the γ-austenite matrix. During the service lifetime of LWRs, those welded components are subjected to thermal aging at temperatures up to 320 °C for a pressurized water reactor (PWR) and 289 °C for a boiling water reactor (BWR). Unfortunately, the duplex structure stainless steel welds are prone to thermal aging embrittlement, which is caused by the instability of ferrite phase upon thermal aging.

The effect of thermal aging on the microstructure and mechanical properties of Type 308/308L welds was extensively studied by Alexander et al. [1]. It was found that aging at 343 °C caused a significant embrittlement, and no saturation of embrittlement was observed after 50,000 h. The related microstructure study showed that the ferrite phase underwent spinodal decomposition along with G-phase precipitation. Accelerated thermal aging at 400 °C for 7000–10,000 h was conducted by Gavenda et al. [2], and the result also consistently showed that the welds' Charpy impact strength and fracture toughness were greatly reduced after thermal aging. Recently studies by Takeuchi [3, 4] showed that a distinct Cr spinodal decomposition occurs in the weld-overlay aged at 400 °C for 10,000 h along with the nucleation and coarsening of G-phase precipitate.

The SS welds of the reactor pressure vessel cladding are also exposed to neutron irradiation, in general, to a relatively lower dose as compared with reactor core components. There have been several studies regarding the neutron irradiation effect on welds fracture toughness [1, 2]. The irradiation decreased materials' Charpy impact energy and resulted in a significant shift of the Charpy impact transition temperature. Transmission electron microscopy examinations conducted by Lee et al. [5] couldn't reveal the nature of fine defects even though micro-hardness tests showed a significant hardening in the δ-ferrite after irradiation. Takeuchi [6] presented the neutron irradiated microstructures in a stainless steel electro-slag weld overlay irradiated to ~0.1 dpa at 290 °C. A slight progression of Cr spinodal decomposition and an increase in the fluctuation of the Si, Ni, and Mn concentrations were observed in the ferrite. Nevertheless, related microstructural studies, particularly at a LWRs relevant condition, are very limited to date.

In this paper, the spinodal decomposition and solute clustering in neutron-irradiated ferrites of a 308L type weld are presented. For comparison, the results from thermal aging condition are also included.

Experimental Details

Materials and Conditions

A Type 304L stainless steel weldment fabricated with ER308L filler metal was used in this study. The 304L SS plates were welded with a conventional submerged arc butt-welding procedure with a double-V joint design. Table 1 lists the chemical composition of the weld metal, and the measured ferrite content is 6.8%. A sample blank was cut from the weldment and thermally aged at 400 °C for 2220 h. By considering a spinodal decomposition activation energy of 164 kJ/mole for the Fe-Cr system, this aging condition shall be equivalent to a 10-year service period at 323 °C in a typical LWR environment [7]. The neutron irradiation was conducted in the Halden reactor at 315 °C to 0.08 dpa (5.6×10^{19} *n/cm*^{2}*, E > 1 meV with an estimated dose rate of* 5×10^{-9} *dpa/s*). Figure 1 of scanning electron microscope (SEM) image shows a duplex grain microstructure of the weld, and the ferrites phases (grey color) are thin plates located at the austenite sub-grain boundaries. No obvious change of this structure was observed after thermal aging or neutron irradiation.

Table 1 Chemical composition (wt%) of 308L weld bulk

C	Mn	P	S	Si	Ni	Cr	Mo	Cu	Ti	Fe	Nb	Ta	N
0.023	2.06	0.032	0.006	0.92	9.30	20.50	0.10	0.09	<0.01	Bal.	0.01	<0.01	0.10

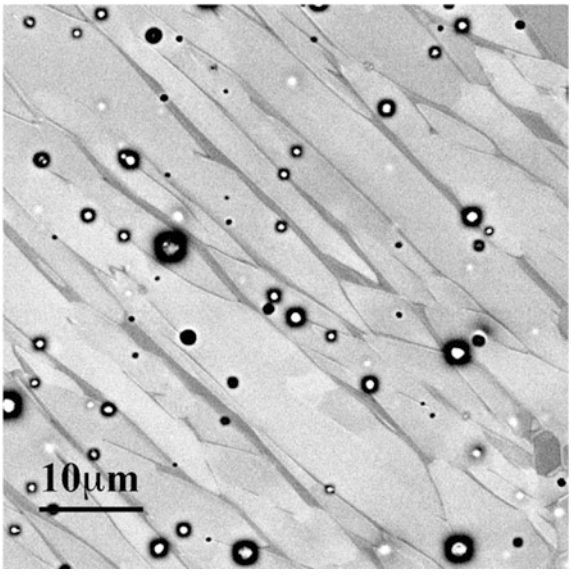

Fig. 1 SEM image of duplex grain structure of 308L weld

Transmission Electron Microscopy

Transmission electron microscopy (TEM) specimens were prepared by using an electropolishing method for the as-welded and thermally aged samples. The electrolyte was 10% perchloric acid balanced with methanol, and the electropolishing was conducted at −20 °C. The irradiated TEM specimens were prepared using a focused ion beam (FEI 3D Quanta FEG FIB). Tecnai TF30-FEG TEM was used to characterize the microstructure. However, it is relatively difficult to study the early stage of spinodal decomposition and very fine precipitate using a TEM, thus the TEM results were mainly used for general microstructure characterization and as a validation on atom probe tomography (APT) results.

Atom Probe Tomography

The APT probe specimens were fabricated using a FIB, and the tips were finished using ion beam imaging for 1 min at beam energy of 2 kV and current of 27 pA to ensure a minimal Ga implantation and ion beam damage. For each sample condition (as-welded, aged and irradiated), a minimum of nine APT tips was fabricated, and at least one dataset of more than 18 M ions was collected for each condition. Both the FIB and APT equipment used for this study are located at the Microscopy and Characterization Suite (MaCS), Center for Advanced Energy Studies (CAES) in Idaho Falls, ID. The 3-D reconstruction and analysis were completed using the Interactive VisuAlization Software (IVAS 3.6.8). The data reconstructions were conducted by following the standard procedure of the Recon Wizard in the software, and the SEM images of APT tips were used for defining tip profile in the 3-D reconstruction.

Results

Table 2 lists the ferrite chemical compositions measured by APT. In general, as compared with the bulk composition of 308L weld (Table 1), the ferrite phase contains less Ni and Mn that are austenite stabilizer. Among the three conditions (i.e., as-welded, thermally aged, and irradiated), except the carbon content, all other

Table 2 Ferrite grain chemical compositions (wt%) measured by APT

Condition	C	Mn	P	S	Si	Ni	Cr	Mo	Cu	Ti	Fe
As-welded	0.044	1.67	0.08	0.053	1.11	5.97	25.16	0.55	0.046	0.01	65.29
Aged	0.018	1.54	0.11	0.057	1.20	5.15	26.80	0.59	0.192	0.01	64.30
Irradiated	0.027	1.53	0.09	0.056	0.94	5.26	24.88	0.67	0.225	0.02	66.29

alloying elements show very consistent weight percentages. Since the APT specimens were lifted from different ferrite grains in several polished TEM disks, this compositional consistency proves that the weld in this study has a homogeneous elemental distribution in the bulk. The large variation in carbon content is perhaps due to the uncertainty associated with the quantitative carbon measurement by APT. The carbon atoms evaporate in the form of single or molecular ions and single pulse can cause multiple carbon ions to evaporate. Carbon atoms also tend to migrate to the APT tip surface under high vacuum [8, 9].

Spinodal Decomposition

Figure 2 shows the comparison of spinodal decomposition among as-welded, aged, and irradiated ferrite grains. The Cr ion map was constructed from a 5 nm thick slice at the middle of each APT tip, and the ions of identified solute clusters (precipitates) were excluded from this spinodal decomposition analysis. Clearly, thermal aging at 400 °C for 2220 h can sufficiently induce a significant separation between Fe and Cr elements, and the ferrite phase decomposes into Cr-rich α' phase and Fe-rich α phase. The spinodal decomposition structure is also consistent with the findings from other researchers, both experimentally and numerically [10, 11]. To better quantify the extent of spinodal decomposition, the radial distribution function (RDF) is used to calculate Cr concentration distribution as a function of radial distance from each referenced Cr ion, and the calculations are averaged over all the detected Cr ions in each dataset. The details of applying RDF to analyze spinodal decomposition was discussed by Zhou [12]. The RDF provides a better quantitative evaluation on spinodal decomposition as compared with other methods, e.g. 1D concentration profiles and frequency distribution [4, 13, 14] because it

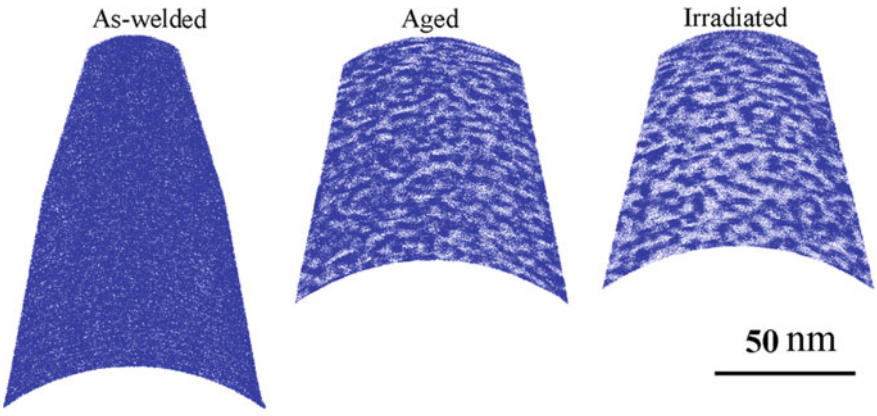

Fig. 2 Spinodal decomposition structure (Cr map) of ferrite grain in the as-welded, aged and irradiated 308L weld

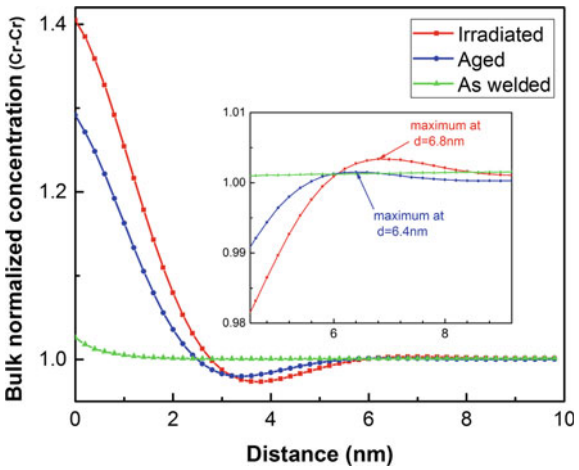

Fig. 3 Radial distribution functions of Cr-Cr ions in aged and irradiated ferrite grains in 308L weld

is a 3-D analysis by including all the identified Fe or Cr ions. Figure 3 shows the Cr-Cr RDF curves for the as-welded, aged and irradiated conditions, respectively. The inset in Fig. 3 highlights the subtle difference of the position of first maximum after *RDF(0)* between aged and irradiated conditions. The maximum indicates a statistically closest distance between two Cr-rich regions and here it corresponds the Cr concentration fluctuation wavelength. We can assume Cr concentration as a sinusoidal wave function [15]:

$$f(\vec{r}) = C_o + \frac{A}{2} \cdot \sin\left(\left(\frac{2\pi}{\lambda}\right)(\vec{r})\right) \tag{1}$$

where, C_o is the average Cr concentration in ferrite phase, A is the concentration fluctuation amplitude, λ is the wavelength, and $\vec{r}$ is a position vector.

The relation between the concentration fluctuation amplitude A and *RDF(0)* is derived by Zhou as [12]:

$$A = C_o\sqrt{2(RDF(0) - 1)} \tag{2}$$

As illustrated in the inset of Fig. 3, the spinodal decomposition wavelength is 6.4 nm for aged condition, which is slightly smaller than the value of 6.8 nm for the irradiated condition. Based on Eq. 2, the spinodal decomposition amplitudes are calculated as 20.7 and 23.9 wt% for the aged and irradiated conditions, respectively. Overall, it appears spinodal decomposition is similar in the irradiated and thermally aged samples.

G-Phase Precipitates

Figure 4 shows clustering of Ni, Mn and Si in both aged and irradiated ferrite grains, and such Ni-Mn-Si enriched solute clusters have been widely observed in a very broad range of neutron-irradiated steels and welds. To quantitatively identify the solute clusters, the maximum separation method (MSM) is used. This approach has been widely accepted by other researchers for characterizing nano-sized solute precipitates using APT [13, 16]. To create a cluster analysis in IVAS software, parameters of "*ions*" (element), "*orders*" (ions), "erosion distance d_e", "d_{max} (nm)", "minimum number of ions in cluster N_{min}" and "envelop parameter L (nm)" have to be specified. For both aged and irradiated welds in this study, element Mn shows a strongly clustering behavior, and thus is chosen as the ion for determining the solute clusters. Figure 5 shows how to determine the parameters of d_{max}, d_e and N_{min} by using the aged weld as an example. To select the suitable orders (ions), the Mn-Mn nearest neighbor distributions for orders of one to ten were examined, and it was found that the 4th order of nearest neighbor shows a clear separation of ions between matrix and cluster regions, as shown in Fig. 5a. The region at near left peak represents the ions in clusters and the region at near right peak corresponds to the ions in matrix. This nearest neighbor distribution is then fitted into two Gaussian distributions. The value of d_{max} is determined as the distance between zero and the crossover of two fitted Gaussian distributions. The value of d_e is the distance between the left Gaussian distribution peak and the crossover of two Gaussian distributions. Envelope parameter L equals to d_{max}. To determine an optimal N_{min}, the number of identified clusters is plotted versus different N_{min} as shown in

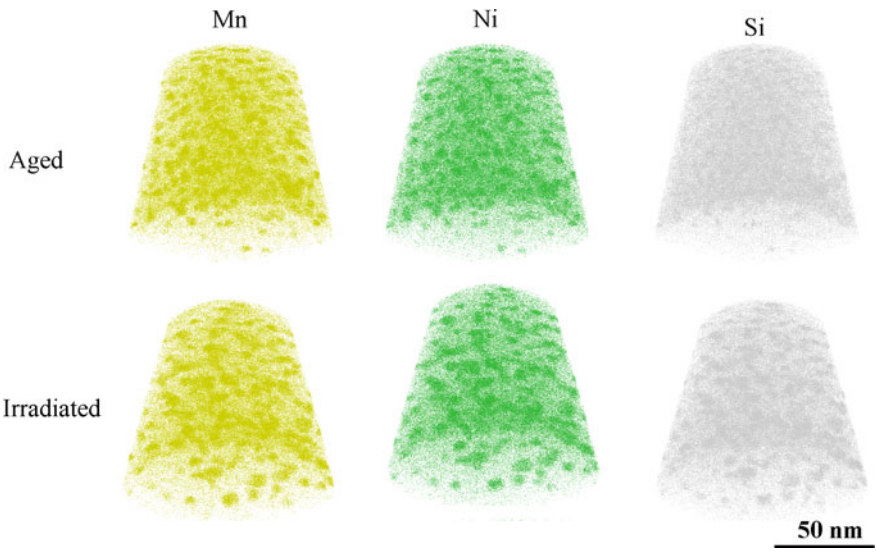

Fig. 4 Mn-Ni-Si clusters in aged and irradiated ferrite grains in 308L weld

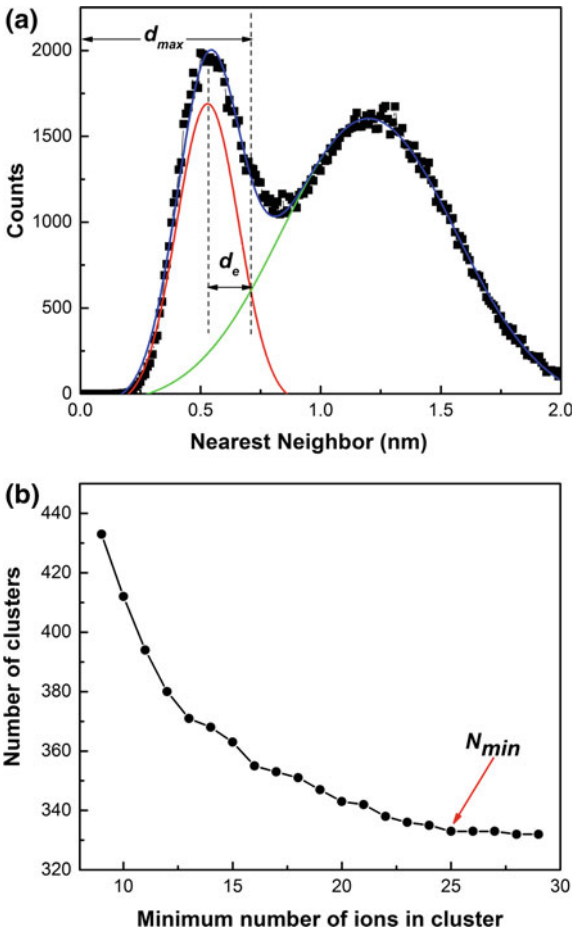

Fig. 5 Solute cluster parameters determination for aged weld 308L: **a** d_{max} (= L) and d_e; **b** N_{min}

Table 3 Parameters for the solute cluster analysis in IVAS

Conditions	Ions	Orders	$d_{max} = L$ (nm)	d_e (nm)	N_{min}
Aged	Mn	4th	0.70	0.18	25
Irradiated	Mn	4th	0.68	0.16	25

Fig. 5b. An optimal N_{min} gives a stable number of clusters by eliminating clusters containing few atoms, and a reasonable choice for N_{min} is 25 for this case. As shown in Fig. 5b, the cluster number doesn't decrease significantly as N_{min} is 25 or larger. Table 3 lists the parameters used in the solute cluster identification for aged and irradiated conditions.

The normalized elemental radial distributions of the identified solute clusters are plotted in Fig. 6. Clearly, there are minor differences in chemical compositions of solute clusters in between aged and irradiated ferrite grains. At the center of solute

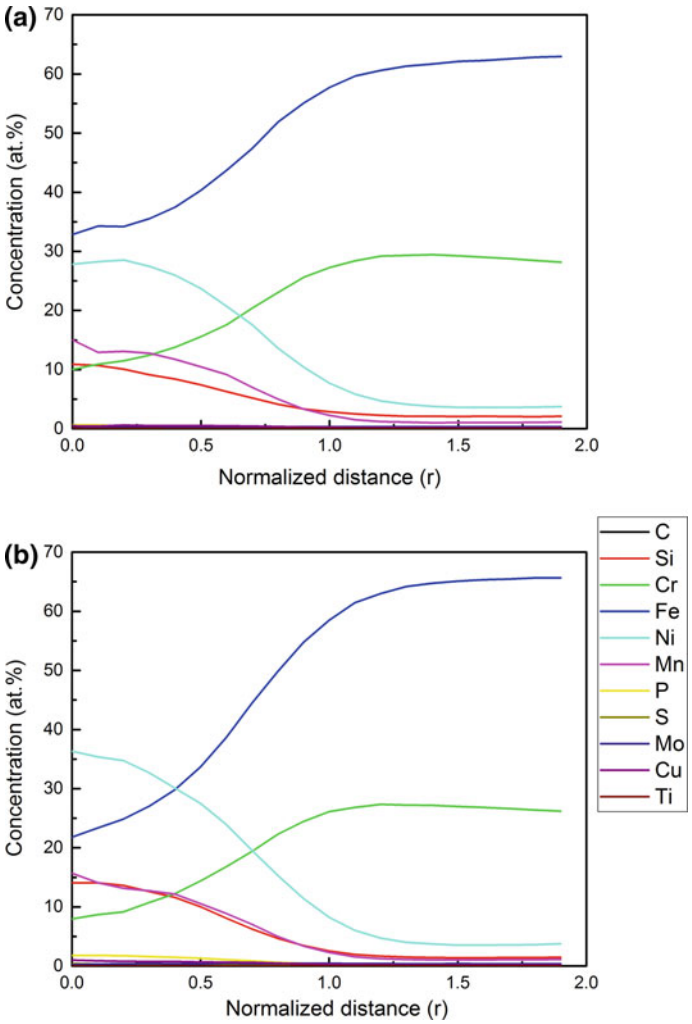

Fig. 6 Normalized radial elemental distribution of the solute clusters: **a** aged and **b** irradiated

Table 4 Chemical composition of identified clusters (wt%)

Condition	C	Mn	P	S	Si	Ni	Cr	Mo	Cu	Ti	Fe
Aged	0.016	7.43	0.176	0.121	2.90	19.15	19.85	0.512	0.484	0.02	49.0
Irradiated	0.021	7.89	0.535	0.139	3.78	22.94	18.49	0.741	0.689	0.02	44.3

clusters (normalized distance equals to zero), much higher concentrations of Ni and Si are observed in the solute clusters in irradiated ferrite grains, while the Mn contents are nearly the same. Table 4 lists the normalized sum of each element in all

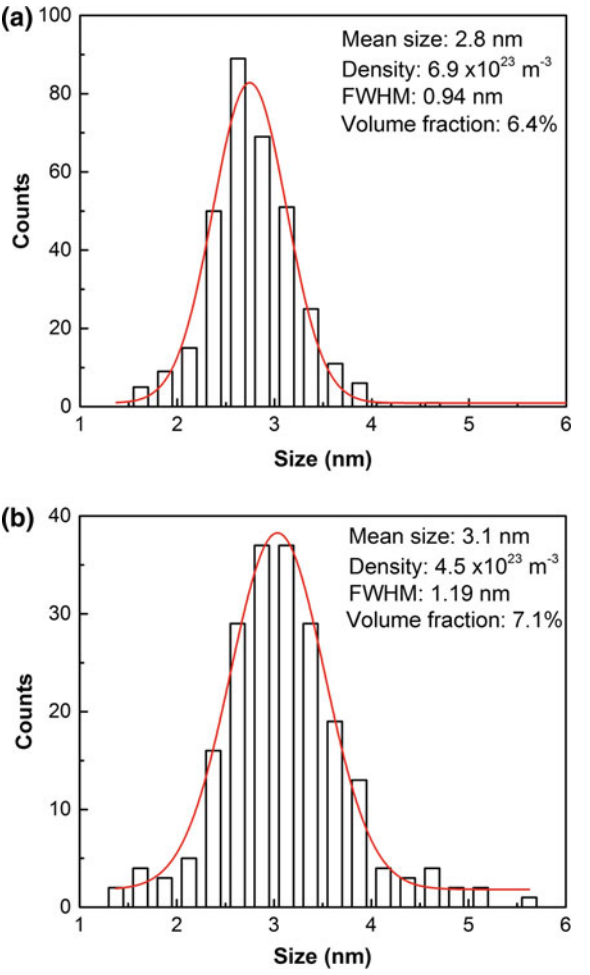

Fig. 7 Size distribution, mean size and number density of G-phase precipitates: **a** aged and **b** irradiated

identified solute clusters, it is found that irradiation promotes more segregations of S, Si, Ni, Cu and Mo into the clusters as compared with aged condition. However, phosphorus shows the most significant segregation into the Ni-Mn-Si solute clusters upon irradiation as compared with thermal aging.

The size distribution, mean size and number density of the solute clusters are summarized in Fig. 7. Obviously, solute clusters in the thermally aged ferrite grain have a narrower size distribution while a higher number density as compared with the clusters in the irradiated ferrite grain. Apparently, the 400 °C thermal aging induces slightly more solute cluster nuclei while the low dose irradiation may promote coarsening. Additional observations are needed to clarify the micromechanisms involving the nucleation and growth of G-phase precipitates.

Transmission Electron Microscopy

The limited TEM results shown in Fig. 8 display a mottled structure in both aged and irradiated ferrite grains, and the contrast of the mottled structure is from a coherent stain field between the α and α′ phases. Given the fact that TEM image is actually a 2-D projection of 3-D structure, the contrast resulting from α-α′ separation is not as evident as that shown in the APT result. Nonetheless, the estimated spinodal decomposition wavelengths from TEM analysis are consistent to that from APT measurement for aged and irradiated ferrite grains. TEM images of Fig. 8 also show nano-sized precipitates, particularly in irradiated specimen. Overall, our TEM results match very well with the APT characterizations. TEM study also shows that, in contrast to ferrite phase, the austenite has nearly no detectable changes upon low dose neutron irradiation or this 400 °C thermal aging.

Discussion

The concurrent evolution between the solute clustering and spinodal decomposition was studied by Danoix and Zhou [10, 17]. It was claimed the G-phase particles were located at α-α′ phase interfaces and no particles were observed within in α or α′ domains. Our study shows that the solute clusters are all located in the Cr-depleted zone, as shown in Fig. 9. As the spinodal decomposition progresses, domains enriched in iron and domains enriched in chromium form over the parent solid solution. It seems that Ni and Mn are rejected from the Cr enriched domains as the α′ phase develops to its equilibrium composition. The solute clusters should nucleate at the α-α′ interfaces and unsymmetrically grow into Fe-rich α phases. It was reported that Si was rejected from as Fe started to enrich in the α phase [18].

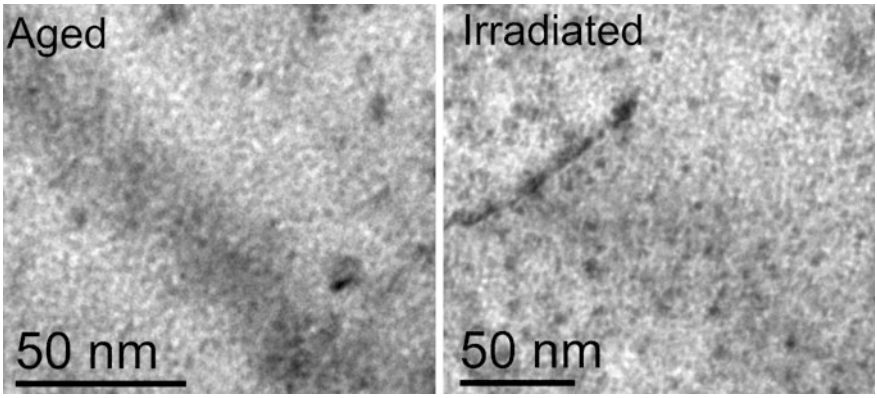

Fig. 8 TEM images of spinodal decomposition (mottled structure) and solute clusters (scattered black dots)

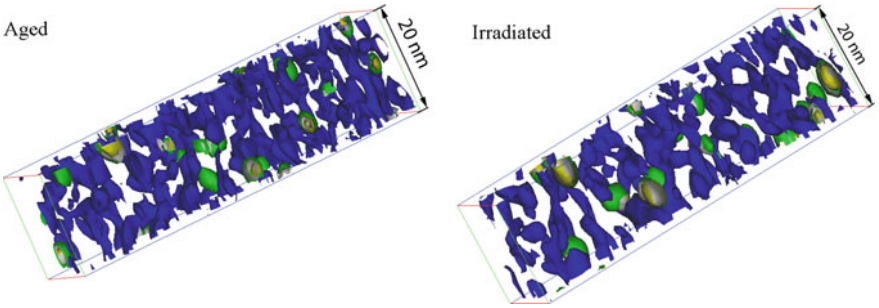

Fig. 9 Iso-surfaces of Mn(Gold)-Ni(Green)-Si(Gray) clusters and interfaces of Cr (Blue) enriched α′ phases: Aged(33.58%Cr-7.47%Mn-13.39%Ni-5.6%Si) and Irradiated (33.57%Cr-6.72% Mn-14.31%Ni-5.74%Si)

However, due to its relatively low concentration in the solute clusters and ferrite matrix, it is difficult to determine where the Si was rejected from which domain in our study. Overall, there is a strong interaction between the spinodal decomposition and solute cluster nucleation and growth.

Based on the microstructural evolution discussed above, a significant embrittlement of the weld is anticipated for both thermally aged and neutron irradiated conditions. Alexander and Nanstad [1] reported that thermal aging of 308 weld materials at 343 °C for up to 50,000 h shows little effect on the yield or ultimate tensile strength or the ductility, in contrast, the materials' Charpy impact toughness was significantly reduced in terms of ductile-to-brittle transition temperature or the upper-shelf energy. The micro-hardness study conducted by Danoix et al. [19] on the aged duplex stainless steel showed that a very good correlation between the hardness of the ferrite grain and the chromium fluctuations was obtained both in the presence and absence of G-phase precipitation, and it was concluded that the spinodal decomposition plays a major role in the hardening process. The α-α′ spinodal decomposition induces a stress field (misfit) that hinders dislocations motions. As discussed by Allen [20] that the cracking susceptibility is strongly influenced by the ferrite phase, which can be hardened by aging or irradiation. In the meantime, the yielding and plastic flow behavior of a duplex microstructure shall be dominated by the austenitic matrix.

Conclusion

In this study, significant microstructural evolution was observed in the ferrite of 308L weld after thermal aging or neutron irradiation. Similar spinodal decomposition and Ni-Mn-Si solute clustering were observed in the ferrite phase of thermally aged and neutron irradiated samples. As compared with the specimen thermally aged at 400 °C for 2220 h, a slightly larger concentration wavelength and

amplitude can be seen in neutron irradiated specimen. The evolution of solute clusters under neutron irradiation and thermal aging is also similar, with a slightly stronger effect on coarsening by neutron irradiation. Irradiation induced segregation involves all alloy elements, including those of minor contents. Thermally induced segregation in aged sample however, only involves the clustering of major ingredients of G-phase precipitates, i.e., Ni, Mn and Si. A strong concurrent behavior between spinodal decomposition and solute cluster nucleation and growth was suspected in both thermally aged and neutron irradiated specimens.

Acknowledgements This research was sponsored by the U. S. NRC under contract #NRC-HQ-14-G-0014. This work was also partially supported by the U.S. Department of Energy, Office of Nuclear Energy under DOE Idaho Operations Office Contract DE-AC07-051d14517, as part of an ATR National Scientific User Facility experiment. The authors would like to thank Joanna Taylor, Jatuporn Burns and Dr. Yaqiao Wu for their invaluable assistance at the CAES facility.

References

1. D.J. Alexander et al., U.S. nuclear regulatory commission (NUREG/CR-6628, 2000)
2. D.J. Gavenda et al., U. S. nuclear regulatory commission (NUREG/CR-6428, 1996)
3. T. Takeuchi et al., Microstructural changes of a thermally aged stainless steel submerged arc weld overlay cladding of nuclear reactor pressure vessels. J. Nucl. Mat. **425**, 60–64 (2012)
4. T. Takeuchi et al., Study on microstructural changes in thermally-aged stainless steel weld-overlay cladding of nuclear reactor pressure vessels by atom probe tomography. J. Nucl. Mat. **415**, 198–204 (2011)
5. J.S. Lee et al., Microstructural characteristic and embrittlement phenomena in neutron irradiated 309L stainless steel RPV clad. J. Nucl. Mater. **326**, 38–46 (2004)
6. T. Takeuchi et al., Effect of neutron irradiation on the microstructure of the stainless steel electroslag weld overlay cladding of nuclear reactor pressure vessels. J. Nucl. Mater. **443**, 266–273 (2013)
7. T.S. Byun, J.T. Busby, ORNL/LTR-2012/440, 2012
8. L. Yao et al., On the multiplicity of field evaporation events in atom probe: a new dimension to the analysis of mass spectra. Phil. Mag. Lett. **90**, 121–129 (2010)
9. B. Gault et al., Impact of directional walk on atom probe microanalysis. Ultramicroscopy **113**, 182–191 (2012)
10. J. Zhou et al., Concurrent phase separation and clustering in the ferrite phase during low temperature stress aging of duplex stainless steel weldments. Acta Mater. **60**, 5818–5827 (2012)
11. G. Bonny et al., On the α-α' miscibility gap of Fe-Cr alloys. Scripta Mater. **59**, 1193–1196 (2008)
12. J. Zhou et al., Quantitative evaluation of spinodal decomposition in Fe-Cr by atom probe tomography and radial distribution function analysis. Microsc. Microanal. **19**, 665–675 (2013)
13. R.P. Kolli, D.N. Seidman, Comparison of compositional and morphological atom-probe tomography analyses for a multicomponent Fe-Cu steel. Microsc. Microanal. **13**, 272–284 (2006)
14. T. Takeuchi et al., Effects of thermal aging on microstructure and hardness of stainless steel weld-overlay claddings of nuclear reactor pressure vessels. J. Nucl. Mat. **452**, 235–240 (2014)
15. J.W. Cahn, On spinodal decomposition. Acta Metall. **9**, 795–801 (1961)

16. Y. Chen et al., Quantitative atom probe tomography characterization of microstructure in a proton irradiated 304 stainless steel. J. Nucl. Mater. **451**, 130–136 (2014)
17. F. Danoix, P. Auger, Atom probe studies of the F-Cr system and stainless steels aged at intermediate temperature: a review. Mater. Charact. **44** (2000)
18. F. Danoix et al., A 3D study of G-phase precipitation in spinodally decomposed α-ferrite by tomographic atom-probe analysis. Microsc. Microanal. Microstruct. **5**, 121–132 (1994)
19. F. Danoix et al., Hardening of aged duplex stainless steels by spinodal decomposition. Microsc. Microanal. **10**, 349–354 (2004)
20. T.R. Allen et al., The effects of low dose rate irradiation and thermal aging on reactor structural alloys. J. Nucl. Mater. **270**, 290–300 (1999)

Microstructural Evolution of Welded Stainless Steels on Integrated Effect of Thermal Aging and Low Flux Irradiation

Martin Bjurman, Kristina Lindgren, Mattias Thuvander, Peter Ekström and Pål Efsing

Abstract The combined effect of thermal aging and irradiation on cast and welded stainless steel solidification structures is not sufficiently investigated. From theory and consecutive aging and irradiation experiments, the effect of simultaneous low rate irradiation and thermal aging is expected to accelerate and modify the aging processes of the ferrite phase. Here, a detailed analysis of long-term aged material at very low fast neutron flux at LWR operating temperatures using Atom Probe Tomography is presented. Samples of weld material from various positions in the core barrel of the Zorita PWR are examined. The welds have been exposed to 280–285 °C for 38 years at three different neutron fluxes between 1×10^{-5} and 7×10^{-7} dpa/h to a total dose of 0.15–2 dpa. The aging of the ferrite phase occurs by spinodal decomposition, clustering and precipitation of e.g. G-phase. These phenomena are characterized and quantitatively analyzed in order to understand the effect of flux in combination with thermal aging.

Keywords Thermal aging · Irradiation · Weld ferrite · Spinodal decomposition · Stainless steel

M. Bjurman (✉) · P. Efsing
Royal Institute of Technology (KTH), Stockholm, Sweden
e-mail: bjurma@kth.se

M. Bjurman
Studsvik Nuclear AB, Nyköping, Sweden

K. Lindgren · M. Thuvander
Chalmers University of Technology, Gothenburg, Sweden

P. Ekström
Swedish Radiation Safety Authority, Solna, Sweden

P. Efsing
Ringhals AB, Väröbacka, Sweden

J.H. Jackson et al. (eds.), *Proceedings of the 18th International Conference on Environmental Degradation of Materials in Nuclear Power Systems – Water Reactors*, The Minerals, Metals & Materials Series, https://doi.org/10.1007/978-3-319-68454-3_54

Introduction

To extend the life of nuclear power plants to 60 years or beyond, verifying the performance of structural materials is critical. One issue is the time dependent thermally induced degradation of mechanical and corrosion properties of cast and welded stainless steel components containing ferrite. The thermal aging phenomenon of δ–ferrite from spinodal decomposition and precipitation of G-phase, rich in Ni, Si, Mn, Mo and Ti (ideally $Ni_{16}Ti_6Si_7$ or $Ni_{16}Mn_6Si_7$), at high temperature applications in the temperature range of 280–500 °C is widely known, and extensive research has been conducted. From theory and consecutive aging and irradiation experiments, the effect of simultaneous low dose rate irradiation and thermal aging is expected to accelerate and modify the aging processes of the ferrite. These studies have generally been conducted with accelerated conditions at higher flux and temperature than in a Light Water Reactor (LWR). In this study, the interaction effects are studied on material extracted from a commercial LWR, with typical dose rates and temperatures of LWRs. The characterization in this paper is focused on the spinodal decomposition and G-phase formation. The implication for LWRs is mainly the reduction of operational life due to an increase in hardness and tensile strength, as well as a decrease in ductility, impact strength, and fracture toughness of the component.

Pieces of material have been harvested from the reactor pressure vessel internals of the Spanish pressurized water reactor (PWR) José Cabrera, also known as Zorita. Material was taken from the baffle plates and the core barrel, and the pieces taken from the latter component contained welds. The Zorita reactor was in operation from 1968 through 2006, when it was permanently shut down. During this period, the pieces cut from the core barrel received fast neutron doses in the range 0.1–2 dpa depending on actual position in the component.

Experimental

Material

Samples were taken at three different locations of the core barrel weld, covering the following doses: 0.15, 1 and 2 dpa. The core barrel was made of plates of Type 304 stainless steel joined by welding. The ferrite content of the weld metal is normal, in the range from 5 to 7% measured using a Ferritescope.

These welds have been exposed to between 280 and 285 °C for 230, 989 effective full power hours (EFPH) of in-service ageing. The temperature difference between the sample positions is significantly less than 5 °C. The exposure of specimens is summarized in Table 1.

Table 1 Irradiation conditions of the investigated welds

Dose (dpa)	Weld section	Temperature	EFPH (h)	Dose rate (dpa/h)
2	W2	280–285 °C	230,989	1E-05
1	W1			5E-06
0.15				7E-07

Instrumentation

Focused Ion Beam Scanning Electron Microscopy (FIB/SEM)

Samples for atom probe tomography (APT) were prepared by the FIB/SEM lift-out technique using a FEI Versa 3D DualBeam. It was necessary to do site-specific preparation as the ferrite volume fraction is rather low and the size of the ferrite dendrites is small, in some cases as thin as 200 nm. 3–6 tips were prepared from each dose level and from these for the 0.15 dpa level, one contained ferrite. For 1 and 2 dpa, ferrite was detected in 3 specimens each.

Atom Probe Tomography

The instrument used is a local electrode atom probe, Imago LEAP 3000X HR, equipped with a reflectron and has a detection efficiency of 37%. Analyses were carried out in voltage pulse mode. The sample temperature was 70 K, the pulse fraction was 20% of the DC voltage, the pulse frequency was 200 kHz in all analyses and the target evaporation rate was 0.2%. The data was analyzed using the IVAS™ 3.6 software.

Results and Discussion

The composition of the ferrite of each measured APT-specimen, including precipitates within the phase, is presented in Table 2. The measured composition varies significantly between specimens due to the local properties of the specific tip extracted. The main composition differences that can affect the interpretation of results between dose levels, are lower Ni- and Si-content of the 1 dpa specimens and generally higher Cr-content of the 2 dpa-specimens.

The APT-analysis of the lowest dose level clearly shows phase separation into α and α' phase as well as formation of G-phase precipitates as illustrated by the blue Cr-atoms and green Ni-atoms in the left atomic map of Fig. 1. The 1 dpa (centre) and 2 dpa maps show significantly larger decomposition and G-phase formation compared to the lowest dose.

Table 2 Composition (at.%) from the APT analyses of the ferrite phase of the respective analyzed specimens

Specimen #/Element	0.15 dpa	1 dpa			2 dpa		
	5826	5923	5924	5970	5956	5964	5973
C	0.07	0.09	0.09	0.03	0.12	0.04	0.02
Mo	0.10	0.08	0.07	0.08	0.08	0.11	0.10
O	0.02	0.04	0.05	0.02	0.07	0.01	0.01
Si	2.55	1.10	0.92	1.20	2.38	2.55	2.46
P	0.07	0.10	0.05	0.16	0.06	0.12	0.14
V	0.07	0.11	0.12	0.11	0.09	0.11	0.09
Mn	0.90	0.89	0.88	0.92	0.68	0.77	0.78
Cr	24.5	24.9	24.2	25.3	25.3	27.0	27.3
Co	0.06	0.05	0.05	0.05	0.05	0.05	0.06
Fe	69.2	70.8	71.9	70.0	68.9	66.7	66.4
Cu	0.04	0.03	0.03	0.03	0.03	0.04	0.03
Ni	2.39	1.74	1.50	2.08	2.17	2.50	2.59

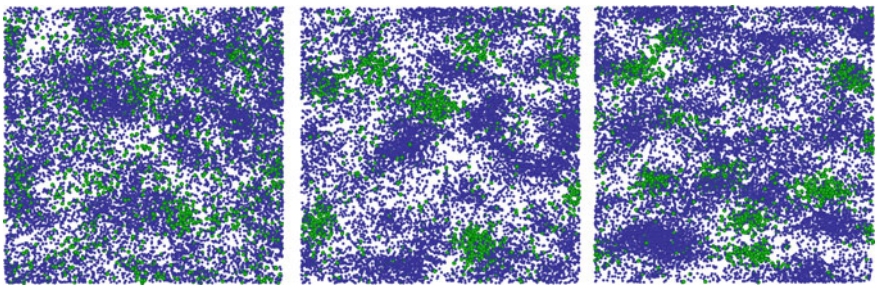

Fig. 1 Atomic maps of projected volumes ($20 \times 20 \times 5$ nm^3) of Cr (blue) and Ni (green) for 0.15 dpa (left), 1 dpa (center) and 2 dpa (right) (Color figure online)

Iso-concentration surface plots, Fig. 2, visually indicate an increase in decomposition with dose, increase in G-phase content and that the position of G-phase precipitates is on the α to α′ phase boundaries, as expected.

The spinodal decomposition wavelength can be regarded as the average distance between α and α' phase and the amplitude is the difference divided by two between the maximum and minimum Cr-content of the α and α′ phase respectively.

Wavelengths and amplitudes are quantified using the radial distribution function (RDF) of Cr [1], and the wavelengths and amplitudes are listed in Table 3. It is observed that the effect of dose on spinodal wavelength is significant between 0.15 dpa and 2 dpa specimens as seen in the left diagram of Fig. 3, where the wave length increasing from 6.4 nm for the lowest dose to 9 nm for the largest wavelength at 2 dpa. These are unfortunately difficult to separate from an effect of increasing Cr-content of bulk ferrite between specimens as seen in the right Fig. 3. The increase of decomposition amplitude with dose and Cr-content are plotted in Fig. 4. Here, the

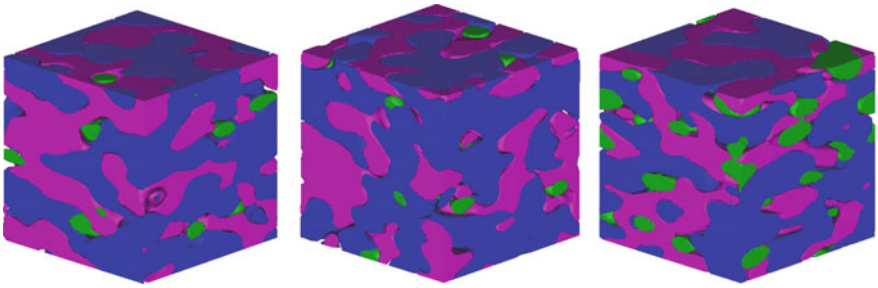

Fig. 2 Iso-concentration plots of 0.15 dpa (left), 1 dpa (center) and 2 dpa (right) respectively showing α (lilac), α′ (blue) and G-phase (green). The size of the box is 20 × 20 × 20 nm^3 (Color figure online)

Table 3 Wavelength and decomposition amplitude for all dose levels

Dose	0.15 dpa	1 dpa			2 dpa		
Specimen #	5826	5923	5924	5970	5956	5964	5973
Wavelength (nm)	6.4	6.5	5.9	7.8	8.9	8.2	9.0
Amplitude (at.%)	43.3	52.2	48.9	49.1	52.1	49.5	50.4

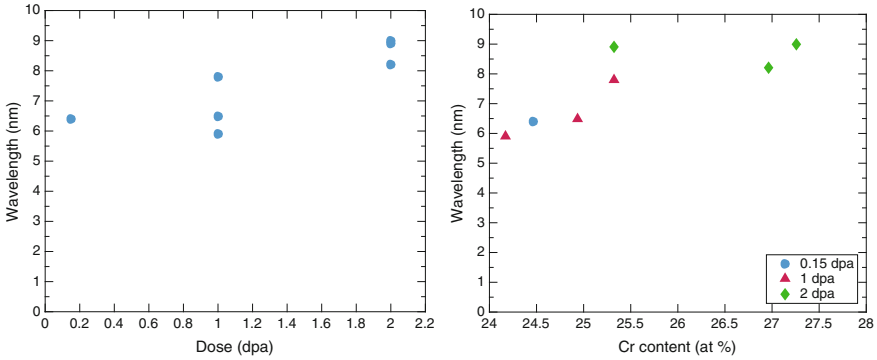

Fig. 3 Decomposition wavelength of Cr as a function of dose (left) and wavelength as a function of Cr-content (right)

effect of Cr-content is very limited but a significantly lower amplitude is seen for the lowest dose.

A comparison of results from this study with literature data from thermally aged components of similar types is done by using an Arrhenius type equation and an activation energy of 243 kJ/mole to recalculate to equivalent aging times and temperatures. Data from aged stainless steel reactor pressure vessel overlay cladding [2], CF3 M [3] and a study of CF8 M [4] using the same evaluation methodology and equipment as used in our experiment, all show a decomposition wave length of <3 nm, and amplitudes of 6 at.% are expected. When comparing

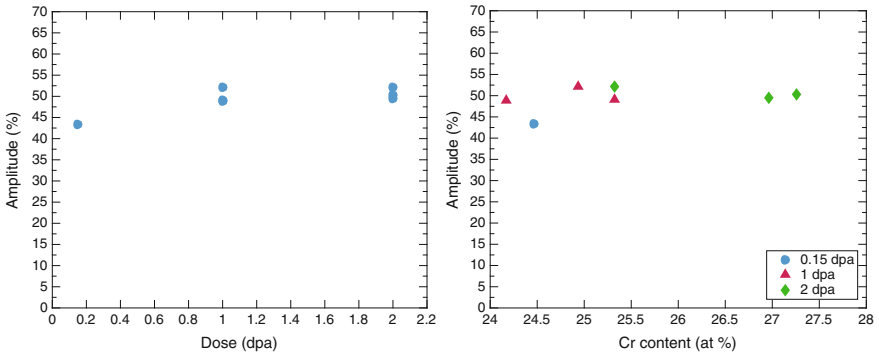

Fig. 4 Decomposition amplitude of Cr as a function of dose (left) and amplitude as a function of Cr-content (right)

these numbers to the obtained wave lengths 5.9–9 nm and decomposition amplitude of 43.3–52.1 at.% measured in this study, it is seen that both decomposition wavelength and amplitude of the current specimens are clearly accelerated by the irradiation for all doses measured and are equivalent to thermal aging times several orders of magnitude above the actual in service times.

G-Phase Formation

The number density of G-phase clusters is as expected similar for all the three dose levels, determined to 4×10^{24}, 2.5×10^{24} and 4×10^{24} m^{-3} for 0.15, 1 and 2 dpa, respectively. From the size distribution in Fig. 5, it is seen that the clusters are still very small at the lowest dose, with a calculated average diameter of 1.4 nm for 0.15 dpa. The average size is in reality smaller than indicated as the clusters are identified using the Maximum separation method [5–7] using Ni, Mn and Si with d_{max} = 0.45 nm and N_{min} = 25. This cut-off size is equivalent to a lower limit of identified clusters of 1.2 nm diameter. Many of the smaller clusters might very well be Ni–Si–Mn-rich clusters, precursors of G-phase, and not crystalline phase (space group $Fm\bar{3}m$). The average size of clusters for 1 and 2 dpa are both 2.0 nm. The G-phase is still growing with dose, which is apparent from Fig. 5, where the number of large clusters is significantly larger for the highest dose. This is also apparent from the right plot in Fig. 6, where the monotonous total increase of Ni in G-phase is compared to the amount in the bulk ferrite. The same monotonous trend is seen for both Mn and Si as well (not shown here).

It can therefore be concluded that the large G-phase particles are coarsening significantly with dose. Significant G-phase formation is common and expected for Mo-containing weld materials, but only to a lesser extent in the Mo-free type weld of this report. G-phase formation is intricately linked to spinodal decomposition by

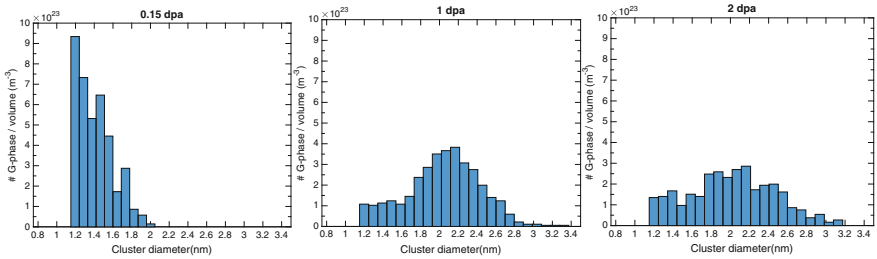

Fig. 5 Size distribution of G-phase in ferrite for 0.15 dpa with average precipitate size 1.41 nm (left), 1 dpa with average size 2.04 nm (center), and 2 dpa with average size of 2.01 nm (right)

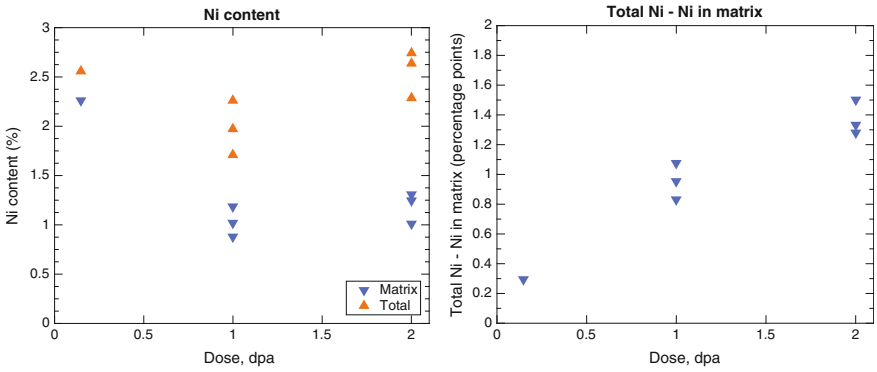

Fig. 6 Ni concentration of the ferrite ("Total") and the ferrite matrix ("Matrix") with respect to dose (left), and the difference of the two (right)

the driving forces of diffusional transport across the α-α′ boundary, but an increase in G-phase is generally indicative of an increase in hardness as well as a reduction in fracture toughness.

Conclusions

In this study, the spinodal decomposition and G-phase formation in the ferrite phase of weld specimens exposed to equal thermal aging and three different fast neutron doses/dose rates have been examined using APT.

It was found that at all of the dose rates tested, the spinodal decomposition and G-phase precipitation increased significantly compared to equivalent thermally aged un-irradiated specimens. An increase in decomposition and G-phase precipitation with dose is seen in the data, but is to date not fully separable from the effect of significant variations in composition between different weld areas of the tested specimens. Further work is ongoing to separate and quantify the compositional and

irradiation effects. Microstructure studies using TEM, SEM/EBSD as well as quantification of mechanical properties and its relation to the microstructure are also planned.

For the low dose rates currently under investigation, the maximum increase in spinodal decomposition is not yet reached at a dose rate of 1×10^{-5} dpa/h or a total of 2 dpa. The lower value of 7×10^{-7} dpa/h at a total of 0.15 dpa is also high enough to substantially alter the rate of spinodal decomposition compared to thermal aging only.

Acknowledgements The authors wish to express their sincere gratitude to Mr. Roger Lundström, who performed specimen extraction and light optical microscopy, and Anders Jenssen for fruitful discussions, both from Studsvik Nuclear AB. EPRI have kindly allowed use of the material. The work was funded by the Swedish Radiation Safety Authority, the Swedish NPPs Materials Group (SUMG) and Studsvik Nuclear AB.

References

1. J. Zhou, J. Odqvist, M. Thuvander, P. Hedström, Quantitative evaluation of spinodal decomposition in Fe–Cr by atom probe tomography and radial distribution function analysis. Microsc. Microanal. **19**, 665–675 (2013)
2. T. Takeuchi, J. Kameda, Y. Nagai, T. Toyama, Y. Matsukawa, Y. Nishiyama, K. Onizawa, Microstructural changes of a thermally aged stainless steel submerged arc weld overlay cladding of nuclear reactor pressure vessels J. Nucl. Mat. **425**, 60–64 (2012)
3. C. Pareige, S. Novy, S. Saillet, P. Pareige, Study of phase transformation and mechanical properties evolution of duplex stainless steels after long term thermal ageing (>20 years). J. Nucl. Mater. **411**(1–3), 90–96 (2011)
4. M. Bjurman, M. Thuvander, F. Liu, P. Efsing, Phase separation study of in-service thermally aged cast stainless steel—Atom probe tomography, in: *Proceedings of the 17th International Symposium on Environmental Degradation of Materials in Nuclear Power Systems*, CNS 2015
5. A. Heinrich, T. Al-Kassab, R. Kirchheim, Investigation of the early stages of decomposition of Cu/0.7 at.% Fe with the tomographic atom probe. Mat. Sci. Eng. **A353** (2003) 92_/98
6. D. Vaumousse, A. Cerezo, P.J. Warren, A procedure for quantification of precipitate microstructures. Ultramicroscopy **95**, 215–221 (2003)
7. J.M. Hyde, C.A. English, An analysis of the structure of irradiation induced Cu-enriched clusters in low and high Nickel welds, Materials Research Society Symposium, 2000, pp. R6.6.1–R6.6.12. Boston

Part VIII
Welds, Weld Metals, and Weld Assessments

The Use of Tapered Specimens to Evaluate the SCC Initiation Susceptibility in Alloy 182 in BWR and PWR Environments

Juxing Bai, Stefan Ritter, Hans-Peter Seifert, Marc Vankeerberghen and Rik-Wouter Bosch

Abstract A better understanding of stress corrosion cracking (SCC) initiation is one of the keys towards developing proactive mitigation techniques for the safe and economic operation of nuclear power plants. However, SCC initiation laboratory studies are very time consuming and require multiple specimens, Hence, in the framework of the European "MICRIN+" research project, an accelerated test method was evaluated for screening the SCC susceptibility in a relatively short time frame. The effects of surface roughness and strain rate on SCC initiation susceptibility in Alloy 182 weld metal were evaluated in simulated BWR and PWR environments. Constant extension rate tensile tests were performed using flat tapered tensile specimens with different surface finishes (ground and polished) in hydrogenated water at 288 and 340 °C. The surface crack distribution and crack length as well as stress thresholds for SCC initiation were analyzed by detailed post-test quantitative characterization. Some test data were analyzed by the EngInit SCC initiation model. The accelerated test technique was successfully applied and revealed very promising results. The highest crack density and lowest stress thresholds for crack initiation were found on the ground surfaces and at the lowest strain rates. A test's load response can be fed to the EngInit model; with parameters to be determined by comparing EngInit's damage to the experimental surface crack distributions. EngInit can potentially be used to link laboratory test results on flat tapered specimens to SCC initiation in components in the field.

Keywords Stress corrosion cracking · Ni-base alloy · BWR · PWR · Hydrogen · Surface finish · Initiation · Constant extension rate tensile test · SCC initiation modeling

J. Bai (✉) · S. Ritter · H.-P. Seifert
Nuclear Energy and Safety Research Division, Paul Scherrer Institute (PSI),
5232 Villigen PSI, Switzerland
e-mail: juxing.bai@psi.ch

M. Vankeerberghen · R.-W. Bosch
SCK•CEN, Boeretang 200, 2400 Mol, Belgium

J.H. Jackson et al. (eds.), *Proceedings of the 18th International Conference on Environmental Degradation of Materials in Nuclear Power Systems – Water Reactors*, The Minerals, Metals & Materials Series, https://doi.org/10.1007/978-3-319-68454-3_55

Introduction

The Ni-based Alloy 182 is widely used in light water reactors as weld filler metal to join the low-alloy steel reactor pressure vessel to both wrought Ni-based alloys (e.g., Alloy 600) and austenitic stainless steels (e.g., AISI 304L, 316L). In recent years several intergranular stress corrosion cracking (SCC) incidents occurred in Alloy 182 dissimilar metal welds in both boiling water (BWRs) [1–4] and pressurized water reactors (PWRs) [5–7], which affected the safe and economic operation of nuclear power plants.

An important parameter that affects SCC initiation of structural materials is the surface condition that strongly depends on the fabrication (e.g. welding technique), machining and surface finishing techniques. The impact of cold-work on SCC has been known for a long time [8]. Numerous field observations clearly show the detrimental role of surface and unintentional bulk deformation on SCC in both BWRs and PWRs [9]. Laboratory investigations have yielded solid evidence that plastic bulk and especially surface deformation promote SCC initiation and growth [10–12]. In practice, cold-worked layers are produced by processes such as abrasive particle blasting, grinding, planning and turning. Thus, the control of nuclear component fabrication, weld repair and SCC mitigation by surface modification require a better understanding of the effect of surface quality on SCC. The nature of the role of cold-work in SCC is quite complex. It affects surface residual stress/strain, yield stress, deformation response, microstructure and also corrosion behavior. This complex role of cold-work on SCC is thus thought to be one of the reasons for the lack of international guidelines on surface quality.

SCC initiation testing under plant relevant conditions is very time consuming and requires multiple specimens. Therefore, accelerated, short-term lab tests under much more aggressive (creviced) environmental, mechanical (e.g., notched, CERT) and material (high cold-work levels) are usually performed that are only qualitative with limited transferability to field components. Within the *MICRIN* + research project (a sub-project of the Euratom 7th Framework Programme project *NUGENIA-PLUS*) the effect of surface condition was evaluated by constant extension rate tensile (CERT) tests with flat tapered tensile specimens [9]. To tie the results of such CERT tests on flat, tapered, tensile specimens to the behavior of components subjected to a different load history, a suitable model is required. EngInit [13, 14] is such a model that aims to make this link. Applying the EngInit model to CERT test results on flat tapered tensile specimens can yield parameter values which subsequently can be used when applying EngInit to components.

In the current paper, results from CERT tests at three different strain rates with Alloy 182 in 288 and 340 °C hydrogenated water are presented and the effects of strain rate and surface finish on the SCC initiation susceptibility are discussed. The load response is fed to an EngInit model and the latter's parameters are determined by fitting the calculated damage distribution to the measured surface crack distribution.

Experimental

Material and Specimen

The Alloy 182 test material is a low-alloy steel reactor pressure vessel nozzle to stainless steel safe end dissimilar metal weld joint from the decommissioned nuclear power plant Lemoniz in Spain. The chemical composition of the Alloy 182 weld metal is summarized in Table 1. Flat tapered specimens with a continuously varying width, but constant thickness along the gauge section were cut by electrical discharge machining (EDM) from the as-welded bulk Alloy 182 weld metal. The dimensions and geometry of the tapered specimens are shown in Fig. 1. The sample axis was perpendicular to the welding direction and the sample plane corresponds to the T-S plane of the weld, as shown in Fig. 1. Figure 2 shows an electron backscatter diffraction (EBSD) analysis of the Alloy 182 weld. The weld consisted of different beads woven together forming a complex pattern. Metallographic analysis revealed the size of the different features, like the size of the grains, dendrites and weld beads. The grains consisted of colonies of dendrites having the same orientation. These grains had a diameter of 40–140 µm and were several mm long. The bead thickness was about 4 mm and the width was around 15 mm. Typically the distances between the dendrite were between 7 and 20 µm. The mechanical properties are summarized in Table 2. The yield stresses of the testing material showed relative large scattering which could be due to the inhomogeneous microstructure. Prior to the SCC testing, the damaged specimen surfaces by EDM were removed by grinding, one site of the specimens was mechanically ground up to 180 grit with emery paper and the other site was given a 1 µm polish finish.

Environment and Methodology of the SCC Initiation Tests

The SCC initiation tests under PWR conditions were performed at SCK•CEN in a stainless steel autoclave, which was attached to a refreshing high-temperature water loop. The test environment was simulated slightly alkaline PWR water under low-flow conditions (20 L/h) at 340 °C with 2 ppm Li, 1000 ppm B and 3.13 ppm H_2, which corresponds to a pH_T of 7.6 an electrochemical corrosion potential (ECP) of −888 mV_{SHE} (Ni stability region). The SCC initiation tests in BWR/HWC environment were performed at PSI in a 1 L stainless steel autoclave with refreshing high-temperature water loop in neutral high-purity water (pH_T = 5.65) under low-flow conditions (6 autoclave exchanges per hour) at 288 °C with

Table 1 Chemical composition of the Alloy 182 test weld in wt.%

Ta	Si	Mn	Cr	Nb	Fe	Ti	Ni
0.022	0.5	6.7	14.7	1.07	9.9	0.33	Bal.

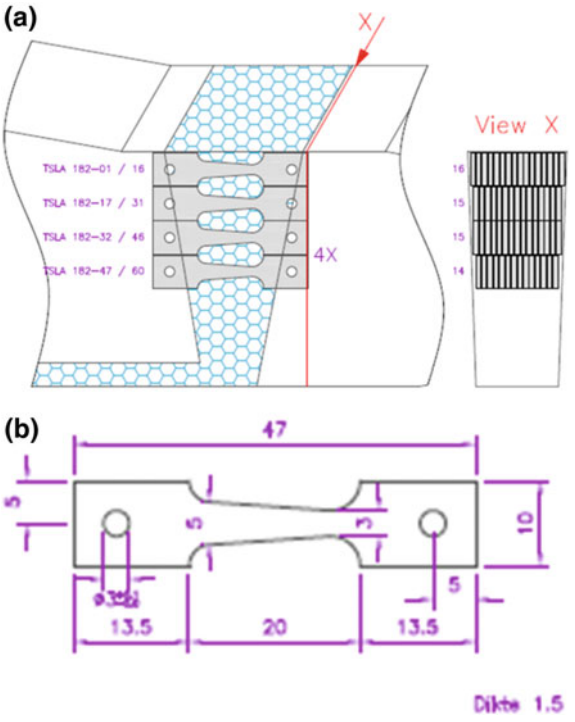

Fig. 1 **a** Orientation of the specimen in the dissimilar metal weld; **b** specimen specifications (all dimensions in mm)

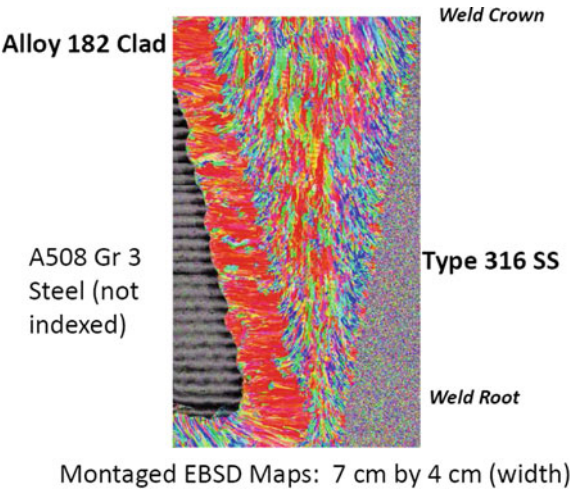

Fig. 2 EBSD analysis of the Alloy 182 weld

0.36 ppm DH and an ECP of −555 mV_{SHE} (Ni/NiO phase transition boundary). During the experiments all important environmental parameters at inlet and (partly at) outlet (DH, DO, conductivity, temperature, pressure, flow) were recorded continuously. The ECP of the specimens, the autoclave potential and the redox

Table 2 Mechanical properties obtained from slow strain rate test at room temperature, 288 and 340 °C in air (mean values from three tests at each temperature)

Test temperature	Yield stress (MPa)	Ultimate tensile strength UTS (MPa)	Uniform strain (%)	Strain to failure (%)
25 °C, Mean value	440	639	24	29
288 °C, Mean value	368	564	22	27.5
340 °C, Mean value	380	588	26.5	31

potential of the high-temperature water environment (Pt-electrode) were measured with a $Cu/Cu_2O/ZrO_2$-membrane electrode.

CERT tests with flat tapered tensile specimens were carried out until specimen failure. The variable cross section of the tensile specimens results in a continuous stress gradient along the gauge section, which is the main advantage of this type of specimen. Before application of the loading, the specimens were pre-oxidized in the specified test environment at a low constant pre-load of 100 N for 7 days to get a uniform and stable oxide film. After the pre-oxidation phase, the specimens were strained at nominal strain rates of 1×10^{-6} s^{-1}, 5×10^{-7} s^{-1} and 1×10^{-7} s^{-1} (nominal strain = $\Delta l/l_0$, l_0 = initial gauge length, Δl = extension after CERT test).

After the CERT tests, the gauge sections of the tapered tensile specimens were examined with a scanning electron microscope (SEM). Surface crack lengths and positions were measured and the number of cracks was counted. From these data, surface crack length density and surface crack number density at different locations along the gauge section were evaluated. For this purpose, the specimen surface was divided in many trapezoidal zones with a length of 0.5 mm along the gauge length. The crack length density and number density were calculated by dividing the total length of cracks in μm and number of cracks in each trapezoidal zone by the corresponding trapezoidal surface area in mm^2, respectively. The maximum true stress experienced at each position of the trapezoidal zones was obtained by dividing the maximum load experienced during the CERT test by the local cross section area after the CERT experiment. To assess the stress threshold for SCC crack initiation, the position of maximum cross-section, where indications of cracking could still be found, was identified by SEM. The corresponding threshold stress in this region was estimated by a simplified method that ignores the moderately tri-axial and non-uniform stress state in the tapered specimen. The maximum critical cross-section is obtained by determining of the boundary between the zone with indication of SCC initiation and without any cracks. As fixed reference point the end of the tapered specimen at the thick side of the gauge section and the distance between the cracking boundary and the reference point was measured. Then this distance is taken and the cross section of the corresponding specimen geometry before the test at this distance from the end of the specimen is taken as critical cross-section. The threshold stress at this specific position was finally obtained by dividing the maximum load experienced during the test by the local critical cross section.

EngInit Model Description

EngInit was originally developed as an engineering model for time-to-failure evaluation of thin-walled, irradiated components of 316 stainless steel under nominal PWR-relevant SCC conditions. The model assumes that damage can be calculated from integrating a damage rate over time, i.e.

$$D(t) = \int_0^t \dot{D}(\tau)\, d\tau$$

The original damage rate was a power-law function of the stress level, i.e.

$$\dot{D} = a\left((\sigma - \sigma_{threshold})/\sigma_{yield}\right)^b,$$

but, for more ductile materials, a strain-based damage rate function could be envisaged, i.e.

$$\dot{D} = a(\varepsilon - \varepsilon_{threshold})^b.$$

The original failure criterion was determined by considering that time-to-failure is inversely proportional to accumulated damage, $t_f \propto 1/D$. This corresponds to failure when the following damage function reaches unity, i.e.

$$Z(t) = t \int_0^t \dot{D}(\tau)\, d\tau \to 1.$$

Time-to-failure, or here, time-to-initiation can also be defined when damage reaches unity, i.e.

$$D(t) = \int_0^t \dot{D}(\tau)\, d\tau \to 1.$$

EngInit is distinct from other models in that it allows the loading history to be taken into account. This is useful for the CERT test on flat, tapered, tensile specimens (as described in Section "Environment and Methodology of the SCC Initiation Tests"). It allows the comparison of static and dynamic loading and the associated difference between the real, constant-load threshold (the one from the model) and the observed threshold in the CERT (see Appendix). Simultaneously, EngInit can be used for post-processing transient finite element stress/strain calculations to determine the achieved damage. This allows for damage evaluation on components subjected to a load history. However, the latter has not been explored for biaxial surface stress situations.

Results and Discussion

Surface Cracking Morphology and Crack Distribution

All specimens failed at the thinnest location along the tapered gauge section. SCC crack initiation has been found in all specimens (both, on the rough/ground and smooth/polished sites). Figure 2 shows light microscope pictures of both ground and polished surfaces of a specimen tested in PWR and BWR/HWC environments. There is a clear difference between the two surface finishes, the ground surfaces turned dark after high-temperature water testing and obviously seemed to be more oxidized, while the polished surfaces were still bright, shiny and light brownish. The difference in surface character might indicate a different corrosion performance between ground and polished surfaces. A typical example of cracking on the ground surface from specimen A182-TSLA-55 tested with $1 \times 10^{-7}s^{-1}$ strain rate is shown in Fig. 3. The cracks show clear intergranular features and normally have substantial crack openings. Figure 4 shows an example of the cracking on the polished surface of the same specimen. The crack has a relatively large opening and is zig-zag shaped (this type of crack is termed as "thick crack"). Beside this crack type, there is a different type of limited intergranular attack observed on polished surfaces, as shown in Fig. 5a. The intergranular cracks seem to be quite shallow and with very little crack openings, and always found to be perpendicular to the main loading direction. This crack type is termed "thin crack" in this paper. The thin cracks can be found on a relative large area in the tapered gauge section. On the polished surface, oxidized grain boundaries are visible under the SEM, as shown in Fig. 5b. The crack surface length versus crack opening width distribution of thick and thin cracks is shown in Fig. 7. For thick cracks, the crack length/crack opening width ratio is typically around 10; for thin cracks, this ratio is typically greater than 70. The crack length distribution of both, thin and thick cracks on the polished surface of the specimen tested in 340 °C hydrogenated water with 1×10^{-7} s^{-1} strain rate is shown in Fig. 8. It can be seen that thin cracks are homogenously distributed over the whole area with cracks, while the length density of thick cracks increases exponentially with applied true stress. It is important to notice, that thin cracks also exist in the high strain/stress region in the tapered gauge section (Fig. 9). The thin cracks seem to represent a limited grain boundary attack at more SCC resistant grain boundaries (for example, low angle grain boundaries), which seem not to grow deep into the bulk material even under very high applied stresses. They were thus not considered as crack initiation and not included in the further quantitative analyses (Fig. 6).

Above the SCC initiation threshold stress, the surface crack length and number density exponentially increased with the applied true stress level for all strain rates and surface finishes. The crack length and number density distribution of both sides of the specimen tested in simulated PWR environment at 340 °C with an extension rate of $1 \times 10^{-7}s^{-1}$ are exemplarily shown in Figs. 10 and 11. This behavior is well predicted using the engineering model *EngInit* developed at SCK•CEN (see Section "EngInit Model").

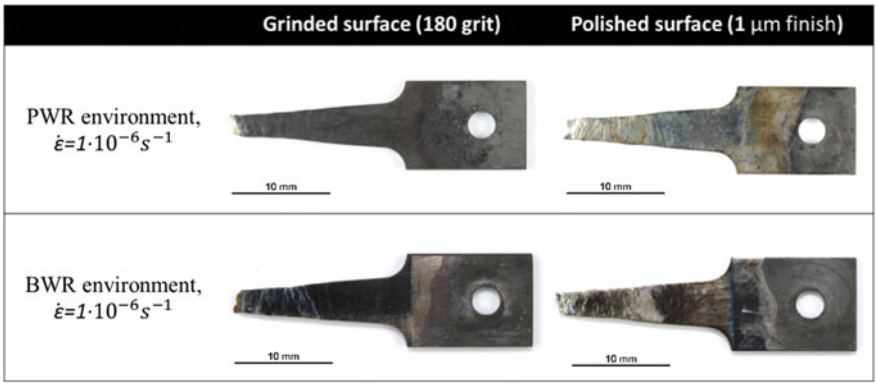

Fig. 3 Light microscope pictures showing two different surfaces of the tapered specimens tested in different environments (upper: specimen tested in simulated PWR environment at 340 °C, lower: specimen tested in simulated BWR/HWC environment at 288 °C)

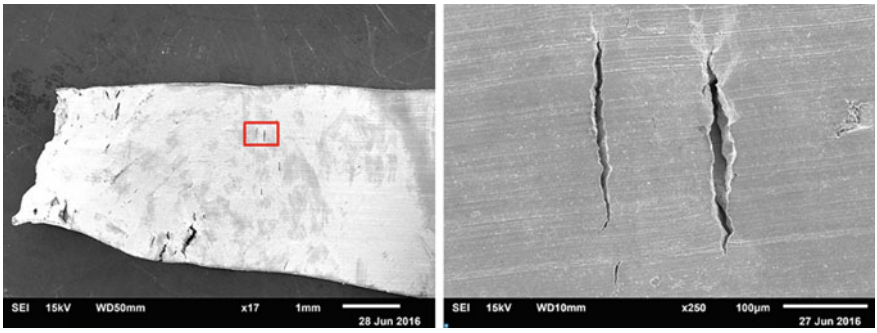

Fig. 4 Typical crack morphology on the ground surface on specimen A182-TSLA-55 (tested under PWR condition with strain rate of 1×10^{-7} s^{-1})

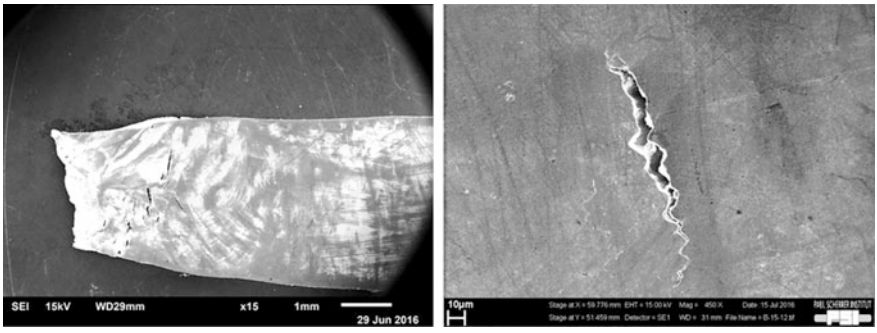

Fig. 5 Typical "thick crack" morphology on the polished surface (1 µm finish) on specimen A182-TSLA-55 (tested under PWR condition with strain rate of 1×10^{-7} s^{-1})

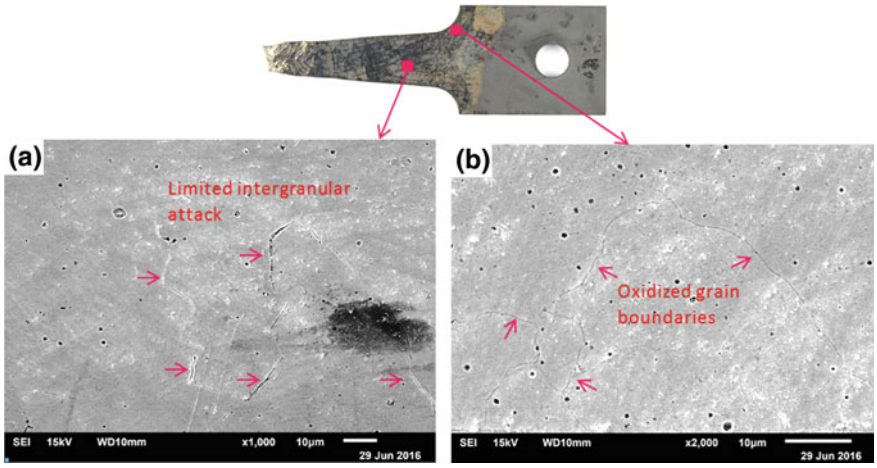

Fig. 6 Limited intergranular attack (thin crack) **a** and oxidized grain boundary **b** on polished surface on specimen A182-TSLA-55 (tested under PWR condition with strain rate of 1×10^{-7} s^{-1})

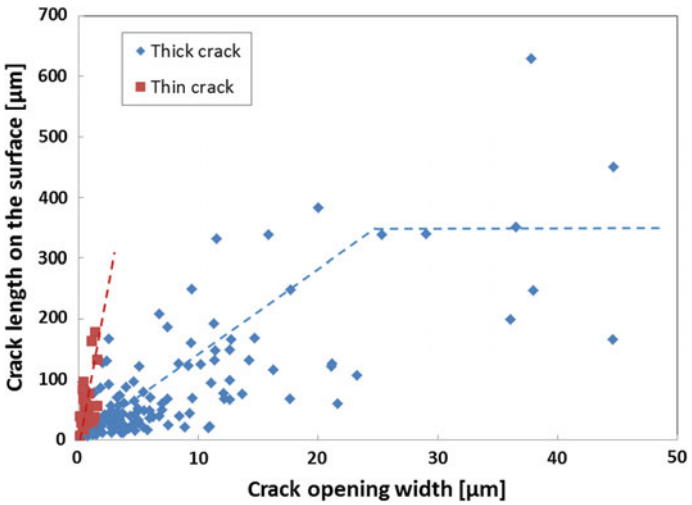

Fig. 7 Crack surface length versus crack opening width distribution of thick and thin cracks

Effect of Strain Rate and Surface Finish

The stress threshold values for SCC initiation are plotted as function of strain rates in Fig. 12. The extrapolation of the stress thresholds to very slow strain rates was used as an estimate for the "constant load" SCC initiation threshold. The "constant load" SCC initiation thresholds at both testing temperatures and surface conditions

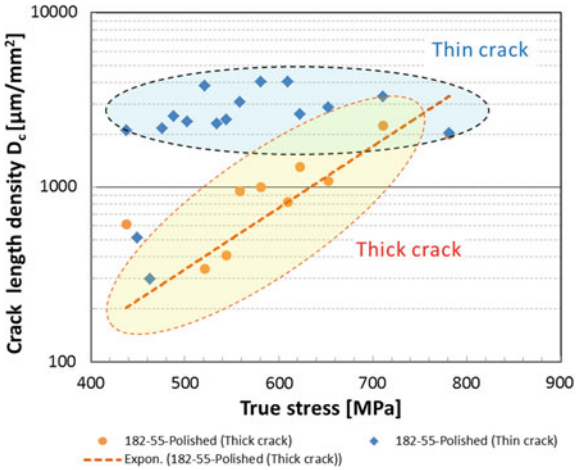

Fig. 8 Crack length density distribution on the polished surface of a specimen tested in 340 °C hydrogenated water (PWR) with 1×10^{-7} s^{-1} strain rate. The thin cracks are homogenously distributed over the whole cracked area, whereas the length density of thick cracks increases exponentially with applied true stress

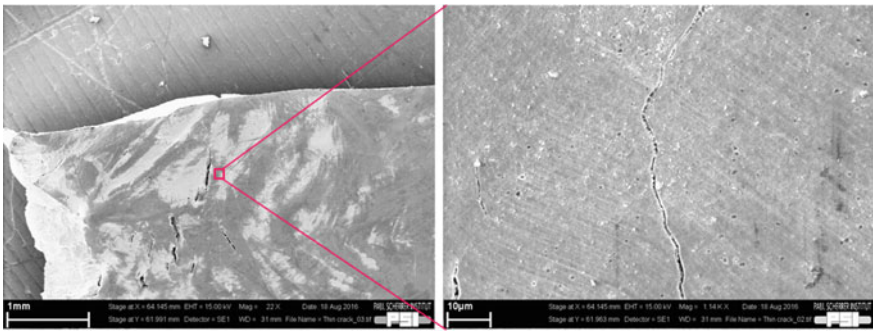

Fig. 9 Example of a thin crack in the high stress/strain region in the tapered gauge section

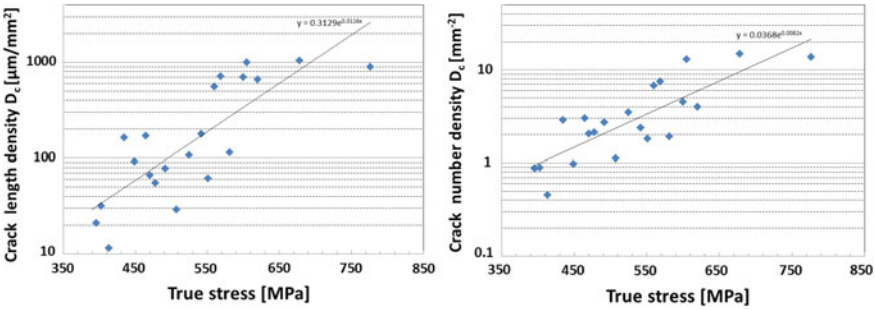

Fig. 10 Crack length (left) and number (right) density versus true stress of specimen A182-TSLA-55 on ground surface (strain rate = 1×10^{-7} s^{-1} PWR, 340 °C)

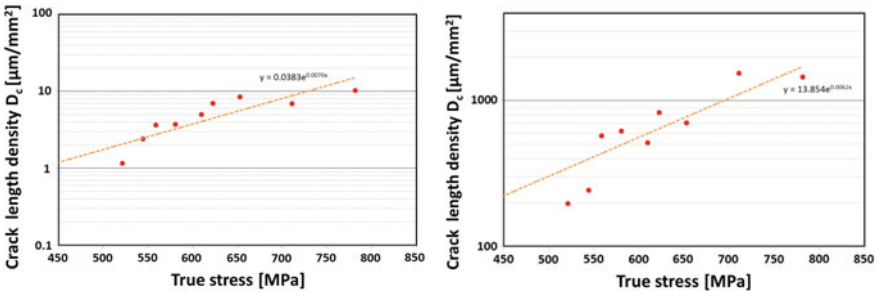

Fig. 11 Crack length (left) and number (right) density versus true stress of specimen A182-TSLA-55 on polished surface (strain rate = 1×10^{-7} s^{-1} PWR, 340 °C)

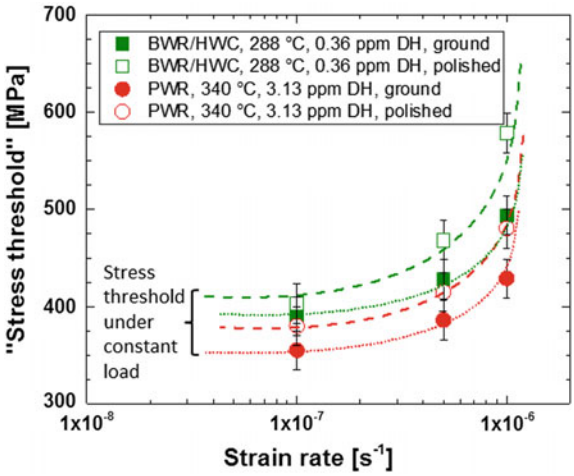

Fig. 12 Threshold stress values for SCC initiation as function of strain rate of the specimens tested under PWR conditions at 340 °C (red points) and BWR/HWC conditions at 288 °C (green points)

are compared in Fig. 13. An estimate of the uncertainty can be made: the intergranular SCC cracks get much shorter and narrower with decreasing distance to the last section, where crack initiation can still be observed. In some cases it was very difficult to unambiguously distinguish real SCC crack initiation from grain boundary attack that results in an uncertainty in threshold stress data for crack initiation in the range of 20 MPa. The stress threshold values for SCC initiation of ground surface at BWR and PWR temperatures were very close or slightly higher than the yield stress, as indicated in Fig. 12. However, due to the relative large scattering range of the measured yield stresses at high-temperatures, definition of a concrete stress/yield stress ratio was difficult.

The polished surfaces showed higher stress threshold values than the ground surfaces for BWR/HWC and PWR conditions, which indicates a higher resistance against SCC. Aggressive grinding causes higher surface layer cold-work level compared to polishing, which may increase the yield stress and thus tend to increase the SCC susceptibility. It is generally accepted that the time to SCC initiation could

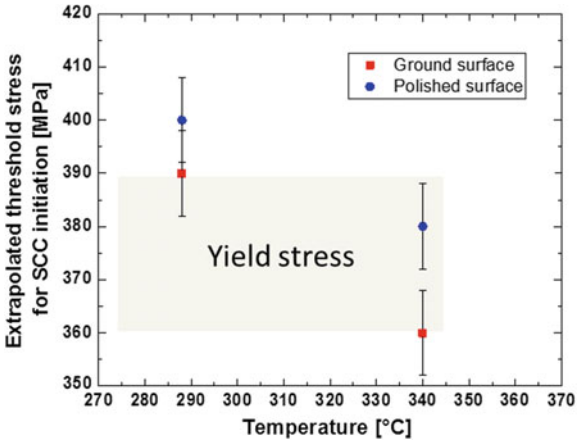

Fig. 13 Extrapolated threshold stress values for SCC initiation of ground and polished surfaces

be very long if loaded below or at the yield stress (no plastic deformation) of the testing material.

Based on these results, the CERT test could be regarded as an attractive option for general assessment of the SCC initiation properties of a material under realistic environmental conditions in relative short time. But one has to keep in mind that the involved dynamic loading with continuous plastic straining is more aggressive than constant loading or displacement. In CERT tests, the degree of environmental degradation is dependent on the test time (strain rate) and the magnitude of the plastic strain. For a given strain, a lower strain rate yields a longer testing time for the environment to act, which would promote SCC. In case of CERT testing with tapered specimen, this would lead to a lower threshold strain/stress value for crack initiation. On the other hand, the limited test duration of this accelerated test might eliminate/oversee certain time-consuming precursor processes that may lead to SCC initiation in long-term test, but not in CERT experiments.

The stress threshold values of both, ground and polished surfaces of specimens tested under PWR conditions are lower than those from tests under BWR/HWC conditions, which indicates the increasing aggressiveness with increasing temperature. The different behavior can also be seen in Fig. 14, where the micrographs of two specimens with the same surface finish, tested at the same strain rate but in the two different environments (BWR/HWC or PWR) are compared. More severe cracking can be observed in the specimen tested at 340 °C (PWR) compared to the one tested at 288 °C (BWR/HWC). This behavior is not surprising, because SCC initiation in Ni alloys is a thermally activated process with a rather high activation energy, i.e., the higher the temperature the higher the susceptibility to SCC. However, it has to be stated that an accurate comparison of temperature effects requires that all parameters which influence SCC, other than temperature, should be maintained constant. Therefore, SCC thermal activation tests in Ni-based alloys should be conducted at a constant ΔECP relative to the Ni/NiO phase transition line. But in the current work, the CERT tests under BWR conditions were conducted

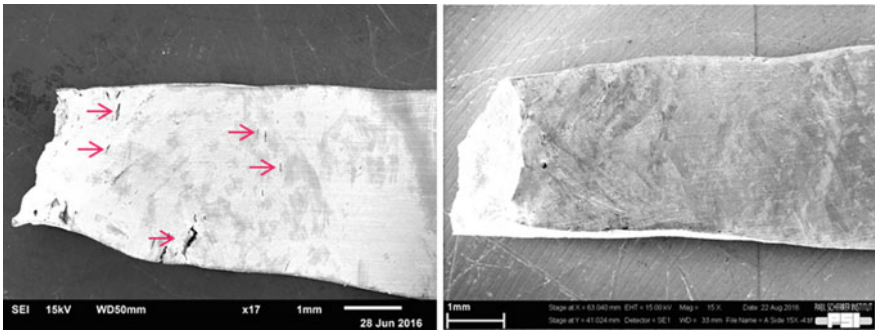

Fig. 14 Low magnification SEM micrographs of specimen A182-TSLA-55 (strain rate = 1×10^{-7} s^{-1}, ground side, PWR, left) and specimen A182-TSLA-59 (strain rate = 1×10^{-7} s^{-1}, ground side, BWR/HWC, right). Many cracks are visible on specimen A182-TSLA-55, indicated with red arrows, but no cracks can be seen on specimen A182-TSLA-59

with a DH level right at Ni/NiO phase transition line, while the tests under PWR conditions were conducted in the Ni stability region with about 20 mV distance to the Ni/NiO phase transition line (the Ni/NiO phase transition boundary is at a DH content of $\sim$1.34 ppm with an ECP −866 mV_{SHE} at a pH_T of 7.6).

EngInit Model

Figure 15 shows a comparison between EngInit-calculated damage distributions and normalized crack length/number density distributions. The horizontal axis is the distance along the specimen length, from 16 mm at the widest part (5 mm) to 30 mm at the narrowest part (3 mm) of the tapered section. The measured crack length and number density distributions are normalized by their peak values along the gauge section. This is done to correspond to damage distributions which are supposed to yield a damage of one at failure. Failure happens in the smallest cross section, hence, towards 30 mm. The primary input to the EngInit calculations are the loading histories as shown in Fig. 16. These are then run through a model with a stress-based damage rate and with failure when damage reaches one. EngInit parameters b (exponent) and σ_t (threshold stress fraction) are respectively set to 4 and 40%. EngInit's a values for the ground specimens are 0.084 (for 1×10^{-6}/s), 0.098 (for 5×10^{-7}/s) and 0.018 (for 1×10^{-7}/s). Hence, it turns out that the a values are displacement rate sensitive. This could be understood as follows. The higher the displacement rate, the more film ruptures and, hence the higher the magnitude of the damage rate (a value). However, with increasing displacement rate the effect saturates. At the lower displacement rate re-passivation enables the healing of damage resulting in a lower a value or damage rate magnitude. Also here the effect will saturate from the point when repair due to re-passivation overtakes

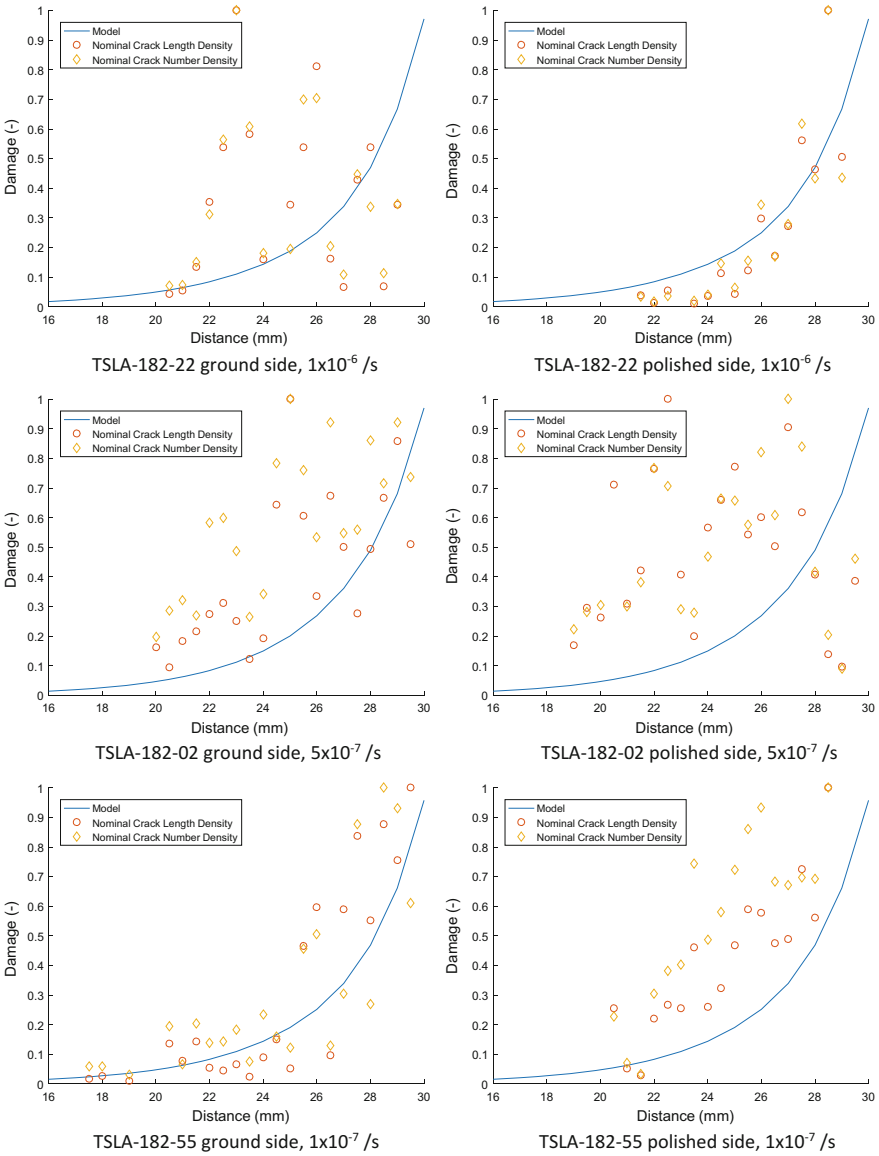

Fig. 15 Approximate fitting (a values only) of the EngInit-calculated damage distribution to normalized crack length and number density distribution (b = 4, σ_t = 0.4). Alloy 182 Lemoniz exposed to simulated PWR water (2 ppm Li, 1000 ppm B, 35 ccH_2/kg at 155 bar and 340 °C). Strain rates: TSLA-182-22: 1 × 10^{-6}/s; TSLA-182-02: 5 × 10^{-7}/s; TSLA-182-55: 1 × 10^{-7}/s

the film rupture rate. As a result one will need to implement a sigmoid type function for the dependence on the local strain rate (which is however different from the displacement rate and depends on the location along the specimen). Figure 17

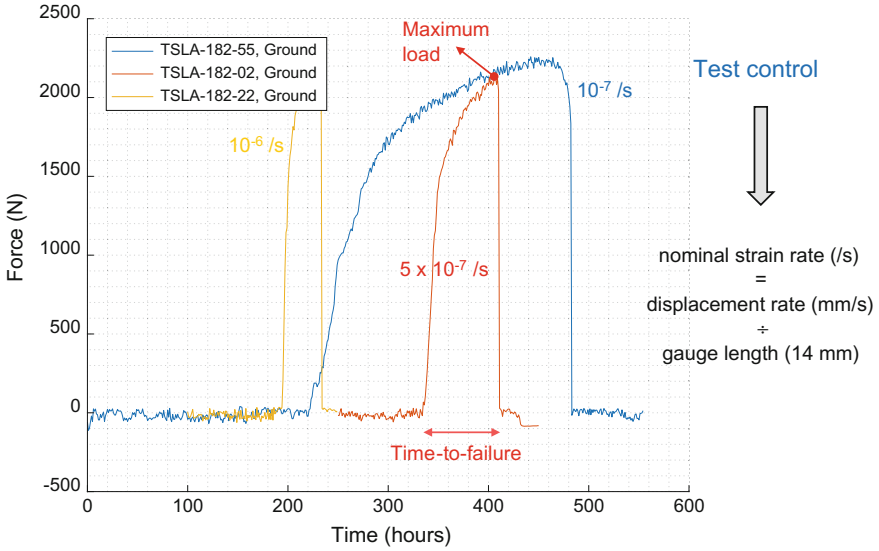

Fig. 16 EngInit's starting point: measured loading histories. Alloy 182 Lemoniz exposed to simulated PWR water (2 ppm Li, 1000 ppm B, 35 ccH_2/kg at 155 bar and 340°C). Strain rates: TSLA-182-22: 1×10^{-6}/s; TSLA-182-02: 5×10^{-7}/s; TSLA-182-55: 1×10^{-7}/s

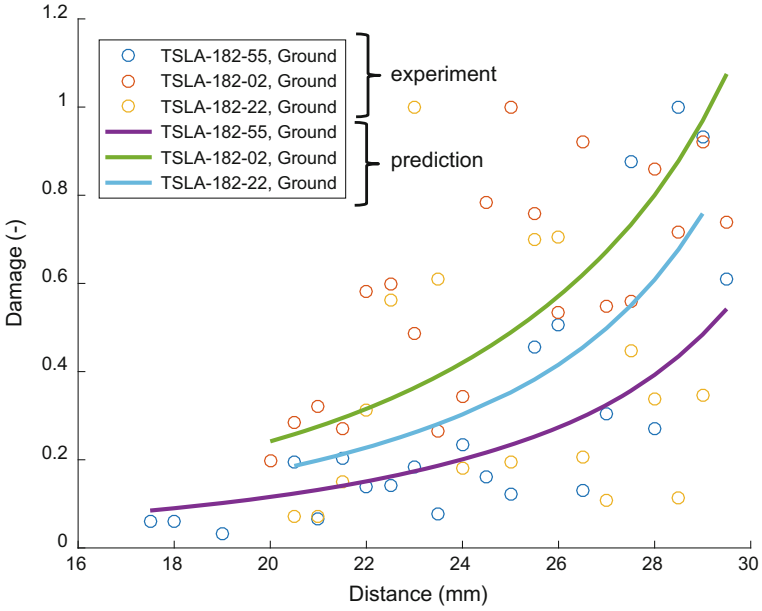

Fig. 17 Approximate fitting of the EngInit-calculated damage distribution to normalized crack length and number density distribution after displacement rate correction. Alloy 182 Lemoniz exposed to simulated PWR water (2 ppm Li, 1000 ppm B, 35 ccH_2/kg at 155 bar and 340 °C). Strain rates: TSLA-182-22: 1×10^{-6}/s; TSLA-182-02: 5×10^{-7}/s; TSLA-182-55: 1×10^{-7}/s

shows the results of an approximate correction for the displacement rate dependency of the damage rate. Note that EngInit, with the same EngInit parameters but different loading histories, reproduces the variance in the measured nominal crack length/number density distributions.

Figure 15 shows approximate (i.e. visual) fitting of normalized crack length or number density distributions to a stress-based EngInit model. Some notes on the fitting are in order. First, one needs to note that damage is commonly assumed to be equal to one at failure or initiation. In EngInit one can adjust parameter values (a, b and σ_t) to yield a damage equal to one (here taken at failure). Secondly, one needs to note that the crack length or number density distributions need to be normalized to yield a maximum value of one. Hence, the shape of the distribution is kept but its maximum value is set to one. Thirdly, one needs to note that subsequent fitting is not trivial. Reasonable all-parameter fits could only be obtained for two of the graphs in Fig. 15 (the bottom left and the top right ones). Hence, in order to progress our research we set the exponent b to 4 and the threshold fraction to 40% of the yield. The former corresponds to a stress dependency observed on steam generator tube failures. The latter is based on a previous fitting of EngInit to O-ring test results on irradiated material, although we need to realize that for nickel-based alloys this value will be higher; see Fig. 11 which would yield values between 80 and 90% (note however the comment made before that a real, constant load threshold might also differ from a visually observed threshold in a CERT test—see Appendix). As a result, only the a parameter had to be fitted, yielding for the ground surface side respectively the values stated above.

Summary and Conclusions

An accelerated SCC initiation testing technique has been applied to study the effect of surface finish and environment on the SCC initiation susceptibility in Alloy 182 weld metal. The results also have been used as input for EngInit model calibration and predictions. The main conclusions can be summarized as follows:

- CERT testing has been performed with Alloy 182 weld metal using flat tapered tensile specimens with different surface finishes at two temperatures (BWR/HWC or PWR conditions) and three different strain rates. The test results revealed decreasing stress thresholds with decreasing strain rates. The methodology of extrapolation of the SCC threshold stress values to constant load (zero strain rate) seemed feasible. The testing technique represents a promising method to screen the SCC initiation susceptibility of light water reactor structural materials in a relative short time frame.
- The polished specimen surfaces showed a lower SCC initiation susceptibility of the Alloy 182 compared to ground surfaces for both BWR/HWC and PWR conditions.

- PWR conditions revealed higher crack densities and lower stress thresholds for SCC initiation than BWR/HWC conditions, which indicates a significant temperature effect of SCC initiation.
- The (preliminary) EngInit model with a stress-based damage rate, a failure criterion set at damage equal to one and a displacement rate dependence on the a value seems to yield a reasonable comparison to experimental normalized crack length/number densities.

Acknowledgements Tracteble Engineering (Belgium) is gratefully acknowledged for providing the Alloy 182 test material. The research leading to these results was partly funded by the European Atomic Energy Community's (Euratom) Seventh Framework Programme FP7/2007–2013 under grant agreement No. 604965. Thanks are also expressed to Yong-Lin Chen (National Tsing-Hua University, Taiwan) and Beat Baumgartner (PSI) for their experimental support.

Appendix: Note on the Real and Apparent Stress Threshold

The real stress threshold, according to the following, stress-based Enginit model is $\sigma_{threshold}^{fraction}$.

$$\dot{D} = \begin{cases} 0 & \sigma \leq \sigma_{threshold}^{fraction} \\ a\left(\sigma^{fraction} - \sigma_{threshold}^{fraction}\right)^{b} & \sigma > \sigma_{threshold}^{fraction} \end{cases}$$

The superscript fraction indicates that the (threshold) stress is expressed as a fraction of the yield stress of the material. The damage rate $\dot{D}$ is zero below the real stress threshold. Accumulated damage is expressed as $D = \int \dot{D}\, dt$.

In a constant stress test, assuming the failure criterion $D_f = 1$, one gets

$$t_f = \begin{cases} \infty & \sigma \leq \sigma_{threshold}^{fraction} \\ \frac{1}{a}\left(\sigma^{fraction} - \sigma_{threshold}^{fraction}\right)^{-b} & \sigma > \sigma_{threshold}^{fraction} \end{cases}$$

Hence, note that one would have to test for an infinitely long time to get at the stress threshold.

Similarly, the threshold might be difficult to access from constant cross-head displacement rate tests where the threshold stress would be evaluated from different tests at a decreasing cross-head displacement rate.

In a constant stress rate test, $\sigma^{fraction} = \dot{\sigma}^{fraction} t$, and assuming the initiation criterion $D = 1$, one gets

$$\sigma_{initiation}^{fraction}(@D=1)=\sigma_{threshold}^{fraction}+\left(\dot{\sigma}^{fraction}\frac{b+1}{a}\right)^{\frac{1}{b+1}},$$

where $\sigma_{initiation}^{fraction}$ is the stress fraction reached at the time to initiation. In the limit, for an infinitely low stress rate, the stress fraction at initiation will equal the stress fraction threshold, i.e.

$$\lim_{\dot{\sigma}^{fraction}\to 0}\sigma_{initiation}^{fraction}=\sigma_{threshold}^{fraction}.$$

Conversely, one can express the associated time as

$$t_{initiation}(@D=1)=\frac{\sigma_{threshold}^{fraction}}{\dot{\sigma}^{fraction}}+\left(\dot{\sigma}^{fraction}\right)^{\frac{-b}{b+1}}\left(\frac{b+1}{a}\right)^{\frac{1}{b+1}}$$

In the limit, for an infinitely low stress fraction rate, the time to initiation will evolve towards infinite, i.e.

$$\lim_{\dot{\sigma}^{fraction}\to 0}t_{initiation}=\infty.$$

Note, from the figure, that one would have to go to a very low stress fraction rate to reach the stress fraction threshold and, conversely, perform an infinitely long test to reach it. In Fig. 18 we assume typical parameters for the stress-based EngInit model, i.e. $a=0.018\ /hour$, $b=4$ & $\sigma_{threshold}^{fraction}=0.4$. From the figure it is not

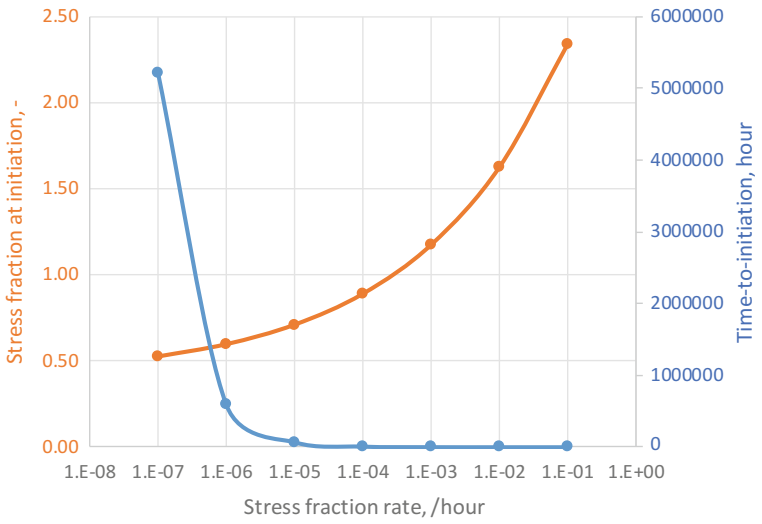

Fig. 18 Stress fraction at initiation and time-to-initiation as function of stress fraction rate

apparent to which value the stress fraction at initiation evolves to at an infinitely low stress fraction rate. Furthermore, note that a stress fraction rate of 10^{-7}/hour corresponds, for a material with a yield stress of 400 MPa, to a stress rate of 40 Pa/hour only. The corresponding time to observe initiation would be 575 years. Visual extrapolation, even on a plot with these low stress fraction rates, does not seem to give the 0.4 real stress fraction threshold! Practical test go down to about 10^{-3}/hour and extrapolating from there is even more difficult.

References

1. O. Runevall, J. Lejon, M. Olsson, K. Tompuri, M. Bjurman, Water chemistry options for internal pump BWRs—the Nordic operational experience, in 20th NPC International Conference, Brighton, UK, 2016
2. H.P. Seifert, S. Ritter, H.J. Leber, S. Roychowdhury, Stress corrosion cracking behavior in the transition region of Alloy 182/low-alloy reactor pressure vessel steel dissimilar metal weld joints in light water reactor environments. Corrosion **71**, 433–454 (2015)
3. H.P. Seifert, S. Ritter, T. Shoji, Q.J. Peng, Y. Takeda, Z.P. Lu, Environmentally-assisted cracking behaviour in the transition region of an alloy182/SA 508 Cl.2 dissimilar metal weld joint in simulated boiling water reactor normal water chemistry environment. J. Nucl. Mater. **378**, 197–210 (2008)
4. R.M. Horn, P.L. Andresen, J. Hickling, BWR Alloy 182 stress corrosion cracking experience, in *5th Int. Symposium on Contribution of Materials Investigation to the Resolution of Problems Encountered in Pressurized Water Reactors* (Fontevraud 5), Fontevraud, France, 2002, pp. 55–67
5. H. Hänninen, P. Aaltonen, A. Brederholm, U. Ehrnstén, H. Gripenberg, A. Toivonen, I. Virkkunen, Dissimilar metal weld joints and their performance in nuclear power plant and oil refinery conditions, in *VTT Research Notes*, VTT, Technical Research Centre of Finland, Espoo, Finland, 2006
6. R. Pathania, A.R. McIlree, J. Hickling, Overview of primary water cracking of Alloys 182/82 in PWRs, in: *5th Int. Symposium on Contribution of Materials Investigation to the Resolution of Problems Encountered in Pressurized Water Reactors* (Fontevraud 5), Fontevraud, France, 2002, pp. 13–27
7. R. Gutti, G. Moffatt, A. McIlree, Metallurgical investigation of cracking in the reactor vessel alpha loop hot leg nozzle to pipe weld at the V.C. summer station, in: *Fontevraud 5 International Symposium*, SFEN, Fontevraud, France, 2002, pp. 29–38
8. P. Berge, Importance of surface preparation for corrosion control in nuclear power stations. Mater. Perform. **36**, 56–62 (1997)
9. S. Berger, R. Kilian, Mitigation of Crack Initiation in LWRs (MICRIN+), in: *EUROCORR 2016*, EFC, Montpellier, France, 2016
10. K. Arioka, T. Yamada, T. Miyamoto, T. Terachi, Dependence of stress corrosion cracking of alloy 690 on temperature, Cold Work, and Carbide Precipitation-Role of Diffusion of Vacancies at Crack Tips. Corrosion **67**, 691–706 (2011)
11. S. Yamazaki, Z. Lu, Y. Ito, Y. Takeda, T. Shoji, The effect of prior deformation on stress corrosion cracking growth rates of alloy 600 materials in a simulated pressurized water reactor primary water. Corros. Sci. **50**, 835–846 (2008)
12. D.J. Paraventi, W.C. Moshier, The effect of cold work and dissolved hydrogen in the stress corrosion cracking of Alloy 82 and Alloy 182 weld metal, in: T.R. Allen, P.J. King, L. Nelson (Eds.) *12th Int. Conference on Environmental Degradation of Materials in Nuclear Power Systems—Water Reactors*, Snowbird, UT, USA, 2005, pp. 543–555

13. M. Vankeerberghen, EngInit-A blueprint for an engineering nmodel for time-to-failure of thin-walled, irradiated components of 316 SS under nominal PWR-relevant SCC conditions, personal communications, (2012)
14. M. Vankeerberghen, R.-W. Bosch, Towards an engineering model for time-to-failure of irradiated components of 316 SS under nominal PWR-relevant conditions, personal communications, (2011)

Effect of Thermal Aging on Fracture Mechanical Properties and Crack Propagation Behavior of Alloy 52 Narrow-Gap Dissimilar Metal Weld

Matias Ahonen, Sebastian Lindqvist, Teemu Sarikka, Jari Lydman, Roman Mouginot, Ulla Ehrnstén, Pekka Nevasmaa and Hannu Hänninen

Abstract Determination of the fracture toughness properties and thermal aging behavior of dissimilar metal weld (DMW) joints is of utmost importance for successful structural integrity and lifetime analyses. This paper presents results from fracture resistance (J-R), fracture toughness (T_0) and Charpy-V impact toughness tests as well as fractography performed for an industrially manufactured narrow-gap DMW mock-up (SA508-Alloy 52-AISI 316L). Tests were performed on post-weld heat treated, 5000 h aged and 10,000 h aged material. The results show that this DMW is tough at the SA 508-Alloy 52 interface, which typically is the weakest zone of a DMW. The DMW joint maintains its high fracture resistance also after thermal aging. Crack propagates for a large part in the carbon-depleted zone (CDZ) of SA 508 but deflects occasionally to the Alloy 52 side due to small weld defects in μm scale. Ductile-to-brittle transition temperature determined from Charpy-V impact toughness tests increases due to thermal aging, but only to a minor extent. No significant change is observed for the T_0 transition temperature due to aging.

Keywords Dissimilar metal weld · Ni-base alloy · Microstructural characterization · Aging

M. Ahonen (✉) · S. Lindqvist · J. Lydman · U. Ehrnstén · P. Nevasmaa
VTT Technical Research Centre of Finland Ltd.,
P.O. Box 1000, VTT, FI-02044 Espoo, Finland
e-mail: matias.ahonen@vtt.fi

T. Sarikka · R. Mouginot · H. Hänninen
Aalto University School of Engineering, P.O. Box 14200, FI-00760 Aalto, Finland

J.H. Jackson et al. (eds.), *Proceedings of the 18th International Conference on Environmental Degradation of Materials in Nuclear Power Systems – Water Reactors*, The Minerals, Metals & Materials Series, https://doi.org/10.1007/978-3-319-68454-3_56

Introduction

Nickel-base alloy weld metals are often used when welding dissimilar metal combinations, such as bainitic pressure vessel steels (low-alloy steels) to stainless steels. In these applications, several inherent properties of nickel-base alloys make them an ideal choice of material. When austenitic stainless steels are welded directly to carbon steels, the difference in coefficient of thermal expansion (CTE) can lead to fatigue and creep failures in the heat-affected zone (HAZ) of the carbon steel [1]. The CTE of Ni lies between those of austenitic stainless steels and carbon steels and thus it provides a smooth transition of CTE across the weld joint and better distributes the thermal stresses that originate from the different CTEs of the joined materials. Nickel-base alloy weld metals also have good corrosion resistance in as-welded condition [2] and good impact toughness at low temperatures [3]. Previously widely used Alloy 600 and its weld metal Alloys 182 and 82 have recently been substituted with higher Cr containing Alloy 690 and its weld metal Alloys 152 and 52 due to their better resistance to stress corrosion cracking (SCC) in light water reactor (LWR) environments [4, 5].

At present, the operational experience of Alloy 52 welds is limited because they have not been in use for an extensive period of time in nuclear reactors. Thus, there is a need to improve the understanding of long-term behavior of Alloy 52 DMWs. It has been previously reported [6], that the fusion zone exhibits a lower fracture resistance with respect to the adjacent SA 508 HAZ and Alloy 52 weld metals. The fracture mechanical testing has demonstrated that DMWs are prone to abrupt crack path deviations from the original cracking plane (i.e., the location of the pre-fatigue crack tip) into the neighboring microstructures. This deflection tendency is shown to be affected by the strength mis-match state. After the crack growth initiates in a J-R test, the crack tends to find its way into the softest zone, the carbon-depleted zone (CDZ), located very close to the fusion line in the low-alloy steel heat-affected zone (LAS HAZ). Furthermore, scanning electron microscopy (SEM) examinations have revealed that crack path deflections occur also to the weld metal side, which is in most cases caused by small weld defects detected in post-test fractography on the fracture surfaces [7].

Thermal aging promotes changes in the microstructures of the different parts of the dissimilar metal weld. The microstructure of the CDZ is different from that of the bainitic LAS base metal. In the CDZ, the carbides have mainly dissolved due to the carbon diffusion towards the Ni-base weld metal, driven by the higher Cr and lower C content of the Ni-base weld metal. Therefore, the CDZ exhibits a ferritic microstructure containing only a small amount of carbides, and its grain size is larger than that of the LAS base metal further away from the fusion boundary outside the HAZ [6].

Several different metallurgical processes can lead to a decrease of the fracture mechanical properties of the RPV steel. These processes include, e.g. precipitation hardening, copper-rich phase precipitation, phosphorous segregation to the grain

boundaries, carbon depletion close to the fusion boundary, and strain aging. Of these P segregation is usually considered the most important mechanism degrading the mechanical properties of the RPV [8, 9]. Thermal aging has been observed to decrease the impact toughness [10] and fracture toughness [9] of the LAS HAZ. Degradation of these properties affects the structural integrity of the component and may cause challenges for the long-term operation of the nuclear power plants. Thus, the knowledge of the aging mechanisms concerning the reactor pressure vessel (RPV) and its weld joints is of utmost importance from the plant life management point of view.

Experimental Methods

The studied material is an industrially manufactured 1:1 scale DMW safe-end mock-up. An optical cross-section image of the mock-up showing the SA 508 low-alloy steel, AISI 308 cladding, Alloy 52 weld metal and AISI 316L stainless steel is presented in Fig. 1 together with a higher magnification optical image showing the LAS HAZ and nominal pre-crack location of the test specimens. The chemical compositions for the materials are presented in Table 1. The weld is manufactured by applying the narrow-gap (NG) gas tungsten arc welding (GTAW) method without buttering and using Alloy 52 as welding consumable. After welding the mock-up was post-weld heat treated at 550 °C for 20 h and at 610 °C for 16 h.

Thermal aging was applied to two separate blocks of the test material. The aging was conducted in a furnace at 400 °C for 5000 and 10,000 h. The temperature during aging was monitored using thermocouples. The aging times were chosen based on the assumption that P segregation is the main mechanism controlling the degradation of fracture toughness of the pressure vessel steel during aging. According to the calculations presented by Joly et al. [8], the aging time of 10,000 h at 400 °C is representative to about 60 years of operation at 325 °C from the P segregation point of view. The specimens for the fracture mechanical testing were cut from the material blocks after thermal aging in order to avoid surface oxidation of the specimens.

This paper concentrates on fracture mechanical characterization of the NG DMW mock-up, fractography and crack path characterization of the fracture mechanical specimens. The applied experimental methods include fracture resistance (J-R), fracture toughness (T_0) and Charpy-V impact toughness testing as well as optical microscopy of the cross-section samples and scanning electron microscopy (SEM) of the fracture surfaces and cross-section samples. J-R testing was performed according to ASTM E 1820-13 standard using 25 mm thick C(T) specimens and by applying unloading compliance method, T_0 tests according to ASTM E1921 standard using 5 × 10 × 55 mm SE(B) specimens and Charpy-V

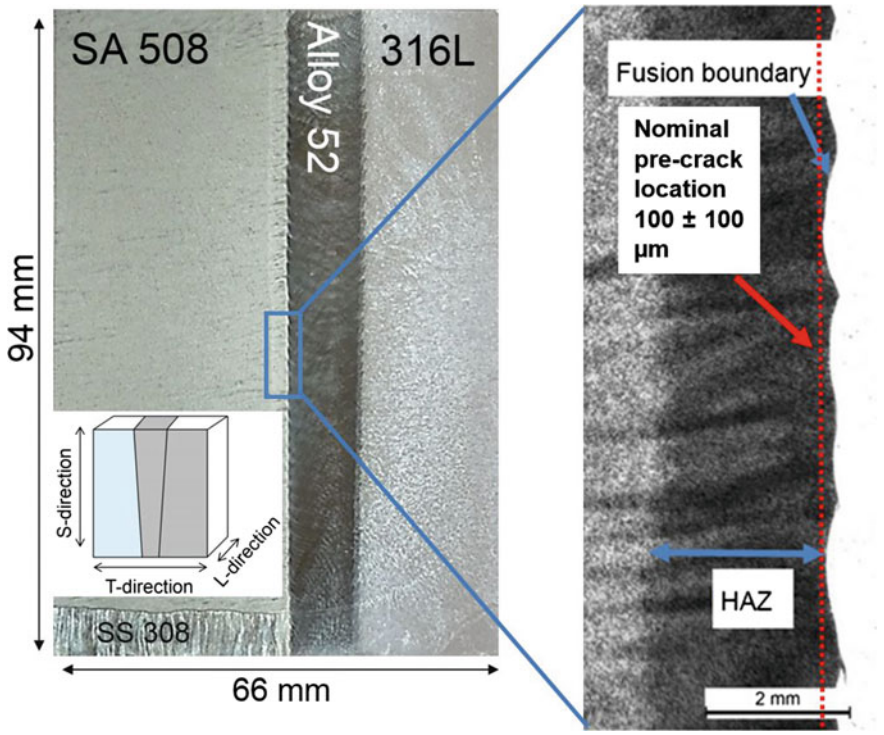

Fig. 1 An optical image on the left, showing the cross-section of the NG DMW mock-up, and a larger magnification optical image on the right, where the HAZ, fusion boundary and nominal pre-crack location are shown. The directions used for determining the specimen orientations are schematically presented in a drawing on the left

impact toughness tests according to SFS-EN ISO 148-1 standard using 10 × 10 × 55 mm CVN specimens. J-R and T_0 specimens were fatigue pre-cracked (to 0.55 and 0.5 W, respectively) and 10% side grooved from both sides. The nominal fatigue pre-crack location (notch location in CVN) was 100 µm ± 100 µm away from the fusion boundary in the LAS side in all test specimens. J-R testing was performed using specimens in both T-L and T-S orientations, whereas the T_0 and Charpy-V specimens were tested only in T-L orientation. J-R tests were conducted in air at 300 °C and T_0 tests at temperatures between −130 and −100°C.

In addition to the fracture mechanical test specimens, cross-section samples were extracted from the mock-up and prepared using standard metallographic sample preparation techniques. More detailed investigations on the microstructural characteristics and hardness properties are reported in a separate paper by Sarikka et al. [11]. Samples for the optical microscopy examination presented in this paper were etched using 2% Nital solution.

Table 1 Chemical compositions of the materials used for manufacturing the studied narrow-gap DMW

wt.%	SA508 Gr. 2	AISI 316L	Alloy 52
C	0.18	0.016	0.023
Si	0.19	0.38	0.15
Mn	1.46	1.62	0.26
P	0.005	0.018	<0.005
S	0.001	0.002	0.0007
Cr	0.12	17.14	29.93
Ni	0.78	11.6	58.86
Mo	0.49	2.36	<0.01
Nb			<0.01
N	0.011	0.068	0.021
Ti	0.002		0.54
Fe	Bal.	Bal.	10.43
Al	0.02		0.66
Co	0.02	0.022	<0.01
Cu	0.06	0.08	<0.01

Results

Fracture Mechanical Testing

The obtained J-R curves and a graph showing the J_{1mm} values for each material condition are presented in Fig. 2a–d. J validity limit for the test specimens was estimated to be 1680 kJ/m^2 based on room temperature tensile properties. J-R test results show that the DMW joint exhibits high fracture resistance values in as-received condition, i.e. after post-weld heat treatment. The J_{1mm} values range between 450 and 600 kJ/m^2, and all the J-R curves are rising (Fig. 2a). There is no significant difference between the results for T-L and T-S orientations, although, on average, the J_{1mm} values in T-L orientation are slightly higher than in T-S orientation. After aging of 5000 h, the J-R curves and J_{1mm} values (Fig. 2b) are quite similar to those obtained for the as-received specimens. The T-L orientation seems to result in somewhat higher J_{1mm} values than T-S orientation (about 550 vs. 450 kJ/m^2) for the 5000 h aged condition. The fracture resistance further decreases slightly for 10,000 h aged specimens (Fig. 2c) compared to as-received and 5000 h aged material. T-L specimens are at the higher end of the scatter also in this set of results. Overall, as illustrated in the plot shown in Fig. 2d, a decreasing trend in J_{1mm} values was observed as a result of thermal aging, although the effect is not large and the values after aging are still at a high level ($\sim$400–500 kJ/m^2), and the J-R curves have still a rising trend.

Charpy-V impact toughness test results are presented for all three conditions (as-received, 5000 h aged and 10,000 h aged) in Fig. 3a. The effect of aging is clear, when considering the change in ductile-to-brittle transition temperature T_{42J}, although the T_{42J} results obtained for the 10,000 h aged material are still clearly

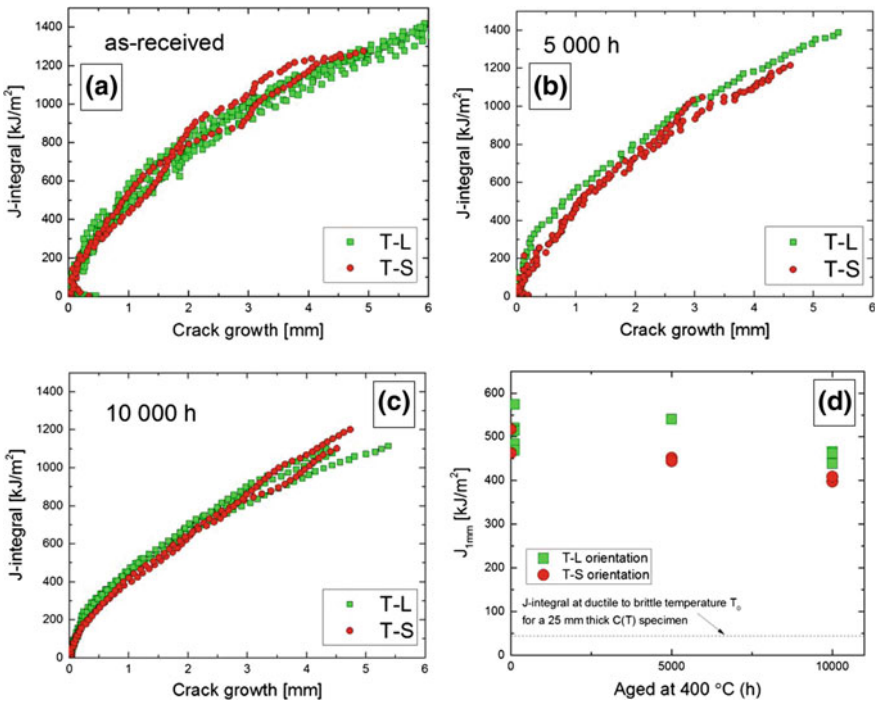

Fig. 2 J-R curves for as-received (**a**), 5000 h aged (**b**) and 10,000 h aged (**c**) DMW where the fatigue pre-crack was located in LAS HAZ, nominally 100 ± 100 μm from the fusion line. The tests were conducted in air at 300 °C. A graph showing the J_{1mm} values obtained from the J-R tests is presented in **d**

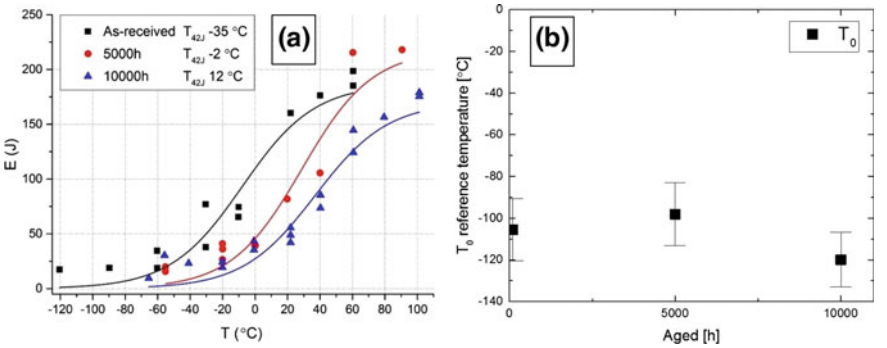

Fig. 3 Charpy-V impact toughness test results for as-received (black), 5000 h aged (red) and 10,000 h aged (blue) NG DMW presented in **a**. Fracture toughness T_0 results as a function of aging time are presented in **b** (Color figure online)

below room temperature. For the as-received material T_{42J} is −35 °C, and after aging for 5000 and 10,000 h the T_{42J} values increase to −2 and +12 °C, respectively. It is notable that the rate of aging appears to decrease after 5000 h, since the difference in T_{42J} is smaller between the results for 5000 and 10,000 h aged material than the difference between the as-received and 5000 h aged material (+14 vs. +33 °C).

The results of the fracture toughness (T_0) tests show that the material maintains its high fracture toughness also after aging. All the obtained results for the three conditions are within the uncertainty limits (2 * standard deviation) of T_0, thus showing that there is no clear evidence of aging in the brittle fracture initiation behavior of the material (Fig. 3b). The nominal pre-crack location for the test specimens is right next to the fusion boundary in the LAS side. In some cases, there was some weld metal visible on the pre-crack surface, but the crack initiated and propagated in all cases entirely in the LAS.

Fracture Surface and Crack Path Characterization

Typical fracture surface and cross-section features of the J-R, T_0 and Charpy-V impact toughness test specimens are presented in the following. A general observation for both ductile (J-R and upper shelf results of Charpy-V tests) and brittle (T_0 and Charpy-V tests showing low impact toughness) cracking was that the cracks tend to follow the CDZ, which is the softest zone of the weld joint. Nominal pre-crack location in all the test specimens was in the LAS, very close to the fusion boundary, nominally 100 ± 100 µm.

Photographs of selected representative J-R test specimen fracture surfaces are presented in Fig. 4a-d. The scale at the side of the images is in 1 mm interval. The first two (4a and 4b) are specimens that are in T-L orientation and the following two (4c and 4d) in T-S orientation. Cracking in J-R testing has initiated almost entirely in the LAS. Cracking was observed to be fully ductile and the dimpled fracture surfaces were formed by microvoid coalescence. The dimples in the LAS part of the fracture surface are smaller than those formed in the Ni-base weld metal.

In J-R testing, after initiation and some crack growth in LAS, cracks partly deflected to the weld metal at certain locations. Those deflections occur where the crack propagates very close to the fusion boundary, as shown in optical cross-section image presented in Fig. 5. The cracking in weld metal also seems to propagate quite often close to the weld pass boundaries (red dashed curves). Similar deflection behavior was also observed in Charpy-V specimens that were tested at higher temperatures and exhibited ductile crack growth. Some crack deflection locations in J-R testing are presented in SEM images shown in Figs. 6–7. With a higher magnification (Fig. 8a and b), it becomes evident that there are typically small weld defects in Alloy 52 at the locations of crack deflection. These small weld

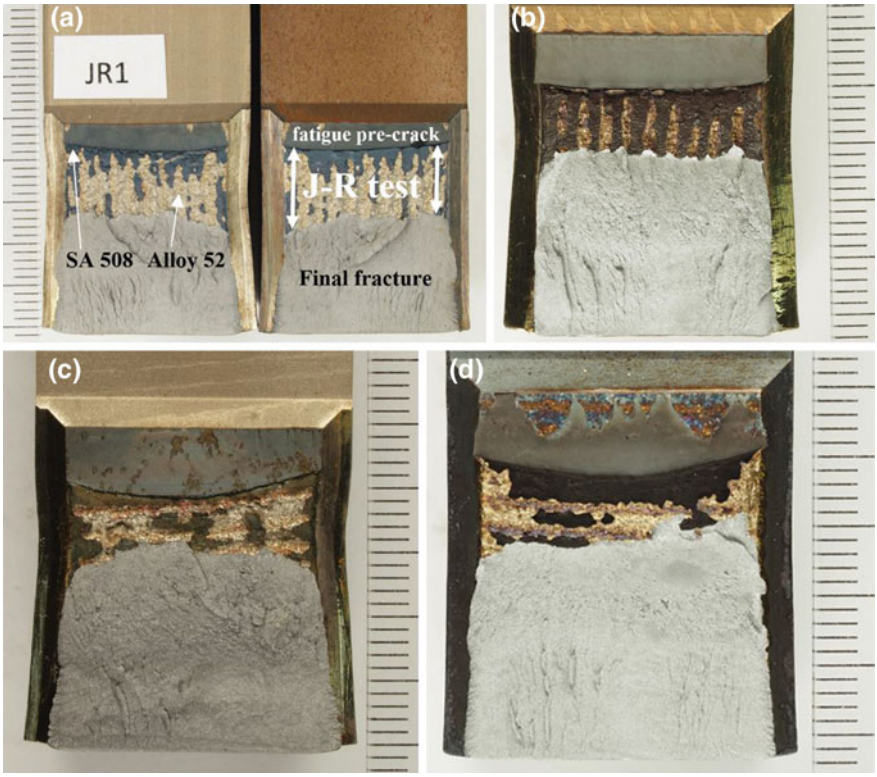

Fig. 4 Photographs of the fracture surfaces of some J-R test specimens. Orientations are T-L in **a** and **b**, and T-S in **c** and **d**. The specimen shown in a was tested in as-received condition and the one shown in b after 5000 h of aging. The specimens presented in **c** and **d** were tested in as-received and 5000 h aged conditions, respectively. Crack growth direction is downwards in these images, and the scale next to the images is in mm interval

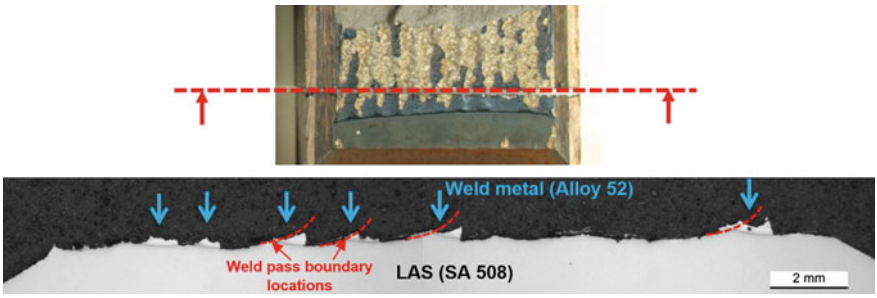

Fig. 5 Optical image of the cross-section of a J-R test specimen (T-L orientation). The photograph above the optical image shows where the cross-section was cut

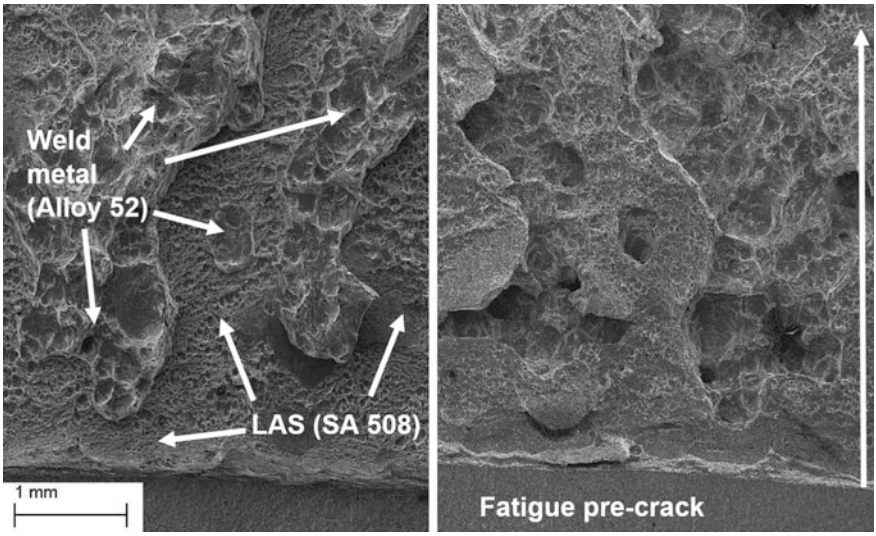

Fig. 6 SEM images from the both sides of the fractured specimen at the same location showing alternating areas of Alloy 52 weld metal and SA 508 low-alloy steel

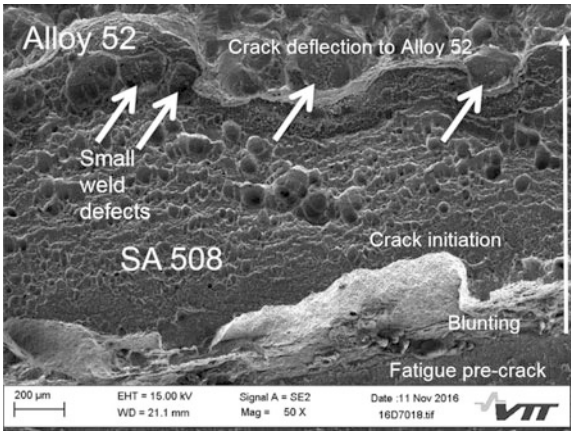

Fig. 7 SEM image of the fracture surface of a J-R test specimen, showing a location at the end of the fatigue pre-crack and the onset of the J-R test crack growth. There are numerous small weld defects at the location of crack deflection to Alloy 52

defects are porosity and they exhibit an appearance typical of a solidification structure. The size of the observed weld defects is smaller than 0.2 mm. It was also observed for the T-L oriented specimens, that once the crack deflected into the weld metal, it typically did not return to the LAS (Fig. 4a and b), although the cracks prefer to grow in CDZ of the LAS HAZ in the beginning of the tests.

The fracture surface appearance of the J-R test specimens tested in as-received and aged conditions was very similar, with the exception that in some T-S

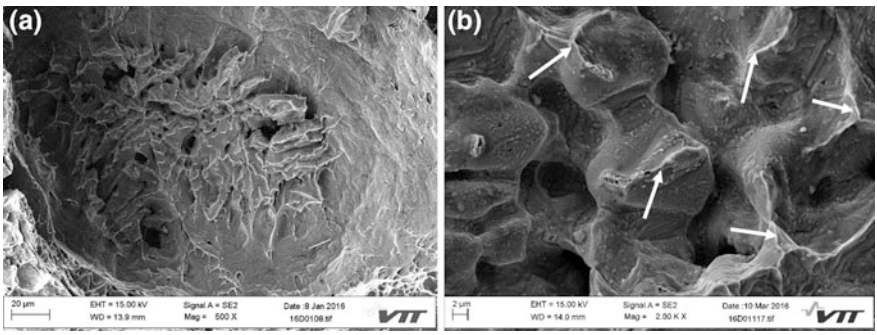

Fig. 8 SEM images of weld defects observed on the fracture surface of J-R test specimens. The morphology of a small (~100 μm) weld defect, located on the bottom of a dimple in Alloy 52, shows typical a solidification structure (**a**). A larger magnification image of another weld defect is shown in (**b**). Carbides are present on the surface and the weld defect has a dendritic and porous appearance. Some parts of the surface show plastic flow (arrows) and have thus been originally attached to the mating fracture surface

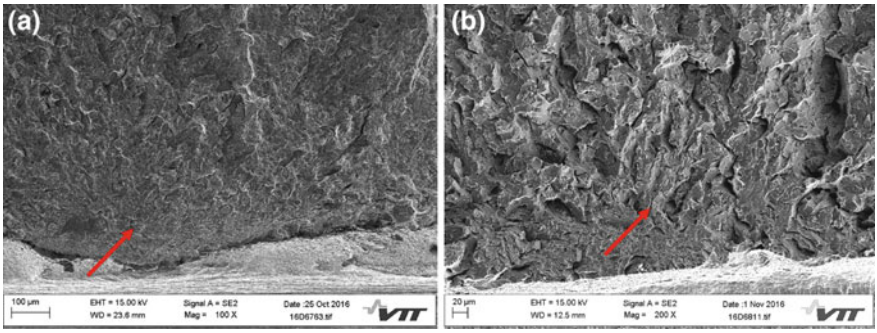

Fig. 9 SEM images of brittle cleavage fracture on Charpy-V specimen (**a**) and T_0 (**b**) test specimen fracture surfaces. The initiation sites are marked with arrows. The specimens were tested in as-received condition

specimens the crack had deflected to the weld metal side later, mainly in the mid-thickness region of the specimen.

In the Charpy-V specimens where brittle fracture was observed, the appearance of the fracture surface was complex. Typical Charpy-V and T_0 specimen fracture surfaces are presented in Figs. 9a and b. Regardless of the exact distance of the notch (Charpy-V) or fatigue pre-crack (T_0), the crack tends to propagate very close to the fusion boundary, i.e. in the CDZ, as shown in the cross-section image, Fig. 10. The cracking was mostly transgranular, but especially in the 10,000 h aged specimen fracture surfaces some areas were showing intergranular (IG) appearance (Fig. 11a and b). Some similar, although not as clear, features indicating possible

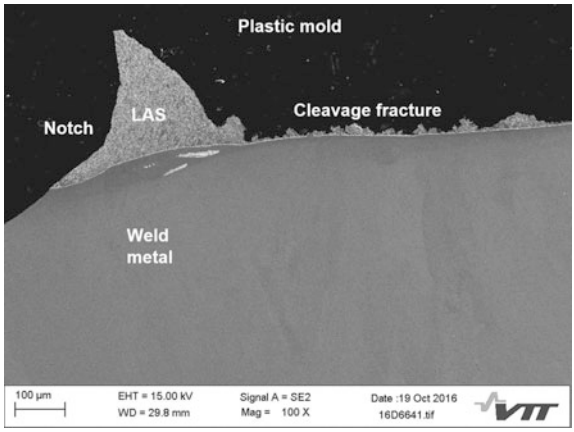

Fig. 10 SEM image of the cross-section of a Charpy-V impact test specimen (as-received condition) showing brittle cleavage fracture after initiation. The cleavage fracture has a serrated cross-section appearance and propagates close (about 0–50 µm) to the fusion boundary in the CDZ

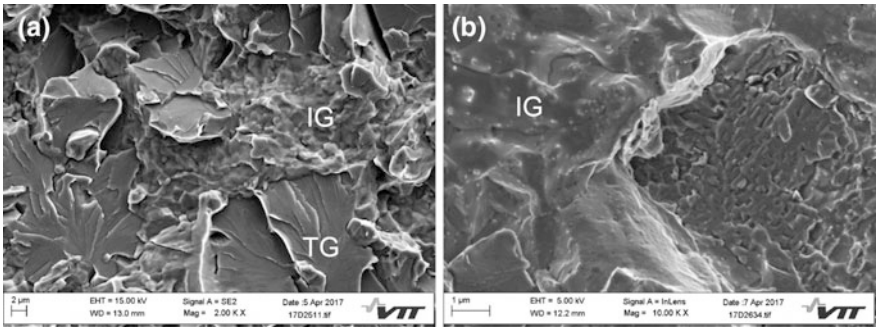

Fig. 11 SEM images showing cleavage and IG fracture on Charpy-V impact toughness test specimen fracture surfaces. The specimens were tested after thermal aging for 10,000 h at 400 °C. Some IG fracture between the cleavage fracture areas is visible in **a**. In **b**, two different appearing areas of IG fracture are present. On the left the appearance is somewhat smooth but tortuous, whereas on the right the appearance is more planar and the carbides are larger

IG cracking were also observed in 5000 h aged Charpy-V specimen fracture surfaces, and even in as-received specimens. In the area shown in Fig. 11a, the fracture surface consists mostly of brittle cleavage fracture, but at some locations the crack seems to prefer the grain boundaries instead of continuing as cleavage fracture. In Fig. 11b, the part on the left has an IG appearance with smooth, slightly tortuous fracture surface with very small ($\sim$0.1 µm) carbides. Instead, the part starting from the middle of the image towards right shows a more planar appearance with larger ($\sim$0.2–0.5 µm) carbides and is probably transgranular fracture.

Discussion

The results obtained from the fracture mechanical testing show that the studied NG DMW exhibits good properties in both as-received and aged conditions. The effect of thermal aging (10,000 h at 400 °C) is evident in J-R and Charpy-V impact toughness tests, but degradation of the measured properties is not substantial. The 10,000 h aged material maintains its high fracture resistance and reasonably low ductile-to-brittle transition temperature T_{42J} (12 °C). Furthermore, because it was observed that the increase of T_{42J} caused by thermal aging was slowing down as the aging time increased, it is assumed that the degradation of impact toughness of the DMW joint due to thermal aging will not be an issue for long-term operation of the nuclear power plant. The fracture toughness T_0 tests did not show a statistically significant difference between the results for as-received and 5000 h and 10,000 h aged material, which further underlines the good fracture mechanical properties of the thermally aged DMW.

The T_0 results obtained for the 10,000 h aged material show a slightly lower T_0 temperature (i.e. better fracture toughness) than the results obtained for the as-received material, which was somewhat unexpected, because the Charpy-V impact toughness tests showed a clear effect of aging. However, the different material behavior in these two types of tests may be explained by the different nature of the test methods. T_0 test measures the fracture toughness, i.e. the material's tendency to cleavage initiation. It is a quasi-static test, measuring the local properties of the material. Charpy-V test is a dynamic test and measures the crack initiation, growth and arrest [12]. Based on that fact it is reasonable to assume, that thermal aging affects the crack growth and crack arrest properties of the LAS HAZ of the DMW, while the tendency to cleavage crack initiation is not markedly affected.

The pre-crack tip or Charpy-V specimen notch location in the tests was 100 μm ± 100 μm away from the fusion boundary in the LAS, but the actual pre-crack tip locations always vary. Even within these rather tight limits, if two cases are at the extremes, i.e. exactly at the fusion boundary versus 200 μm away in LAS HAZ, the results may be slightly different due to the different crack path and different hardness (i.e. different local strength mismatch) of the joint at different distances from the fusion boundary [11]. As shown in Fig. 10, the crack tends to grow in the CDZ very close to the fusion boundary. In some cases, there was some weld metal visible on the pre-crack surface (Fig. 4d). In J-R tests that was not observed to have an effect on J_{1mm} values. In T_0 tests, the crack initiated and propagated in all cases entirely in the LAS, although in some specimens a small part of the pre-crack fracture surface was on the weld metal side of the fusion boundary. In addition, the T_0 results fit well with the other results where the pre-crack was entirely in the LAS. However, the distance of the pre-crack to the fusion boundary may affect the results to some degree, and can explain the large scatter of the test results for the 10000 h aged material. Further studies on the exact location of the pre-crack of the test specimens are under way.

IG fracture was observed in the Charpy-V test specimen fracture surfaces along with cleavage fracture, which still was the dominant fracture mechanism in all brittle appearing specimens. Complex features, that are not cleavage fracture but have characteristics of IG fracture and, in some cases plastic flow, were observed already in the as-received material specimens and in 5000 h aged specimens. A significant amount (>10%) of IG fracture between the cleavage fracture areas was observed in the 10000 h aged specimens, which may indicate that thermal aging promotes brittle IG fracture as is suggested in literature [8, 9]. However, the Charpy-V test specimen fracture surfaces require more thorough characterization in order to quantitatively assess the proportion and characteristics of IG fracture in the specimens of different conditions, and also the effect of test temperature on the extent of IG fracture.

The tendency of the crack to preferential propagation in the CDZ is very strong, because the cracks followed this softest zone in different types of mechanical tests. In J-R testing the cracks propagated in CDZ after blunting, as observed from the fracture surface and cross-section examinations. Wang et al. [13] performed J-R tests using SE(B) specimens with different pre-crack locations and observed, that the cracks always deflect towards the lowest strength in a NG DMW joint, which is in line with the results obtained in this study. It is assumed that the wavy shape of the fusion boundary, which is formed in multi-pass welding, is promoting the crack deflections in conjunction with the small weld defects that were observed repeatedly at the locations of crack deflection. Cross-section optical examination results indicate that the weld pass boundary areas provide a preferred cracking path to the surrounding weld metal. At the locations where the crack deflected into the weld metal it typically did not return to the LAS later in the test, although the cracks prefer to propagate in CDZ of the LAS HAZ in the beginning of the tests. It has been reported earlier [6, 7, 11] that there is a hard zone in the weld metal close to the fusion boundary. The crack path examinations suggest that in J-R testing, owing to local hardness (and strength) mismatch, it is energetically more advantageous for the crack to continue growing in the Alloy 52 weld metal, once the crack deflection has occurred, than to come back to the LAS by penetrating through the hard zone of the weld metal close to the fusion line.

Conclusions

Based on the obtained results the following conclusions are drawn:

- The effect of thermal aging on the fracture resistance of the studied NG DMW is evident but not substantial. The J-R testing results at 300 °C for the material aged for 10000 h at 400 °C show J_{1mm} values in the range of about 400–500 kJ/m^2, which is about 10–20% lower than the values obtained for the as-received material. T-S orientation results in slightly lower values than T-L orientation. All the J-R curves are rising.

- Ductile-to-brittle transition temperature (T_{42J}) measured after 10000 h aging is 12 °C, which gives a ΔT_{42J} of 47 °C as compared to the as-received material. The results obtained for the as-received, 5000 h aged and 10000 h aged material show that the degrading effect of thermal aging on Charpy-V impact toughness decreases as function of aging time.
- Fracture toughness T_0 was not significantly affected by thermal aging. Thus, it is assumed that thermal aging may promote brittle crack propagation and degrade material's capability to arrest the growing cracks at low temperatures, whereas the brittle crack initiation tendency of the material is not markedly affected.
- CDZ is the preferred crack path in all types of tests applied in this study. However, crack deflections to the weld metal side of the fusion boundary occur due to the small defects observed in the weld metal in tests, where the fracture mode is ductile. Crack deflections were typically associated to the weld pass boundary regions.

Acknowledgements This study has been made in collaboration between VTT Technical Research Centre of Finland Ltd and Aalto University School of Engineering within the Nickel-base Alloy Welding Forum (NIWEL) research project funded by TEKES, Finnish (Teollisuuden Voima Oyj and Fortum Oyj) and Swedish (Ringhals AB and OKG AB) energy industry. The authors wish to express their gratitude for the funding and participation of all the participants of the project.

References

1. J.C. Lippold, et al., *Welding Metallurgy and Weldability of Stainless Steels* (Wiley Hobocken, N.J., USA, 2005). ISBN 0-47147379-0
2. S. Kiser, Nickel-alloy consumable selection for severe service conditions. Welding J. **69**(1), 30–35 (1990)
3. J. Hilkes et al., Electrodes for Welding 9% Nickel Steel. Welding J. **83**(1), 30–37 (2004)
4. P.L. Andresen, et al., PWSCC of Alloys 690, 52 and 152. in *Proceedings of the 13th International Symposium on Environmental Degradation of Materials in Nuclear Power Systems - Water Reactors, Whistler, Canada,* CNS-SNC (CD-ROM), Canada, April 19–23, 2007
5. D. Buisine, et al., French Steam Generator Tubes: An Overview of Degradations. in: *Proceedings of the 7th Fontevraud Conference, Avignon, France,* SFEN (CD-ROM), France, September 26–30, 2010
6. Hänninen et al., Structural Integrity of Ni-base Alloy Welds. VTT Technology 175. VTT Technical Research Centre of Finland, Espoo, 2014, p. 257. ISBN 978-951-38-8259-4
7. M. Ahonen, et al.. Fracture Mechanical and Microstructural Characterization of Narrow-gap Safe-end Dissimilar Metal Weld. in *Proceedings of Baltica X—2016—Life Management and Maintenance for Power Plants*, Helsinki, Finland, June 7–9, 2016
8. P. Joly, et al., Fracture Toughness in the Ductile-brittle Transition and Thermal Ageing Behaviour of Decarburized Heat Affected Zone of Alloy 52 Dissimilar Metal Welds of Nuclear Components. in *Proceedings of the ASME-2014 Pressure Vessel and Piping Conference,* Anaheim, CA, USA July 20–24, 2014
9. J.A. Hudson et al., Thermal ageing effects in structural steels. Theoret. Appl. Fract. Mech. **10**, 123–133 (1988)

10. G. Gage, et al., Thermal Ageing Embrittlement of the Heat-Affected-Zone in a PWR RPV Steel Weldment. Nuclear Power Plant Life Extension, Snowbird, Utah, USA July 31-August 3, 1988
11. T. Sarikka, et al., Microstructural Characterization of Alloy 52 Narrow-Gap Dissimilar Metal Weld after Aging. in *Proceedings of the 18th International Symposium on Environmental Degradation of Materials in Nuclear Power Systems—Water Reactors,* Portland, Oregon, USA August 13–17, 2017. (Submitted)
12. K. Wallin, *Fracture Toughness of Engineering Materials: Estimation and Application*. (EMAS, UK, Publishing, 2011), p. 543. ISBN 0-9552994-6-2
13. H.T. Wang et al., An experimental investigation of local fracture resistance and crack growth paths in a dissimilar metal welded joint. Mater. Des. **44**, 179–189 (2013)

Distribution and Characteristics of Oxide Films Formed on Stainless Steel Cladding on Low Alloy Steel in Simulated PWR Primary Water Environments

Qi Xiong, Hongjuan Li, Zhanpeng Lu, Junjie Chen, Qian Xiao, Jiarong Ma, Xiangkun Ru and Xue Liang

Abstract The properties of oxide film formed on stainless steel (SS) cladding on low alloy steel (LAS) after immersion in simulated PWR primary water environments with different dissolved oxygen contents are investigated. The HAZ in the LAS consist of overheated crystal region, complete recrystallized region and incompletely recrystallized region, while SS cladding consist of austenite zone and austenite and ferrite mixing zone. Pitting appeared on 309L SS after immersion in high temperature water due to the dissolution of inclusions existed previously on 309L SS which contain higher ferrite content. Raman spectra and TEM results show that the outer layer is mainly Fe-rich spinel oxides while the inner layer is mainly Cr-rich oxides. Ni is mainly concentrate at the oxide/substrate interface due to the low oxygen affinity. The inner oxide layer on 308L SS is thinner than that on 309L SS, implying that ferrite distributed on austenite is not favorable for the growth of oxides. Reducing the oxygen content in PWR primary water favored the formation of spinel oxides.

Keywords Stainless steel cladding · Pressurized water reactor · Low alloy steel · Oxide film · High temperature water

Q. Xiong · H. Li · Z. Lu (✉) · J. Chen · Q. Xiao · J. Ma · X. Ru
Institute of Materials School of Materials Science and Engineering,
Shanghai University, Shanghai 200072, China
e-mail: zplu@t.shu.edu.cn

Q. Xiong · H. Li · Z. Lu · J. Chen · Q. Xiao · J. Ma · X. Ru
State Key Laboratory of Advanced Special Steels,
Shanghai University, Shanghai 200072, China

Z. Lu · X. Liang
Key Laboratory for Microstructure, Shanghai University, Shanghai 200444, China

J.H. Jackson et al. (eds.), *Proceedings of the 18th International Conference on Environmental Degradation of Materials in Nuclear Power Systems – Water Reactors*, The Minerals, Metals & Materials Series, https://doi.org/10.1007/978-3-319-68454-3_57

Introduction

The dissimilar welded joints of pressurized water reactor (PWR) nuclear power plant have become the most easily damaged parts in primary water environment due to its unique material properties. Most of the problems are associated with deterioration of piping systems connecting the nuclear reactor vessel [1, 2]. In PWR nuclear power plants, low alloy steel (like A508 III) are widely used in reactor pressure vessel, voltage regulator and steam generator shell because of its high strength, good ductility and low price. Stainless steel (like 309L/308L SS) exists in the inner wall of the pipe or container as anti-corrosion layer [3–5]. Low alloy steel and stainless steel dissimilar joints exist on the key parts of many connections, such as the connections of safe end and reactor pressure vessel nozzle. Cracking and leakage accidents of primary water nozzle safe end in PWR nuclear power plant have been reported [6, 7]. The main factors that cause the failure of welds are sensitive microstructure, stress/strain and corrosive environment. In order to understand the failure mechanism of the dissimilar joints, many works have been done by previous researchers [8–10]. The physicochemical properties and chemical compositions of LAS base metal and stainless steel cladding are quite different. Complex microstructure appeared near the fusion zone and the HAZ has been found to be the weakness part of SCC. Most studies have focused on microstructure and stress corrosion, little is known about the properties of oxide film on LAS-SS dissimilar joints in high temperature water. The properties of oxide films are closely related to the initiation of a crack. In this work, the microstructure and the characteristics of oxide films formed on stainless steel cladding on low alloy steel in simulated primary water have been studied by metallographic examination, scanning electron microscopy (SEM), Raman spectroscopy, focused ion beam (FIB) sampling and transmission electron microscope (TEM) observation.

Experimental Procedure

Materials

This work has been conducted on low alloy steel with stainless steel cladding (A508III/309L/308L) from nuclear power station safe end dissimilar metal welded joint simulation specimen, Low alloy steel base metal was Mn-Ni-Mo forgings, the main chemical compositions of each part were listed in Table 1, Considering the elements (especially Cr and Ni)dilution of dissimilar metal welding, the first cladding layer on A508III was 309L SS which contained higher content of Cr and Ni as the isolation layer with a thickness of 2.5 mm, then followed by a layer of 308L SS as the corrosion resistant layer, and post weld heat treatment (PWHT) was carried out subsequently, the PWHT condition is shown in Table 2.

Table 1 Chemical composition of the substrate and the cladding material (wt%)

Material	Fe	Cr	Ni	Mn	Si	C	P	Mo	Cu	Co
A508III	97	0.164	0.82	1.40	0.235	0.192	0.01	0.491	0.039	0.022
309L	60.2	23.94	13.48	1.67	0.40	0.016	0.011	0.031	0.044	0.04
308L	66.8	20.38	10.32	1.76	0.37	0.02	0.014	0.022	0.029	0.04

Table 2 The conditions of post weld heat treatment

Starting temperature	350 °C
Heating rate	≤ 50 °C/h
Temperature	595–620 °C
Time	40–40.5 h
Cooling rate	≤ 55 °C/h
Down to	350 °C
Then air cooling	

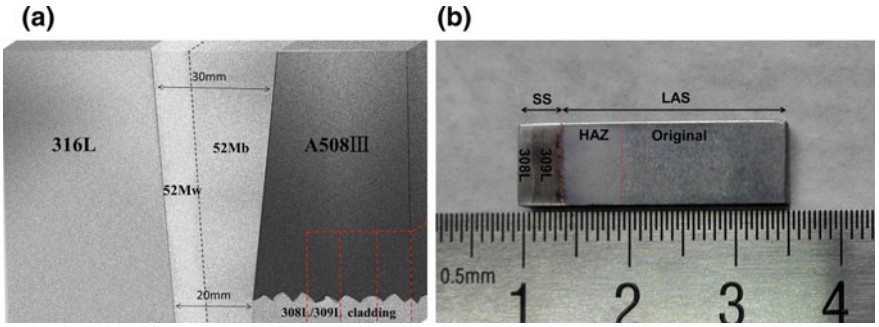

Fig. 1 The macrograph of sample (**a**) sampling location, (**b**) metallographic sample

Figure 1(a) shows the plate weld specimen and the red boxes was the sampling location. The specimens with a size of 25 mm × 8 mm × 3 mm were cut from a plate sample. The physical picture of experimental sample A508III/309L/308L is shown in Fig. 1b. In order to reveal the microstructure, the samples were prepared by grinding and polishing. Before optical microscope observations, different parts of dissimilar metal joint would be etched separately, the low alloy steel side was etched by 4% nital solution, and the stainless steel was electro-etched in 40% NaOH solution for 30 s with DC 5–6 V. The macrograph of metallographic sample is shown in Fig. 1b, the HAZ in A508III was about 5 mm in width. The composition and microstructural features were then examined by metallurgical microscope, scanning electron microscopy and energy dispersive spectroscopy (EDS).

Immersion Tests in Simulated PWR Primary Water Environments

Immersion tests in simulated primary water environments at 290 °C were conducted to study the characteristics of oxide film. The samples were punched with a diameter ϕ2 circular hole in low alloy steel side for facilitate hanging in the autoclave. The specimens were polished with metallographic sandpaper to 1500 grit, cleaned with deionized water and alcohol, and then dried with cool air. Immersion tests were carried out in oxygen-containing PWR water and deaerated PWR water respectively. The solution for immersion tests was made up by adding 2 ppm lithium (with $LiOH{\cdot}H_2O$) and 1200 ppm boron (with H_3BO_3) to deionized water, before pouring the solution (1 L) into the autoclave (2 L), in order to prevent the samples contact kettle wall or other metal, samples were hung in the autoclave with small hooks which were wrapped in PTFE. For the immersion tests in oxygen-containing PWR water, the autoclave was at first opened for releasing the air and then closed and then slowly heated to 290 °C at ~7.2 MPa. For the tests in the deaerated PWR water, deaeration of the water in the autoclave was achieved by purging N_2 gas for 2 h before heating. The oxygen content in the deaerated PWR water was expected to be below 10 ppb. The oxygen content in oxygen-containing naturally exposed solution in autoclave was lower than that at room temperature, but it was expected to be at ppm level [11], which was higher than that in deaerated water significantly. It can be used for analysing the effects of environmental conditions on oxidation of various parts of the weld. Immersion tests were carried out for 168 h. After the tests, the oxidized samples were cleaned with deionized water, rinsed in acetone and dried with cold air. The distribution and characteristics of oxide films formed on specimens were analyzed by Raman spectra, SEM-EDS and TEM.

Results and Discussion

Microstructure Observation

The details of the A508III/309L/308L weld block are shown in Fig. 1b, it can distinguish 308L SS, 309L SS, fusion line and HAZ of low alloy steel from the metallographic sample. Figure 2a–c shows the microstructure of HAZ in low alloy steel, decarburization zone formed by the migration of carbon atoms from low alloy steel to stainless steel [12] about 200–300 μm in width was formed near the fusion line. Ferrite grains grew up formed the overheated crystal region because of the high temperature near the weld line during the welding process. As shown in Fig. 2b, the microstructure in the range of 0.5–4.5 mm from the fusion line consisted of bainite with fine grains as a result of recrystallization. Figure 2c shows the intercritically reheated coarse-gain heat-effected zone (ICCGHAZ) between HAZ

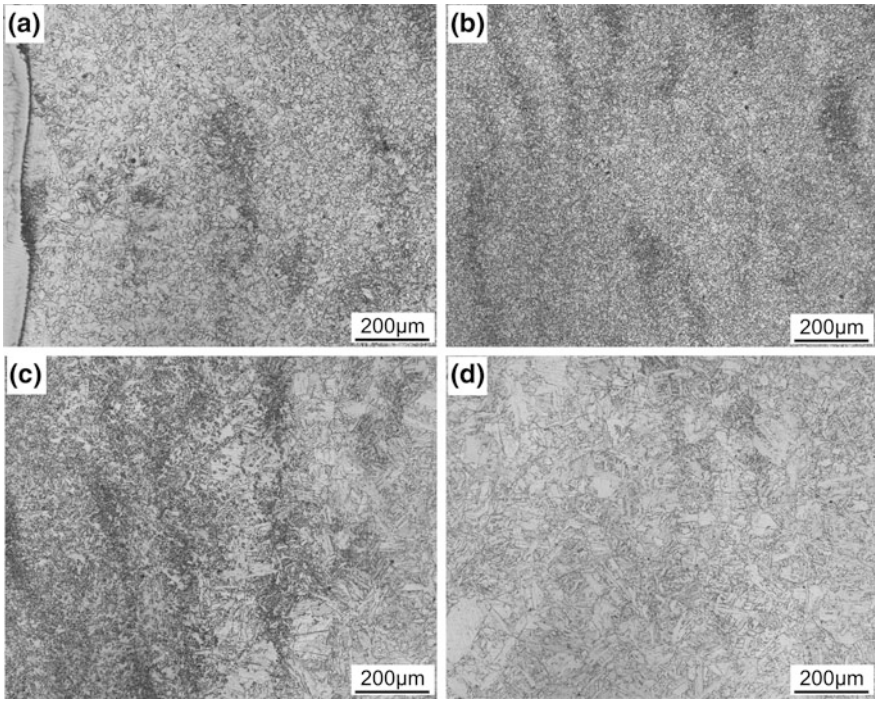

Fig. 2 Optical micrographs of A508III (**a**) microstructure near the weld line, (**b**) HAZ of A508III which is far away from the weld line, (**c**) ICCGHAZ of A508III and (**d**) unheated effect zone of A508III

and base metal, ICCGHAZ was composed of ferrites and coarse carbons due to incompletely recrystallization. Figure 2d shows the unheated effect zone of A508 III, it mainly consisted of bainite and ferrite.

The microstructure of stainless steel is shown in Fig. 3. The stainless steel part near the fusion line (180–200 μm thick) consisted of austenite (A) and the other region of 309L SS consisted of austenite and ferrite (A + F) as shown in Fig. 3b. From Fig. 3c and d, the ferrite was vermicular on 309L SS while dendritic on 308L SS. By metallographic method, statistical results shown the ferrite content on 309L SS and 308L SS were about 9 and 12% respectively. Relevant research has found the distribution of ferrite on austenite stainless was related to the ratio of Cr_{eq}/Ni_{eq} and welding speeds [13–15]. Inclusions that have been identified mainly to be SiO_2 and MnS by EDS were found in 309L SS, as shown in Fig. 4a, which were not found in 308L SS owning to the different welding process. Nonmetallic inclusions were detrimental to the corrosion resistance of steels, including pitting corrosion, stress corrosion cracking and hydrogen-induced cracking [16, 17]. Figure 4b shows the main alloying elements distribution near the fusion zone, the element concentration gradient was 40–100 μm width mainly appeared in the carbon-rich zone.

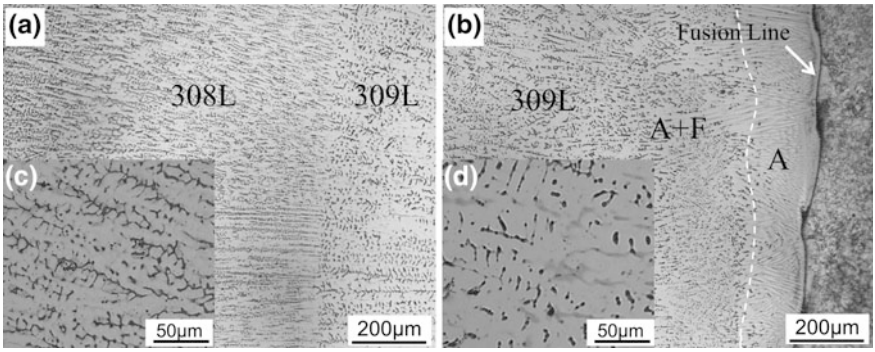

Fig. 3 Optical micrographs (**a**) 309L SS and 308L SS, (**b**) 309L SS near the fusion line, (**c**, **d**) the details of the micrographs for 308L SS and 309L SS respectively

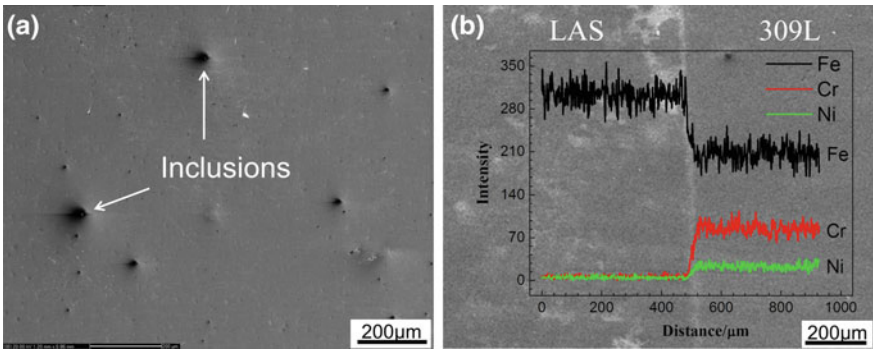

Fig. 4 SEM micrographs and EDS spectrum image (**a**) SEM of 309L surface, (**b**) the SEM-EDS near the fusion zone

Relationship Between Microstructure and Distribution of Oxide Film

Tests in the Oxygen-Containing PWR Water

After the immersion test in oxygen-containing PWR water at 290 °C for 168 h, oxide films formed on the weld specimen were characterized. Figure 5a shows the low magnification overall view of corrosion, the interface of oxide films on different parts of the weld was clear. Small and fine oxide particles were distributed on the oxide film surface of A508III, as shown in Fig. 5b. Corrosion pits with a diameter about 100 μm start appeared on A508III at 2–3 mm distance from the weld line (shown in Fig. 6a), while pits were not observed on A508III in deaerated water condition. EDS results shown that the inside of the corrosion pits was mainly iron oxides, which indicated that the accelerated corrosion of sensitive site happened on

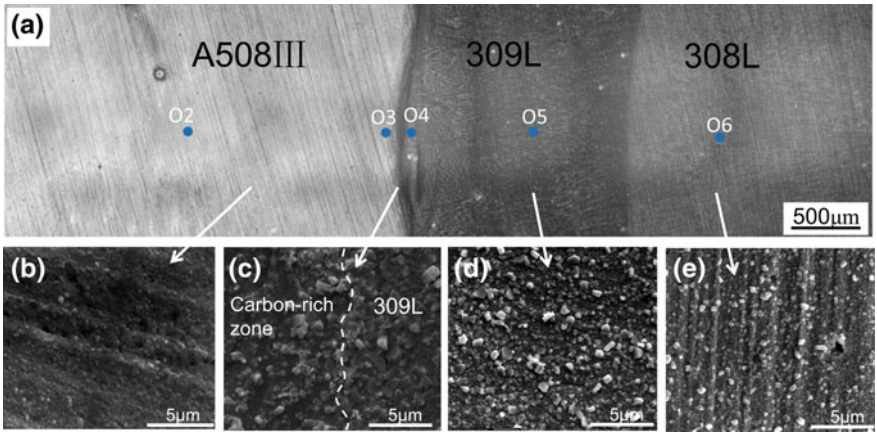

Fig. 5 The morphologies of corrosion film on the weld after immersion in the oxygen-containing high temperature water at 290 °C for 168 h (**a**) low magnification overall view of corrosion, (**b**) A508III, (**c**) weld, (**d**) surfacing layer on 309L SS, (**e**) surface layer on 308L SS

the surface of low alloy steel in oxygen-containing condition. The surface of 309L/308L SS was mainly covered with faceted particles of different sizes. EDS analysis showed that the chemical composition of outer particles on 309L SS was 59.77 wt% Fe, 18.08 wt% O, 12.28 wt% Cr and 7.02 wt% Ni. While the inner layer with fine oxides gave the main compositions of 54.34 wt% Fe, 10.08 wt% O, 20.68 wt% Cr and 10.95 wt% Ni, which indicated that the faceted particles were might mainly composed of Fe, Cr, Ni and O, Lower Cr and Ni content was found in the outer layer compared to matrix, whereas the content of Cr and Ni in the inner layer oxide film was closed to the matrix component. The distribution of oxide near the fusion line is displayed in Fig. 5c, oxide film on carbon-rich zone like the transition region covered with few faceted oxide particles because of the migration of Cr and Ni from SS to LAS. The large oxide particles inhomogeneous distributed on 309L SS were more than those on 308L SS as shown in Fig. 5d and e. Corrosion pits have been found only on 309L SS surface after immersion, its average size was about 20 μm in diameter, as shown in Fig. 6b.

Immersion in the Deaerated High Temperature Water at 290 °C for 168 H

Figure 7 shows the morphologies of film on weld surface after immersion in deaerated PWR water. Oxide particles on LAS-SS weld surface were larger. Oxide particles on 309L SS were denser than those on 308L SS obviously, and the higher content of Cr and Ni in 309L may be the factor. The different content of ferrite in 309L SS and 308L SS may be another factor that affect the forming of face oxide particles. Previous works have been reported that the interaction between the

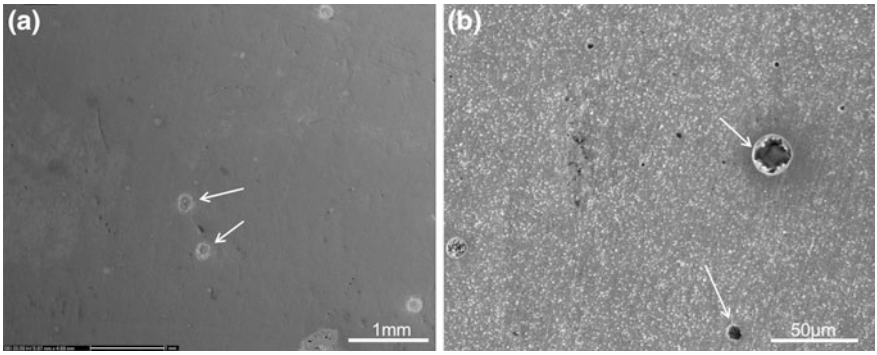

Fig. 6 Pitting of surface after immersion in the oxygen-containing high temperature water (**a**) A508III, (**b**) 309L SS

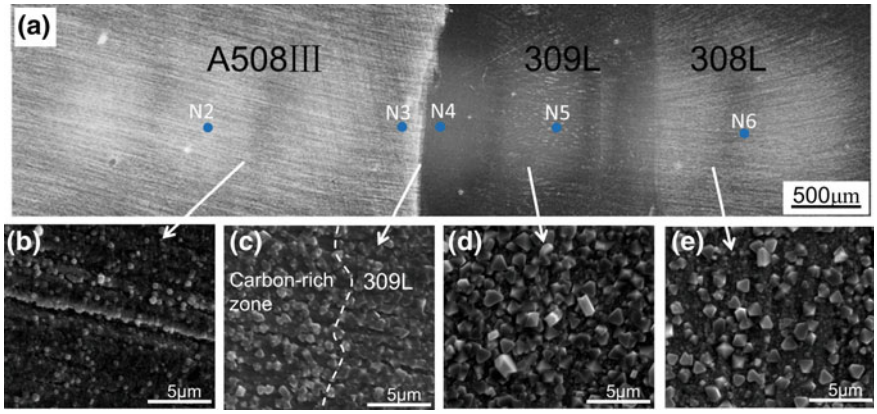

Fig. 7 The morphologies of the surface film on the weld after immersion in the deaerated PWR water at 290 °C for 168 h (**a**) low magnification overall view of corrosion, (**b**) low alloy steel, (**c**) near the weld fusion line, (**d**) surface layer on 309L SS, (**e**) surface layer on 308L SS

Table 3 Chemical composition of inclusions and pits on 309L SS after immersion (wt%)

	Fe	Cr	Ni	Mn	Si	O	Al
Inclusions	9.41	6.50	0.81	32.42	17.86	27.09	3.40
Pits	22.22	22.55	1.92	7.56	0.63	20.48	2.74

austenite and the ferrite would affect the corrosion potential of dual-phase steel [18, 19]. Corrosion pits could be found only on 309L SS, and the size and distribution of pits were similar to the inclusions on 309L, as shown in Fig. 4a. EDS results were displayed in Table 3. The preferential dissolution of Si in oxide films in high temperature water has been reported [20]. The decrease of Si and Mn in pits revealed that inclusions were dissolved in oxygen-containing and deaerated high temperature water.

The Effect of Oxygen Content on the Oxide Film of Welding

Figure 8 shows the Raman spectroscopy results of oxide film formed on A508III after immersion, and O1, O2, O3 and N1, N2, N3 indicating the different locations of detection from the fusion line, as shown in Fig. 5a and Fig. 7a, O1 and N1 were out of those pictures. It can found that the film formed on HAZ and base metal has no sharp distinction. According to the Raman characteristic peaks, 295,550 and 680 cm^{-1} were the characteristic peaks of Fe_3O_4, while 300 and 670 cm^{-1} were the characteristic peaks of Fe_2O_3. From the Fig. 8a, Fe_2O_3 and Fe_3O_4 were detected on A508III surface film in oxygen-containing PWR water while Fe_3O_4 was detected on A508III surface film in deaerated condition. From the potential-pH diagram [21], Fe_2O_3 was more stable in oxygen-containing high temperature water and Fe_3O_4 was more stable in deaerated high temperature water. The relative intensity of the Raman characteristic peak was correlated to the proportion of the corresponding oxide structure, as shown in Fig. 8. In oxygen-containing PWR water, A508III surface oxide film was mainly Fe_2O_3, while in deaerated PWR water was mainly Fe_3O_4.

The films on 309L/308L SS surface were characterized by Raman spectroscopy. O4, O5, O6 and N4, N5, N6 indicating the different locations of detection from the fusion line, the corresponding detection position is shown in Fig. 5a and Fig. 7a. As shown in Fig. 9, the Raman peaks at 320, 472, 550, 570, and 676 cm^{-1} were characteristics of spinel with AB_2O_4. According to EDS results, spinel should be $(Fe, Ni)(Fe, Cr)_2O_4$ which formed on both 309L SS and 308L SS in deaerated water was larger in size and denser in distribution than that in oxygen-containing water. It was indicated that low oxygen content was favorable for the formation of spinel. Oxide concentration has great effect on the electrochemical corrosion potential of metal in high temperature water [22]. Spinel was more stable at low dissolved oxygen concentration in PWR water [23].

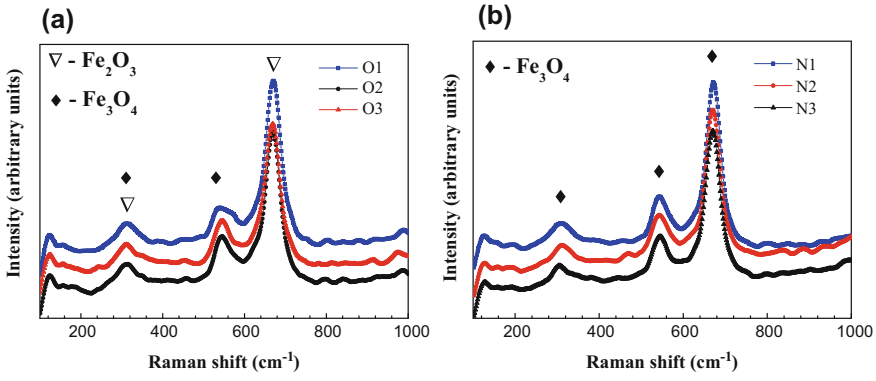

Fig. 8 The Raman spectroscopy results of the surface film on A508 III steel after 168 h immersion, (**a**) in oxygen-containing water, (**b**) in deoxygenized water

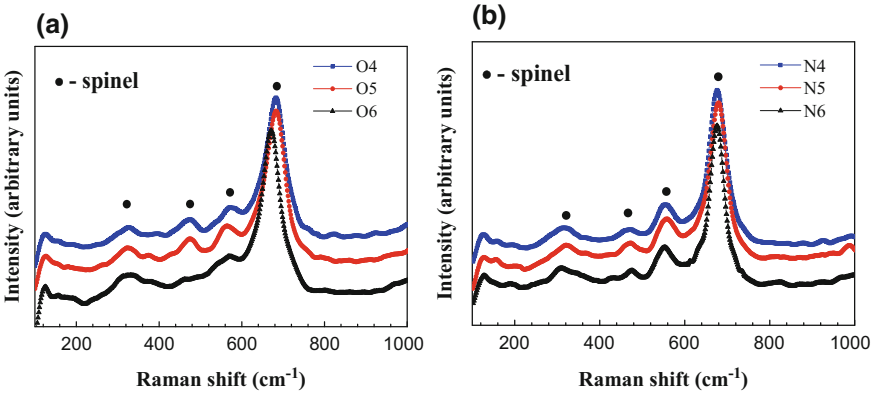

Fig. 9 The Raman spectra of the surface films on 309L/308L SS after 168 h immersion, (**a**) in oxygen-containing PWR water, (**b**) in deaerated PWR water

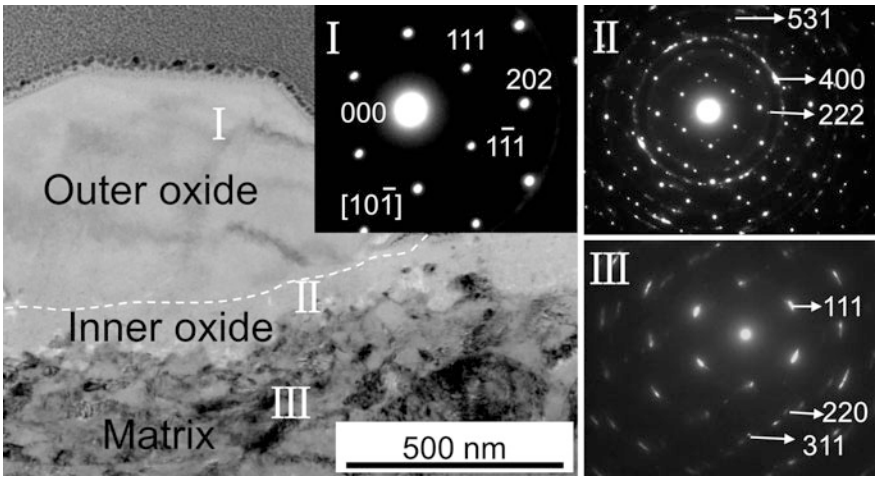

Fig. 10 TEM image and corresponding electron diffraction patterns of the oxide film on 309L SS after exposure in deaerated water at 290 °C. The white dotted line indicates the interface of the outer-layer and the inner-layer oxide film

TEM images of oxide film formed on SS surface after immersion in deaerated water conditions are displayed in Figs. 10 and 11. The white region was the oxides with the duplex structure. The outer layer was composed of large and dispersive oxide particles that were determined to be spinel-type structure by the diffraction pattern (as shown in Figs. 10I and 11I). Combined with TEM-EDS results, those particles should be (Fe, Ni) $(Fe, Cr)_2O_4$, which was consistent with the Raman spectroscopy results. TEM results show that the inner layer of the oxide film on 309L SS was about 140 ± 20 nm thick (region II in Fig. 10), whereas that of 308L

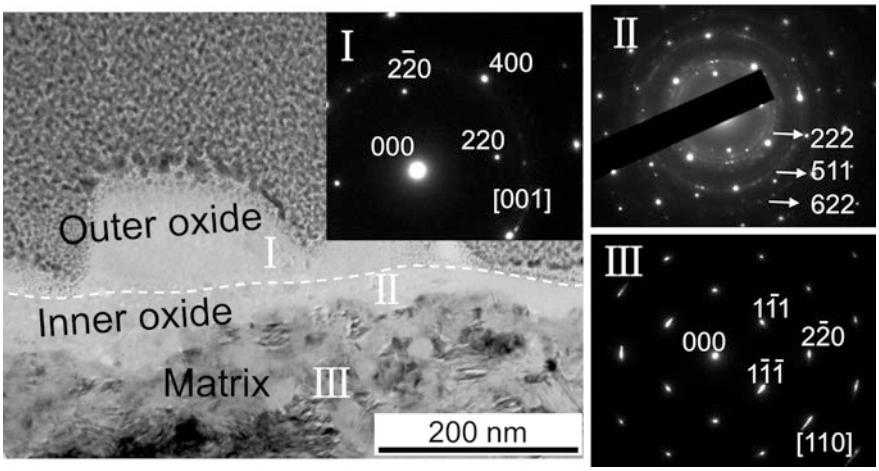

Fig. 11 TEM image and corresponding electron diffraction patterns of the oxide film on 308L SS after exposure in deaerated water at 290 °C. The white dotted line indicates the interface of the outer-layer and the inner-layer oxide film

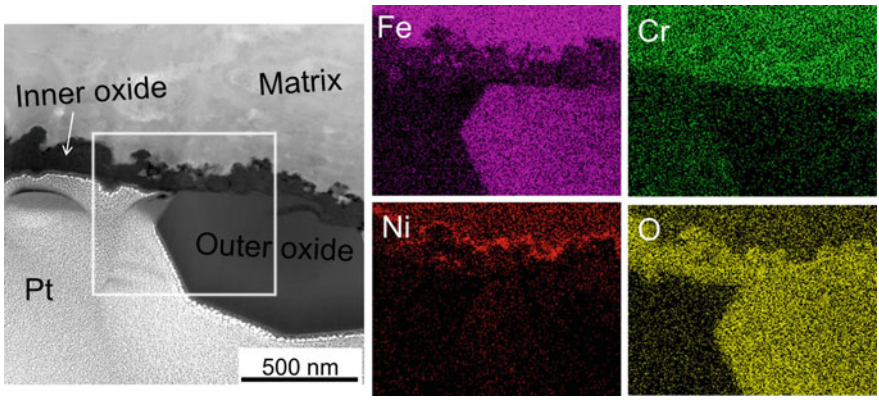

Fig. 12 STEM-HAADF images of the oxide film on 309L SS and the corresponding EDS mappings for Cr, Ni, Fe, and O after immersion in deaerated PWR water at 290 °C

SS was about 60 ± 30 nm thick (region II in Fig. 11). The SAED pattern of region II from the inner layer showed diffraction ring which indicated the presence of fine spinel oxides in the inner layer, and the dark area (region III) was matrix with FCC structure which mean the matrix of 309L SS and 308L SS in the cross sectional analysis was austenite.

Figures 12 and 13 show the EDS mappings of the oxide layers on 309L SS and 308L SS respectively. EDS results show that the outer oxide layer was rich in Fe and the inner layer was rich in Cr. It was worth noting that Ni-enriched layer

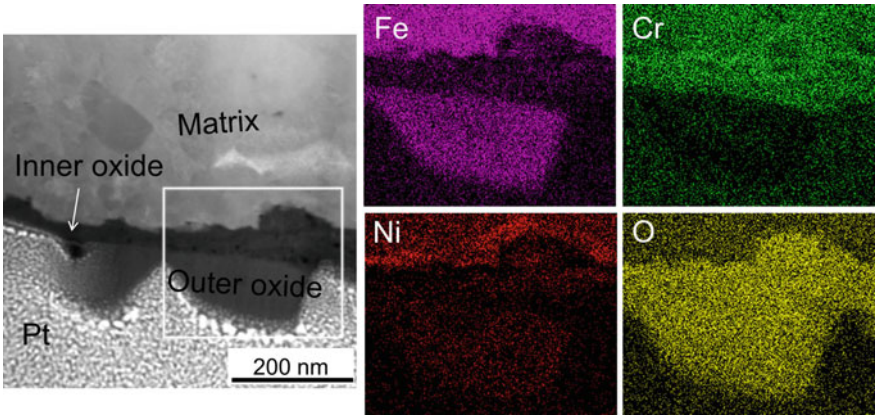

Fig. 13 STEM-HAADF image of the oxide film on 308L SS and the corresponding EDS mappings for Cr, Ni, Fe and O after immersion in deaerated PWR water at 290 °C for 168 h

appeared at the interface between the inner layer and the matrix. The oxidation rate of Ni was lower than that of Fe and Cr in the oxidation process, because of the low oxygen affinity Ni was the least likely to be oxidized compared with Fe and Cr [24, 25], therefore the migration rate of Ni into the oxide films was very low, resulting in the enrichment of Ni in the interface of inner layer and matrix. The enrichment of Cr in the inner layer contributed to the corrosion resistance. Das et al. [26] have found that it was slower for atoms to diffuse in Cr-rich oxide than in Fe or Ni-rich oxide, and a Cr-rich oxide layer protective and limits oxide growth. Han et al. [20] reported that the inner layer of the oxide film formed on 316L SS with a higher Cr content was thinner than that on 9Cr-26Ni-1.5Mo-5Si alloy. In this work, the inner layer of 308L SS was thinner than that of 309L SS, but there was no significant difference in the Cr content of the inner layer of 309L and 308L SS. This can be due to the galvanic interaction influence of α-phase in stainless steel. Previous researchers have studied the electrochemical properties between ferrite and austenite [27, 28], α-phase improved the open circuit potential of γ- phase and the passive film impedance of single γ-phase increased after the contact of the two phases. The oxide film on the duplex stainless steel showed better corrosion resistance. Compared with 309L SS, the ferrite content in 308L SS was higher, which indicated lower growth rate of oxide film on 308L SS than on 309L SS, therefore the inner oxide layer on 308L SS was thinner than that on 309L SS.

Conclusions

Oxide film formed on stainless steel cladding on low alloy steel after immersion in simulated PWR primary water environments with different dissolved oxygen contents were studied. The HAZ in the A508III consist of overheated crystal region,

complete recrystallization region and incompletely recrystallization region. While SS cladding consist of austenite zone, austenite and ferrite mixing zone. Ferrite content is higher in 308L SS than that in 309L SS with surface inclusions that are mainly SiO_2 and MnS. Pitting appeared on 309L SS after immersion in oxygen-containing high temperature water due to the dissolution of inclusions. The oxide film is divided into two layers, with the outer layer mainly Fe-rich spinel oxide and the inner layer is mainly Cr-rich oxides. Ni enrichment is evidenced at the oxide/substrate interface. The inner oxide layer on 308L SS is thinner than that on 309L SS, implying that ferrite distributed in the austenite is not favorable for the growth of oxides. Reducing the oxygen content in PWR primary water favored the formation of spinel oxides.

Acknowledgements This work was supported by Shanghai Municipal Commission of Economy and Informatization No. T-221715003, National Natural Science Foundation of China (51571138), and the International Cooperative Project sponsored by Science and Technology Commission of Shanghai Municipality No. 13520721200.

References

1. K.S. Kim et al., Residual stress analysis of an overlay weld and a repair weld on the dissimilar butt weld. Nucl. Eng. Des. **239**(12), 2771–2777 (2009)
2. H. Xue et al., The effect of single tensile overload on stress corrosion cracking growth of stainless steel in a light water reactor environment. Nucl. Eng. Des. **241**(3), 731–738 (2011)
3. J.C. Lippold, D.J. Kotecki, *Welding Metallurgy and Weldability of Stainless Steels* (Wiley, New Jersey, NJ, 2015), p. 376
4. R. Kaçar, O. Baylan, An investigation of microstructure property relationships in dissimilar welds between martensitic and austenitic stainless steels. Mater. Des. **25**(4), 317–329 (2004)
5. K.H. Lee et al., Analysis of the master curve approach on the fracture toughness properties of SA508 Gr.4 N Ni-Mo-Cr low alloy steels for reactor pressure vessels. Mater. Sci. Eng. A **527** (15), 3329–3334 (2010)
6. G.V. Rao et al., Experience with Bimetallic Weld Cracking. in *Proceedings of International Symposium Fontevraud III,* (French Nuclear Energy Society, France, 1994) **1**, pp. 146–153
7. O.D. Bouvier, B. Yrieix, Grain Boundary Defects Initiation at the Outer Surface of Dissimilar welds. in *Proceedings of the Seventh International Symposium on Environmental Degradation of Materials in Nuclear Power Plants: Water Reactors meeting*, (NACE International, Houston, 1995) **1**, pp 93–104
8. A. Laukkanen et al., Characteristics relevant to ductile failure of bimetallic welds and evaluation of transferability of fracture properties. Nucl. Eng. Des. **237**(237), 1–15 (2007)
9. G.F. Li, E.A. Charles, J. Congleton, Effect of post weld heat treatment on stress corrosion cracking of a low alloy steel to stainless steel transition Weld. Corros. Sci. **43**(10), 1963–1983 (2001)
10. R.H. Khalid et al., Microstructural evolution during friction surfacing of austenitic stainless steel AISI 304 on low carbon steel. Metallurg. Mater. Trans. A **44**(1), 345–350 (2013)
11. H.S. Peavy, D.R. Matthews, G. Tchobanoglous, *Environmental Engineering* (McGraw–Hill Book Company, New York, NY, 1985), p. 694
12. Y. You, R.K. Shiue, The study of carbon migration in dissimilar welding of the modified 9Cr-1Mo steel. J. Mater. Sci. Lett. **20**(15), 1429–1432 (2001)

13. J.W. Fu, Y.S. Yang, J.J. Guo, Formation of a blocky Ferrite in Fe–Cr–Ni alloy during directional solidification. J. Cryst. Growth **331**(14), 3661–3666 (2009)
14. A. Hunter, M. Ferry, Phase formation during solidification of AISI 304 austenitic stainless steel. Scripta Mater. **46**(4), 253–258 (2009)
15. N. Suutala, Effect of solidification conditions on the solidification mode in austenitic stainless steels. Metallurg. Mater. Trans. A **14**(1), 191–197 (1983)
16. S.Q. Zheng et al., Mechanism of (Mg, Al, Ca)-oxide inclusion-induced pitting corrosion in 316L stainless steel exposed to sulphur environments containing chloride Ion. Corros. Sci. **67** (1), 20–31 (2013)
17. M. Elbouj, R.W. Revie, Metallurgical factors in stress corrosion cracking (SCC) and hydrogen-induced cracking (HIC). J. Solid State Electrochem. **13**(7), 1091–1099 (2009)
18. C.T. Kwok et al., Pitting and galvanic corrosion behavior of laser-welded stainless steels. J. Mater. Process. Technol. **176**(1–3), 168 (2006)
19. C.T. Kwok, et al., Investigation of Galvanic Corrosion in Laser-Welded Stainless Steel Sheets. in *Paper presented at Fifth International Symposium on Laser Precision Microfabrication*, 2004, p. 5662
20. G.D. Han et al., Properties of oxide films formed on 316L SS and model alloys with modified Ni, Cr and Si contents in high temperature water. Corros. Sci. **106**, 157–171 (2016)
21. N. Toshiyasu, K. Toshiaki, Clarification of chemical state for alloying elements in iron rust using a binary-phase potential–pH diagram and physical analyses. Corros. Sci. **45**(5), 1073–1084 (2003)
22. Y.J. Kim, P. Andresen, Data quality, issues and guidelines for ECP measurement in high temperature water. Corrosion **59**, 584–597 (2003)
23. B. Beverskog, I. Puigdomenech, Revised pourbaix diagrams for iron at 25–300 °C. Corros. Sci. **38**, 2121–2135 (1996)
24. M.C. Sun et al., Oxidation of 316 stainless steel in supercritical water. Corros. Sci. **51**(5), 1069–1072 (2009)
25. K.I. Choudhry et al., Corrosion of engineering materials in a supercritical water cooled reactor: Characterization of oxide scales on alloy 800H and stainless steel 316. Corros. Sci. **100**(11), 222–230 (2015)
26. N.K. Das et al., Early stage SCC initiation analysis of FCC Fe–Cr–Ni ternary alloy at 288 °C: A quantum chemical molecular dynamics approach. Corros. Sci. **51**(4), 908–913 (2009)
27. Q.S. Guo et al., Galvanic effect between ferrite and austenite in 2205 duplex stainless steel. Corros. Protect. **36**(12), 1119–1123 (2015)
28. Y. Wang, X.Q. Cheng, X.G. Li, Electrochemical behavior and compositions of passive films formed on the constituent phases of duplex stainless steel without coupling. Electrochem. Commun. **57**, 56–60 (2015)

Microstructural Characterization of Alloy 52 Narrow-Gap Dissimilar Metal Weld After Aging

Teemu Sarikka, Roman Mouginot, Matias Ahonen, Sebastian Lindqvist, Ulla Ehrnstén, Pekka Nevasmaa and Hannu Hänninen

Abstract The safe-end dissimilar metal weld (DMW) joining the reactor pressure vessel to the main coolant piping is one of the most critical DMWs in a nuclear power plant (NPP). DMWs have varying microstructures at a short distance across the ferritic-austenitic fusion boundary (FB) region. This microstructural variation affects the mechanical properties and fracture behavior and may evolve as a result of thermal aging during long-term operation of an NPP. This paper presents microstructural characterization performed for as-manufactured and 5000 h and 10,000 h thermally aged narrow-gap DMW representing a safe-end DMW of a modern pressurized water reactor (PWR) NPP. The most significant result of the study is that the thermal aging leads to a significant decrease in a hardness gradient observed across the ferritic-austenitic FB of the as-manufactured DMW.

Keywords Dissimilar metal weld · Ni-base alloy · Microstructural characterization · Aging

Introduction

The main structural materials used in the primary circuit of pressurized water reactor (PWR) nuclear power plants (NPP) consist of ferritic low-alloy steels (LAS), stainless steels (SS), and Ni-base alloys [1]. LASs alloyed with small amounts of Cr, Ni, Mo, and V are used for structural components due to their high strength. Austenitic SSs are used for core components, piping, and

T. Sarikka (✉) · R. Mouginot · H. Hänninen
Aalto University School of Engineering, P.O. Box 14200, 00760 Aalto, Finland
e-mail: teemu.sarikka@aalto.fi

M. Ahonen · S. Lindqvist · U. Ehrnstén · P. Nevasmaa
VTT Technical Research Centre of Finland Ltd, VTT,
P.O. Box 1000, FI-02044 Espoo, Finland

J.H. Jackson et al. (eds.), *Proceedings of the 18th International Conference on Environmental Degradation of Materials in Nuclear Power Systems – Water Reactors*, The Minerals, Metals & Materials Series, https://doi.org/10.1007/978-3-319-68454-3_58

corrosion-resistant claddings of the reactor pressure vessel (RPV), pressurizer, and steam generators. Ni-base alloys are, again, used for high-strength components and welds, especially when high corrosion resistance is required [2]. Dissimilar metal welds (DMW) are welds in which a combination of these materials with different compositions and crystal structures are joined together. There has been a number of DMW failures observed in NPPs during their service lives and, due to that, DMWs are among the first entries on the IAEA list of critical items in PWR NPPs [3].

A typical example of a DMW in an NPP is the RPV nozzle to safe-end weld between SS-cladded ferritic RPV steel and austenitic SS piping using Ni-base alloy filler metal. These alloys have significantly different compositions, especially regarding the C, Cr, and Ni contents and due to that, a composition gradient forms at the interface and a complex microstructure results from the mixing and diffusion of alloying elements. The reduced Cr and Ni contents in the transition region due to dilution effects tend to increase the stress corrosion cracking (SCC) susceptibility with respect to the bulk weld metal [4]. Simultaneously, the formation of hard and soft layers, driven by the composition gradients and microstructures, leads to mechanically weak points in the un-mixed zone (UMZ) or partially melted zone (PMZ) and increases the strength mismatch at the ferritic-austenitic interface. Hence, the interface is more complex than that of a similar metal weld interface and the key microstructural factors in the formation of the hard and soft zones are carbon-depleted zone (CDZ), martensitic zone, C build-up zone and Type II boundaries [4–7]. The CDZ results from the carbide dissolution and migration of C from the HAZ of the ferritic steel to the Ni-base weld metal near the fusion boundary. The difference in composition results in different C activity promoting the diffusion of C leaving a layer of ferritic grains with low hardness to the HAZ of ferritic steel [5]. This phenomenon is further increased by post-weld heat treatment (PWHT) [8]. Martensitic regions have often been observed within the UMZs of DMWs. The existence of a martensitic region is due to the formation of intermediate compositions with high hardenability at the ferritic-austenitic interface and further transforming to martensite upon rapid cooling during a welding thermal cycle [9].

The use of Ni-base alloy weld metals has reduced the width of the martensitic region and the migration of C from the ferritic side compared to stainless steel weld metals. On the other hand, low diffusivity of C in Ni-base alloys results in an accumulation of C close to the ferritic-austenitic fusion boundary, which may lead to the formation of C build-up of about 1.5 wt% C in the Ni-base alloy weld metal next to the fusion boundary. A narrow planar solidification front of about 3–5 μm can also be observed close to the fusion boundary inside the weld metal. It shows neither dendritic structure nor precipitation, and has very steep composition gradients and high hardness levels due to the C build-up [10, 11]. The precipitation of carbides when the solubility limit of C is exceeded is also associated with high hardness levels and brittle microstructures susceptible to hydrogen-assisted cracking [12, 13]. Type II boundaries are essentially grain boundaries parallel to the fusion boundary in the weld metal. They result from the different crystal structure of

the metals across the interface. After austenitization of the ferritic steel at high temperature, the original fusion boundary becomes an austenitic-austenitic boundary, which can migrate into the austenitic weld metal. The distance between the Type II boundary and the fusion boundary is therefore controlled by the composition and temperature gradients within the transition region. They are a common feature affecting the failure of DMWs and the presence of Type II boundaries reduces SCC resistance and can lead to intergranular (IG) cracking under simulated reactor coolant conditions [14].

DMWs have been related to a number of incidents involving IG cracking of austenitic SS piping [2, 15, 16] with sensitive microstructures found in the HAZ of SS and Ni-base alloys and within the weld metal [17, 18]. Ni-base weld metal Alloys 82 and 182 have previously increased the service life of DMWs by reducing C migration at the interface and differential thermal expansion strains [19], but they are susceptible to SCC and cracking incidents concerning Alloys 600 and 182 used in the RPV head penetrations have been observed in many plants [2, 16]. Intergranular stress corrosion cracking (IGSCC) initiated mostly in the HAZ of Alloy 600 welded with Alloys 182 and 82, due to the presence of corrosion environment, residual stress, and material sensitization effects. This type of IGSCC in high temperature and in pressurized water environment is called primary water SCC (PWSCC) [20, 21]. DMW interfaces are generally susceptible to SCC as they are present as narrow transition zones in terms of chemical composition, crystal structure, and different thermal expansion coefficient.

Following the improvements in the chemical compositions to reduce the effect of SCC, higher Cr containing Alloy 690 has replaced Alloy 600 and Alloy 52, 152, and 52 M filler metals are used in modern NPP DMWs [22]. With higher Cr content, they show better SCC resistance with significant improvement in crack initiation times and crack growth rates (CGR) [23]. However, the thermal stability of Alloy 690 in the long-term performance of NPPs operating as long as 60–80 years remains questionable [24]. In addition, the susceptibility of welds to SCC depends not only on the properties of the base and weld metals, but also on the microstructural changes taking place at the weld interface during welding and PWHT. The behavior of higher Cr containing Alloys 690, Alloy 52, and 152 after long-term exposure to the PWR conditions, and especially thermal aging, is therefore of major importance, especially since there is still little knowledge about the long-term behavior of such DMWs, and no long-term in-service experience is yet available.

Experimental Methods

Microstructural characterization was performed to an as-manufactured and thermally aged narrow-gap DMW mock-up representing a safe-end DMW of a modern PWR NPP. The thermal aging was performed at a temperature of 400 °C for

durations of 5000 h and 10,000 h. Aging parameters (10,000 h and 400 °C) were chosen equivalent to 60 years of operations at PWR in-service temperature in terms of GB segregation of phosphorous in RPV steel, which is assumed to be the governing factor for the structural integrity of the DMW [25]. The DMW mock-up consisted of SA 508 ferritic RPV steel and Type 316L SS base metals, SS 309L/308L cladding on the RPV steel, and Alloy 52 weld metal without any buffer. A cross-section of the DMW mock-up is presented in Fig. 1 and chemical compositions of the base and weld materials are presented in Table 1. The samples from each weld condition were extracted by electrical discharge machining (EDM), ground with SiC paper up to 4000 grit, polished with diamond polishing paste up to 0.25 μm, and finally polished in a vibratory polisher using colloidal silica suspension. The microstructural characterization was performed using light optical microscopy (LOM) and scanning electron microscopy (SEM) with energy-dispersive X-ray spectroscopy (EDS) and electron backscatter diffraction (EBSD). The microhardness measurements were performed using an instrumented microhardness tester equipped with a Vickers tip with an indentation load of 350 mN. The nanoindentation measurements were performed using a CSM nanoindentation tester equipped with a Berkovich tip with an indentation load of 1.5 mN.

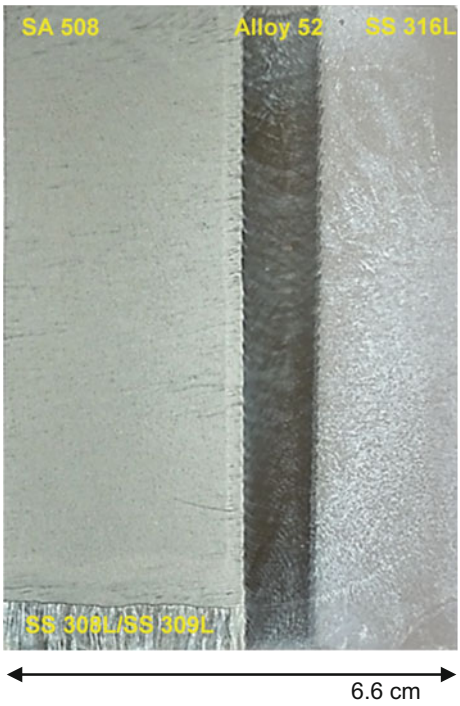

Fig. 1 A cross-section macrograph of the studied DMW

Table 1 Chemical compositions (in wt%) of the materials used in the studied DMW

	SA 508 Gr. 2	AISI 316 L	AISI 308 L	Alloy 52
C	0.21	0.023	0.007	0.023
Si	0.17	0.53	0.37	0.15
Mn	0.78	1.29	1.9	0.26
P	0.002	0.031	0.013	<0.005
S	0.009	0.002	0.001	0.0007
Cr	0.45	17	20.3	29.93
Ni	0.85	10.1	10.3	58.86
Mo	0.62	2.04	0.1	<0.01
Nb				<0.01
N	0.014	0.04	0.04	0.021
Ti	0.002			0.54
Fe	Bal.	Bal.	Bal.	10.43
Al	0.016			0.66
Co	<0.003			<0.01
Cu	0.06		0.05	<0.01

Results

Characterization of the SA 508 HAZ

As shown in Fig. 2, the HAZ of the SA 508 extends about 2.5 mm from the fusion boundary to the base metal. The SA 508 base metal (about 240 HVIT) consists of coarse ferrite grains and bainite clusters. Starting from the SA 508 base metal, the microstructure refines progressively towards the fusion boundary due to the heat input from the welding process. First, a partially grain-refined zone exists followed by a grain-refined zone of higher hardness (about 280 HVIT). Closer to the fusion boundary, the heat input during welding has caused grain coarsening and immediately adjacent to the fusion boundary is a CDZ (about 230 HVIT) with coarse grains from which C has diffused to the higher Cr containing Alloy 52 weld metal side of the interface. The presence of lighter and darker bands in the SA 508 HAZ, obviously resulting from macro-segregation during manufacturing, should also be noted. The darker bands have a smaller grain size and are harder (about 300 HVIT) than the rest of the HAZ.

PWHT used to temper DMWs is a standard procedure used for residual stress relaxation of the components, resulting in widening of the CDZ in the SA 508 HAZ [11]. As can be seen in Fig. 3, a CDZ of about 60–70 µm wide is visible in the SA 508 side of the ferritic-austenitic interface of the studied DMW. However, thermal aging at 400 °C for 10,000 h does not seem to influence the width of the CDZ. In addition, a comparison of the microstructures in the SA 508 HAZ between the as-manufactured and the 10,000 h aged DMW does not reveal noticeable changes using LOM or SEM, as shown in Fig. 4.

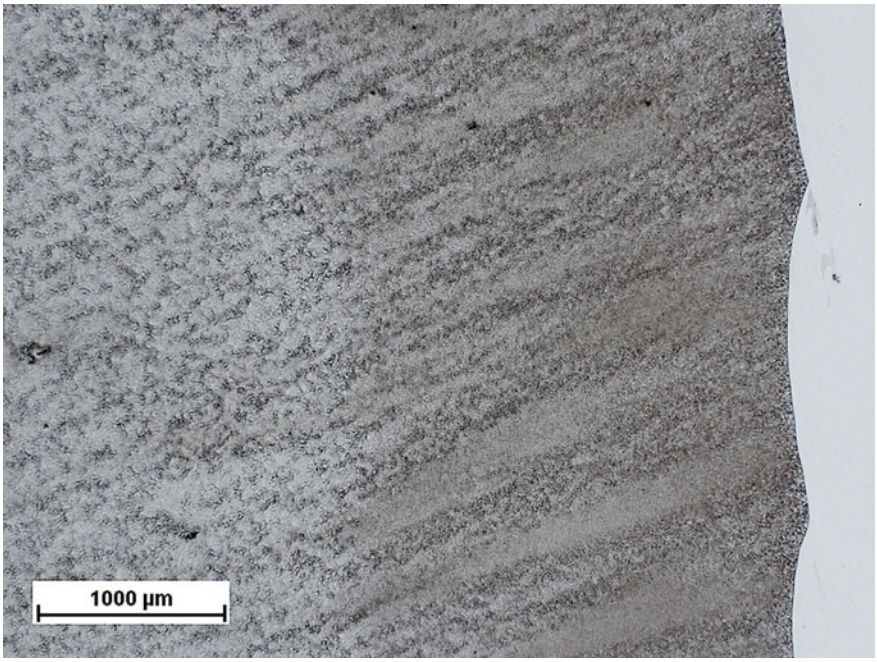

Fig. 2 Optical image showing the ferritic-austenitic interface of the DMW mock-up before aging

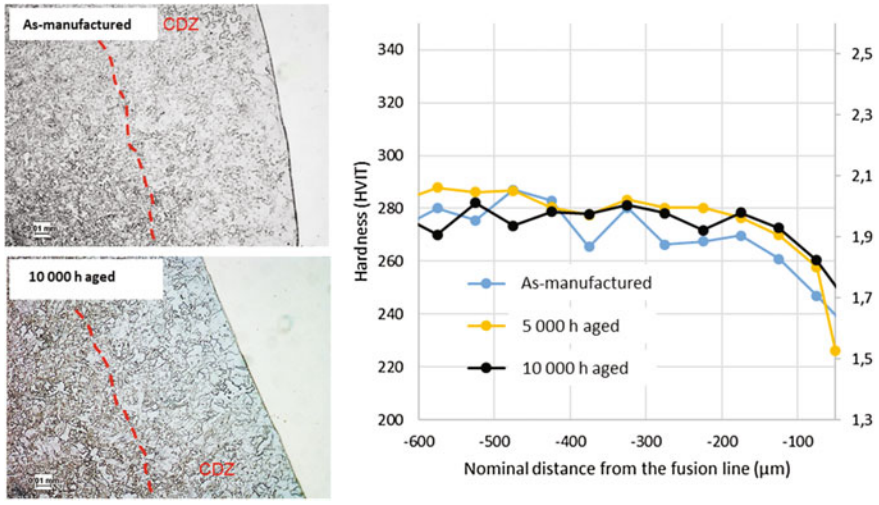

Fig. 3 Optical images of the SA 508-Alloy 52 weld metal interface in as-manufactured and at 400 °C for 10,000 h thermally aged conditions with corresponding hardness profiles. The thermal aging seems to have no effect on the CDZ

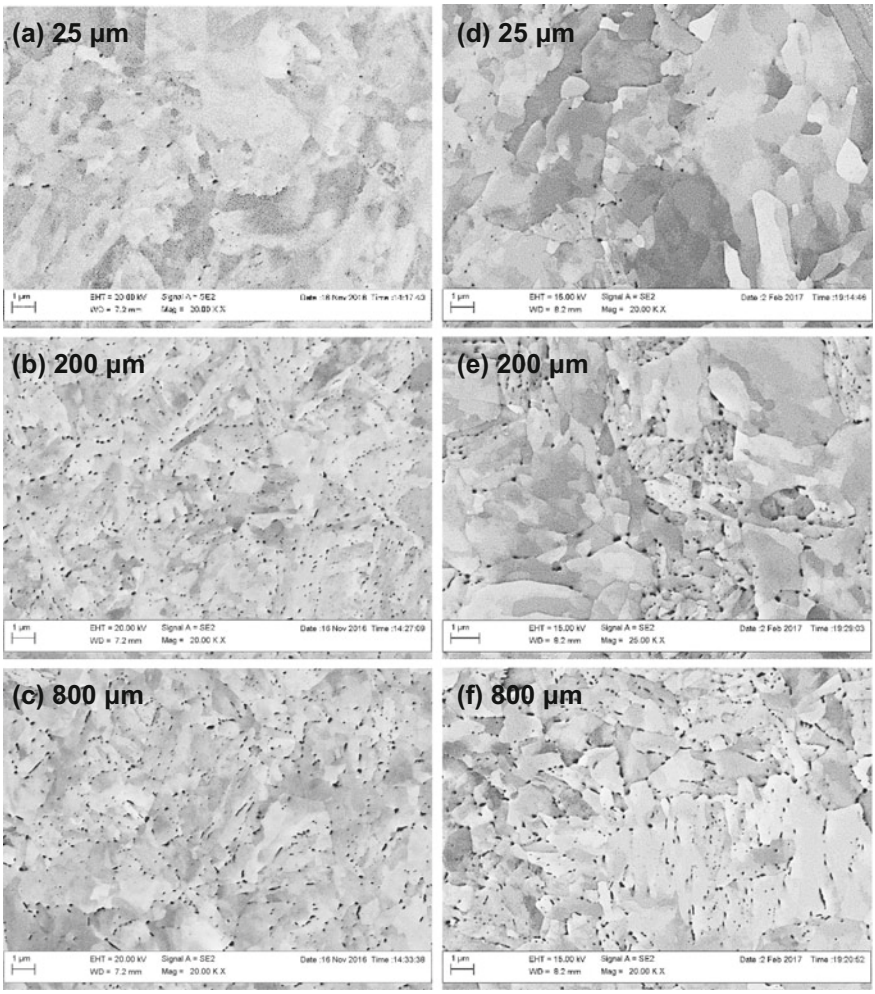

Fig. 4 SEM images showing the SA 508 HAZ microstructure in the as-manufactured (left) and at 400 °C for 10,000 h thermally aged (right) conditions taken next to the fusion boundary (**a** and **d**), 200 µm from the fusion boundary (**b** and **e**), and 800 µm from the fusion boundary (**c** and **f**)

Characterization of Alloy 52 Weld Metal

Microhardness measurements were carried out on the Alloy 52 weld metal in the studied conditions and the results are presented in Table 2. The hardness of the Alloy 52 weld metal increases from the weld crown to the weld root, with thermal aging having small or no influence on the weld metal hardness. Thermal aging at 400 °C has an insignificant influence on the microstructure outside the fusion zone, as shown in Fig. 5, and on the hardness levels in the Alloy 52 weld metal.

Table 2 Microhardness variation in Alloy 52 weld metal from the weld crown to the weld root, before and after aging at 400 °C for 5000 and 10,000 h

	Crown		Center		Root	
	Mean HVIT	SD	Mean HVIT	SD	Mean HVIT	SD
As-manufactured	232	8	247	14	268	10
5000 h	243	13	249	8	270	15
10,000 h	239	15	245	17	257	12

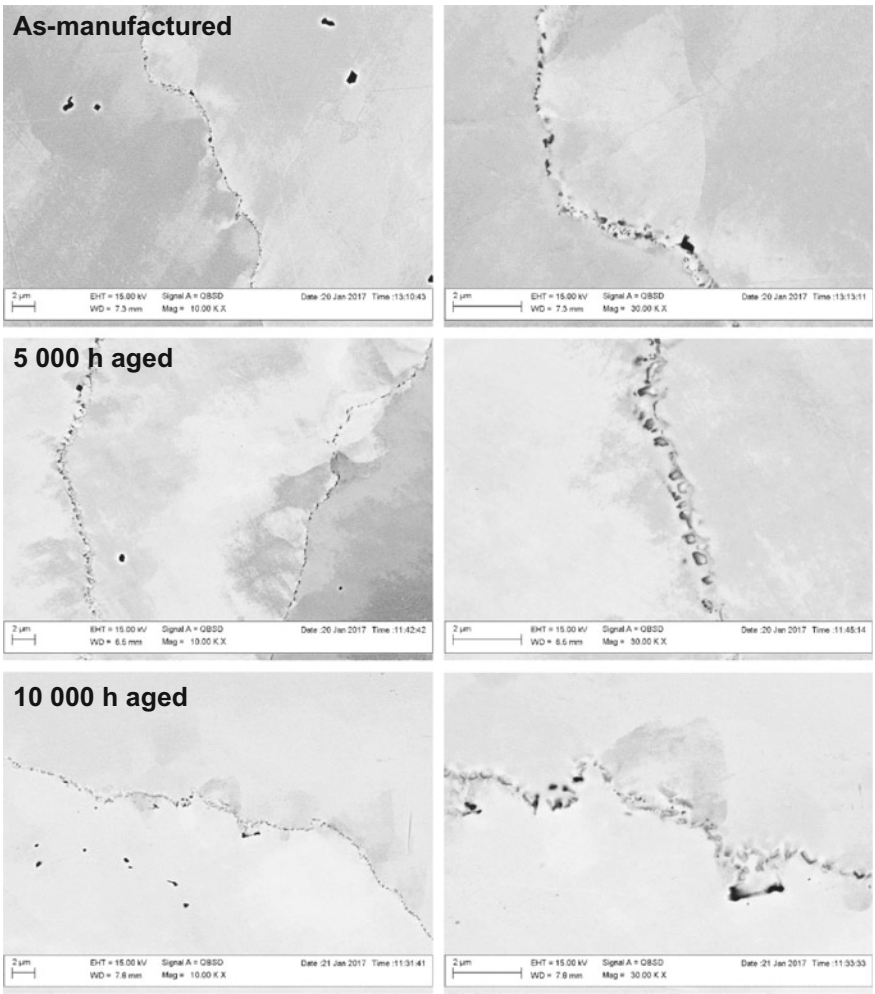

Fig. 5 SEM imaging showing GBs in Alloy 52 weld metal in as-manufactured condition and after aging at 400 °C for 5000 and 10,000 h

However, transition zones in DMWs are traditionally susceptible to metallurgical changes and represent a critical location that must be investigated along with the weld metal [11, 26]. The transition zone from the SA 508 to the Alloy 52 weld metal is of particular interest since it joins two materials with different lattice structures and very different composition.

Characterization of the Ferritic-Austenitic Interface

Along with the formation and development of a PMZ, the existence of the weld passes modifies the composition gradients at the pass boundaries across the SA 508-Alloy 52 interface significantly. The PMZ has a composition still close to that of SA 508, and is comprised mostly of ferritic grains. The Fe- and Ni-composition gradients from SA 508 to the Alloy 52 weld metal are less steep beyond the PMZ when compared to a fusion boundary location without a PMZ. An EDS elemental map presented in Fig. 6 shows that this phenomenon is a result of the location of the PMZ at the start of a weld pass. The weld pass sweeps material from SA 508 into the weld metal generating the PMZ but also mixing more SA 508 into the weld. It results in a significant local Fe enrichment in the weld metal, which then results in a formation of martensite-like layers that are harder than the surrounding base and weld metal.

Micro- and Nanohardness Profiles

The results of metallurgical changes in the narrow transition zones of DMWs are often visible as changes in hardness across the interface. Figure 7 shows microhardness profiles across the SA 508-Alloy 52 interface in the as-manufactured condition and after aging. The lowest hardness is found in SA 508 (220–230 HVIT) and the highest hardness in Alloy 52 weld metal (536 HVIT). The high range in the SA 508 HAZ hardness is due to the banded microstructure. The thermal aging affects the hardness profiles significantly, as the hardness peak on Alloy 52 weld metal side of the fusion boundary lowers as a result of aging for 5000 h (377 HVIT) and further upon aging for 10,000 h (331 HVIT) at 400 °C.

Significant changes occurring over narrow transition zones adjacent to the interface make the use of nanoindentation particularly useful. A smaller load and, thus, also smaller indentation size enables measurements with a better spatial resolution and characterization, for example, of the width of the hard layers and their position compared to the fusion boundary more precisely. Figure 8 shows hardness profiles across the SA 508-Alloy 52 interface obtained using nanoindentation. Before aging, a clear hardness peak (858 HVIT) starting from the fusion boundary and extending to some tens of μm away from the fusion boundary is observed on the Alloy 52 weld metal side. After 5000 h at 400 °C, the hardness peak in the

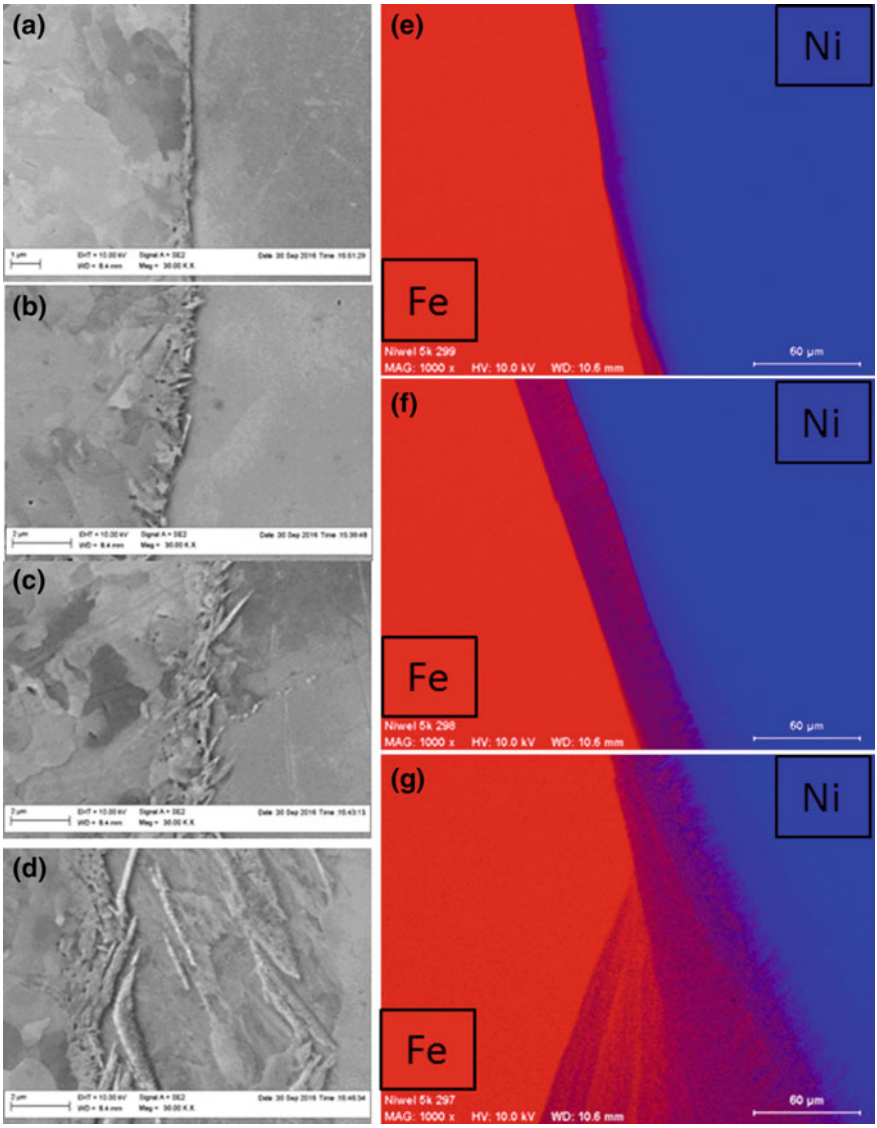

Fig. 6 SEM images of the different levels of PMZ observed at the fusion boundary between SA 508 and Alloy 52 in 5000 h at 400 °C aged interface with **a** a clean fusion boundary without PMZ, **b** the start of a feather-like layer, **c** a visible PMZ and **d** a large PMZ starting to be swept into the weld metal. EDS mapping of the start of a weld pass in the 5000 h at 400 °C aged interface showing the transition from a) a clean fusion boundary to **b** a PMZ and eventually to **c** a SA 508 swirl in the weld metal. The beginning of the weld pass increases the dilution of Fe (red) from the SA 508 to the Ni-rich (blue) weld metal (Color figure online)

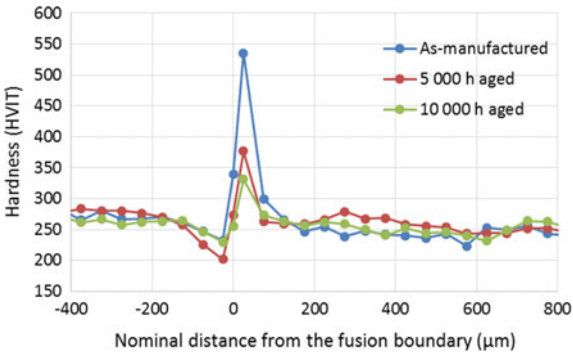

Fig. 7 Comparison of the microhardness profiles of as-manufactured, 5000 h aged, and 10,000 h aged at 400 °C SA 508-Alloy 52 weld metal interface

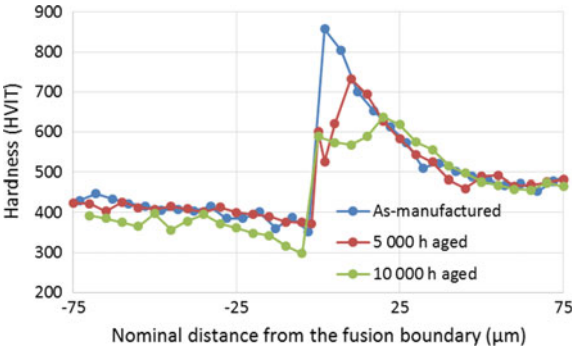

Fig. 8 Comparison of the nanoindentation hardness profiles of as-manufactured, 5000 h aged, and 10,000 h aged at 400 °C SA 508-Alloy 52 weld metal interface

Alloy 52 weld metal is lower (733 HVIT) and the width of the hard layer is narrower (about 5 µm). In addition, the hard layer is not adjacent to the fusion boundary anymore, but starts rather about 10 µm into the weld metal. The CDZ reaches softer values (319 HVIT) than in the as-manufactured condition (330 HVIT), although the average hardness is similar. After 10,000 h at 400 °C, the same trend is observed, i.e., the hardness peak in the Alloy 52 weld metal is lower (637 HVIT) and pushed further into the weld metal (about 20 µm). The CDZ reaches even lower values (280 HVIT).

Discussion

The main conclusion of the microstructural characterization is that the thermal aging at 400 °C for up to 10,000 h does not influence the hardness of the SA 508 HAZ or the Alloy 52 weld metal outside the fusion region and does not change the microstructure to the extent, which can be clearly detected using LOM and SEM. Microstructural characteristics of the Alloy 52 weld metal, the SA 508 HAZ, and the fusion boundary region showed no significant differences after the thermal

aging. Local grain boundary migration was observed in the aged Alloy 52 weld metal, however, it was also observed locally in the as-manufactured Alloy 52 weld metal. Hence, it is difficult to directly determine whether the grain boundary migration has occurred as a result of PWHT or as a result of thermal aging, or both. There was a notable variation in the local distribution of grain boundary carbides within the Alloy 52 weld metal. That makes stating whether thermal aging has caused precipitation or growth of grain boundary carbides difficult, especially compared to bulk metal alloys, such as solution annealed Alloy 690. It can be said, though, that the carbide precipitation or growth resulted from the thermal aging was not substantial. This is expected, since the observable effect of thermal aging for up to 10,000 h on the microstructure of Alloy 690, with a similar composition as Alloy 52, becomes significant at temperatures clearly higher than 400 °C [27]. Therefore, the thermal aging of Alloy 52 at 400 °C for 10,000 h is not enough to produce major visible changes in the microstructure using LOM and SEM, such as significant carbide precipitation or growth. Although the aging at this temperature does not produce visible microstructural changes in the material, it definitely can have an effect on the material properties through short-range ordering (SRO) [27] and diffusion of elements across the fusion boundary.

The SA 508-Alloy 52 near-interface region is, however, significantly affected by the thermal aging, which is clearly found to reduce the mechanical mismatch present at the interface of the as-manufactured condition DMW. The hardness peak in Alloy 52 weld metal decreases from 536 HVIT before aging to 377 HVIT after 5000 h at 400 °C and to 331 HVIT after 10,000 h. A similar trend is observed in the nanoindentation measurements, which additionally show that the position of the hardness peak in Alloy 52 weld metal moves further away from the fusion boundary due to thermal aging. A summary of the main hardness results is presented in Table 3.

Concerning the interface region, there is a clear correlation between the microstructural understanding and the microhardness and nanoindentation measurement results. The PWHT performed to DMW components promotes the diffusion of C from the relatively high-C/low-Cr SA 508 side of the weld interface to the low-C/high-Cr Alloy 52 weld metal side. It results in a CDZ in the SA 508 adjacent to the fusion boundary, while the C that has diffused piles up in the planar growth zone in the weld metal directly adjacent to the fusion boundary leading to a significant hardness peak in the Alloy 52 weld metal adjacent to the fusion boundary. Associated to the low hardness of the SA 508 CDZ, it creates a strong hardness mismatch at the DMW interface. This is shown in the hardness map and the EDS

Table 3 Summary of the peak hardness results and their locations at the SA 508-Alloy 52 weld metal

	HVIT (350 mN)	HVIT (1.5 mN)	Location	Distance from fusion boundary (μm)
As-manufactured	536	858	Alloy 52	0–2
5000 h aged	377	733	Alloy 52	10
10,000 h aged	331	637	Alloy 52	20

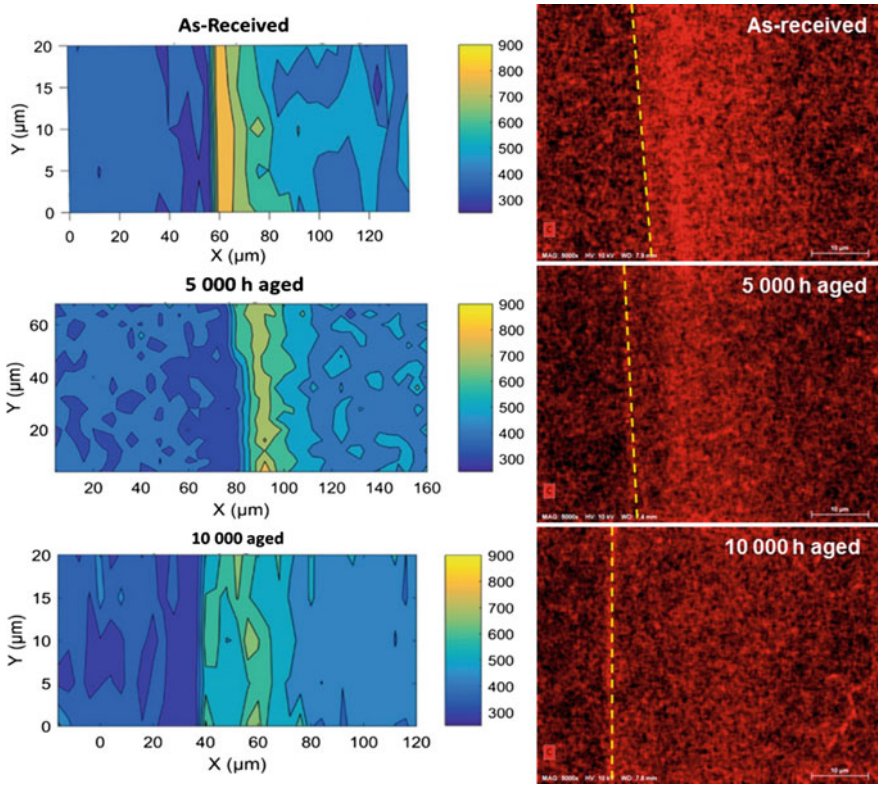

Fig. 9 Nanoindentation hardness profile (1.5 mN) across the SA 508-Alloy 52 interface in all conditions with the corresponding EDS maps showing distribution of C next to the fusion boundary (yellow dashed line represents the fusion boundary). A clear correlation is seen between the hard layer in Alloy 52 weld metal near the FB and the C-rich layer in the EDS maps (Color figure online)

map of C across the ferritic-austenitic interface of the as-manufactured and aged conditions presented in Fig. 9. The formation of a CDZ on the SA 508 side and the diffusion of C to the weld metal leads to a conclusion that the thermal aging reduces the hardness peak in the weld metal side by allowing carbon to diffuse further into the weld metal, thereby lowering the hardness peak and moving it further away.

Conclusions

The influence of the thermal aging at 400 °C for 5000 h and 10,000 h on the microstructure and hardness of a Ni-base alloy DMW was characterized with a focus on the SA 508-Alloy 52 interface. The aging parameters (10,000 h and 400 °C) were

chosen so that they would be equivalent to 60 years of operations at PWR in-service temperature in terms of GB segregation of phosphorous in RPV steel, which is assumed to be the governing factor for the structural integrity of the DMW. The main conclusions are summarized as follows:

- The thermal aging did not result in significant changes in the microstructure observable with LOM or SEM nor did it cause any notable changes in the hardness level of the Alloy 52 weld metal (about 230–270 HVIT according to microhardness measurements) or the SA 508 HAZ (about 240 HVIT according to microhardness measurements) outside the fusion zone.
- The SA 508-Alloy 52 interface was found, on the other hand, to be significantly affected by the thermal aging. A high hardness mismatch resulted from the diffusion of C from the SA 508 HAZ to the Alloy 52 weld metal upon PWHT, with C pile-up observed next to the ferritic-austenitic interface, leading to a significant hardness peak in the weld metal side of the interface. Thermal aging at 400 °C for 10,000 h reduced the observed hardness peak significantly (about 220 HVIT according to nanoindentation) while shifting it further away from the fusion boundary. The diffusion of C further into the weld metal is the main mechanism to explain the phenomenon.
- Concerning the thermal aging at 400 °C of the Alloy 52 weld metal, no detrimental effect was noticed, while thermal aging clearly reduces the hardness mismatch and hence strength mismatch at the ferritic-austenitic interface, which is likely beneficial for both the mechanical properties and EAC resistance.

Acknowledgements This study, carried out in parallel with that presented by Ahonen et al. on mechanical behavior, has been made in collaboration between Aalto University School of Engineering and VTT Technical Research Centre of Finland Ltd within the Nickel-base Alloy Welding Forum (NIWEL)-research project funded by TEKES, Finnish (Teollisuuden Voima Oyj and Fortum Oyj) and Swedish (Vattenfall AB and OKG AB) energy industry. The authors wish to express their gratitude for the funding and participation to the project.

References

1. D. Féron (ed.), *Overview of Nuclear Materials and Nuclear Corrosion Science and Engineering*. (Nuclear Corrosion Science and Engineering. Elsevier, 2012), pp. 31–56
2. D.D. MacDonald, G.A. Cragnolino, *Corrosion of Steam Cycle Materials*, ed by P. Cohen, ASME Handbook on Water Technology for Thermal Power Systems. ASME. pp. 659–1031
3. IAEA, Cost Drivers for the Assessment of Nuclear Power Plant Life Extension. IAEA-TECDOC-1309. (International Atomic Energy Agency, 2002), p. 84. ISBN 92-0-114402-4
4. Q. Peng, et al., SCC behavior in the transition region of an alloy 182-SA 508 Cl.2 dissimilar weld joint under simulated BWR-NWC conditions. in *Proceedings of the 12th International Conference on Environmental Degradation of Materials in Nuclear Power Systems-Water Reactors*, 2005 pp. 589–599
5. C.D. Lundin, Dissimilar metal welds-transition joints literature review. Welding J. **61**(2), 58–63 (1982)

6. R. Rajeev et al., Origin of hard and soft zone formation during cladding of austenitic/Duplex stainless steel on plain carbon steel. Mater. Sci. Technol. **17**(8), 1005–1011 (2001)
7. T. Sarikka et al., Microstructural, mechanical, and fracture mechanical characterization of SA 508-alloy 182 dissimilar metal weld in view of mismatch state. Int. J. Press. Vessels Pip. **145**, 13–22 (2016)
8. C. Sudha et al., Systematic study of formation of soft and hard zones in the dissimilar weldments of Cr–Mo steels. J. Nucl. Mater. **302**, 193–205 (2002)
9. T.W. Nelson, el al., Investigation of boundaries and structures in dissimilar metal welds. Sci Technol Welding Joining. **3**(5) 249–255 (1998)
10. B.T. Alexandrov et al., Fusion boundary microstructure evolution associated with embrittlement of Ni-base alloy overlays applied to carbon steel. Welding World **57**(1), 39–53 (2012)
11. T. Sarikka, Effect of Strength Mismatch on Fracture Behavior of Ferrite-Austenite Interface in Ni-Base Alloy Dissimilar Metal Welds. Aalto University Publication Series. Doctoral Dissertations. p. 135. ISBN 978-952-60-6983-8
12. T.W. Nelson et al., Nature and evolution of the fusion boundary in ferritic-austenitic dissimilar metal welds—Part 1: Nucleation and growth. Welding J. **78**, 329–337 (1999)
13. T.W. Nelson et al., Nature and evolution of the fusion boundary in ferritic-austenitic dissimilar metal welds—Part 2: on-cooling transformations. Welding J. **79**, 267–277 (2000)
14. W.C. Chung et al., Microstructure and stress corrosion cracking behavior of the weld metal in alloy 52-A508 dissimilar welds. Mater. Trans. **52**(1), 12–19 (2011)
15. U. Ehrnstén, *Corrosion and Stress Corrosion Cracking of Austenitic Stainless Steels*. ed by T. R. Allen, R.E. Stoller, S. Yamanaka, eds. Comprehensive Nuclear Materials, vol 5, (Elsevier, 2012), pp. 93–104
16. S. Fyfitch, *Corrosion and Stress Corrosion Cracking of Ni-base Alloys*. ed by T.R. Allen, R. E. Stoller,S. Yamanaka, Comprehensive Nuclear Materials, vol 5, (Elsevier, 2012), pp. 69–92
17. P.M. Scott, Environment-Assisted Cracking in Austenitic Components. Int. J. Press. Vessels Pip. **65**(3), 255–264 (1996)
18. Z. Lu et al., Characterization of microstructure, local deformation and microchemistry in alloy 690 heat-affected zone and stress corrosion cracking in high temperature water. J. Nucl. Mater. **465**, 471–481 (2015)
19. B.E. Payne, Nickel-base welding consumables for dissimilar metal welding applications. Metal Construct. **1**(12), 79–87 (1969)
20. F. Scenini, et al., Alloy Oxidation Studies Related to PWSCC. in *Proceedings of the 12th International Conference on Environmental Degradation of Materials in Nuclear Power Systems-Water Reactors*, 2005, pp. 891–902
21. P.L. Andresen, et al., Effects of PWR Primary Water Chemistry on PWSCC of Ni Alloys. in *13th International Conference on Environmental Degradation of Materials in Nuclear Power System*, (Whistler, British Columbia, 2007) pp. 1–21
22. H.T. Lee, J.L. Wu, Intergranular corrosion resistance of nickel-based alloy 690 weldments. Corros. Sci. **52**(5), 1545–1550 (2010)
23. G. Sui et al., Stress corrosion cracking of alloy 600 and alloy 690 in hydrogen/steam at 380 °C. Corros. Sci. **39**(3), 565–587 (1997)
24. G.A. Young, et al., The Kinetics of Long Range Ordering in Ni-Cr and Ni-Cr-Fe Alloys. in *Proceedings of the 16th Annual Conference on the Environmentally Assisted Cracking of Materials in Nuclear Power Systems-Water Reactors*, 2013, pp. 1–22
25. P. Joly et al., *Thermal Ageing Effects: Examples on Materials of PWR and Preventive Measures in the Design of EPR Plants* (DOI, Materials Innovation for Nuclear Optimized Systems, 2013). doi:10.1051/epjconf/20135104004
26. R. Mouginot, et al., Characterization of a Ni-base NG-DMW of Modern PWR. in *International Symposium Fontevraud 8 on Contribution of Materials Investigations and Operating Experience to LWRs' Safety, Performance and Reliability*, (SFEN, Avignon, France, 2014), p. 14
27. R. Mouginot et al., Thermal ageing and short-range ordering of alloy 690 between 350 and 550 & #xB0;C. J. Nucl. Mater. **485**, 56–66 (2017)

A Statistical Analysis on Modeling Uncertainty Through Crack Initiation Tests

Jae Phil Park, Chanseok Park and Chi Bum Bahn

Abstract Because a large time spread in most crack initiation tests makes it a daunting task to predict the initiation time of cracking, a probabilistic model, such as the Weibull distribution, has been usually employed to model it. In this case, although it might be anticipated to develop a more reliable cracking model under ideal cracking test conditions (e.g., large number of specimen, narrow censoring interval, etc.), it is not straightforward to quantitatively assess the effects of these experimental conditions on model estimation uncertainty. Therefore, we studied the effects of some key experimental conditions on estimation uncertainties of the Weibull parameters through the Monte Carlo simulations. Simulation results suggested that the estimated scale parameter would be more reliable than the estimated shape parameter from the tests. It was also shown that increasing the number of specimen would be more efficient to reduce the uncertainty of estimators than the more frequent censoring.

Keywords Weibull distribution · Estimation · Monte carlo simulation

Nomenclature

CDF	Cumulative distribution function
$F(\cdot)$	Cumulative distribution function of Weibull distribution
ECF	End cracking fraction
$\hat{\eta}$	Estimator of Weibull scale parameter
$\hat{\beta}$	Estimator of Weibull shape parameter
EVD	Extreme value distribution
EVD_m	Extreme value distribution for minima

J.P. Park (✉) · C.B. Bahn
School of Mechanical Engineering, Pusan National University,
46241 Busan, Republic of Korea
e-mail: bahn@pusan.ac.kr

C. Park
Department of Industrial Engineering, Pusan National University,
46241 Busan, Republic of Korea

J.H. Jackson et al. (eds.), *Proceedings of the 18th International Conference on Environmental Degradation of Materials in Nuclear Power Systems – Water Reactors*, The Minerals, Metals & Materials Series, https://doi.org/10.1007/978-3-319-68454-3_59

GEVD	Generalized extreme value distribution
iid	Independent and identically distributed
s_i	Last censoring time of i_{th} suspended specimen
LCI	Length of censoring interval
$L(\cdot)$	Likelihood function
μ	Location parameter of generalized extreme value distribution
$l(\cdot)$	Log-likelihood function
LB	Lower bound
c_{j_L}	Lower bound time of censoring interval for j_{th} cracking
MLE	Maximum likelihood estimation
C	Number of interval-censored cracked specimens
S	Number of suspended specimens
PDF	Probability density function
$g(\cdot)$	Probability density function of generalized extreme value distribution
$\text{RE}(\cdot)$	Relative error
$\text{RE}_{50\%}$	Relative error of median estimates
$\text{RLCI}_{90\%}$	Relative length of 90% confidence interval
RTD	Relative test duration
σ	Scale parameter of generalized extreme value distribution
η	Scale parameter of Weibull distribution
ξ	Shape parameter of generalized extreme value distribution
β	Shape parameter of Weibull distribution
SCC	Stress corrosion cracking
t	Time
η_{true}	True Weibull scale parameter
β_{true}	True Weibull shape parameter
UB	Upper bound
c_{j_U}	Upper bound time of censoring interval for jth cracking
x	Variable of generalized extreme value distribution

Introduction

It is widely known that stress corrosion cracking (SCC) can result in loss-of-coolant accidents in nuclear reactors [1–3]. Thus, the prediction of the SCC initiation time is a very important task for several researchers in nuclear science. However, this is a difficult task due to the complex mechanism of SCC initiation, which is not clearly identified yet. Therefore, empirical SCC initiation models are generally adopted for this purpose [4–6].

However, most SCC experiments showed non-negligible scatter with respect to cracking time [7], although all of the experimental conditions (e.g., temperature, tensile stress, etc.) were strictly controlled. Therefore, a probabilistic model was frequently used as an SCC initiation model to quantitatively consider the time

scatter. Particularly, the Weibull distribution [8], which can generally consider the effect of the time-dependent degradation of a material, is widely accepted as a probabilistic model of SCC initiation time [6, 9, 10].

To obtain the model parameters of SCC initiation (i.e., Weibull parameters in this case), a cracking test must be performed. The typical procedure of a cracking test involves an interval-censored reliability test. This implies that several stressed specimens (e.g., U-bend or constant tensile stress specimens) are exposed to a corrosive environment and censored at every scheduled time. Following the test, the testing results can be used to estimate the Weibull parameters typically using the maximum likelihood estimation (MLE) [11]. It is expected that the reliability of the estimated Weibull parameters would increase with an increase in the number of test specimens and a smaller length of the censoring interval (LCI). The LCI is defined as a length of time interval between one censoring time and the next censoring time. Thus, smaller LCI indicates frequent censoring on specimens. However, there is no theory yet available to calculate the exact estimation uncertainties for the estimated Weibull parameters with interval-censored data [11]. Therefore, in this study, the effects of some key experimental conditions on estimation uncertainties of Weibull parameters were investigated through the Monte Carlo simulation.

Theoretical Background of the Weibull Distribution

In this section, we will discuss the reason for the suitability of the Weibull distribution as an SCC initiation model.

Extremal Types Theorem

According to the well-known central limit theorem [12], the distribution of an independent and identically distributed (iid) sample mean can be approximated to the normal distribution with a large sample. A similar theorem known as the *extremal types theorem* exists for the distribution of sample maxima (or minima). The extremal types theorem [13] states that the location scale families of only three distributions are possible limits for the distribution of sample maxima (or minima).

Figure 1 shows the schematic illustration of the extremal types theorem for sample minima. Three possible cases for the distribution of sample minima include the following:

- If the unbounded lower tail of a parent distribution is light-tailed (i.e., falls off exponentially or faster [14]), then the distribution of sample minima is approximated to a Type I extreme value distribution for minima (Type I EVD_m, i.e., the smallest extreme value distribution) that has an unbounded domain.

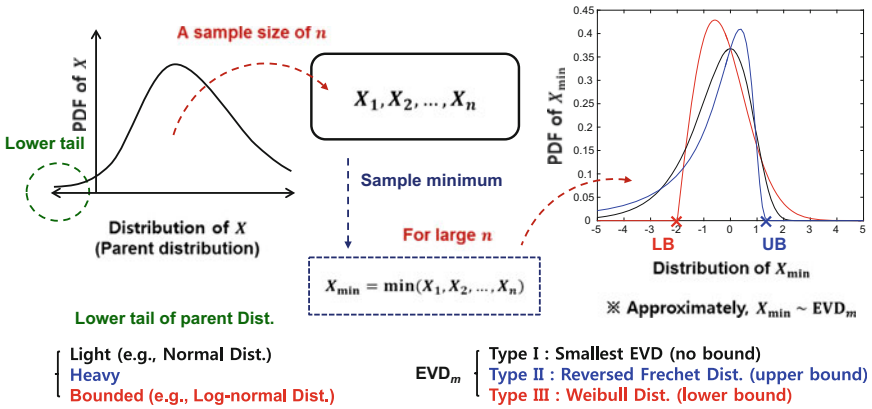

Fig. 1 Schematic illustration of the extremal types theorem for sample minima [15]

- If the unbounded lower tail of the parent distribution is heavy-tailed, then the distribution of the sample minima is approximated to a Type II EVD_m (i.e., reversed Fréchet distribution) that has an upper bound.
- If the lower tail of the parent distribution is bounded (e.g., uniform distribution), then the distribution of the sample minima is approximated to a Type III EVD_m (i.e., Weibull distribution) that has a lower bound.

Weibull Distribution

McFadden [16] proved that all three types of EVD could be expressed as a one functional form, namely the generalized extreme value distribution (GEVD). The probability density function (PDF) of GEVD for the sample minima case could be expressed as follows:

- Type I EVD_m: smallest extreme value distribution $(\xi = 0)$:

$$g(x;\, \mu,\, \sigma,\, 0) = \left(\frac{1}{\sigma}\right)\exp\left[-\exp\left(\frac{x+\mu}{\sigma}\right) + \left(\frac{x+\mu}{\sigma}\right)\right], \quad x \in \mathbb{R}, \tag{1}$$

- Type II EVD_m: reversed Fréchet distribution $(\xi > 0)$:

$$g(x;\, \mu,\, \sigma,\, \xi) = \left(\frac{1}{\sigma}\right)\exp\left[-\left(1-\xi\left(\frac{x+\mu}{\sigma}\right)\right)^{-\frac{1}{\xi}}\right]\left[1-\xi\left(\frac{x+\mu}{\sigma}\right)\right]^{-\frac{1}{\xi}-1}, \; x \le \mu - \frac{\sigma}{\xi}, \tag{2}$$

- Type III EVD_m: Weibull distribution $(\xi < 0)$:

$$g(x;\, \mu,\, \sigma,\, \xi) = \left(\frac{1}{\sigma}\right)\exp\left[-\left(1-\xi\left(\frac{x+\mu}{\sigma}\right)\right)^{-\frac{1}{\xi}}\right]\left[1-\xi\left(\frac{x+\mu}{\sigma}\right)\right]^{-\frac{1}{\xi}-1},\ x \geq \mu - \frac{\sigma}{\xi}, \quad (3)$$

where x denotes the variable, $\mu \in \mathbb{R}$ denotes the location parameter, $\sigma > 0$ denotes the scale parameter and $\xi \in \mathbb{R}$ denotes the shape parameter. The type of EVD is determined by the sign of ξ. Specifically, the Type III EVD_m in Eq. (3) can be converted to a widely-known functional form of the Weibull distribution by parameter substitution as given by:

$$x = t - 2\eta,\ \mu = \eta,\ \sigma = \frac{\eta}{\beta},\ \xi = -\frac{1}{\beta}. \quad (4)$$

Following the substitution, a two-parameter Weibull distribution that is frequently used as a cracking probability model is obtained with the following cumulative distribution function (CDF):

$$F(t;\, \beta,\, \eta) = 1 - \exp\left[-\left(\frac{t}{\eta}\right)^{\beta}\right], \quad (5)$$

where $t \geq 0$ denotes time, $\beta > 0$ denotes the shape parameter and $\eta > 0$ denotes the scale parameter of the Weibull distribution.

In application to cracking tests, the cracking time of a specimen indicates the earliest cracking time of it (i.e., the minimum cracking time). Therefore, the distribution of cracking time at a macroscopic scale (e.g., at engineering scale) will follow the EVD_m irrespective of the distribution of cracking time at a microscopic scale (e.g., at a grain boundary scale) because there are a lot of microscopic candidates of cracking on an SCC specimen having macroscopic scale. Furthermore, it is obviously impossible for the cracking time to correspond to a negative value, which means the lower tail of the parent distribution (i.e., distribution of cracking time at a microscopic scale) is bounded. Therefore, the distribution of cracking time at a macroscopic scale corresponds to the Type III EVD_m (i.e., Weibull distribution). Furthermore, it is interesting that, when iid Weibull distributed samples (e.g., cracking time) are selected, then the distribution of the sample minima also follows the Weibull distribution [11]. Thus, if the cracking mechanism is governed by the weakest link behavior [11], then this fact could be a strong basis to justify the use of the Weibull distribution as an appropriate statistical model of crack initiation time.

Estimation of Weibull Parameters

As previously mentioned, maximum likelihood estimation (MLE) is usually used to estimate the Weibull parameters from the given test data for its good estimation efficiency [17, 18]. MLE method uses the cracking time information of each specimen. The MLE method estimates the parameters of the Weibull distribution directly by using the likelihood function. The likelihood function for the interval-censored case is given by [13]:

$$L(\beta,\eta)=\prod_{i=1}^{S}[1-F(s_i;\beta,\eta)]\cdot\prod_{j=1}^{C}[F(c_{j_U};\beta,\eta)-F(c_{j_L};\beta,\eta)] \tag{6}$$

where S is the number of suspended (i.e., uncracked until the last censoring time) specimens, s_i is the last censoring time of i_{th} suspended specimen, C is the number of interval-censored cracked specimens, and c_{j_U} and c_{j_L} are the upper and lower bound times, respectively, of the censoring interval for the j_{th} cracking. The sum of S and C is equal to the total number of specimens.

The use of log-likelihood is convenient to determine the Weibull parameters that maximize the likelihood function [i.e., $\arg\max_{(\beta,\eta)} L(\beta,\eta)$]. The log-likelihood function is as follows:

$$l(\beta,\eta)=\ln L(\beta,\eta)=\sum_{i=1}^{S}\ln[1-F(s_i;\beta,\eta)]+\sum_{j=1}^{C}\ln[F(c_{j_U};\beta,\eta)-F(c_{j_L};\beta,\eta)]. \tag{7}$$

The maximum likelihood point is obtained where both partial derivatives of $l(\beta,\eta)$ reach zero. Therefore, the maximum likelihood point is given by:

$$\begin{cases}\frac{\partial}{\partial\beta}l(\beta,\eta)=0\\ \frac{\partial}{\partial\eta}l(\beta,\eta)=0.\end{cases} \tag{8}$$

Substituting Eqs. (5) and (7) into Eq. (8), we can obtain the final simultaneous equation:

$$\begin{cases}\sum_{i=1}^{S}\left[-\left(\frac{s_i}{\eta}\right)^{\beta}\ln\left(\frac{s_i}{\eta}\right)\right]+\sum_{j=1}^{C}\left[\frac{-\left(\frac{c_{j_L}}{\eta}\right)^{\beta}\ln\left(\frac{c_{j_L}}{\eta}\right)\exp\left[-\left(\frac{c_{j_L}}{\eta}\right)^{\beta}\right]+\left(\frac{c_{j_U}}{\eta}\right)^{\beta}\ln\left(\frac{c_{j_U}}{\eta}\right)\exp\left[-\left(\frac{c_{j_U}}{\eta}\right)^{\beta}\right]}{\exp\left[-\left(\frac{c_{j_L}}{\eta}\right)^{\beta}\right]-\exp\left[-\left(\frac{c_{j_U}}{\eta}\right)^{\beta}\right]}\right]=0\\ \sum_{i=1}^{S}\left[\left(\frac{\beta}{\eta}\right)\left(\frac{s_i}{\eta}\right)^{\beta}\right]+\sum_{j=1}^{C}\left[\left(\frac{\beta}{\eta}\right)\frac{\left(\frac{c_{j_L}}{\eta}\right)^{\beta}\exp\left[-\left(\frac{c_{j_L}}{\eta}\right)^{\beta}\right]-\left(\frac{c_{j_U}}{\eta}\right)^{\beta}\exp\left[-\left(\frac{c_{j_U}}{\eta}\right)^{\beta}\right]}{\exp\left[-\left(\frac{c_{j_L}}{\eta}\right)^{\beta}\right]-\exp\left[-\left(\frac{c_{j_U}}{\eta}\right)^{\beta}\right]}\right]=0.\end{cases} \tag{9}$$

It would be extremely difficult to determine a general analytical solution for Eq. (9); therefore, we used a numerical approach. In this case, the MATLAB (R2015b, MathWorks, Natick, MA, USA, 2015) offers the numerical nonlinear simultaneous equation solver *fsolve*.

Monte Carlo Simulation

Experimental Factors

Experimental factors (e.g., number of specimens) can affect the uncertainties of Weibull estimators. In the present study, a Monte Carlo simulation was performed to investigate their corresponding quantitative effects. The experimental factors considered in the simulation study include (1) true Weibull parameters; (2) the number of specimens; (3) end cracking fractions (ECF); and (4) length of censoring interval (LCI).

True Weibull Parameters

As previously mentioned, it could be reasonably assumed that the inherent cracking probability was Weibull distributed at a macroscopic scale. The study investigated as to whether the estimation uncertainties were affected by the parameters of the given Weibull distribution (i.e., inherent cracking probability behavior). These were termed as the true Weibull parameters (β_{true}, η_{true}), which are generally unknown to experimenters.

It should be noted that the scale parameter η was considered as a nuisance parameter in several applications [19]. For example, if the relative errors (RE) of estimators that were defined as follows:

$$\text{RE}(\hat{\beta}) = \frac{\hat{\beta} - \beta_{\text{true}}}{\beta_{\text{true}}};\ \text{RE}(\hat{\eta}) = \frac{\hat{\eta} - \eta_{\text{true}}}{\eta_{\text{true}}}, \tag{10}$$

were affected by the value of the true scale parameter (η_{true}), then only changing the time unit (e.g., hours to seconds) could affect the relative estimation errors. This is contradictory. Therefore, the η_{true} is just a scale factor, and relative estimation errors should not be affected by the value of η_{true} [17]. Without loss of generality, the value of η_{true} was fixed at 100 in this simulation study.

Nevertheless, the value of the true Weibull shape parameter (β_{true}) could be a factor affecting the relative estimation errors. Therefore, the shape parameter was a main parameter of the Weibull distribution [19]. Several values of β_{true} (2, 3 and 4) were selected as the simulation inputs. In previous studies, the value of the estimated Weibull shape parameter for an SCC initiation time ranged from two to four [6, 20–22].

Number of Specimens

It is expected that the estimated Weibull parameters (i.e., $\hat{\beta}$, $\hat{\eta}$) could be reliable with a large number of specimens. However, the SCC initiation test for nuclear reactor materials requires a corrosive environment with high temperatures and pressures. Thus, it is difficult to test a large number of specimens simultaneously. Hence, the simulation range of the specimen number was set from 5 to 50.

End Cracking Fraction

During the performance of the SCC test, cracking does not necessarily occur for every specimen within the available testing time. Thus, the test duration was considered as a factor of estimation uncertainties in an earlier study [18]. However, the results indicated that there were deficiencies to using the test duration as a factor of estimation uncertainties. First, experimenters do not know their relative test duration (RTD), which is defined as follows:

$$\mathrm{RTD} = \frac{\text{test duration}}{\eta_{\text{true}}}, \tag{11}$$

this is because the experimenters do not know the exact value of η_{true}. Additionally, it is possible to continue the simulation even after all of the specimens cracked when the test duration is used as a fixed input for a simulation study [18]. Therefore, the end cracking fraction (ECF) is considered as an alternative factor of estimation uncertainties. The ECF is a proportion of cracked specimen at the end of a test, which used for a criterion of the test termination. For example, if the value of ECF corresponded to 0.6, then the test ended when more than or equal to 60% of the specimens cracked. The simulation range for ECF was set from 0.6 to 1.0.

Length of Censoring Interval

It is expected that a shorter LCI is better to estimate reliable Weibull parameters. We considered a situation that the SCC test was carried out by inserting a large number of U-bend specimens into the autoclave. To censor the specimens, the experiment has to be stopped. Therefore, frequent censoring causes inconveniences for experimenters, and hence it is important to set a reasonable LCI for a cracking test. Although there are some advanced test methods (e.g., direct current potential drop) which can measure the crack initiation time without stopping the experiment, however, it is difficult to test a lot of specimens simultaneously through that kind of advanced test methods. Therefore, one of the interesting motivation of the simulation study is to find which of the following is more helpful to estimate the more reliable Weibull model – ‘a lot of inaccurate cracking time data’ or ‘a few accurate cracking time data’.

Thus, in order to investigate the general effect of LCI, the simulation range for starting LCI was set from 5 to 50% of η_{true}, although the value of η_{true} was unknown in the real testing case. It is assumed that length of censoring interval does not vary with time.

Simulation Procedure

Table 1 shows the simulation range of the study. A total of 900 (= 1 × 3 × 10 3 × 10) experimental cases were considered, and 20,000 random iterations were performed for each experimental case. From the resulting simulation data, the Weibull estimators (i.e., $\hat{\beta}, \hat{\eta}$) were calculated by the MLE method. Figure 2 shows the schematic procedure of the simulation study. The simulation procedure can be summarized as follows:

(1) Based on the assumed true Weibull distribution (see black solid lines in Fig. 2) and given experimental condition (e.g., number of specimens, ECF), we obtain the result of virtual cracking time data through the Monte Carlo simulation (see black squared dots in Fig. 2).
(2) We estimate the Weibull parameters by MLE method with the previous cracking time data (see red solid lines in Fig. 2).
(3) We iterate (1) and (2) 20,000 times to obtain a distribution of Weibull estimates at the given experimental condition.
(4) With changing to another experimental condition, we iterate the above procedure 900 times.

Table 1 Experimental factors considered in the Monte Carlo simulation

True Weibull parameters		Number of specimens	ECF	LCI (% of η_{true})
η_{true} (Dim'less time)	β_{true}			
100	2	5	0.6	5
–	3	10	0.8	10
–	4	15	1.0	15
–	–	20	–	20
–	–	25	–	25
–	–	30	–	30
–	–	35	–	35
–	–	40	–	40
–	–	45	–	45
–	–	50	–	50

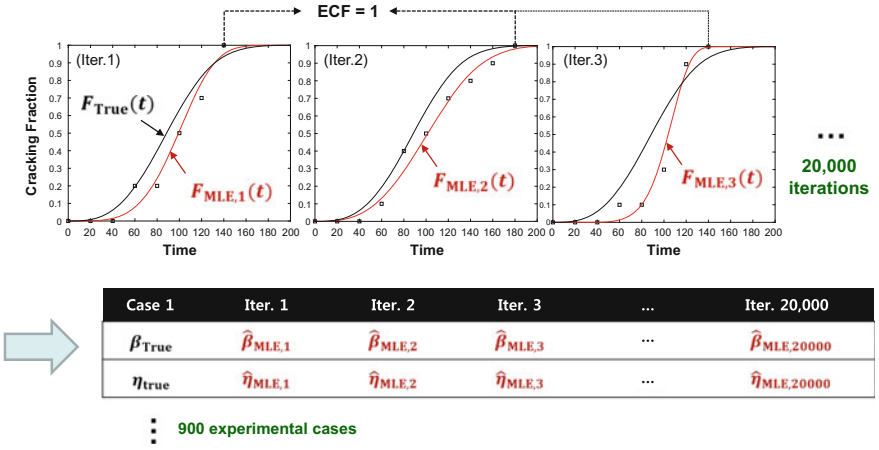

Fig. 2 Schematic procedure of the Monte Carlo simulation (β_{true} : 3; LCI: 20% of η_{true}; ECF: 1.0)

Results and Discussion

From the random simulation results, the 5th, 50th and 95th percentiles ($\hat{\beta}_{5\%}$, $\hat{\beta}_{50\%}$, $\hat{\beta}_{95\%}$; $\hat{\eta}_{5\%}$, $\hat{\eta}_{50\%}$, $\hat{\eta}_{95\%}$) of 20,000 replicates of Weibull estimates could be derived for each experimental case. The selected median estimates (i.e., $\hat{\beta}_{50\%}$, $\hat{\eta}_{50\%}$) were converted to the relative error ($\text{RE}_{50\%}$) to represent the bias of estimators, which is defined as follows:

$$\text{RE}_{50\%}(\hat{\beta}) = \text{RE}(\hat{\beta}_{50\%}) = \frac{\hat{\beta}_{50\%} - \beta_{\text{true}}}{\beta_{\text{true}}};\ \text{RE}_{50\%}(\hat{\eta}) = \text{RE}(\hat{\eta}_{50\%}) = \frac{\hat{\eta}_{50\%} - \eta_{\text{true}}}{\eta_{\text{true}}} \tag{12}$$

In order to quantify the dispersion of estimators, a relative length of a 90% confidence interval ($\text{RLCI}_{90\%}$) was utilized, which is defined as follows:

$$\text{RLCI}_{90\%}(\hat{\beta}) = \text{RE}(\hat{\beta}_{95\%}) - \text{RE}(\hat{\beta}_{5\%});\ \text{RLCI}_{90\%}(\hat{\eta}) = \text{RE}(\hat{\eta}_{95\%}) - \text{RE}(\hat{\eta}_{5\%}). \tag{13}$$

As an example, Fig. 3 shows the effect of the number of specimens on estimation uncertainties when the other experimental factors are fixed at the certain values. It is well represented that as the number of specimens is large, estimators becomes reliable (i.e., little bias and short length of confidence interval). For estimating the shape parameter β, it is likely that the shape parameters are overestimated when the number of specimens is relatively low (i.e.,$\text{RE}_{50\%}(\hat{\beta}_{\text{MLE}}) > 0$). For the scale parameter η estimation, the bias is barely noticeable even when the number of specimens is low [i.e., $\text{RE}_{50\%}(\hat{\eta}_{\text{MLE}}) \approx 0$]. The relative length of 90% confidence interval (i.e., $\text{RLCI}_{90\%}(\hat{\eta}_{\text{MLE}})$) are much lower than that of the shape parameter β (i.e., $\text{RLCI}_{90\%}(\hat{\beta}_{\text{MLE}})$).

Uncertainty of $\hat{\beta}_{MLE}$

Figure 4 shows the contour plots of $RE_{50\%}(\hat{\beta}_{MLE})$, indicating a relative estimation bias in the Weibull shape parameter. It was likely that $\hat{\beta}_{MLE}$ showed a tendency to be overestimated irrespective of the value of ECF and β_{true} when the number of specimens was relatively small. It is shown that the value of LCI does not much affect $RE_{50\%}(\hat{\beta}_{MLE})$ especially when the ECF is relatively high. The unusual result that occurred in the long LCI region may not be reliable due to the low convergence ratio [15].

Figure 5 shows the contour plots of $RLCI_{90\%}(\hat{\beta}_{MLE})$. As expected, the dispersion in $\hat{\beta}$ was large when the number of specimens was relatively small. In contrast, the effect of LCI was not noticeable. Additionally, some critical regions were observed, in which very wide $RLCI_{90\%}(\hat{\beta})$ were produced [18]. The gradients of $RLCI_{90\%}(\hat{\beta})$ were very high around the critical region. It is likely that this critical region was an inherent behavior of estimation uncertainty because another estimation method, which has a unity convergence ratio for the same experimental condition, also showed the critical region [15]. Experimenters should plan the crack initiation testing so that they can avoid this critical region. We suggest that it is very dangerous to estimate β with less than ten specimens regardless of the censoring interval and ECF.

Uncertainty of $\hat{\eta}_{MLE}$

Figures 6 shows the contour plots of $RE_{50\%}(\hat{\eta}_{MLE})$. The simulation results indicated that the value of $RE_{50\%}(\hat{\eta}_{MLE})$ was almost zero in every experimental condition.

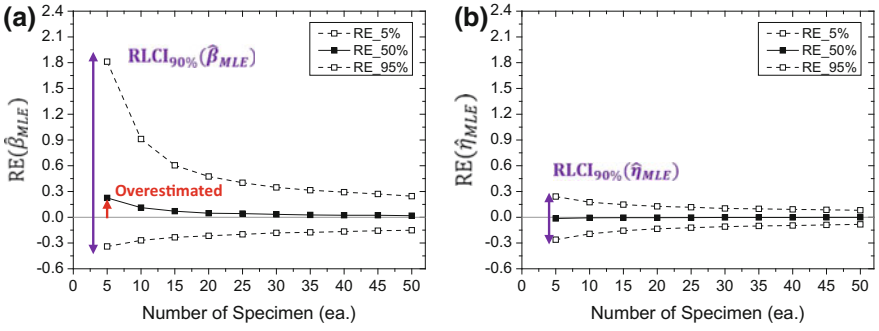

Fig. 3 Effects of the number of specimens on (a) $RE(\hat{\beta})$ and (b) $RE(\hat{\eta})$ (β_{true} : 3; LCI: 20% of η_{true}; ECF: 1.0)

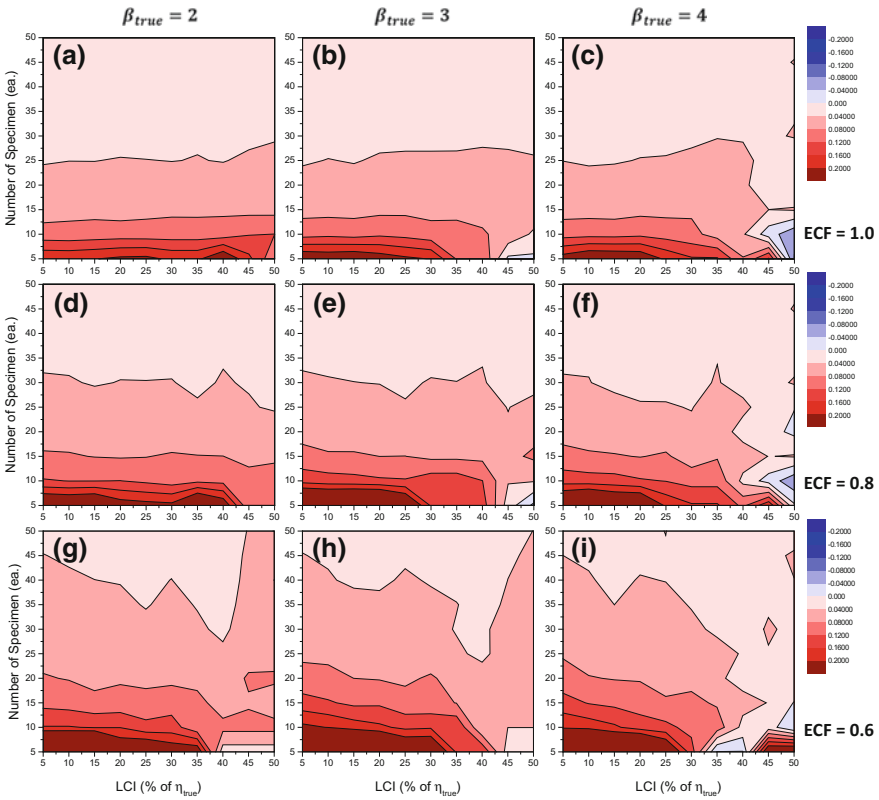

Fig. 4 Effects of the number of specimens and LCI on $RE_{50\%}(\hat{\beta}_{MLE})$ when ECF = 1.0 and (a) $\beta_{true} = 2$, (b) $\beta_{true} = 3$, (c) $\beta_{true} = 4$; when ECF = 0.8 and (d) $\beta_{true} = 2$, (e) $\beta_{true} = 3$, (f) $\beta_{true} = 4$; when ECF = 0.6 and (g) $\beta_{true} = 2$, (h) $\beta_{true} = 3$, (i) $\beta_{true} = 4$ [15]

This suggests that $\hat{\eta}_{MLE}$ is always unbiased irrespective of the combination of experimental conditions in the simulation range.

Figure 7 shows the contour plots of $RLCI_{90\%}(\hat{\eta}_{MLE})$. When compared to the case of $RLCI_{90\%}(\hat{\beta}_{MLE})$, the overall value of $RLCI_{90\%}(\hat{\eta}_{MLE})$ was quite small. This indicates that the estimated scale parameter is more reliable than the shape parameter under the same experimental conditions [18]. The dispersion in $\hat{\eta}_{MLE}$ was large when: (1) the number of specimens was small; (2) the value of ECF was low; and (3) the value of β_{true} was small. LCI showed no noticeable effect on $RLCI_{90\%}(\hat{\eta}_{MLE})$. The critical region did not appear in the case of $RLCI_{90\%}(\hat{\eta}_{MLE})$. The simulation result suggests that a relatively reliable $\hat{\eta}$ could be obtained with only five specimens regardless of the other experimental conditions.

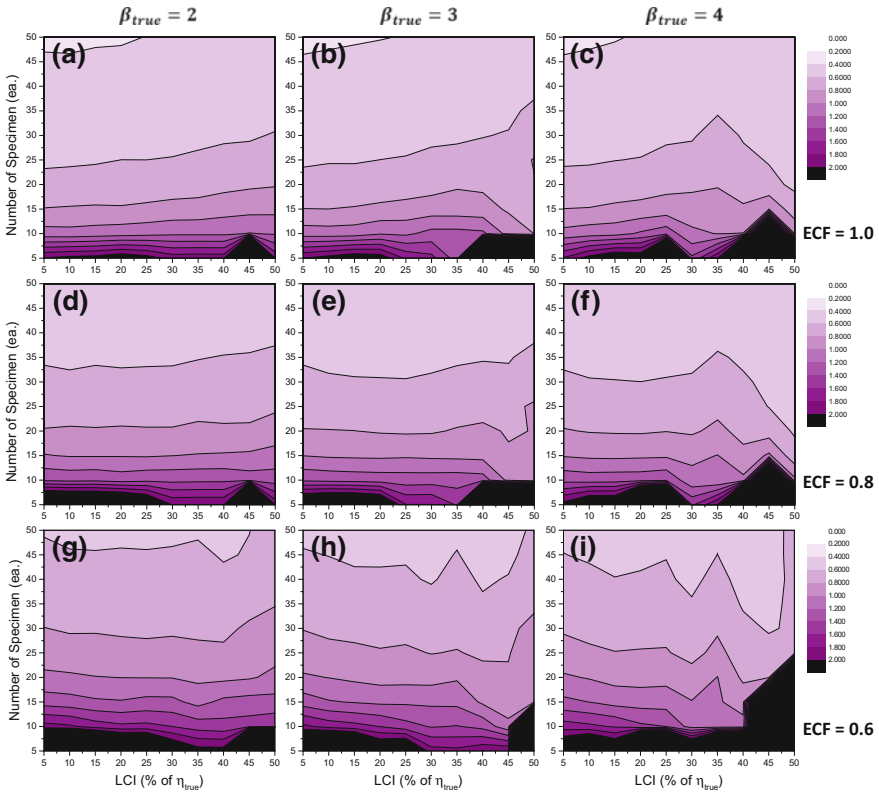

Fig. 5 Effects of the number of specimens and LCI on $\mathrm{RLCI}_{90\%}(\hat{\beta}_{\mathrm{MLE}})$ when ECF = 1.0 and (a) $\beta_{\mathrm{true}} = 2$, (b) $\beta_{\mathrm{true}} = 3$, (**c**) $\beta_{\mathrm{true}} = 4$; when ECF = 0.8 and (d) $\beta_{\mathrm{true}} = 2$, (e) $\beta_{\mathrm{true}} = 3$, (f) $\beta_{\mathrm{true}} = 4$; when ECF = 0.6 and (g) $\beta_{\mathrm{true}} = 2$, (h) $\beta_{\mathrm{true}} = 3$, (i) $\beta_{\mathrm{true}} = 4$ [15]

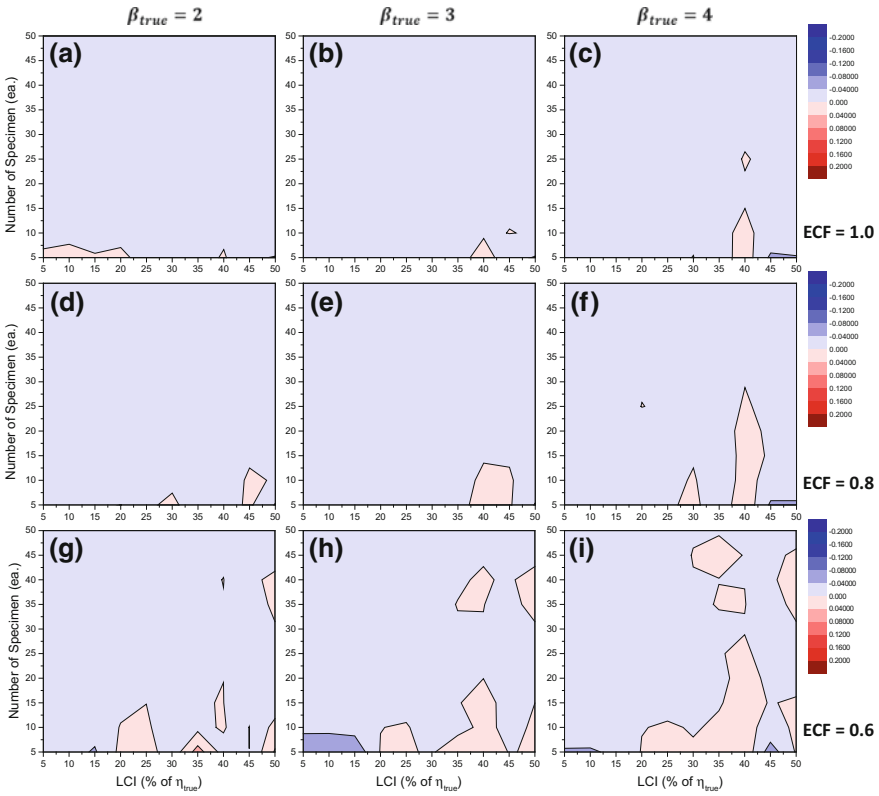

Fig. 6 Effects of the number of specimens and LCI on $RE_{50\%}(\hat{\eta}_{MLE})$ when ECF = 1.0 and (a) $\beta_{true} = 2$, (b) $\beta_{true} = 3$, (c) $\beta_{true} = 4$; when ECF = 0.8 and (d) $\beta_{true} = 2$, (e) $\beta_{true} = 3$, (f) $\beta_{true} = 4$; when ECF = 0.6 and (g) $\beta_{true} = 2$, (h) $\beta_{true} = 3$, (i) $\beta_{true} = 4$ [15]

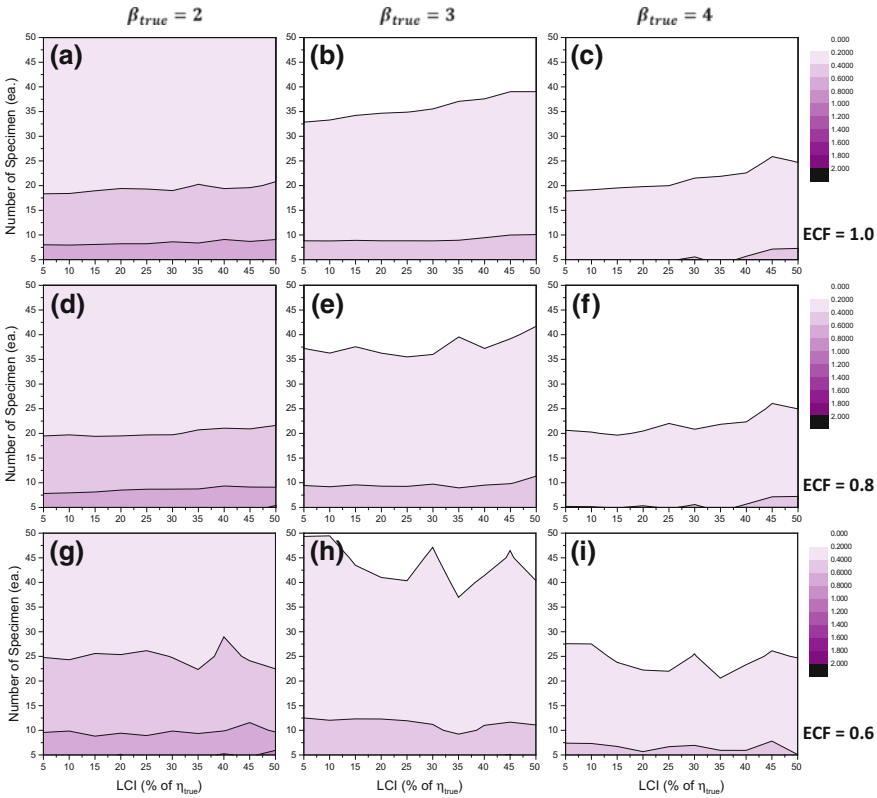

Fig. 7 Effects of the number of specimens and LCI on $\mathrm{RLCI}_{90\%}(\hat{\eta}_{\mathrm{MLE}})$ when ECF = 1.0 and (a) $\beta_{\mathrm{true}} = 2$, (b) $\beta_{\mathrm{true}} = 3$, (c) $\beta_{\mathrm{true}} = 4$; when ECF = 0.8 and (d) $\beta_{\mathrm{true}} = 2$, (e) $\beta_{\mathrm{true}} = 3$, (f) $\beta_{\mathrm{true}} = 4$; when ECF = 0.6 and (g) $\beta_{\mathrm{true}} = 2$, (h) $\beta_{\mathrm{true}} = 3$, (i) $\beta_{\mathrm{true}} = 4$ [15]

Conclusions

The main goal of this study is to provide quantitative estimation uncertainties for experimenters developing a Weibull distribution model via cracking tests. The MLE method was performed with respect to the Weibull estimation. Monte Carlo simulations were used in order to quantify uncertainties estimators in various experimental conditions by considering the effects of: (1) true Weibull parameters; (2) the number of specimens; (3) end cracking fractions; and (4) length of censoring interval. The following conclusions were drawn from the study:

- The Weibull distribution was appropriate for the statistical model of crack initiation time at a macroscopic scale.
- In the simulation range, $\hat{\beta}_{\mathrm{MLE}}$ showed a tendency to be overestimated and dispersed when the number of specimens was small and the value of ECF was low. The value of LCI does not much affect bias of $\hat{\beta}_{\mathrm{MLE}}$ especially when the ECF is relatively high. It was shown that there were critical regions, in which the dispersions were extremely large. Thus, experimenters should avoid this critical region when establishing an SCC test plan. We suggest that it is very dangerous to estimate β with less than ten specimens regardless of the censoring interval and ECF.
- $\hat{\eta}_{\mathrm{MLE}}$ showed almost zero bias in all simulation ranges. In most cases, the LCI did not affect the estimation uncertainty of $\hat{\eta}$. The overall bias and dispersion of $\hat{\eta}$ were much lower than those of $\hat{\beta}$ in the simulation study range. Therefore, the estimated scale parameter would be more reliable than the estimated shape parameter from the cracking tests. Actually, the simulation result suggests that a relatively reliable $\hat{\eta}$ could be obtained with only five specimens regardless of the other experimental conditions. Therefore, It was shown that increasing the number of specimen would be more efficient to reduce the uncertainty of estimators than the more frequent censoring.

Acknowledgements This work was supported by the Nuclear Safety Research Program through the Korea Foundation of Nuclear Safety (KOFONS) granted financial resource from the Nuclear Safety and Security Commission (NSSC), Republic of Korea (No. 1403006), and was supported by "Human Resources Program in Energy Technology" of the Korea Institute of Energy Technology Evaluation and Planning (KETEP), who granted the financial resources from the Ministry of Trade, Industry & Energy, Korea. (No. 20164010201000).

References

1. W. Lunceford, T. DeWees, P. Scott, EPRI Materials Degradation Matrix, Rev. 3. EPRI, Palo Alto, CA, USA 3002000628, 2013
2. P. Scott, M.-C. Meunier, Materials Reliability Program: Review of Stress Corrosion Cracking of Alloys 182 and 82 in PWR Primary Water Service (MRP-220). EPRI, Palo Alto, CA, USA Rep. No. 1015427, 2007

3. K.J. Kim and E.S. Do, Technical Report: Inspection of Bottom Mounted Instrumentation Nozzle (in Korean). Korea Institute of Nuclear Safety (KINS), Daejeon, Korea KINS/RR-1360, 2015
4. C. Amzallag, S.L. Hong, C. Pages, A. Gelpi, Stress Corrosion Life Assessment of Alloy 600 PWR Components. in *9th International Symposium on Environmental Degradation of Materials in Nuclear Power Systems—Water Reactors*, 1999, pp. 243–250
5. Y.S. Garud, Stress Corrosion Cracking Initiation Model for Stainless Steel and Nickel Alloys. EPRI, Palo Alto, CA, USA 1019032, 2009
6. M. Erickson, F. Ammirato, B. Brust, D. Dedhia, E. Focht, M. Kirk, et al., Models and Inputs Selected for Use in the xLPR Pilot Study. EPRI, Palo Alto, CA, USA 1022528, 2011
7. G. Troyer, S. Fyfitch, K. Schmitt, G. White, C. Harrington, Dissimilar Metal Weld PWSCC Initiation Model Refinement for XLPR Part I: A Survey of Alloy 82/182/132 Crack Initiation Literature. in *17th International Conference on Environmental Degradation of Materials in Nuclear Power Systems—Water Reactors*, Ottawa, Ontario, Canada, August 9–13, 2015
8. W. Weibull, A statistical distribution function of wide applicability. J. Appl. Mech. **18**, 293–297 (1951)
9. E. Eason, Materials Reliability Program: Effects of Hydrogen, pH, Lithium and Boron on Primary Water Stress Corrosion Crack Initiation in Alloy 600 for Temperatures in the Range 320–330°C (MRP-147). EPRI, Palo Alto, CA, USA 1012145, 2005
10. I.S. Hwang, S.U. Kwon, J.H. Kim, S.G. Lee, An intraspecimen method for the statistical characterization of stress corrosion crack initiation behavior. Corrosion **57**, 787–793 (2001)
11. J. McCool, *Using the Weibull distribution: reliability, modeling, and inference* (Wiley, Hoboken, N.J., USA, 2012)
12. S.M. Ross, *Introduction to Probability and Statistics for Engineers and Scientists*, 4th edn. (Elsevier Academic Press, USA, 2009)
13. R.A. Fisher L.H.C. Tippett, Limiting Forms of the Frequency Distribution of the Largest or Smallest Member of a Sample. in *Mathematical Proceedings of the Cambridge Philosophical Society*, 1928, pp. 180–190
14. R.L. Wolpert, *Extremes*, Available online: https://www2.stat.duke.edu/courses/Fall15/sta711/lec/topics/extremes.pdf, 2014
15. J.P. Park, C. Park, J. Cho, C.B. Bahn, Effects of cracking test conditions on estimation uncertainty for Weibull parameters considering time-dependent censoring interval. Materials **10**, 3 (2016)
16. D. McFadden,Modeling the Choice of Residential Location. *Transportation Research Record* 1978
17. U. Genschel, W.Q. Meeker, A comparison of maximum likelihood and median-rank regression for Weibull estimation. Q. Eng. **22**, 236–255 (2010)
18. J.P. Park, C.B. Bahn, Uncertainty evaluation of Weibull estimators through Monte Carlo simulation: applications for crack initiation testing. Materials **9**, 521 (2016)
19. F.R. Hampel, E.M. Ronchetti, P.J. Rousseeuw, W.A. Stahel, *Robust statistics: the approach based on influence functions* vol 114, Wiley, 2011
20. J.D. Hong, C. Jang, T.S. Kim, PFM application for the PWSCC integrity of Ni-Base alloy welds—development and application of PINEP-PWSCC. Nuclear Eng. Technol. **44**, 961–970 (2012)
21. K. Dozaki, D. Akutagawa, N. Nagata, H. Takihuchi, K. Norring, Effects of dissolved hydrogen condtent in PWR primary water on PWSCC initiation property. E-J. Adv. Main. **2**, 65–76 (2010)
22. Y.S. Garud, SCC initiation model and its implementation for probabilistic assessment. in *ASME Pressure Vessels & Piping Division*, July 18–22, 2010

Part IX
Plant Operating Experience

Laboratory Analysis of a Leaking Letdown Cooler from Oconee Unit 3

James Hyres, Rocky Thompson and Jim Batton

Abstract This paper covers the results of laboratory examinations performed on a leaking letdown cooler from Oconee Unit 3. The laboratory scope included dewatering, pressure testing, visual inspections, metallography, Vickers micro-hardness, scanning electron microscopy (SEM), energy dispersive spectroscopy (EDS), X-Ray Diffraction (XRD), and Optical Emission Spectroscopy (OES). The laboratory examinations identified one tube containing a through-wall crack. The most likely cause of the crack appeared to be OD-initiated caustic stress corrosion cracking (SCC). The presence of heavy deposits on the tube OD surface and heat tinting on the primary and secondary flow seals indicated boiling occurred near the tight radius region of the bundle. Once boiling occurred, caustic-forming species such as calcium phosphate deposited and concentrated on the tube OD surface. The literature indicates as caustic concentrations approach $\sim$20%, the conditions become favorable for caustic SCC to occur in austenitic stainless steels such as Type 316L.

Keywords Letdown cooler · Type 316L stainless steel tubing · Intergranular stress corrosion cracking · Caustic stress corrosion cracking

Introduction

Oconee is a three-unit pressurized water reactor (PWR) plant with Babcock & Wilcox (B&W) 177FA nuclear steam supply systems (NSSS). The reactor coolant system (RCS) letdown water for each unit flows from the cold leg of one of the two

J. Hyres (✉)
BWX Technologies, Inc., 2016 Mt. Athos Road, Lynchburg, VA 24504-5447, USA
e-mail: jwhyres@bwxt.com

R. Thompson
Duke Energy, 526 South Church Street, Charlotte, NC 28202, USA

J. Batton
Duke Energy, Oconee Nuclear Station, Seneca, SC 29672, USA

J.H. Jackson et al. (eds.), *Proceedings of the 18th International Conference on Environmental Degradation of Materials in Nuclear Power Systems – Water Reactors*, The Minerals, Metals & Materials Series, https://doi.org/10.1007/978-3-319-68454-3_60

once-through steam generators and through two parallel letdown coolers to cool the water before entering the purification and deborating demineralizers.

Forty-two (42) failures of letdown coolers have occurred in B&W plants since 1977 (Refs. [1–3]). Of these, 27 (or 64%) of the failures have occurred at the Oconee plants. OD-initiated high cycle fatigue at tube-to-tube stitch welds was identified as the cause of early failures by the destructive examination of letdown coolers from Crystal River-3 and Three Mile Island-1 (TMI-1). A number of recommendations were developed and implemented at B&W plants to minimize or prevent additional tube failures by high cycle fatigue.

For a while these recommendations appeared to be effective. Oconee reported no letdown cooler failures between 1997 and 2003. However, failures reoccurred from 2003 to 2014. Similar letdown coolers are in service at Davis-Besse and ANO-1. ANO-1 has experienced no failures to date; Davis-Besse reported a cooler failure in 2009. The cause of failure was not determined, but assumed to be due to high cycle fatigue.

Due to the recent poor reliability of the letdown coolers at Oconee and since no letdown cooler from any B&W plant had been destructively examined since 1987, it was decided to destructively examine the archived Oconee 3A letdown cooler which had a known leak in order to determine the cause of the tube failure. Leakage was discovered in the 3A letdown cooler in July 2003. This letdown cooler was in service from 1994 until the EOC 22 Refueling Outage in spring 2006, when it was removed and replaced with another cooler.

Letdown Cooler Description and Metallurgy

The 3A letdown cooler was manufactured by Graham Manufacturing Company in 1994. It is a compact counter flow heat exchanger having a Helicoil tube bundle design consisting of thirty (30) seamless Type 316L stainless steel tubes, each having a 19 mm (0.750 in) OD and 1.8 mm (0.072 in) wall thickness, and measuring approximately 18 m (60 feet) long. The tubes were procured in the solution annealed condition, i.e. heated at 1038 °C (1900 °F) followed by rapid quenching to below 427 °C (800 °F) in less than 3 min. When rolled into the bundle, each tube contains approximately nine (9) coils. Once coiled, the entire tube bundle is stress relieved at 1093 °C (2000 °F) for 32 min, followed by rapid cooling to below 427 °C (800 °F).

Each tube is tack-welded to a support bar on the inlet and outlet ends, and then formed at a 90° angle toward the inlet and outlet tubesheets. The tubes are roll expanded (2–5% wall reduction) nominally 3.8 cm (1.5 in) into the 4.8 cm (1.88 in) thick tubesheets and then seal welded. The bundle is encased within a 13 mm (0.5 in) thick carbon steel shell containing inlet and outlet ports for the primary and secondary fluids. The as-manufactured cooler weighs approximately 3000 kg (6600 lb).

Primary inlet flow (RCS) is from the center of the bundle outward. Secondary side cooling water (Component Cooling) flows in the opposite direction, from the

outer periphery of the cooler, spiraling inward toward the center. A thin stainless steel baffle plate between the outer 2 and 3 coils of the tubes helps direct the cooling water flow inward toward the center. The cooling water exits the central cavity through the outlet nozzle located on the same side as the inlet nozzle.

Letdown Cooler Operating Conditions

RCS letdown fluid enters the tubes nominally at 14.9 MPa (2155 psig) and 291 °C (555 °F). Treated Component Cooling water flows on the shell side. The operating conditions on the shell side of the letdown cooler are 71 °C (160 °F) measured at the cooler outlet and 0.48–0.62 MPa (70–90 psia) (pressure estimated in the cooler), which corresponds to a saturation temperature of 149–160 °C (300–320 °F). The RCS temperature is 291 °C (555 °F) at the cooler inlet and decreases as the fluid cools as it passes through the tubes. Localized boiling of the Component Cooling water (producing some superheated steam) occurs on the tube surface at the RCS inlet end of the letdown cooler where both the RCS temperature and the OD of the tube wall equal or exceed the saturation temperature at the shell side operating pressure. In this respect, letdown cooler design operating conditions in the B&W NSSS differ from other PWR and even BWR designs that have stepwise cooling and pressure reduction of the letdown water via a regenerative heat exchanger in order to prevent localized boiling conditions from occurring.

From 1994, when the 3A letdown cooler went into service, until April 2003, the secondary side Component Cooling water chemistry was potassium chromate (100–500 ppm as CrO_4), sodium phosphate (100–300 μg/L as PO_4), and pH ~10 in accordance with Ref. [4]. In May 2003, chromate chemistry was replaced with molybdate (500–1000 μg/L MoO_4)-azole (tolyltriazole) chemistry at pH 9.0–11 in accordance with Ref. [5]. Makeup water to the Component Cooling system is high purity demineralized water. After the letdown cooler leak developed, boric acid from RCS in-leakage was introduced into the Component Cooling water (secondary side) system until the leaking cooler was removed from service. The Component Cooling system operates at a lower pressure than the raw water system, which acts as its heat sink.

Results

Receipt, Dewatering, and Pressure Testing

Figure 1 is a receipt photograph taken of the cooler showing the primary side inlet and outlet manifolds. The tubes were dewatered prior to pressure testing, and then each tube was individually pressure tested with 206 kPa (30 psi) helium for

Fig. 1 Receipt photograph showing the primary flow seal side of the letdown cooler. The primary inlet (near center) and outlet (toward bottom) manifolds are visible

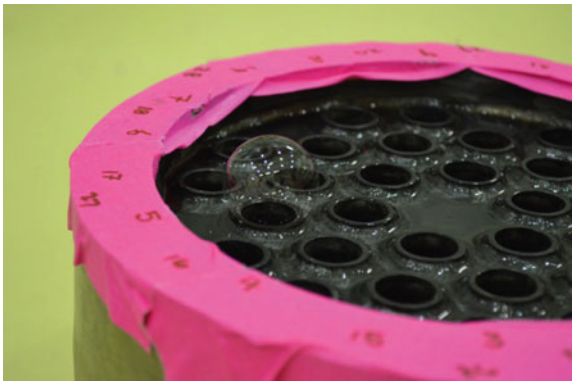

Fig. 2 Photograph taken during the shell-side pressure test. A bubble formed at the end of tube #17, indicating a through-wall defect

~15 min to identify leaking tubes. One tube, identified as Tube #17 in the laboratory, failed the pressure test. The shell side was also pressurized with 206 kPa (30 psi) of helium. Soap bubbles were used to check the integrity of each tube, the tubesheet seal welds, and the weld joining the tubesheet to the shell wall. This test also confirmed the leak in Tube #17 (see Fig. 2). No other leaks were identified.

Cooler Disassembly

The letdown cooler shell was cut just above the primary side end plate and then removed to access the tube bundle. Figures 3, 4 and 5 show the tube bundle and its central cavity. White-to-brown deposits were found on the tubes in the tight radius region on the inlet ends. The deposits were most heavily concentrated on the tube intrados, which corresponds to the underside (i.e., 6:00 position) of the tubes in-service. Few or no deposits were present on the tube extrados. The leak in Tube

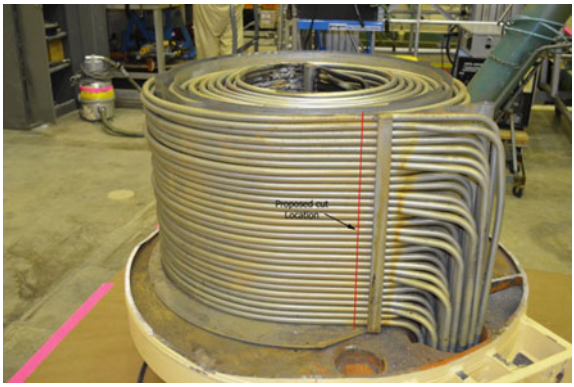

Fig. 3 The letdown cooler after shell removal. The cut location to isolate the tubes is indicated

Fig. 4 The central cavity near the inlet side of the tube bundle. The tube #17 leak location is indicated

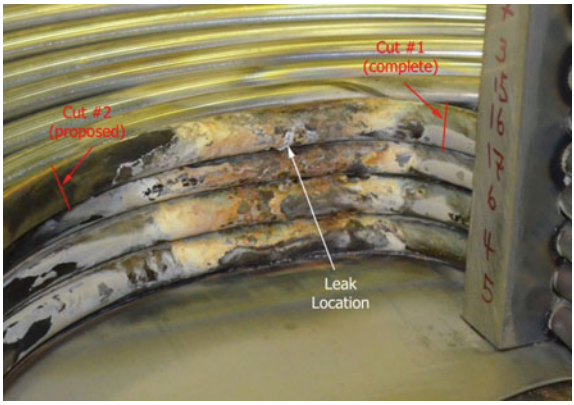

Fig. 5 Higher magnification view of the tube #17 leak location. Cut locations for the destructive examinations are indicated

#17 was located in the deposit-covered region of the tubes as indicated in Fig. 5. Evidence of heat tinting was also found near the tight radius area of the tube bundle corresponding to the Tube #17 leak location (Figs. 6 and 7).

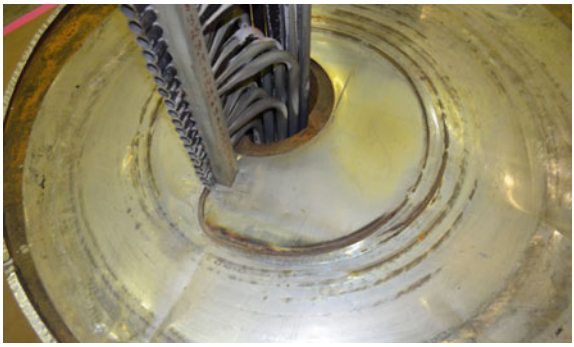

Fig. 6 View of the primary flow seal after removing the tubes

Fig. 7 Higher magnification view of the tight radius region showing the most pronounced heat tinting

The bulk residual stresses were relatively low as evidenced by the tubes not "springing open" after they were cut at the outlet and inlet side support bars in order to remove them. The tube bundle stress relief treatment was therefore concluded to have been effective.

Visual Examinations on Leaking Tube Section

Visual examination of the OD surface of the 5.1 cm (2 in) section of Tube #17 revealed three circumferential cracks in the tube intrados (see Figs. 8 and 9). Visual examination under higher magnification revealed the cracking to be jagged with a minor branch at one tip of the through-wall crack (see Fig. 10). IGA-like features were also found on the OD surface at the opposite end of the crack. This finding indicated corrosion was associated with the cracking, which likely initiated on the tube surface exposed to the Component Cooling water (see Fig. 11).

The tube section was cut open clamshell-style to permit visual examination of the ID surface (see Fig. 12). One crack was found (see Fig. 13), which was the through-wall leak identified during pressure testing. Cuts were then made through the cracked region in order to produce a through-wall open crack specimen and two

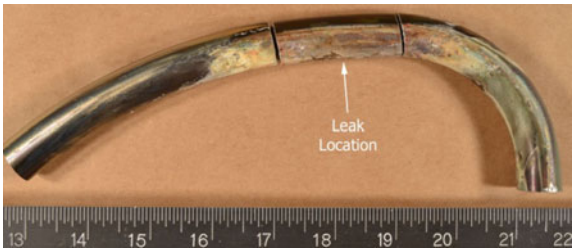

Fig. 8 Initial cuts to isolate the through-wall crack region

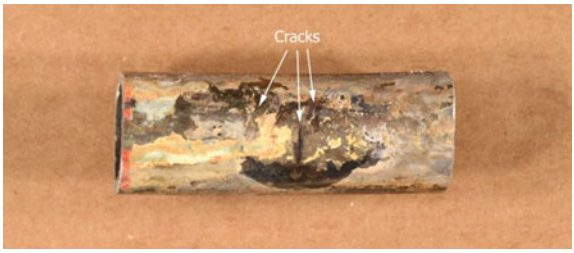

Fig. 9 Resulting piece as viewed from the tube #17 intrados. Three cracks were visible in this area

Fig. 10 Higher magnification view of the tube #17 cracks

metallographic mounts, one through the through-wall crack tip and one through a secondary crack (see Fig. 14).

SEM/EDS Examinations

High magnification Scanning Electron Microscopy/Energy Dispersive X-ray Spectroscopy (SEM/EDS) examinations were performed on the opened through-wall crack, OD surface deposits, and a cross section prepared through a

Fig. 11 IGA-like features were observed at one of the crack tips

Fig. 12 Photograph taken after cutting the piece open clamshell-style to reveal the ID surface. The through-wall crack location is indicated

Fig. 13 Higher magnification view of the through-wall leak location

secondary crack. The secondary electron (SE) imaging technique was employed to characterize the open crack surface topography. The mounted sample was analyzed in the as-polished condition using backscattered electron imaging (BSE).

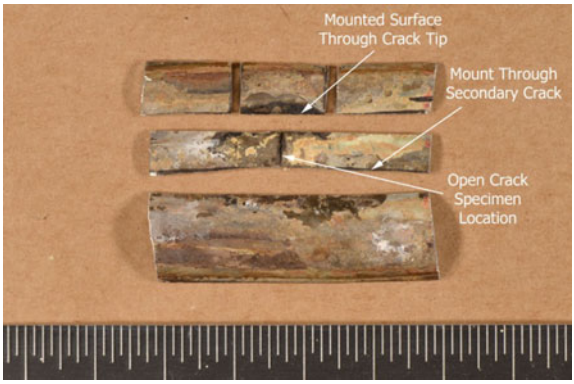

Fig. 14 Photograph showing the additional sections made through the leak location

Opened Through-Wall Crack

Low magnification optical microscopy and low magnification SEM both revealed that the through-wall cracking was intergranular from OD to ID (see Figs. 15, 16, 17 and 18). Pitted features on many grain facets indicated corrosive attack occurred at some point after the crack formed. Secondary cracking was also noted in several locations, a characteristic typical of stress corrosion cracking (SCC) in austenitic stainless steels.

EDS analysis of the heavily deposited region on the opened fracture surface showed the deposits were composed of major amounts of O, Cr, Fe, and Ni, with minor amounts of Mo, and trace amounts of Si, Ti, Cu, Zn, and Sn (see Fig. 19 for a typical EDS spectrum). No evidence of deleterious soluble species such as chloride was found in the areas examined. It should be noted that the escaping fluid through the crack would likely remove deposited soluble species from the crack surfaces.

Fig. 15 Photograph of the opened through-wall crack. Cracking is intergranular in nature

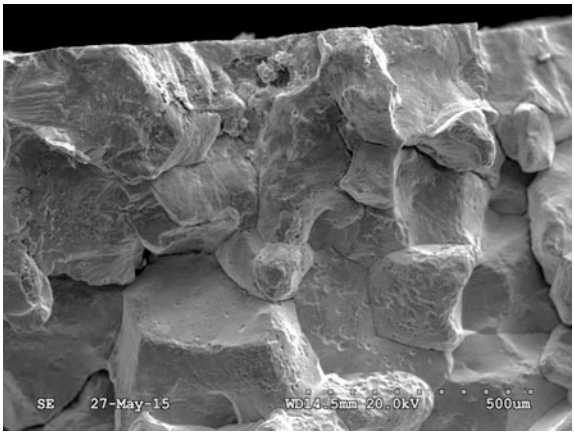

Fig. 16 SEM image of the opened crack taken near the tube ID surface

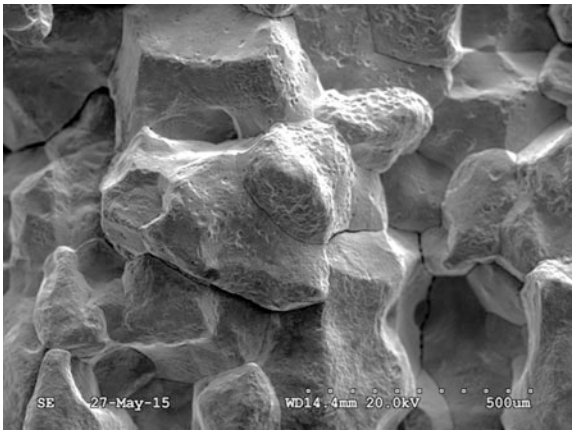

Fig. 17 SEM image of the opened crack taken in the mid-wall region

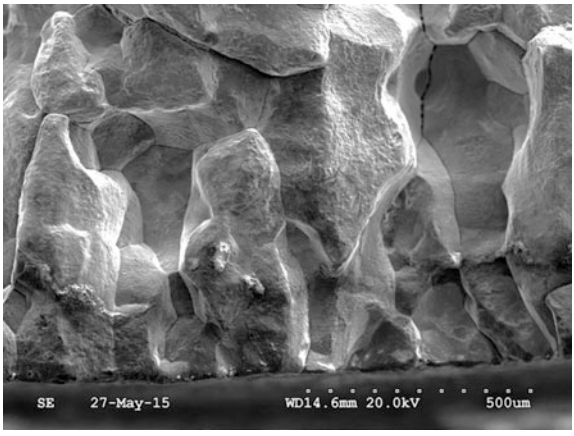

Fig. 18 SEM image of the opened crack taken near the tube OD surface

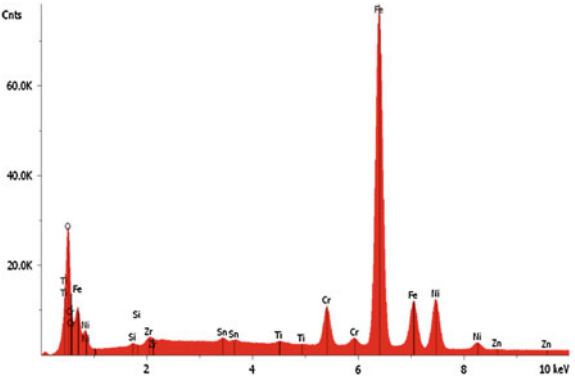

Fig. 19 EDS spectrum results for a heavily deposited region on the opened through-wall crack

OD Deposits

Deposits collected from the OD surface of Tube #17 in the through-wall crack region were affixed to a specimen stub using double-sided carbon tape. EDS analyses of regions of interest found that the deposits consisted of major amounts of O and Ca, with minor amounts of Mg, Si, P, Fe, Cu, Zn, and Ba, along and trace amounts of Al, Cr, Ni, and Cu. The presence of Mg, Ca, and Si indicated in-leakage of raw water into the Component Cooling water system. The presence of phosphorus in the deposits was consistent with deposition occurring during the time period that CrO_4–PO_4 chemistry was employed. Barium was also identified during the 1987 letdown cooler examination (Ref. [1]). A definitive source for the barium and its potential impact on the tube cracking could not be conclusively determined.

Secondary Crack Cross Section

An axial cross section through a secondary crack in Tube #17 was prepared for SEM/EDS examination by placing the specimen in conductive copper mounting material, and then grinding and polishing using standard techniques. The cross section was examined in the as-polished condition. Figure 20 shows the cracking clearly initiated on the OD surface and propagated toward the ID surface. Shallow penetrations were noted mostly on the OD surface, but a few were also present on the ID surface. Very minor surface cold work was evident on the OD surface in this region.

The cracking contained several shallow branches, three of which were selected for higher magnification inspections. All three tips were intergranular in nature and exhibited a similar blunted morphology (see Fig. 21). Blunted crack tips are typically associated with inactive crack growth.

The EDS results indicated the base metal contained major amounts of Cr, Fe, and Ni with minor amounts of Mn and Mo, as well as trace amounts of Mg, Si, V,

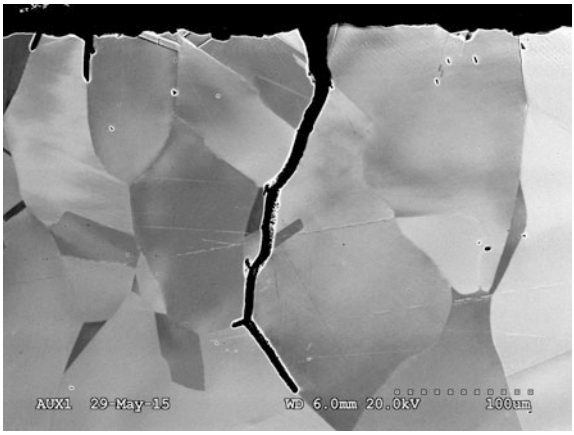

Fig. 20 Secondary crack cross section showing crack propagation from OD (top) toward the ID

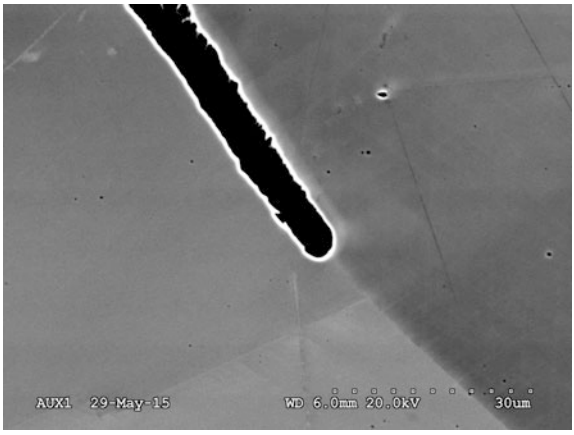

Fig. 21 Secondary crack tip cross section at higher magnification

and Cu. No evidence of deleterious species and/or de-alloying was identified within or adjacent to the cracking, or ahead of the crack tip within the grain boundaries.

Metallographic Examinations

Metallographic cross sections were prepared through various regions of interest in the tubes to characterize the crack region, tubes adjacent to the leaking tube, a tube near the center of the tube bundle, and tubes adjacent to the primary and secondary flow seals. Features specific to the pluggable cooler design were also investigated. Results for two of the cross sections, the through-wall crack tip and a secondary crack, are presented in this paper.

Mounts were examined in the as-polished condition and after electrolytic etching with 10% oxalic acid (~6 V for ~15 s) to reveal the material microstructure. The secondary crack cross section was also etched according to ASTM A 262 Practice A to assess material sensitization. This procedure involved oxalic etching at 0.5 Å for 90 s.

Through-Wall Crack Tip

The through-wall crack tip region exhibited a few branches, but was generally straight and unbranched for much of its length (see Figs. 22 and 23). Secondary cracking was noted on the OD surface as well. Intergranular cracking and branching are evident near the OD, but the latter half of the crack was clearly straight and transgranular. There was also evidence of cold work on the OD surface, as evidenced by the presence of disturbed grains in this area.

Fig. 22 Micrograph of the cross section prepared through the tube #17 through-wall crack tip. OD surface is along top edge. Electrolytic 10% oxalic etch

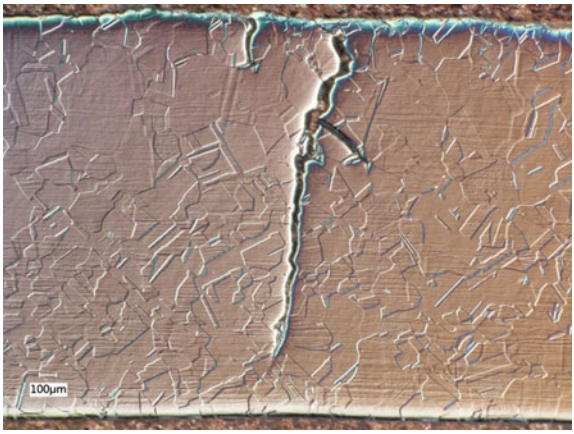

Fig. 23 Same area as Fig. 24, using Differential Interference Contrast (DIC) illumination

Secondary Crack

The cross section of a secondary crack in Tube #17 is shown after standard oxalic etching in Fig. 24 and after ASTM A 262 etching in Fig. 25. The cracking extended nearly through-wall in this plane. The grain boundaries exhibited a step structure after the ASTM A 262 etch, indicating that the material microstructure was non-sensitized.

Vickers Microhardness

Vickers microhardness (100 g load) traverses were taken on the polished cross section prepared from Tube #17. An OD-to-ID traverse indicated elevated hardness near the OD surface (285 HV) due to surface cold work. The bulk hardness for tube

Fig. 24 Tube #17 secondary crack. Electrolytic 10% oxalic etch

Fig. 25 Same area as Fig. 24, after etching per ASTM A 262, Practice A. No evidence of ditching was noted at the grain boundaries

#17 was approximately 150–160 HV, compared to 140–150 HV for the other the other tubes tested. Elevated hardness generally increases a material's susceptibility to SCC.

Optical Emission Spectroscopy (OES)

OES Chemical analysis was performed on three tube specimens (tube #17 and two adjacent tubes, #6 and #16). The results were all within the specified limits for Type 316L tubing per ASTM A 213. Of specific interest was the carbon content, which was consistent for all three tubes (0.018 wt%) and within specification for Type 316L stainless steel.

Analysis of OD Deposits

A clean razor knife was used to scrape deposits from the OD surface of tube #17 and two adjacent tubes, #6 and #16. Powder X-ray diffraction (XRD) was performed to identify the crystalline phase compositions of the tube deposit samples removed from the OD surface of tube #6, tube #16, and tube #17. Approximately 0.01–0.02 grams of powder was used for the analysis of the three samples. Samples were prepared using a greased microscope slide due to the small amount of available deposits.

The powder specimens were scanned by X-ray diffractometry, using a Philips X'Pert Diffractometer System, and the heights of selected peaks were measured. To minimize preferred orientation effects, several peaks from each phase were included. Empirically derived relative intensity factors were applied to the sums of the peak heights for each phase detected and the volume percent of the phases were normalized to give a total of 100%.

Utilizing a copper target X-ray tube operating at 40 kV and 40 mA, the samples were scanned over an angular range from 5° to 90° 2θ at a step size of 0.010° and a dwell time of 3.5 s per step. Cu Kα radiation was used. Qualitative results of the samples indicated calcium phosphate, $Ca_3(PO_4)_2$, was the major constituent in all three specimens. Other compounds identified included: tri-calcium silicate (Ca_3SiO_5), silicon dioxide (SiO_2), magnetite (Fe_3O_4), potassium, and chromium.

Discussion

Pressure testing and subsequent destructive examinations revealed a single through-wall crack in one of the letdown cooler tubes, identified as tube #17 in the laboratory. The through-wall crack was located in a heavily-deposited region of the

tube bundle central cavity near the primary inlet. Low magnification visual inspections revealed at least three cracks on the tube #17 OD surface; only one crack was visible on the tube ID surface. This observation indicated crack propagation was most likely OD to ID.

The open crack SEM examinations showed the through-wall portion of the cracking was intergranular from OD to ID. Shallow pitting present on grain facets indicated chemical attack occurred at some point after the crack formed. Cross-sectional examination of the through-wall crack tip region revealed cracking was mixed intergranular/transgranular in nature, as evidenced by the relatively straight, non-branching nature of the crack. OD intergranular attack (IGA) and intergranular secondary cracking were also identified.

Analysis of the deposits by XRD indicated a major constituent was calcium phosphate. The EDS data collected from the deposits indicated in-leakage of raw water as evidenced by the presence of Mg, Ca, and Si. No chlorine was detected on the though-wall open crack or the OD deposits located near the cracking.

Based on the laboratory findings, the most likely cause of the cracking appears to be OD-initiated caustic SCC. The presence of heavy deposits on the tube OD surface and heat tinting on the primary and secondary flow seals indicate boiling occurred near the tight radius region of the bundle. Once boiling occurs, there is the potential for caustic-forming species such as calcium phosphate to deposit and concentrate. As the caustic concentration approaches $\sim$20%, the conditions become favorable for cracking/IGA to occur.

For stress corrosion cracking to occur, three conditions must be present: (1) a susceptible material, (2) tensile stress, and (3) an environment known to cause stress corrosion cracking. Each of these conditions is discussed below.

Material

Cracking through the failed tube was primarily intergranular with a minor amount of transgranular propagation near the crack tips. This crack morphology is consistent with the literature, which indicates caustic SCC can produce both types of cracking in stainless steels (Ref. [6]). Ref. [7] indicates SCC caused by concentrated caustic in stainless and low-alloy steels is often observed to be intergranular in nature.

Conversely, chloride-induced SCC generally follows a transgranular path in non-sensitized, low carbon grades of austenitic stainless steels (Ref. [8]). This is because the low carbon grades are less likely to become sensitized, or chromium depleted, at the grain boundaries. (In contrast, chloride-induced SCC typically produces intergranular cracking in sensitized stainless steels.) Indeed, the ASTM A 262 Practice A test results revealed no evidence of sensitization in the tube material. Further, the tube material carbon content was 0.018% by weight, which is below the 0.02% solubility limit of carbon in austenite. Consequently, reducing the carbon

level to below 0.02% by weight is the recommended threshold to prevent sensitization of austenitic stainless steels by processes such as welding (Ref. [8]).

The failed tube contained evidence of surface cold work on the OD, with a maximum measured hardness of 285HV. Surface cold work was not identified in other tubes tested. In addition, the bulk hardness of the failed tube was slightly higher (150–160HV) compared to the other tubes tested (140–150HV). Elevated hardness due to strain hardening has been linked to intergranular cracking in non-sensitized Type 304L and Type 316L austenitic stainless steels (Ref. [9]).

Tensile Stress

Since the tubes are stress relieved after the coiling operation, the most likely source of tensile stress is operating stresses. Minimal "spring open" was noted during the tube sectioning operations, indicating minimal bulk residual stresses were present in the tube material and that the stress relief treatment was effective.

Environment

Because of the low operating pressure of the letdown cooler shell side (0.48–0.62 MPa, 70–90 psia) and the high RCS inlet temperature (291 °C, 555 °F) on the tube side, localized boiling will occur on the OD surface (Component Cooling water side) of the letdown cooler tubes until the RCS is cooled to less than the shell side saturation temperature. Non-volatile species in the Component Cooling water concentrate as the water boils until their solubility limits are exceeded and they precipitate on the tube surfaces.

The tube deposits appeared porous based on visual examination. Evidence of corrosive attack was present on the tube OD surface underneath deposits which is consistent with attack after the deposits precipitated. Boiling continued to occur at the tube surface within the pores of the deposits, forming concentrated caustic solutions that could attack the tube.

There was evidence of chemical attack in tubes located toward the primary flow seal end of the tube bundle. No attack was observed near the center of the bundle or at the opposite end of the bundle. This observation indicates the tubes toward the primary flow seal side of the tube bundle experienced the highest in-service temperatures and therefore were the most susceptible to corrosive attack. The apparent temperature gradient across the tube bundle may be attributable to the varying lengths of tubing from the inlet end to the tight radius region, i.e. the tube length is shorter on the primary flow seal side compared to the secondary flow seal side.

The XRD results for the heavy tube deposits indicated they were largely composed of calcium phosphate, $Ca_3(PO_4)_2$, with lesser amounts of tri-calcium silicate, Ca_3SiO_5, and silica, SiO_2. The source of the phosphate is the sodium phosphate

Table 1 Oconee nuclear station raw water chemistry

Parameter	mg/L	mole/L	pH
HCO_3^-	9.70	0.159	
SiO_2	7.36	0.123	
Na^+	1.75	0.0761	
Cl^-	1.13	0.0319	
Ca^{+2}	1.28	0.0319	
Mg^{+2}	0.62	0.0255	
SO_4^{-2}	1.62	0.0169	
K^+	0.62	0.0159	
pH			7.1

added for pH buffering of the Component Cooling water during the time period that potassium chromate was used as a corrosion inhibitor in the system. In-leakage of raw water into the Component Cooling water is the only plausible source of Ca, Mg, and Si (see Table 1). A review of historical Component Cooling water system chemistry data (Ref. [10]) did reveal specific raw water in-leakage events via Component Cooler tube leaks that occurred after the 3A letdown cooler was removed from service in 2006; however, no specific leak events were found in the reported chemistry data for the time period that the letdown cooler was in service. Tube-to-tubesheet joint leakage of the Component Coolers (the joints are not seal welded) is therefore the likely chronic source of Ca, Mg, and Si by low level raw water in-leakage.

MULTEQ simulations (static model with steam removed) of Component Cooling water containing sodium phosphate and faulted with raw water of the chemistry shown in Table 1 do predict calcium phosphate as a major precipitate with lesser amounts of calcium silicate (in agreement with the XRD findings) and a caustic pH at system temperature. With the current molybdate-azole chemistry faulted with raw water, MULTEQ simulations still predict a caustic pH, but with silica and $CaMg(SiO_3)_2$ as the major precipitates.

As the caustic concentration approaches ~20%, the conditions become favorable for cracking and IGA to occur in austenitic stainless steels. According to Ref. [8], the 1970s witnessed increased interest in caustic SCC as a result of the use of austenitic alloys in heat-exchanger systems of water-cooled nuclear power plants. It is well known from conventional boiler technology that boiling and steam blanketing at heat-transfer surfaces give rise to very high local caustic concentrations. The data show that there is an inherent danger of caustic SCC in strong caustic solutions when the temperature approaches 100 °C (212 °F). Non-sensitized Type 304 stainless steel components have failed at caustic concentrations about 20% (NaOH) at 100 °C (212 °F). Alloys containing nickel concentrations of 30% by weight or higher exhibit increased resistance to caustic SCC (Ref. [6]).

Reference [11] states: "Susceptibility of austenitic stainless steels to caustic SCC usually becomes a problem when the caustic concentration exceeds approximately 25% and temperatures are above 100 °C (212 °F)." A case history involving a Type 316L weld HAZ revealed cracking to be branching and intergranular. The lowest

reported temperature for a caustic SCC failure of stainless steel with <1 ppm Cl present was 120 °C (Ref. [12]), which is lower than the steam saturation temperature (149–160 °C) in the region of the letdown cooler where heavy deposition and SCC were observed.

Conclusions

A stress-relieved Type 316L stainless steel tube in the Oconee Nuclear Station 3A letdown cooler developed a through-wall leak most likely due to OD-initiated caustic stress corrosion cracking (SCC) based on the laboratory analyses. The through-wall cracking was intergranular in nature and developed within a heavily deposited region of the tube that experienced the highest operating temperatures and localized boiling of the Component Cooling water at the OD surface. Highly caustic conditions were created in the region of localized boiling when caustic forming impurities (Ca, Mg) entered the Component Cooling water via raw water in-leakage. Calcium combined with the phosphate, being used for pH buffering at the time, to form calcium phosphate deposits where boiling occurred. Other raw water impurities formed deposits such as tri-calcium silicate and silica in the boiling region. The occurrence of caustic SCC of austenitic stainless steel tubing under these conditions is consistent with the literature, which indicates that caustic conditions approaching 20% and higher are favorable for SCC and IGA. Elevated hardness levels present at the tube OD due to surface cold work increased the tube's susceptibility to SCC.

Remedial measures developed from this work and implemented at the plant were: (1) to maintain a minimum concentration of borate in the Component Cooling water in order to buffer the pH and prevent caustic conditions from occurring in the region of localized boiling and (2) to lower the control limit for chloride in order to more quickly prompt action to isolate and repair leaks, since an increasing chloride concentration in the Component Cooling water would be indicative of significant raw water in-leakage into the system.

It was also recommended that: (1) the tubesheets of the Component Coolers be coated in order to mitigate raw water in-leakage through tube-to-tubesheet joints and (2) the tubing material for future replacement letdown coolers be changed from Type 316L to an alloy that contains at least 30% nickel by weight to prevent caustic SCC.

References

1. C.R. Frye, Examination of Letdown Coolers A and B from Crystal River Unit 3, Babcock & Wilcox Report No. RDD:88:5105–01:01, 9 Oct 1987
2. C.R. Frye, Laboratory Comparison of Material from Two Failed Let Down Coolers. Babcock & Wilcox Report No. RDD:88:5178-01:02, 16 Oct 1987

3. R.B. Camper, A B&W Review of Graham Letdown Coolers. B&W No. 47-1170720-00, Jan 1998
4. BAW-1385, Water Chemistry Manual for 177FA Plants, Rev. 6, B&W Nuclear Technologies, Dec 1992
5. EPRI Report 1007820, Closed Cooling Water Chemistry Guideline—Revision 1, Apr 2004
6. R.B. Rebak, Industrial Experience on the Caustic Cracking of Stainless Steels and Nickel Alloys—A Review. UCRL-PROC-216072, Corrosion/2006, 11 Oct 2005
7. K.A. Esaklul (ed.), *Handbook of Case Histories in Failure Analysis,* vol. 2 (ASM International, 1993)
8. R.H. Jones, *Stress Corrosion Cracking*. (ASM International, 1992), pp. 102, 114, 352
9. T. Couvant, et al. Investigations on the Mechanisms of PWSCC of Strain Hardened Austenitic Stainless Steels, in *Proceeds of the 13th International Conference on Environmental Degradation of Materials in Nuclear Power Systems* (2007)
10. R. Thompson, Evaluation of ONS-3 Component Cooling System Water Chemistry, August 2015
11. ASM Handbook, Corrosion, vol. 13, 1987, p. 353
12. D.R. McIntyre, MTI Publication No. 27, Experience Survey—Stress Corrosion Cracking of Austenitic Stainless Steels in Water (1987)

Root Cause Analysis of Cracking in Alloy 182 BWR Core Shroud Support Leg Cracks

Martin Bjurman, Daniel Jädernäs, Kwadwo Kese, Anders Jenssen, Jiaxin Chen, Massimo Cocco and Hanna Johansson

Abstract Cracks were found in the Alloy 182 weld and buttering of two core shroud support legs in the Forsmark BWR Unit 1. This paper presents the root cause analysis based on mechanical and metallurgical analysis by Microscopy, Electron Backscatter Diffraction, and micro- and nano-indentation analysis along the crack path. The High Resolution Analytical Transmission Electron Microscopy examinations on the oxides are presented in detail in another paper at this conference. The morphology of the cracks, local hardness, crystallographic orientations and compositions along the crack path and crack tip regions were examined. The crack penetrated the boat keel surface into the A182 Low Alloy Steel mixing zone. Cracking was identified as IGSCC and signs of grinding and elevated micro-hardness near the boat top surface region were detected. Plastic deformation was observed in a crack tip region in a sample section with the largest crack depth, while not at the crack periphery.

Keywords Crack · Alloy 182 · Failure analysis · BWR · Core shroud · Support leg · SEM

Introduction

During the outage of 2011, cracks were found in two core shroud support legs in Forsmark BWR Unit 1. To remove the cracks and to obtain samples for failure analysis, boat samples were extracted by electro discharge machining (EDM). Figure 1 shows a photograph of such a crack and its relative location in one core

M. Bjurman (✉) · K. Kese · A. Jenssen · J. Chen
Studsvik Nuclear AB, Nyköping, Sweden
e-mail: bjurma@kth.se

D. Jädernäs
Idaho National Laboratory, Idaho Falls, USA

M. Cocco · H. Johansson
Forsmark Kraftgrupp AB, Forsmark, Sweden

J.H. Jackson et al. (eds.), *Proceedings of the 18th International Conference on Environmental Degradation of Materials in Nuclear Power Systems – Water Reactors*, The Minerals, Metals & Materials Series, https://doi.org/10.1007/978-3-319-68454-3_61

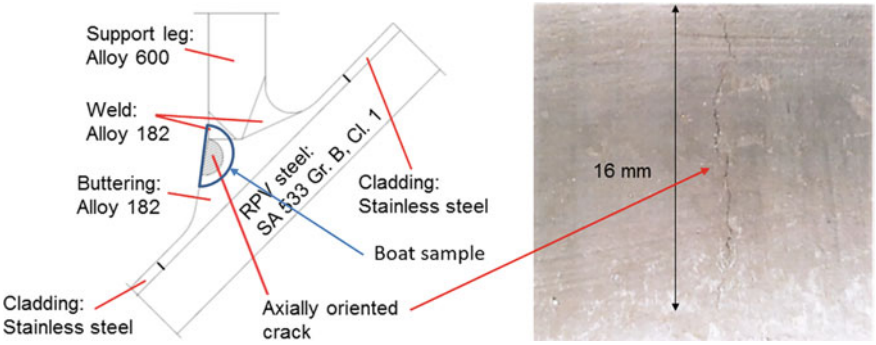

Fig. 1 Photograph and schematic drawing of the crack surface and its location in one core shroud support leg examined in this study. The extracted boat is presented in Fig. 2

shroud support leg. The surface crack had a length of 16 mm and was confined only to the buttering. The long crack started at the wetted surface, extended 20 mm in depth and appeared to end at approximately 0.5 mm from the boat keel and did not contain the interface between RPV steel and Alloy 182. After extraction from the plant, the crack was examined by using Stereo Light Optical Microscopy (LOM), Focused Ion Beam (FIB), Electron Backscatter Diffraction (EBSD), Micro/Nano-Indentation, Scanning Electron Microscopy (SEM) and Analytical Transmission Electron Microscopy (ATEM). The ATEM-analyses are reported separately in another paper [1] in this conference. In this paper, the influence of crack morphology, local hardness, crystallographic orientations and compositions along the crack path and crack tip regions on initiation and propagation cracking are discussed. The second boat sample extracted revealed a similar size crack that penetrated both buttering and weld but was not examined in depth.

Experimental

Material and Examined Locations

The boat sample was a buttering, heat-treated with RPV and attachment weld, both of Alloy 182. The buttering was welded onto the LAS and ground to shape followed by the RPV heat treatment for 7 h at 625 °C. The support leg made from Alloy 600 was then fitted followed by the attachment welds of Alloy 182 conducted on site. The geometry is depicted in Fig. 1.

Equipment

A field emission type Scanning Electron Microscope SEM (Zeiss Auriga Cross Beam FEG-SEM) was used for high-resolution imaging and EBSD measurement (using a Hikari EBSD camera with software TSL OIM Analysis 7.2.0). Other attachments to the FEG-SEM were EDS, WDS, FIB, Pt-gas injection system and micromanipulator. The equipment was operated at 5–20 kV electron acceleration voltage.

EBSD maps were acquired using different step sizes, 2 and 0.1 μm, respectively. These values are important to keep in mind since the resolution in EBSD is never better than the step size used. The small step size was used for the detailed maps and the large step size was used for the overview maps presented later.

Light optical microscopy examinations were conducted in a Reichert Polyvart MET (presently Leica) microscope, equipped with a Leica DFC digital camera.

Nano-indentation experiments were performed at room temperature using a Hysitron TriboIndenter TI–950 instrument. The instrument incorporates both a nano-indentation system and a scanning probe microscopy (SPM) system. Both systems use a common diamond Berkovich tip mounted in a Macor® body. In the present study, hardness H and effective modulus E^* are reported.

Micro-hardness measurements were made using a Vickers indenter, an Anton Paar model MHT–10 with a load force of 0.98 N, installed at the Leica MeF4 fully integrated inverted remote controlled microscope with Leica DFC 280 camera. This system is installed in a hot cell at Studsvik.

Results

Crack Path and Microstructure

A schematic drawing of the boat sample in-half is shown in Fig. 2. The boat sample was sectioned into seven parallel pieces and labeled accordingly. The microscopy presented below is conducted on the sectioning surfaces illustrated by the white bands between numbered pieces.

All six cross-sections examined had similar appearance in etched state as illustrated for cross-section #4_5 in Fig. 3. The crack plane normal is through the bead. At the weld bead interfaces, where the grain structure abruptly changed, the crack propagation was retarded and changed direction. For the cross-sections at either end of the boat sample, Samples #2, #3 and #6, the change in the direction of crack advance at each bead was more pronounced than for the other more centrally positioned cross-sections. Hence, the distance between cracks in different beads was larger. This could in part be due to crack propagation in the L–T direction compared to L–S propagation in Samples #4 and #5.

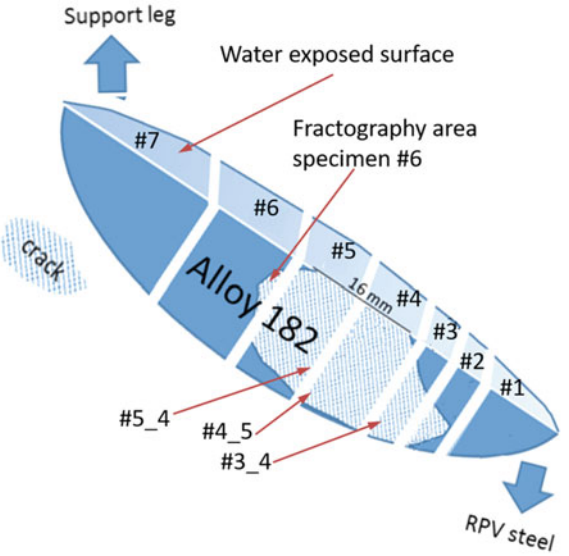

Fig. 2 The crack area and the examined locations in the boat sample in-half. The pieces are numbered #1–#7 and cross sections according to Specimen number 3_facing specimen 4 is written #3_4

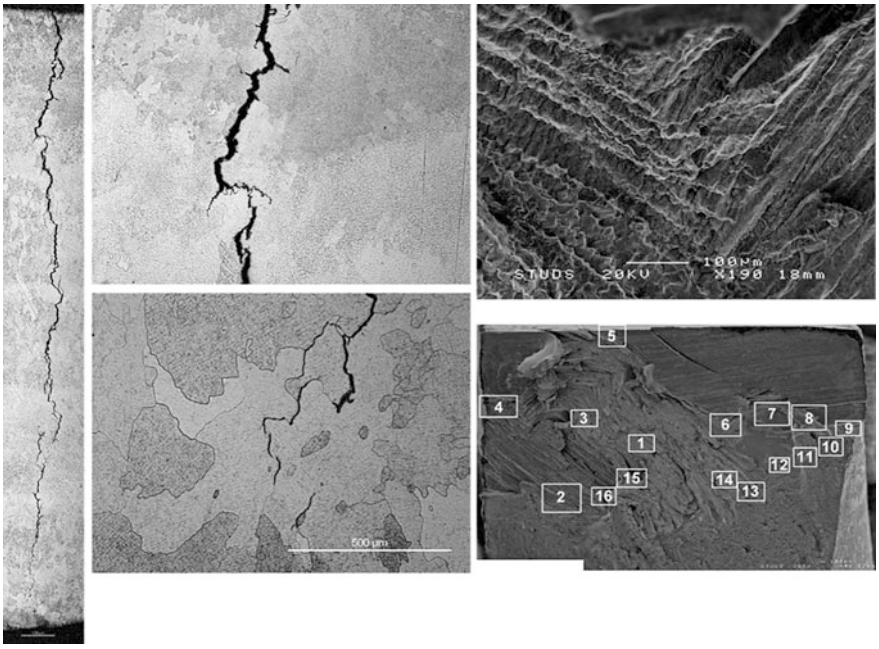

Fig. 3 LOM images of the etched cross-section #4_5. Overview image (left) and some detailed views (center). SEM secondary electron (SE) images showing an overview of the fracture surface from specimen #6 (lower right) and detail at Location 6 (upper right) of dendritic appearance at the boundary between two grains

The crack size in relation to the boat and cross section positions as shown in Fig. 2 was derived from cross section examinations and fracture surfaces. In short, the entire crack was approximately 16 mm long on the wetted surface of the sample, whereas its length was more than 33 mm under this surface. The depth exceeded 15 mm, penetrating the surface of the sample facing the RPV. A 21 mm long semi-continuous crack was visible on the surface facing the RPV, which probably was in the mixed zone between Alloy 182 and RPV steel. Because the cracks observed on cross-sections adjacent to this region did not grow through the boat sample thickness, it suggests that the missing part of the crack may be relatively small. According to the plant ultrasonic testing (UT) from the outside of the RPV, the crack did not extend into the low alloy steel. However, a small indication was subsequently found on the replica of the EDM-surface in the reactor. This indication was successfully removed during the following outage.

The crack grew in the buttering and it did not extend into the weld. The approximate location of the transition zone between buttering and weld is indicated in the right image of Fig. 3 with detail of region 6 above. These micrographs are representative of the intergranular cracking observed, and exhibit the typical IGSCC-appearance of Alloy 182. Cracking was fully intergranular with a readily recognizable dendrite structure. No indications of fatigue striations, ductile failure or cleavage were found on the fracture surface.

SEM-EDS/EBSD

SEM-EDS and EBSD measurements were carried out on the cross sections that faced the support leg of cross-sections #3_4 and #4_5. EBSD was applied on the samples to measure the strain distribution in the sample, and particularly in the areas surrounding the crack and in front of the crack tip. As can be observed in the inverse pole figure maps in Figs. 4 and 5, the weld is characterized by large, irregularly shaped grains with a relatively distinct texture on both cross sections.

As the weld buttering was heat-treated together with the pressure vessel, precipitates that accordingly formed or changed are of special interest for the discussion of their possible roles in the crack initiation and propagation processes. EDS mapping of the cross sections revealed secondary Ti precipitates (carbide) and the Nb (nitride type), see Fig. 6.

Furthermore, inhomogeneity was observed in the Fe and Cr composition, probably correlating to the dendritic grain structure and Si, and partly Nb and Ti, anti-correlate with the Fe and Cr variations observed. In the middle of the weld in the thickness direction, a shift in elemental composition was observed with higher Ni and lower Fe towards the wetted surface (region 1); see Fig. 5. The appearance of the secondary phase particles also changes at this location. Still, densities and distributions of precipitates can be regarded as normal. In addition, no grain boundary Cr-depletion was detected. Furthermore, a region with an even higher Fe content close to the EDM surface was observed, indicating the mixing with the

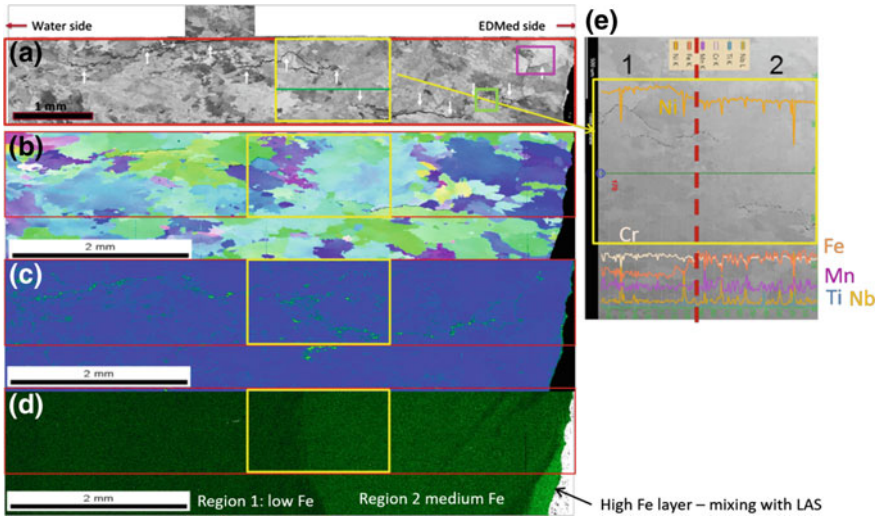

Fig. 4 . Crossection #3_4, **a** SEM image of cracked region (red box) and its relation to areas examined by EBSD-EDS, detail of EDS-map (yellow box), crack tip (pink box) and nano-indentation (green and pink box). **b** Inverse pole figure map, **c** Kernel average misorientation or grain average misorientation map, **d** Fe EDX-map, and **e** EDS line profiles at the position indicated by a green line

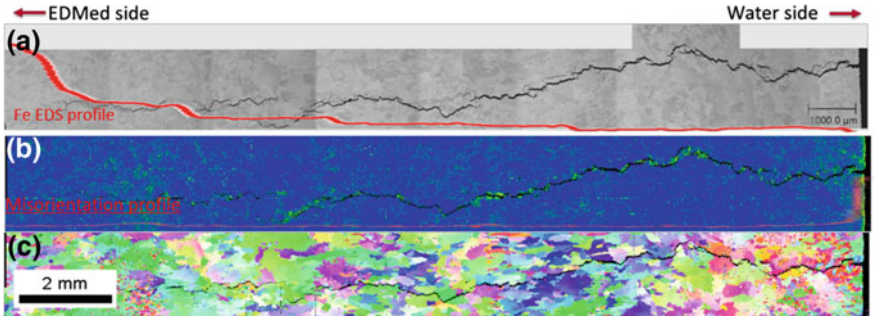

Fig. 5 Cross-section #4_5. **a** SEM-image of cracked region and a EDS Fe-plot (red) of the composition averaged along the crack. **b** Local misorientation map and misorientation profile (in red) of the cracked region, and **c** Inverse pole figure map of the cracked region

underlying LAS inside the boat sample. This is also visible in the Fe-map of Fig. 4 for cross-section #3_4 and in Fe-EDS-map of Fig. 5 for cross-section #4_5.

By studying the images, Figs. 4, 5 and 6, we may conclude that the cracking was intergranular and it propagated in the high angle main grain boundaries, but not in the dendritic grain boundaries. Indications of hot-cracking in Alloy 182 have previously been found in Ringhals BWR unit 1 and PWR units 2 and 4 [2], but none

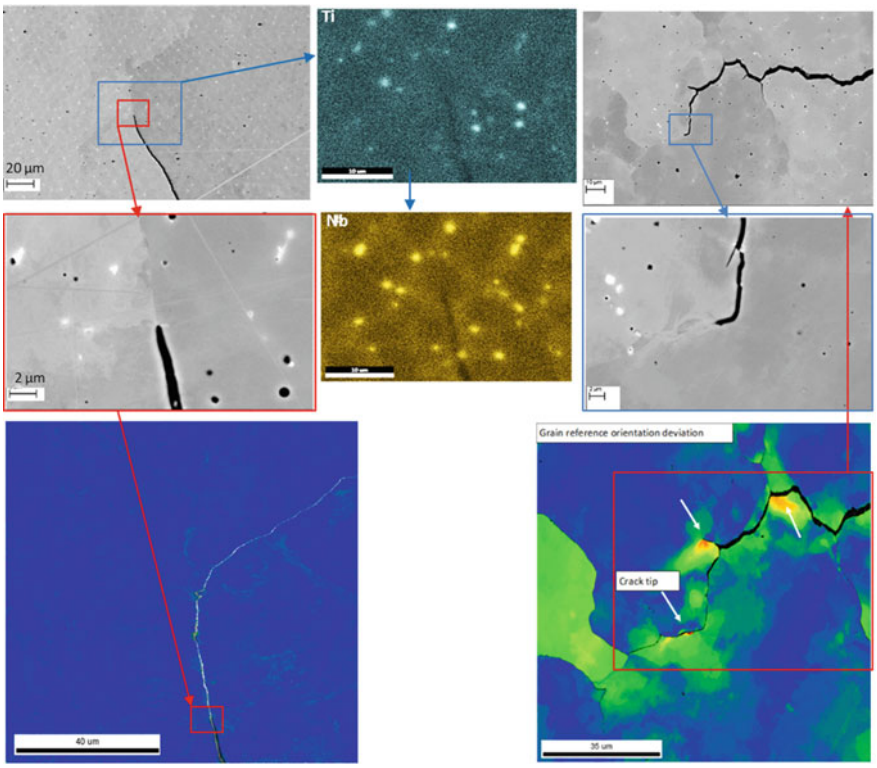

Fig. 6 (Left) Crack-tip SEM images and local misorientation maps in cross section #3_4 with virtually no deformation observed in this region. (Center) EDS maps of cross section #3_4 with Ti and Nb maps indicating precipitates. (Right) Crack-tip SEM images and grain reference orientation deviation map in the crack tip region of #4_5

of the cross-sections examined in this work revealed any evidence for weld repair-induced cracking or hot-cracking.

Plastic strain was measured at the crack tips in two cross-sections oriented upward in the reactor of cross-section #4_5 (the central part of the boat sample), and cross section #3_4 (at the crack flank). The results are presented in Fig. 5. Sizeable localized deformation at the crack tip region was detected only in cross-section #4_5. The absence of such deformation at the crack periphery (e.g. cross-section #3_4) was verified by a nano-indentation experiment as discussed below. Therefore, cracking at the central part of the boat sample might have occurred at higher stress while the cracking at the flanks occurred at a relatively low K, given Alloy 182's documented susceptibility to IGSCC.

It can be seen in Fig. 5 that the local misorientation of Sample #3 is higher around the crack compared to the rest of the material. There appeared more grain misorientation in the region close to the wetted surface than in the rest of the sample, which would indicate a higher strain in this region. This appears to be in

agreement with the micro-hardness measurements, which showed increased hardness at the wetted surface.

The characteristics of the crack in cross-section #4_5, Fig. 5, are slightly different from that in cross-section #3_4. An increased lattice misorientation, thus more plastic deformation, can be observed in the crack tip region but not seen in cross-section #3_4 Secondary cracks were also observed in other locations along the main crack, where the direction of the main crack changed. These secondary cracks show a high local strain indicating that a relatively high load was applied without further crack propagation in that plane.

Initiation occurred in the buttering that was post weld heat treated, but generally, no adverse effects are anticipated from PWHT on SCC initiation and propagation. Work on the effect of PWHT on crack initiation, mainly relevant for PWR environments, showed limited but a slightly beneficial effect of PWHT. Work on the effect of PWHT on crack initiation, mainly relevant for PWR environments, showed limited but a slightly beneficial effect of PWHT. Cassagne observed that PWHT increased the time to cracking by a factor of 4 [3]. Mills et al. reported a delay in the onset of SCC by the reduction of surface stress [4].

Cracking was oriented axially relative to the support leg, and the general orientation of crack propagation was towards the RPV steel in the central part and parallel with the RPV/Alloy 182 interface at the flanks. The direction of welding was transverse to the axial direction of the support leg and the cracks propagated within each bead separately, probably because the transition between different solidification structures was less favorable. This occurs even though EBSD-results show that the transition is close to epitaxial. Cracking at the flanks would become somewhat more branched than in the central region of the boat sample. Therefore, the cracking might have propagated downwards more rapidly in the boat central region than at the flanks, which would be followed by slow cracking as the driving force was reduced.

Mechanical Properties

Micro hardness measurements made on crossection #5_4 from the wetted surface down along the crack are presented in Fig. 7. The average hardness was 259 ± 6 HV, with a much higher hardness 299 ± 8 HV close to the surface region. This observation seems to agree with the higher degree of plastic strain found in the EBSD measurements. Hardness values were generally high compared to those previously seen. Hardness measurements were made during the construction of Forsmark 1 on a mock-up containing buttering and weld were; 220 HV in the buttering, 260 HV in the weld, and in the heat affected zone (HAZ) 260–330 HV. Values in the range 200–230 HV are commonly seen in the literature. It is unclear whether the increased average hardness is related to any manufacturing or material aging issues.

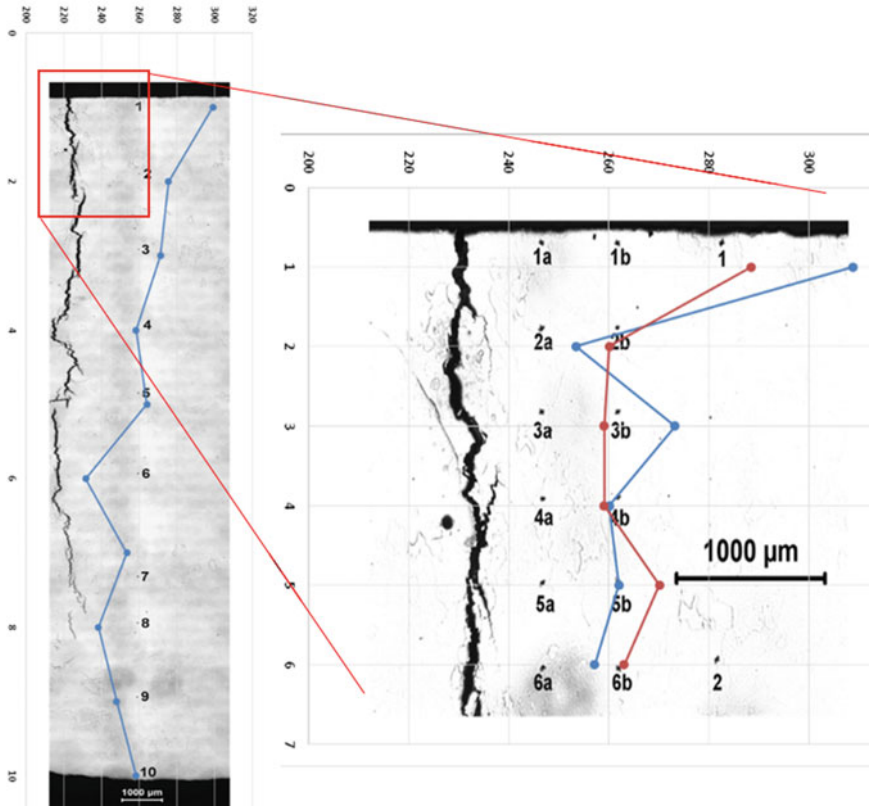

Fig. 7 Hardness profiles from the surface of cross-section #5_4. Left: Full cross-section from wetted surface to keel. Right: Detailed hardness profiles in the surface region

Elevated surface hardness could be induced by surface deformation through e.g. machining or grinding. Grinding effects are reasonable, since the buttering was ground or machined after welding, then subjected to the PWHT, and finally the support leg was welded to the buttering. The weld was probably ground, which means that part of the buttering would have been machined and/or ground two times.

Nano-indentation experiments were performed on Sample #3_4 on which EBSD and SEM/EDS studies had already been made, the testing positions are indicated in Fig. 4. The measurements were conducted on (a), a reference region far from any visible crack, (b), a region close to a visible crack as well as (c), where a sharp change in Fe content across a region that had been observed in the SEM/EDS. Hardness is known to be influenced by the presence of residual or applied stresses in a material.

Measurements close to the crack tip, Fig. 8a, shows no systematic trend in hardness variations around the crack tip. The average hardness's in horizontal and vertical directions show no significant difference. Results of hardness measurement at a crack branching location where crack deflection occurred Fig. 8b, no hardness gradient could be seen in the region adjacent to the crack at the location of crack path deviation. From Fig. 8c, it is seen that no gradients are present with Fe-content either.

FEM calculations showed that the highest stresses occur in the site produced welds, on both the upper and the lower sides of the support, not at the buttering. This might suggest that the buttering was more sensitive to crack initiation than the surrounding material. This could be due to the heat treatment applied, but fitting-stresses and other unknown stresses might have contributed to the location of cracking. The surface condition (cold work) could also have been different between weld and buttering.

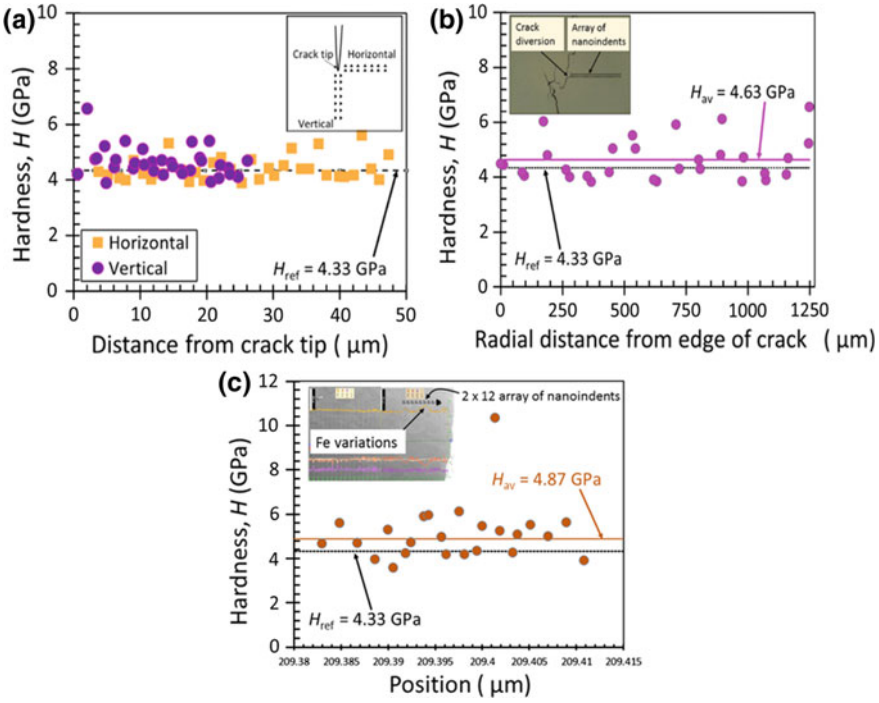

Fig. 8 Hardness of cross-section #3_4, positions in the cross section are shown in Fig. 4, **a** Close to a crack tip measured in two directions as a function of distance from the crack tip. **b** Hardness as a function of distance from edge of crack at a location where crack deflection occurred. **c** Hardness in a region of high and varying Fe-content

Conclusions

In this study, the root cause of cracks found in the Alloy 182 weld and buttering of two core shroud support legs in the BWR Forsmark 1 was investigated. Based on the experimental results obtained, the following conclusions may be drawn:

(1) The as-received boat sample from Forsmark did not contain the entire crack formed in the support leg, and the crack reached the mixed zone between LAS and Alloy 182, but did not significantly penetrate the LAS.
(2) The type of cracking is intergranular stress corrosion cracking (IGSCC).
(3) There was no evidence of hot cracking, weld repair-induced initiation of cracking or any significant microstructural deviations from expected, that are likely causes for the cracking, but a significant shift in composition was noted within the buttering.
(4) There is localized plastic deformation in the crack tip region at the central part of the boat sample whereas no plastic deformation is detected at the crack flanks.
(5) Hardness measurements of the buttering showed increased average hardness compared to literature and results from mockup measurements.
(6) There is elevated hardness and evidence of plastic deformation at the surface of the buttering.

Acknowledgements The authors wish to express their sincere gratitude to Mr. Roger Lundström and Mr. Michael Jakobsson at Studsvik Nuclear AB who performed light optical microscopy work, Prof. Esteban Broitman at, formerly Linköping University who helped with nano-indentation measurement and scientific discussion about the result, and to Dr. J. Öijerholm at Studsvik Nuclear AB for his technical and administrative support.

References

1. J. Chen et al., Microstructure of Oxide Films Formed in Alloy 182 BWR Core Shroud Support Leg Cracks, in *Paper Presented in this Conference*
2. A. Jenssen et al., Assessment of Cracking in Dissimilar Metal Welds, in *10th International Conference on Environmental Degradation of Materials in Nuclear Power Systems-Water Reactors* (NACE International, Houston, TX, USA, 2002)
3. T. Cassagne et al., Stress Corrosion Crack Growth Rate Measurements in Alloys 600 and 182 in Primary Water Loops under Constant Load, in *Proceedings of the 9th International Symposium on Environmental Degradation of Materials in Nuclear Systems-Water Reactors* (The Minerals, Metals & Materials Society, Warrendale, PA, 1999), pp. 217–224
4. W.J. Mills, C.M. Brown, Stress Corrosion Crack Growth Rates or Alloy 82H Welds in High Temperature Water, in *Proceedings of I1th International Conference on Environmental Degradation of Materials in Nuclear Power Systems-Water Reactors* (ANS, 2003), pp. 1240–1254

Microbially Induced Corrosion in Firefighting Systems—Experience and Remedies

Ulla Ehrnstén, Leena Carpén and Kimmo Tompuri

Abstract Firefighting water systems are important safety systems in all industries, including nuclear power plants (NPPs). However, they are susceptible to microbially induced corrosion, which is a degradation mode needing special attention. Leakages were observed in a fire fighting system made from stainless steel at a nuclear power plant shortly after maintenance and modernization work, which included replacement of part of the old carbon steel pipelines with stainless steel pipelines, as well as exchange of some Type 304 stainless steel pipes with Type 316 pipes due to relining parts of the system. The failure analysis revealed sub-surface corrosion cavities with pinholes at the inner surface and finally penetrating the whole pipe wall thickness. It was concluded that the reason for the leaks was due to microbially induced corrosion, (MIC). The paper will present the results from failure analyses, explain the remedial actions taken at the power plant, and discuss the implication of these findings on new similar systems, including the importance of avoiding iron deposits and optimization of water quality.

Keywords Stainless steel · Microbially induced corrosion · Ageing management

Introduction

Firefighting water systems (FFWS) are important safety systems in industry, including NPP's. The FFWS consists of a water reservoir, from which the firefighting water is fed into the main piping. The main piping distributes water into the sprinkler system, which consists of a large amount of piping of smaller size than the main piping and numerous spray nozzles at the end of the sprinkler piping.

U. Ehrnstén (✉) · L. Carpén
VTT Technical Research Centre of Finland, VTT,
P.O. Box 1000, Kivimiehentie 3, 02044 Espoo, Finland
e-mail: ulla.ehrnsten@vtt.fi

K. Tompuri
Teollisuuden Voima Oyj, 27160 Olkiluoto, Eurajoki, Finland

J.H. Jackson et al. (eds.), *Proceedings of the 18th International Conference on Environmental Degradation of Materials in Nuclear Power Systems – Water Reactors*, The Minerals, Metals & Materials Series, https://doi.org/10.1007/978-3-319-68454-3_62

The FFWS contains also hundreds of valves and several pumps. The typical total length of a FFWS is more than 1000 meters and the total water volume in the piping is in the order of 100 m^3. The FFWS are moderately pressurized, between 12 and 16 bars. The material choices differ from plant to plant, but commonly carbon steel, galvanized steel, and stainless steels are used for the large diameter piping, while copper is also used for small diameter piping. The valves are made of cast iron, carbon steel, or stainless steel, with or without rubber coating, while the smaller valves typically are made from brass. The main piping is continuously filled with water, while there are differences between plants concerning the sprinkler system, which can either be water filled or dry. In most plants, the water is not circulated, but stagnant [1]. The water used in the FFWS typically varies, and can be alkalized treated raw water, desalinated water or demineralized water. In addition, biocides are used in some systems. It is quite common that the water treatment has changed, i.e. improved, over the years, either as part of continuous improvement or as mitigation to observed corrosion problems.

FFWS are susceptible to corrosion. Corrosion can be caused by many factors or the combination of these factors, such as pipe weld seam corrosion, residual water in dry pipe systems, trapped air in wet pipe systems, corrosive water chemistry, periodically supplying oxygenated water into the system (e.g. in connection to functionality tests), stagnant water and MIC. The corrosivity of FFWS water is significantly influenced by water quality and chemistry parameters, such as concentration of dissolved gases (O_2, CO_2), solids (hardness and deposits) and micro-organisms [2]. Considering stainless steels, the most important chemical component in waters is the chloride content and the presence of possible inhibitive anions, like sulfates. Stainless steels usually have an excellent corrosion resistance in cold, flowing, low-chloride containing water. In stagnant water, however, the corrosion resistance evidently diminishes. Increase in temperature or chloride content accelerates localized corrosion. In addition, thiosulfate is known to have a detrimental effect on the pitting corrosion resistance of stainless steel if it exists in a certain ratio to chloride and/or sulfate. MIC is one—corrosion mode, which stainless steel FFWS are especially susceptible. Microbes, which are numerous in natural waters, can change the environments corrosiveness either chemically or physically. Microbial colonization results in increase of the open circuit potential to above the pitting potential of stainless steels [3]. Further, stainless steel welds, and especially heat affected zones with heat tints are vulnerable to MIC [2, 4]. There are several types of microbes causing MIC, and the literature on the mechanisms is ample [3–8].

Microbially induced corrosion (MIC) has been a known degradation mode of stainless steels since the 1970s. However, it was not widely well known, nor considered, when a large amount of the current NPP-fleet was designed, or taken into consideration in early operational guidelines. The nuclear industry started to look into this topic in the mid 1980s. The oldest reference found in the open literature on MIC in the nuclear industry, is from 1983 [9]. This reference described a leakage that had been observed in the essential raw cooling water system made from Type 316 stainless steel at Watts Bar NPP. The leakage was evaluated to be

due to MIC, and a non-conformance report was submitted to the NRC. A special program was initiated which included looking for remedies for MIC and performing structural analyses to determine the possible consequences from MIC. The conclusion from the tests performed was that a combination of sodium hypochlorite and sodium bromide would decrease the total counts of active bacteria with no significant corrosive effects on system materials. Consequently, a new bromine/chlorine biocide injection system was installed in October 1990, resulting in about 90% decrease in the bacteria amount. As part of the remedy program at the plant, all systems were reviewed in terms of susceptibility to MIC, and the fire protection system was identified as one of the systems with a risk for MIC [9].

The oldest report on MIC publicly available on the EPRI web site is from 1986 [8]. This report contains results from a survey on observed MIC in different systems and materials. The performed survey reported MIC in stainless steel piping, tanks, stray pond components, and heat exchanger tubes. The report contains also instructions on how to recognize MIC, and advice for remedies, including mechanical treatment, use of biocides and of corrosion inhibitors. The lack of transferability of mitigation methods from laboratory to operation is highlighted, as is the need to consider the risk for MIC in all phases of component lifetime, as the root cause is seldom only the normal operation, but the manufacturing, pressure tests, pre-operation phases or maintenance. Ozone was, in this report, especially recommended for stainless steel systems, both for normal operation as well as for pressure tests etc., but also borate and hydrogen peroxide are recommended for pre-operation phases [10]. Since that, MIC has been on EPRI´s agenda, and courses on the topic are held regularly and reports are published. Several organizations globally have published documents and standards attempting to address these problems. However, there is currently no agreed-upon common strategy for effective mitigation of corrosion problems in FFWS [2].

In 2006, EPRI made a report from 2004 publicly available on water treatment strategies presenting an overview of MIC, microorganism control, and remedial alternatives [10]. The report is intended as a support for the licensees concerning lifetime management of service water systems, circulating water systems and fire protection systems. The report emphasizes the importance of preventing MIC, instead of mitigating it, when it has occurred. One reason for this is the population dynamics. Typical for MIC-cases is that they are discovered only when the amount of microorganisms have increased to a stationary phase, which makes solving the problem most difficult. The growth curve of microorganisms consists typically of a slow phase where the reproduction rate and death rate of the microorganisms are relatively equal and at a low level. Usually the population remains low for an extended period without approaching the critical population level where potential microbiological problems are likely to occur. In response to a change in the growth-limiting factors of the environment, reproduction rates may be stimulated and the population enters into a fast growing phase. It is at this point, when the population exceeds the critical level, that problems begin to appear in the system. Once the limit of the environment for supporting an increasing population has been reached, the microflora enters into a stationary phase [10]. It is the stationary phase

of the growth cycle when most of the chronic or mature microbiological problems persist. However, there is no clear correlation between the amount of bacteria and corrosion. More important is what is the activity of the microbial community and especially that of the microbes attached to the surfaces forming biofilms. Though experience has shown that there appears to be a correlation between how long the MIC existed before mitigation was implemented and the length of time required for a successful on-line mitigation program. The longer MIC has existed, the longer the time required mitigating it. Experiences have shown that some on-line programs have been completed within a six-week period. In other cases where the MIC was a relatively severe chronic problem, periods up to nine months were required for mitigation [10]. Use of biocides is one recommended mitigation method. It is important, though, to combine this with mechanical cleaning, as most biocides does not penetrate tubercles and biofilms [11–13].

Background on the Leak in a NPP Firefighting Water System

The FFWS at the plant in question was originally constructed from carbon steel, which had gradually been replaced by stainless steel pipes. Modernization and re-lining of the FFWS included also partial exchange of the Ø140 × 3 mm piping in the sprinkler system from EN 1.4301 (similar to SIS 2333 and Type 304) to EN 1.4401 (similar to Type 316) stainless steel. About two years after the exchange, in 1997, leakages in both the old EN 1.4301 (Type 304) as well as in the new EN 1.4401 (Type 316) piping were observed. The leakage was always on the lower side of the piping, in the heat affected zone (HAZ) of the welds. The water inside the FFWS was stagnant tap water, which had been chlorinated using ammonium hypochlorite since the exchange of the piping, but not earlier. The system is emptied yearly and filled with fresh water. Two failure analyses were performed in addition to a survey on FFWS in the Nordic NPPs [1, 11]. After the first failure analysis was performed, indicating that the reason may be microbially induced corrosion (MIC), an extended failure analysis on additional samples was launched including experts on MIC in the investigations, as well as analysis of the water, of the deposits in the piping and electrochemical investigations.

Failure Analyses of the Firefighting System Leak

A total of seven samples from the piping from the FFWS, made from ∅140 × 3 mm stainless steel piping of EN 1.4401/Type 316 were investigated. The investigations performed comprised determination of the chemical composition of the material, visual examination, scanning electron microscopy (SEM), analysis

of the corrosion products using energy dispersive analysis (EDS) and light optical microscopy of a cross-section. Swab samples from the piping were analyzed for bacteria and water samples were analyzed for its composition. Additionally, polarization curves were performed for determination of corrosion potential values, e.g., pitting and repassivation potential.

Results from the Failure Analysis

The chemical composition of the material is presented in Table 1. The composition fulfils the requirements of EN 1.4401 (Type 316) stainless steel. The visual inspection of one of the pipe samples revealed two perforations on the outer surface of the sample. These perforations were situated at the heat affected zone close to the fusion line of the weld. Significant reddish brown deposit was seen on the opposite inner side, Fig. 1. Typically, the openings of the pits were very small but had large subsurface cavities, Fig. 2. Selective corrosion was also observed, where the austenite had dissolved, leaving a ferrite skeleton behind, Fig. 3. The findings from the other studied samples were similar.

The microstructure of the pipe material was normal austenitic structure. Pits were located in the heat affected zone of the welds, and there were clear signs of oxidation of heat affected zone (heat tints) but no welding defects were observed in the failure areas. Dark brown circular deposit rings typically surrounded the pits and the inner surfaces were most of the times covered with thin, rather smooth layer of yellowish brown deposit. Sulfur and occasionally high amounts of manganese as well as small amounts of phosphate were detected on the deposits, in or surrounding the pits.

The result from the water analysis is presented in Table 2. The results indicates a water quality, which should not pose any corrosion issues for EN 1.4301/Type 304 or EN 1.4401/Type 316 stainless steel, although the pH is not exactly in the most optimal region for chlorination, which is considered to be 6.0–7.5 [10].

The results from the bacteria counts from different samples are presented in Table 3. High amounts of aerobic (and heterotrophic aerobic) bacteria were detected in the sample taken from the pipe inner surface, especially when the surface was still moist. Sulfate reducing bacteria were also detected in the sample taken from the moist inner surface, although the count was small. However, the

Table 1 Chemical composition of the EN 1. 4401 (Type 316) piping specimen (wt%)

	C	Si	Mn	S	P	Fe	Cr	Ni	Mo	Cu	Ti	Co
FFWS sample	0.032	0.67	1.45	0.007	0.034	Bal.	16.89	10.70	2.47	0.21	0.017	0.23
EN 1.4401	<0.07	<1.0	<2.0	<0.045	<0.030	Bal.	16.5–18.5	10.0–13.0	2.00–2.50			

Fig. 1 Appearance of the inner surface of a leaking FFW pipe made from EN 1.4401 stainless steel. The reddish area is the lower side of the pipe in the piping

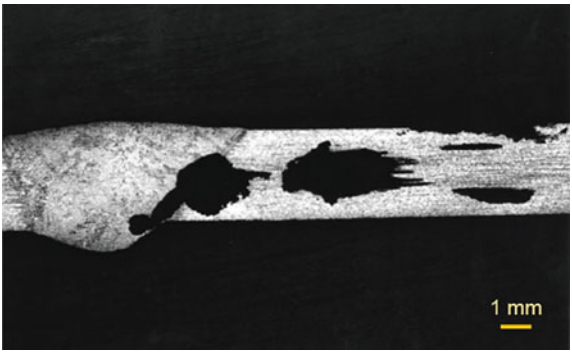

Fig. 2 Photograph of the cross-section from a leaking EN 1.4401 pipe, showing a very small pit mouth and a large sub-surface cavity

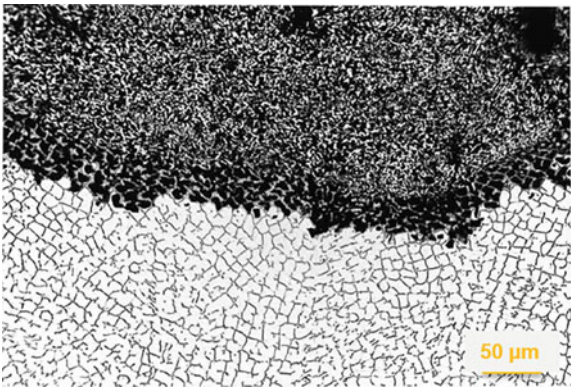

Fig. 3 Selective corrosion of the stainless steel weld metal, where the austenite phase has dissloved, leaving a ferrite skeleton behind

system had been opened half an hour prior sampling, which might have had an influence to the low amounts of anaerobic bacteria detected. The amount of aerobic bacteria was also rather high in the sample from the inner surface. Further, iron bacteria (bacteria growing on ferrous sulfide medium) was verified on the inner

Table 2 Results from water analysis

pH	Fe (mg/l)	Mn (mg/l)	Ca (mg/l)	Mg (mg/l)	Cl^- (mg/l)	SO_4^{2-} (mg/l)	HCO_3 (mg/l)	NO_2 (mg/l)	NO_3 (mg/l)
7.8	0.05	0.02	12	4.7	24	27	26	<0.01	<1

Table 3 Results from bacteria counts, CFU = Colony forming units

	Type of bacteria				
Location	Aerobic (cfu/ml)	Heterotrophic aerobic (cfu/ml)	Anaerobic (cfu/ml)	Sulfate reducing (cfu/ml)	Iron (Y = detected)
Pipe inner surface	1.1–7.3 10^3		5.5–9.5	0.5	
Moist pipe inner surface	4.3×10^6	4.3×10^5			Y
Dry deposit	20				
Water		2.4×10^5	0.1–1	0.2–4.1	

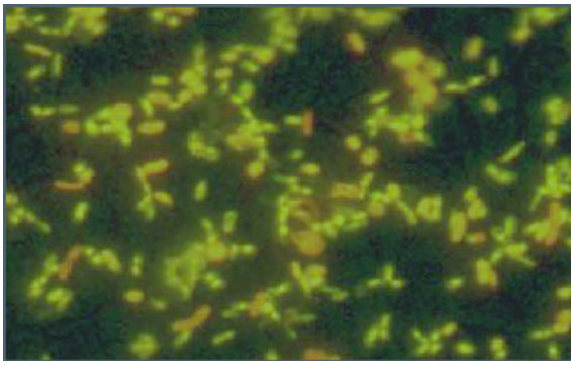

Fig. 4 A colony of bacterial cells and starting biofilm formation in the deposit analyzed from the failure area on the inner surface of fire extinguishing pipe

surface. Large numbers of individual rod-shaped bacteria as well as cell aggregates and starting biofilm formation on the stainless steel coupons incubated six (6) days in iron bacteria culture medium could be seen under the epifluorescence microscopy, Fig. 4.

The results from the electrochemical measurements clearly show that the iron deposit on the surface lowered both the pitting initiation potential, E_{pn}, (+540 mV_{SCE} vs. +680 mV_{SCE}) and the repassivation potential, E_{pp}, (+100 mV_{SCE} vs. +185 mV_{SCE}). In addition, the effect of the heat tint in the HAZ is clearly seen, resulting in a pitting initiation potential of +316 mV_{SCE} and a repassivation potential of −50 mV_{SCE}, Table 4.

Table 4 The pitting initiation potential (E_{pn}), repassivation potential (E_{pp}), and open circuit potential (E_{oc}) determined for stainless steel sample in water containing chloramine

Water/test	E_{pn} (mV_{SCE})	E_{pp} (mV_{SCE})	E_{oc} (mV_{SCE})
Water + 200 Cl	680	185	−9
Water + 200 Cl + deposit	540	100	−17
Water + 200 Cl + weld + deposit	316	50	54

Discussion

The leakage in the EN 1.4401/Type 316 stainless steel piping occurred after a relatively short time of usage in water with low chloride content. The water is not regarded as corrosive to neither EN 1.4301 (Type 304) nor EN 1.4401 (Type 316) stainless steel. However, the water in the FFW system is stagnant most of the time and only occasionally circulated. The corrosion resistance of stainless steels is clearly diminished in stagnant water with possibility for deposit formation. During long stagnant periods, bacterial activity may increase, as was confirmed from the swab samples. The water in the FFW system contained also a high amount of precipitated iron. The high concentration of iron in the water can offer suitable conditions for iron oxidizing bacteria. Besides, iron hydroxides can behave as anion selective membrane at neutral pH and had been shown [14] playing a certain role for the occurrence of localized attack of stainless steel. The iron is obviously corrosion products from the steel components in the system.

The conclusion is thus, that the through-wall pitting in the EN 1.4401/Type 316 stainless steel was remarkably affected by microbial activity. The presence of precipitated iron and remains of oxidized regions (heat tint areas) of welded structures have increased the susceptibility for pitting. Despite being drinking-water quality, the water seemed to contain enough sulfates for sulfate-reducing bacteria which can obtain their energy by oxidizing organic compounds or molecular hydrogen (H_2) while reducing sulfate (SO_4^{2-}) to hydrogen sulfide (H_2S). In a sense, these organisms “breathe” sulfate rather than oxygen in a form of anaerobic respiration. Relatively large amount of suspend solids and debris also help local conditions build up for colonies. Similar cases has since been reported in the literature [15, 16].

The recommendations given by the researchers were as follows. The best way to prevent forming of deleterious oxide layers is to remove oxygen from the piping by shielding gas flushing before welding and using backing gas during the whole welding and as well as little time after welding. The oxidization of root can be reduced also by using root paste. This paste reacts with the welding heat and forms a slag layer on the root side of the weld. However, the results achieved with root paste are not anywhere near to the results achieved by using the backing gas. Alternatively, the heat tints can be removed by pickling after welding. However, this is not always possible while considering the welding of piping. To avoid this kind of failures one should use water as clean as possible with low amounts of

solids, chlorides, manganese, and iron, as well as a low amount of organic substances and avoid stagnant conditions or very low flow conditions. If the continuous flow is not possible, the water should be changed frequently enough and the amounts of bacteria should be checked regularly and when necessary to treat the water to minimize the bacterial activity.

Remedies and Implications

After the first corrosion problems in the FFWS were detected, counteractions were implemented at the plant. First, mild sanitation using chloramine addition to the firefighting system was taken into use. Chloramine is a so-called oxidizing biocide and disinfectant, but simultaneously a pH-neutral agent in the water. The laboratory tests performed as part of the investigations confirmed, that chloramine treated water will not cause pitting, and could therefore not alone be the reason for the earlier observed pitting and leaks.

After sanitation, some defected pipes were exchanged to stainless steel of Type SIS 2333 (similar to EN 1.4301 and Type 304). Shielding gas was used during welding of all welds to avoid heat tints in the HAZ. The weld areas were also mechanically polished on the inner surface. Then the systems were rinsed with demineralized water, which was also left inside the piping. All firefighting systems are now pressurized with demineralized water. Water of drinking water quality will be used as water for firefighting, while the system is filled with demineralized water during stand-by conditions.

Lessons learned were taken into account in a new build project. All welded piping is made of austenitic steel of type EN 1.4571, similar to Type 316Ti. Shielding gas was used for all stainless steel welds to prevent possible heat tint. In addition, non-welded components are used, e.g. screwed, coupled, pressed or flanged components, all made of stainless steel or EN 1.4401 (similar to Type 316) or EN 1.4571 (similar to Type 316Ti). Crevices are known to enhance the risk for MIC, as microbes can adhere to crevices more easily than on flat surfaces [17]. However, the risk for MIC is minimized through water quality, and therefore these joints are not considered to be at risk for MIC. The local water quality gives the basis for the material selection and design. In the new FFWS demineralized water filling and recirculation in the main loops is used.

Some new builds also rely on galvanized steel-based system. The most critical criterion is the water hardness. If the firewater is hard, galvanized materials might be used. However, in soft water which does not have protective amounts of Calcium/Magnesium, galvanized steel might not be the optimized solution, as these would corrode in these circumstances. Unlike the waters in Central Europe which are hard, the raw water in Nordic countries is typically soft, i.e., has a low hardness and low pH (<7), which precludes the use of galvanized materials due to corrosion issues.

All firefighting systems at the plant are included in the plant chemistry-monitoring program. The main diagnostic parameter is the conductivity, which is used to control the total salinity in the firefighting systems. Some plants also monitor pH, suspended solids, as well as chloride and sulfate concentrations.

Acknowledgements The work was performed for Teollisuuden Voima. This publication has been prepared as part of the Finnish national research program on reactor safety, SAFIR 2018, project THELMA. The funding is highly appreciated.

References

1. U. Ehrnstén et al., A Survey Of Corrosion in Fire Fighting Water Systems in Nuclear Power Plants, VTT report VALC 613 (1999)
2. P. Su, D.B. Fuller, Corrosion and Corrosion Mitigation in Fire Protection Systems, FM Global technical report, project ID 0003040794, 2nd edn (July 2014)
3. L. Carpén et al., Effects of Leptothrix discophora on the potential behavior of stainless steel. Mater. Corros. **54**, 515519 (2003)
4. T. Hakkarainen, L. Carpén, Effects of Heat Tints on Pitting Susceptibility of Stainless Steel, in *7th International Symposium on Electrochemical Methods in Corrosion Research*, EMCR2000, Paper No. 061 (Budapest, Hungary May 28–June 1 2000)
5. L. Carpén et al., Simulation of MIC at Splash Zone Areas of the Paper Industry, CORROSION 2001, Paper no. 245, (NACE International, Houston, TX, 2001)
6. T. Hakkarainen, Microbiologically influenced corrosion of stainless steels—What is required for pitting? Mater. Corros. **54**(7), 503–509 (2003)
7. J. Roland, P.E. Huggins, Microbiological Influenced Corrosion. What it is and how it works, http://www.sprinklernet.org/technical/mic/articles/article4.html
8. D.H. Pope, A Study of Microbiologically Influenced Corrosion in Nuclear Power Plants and a Practical Guide for Countermeasures, EPRI NP-4582 (May 1986)
9. S. Ferrel, Microbiologically induced corrosion (MIC) special program (SP) final report, 1993. https://www.nrc.gov/docs/ML0732/ML073230496.pdf. Accessed 6 Mar 2017
10. R. Lutey, Water Treatment Strategies: Microorganism Control, EPRI (Palo Alto, CA 2004), 1009598
11. L. Carpén, Corrosion of Stainless Steel in Fire Protection Systems, VTT Research report VTT-R-01556-08, VTT (1998)
12. L. Carpén et al., Microbially induced corrosion (MIC) in austenitic stainless steel used as fire extinguishing pipes, Eurocorr 2001, the European Corrosion Congress, Riva del Garda, Italy, Sept 30–Oct 4 2001 (AIM, Associazione Italiana de Metallurgia, 2001)
13. D.H. Pope, R.M. Pope, Microbiologically Influenced Corrosion in Fire Protection Sprinkler Systems, Corrosion 2000, Paper No. 00401 (NACE International, Houston, TX, 2000)
14. M.H. Renner, Corrosion Engineering Aspects Regarding MIC Related Failures of Stainless Steels. Corrosion, Paper No. 285 (NACE International, Houston, TX, 1998)
15. R.I. Garber, D.G. Chakrapani, Some Recent Failures of Fire Sprinkler System Components: Corrosion Case Histories, Corrosion, Paper No 04511 (NACE International, Houston, TX, 2004)
16. L. Hilbert et al., Unexpected Corrosion of Stainless Steel in Low Chloride Waters—Microbial Aspects. Eurocorr 2009. The European Corrosion Congress, 6–10 Sept 2009, Nice, France. EFC. Nice, FR, 16 s, 2009
17. G. Kobrin (ed.), *A Practical Manual on Microbiologically Influenced Corrosion* (Nace International, Houston, TX, 1993)

Managing the Ageing Degradation of Concealed Safety Relevant Cooling Water Piping in European S/KWU LWRs

Martin Widera, Gerd Ahlers, Bernd Gruhne and Thomas Wermelinger

Abstract Safety relevant cooling water piping is designed to transport excess heat both from the reactor core and the fuel pool under all operational and emergency conditions. Plain carbon steels are used, with or without different types of protective coating systems. Outside of the reactor building, such piping is often buried or concealed, which also gives additional protection against damage. Relevant ageing mechanisms are shallow pit corrosion and microbiological induced corrosion (MIC). While these ageing mechanisms can lead to localized leaks and limited loss of cooling water, neither the mechanical integrity nor the cooling ability of the systems are compromised. The extent and ageing management of the mechanisms are described, based on more than 30 years of operating experience. This includes NDT results and post service examinations after retrofits. Based on this positive operational experience, two different NDT concepts are recommended to manage the long time operational ageing.

Keywords EU TPR · WENRA · Ageing management · KTA 1403 · S/KWU · LWR · Cooling water piping · Concealed piping · Buried piping · Carbon steel · Cement mortar lining · Shallow pit corrosion · MIC · NDT · Operating experience

M. Widera (✉)
RWE Power AG, Huyssenallee 2, 45128 Essen, Germany
e-mail: martin.widera@rwe.com

G. Ahlers
PreussenElektra GmbH, Tresckowstrasse 5, 30457 Hannover, Germany

B. Gruhne
EnBW Kernkraft GmbH Kernkraftwerk Neckarwestheim, Im Steinbruch, 74382 Neckarwestheim, Germany

T. Wermelinger
Kernkraftwerk Gösgen-Däniken AG, 4658 Däniken, Switzerland

J.H. Jackson et al. (eds.), *Proceedings of the 18th International Conference on Environmental Degradation of Materials in Nuclear Power Systems – Water Reactors*, The Minerals, Metals & Materials Series, https://doi.org/10.1007/978-3-319-68454-3_63

Background: The EU Topical Peer Review 2017—Ageing Management (AM)

The European Union's Nuclear Safety Directive (NSD) 2014/87/EURATOM requires the member states to undertake topical peer reviews (TPR) every 6 years with the first starting in 2017. For the first TPR, ageing management (AM) was chosen as the topic. In addition to EU members, Switzerland also committed to contribute National Assessment Reports (NARs) [1]. For more information see the final WENRA NAR Technical Specification from December 2016 [2].

The first stage of the TPR is to generate the NARs until end of 2017, which will be published in 2018. For LWRs, the following four systems, structures and components (SSC) will be covered as examples for ageing management:

- Electrical cables
- Concealed pipework
- Reactor pressure vessel
- Concrete containment structures.

With these four SSCs selected is to provide examples of how implementation of the overall ageing management program performs in practice.

The present paper gives an overview of the status of the ageing management of concealed steel pipework in S/KWU LWRs. It uses information coming from the VGB report (VGB PowerTech e.V., www.vgb.org) produced as basic input to the German NAR as well as recent VGB work concerning definition of proper NDT measures concerning ageing management of concealed safety relevant cooling lines for European S/KWU LWRs, based on good operational experience. The present paper will cover operating S/KWU LWRs in Germany and Switzerland as well as operating experience for such LWRs which are not in operation anymore. The main results are also transferable to the operating S/KWU PWR in the Netherlands. This results in coverage of 8 operating PWRs and 2 operating BWRs, all participating in the EU TPR.

AM in German NPPs

This section describes ageing management as being performed in Germany according to German Nuclear Safety Standards Commission code KTA 1403 [3]. Ageing management in Switzerland is based on Swiss Guideline ENSI B-01 [4], in the Netherlands based on Dutch Guideline NVR.NS-G-2.12 [5], which is derived from IAEA Safety Guide NS-G-2.12 (2009) [6]. The methodologies of ageing management described in those three papers are not identical, but lead to comparable results. In the following, the German approach in [3] is described.

In Germany, AM in NPPs became a topic of debate in the late 1990s. Reason for this debate was the introduction of regulations of the USNRC concerning AM used as a basis for life time extension of NPPs in the USA, see also [7].

Although AM was comprehensively practiced on a high level in German NPPs from their start of operation in form of operational surveillance, staggered and non-destructive testing, and preventive maintenance programs, the nuclear code KTA 1403 "Ageing Management in Nuclear Power Plants" was finalized in 2010, when lifetime extension was still a topic for German plants. This lead to a formal management process which united the existing and approved activities in order to cope with relevant ageing mechanisms [7].

Scope of Ageing Management for Concealed Pipework

Concealed piping in S/KWU LWRs can be divided into two classes based on their installation:

- buried piping
- piping in accessible and non-accessible covered channels, mostly made from concrete.

According to KTA 1403 [3], all mechanical systems and components shall be assigned to either one of the three AM classes, M1 to M3:

- M1 are mechanical systems and components of the pressure containing boundary and of outer systems, whose failure is not covered by plant design. The best example is the reactor pressure vessel.
- M2 are safety relevant mechanical systems and components. Those are mainly systems responsible for mastering of accidents, e.g. emergency coolant lines. Due to redundant design, a single failure of one system would not be critical. Other systems containing radioactivity are also assigned to M2, e.g. disposal lines.
- M3 are all other mechanical systems and components. They are not part of AM according to KTA 1403.

Main results of applying this AM classification to concealed piping of S/KWU LWRs today in operation are:

There are no concealed M1 systems/components. M2 systems in covered channels like steam generator emergency feed water lines are in general accessible from the outside. Buried M2 systems needed for managing design basis accidents are the safety relevant cooling water lines, which are needed to remove decay heat after a design base accident. They are often not accessible from the outside. Most of them are made of steel, although in limited cases pre-stressed concrete piping was used. Other buried M2 systems, such as disposal lines, are not needed for accident scenarios.

Therefore, the safety relevant cooling water lines are in terms of safety relevance and service/NDT accessibility the leading covered systems in AM. Those lines made from steel are used as NAR example.

The safety relevant cooling water system of S/KWU LWRs consists of several redundant lines. Its duty is to remove, under all operational and emergency conditions, excess heat originated from the fuel in the reactor core and the fuel pool, and transmit the excess heat, via intermediate cooling systems, to the heat sink. The heat sink, which is site dependent, is typically a river or a set of air cooled cell coolers. This is done using either conditioned river water or raw water, see also [8].

Target of the AM is to prevent a large break of such a safety relevant cooling line due to ageing. This is done despite the fact, that a single failure would not compromise the ability to manage a design basis accident. Anyway, any local (water) leakages of these lines neither compromise their functionality nor the fulfillment of their protection targets.

AM Approach for Safety Relevant Cooling Water Lines

The knowledge basis for finding appropriate AM measures is the systematical analysis and evaluation of the effective damage mechanisms of the specific systems, based on their condition. This includes according to KTA 1403:

- the knowledge about the requirements and specifications (design, materials, manufacturing)
- the knowledge about the operational conditions since (including) commissioning
- the knowledge about relevant damage mechanisms and how to avoid them
- the design concerning damage mechanisms
- the current state of knowledge about the damage mechanisms.

With this knowledge base, the applied approach for fulfilling the AM target defined at the end of Chap. 3 includes:

- representative surveillance of consequences of damage mechanisms, by e.g. operational monitoring, NDT and laboratory examination
- observance of findings from operation of other NPPs,
- tracking the knowledge of potential damage mechanisms

Chapter 5 gives information about necessary and available quality. In Chap. 6, the potential and effective damage mechanisms are described. Chapter 7 shows operational experience concerning these damage mechanisms, derived especially from elder S/KWU plants now out of service. In Chap. 8, the chosen monitoring and NDT measures will be explained.

Requirements and Specifications of Safety Relevant Cooling Water Lines

The design of safety relevant cooling water lines is based on decades of good operational experience with cooling water lines in fossil power plants, other industrial plants such as in the chemical industry and also in the public water supply.

Safety relevant cooling water lines of German S/KWU NPPs have nominal diameters up to 1200 mm. The nominal operational conditions are pressure up to 6 bar and temperatures up to around 30 °C, design values are normally 10 bar and 50–80 °C. Due to these low operational parameters, these systems are low energy systems, according to German nuclear code, see e.g. [9]. This means that there is no mechanical loading which could cause a catastrophic failure of the system by itself.

These systems are made of usual industry grade carbon steels. Depending on specific site, different coating systems are applied from outside and from inside, examples are:

- Inside coatings: (no coating), zinc coating, rubber coating, epoxy based coatings, polyethylene in-liners, cement mortar coating
- Outside coatings: bitumen based coatings, tar-epoxy based coatings

Carbon steel piping with no inner coating has been applied for higher diameter piping only in elder S/KWU plants today out of service. Their operational experience serves as lower bound for piping with inner coatings. Preferred solution for higher diameter piping in later S/KWU LWRs today in operation in Germany is welded carbon steel piping with inner cement mortar coating.

Such carbon steel piping with inner cement mortar coating has been produced and used in Germany with good success for more than 100 years, with enhanced application since the mid 1960s. Thus for S/KWU LWRs, the piping specification was based on well proven German industrial standards (DIN).

Outer coatings (bitumen/tar-epoxy) have been always used for these systems. In addition, in some S/KWU LWRs cathodic protection systems are in use for the buried sections of the safety relevant cooling water system. The long and very good operational experience with such systems started in Germany 1906 in service water supply.

Installation of the buried system parts was also designed and performed according to well proven DIN standards. Preparation of the piping beds including use of geotextile base mats and repeated compaction of the sand bed to prevent local settling and use of stone free sands and stone free coverage soil to prevent mechanical damage to the outer coating of the pipes.

The design specification for each individual plant based on this set of DIN standards was prepared and approved by the inspection authority. The appropriate implementation of the specification during manufacture, installation of the piping was supervised by authorized experts working for the inspection authority.

Thus the available quality of the buried safety relevant cooling systems of German S/KWU LWRs is based on decades of German industrial experience and according to well established and approved DIN standards. Also according to today's state of knowledge, they possess the necessary quality to further withstand the damage mechanisms (see Chap. 6) for at least the remaining operating time of Germany's LWRs (end of 2022), originally designed for 40 years. At the moment, an end of life of the piping is not predictable. This is also confirmed by operational experience from older S/KWU LWRs, see Chap. 7.

Safety Relevant Cooling Water Lines: Damage Mechanisms

As mentioned before, the damage mechanisms for cooling water lines made from usual carbon steels and with different coating systems are well known for decades not only from NPPs worldwide, but also from fossil power plants, the chemical industry and also from water supply.

Designed as low energy system with a low operating temperature around 30 °C, typical temperature dependent damage mechanisms like (thermal) fatigue, creep or thermal ageing cannot occur. Radiation induced mechanisms are not possible. By design limitation of the flow velocity, all wear related mechanisms such as erosion or erosion corrosion cannot occur. By materials choice, low operating temperature, and cooling water chemistry control, stress corrosion cracking mechanisms cannot occur either.

Thus, only corrosive damage mechanisms without mechanical loading remain possible. Design uses well proven increases in wall thickness to account for wall thickness loss due to uniform surface corrosion.

So, two well-known effective corrosion mechanisms in carbon steel water piping remain possible and can occur:

- shallow pit corrosion from inside, and
- microbiological induced corrosion (MIC) from inside

For carbon steel piping, MIC is not a solitary mechanism, but it always works in conjunction with shallow pit corrosion, enhancing the damage progress. This works by forming localized bio films and subsequently by acidic excretions of the microorganisms enhancing the corrosion process under the film.

Shallow pit corrosion can lead to localized leaks. Such localized leaks do not compromise the load bearing ability of the piping nor the functionality.

Damage mechanisms concerning the coatings are:

- mechanical damage from the outside or inside (this is not classified as ageing)
- ageing of polymer based inside coatings, leading to e.g. adhesion loss, bubble formation, local open surfaces
- cracking and disruption of cement mortar on the inside

Possible consequence of damage to coatings is the onset of shallow pit corrosion in the localized exposed areas of the carbon steel pipe.

Operational Experience

So far, the operational experience of safety relevant cooling systems in German S/KWU LWRs is good, especially concerning the younger NPPs which are currently still in operation.

The operational experience from older S/KWU covers the still operating units. In several of the older LWRs, operational monitoring repeatedly found some localized piping damage in the form of small leaks or even droplet leaks, all starting from inside. Such damage was found in piping without inner coating or with inner coatings based on tar-epoxy, rubber, or zinc. Starting with a notification letter of German Federal Ministry's Expert organization GRS in 2007, the German NPP operators started a comprehensive assessment program of those systems. This included representative NDT with video camera crawlers from inside and in a few cases also by local excavations from outside.

Limited leaks in buried piping (nominal diameter ND $\geq$ 400 mm) have been observed only in older plants, which are no longer operating. So far, no leaks have been found in buried higher diameter piping (ND $\geq$ 400 mm) with cement mortar coating.

In an older German S/KWU PWR, which is not in operation today, a retrofit of the buried safety relevant cooling water lines was started in 2008 after more than 30 years of operation as an optimization measure for a possible extended plant operation. As part of the program, systematic examinations have been conducted on the excavated sections.

Figures 1 to 4 show some typical results of the post service examinations, performed by AREVA Germany.

Fig. 1 Specimen cutting of an ND 500 × 6.3 mm elbow for post service examination, after excavation and partial dismantling of the outside coating (left), and inner surface after cutting and before sand blasting (right)

As Fig. 1 implies, the excavated old pipe was designed without an inner coating. In addition, this old line did not use an active cathodic system for protection of the outer surface, but only an outside coating. In this case, a ND 500 mm elbow with a nominal wall thickness of 6.3 mm was examined.

After sand blasting the surfaces, systematic wall thickness measurement was performed, Fig. 2. Average wall thickness of 5.7 mm and a minimum wall thickness of 4.3 mm were measured. The cross section in this area shows that on the inner surface, the deepest attack are grooves formed into the weld metal, Figs. 3 and 4 (left). This is a form of shallow pit corrosion attack which is repeatedly seen in non-coated piping. The location with the deepest attack found in the elbow was in the groove area, with a remaining wall thickness of 2.3 mm, which is sufficient to not cause a leak. On the inner surface the attack is quite smooth but visible compared to the weld, Figs. 3 and 4 (middle). On the outer surface of that elbow, a slight shallow pit corrosion was found, leading to a minimum wall thickness of 5.1 mm, Figs. 3 and 4 (right).

In total, the quality of this specific elbow after more than 30 years of service is—despite the facts that it was designed without an inner coating and operated without active cathodic protection—still in quite good condition and would fulfill the requirements for continued operation. Explanation for this is the known behavior of uncoated cooling water piping in which a protective oxide layer forms on the corrosion spots which, while looking aesthetically unpleasing, see also Fig. 1, becomes an effective barrier slowing down oxygen diffusion to the metal surface and thus minimizing the localized shallow pit corrosion rate, as long it is not mechanically removed.

Based on the results of these examinations it became obvious that the actual quality of the buried piping was better than expected from inside camera inspections.

To confirm these positive results, an additional representative NDT program was conducted on the remaining lines. At several localized excavations UT wall thickness measurements were performed from the outer side of the piping. The results confirmed the positive laboratory findings. So it had become clear that even after more than 30 years of service of this system made of carbon steel pipes

Fig. 2 Strip from elbow ND 500 × 6.3 mm, inner surface after sand blasting and wall thickness measurement, markings show measured minimum wall thickness values

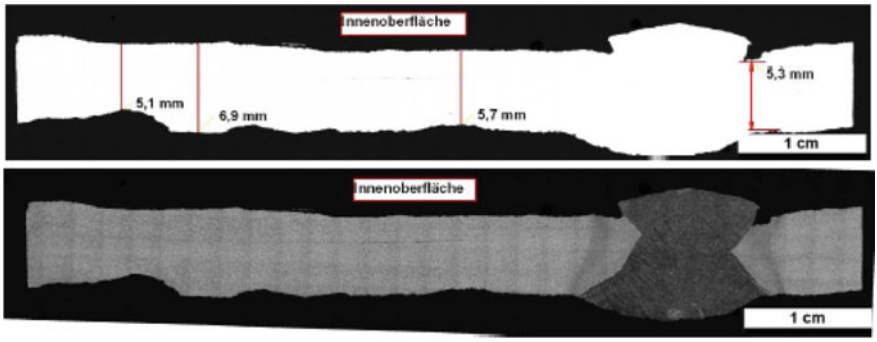

Fig. 3 Cross section thru strip in Fig. 2 in the region of lowest measured wall thickness, before and after etch, with optically measured wall thickness values

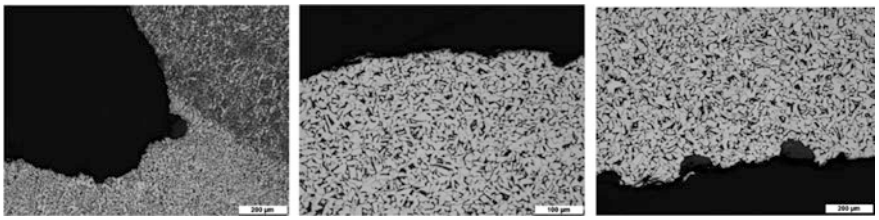

Fig. 4 Details from cross section Fig. 3, inner surface weld area (left), and base metal (middle), outer surface (right)

without inner coating the actual condition was much better than predicted from inside camera inspections and was adequate for further service. Therefore the retrofit was stopped in confirmation by the inspection authority.

Monitoring and NDT

Monitoring and NDT are used either to minimize or to detect damage caused by various degradation mechanisms.

Operational surveillance of the safety relevant cooling water system includes

- monitoring operational parameters as pressure, temperatures and mass flows
- monitoring of the cooling water chemistry (e.g. pH and Chloride content) using laboratory analysis.

Possible consequences of damage mechanisms are monitored by

- survey walk-downs along representative system parts in buildings
- NDT (see below), and periodic functional tests and leak tests.

Additional measures are possible by

- integral leak detection via differential pressure measurement
- survey walk-downs along buried lines looking for signs of big leaks.

The challenge of performing NDT on buried piping is that they are not accessible from outside and access from the inside is limited to the first few meters which can be reached by endoscope or video-scope.

For finding suitable NDT techniques, VGB work panel on component integrity and his NDT work group made in 2015 an evaluation including results of a 2012 GRS evaluation [10]. The choice of NDT techniques was done according to KTA 3211.4 [11].

Beside the lack of accessibility from outside, it is also important neither to damage the inside coating while using crawler systems including any cleaning steps, nor to damage protective oxide layers, see Sect. 7. Other NDE e.g. radiographic testing (RT) in buried sections is not feasible. Eddy current testing (ET) of ferritic piping would need a crawler driven heavy equipment for magnetic saturation, thus imposing substantial damage risk to the coating and protective oxide layers.

As final result of the VGB evaluation, two NDT techniques for two different cases have been recommended for practical AM use, in order to exclude a large-scale failure of the piping:

Case 1: Piping or pipe sections without inner coating:

Ultrasonic wall thickness testing from the outside in system parts in buildings can be used as representative NDT for buried parts. In addition, these results are bounding in the case of a cathodic protection system in use in the buried sections. This method is especially well suited for uncoated weld areas of cement mortar coated pipes (according to DIN) and recommended as an alternative to visual testing from the inside, see case 2.

Case 2: Piping with inner coating:

Visual testing (VT) from inside is well suitable to get a direct view on the piping or on the coating. Different techniques are usable including limited direct access. For deeper insight, the use of borescope or video-scope VT systems is necessary, and video-scope equipped pig systems are needed to enter buried sections. The applied VT techniques and systems have to be selected both plant specific and diameter dependent. Any form of mechanical cleaning, including water jet cleaning, is not recommended in order neither to damage coatings or protective oxide layers nor to plug heat exchangers by the generated deposits.

In all operating German LWRs, additional periodic NDT measures according to these 2015 recommendations have been already introduced.

These AM NDT measures together with the operational surveillance and the periodic functional test and leak tests assure the detection of damage before any gross failure can occur.

Discussion and Summary

The ageing management of concealed safety relevant cooling water steel piping in S/KWU LWRs already started with proper design, choice of materials and coatings, production and installation. The whole design was based on decades of good industrial experience with cooling water lines, with know-how summarized in industrial codes. By using this know-how, appropriate provision was granted to withstand the well-known ageing mechanisms of such piping.

Since the start of operation, there has been regular, periodic monitoring and evaluation of these damage mechanisms by operational surveillance and NDT. Thus any degradation relevant for integrity behavior can be detected early enough in order to avoid a large break of such a line.

Information coming from the fleet, especially evaluations from operational behavior in 2007, was used to re-evaluate the condition of the systems. This included NDT examinations and also post service examinations of pipe sections during retrofit measures. Such examinations presented in this paper from an older, now out of service plant, show that even for buried piping without an inner coating and operated without active cathodic protection, would after more than 30 years still serve the requirements for continued service.

In total, the AM of the buried carbon steel based safety relevant cooling water lines of the S/KWU fleet showed that after more than 30 years of operation that the damage mechanisms had been sufficiently managed. Only limited local leaks occurred. There is no area-wide damage, which could cause a break of such a line. Moreover, the limited leaks did not have negative influence on system functionality or accident management. This was also confirmed by German Federal Ministry's Expert organization GRS in [10].

In addition, in all operating German LWRs, additional periodic NDT measures according to the 2015 recommendations have been introduced. This adds another safety margin to the AM measures concerning detection of damage mechanisms before any gross failure can occur.

Acknowledgements Special thanks of the authors are going both to AREVA Germany Materials Laboratory and to the ordering German NPP for giving permission to use their photographs.

References

1. www.ensi.ch
2. Topical Peer Review 2017, Ageing Management, Technical Specification for the National Assessment Reports, RHWG Report to WENRA, 21. December 2016. www.wenra.org, www.ensreg.eu
3. KTA 1403 (2010–11), Alterungsmanagement von Kernkraftwerken (Ageing Management in Nuclear Power Plants), www.kta-gs.de
4. Alterungsüberwachung, Richtlinie für die schweizerischen Kernanlagen, ENSI-B01/d, Ausgabe August 2011, www.ensi.ch

5. Verouderingsbeheer voor kernenergiecentrales, Veiligheidsrichtlijn NVR.NS-G-2.12, Jan 2011, Ministerie van Economische Zaken, Landbouw en Innovatie, Den Haag, (2011)
6. IAEA Safety Standards, Ageing Management for Nuclear Power Plants, Safety Guide No. NS-G-2.12, Wien, (2009). www.iaea.org
7. P. Barreiro et al., Nutzen des Alterungsmanagements in deutschen Kernkraftwerken. VGB PowerTech **5**, 26–32 (2013)
8. VGB Kühlwasserrichtlinie – Wasserbehandlung und Werkstoffeinsatz in Kühlwassersystemen (VGB-R 455 P), Zweite überarbeitete Ausgabe 05/2000, VGB PowerTech Service GmbH, Essen
9. Rahmenspezifikation Basissicherheit, 24.05.1979, 2nd Appendix in: RSK-Leitlinien für DWR, 09/79, In: RSK-Leitlinien für Druckwasserreaktoren, 11/96, www.rskonline.de
10. GRS-Bericht A-3634, Betriebserfahrungen mit Komponenten der sicherheitstechnisch wichtigen Nebenkühlwassersysteme in deutschen Anlagen mit DWR und SWR, Gesellschaft für Anlagen- und Reaktorsicherheit GmbH, Köln, Februar 2012. www.grs.de
11. KTA 3211.4 (2013–11), Druck- und aktivitätsführende Komponenten von Systemen außerhalb des Primärkreises, Teil 4: Wiederkehrende Prüfungen und Betriebsüberwachung, (Pressure and Activity Retaining Components of Systems Outside the Primary Circuit—Part 4: Inservice Inspections and Operational Monitoring), www.kta-gs.de

Identification of PWR Stainless Steel Piping Safety Significant Locations Susceptible to Stress Corrosion Cracking

R. Hosler, A. Kulp, P. Stevenson and S. Petro

Abstract Stress corrosion cracking (SCC) of stainless steel was originally considered only an issue with boiling water reactors (BWRs), but operating experience has shown that this phenomenon also occurs in pressurized water reactors (PWRs), such as in off-chemistry locations of stagnant branch connection piping. In this paper, the safety significant stainless steel piping locations susceptible to SCC are identified for three representative PWR plants (Plant A [Babcock and Wilcox-designed], Plant B [Westinghouse-designed], and Plant C [Combustion Engineering-designed]). For the purpose of this paper, "safety significant" is defined as having a high consequence of failure as determined by the plant's risk-informed in-service inspection (RI-ISI) program. Weld locations are considered susceptible to SCC when the water is stagnant and ≥ 200 °F during steady-state reactor operation. The results of this work will be used to develop guidance for selection of welds to inspect when addressing currently existing inspection requirements.

Keywords SCC susceptibility · Stainless steel · Primary piping

Purpose

The purpose of this paper is to identify the weld locations of stainless steel piping at Plant A, Plant B, and Plant C that meet all three of the following criteria (1) high consequence of failure as determined by the RI-ISI process, (2) temperature ≥ 200 °F during steady-state reactor operation, and (3) typically stagnant during steady-state

R. Hosler (✉) · A. Kulp
AREVA, Paris, France
e-mail: ryan.hosler@areva.com

P. Stevenson
Westinghouse, Monroeville, US

S. Petro
AEP, Columbus, US

J.H. Jackson et al. (eds.), *Proceedings of the 18th International Conference on Environmental Degradation of Materials in Nuclear Power Systems – Water Reactors*, The Minerals, Metals & Materials Series, https://doi.org/10.1007/978-3-319-68454-3_64

reactor operation. The resultant list of stainless steel weld locations will be considered susceptible to ID-initiated stress corrosion cracking (SCC) and to have a high consequence of failure.

The results of this work can be used as guidance for selection of welds to inspect when addressing currently existing inspection requirements.

Background

Following the occurrence of several reports in the United States (U.S.) PWR fleet of SCC of pressure boundary stainless steel piping, the Nuclear Regulatory Committee (NRC) requested that the industry consider the issue [1]. While the NRC information notice did not require any response, the industry decided to proactively address the issue via the PWROG Materials Committee.

Outside-diameter (OD) initiated SCC was addressed (at least temporarily) by the OD-initiated SCC Interim Strategy, which was issued as an NEI 03-08 Good Practice Recommendation [2]. The Interim Strategy ensures a consistent minimum level of awareness is communicated to appropriate site organizations regarding OD-initiated SCC operating experience and provides a consistent and minimum set of attributes for identifying OD-initiated SCC for consideration by the plants.

Inside-diameter (ID) initiated SCC is being addressed by the PWROG Materials Committee and this paper summarizes the current state of that process.

Note that the ID-initiated SCC susceptibility screening criteria used in this document (i.e., stainless steel, ≥ 200 °F, and stagnant) is a simplified version of the criteria developed previously [3]. These simplified criteria were developed because it is not practical to obtain the detailed inputs required to implement the original screening criteria, such as the exact material properties, environmental conditions, and stress levels at all stainless steel piping locations. The following assumptions were made to develop the simplified criteria:

1. Austenitic stainless steel (regardless of the presence of sensitization) is susceptible to SCC (in conjuncture with an aggressive environment and a sustained tensile stress). Note that, while sensitization can increase susceptibility to SCC, it is not required, which is supported by an operating experience review of SCC in stagnant PWR piping that found sensitization was a contributing factor in 12 of 47 events (with an additional 55 events marked as "unknown") [4].
2. The water chemistry (i.e., dissolved oxygen and chloride concentrations) in high temperature (≥ 200 °F) stagnant locations is assumed to be sufficiently aggressive to drive SCC (in conjunction with a susceptible material and a sustained tensile stress). This assumption is reasonable since operating experience indicates SCC does occur in stagnant locations [4].
3. Weld residual stress in the heat-affected zone results in a sufficiently high sustained tensile stress to drive SCC (in conjunction with a susceptible material and an aggressive environment). This assumption is reasonable since laboratory

studies and operating experience indicate that weld residual stress is sufficient to drive SCC in stainless steel when the environment is sufficiently aggressive [3].

Since (based on the assumptions above) all three required components of SCC (i.e., susceptible material, aggressive environment, and sustained tensile stress) are only present at the weld locations (including the adjacent base metal), consideration of the RI-ISI process (which focuses on weld locations) is appropriate.

Methodology

Three representative plants were selected (one from each design: B&W, Westinghouse, and CE) that have RI-ISI programs that have scope that include at least ASME Class 1 and Class 2 piping.

The following methodology was followed for each selected plant:

1. Obtain the list of all weld locations within the scope of the plant-specific RI-ISI program and the corresponding plant-specific RI-ISI drawings
2. Filter the list so that only weld locations remain that meet the following criteria:
    a. Stainless steel (Per the plant-specific RI-ISI documentation)
    b. High consequence of failure (Per the plant-specific RI-ISI documentation)
    c. Temperature ≥ 200 °F during normal reactor operation
        i. This temperature was selected based on original screening criteria [3]
        ii. Typical temperatures are to be obtained from plant-specific RI-ISI documentation; if temperature is not reported in the RI-ISI documentation, then the typical temperature was estimated based on System Engineer knowledge of system operations; in some cases, assumptions are made to estimate the likely temperature (see Section "Justified Assumptions")
    d. Typically stagnant during normal reactor operation (per System Engineer judgment)
        i. Per system engineer judgment, stagnant locations were put in three categories:
            1. Category 1: typically flushed/drained/operated more than once per fuel cycle
            2. Category 2: typically flushed/drained/operated once per fuel cycle
            3. Category 3: typically flushed/drained/operated less than once per fuel cycle

3. The following "stagnant" locations were screened out and, thus, not included in the final list:
   a. Category 1 locations (See Section "Justified Assumptions", Assumption 2)
   b. Stagnant locations in pressurizer steam space (See Section "Justified Assumptions", Assumption 3)
   c. Select welds near the branch connection (See Section "Justified Assumptions", Assumption 4)
4. The resultant list represents weld locations that have a high consequence of failure (i.e., rupture) and are susceptible to SCC. These weld locations were then highlighted in the figures of the piping.

Justified Assumptions

1. When two adjacent valves represent the pressure boundary, the welds between the valves are considered to be <200 °F (with the exception of the isolation valve to pipe weld opposite the branch connection).

This assumption is justified since both valves are typically closed during steady state plant operation and, thus, the water in the piping between the two valves will attempt to equilibrate with the building temperature, typically ~ 120 °F, which is well below 200 °F. While these welds may spend some limited time above 200 °F, the impact on SCC susceptibility will be negligible since SCC is a thermally activated, time dependent phenomenon (typically taking several years at elevated temperature, and requiring increasing time with decreasing temperature) [4]. Note that, while valve leakage may allow some high temperature coolant to enter the piping between the valves, this potential introduction is not expected to increase the temperature sufficiently to have a significant impact on SCC susceptibility.

The temperature at the valve to pipe weld at the first isolation valve (opposite the branch connection) can be greater than 200 °F due to conduction of heat through the valve from the coolant in contact with the primary loop on the other side of the valve. This is supported by several cases of SCC in this type of weld and temperature measurements ranging from 248 °F to 347 °F [4].

2. Weld locations typically flushed/drained/operated more than once per fuel cycle (stagnant Category (1) likely have adequate water chemistry control to mitigate the risk of SCC. Note that this is only true when the source of introduced coolant is deoxygenated. For example, this assumption is not applicable in the case of the coolant source being the makeup tank, which is commonly oxygenated.

The only piping screened as Category 1 was the portion of the pressurizer spray line that is bypassed when pressurizer spray is not actuated. It was appropriate to screen this piping as not susceptible to SCC because the source of introduced coolant (i.e., pressurizer spray line) is deoxygenated. Furthermore, this segment of

piping has no reported SCC per operating experience [4]. Therefore, the focus of this work will be on the more susceptible locations (i.e., Category 2 and 3), which can act as a leading indicator for Category 1 locations.

3. Stagnant locations in the pressurizer steam space likely have adequate water chemistry control to mitigate the risk of SCC.

The concern with stagnant locations is that contaminants (such as chlorides) can concentrate over time. However, the pressurizer water chemistry is controlled and, thus, the chemistry in the steam space (which is a function of water chemistry in the pressurizer) should also have minimal contaminants. While it may be possible for contaminants in the steam space to concentrate over time, this is not expected to be a concern since a review of 137 SCC events found that none occurred in pressurizer steam space [4].

4. Branch piping welds from the connected flowing line up to and including the welds on both ends of the first elbow likely have adequate water chemistry control to mitigate the risk of SCC.

Given the close proximity to the flowing line and the phenomenon of swirl penetration [5], sufficient mixing with the bulk coolant is anticipated to avoid the concentration of contaminants up to and including the welds of the first elbow of the branch line. Note that the determination of the depth of swirl penetration is complex and is dependent on many factors that are specific to a given branch line. The selection of the first elbow is considered a reasonable approximation for the depth of swirl penetration for the purposes of this document (i.e., screening for stagnation and, thus, SCC susceptibility).

Note that this assumption is not applicable to branch lines connected to a low flow line (e.g., auxiliary spray line branching off the pressurizer spray line) because the swirl penetration depth in this case is expected to be minimal and to only extend to the first branch weld.

Beyond the depth of swirl penetration, stagnant coolant in branch piping will have some mixing due to convection. The change in temperature from the hot water at the swirl penetration to the cooler water at the isolation valve will result in some flow, which could potentially reduce the concentration of aggressive species in the coolant screened as stagnant. However, this change in temperature (and resultant flow) is expected to be very small since the lines of interest are relatively short and likely insulated. Therefore, while such mixing is possible, there is not sufficient information to use convection to screen out these welds at this time.

5. All screened-in locations (i.e., welds susceptible to SCC with a high consequence of failure) are assumed to be in insulated piping. Screened-in weld locations are not applicable at units where those weld locations are not insulated. This is because the temperature in un-insulated lines will be below 200 °F in all locations that are truly stagnant (i.e., not impacted by swirl penetration).
6. All stagnant branch piping is assumed to be ≥ 200 °F up to the first isolation valve (with the exception of some welds near the end of particularly long branch lines). “Long” branch lines will be defined in Section “Results”.

For the purpose of this report, it is conservative to assume that all welds in a stagnant branch line connected to flowing primary water are above 200 °F (i.e., in the temperature range for SCC susceptibility).

However, some welds on long branch lines are known to be below 200 °F (e.g., auxiliary spray line) as evidenced by SCC initiating on the outer surface, which can only occur at temperatures where deliquescence can occur (i.e., below 200 °F) [3]. As discussed in Section "Results", select welds are screened out because the temperature is likely below 200 °F.

Results

Plant-specific RI-ISI documentation was used to filter out all weld locations that do not have a high consequence of failure. The material (i.e., stainless steel or not stainless steel) and the typical steady state temperature of each weld location were determined using plant-specific RI-ISI documentation and the associated plant-specific RI-ISI drawings. In cases where the plant-specific RI-ISI documentation did not clearly identify the typical steady state temperature for select stainless steel weld locations, the value was estimated based on the expertise of Systems Engineers who used their knowledge of plant systems operation and plant-specific RI-ISI drawings. The determination of the typical flow conditions (i.e., flowing or stagnant) and, as appropriate, the degree of stagnation (i.e., Category 1, 2, or 3, as discussed in Section "Methodology") for high temperature (i.e., typically $\geq$ 200 °F during steady state conditions) stainless steel weld locations, was made based on the expertise of Systems Engineers who used their knowledge of plant systems operation and plant-specific RI-ISI drawings. The assumptions in Section "Justified Assumptions" were also used in the determination of the typical temperature and presence of stagnation.

Several tables were created that list the stainless steel weld locations for Plant A (Section "Plant A (B&W Unit) Results"), Plant B (Section "Plant B (Westinghouse Unit) Results"), and Plant C (Section "Plant C (CE Unit) Results") that meet all of the following criteria: 1) high consequence of failure, (2) typical temperature is 200 °F during steady state reactor conditions, and (3) stagnant. The tables also report the weld locations that were inspected to meet the requirements of ASME Section XI and the weld locations that are now inspected to comply with the plant-specific RI-ISI program. Following each table, there are one or more figures that illustrate the results of the preceding table (weld locations of interest are highlighted in the figures).

Plant A (B&W Unit) Results

The Core Flood System and Reactor Coolant System included weld locations that screened in as being both susceptible to ID-initiated SCC and having a high

consequence of failure. The remaining plant systems with ASME Class 1 and/or Class 2 piping did not include any weld locations that screened in.

Table 1 lists the weld locations screened in for the Core Flood System, which are shown in Fig. 1 (1D-ISI-CF-001) and Fig. 2 (1D-ISI-CF-002). Note that weld CF-096 (which was part of a recent modification at Plant A) meets all the criteria for SCC susceptibility, but this weld was not included in the Plant A RI-ISI Program documentation supplied for this report. For completeness, weld CF-096 is included herein.

Table 2 lists the weld locations screened in for the Reactor Coolant System drain lines, which are shown in Fig. 3 (1D-ISI-RC-002) and Fig. 4 (1D-ISI-RC-004).

Table 3 lists the weld locations screened in for the Reactor Coolant System pressurizer auxiliary spray line, which is shown in Fig. 5 (1D-ISI-RC-005). Note that the welds in this line are assumed to be below 200 °F beyond the secondary shield wall, which is a reasonable delineation in that the welds that are screened in are a leading indicator of SCC given their higher temperature.

Table 4 lists the weld locations screened in for the Reactor Coolant System pressurizer drain line, which is shown in Fig. 6 (1D-ISI-RC-005). Note that the welds in this line are assumed to be below 200 °F beyond the elbow of the second drop in elevation, which is a reasonable delineation in that the welds that are screened in are a leading indicator of SCC given their higher temperature.

Table 1 Core flood system screened-in weld locations

Weld location	Drawing	Pipe size (in.)	Material	Steady state temp (°F)	Stagnant category 2—drained/flushed once per fuel cycle, category 3—drained/flushed less than once per fuel cycle
CF0096WELD	1D-ISI-CF-001	14	SS	≥ 200	2 (used when DHR initiated during cooldown)
CF0004WELD	1D-ISI-CF-001	14	SS	≥ 200	2 (used when DHR initiated during cooldown)
CF0005WELD	1D-ISI-CF-001	14	SS	≥ 200	2 (used when DHR initiated during cooldown)
CF0006WELD	1D-ISI-CF-001	14	SS	≥ 200	2 (used when DHR initiated during cooldown)
CF0007WELD	1D-ISI-CF-001	14	SS	≥ 200	2 (used when DHR initiated during cooldown)
CF0008WELD	1D-ISI-CF-001	14	SS	≥ 200	2 (used when DHR initiated during cooldown)
CF0023WELD	1D-ISI-CF-002	14	SS	≥ 200	2 (used when DHR initiated during cooldown)

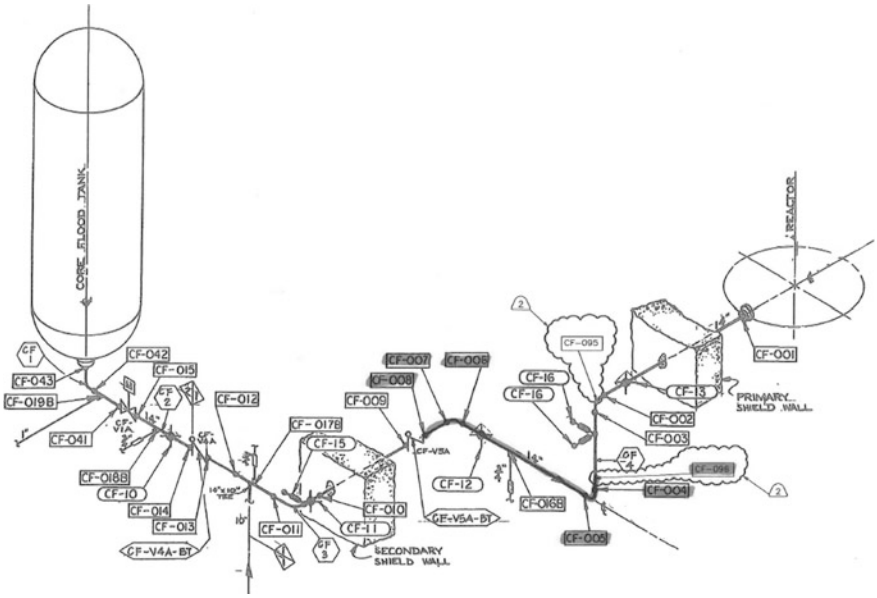

Fig. 1 Schematic of 1D-ISI-CF-001

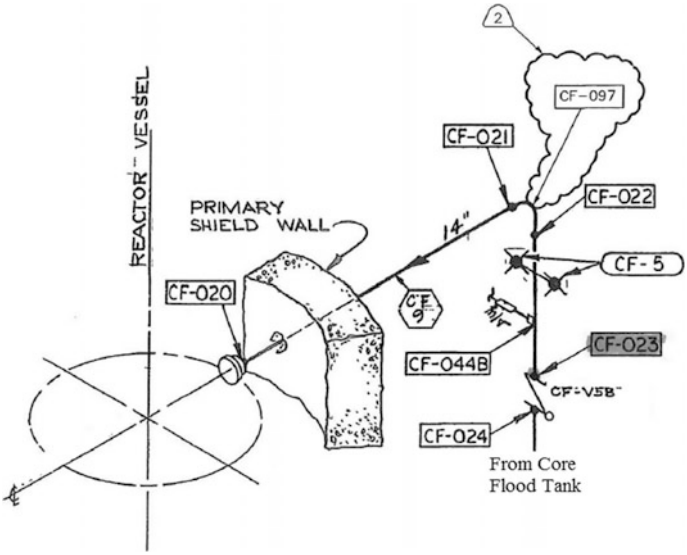

Fig. 2 Schematic of 1D-ISI-CF-002

Table 2 Reactor coolant system drain lines screened-in weld locations

Weld Location	Drawing	Pipe size (in.)	Material	Steady state temp (°F)	Stagnant category 2—drained/flushed once per fuel cycle, category 3—drained/flushed less than once per fuel cycle
RC0175WELD	1D-ISI-RC-002	2	SS	≥ 200	3 (used to drain RCS loops for maintenance)
RC0176WELD	1D-ISI-RC-002	2	SS	≥ 200	3 (used to drain RCS loops for maintenance)
RC0177WELD	1D-ISI-RC-002	2	SS	≥ 200	3 (used to drain RCS loops for maintenance)
RC0178WELD	1D-ISI-RC-002	2	SS	≥ 200	3 (used to drain RCS loops for maintenance)
RC0179WELD	1D-ISI-RC-002	2	SS	≥ 200	3 (used to drain RCS loops for maintenance)
RC0180WELD	1D-ISI-RC-002	2	SS	≥ 200	3 (used to drain RCS loops for maintenance)
RC0188WELD	1D-ISI-RC-002	2	SS	≥ 200	3 (used to drain RCS loops for maintenance)
RC0189WELD	1D-ISI-RC-002	2	SS	≥ 200	3 (used to drain RCS loops for maintenance)
RC0190WELD	1D-ISI-RC-002	2	SS	≥ 200	3 (used to drain RCS loops for maintenance)
RC0191WELD	1D-ISI-RC-002	2	SS	≥ 200	3 (used to drain RCS loops for maintenance)
RC0290WELD	1D-ISI-RC-002	2	SS	≥ 200	3 (used to drain RCS loops for maintenance)
RC0199WELD	1D-ISI-RC-004	2	SS	≥ 200	3 (used to drain RCS loops for maintenance)
RC0207WELD	1D-ISI-RC-004	2	SS	≥ 200	3 (used to drain RCS loops for maintenance)
RC0208WELD	1D-ISI-RC-004	2	SS	≥ 200	3 (used to drain RCS loops for maintenance)
RC0209WELD	1D-ISI-RC-004	2	SS	≥ 200	3 (used to drain RCS loops for maintenance)
RC0210WELD	1D-ISI-RC-004	2	SS	≥ 200	3 (used to drain RCS loops for maintenance)
RC0211WELD	1D-ISI-RC-004	2	SS	≥ 200	3 (used to drain RCS loops for maintenance)
RC0212WELD	1D-ISI-RC-004	2	SS	≥ 200	3 (used to drain RCS loops for maintenance)

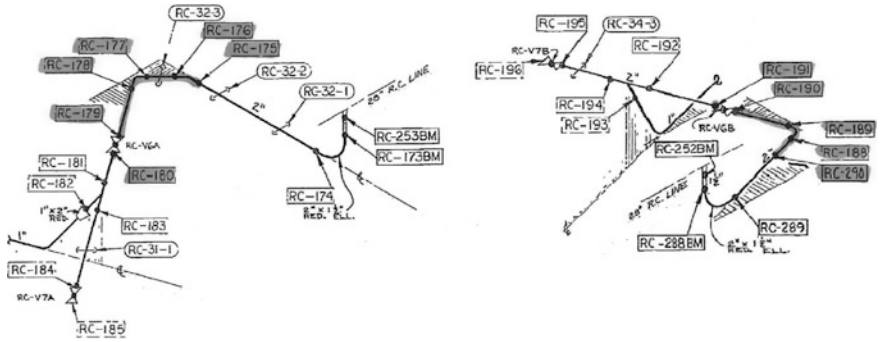

Fig. 3 Schematic of 1D-ISI-RC-002

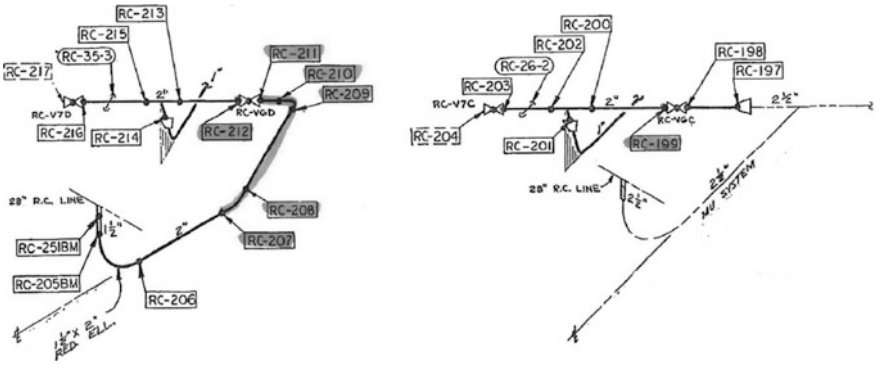

Fig. 4 Schematic of 1D-ISI-RC-004

Table 3 Reactor coolant system pressurizer auxiliary spray screened-in weld locations

Weld Location	Drawing	Pipe size (in.)	Material	Steady state temp (°F)	Stagnant category 2—drained/flushed once per fuel cycle, category 3—drained/flushed less than once per fuel cycle
SP0062SWELD	1D-ISI-RC-005	1.5	SS	≥ 200	2 (used during cooldown)
SP0063SWELD	1D-ISI-RC-005	1.5	SS	≥ 200	2 (used during cooldown)
SP0067SWELD	1D-ISI-RC-005	1.5	SS	≥ 200	2 (used during cooldown)
SP0068SWELD	1D-ISI-RC-005	1.5	SS	≥ 200	2 (used during cooldown)

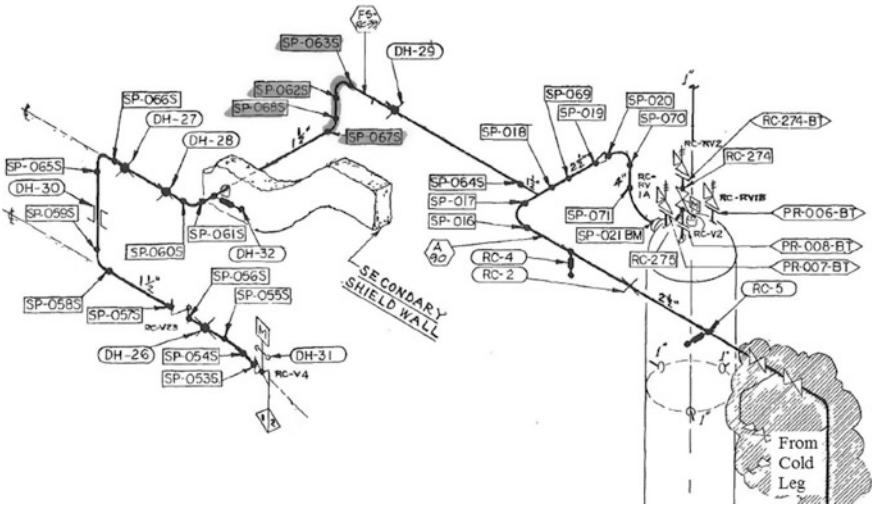

Fig. 5 Schematic of 1D-ISI-RC-005 (Pressurizer Auxiliary Spray)

Table 4 Reactor Coolant System Pressurizer Drain Lines Screened-In Weld Locations

Weld Location	Drawing	Pipe size (in.)	Material	Steady state temp (°F)	Stagnant category 2—drained/flushed once per fuel cycle, category 3—drained/flushed less than once per fuel cycle
SR0011WELD	1D-ISI-RC-005	2	SS	≥ 200	3 (Used to drain the PZR for maintenance)
SR0012WELD	1D-ISI-RC-005	2	SS	≥ 200	3 (Used to drain the PZR for maintenance)
SR0013WELD	1D-ISI-RC-005	2	SS	≥ 200	3 (Used to drain the PZR for maintenance)
SR0014WELD	1D-ISI-RC-005	2	SS	≥ 200	3 (Used to drain the PZR for maintenance)
SR0015WELD	1D-ISI-RC-005	2	SS	≥ 200	3 (Used to drain the PZR for maintenance)
SR0016WELD	1D-ISI-RC-005	2	SS	≥ 200	3 (Used to drain the PZR for maintenance)
SR0017WELD	1D-ISI-RC-005	2	SS	≥ 200	3 (Used to drain the PZR for maintenance)

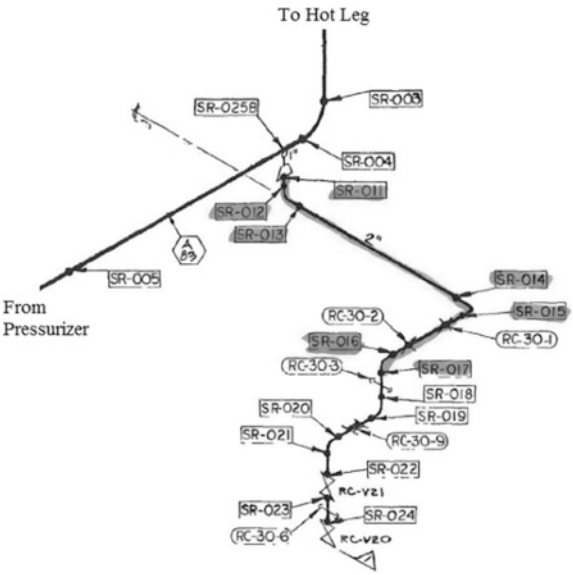

Fig. 6 Schematic of 1D-ISI-RC-005 (Pressurizer Drain Line)

Plant B (Westinghouse Unit) Results

The Residual Heat Removal System, Safety Injection System, and Chemical and Volume Control System included weld locations that screened in as being both susceptible to ID-initiated SCC and having a high consequence of failure. The remaining plant systems with ASME Class1 and/or Class 2 piping did not include any weld locations that screened in.

Table 5 lists the weld locations screened in for the Residual Heat Removal System, which are shown in Figs. 7 and 8. Note that the welds in these lines are assumed to be below 200 °F when located in the containment basement, which is a reasonable delineation in that the welds that are screened in are a leading indicator of SCC given their higher temperature.

Table 6 lists the weld locations screened in for the Safety Injection System, which are shown in Figs. 9, 10 and 11.

Table 7 lists the weld locations screened in for the Chemical and Volume Control System, which are shown in Fig. 12. Note that the welds in this line are assumed to be below 200 °F beyond the elbow of the second drop in elevation, which is a reasonable delineation in that the welds that are screened in are a leading indicator of SCC given their higher temperature.

Table 5 Residual Heat Removal System Screened-In Weld Locations

Weld Location	Drawing	Pipe size (in.)	Material	Steady state temp (°F)	Stagnant category 2—drained/flushed once per fuel cycle, category 3—drained/flushed less than once per fuel cycle
RHR-W004	ISIM-957-1-1	8	SS	≥ 200	2-Flow when RHR is initiated during cooldown
RHR-W005	ISIM-957-1-1	8	SS	≥ 200	2-Flow when RHR is initiated during cooldown
RHR-W006	ISIM-957-1-1	8	SS	≥ 200	2-Flow when RHR is initiated during cooldown
RHR-W028	ISIM-957-1-1	8	SS	≥ 200	2-Flow when RHR is initiated during cooldown
RHR-W029	ISIM-957-1-1	8	SS	≥ 200	2-Flow when RHR is initiated during cooldown
RHR-W030	ISIM-957-1-1	8	SS	≥ 200	2-Flow when RHR is initiated during cooldown

NR Not Reported

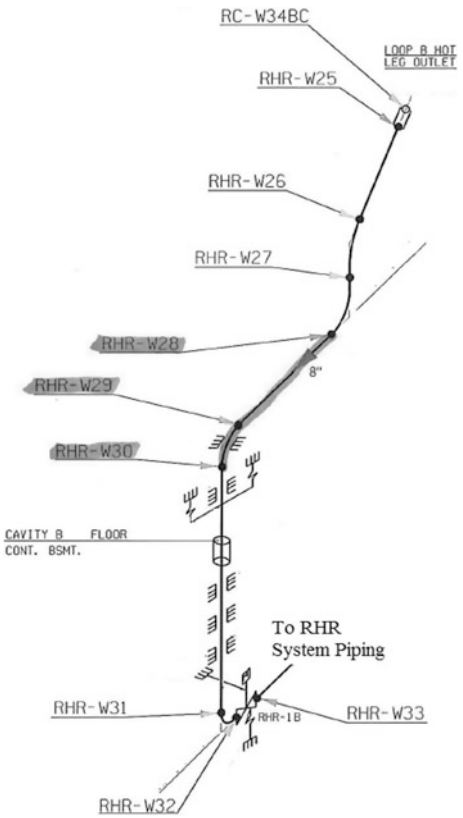

Fig. 7 Schematic of ISIM-957-1-1

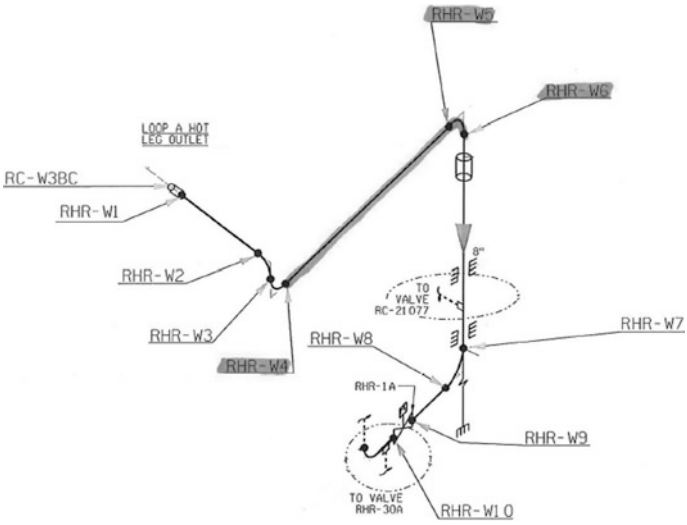

Fig. 8 Schematic of ISIM-957-1-1

Table 6 Safety Injection System Screened-In Weld Locations

Weld Location	Drawing	Pipe size (in.)	Material	Steady state temp (°F)	Stagnant category 2—drained/flushed once per fuel cycle, category 3—drained/flushed less than once per fuel cycle
SI-W120	ISIM-935	12	SS	≥ 200	2-Flow when RHR is initiated during cooldown
SI-W121	ISIM-935	12	SS	≥ 200	2-Flow when RHR is initiated during cooldown
SI-W108	ISIM-938-2-1	4	SS	≥ 200	2-used during start-up, cooldown, and DBAs
SI-W048	ISIM-939-1	6	SS	≥ 200	3-Flow when SI is initiated during a DBA

NR: Not Reported

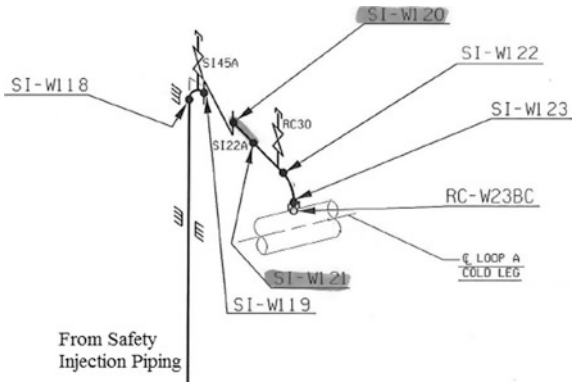

Fig. 9 Schematic of ISIM-935

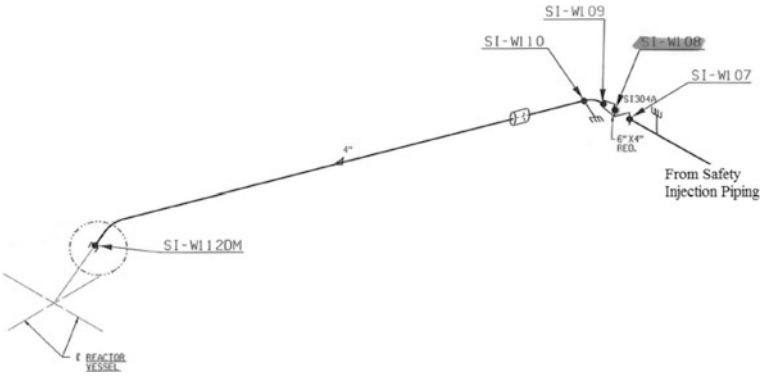

Fig. 10 Schematic of ISIM-938-2-1

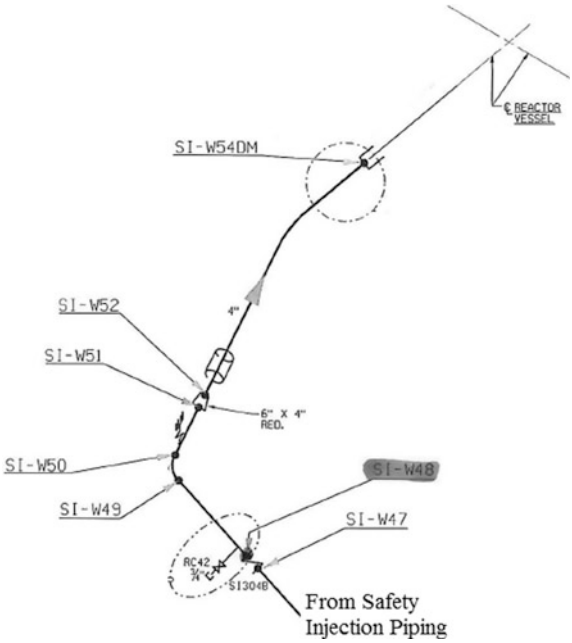

Fig. 11 Schematic of ISIM-939-1

Plant C (CE Unit) Results

The Safety Injection System, Shutdown Cooling System, and Reactor Coolant System include weld locations that screened in as being both susceptible to ID-initiated SCC and having a high consequence of failure. The remaining plant systems in the RI-ISI program (Charging System, Fire Protection System, Feedwater System) with ASME Class1 and/or Class 2 piping did not include any weld locations that were screened in.

Table 8 lists the weld locations screened in for the Safety Injection System, which are shown in Figs. 13, 14, 15 and 16.

Table 9 lists the weld locations screened in for the Shutdown Cooling System, which are shown in Fig. 17.

Table 10 lists the weld locations screened in for the Reactor Coolant System, which are shown in Figs. 18, 19, 20, 21 and 22.

Table 7 Chemical & Volume Control System Screened-In Weld Locations

Weld Location	Drawing	Pipe size (in.)	Material	Steady state temp (°F)	Stagnant category 2—drained/flushed once per fuel cycle, category 3—drained/flushed less than once per fuel cycle
CVC-W167S	ISIM-874-3	2	SS	≥ 200	2-Flow initiated during plant cooldown
CVC-W168S	ISIM-874-3	2	SS	≥ 200	2-Flow initiated during plant cooldown
CVC-W169S	ISIM-874-3	2	SS	≥ 200	2-Flow initiated during plant cooldown
CVC-W170S	ISIM-874-3	2	SS	≥ 200	2-Flow initiated during plant cooldown
CVC-W171S	ISIM-874-3	2	SS	≥ 200	2-Flow initiated during plant cooldown
CVC-W172S	ISIM-874-3	2	SS	≥ 200	2-Flow initiated during plant cooldown
CVC-W173S	ISIM-874-3	2	SS	≥ 200	2-Flow initiated during plant cooldown
CVC-W174S	ISIM-874-3	2	SS	≥ 200	2-Flow initiated during plant cooldown
CVC-W175S	ISIM-874-3	2	SS	≥ 200	2-Flow initiated during plant cooldown
CVC-W176S	ISIM-874-3	2	SS	≥ 200	2-Flow initiated during plant cooldown
CVC-W177S	ISIM-874-3	2	SS	≥ 200	2-Flow initiated during plant cooldown
CVC-W178S	ISIM-874-3	2	SS	≥ 200	2-Flow initiated during plant cooldown

NR: Not Reported

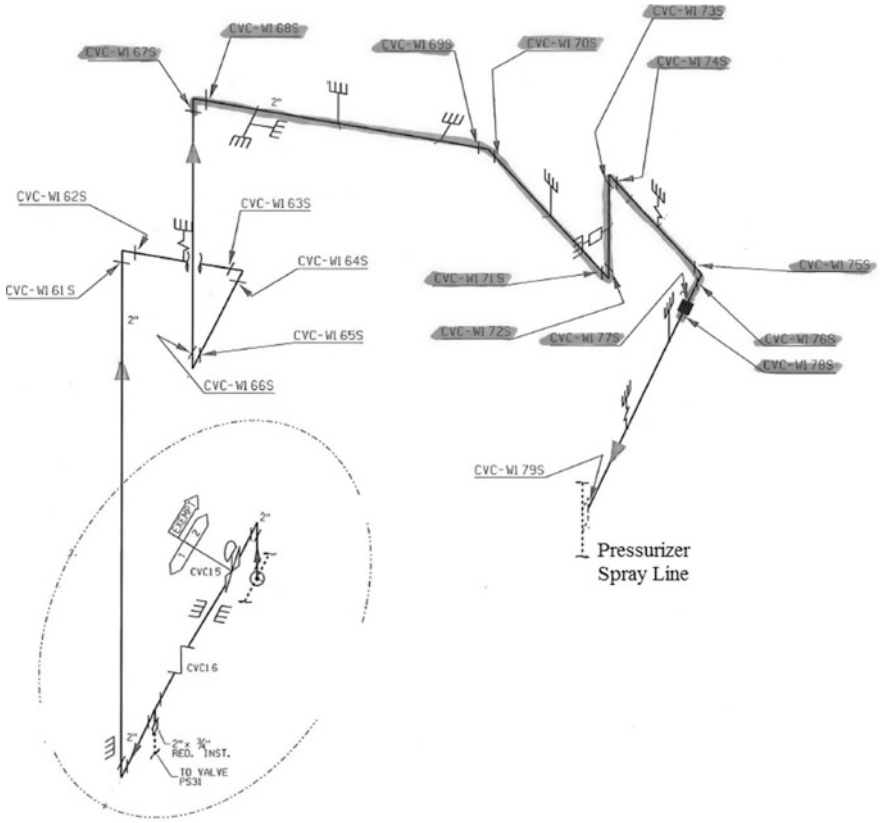

Fig. 12 Schematic of ISIM-874-3 (Pressurizer Auxiliary Spray)

Table 8 Safety Injection System Screened-In Weld Locations

Weld Location	Drawing	Pipe size (in.)	Material	Steady state temp (°F)	Stagnant category 2—drained/flushed once per fuel cycle, category 3—drained/flushed less than once per fuel cycle
BSI-C-1009	25203-29527-00017	12	SS	≥200	3
BSI-C-1011	25203-29527-00017	12	SS	≥200	3
BSI-C-1013	25203-29527-00017	12	SS	≥200	3
BSI-C-3006	25203-29527-00018	12	SS	≥200	3
BSI-C-3008	25203-29527-00018	12	SS	≥200	3
BSI-C-3010-A	25203-29527-00018	12	SS	≥200	3
BSI-C-2009	25203-29527-00019	12	SS	≥200	3
BSI-C-2009A	25203-29527-00019	12	SS	≥200	3
BSI-C-2011	25203-29527-00019	12	SS	≥200	3
BSI-C-4006	25203-29527-00020	12	SS	≥200	3
BSI-C-4008	25203-29527-00020	12	SS	≥200	3
BSI-C-4009	25203-29527-00020	12	SS	≥200	3
BSI-C-4010A	25203-29527-00020	12	SS	≥200	3
BSI-C-4011	25203-29527-00020	12	SS	≥200	3

NR: Not Reported

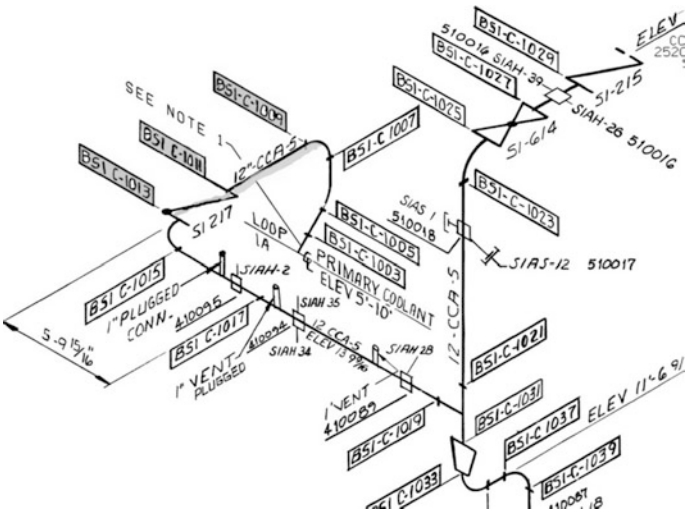

Fig. 13 Schematic of 25203-29527-00017

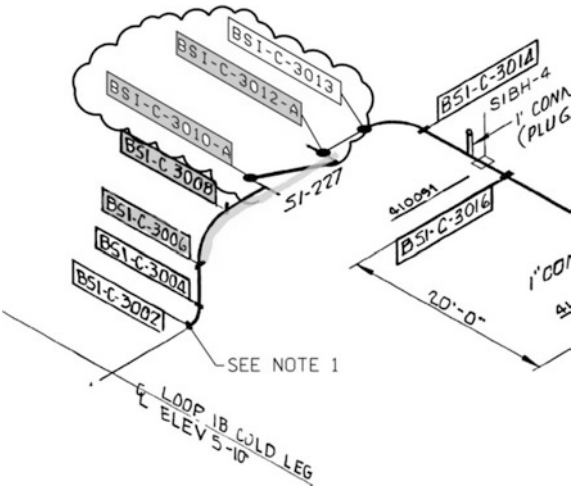

Fig. 14 Schematic of 25203-29527-00018

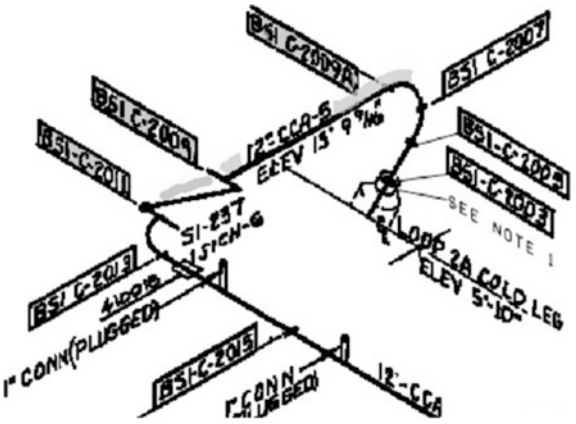

Fig. 15 Schematic of 25203-29527-00019

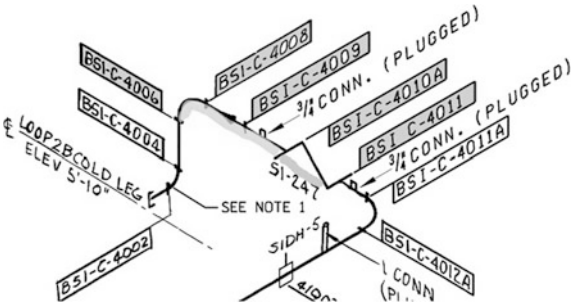

Fig. 16 Schematic of 25203-29527-00020

Table 9 Shutdown Cooling System Screened-In Weld Locations

Weld Location	Drawing	Pipe size (in.)	Material	Steady state temp (°F)	Stagnant category 2—drained/flushed once per fuel cycle, category 3—drained/flushed less than once per fuel cycle
BSD-C-2009	25203-29527-00021	12	SS	≥200	2
BSD-C-2011	25203-29527-00021	12	SS	≥200	2
BSD-C-2013	25203-29527-00021	12	SS	≥200	2
BSD-C-2015	25203-29527-00021	12	SS	≥200	2
BSD-C-2017	25203-29527-00021	12	SS	≥200	2
BSD-C-2019	25203-29527-00021	12	SS	≥200	2
BSD-C-2021	25203-29527-00021	12	SS	≥200	2
BSD-C-2021A	25203-29527-00021	12	SS	≥200	2

NR: Not Reported

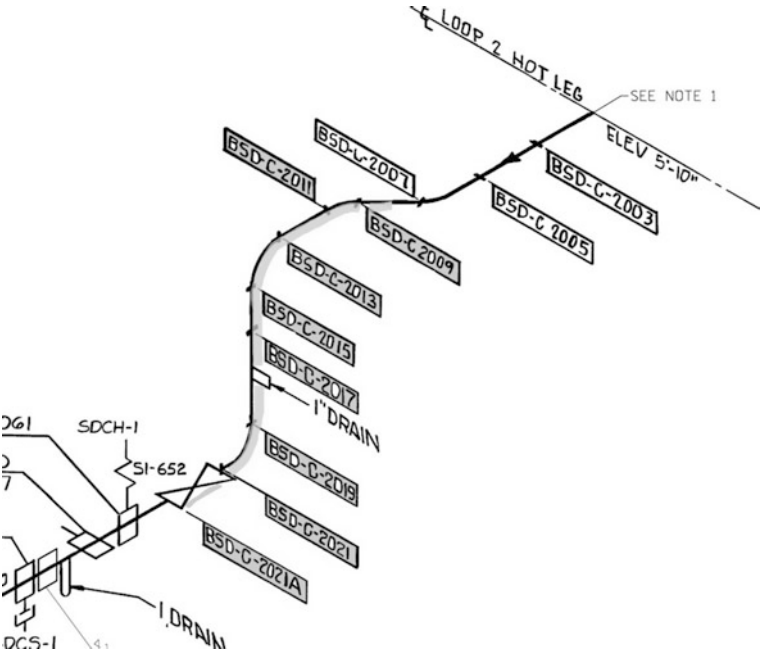

Fig. 17 Schematic of 25203-29527-00021

Table 10 Reactor coolant system screened-in weld locations

Weld Location	Drawing	Pipe size (in.)	Material	Steady state temp (°F)	Stagnant category 2—drained/flushed once per fuel cycle, category 3—drained/flushed less than once per fuel cycle
BPD-C-3004	25203-29527-00030	2	SS	≥ 200	3
BPD-C-3006	25203-29527-00030	2	SS	≥ 200	3
BPD-C-1005	25203-29527-00031	2	SS	≥ 200	3
BPD-C-1007	25203-29527-00031	2	SS	≥ 200	3
BPD-C-1009	25203-29527-00031	2	SS	≥ 200	3
BPD-C-1011	25203-29527-00031	2	SS	≥ 200	3
BPD-C-1013	25203-29527-00031	2	SS	≥ 200	3
BPD-C-1021	25203-29527-00032	2	SS	≥ 200	3
BPD-C-1023	25203-29527-00032	2	SS	≥ 200	3
BPD-C-2005	25203-29527-00034	2	SS	≥ 200	3
BPD-C-2007	25203-29527-00034	2	SS	≥ 200	3
BPD-C-4008	25203-29527-00035	2	SS	≥ 200	3
BPD-C-4010	25203-29527-00035	2	SS	≥ 200	3

NR: Not Reported

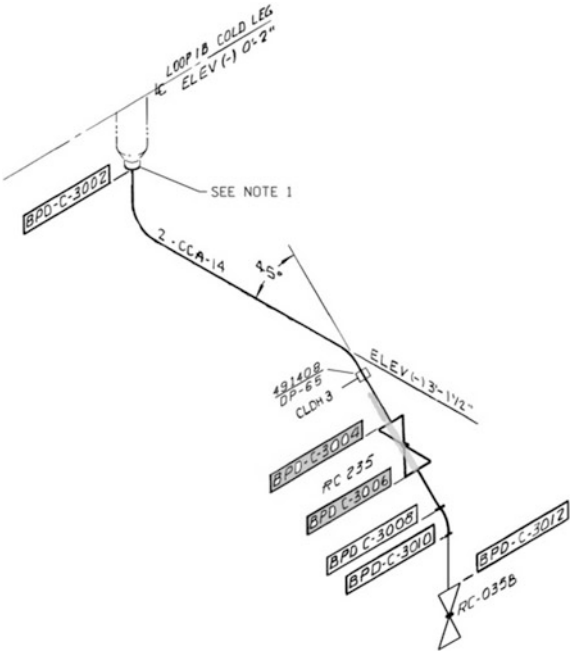

Fig. 18 Schematic of 25203-29527-00030

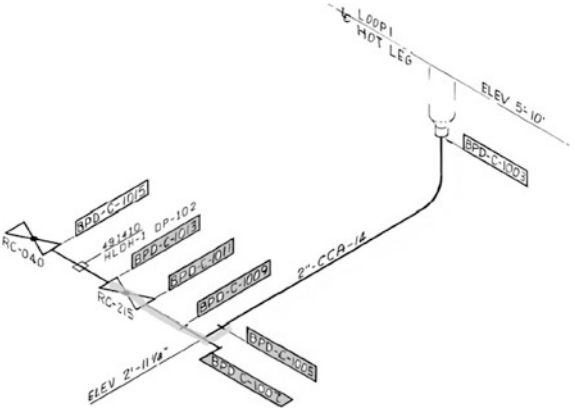

Fig. 19 Schematic of 25203-29527-00031

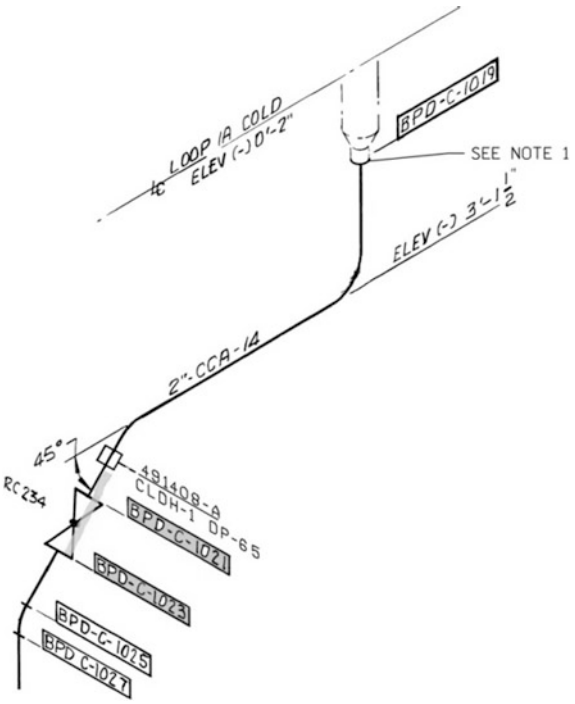

Fig. 20 Schematic of 25203-29527-00032

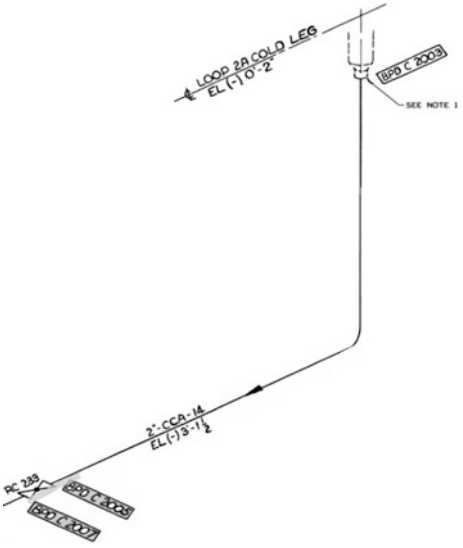

Fig. 21 Schematic of 25203-29527-00034

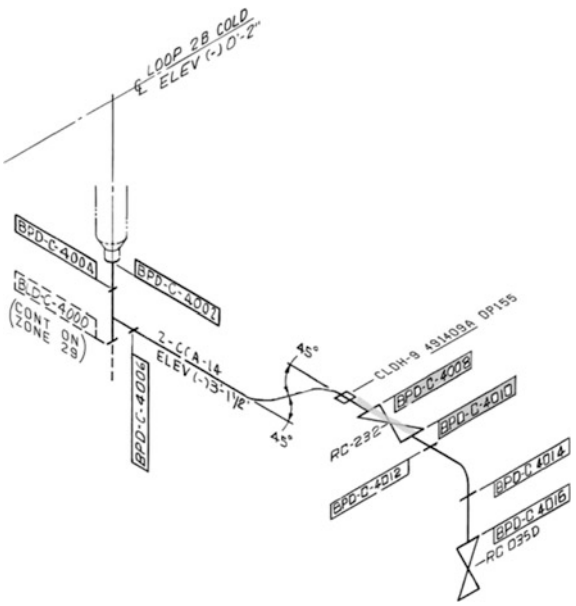

Fig. 22 Schematic of 25203-29527-00035

Discussion & Conclusions

Based on the results of the methodology followed in this paper, Plant A (Babcock & Wilcox-designed), Plant B (Westinghouse-designed), and Plant C (Combustion Engineering-designed) all contain several stainless steel weld locations in multiple systems that are both susceptible to SCC and have a high consequence of rupture, as shown in Tables 11, 12 and 13. Note that SCC in stainless steel piping resulting in rupture is very unlikely due to high flaw tolerance of austenitic stainless steel, which is supported by extensive operating experience in light water reactors.

Table 11 Plant A (B&W) Results Summary

System	Location	Stagnant category	Pipe size (in.)	Number of Welds Screened In
CF	From RV to Valve	2	14	7
RC	Drain Lines (Up to Valve)	3	2	14
RC	Drain Lines (Between Valves)	3	2	4
RC	Pressurizer Auxiliary Spray	2	1.5	4
RC	Pressurizer Drain Line	3	2	7

Table 12 Plant B (Westinghouse) Results Summary

System	Location	Stagnant category	Pipe Size (in.)	Number of welds screened in
RHR	From HL to Valve	2	8	6
SI	From CL or RV to Valve	2/3	4/6/12	4
CVC	Pressurizer Auxiliary Spray	2	2	12

Table 13 Plant C (CE) Results Summary

System	Location	Stagnant category	Pipe size (in.)	Number of welds screened in
SI	From CL to Valve	3	12	15
SDC	From HL to Valve	2	12	8
RC	Drain Lines	3	2	13

Volumetric inspection of select weld locations in ASME Code Class 1 stainless steel piping is currently required for pipe sizes $\geq$ 1 NPS (excluding socket welds) and is performed either through RI-ISI or ASME Code Section XI B-J (along with the one-time inspection for small bore piping from the GALL). The results of this work will be used to develop a resource guide to be used as a tool for assisting in the selection of welds to inspect when addressing currently existing inspection requirements. Note that the intention of the resource guide is not to require additional inspections, but rather to support in the weld location selection process.

References

1. NRC Information Notice 2011–04, Contaminants and Stagnant Conditions Affecting Stress Corrosion Cracking In Stainless Steel Piping In Pressurized Water Reactors. (ML103410363)
2. PWR Owners Group Materials Subcommittee Interim Strategy for Identifying Outside Diameter Initiated Stress Corrosion Cracking (ODSCC) of Stainless Steel Systems, NEI 03–08 Good Practice Recommendation
3. R. Hosler, S. Fyfitch, H. Malikowski, and G. Ilevbare, Review of Stress Corrosion Cracking of Pressure Boundary Stainless Steel in Pressurized Water Reactors and the Need for Long-term Industry Guidance, In 16th International Conference on Environmental Degradation of Materials in Nuclear Power Systems-Water Reactors, 2013
4. Materials Reliability Program, *Stress Corrosion Cracking of Stainless Steel Components in Primary Water Circuit Environments of Pressurized Water Reactors (MRP-236)* (Palo Alto, CA, EPRI, 2007), p. 1015540
5. Materials Reliability Program, *Management of Thermal Fatigue in Normally Stagnant Non-Isolable Reactor Coolant System Branch Lines—Supplemental Guidance (MRP-146S)* (Palo Alto, CA, EPRI, 2009), p. 1018330

Part X
IASCC Testing—Characterization

On the Use of Density-Based Algorithms for the Analysis of Solute Clustering in Atom Probe Tomography Data

Emmanuelle A. Marquis, Vicente Araullo-Peters, Yan Dong, Auriane Etienne, Svetlana Fedotova, Katsuhiko Fujii, Koji Fukuya, Evgenia Kuleshova, Anabelle Lopez, Andrew London, Sergio Lozano-Perez, Yasuyoshi Nagai, Kenji Nishida, Bertrand Radiguet, Daniel Schreiber, Naoki Soneda, Mattias Thuvander, Takeshi Toyama, Faiza Sefta and Peter Chou

Abstract Because atom probe tomography (APT) provides three-dimensional reconstructions of small volumes by resolving atomic chemical identities and positions, it is uniquely suited to analyze solute clustering phenomena in materials. A number of approaches have been developed to extract clustering information from the 3D reconstructed dataset, and numerous reports can be found applying these methods to a wide variety of materials questions. However, results from clustering analyses can differ significantly from one report to another, even when performed on similar microstructures, raising questions about the reliability of APT

E.A. Marquis (✉) · V. Araullo-Peters · Y. Dong
Department of Materials Science and Engineering, University of Michigan, Ann Arbor, MI 48109, USA
e-mail: emarq@umich.edu

A. Etienne · B. Radiguet
Groupe de Physique Des Matériaux, UMR CNRS 6634, Université de Rouen, Saint Etienne du Rouvray Cedex, France

S. Fedotova · E. Kuleshova
Russian Research Center 'Kurchatov Institute', Pl. Kurtachova, 123 182 Moscow, Russian Federation

K. Fujii · K. Fukuya
Institute of Nuclear Safety System Inc., 64 Sata, Mihama 919-1205, Japan

A. Lopez
DEN-Service D'Etudes Des Matériaux Irradiés, CEA, Université Paris-Saclay, F-91191 Gif-Sur-Yvette, France

A. London · S. Lozano-Perez
Department of Materials, University of Oxford, Parks Road, Oxford OX1 3PH, UK

Y. Nagai · T. Toyama
The Oarai Center, Institute for Materials Research, Tohoku University, Oarai, Ibaraki 311-1313, Japan

J.H. Jackson et al. (eds.), *Proceedings of the 18th International Conference on Environmental Degradation of Materials in Nuclear Power Systems – Water Reactors*, The Minerals, Metals & Materials Series, https://doi.org/10.1007/978-3-319-68454-3_65

to quantitatively describe solute clustering. In addition, analysis details are often not provided, preventing independent confirmation of the results. With the number of APT research groups growing quickly, the APT community recognizes the need for educating new users about common methods and artefacts, and for developing analysis and data reporting protocols that address issues of reproducibility, errors, and variability. To this end, a round robin experiment was organized among ten different international institutions. The goal is to provide a consistent framework for the analysis of irradiated stainless steels using APT. Through the development of more reliable and reproducible data analysis and through communication, this project also aims to advance the understanding between irradiated microstructure and materials performance by providing more complete quantitative microstructural input for modeling. The results, methods, and findings of this round robin will also apply to other clustering phenomena studied using APT, beyond the theme of radiation damage.

Keywords Atom probe tomography · Cluster analysis

Introduction

Atom probe tomography (APT) has transformed the analysis of irradiated microstructures with its unique chemical and spatial sensitivity that enable the detection of small solute atom clusters. It has provided key insights into the development of solute clusters in irradiated reactor pressure vessel (RPV) steels [1], irradiated austenitic stainless steels [2–4], or oxide dispersion-strengthened steels [5, 6]. APT generates three-dimensional reconstructions of atomic position and chemistry from needle-shaped samples using a combination of field evaporation, time-of-flight mass spectrometry, position-sensitive detection, and a reconstruction algorithm. As with any other experimental method, analysis of the APT data

K. Nishida · N. Soneda
Materials Science Research Laboratory, Central Research Institute of Electric Power Industry, Nagasaka, Japan

D. Schreiber
Energy and Environment Directorate, Pacific Northwest National Laboratory, Richland, WA 99352, USA

M. Thuvander
Department of Physics, Chalmers University of Technology, SE-412 96 Göteborg, Sweden

F. Sefta
Departement Métallurgie, EDF—R&D, Avenue Des Renardières—Ecuelles, 77818 Moret-Sur-Loing, France

P. Chou
Electric Power Research Institute, Palo Alto, CA 94304, USA
e-mail: pchou@epri.com

requires an understanding of the mechanisms of data generation along with possible limitations and artefacts, a definition of the objects of interest, and a data processing method to quantify the objects. Data generation is beyond the scope of this paper, and we will refer the reader to existing monographs, e.g. [7]. However, it is important to recognize that the physical processes controlling movement and evaporation of atoms under an applied electric field and the limitations inherent to the reconstruction algorithms may result in artefacts and errors in the reconstructed data, with significant consequences on the outcome of the data analysis procedure. Obvious artefacts manifest themselves as variations in the reconstructed atomic density and variations in solute concentrations that depend on crystallographic orientation. Additional sources of errors may be less evident. A number of mechanisms have been identified with significant effects on the spatial and chemical accuracy of the reconstructed data, which includes localized hopping of atoms on the sample surface prior to evaporation (roll-up motion) [8], longer range surface diffusion [9], local changes in the field distribution, particularly near terrace edges [10, 11], non-uniform evaporation due to evaporation field differences between phases or crystallographic orientation [12, 13], or detection biased against multiple events [14]. This paper summarizes the round robin experiment on data analysis procedures only; therefore, most of these effects will not be considered.

For density-based methods, solute cluster is defined as a region where solute atoms are spatially closer to one another than they would be when randomly distributed. Two main methods are commonly used to analyze clusters. The first, the "maximum separation method", relies on three parameters (O, d_{max}, and N_{min}). The order, O, defines the number of nearest neighbors considered. If O solute atoms are within the critical distance, d_{max}, of another solute atom, then these atoms are part of the same cluster [15–18]. A cluster requires a minimum number of atoms, N_{min}, to avoid counting statistically random occurrences of a few atoms being close together. The second, the "local concentration method", relies on an analysis of the local solute concentrations. Clustered atoms are defined by the concentration or density of neighboring solutes being higher than a critical threshold concentration, C_{th} or number of atoms, N_{th} [19–21], and by a minimum number of solute atoms, N_{min}. A combination of both methods, also called the "iso-position method", filters solute atoms with a high local concentration before applying an envelope algorithm [6] or maximum separation method to increase the contrast between clusters and matrix [4, 22]. Variations on these cluster-finding algorithms, such as Fourier transform and auto-correlation functions [23], pair correlation functions [24, 25], Delaunay tessellation [26], iso-concentration surfaces and proximity histograms [27], and frequency distributions [28] have also been developed for the detection and analysis of solute clusters in APT data; however these are beyond the scope of this round robin experiment.

In either of the two approaches described above, the selection of the analysis parameters is an important step that can significantly modify the outcome of the analysis. A number of studies have been dedicated to defining objective methods of selection. Using a small set of synthetic microstructures, Hyde et al. found that d_{max} has the largest influence on the outcome [29]. The selection of N_{min} and the

resulting error on the number density of precipitates were addressed by Cerezo and Davin by comparing the outcomes of the cluster search algorithm performed on an experimental dataset and on a random solid solution. The N_{min} value should minimize the number of random occurrences in the matrix [16, 17] and Styman et al. refined this step by adding a comparison of cluster compositions in the experimental and randomized datasets [30]. The generation of a random dataset is generally done by re-assigning the measured time-of-flight values at random—as this retains the correct overall composition—while keeping the detected positions, although one should consider the multiplicity of possible random datasets giving rise to a range of possible N_{min} values [31]. Different methods have been proposed for the objective selection of a d_{max} value. These have relied largely on the interpretation of the distribution of nearest neighbor distances (NND) to enable a selection of d_{max} that minimizes the inclusion of random clusters, and the splitting or merging of clusters [32]. As a variation on this approach, Jägle proposed to re-examine the NNDs by fitting the part of the distribution pertaining to the matrix rather than selecting a d_{max} value based on the comparison with a randomized dataset [33]. Alternatively, Kolli suggested using the variations of the number of clusters to find an optimum value [34]. Following observations that optimized values of d_{max} and N_{min} are correlated [29], Williams et al. proposed to compare the observed number of clusters with the expected number of cluster in a randomized dataset by sweeping through a wide range of the parameter space [31].

Despite the number of proposed methods, a challenge remains that no standardized approach to the analysis of solute clusters can be applied, as no single method works for all microstructures of interest. As illustrated below, the maximum separation method is well-suited for microstructures where the solute density contrast between clusters and matrix is significant, but fails when that contrast is reduced. Therefore, not all microstructures will be amenable to this technique and its limitations require clarification. In addition, incomplete reporting of the analysis procedures is apparent in the open literature, raising a range of concerns from data interpretation, validity, to reproducibility. In particular, the absence of details and error or variability analyses limit the reader's assessment of data quality and of appropriateness for comparison against other work or future work.

In this context, the present round robin experiment, conducted among ten international research groups, has several objectives: provide an educational platform for new users, bring awareness about current common methods and their limitations, test the variability of the traditional cluster search methods used by the APT community when applied to irradiated stainless steels, clarify the range of applications suitable to the use of this algorithm, recommend best practices in the use of these methods, and provide a template for reporting data that will assist future researchers in need of re-interpretation of published data.

Experimental

The current round-robin explores the use of the maximum separation method as implemented in the Cameca software IVAS [35] and the concentration/density methods implemented in the Rouen GPM 3Dsoft software [36]. The maximum separation method or iso-position method can also be performed using open software, such as 3Depict [37]. In order to limit the effects of specimen preparation, data collection, and data reconstruction, a series of synthetic datasets were created to simulate increasingly challenging clustering behaviors. The dataset contained two elements (A and B) where B exhibits clustering tendency and is therefore selected as the core atom in the cluster search algorithms. For each dataset, a fixed number of clusters were randomly distributed in the volume, with a minimum separation distance between clusters. The radii of the clusters were assigned based on a gaussian size distribution. Each cluster was assigned the same concentration with the appropriate number of atoms randomly assigned A or B within the clusters. The only artefact introduced in the data is a random Gaussian translation of the atoms around their atomic lattice sites that is more pronounced for the solute atoms. A translation using a normal distribution with a variance of $\pm a$ for x and y and $\pm a/2$ for z—where a is the lattice parameter—was then imposed on the positions of all A atoms and B atoms in solution. A larger delocalization was applied to B atoms in clusters with a variance of $\pm 2a$ for x and y and $\pm a$ for z. To account for the detection efficiency of the currently most used commercial LEAP 4000 HR instrument, 63% of the atoms were removed at random. Details regarding the datasets can be found in Table 1.

The datasets, shown in Fig. 1, were distributed to the round robin participants without any prior information regarding their microstructures. Participants were asked to analyze the clustering behavior of B atoms in terms of number of clusters, average cluster size, and average cluster composition. The analysis methods used by the participants were either the maximum separation distance as implemented in the IVAS software or the iso-position method as implemented in the GPM 3Dsoft software. Some participants used iso-concentration surfaces (iso-surfaces) to guide their analyses. Atoms on the edges of the volumes were counted as whole or half.

Table 1 Cluster characteristics in synthetic datasets (nominal values)

Dataset	Number of clusters	Radius (nm)	Composition of clusters (matrix) (at.%)	Minimum inter-cluster spacing (nm)
1	176	1.1 ± 0.1	75 (<0.07)	5
2	96	1.2 ± 0.1	20 (<0.07)	6
3	275	1.2 ± 0.1	40 (<0.07)	2.2
4	169	1.0 ± 0.1	30 (10)	6

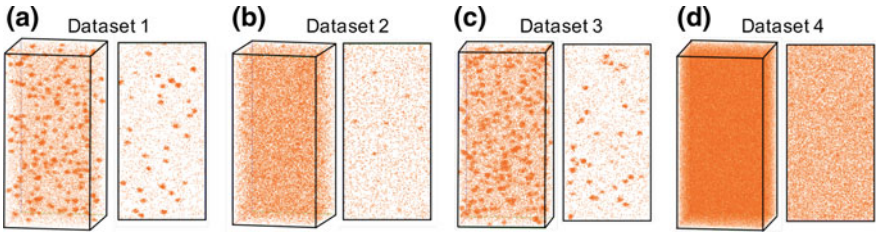

Fig. 1 Reconstructions and slices for Dataset 1 (**a**), Dataset 2 (**b**), Dataset 3 (**c**), and Dataset 4 (**d**). Dataset dimensions are 50 nm × 50 nm × 100 nm. Slices are 10 nm thick

Results

Cluster Identification

Dataset 1 The high solute density contrast between clusters and matrix translated into a bimodal distribution of the first nearest neighbor distance (NND); Fig. 2a. For most participants, a comparison with a randomized dataset guided the selection of d_{max} and N_{min} values. Some participants selected a higher value of O without significant effect on the outcome since the contrast between matrix and clusters was already significant with O = 1. The values of N_{min} ranged from 6 to 20 atoms, without a strong effect on the outcome due to the clear contrast between the size distribution of random clusters and that of the true clusters (Fig. 3). Overall, the stability of this system with respect to the parameters within a relatively wide range of values led to the convergence of the answers; and the number and size of the clusters identified by participants were relatively close to the set value (Table 2). Indeed, a sensitivity analysis with respect to d_{max} and N_{min} for O = 1 showed a wide area of constant cluster density (Fig. 4a). The selection of the d_{max} value mostly affected the number of clusters and the measured average cluster size. Figure 5a illustrates the dependence of the number of detected clusters and size on the d_{max} value for all choices of N_{min} and O by the participants. Within the stable region, i.e. for d_{max} values greater than 0.7 nm, the deviation from the set number of clusters was $\sim$1%, while the size of the cluster was systematically under-estimated by up to 6%. One answer significantly deviated from the others, and was found to be outside the range of stability.

Dataset 2 The solute density contrast between matrix and clusters was lower than in the previous case. As illustrated with the NND distributions, a higher order value was required to set the experimental distribution differently enough from the random distribution (Fig. 2b). The sensitivity analysis with respect to d_{max} and N_{min} at constant O showed that the number of clusters continuously changes with d_{max}, N_{min} and did not exhibit a stable region (Fig. 4b). Therefore, a visual check was used by most participants to find the values of the analysis parameters. The reported number of clusters was slightly underestimated. The average of reported cluster size

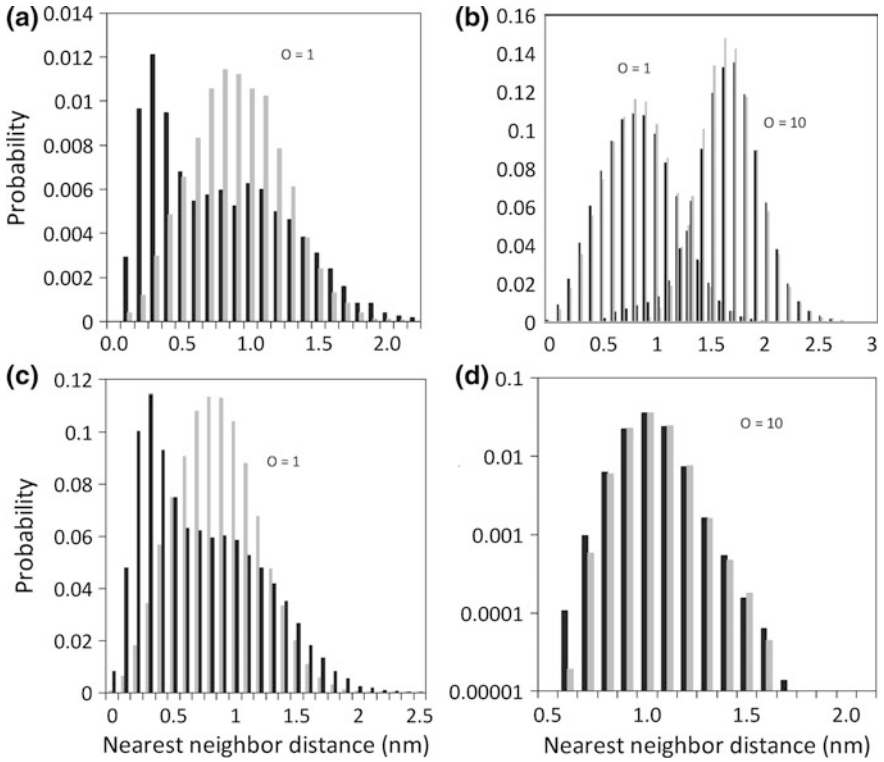

Fig. 2 Nearest neighbor distributions for Dataset 1 (**a**), Dataset 2 (**b**), Dataset 3 (**c**), and Dataset 4 (**d**). The grey bars represents random distributions

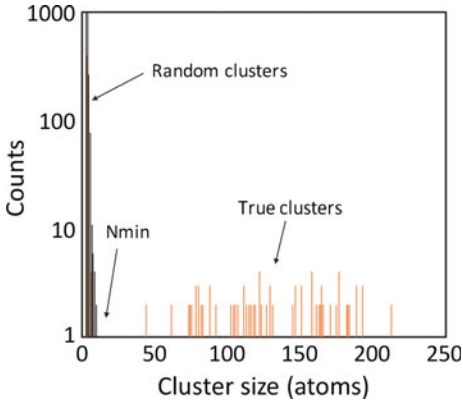

Fig. 3 Size distribution of the clusters for Dataset 1 (d_{max} = 0.7 nm, O = 1)

Table 2 Reported cluster search parameter values and cluster characteristics

		Number of clusters	Size (in atoms)	Cluster concentration	Matrix concentration
Dataset 1	Nominal	176	139	75	0.42
	Mean	178	121	48.9	0.44
	Standard deviation	5.4	16.3	11.1	0.03
	Spread	15	49.4	25.4	0.04
Dataset 2	Nominal	96	30	20	0.67
	Mean	86.6	35.3	24.1	0.66
	Standard deviation	3.8	10.3	12.7	0.01
	spread	11	26	33.1	0.03
Dataset 3	Nominal	275	44	40	0.41
	Mean	265.5	78	30.5	0.44
	Standard deviation	23.2	22.1	10.8	0.04
	spread	83	75	14.1	0.11
Dataset 4	Nominal	169	30	30	9.88
	Mean	103.3	89.6	44.2	9.91
	Standard deviation	41.8	66.2	11.3	0.06
	Spread	124	186.3	31.8	0.16

was close to the actual value, with a smaller spread than in Dataset 1 (Table 2). Here, even though the number of clusters was rightly identified using a wide range of d_{max} values, the narrower range of intermediate d_{max} values yielded answers close to the nominal value both in terms of number of clusters and cluster sizes (Fig. 5b). Larger value of d_{max} tended to include too many matrix atoms due to the smaller difference in the NND between the clusters and matrix. The deviation from the set number of clusters was $\sim$10%, while the size of the cluster was overestimated by 16%.

Dataset 3 Here, some clusters were allowed to be closer in space (Fig. 1c), leading to possible merger of clusters through the search algorithm if too large of a d_{max} value was selected. While an objective selection of d_{max} was in principle possible due to the bimodal distributions of NNDs (Fig. 2c), both the number and size of the clusters were highly dependent on the selection of the d_{max} value (Figs. 4c and 5c). The reported numbers of clusters and cluster sizes varied widely, as only a very narrow range of parameter values led to answers close to the nominal value without the use of additional corrections to account for cluster merging. Small d_{max} values yielded cluster sizes that were close to the actual number but meanwhile significantly overestimated the number of clusters. On the other hand, larger d_{max} value merged clusters that were spatially close to each other and therefore overestimated the cluster size. Only one participant manually split clusters when they appeared to be merged.

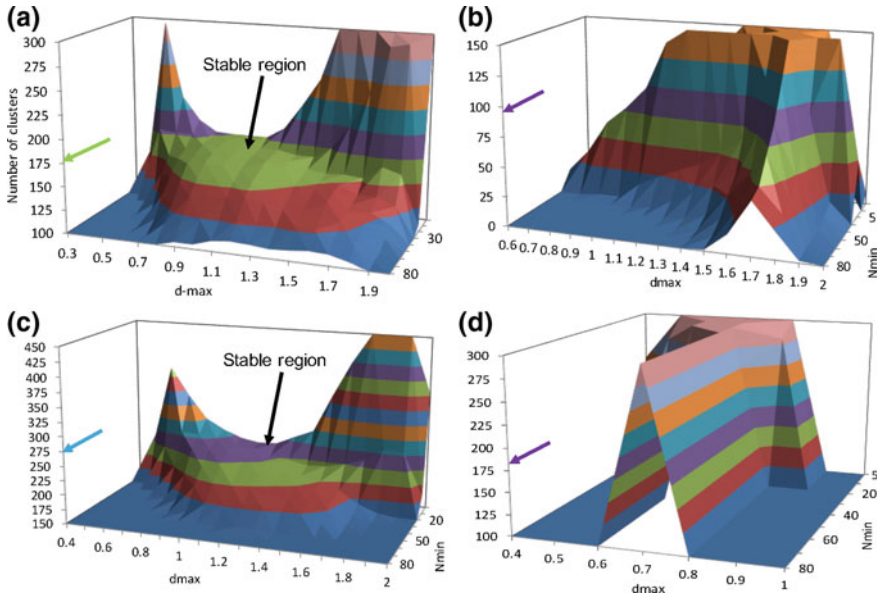

Fig. 4 Sensitivity analysis with respect to d_{max} and N_{min} for the maximum separation distance, applied to Dataset 1 with O = 1 (**a**), Dataset 2 with O = 5 (**b**), Dataset 3 with O = 1 (**c**), and Dataset 4 with O = 10 (**d**). Arrows point to the nominal number of clusters

Dataset 4 The cluster microstructure in this dataset presented the challenge of a high matrix solute concentration. As a result, the distribution of NND failed to show significant deviation from the random distribution, even to orders as high as 10 (Fig. 2d). Participant selection of parameters for d_{max} was therefore arbitrary and so were the outcomes, as illustrated with the steep variations with d_{max} and N_{min} (Figs. 4d and 5d). Alternatively, the concentration-based method could be applied to this dataset while maintaining an objective selection of parameter values, and two participants provided answers that were closer to the nominal value. As illustrated in Fig. 6, the use of the local concentration highlighted the clusters while reducing the matrix background. The selection of a maximum separation distance could become objective again, and the comparison with randomized datasets could be used for selecting the threshold concentration (25 at.% in Fig. 6); the maximum separation method was subsequently applied to the filtered atoms.

Cluster Composition

Participants used three different methods to estimate cluster compositions. The inclusion method implemented in the IVAS software requires two additional parameters: an inclusion distance $L \leq d_{max}$, and an erosion distance, $e \leq L$, to

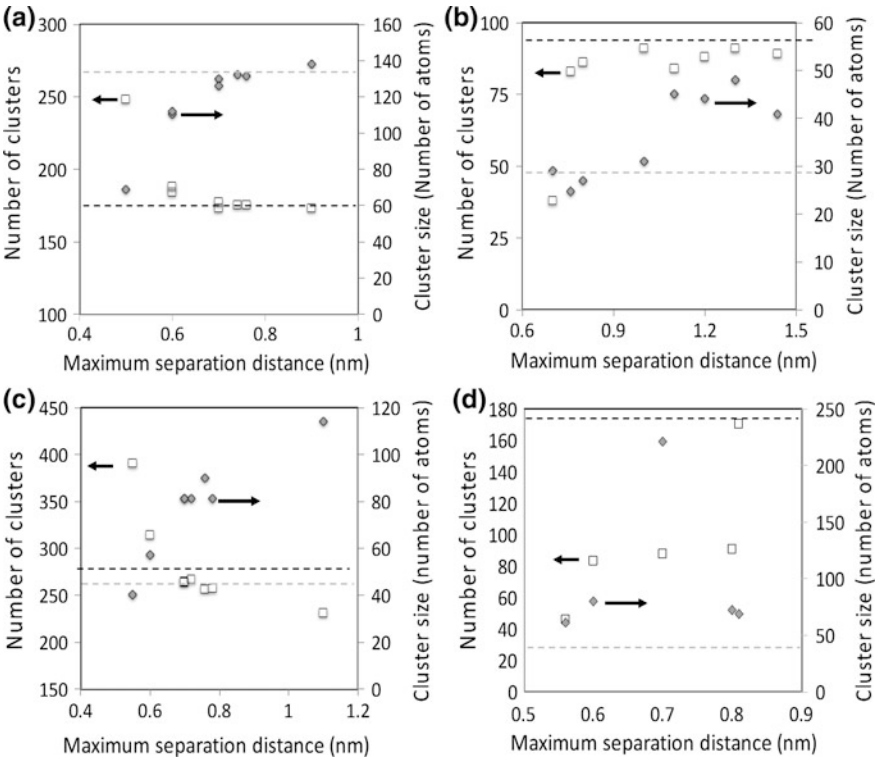

Fig. 5 Reported number of clusters and cluster sizes as a function of the selected d_{max} values in the case of the maximum separation distance for Dataset 1 (**a**), Dataset 2 (**b**), Dataset 3 (**c**), and Dataset 4 (**d**). Dashed lines corresponds to nominal values, and arrows indicate the relevant axis

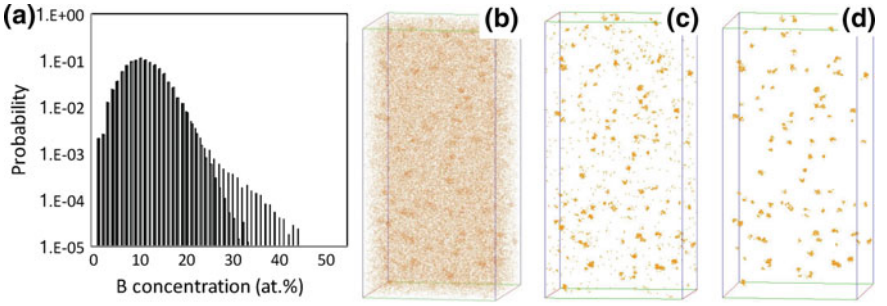

Fig. 6 Local concentration measured in 0.75 nm radius spheres around each B atom. Open circles are for the random dataset. (**a**); Overall dataset (**b**) B atoms with local B concentration >25 at.% (**c**) identified clusters using maximum separation method on the B atoms shown in (**c**) (**d**)

erode the cluster matrix interface [16]. The value of L should maximize the inclusion of all atoms within the clusters while minimizing neighboring cluster overlap. The second method consisted of calculating radial average concentration profiles from the center of clusters, while the third method relied on generating proximity histograms based on an iso-concentration surface whose position depends on the selection of a bin size and a delocalisation distance [27]. We note that other methods have been described, including the use of NNDs for estimating both matrix and cluster concentrations [38].

For all cases, the reported cluster compositions, summarized in Table 2 and Fig. 7, strongly depended on the method used. The inclusion method performed most poorly with the largest deviations from the set compositions. It appeared to strongly underestimate the higher cluster concentrations while it significantly overestimated the more dilute cluster compositions. The other methods behaved comparably. The compositions reported using the radial concentration method were systematically above the two methods, with a deviation that increased with increasing cluster concentration. Best results were obtained for the intermediate concentrations with deviations up to 15% from the set values, while deviations of 20 and 25% were noted for the lowest concentration at 20% and highest concentration at 75% respectively.

Discussion and Recommendations

The results of this round robin experiment show that a narrower range of outcomes with higher fidelity are reported for microstructures with high solute density contrast, and significantly wider spread are reported for more complex microstructures (cluster proximity or concentrated matrix composition). The synthetic datasets used in this study highlight a number of limitations in the application of the maximum

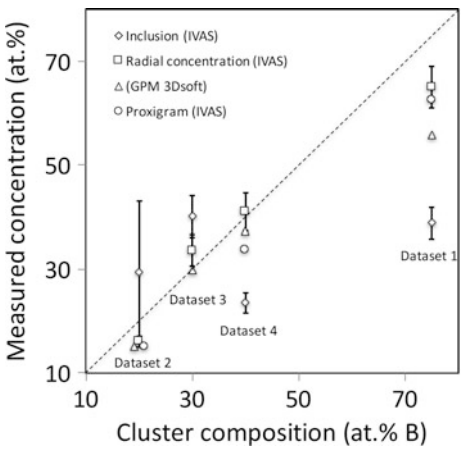

Fig. 7 Reported versus nominal compositions for the four datasets

separation method as implemented in the IVAS software, which is still the most widely applied analysis method in the literature. Not all microstructures are amenable to this method, and its application becomes questionable for dataset where the matrix composition is no longer dilute. In this case, other methods may be applied; we illustrate here how the use of local composition to filter solute atoms increases the contrast between matrix and clusters, providing more stable and reliable answers. The selection of the appropriate cluster analysis method is crucial to understanding the microstructure.

We also note that effects of commonly observed artefacts on the quality and stability of the outcomes were not tested in the present experiment but should be taken into account. In particular, the effect of density variations (both in terms of overall density or relative solute density), such as those observed at crystallographic poles or zone lines, should be carefully considered in future analyses. At times, however, relative changes in density due to evaporation artefacts can play in our favor, as in the case of lower-evaporation-field clusters that are reconstructed with increased atomic density, thereby increasing the contrast in comparison to matrix solute atoms. We also did not test whether these methods would be amenable to microstructures with multiple populations of clusters of different solute densities.

Cluster Detection and Counting

In light of the present findings, we suggest following a workflow to remediate the lack of information reporting and to provide guidance for researchers new to the field of APT. This workflow is relevant to the use of the maximum separation and iso-position methods.

- High contrast datasets may be analyzed by the maximum separation method as implemented in the IVAS software while lower contrast dataset would be best analyzed using concentration filtering, followed by the maximum separation method as implemented in the IVAS software or by the GPM 3Dsoft iso-position method.
- For both methods, because of the strong dependence of the outcome on values of the analysis parameters, a *description or justification of the methods by which parameters are selected* is required for completeness, so the results can be reproduced. In addition, *a sensitivity analysis* with respect to the parameters is highly recommended as additional justification for the selection of the parameters' values and as a measure of the uncertainty.
- In both methods, an approach to selecting values of d_{max}, O, N_{min} or C_{th}, based upon *comparison with randomized datasets,* to minimize the number of random occurrences, is recommended. We note here that the concentration of the random dataset may be considered carefully when the overall solute concentration is not dilute. The use of a random dataset keeping the overall solute concentration might artificially increase the detection of random clusters.

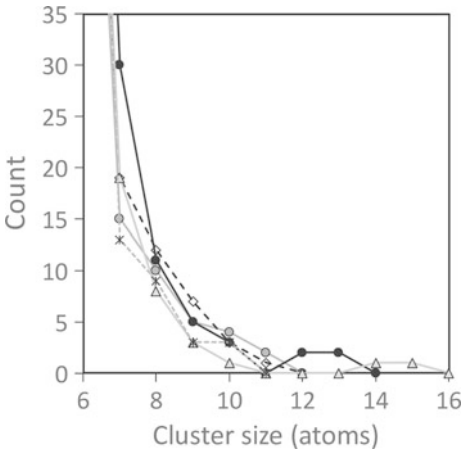

Fig. 8 Cluster size distribution for 6 different instances of a random solid solution from Dataset 2 using O = 5 and d_{max} = 1.0 nm

– Once parameters are set and selected, a check of the randomness of the matrix could be valuable [33] as well as *visual inspection*.
– In the case of clusters that are close spatially, there is no automated procedure to correct for possible merging of clusters. One may use either manual visual inspection or automated measurements of size, aspect ratio, or concentration to determine the likelihood that the cluster resulted from a merge.

Additional steps, if performed, could provide further information and quantification of uncertainty. These include the use of several instances of a random solid solution to highlight the range of N_{min} values that should be considered when reporting the number and size of clusters (Fig. 8).

Cluster Composition

Concentration measurements were most susceptible to the selected analysis methods due to the blurred cluster interfaces. Small clusters and precipitates are prone to evaporation artefacts, such as preferential evaporation or retention leading to change in curvature and to non-uniform projection with overlap of matrix and cluster atoms over distances that may be comparable to the average cluster size. In the best-case scenario, this leads to a broadening of the interface while the cluster's core still reflects the original composition. In the vast majority of cases, the reconstructed width of an interface is 2 to 3 nm even though the structure of interface might be atomically sharp by another imaging technique. It is therefore evident that the accurate quantification of the composition of clusters within this size range may be challenging. Here, evaporation artefacts were enhanced by varying the delocalization of the matrix and cluster atoms.

While the maximum separation method is reasonable for determining the number and locations of clusters in high contrast microstructures, it is not recommended for compositional measurements. The iso-position method and the radial concentration profile provided more accurate answers. Here again, however, we emphasize the need for thorough reporting of the method by which composition is measured (e.g. radius over which composition is assessed in the case of the radial concentration profile) and for provision of additional data that will enable future analysis and interpretation. A minimum requirement would be the composition profile averaged for all clusters and the dependence of the maximum core composition with cluster size.

Because the inclusion and erosion methods have been used in a large number of studies, it is worth discussing the effects of the inclusion and erosion parameters if one were to interpret compositional values previously published. The IVAS software limits the value of the erosion parameter, e, to the range of [0, L], where L is the inclusion distance and $L \leq d_{max}$. Given these constraints, for clusters smaller than 2 nm, the nominal cluster composition can rarely be attained for reasonable values of $L \sim d_{max}/2$, that ensures that most atoms inside the cluster are counted without creating overlap between neighboring clusters. Using Dataset 1 for illustration, all methods systematically underestimated the cluster composition (75% B; Fig. 7), the reason being the inclusion of matrix atoms along the broad interface. A d_{max} value of 0.8 nm with $N_{min} = 10$ was selected for the purpose of illustrating the effects of L and e on the measured cluster compositions. As expected when the value of e increases while keeping L constant (Fig. 9b), the B concentration in the clusters increases due to the removal of the matrix atoms near the interface. The deviation from the target value should scale with the size. With larger clusters, the number of near surface atoms contributing to the deviation gets smaller relative to the number of bulk atoms with the appropriate concentration. In Fig. 9a, where L = e, one can see that for L values smaller or equal to 0.2 nm, higher concentrations can be obtained. However, these are artefacts due to the exclusion of A atoms within the clusters, artificially increasing the B concentration. In Dataset 2, different results are observed (Fig. 9c, d). The data were analyzed using a higher order of O = 5 with a $d_{max} = 1.0$ nm. For a fixed value of the inclusion distance L = 1.0 nm, increasing the erosion distance, e, increases the measured average concentration but leads to lower concentrations than expected in all cases, except for e = 1.0 nm at which point the matrix atoms near the surface are removed in excess (Fig. 9c). However, setting L = e allows one to find any concentration above the expected concentration (Fig. 9d). The rapid increase in concentration for L = e < 0.2 nm is due to the exclusion of A atoms that are within the clusters.

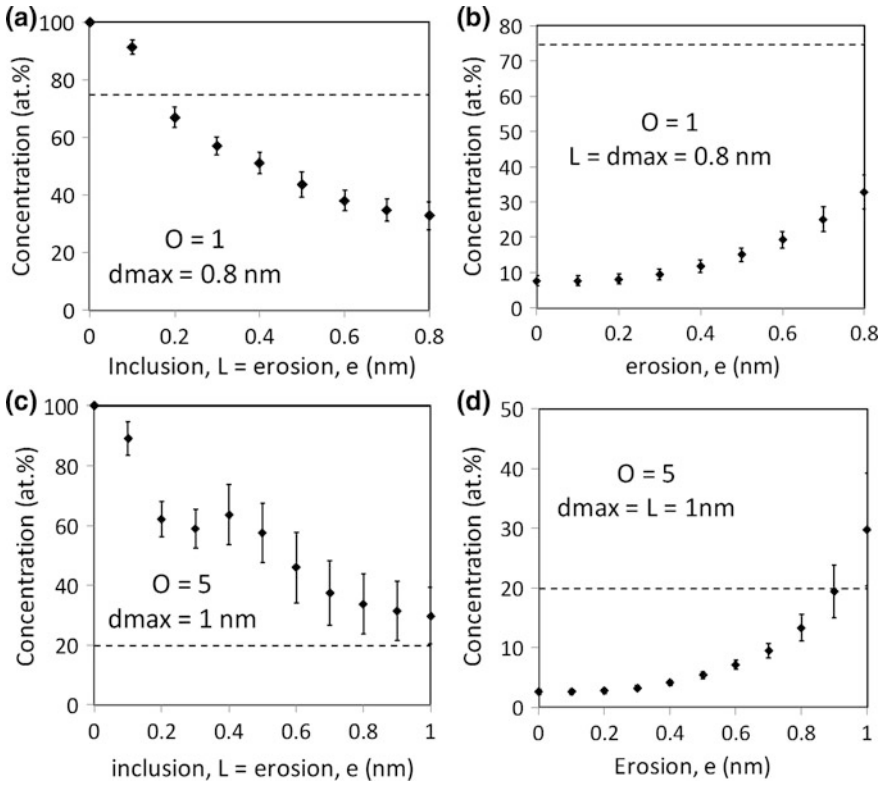

Fig. 9 Concentrations measured using the d_{max}-L-e method. Dataset 1 cluster compositions as a function of e when d_{max} = L = 0.8 nm (**a**); Dataset 1 cluster compositions as a function of e = L when d_{max} = 0.8 nm (**b**). Dataset 2 cluster compositions as a function of e when d_{max} = L = 1.0 nm (**c**); Dataset 2 cluster compositions as a function of e = L when d_{max} = 1.0 nm (**d**)

Conclusions

Ten international research groups independently analyzed four synthetic datasets created to test the reproducibility, accuracy, and validity of two widely used clustering analysis methods, the maximum separation method and the iso-position method, to identify and measure number density, size, and composition of the cluster populations. This round-robin experiment highlighted the ability of the maximum separation distance to reliably find clusters in microstructures with compositionally highly concentrated clusters in a dilute (low background) matrix. For datasets with higher concentration backgrounds, the iso-position method is recommended, as it reduces the microstructure to one with low background, where the maximum separation method can be applied.

We emphasize the need for thorough reporting of the analysis methods, which includes detailed justification of the method and parameters used. The information is not only essential for the reproducibility of the results, but also ensures that the data presented could be accurately interpreted by future researchers. Minimum information would include:

- Core atoms (or relevant mass to charge ranges)
- Analysis method and any variation on the common approach
- Generation of a randomized dataset for comparison with experimental data to select analysis parameters
- Sensitivity analysis to further refine and justify the choice of parameters, and estimating the uncertainty
- Method used to define N_{min}
- Specification of how edge clusters are counted and how many are found
- Specification of how merged or split clusters were accounted for.

Acknowledgements The authors acknowledge the voluntary participation by the members of the APT Round Robin and financial support of EPRI and EDF for the analysis of the aggregate results.

References

1. J. Hyde, M. Burke, B. Gault, D.W. Saxey, P. Styman, K. Wilford, T. Williams, Ultramicroscopy **111**, 676–682 (2011)
2. A. Etienne, B. Radiguet, P. Pareige, J.P. Massoud, C. Pokor, J. Nucl. Mater. **382**, 64–69 (2008)
3. T. Toyama, Y. Nozawa, W. Van Renterghem, Y. Matsukawa, M. Hatakeyama, Y. Nagai, A. Al Mazouzi, S. Van Dyck, J. Nucl. Mater. **418**, 62–68 (2011)
4. Y. Chen, P.H. Chou, E.A. Marquis, J. Nucl. Mater. **451**, 130–136 (2014)
5. D.J. Larson, P.J. Maziasz, I.S. Kim, K. Miyahara, Scripta. Mater. **44**, 359–364 (2001)
6. M.K. Miller, E.A. Kenik, Microsc. Microanal. **10**, 336–341 (2004)
7. B. Gault, M.P. Moody, J.M. Cairney, S.P. Ringer, Atom Probe Microscopy, Springer, 2012
8. A.R. Waugh, E.D. Boyes, M.J. Southon, Surf. Sci. **69**, 109–142 (1876)
9. B. Gault, F. Danoix, K. Hoummada, D. Mangelinck, H. Leitner, Ultramicroscopy **113**, 182–191 (2012)
10. D.J. Rose, J. Applied Phys. **27**, 215–220 (1956)
11. F. Vurpillot, A. Bostel, E. Cadel, D. Blavette, Ultramicroscopy **84**, 213–224 (2000)
12. M.K. Miller, M.G. Hetherington, Surf. Sci. **246**, 442–449 (1991)
13. F. Vurpillot, A. Bostel, D. Blavette, Appl. Phys. Lett. **76**, 3127–3129 (2000)
14. D.W. Saxey, Ultramicroscopy **111**, 473–479 (2011)
15. A. Heinrich, T.a. Al-Kassab, R. Kirchheim, Mater. Sci. Eng. A **35,** 92–98 (2003)
16. D. Vaumousse, A. Cerezo, P.J. Warren, Ultramicroscopy **95**, 215–221 (2003)
17. A. Cerezo, L. Davin, Surf. Interf. Anal. **39**, 184–188 (2007)
18. L.T. Stephenson, M.P. Moody, P.V. Liddicoat, S.P. Ringer, Microsc. Microanal. **13**, 448–463 (2007)
19. D. Blavette, S. Chambreland, Journal de Physique Colloques **47**, C7–503 (1986)
20. B. Radiguet, A. Barbu, P. Pareige, J. Nucl. Mater. **360**, 104–117 (2007)
21. J.M. Hyde, A. Cerezo, T.J. Williams, Ultramicroscopy **109**, 502–509 (2009)

22. E. Meslin, B. Radiguet, M. Loyer-Prost, Acta Mater. **61**, 6246–6254 (2013)
23. F. Vurpillot, F. De Geuser, G. Da Costa, D. Blavette, J. Microscopy-Oxford **216**, 234–240 (2004)
24. F. De Geuser, W. Lefebvre, D. Blavette, Phil. Mag. Lett. **86**, 227–234 (2006)
25. L. Couturier, F. De Geuser, A. Deschamps, Mater. Charact. **121**, 61–67 (2016)
26. W. Lefebvre, T. Philippe, F. Vurpillot, Ultramicroscopy **111**, 200–206 (2011)
27. O.C. Hellman, J.A. Vandenbroucke, J. Rüsing, D. Isheim, D.N. Seidman, Microsc. Microanal. **6**, 437–444 (2000)
28. M.P. Moody, L.T. Stephenson, A.V. Ceguerra, S.P. Ringer, Microsc. Res. Tech. **71**, 542–550 (2008)
29. J.M. Hyde, E.A. Marquis, K.B. Wilford, T.J. Williams, Ultramicroscopy **111**, 440–447 (2011)
30. P.D. Styman, J.M. Hyde, K. Wilford, G.D.W. Smith, Ultramicroscopy **132**, 258–264 (2013)
31. C.A. Williams, D. Haley, E.A. Marquis, G.D. Smith, M.P. Moody, Ultramicroscopy **132**, 271–278 (2013)
32. R.K. Marceau, L.T. Stephenson, C.R. Hutchinson, S.P. Ringer, Ultramicroscopy **111**, 738–742 (2011)
33. E.A. Jaegle, P.P. Choi, D. Raabe, Microsc. Microanal. **20**, 1662–1671 (2014)
34. R.P. Kolli, D.N. Seidman, Microsc. Microanal. **13**, 272–284 (2007)
35. D.J. Larson, T. Prosa, R. Ulfig, B. Geiser, T.F. Kelly, Local Electrode Atom Probe Tomography (Springer, 2014)
36. W. Lefebvre-Ulrikson, F. Vurpillot, X. Sauvage, Atom Probe Tomography Put Theory into Practice (Elsevier, 2016)
37. D. Haley, 3Depict—Visualisation & Analysis for Atom Probe, 2010
38. T. Philippe, F. De Geuser, S. Duguay, W. Lefebvre, O. Cojocaru-Miredin, G. Da Costa, D. Blavette, Ultramicroscopy **109** (2009)

Comparative Study on Short Time Oxidation of Un-Irradiated and Protons Pre-Irradiated 316L Stainless Steel in Simulated PWR Water

M. Boisson, L. Legras, F. Carrette, O. Wendling, T. Sauvage, A. Bellamy, P. Desgardin, L. Laffont and E. Andrieu

Abstract Achieving a better understanding of the Irradiation Assisted Stress Corrosion Cracking resistance is one of the issues to improve the durability of Pressurized Water Reactors. To do so, assessing the interaction of irradiation defects with oxidation of internal vessel bolts, made of 316L alloy, is crucial. In this work we studied the effect of protons pre-irradiations at 1 dpa on the very first steps of oxidation (1 min < t < 24 h) in simulated PWR environment. The morphology of the oxide layer was investigated using optical microscopy and Scanning Electron Microscopy. The oxidation kinetics for short term oxidation is discussed based on the obtained results. It was observed that crystallographic orientation has an effect on the oxidation process. The level of cold-work and the presence of precipitates were taken into account and both seemed to accelerate the oxidation kinetic. Finally, irradiation also tended to speed-up the oxidation phenomenon.

Keywords Irradiation · Oxidation · Austenitic stainless steel · IASCC

Introduction

Austenitic stainless steels are widely used as structural materials in Pressurized Water Reactors (PWRs) because of their good mechanical properties and their resistance to corrosion. In PWRs the lower core internals, including baffle bolts, are made of austenitic stainless steels. Baffle former bolts have in some cases failed by

M. Boisson (✉) · L. Legras · F. Carrette
EDF R&D, EDF Lab Les Renardières—MMC, Avenue Des Renardières—Ecuelles, 77818 Moret Sur Loing, France
e-mail: marylou.boisson@edf.fr

O. Wendling · T. Sauvage · A. Bellamy · P. Desgardin
CNRS, CEMHTI UPR3079, Univ. Orléans, F-45071 Orléans, France

M. Boisson · L. Laffont · E. Andrieu
CIRIMAT, Université de Toulouse, CNRS, INPT, UPS, ENSIACET, 4 Allée Emile Monso BP 44362, 31030 Toulouse Cedex 4, France

J.H. Jackson et al. (eds.), *Proceedings of the 18th International Conference on Environmental Degradation of Materials in Nuclear Power Systems – Water Reactors*, The Minerals, Metals & Materials Series, https://doi.org/10.1007/978-3-319-68454-3_66

intergranular cracking due to Irradiation Assisted Stress Corrosion Cracking (IASCC). Indeed, in service bolts are subjected to mechanical loadings, irradiation and primary environment. Due to their close vicinity to the core, they are subjected to very high neutron irradiation of up to 80 dpa during the lifetime of the plant. Irradiation leads to several well-known modifications of the material's microstructure and microchemistry such as dislocations loops, cavities, radiation induced segregation (RIS) etc. which in turn lead to changes in the mechanical properties [1–11]. These changes may also affect the oxidation process.

Since the formation of a passive layer on stainless steel is a key phenomenon in the corrosion behavior, it is necessary to better understand the impact of irradiation on the oxidation phenomenon. Potter and Mann [12], were among the first to describe the oxide layer formed as duplex with an outer part iron rich and an inner part chromium rich. Since then, the structure of the oxide film has been studied in several works and is reported to be a duplex oxide composed of an outer layer of (Fe_3O_4) crystallites and a continuous inner layer of an AB_2O_4 spinel (A and B = Fe, Cr and Ni) rich in chromium. Perrin, Gupta and Dumerval [13–15], have studied the effect of the irradiation on the oxide formed on austenitic stainless steels for long time oxidations. These oxide have been shown to have the same duplex structure and composition as those formed on un-irradiated steels. Moreover, they observed that the inner layer is thinner and richer in chromium on the irradiated area. Furthermore, the crystallographic orientation of the metal has been shown to impact the oxide formation in several studies dedicated to nickel based alloys [16, 17] or austenitic stainless steels [18, 19]. Since stainless steels are known to have an oxidation behavior close to that of nickel based alloys, as both form a duplex oxide scale, it was expected that the crystallographic orientation would impact the stainless steel oxidation mechanism. When dealing with the outer oxide scale made of crystallites, these works showed that orientations closed to [110] have the fastest kinetics while those closed to [111] have the slowest.

Although several authors have already studied the oxide layers formed on austenitic stainless steels without irradiation, the very first steps of oxidation and the impact of irradiation have not yet been well understood. Indeed, for the time being, most of the studies have looked at long exposure times. Studying short oxidation times is thought to be better to understand the first steps of the underlying mechanisms of the oxide formation and growth. Among the few authors that have studied those first steps, Soulas [18, 19], investigated oxidations ranging from 1 min to 24 h and proposed a mechanism for short times oxidation. From the oxide structural and chemical characterizations, he concluded that the native inner layer is chromium enriched and amorphous and will tend to grow as the oxidation progress. When thickening, this inner layer will then crystallize and be composed of nano-grains and, in parallel, crystallites will nucleate and grow at the surface of the oxide. Those nano-grains will evolve into a monocrystalline layer and finally be in epitaxy with the underlying metal grain as the oxidation continues. During the same time, the outer oxide will coalesce and form well shaped and facetted crystallites.

The present study focuses on the oxidation mechanisms of austenitic stainless steel for short time exposure (from 5 min to 24 h) without applied stresses, with

and without irradiation. The aim is to better understand the oxidation process occurring in simulated PWR environment on proton pre-irradiated 316L stainless steel. The crystallographic orientation has been taken into account by mapping some areas of the samples prior to oxidation. Proton implantations have been performed up to 1 dpa at the CEMHTI (Conditions Extrêmes et Matériaux: Haute Température et Irradiation) of Orléans—France to simulate the irradiation occurring in PWRs. Oxidation times of 5 min, 1 h and 24 h have been realized in PWR simulated environment. The outer oxide layers were characterized using optical microscopy and SEM on both irradiated and un-irradiated regions. The cold-work induced by Vickers indents prior to exposure and the influence of the presence of precipitates were also studied to highlight any impact on the oxidation process.

Experimental Methods

Materials

The material investigated is a commercial heat of solution annealed Type 316L from Creusot Loire Industrie provided by EDF R&D. The chemical composition of the alloy is presented in the following Table 1.

Experimental Protocols

Sample Preparation

Three samples destined to be irradiated were machined by Electro Discharge Machining with the following dimensions: 10.85 mm × 11.85 mm × 0.6 mm. Samples were polished from 800 grid SiC paper to 1 µm diamond paste on one side and from 800 grid SiC paper down to colloidal silica (0.04 µm) on the side which was irradiated. The polishing procedure used has been reviewed on a previous work [20]. This polishing induces no strain hardening and few dislocations enabling a study without induced residual stresses.

Table 1 Composition of 316L alloy in weight percent

C	S	N	P	Mn	Si	Ni	Cr	Mo	Cu	Co
0.026	0.004	0.050	0.033	1.80	0.42	11.35	16.3	2.48	0.02	0.06

Proton Irradiation

Some samples were irradiated with proton at the CEMHTI of Orléans to a dose of 1 dpa. Thin samples were required to insure a good thermal transfer. These irradiations were performed at 380 °C and with a dose rate close to 8.5×10^{-6} dpa s^{-1}. The irradiation temperature was chosen according to the equations proposed by Was [21, 22], in order to simulate neutron irradiation occurring in PWRs; see Eqs. 1 and 2 in which K_0 is the damage rate (dpa/s), k Boltzmann's constant (8.617×10^{-5} eV/K), E_m^v the vacancy migration energy ($\sim$1.3 eV), and E_f^v the vacancy formation energy ($\sim$1.9 eV). The damage rate K_{01} was fixed at 4.5×10^{-8} dpa/s and T_1 was fixed at 288 °C to simulate neutron irradiation. The two equations allow optimization of the irradiation conditions to better simulate the Frank loop size and density (Eq. 1), and the radiation induced segregation (Eq. 2). Due to technical issues, the targeted dose rate of 1.4×10^{-5} dpa s^{-1} was not achievable. The irradiations were therefore performed close to 8.5×10^{-6} dpa s^{-1} and the ideal irradiation temperature would have been 370 °C.

$$(loops)T_2 - T_1 = \frac{\frac{kT_1^2}{E_m^v + 2E_f^v} ln\left(\frac{K_{0_2}}{K_{0_1}}\right)}{1 - \frac{KT_1}{E_m^v + 2E_f^v} ln\left(\frac{K_{0_2}}{K_{0_1}}\right)} \quad (1)$$

$$(RIS)T_2 - T_1 = \frac{\frac{kT_1^2}{E_m^v} ln\left(\frac{K_{0_2}}{K_{0_1}}\right)}{1 - \frac{KT_1}{E_m^v} ln\left(\frac{K_{0_2}}{K_{0_1}}\right)} \quad (2)$$

An irradiation dose of 1 dpa was chosen to be close to the saturation of the dislocation loops and the RIS phenomenon as the loop size and density saturation occur at approximately 1 dpa and the RIS tends to saturate between 0 and 5 dpa [1, 4, 5, 23, 24].

Irradiated samples were then polished with colloidal silica to remove the possible oxide formed during the irradiation and to reach the irradiated area at the desired dose at a depth of about 2 µm. The duration of this mechanical polishing was obtained after calibrating the polishing kinetics using Vickers indentation of 500 g to measure the abraded depth.

Stopping and Range of Ions in Matter (SRIM) calculations were performed with Kinchin-Pease cascades to obtain the damage profile and using a displacement energy of 40 eV [25–27]. The total penetration depth of the 1 meV protons was about 15 µm. The irradiated zone in each sample was of 4 mm in diameter, so that all samples had both irradiated and un-irradiated regions. This enables comparative studies of the oxides formed on irradiated and un-irradiated areas on the same sample. In order to locate the irradiated regions, four indentations were performed on each sample around the irradiated spot visible after exposure to simulated PWR environment. Global aspect of the samples after exposure from 5 min to 24 h are presented on Fig. 1.

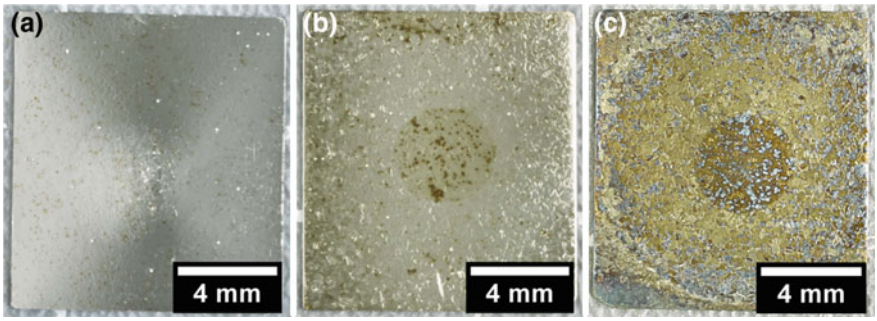

Fig. 1 Pictures of the irradiated samples after **a** 5 min oxidation **b** 1 h oxidation **c** 24 h oxidation

EBSD Mapping

Electron backscatter diffraction (EBSD) mapping was carried out before oxidation using a SEM TESCAN Mira3 to take into account crystallographic orientation effects on oxidation kinetics. An average of 22 EBSD maps of 2 mm $\times$ 2 mm were acquired on each sample and Vickers indents were realized on strategic spots of the samples both to help navigate at a microscopic level after oxidation and to explore the effect of local pre-straining on the associated oxidation behavior.

Oxidation Procedure

Before oxidation, the native chromium rich oxide formed during mechanical polishing by colloidal silica was removed using argon ion polishing (4.5 keV, 90 s, 50° rocking angle, 25 rocks/s 30 rpm using Gatan PECS). Oxidations were performed in simulated PWR environment (325 °C, 155 bars, 1000 ppm B, 2 ppm Li, 30 cc/kg H_2, $O_2 \leq 5$ ppb and $pH_{325\,°C} = 7{,}3$) using a specific oxidation loop developed at EDF R&D and called "TITANE loop" [28]. The high pressure and high temperature part of the loop is made of Titanium to avoid metallic contamination from the circuit. The ion concentration in the water is controlled through ion resins filters avoiding any redeposition problems or supersaturation of the medium. The chemistry of the medium is controlled before and after each oxidation test. A small cell is coupled to the main loop to carry out short time oxidations (down to 1 min). In this cell the samples are in contact with the PWR simulated media only during the oxidation time and not during the conditioning and deconditioning phases of the primary water of the loop. To do so, samples were heated to test temperature under Argon flux and 5% hydrogen to avoid oxidation and at the end of the exposure the medium is flushed out by an argon flux. Oxidation times ranging from 5 min to 24 h were performed (5 min, 1 h and 24 h).

Experimental Techniques

Macroscopic Studies

After oxidation the samples were observed with optical microscopy to assess the oxidation quality and to give an overview of the oxidation effects. The images were compared to the EBSD maps to pinpoint any relation between the oxide layer (estimated using the reflexivity differences) and the crystallographic orientation of the substrate.

Microscopic Studies

All samples were observed with a FEI Dual Beam Helios nanolab 600 after oxidation. The size, density and morphology of the external crystallites were observed with this microscope. Images were acquired on specific grain orientation by using the EBSD maps acquired before oxidation. SEM was used to look closely at the impact of strain induced by the Vickers indentation performed before oxidation and the influence of the presence of precipitates on the oxidation phenomenon.

Results

Surface Observations Using Optical Microscopy

Metallographic Observations

In Fig. 2, the irradiated area appears darker on each sample regardless of the oxidation time. Preferential oxidation seems to happen near the precipitates and is enhanced in the irradiated region as visible on Fig. 2. Moreover, on each optical image the coloration of one grain from another is different both on the irradiated and un-irradiated regions. The grain or area coloration may signify when it is darker that the oxide formed is thicker and thus decreases the light-reflecting ability on those regions. The morphology of the crystallites or even the chemistry of the oxides may also play a role in the coloration change.

Observations Using the Crystallographic Orientation of the Underlying Metal

In this work three specific grain orientations of the alloy have been studied: [100], [110] and [111]. As reported previously, the observed coloration is related to the light reflecting ability of a specific area. When looking closely at the grain

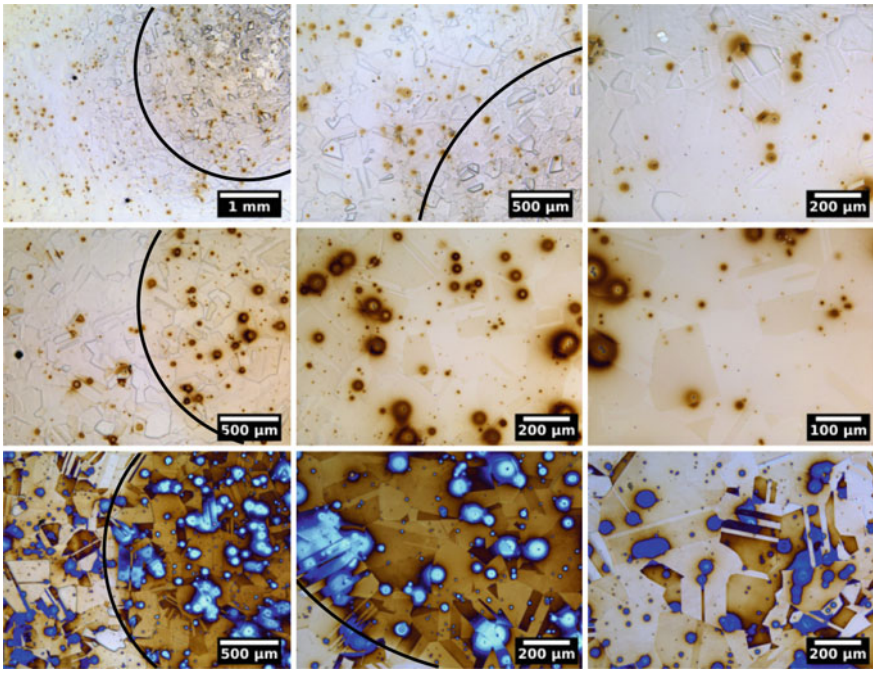

Fig. 2 Optical images of the samples, first to last row 5 min oxidation, 1 h oxidation and 24 h oxidation, respectively

coloration as compared to their orientation with the EBSD maps acquired before oxidation it appears that some orientations are more sensitive to oxidation than others (cf. Fig. 3). Indeed, grain orientation close to [100] come up darker than any of the two others studied orientations as opposed to [111] grain orientation which is the lighter (shown by the arrows on Fig. 3). This oxidation behavior is the same for irradiated as well as unirradiated areas, since no differences were observed in this respect between the two areas. The orientation effect can also distinctively be seen by looking closely at twins and especially on those which have a precipitate close by causing an advanced oxidation. On those twinned grains the oxidation is preferential on only one of the two orientations leading to the conclusion that orientation plays a role in the oxide formation and growth. These results clearly suggest that grain orientation affects the oxide growth, structure, morphology or chemistry for both irradiated and unirradiated area.

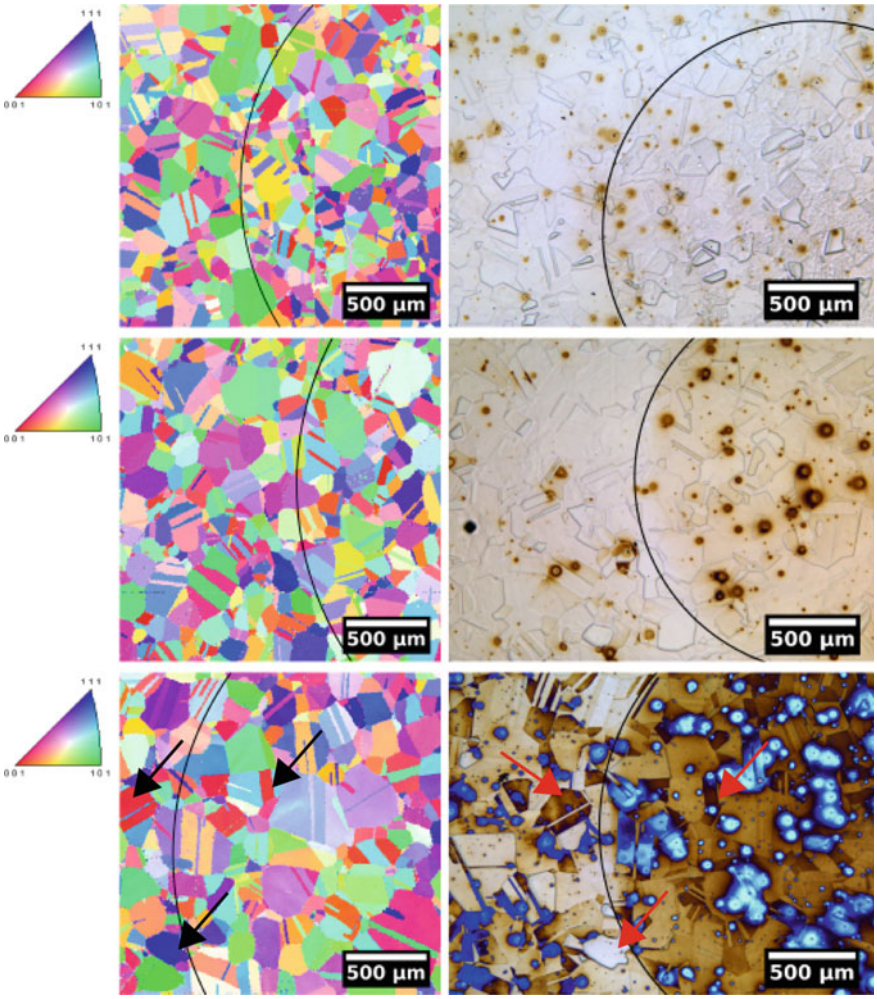

Fig. 3 EBSD maps and optical microscopy images on the same area for first row 5 min oxidation sample middle row 1 h oxidation sample and third row 24 h oxidation sample

Surface Observations Using SEM

Un-Irradiated Area Without Cold-Working

The three oxidation times were studied with SEM on specific grain orientations ([100], [110] and [111]). The SEM micrographs are presented on Figs. 4, 5 and 6 for 5 min, 1 and 24 h oxidation respectively. Regardless of the oxidation time or the orientation of the underlying grains, crystallites are present on top of all the samples. For the 5 min oxidation test the crystallites formed are small, overall

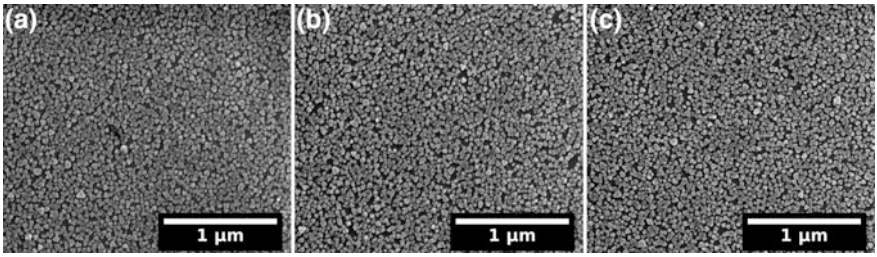

Fig. 4 SEM images of the sample oxidized 5 min on grains **a** [100] **b** [110] and **c** [111]

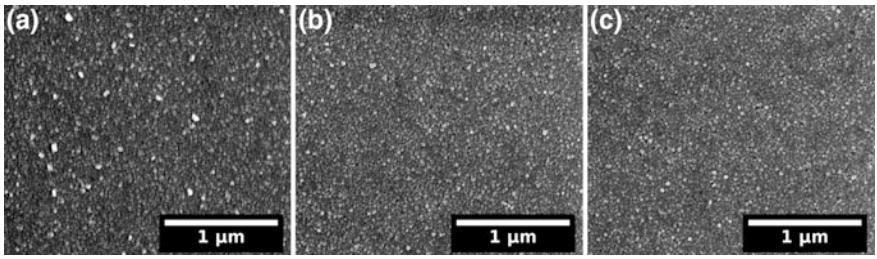

Fig. 5 SEM images of the sample oxidized 1 h on grains **a** [100] **b** [110] and **c** [111]

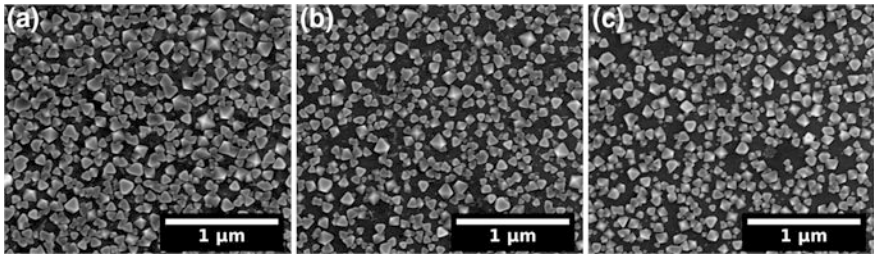

Fig. 6 SEM images of the sample oxidized 24 h on grains **a** [100] **b** [110] and **c** [111]

triangular and relatively dense ($\sim$30 nm in size and an overall coverage of the surface of $\sim$56–62%). After 1 h oxidation, the outer oxide is denser and covers the whole surface but the crystallites size is much smaller, about 5–20 nm. The crystallites are more globular than after 5 min oxidation. Finally, after 24 h oxidation the crystallites are well shaped and faceted, their size is much larger and their density decrease. Moreover, they are bigger and denser on the [100] grain than on the other two orientations. The outer oxide size is close to 87 nm on grain [100] while approximately 74 nm on grains [110] and [111]. As far as the density, the coverage is almost 56% for the [100] grain against a coverage of 42% on [110] and [111] grains. No clear differences in shapes or morphologies of the outer oxides is noticed as a function of the grain orientation for all three oxidation durations.

While clear differences were previously seen with optical microscopy and a crystallographic orientation impact on the oxide was highlighted, the SEM observations of the outer oxide do not concur as for the grain orientation. Since no obvious differences in the crystallites morphologies were seen, it seems that the grain contrast observed on the optical image cannot be explained with the outer oxide thickness or roughness. Advanced characterizations of the inner and outer oxide structure, thickness and chemistry have to be done to conclude on the grain orientation effect.

As previously seen on the optical images of the oxidized samples, the oxidation behavior seem to be impacted by the presence of inclusions. To better understand this, the inclusions were analyzed using EDXS before and after oxidation. Most of them consist of MnS precipitates and Cr, Mn, Ti, Al oxides (cf. Fig. 7). The latter tended to grow on MnS inclusions. After oxidation no or few residuals MnS precipitates were found indicating that they were completely oxidized during the corrosion test. In austenitic stainless steels, MnS precipitates are known to generate pitting [29–31]. This corrosion process is likely to be observed in the present study. It seems to induce local changes in the oxidation kinetic by speeding it up.

These observations were confirmed with more SEM observations as presented in Fig. 8. Some precipitates are still present but other have been dislodged during the polishing. Both cases may impact the local oxidation behavior of those areas. In the near vicinity of the precipitates or dislodged precipitates the outer oxide is denser and crystallites are bigger. Distribution and coverage gradients of the oxide is seen by moving gradually away from those areas. The oxidation appears more advanced on these regions indicating that inclusions or holes suspected to contain an inclusion lead to a speeding up of the oxidation kinetic.

Un-Irradiated Area with Cold-Working

As presented in the experimental protocol, Vickers indentations have been made on the samples in order to get geographic markers that helps to navigate. After oxidation these indents were observed and some SEM images are presented in Fig. 9 and Fig. 10. As visible on Fig. 9a, some plastic strain was induced by the indentation of the material and results in the appearance of slip bands. Figure 9b presents a similar area on an oxidized sample. Crystallites seem to nucleate preferentially on

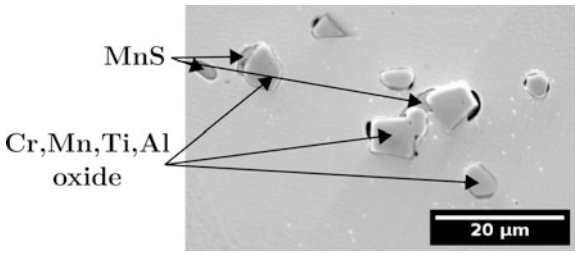

Fig. 7 SEM image of inclusions before oxidation

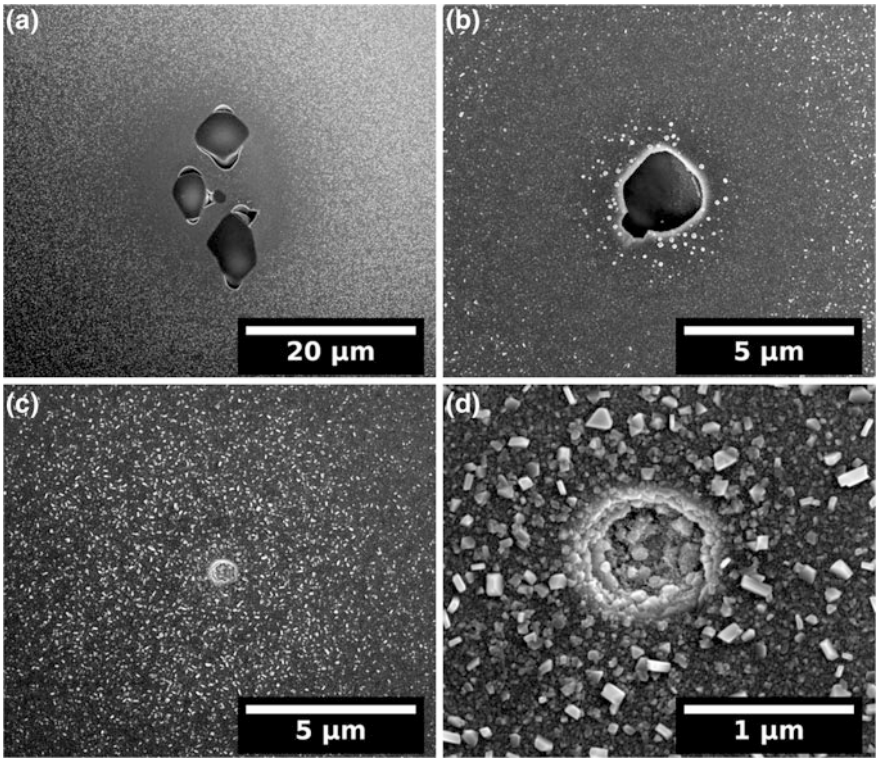

Fig. 8 SEM image of inclusions and dislodged inclusions after oxidation

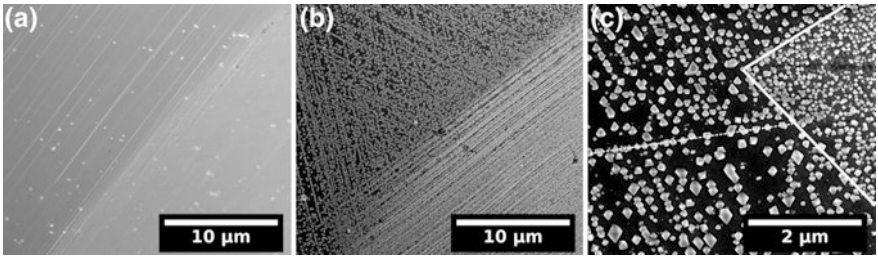

Fig. 9 SEM images of a Vickers indent on a **a** un-oxidized sample **b** oxidized sample **c** oxidized samples with a grain boundary (dashed line) close to the indent (solid line)

these slip bands. Moreover, really close to the indent a grain boundary can be seen on Fig. 9c and crystallites have different shapes on either side of the grain boundary.

No differences in size or shape of the crystallites can be noticed between the oxide formed on the grains and the oxide on top of the slip bands (see Fig. 10).

However, crystallites that grow on top of the slip bands start to naturally coalesce (cf. Fig. 10d). As a strain gradient is present around the indents, several images were acquired first near the indent (Fig. 10a, b), and then a bit further away (Fig. 10c, d). Figure 10a was taken near the indent while the image of Fig. 10c was captured further off and it clearly appears that the outer oxide is denser but also smaller near the indent. The coverage is close to 25% for the oxide formed near the indent on Fig. 10a against 18% for Fig. 10c. As for the crystallites size, it doubles further away from the indent ($\sim$110 nm on Fig. 10b against 235 nm on Fig. 10d). In both cases the crystallites formed on cold-worked material are bigger than the ones on stress free area where the crystallite size was smaller than 80 nm for the same oxidation time. Figure 10a also has the advantage of presenting a clear grain boundary in its middle. As the grains on either side have different crystallographic orientations the slip bands are formed according to the grain orientation. The outer oxide alignment is not the same and the grain boundary clearly act as a barrier. Moreover, the outer oxide morphology and density from one grain to another are not the same.

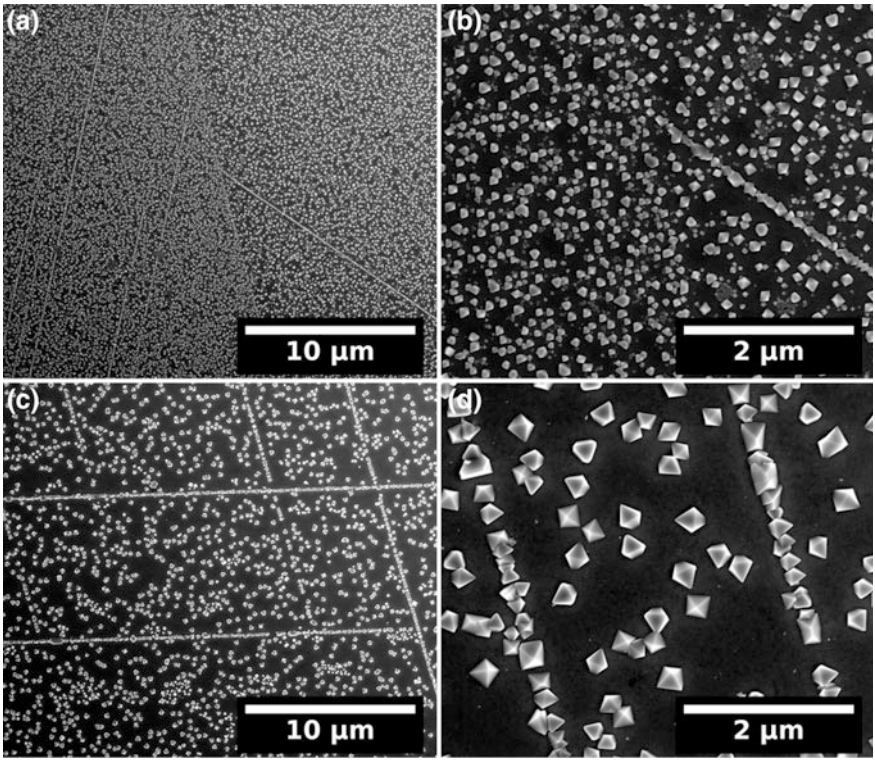

Fig. 10 SEM images on an oxidized sample of **a** a Vickers indent **b** a grain boundary close to the indent **c** and **d** area further off the indent

In presence of cold-work the outer oxide tends to preferentially grow on top of the slip bands and the crystallites are bigger, well-shaped and geometrical. It also highlights that the crystallographic orientation of the substrate impacts the oxide formation. Furthermore, the crystallites are smaller and denser as the cold-work increase. All these results suggest that the oxidation kinetic is modified when cold-work is present.

Irradiated Area Without Cold-Working

The oxide formed on the irradiated area was compared to the oxide developed outside this region. Figs. 11, 12 and 13 present the outer oxide after 5 min, 1 h and 24 h oxidation respectively. For the sample oxidized 5 min, the [100] grain is the only one to present a clear difference between the un-irradiated and the irradiated areas. On the irradiated [100] grain the morphology of the crystallites is more faceted and they appear mostly as square based pyramids. The rest of the outer oxide is globular and looks like nuclei on this irradiated grain. If a different morphology was observed no change in size was noticed with or without irradiation on the [100] grains. Comparatively, the other two orientations do not present any irradiation effect on the outer oxide, as the crystallite size and shape are equivalent. This observation seems to highlight that irradiation is likely to accelerate the oxidation kinetic. On the 1 h oxidized sample no difference are highlighted between irradiated and un-irradiated grains (see Fig. 12). Finally, for the 24 h oxidized sample (see Fig. 13) the outer oxide is denser on the irradiated grains but the

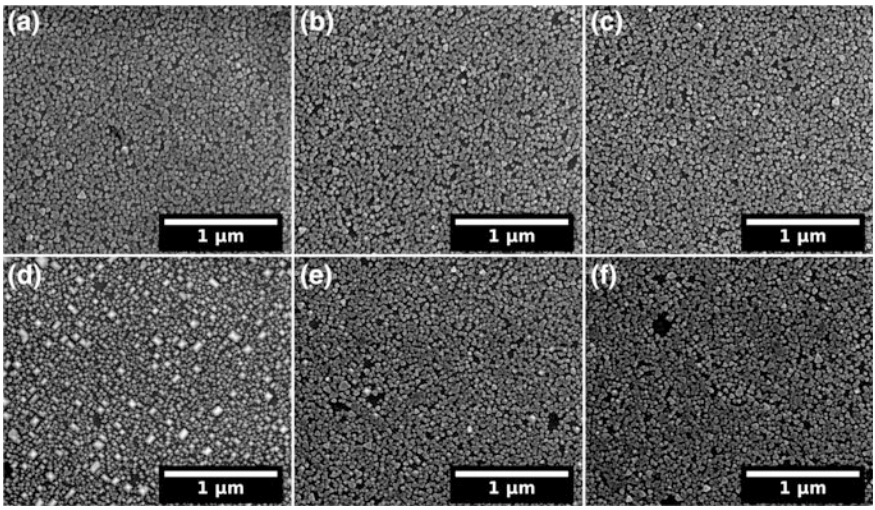

Fig. 11 SEM images of the outer oxide formed after 5 min oxidation on a grain **a** [100] un-irradiated **b** [110] un-irradiated **c** [111] un-irradiated **d** [100] irradiated **e** [110] irradiated **f** [111] irradiated

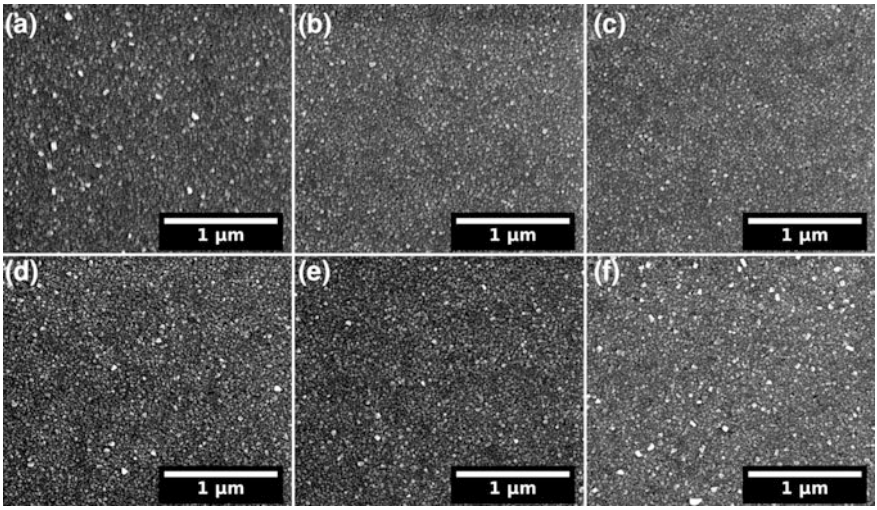

Fig. 12 SEM images of the outer oxide formed after 1 h oxidation on a grain **a** [100] un-irradiated **b** [110] un-irradiated **c** [111] un-irradiated **d** [100] irradiated **e** [110] irradiated **f** [111] irradiated

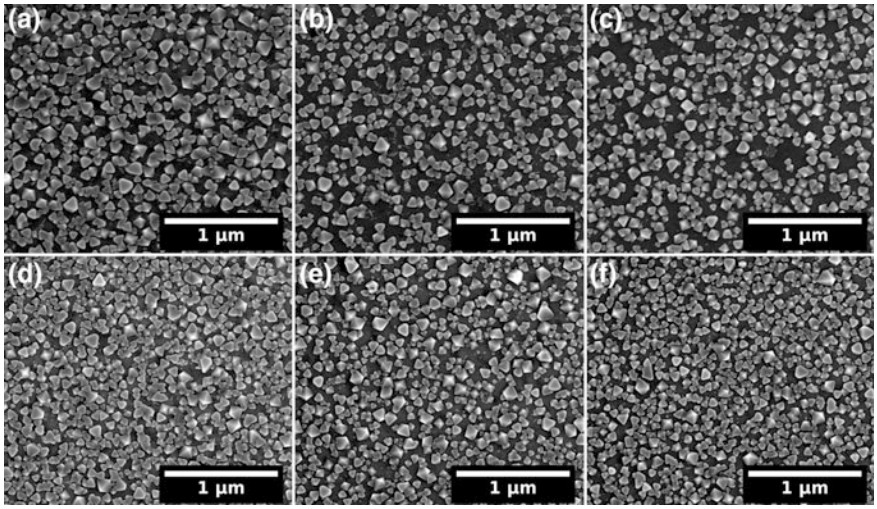

Fig. 13 SEM images of the outer oxide formed after 24 h oxidation on a grain **a** [100] un-irradiated **b** [110] un-irradiated **c** [111] un-irradiated **d** [100] irradiated **e** [110] irradiated **f** [111] irradiated

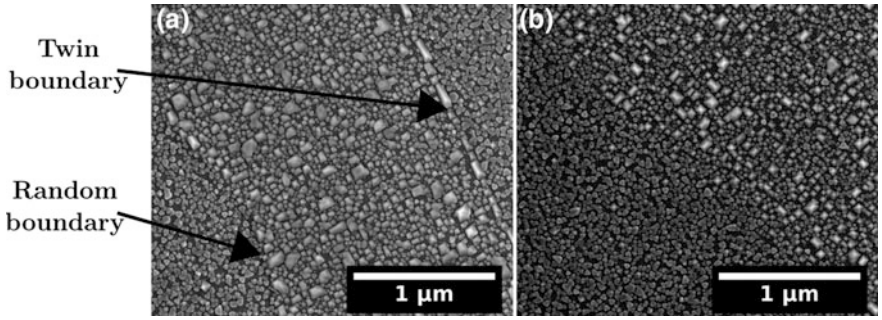

Fig. 14 SEM images of the outer oxide formed after 5 min oxidation on the irradiated area for **a** and **b** grain boundaries between a random grain and a grain whose orientation was close to [100]

crystallites size are really close. This result tends to indicate that irradiation accelerates the oxidation kinetic.

As the crystallites on the irradiated area of the 5 min oxidized sample were the most affected by the irradiation as compared to the other oxidation durations, some investigations were made on this region. It clearly appears on Fig. 14 that the crystallographic orientation plays a role in the development of the outer oxide. The grain boundaries are easily visible thanks to the change in shape and size of the crystallites. Moreover on Fig. 14a, two different behaviors at grains boundaries can be observed. On the twin boundary on the right side, crystallites seem to coalesce and tend to grow up rapidly. This may indicate that the grain boundary nature influence the oxidation kinetic.

Discussion

Effect of Oxidation Time

Morphological evolution of the outer oxide layers and oxidation kinetics as a function of the oxidation time were studied. Short oxidation times were investigated in this work (5 min, 1 h and 24 h) (cf. Figs. 4, 5 and 6). It appears that at 5 min oxidation, crystallites are formed and are relatively small ($\sim$30 nm in size). The overall coverage of the surface is about $\sim$56 at 62% and the crystallites are for the majority geometrical. After 1 h oxidation, the outer oxide is more globular, denser and cover the whole surface but the crystallites are smaller than after 5 min oxidation. It might be because the crystallites, have gone through a dissolution/reprecipitation phenomenon as their size and globular morphology suggest. Finally, after 24 h oxidation the crystallites are well shaped and faceted, their size is much larger and their density decrease. Moreover they are bigger and denser on the [100] grain than on the other two. This observation highlights the growth and coalescence phenomenon of the crystallites.

Comparing these results to the ones obtained by Soulas [18] on the same heat with different the grain size, it appears that the oxidation kinetics seems slightly different. As observed by Soulas, the crystallites becomes more faceted and less dense as the oxidation time increases. But for same oxidation times in these two studies, the outer oxide does not possess the exact same size or morphology. Moreover, through the cold-work and irradiation acceleration of the oxide kinetics, crystallographic orientation seems to be the next step in the oxidation kinetic as proposed by Soulas [18].

Crystallographic Orientation Effect

Since grain coloration is not the same for every grain (see Figs. 2 and 3) and is dependent of the crystal orientation, it can be assumed that the thickness, chemistry or morphology of the oxide differ according to the underlying grain orientation. Therefore, some grain orientations are preferentially oxidized as compared to other orientations.

Soulas [18, 19], also studied the effect of crystallographic orientations in his work and their impact on the duplex oxide. He showed that the structure and chemistry of the oxide were independent to crystallographic orientation of the underlying metal grain but that their thickness (inner oxide), morphology, density and size (outer oxide) were depending on the crystallographic orientation of the metal grain on which the oxide grew. Soulas concluded that the [111] grains had the fastest oxidation kinetics for short time exposure. From the optical images as compared to EBSD maps acquired before oxidation Soulas suggested that the darker grains corresponding to [111] grain orientations were the thicker and confirmed this by a TEM study on the inner oxide. But, in the present work, as the darker grains are [100] orientation they should have the thicker inner oxides. Further analysis have to be carried out to verify this point and to better understand the oxidation kinetics difference depending on the crystallographic orientation of the sub lying grain of metal.

Inclusions Effect

Results from optical microscopy and SEM indicate that the presence of inclusions modify the density and morphology of the oxide formed (see Fig. 8). Since there is a gradient of density and size of oxide crystallites around these inclusions, the outer oxide appearance as well as oxidation kinetic seems to be modified. These precipitates may locally change the chemistry of the boundary layer in the media when MnS precipitates oxidize, affecting the oxidation process. By looking at the higher outer oxide density around precipitates, the conclusion that the dissolution of MnS inclusions speeds-up the oxidation process can be drawn. Indeed, these are known

to induce pitting, releasing Mn cations into the media. No high Mn cations content was found in the media after oxidation since the measured concentration was below 10 ppb. But if they are released in the boundary layer, the Mn might also reprecipitate and affect the oxidation process.

Cold-Work Effect

The cold-work induced by Vickers indentation before the oxidation have an impact on the crystallites formed. The strain due to the indentation caused the formation of slip bands in the material on which the crystallites tend to preferentially grow (see Fig. 9). Since the inner layer may grow by anionic diffusion and the outer layer may grow by mixed diffusion (anionic and cationic), the slip bands would act as a preferential diffusion path, explaining the formation and coalescence of well-aligned crystallites along those slip bands. It was noticed in this study that the more the cold work there is the more the crystallites are small and dense (cf. Fig. 10) which could be because of the high density of defects induced by the cold-working leading to numerous preferential nucleation sites.

Comparing the cold-worked and unstrained areas shows that the presence of strain induced growth of bigger crystallites which are well-shaped and more geometrical. In addition, the outer oxide formed on strained area is dependent on the orientation of the underlying grain. Indeed, grain boundaries are highlighted and the morphology and density of the outer oxide differ from one grain to another. Since this is not the case on strain free regions, it suggests that the oxidation is more advanced on cold-work regions. Based on these results and as the literature suggested [17, 32–34], cold-work impact the oxide formed and seems to accelerate the oxidation process.

Irradiation Effect

On optical micrographs, the irradiated areas observed have different colorations than the un-irradiated one as seen on Fig. 2. It clearly attests to differences between the oxides formed on these regions. Moreover, the preferential oxidation occurring near inclusions is enhanced on the irradiated area attesting to a more advanced oxidation process. From the SEM study the same conclusion can be drawn (cf. Figs. 11, 12 and 13). The outer oxides on [100] grains differ for the irradiated and un-irradiated area on the sample oxidized 5 min as seen on Fig. 14. Those formed on the irradiated grain are well shaped and with a different morphology than on the other grains. It might indicate that [100] have the fastest kinetic regarding the outer oxide.

Perrin et al. [13] studied a longer oxidation time with protons pre irradiated samples and observed the outer layers. Many crystallites had grown onto the

irradiated area as the irradiation defects acted as preferential nucleation sites. As observed by Perrin et al., Dumerval [15] also concluded that irradiation defects close to the surface would impact the nucleation and growth of the outer layer. In their study, crystallites were smaller on irradiated regions. Gupta [14], also conducted oxidation test on irradiated material and draw the same conclusion that irradiation decreased the crystallites size. Comparing these results to the one obtained in this work it appears that no change in term of in size or density was seen for most of the studied samples. It might be because the oxidation time used in on these papers are much longer than the ones performed here, hence the outer layer would still grow on un-irradiated samples but reach faster a stationary state for the irradiated area which seems to show the fastest kinetics.

This study seems to indicate that irradiation causes to accelerate the oxidation kinetic and that samples are more oxidized on the irradiated region. More detailed investigations have to be done to compare the chemistry and thickness, on a same grain orientation between the irradiated and un-irradiated areas and finally in order to conclude on the consequence of irradiation on the oxide layers.

Conclusion

This study assessed the effect of proton pre-irradiation, cold-work and inclusions on 316L stainless steel on the oxidation process. Three oxidation tests of 5 min, 1 h and 24 h in PWR primary simulated media have been performed on stainless steel samples, which were protons irradiated on a small area allowing to study on one sample both un-irradiated and irradiated regions after oxidation. Moreover, indentations were used to investigate the effect of cold-work induced before oxidation. To better understand the crystallographic orientation effect, and the irradiation impact on the oxides further analysis, as TEM study, have to be carried out to study the thickness, structure and chemistry of the oxide layer, both internal and external. Since the initiation of IASCC crack implies the oxide scale breakdown, it is important to investigate the oxidation mechanism as well as the nature and structure of the oxide formed on the surface and at grain boundaries where the cracks are likely to occur. TEM studies of the oxide scale and inner oxide/metal interface as well as the oxide formed at grain boundaries and RIS on these will be needed to better understand the impact of irradiation on the oxidation mechanism and correlate the results to the IASCC mechanism. As of now, the following results were observed using optical microscopy, EBSD mapping and SEM:

- Crystallites are formed at the surface for all oxidation times and as the oxidation duration increases, the outer oxide becomes more faceted and well-shaped.
- A crystallographic orientation effect on the oxide formed was highlighted using optical microscopy and EBSD mapping. Looking at irradiated or cold-wok area revealed that the outer oxide morphology is dependent of the underlying metal grain orientation. Moreover, from observations on the irradiated area of the

5 min oxidized sample showed that the outer oxide is likely to have the fastest kinetic on [100] grain.

- Inclusions and especially MnS seems to be oxidized during the tests inducing a preferential oxidation around precipitates. Inclusions tends to accelerate the oxidation process and highlight even more the crystallographic orientation of the underlying metal grain impact on the oxidation kinetic.
- Cold-work caused the formation of well aligned crystallites on top of the slip bands and the induced defects of the cold-working acted as preferential nucleation sites for the crystallites. Overall the cold-work is responsible for a more advanced oxidation.
- Irradiation tended to accelerate the oxidation kinetic.

Acknowledgements The authors would like to thank O. Wendling, T. Sauvage, A. Bellamy and P. Desgardin for setting up the irradiation experiment and carrying out the irradiations and, T. Girard (EDF R&D) for conducting the oxidation tests. The authors would also like to acknowledge M. Mahé (EDF R&D) for the EDXS analysis of the precipitates.

References

1. S.M. Bruemmer et al., Radiation-induced material changes and susceptibility to intergranular failure of light-water-reactor core internals. J. Nucl. Mater. **274**(3), 299–314 (1999)
2. G.S. Was, P.L. Andresen, Irradiation-assisted stress-corrosion cracking in austenitic alloys. JOM **44**(4), 8–13 (1992)
3. C. Pokor et al., Irradiation damage in 304 and 316 stainless steels: experimental investigation and modeling. Part I: Evolution of the microstructure. J. Nucl. Mater. **326**(1), 19–29 (2004)
4. D.J. Edwards, E.P. Simonen, S.M. Bruemmer, Evolution of fine-scale defects in stainless steels neutron-irradiated at 275 °C. J. Nucl. Mater. **317**(1), 13–31 (2003)
5. S.J. Zinkle, P.J. Maziasz, R.E. Stoller, Dose dependence of the microstructural evolution in neutron-irradiated austenitic stainless steel. J. Nucl. Mater. **206**(2), 266–286 (1993)
6. S.J. Zinkle, R.L. Sindelar, Defect microstructures in neutron-irradiated copper and stainless steel. J. Nucl. Mater. **155**, 1196–1200 (1988)
7. A. Etienne, *Etude des effets d'irradiations et de la nanostructuration dans des aciers austénitiques inoxydables* (Ph.D thesis, Université de Rouen, Rouen, 2009)
8. P.J. Maziasz, Overview of microstructural evolution in neutron-irradiated austenitic stainless steels. J. Nucl. Mater. **205**, 118–145 (1993)
9. T.R. Allen et al., The effect of dose rate on the response of austenitic stainless steels to neutron radiation. J. Nucl. Mater. **348**(1–2), 148–164 (2006)
10. B.H. Sencer et al., Microstructural origins of radiation-induced changes in mechanical properties of 316 L and 304 L austenitic stainless steels irradiated with mixed spectra of high-energy protons and spallation neutrons. J. Nucl. Mater. **296**(1–3), 112–118 (2001)
11. D.J. Edwards et al., Influence of irradiation temperature and dose gradients on the microstructural evolution in neutron-irradiated 316SS. J. Nucl. Mater. **317**(1), 32–45 (2003)
12. E.C. Potter, G.M.W. Mann, Oxidation of mild steel in high-temperature aqueous systems. in Presented at the 1st International Congress of Metallic Corrosion (London, 1961) 417
13. S. Perrin et al., Influence of irradiation on the oxide film formed on 316 L stainless steel in PWR primary water. Oxid. Met. **80**(5–6), 623–633 (2013)

14. J. Gupta, *Intergranular Stress Corrosion Cracking of Ion Irradiated 304L Stainless Steel in PWR Environment* (Ph.D thesis, Institut National Polytechnique de Toulouse, Toulouse, 2016)
15. M. Dumerval, Effet des défauts d'implantation sur la corrosion des aciers inoxydables austénitiques en milieu primaire des réacteurs à eau pressurisée (Ph.D thesis, Université de Grenoble, Grenoble, 2014)
16. A. Machet, Etude des premiers stades d'oxydation d'alliages inoxydables dans l'eau à haute température (Ph.D thesis, Université Pierre et Marie Curie—Paris VI, Paris, 2004)
17. S. Gardey, Etude de la corrosion généralisée des alliages 600, 690 et 800 en milieu primaire—Contribution à la compréhension des mécanismes (Ph.D thesis, Université Pierre et Marie Curie, Paris, 1998)
18. R. Soulas, Effet de la cristallographie sur les premiers stades de l'oxydation des aciers austénitiques 316L, (Ph.D thesis, Institut National Polytechnique de Grenoble, Grenoble, 2012)
19. R. Soulas et al., TEM investigations of the oxide layers formed on a 316L alloy in simulated PWR environment. J. Mater. Sci. **48**(7), 2861–2871 (2013)
20. X. Sun, *Study of deformed layer formed during mechnical stages of specimen preparation for EBSD and TEM* (Report EDF R&D and PHELMA, Moret Sur Loing, 2016)
21. G.S. Was, T.R. Allen, Radiation damage from different particle types, Radiat. Eff. Solids—NATO Science Series II—Mathematics, Physics and Chemistry (235, Springer, 2007), 65–98
22. G.S. Was, *Fundamentals of Radiation Materials Science* (Springer, Berlin, 2007)
23. G.S. Was et al., Emulation of neutron irradiation effects with protons: validation of principle. J. Nucl. Mater. **300**, 198–216 (2002)
24. B.H. Sencer et al., Proton irradiation emulation of PWR neutron damage microstructures in solution annealed 304 and cold-worked 316 stainless steels. J. Nucl. Mater. **323**(1), 18–28 (2003)
25. J.F. Ziegler, J.P. Biersack, in *The Stopping and Range of Ions in Matter*,ed. by D.A. Bromley. Treatise on Heavy-Ion Science (6: Astrophysics, Chemistry, and Condensed Matter, Boston, MA: Springer US, 1985), 93–129
26. J.F. Ziegler, M.D. Ziegler, J.P. Biersack, SRIM – The stopping and range of ions in matter (2010). Nucl. Instrum. Methods Phys. Res. Sect. B: Interact. Mater. Atoms **268**(11–12), 1818–1823 (2010)
27. R.E. Stoller et al., On the use of SRIM for computing radiation damage exposure. Nucl. Instrum. Methods Phys. Res. Sect. B **310**, 75–80 (2013)
28. T. Couvant, A. Herbelin, Adaptation d'une cellule d'oxydation sur la boucle Titane - Cahier des clauses techniques particulières (Note EDF, EDF R&D, Moret-sur-Loing, H-T29-2007-03241-FR, 2008)
29. G. Wranglen, Pitting and sulphide inclusions in steel. Corros. Sci. **14**(5), 331–349 (1974)
30. J. Stewart, D.E. Williams, The initiation of pitting corrosion on austenitic stainless steel: on the role and importance of sulphide inclusions. Corros. Sci. **33**(3), 457–474 (1992)
31. T.L. Sudesh, L. Wijesinghe, D.J. Blackwood, Real time pit initiation studies on stainless steels: the effect of sulphide inclusions. Corros. Sci. **49**(4), 1755–1764 (2007)
32. M. Warzee et al., Effect of surface treatment on the corrosion of stainless steels in high-temperature water and steam. J. Electrochem. Soc. **112**(7), 670–674 (1965)
33. S.E. Ziemniak, M. Hanson, P.C. Sander, Electropolishing effects on corrosion behavior of 304 stainless steel in high temperature, hydrogenated water. Corros. Sci. **50**(9), 2465–2477 (2008)
34. S. Ghosh, M.K. Kumar, V. Kain, High temperature oxidation behavior of 304L stainless steel—Effect of surface working operations. Appl. Surf. Sci. **264**, 312–319 (2013)

Hydrogen Trapping by Irradiation-Induced Defects in 316L Stainless Steel

Anne-Cécile Bach, Frantz Martin, Cécilie Duhamel, Stéphane Perrin, François Jomard and Jérôme Crépin

Abstract The irradiation-induced defects in stainless steel internal components of pressurized water reactors combined with hydrogen uptake during the oxidation process could be a key parameter in the mechanism for Irradiation-Assisted Stress Corrosion Cracking (IASCC). The ultimate aim of this study is to characterize the effects of irradiation defects on hydrogen uptake during the oxidation of an austenitic stainless steel (SS) in primary water. The focus was made on the interactions between hydrogen and these defects. A heat-treated 316L SS containing a low amount of defects is compared with ion implanted samples. Both materials were characterized by Transmission Electron Microscopy (TEM). Hydrogen uptake was then promoted by cathodic charging using deuterium as isotopic tracer for hydrogen. The deuterium distribution was first characterized by SIMS (Secondary Ion Mass Spectrometry) profiles. This technique highlighted some deuterium segregation in link with the localization of implantation-induced defects, i.e. dislocation loops and cavities. Using TDS (Thermal Desorption Spectrometry) experimental results and literature data, a numerical model was used to simulate the deuterium profiles, providing diffusion and trapping/detrapping information associated with irradiation defects in the 316L SS.

A.-C. Bach (✉) · F. Martin
DEN-Service de la Corrosion et du Comportement des Matériaux dans leur Environnement (SCCME), CEA, Université Paris-Saclay, 91191 Gif-sur-Yvette, France
e-mail: annececile.bach@cea.fr

A.-C. Bach · C. Duhamel · J. Crépin
MINES ParisTech, PSL Research University MAT- Centre des matériaux, CNRS UMR 7633, BP 87, 91003 Evry, France

S. Perrin
Laboratoire d'étude des Ciments et Bitumes pour le Conditionnement, CEA, DEN, DE2D, SEAD, 30207 Bagnols-sur-Cèze, France

F. Jomard
Groupe d'Etude de la Matière Condensée, CNRS, UVSQ, 45 Avenue des Etats-Unis, 78035 Versailles cedex, France

J.H. Jackson et al. (eds.), *Proceedings of the 18th International Conference on Environmental Degradation of Materials in Nuclear Power Systems – Water Reactors*, The Minerals, Metals & Materials Series, https://doi.org/10.1007/978-3-319-68454-3_67

Keywords Hydrogen trapping · Irradiation defects · Austenitic stainless steel · Thermal desorption · Modeling

Introduction

Austenitic stainless steels are currently used for several structural components of Light Water Reactors (LWR) as the vessel internals and the associated baffles and bolts in the reactor core. In Pressurized Water Reactor (PWR) the austenitic stainless steels (SS) are exposed to primary water, which is an aqueous solution containing dissolved hydrogen at a temperature ranging between 290 and 325 °C and a pressure of about 155 bar. These materials are subjected to a corrosive environment, mechanical and thermal stresses and also to the neutron flux emitted by the nuclear fuel in the reactor core. Since the eighties, some cracks have been observed on SS baffles and bolts in the reactor core. They could result from a phenomenon denoted Irradiation-Assisted Stress Corrosion Cracking (IASCC) although all the mechanisms are not totally understood yet [1, 2].

Although the effect of hydrogen altering mechanical properties of materials at room temperature [3–5] is well known, its role in the mechanisms of crack initiation and propagation during Stress Corrosion Cracking (SCC) or IASCC is complex and is not a general consensus. A part of absorbed hydrogen localized near a crack tip could act via the classical decohesion mechanism and/or by increasing the local plasticity. Several studies made on nickel-base alloys [6, 7] or stainless steels [8] in primary water showed an effect of hydrogen on crack initiation and propagation during SCC. Zhong et al. [8] studied a 316 stainless steel using Slow Strain-Rate tests in simulated PWR primary water. They highlighted the possible mitigation of the crack initiation by increasing the dissolved hydrogen level and a maximum in the crack growth rate at a dissolved hydrogen content of about 15 cm^3 (STP) H_2/kg H_2O,. Rios et al. [7] found the same behavior for the crack growth rate in Alloy 600, reaching a maximum for an intermediate hydrogen overpressure (4 bar) but showed, in contrast to Zhong, an important reduction of crack initiation time with hydrogen (maximum for 1 bar H_2). Thus the effects of hydrogen are not clearly determined yet but the information available indicates hydrogen is absorbed in the alloy during PWR oxidation process. Indeed, a recent study of Dumerval et al. [9] highlighted, thanks to the GD-OES (Glow discharge Optical Emission Spectroscopy) technique, that a non-negligible amount of hydrogen was incorporated and trapped underneath the oxide/alloy interface during oxidation of 316L SS in simulated PWR primary conditions. Indeed, the primary water is a potential huge source of hydrogen (water and dissolved hydrogen) which can dissociate, for instance in the oxidation process, then diffuse in the alloy and interact with structural defects where it could be trapped. As an illustration, in Dumerval's work [9], the accumulation of hydrogen near the oxide/alloy interface was assigned to trapping at vacancies that were created by cationic growth of the oxide layer.

During in-core nuclear power plant exposure conditions, interactions of neutrons with the alloy atoms induce the creation of structural defects such as vacancies, interstitials, cavities, He bubbles, black dots, dislocation loops… [10–14]. All these defects could be additional trapping sites for hydrogen. The main difficulty in studying hydrogen uptake during PWR exposure stands in the activation of materials under neutron flux that renders analysis much more complex than a 'simple' autoclave exposure. For this reason, a way to cover the whole effects that could affect the integrity of the vessel internals is to study these effects separately then combined in a segmented way, allowing the behavior comparison between pre-irradiated materials and a reference material.

To emulate neutron irradiation defects while avoiding difficulties of neutron irradiation experiments (time, cost, activation…), ion implantation of light or heavy ions are often used. Light ion implantation, like protons, lead to the formation of dislocation loops with a density and a mean size in the same order of magnitude that those created by neutrons irradiation as explained by Was [15, 16]. Moreover some other irradiation characteristics are also in good agreement with neutron-irradiation results like grain boundary microchemistry or radiation hardening. However, it is difficult to reach relevant damage and damage rate with proton implantations so heavy ion implantations are sometimes used. They allow the creation of a lot of damages in short times but their penetration depth is smaller (1–2 μm) than for neutron irradiation. The implanted microstructure presents the same type of defects (dislocation loops and cavities) as neutron-irradiated material.

For this study, although there exist some differences with neutron induced defects, iron ion implantation was chosen to create defects with quite similar nature and relevant in terms of density and size to start to investigate the interactions between hydrogen and irradiation defects. Iron ions were also chosen to minimize the modifications induced by implantation on the average alloy composition (main alloying element).

The aim of this study is to highlight the hydrogen trapping related to implantation-induced defects and thus characterize the interactions between hydrogen and these defects thanks to numerical simulations. For that, deuterium was used as a hydrogen isotopic tracer. The deuterium uptake was promoted in the 316L SS by room temperature cathodic charging.

Materials and Methods

Materials

Reference Material

An industrial grade of 316L SS was used in this study. Its chemical composition is given in Table 1. Large samples (110 mm × 22 mm × 1.5 mm) were cut by

electrical discharge machining and then polished with SiC paper up to grade 1200. A first thermal treatment of 1 h at 1080 °C, followed by oil quenching, was performed to annihilate dislocations and dissolve carbides. Then a second treatment of 15 h at 300 °C was done to evacuate thermal vacancies possibly retained in the alloy during quenching. Thanks to these two thermal treatments, a reference material with a minimal quantity of defects was obtained. Coupons of 20 mm 20 mm × 1.5 mm were then cut with a low-speed precision cut-off machine, to minimize the creation of new defects, and polished with SiC paper up to grade 2000 and diamond paste down to 3 μm, followed by a mirror finish on a vibratory table with a suspension of colloidal silica.

Implanted Material

5 MeV Fe^{3+} ion implantations were performed on this reference material, at JANNuS-Saclay (Joint Accelerators for Nanoscience and Nuclear Simulation), CEA, France, to create sub-surface defects. An implantation temperature of 500 °C was used, in order to compensate for the effect of higher dose rate with ion irradiation on microstructural evolution, with a total dose of 4×10^{15} at. cm^{-2} and a mean flux of 7×10^{11} at. $cm^{-2} \cdot s^{-1}$. Using SRIM Monte Carlo simulation code as detailed in Stoller's work [17], theoretical damages induced by implantation were estimated in dpa (displacement per atom). With our implantation conditions, damages reached up to 4.5 dpa at $\sim$1.2 μm depth as presented in Fig. 1.

Five Faraday cups were used in the specimen chamber to monitor the irradiation beam current. It was checked at every 10 min to extrapolate the actual value of implantation dose. Irradiation temperature was controlled by one thermocouple in the sample support and monitored by an IR camera. The setpoint temperature had to be reduced at the beginning of the experiment to compensate for implantation-induced heating.

TEM Observations

A Transmission Electron Microscopy (TEM) thin foil was prepared by the Focused Ion Beam (FIB) technique, allowing us to characterize the distribution of implantation-induced defects in depth (from the surface). In order to check that the FIB technique did not introduce defects in the material similar to those created by ion implantation, TEM observations in the conditions described below were made on the non-implanted zone of the thin foil. These examinations did not reveal the presence of dislocation loops, and no cavities were observed, so we assumed that damages induced by FIB were negligible in this study.

TEM observations were carried out using a FEI TECNAI F20-ST field emission gun microscope operated at 200 kV. Irradiation-induced defects were characterized, particularly the Frank faulted loops. For that, the rel-rod dark field technique was

Table 1 Nominal composition of the industrial 316L SS in wt% obtained by Optical Emission Spectrometry

	C	Si	Mn	S	P	Ni	Cr	Ti	Co	Al	Cu	Mo	Fe
Nominal	0.019	0.33	1.33	<0.003	0.025	10.36	16.94	0.024	0.10	<0.01	0.23	2.08	Bal.
Measurement uncertainty	± 0.003	± 0.01	± 0.02	–	± 0.003	± 0.15	± 0.15	± 0.003	± 0.01	–	± 0.01	± 0.03	–

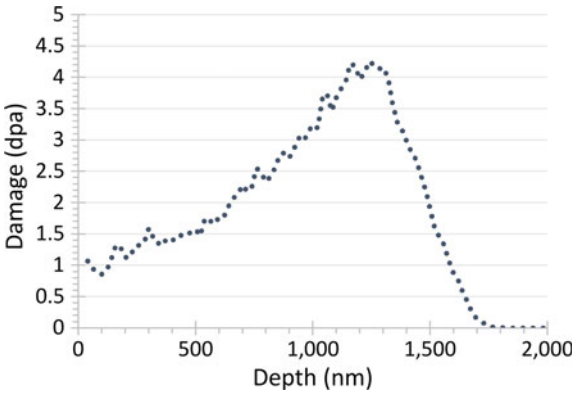

Fig. 1 SRIM calculation of the damage profile (dpa) for the Fe^{3+} implantation at 5 MeV and a dose of 4×10^{15} at. cm^{-2} used in this study

used. The {111} stacking fault of each loop can produce rel-rods on the diffraction pattern. By tilting the TEM specimen, one rel-rod can be intensified (two beam condition) and used to image the corresponding Frank loops in dark field. This investigation technique is more detailed in [11].

Cathodic Charging at 25 °C and Aging

In order to study the interactions between implantation-induced defects and hydrogen, deuterium was introduced in both reference and implanted samples by cathodic charging at 25 °C in a deaerated (Ar bubbling) 0.1 M NaOD solution. A cathodic current density j of 1 mA · cm^{-2} was chosen to enhance hydrogen adsorption on the surface from the proton discharge in Volmer-Tafel electrochemical domain.

Directly after cathodic charging, samples were quickly transferred and stored in liquid nitrogen (77 K) in order to prevent deuterium desorption and further internal diffusion. These specimens were then analyzed by Thermal Desorption Spectrometry (TDS) or by Secondary Ion Mass Spectrometry (SIMS). For this technique, an additional aging step of 24 h at 40 °C under vacuum was done to let a part of charged deuterium diffuse and desorb. All the charging and aging conditions are presented in Table 2.

Table 2 Typical experimental deuterium cathodic charging and aging conditions

	Solution	T [°C]	t [h]	j [mA · cm^{-2}]	Aging
TDS samples	0.1 M NaOD	25	1	1	/
SIMS samples	0.1 M NaOD	25	3	1	24 h at 40 °C

TDS

After deuterium cathodic charging, samples of reference material were analyzed by Thermal Desorption Spectrometry (TDS). It consists of monitoring the deuterium D_2 (m/z = 4) desorption flux as a function of time and temperature with a quadrupole mass spectrometer (Inficon™ Transpector 2). For this study, the specimens were subjected to a temperature ramp of 10 °C/min from room temperature to 1000 °C. Thanks to calibrated D_2 leaks, the signal given by the spectrometer (ionic current in A cm^{-2}) can be converted into a quantified flux (mol(D) · cm^{-2} · s^{-1}).

SIMS

SIMS (Secondary Ion Mass Spectrometry) analyses were conducted on the reference and implanted samples after deuterium charging and aging with a CAMECA IMS7f device. A primary Cs^+ ion beam (40 nA) was used over a 125 × 125 μm^2 surface and the analyzed surface was limited to a 33 μm diameter circle via a system of diaphragms. Several elements were analyzed: ^1H, ^2H (or D), ^{12}C, ^{16}O, ^{52}Cr, ^{56}Fe, ^{58}Ni. To compare the results of the different samples by avoiding the influence of small variations of experimental parameters, the signal intensities were normalized to the highest signal (^{58}Ni) deep in the bulk.

After the analysis, the average crater depth was measured with a stylus profiler (Dektak©, Bruker™), addressing an average sputtering rate used to convert the abrasion time (s) into depth from the surface (nm).

Results and Discussion

Microstructural Characterization

Reference Samples

After thermal treatments, the reference material was characterized by optical and electron microscopies. The mean grain size was estimated at 26 ± 6 μm from a polished and electrochemically attacked (oxalic acid) sample. The material presented an austenitic structure with around 3% of ferrite and scarce Ti(C, N) precipitates. A thin foil of the reference material was prepared by electrolytic thinning. TEM observations revealed the presence of some dislocation lines which were not counted, but their density being globally very low, the reference material will be considered defectless with respect to dislocations.

Fe^{3+} Implanted Samples

TEM observations were performed on a thin foil of a Fe^{3+} implanted sample. Figure 2 shows a TEM dark-field image of the sub-surface (surface is highlighted by the dashed line). It evidences the presence of faulted Frank loops with a wide range of sizes. Only one loop family on the existing four was characterized here which is assumed to represent 1/4 of the total number of Frank loops. The loop density and size were estimated as a function of their distance from the implanted surface as shown in Fig. 3. Considering a thin foil thickness of about 100 nm, the total average density and mean diameter of dislocation loop observed on the whole

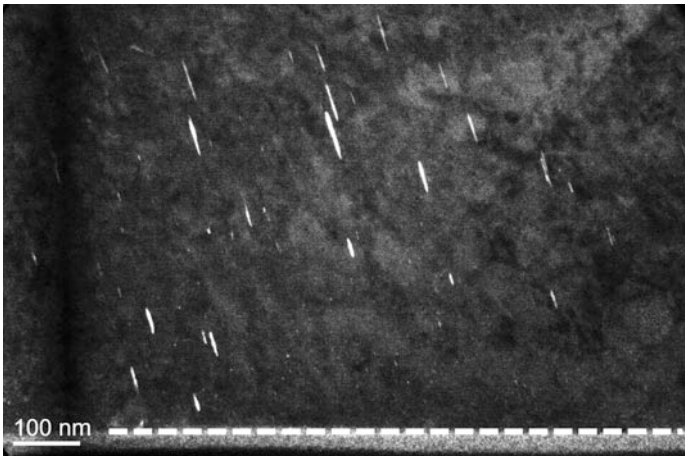

Fig. 2 TEM dark field micrograph of the implanted zone near the surface (white dashed line at the bottom) evidencing Frank loops (white lines) (Color figure online)

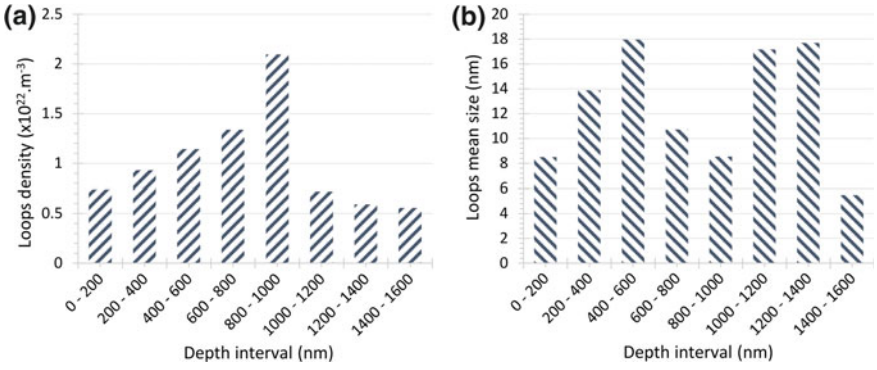

Fig. 3 Evolution of Frank loops density **a** and mean size **b** as a function of the depth in the Fe^{3+} implanted sample

implanted zone were estimated to be around $1.0 \pm 0.1 \times 10^{22}$ m^{-3} and 13 nm, respectively. The standard deviation related to the mean size of dislocation loops is 15 nm, showing a high variability of the dislocation loops size. The mean size of Frank loops is similar to the values reported by Chen et al. (10–12.5 nm) and Miura et al. (9.5 nm), on 316 grade SS irradiated with 3 MeV Fe at 400 °C and 2.8 MeV Fe at 300 °C, respectively [18, 19]. The loop density was between a factor 10 and 100 lower in this study, which could be due to the higher irradiation temperature. For comparison, 10 MeV Fe implantation at 450 °C in Gupta et al. work [20] lead to an average loops density of 5×10^{21} m^{-3}, closer to the results of this study.

The shape of the loop density distribution is in good agreement with the damage distribution given by SRIM simulation for ion implantation even though the highest density of defects is shifted to a somewhat lower depth between 800 and 1000 nm. An interesting thing to see is the decrease of the loop mean size between 600 and 1000 nm which could be related to the highest density of defects in this zone. There are more dislocation loops but they are smaller.

Besides, complimentary TEM observations, which would need further work, revealed the presence of numerous large cavities (up to diameter of 15 nm) in the implantation-affected zone as shown in the overfocused bright field image in Fig. 4. Cavity population is not fully characterized yet but their density seems to be high between 650 and 1050 nm from the surface.

Hydrogen Trapping by Irradiation-Induced Defects

The deuterium and hydrogen signals obtained by SIMS on the deuterium charged reference sample after 24 h aging at 40 °C are presented in Fig. 5. Both signals are

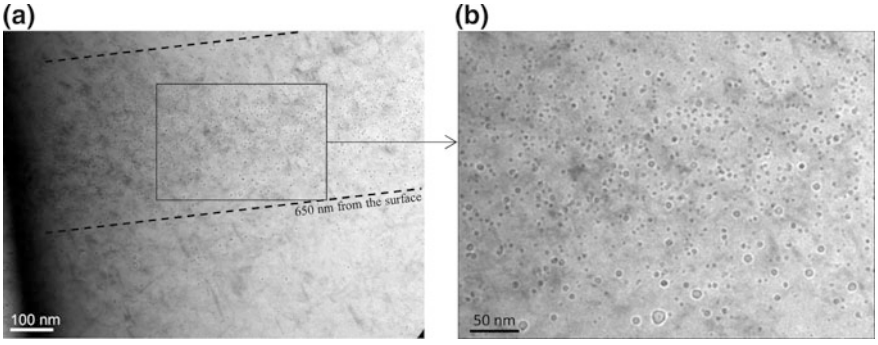

Fig. 4 Bright field TEM micrographs in overfocused conditions of the implanted zone evidencing the presence of numerus cavities between 650 and 1050 nm from the surface (dashed lines), **b** shows an area with cavities at higher magnification

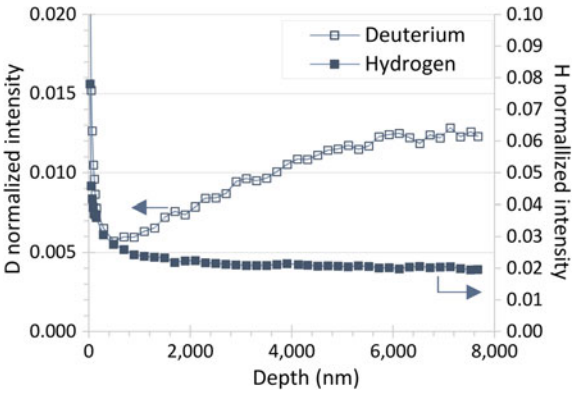

Fig. 5 SIMS deuterium (empty squares) and hydrogen (full squares) profiles in a reference sample after D cathodic charging and aging for 24 h at 40 °C (Color figure online)

normalized to the ^{58}Ni signal and are not equivalent to concentrations because of the differences of sputtering and ionization rates. Hydrogen found in the specimen comes from the omnipresence of this element in the environment, mostly at the extreme surface, due to pollutions or water residues adsorbed on the surface. On the other hand, the deuterium profile, originating exclusively from the cathodic charging, shows an accumulation deeper in the alloy with a maximum for around 7 µm from the surface. This shape may be the result of deuterium interstitial diffusion during the aging step, out of the sample by its free surface and also deeper in the alloy (decreasing and shifting bell shape).

SIMS analyses have also been conducted on the implanted sample after an identical deuterium charging and aging procedure. Figure 6 presents the deuterium profiles obtained on the charged implanted sample after aging, along with the one of the reference sample previously showed. It can be seen that, for the implanted specimen, a significant deuterium accumulation is observed between 600 and 1200 nm from the surface. This profile is in good agreement with the localization of implantation-induced defects and thus highlights the trapping of deuterium by these

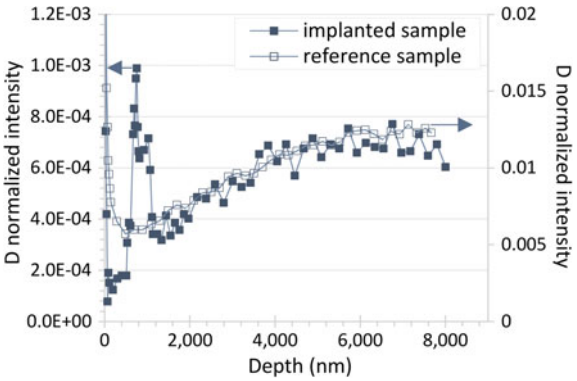

Fig. 6 SIMS deuterium profiles of reference (empty squares) and implanted (full squares) samples after D cathodic charging and 24 h aging at 40 °C

defects. The non-trapped deuterium can still diffuse and lead, deeper in the alloy, to a residual profile similar to the one on the reference sample.

Hydrogen trapping by implantation-induced defects have already been evidenced by Jambon et al. [21] who worked on a nickel-base alloy and highlighted, thanks to SIMS analyses, hydrogen trapping related with defects induced by a previous Ni ion implantation.

Simulation of Diffusion and Trapping

To characterize the hydrogen trapping by irradiation-induced defects, a numerical model [22] was used to simulate the hydrogen diffusion and trapping in both implanted and non-implanted materials. For that, each experimental step, experimented by the samples, was taken into account in the simulations. To begin with, hydrogen diffusion coefficient in the studied SS was determined from the simulation of reference material experiments, then, thanks to additional trapping terms, hydrogen trapping by implantation-induced defects was simulated.

Determination of the Diffusion Constants

The first step to apply the numerical model on the implanted sample was to determine the pre-exponential constant D_0 and the activation energy E_a used to calculate, with an Arrhenius law, the diffusion coefficient (D) of the deuterium in 316L stainless steel (1). In this way, a "pure diffusion" system was considered and the classical Fick's second law (2) was used in the model to simulate the entire experimental sample history (i) cathodic charging by one surface under constant hydrogen surface concentration, then (ii) aging at 40 °C for 24 h in vacuum, under a null hydrogen surface concentration imposed by instantaneous surface recombination and release in vacuum of the desorbing hydrogen.

$$D = \boldsymbol{D}_0 \exp\left(\frac{-\boldsymbol{E_a}}{RT}\right) \tag{1}$$

$$\frac{\delta C_L}{\delta t} = D\frac{\delta^2 C_L}{\delta x^2} \tag{2}$$

where C_L represents the local interstitial deuterium concentration.

Two experimental results on the defect-free reference material were used and simulated, then fitted thanks to D_0 and E_a adjustments. The first experiment used was a TDS deuterium spectrum (normalized to its maximum desorption rate) obtained with a reference sample just after a deuterium cathodic charging of 1 h at 25 °C (no aging) and the second one was the deuterium depth profile obtained by

SIMS on a reference sample, deuterium-charged then aged at 40 °C for 24 h, as presented in the previous section.

Most experimental conditions of these experiments were incorporated into the modeling to be as close as possible to the reality in order to consider that there are only D_0 and E_a which can improve the simulated results. After adjustments of these constants from values given by the literature [23] to best fit the experimental TDS curve and the SIMS profile, a matching couple of values was found: $D_0 = 1.4 \times 10^{-5}$ cm^2 · s^{-1} and $E_a = 40$ kJ mol^{-1}. The comparison between experimental and simulated results considering this set of diffusion constants for the two experiments is shown in Fig. 7. Some slight discrepancies between experimental and simulated results appear at the end of the deuterium desorption peak (Fig. 7a) and principally near the surface in the deuterium depth profile (Fig. 7b). These differences could originate from the fact that the reference material is not fully defect-free but this effect should be of the second order. The difference in the deuterium concentration profiles close to the surface may be assigned to the presence of a nanometric oxide layer on the surface. First, it could explain the deuterium amount at the very extreme surface (below 50 nm) on the SIMS profile: some deuterium may be present in a surface hydroxide layer or in solution in the oxide layer but this high deuterium concentration decreases rapidly after a few nanometers. Then, due to a slower diffusion rate in the oxide layer or a slower recombination rate at the oxide surface [7, 24], the desorption from the bulk may be slower, inducing some deuterium accumulation below the oxide layer. These two phenomena have not been taken into account in the modeling yet and could explain the discrepancies seen on the deuterium concentration profiles. However, there is globally a fairly good agreement between the experimental and the simulated data with the determined set of diffusion parameters.

These values determined here for the diffusion of deuterium in 316L stainless steel are in good agreement with literature data [25–28]. For instance, Forcey et al.

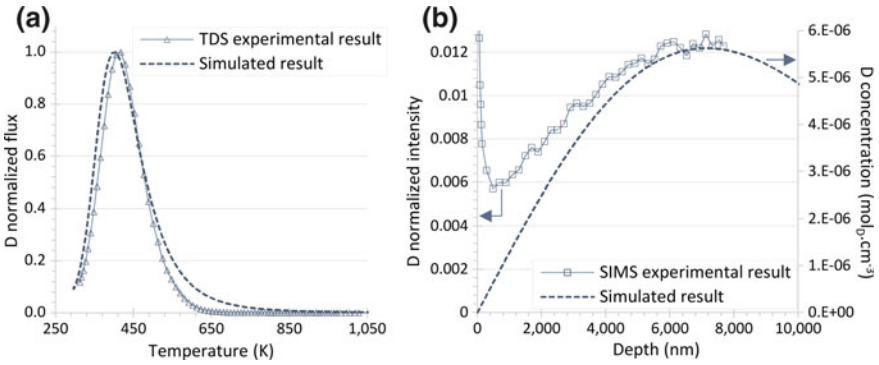

Fig. 7 Comparison between experimental and simulated results for **a** TDS deuterium spectrum just after cathodic charging and **b** SIMS deuterium depth profile after cathodic charging and 24 h aging at 40 °C

found for the diffusion of hydrogen in an annealed 316L SS an activation energy of 42.5 kJ mol^{-1} but a higher pre-exponential constant of 7.7×10^{-4} $cm^2 \cdot s^{-1}$ (these values are assumed to be valid between 250 and 600 °C).

Assuming interstitial diffusion is not affected by the presence of traps, provided they are considered a dilute system in the matrix, the diffusion parameters determined in this study with "pure diffusion" system were then directly injected in the numerical model for the simulation of diffusion and trapping of deuterium in the 316L stainless steel.

Diffusion and Trapping of Deuterium in the Implanted Material

To add the trapping phenomenon to the diffusion of deuterium in stainless steel, the set of McNabb and Foster's equations was used [29]. It corresponds to the second Fick's law with a trapping term (3) coupled with the kinetic equation of the deuterium trapping/detrapping (4).

$$\frac{\delta C_L}{\delta t} + N\frac{\delta \theta}{\delta t} = D\frac{\delta^2 C_L}{\delta x^2} \tag{3}$$

$$\frac{\delta \theta}{\delta t} = k(1-\theta)C_L - p\theta \tag{4}$$

where C_L represents the local interstitial deuterium concentration, N is the trap site density, θ the trap occupancy, D the interstitial diffusion coefficient, k and p the respective trapping and detrapping kinetic constants associated with one type of trap site, both following an Arrhenius law (5 and 6).

$$k = k_0 \exp\left(\frac{-E_k}{RT}\right) \tag{5}$$

$$p = p_0 \exp\left(\frac{-E_p}{RT}\right) \tag{6}$$

To start the simulation of deuterium diffusion and trapping by irradiation defects, only Frank dislocation loops were considered. The values of the parameters k_0, E_k, p_0 and E_p for dislocation loops did not exist in the literature but were available for edge dislocations in a nickel-based alloy in Hurley's work [23], see Table 3. Concerning the density of traps N, the experimental characterizations of the dislocation loops presented in Section "Fe^{3+} implanted samples". were used. For practical reasons, we considered a dislocation loop of perimeter l equivalent to an edge dislocation of length l and so the dislocation linear density was calculated as a function of depth as shown in Fig. 8. As explained in ref. [23, 30, 31], the experimental dislocation linear density can be converted into an amount of trap sites per volume unit in order to put it in the numerical model.

Table 3 Trapping and detrapping kinetic constants for trapping at dislocations in A600 nickel-based alloy [23]

Dislocations trapping (k)		Dislocations detrapping(p)	
k_0 ($cm^3 \cdot mol^{-1} \cdot s^{-1}$)	E_k ($kJ \cdot mol^{-1}$)	$p_0(s^{-1})$	$E_p(kJ \cdot mol^{-1})$
$(1.5 \pm 0.2)\ 10^6$	42 ± 4	$(1.5 \pm 0.2)\ 10^6$	76 ± 4

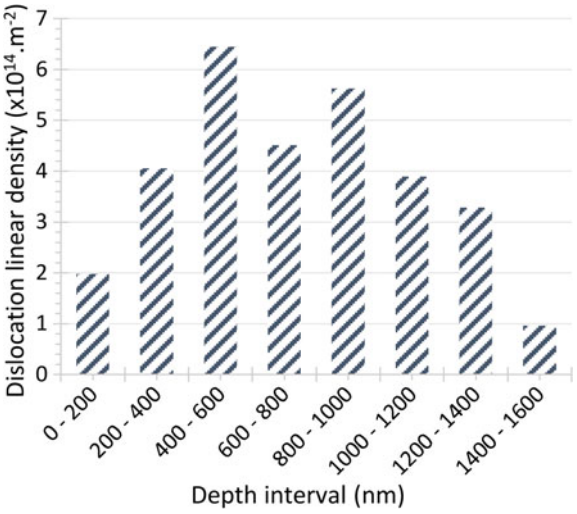

Fig. 8 Evolution of the equivalent dislocation linear density as a function of depth in the implanted sample

The result of the simulation of deuterium depth profile after 3 h at 25 °C cathodic charging and aging for 24 h at 40 °C with these parameters is presented in Fig. 9, along with the SIMS experimental deuterium profile. The experimental concentration profile is on average well-reproduced by the simulation using this preliminary set of parameters. Deeper than 3 μm from the surface, the two profiles are quite well-superimposed indicating a good reproduction by simulation of the interstitial deuterium profile, validating the hypothesis made on the invariance of diffusion coefficient. The zone where deuterium is trapped by implantation-induced defects is broader with simulation than in reality but the balance between interstitial and trapped deuterium is respected. With the current data, the trapping and detrapping kinetic parameters, k and p, extracted from literature, seem applicable to dislocation loops.

However, since the only defects considered at the moment were dislocation loops, the simulation may be improved with considering also trapping of hydrogen by the cavities identified earlier in the paper. As cavities are significantly present in the depth range 600–1200 nm, which seems also to be the location of trapped deuterium on the SIMS concentration profile (Fig. 9), their effect on trapping may need to be considered. On-going work is focusing on this subject.

In the present study, we chose to perform ion implantation and hydrogen cathodic charging separately and assumed in the modelling that hydrogen

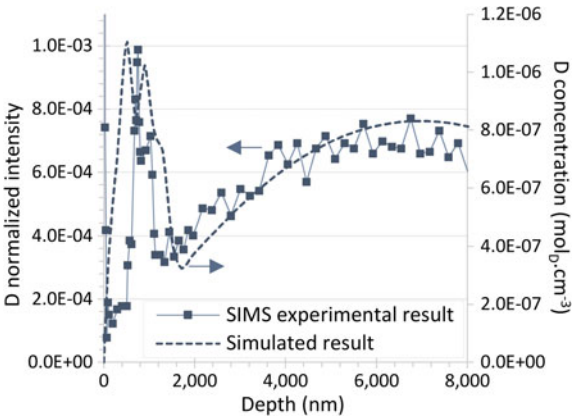

Fig. 9 Comparison between SIMS (closed squares) and simulated (dotted line) deuterium depth profiles after cathodic charging of 3 h at 25 °C and aging for 24 h at 40 °C

introduced in the alloy do not modify the defects population characterized after ion implantation. Nevertheless, in PWR primary medium, hydrogen uptake occurs simultaneously with neutron irradiation and the interaction between this element and irradiation defects could modify the final alloy damaged microstructure. For example, Kato et al. [32] studied the interactions between hydrogen and implantation-induced defects by H^+ and H_2^+ implantations in various annealed stainless steels. They showed that hydrogen modifies the cavity population and allows cavities to form at the grain boundaries. Thus, another way to improve the modelling will be to consider the hydrogen effects on implantation-induced defects and it will start by TEM characterizations of defects in an implanted sample after hydrogen charging, in order to adjust trapping site density and location in the simulation.

Conclusion

In this work, to study the interactions between hydrogen and irradiation-induced defects, an annealed 316L stainless steel was implanted with 5 MeV Fe^{3+} ions at 500 °C in order to simulate defects created by neutron irradiation. The implanted microstructure was characterized by TEM and then deuterium cathodic charging and SIMS analyses allowed to focus on hydrogen trapping by implantation-induced defects.

SIMS analyses performed on both implanted and non-implanted model materials after deuterium cathodic charging and an aging step highlighted a strong trapping of hydrogen in link with the implantation defects but not in the whole implanted zone. A numerical model used to simulate diffusion and trapping of hydrogen in materials was used to determine hydrogen interstitial diffusion coefficient and study trapping parameters. For that, the experimental conditions and real dislocation loop density were injected in the model. There is globally a fairly good agreement between the

experimental and the simulated data using the following adjusted diffusion parameters: $D_0 = 1.4 \times 10^{-5}$ cm^2 $\cdot$ s^{-1} and $E_a = 40$ kJ $\cdot$ mol^{-1}, and trapping parameters extracted from literature. Some differences remain certainly due to the presence of numerous cavities in the implanted zone which have not been taken into account in the model yet.

Acknowledgements The authors would like to thank Y. Serruys, E. Bordas and Team JANNuS (DMN/JANNUS, CEA Saclay) for their support and assistance in conducting the Fe irradiation. The authors would also like to acknowledge K. Rousseau(SERMA TECHNOLOGIES, Grenoble, France) for TEM FIB sampling.

References

1. P. Scott, A review of irradiation assisted stress corrosion cracking. J. Nucl. Mater. **211**(2), 101–122 (1994)
2. G.S. Was, Y. Ashida, P.L. Andresen, Irradiation-assisted stress corrosion cracking. Corros. Rev. **29**(1–2), 7–49 (2011)
3. G. Pressouyre, Trap theory of hydrogen embrittlement. Acta Metall. **28**(7), 895–911 (1980)
4. A.-M. Brass, J. Chene, Hydrogen uptake in 316L stainless steel: consequences on the tensile properties. Corros. Sci. **48**(10), 3222–3242 (2006)
5. I.M. Robertso, P. Sofronis, A. Nagao, M.L. Martin, S. Wang, D.W. Gross, K.E. Nygren, Hydrogen embrittlement understood. Metall. Mater. Trans. B **46**(3), 1085–1103 (2015)
6. N. Totsuka, Z. Szklarska-Smialowska, Effect of electrode potential on the hydrogen-induced IGSCC of alloy 600 in an aqueous solution at 350 °C. Corrosion **43**(12), 734–738 (1987)
7. R. Rios, T. Magnin, D. Noel, O. de Bouvier, Critical analysis of alloy 600 stress corrosion cracking mechanisms in primary water. Metall. Mater. Trans. A **26**(4), 925–939 (1995)
8. X. Zhong, S.C. Bali, T. Shoji, Effects of dissolved hydrogen and surface condition on the intergranular stress corrosion cracking initiation and short crack growth behavior of non-sensitized 316 stainless steel in simulated PWR primary water. Corros. Sci. **118**, 143–157 (2017)
9. M. Dumerval, S. Perrin, L. Marchetti, M. Tabarant, F. Jomard, Y. Wouters, Hydrogen absorption associated with the corrosion mechanism of 316L stainless steels in primary medium of Pressurized Water Reactor (PWR). Corros. Sci. **85**, 251–257 (2014)
10. N. Hashimoto, E. Wakai, J.P. Robertson, Damage structure in austenitic stainless steel 316LN irradiated at low temperature in the HFIR. J. Electron. Microsc. (Tokyo) **48**(5), 575 (1999)
11. D.J. Edwards, E.P. Simonen, S.M. Bruemmer, Evolution of fine-scale defects in stainless steels neutron-irradiated at 275 °C. J. Nucl. Mater. **317**(1), 13–31 (2003)
12. G.S. Was, P.L. Andresen, Stress corrosion cracking behavior of alloys in aggressive nuclear reactor core environments. Corrosion **63**(1), 19–45 (2007)
13. O.K. Chopra, A.S. Rao, A review of irradiation effects on LWR core internal materials—IASCC susceptibility and crack growth rates of austenitic stainless steels. J. Nucl. Mater. **409**(3), 235–256 (2011)
14. Y. Dong, B.H. Sencer, F.A. Garner, E.A. Marquis, Microchemical and microstructural evolution of AISI 304 stainless steel irradiated in EBR-II at PWR-relevant dpa rates. J. Nucl. Mater. **467**(2), 692–702 (2015)
15. G.S. Was, J.T. Busby, T. Allen, E.A. Kenik, A. Jenssen, S.M. Bruemmer, J. Gan, A.D. Edwards, P.M. Scott, P.L. Andreson, Emulation of neutron irradiation effects with protons: validation of principle. J. Nucl. Mater. **300**(2), 198–216 (2002)

16. G.S. Was, *Fundamentals of Radiation Materials Science: Metals and Alloys* (Springer Science & Business Media, 2007)
17. R.E. Stoller, M.B. Toloczko, G.S. Was, A.G. Certain, S. Dwaraknath, F.A. Garner, On the use of SRIM for computing radiation damage exposure, Nucl. Instrum. Methods Phys. Res. Sect. B Beam Interact. Mater. At., **310**, pp. 75–80 (2013)
18. D. Chen, K. Murakami, K. Dohi, K. Nishida, N. Soneda, Z. Li, L. Liu, N. Sekimura, Depth distribution of Frank loop defects formed in ion-irradiated stainless steel and its dependence on Si addition. Nucl. Instrum. Methods Phys. Res. Sect. B Beam Interact. Mater. At., **365**, pp. 503–508 (2015)
19. T. Miura, K. Fujii, H. Nishioka, K. Fukuya, Effects of hydrogen on interaction between dislocations and radiation-induced defects in austenitic stainless steels. J. Nucl. Mater. **442** (1–3), pp. S735–S739 (2013) (Supplement 1)
20. J. Gupta, J. Hure, B. Tanguy, L. Laffont, M.-C. Lafont, E. Andrieu, Evaluation of stress corrosion cracking of irradiated 304L stainless steel in PWR environment using heavy ion irradiation. J. Nucl. Mater. **476**, 82–92 (2016)
21. F. Jambon, L. Marchetti, M. Sennour, F. Jomard, J. Chêne, SIMS and TEM investigation of hydrogen trapping on implantation defects in a nickel-based superalloy. J. Nucl. Mater. **466**, 120–133 (2015)
22. C. Hurley, F. Martin, L. Marchetti, J. Chêne, C. Blanc, E. Andrieu, Numerical modeling of thermal desorption mass spectroscopy (TDS) for the study of hydrogen diffusion and trapping interactions in metals. Int. J. Hydrog. Energy **40**(8), 3402–3414 (2015)
23. C. Hurley, Kinetic study of hydrogen-material interactions in nickel base alloy 600 and stainless steel 316L through coupled experimental and numerical analysis (Ph-D thesis, Institut National Polytechnique de Toulouse 2015)
24. W.A. Swansiger, R. Bastasz, Tritium and deuterium permeation in stainless steels: influence of thin oxide films. J. Nucl. Mater. **85**, 335–339 (1979)
25. P. Tison, Influence de l'hydrogène sur le comportement des métaux (Ph-D thesis, Université Pierre et Marie Curie Paris 6, 1984)
26. C. Shan, A. Wu, Q. Chen, The behavior of diffusion and permeation of tritium through 316L stainless steel. J. Nucl. Mater. **179**, 322–324 (1991)
27. K.S. Forcey, D.K. Ross, J.C.B. Simpson, D.S. Evans, Hydrogen transport and solubility in 316L and 1.4914 steels for fusion reactor applications. J. Nucl. Mater. **160**(2), 117–124 (1988)
28. D.M. Grant, D.L. Cummings, D.A. Blackburn, Hydrogen in 316 steel—diffusion, permeation and surface reaction. J. Nucl. Mater. **152**(2), 139–145 (1988)
29. A. McNabb, P.K. Foster, A new analysis of the diffusion of hydrogen in iron and ferritic steels. Trans. Metall. Soc. AIME **227**, 618–627 (1963)
30. A.H.M. Krom, A. Bakker, Hydrogen trapping models in steel. Metall. Mater. Trans. B **31**(6), 1475–1482 (2000)
31. J. Chêne, A.M. Brass, Hydrogen transport by mobile dislocations in nickel base superalloy single crystals. Scr. Mater. **40**(5), 537–542 (1999)
32. T. Kato, K. Nakata, J. Kuniya, S. Ohnuki, H. Takahashi, Cavity formation by hydrogen injection in electron-irradiated austenitic stainless steel. J. Nucl. Mater., **155–157**, Part 2, pp. 856–860 (1988)

Grain Boundary Oxidation of Neutron Irradiated Stainless Steels in Simulated PWR Water

Takuya Fukumura, Koji Fukuya, Katsuhiko Fujii, Terumitsu Miura and Yuji Kitsunai

Abstract To elucidate the mechanisms of irradiation assisted stress corrosion cracking (IASCC), stress corrosion cracking (SCC) tests on 3 dpa, 19 dpa and 73 dpa neutron-irradiated 316 stainless steel were performed and the effects of irradiation on grain boundary (GB) oxidation were investigated. O-ring specimens were prepared from irradiated flux thimble tubes and a constant load SCC test was performed in a simulated pressurized water reactor primary water at 320 °C. After the SCC test, the oxidation condition of GBs was examined by transmission electron microscopy. Evidence of GB oxidation was found in all examined GBs, even at the relatively low dose of 3 dpa. The morphology of GB oxidation was sharp wedge-shaped. The average GB oxidation length at 3 dpa, 19 dpa and 73 dpa were 100 nm, 340 nm and 400 nm, respectively, indicating the promotion of GB oxidation due to irradiation. In the GB oxide, Fe and Ni depletion and Cr enrichment were observed. Also, Ni enrichment on GB was observed in front of the GB oxidation.

Keywords Irradiation assisted stress corrosion cracking · Stainless steel · Corrosion · PWR · Grain boundary

Introduction

Irradiation assisted stress corrosion cracking (IASCC) is one of the major concerns for the structural integrity of core internals in light water reactors. IASCC of the baffle former bolt (BFB) is known to occur in pressurized water reactors (PWRs) [1]. Many studies have been carried out to clarify the conditions and mechanism of

T. Fukumura (✉) · K. Fukuya · K. Fujii · T. Miura
Institute of Nuclear Safety System, Inc, 64 Sata, Mihama-Cho, Fukui 919-1205, Japan
e-mail: fukumura@inss.co.jp

Y. Kitsunai
Nippon Nuclear Fuel Development Co., Ltd, 2163 Narita-Cho, Oarai-Machi, Higashi-Ibaraki-Gun, Ibaraki-Ken 311-1313, Japan

J.H. Jackson et al. (eds.), *Proceedings of the 18th International Conference on Environmental Degradation of Materials in Nuclear Power Systems – Water Reactors*, The Minerals, Metals & Materials Series, https://doi.org/10.1007/978-3-319-68454-3_68

IASCC initiation in PWR environment [2–5]. The threshold of IASCC initiation stress is known to decrease rapidly up to about 20 dpa and then decrease gently over about 40 dpa [6–10].

IASCC is a complex phenomenon in which material properties, stress and water conditions are simultaneously changed by irradiation and its mechanisms are not yet well understood. Recent studies have focused on the combination of high local stress/strain concentration at grain boundaries (GBs) caused by heterogeneous deformation [11, 12] and degradation of GB binding strength due to various factors. One such factor is considered to be GB oxidation in high-temperature water. Previously, GB oxidation was observed in about 20 dpa irradiated stainless steel [13]. Therefore, an understanding of corrosion behavior is considered to be very important, but there have been very few studies on the corrosion behavior of irradiated stainless steel.

Previous studies showed that the oxide film of irradiated stainless steel consists of two layers, a Cr-rich spinel inner layer and an Fe-rich spinel outer layer, and that the amount of surface corrosion products increases with increasing dose [13]. This paper shows experimental results of the GB oxidation behavior of neutron irradiated stainless steel in simulated PWR primary water.

Experimental Procedure

Test Materials

The material examined was cold-worked type 316 stainless steel taken from flux thimble tubes (FTTs) that had been in service in a PWR. The specimens were prepared from regions irradiated to 3, 19 and 73 dpa. Laboratory data indicate that the initiation of IASCC in PWR environment occurs at doses around 3 dpa. At very high doses (>40 dpa), the susceptibility to cracking appears to have reached saturation. The doses of 3 dpa, 19 dpa and 73 dpa were selected for low dose, middle dose and high dose, respectively. The chemical composition of the test material is shown in Table 1 and the irradiation conditions are shown in Table 2.

Table 1 Chemical composition (wt%)

C	Si	Mn	P	S	Ni	Cr	Mo	Fe
0.04	0.62	1.63	0.022	0.006	12.61	16.94	2.22	Bal.

Table 2 Irradiation conditions

Dose (dpa)	Dose rate (dpa/s)	Temperature (°C)
3	8.7×10^{-9}	323
19	4.8×10^{-8}	323
73	1.5×10^{-7}	297

The FTT materials were cut into O-ring type specimens, 7.6 mm in outer diameter, 5.1 mm in inner diameter and 2 mm in length. The cut surfaces were mechanically polished.

The specimens were immersed in simulated PWR primary water (2.7 ppm dissolved hydrogen, 500 ppm B as boric acid, 2 ppm Li as LiOH, pH 6.9 at room temperature and less than 1 ppb dissolved oxygen) at 320 °C for 1149 h under a constant load condition. The applied stress was 900 MPa at maximum in the specimens.

Analysis

After the SCC test, specimen surfaces were examined using an optical microscope and a scanning electron microscope (SEM), and the cross-sections of near surface GB were examined using a transmission electron microscope (TEM) with an energy dispersive X-ray spectrometer (EDS). A focused ion beam (FIB) fabrication system was used for preparing trenches for near-surface cross-sectional observations. Surface oxidation behavior, oxide layer structure, composition, thickness and GB oxidation behavior were evaluated. For the examinations, the outer peripheral area and mid-thickness area at 90° away from the loading axis were selected as shown in Fig. 1. These areas were selected to avoid the contact effect of the specimen and loading bar. The finite element method (FEM) analysis showed tensile stress at the

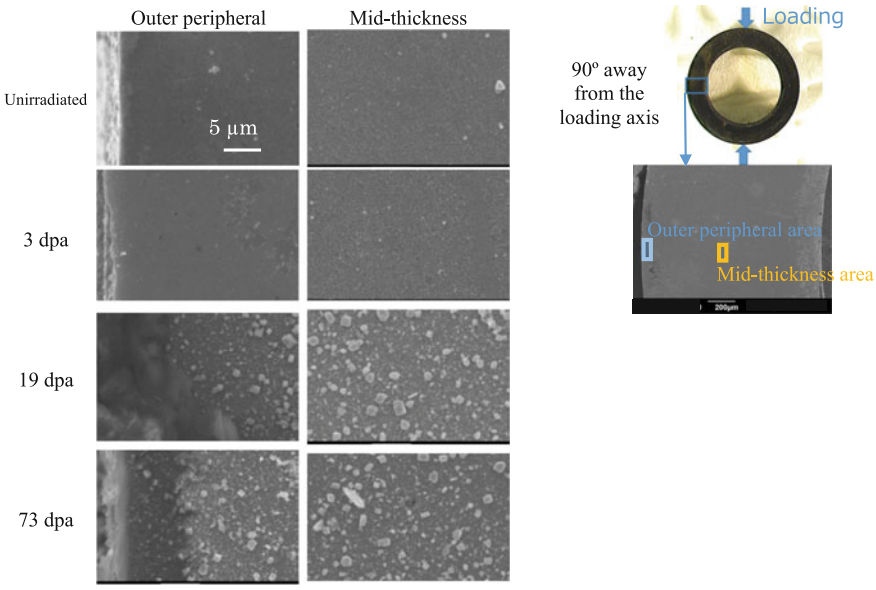

Fig. 1 SEM observation of surface corrosion products

outer peripheral area and mid-thickness area at 90° away from the loading axis of about 400 MPa and 0 MPa, respectively. The maximum tensile stress of 900 MPa was applied in the inner peripheral area at 0° and 180° away from the loading axis in the specimen.

Experimental Results

Surface Oxidation

IASCC cracks were observed in the 19 and 73 dpa specimens on the inner peripheral surface near 0° and 180° position and on the outer peripheral surface near 90° and 270° position, but not in the 3 dpa specimen. Considering that the maximum initial stress was about 900 MPa, initiation of IASCC is reasonable based on results of previous testing [4, 8]. More surface corrosion products were observed in the 19 dpa and 73 dpa specimens than in the unirradiated and 3 dpa specimens as shown in Fig. 1, indicating that general corrosion is promoted due to irradiation. The surface corrosion products were identified in a previous study as Fe-rich spinel oxide particles [13].

Inner Layer Thickness

TEM images of cross-sections of the near-surface oxide layer are shown in Fig. 2, in which Z-contrast images are shown for the 3 dpa, 19 dpa and 73 dpa specimens. The oxide film thickness in the 19 dpa and 73 dpa specimens was thicker than in the 3 dpa specimen. The surface oxide film consisted of a dual structure, an outer layer and an inner layer. The outer oxide layer consisted of Fe-rich spinel oxide particles and the inner oxide layer consisted of Cr-rich spinel oxide fine grains.

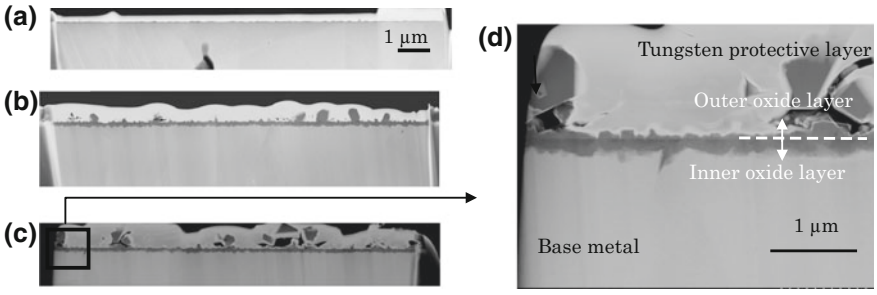

Fig. 2 TEM images of cross-section near-surface oxide layer. **a** 3 dpa Z-contrast image, **b** 19 dpa Z-contrast image, **c** and **d** 73 dpa Z-contrast image

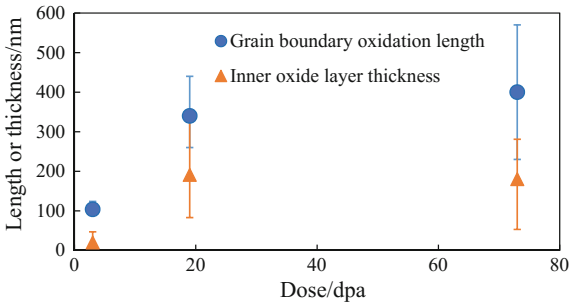

Fig. 3 Inner oxide layer thickness and GB oxidation length against dose

The outer oxide layer is considered to be formed by the re-precipitation of ferrous ions dissolved by corrosion, and the inner oxide layer to be formed by the inward diffusion of oxygen. Both the outer and inner oxide layers are formed through the corrosion process. However, since the outer oxide layer could be affected by water chemistry in the test facility, the thickness of the inner oxide layer was selected as the index of general corrosion.

The average thickness and range of the inner oxide layer of the outer peripheral and mid-thickness locations in the 3 dpa specimen were 23 nm (6–47 nm) and 17 nm (7–34 nm), respectively, those of the 19 dpa specimen were 225 nm (145–334 nm) and 158 nm (83–219 nm), respectively and those of the 73 dpa specimen were 196 nm (116–581 nm) and 158 nm (53–237 nm), respectively. The inner oxide layer thickness becomes thicker with increasing dose shown as Fig. 3, indicating that general corrosion is promoted due to irradiation. The inner oxide layer thickness of peripheral area in 3 dpa specimen was slightly thicker than that of mid-thickness area. It might indicate that general corrosion is slightly promoted due to stress. On the other hand, stress changed with crack propagation in 19 dpa and 73 dpa specimens so that the effect of stress on inner layer thickness was not clear.

Cross-Sectional Observation of Gb Oxidation

TEM images of cross-sections near GBs in the 3 dpa, 19 dpa and 73 dpa specimens are shown in Fig. 4. GB oxidation was observed in all examined GBs: 9 GBs in the 3 dpa specimens, 3 GBs in the 19 dpa specimens and 4 GBs in the 73 dpa specimens. The average and range of GB oxidation length are about 100 nm (90–120 nm) in the 3 dpa specimen, are about 340 nm (260–440 nm) in the 19 dpa specimen and are about 400 nm (250–570 nm) in the 73 dpa specimen. Comparing the GB oxidation length of the outer peripheral and mid-thickness areas in the 3 dpa specimen, no significant difference was found, indicating that the tensile stress of 400 MPa had no effect on GB oxidation at 3 dpa. The GB oxidation length plotted against dose is shown in Fig. 3. The GB oxidation length becomes longer with increasing dose in the same manner as inner oxide layer thickness. It was also confirmed that GB oxidation is promoted due to irradiation.

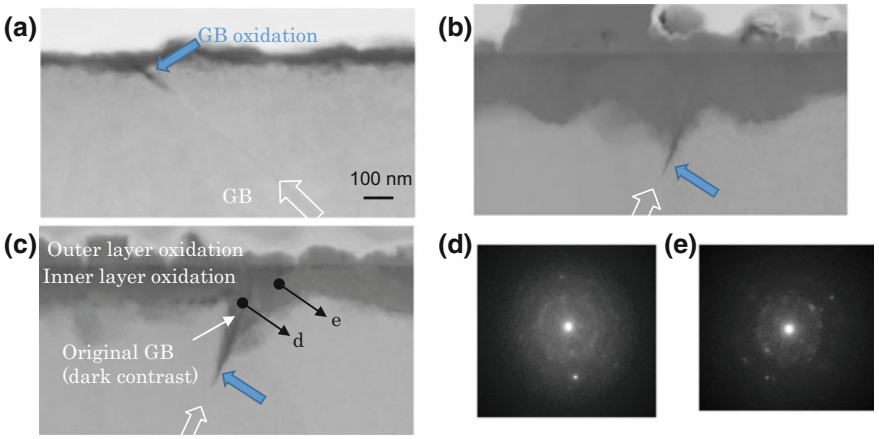

Fig. 4 GB cross-sectional TEM images. **a** Z-contrast image in 3 dpa specimen, **b** Z-contrast image in 19 dpa specimen, **c** Z-contrast image in 73 dpa specimen, **d** selected area diffraction pattern of GB oxide in 73 dpa specimen, **e** selected area diffraction pattern of inner layer oxide in 73 dpa specimen

Gb Oxide Structure and Chemical Composition

Selected area diffraction pattern examples of GB oxide and inner layer oxide in the 73 dpa specimen are shown in Fig. 4d, e. The diffraction pattern show that GB oxide consists of a fine grain spinel structure of the same type as the inner oxide layer.

EDS elemental mapping analysis of the cross-section and line analysis along a GB in the 3 dpa specimen are shown in Fig. 5. At the GB oxide, Cr enrichment, Fe and Ni depletion and slight Si enrichment were observed. On the other hand, at the GB oxide front, which means ahead of the GB oxide tip on the non-oxidized part of the GB, significant Ni enrichment about 200 nm long along the GB was observed with Fe and Cr depletion. The same elemental changes were observed in the 19 dpa and 73 dpa specimens.

EDS element analysis example across an oxidized GB in the 3 dpa specimen is shown in Fig. 5c. The analyzed positions is 50 nm inward from the GB oxide tip. The concentration of Fe, Cr, Ni, Si and O on GB was 20, 25, 8, 5 and 10 wt%, respectively. The width of concentration change was about 20 nm.

A comparison of the distribution of elements along GBs in the 3 dpa, 19 dpa and 73 dpa specimens is shown in Fig. 6. In this figure, normalized ratios of each element are plotted. For example, the Fe ratio is defined as:

$$R_{Fe} = \frac{C_{Fe}}{C'_{Fe}}$$

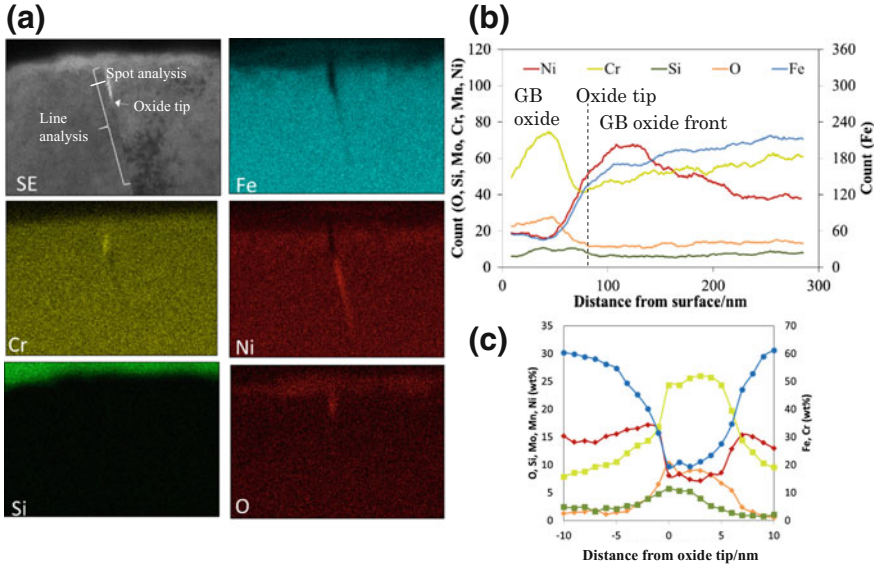

Fig. 5 EDS element analysis of GB oxidation in 3 dpa specimen. **a** mapping analysis, **b** line analysis along a GB, **c** spot analysis across a GB

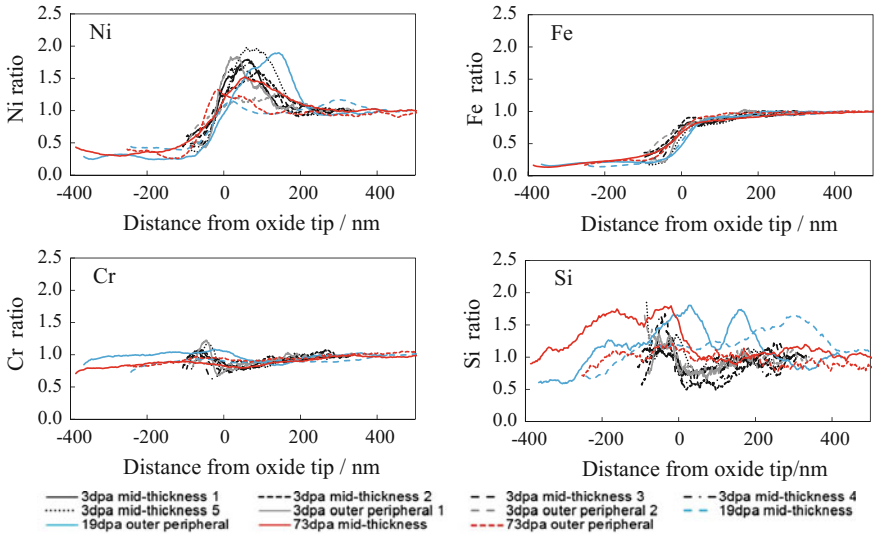

Fig. 6 Comparison of element distribution along GBs. **a** Ni ratio, **b** Fe ratio, **c** Cr ratio, **d** Si ratio

R_{Fe}: Fe ratio
C_{Fe}: Count of Fe at an arbitrary position on GB
C'_{Fe}: Count of Fe at the most distant position from the GB

Ni is depleted near the surface, and the Ni peak is located between the oxide tip and 200 nm from the oxide tip. The Cr peak is in the GB oxide. Fe is depleted near the surface and the Fe ratio goes up to 1 rapidly near the oxide tip. The Si peak is in the GB oxide. There are some differences in the value of element ratio or range of change, however, no significant difference in profile of element ratio along the distance is observed among the 3 dpa, 19 dpa and 73 dpa specimens, neither at the mid thickness, or atthe outer peripheral area. This indicates that the basic mechanism of GB oxidation is not changed due to irradiation up to 73 dpa or due to the stress of 400 MPa in the 3 dpa specimen.

Discussion

The inner layer thickness increased with dose as shown in Fig. 3, indicating the general corrosion was promoted by irradiation. In high-temperature water, Fe dissolves into water as Fe^{2+}, and then finally re-precipitates as Fe-rich spinel outer oxide via Scikorr's reaction, while O diffuses into metal then forms Cr-rich spinel inner oxide. It is considered that irradiation induced lattice defects such as cavities and dislocation loops are likely to affect the diffusion path. These defects provide additional diffusion paths, resulting in some enhancement of solute diffusion and corrosion processes.

Grain boundary oxidation is confirmed to occur at the relatively low dose of 3 dpa. It is also confirmed that the GB oxidation is promoted by irradiation in the same fashion as general corrosion, as shown in Fig. 3. On the other hand, the Cr enrichment, Fe depletion, Ni depletion and Si enrichment along GB in GB oxide and Ni enrichment in front of GB oxide were not changed at doses of 3 to 73 dpa as shown in Fig. 6. This suggests that the basic process of GB oxidation does not change at doses ranging from 3 to 73 dpa.

The basic process of GB oxidation is considered to occur by Fe dissolution and O internal diffusion along GB, in the same fashion as general corrosion, to form Fe depletion and Cr-rich oxide on GB. When Fe dissolves into water, vacancies are formed and they diffuse along GB. In high-temperature water with hydrogen, metal Ni is thermodynamically stable. Therefore, it is considered that Cr preferentially forms oxides, and that a part of Ni diffuses ahead of the GB oxide with vacancies to form Ni enrichment. On the other hand, Cr diffuses from the non-oxidized GB region to the GB oxide in order to mitigate the vacancy concentration gradient.

It is considered that GB oxidation was promoted by GB composition changes due to radiation induced segregation (RIS). Fe and Cr depletion, and Ni and Si enrichment on GB were occurred due to RIS. The relationship between the degree of GB segregation of Cr, Ni, Si and GB oxidation length is shown in Fig. 7. The

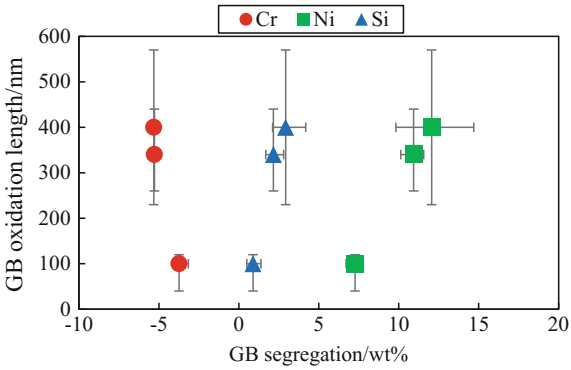

Fig. 7 Relationship between GB segregation and GB oxidation length

data of RIS were published previously for the same FTT material [16]. The increase in GB oxidation with dose is likely to correspond to the degree of RIS. Terachi et al. [14] reported that the surface of stainless steel with lower Cr content was covered with a thicker oxide layer after exposure in simulated PWR primary water, and deduced that general corrosion was promoted by lower Cr content in the metal. Although there was a possible difference between the corrosion process on in-grain and GB, it is likely that preferential oxidation can occur at Cr-depleted GB due to RIS. Although the degree of Cr segregation does not change significantly from 25 dpa to 73 dpa, the GB oxidation length increased by about 20%. It is difficult to explain quantitatively the promotion of GB oxidation at high dose only by Cr depletion. The evolution of segregation of Ni and Si at GB at high dose may be related to the promotion of GB oxidation. It is known that Cr affects corrosion resistance and that Si has high oxidation potential. A high Ni content may result in corrosion enhancement, in analogy with Alloy 600 that easily undergoes GB oxidation. More detailed studies are needed regarding how Cr, Ni and Si segregation are related to the promotion of GB oxidation.

For the effect of stress on GB oxidation, the difference in GB oxidation length was not significant with and without 400 MPa tensile stress in the 3 dpa specimen. The inner oxide of the area subjected to 400 MPa tensile stress was slightly thicker than that in the area without stress in the 3 dpa specimen. Thus, it was found that 400 MPa tensile stress in the 3 dpa specimen promotes general corrosion on the surface, but does not promote GB oxidation. One possible reason for this different corrosion behavior between surface general corrosion and GB oxidation is that the effect of RIS on GB oxidation might be greater than that of stress. However, the effect of stress on GB oxidation has not been well examined yet and awaits further study.

Figure 8 shows changes in various properties including IASCC with dose in the FTT materials examined in this study. The IASCC initiation threshold stress decreases significantly until about 20 dpa and seems to decrease slowly or to saturate over about 40 dpa. The change in IASCC initiation stress cannot be explained fully by any single factor. The GB oxidation length shows the similar

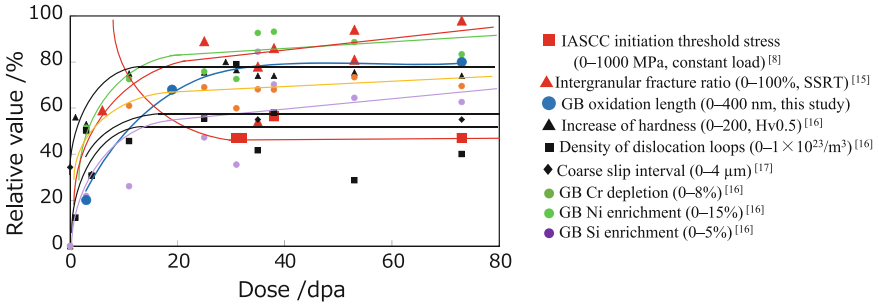

Fig. 8 Comparison of trend due to irradiation between IASCC characteristics (IASCC initiation threshold stress and intergranular fracture ratio), GB oxidation length, increase of hardness, density of dislocation loops, coarse slip interval and GB segregation (Cr, Ni, Si)

change in IASCC initiation stress. The GB oxidation might be related to degradation of the GB binding strength. In a future study, the effect of GB oxidation on degradation of GB binding strength will be evaluated.

Conclusions

GB oxidation behaviors of stainless steel irradiated to 3 dpa, 19 dpa and 73 dpa in a simulated PWR primary water were investigated.

GB oxidation length increased with increasing dose the same as inner oxide layer thickness. The promotion of GB oxidation due to irradiation was confirmed.

Element distribution near GB oxidation was not changed due to irradiation. The basic oxidation process is not considered to be changed due to irradiation.

References

1. R. Cauvin, O. Goltrant, Y. Rouillon, E. Verzaux, A. Cazus, P. Dubuisson, P. Poitrenaud, S. Bellet, Fontevraud 3. FNES **1**, 54–65 (1994)
2. O.K. Chopra, A.S. Rao, A review of irradiation effects on LWR core internal materials—IASCC susceptibility and crack growth rates of austenitic stainless steels. J. Nucl. Mater. **409**, 235–256 (2011)
3. G.S. Was, S.M. Bruemmer, Effects of irradiation on intergranular stress corrosion cracking. J. Nucl. Mater. **216**, 326–347 (1994)
4. K. Fukuya, H. Nishioka, K. Fujii, Irradiation Behavior of Stainless Steels in Light Water Reactor, INSS MONOGRAPHS No. 4 (2009)
5. K. Fukuya, Current understanding of radiation-induced degradation in light water reactor structural materials. J. Nucl. Sci. Technol. **50**, 213–254 (2013)
6. J. Conermann, R. Shogan, K. Fujimoto, T. Yonezawa, Y. Yamaguchi, Irradiation Effects in a Highly Irradiated Cold Worked Stainless Steel Removed from a Commercial PWR, Proc. of

the 12th International Conference on Environmental Degradation of Materials in Nuclear Power System—Water Reactors, pp. 277–284 (2005)
7. P. Freyer, T. Mager, M. Burke, Hot Cell Crack Initiation Testing of Various Heats of Highly Irradiated 316 Stainless Steel Compositions Obtained from Three Commercial PWRs, Proc. of 13th Int. Conf. on Environmental Degradation of Materials in Nuclear Power Systems (2007)
8. H. Nishioka, K. Fukuya, K. Fujii, T. Torimaru, IASCC Initiation in Highly Irradiated Stainless Steels under Uniaxial Constant Load Conditions. J. Nucl. Sci. Technol. **45**(10), 1072–1077 (2008)
9. K. Takakura, K. Nakata, K. Fujimoto, K. Sakima, N. Kubo, IASCC Properties of Cold Worked 316 Stainless Steel in PWR Primary Water, Proc. of 14th Int. Conf. on Environmental Degradation of Materials in Nuclear Power Systems, pp. 1207–1218, (August 23–27, 2009)
10. R.W. Bosch, M. Vankeeberghen, R. Gerard, F. Somville, Crack initiation testing of thimble tube material under PWR conditions to determine a stress threshold for IASCC. J. Nucl. Mater. **461**, 112–121 (2015)
11. K. Fukuya, H. Nishioka, K. Fujii, T. Miura, Y. Kitsunai, Local strain distribution near grain boundaries under tensile stresses in highly irradiated SUS316 stainless steel. J. Nucl. Mater. **432**, 67–71 (2013)
12. Z. Jiao, G. Was, T. Miura, K. Fukuya, Aspects of ion irradiations to study localized deformation in austenitic stainless steels. J. Nucl. Mater. **452**, 328–334 (2014)
13. K. Fukuya, H. Nishioka, K. Fujii, Y. Kitsunai, Characterization of surface oxides formed on irradiated stainless steels in simulated PWR primary water, Proc. of Fontevraud 8 (2014)
14. T. Terachi, T. Yamada, T. Miyamoto, K. Arioka, K. Fukuya, Corrosion Behavior of Stainless Steels in Simulated PWR Primary Water, Effect of Chromium Content in Alloys and Dissolved Hydrogen, J. Nucl. Sci., Technol., vol. 45, no. 10, pp. 975–984 (2008)
15. K. Fukuya, M. Nakano, K. Fujii, T. Torimaru, IASCC Susceptibility and Slow Tensile Properties of Highly-irradiated 316 Stainless Steels. J. Nucl. Sci. Technol. **41**, 673–681 (2004)
16. K. Fukuya, K. Fujii, M. Nishioka, Y. Kitsunai, Evolution of Microstructure and Microchemistry in Cold-worked 316 Stainless Steels under PWR Irradiation. J. Nucl. Sci. Technol. **43**, 159–173 (2006)
17. H. Nishioka, K. Fukuya, K. Fujii, T. Torimaru, IASCC properties and mechanical behavior of stainless steels irradiated up to 73 dpa, *Proc. of 13th Int. Conf. on Environmental Degradation of Materials in Nuclear Power Systems,* 19–23, August (2007)
18. K. Arioka, T. Yamada, T. Terachi, Dependence of Stress Corrosion Cracking for Cold-Worked Stainless Steel on Temperature and Potential, and Role of Diffusion of Vacancies at Crack Tips. Corrosion **64**, 691–706 (2008)
19. K. Fujii, K. Fukuya, Development of micro tensile testing method in an FIB system for evaluating grain boundary strength. Mater. Trans. **52**(1), 20–24 (2011)

Irradiation Assisted Stress Corrosion Cracking (IASCC) of Nickel-Base Alloys in Light Water Reactors Environments—Part I: Microstructure Characterization

M. Song, M. Wang, G.S. Was, L. Nelson and R. Pathania

Abstract Nickel-base alloys, 625DA and 625Plus have received renewed interest as potential structural materials in nuclear reactors to replace the austenitic stainless steels, which show high susceptibility of irradiation-assisted stress corrosion cracking (IASCC). We investigated the microstructural response of both alloys after 2 MeV protons irradiated to 5dpa at 360 °C in the Michigan Ion Beam Laboratory (MIBL). Transmission electron microscopy was performed on plan-viewed samples with a depth range 9–12 μm prepared by jet-polishing. Detailed analysis included changes in phases, dislocation loops, voids swelling, and radiation induced segregation (RIS). Nano-scaled irradiation-induced precipitates and dislocation loops were pervasive. Voids were absent in these alloys. RIS occurred at random high angle grain boundaries examined. A complete characterization of the irradiated microstructure is required to understand their mechanical and IASCC behavior.

Keywords Microstructure · Nickel-base alloy · Precipitates · Proton irradiation · IASCC

Introduction

Nickel-base alloys 625 and derivatives were considered as versatile alloys because of their unique combination of high strength, good fracture toughness, outstanding fatigue and thermal fatigue strength, and superb resistance to corrosion at a broad range of corrosive medium with different temperatures and pressures. These advantages make them widely applied in marine, chemical processing, aerospace,

M. Song (✉) · M. Wang · G.S. Was
University of Michigan, 2355 Bonisteel Blvd, Ann Arbor, MI 48109, USA
e-mail: meowsong@umich.edu

L. Nelson
JLN Consulting, Mills River, NC 28759, USA

R. Pathania
Electric Power Research Institute, 3420 Hillview Ave, Palo Alto, CA 94304-1338, USA

J.H. Jackson et al. (eds.), *Proceedings of the 18th International Conference on Environmental Degradation of Materials in Nuclear Power Systems – Water Reactors*, The Minerals, Metals & Materials Series, https://doi.org/10.1007/978-3-319-68454-3_69

and oil and gas industries [1–4]. Alloy 625 has demonstrated better resistance in irradiation-assisted stress corrosion cracking (IASCC) in comparison with alloy X750 [5], therefore these alloys has received renewed interest recently as potential structural materials to replace the austenitic stainless steels in light water environments, where the austenitic stainless steels show high susceptibility of IASCC [6–8]. IASCC is considered as one of the primary degradation mechanisms of core components [9–12].

Alloy 625 is commercially available in several versions according to its different thermal-mechanical processing. Alloy 625 is commonly referred as the solution annealed and water quenched version. An annealed and aged version is named 625Plus, which is precipitation hardened. Alloy 625 can also be processed through a single-step ageing after hot-work to achieve another high strength version, which is referred to as 625 Direct Aged (DA). These precipitation hardened alloy 625 commonly derive their strength from nano-sized $D0_{22}$-ordered Ni_3(Nb, Ti, Al) (γ'') precipitates.

Under irradiation, numerous defects are generated including point defects and their clusters such as voids, dislocation loops or stacking fault tetrahedral [13]. These point defects and clusters are the major cause for radiation embrittlement and swelling. Irradiation can also change the pre-existing precipitates by dissolution or disordering, or transform them to new precipitates [14], which can also affect the performance. Thus, the irradiation induced microstructure must be well understood.

Although both nickel-base alloys 625Plus and 625DA have been used for decades, the irradiated microstructures of these alloys have seldom been studied. Here, we performed a detailed study of the irradiation induced microstructure of these alloys. The results will help to understand the performance these alloys during service in reactors.

Experimental

Alloy 625Plus heat 215846 was provided by Carpenter Technology Corporation, and alloy 625DA heat JG81 was supplied by Bechtel Marine Propulsion Corp (BMPC). The chemical compositions (wt%) are tabluated in Table 1. Although within the same category, 625Plus and 625DA were examined with different chemcial compositions. Table 2 summarizes the heat treatment history of both alloys. Alloy 625Plus was heat treated by a high tempearture solution anneal plus step two aging treatment. Alloy 625DA was directly aged for over 80 h after hot-work without a solution anneal.

The proton irradiation experiments were conducted using a 3 MV NEC Pelletron accelerator in the Michigan Ion Beam Laboratory (MIBL) at the University of Michigan. Irradiations were conducted with 2 MeV protons at a dose rate of about 1.3×10^{-5} dpa/s at 360 °C. The temperature is selected to simulate the neutron radiation at around 300 °C with compensation of the dose rate effect. The dose and dose rate were estimated using SRIM 2013 (full cascade option) [15]. The resulting

Table 1 Chemical composition of alloys investigated (wt%)

Alloy	Heat	Ni	Cr	Mo	Fe	Nb	Ti	Al	Ta	C	Si	Mn	Co	P	S	Cu	Mg	B
625DA	JG81	62.4	20.8	8.4	3.9	3.6	0.31	0.33	0.03	0.036	0.06	0.08	0.05	0.009	0.0004	0.05	0.0039	0.0023
625Plus	215846	60.4	21.0	8.0	5.7	3.4	1.28	0.2	–	0.008	0.03	0.02	–	0.001	0.0005	–	–	–

Table 2 Heat treatment history of the alloys

Alloy	Heat treatment history
625 Plus	1038 °C 2 h, fan cool, 735 °C 8 h, cool at 56 °C/h to 621 °C for 8 h, AC
625 DA	Aged at 649–667 °C for 81 h, AC

damage layer was approximately 20 microns with relatively uniform damage in the first 15 microns.

Specimens with dimensions of 2 × 2 × 20 mm were cut from the as-received (AR) billet using electro discharge machining (EDM). Samples for optical microscopy were prepared by mechanical grinding up to 800 grit, and followed by cloth polishing with 1 μm diamond paste, and finally vibration polishing. These samples were electrolytically etched in a solution of 10 g citric acid and 10 g ammonium sulfate per liter of water at 5–10 V and a current density of $\sim 0.01 A/cm^2$. The finished samples exhibited a dull golden color. Electron transparent disks were prepared by mechanical grinding of 3 mm disks down to tens of μm. The disks were then perforated in a TenuPol-5 twinjet polisher with the same electropolishing solution at 0 °C and 10–20 V. The irradiated samples were prepared by back thinning of the un-irradiated side to a thickness of around 60 μm with fine grid sand paper to avoid mechanical deformation of the specimens. The irradiated side was then electro-polished to the depth at which observations would be made (typically ~10 μm). The as-ground disks were back thinned by twin jet polisher until perforation.

Scanning electron microscope (SEM) experiments were performed using an FEI Helios 650 Nanolab system equipped with both energy-dispersive X-ray (EDX) spectroscopy. The electron back scatter diffraction (EBSD) maps were collected with an operating voltage of 20 kV and a working distance of 15 mm. The step size for EBSD collection was typically around 1 μm. Transmission electron microscopy (TEM) was performed using a JEOL 3011 microscope operated at 300 kV with an energy-dispersive X-ray spectroscopy (EDX) detector. The smallest objective aperture was used for the dark field imaging. The exposure time was set to 4 s. High resolution (HR) TEM was performed on a JEOL3100R05 double Cs corrected TEM/Scanning TEM (STEM).

Results

As-Received Microstructure

Grain Structure

Both nickel-base alloys possess high length fraction of annealing twin boundaries. The regular high angle grain boundaries (GB) constituted a length fraction of 22% in alloy 625Plus, and 46% in alloy 625DA. It was easy to distinguish these random

Table 3 Grain boundary character from EBSD measurements

ID	LAGB		HAGB		Special GB		Random High angle		Area (μm^2)
	L (μm)	Fraction, %	L(μm)	Fraction, %	L(Σ3 + Σ9)	Fraction, %	L (μm)	Fraction, %	
625Plus	743	1.1	67,800	98.9	50,117 + 2369	76.6	15,314	22.3	1,012,842
625DA	229	2.8	7990	97.2	4021 + 209	51.5	3760	45.7	13,457

LAGB: low angle grain boundary, grain boundaries lower than 15° and above 2°
HAGB: high angle grain boundary, grain boundaries larger than 15°

high angle grain boundaries from twin boundaries, as the latter typically appeared as straight lines in the TEM. The EBSD results showed that the length fraction of twin boundary (TB), mainly Σ3 boundary, was above 50% of the total length of GB. Better corrosion resistance was achieved in alloy 600 with a high fraction of these kinds of coincidence site lattice (CSL) boundaries during practical applications [16]. Although alloys 625 are precipitated hardened, a similar effect is still expected because CSL boundaries are always low energy boundaries and more stable compared to other high angle grain boundaries. All the statistical data are listed in Table 3, which is related to the GB information. It was noticed that the length fraction of low angle boundaries was less than 3% for all alloys. Another character of grain boundary is the composition. Enrichment of Cr and Mo and depletion of Ni was observed in the as-received conditions in both alloys.

Second Phases

A general feature of both nickel-base alloys was the formation of (Nb,Ti)(C,N) stringers along the extrusion or rolling direction as shown in Fig. 1. More particles were observed in alloys 625 DA compared to that in alloy 625Plus. These carbonitrides were formed during the solidification process and were hard to remove

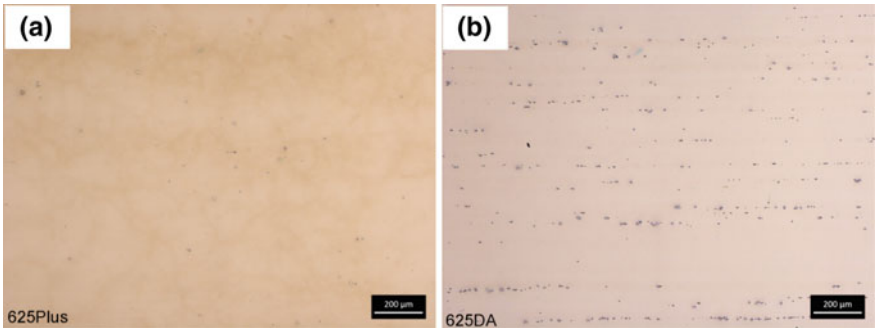

Fig. 1 Optical images of **a** alloy 625Plus and **b** alloy 625DA

by the subsequent heat treatments. The average grain size was measured by a linear interception method with at least 200 grains involved for each alloy. Alloy 625Plus showed the largest average grain size of around ~120 μm. Alloy 625DA showed the smallest average grain size of around ~12 μm.

Substantial amounts of precipitates were observed within the matrix in both alloys, with a density on the order of $10^{22}/m^3$. Extracted particles are shown in Fig. 2. The inserted selected area diffraction pattern (SADP) corresponds well to the γ″ and γ′. γ′ phase has been excluded from further analysis of these alloys. EDX results suggests that these particles were enriched in Nb and Ti, which corresponded well to the chemical composition of Ni_3(Nb, Ti, Al) (γ″) precipitate. All the EDX results are summarized in Table 4. Due to the signal from the pole piece in the microscope, Fe content was not properly measured and assumed zero for the analysis. The statistical results are given in Fig. 3, and were based on measurements of about 400 particles in each case. The precipitates in alloy 625Plus and 625DA show a similar size with around ~12 nm in diameter. But the particle density is higher in alloy 625Plus, $(4.5 \pm 3.5) \times 10^{22}/m^3$ than that in alloy 625DA, $(2.1 \pm 0.2) \times 10^{22}/m^3$.

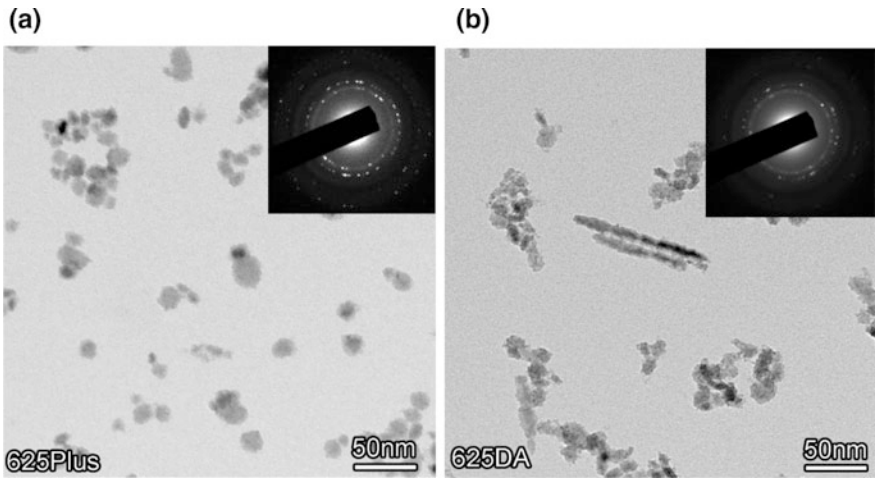

Fig. 2 Bright field of the extracted particles in **a** alloy 625Plus and **b** alloy 625DA

Table 4 Chemical composition of nano-sized precipitates in the alloys (wt%). The Fe is assumed to be zero in the alloys

Alloy	Ni	Cr	Mo	Nb	Ti	Al
625Plus	50.7 ± 5.0	8 ± 0.8	10.9 ± 2.3	23.5 ± 3.0	5.9 ± 0.2	0.2 ± 0.2
625DA	47.1 ± 5.8	9.9 ± 2.9	11.7 ± 1.6	27.3 ± 2.9	2.7 ± 0.7	0.4 ± 0.3

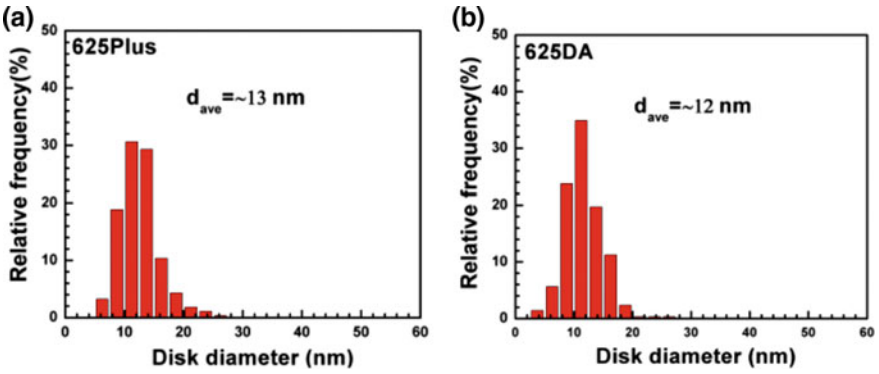

Fig. 3 Disk diameter distribution of γ″ and γ′ precipitates **a** 625Plus and **b** 625DA

Radiation-Induced Microstructure

Dislocation Loops

Faulted, Frank-loops are frequently observed in irradiated austenitic steels [17, 18] and nickel-base alloys [19]. The habit plane is the {111} close packed plane. These loops are easily observed by the Rel-rod method, which takes advantage of the diffraction pattern of stacking faults and creates a streaked line between the major diffraction spots. According to the crystallography of the FCC structure, only one quarter of the total loops is imaged at a time, so the loop density should be calculated by multiplying by a factor of 4. Figure 4 shows a typical Rel-rod image of dislocation loops in alloy 625Plus, which is typical for both alloys investigated. All the loops are inclined in the same direction as all of them shared the same habit plane. The size distributions of loops for different alloys are shown in Fig. 5.

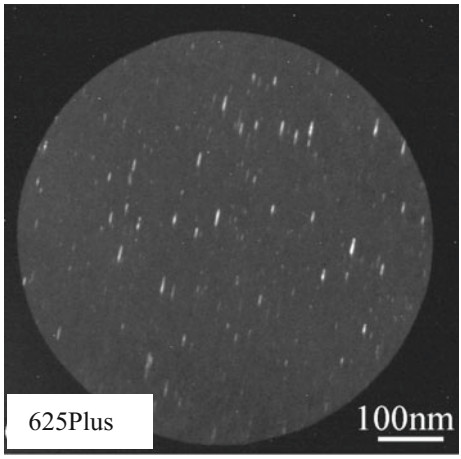

Fig. 4 Faulted loops in alloy 625Plus. These loops are observed through the rel-rod method. The alloys are irradiated at 360 °C to around 5 dpa by protons

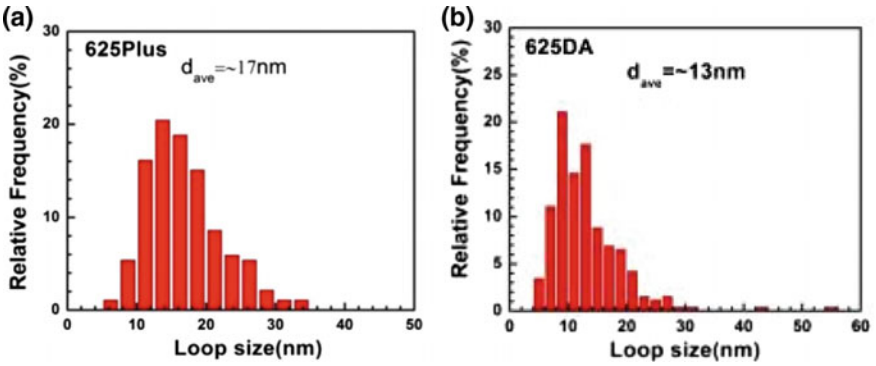

Fig. 5 Statistical study of the dislocation loops in **a** alloy 625 Plus and **b** alloy 625DA. These alloys are irradiated at 360 °C to about 5 dpa by protons

Smaller loops with higher density were observed in alloy 625DA (size: (13 ± 5.8) nm; density: (10.2 ± 1.1) × $10^{22}/m^3$) compared with 625Plus (size: (16.7 ± 5.4 nm); density: (3.1 ± 0.8) × $10^{22}/m^3$).

Precipitates

The irradiated microstructure of alloy 625Plus is shown in Fig. 6a as an example. No significant size or density change of γ″ phase was observed in the alloys studied. Part of the precipitates was not observed in the dark field. These missing spots deviated from the standard diffraction condition as shown in Fig. 6b. This could be due to partial re-solution of the phase that broke the ordered structure. A new precipitate was observed in these alloys. A typical [001] zone axis is shown in the upper right corner of Fig. 6a. The superlattice reflections at {100}, {110}, ½{201} are from the three variants of γ″ phase.

In addition to these superlattice reflections, another group of spots at 1/3{220} position were also observed in Fig. 6a. These diffraction spots are associated with variants 1 and 2 of the Ni_2Cr phase, which is a long range ordered (LRO) phase. These precipitates (shown in Fig. 6d) are randomly distributed within the matrix. There is no clear evidence that the formation of this LRO phase was associated with the pre-existing γ″ phase. A slightly larger size was observed in alloy 625DA (~11 nm) than in the alloy 625Plus (~6 nm). The density was about the same, $10^{23}/m^3$.

Radiation-Induced Segregation

Before irradiation, there was a slight enrichment of Cr and Mo and corresponding depletion of Ni in the as-received condition, as shown in Fig. 7a. Following

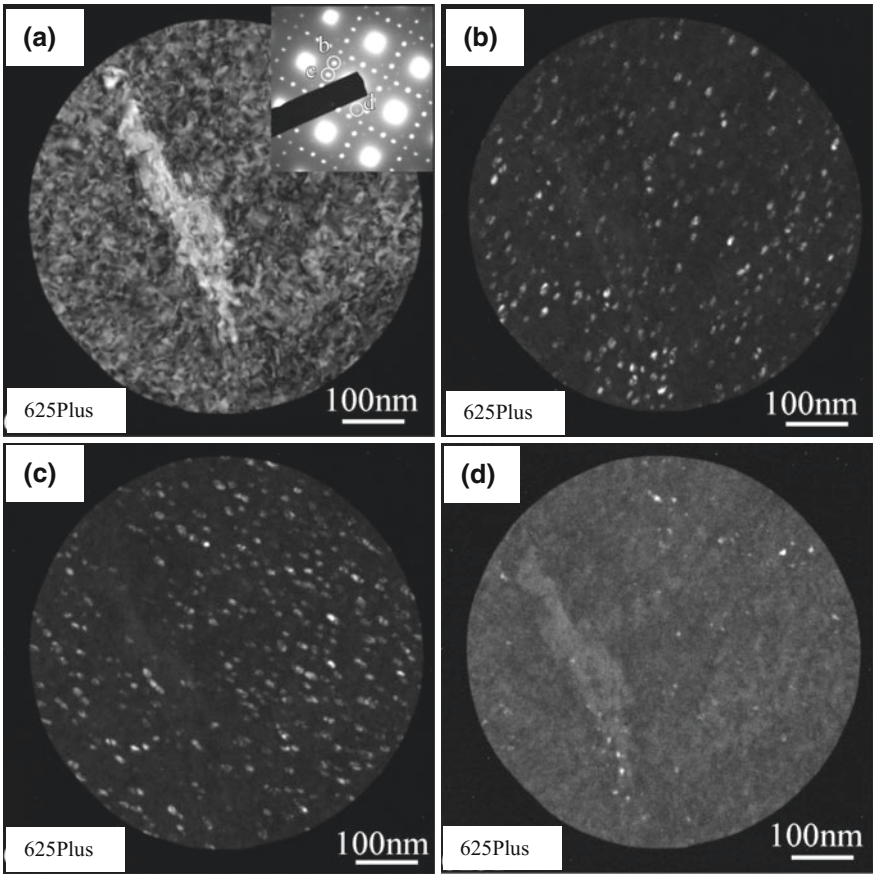

Fig. 6 Distribution of long range-order phase in 625Plus after 5 dpa 360 °C proton irradiation. **a** Bright field image and **b**–**c** dark field image of pre-existing γ'' and **d** dark field of three variants of long range order phase respectively

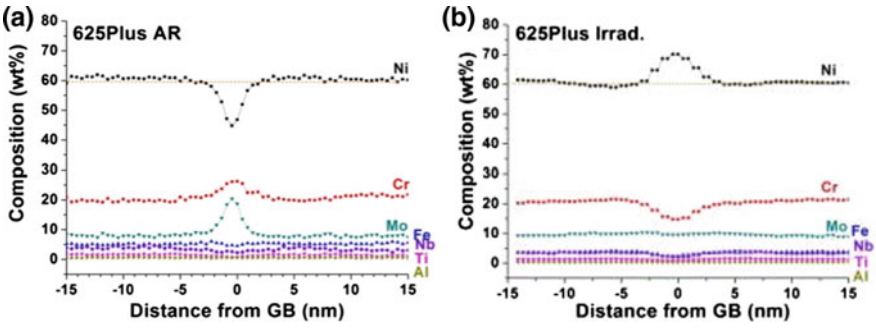

Fig. 7 RIS in alloy 625Plus **a** as-received and **b** after irradiation

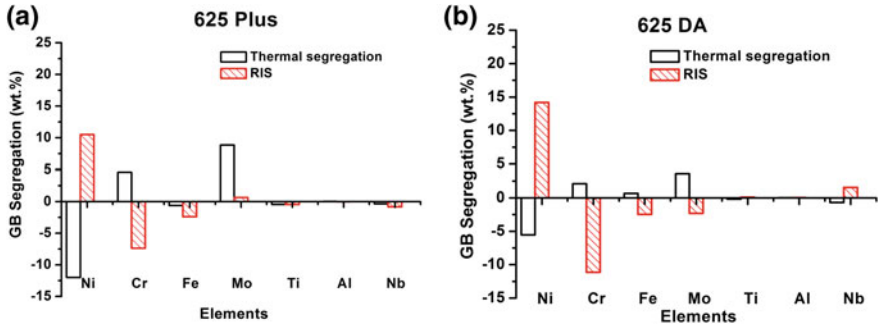

Fig. 8 Comparison of thermal segregation and RIS in nickel-base alloys **a** alloy 625Plus **b** alloy 625DA

irradiation, GB concentrations of Ni were enriched above the bulk level and those for Cr and Fe were depleted in Fig. 7b. Quantitative results of alloy 625Plus and 625DA are shown in Fig. 8. Mo is a slow diffuser which was enriched in the as-received condition and depleted along with Cr in the irradiated condition. Depending on the degree of original enrichment, the Mo may show above or below the bulk level after irradiation. The segregation of other elements is insignificant or beyond the resolution of the instrumentation.

Discussion

Radiation-induced dissolution of γ'' is insignificant in these nickel-base alloys. It was reported that γ'' phase were totally dissolved in alloy 718 after 10dpa Fe ion irradiation [20]. It should be noted that the cascade structure is different during proton and heavy ion damage. Therefore, the efficiency for precipitation dissolution is different between proton and heavy ion. If the irradiation goes to higher doses, these phases may dissolve eventually.

The irradiated microstructures are very sensitive to the chemical composition. Both alloys are close to each other in chemical composition. However, significant difference of microstructure was observed after irradiation. The loops were smaller in alloy 625DA in comparison to alloy 625P. But the loop density was very high in alloy 625DA. This suggests that the pre-existing precipitates may act as sinks for the irradiation induced defects or clusters at 360 °C. Alloy 625Plus with higher density of γ'' phase shows a lower density of irradiation induced loops. The newly formed (LRO) phase is even more sensitive to the chemical composition. The volume fraction of LRO in alloy 625DA was around 5% while it was just around 1.2% in alloy 625P. It is proposed that the Fe element may strongly inhibit the formation of the LRO phase.

RIS among both alloys is quite similar. However, the behavior of various elements under radiation is very interesting and can be understood simply through the solute size effect [13] in which elements with larger radius preferentially diffuse away from GB while smaller atoms preferentially diffuse towards the GB. The response of Mo was confusing without the thermal segregation data. Due to its slow diffusivity, Mo can show either higher or lower than the bulk value after irradiation. But the absolute value decreased which suggested that Mo diffused away together with Cr from GB.

Conclusions

Significant irradiation-induced microstructural changes were observed in both nickel-base alloys 625Plus, and 625DA following 5 dpa proton irradiation. The dissolution of γ'' was insignificant. Loops of larger size with lower density were formed in alloy 625Plus compared with those formed in alloy 625DA. Although the density was similar for both alloys, the diameter of LRO phase was larger in alloy 625DA than that in alloy 625Plus, resulting in a factor of four difference in volume fraction. The LRO phase is very sensitive to the chemical composition. RIS was significant among both alloys. Enrichment of Ni, depletion of Cr and Fe were observed after irradiation. Mo is a slow diffuser and can be either higher or lower than bulk values after irradiation. No voids were observed at these doses for both alloys.

Acknowledgements The authors acknowledge the financial support by EPRI (contracts 10002164 and 10002154), and DOE (contract 4000136101), and gratefully acknowledge O. Toader, T. Kubley, E. Uberseder and D. Woodley for their assistance with the proton irradiations. Access to the microscopes of the Michigan Center for Materials Characterization (MC^2) at University of Michigan is also acknowledged. The technical assistance on FEI Talos Microscope from Dr. C. M. Parish at Oak Ridge National Laboratory is greatly appreciated. This work was also supported by the U.S. Department of Energy, Office of Nuclear Energy under DOE Idaho Operations Office Contract DE-AC07-051D14517 as part of a Nuclear Science User Facilities experiment.

References

1. L.E. Shoemaker. Alloys 625 and 725: trends in properties and applications, Superalloys 718, 625, 706 and derivatives 409–418 (2005)
2. R.B. Bhavsar, A. Collins, S. Silverman. Use of alloy 718 and 725 in oil and gas industry, Superalloys 718, 625, 706 and Various Derivatives 47–55 (2001)
3. G. Smith, D. Tillack, S. Patel. Alloy 625: impressive past, significant presence, awesome future, Superalloys 718,625,706 and various derivatives 35–46 (1991)
4. J.M. Rakowski, C.P. Stinner, M. Lipschutz, J. Preston Montague. The use and performance of wrought 625 alloy in primary surface recuperators for gas turbine engines, Superalloys 718, 625, 706 and derivatives 271–286 (2005)

5. R. Bajaj, W. Mills, M. Lebo, B. Hyatt, M. Burke, Irradiation-assisted stress corrosion cracking of HTH Alloy X-750 and Alloy 625. Seventh International Symposium on Environmental Degradation of Materials in Nuclear Power Systems-Water Reactors. **2**, 1093–1107 (1995)
6. S. Bruemmer. New Issues Concerning Radiation-Induced Material Changes and Irradiation-Assisted Stress Corrosion Cracking in Light Water Reactors. Proc. 10th Int. Conf. Environmental Degradation of Materials in Nuclear Power Systems—Water Reactors (Houston, TX: NACE, 2002), 2002
7. O. Chopra, A. Rao, A review of irradiation effects on LWR core internal materials–Neutron embrittlement. J. Nucl. Mater. **412**, 195–208 (2011)
8. O. Chopra, A. Rao, A review of irradiation effects on LWR core internal materials–IASCC susceptibility and crack growth rates of austenitic stainless steels. J. Nucl. Mater. **409**, 235–256 (2011)
9. P. Scott, A review of irradiation assisted stress corrosion cracking. J. Nucl. Mater. **211**, 101–122 (1994)
10. E. Kenik, R. Jones, G. Bell, Irradiation-assisted stress corrosion cracking. J. Nucl. Mater. **212**, 52–59 (1994)
11. G.S. Was, S.M. Bruemmer, Effects of irradiation on intergranular stress corrosion cracking. J. Nucl. Mater. **216**, 326–347 (1994)
12. J. Busby, G. Was, E. Kenik, Isolating the effect of radiation-induced segregation in irradiation-assisted stress corrosion cracking of austenitic stainless steels. J. Nucl. Mater. **302**, 20–40 (2002)
13. G.S. Was, *Fundamentals of radiation materials science: metals and alloys* (Springer, Berlin, 2016)
14. K.C. Russell, Phase stability under irradiation. Prog. Mater Sci. **28**, 229–434 (1984)
15. J.P.B. J.F.Ziegler. SRIM 2013 Program, IBM Corporation, Yorktown, NY
16. P. Lin, G. Palumbo, U. Erb, K. Aust, Influence of grain boundary character distribution on sensitization and intergranular corrosion of alloy 600. Scr. Metall. Mater. **33**, 1387–1392 (1995)
17. Z. Jiao, G. Was, The role of irradiated microstructure in the localized deformation of austenitic stainless steels. J. Nucl. Mater. **407**, 34–43 (2010)
18. Z. Jiao, J. Busby, G. Was, Deformation microstructure of proton-irradiated stainless steels. J. Nucl. Mater. **361**, 218–227 (2007)
19. G.S. Was, *Fundamentals of radiation materials science: metals and alloys* (Springer, Berlin, 2007)
20. J. Hunn, E. Lee, T. Byun, L. Mansur, Ion-irradiation-induced hardening in Inconel 718. J. Nucl. Mater. **296**, 203–209 (2001)

Irradiation Assisted Stress Corrosion Cracking (IASCC) of Nickel-Base Alloys in Light Water Reactors Environments Part II: Stress Corrosion Cracking

Mi Wang, Miao Song, Gary S. Was, L. Nelson and R. Pathania

Abstract Radiation-induced microstructural changes control the Irradiation Assisted Stress Corrosion Cracking (IASCC) of core materials, which is a key factor in the extension of the operating lifetime of Light Water Reactors (LWRs). Nickel-base alloys are considered as potential structural materials to replace highly IASCC susceptible austenitic stainless steels. Constant extension rate tensile (CERT) tests were conducted on proton irradiated high strength nickel-base alloy 625 with two different heat treatment conditions (625Plus and 625DA) in both simulated BWR NWC and PWR primary water. Crack length per unit area and fraction of grain boundaries that cracked were used to assess the IASCC susceptibility. Both 625Plus and 625DA showed a very high IASCC susceptibility. 625DA also exhibited greater changes in all microstructure features than 625Plus.

Keywords Nickel-base alloys · Irradiation-assisted stress corrosion cracking · Mechanical properties · LWRs

Introduction

The life extension of existing reactors and design of next generation nuclear reactors require advanced materials that can maintain structural integrity in harsh radiation environments. Austenitic stainless steels used in core components have proved to be problematic, especially at high irradiation doses [1–3]. The fracture toughness of Type 304L SS drops to extremely low values after just 4 dpa irradiation [4]. Void swelling may become significant at higher doses [5]. More

M. Wang (✉) · M. Song · G.S. Was
University of Michigan, Ann Arbor, MI 48109, USA
e-mail: miwan@umich.edu

L. Nelson
JLN Consulting, Mills River, NC 28759, USA

R. Pathania
Electric Power Research Institute, 3420 Hillview Ave, Palo Alto, CA 94304-1338, USA

J.H. Jackson et al. (eds.), *Proceedings of the 18th International Conference on Environmental Degradation of Materials in Nuclear Power Systems – Water Reactors*, The Minerals, Metals & Materials Series, https://doi.org/10.1007/978-3-319-68454-3_70

importantly, IASCC has been observed to occur quite early in life [4]. It is identified as one of the primary degradation mechanisms of core components made of stainless steels and nickel-base alloys, which are used in control rod blades, neutron source tubes, baffle bolts, and springs in light water reactors systems [6–9]. Thus, replacement of these components may become a necessity.

Due to the generally poor performance of high strength alloys like alloy X-750 in nuclear reactors, alloy 625 has received renewed interest as a potential structural material to replace austenitic stainless steels in core components [1] because of their high strength, good fracture toughness and resistance to corrosion over a broad range of severe environments [10–12]. Alloy 625 is available commercially in a variety of thermal-mechanical treatments. Alloy 625Plus is a solid solution and aged version of alloy 625. This alloy can also be processed through a direct aging procedure after hot-working to achieve a high strength and is referred to as 625 Direct Aged (DA). This paper examines the IASCC susceptibility of the two high strength nickel-base alloys, 625Plus and 625DA in LWRs environments.

Experimental

Materials and Samples Design

Alloy 625Plus heat 215,846 was provided by Carpenter Technology Corporation, and alloy 625DA heat JG81 was supplied by Bechtel Marine Propulsion Corp (BMPC). The chemical compositions and thermal treatments of 625Plus and 625DA are listed in Tables 1 and 2, respectively. The grain size of alloy 625Plus was about 120 μm while 625DA had a much smaller grain size, around 12 μm. More detail information on the alloy microstructures and processing conditions is presented in the Part I paper [13].

Samples were made by the standard design used for proton irradiations at the Michigan Ion Beam Laboratory (MIBL) at the University of Michigan. All the samples were machined with the tensile axis oriented in the extrusion direction. The tensile samples have a square gage section of 2 mm, a gage length of 21 mm and threaded ends, as shown in Fig. 1. Before irradiation, all the samples were mechanically polished with silicon carbide abrasive paper from 360 to 4000 grit then electropolished to obtain a mirror finish.

Proton Irradiation Experiment

The proton irradiation experiments were conducted using a 3 MV NEC Pelletron accelerator in the Michigan Ion Beam Laboratory (MIBL) at the University of Michigan. Irradiations were conducted with 2 meV protons to a dose of 5 dpa at a

Table 1 Chemical compositions of alloys 625Plus and 625DA (wt%)

Condition	Ni	Cr	Mo	Fe	Nb	Ti	A1	Ta	C	Si	Mn	Co	P	S	Cu	Mg	B
625Plus	60.38	20.99	8.02	Bal.	3.4	1.28	0.2	–	0.008	0.03	0.02	–	0.001	0.0005	–	–	–
625DA	62.41	20.76	8.39	3.88	3.58	0.31	0.33	0.03	0.036	0.06	0.08	0.05	0.009	0.0004	0.05	0.0039	0.0023

Table 2 Heat treatment of alloys 625Plus and 625DA

Alloy	Thermal mechanical treatments (TMTs)
625Plus	1038 °C/2 h + 725 °C/8 h + 621 °C/8 h
625DA	Hot working + 648–667 °C/8 h

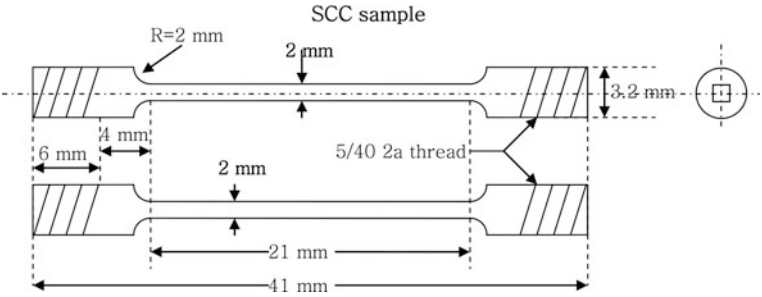

Fig. 1 Schematic diagram of tensile sample

dose rate of about 1.3×10^{-5} dpa/s at 360 °C. The dose and dose rate were estimated using SRIM 2013 (full cascade option) [14]. The resulting damage layer was approximately 20 microns with relatively uniform damage in the first 15 microns.

Hardness Measurement

Microhardness was measured using a Vickers Hardness indenter (MICROMET II) with a load of 25 g. The lower load (25 g) was chosen to confine the plastic zone ahead of the indenter tip to a depth within the proton irradiated range ($\sim$20 μm) to ensure that the unirradiated region was not being sampled.

CERT Test and Crack Characterization

Constant extension rate tensile (CERT) tests were performed using the CERT I and CERT II systems in the High Temperature Corrosion Laboratory (HTCL) at the University of Michigan. CERT I and CERT II systems share the same design and are capable of straining four samples in parallel providing identical conditions within a given test, respectively. However, CERT I system was assigned to a BWR NWC environment while CERT II system was a PWR primary water environment. Each system consists of a 4 L stainless steel autoclave that was connected to a flowing water loop fed from an external water column in which the addition of gas was made. CERT experiments were conducted at a strain rate of 1×10^{-7} s^{-1}

Table 3 Conditions of CERT test for simulated BWR NWC and PWR primary water environments

Parameter	BWR NWC	PWR primary water
Temperature (°C)	288	320
Pressure (psi)	1500	2000
Inlet conductivity (μS/cm)	<0.1	20–30
Outlet conductivity (μS/cm)	<0.1	20–30
O_2 concentration (ppb)	2000	<5
H_2 concentration (cc/kg)	–	35
Boron (ppm)	–	900–1100
Lithium (ppm)	–	2–3
pH at 25 °C	7.0	6–6.7

in either simulated BWR NWC (288 °C, 1500 psi, 2000 ppb dissolved oxygen) or PWR primary water environment (320 °C, 2000 psi, 35 cc/kg dissolved hydrogen, 1000 ppm [B] and 2 ppm [Li]) to about 4% plastic strain. The conductivity, oxygen content, hydrogen content, and B and Li concentrations were chosen to be representative of both reactors cores. The specific conditions are listed in Table 3. After the CERT test, the gage section of each tensile sample (about 1 mm^2 area) in both irradiated and unirradiated areas were characterized in an SEM (JEOL JSM-6480) to determine the surface morphology and cracking susceptibility.

Results

Irradiation Hardening

Irradiation hardening measurements of alloy 625Plus and 625DA are plotted in Fig. 2. As precipiate hardened alloys, both alloys showed small increases in hardness after 5 dpa irradiation. 625DA exhibited an increase in hardness of 150 Hv versus 60 Hv for 625Plus.

CERT Test Results

CERT tests on high strength nickel-base alloys, 625Plus and 625DA were completed in both BWR NWC and PWR primary water environments. Two samples of each alloy were tested for each environment. All alloys were strained to a plastic strain close to 4% as determined by the linear variable differential transducer (LVDT), and later verified from the fiducial marks on the samples. The stress-strain curves of each alloy are shown in Fig. 3. The apparent yield stress of 625Plus and 625DA were about same, around 750 MPa.

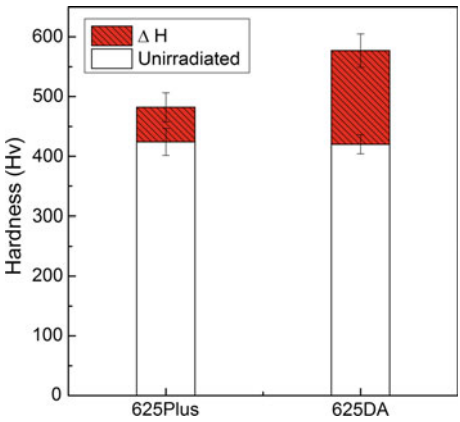

Fig. 2 Hardening measurements for alloys 625Plus and 625DA before and after irradiation to 5 dpa

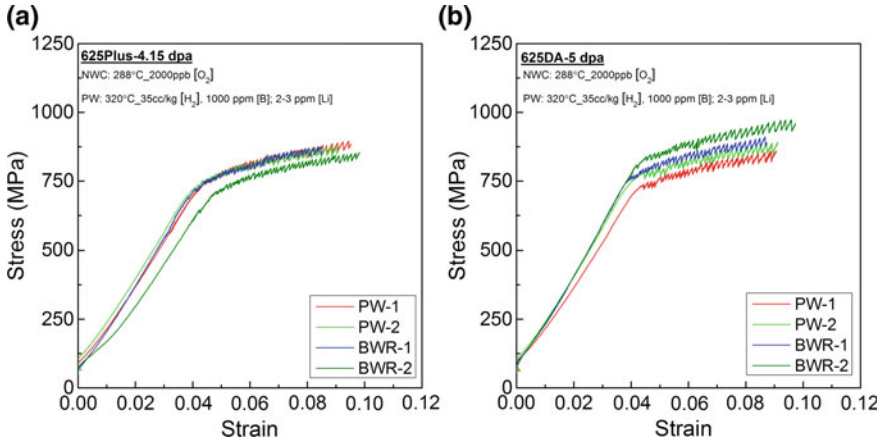

Fig. 3 Stress-strain curve of alloy 625Plus in (**a**) and 625DA in (**b**) in both BWR NWC and PWR primary water environments

Because only 1% of the thickness of the alloy was actually irradiated by the proton beam (20 μm irradiation depth over 2 mm bar thickness), the yield strengths obtained were not expected to show any effect of irradiation. The serrations in the plastic deformation region were due to dynamic strain aging of the alloys.

Cracking Behavior

Cracks were observed in both unirradiated and irradiated areas for both high strength nickel-base alloys in BWR NWC and PWR primary water environments. Micrographs of these cracks are shown in Fig. 4 for BWR NWC, and in Fig. 5 for

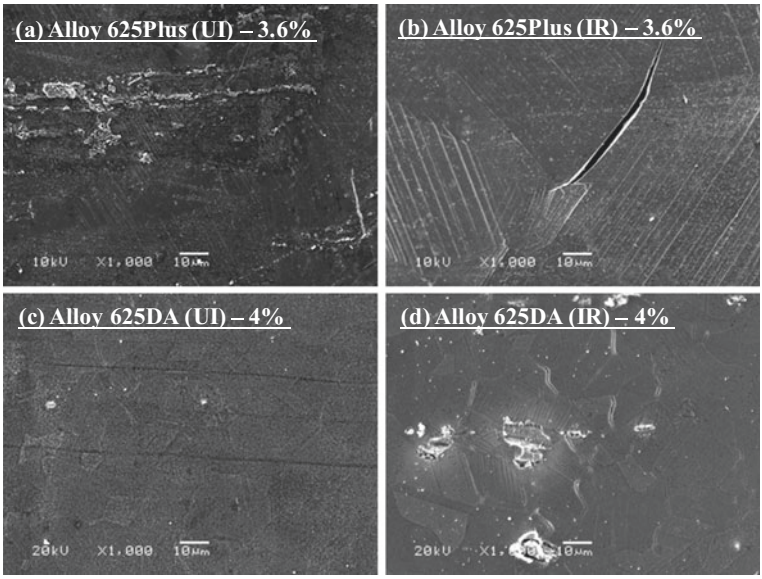

Fig. 4 SEM mircrographs of high strength nickel-base alloys 625Plus in (**a**) and (**b**), and 625DA in (**c**) and (**d**), irradiated to a dose of 5 dpa and strained to about 4% in BWR NWC environment, stress direction: horizontal, *UI* unirradiated area, *IR* irradiated area

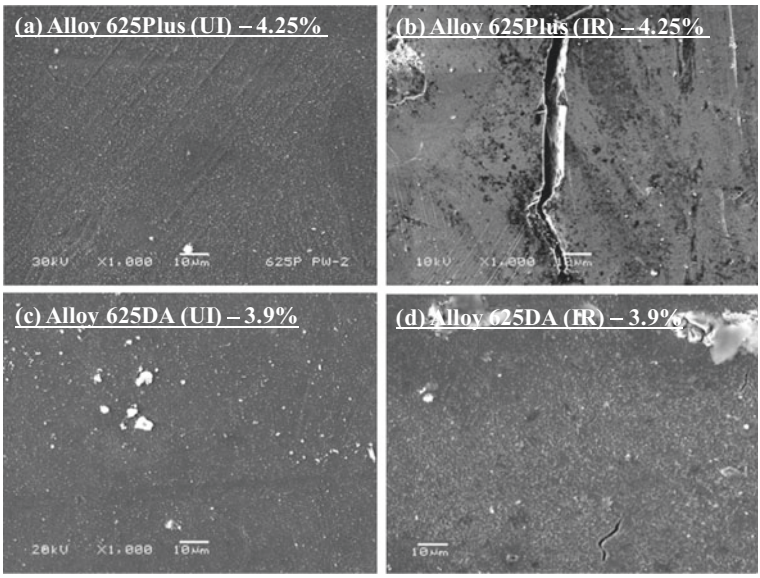

Fig. 5 SEM mircrographs of high strength nickel-base alloys 625Plus in (**a**) and (**b**), and 625DA in (**c**) and (**d**), irradiated to a dose of 5 dpa and strained to about 4% in PWR primary water environment, stress direction: horizontal, UI unirradiated area, IR irradiated area

PWR primary water. The strain (stress) direction was horizontal in these micrographs. For both BWR NWC and PWR primary water environments, the surface was covered with oxide crystallites. The oxide formed on nickel-base alloys should consist of a duplex oxide: an inner layer of continuous Cr-rich oxide with a discontinuous external layer with composition, morphology and microstructure depending on the environment and exposure duration [15, 16]. However, most of the external oxide should be an iron-rich spinel oxide, typically of the form of $Ni_{1-x}Fe_{2+x}O_4$, which may be the small crystallites observed on the surface [17–19].

The morphology of the cracks for each alloy was different for the irradiated and unirradiated areas. For both alloys, the number of cracks in the irradiated area was greater than in the unirradiated area. Crack opening was also greater in the irradiated area (several microns) compared to the unirradiated area (less than one micron). In the irradiated area, the cracks on alloy 625Plus were wide and long, with lengths of tens to hundreds of micrometers in both water environments. Alloy 625DA had a very small grain size, so most cracks were small and extended along several facets. In the unirradiated area, cracks for all the alloys were fairly very short and narrow.

IASCC Susceptibility

Crack characterization for each condition includes the following parameters:

- average crack length;
- crack density: the number of cracks observed per unit area;
- crack length per unit area: the total crack length divided by the analyzed area;
- fraction of grain boundary length that cracked.

The most representative metric to describe the cracking susceptibility is crack length per unit area, which measures the extent of cracking by incorporating both the density and the length of cracks. For all the alloys, the crack length per unit area was much higher in the irradiated area than in the unirradiated area. The IASCC susceptibility of nickel-base alloys, determined by crack length per unit area, in BWR NWC and PWR primary water is plotted in Fig. 6, in which "UIA" refers to the unirradiated area and "IA" refers to the irradiated area.

By crack length per unit area, alloy 625DA was more susceptible than alloy 625Plus to IASCC in both BWR NWC and PWR primary water environments, especially in NWC. Moreover, for these high strength nickel-base alloys, the cracking susceptibility was always higher in BWR NWC than in PWR primary water environment. It was quite reasonable since the NWC environment is far more aggressive [20, 21] than primary water and resulting in more and longer cracks.

Another metric to measure cracking susceptibility is fraction of grain boundary length that cracked. This metric eliminates the influence of grain size in the data. The ratio between cracked grain boundary length and random high angle grain boundary (HAGB) length is shown in Fig. 7. The random HAGB length was

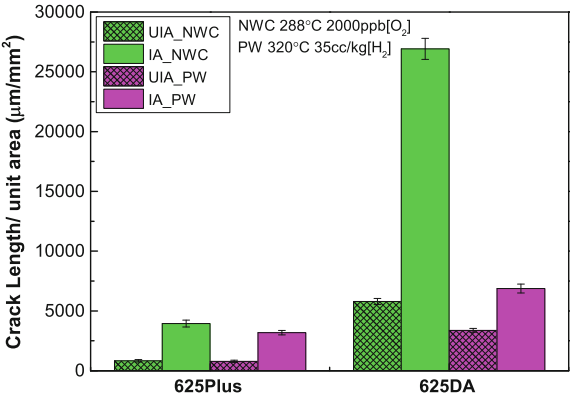

Fig. 6 Crack length per unit area in both irradiated (IA) and unirradiated (UIA) areas of alloys 625Plus and 625DA irradiated to a dose of 5 dpa and strained to 4% in both BWR NWC and PWR primary water environments

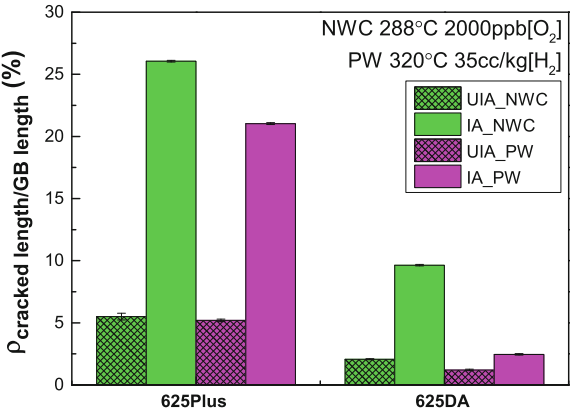

Fig. 7 Ratio between cracked length and random HAGB length in both irradiated and unirradiated areas of alloys 625Plus and 625DA irradiated to a dose of 5 dpa and strained to 4% in both BWR NWC and PWR primary water environments

obtained from the EBSD results which were presented in the Part I [13]. By fraction of grain boundary length that cracked, it showed that 625Plus had a higher ratio of grain boundary cracking. In other words, alloy 625Plus had a higher IASCC susceptibility in both BWR NWC and PWR primary water environments.

Discussion

Two parameters were used to evaluate the IASCC behavior, the crack length per unit area, and the fraction of cracked grain boundary. These two parameters provide somewhat different information. Crack length per unit area is the total length of all the cracks in the sample per unit area observed. It combines both the crack density and the crack length and in fact, is approximately equal to the product of the average of both. It directly indicates the performance of the alloy from the application/engineering point of view. Fraction of cracked grain boundary, on the

other hand, is a measure of the fraction of the total grain boundary length that has cracked and is independent of grain size. As noted, 625Plus and 625DA had very different grain sizes. Usually, grain size has an influence on SCC behavior, with increasing SCC susceptibility with grain size [22]. But, some processes used to reduce grain size may leave defects on grain boundaries (such as, precipitates, carbides, etc.,) which would cause an increase on IASCC susceptibility. Therefore, for a given alloy, if either the value of cracking length per unit area or fraction of cracked grain boundary is high, the IASCC susceptibility is high.

Figure 8 illustrates a direct ranking of IASCC susceptibility versus microstructural changes due to radiation. All the microstructure data represented came from the Part I paper [13]. Using the metric of crack length per unit area, 625DA was higher in cracking susceptibility. Also, 625DA had higher hardness after irradiation and more radiation hardening. Moreover, 625DA also had more significant microstructural changes due to irradiation, the change in existing precipitates (γ'' phase), formation of radiation-induced long range order (LRO) phase, formation of dislocation loops, and the lowest Cr concentration at the grain boundary. Thus, it was not a surprise that the alloy that had significant changes in microstructure features due to radiation also had a very high IASCC susceptibility. However, it also made it impossible to determine the specific microstructural feature or combination of features that control the IASCC behavior.

Using the metric of fraction of cracked grain boundary, 625Plus was more susceptible to IASCC in both water environments. Once the crack length was normalized to the high angle grain boundary (HAGB) length, it was considered that the grain size effect was eliminated. As listed in Fig. 8, the grain size of 625Plus was 10 times larger than that for 625DA. In addition, the HAGB length per unit area of 625DA was around 20 times more than that of 625Plus (EBSD results presented in the Part I paper [13]). Therefore, the IASCC susceptibility ranking of

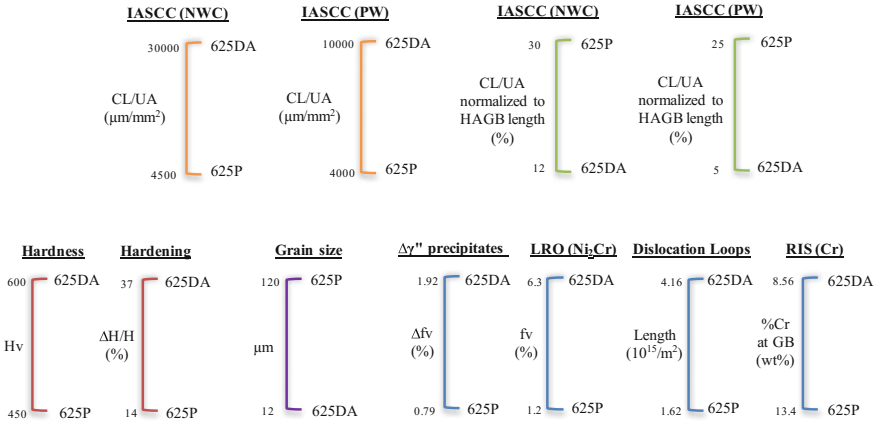

Fig. 8 IASCC behavior of high strength nickel-base alloys versus microstructural features due to radiation

625DA dropped while 625Plus increased due to the mathematic calculation. It should also be noted that over 25% of the random HAGB length (Fig. 7) in alloy 625Plus was cracked after an irradiation dose of 5 dpa. Although the microstructural changes induced by irradiation might not be that significant in 625Plus, it was still considered as highly susceptible to IASCC in LWRs environments.

Conclusion

Evaluation of IASCC behavior of the high strength nickel-base alloys 625Plus and 625DA, in both BWR NWC and PWR primary water was made following proton irradiation to 5 dpa.

- Alloy 625Plus and alloys 625DA were both highly susceptible to IASCC;
- While the IASCC susceptibility of 625DA correlated with the degree of irradiation-induced microstructural changes, the dominant feature or combintaion of features could not be identified;
- High potential environment significant enhanced cracking behavior as IASCC susceptibility was higher in BWR NWC than in PWR primary water.

Acknowledgements Support for this work was provided by the Electric Power Research Institute (contract no: 10002164 and 10002154) and Department of Energy (contract no: 4000136101). The authors gratefully acknowledge the facilities provided by the Michigan Ion Beam Laboratory and the High Temperature Corrosion Laboratory at the University of Michigan. The authors would also like to thank Dr. Ovidiu Toader of the Michigan Ion Beam Laboratory and Mr. Alex Flick of the High Temperature Corrosion Laboratory for their invaluable support in conducting the experiments.

Reference

1. S. Bruemmer, New issues concerning radiation-induced material changes and irradiation-assisted stress corrosion cracking in light water reactors, in Proceeding of 10th International Conference on Environmental Degradation of Materials in Nuclear Power Systems—Water Reactors. (Houston, TX, 2002)
2. O. Chopra, A. Rao, A review of irradiation effects on LWR core internal materials—Neutron embrittlement. J. Nucl. Mater. **412**, 195–208 (2011)
3. O. Chopra, A. Rao, A review of irradiation effects on LWR core internal materials—IASCC susceptibility and crack growth rates of austenitic stainless steels. J. Nucl. Mater. **409**, 235–256 (2011)
4. P. Andresen, F. Garner, J. Gorman, S. Maloy, J. Nelson, L. Tan, T. Toloczko, G. Was, Technical report: critical issues report and roadmap for the advanced radiation-resistant materials program, EPRI, Palo Alto, CA: 2012. 1026482, (2012)
5. F. Garner, B. Oliver, L. Greenwood, D. Edwards, S. Bruemmer, M. Grossbeck (2002) Generation and retention of helium and hydrogen in austenitic steels irradiated in a variety of LWR and test reactor spectral environments. Pacific Northwest National Laboratory (PNNL), Richland, WA (US)

6. P. Scott, A review of irradiation assisted stress corrosion cracking. J. Nucl. Mater. **211**, 101–122 (1994)
7. E. Kenik, R. Jones, G. Bell, Irradiation-assisted stress corrosion cracking. J. Nucl. Mater. **212**, 52–59 (1994)
8. G. Was, S. Bruemmer, Effects of irradiation on intergranular stress corrosion cracking. J. Nucl. Mater. **216**, 326–347 (1994)
9. J. Busby, G. Was, E. Kenik, Isolating the effect of radiation-induced segregation in irradiation-assisted stress corrosion cracking of austenitic stainless steels. J. Nucl. Mater. **302**, 20–40 (2002)
10. G. Smith, D. Tillack, S. Patel, Alloy 625: impressive past, significant presence, awesome future, in *Superalloys 718,625,706 and Various Derivatives. The Minerals*. (Metals and Materials Society, 1991), pp. 35–46
11. L. Shoemaker, Alloys 625 and 725: trends in properties and applications, in *Superalloys 718, 625, 706 and Derivatives. The Minerals*, (Metals and Materials Society, 2005), pp. 409–418
12. J. Rakowski, C. Stinner, M. Lipschutz, J. Preston Montague, The use and performance of wrought 625 alloy in primary surface recuperators for gas turbine engines, in *Superalloys 718,625,706 and Derivatives*, (2005), pp. 271–286
13. M. Song, M. Wang, G. Was, Irradiation assisted stress corrosion cracking (IASCC) of nickel-base alloys in light water reactors (LWRs) environments Part I: microstructure characterization, in *Proceeding of 18th International Conference on Environmental Degradation of Materials in Nuclear Power Systems—Water Reactors*. (Portland, Oregon, 2017)
14. J.S.R.I.M. Ziegler, *Program* (IBM Corporation, Yorktown, NY, 2013)
15. F. Carrette, M. Lafont, G. Chatainier, L. Guinard, B. Pieraggi, Analysis and TEM examination of corrosion scales grown on Alloy 690 exposed to pressurized water at 325 °C. Surf. Interface Anal. **34**, 135–138 (2002)
16. A. Machet, A. Galtayries, S. Zanna, L. Klein, V. Maurice, P. Jolivet, M. Foucault, P. Combrade, P. Scott, P. Marcus, XPS and STM study of the growth and structure of passive films in high temperature water on a nickel-base alloy. Electrochim. Acta **49**, 3957–3964 (2004)
17. L. Marchetti, S. Perrin, Y. Wouters, F. Martin, M. Pijolat, Photoelectrochemical study of nickel base alloys oxide films formed at high temperature and high pressure water. Electrochim. Acta **55**, 5384–5392 (2010)
18. M. Sennour, L. Marchetti, F. Martin, S. Perrin, R. Molins, M. Pijolat, A detailed TEM and SEM study of Ni-base alloys oxide scales formed in primary conditions of pressurized water reactor. J. Nucl. Mater. **402**, 147–156 (2010)
19. Marchetti-Sillans L (2007) Ph.D. thesis: Corrosion généralisée des alliages à base nickel en milieu aqueux à haute température: apport à la compréhension des mécanismes. École Nationale Supérieure des Mines Saint-Etienne
20. Macdonald D (2016) The electrochemical nature of stress corrosion cracking. in *Stress Corrosion Cracking of Nickel Based Alloys in Water-Cooled Nuclear Reactors: The Coriou Effect*. *239*
21. G. Was. Irradiation assisted corrosion and stress corrosion cracking (IAC/IASCC) in nuclear reactor systems and components, in *Nuclear Corrosion Science and Engineer* (Woodhead Publishing, 2012)
22. G. Was, *Fundamentals of radiation materials science* (Springer, Metals and Alloys, 2007)

Solute Clustering in As-irradiated and Post-irradiation-Annealed 304 Stainless Steel

Yimeng Chen, Yan Dong, Emmanuelle Marquis, Zhijie Jiao, Justin Hesterberg, Gary Was and Peter Chou

Abstract A commercial purity 304SS was irradiated to 5 dpa Kinchin-Pease (10 dpa full-cascade) using 2 meV protons at 360 °C. Post-irradiation annealing (PIA) was applied to reduce or remove IASCC susceptibility. This paper focuses on the links between irradiation-induced hardening and irradiated microstructures of the as-irradiated and PIA conditions; the irradiated microstructure is assessed by transmission electron microscopy (TEM) and atom probe tomography (APT). Dislocation loops, Ni–Si clusters, and Cu-enriched clusters are present in the as-irradiated condition. When the dislocation loops are removed by PIA, ~40% of the as-irradiated hardness remains and can be rationally attributed to the solute clusters still present in the PIA microstructure. The observations indicate that hardening in the as-irradiated condition is controlled by both dislocation loops and solute clusters and suggest that radiation-induced solute clusters may be important to detailed understanding of IASCC (irradiation-assisted stress corrosion cracking).

Keywords IASCC · Irradiated stainless steel · Solute clusters · Dislocation loops · Hardness · Atom probe tomography

Y. Chen · Y. Dong · E. Marquis
Department of Materials Science and Engineering, University of Michigan, Ann Arbor, MI 48109, USA

Z. Jiao · J. Hesterberg · G. Was
Department of Nuclear Engineering and Radiological Sciences, University of Michigan, Ann Arbor, MI 48109, USA

P. Chou (✉)
Electric Power Research Institute, Palo Alto, CA 94304, USA
e-mail: pchou@epri.com

Present Address:
Y. Chen
CAMECA Instruments, Inc, Madison, WI 53711, USA

J.H. Jackson et al. (eds.), *Proceedings of the 18th International Conference on Environmental Degradation of Materials in Nuclear Power Systems – Water Reactors*, The Minerals, Metals & Materials Series, https://doi.org/10.1007/978-3-319-68454-3_71

Introduction

Studies in the literature have concluded that, in the context of stainless steels in light-water reactors (LWR), irradiation-induced hardening, dislocation loop density and size, and radiation-induced grain-boundary segregation, as determined by transmission electron microscopy (TEM), no longer change significantly past 5 dpa [1–3]. However, studies of IASCC crack initiation of field-retrieved stainless steels suggest that fluence is an important factor up to 20–25 dpa or above [4–6]. It is therefore not possible to diagnose relative degrees of IASCC susceptibility based on these microstructural parameters.

More recently, a small number of researchers have applied atom probe tomography (APT), in conjunction with TEM, to characterized the microstructure of irradiated stainless steels relevant to LWRs [7–13]. The studies consistently identified radiation-induced solute clusters at number densities comparable to or greater than those of Frank loops, which has been regarded as the dominant irradiation-induced defect in the matrix. In addition, the aggregate data suggest that the number density of radiation-induced solute clusters continue to increase beyond 5 dpa, when the Frank loop number density and size saturate. It is therefore important to establish whether clusters affect irradiated materials behavior, particularly at doses ≥ 5 dpa. If they do, then solute clusters, together with Frank loops, may influence IASCC susceptibility at higher doses.

Consequently, a study was initiated on a proton-irradiated commercial purity 304 stainless steel (CP304) in as-irradiated and several post-irradiation-annealed (PIA) conditions: IASCC susceptibilities of the different conditions were assessed by CERT in BWR NWC, incrementally strained up to 10%; the irradiated microstructures of the matrix were characterized by TEM (for Frank loops) and APT (for solute clusters); localized deformation was quantified by the % of slip steps on the surface with height >280 nm after CERT (and oxide stripping); and hardness values were determined [14]. Radiation-induced segregation (RIS) at grain-boundaries was not evaluated since prior PIA studies [15, 16] indicated that it does not exert a strong influence on IASCC. The relationship between IASCC and two aspects of PIA, irradiation-induced hardening and localized deformation has already been reported [17]. This paper focuses on the link between irradiation-induced hardening, and irradiated microstructure.

Experimental Method

This study uses a commercial purity 304SS (Table 1) whose IASCC susceptibility is known from previous studies [18–21]; Cu was not reported by the bulk analysis associated with the material certificate, but was detected and quantified by APT to be 0.40 at.% (0.46 wt.%) in earlier work [9, 11]. Proton irradiation was conducted at the Michigan Ion Beam Laboratory, where samples were irradiated to 5 dpa

Table 1 Chemical composition of the test material

Alloy		Fe	Cr	Ni	Mn	Si	P	S	C
CP304	wt.%	Bal.	18.30	8.50	1.38	0.65	0.03	0.03	0.04
	at.%	69.8	19.3	7.9	1.4	1.27	0.05	0.05	0.18

Kinchin-Pease (10 dpa full-cascade) [22][1] at 360 °C using 2 meV protons and a dose rate of 1.2×10^{-5} dpa/s. The proton range was ~20 microns; the damage rate was nearly uniform through the first 15 microns [23].

PIA was conducted at four different temperatures: 450, 500, 550 and 600 °C for durations up to 100 h. Hardness values were measured for the as-irradiated condition and all of the PIA conditions; whereas CERT, microstructural characterization and localized deformation measurements were conducted on the as-irradiated condition and selected PIA conditions.

Faulted (Frank) dislocation loops were characterized by TEM using the rel-rod dark field technique, as described in [19].

Needle-shaped APT specimens were prepared by the standard lift-out method and by focused ion beam milling on a FEI Helios NanoLab dual beam microscope [24]. Specimens were prepared from the relatively flat dose rate region at about 10 µm under the irradiated surface. APT specimens were analyzed using a LEAP-4000XHR microscope operated in electrical mode with a voltage pulse fraction of 20%. Specimen temperature was maintained at 35 K and detection rate was kept constant at 0.005 atom/pulse. Reconstruction of the relative atom positions from the raw data was performed using the commercial software, IVAS 3.6.4 from CAMECA™. Values of the reconstruction parameters were selected to produce a uniform reconstructed density, so that the shape of the reconstructed Ni/Si clusters is isotropic on average. These conditions were satisfied with a combination of an image compression factor between 1.1 and 1.3, an evaporation field value of 33 V/nm for Fe [25], and a k-factor between 3.7 and 4.

The microstructures of irradiated 304 stainless steels are complex; in this study, it consists of Cu-rich clusters, Si and Ni-rich clusters, and dislocations with solute segregation. To ensure that the observed microstructures can be compared from one dataset to another, or between alloy compositions, or irradiation conditions, a standardized approach to define the parameters used in the cluster searching algorithm is required. Each element and associated microstructural feature requires different analysis methods for which the parameter selections are described in detail in [11]. In brief, a qualitative analysis of solute distributions is first carried out using the local concentration (LC) method, which can be utilized for visualization

[1]There are two options in SRIM for calculations of dose: "full-cascade" and "Kinchin-Pease." A large number of studies across the years that applied proton-irradiation to investigate radiation damage calculated dose using the full-cascade option. However, a recent publication by Stoller et al. [22] established that the Kinchin-Pease option is more appropriate when comparing ion and neutron displacement damage. The Kinchin-Pease (K-P) value is a factor of 2 less than the full-cascade value; that is, 10 dpa (full-cascade) corresponds to 5 dpa (K-P).

purposes. Quantitative analyses of Cu and Si solute clustering and segregation are then performed using the MSM (maximum separation method) algorithm associated with a modified parameterization approach, while combined data filtering and cluster searching is applied to the analysis of the Ni distribution.

Results and Discussion

Dislocation Loops by TEM

The number of dislocation loops quickly decreases with annealing condition. Table 2 summarizes the TEM measurement of Frank loops in the as-irradiated and post-irradiation annealed conditions. After PIA at 550 °C:1 h, they have been essentially removed; only 1.8% of the as-irradiated number density remain; their diameter is twice as large those in the as-irradiated condition, reflecting the preferential removal (coarsening) of the size distribution even as the total number densities decrease after PIA. Dislocation loops could not be confirmed after PIA at 600 °C:10 h, which resulted in mostly twins, stacking faults, and dislocations.

Solute Distributions by APT

APT provides a complementary view of the various features constituting the microstructure and was used to quantify the microstructure in the as-irradiated and annealed conditions. Figure 1 shows representative spatial distributions of Ni, Si, and Cu atoms in 10 nm slices of APT reconstructed volumes for the as-irradiated and annealed conditions.

In the as-irrdaiated condition, Cu forms 1–2 nm clusters. The distributions of Ni and Si are correlated at Ni/Si clusters and dislocation loops. TEM did not detect the structure of these nano-sized clusters by nano-beam diffraction, dark field imaging,

Table 2 Average Frank dislocation loop sizes and densities in CP304 irradiated to 5 dpa (K-P) at 360 °C and after various post-irradiation annealing conditions

PIA condition	Number of loop characterized	Average loop diameter (nm)	Error of mean (nm)	Loop density (m^{-3})	Remaining loop density (%)
As-irradiated	221	7.4	0.2	5.3E22	100
500°C:1 h	146	8.9	0.2	1.2E22	22.6
500°C:15 h	35	10.0	0.3	4.2E21	7.9
550°C:1 h	35	14.6	0.8	9.5E20	1.8
600°C:10 h*	–	–	–	–	

*Stacking faults observed, loops negligible

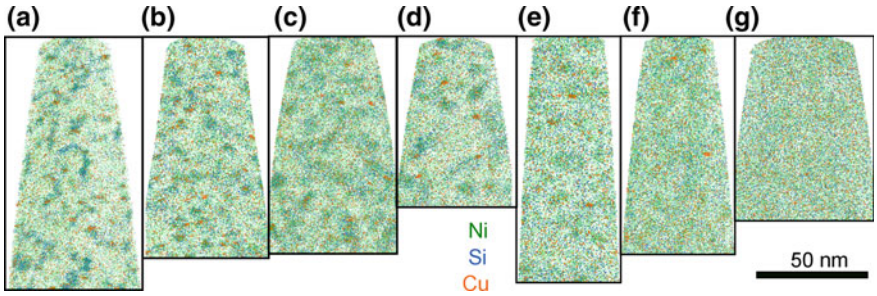

Fig. 1 5 nm thick slices from representative APT datasets obtained in the **a** as-irradiated, and **b–g** six post irradiation annealing conditions in the order of increasing Fe diffusion distance (500 °C: 1 h, 550 °C: 1 h, 500 °C: 15 h, 500 °C: 100 h, 600 °C: 1 h, and 600 °C:10 h)

or selected area diffraction with extended exposure times. Additionally, Mn is found to be depleted at the dislocations, while carbon is found uniformly distributed. A previous analysis of this condition revealed that about 30% of the Cu clusters appear to be in contact with Ni/Si clusters or dislocations.

Table 3 summarizes APT-determined number densities and volume fractions of Cu clusters, Ni/Si clusters, and the line density of Si decorated dislocation loops in the as-irradiated condition. APT chemical analysis confirms that Ni and Si co-segregate to clusters with a measured Ni/Si ratio of 3.6 ± 1.4, where 1.4 is the standard deviation over the cluster population. The volume fraction of Ni/Si-rich clusters can be calculated from the atomic volumes of Ni and Si atoms forming clusters, divided by the total volume of the APT dataset. The number density of Cu clusters is determined to be $1.3 \pm 0.2 \times 10^{24}$ m^3, and the volume fraction is 0.11 ± 0.01%, calculated from the number of Cu atoms forming the clusters times the atomic volume of Cu and divided by the total volume of the APT dataset; the error is derived from the standard deviation from 3 datasets.

Characterizing dislocations by APT is also possible due to solute segregation to dislocation lines. Without segregation however, there would be an inherent ambiguity as to the absence or presence of dislocations. The present observations reveal Ni and Si segregation to linear features, interpreted as dislocations. Some dislocations appear as full loops, as have been previously observed in irradiated 316 and 304 stainless steels [9, 26] while others are just linear features or incomplete loops. The quantitative analyses of dislocation number density, line density and loop size proposed here assume that all dislocations exhibit Ni and Si segregation. As prior results for the same class of material show similar loop sizes and densities as measured by TEM [27], a reasonable comparison between TEM and APT measurements can be confirmed. It is worth noting that a more complex microstructure with a higher number density of dislocations can be expected if the materials are processed by cold-work, for instance bolts used in pressurized water reactors are cold-worked 316 stainless steels [28].

Within this study, the number density and size of dislocation loops in the as-irradiated condition as determined by TEM and APT can be compared via

Table 3 Cluster and dislocation number densities, sizes and compositions measured in the as-irradiated alloy by APT

Cu clusters			Dislocation loops			Ni-rich clusters			
Number density (10^{24} m^{-3})	Volume fraction (%)	Size (nm)	Number density (10^{22} m^{-3})	Loop diameter (nm)	Line density (10^{15} m^{-2})	Number density (10^{24} m^{-3})	Volume fraction (%)	Size (nm)	Ni/Si ratio
1.3 ± 0.2	0.11 ± 0.01	1.5 ± 0.2	5.7 ± 1.8	9.4 ± 3.2	4.0 ± 1.7	0.83 ± 0.03	0.96 ± 0.01	2.8*	3.6 ± 1.4

The errors are the standard deviation from multiple dataset/results

*The average diameter of the Ni–Si clusters was derived from the number density and volume fraction, assuming spherical clusters

Tables 1 and 3, respectively. The number densities correspond quite well while the loop diameters do not correspond as well. And it should also be noted that the TEM rel-rod dark field technique identifies only Frank loops whereas APT detects all loops decorated by segregation and may therefore include both Frank loops and perfect loops.

Cu-Rich Clusters

As mentioned above, Cu forms nanoscale clusters. Visually in Fig. 1, where results are presented in order of increasing Fe diffusion length, the number densities decrease with annealing, and the Cu clusters are completely dissolved after annealing at 600 °C for 10 h. Quantitatively, the evolution of the spatial distribution of Cu is assessed by measuring the deviation of the normalized distribution of Cu–Cu nearest neighbor distances (NND) with the distribution expected from a random solid solution (Fig. 2a). The as-irradiated condition shows the largest deviation due to Cu clustering while at the 600 °C:10 h PIA condition, the distribution is essentially coincident with the random distribution, indicating the predominant, if not complete, dissolution of Cu clusters. The number of clusters,

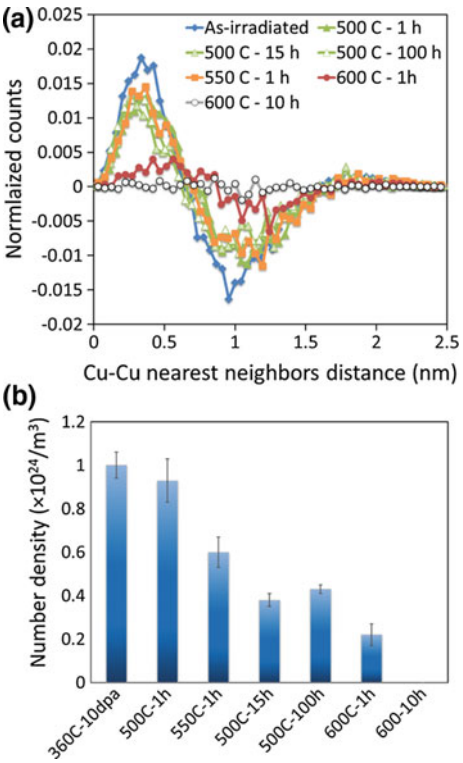

Fig. 2 Cu cluster analysis: **a** Cu–Cu 1st order NND analysis calculated by subtracting the randomized data from the normalized NND distributions; **b** number density of identified Cu clusters

determined by a cluster search algorithm, decreases with diffusion distance (Fig. 2b).

Irradiation-induced Cu precipitation is a well-known phenomenon in neutron and proton irradiated steels, leading to precipitation hardening, particularly for ferritic reactor pressure vessel (RPV) steels [29, 30]. In RPV steels, APT observations suggest that Cu precipitation is often associated with Mn, Si and Ni clusters [31]. However, in the present case, the distribution of Cu clusters is mainly independent of the other solute-rich features. Comparison with previous measurements on the same alloy proton-irradiated to 2.5 dpa (Kinchin-Pease) [9] indicates a tenfold increase in the number density of Cu clusters from 2.5 to 5 dpa (K-P). While the analysis methods for APT data are different between the two studies, the trend with dose is significant. In lower Cu alloys, such as a 316 with 0.21 at.% Cu, no Cu clusters were observed after neutron irradiation at 360 °C to 12 dpa [32] or self-ion irradiation at 350 °C to 10 dpa (K-P) [26]. Their irradiation response is therefore highly sensitive to the alloy composition. Such observations have potential implications for heat-to-heat variations in the performance of irradiated stainless steels.

Ni/Si-Rich Clusters

The evolution of the spatial distribution of Ni with PIA conditions is illustrated by the difference between the measured distribution of nearest neighbor distances and a random distribution in Fig. 3a. Ni clustering is evident at all conditions until 600 °C:10 h. The normalized radial distribution functions (RDFs) emphasizes the decrease in the amplitude of the concentration fluctuation with increasing diffusion distance (Fig. 3b).

Si clusters can be clearly distinguished in the Si atom map of the as-irradiated condition in Fig. 1. As the temperature and aggressiveness of the PIA increase,[2] the clusters appear more diffuse, until at 600 °C, the Si atom map is almost uniform. Correspondingly, the normalized Si–Si nearest neighbor distance distributions is biased toward smaller distances in the as-irradiated condition, and shifts closer to the random distribution as the temperature and aggressiveness of the PIA increase; in particular, the distribution of the PIA condition 500 °C:100 h is only slightly different from random, while the distribution of the PIA condition 600 °C:1 h is essentially coincident with the random distribution, indicating the predominant, if not complete, disappearance of Si clustering (Fig. 4).

Ni-rich clusters are found either on dislocation loops or in the matrix. On dislocation loops, while Si shows almost continuous distribution along the dislocation line, the distribution of Ni is more localized into clusters on either side of the dislocation plane; as indicated previously, the linear density of these Ni-rich

[2]The aggressiveness of post-irradiation annealing condition is captured by the parameter $\sqrt{D_{Fe}t}$, the "iron diffusion distance" [16].

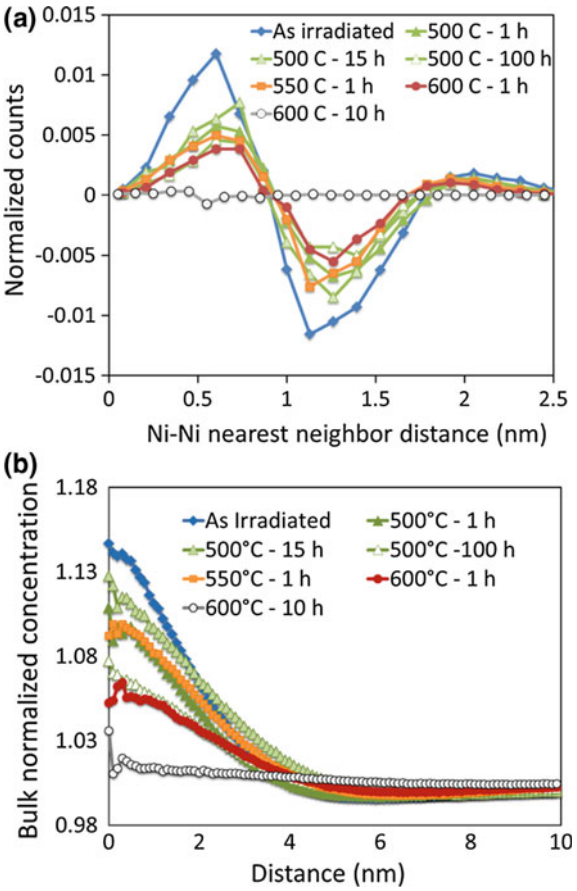

Fig. 3 Ni analysis: **a** 1st order NND analysis and **b** RDFs of bulk normalized Ni concentration for APT datasets collected from different annealing conditions

clusters on dislocations is 12 clusters per 100 nm, measured from 6 individual dislocation fragments and loops. This may support the hypothesis that dislocations serve as nucleation sites for precipitation [33]. Ni and Si rich clusters have been previously reported in neutron irradiated 304 stainless steels and the structure was identified to be that of the γ' phase by TEM [10, 34]. In this study, the Ni/Si ratio of the (as-irradiated) Ni-rich clusters is 3.6 ± 1.4, which is higher than 3 for the Ni_3Si γ' phase. However, the clusters were identified based on Ni atoms, which leads to preferential inclusion of Ni atoms over other solute elements, resulting in higher Ni/Si ratios. Toyama et al. reported Mn enrichment in over half of the Ni/Si-rich clusters in a 304SS irradiated by neutrons at 300 °C to 24 dpa [10]. In contrast, Mn depletion is observed in all of the Ni/Si clusters in the material of this study [CP304, proton-irradiated to 5 dpa (K-P) at 360 °C].

In LWR-irradiated 304/316SS, Ni/Si-rich clusters, identified as γ', are consistently reported by TEM only at doses ≥ 12 dpa [28]. At lower doses, TEM detection of γ' is inconsistent; some studies report and quantify their presence while

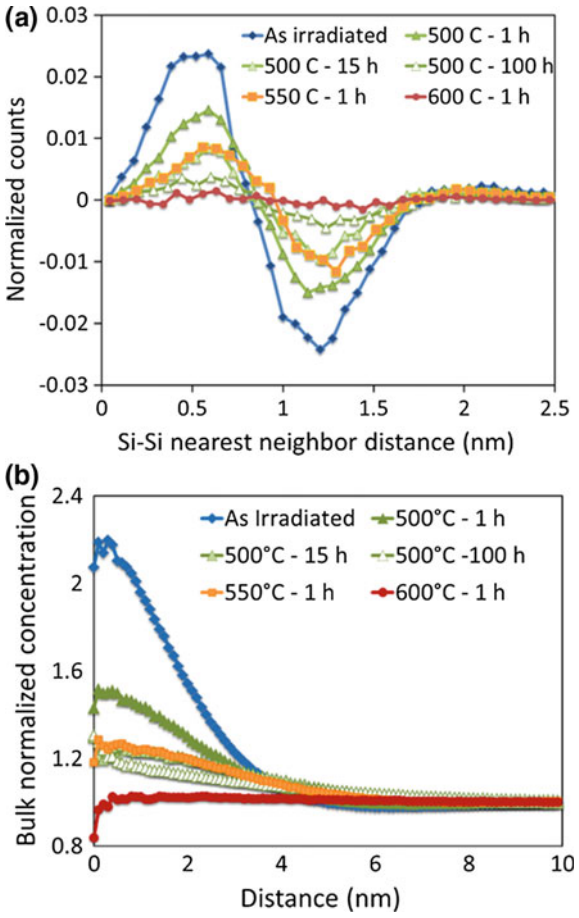

Fig. 4 Si analysis: **a** 1st order NND analysis and **b** RDFs of bulk normalized Si concentration for APT datasets collected from different annealing conditions

others do not, and the number densities of γ' measured by TEM are low compared to dislocation loops; therefore, their influence has been considered negligible. For example, in one study of several BWR-irradiated stainless steels in the range of 3.5–13 dpa, TEM did not detect γ'in all conditions, and when detected, their number densities are factors of 20–200X lower than Frank loops [35]. In contrast, APT detects Ni/Si clusters consistently and at much higher densities relative to dislocation loops. For example, Toyama[3] reported a Ni/Si cluster density of 4.2×10^{23} m^{-3} compared to Frank loop density of 0.61×10^{23} m^{-3} (cluster/loop ratio of 6.9; PWR neutron-irradiated 304SS, 24 dpa, 300 °C). In this study of proton-irradiated CP304 [5 dpa (K-P), 360 °C], in the as-irradiated condition, both

[3]Toyama et al. reported two types of Ni/Si clusters, one that contained Mn and P and another that contained neither. However, they did not draw a distinction between the two populations in subsequent analysis.

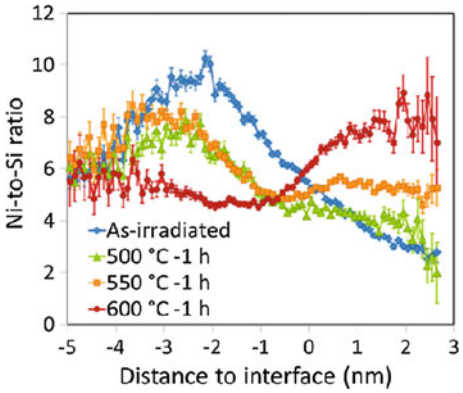

Fig. 5 Proxigram profile of Ni-to-Si ratio calculated from Ni iso-concentration surface with an iso-value of 10.80 at.%

Ni/Si clusters and Cu-clusters are much more numerous than Frank loops (cluster/loop ratios of 14.6 and 22.8 respectively, from the values in Table 3).[4]

The γ′ phase can be characterized using traditional TEM dark field technique. However, because of the resolution limitation of traditional TEM, precipitates less than 2 nm and solute clusters may be difficult to characterize. For instance, the average size of γ′ in a CW 316SS irradiated to 25 dpa in a PWR is around 2 nm [27], and there is high probability of missing small precipitates using TEM. Fukuya et al. [27] found that the average size of γ′ is nearly constant after annealing at 400, 500 and 550 °C for an hour, with slight increases in number density. Renterghem et al. [34] applied PIA to a CW 316SS irradiated to 80 dpa in a PWR and also found that the size of γ′ barely changed after annealing at 500 °C for 6 h and increased slightly after annealing at 550 °C for 6 h; the γ′ appeared to dissolve after annealing at 550 °C for 6 h.

In our study of Ni/Si-rich clusters, their dissolution involves the diffusion of Si and of Ni at different rates. Figure 5 highlights the regions of highest Ni and Si concentration after annealing for 1 h at different temperatures. In the as-irradiated state, the Ni/Si ratio in the clusters is ~3, which would be consistent with the stoichiometry of the γ′ phase. The faster diffusion of Si results in a Ni/Si ratio that is even higher than the ratio expected in the matrix that, based on the alloy composition, is about 6. The changing nature and chemistry of the clusters with annealing time raises the question of how to model their hardening effect. While they may be

[4]Because of cluster/loop ratio they measured (loops by TEM and solute clusters by APT) was high, Toyama et al. "strongly suggested that Ni–Si precipitates mainly exist at sites independent of Frank loops", although the suggestion was not directly verified by APT observation. In our study, the average linear density of Ni-rich clusters (actually Ni/Si rich clusters) on dislocations was determined by APT to be 12 clusters per 100 nm; and the cluster/loop ratio of proton-irradiated CP304 (14.6) is, in fact, higher than that measured by Toyama et al. for neutron-irradiated 304SS (6.9). In proton-irradiated CP304, the average dislocation loop diameter 9.4 nm according to APT (Table 3) [or 7.4 nm according to TEM (Table 2)]. Therefore, there are ~3.5 clusters are associated with the average dislocation loop. It follows that approximately (3.5/14.6) × 100% = 24% of the clusters are associated with dislocation loops, while the majority, ~76%, are "free clusters".

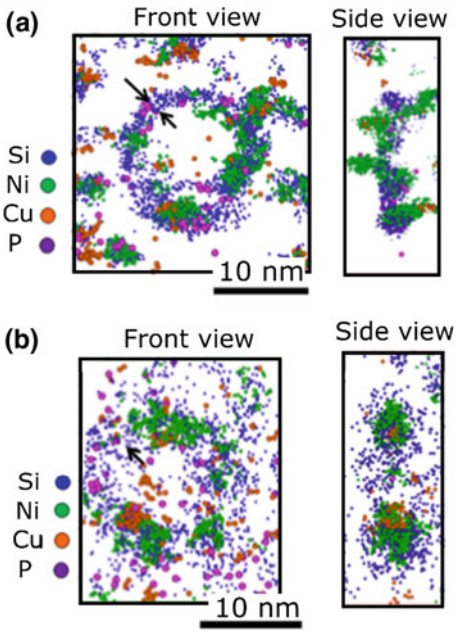

Fig. 6 LC-filtered atomic maps showing the elemental distributions in **a** an as-irradiated sample (image courtesy from Ref. [11]) and **b** a sample after 15 h of annealing at 500 °C. The concentration thresholds used for generating the atomic maps were: $C_{th}(Si) = 6.3$ at.%, $C_{th}(Ni) = 23$ at.%, $C_{th}(Cu) = 3$ at.% and $C_{th}(P) = 2$ at.%

an ordered γ' phase initially—although electron diffraction could not confirm this the diffusion of Si away from the clusters even at 500 °C would suggest that the structure is not preserved. This change in structure could be associated with a significant change in the hardening contribution.

The diffusion of Si is also visible when analyzing dislocation loops. Remember that dislocations were identified by the segregation of Ni and Si. Figure 6 compares two dislocation loops, the first observed in the as-irradiated state and the second after annealing at 500 °C for 15 h. After annealing, it is clear that Si has diffused away; and although the dislocation loop is barely visible, the clusters decorating the dislocations are still clearly identified, thanks to the slower diffusing Ni. While Si segregation decreased, whether the dislocation loop still exists cannot be determined from the data. In general, the dissolution of Ni/Si clusters appears to have a slower rate compared to the annihilation of dislocation loops, which suggests that the clusters play a critical role in controlling the mechanical property of the materials after PIA.

PIA Effect on Irradiation Hardening

Irradiation hardening originates from radiation-induced defects, including dislocation loops and clusters/precipitates.[5] PIA reduces the defect populations and thereby decreases the irradiation hardening. Remaining irradiation hardening is expressed as % of $\Delta\sigma_{y,\ irrad}$, where $\Delta\sigma_{y,\ irrad} = \sigma_{y,\ irrad} - \sigma_{y,\ unirrad}$.

Table 4 summarizes the available TEM and APT microstructural data for the as-irradiated and PIA conditions. The APT results described in Section "Ni/Si-rich Clusters" (and Fig. 5 in particular) suggest that after PIA at 550 °C:1 h, Si has diffused away from the Ni/Si clusters, but Ni clustering remains; and at the same time, TEM indicates the near disappearance of dislocation loops. Because composition (and potentially the structure) of the Ni/Si clusters are changing, the authors decided to be conservative, and only APT data associated with the as-irradiated condition (and also the number density after PIA at 500 °C:1 h) are quantified. The Cu-rich clusters remain better defined across the PIA conditions; therefore, more detailed information can be provided.

Figure 7 plots the data for Frank loops and Cu clusters versus Fe diffusion distance $\sqrt{D_{Fe}t}$ (representing the different PIA conditions); D_{Fe} is the diffusivity of iron in austenitic stainless steels at the annealing temperature [16] and t is the annealing time. Frank loops and Cu clusters follow somewhat different trends. The loops are removed faster and are gone at an iron diffusion distance of $\sim 10^{-9}$ m, while the Cu clusters still persist. Ni clusters with high Ni/Si ratios, reflecting the departure of Si, also remain, although not quantified in Table 4 or in this figure. Figure 8 is the companion figure where the microstructural quantities are correlated to the (remaining) irradiation hardening. When the dislocation loops have been removed (zero on the y-axis), ~40% of the original irradiation hardening still remains; at the same time, Cu-enriched clusters, although their number densities have decreased significantly, have not been entirely removed, and Ni clusters with high Ni/Si ratios also remain. These clusters are therefore correlated with the remaining hardening. The association in this way of ~40% of the original irradiation hardening with clusters should be a lower bound estimate because they were more numerous in the as-irradiated condition.

This result is broadly consistent with the APT study of Toyama et al. [10] who conducted PIA on material retrieved from a 304SS fuel wrapper plate of a commercial PWR, irradiated to 24 dpa at 300 °C. Interpreting their results according to the dispersed barrier model, they can attribute almost 50% of the irradiation-induced increase in yield strength to Ni/Si clusters. Toyama et al. do not address the changing composition of Ni–Si clusters during PIA.

[5]In this paper, "clusters" and "precipitates" will be used interchangeably.

Table 4 Summary of available TEM, APT, and hardness data

PIA condition ($\sqrt{D_{Fe}t}$)	Cu clusters (APT)			Ni–Si clusters (APT) [2]			Dislocation loops (TEM)		ΔHardness (Measured)	ΔYS (Converted) [3]
	Number density (m^{-3})	Vol fraction (%)	Size (m)	Number density (m^{-3})	Vol fraction (%)	Size (m)	Number density (m^{-3})	Size (m)	ΔHv (kg mm^{-2})	MPa
As-irradiated	1.3E+24	0.11	1.5E-09	8.3E+23	0.96	*2.8E-09*	5.3E+22	7.4E-09	211	*639.3*
500 °C:1 h (*1.0E-10 m*)	1.1E+24	0.09	Unchanged See note [1]	3.0E+23	N/A		1.2E+22	8.9E-09	120	*363.6*
500 °C:15 h (*3.9E -10 m*)	5.0E+23	0.065		See note [2]			4.2E+21	1.0E-08	99	*300.0*
550 °C:1 h (*3.9E-10 m*)	7.0E+23	0.058					9.5E+20	1.5E-08	95	*287.9*
500 °C:100 h (*1.0E-9 m*)	6.4E+23	0.08					N/A			
600 °C:1 h (*1.3E-9 m*)	1.6E+23	0.016								
600 °C:10 h (*4.1E-9 m*)	Not observed	Not observed	Not observed	Not observed	Not observed	Not observed	Not observed	Not observed	20	*60.6*

[1] Changes in the size of the Cu-clusters across the PIA conditions are too small to attribute significance. Therefore, the average diameter of the Cu clusters is considered to be unchanged

[2] Quantification of the Ni–Si clusters in the course of PIA is difficult; for example, their boundary with the matrix becomes increasingly diffuse and their compositions change. However, it is clear that Ni–Si clusters do not disappear until 600 °C:1 h; and when Si clustering disappears at 600 °C:1 h, some Ni clustering remains. The average diameter of the Ni–Si clusters in the as-irradiated condition was derived from the number density and volume fraction, assuming spherical clusters; the italicized font indicates a calculated value

[3] Converted according to the empirical relation $\Delta\sigma_y = 3.03\Delta H_v$ [36]; the italicized font indicates a calculated value

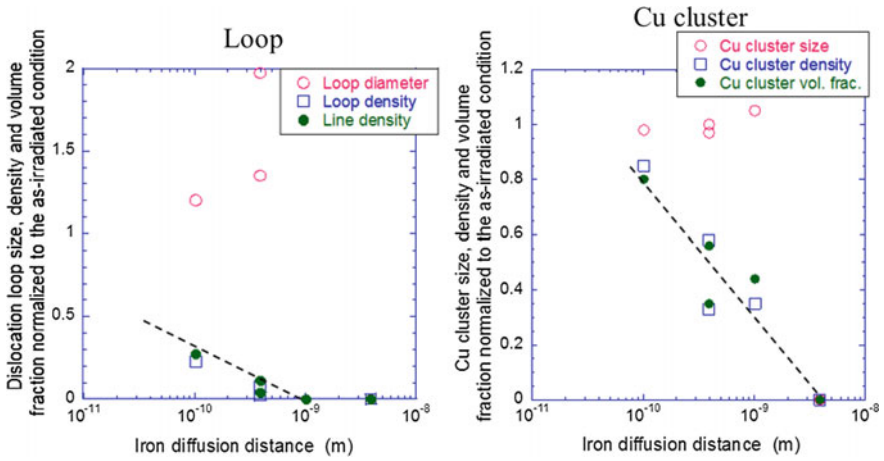

Fig. 7 Plots of the sizes, number densities, and line density or volume fractions of Frank loops and Cu-enriched clusters as a function of iron diffusion distance of the PIA conditions. The values on the y-axis have been normalized against the respective values in the as-irradiated condition. (*Note* the scales of the y-axis of the two plots are different). The dashed lines simply denote the trend

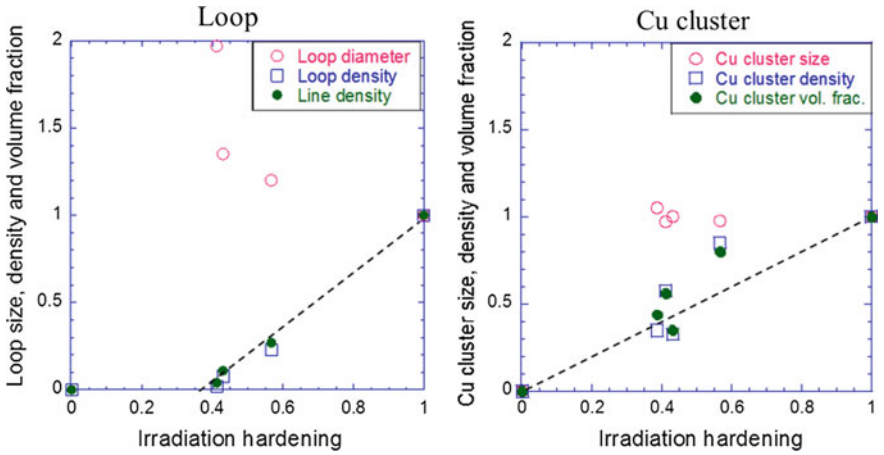

Fig. 8 Plots of the sizes, number densities, and line density or volume fractions of Frank loops, and Cu-enriched clusters against the (remaining) irradiation hardening, after PIA. The values on the x and y axes have been normalized against the respective values in the as-irradiated condition. For example, the irradiation hardening value 1 represents the as-irradiated state, and the irradiation hardening value 0 represents the non-irradiated condition. The dashed lines simply denote the trend

The Dispersed Barrier Model

In the dispersed barrier model, the irradiated yield strength contribution of an independent defect type i (where i = Frank loops, precipitates, voids, etc.) is expressed as:

$$(\Delta\sigma_y)_i = \alpha_i M \mu b (N_i d_i)^{0.5} \quad (1)$$

where α_i is the strength (hardening) coefficient, N_i is the number density, and d_i is the diameter; the remaining parameters are associated with the matrix (i.e. do not change with the type of defect) and consist of the Taylor's factor M (3.06), the shear modulus μ (76 GPa), and the magnitude of Burgers vector b (0.255 nm). The overall irradiated yield stress is the root mean square of the independent contributions:

$$\Delta\sigma_y = \left[\Sigma(\Delta\sigma_y)_i^2\right]^{0.5} \quad (2)$$

The hardening coefficients α_i are determined by fitting to microstructural observations (to date, predominantly by TEM). The α_i values of Lucas et al. [37] and Fukuya et al. [27] are frequently cited, but as Fukuya et al. themselves noted, there is no definitive set of values although there is a range.

The dispersed barrier model assumes independent microstructural defect populations. The APT analyses showed dislocation loops are decorated by Ni/Si clusters and they are therefore not independent.[6] However, the dispersed barrier model does demonstrate that Frank loops alone cannot account entirely for the as-irradiated hardness/yield strength and therefore indicates that solute clusters make a significant contribution.

Table 5 provides values for the barrier strengths for Frank loops, γ' (Ni_3Si), and Ni/Si clusters used in three studies. The biggest difference is in the value of Ni/Si clusters/precipitates. Toyama et al. had to modify the strength coefficient of Ni/Si clusters they observed by APT to a value significantly lower than the strength coefficient assigned to γ' identified by TEM (0.11 vs. 0.4). Because the APT-detected number density of Ni/Si clusters is so large, a strength coefficient of 0.4 would dramatically over-predict $\Delta\sigma_{y,\ irrad}$.

In Table 6, the barrier strengths used by Toyama et al. [10] is applied to the as-irradiated condition of this study; $\alpha_{cluster}$ = 0.11 is applied to both the Ni/Si and the Cu-enriched clusters. The match between the overall calculated irradiated yield strength and the overall measured yield strength (converted from hardness measurements[7]) is quite good, being different by only 6%. According to this

[6]The model also does not account for any changes in hardness associated with the loss of solution hardening in the matrix when solutes are removed from the matrix to form clusters/precipitates.

[7]Converted according to the empirical relation $\Delta\sigma_y = 3.03\ \Delta H_v$ [36].

Table 5 Strength coefficients for Frank Loops, γ' (Ni_3Si), and Ni/Si clusters

	Strength coefficients (α_i)		
	Lucas et al. [37]	Fukuya et al. [16]	Toyama et al. [10]
Frank loops [TEM]	0.45	0.5	0.45
γ' (Ni_3Si) [TEM]	0.4	0.4	
Ni/Si clusters [APT]			0.11

Table 6 The dispersed barrier model (Eqs. 4.2 and 4.3) applied to the as-irradiated condition of this study using the strength coefficients of Toyama et al. (Table 5), assuming the same barrier strength for Ni/Si clusters and Cu clusters

	As-irradiated	
	$(Nd)^{0.5}$ [m^{-1}]	ΔYS [MPa]
Cu clusters (APT)	4.42E + 07	288.1
Ni–Si clusters (APT)	4.83E + 07	314.8
Dislocation loops (TEM)	1.98E + 07	528.5
Overall ΔYS (Calculated)		679.3
Overall (from Hardness)*		639.3
Overall ΔYS (Calc)/ΔYS(Hardness)		1.06

*Converted according to the empirical relation $\Delta\sigma_y = 3.03\Delta H_v$ [36]

deconvolution, the contribution of clusters (Ni/Si and Cu clusters) to irradiated yield strength (before the root-mean square summation of Eq. 2) is actually slightly larger than the contribution of Frank loops (somewhat over 50%)[8]; 288.1 + 314.8 = 602.9 MPa for Ni/Si and Cu clusters and 528.5 MPa for Frank loops. The results are consistent with Fig. 8 which correlates ~40% of the irradiated yield strength with clusters (likely a lower bound estimate, as noted earlier).

The apparent success in applying Toyama's barrier strengths to the as-irradiated condition of this study is encouraging, but additional analysis and data will be necessary to establish whether the values can be applied more generally.

Conclusions

A commercial purity 304SS was irradiated to 5 dpa (K-P) using 2 meV protons at 360 °C and examined in as-irradiated and post-irradiation-annealed conditions. In the as-irradiated condition, Ni–Si-enriched and Cu-enriched clusters were detected clearly by APT, both at number densities significantly greater than Frank loops (quantified by TEM). Cu is an impurity not listed in the material certificate of this

[8]An exact percentage contribution is difficult to provide because of the root-mean-square summation of the contributions of Frank loop and clusters.

heat of stainless steel. APT data indicate that ~25% of Ni–Si clusters decorate Frank loops and thereby suggesting that the rest are "free" clusters.

With increasing degree of post-irradiation annealing (PIA), as assessed by the diffusion distance of iron ($\sqrt{D_{Fe}t}$), the number densities of all features decrease, but the loops are removed fasters than clusters; they are essentially gone (reduced to 1.8% of the as-irradiated condition) after PIA at 550 °C:1 h. However, ~40% of the as-irradiated hardness still remains and can be rationally attributed to the solute clusters still present in the microstructure.

The results of this study are broadly consistent with the observations of Toyama et al., who applied PIA to neutron-irradiated 304SS and attributed almost 50% of the as-irradiated yield strength to radiation-induced solute clusters. The barrier strengths of Toyama et al., fitted to their TEM observation of Frank loops and APT observation of solute clusters, are also consistent with the data of this study.

The observations indicate that hardening in the as-irradiated condition is controlled by both dislocation loops and solute clusters and suggest that radiation-induced solute clusters may be important to detailed understanding of IASCC (irradiation-assisted stress corrosion cracking).

Acknowledgements The work presented in this paper was funded by the Electric Power Research Institute.

References

1. S.M. Bruemmer, E.P. Simonen, P.M. Scott, P.L. Andresen, G.S. Was, J.L. Nelson, J. Nucl. Mater. **274**, 299–314 (1999)
2. P. Scott, *Final Review of the Cooperative Irradiation-Assisted Stress Corrosion Cracking Research Program*. EPRI, Palo Alto, CA: 2010. 1020986
3. K. Fukuya, J. Nucl. Sci. Technol. **50**(3), 213–254 (2013)
4. C. Pokor, G. Courtemanche, B. Tanguy, J.-P. Massaud, N. Monteil, IASCC of Core Internals of PWRs: EDF R&D and Engineering program to assess internals lifetime management, in Fontevraud 7 Symposium—Contribution of Materials Investigations to Improve the Safety and Performance of LWRs, Avignon, France, 26–30 September 2010, Paris, France, SFEN
5. O.K. Chopra, A.S. Rao, J. Nucl. Mater. **409**, 235–256 (2011)
6. R.W. Bosch et al., J. Nucl. Mater. **461**, 112–121 (2015)
7. A. Etienne, B. Radiguet, P. Pareige, J.-P. Massoud, C. Pokor, J. Nucl. Mater. **382**, 64–69 (2008)
8. G. Was, Z. Jiao, *Potential for Atom Probe Tomography in Understanding Irradiation Assisted Stress Corrosion Cracking: Characterization of Proton-Irradiated, Si-Containing Stainless Steels.* EPRI, Palo Alto, CA: 2011. 1022815
9. Z. Jiao, G.S. Was, Acta Mater. **59**(3), 1220–1238 (2011)
10. T. Toyama, Y. Nozawa, W. Van Renterghem, Y. Matsukawa, M. Hatakeyama, Y. Nagai, A. Al Mazouzi, S. Van Dyck, J. Nucl. Mater. **418**, 62–68 (2011)
11. Y. Chen, P.H. Chou, E.A. Marquis, J. Nucl. Mater. **451**, 130–136 (2014)
12. P. Chou, N. Soneda, K. Nishida, K. Dohi, E.A. Marquis, Y. Chen, Proceedings of Fontevraud 8 Conference: Contribution of Materials Investigations and Operating Experience to LWR's Safety, Performance and Reliability, Avignon, France, 15–18 September 2014
13. K. Fujii, K. Fukuya, J. Nucl. Mater. **469**, 82–88 (2016)

14. Z. Jiao, G. Was, Y. Chen, E. Marquis, *Program on Technology Innovation: Effects of Post Irradiation Annealing on IASCC.* EPRI, Palo Alto, CA: 2015. 3002005475
15. J.T. Busby, G.S. Was, E.A. Kenik, J. Nucl. Mater. **302**, 20–40 (2002)
16. K. Fukuya, M. Nakano, K. Fujii, T. Torimaru, Y. Kitsunai, J. Nucl. Sci. Technol. **41**, 1218–1227 (2004)
17. Z. Jiao, J. Hesterberg, G. Was, Effect of Post-Irradiation Annealing on Hardening, Localized Deformation and IASCC of a Proton-Irradiated 304 Stainless Steel, 17th International Conference on Environmental Degradation of Materials in Nuclear Power Systems—Water Reactors, Ottawa, Ontario, Canada, 9–13 August 2015
18. Z. Jiao, G.S. Was, J. Nucl. Mater. **382**, 203–209 (2008)
19. Z. Jiao, G.S. Was, J. Nucl. Mater. **407**, 34–43 (2010)
20. Z. Jiao, G.S. Was, J. Nucl. Mater. **408**, 246–256 (2011)
21. Z. Jiao, M. McMurtrey, G.S. Was, Scripta Mater. **65**, 159–162 (2011)
22. R.E. Stoller, M.B. Toloczko, G.S. Was, A.G. Certain, S. Dwaraknath, F.A. Garner, Nucl. Instrum. Methods. Phy. Res. B **310**, 75–80 (2013)
23. G. Gupta, Z. Jiao, A.N. Ham, J.T. Busby, G.S. Was, J. Nucl. Mater. **351**, 162–173 (2006)
24. K. Thompson et al., Ultramicroscopy **107**(2–3), 131–139 (2007)
25. T. Tsong, Surf. Sci. **70**(1), 211–233 (1978)
26. A. Etienne, B. Radiguet, P. Pareige, J. Nucl. Mater. **406**(2), 251–256 (2010)
27. K. Fukuya, K. Fujii, H. Nishioka, Y. Kitsunai, J. Nucl. Sci. Technol. **43**(2), 159–173 (2006)
28. D.J. Edwards, E.P. Simonen, F.A. Garner, L.R. Greenwood, B.M. Oliver, S.M. Bruemmer, J. Nucl. Mater. **317**(1), 32–45 (2003)
29. T. Takeuchi et al., J. Nucl. Mater. **402**(2), 93–101 (2010)
30. P. Auger et al., J. Nucl. Mater. **225**, 225–230 (1995)
31. K. Fujii et al., J. Nucl. Mater. **340**(2), 247–258 (2005)
32. A. Etienne, B. Radiguet, P. Pareige, J.-P. Massoud, C. Pokor, J. Nucl. Mater. **382**(1), 64–69 (2008)
33. E. Kenik, J. Busby, Mater. Sci. Eng. R **73**(7), 67–83 (2012)
34. W. Van Renterghem, M.J. Konstantinović, M. Vankeerberghen, J. Nucl. Mater. **452**, 158–165 (2014)
35. A. Jenssen, J. Stjärnsäter, T. Torimaru, Y. Kitsunai, *BWRVIP-221: BWR Vessel and Internals Project, Crack Growth in High Fluence BWR Materials—Phase1: Crack Growth Rate Testing of Types 304L and 316L at Doses Ranging from 3.5 to 13 dpa.* EPRI, Palo Alto, CA: 2009. 1019079
36. J.T. Busby, M.C. Hash, G.S. Was, J. Nucl. Mater. **336**, 267–278 (2005)
37. G.E. Lucas, J. Nucl. Mater. **205**, 287 (1993)

Part XI
IASCC Testing—Initiation and Growth

Irradiation-Assisted Stress Corrosion Cracking Initiation Screening Criteria for Stainless Steels in PWR Systems

Steve Fyfitch, Sarah Davidsaver and Kyle Amberge

Abstract The Irradiation-Assisted Stress Corrosion Cracking (IASCC) initiation data for austenitic stainless steels in Pressurized Water Reactor (PWR) primary water environments were collected from available research programs and evaluated by the Electric Power Research Institute (EPRI) Materials Reliability Program (MRP). The objective was to determine the relationship between applied tensile stress, neutron fluence, and initiation of IASCC at nominally constant load. Analysis of the available data shows that the applied tensile stress level for initiation of IASCC decreases with increasing neutron dose in PWR environments above the PWR threshold for IASCC of three displacements per atom (dpa). An apparent asymptotic value between approximately 30 and 35% of irradiated yield strength has been observed for neutron dose levels between approximately 10 and 100 dpa. Maximum testing times up to approximately 5000 h are now available, but these still are several orders of magnitude less than 60–80 year operating times. However, the results from this study can currently be used by the nuclear industry to assess the effects of irradiation on austenitic stainless steels in PWR systems as an indicator of the combination of stress and neutron dose at which IASCC becomes possible, particularly for subsequent license renewal (SLR) evaluations.

Keywords IASCC · Initiation · Stainless steel · PWR

Introduction

Irradiation-assisted stress corrosion cracking (IASCC) is an age-related degradation mechanism where materials exposed to neutron radiation become more susceptible to stress corrosion cracking (SCC) with increasing fluence [1]. IASCC, like primary

S. Fyfitch (✉) · S. Davidsaver
AREVA Inc, P.O. Box 10935, Lynchburg, VA 24506-0935, USA
e-mail: steve.fyfitch@areva.com

K. Amberge
Electric Power Research Institute, 3420 Hillview Avenue, Palo Alto, CA 94304-1395, USA

J.H. Jackson et al. (eds.), *Proceedings of the 18th International Conference on Environmental Degradation of Materials in Nuclear Power Systems – Water Reactors*, The Minerals, Metals & Materials Series, https://doi.org/10.1007/978-3-319-68454-3_72

water stress corrosion cracking (PWSCC), is a distinctive subset of SCC. Despite numerous investigations and research efforts, details of the IASCC mechanism in pressurized water reactors (PWRs) remain speculative [2–9]. The current consensus is that IASCC results from a synergistic effect of irradiation damage to the material, water environment with possible radiolysis effects, and stress state.

Various austenitic stainless steels (e.g., Types 304, 316, and 347) are used in PWR locations that receive potentially high levels of neutron exposure. There are three major ways that neutron irradiation affects an austenitic stainless steel material PWR component item:

a. Irradiation creates vacancy and interstitial loops, leading to radiation-induced hardening and, at very high neutron exposures, dislocation channeling with stress [10].
b. Irradiation changes the local alloy chemical composition near point defect traps, especially around the grain boundaries [11].
c. Irradiation produces transmutation products, including hydrogen and helium [12].

Irradiation can also lead to precipitation of new phases [13] or destabilization of the phases already present [14]. However, these are generally considered secondary effects. Although the exact mechanism of IASCC in PWRs is not yet known, both hardening and radiation-induced segregation (RIS) could play a role [15]. Operating experience and irradiated material test results suggest that IASCC may be of most concern in the later stages of reactor vessel internals component item life in PWRs.

IASCC was first observed in Type 304 stainless steel fuel cladding in the early 1960s in both boiling water reactors (BWRs) and PWRs [4]. Since then, IASCC failures have been reported for a number of other reactor vessel internals component items made from various stainless steels and nickel-based alloys in various types of reactors. More detailed historical reviews of intergranular cracking attributed to IASCC in BWRs and PWRs can be found in other publications [3, 4]. As demonstrated in numerous laboratory tests on irradiated materials with constant loading, constant deformation, and slow strain rates, there appears to be a neutron fluence threshold value below which the materials can be considered not susceptible to IASCC in a PWR primary environment [16–23]. However, it should be noted that full susceptibility to IASCC does not appear suddenly at a threshold level. Instead, susceptibility begins to be measureable at this threshold neutron fluence level and escalates with increasing neutron fluence over several tens of dpa.

It is therefore recognized that a certain neutron fluence level is a necessary precondition for the occurrence of IASCC, rather than SCC. Approximate fluence levels for observed occurrences of IASCC in both BWRs and PWRs are plotted in Fig. 1 [24]. Due to different water chemistry and operational conditions, a neutron fluence threshold for IASCC in PWRs differs considerably from that in BWRs where oxygen and hydrogen peroxide are present. For austenitic stainless steel, the PWR industry has agreed upon a “practical IASCC threshold” screening value of approximately three dpa, below which no significant degradation of the resistance to SCC is observed.

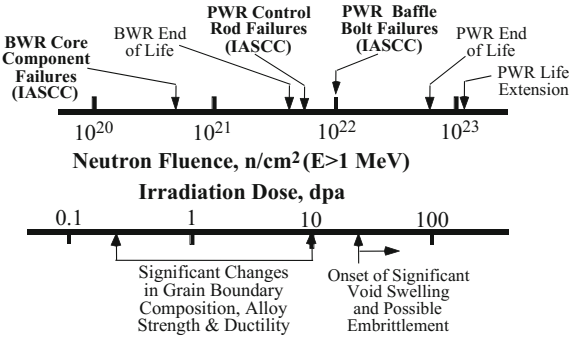

Fig. 1 Neutron fluence effects on IASCC susceptibility in BWR and PWR environments [24]

IASCC Initiation Data Sources

As noted in an earlier publication [25], a number of experimental programs have been conducted since the 1990s in an attempt to characterize the IASCC behavior of austenitic stainless steels with respect to neutron fluence, temperature, degree of cold-work, and material type. This led to development of an EPRI-sponsored database and an analysis of the available test data applicable to IASCC initiation, which was compiled in an EPRI report in 2007 [26]. The existing EPRI database comprises the following materials and test specimens:

- ASTM austenitic stainless steels (Types 304, 316, 347, 308, Coreloy, and CF8)
- Russian austenitic stainless steels (KhN35 V, 14Kh17N2, 08Kh18N10, Sv08Kh19N10, and Sv04Kh19N11)
- Slow strain-rate tensile tests (SSRTs)
- Constant extension rate tests (CERTs)
- Constant load crack initiation tests using O-ring and uniaxial constant load tensile specimens
- Cold-worked, solution-annealed, heat-affected-zone, and weld material test specimens.

Details of the testing can be obtained from the source documents listed in Ref. [26].

Additional test programs have since been completed, which have resulted in a larger database of IASCC initiation data, particularly for dose values where data had been lacking (i.e., in the range of 45–55 and 80–100 dpa). These new data have been compiled and will be published in a revision to EPRI document MRP-211 [26, 27]. A summary of the most recently available data sources is provided in Table 1.

Table 1 Recently published IASCC initiation data sources (2007–2016)

Reference source	Materials tested	Testing method	Test temperature (°C/°F)	Dose (dpa)	Exposure time (h)
MRP-224 (multiple sources) [28]	316CW, 304SA, 304L SA, 308, CF8, Coreloy, 316 Modified	O-Ring, Tensile	290/554, 340/644, 325/617, 330/626	0.1–76	2–3928
Nishioka [29]	316CW	Tensile	320/608	31–73	9–1708
Pokor [30]	304L SA	Tensile	290/554, 340/644	3.2–32.2	2–5012
Karlsen [31]	304 SA, 304L SA	Tensile	325/617, 330/626	11–16	490–2112
Fujii [32]	316 CW	Tensile	320/608	38	46–1050
Bosch [33]	316L CW	O-Ring	320/608	45–80	15–4350
MRP-413 [34]	316 CW	O-Ring, Tensile	340/644	62–100	2–4298

Note That the maximum exposure times vary with each data set, and that the maximum exposure time in the database is approximately 5000 h (about 7 months). The test temperatures range from 290 °C (554 °F) to 340 °C (644 °F) and the test environments are PWR primary water conditions

Analysis of PWR IASCC Initiation Data Trends

In Ref. [25], a figure of the available IASCC initiation data as a function of test time was prepared and the indications at that time were that cracking would not occur in specimens stressed below an apparent threshold of approximately 50% of the irradiated yield strength (at test temperatures from 290 to 340 °C (544–644 °F), for test times up to approximately 4000 h). It was also noted that with the available database, it was not possible to determine if a threshold closer to 40% would be valid to operating times of approximately 600,000 to 700,000 h (or, about 60 to 80 years).

Since that time, additional investigations have been performed with higher dose materials (i.e., greater than 65 dpa) and test times to slightly over 5000 h. These new data are added to the prior database and provided as Fig. 2. The new test results provide further insight into the effect of longer testing times, but the general trend that the time to initiate IASCC decreases with both increasing dose and stress level has remained the same. This trend has also been seen by others [33, 35]. Note however that the apparent threshold stress for IASCC initiation has dropped to approximately 35% of the irradiated yield strength for one data set and additional testing at much longer exposure times may or may not lead to a further drop in this apparent threshold stress.

These same data are presented in Fig. 3, which shows IASCC flaw initiation data as a function of irradiation damage. Variations of this figure by other investigators have led to differing conclusions regarding a saturation stress level (e.g., Ref. [33]),

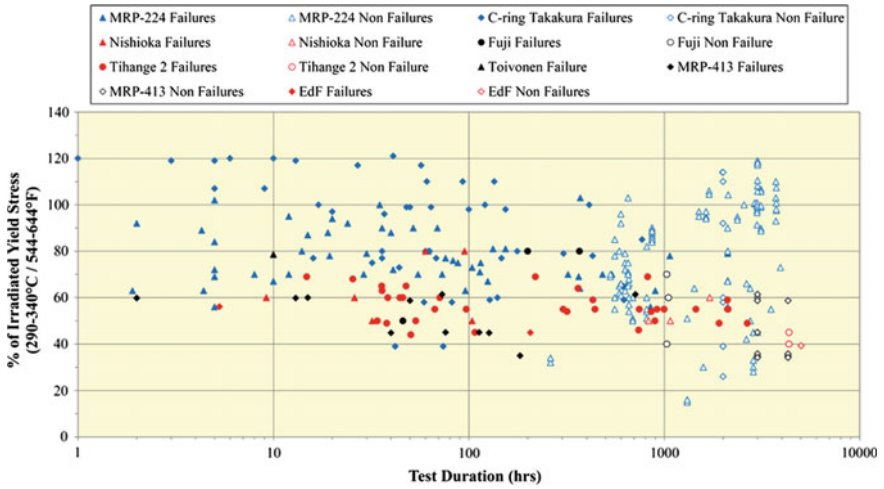

Fig. 2 IASCC initiation data stress versus time to cracking—constant-load tests [27]

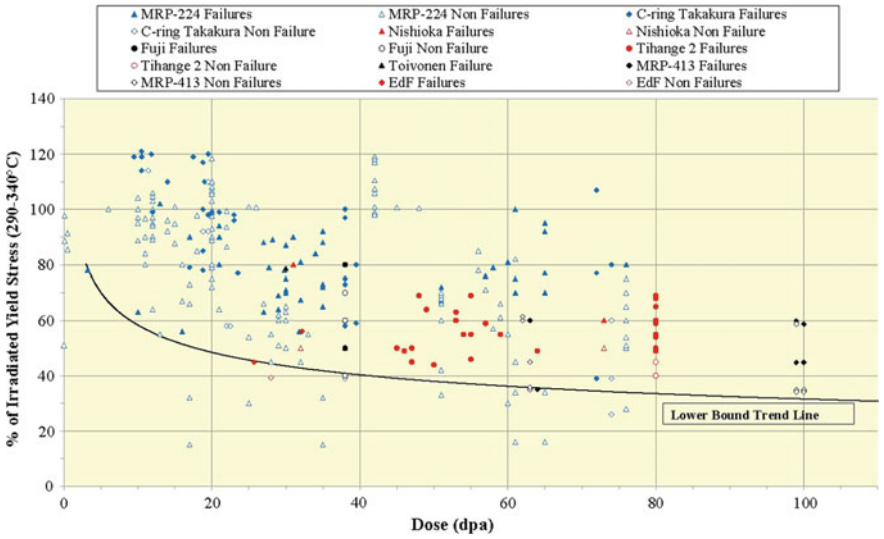

Fig. 3 IASCC initiation data stress versus dose—constant-load tests [27]

but all tend to agree that adequate data are not currently available to determine if the stress threshold saturates above a dose of about 30 dpa or whether a small further decrease in stress threshold will continue to occur with increasing dose levels. Considerations for why IASCC initiation may not saturate but continue to increase with dose level include:

- Local alloy chemical composition at grain boundaries (i.e., RIS) continues to change with dose
- Microstructural features (Frank loops, dislocation density, precipitates, etc.) continue to evolve with dose
- Transmutation products, particularly helium and hydrogen levels, increase with dose.

Yonezawa et al. [36] have evaluated SSRT test results and have shown that there appears to be a relationship between IASCC initiation (as measured by the observed fraction of intergranular cracking area) and temperature; however, since the majority of data in the EPRI-sponsored database have been tested at 340 °C (644 °F), it was concluded that there are insufficient available data to clearly determine the effect of temperature on IASCC initiation.

Takakura et al. [35] have shown that the test data on flux thimble tube (FTT) specimens are generally conservative relative to results on baffle-to-former bolt (BFB) specimens (Fig. 4). Since the majority of the database is comprised of FTT specimen results, a lower bound curve fit to these data is expected to be conservative for highly irradiated PWR component items. Based on this type of analysis, a trend curve for screening IASCC initiation of austenitic stainless steels in PWRs is proposed. This curve is based on a conservative fit to the industry database and truncated at 3 dpa (i.e., the "practical" IASCC threshold dose for PWR environments).

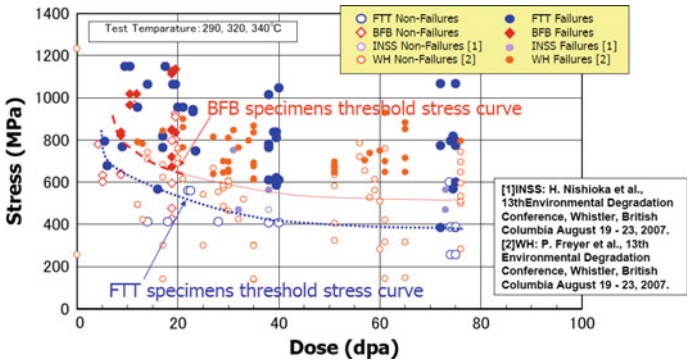

Fig. 4 IASCC initiation data stress versus dose for Baffle-to-Former Bolt (BFB) and Flux Thimble Tube (FTT) specimens—constant-load tests [35]

Summary

A review of IASCC initiation test data compiled from both the literature and a number of EPRI-sponsored test programs was performed. These data were assessed against relevant environmental conditions such as neutron fluence, neutron flux, temperature, and stress.

The available IASCC initiation data have been obtained primarily on Type 316 cold-worked stainless steel FTTs, and data on other austenitic stainless steels used in PWRs, such as solution-annealed Type 304 and Type 347, are limited. Also, there are minimal data on CASS, stainless steel weld materials, and weld HAZ materials. There are obviously strong heat-to-heat differences in IASCC susceptibility, but insufficient data are available to evaluate this in detail.

The available data also could not be used to clearly define an effect of temperature on IASCC initiation, although it appears that higher temperatures [e.g., 340 °C (644 °F)] will initiate IASCC at lower fluence levels sooner than lower temperatures [e.g., 290 °C (554 °F)]. In addition, most of the data have been obtained on materials irradiated below 325 °C (617 °F). At higher irradiation temperatures and high fluence, precipitate phases, voids, and cavities may play a more prominent role in material IASCC susceptibility, for example by producing supplementary hardening. Consequently, the database does not include such potential effects, which have been observed in stainless steels irradiated to high fluence levels at temperature above 325 °C (617 °F).

Based on the currently available data, opinions differ as to whether neutron spectrum has any discernable effect on the IASCC susceptibility of austenitic stainless steels. Additional data are needed to clarify this. The available data seem to indicate that materials irradiated in fast breeder reactors show lower susceptibility to IASCC initiation than PWR irradiation. In addition, testing at low stress for much longer exposure times would be needed to determine the stress levels necessary to initiate cracking at the longer times associated with PWR SLR.

A lower bound trend curve was developed, which suggests that IASCC crack initiation would not occur in austenitic stainless steel materials irradiated to about 80 dpa when loaded to below a stress threshold of approximately 35% of the irradiated yield strength. The data are insufficient to determine whether a small further decrease in stress threshold will continue to occur with increasing dose levels representative of PWR SLR. Several potential reasons for why IASCC initiation may not saturate but continue to increase with dose level have also been identified. However, the results from this study can currently be used by the nuclear industry to assess the effects of irradiation on austenitic stainless steels in PWR systems as an indicator of the combination of stress and neutron dose at which IASCC becomes possible, particularly for SLR evaluations.

Acknowledgements This work was performed for the EPRI MRP. The authors acknowledge the following core members that participated in the analysis of the data during expert panel deliberations:

• D. Brimbal and G. Troyer of AREVA
• J. Rashid of ANATECH Corp (a Structural Integrity Associates Company)
• M. Burke, R. Lott, and J. McKinley of Westinghouse
• P. Chou, J. Smith, and C. Topbasi of EPRI
• J.P. Massoud and F. Sefta of EDF
• P. Efsing, G. Gardner, H. Malikowski, and T. Wells for utility oversight.

The authors also acknowledge the support of T. Natour (AREVA project management) and D. Burak (AREVA) in preparation of this paper.

References

1. M.B. McNeil, Irradiation assisted stress corrosion cracking. Nucl. Eng. Des. **181**, 55–60 (1998)
2. P.M. Scott, *A Review of Irradiation Assisted Stress Corrosion Cracking of Austenitic Materials for PWR Core Internals* (Framatome, France, Eurocorr, 1996)
3. P.M. Scott, A review of irradiation assisted stress corrosion cracking. J. Nucl. Mater. **211**, 101–122 (1994)
4. P.L. Andresen, *Irradiation-assisted stress-corrosion cracking*, ed. R.H. Jones. Stress Corrosion Cracking—Materials Performance and Evaluation (American Society for Metals, Metals Park, OH, 1992), pp. 182–210
5. J.L. Nelson, P.L. Andresen, *Review of current research and understanding of irradiation-assisted stress corrosion cracking*. Proc. 5th Int. Symp. on Environmental Degradation of Materials in Nuclear Power Systems—Water Reactors, Monterey California, August, 1991, NACE, pp. 10–26
6. Meeting Notes of the JOBB Task Team With EDF on Baffle/Former Bolts, April 3–4, 1997, Moret-Sur-Loing, France, EPRI
7. P.L. Andresen, F.P. Ford, S.M. Murphy, J.M. Perks, *State of Knowledge of Radiation Effects on Environmental Cracking in Light Water Reactor Core Materials*. Proc. 4th Int. Symp. on Environmental Degradation of Materials in Nuclear Power Systems—Water Reactors, Jekyll Island, Georgia, August, 1989, NACE, pp. 1–83 through 1–121
8. H. Hanninen, I. Aho-Mantilla, *Environmental-Sensitive Cracking of Reactor Internals*. Proc. 3rd Int. Symp. on Environmental Degradation of Materials in Nuclear Power Systems—Water Reactors, Traverse City, Michigan, August 30–September 3, 1987, AIME, pp. 77–92
9. S.M. Bruemmer, et al., *Reviews for the Understanding and Evaluation of Irradiation-Assisted Stress Corrosion Cracking*. Critical Issue Reviews for the Understanding and Evaluation of Irradiation-Assisted Stress Corrosion Cracking, EPRI TR-107159, 4068, Final Report, November, 1996
10. J.I. Cole et al., *Deformation Temperature, Strain Rate, and Irradiation Microstructure Effects on Localized Plasticity in 304L SS*. Proc. 7th Int. Symp. On Environmental Degradation of Materials in Nuclear Power Systems—Water Reactors, NACE, 1995
11. E.P. Simonen, S.M. Bruemmer, *Kinetic Evaluation of Intergranular Fracture in Austenitic Stainless Steels*. Proc. 7th Int. Symp. On Environmental Degradation of Materials in Nuclear Power Systems—Water Reactors, NACE, 1995
12. P.J. Maziasz, Overview of microstructural evolution in neutron-irradiated austenitic stainless steels. J. Nucl. Mater. **205**, 118–145 (1993)

13. F.A. Garner, *Irradiation Performance of Cladding and Structural Steels in Liquid Metal Reactors*. Materials Science and Technology, vol. 10A (VCH, Weinheim, 1994), pp. 422–543
14. W.J.S. Yang, Grain boundary segregation in solution-treated Nimonic PE16 during irradiation. J. Nucl. Mater. **108–109**, 339–346 (1982)
15. Critical Issue Reviews for the Understanding and Evaluation of Irradiation-Assisted Stress Corrosion Cracking, EPRI TR-107159, November 1996
16. Materials Reliability Program: Hot Cell Testing of Baffle/Former Bolts Removed From Two Lead Plants (MRP-51), EPRI Report 1003069, 2001
17. Materials Reliability Program: Characterization of Type 316 Cold-Worked Stainless Steel Highly Irradiated Under PWR Operating Conditions (MRP-73), EPRI Report 1003525 (2002)
18. Materials Reliability Program: Characterization of Decommissioned PWR Vessel Internals Material Samples—Tensile and SSRT Testing (MRP-129), EPRI Report 1008205 (2004)
19. Materials Reliability Program: Crack Initiation Testing and Slow Strain Rate Tensile (SSRT) Testing of Boris-60 Irradiated Materials, and Effect of Hydrogen on IASCC Susceptibility (MRP-159), EPRI Report 1010096 (2005)
20. P.M. Scott, M.-C. Meunier, D. Deydier, S. Silvestre, A. Trenty, *An Analysis of Baffle/Former Bolt Cracking in French PWRs*, ed. by R.D. Kane. ASTM STP 1401 Environmentally Assisted Cracking: Predictive Methods for Risk Assessment and Evaluation of Materials, Equipment and Structures, ASTM (2000), pp. 210–223
21. R.P. Shogan, T.R. Mager, *Susceptibility of Type 316 Stainless Steel to Irradiation Assisted Stress corrosion Cracking in a PWR Environment*. Proc. 10th Int. Conference on Environmental Degradation of Materials in Nuclear Power Systems—Water Reactors, 2002
22. H. Kanasaki, et al., *Fatigue and Stress Corrosion Cracking Behaviors of Irradiated Stainless steels in PWR Primary Water*. Proceedings of ICON 5: 5th International Conference on Nuclear Engineering, 1997
23. K. Fukuya et al., IASCC susceptibility and slow tensile properties of highly-irradiated 316 stainless steels. J. Nucl. Sci. Technol. **41**(6), 673–681 (2004)
24. S.M. Bruemmer et al., Radiation-induced material changes and susceptibility to intergranular failure of light-water-reactor core internals. J. Nucl Mater **274**, 299–314 (1999)
25. S. Fyfitch et al., *Criteria for Initiation of Irradiation-Assisted Stress Corrosion Cracking in Stainless Steels in PWR Systems*. Proc. 14th Int. Conference on Environmental Degradation of Materials in Nuclear Power Systems–Water Reactors, 2009
26. Materials Reliability Program: PWR Internals Age-Related Materials Properties, Degradation Mechanisms, Models, and Basis Data—State of Knowledge (MRP-211). EPRI, Palo Alto, CA: 2007. 1015013
27. Materials Reliability Program: PWR Internals Age-Related materials Properties, Degradation Mechanisms, Models, and Basis Data—State of Knowledge (MRP-211, Rev. 1). EPRI, Palo Alto, CA: 2017. 3002010270
28. Materials Reliability Program: Analysis of IASCC Initiation Data for Irradiated Stainless Steels (MRP-224). EPRI, Palo Alto, CA: 2007. 1015480
29. H. Nishioka et al., IASCC initiation in highly irradiated stainless steels under uniaxial constant load conditions. J. Nucl. Sci. Technol. **45**(10), 1072–1077 (2008)
30. C. Pokor et al., *Determination of the time to Failure Curve as a Function of Stress for a Highly Irradiated AISI 304 Stainless Steel after Constant Load Tests in Simulated PWR Water Environment*, Fontevraud 7, Avignon, France, September 26–30, 2010
31. T.M. Karlsen, *Halden In-Reactor Constant Load Test for CIR II.* CIR II Extension Program Steering Committee Meeting, EDF, Les Renardieres, November 18–19, 2009, CIR Meeting CD
32. K. Fujii et al., *Effects of Dissolved Hydrogen on IASCC Behavior*, Fontevraud 7, Avignon, France, September 26–30, 2010
33. R.W. Bosch et al., Crack initiation testing of thimble tube material under PWR conditions to determine a stress threshold for IASCC. J. Nucl. Mater. **461**, 112–121 (2015)

34. Materials Reliability Program: Effect of Lithium Concentration on IASCC Initiation in Irradiated Stainless Steel (MRP-413): EPRI, Palo Alto, CA: 2016. 3002008082
35. K. Takakura et al., *IASCC Properties of Cold Worked 316 Stainless Steel in PWR Primary Water*. Proc. 14th Int. Conference on Environmental Degradation of Materials in Nuclear Power Systems—Water Reactors, 2009
36. T. Yonezawa et al., *IASCC Susceptibility and It's Improvement of Austenitic Stainless Steels for Core Internals of PWR*. International Symposium: Contribution of Materials Investigation to the Resolution of Problems Encountered in PWR Plants, Fontevraud 4, SFEN, 1998

Novel Technique for Quantitative Measurement of Localized Stresses Near Dislocation Channel—Grain Boundary Interaction Sites in Irradiated Stainless Steel

D.C. Johnson and G.S. Was

Abstract A process for quantitatively measuring the residual stress near dislocation channel—grain boundary interaction sites has been developed especially for irradiated stainless steel using High Resolution Electron Backscatter Diffraction (HREBSD). Tensile stress acting normal to the grain boundary at 15 different discontinuous channel—grain boundary sites were observed to be highly elevated, with peak stresses reaching ~2 GPa, which is roughly an order of magnitude greater than the stresses observed at sites where slip transfer occurred at the grain boundary. A clearly observable difference can be made between the stress profiles present at discontinuous and continuous channel—grain boundary interaction sites. This difference is consistent with the theory that high tensile stress at the grain boundary may be a key driving factor for the initiation of irradiation assisted stress corrosion cracks.

Keywords Irradiation assisted stress corrosion cracking · Localized deformation · High resolution electron backscatter diffraction · Austenitic steel

Introduction

Current generation light water reactors continue to produce a large amount of electrical power in the United States as well as many other countries across the world [1]. Although commercial light water reactors have been reliably running for several decades, many material degradation mechanisms have led to the premature failure of internal core components over the years. In particular, Irradiation Assisted Stress Corrosion Cracking (IASCC) has been observed and studied in both boiling water reactor (BWR) and pressurized water reactor (PWR) designs since the early

D.C. Johnson (✉) · G.S. Was
Department of Nuclear Energy and Radiological Sciences, University of Michigan, Ann Arbor, MI 48109, USA
e-mail: dcoulson@umich.edu

J.H. Jackson et al. (eds.), *Proceedings of the 18th International Conference on Environmental Degradation of Materials in Nuclear Power Systems – Water Reactors*, The Minerals, Metals & Materials Series, https://doi.org/10.1007/978-3-319-68454-3_73

1960's [2]. Even after decades of researching IASCC, the fundamental processes which determine crack initiation in austenitic stainless steel are still poorly understood.

Recently, localized deformation has been highlighted as a potentially key factor in the IASCC initiation process. Irradiation causes a change in the deformation mode from homogeneous slip to localized heterogeneous deformation [3, 4]. A majority of the deformation in the material is localized to very small bands called dislocation channels, which are shown in Fig. 1. These dislocation channels can have multiple types of interactions when they intersect with grain boundaries in the material. The first option is that the dislocation activity is able to propagate across the grain boundary into the adjacent grain, resulting in visual continuity of the dislocation channel. This is referred to as a continuous dislocation channel. Dislocations can also be completely arrested at the grain boundary and prevented entirely from propagating into the adjacent grain, and are referred to as discontinuous channels. Examples of both continuous and discontinuous dislocation channels are presented in Fig. 2. Studies performed by McMurtrey et al. have shown that the IASCC susceptibility at discontinuous channel sites is far greater than at continuous channel sites in the same material [5]. Work performed by West et al. showed a strong dependence between crack initiation and orientation of the grain boundary trace with respect to the loading axis [6]. Cracking susceptibility increased as the grain boundary was oriented more perpendicular to the loading axis, where the normal tensile stress acting on the grain boundary was greatest. This is consistent with discontinuous channel sites showing higher susceptibility to crack initiation since the pile-up of dislocations at the grain boundary will create a strong local stress field which can help to crack the grain boundary.

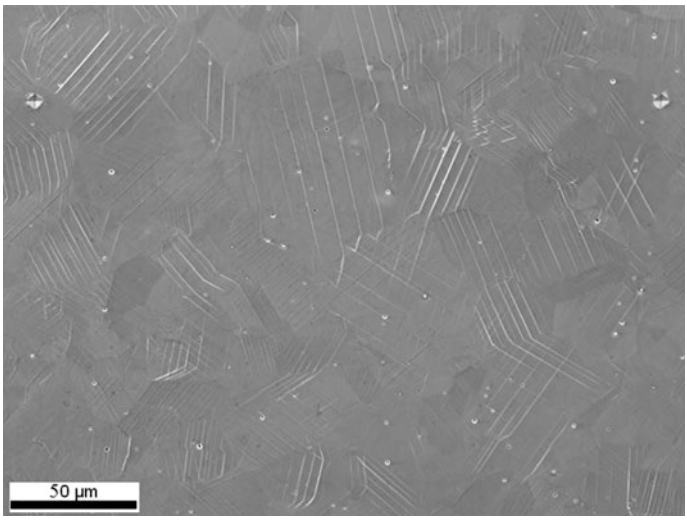

Fig. 1 SEM of DC after argon strain

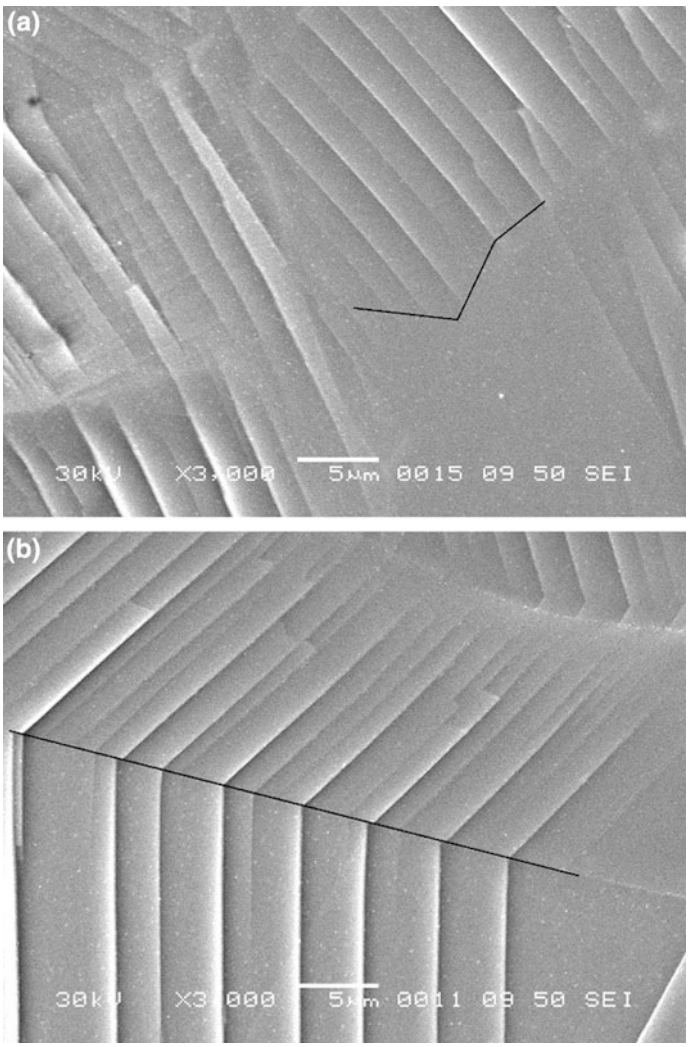

Fig. 2 **a** Discontinuous channels **b** continuous channels

Until recently, it was not possible to accurately measure localized residual stresses on the sub-micron length scale in metals. Using a technique developed by Wilkinson, Meaden, and Dingley called High Resolution Electron Backscatter Diffraction (HREBSD), it is possible to quantitatively measure residual elastic stresses at a small length scale [7–9]. Small changes in the Kikuchi band structure are measured using cross correlation and those changes are related to deformation in the crystal lattice. This technique has been applied for the first time in irradiated stainless steel in an attempt to uncover the difference in stress state present at the interaction site between dislocation channels and grain boundaries.

Experimental Procedures

A lab purity alloy of $Fe_{13}Cr_{15}Ni$, with composition as shown in Table 1, was used throughout this study. A bulk sample of $Fe_{13}Cr_{15}Ni$ was cold rolled and then solution annealed at 950 °C for 30 min to increase the average grain size to 25 microns. From the solution annealed bulk sample, tensile and TEM bar samples were electrical discharge machined (EDM) as shown in Fig. 3a. The gauge section was polished flat using successively finer grit SiC paper starting with 320 grit and ending with 4000 grit. Samples were electropolished using a 10% perchloric acid 90% methanol solution at −40 °C for 30 s to achieve a mirror finish.

Samples were then loaded onto a stage, with the geometry shown in Fig. 3b, and irradiated with 2 meV protons to a total dose of 5 dpa at 360 °C at a dose rate of 1.0×10^{-5} dpa/s at the University of Michigan Ion Beam Laboratory (MIBL). The damage level is calculated at 60% of the Bragg peak using the SRIM simulation program and a displacement energy of 40 eV as outlined in Ref. [10]. The temperature is tightly controlled during the experiment to best replicate the damage observed in neutron irradiated material under typical reactor conditions [11].

Table 1 $Fe_{13}Cr_{15}Ni$ alloy composition

Alloy composition (wt%)									
Cr	Ni	Mo	Cu	Al	Si	S	P	Mn	C
13.41	15.04	0.01	0.01	<0.01	0.1	<0.005	<0.01	1.03	0.016

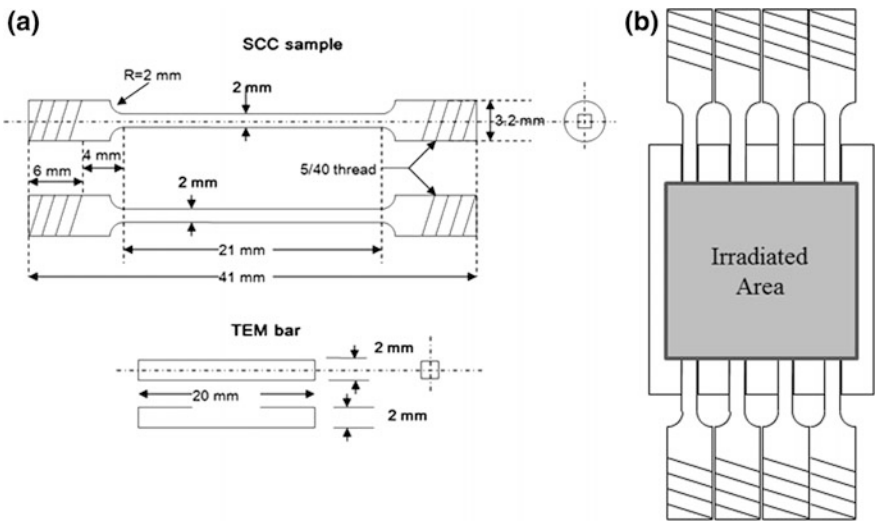

Fig. 3 SCC and TEM bar design and irradiation stage

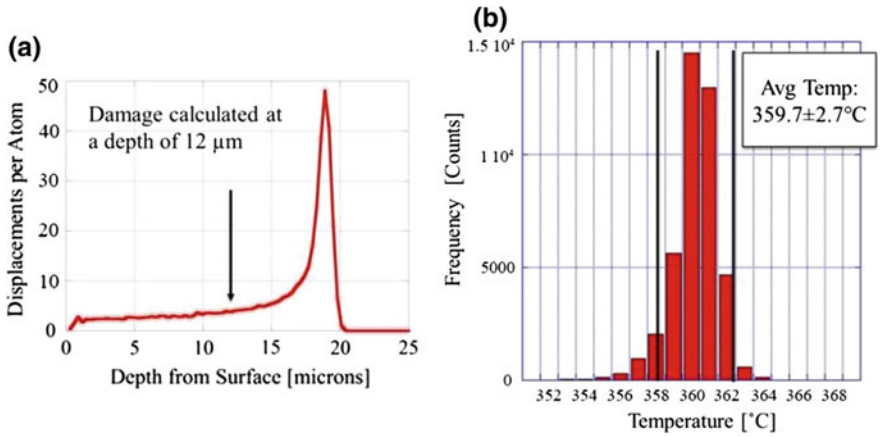

Fig. 4 SRIM profile and temperature distribution

The SRIM damage profile is presented in Fig. 4a, and a histogram of the stage average temperature history is shown in Fig. 4b.

Post irradiation, a hardness indenter is used to place an array of equally spaced indents along the irradiated portion of the tensile bar. 10 unique regions are mapped out by placing 22 identical indents which have a vertical spacing of 1.5 mm and a horizontal spacing of 0.7 mm. Each region has the grain structure mapped by EBSD using a Phillips XL30 FEG SEM and TSL OIM 5 software with a coarse step size of 4 microns. Fully characterized tensile bars are then loaded into an autoclave for Constant Extension Rate Tensile (CERT) tests which are operated in a high purity argon environment at 288 °C and with a strain rate of 3×10^{-7} s^{-1}. After straining, an Olympus LEXT confocal microscope is used to determine the location and interaction type of the dislocation channels at grain boundaries.

The generated dislocation channels can have a surface step height greater than 400 nm [12], which can result in beam shadowing during HREBSD analysis. Therefore, the top ~200 nm of the sample surface is removed by mechanical polishing with 20 nm colloidal silica solution. To ensure that the desired amount is removed from the surface, the depths of the hardness indents used for marking the EBSD regions are measured before and after polishing with an Olympus LEXT confocal laser microscope. Guo et al. showed that the stress field generated by dislocations piling up at a grain boundary is not limited to the surface region of the sample [13], and penetrates several microns into the material. Therefore, the stress field generated by dislocation channels should still be present after removing a small layer from the surface.

Specific boundaries of interest are relocated using the hardness indents as landmarks along with EBSD scans and confocal images, since the polishing step removes many of the channels completely. After relocation, a ~20 μm × 20 μm area is scanned with a 100 nm step size with the grain boundary of interest roughly in the center of the scan. Raw Kikuchi patterns are collected at each point during the

EBSD scanning and are analyzed offline using the CrossCourt3 (CC3) software package developed by BLG Vantage and 50 regions of interest for cross correlation. The 50 regions of interest are used to develop a best fit distortion tensor by comparing the raw EBSD pattern selected as the reference with every other pattern collected from that same grain. Distortion tensor results from CC3 were combined with anisotropic elasticity coefficients for stainless steel [14] to calculate the residual tensile stress acting perpendicular to the grain boundary. Calculated stress tensors are transformed such that the principle stresses are resolved normal to the grain boundary surface trace and all points with a calculated mean angular error greater than 10^{-3} rad were removed from analysis due to the large calculation errors for these points.

Results and Discussion

Figure 5a shows the CC3 calculated tensile stress acting normal to the grain boundary near a discontinuous dislocation channel-grain boundary (DC-GB) interaction site after a successful HREBSD scan. Since the grain boundary plane with respect to the loading axis is unknown, the principle stresses are rotated to be perpendicular to the grain boundary trace angle. The quoted magnitudes of the calculated tensile stress assume that the grain boundary plane angle is perpendicular

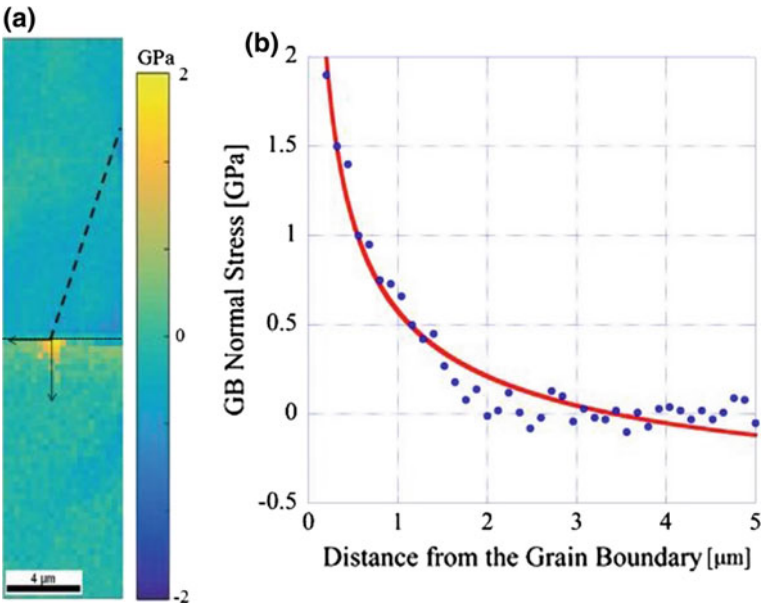

Fig. 5 Raw CC3 stress map and stress profile w GB

with the sample surface, and are therefore upper bound values. Location of the dislocation channel is marked by a black dashed line.

The main observable feature in this scan is a high tensile stress at the intersection point between the discontinuous channel and the grain boundary. A majority of the elevated stress is dissipated over the first 2–3 microns before reaching a quasi-static background level near 0 GPa. Shear stresses were also observable in the CC3 calculated stress tensor, however the magnitude of these stresses was only on the order of 30% of the tensile stresses. The stress was measured as a function of distance from the grain boundary moving in a direction which is perpendicular to the grain boundary, and is plotted in Fig. 5b. The peak grain boundary normal stress is observed to be 1.91 GPa for this example and 0.71 GPa for the shear stress component. This is much larger than the shear stresses observed by Guo et al. [13] in titanium, which ranged from 0.15 GPa to 0.60 GPa. This difference is most likely due to the larger degree of slip localization in irradiated stainless steel, which results in larger dislocation pile-ups.

Theoretical work by Eshelby et al. [15] produced an analytical solution to the pile-up of dislocations at an immovable barrier, similar to the case here in which dislocations are blocked by a grain boundary. In the Eshelby model, the number of dislocations, n, are constrained to lie in the same slip plane under the combined action of their mutual repulsion and the force of an applied stress. The resulting stress field present on the other side of the stationary barrier was found to be closely approximated by $r^{-1/2}$ dependence, where r is the distance from the dislocation pile-up. The raw data presented in Fig. 5b was fit with a least squares algorithm to a function of the form:

$$\sigma_N = A + \frac{K}{\sqrt{r+B}}[GPa] \tag{1}$$

where σ_N denotes the grain boundary normal stress, K is the stress intensity factor that describes resistance to slip transfer of this grain boundary, A allows for uncertainty in the stress state of the selected reference pattern, and B allows for uncertainty of the exact location of the grain boundary beneath the resolving limit of your EBSD step size. The data shown in Fig. 5b and other subsequent scans show agreement with Eq. (1) for discontinuous channel interaction sites. The fitting parameters A, B, and K are −0.539 GPa, 0.035 μm, and 0.8774 MPa$\sqrt{m}$ respectively. In addition to the scan presented in Fig. 5, 14 additional HREBSD scans have been made near other discontinuous DC-GB interaction sites and 10 continuous DC-GB interaction sites. The GB normal stress profiles for each of these scans are presented in Fig. 6, with all data presented in red coming from continuous channel sites and all data presented in blue coming from discontinuous channel sites. A clear distinction can be made between the behavior at discontinuous and continuous channel sites. At all discontinuous sites, there is a clearly visible elevation in the GB normal stress which reaches a peak value at the site of intersection and dissipates over the first few microns in the adjacent grain. The range of K values for these additional scans range from 0.49 to 1.42 MPa$\sqrt{m}$. At continuous

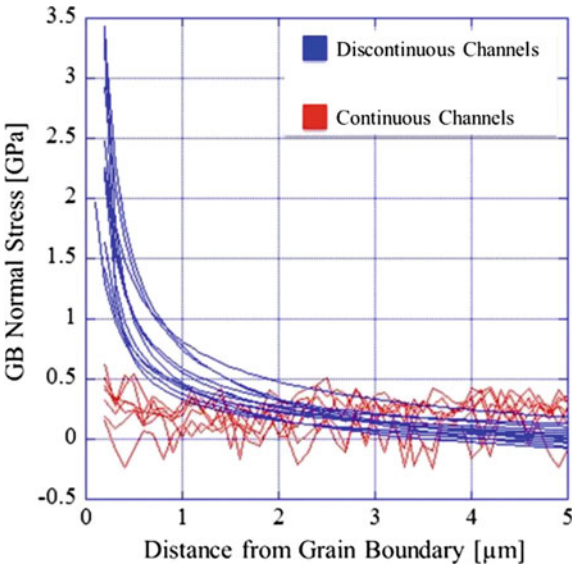

Fig. 6 Compilation of GB normal stress from HREBSD scans

channel sites, however, no appreciable GB normal stress is observed, and no Eshelby fit can be performed on these data. This flat profile near continuous channels is also observed by Guo et al. [13] who saw no stress elevation near slip transmission sites.

Conclusions

A process has been developed to quantitatively measure the residual stresses near dislocation channel—grain boundary interaction sites in irradiated stainless steel using HREBSD. By removing channel steps to eliminate shadowing during EBSD scanning of the sample surface and using unique markers to relocate specific grain boundaries of interest, it is possible to measure tensile stresses acting normal to the grain boundary at both continuous and discontinuous channel—grain boundary interaction sites. Elevated tensile stresses are observed at discontinuous channel sites, while no appreciable elevation in tensile stress is observable at continuous channel sites. The profile of the elevated stress observed near discontinuous channels is consistent with the model proposed by Eshelby in the early 1950's and other results published on non-irradiated materials. The model proposed by Eshelby is not specific to irradiated materials, and only details the behavior dislocations piling up at a grain boundary. However, the complex microstructure prevalent in irradiated materials leads to the restriction of dislocation mobility and a higher degree of localized deformation. Therefore, larger dislocation pile-ups can be generated in irradiated materials, resulting in higher local levels of stress which can

affect the cracking susceptibility of certain grain boundaries. The results presented on both continuous and discontinuous stress profiles are consistent with the enablement of IASCC by a high local tensile stress at the grain boundary.

Acknowledgements The authors would like to acknowledge Alexander Flick for his assistance conducting constant extension rate tests in the High Temperature Corrosion Laboratory at the University of Michigan as well as the staff of the University of Michigan Ion Beam Laboratory, Ovidiu Toader, Fabian Naab, Thomas Kubley, and Ethan Uberseder for assistance in performing proton irradiations. This work was supported by the U.S. Department of Energy, Office of Science, Basic Energy Sciences, under grant DE-FG02-08ER46525.

References

1. N.S. Caetano, T.M. Mata, A.A. Martins, M.C. Felgueiras, Energy Procedia **107**, 7 (2017)
2. P.L. Andresen, F.P. Ford, K. Gott, R.L. Jones, P.M. Scott, T. Shoji, R. W. Staehle, R.L. Tapping, Expert Panel Report on Proactive Materials Degradation Assessment, BNL-NUREG-77111-2006
3. T. Miura, K. Fujii, K. Fukuya, Y. Ito, J. Nucl. Mater. **210**, 386–388 (2009)
4. N. Hashimoto, T.S. Byun, JNM **960**, 367–370 (2007)
5. M.D. McMurtrey, G.S. Was, B. Cui, I.M. Robertson, L. Smith, D. Farkas, Int. J. Plast **56**, 219 (2014)
6. E.A. West, M.D. McMurtrey, Z. Jiao, G.S. Was, Metall. Mater. Trans. A **43**, 136 (2012)
7. A.J. Wilkinson, G. Meaden, D.J. Dingley, Ultramicroscopy **106**, 307 (2006)
8. A.J. Wilkinson, G. Meaden, D.J. Dingley, Mater. Sci. Technol. **22**, 1271 (2006)
9. J. Kacher, C. Landon, B.L. Adams, D. Fullwood, Ultramicroscopy **109**, 1148 (2009)
10. R.E. Stoller, M.B. Toloczko, G.S. Was, S. Dwaraknath, F.A. Garner, Nucl. Inst. Methods Phys. Res. B **310**, 75 (2013)
11. G.S. Was, J. Mater. Res. **30**, 1158 (2015)
12. Z. Jiao, G.S. Was, JNM **382**, 203 (2008)
13. Y. Guo, T.B. Britton, A.J. Wilkinson, Acta Mater. **76**, 1 (2014)
14. K. Benyelloul, H. Aourag, Comput. Mater. Sci. **67**, 353 (2013)
15. J.D. Eshelby, F.C. Frank, F.R.N. Nabarro, Philos. Mag. **42**, 351 (1951)

IASCC Susceptibility of 304L Stainless Steel Irradiated in a BWR and Subjected to Post Irradiation Annealing

Justin R. Hesterberg, Zhijie Jiao and Gary S. Was

Abstract Post-irradiation annealing (PIA) was conducted to investigate the cause of irradiation-assisted stress corrosion cracking (IASCC). The effects of PIA on irradiation hardening, dislocation channel formation, and IASCC susceptibility were examined for a 304L stainless steel irradiated to 5.9 dpa in the Barsebäck-1 reactor (Sweden). The annealing treatments were performed at temperatures in the range 450–600 °C and times ranging from 1–20 h. Longer annealing times and higher temperatures, as represented by iron diffusion distance, resulted in a significant reduction in irradiation hardening. IASCC susceptibility was measured for the as-irradiated and two PIA conditions (500 °C: 1 h and 550 °C: 20 h) via interrupted CERT tests under simulated BWR-NWC conditions. The annealing treatments progressively reduced IASCC susceptibility (as measured by the final intergranular fracture fraction) and dislocation channel density.

Keywords IASCC · Irradiation · Hardening · Dislocation channels · Post-irradiation annealing · Neutron-irradiated · Stainless steel

Introduction

Stainless steel components of nuclear reactors undergo an increased susceptibility to irradiation-assisted stress corrosion cracking (IASCC) after being irradiated to approximately 1 dpa in BWR reactors and about 4 dpa in PWR reactors [1]. While this phenomenon has been studied for many years, IASCC remains a complex problem which has yet to be fully understood. The complexity is largely due to the multiple irradiation effects which concurrently evolve during an irradiation. Previous research on this topic has largely focused on three interconnected factors: radiation-induced segregation, irradiation hardening, and localized deformation,

J.R. Hesterberg (✉) · Z. Jiao · G.S. Was
University of Michigan, 2355 Bonisteel Blvd., Ann Arbor, MI 48109-1204, USA
e-mail: jhesterb@umich.edu

J.H. Jackson et al. (eds.), *Proceedings of the 18th International Conference on Environmental Degradation of Materials in Nuclear Power Systems – Water Reactors*, The Minerals, Metals & Materials Series, https://doi.org/10.1007/978-3-319-68454-3_74

which are each considered to play a role, though each of them alone is insufficient to fully explain IASCC susceptibility [2].

The first factor, and perhaps most widely studied, is radiation induced segregation (RIS). Undersized atoms, like nickel and silicon, will enrich at grain boundaries or matrix sinks, while oversized atoms, like chromium and manganese, will deplete [3]. This reduction of chromium at grain boundaries below a threshold value may limit passivation, thus making the grain boundary a preferential site for oxidation and easier cracking. However, recent studies have shown clear evidence that radiation-induced segregation at grain boundaries alone cannot explain IASCC susceptibility [4, 5], though the wider influence of solute clusters at matrix sinks is less understood [6, 7].

The second factor is irradiation hardening [8]. During irradiation, a large amount of dislocation loops, solute clusters, and precipitates are introduced in the material, thus causing an increase in the hardness and yield stress of the material. As IASCC susceptibility has been observed to increase with yield stress [9], this hardening has often been cited as a key factor of IASCC. However, post-irradiation annealing experiments have shown that IASCC is often reduced faster than hardening [4, 5, 10, 11]. This implies that the hardening alone does not control the IASCC susceptibility, but that the irradiation defects themselves may play a more specific role in the IASCC process, above their bulk contribution of hardening.

The third irradiation effect often considered is the development of localized deformation with the addition of strain, most often in the form of dislocation channels [12–18]. These channels form as preferred paths of dislocation movement through the irradiated microstructure, and thus can result in enhanced stress concentrations at the grain boundary, and possibly cause initiation of an intergranular crack. Recent research on the role of dislocation channeling, has also shown the channel interaction with a grain boundary, i.e. whether or not the channel can continue into the neighboring grain, is important in determining the susceptibility to crack initiation [16, 17].

In this paper, post-irradiation annealing (PIA) treatments are applied to an irradiated 304L stainless steel to investigate the effect on hardness, IASCC susceptibility, and the dislocation channel evolution. Annealing treatments on both proton and neutron irradiated material have been shown to decrease the hardness and yield stress through the dissolution of irradiation defects, reduce radiation-induced segregation, and decrease or eliminate the IASCC susceptibility [4, 5, 10, 11, 19–21]. The effect of annealing treatments on the dislocation channel formation and evolution have not been previously investigated.

Experiment

The material is a 304L stainless steel taken from a control rod irradiated in the decommissioned Barsebäck 1 BWR in Sweden, received through Studsvik Nuclear AB. The material was irradiated to a fluence (E > 1 MeV) of 4.16×10^{21} n/cm^2

Table 1 Chemical composition of the irradiated 304L stainless steel via APT [22] in wt%. Additional impurities of aluminum and copper were identified via APT, as compared to the original ladle analysis

Element	Fe	Cr	Ni	Mn	Si	Co	Cu	C	P	Al	S
Concentration (wt%)	68.01	18.34	11.6	1.13	0.40	0.15	0.12	0.035	0.02	0.02	0.001

over its lifetime, thus corresponding with a dose of 5.9 dpa. The composition of the material, as measured by post-irradiation APT, is given in Table 1 [22].

Micro-hardness measurements were performed to generalize the changes in the bulk irradiated microstructure following the annealing treatments. Each specimen was measured at a load of 200 gf, with at least 30 independent indents, whereas the average hardness and standard deviation was then recorded. The annealing conditions examined covered four different temperatures: 450 °C, 500 °C, 550 °C, and 600 °C with times: 1, 5, and 20 h at each temperature. To compare different annealing times and temperatures, iron diffusion distance (d) was calculated: $d = \sqrt{Dt}$, where t is the annealing time and D the iron self-diffusion coefficient given by $D = D_o e^{-Q/kT}$, with T the annealing temperature, k the Boltzmann constant, Q the migration energy of 2.95 eV, and D_o equals 4.9×10^5 m^2/s as used by Fukuya et al. [5].

For IASCC susceptibility testing, multiple miniature tensile specimens were fabricated with a gauge length of 12 mm and a nominal diameter of 2.0 mm and were subjected to the different thermal treatments. After annealing, the tensile specimens were tested via interrupted constant extension rate tensile tests (CERT) until failure in a simulated BWR-NWC water environment (288 °C, 2000 ppb dissolved oxygen, and conductivity of 0.2 μS/cm) under an applied strain rate of 3.0×10^{-7} s^{-1}. Following the failure of a tensile specimen the individual stress-strain curves of the interrupted CERT tests were compiled to create a singular stress-strain curve for the specimen.

For this study, the straining experiments were completed in small stress/strain increments, such that we could more precisely identify point of crack initiation and study the development of the localized deformation, as opposed to straining the specimens directly to failure. After each stress/strain increment the specimen was removed from the autoclave and examined using a JEOL JSM-6480 SEM. This examination recorded any sites of crack initiation and changes in the localized deformation. The localized deformation was measured as an areal density of dislocation channels, whereas individual channels were identified by either their discontinuity at a grain boundary or their change in slip direction when continuing across a boundary.

Results and Discussion

Irradiation Hardening

Vickers micro-hardness has been often used in the literature as a simple method to evaluate the generalized changes in the bulk irradiated microstructure following PIA treatments. Prior studies have shown that a greater reduction in hardening corresponds to a greater removal of irradiation defects such as dislocation loops, solute clusters, and precipitates [4, 5, 11]. The selected range of annealing temperatures and times were expected to fully bound the complete removal of irradiation hardening. The hardness measurements for the selected temperatures and times (1, 5, and 20 h) are shown in Fig. 1, where the irradiation hardening is compared as a percentage of the as-irradiated condition. Overall, it was observed that annealing at 450 °C, had a minimal impact on the irradiation hardening at times up to 20 h. However, temperatures of 500 °C, 550 °C, and 600 °C showed a successively greater removal of hardening with increasing time and temperature. Following annealing at 600 °C: 20 h, the measured hardness had returned to a value expected for an unirradiated 304L stainless steel ($\sim$165 H_v), indicating a full removal of the irradiation damage.

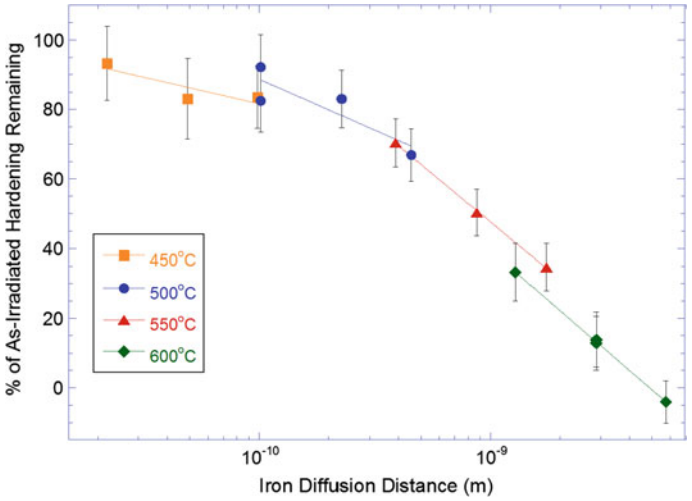

Fig. 1 Reduction in the residual irradiation hardening due to specific annealing treatments, the iron diffusion distance increases at each temperature with annealing times of 1, 5 and 20 h. Overall the hardness was seen to decrease with increasing temperature and time

Tensile Straining

Stress-strain curves for each of the tested conditions in simulated BWR-NWC environment are shown in Fig. 2. Note that due to the interrupted CERT testing the final stress-strain curves were compiled of several independent straining increments, thus causing the segmented appearance. The elastic deformation portion of each curve has been corrected to subtract system compliance by normalizing to the expected Young's modulus for an austenitic stainless steel, note that the slight changes in the Young's modulus due to irradiation were not accounted. Mechanical properties of the varying annealing treatments, as determined from the CERT tests, are summarized in Table 2. The table is organized by annealing condition, showing the yield stress, maximum stress, uniform and total elongation.

The as-irradiated condition displayed a yield stress drop and subsequent strain softening, as typical of the irradiated condition of a solution-annealed steel. Annealing at 500 °C:1 h slightly reduced the yield stress, while completely removing the yield stress drop and strain softening behavior, instead displaying an extremely slight strain hardening behavior. Annealing at 550 °C:20 h caused a large increase in the yield stress and specimen elongation. Furthermore, this condition displayed a clear strain hardening behavior, up till 8.8% plastic strain.

Following the final failure of the specimens, the fracture surfaces were fully examined by SEM, as shown in Fig. 3. The fracture surface was quantified in accordance to the relative area of each fracture type: intergranular (IG), transgranular (TG), mixed IG/TG, and ductile failure. Examples of each type of fracture can be seen in Fig. 4. The results of the fractography classification and reduction of

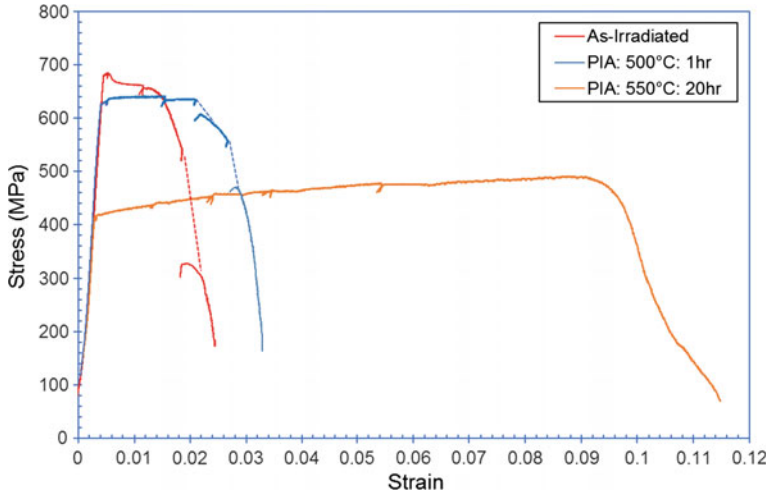

Fig. 2 Change in the stress strain behavior under simulated BWR-NWC conditions due to specific annealing treatments: 500 °C: 1 h and 550 °C: 20 h. Overall a clear change in the mechanical behavior, yield stress, and elongation was observed

Table 2 Changes in the mechanical properties and fracture classification due to the varying annealing treatments, as determined from the CERT tests under simulated BWR-NWC environment

Tensile specimen	σ_y (MPa)	σ_{UTS} (MPa)	ε_{total} (%)	$\varepsilon_{uniform}$ (%)	% RA	Brittle fracture type (%)		
						Intergranular	Mixed	Transgranular
As-Irradiated	685.5	685.5	2.00	0.00	28.6	48.40	28.62	3.62
PIA: 500 °C: 1 h	633.4	642.4	2.58	0.95	46.8	34.86	12.82	36.58
PIA: 550 °C: 20 h	421.3	491.5	11.01	8.78	73.0	20.60	25.04	35.28

area analysis after CERT are summarized in Table 2. While the as-irradiated fracture surface was 48.4% purely intergranular, annealing at 500 °C: 1 h and 550 °C:20 h, decreased the percentage of pure intergranular fracture to 34.9% and 20.6%, respectively. The degree of mixed mode fracture seemed to vary between the studied conditions while the about of transgranular fracture was significantly enhanced after annealing to ~30% of the fracture area for both PIA conditions. The percentage of ductile fracture did not seem effected by the annealing, and thus remained constant at 15–20% of the fracture surface.

Localized Deformation

The areal density of dislocation channels was measured via SEM following each stress/strain increment. Due to the highly-strained region that occurs during the advancement of a crack tip, measurements of the dislocation channel density were only taken for increments which displayed no significant crack growth. The measured dislocation channel densities following each measured strain increment are shown in Table 3. As multiple specimens exhibited regions of enhanced strain, where the eventual crack initiation later occurred, the measured channel densities are averaged over the region where crack initiation was later observed, rather than over the entire gage length.

A comparison of the dislocation channel density as a function of strain for the examined conditions: as-irradiated, 500 °C: 1 h, and 550 °C: 20 h, is shown in Fig. 5. It is observed that the as-irradiated and PIA: 500°C: 1 h conditions have similar dislocation channel densities, though there is a slight reduction for the 500 °C: 1 h condition. In comparison, the 550 °C: 20 h condition has a significantly reduced dislocation channel density regardless of the plastic strain. This result seems to suggest that the density of dislocation channels is primarily affected by the irradiation hardening, and hence the population of irradiation defects. This agrees with previous work by Jiao et al. [15], where the dislocation loop density was the primary contributor to the development of localized deformation.

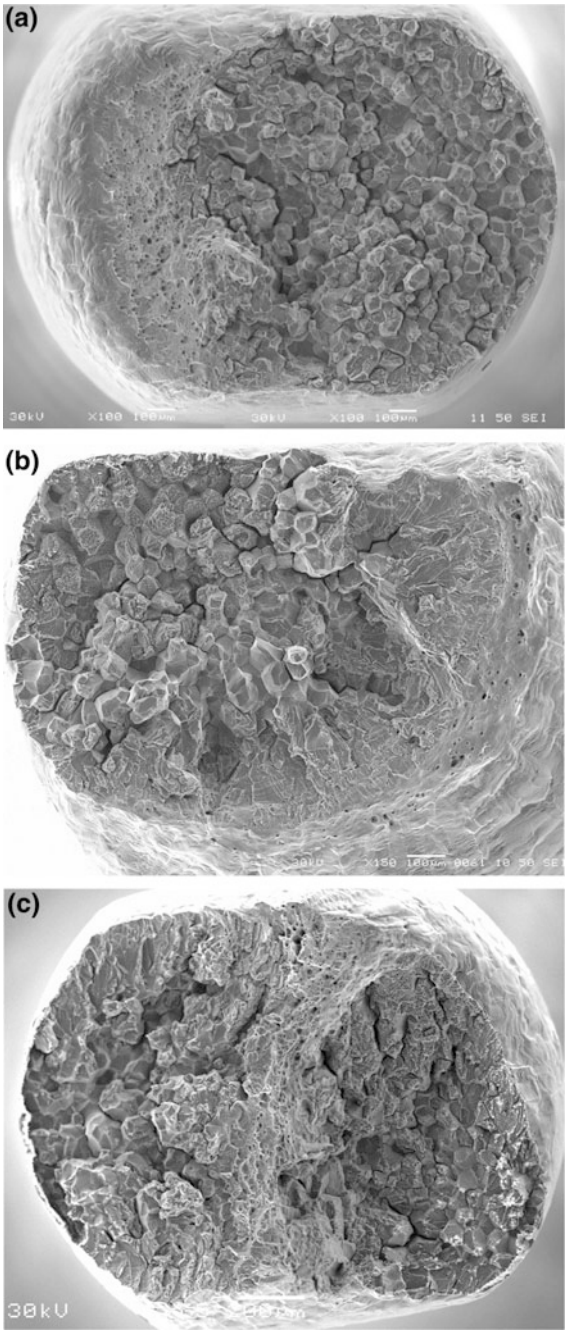

Fig. 3 Comparison of the final fracture surface of the CERT tensile specimens: **a** as-irradiated, **b** PIA: 500°C: 1 h and **c** PIA: 550 °C: 20 h. Overall, a clear reduction but not full removal of intergranular failure was observed with increasing PIA treatments. The 550 °C: 20 h fracture surface (c) displays two regions of IG cracking as independent cracks advanced from opposite side, before the specimen failed as a shear between each separate crack planes

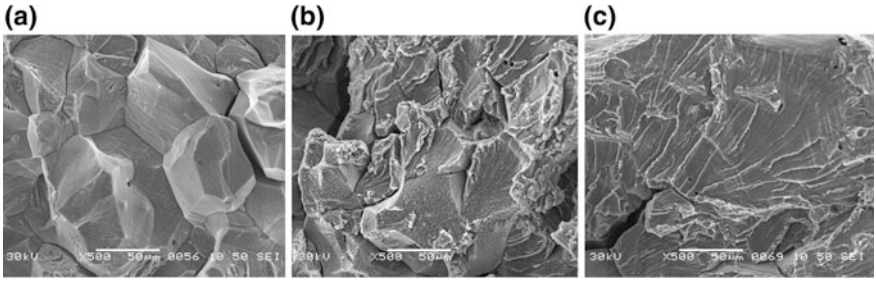

Fig. 4 Sample images of the three primary modes of failure that were observed during the crack growth of the as-irradiated and PIA specimens: **a** intergranular, **b** mixed intergranular-transgranular, **c** transgranular

Table 3 Dislocation channel densities of the examined strain increments and annealing conditions

Specimen	Plastic strain (%)	Channel density (#/mm^2)
As-Irradiated	0.00	121 ± 19
	0.77	1337 ± 169
500 °C: 1 h	0.00	3.5 ± 2.9
	1.00	1903 ± 246
	1.50	2462 ± 232
550°C: 20 h	0.00	8.8 ± 5.5
	1.00	132 ± 46
	2.00	174 ± 76
	3.00	499 ± 115
	5.00	585 ± 136

IASCC Susceptibility

The IASCC susceptibility of neutron-irradiated tensile specimens is often measured as the percentage of intergranular fracture on the fracture surface in literature. As such, for the sake of comparing to previous PIA results, this value will be utilized for comparing the relative change in IASCC susceptibility. It is worth noting that this method of characterizing IASCC susceptibility by %IG does list a higher susceptibility for the 550 °C: 20 h condition than expected. This tensile specimen initiated multiple cracks and two cracks appeared to grow from opposite sides of the tensile specimen slightly off plane from one another. After both cracks progressed through roughly 50% of the cross section, the specimen failed as a shear between the two separate crack planes. As such the final cross section displays two independent crack fronts, and thus a higher percentage of pure intergranular fracture.

Other features of the CERT test support the trend in %IG i.e. yield stress, elongation, and reduction in area. Following the annealing treatment at 500 °C: 1 h, there was not a large decrease in yield stress (<10%), however, significant changes were observed in the strain hardening behavior, leading to ~30% increase in

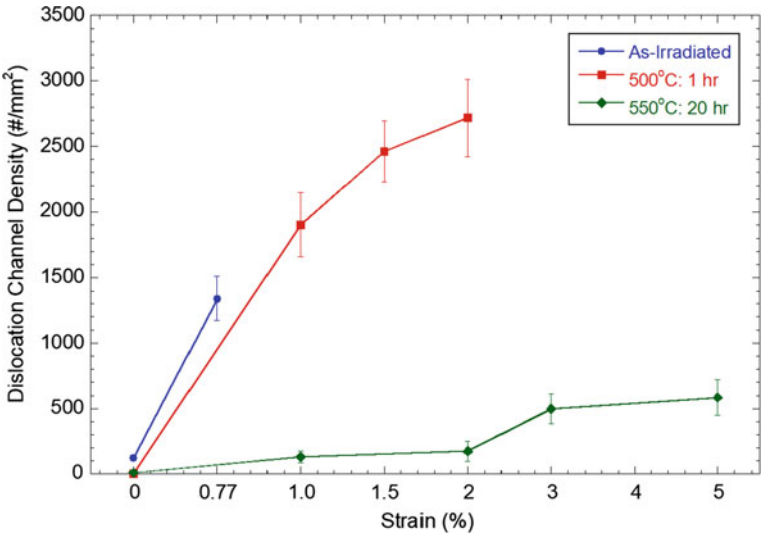

Fig. 5 Comparison of the dislocation channel densities with strain for the examined conditions: as-irradiated, 500 °C: 1 h, and 550 °C: 20 h. The density of dislocation channels was significantly decreased with increased annealing

elongation and 63% increase in the reduction of area as compared to the as-irradiated condition. Similarly, following annealing at 550 °C: 20 h a ~40% reduction in the yield stress, 450% increase in elongation, and 155% increase in the reduction of area was observed than compared to the as-irradiated condition. Clearly, these mechanical properties display a much larger change in the IASCC susceptibility than indicated by the intergranular fracture area.

Figure 6 compares the residual hardening and IASCC susceptibility of multiple irradiated 300-series stainless steels examined in literature following PIA treatments [5, 11, 19–21], the annealing times and temperatures are normalized by the iron diffusion distance as previously described. Due to both the low initial susceptibility of our examined material, and its apparent resistance to IASCC mitigation, the difference between our results versus the PIA literature on neutron-irradiated materials [5, 11, 19–21] is quite evident. The 500 °C: 1 h condition displayed ~70% of the as-irradiated susceptibility, while the 550 °C:20 h condition has ~40% of IASCC susceptibility remaining. The 500 °C: 1 h condition fits within the range of literature data, though it clearly lies near the upper limit. Both due to its relatively high %IG and the lack of more literature after high temperature annealing, the 550 °C:20 h clearly lies outside the literature trend as the other high temperature specimens have been fully mitigated of IASCC susceptibility. Despite previous literature suggesting that IASCC susceptibility decreases more rapidly following annealing treatments than the residual irradiation hardening, our data displays a similar decrease in both quantities following annealing up to 550 °C: 20 h.

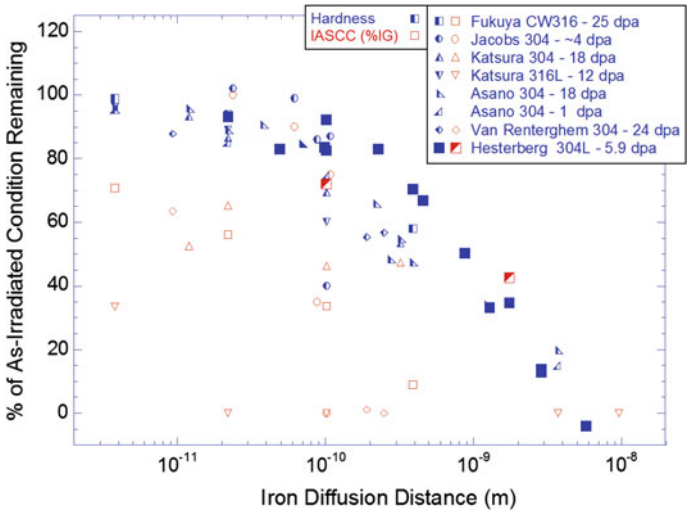

Fig. 6 Comparison of the residual hardening and IASCC susceptibility of multiple irradiated 300-series stainless steels examined in literature following PIA treatments [5, 11, 19–21], the annealing times and temperatures have been normalized by the iron diffusion distance as previously described

Conclusions

Annealing at 450 °C did not significantly reduce the irradiation hardening, while annealing at temperatures of 500 °C to 600 °C was observed to increasingly reduce the hardening with annealing temperature and time. Irradiation hardening was fully removed after a 600 °C: 20 h annealing.

Straining the as-irradiated condition resulted in a yield stress drop, followed by strain softening until final fracture at ~2% plastic strain; the final fracture had a moderate IASCC susceptibility with 48.4% of the final fracture surface displaying purely intergranular failure. Annealing at 500 °C: 1 h did not result in a significant reduction of irradiation hardening, but caused an increase in the ductility and strain hardening, and a reduction in the intergranular fracture to 34.9% of the final fracture area. Annealing at 550 °C: 20 h caused a significant reduction in irradiation hardening, as well as a further increase in the ductility and strain hardening capability of the material and reduction in the relative area of intergranular fracture to 20.6%.

The dislocation channel density was observed to decrease with additional annealing, roughly corresponding to the decrease in irradiation hardening. Overall, the irradiation hardening, dislocation channel densities, and IASCC susceptibility were all reduced following post-irradiation annealing up to 550 °C, but the IASCC susceptibility was not fully mitigated, in contrast to similar materials previously examined in literature.

Acknowledgements The authors would like to thank Alex Flick for assistance in operation of the CERT experiments at the Irradiated Materials Testing Laboratory and the University of Michigan. Gratitude is also extended to Maxim Gussev and the technical support staff at the Low Activity Materials Development and Analysis Laboratory at Oak Ridge National Laboratory for assistance with specimen handling and preparation. Support for this project was provided by funding from the Nuclear Energy University Programs (project number: DE-AC07-05ID14517) and under appointment to the Rickover Fellowship Program in Nuclear Engineering sponsored by Naval Reactors Division of the U.S. Department of Energy.

References

1. P. Scott, A review of irradiation assisted stress corrosion cracking, J. Nucl. Mater. **211**, 101–122 (1994). http://www.sciencedirect.com/science/article/pii/0022311594903603 (Accessed 31 July 2012)
2. K. Fukuya, Current understanding of radiation-induced degradation in light water reactor structural materials. J. Nucl. Sci. Technol. **50**, 213–254 (2013)
3. D. Damcott, T. Allen, G. Was, Dependence of radiation-induced segregation on dose, temperature and alloy composition in austenitic alloys. J. Nucl. Mater. **225**, 97–107 (1995). doi:10.1016/0022-3115(94)00690-3
4. J. Busby, G. Was, E. Kenik, Isolating the effect of radiation-induced segregation in irradiation-assisted stress corrosion cracking of austenitic stainless steels. J. Nucl. Mater. **302**, 20–40 (2002). doi:10.1016/S0022-3115(02)00719-5
5. K. Fukuya, M. Nakano, K. Fujii, T. Torimaru, Y. Kitsunai, Separation of Microstructural and Microchemical Effects in Irradiation Assisted Stress Corrosion Cracking using Post-irradiation Annealing. J. Nucl. Sci. Technol. **41**, 1218–1227 (2004). doi:10.1080/18811248.2004.9726351
6. T. Toyama, Y. Nozawa, W. Van Renterghem, Y. Matsukawa, M. Hatakeyama, Y. Nagai et al., Irradiation-induced precipitates in a neutron irradiated 304 stainless steel studied by three-dimensional atom probe. J. Nucl. Mater. **418**, 62–68 (2011). doi:10.1016/j.jnucmat.2011.07.027
7. Y. Chen, P. Chou, E. Marquis, Quantitative atom probe tomography characterization of microstructures in a proton irradiated 304 stainless steel. J. Nucl. Mater. **451**, 130–136 (2014). doi:10.1016/j.jnucmat.2014.03.034
8. G. Was, J. Busby, Role of irradiated microstructure and microchemistry in irradiation-assisted stress corrosion cracking. Philos. Mag. **85**, 443–465 (2005). doi:10.1080/02678370412331320224
9. G. Was, Y. Ashida, P. Andresen, Irradiation assisted stress corrosion cracking. Corros. Rev. **29**, 7–49 (2011). doi:10.1515/CORRREV.2011.020
10. Z. Jiao, Y. Chen, J. Hesterberg, E. Marquis, G. Was, Post-Irradiation Annealing in Mitigation of IASCC of Proton-Irradiated Stainless Steel, In: 16th Int. Conf. Environ. Degrad. (2013)
11. W. Van Renterghem, A. Al Mazouzi, S. Van Dyck, Influence of post irradiation annealing on the mechanical properties and defect structure of AISI 304 steel. J. Nucl. Mater. **413**, 95–102 (2011). doi:10.1016/j.jnucmat.2011.04.006
12. T. Onchi, K. Dohi, N. Soneda, M. Navas, M. Castaño, Mechanism of irradiation assisted stress corrosion crack initiation in thermally sensitized 304 stainless steel. J. Nucl. Mater. **340**, 219–236 (2005). doi:10.1016/j.jnucmat.2004.11.012
13. L. Fournier, M. Savoie, D. Delafosse, Influence of localized deformation on A-286 austenitic stainless steel stress corrosion cracking in PWR primary water. J. Nucl. Mater. **366**, 187–197 (2007). doi:10.1016/j.jnucmat.2007.01.001
14. Z. Jiao, G. Was, Impact of localized deformation on IASCC in austenitic stainless steels. J. Nucl. Mater. **408**, 246–256 (2011). doi:10.1016/j.jnucmat.2010.10.087

15. Z. Jiao, G. Was, The role of irradiated microstructure in the localized deformation of austenitic stainless steels. J. Nucl. Mater. **407**, 34–43 (2010). doi:10.1016/j.jnucmat.2010.07.006
16. M. McMurtrey, G. Was, L. Patrick, D. Farkas, Relationship between localized strain and irradiation assisted stress corrosion cracking in an austenitic alloy. Mater. Sci. Eng. A **528**, 3730–3740 (2011). doi:10.1016/j.msea.2011.01.073
17. K. Stephenson, G. Was, Relationship Between Dislocation Channeling and IASCC in Neutron Irradiated Stainless Steel, In: 16th Int. Conf. Environ. Degrad. (2013)
18. M. McMurtrey, G. Was, B. Cui, I. Robertson, L. Smith, D. Farkas, Strain localization at dislocation channel-grain boundary intersections in irradiated stainless steel. Int. J. Plast **56**, 219–231 (2014). doi:10.1016/j.ijplas.2014.01.001
19. R. Katsura, Y. Ishiyama, N. Yokota, T. Kato, K. Nakata, K. Fukuya, et al., Post-Irradiation Annealing Effect of Austenitic Stainless Steels on IASCC, Corrosion. (1998). http://www.onepetro.org/mslib/servlet/onepetropreview?id=NACE-98132 (Accessed 31 July 2012)
20. K. Asano, R. Katsura, M. Kodama, S. Nishimura, K. Fukuya, K. Nakata, Post-irradiation annealing effects on hardness and intergranular corrosion in type 304 stainless steel, in: 7th Int. Conf. Environ. Degrad. Mater. Nucl. Power Syst. 1033–1042 (1995)
21. A. Jacobs, G. Wozadlo, G. Gordon, Low-Temperature Annealing: A Process to Mitigate Irradiation-Assisted Stress Corrosion Cracking. Corrosion **51**, 731–737 (1995). doi:10.5006/1.3293549
22. N. Soneda, K. Nishida, P. Chou, Characterization of solute atom distribution in grain interior of neutron-irradiated 304L and 304 stainless steels (2011)

Irradiation Assisted Stress Corrosion Cracking Susceptibility of Alloy X-750 Exposed to BWR Environments

S. Teysseyre, J.H. Jackson, P.L. Andresen, P. Chou and B. Carter

Abstract The effect of irradiation on stress corrosion cracking susceptibility and fracture toughness of alloy X-750 has been investigated. The material has been irradiated at a target temperature of 288 °C in the Advanced Test Reactor at Idaho National Laboratory to a fluence of approximately 1.93×10^{20} n/cm^2 (E >1 meV). Stress corrosion cracking crack growth rates were determined in both unirradiated and irradiated materials in normal water chemistry and hydrogen water chemistry environments. Although the effect of irradiation on tensile properties and fracture toughness was observed, there was no significant effect of irradiation observed on the propagation rate of stress corrosion cracks.

Introduction

Nickel based alloy X-750 is used in commercial boiling water reactors (BWR) in locations where it is exposed to varying levels of neutron irradiation. To address the knowledge gaps associated with the effect of irradiation of X-750 on stress corrosion cracking susceptibility and fracture toughness, a Nuclear Science User Facilities (NSUF) project was designed in collaboration with the Electric Power Research Institute (EPRI) to irradiate and test X-750. This pilot project is being conducted in three phases. Phase I included the fabrication of specimens and

S. Teysseyre (✉) · J.H. Jackson
Idaho National Laboratory, Idaho Falls, ID, USA
e-mail: sebastien.teysseyre@inl.gov

P.L. Andresen
GE Global Research Center, New York, USA

P. Chou · B. Carter
Electric Power Research Institute, Palo Alto, USA

J.H. Jackson et al. (eds.), *Proceedings of the 18th International Conference on Environmental Degradation of Materials in Nuclear Power Systems – Water Reactors*, The Minerals, Metals & Materials Series, https://doi.org/10.1007/978-3-319-68454-3_75

established the baseline fracture toughness and crack growth rates (CGR) of unirradiated material. Phase II involved the design and fabrication of specimen holders and performance of a safety analysis of the experiment in preparation for irradiation of tensile and compact tension specimens utilizing the Loop 2A that is located in the Advanced Test Reactor (ATR) center flux trap. In the current and final Phase III, post irradiation examination including tensile testing, crack growth rate (CGR) testing, fracture toughness testing, and TEM analyses is being conducted.

Experimental Procedures

Material and Irradiation Conditions

Several sections of Inconel[1] alloy X-750 were provided to Idaho National Laboratory (INL) by General Electric Global Research Center (GE-GRC). These sections were removed by GE-GRC from a spare upper support bracket that was purchased from Southern Co. by EPRI. The material was delivered in the High Temperature Heat-Treatment (HTH) condition which consists of a 35% minimum reduction hot roll; solution anneal at 1107 °C for 1 h and rapid cool; aging at 704 °C for 20 h and air cool. The composition for this material is given in Table 1 and additional microstructural details may be found in [1].

The irradiation program included three target fluences (5.0×10^{19} n/cm^2, 2.0×10^{20} n/cm^2, and 1.0×10^{21} n/cm^2, E >1 meV) to be performed in Loop 2A of the ATR center flux trap at a target irradiation temperature of 288 °C. The control of the irradiation temperature was not optimum during the experiment which led to several of the specimens reaching a temperature of 340 °C in the first irradiation cycle and most specimens achieving a temperature of ~265 °C during the second irradiation cycle. The data presented in this paper only includes the specimens irradiated to the intermediate fluence (actual measured fluence was 1.93×10^{20} n/cm^2) which corresponds to a dose of 0.28 dpa using the correlation of 6.84×10^{20} n/cm^2 (E >1 meV) per dpa.

Fracture Toughness and IASCC Testing

Fracture toughness and IASCC testing were performed on 0.4T CT specimen with side grooves along the crack path. The stress corrosion cracking tests were performed in controlled water chemistry testing loops. The water was continuously

[1]Inconel is a registered trademark of Special Metals Incorporated.

Table 1 Composition of alloy X750 (wt%)

Al	C	Nb + Ta	Co	Cr	Cu	Fe	Mg	Ni	P	S	Si	Ti	Ta	Others
0.77	0.04	0.99	0.726	14.99	0.0151	7.8	0.197	70.8	<0.005	0.002	0.253	2.42	<0.01	0.97

refreshed with a flow rate of approximately 200 ml/min for a 4 l autoclave and the water chemistry was continuously monitored and controlled. Dissolved gas concentration was controlled by applying an overpressure of mixed gas at room temperature before the water flowed to the high pressure high temperature part of the loop. The ion content was controlled by flowing water through an ion exchange column to remove corrosion products and by adding a controlled amount of sulfate (SO_4) when desired for crack growth rate control. Typically the tests were performed in normal water chemistry (NWC) with 2 ppm dissolved oxygen in pure water and hydrogen water chemistry (HWC) with approximately 63 ppb dissolved hydrogen in pure water. In order to facilitate intergranular cracking engagement and to remain consistent with the methodology employed by Andresen [1] previously with this material, sulfate addition (up to 30 ppb) was occasionally used. Test control and monitoring was accomplished using the AT5 software [2, 3] provided by the GE Global Research Center (GE-GRC). This software utilizes reversing, direct current potential drop (DCPD) to measure crack growth during CGR and J-R tests.

The tests were generally performed in four steps: (1) initiation of a fatigue crack in environment for irradiated specimens or in air for unirradiated specimens, (2) transition from fatigue to stress corrosion cracking in the environment, (3) stress corrosion cracking in the various environments and conditions of interest, and (4) post-test fatigue.

Typically, a crack was initiated and extended by fatigue from the machined notch by a three step fatigue program. After several days in the environment to assure stabilization of the corrosion potential, crack extension was continued in the environment with a frequency that decreased from 0.1 to 0.001 Hz followed by introduction of a hold time of 9000s at Kmax to transition the transgranular fatigue crack to an intergranular stress corrosion crack. The experiment was then performed at a constant K. The series of steps followed to prepare a specimen for a SCC test under a constant K applied of 25 ksi$\sqrt{\text{in}}$ is presented in Table 2.

The targeted constant K was maintained while the specimen was held in NWC and HWC. At the end of the test, the specimen was ruptured by fatigue and the fracture surface was analysed using optical and scanning electron microscopy. From the fracture surface, the percentage difference (error) between the propagated crack as determined with the DCPD technique and the actual measured crack propagation was determined as (actual–DCPD)/actual $\times$ 100. This post-test computed error was used as a basis to compensate for the commonly observed discrepancy between DCPD measured crack lengths and the actual physically

Table 2 Example of crack conditioning steps for a constant K = 25 ksi$\sqrt{in}$ experiment

Step #	K_{max} (ksi$\sqrt{in}$)	Ratio K_{min}/K_{max}	Frequency (Hz)	Holding time (s)
1	23	0.2	1	0
2	24	0.4	1	0
3	25	0.6	1	0
4	25	0.6	0.1	0
5	25	0.6	0.01	0
6	25	0.6	0.001	0
7	25	0.6	0.001	9000
8	**Constant 25**	**1**		

measured crack length. Crack growth rates were corrected using this calculated difference.

Fracture toughness tests for unirradiated specimens were performed using a dual zone high temperature box furnace for temperature control. The crack tip temperature was monitored during testing for all specimens by welding a type K thermocouple spanning the crack path and approximately 5 mm ahead of the notch tip as well as an additional type K thermocouple welded to the top edge of the specimen to ensure negligible temperature gradient within the specimen. All tests were performed according to American Society for Testing of Materials (ASTM) Standard E1820-09 "Standard Test Method for Measurement of Fracture Toughness" [4]. Fracture toughness tests with irradiated specimens were performed using the same system used for IASCC testing but in air. Specimen temperature was controlled by controlling the temperature of the autoclave with a thermocouple located near, but not attached to, the specimen. Elongation and strain rate were determined by crosshead displacement and crack growth was measured by DCPD technique.

Tensile Testing

Tensile properties of the unirradiated specimens were performed according to the ASTM Standard E8 "Standard Test Methods for Tension Testing of Metallic Materials" [5]. The specimens were dogbone specimens with a cylindrical gage section. The nominal gage cross section was 0.25 in. and the gage length was 1 in. The specimens were machined with their tensile axis along the longitudinal (L), or rolling direction, to coincide with the L-T orientation of the CT specimens used in fracture testing and SCC testing. For characterization of tensile properties of the irradiated specimens, crosshead displacement was the method used for measuring elongation during remote tensile testing.

Results and Discussion

Tensile Tests

The results of the tensile tests performed at 288 °C are shown in Fig. 1 and summarized in Table 3. Testing performed with unirradiated specimens provided very similar results. Two tensile tests were performed and results were identical to those obtained by M. Morra [6]. Only one representative data set is shown in this table. The average 0.2% offset yield strength (σ_y) for alloy X-750 was 713.5 MPa, the average tensile strength (σ_{ult}) was 1079 MPa, and the average strain to failure (ε_f) was 31.1%. After irradiation, irradiation hardening and reduction of strain to failure were observed. The 0.2% offset yield strength increased to 972 MPa and

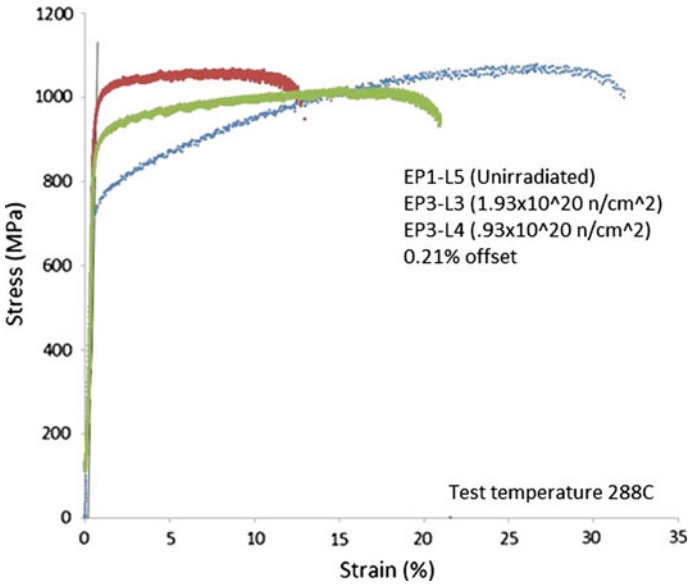

Fig. 1 Strain-stress curves obtained at 288 °C with unirradiated and irradiated X750

Table 3 Tensile properties at 288 °C as a function of dose

Specimen ID	Dose (dpa)	0.2% YS (Mpa)	UTS (Mpa)	Elongation (%)
EP1-L5	0	715	1082	30
EP1-L3	0.28	962	1067	13
EP1-L4	0.28	877	1023	21

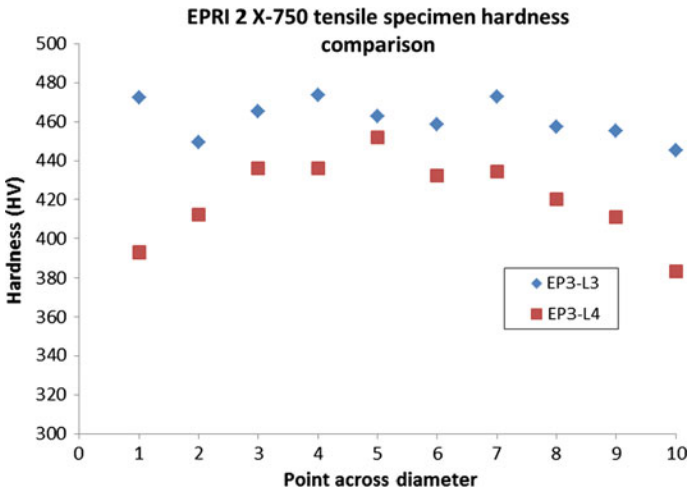

Fig. 2 Hardness measurements taken across the cross section of the tested specimens

strain to failure decrease to 13%. However, there was a noticeable difference between the two tests performed. Similarly, differences were observed in the hardness measurements taken across the specimen (cross sections of the tensile specimens' head) as shown in Fig. 2. Although the hardness is similar in the center of the specimens, the surface hardness of specimen EP1-L3 is about 470HV while it is only 390HV on specimen EP1-L4.

Fracture Toughness

For all tests performed with unirradiated specimens, J_Q was qualified as J_{IC}, a geometry independent fracture toughness because all specimens met the requirements for this qualification per ATSM E1820-09. The test performed with irradiated specimens did not meet the standard therefore J_Q is reported because the curvature of the final crack front exceeded the allowable deviation of the crack length value. The representative fracture toughness results for irradiated and unirradiated specimens are summarized in Table 3. Fracture toughness (J_{IC}, J_Q) generally decreased and tearing modulus which is an indication of residual toughness also decreased. Figure 3 shows an overlay plot of the full J-R curves for unirradiated and irradiated testing (Table 4).

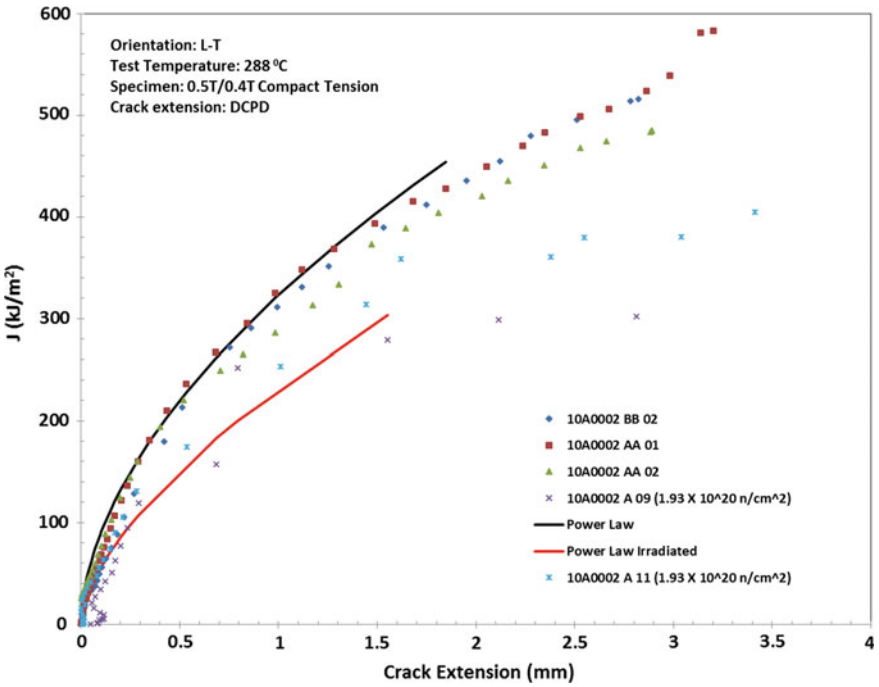

Fig. 3 Overlay plot showing effect of irradiation to 0.28 dpa on X-750

Table 4 Fracture toughness results at 288 °C

Dose (dpa)	J_{IC} or J_Q (kJ/m^2)	Tearing modulus
0	163.5	78
0	160.8	70
0	132.6	81
0.28	99.39	55
0.28	121	60

SCC and IASCC Testing

Unirradiated X-750 exhibited high crack growth rates that were consistent with the crack growth rates determined elsewhere (1). Figure 4 shows an example of the response of a specimen tested under a constant applied K = 27.5 Mpa$\sqrt{m}$ (25 ksi$\sqrt{in}$) in BWR water containing 10 ppb sulfate both in NWC and HWC. The CGR (1.5×10^{-6} mm/s) measured in NWC is reduced to 5.3×10^{-8} mm/s when the environment is changed to HWC. This behavior has been reproducible over the

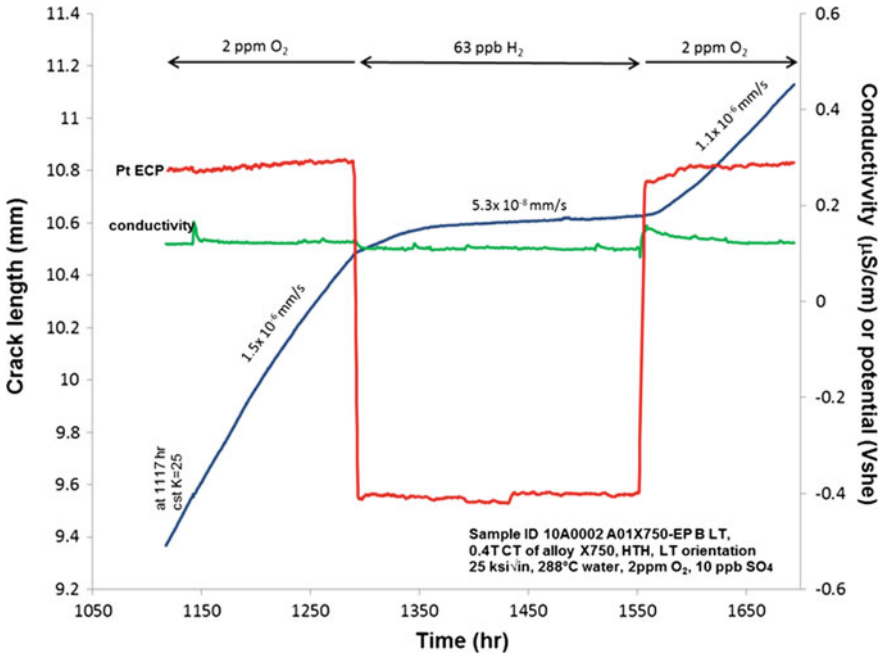

Fig. 4 Crack length versus time obtained with unirradiated X-750

various test performed within this project. The various CGRs measured in NWC range from 8.8×10^{-7} mm/s to 1.8×10^{-6} mm/s and from 1.3×10^{-8} mm/s to 1.3×10^{-7} mm/s in HWC, respectively. On average the change in crack growth rate via reduction of ECP is about a factor of 22.

Irradiated specimens exhibited similar crack growth rates to the unirradiated materials. Under a constant applied K of 27.5 Mpa$\sqrt{}$m (25 ksi$\sqrt{}$in), crack growth rates of 1.6×10^{-6} mm/s were measured in NWC. The crack growth rate decreased sharply to 5.9×10^{-8} mm/s when testing was performed in HWC. The ECP benefit obtained was observed under various applied constant K (Fig. 5).

The comparison of all crack growth rates generated in this study confirms that there is no significant change in CGR after irradiation to 1.9×10^{20} n/cm^2 (Fig. 6) and the K dependency remains the similar (Fig. 7).

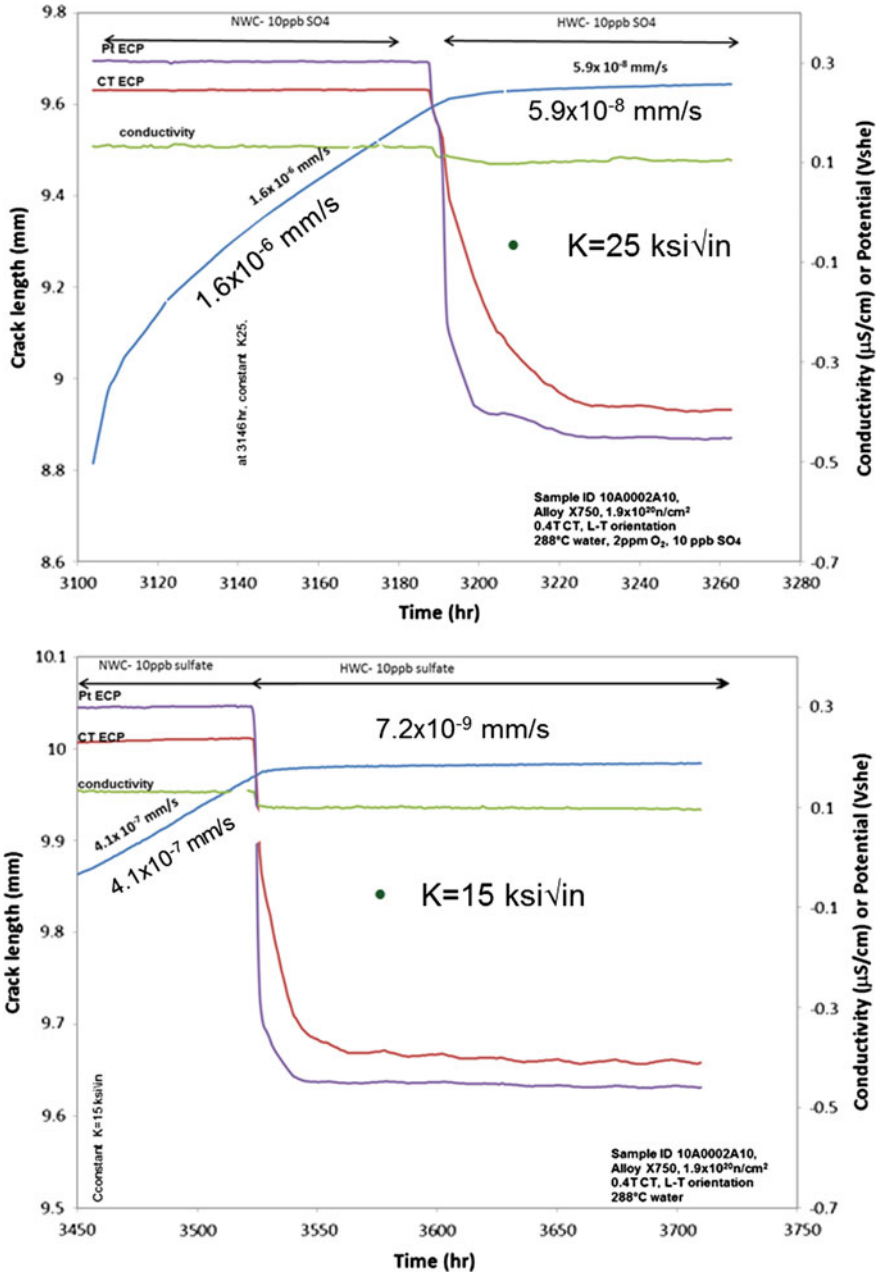

Fig. 5 Crack length versus time for irradiated X-750

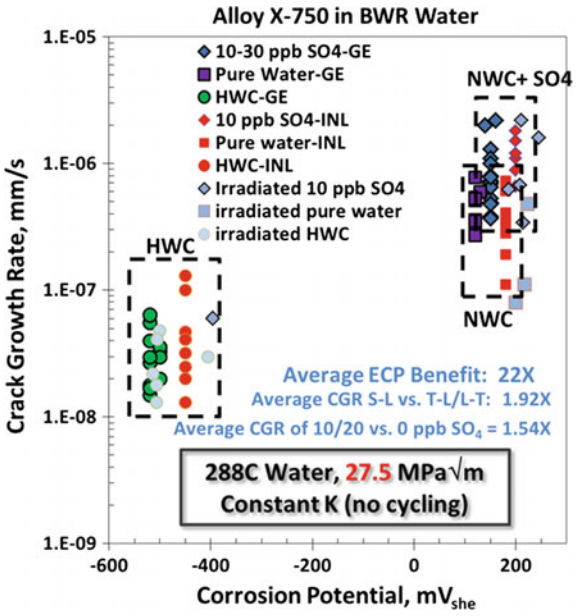

Fig. 6 Effect of corrosion potential on crack growth rate, GE data from (1)

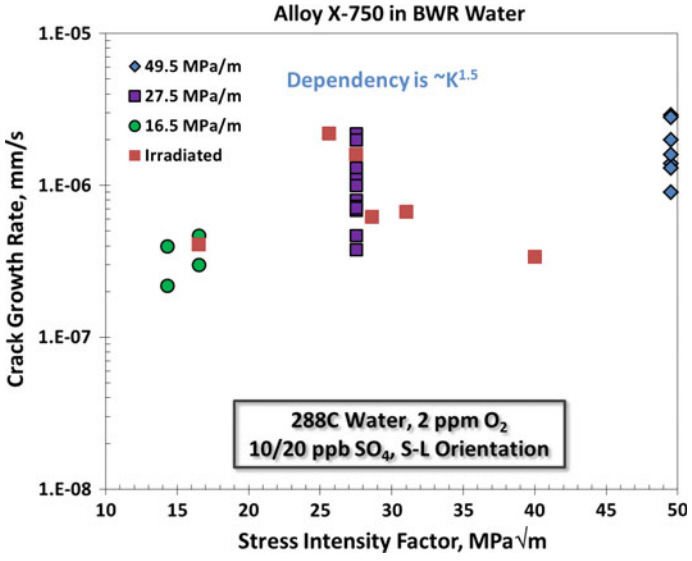

Fig. 7 K dependency for unirradiated and irradiated X-750 tested in BWR NWC water

Conclusions

X-750 specimens irradiated to the fluence of 1.93 x 10^{20} n/cm^2 did not exhibit an increased CGR compared to unirradiated X-750 (HTH) tested in both NWC and HWC conditions. The effectiveness of the HWC mitigation was retained after irradiation as the influence of corrosion potential remained unchanged. The K dependency did not appear affected by irradiation. However, irradiation hardening was observed along with a nominal reduction of fracture toughness to approximately 72% (average) of the unirradiated values.

Acknowledgements This work was supported under a Cooperative Research and Development Agreement between the Idaho National Laboratory (under the Nuclear Science User Facilities) and the Electric Power Research Institute.

References

1. P.L. Andresen, J. Flores-Preciado, M. Morra, R. Carter, Microstructure and SCC of Alloy X-750. in *15th International Conference on Environmental Degradation of Materials in Nuclear Power Systems-Water reactors*, 2011
2. P.L. Andresen, The Effects of Aqueous Impurities on Intergranular Stress Corrosion Cracking of Sensitized Type 304 Stainless Steel. Final Report NP3384 Contract T115-3, EPRI, 1983
3. P.L. Andresen, C.L. Briant, Environmentally assisted cracking of types 304L/316L/316NG stainless steel in 288 °C water. Corrosion **45**, 448–463 (1989)
4. Standard test method for measurement of fracture toughness. ASTM E 1820–09. (ASTM International, West Conshohocken, PA, 2009)
5. Standard Test Methods for Tension Testing of Metallic Materials. ASTM E 8–04. (ASTM International, West Conshohocken, PA, 2004
6. BWRVIP-240: BWR Vessels and Internals Project, Metallurgical Analyses and Macro and Microstructural Mapping of Alloy X-750 and Alloy XM-19 Plates. (EPRI, Palo Alto, CA, 2010). 1021003

Evaluation of Crack Growth Rates and Microstructures Near the Crack Tip of Neutron-Irradiated Austenitic Stainless Steels in Simulated BWR Environment

Yasuhiro Chimi, Shigeki Kasahara, Hitoshi Seto, Yuji Kitsunai, Masato Koshiishi and Yutaka Nishiyama

Abstract In order to understand irradiation-assisted stress corrosion cracking (IASCC) growth behavior, crack growth rates (CGRs), locally deformed microstructure, and oxide film properties for neutron-irradiated austenitic stainless steels (SSs) are investigated. Crack growth rate tests have been performed in simulated Boiling Water Reactor (BWR) water conditions (at ~288 °C) on a neutron-irradiated 316L SS at ~12–14 dpa. After the crack growth rate tests, the microstructures near the crack tip of the CT specimens are examined with scanning transmission electron microscope (FE-STEM). In comparison with a previous study at <~2 dpa, the irradiated 316L SS at ~12 dpa shows a less benefit of low electrochemical corrosion potential (ECP) conditions on CGR. An inactive crack tip immersed over 1000 h was filled with oxides, while almost no oxide film was observed near the active crack front in the low-ECP conditions. In addition, a high density of deformation twins and dislocations were found near the fracture surface of the crack front. It is considered that both localized deformation and oxidation are possible dominant factors for the SCC crack growth in highly irradiated SSs.

Keywords IASCC · Crack growth rate · Microstructure · Localized deformation · Oxide film · Austenitic stainless steel · Neutron irradiation · BWR

Introduction

Austenitic stainless steels (SSs) used in reactor core internals, such as core shroud of Boiling Water Reactors (BWRs), are exposed to neutron irradiations during plant operations. After long-term operations, the properties of the SSs can be changed, leading to hardening, embrittlement, segregation, and irradiation-assisted stress

Y. Chimi (✉) · S. Kasahara · Y. Nishiyama
Japan Atomic Energy Agency (JAEA), Ibaraki, Japan
e-mail: chimi.yasuhiro@jaea.go.jp

H. Seto · Y. Kitsunai · M. Koshiishi
Nippon Nuclear Fuel Development (NFD), Ibaraki, Japan

J.H. Jackson et al. (eds.), *Proceedings of the 18th International Conference on Environmental Degradation of Materials in Nuclear Power Systems – Water Reactors*, The Minerals, Metals & Materials Series, https://doi.org/10.1007/978-3-319-68454-3_76

corrosion cracking (IASCC). For irradiated SSs, crack growth rates (CGRs) increase with increasing neutron dose and show a tendency toward saturation at high doses [1, 2]. In addition, highly irradiated SSs have small or no beneficial effect of hydrogen water chemistry (HWC) or a low electrochemical corrosion potential (ECP) on CGRs [3–5].

When applying stress and strain on highly irradiated SSs, on the other hand, it is known that localized deformation is occurred due to introducing dislocation channels [1, 6]. The localized deformation is evaluated as the most important factor in IASCC by the correlation strength of localized deformation with IASCC [7]. Recently, we have observed the microstructures under visible slip steps on strained tensile specimens made of neutron-irradiated 316L SSs [8, 9]. The microstructures could change with neutron dose, i.e., the microstructure for low dose of ~1 dpa shows tangling of dislocations, while the microstructure for high dose of ~12 dpa consists of dislocation channels [8, 9]. Moreover, we have found that oxidation could be enhanced in the locally deformed areas around grain boundaries (GBs) with high local strain for highly irradiated SSs [8, 9]. From these results, it is considered that the CGRs could be related to microstructures of locally deformed areas and oxide films. However, there are few microstructural data near the crack tip of the CGR test specimen in neutron-irradiated SSs.

In the present study, to investigate the effects of locally deformed microstructure and oxide film properties on CGRs, crack growth rate tests are performed on irradiated specimens and microstructural observations are carried out near the crack tips.

Experimental Procedure

Specimens

Figure 1 shows the compact tension (CT) specimen with a thickness of B = 5.6 mm used for crack growth rate tests. The material was a 316L SS, identical to the heat used in a previous project [3]. The specimens were irradiated with neutrons at ~561 K (~288 °C) in the Japan Materials Testing Reactor (JMTR) up to a neutron dose of ~12–14 dpa. The chemical composition of the material is shown in Table 1.

Crack Growth Rate Tests

Crack growth rate tests of three specimens (ID: A410, A412, and A425) were carried out using a high-temperature and high-pressure water loop with an autoclave in a hot cell. The simulated BWR water conditions were employed as the

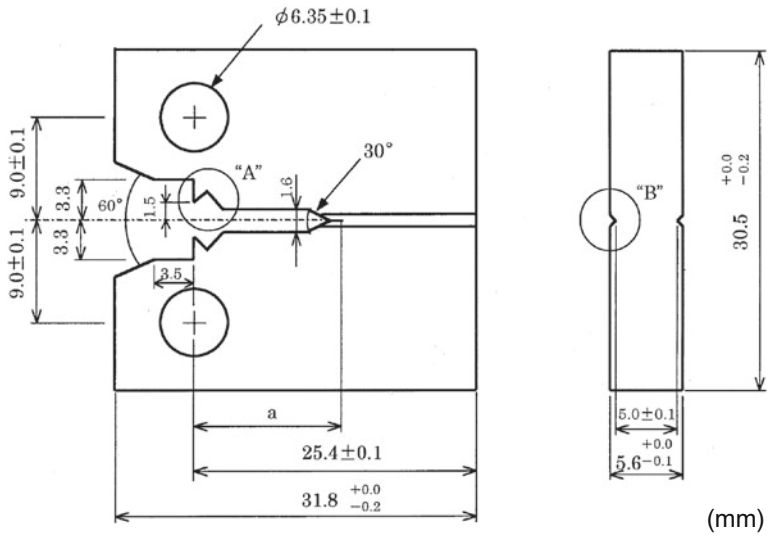

Fig. 1 Schematic of the CT specimen used in this study

Table 1 Chemical composition of the material used in the present study

Material	Chemical composition (wt.%)								
	C	Si	Mn	P	S	Ni	Cr	Mo	Co
316L SS	0.008	0.43	0.83	0.023	0.001	12.55	17.54	2.11	0.02

temperature at $\sim$561 K, the inlet conductivity of $\leq$0.1 μS/cm, the outlet conductivity of $\leq$0.2 μS/cm, under controlling inlet concentrations of dissolved oxygen (DO) or dissolved hydrogen (DH). The ECP of the specimens was monitored using internal Ag/AgCl reference electrodes in the autoclave. For a high-ECP condition, the DO was controlled to be 32 ppm. The DO was maintained at <10 ppb and DH was controlled to be 50 ppb for low-ECP conditions. Crack lengths of the CT specimens were monitored by reversing direct-current potential drop method (PDM) during the tests. In the beginning of the test, a pre-crack was introduced in situ in simulated BWR water by cyclic loading with loading ratio of 0.7 (R = 0.7) and frequencies of 0.01–0.0001 Hz. The maximum stress intensity factor (K) was the initial K for the following constant load test. The in situ pre-crack length was $\sim$0.4 mm, which exceeded the plastic zone due to fatigue pre-cracking in air. After the crack growth became stable, a constant load was applied to the specimen. The ranges of K were 10–20 MPa$\sqrt{m}$ for a low-K condition and 20–30 MPa$\sqrt{m}$ for a high-K condition. The concentrations of chemical species such as SO_4^{2-}, NO_3^-, and Cl^- in the sampling water were <5 ppb during the tests. After the crack growth rate tests, the CT specimens were broken open, and the fracture surfaces were observed by optical microscope and scanning electron microscope

(SEM). The PDM signals were corrected with the crack length measurements from the fracture surface. The CGRs were calculated based on the corrected PDM results.

Microstructural Observations

A schematic flow of the microstructural observation procedure for the CT specimens A412 and A425 after the crack growth rate tests is shown in Fig. 2. Each CT specimen was cut in half in the direction perpendicular to the crack plane before being broken open along the crack plane as shown in Fig. 2. The fracture surface of each broken-open CT halves was observed by optical microscope and SEM. The PDM signals were corrected with the crack length measured from the intergranular (IG) crack region in the specimen, assuming a homogeneous crack growth throughout the whole specimen thickness. A cross-sectional view in the direction perpendicular to the crack plane on the bifurcation of the crack was observed using optical microscope and SEM. The microstructural observations using scanning transmission electron microscope (FE-STEM) and energy dispersive X-ray spectroscopy (EDX) were performed on the specimens from the fracture surfaces and the cross-sections of the CT halves. The focus was on the deformed microstructures and oxide films near the crack tip. The EDX mapping was obtained by 256 × 200 pixels. STEM thin films were prepared from the fracture using a focused ion beam (FIB) technique.

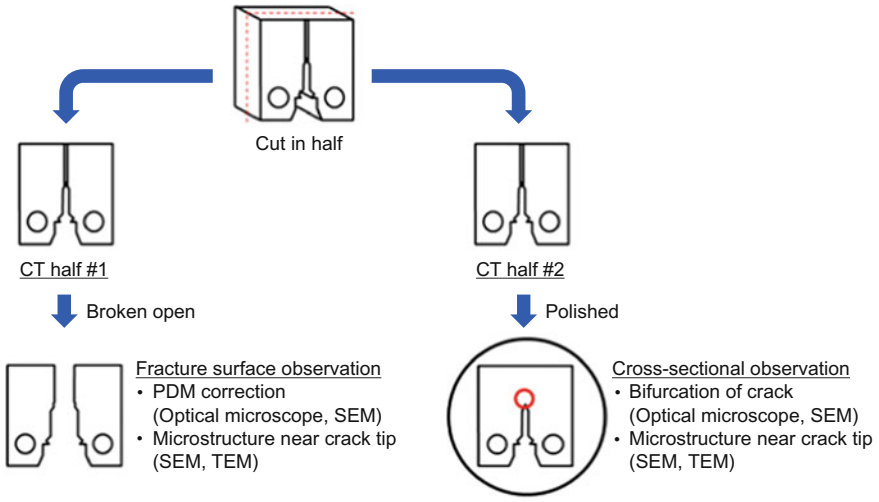

Fig. 2 Schematic flow of microstructural observation procedure for specimens A412 and A425

Results and Discussion

Crack Growth Rates

The specimens, test conditions, and results of the crack growth rate tests are summarized in Table 2. The time evolution of the crack lengths for the specimens A410, A412, and A425 is shown in Figs. 3, 4 and 5, respectively. The CGRs were calculated by linear fitting of the crack lengths in the time periods at constant load conditions shown in the figures. The values of ECP and K reported in Table 2 were average values of the test periods. For the specimens A410 and A412, the CGRs decreased by more than one order of magnitude when switching from a high-ECP condition to low-ECP conditions. For the specimen A425, on the other hand, the crack growth test was performed only in a low-ECP condition. The CGR was stable from the early stage of the test as shown in Fig. 5 and showed a similar value to the specimen A412. Thus, the CGR is almost independent of the history of water condition.

The fracture surface of the specimen A410 is shown in Fig. 6. An IG crack region can be seen during in situ pre-cracking in simulated BWR water after the fatigue pre-cracking in air. The specimens A412 and A425 were cut in half perpendicular to their crack planes. The photos of CT halves and the SEM images of the fracture surfaces are shown in Figs. 7 and 8 for the specimens A412 and A425, respectively. There are some larger oxides in the upper SEM images in Fig. 7b than the other regions in Figs. 7 and 8. It is consistent with the fact that the region around the upper SEM images in Fig. 7b has been experienced the high-ECP condition during the test.

The CGR data obtained in the present study is plotted against neutron dose in Fig. 9. In comparison, the CGR data from literature [3] are also shown in the figure. In the high-ECP condition, the CGRs are still increasing up to ~12 dpa for both the high- and low-K conditions. The beneficial effect of a low-ECP environment on

Table 2 Summary of the crack growth tests in the present study

Specimen ID	Neutron dose (E > 1 MeV)	Water condition*	ECP_{ave} (mV_{SHE})	K_{ave} ($MPa\sqrt{m}$)	CGR (m/s)
A410	11.9 dpa (7.14×10^{25} n/m^2)	High ECP	230	25.8	8.3×10^{-9}
		Low ECP 1	−60	30.0	7.8×10^{-10}
		Low ECP 2	−170	35.0	1.2×10^{-9}
A412	12.2 dpa (7.38×10^{25} n/m^2)	High ECP	230	13.4	6.5×10^{-9}
		Low ECP 1	−530	14.8	7.2×10^{-11}
		Low ECP 2	−630	15.0	7.1×10^{-11}
A425	13.7 dpa (8.23×10^{25} n/m^2)	Low ECP 1	−620	16.8	1.3×10^{-10}

*High ECP (32 ppm DO), Low ECP 1 (<10 ppb DO), and Low ECP 2 (<10 ppb DO and 50 ppb DH)

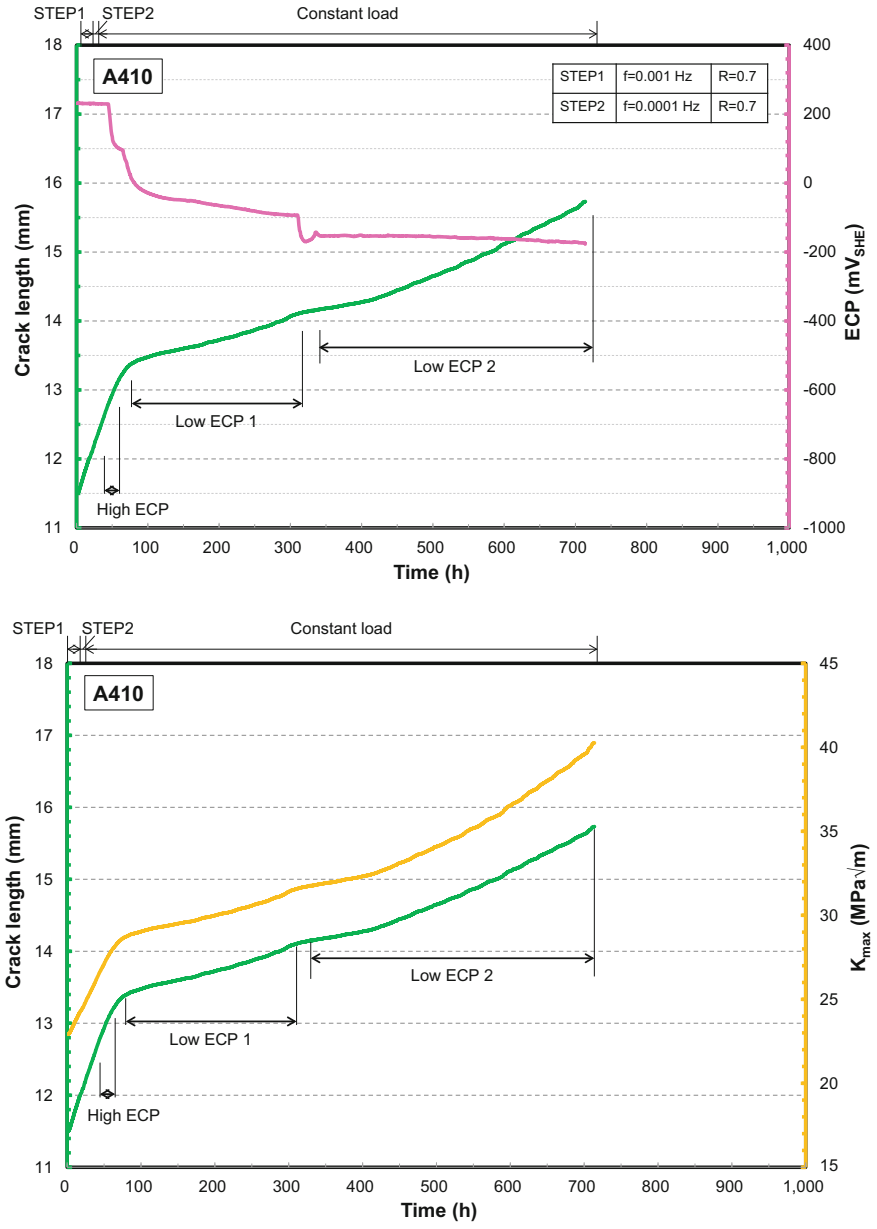

Fig. 3 Crack growth data for specimen A410

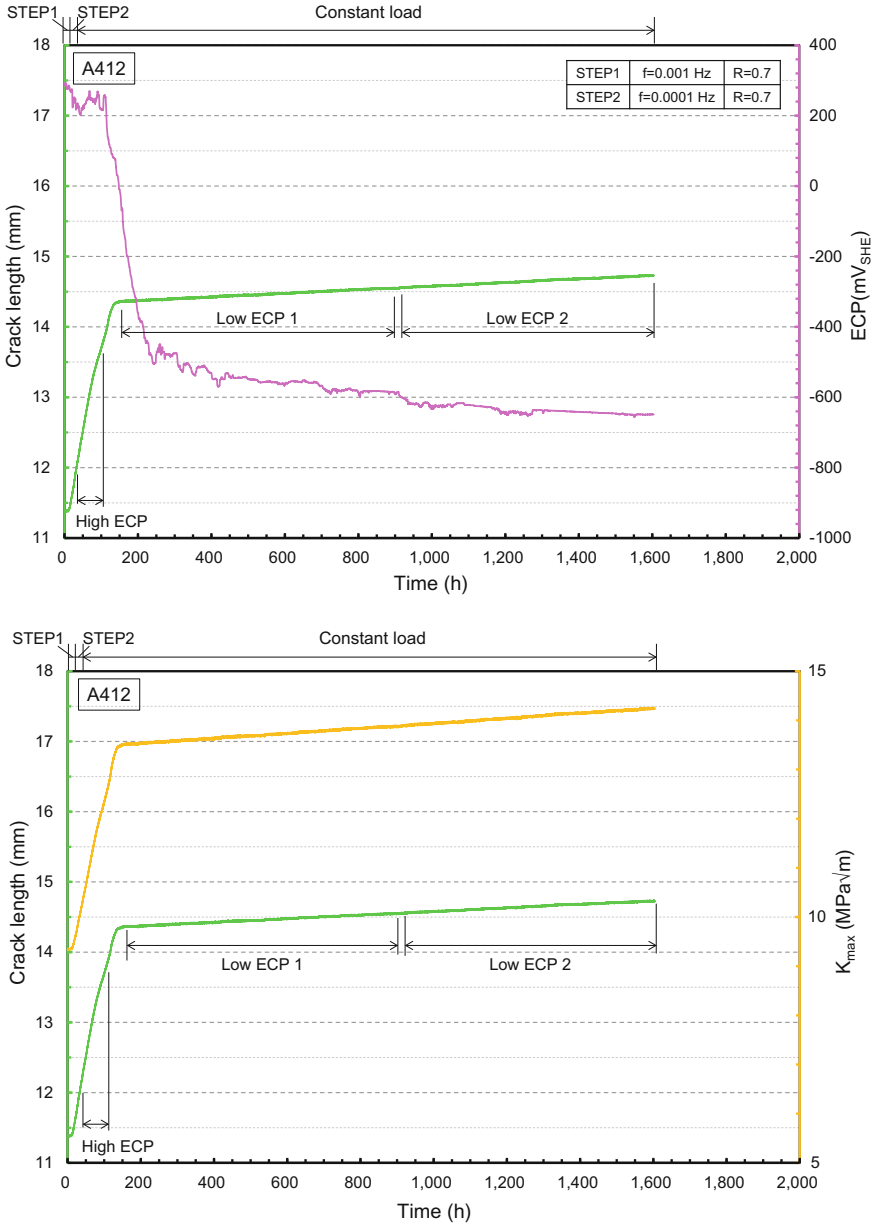

Fig. 4 Crack growth data for specimen A412

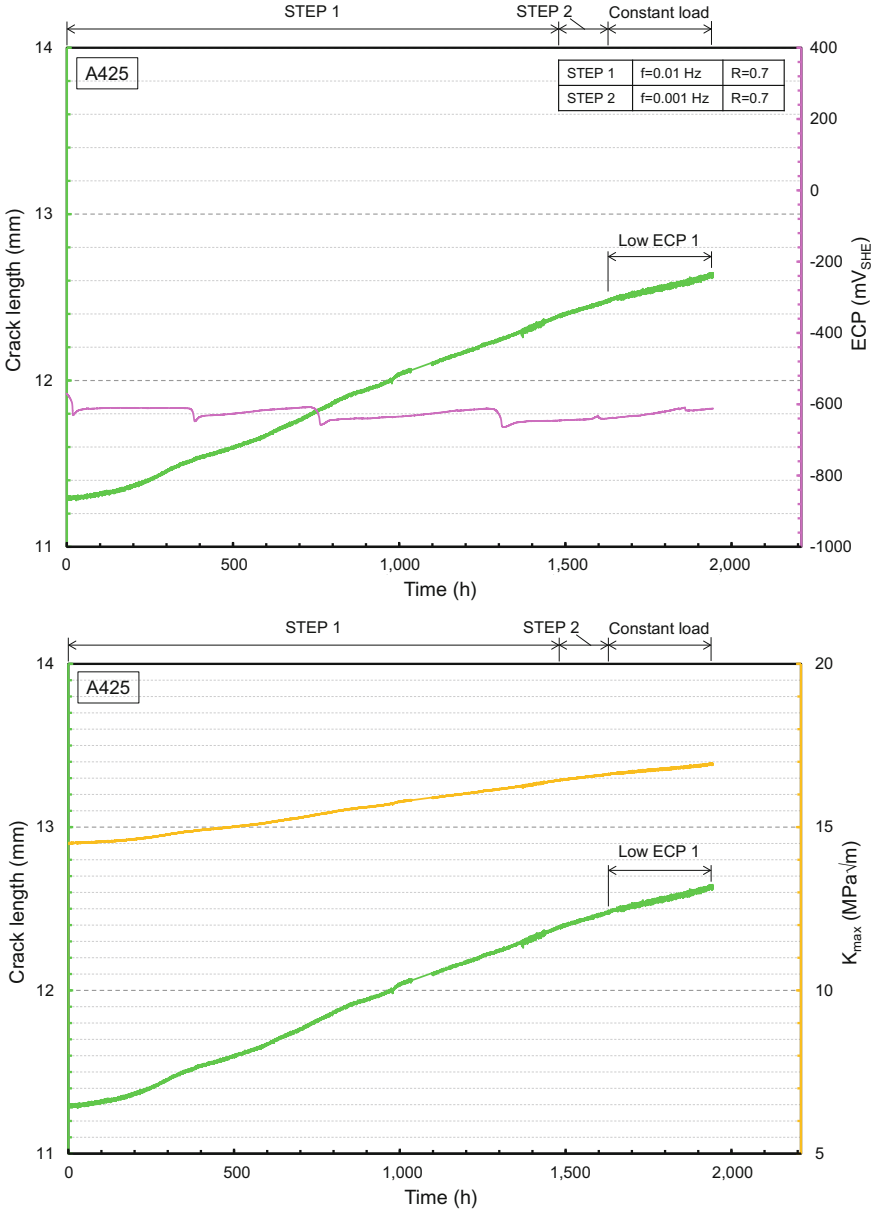

Fig. 5 Crack growth data for specimen A425

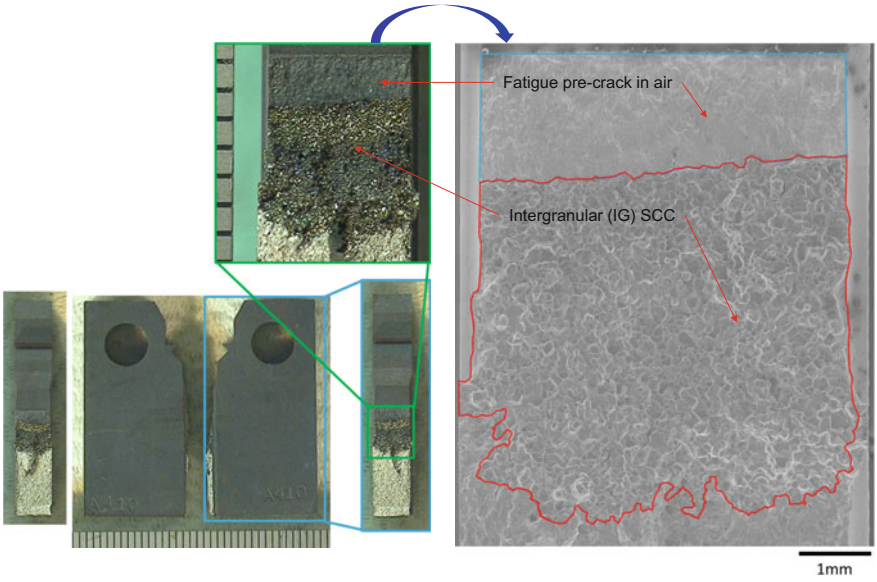

Fig. 6 Fracture surface of specimen A410

CGR is prone to be smaller for higher neutron dose and for higher K condition. In the low-ECP conditions, it is possible that the contribution of an environmental factor to the CGR becomes smaller.

Microstructures

Figure 10 shows FE-STEM images of a region near the crack tip (crack front), which is shown as a red box in the lower-right SEM image in Fig. 7b, in a broken-open CT half of the specimen A412. There are dislocations near the fracture surface. It is considered that the dislocations could be introduced by plastic deformation in the plastic zone in the vicinity of the crack front. A number of deformation twin bands were observed about ~3 μm below the fracture surface. No dislocation channel or surface step was observed in this region. This observation was different from what observed in a previous study where defect-free channels were found in a strained tensile specimen at ~12 dpa [8, 9]. The difference in the microstructures between the CT fracture surface and the surface of the strained tensile specimen might be attributed to the difference in the loading direction towards the surface.

A cross-sectional view of the crack plane of the specimen A412 is shown in Fig. 11. There are one or two continuous main cracks with many branches. A crack tip in the middle part of the cracks (i.e., an inactive crack tip), which experienced

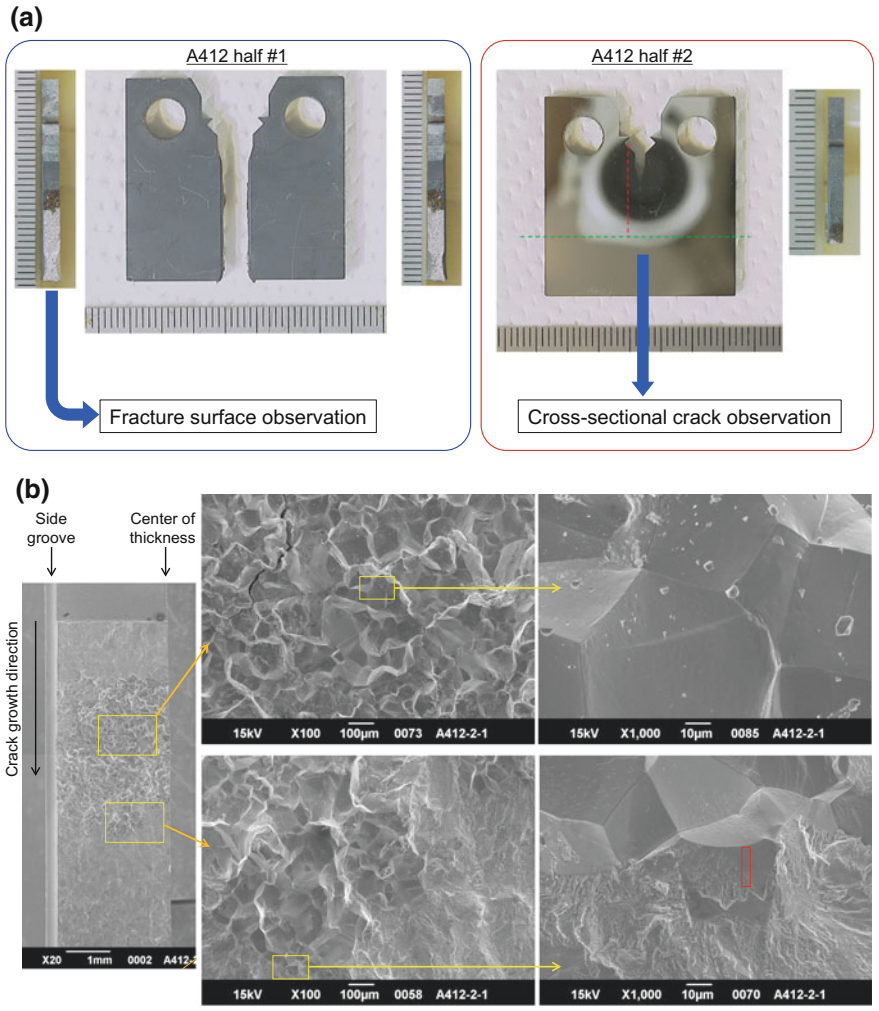

Fig. 7 Photos of CT halves and SEM images of fracture surface for specimen A412. A red box in lower-right SEM image indicates a region near crack front observed by FE-STEM (see Fig. 10). **a** Photos of CT halves **b** SEM images of fracture surface

both the high- and low-ECP conditions over 1000 h, was observed by FE-STEM. Figure 12 shows the FE-STEM image and the EDX mapping around the crack tip. The crack tip is filled with oxides and there are two twins and a Ni-rich region ahead of the crack tip. To analyze the crack tip in detail, the STEM-EDX line profile was measured near the crack tip along the GB as shown in Fig. 13. A Ni-rich

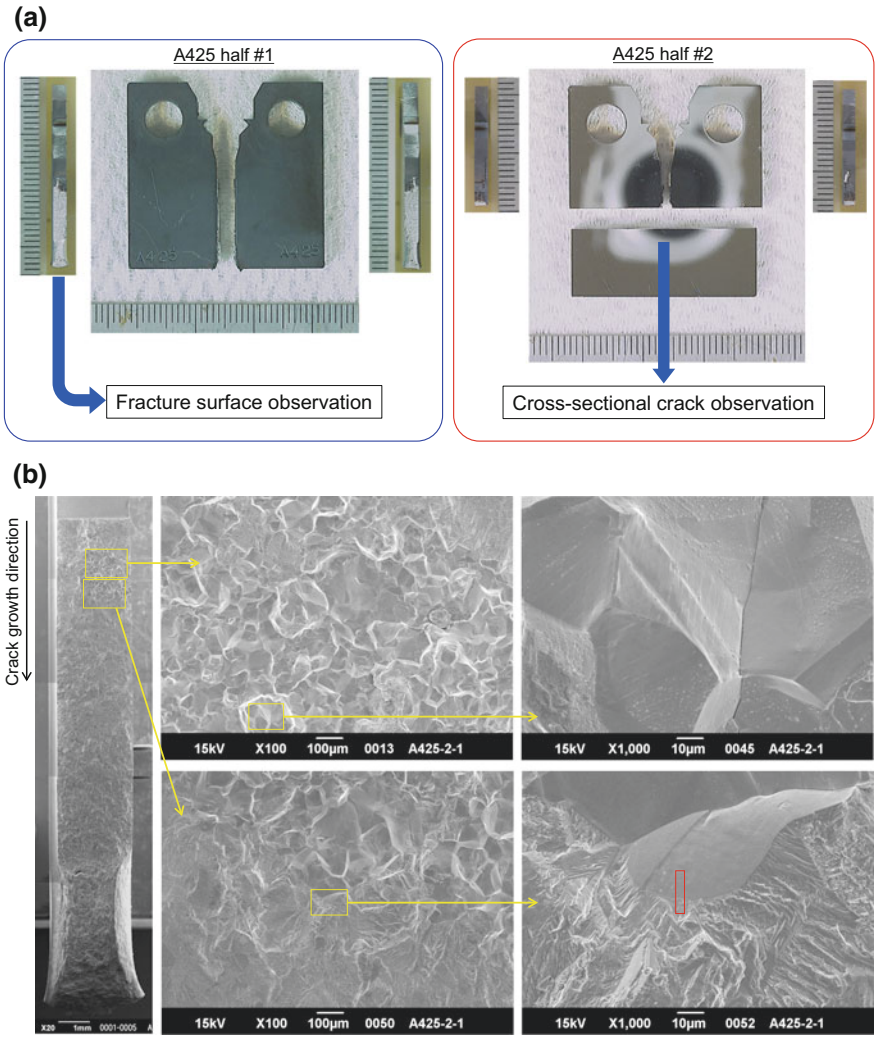

Fig. 8 Photos of CT halves and SEM images of fracture surface for specimen A425. A red box in lower-right SEM image indicates a region near crack front observed by FE-STEM (see Fig. 14). **a** Photos of CT halves **b** SEM images of fracture surface

metal region can be seen ahead of the crack tip. From the diffraction patterns also shown in the figure, the oxides inside the crack are found to be Cr-rich spinel oxides, which is similar to that observed in inactive SCC cracks in actual nuclear power plants (NPPs), [10]. A Ni enriched zone ahead of crack tip is suggested to be a signature of a slow growing crack in high temperature deaerated water environment [11]. The present result is consistent with the analyses of inactive SCC cracks in actual NPPs and a slow growing crack.

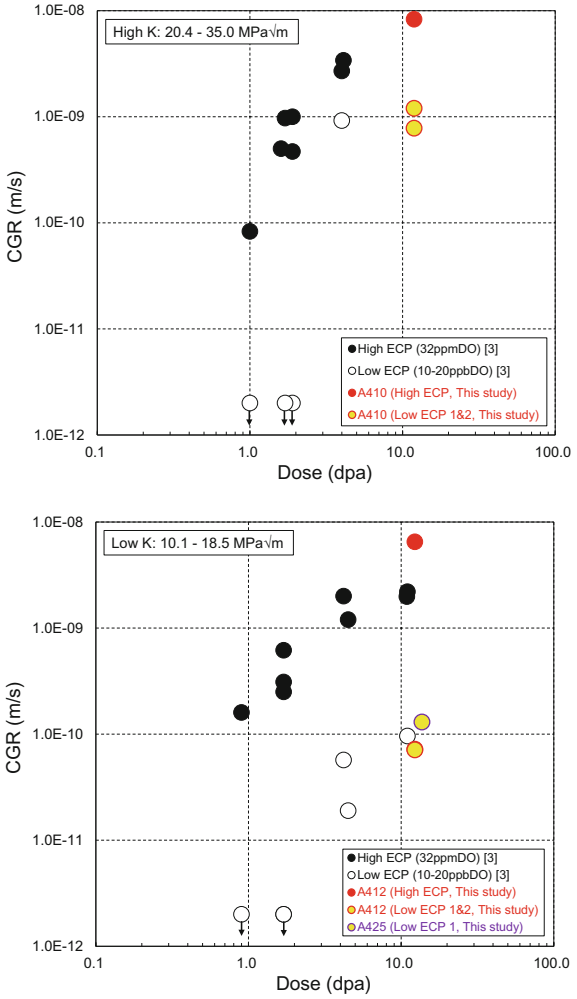

Fig. 9 CGR data plotted against neutron dose

FE-STEM images of a region near crack front, which is shown as a red box in the lower-right SEM image in Fig. 8b, in a broken-open CT half of the specimen A425 are shown in Fig. 14. The EDX line profile around the crack front is also shown in the figure. It is found that there are very thin or almost no oxide films and no Ni-rich metal region ahead of the crack front. This result is different from the observations of the inactive crack tip (Fig. 13). It is considered that the reason for the difference is the water chemistry and the immersion time. Moreover, there are no deformation twin bands near the crack front. This result is different from the introduction of a number of deformation twins near the crack front in the specimen A412. It is noted here that the discontinuous dislocation channels across the grain boundary can be introduced [12]. Therefore, both types of grains with and without

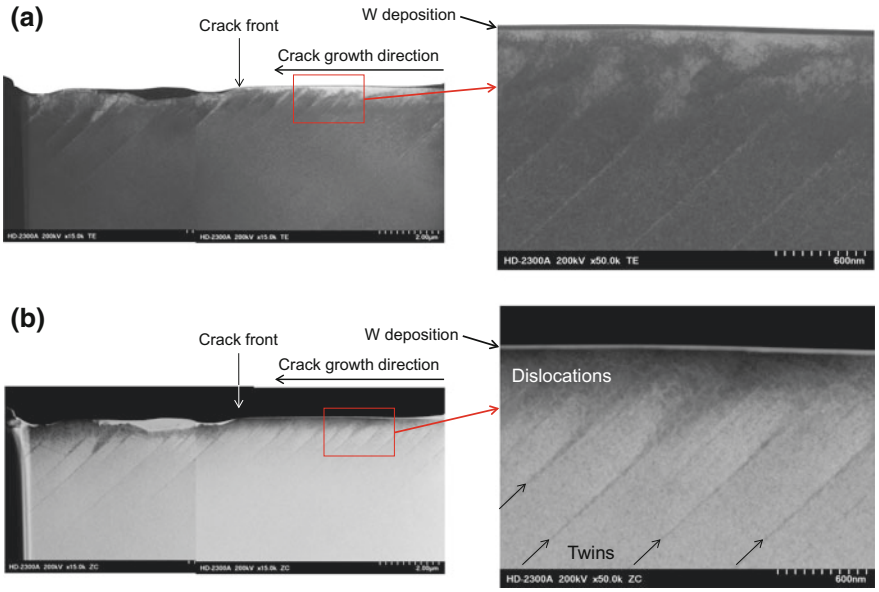

Fig. 10 FE-STEM images of a region near crack front in specimen A412. **a** Transmission electron (TE) images **b** Z-contrast (ZC) images

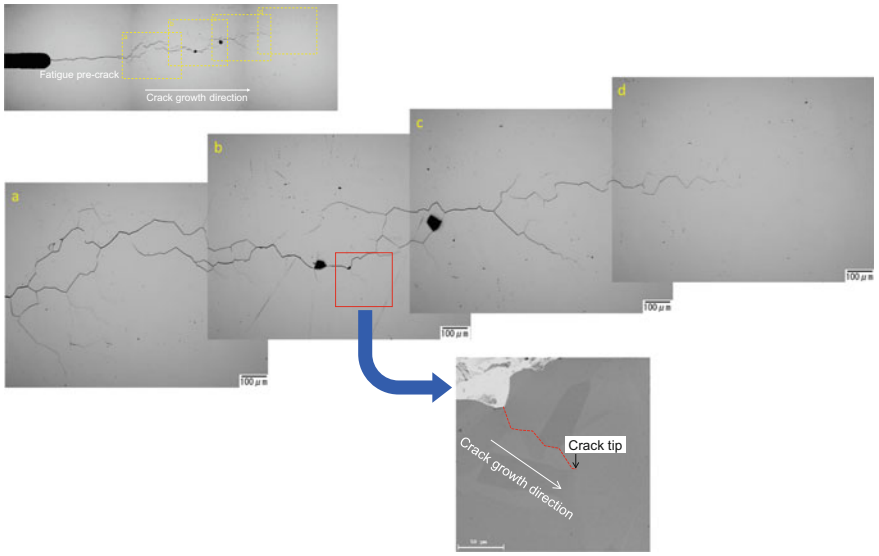

Fig. 11 Cross-sectional view of cracks in specimen A412

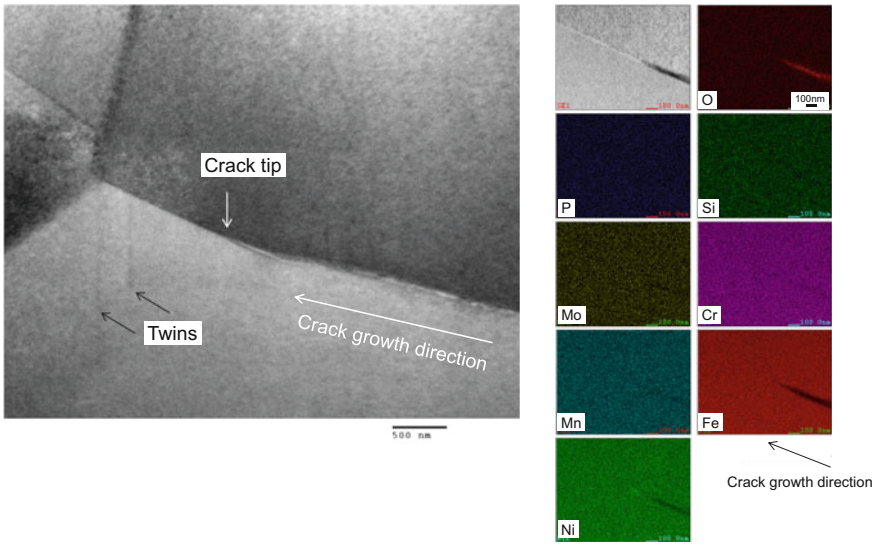

Fig. 12 FE-STEM image and EDX mapping around a crack tip in specimen A412

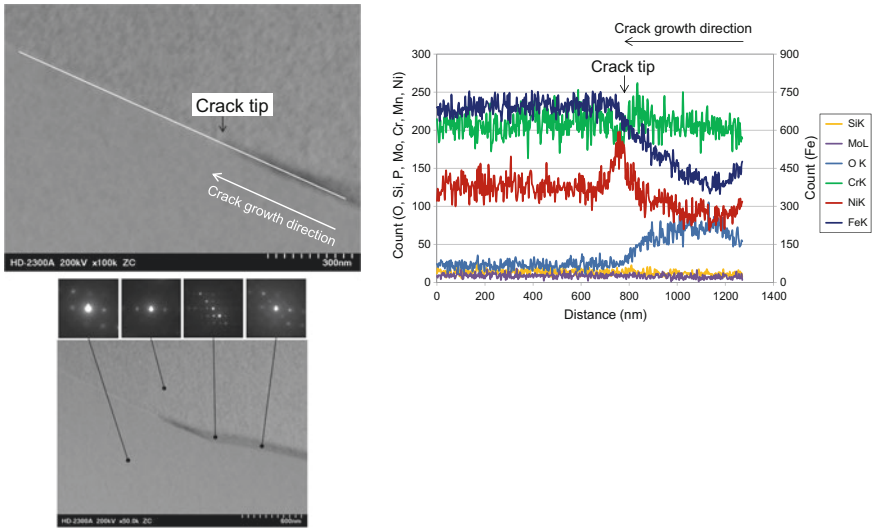

Fig. 13 STEM-EDX line profile near a crack tip along a GB in specimen A412

deformation twins can be found along the IG crack. The present results indicate that both localized deformation and oxidation are possible dominant factors for the SCC crack growth in highly irradiated SSs.

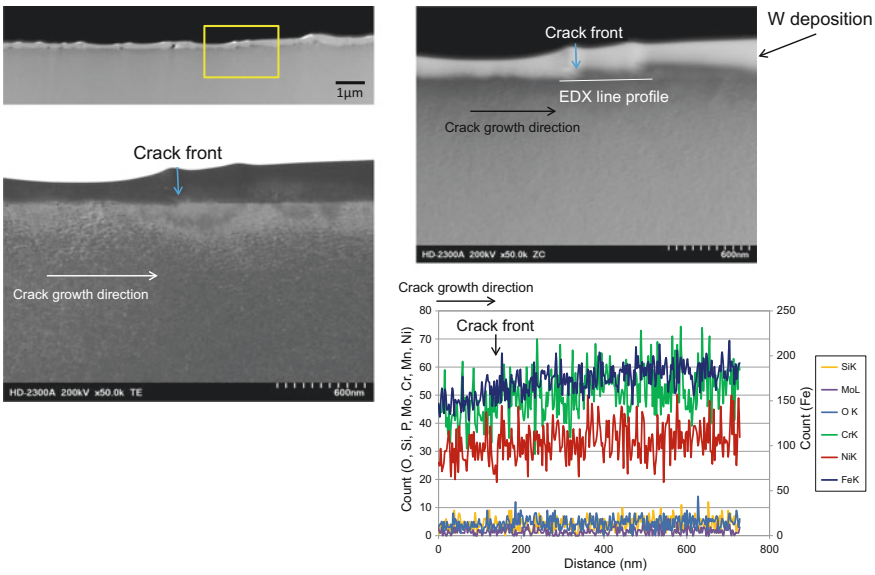

Fig. 14 FE-STEM images of a region near crack front in specimen A425

Summary

In order to understand IASCC growth behavior, on the effect of localized deformation and oxidation on CGRs was investigated. The CGR data were obtained from crack growth rate tests on neutron-irradiated 316L SSs in simulated BWR environments, and the microstructure around crack tip was observed with FE-STEM. The benefit of a low-ECP condition on CGR was small for high dose specimens and at high Ks. From the microstructural observations, the inactive crack tip immersed over 1000 h was filled with oxides, while almost no oxide film was observed near the active crack front in the low-ECP conditions. In addition, a high density of deformation twins and dislocations were found near the fracture surface of the crack front. It is considered that both localized deformation and oxidation are possible dominant factors for the SCC crack growth in highly irradiated SSs.

Acknowledgements A part of this study was conducted under a contract with the Nuclear Regulation Authority of Japan.

References

1. K. Fukuya, Current understanding of radiation-induced degradation in light water reactor structural materials. J. Nucl. Sci. Technol. **50**(3), 213–254 (2013)
2. S. Ooki et al., Study on SCC growth behavior of BWR core shroud, in *Proc. 12th Int. Conf. on Environmental Degradation of Materials in Nuclear System—Water Reactors*, TMS, 2005, pp. 365–376
3. K. Takakura et al., Crack growth behavior of neutron irradiated L-grade austenitic stainless steels in simulated BWR conditions, in *Proc. 14th Int. Conf. on Environmental Degradation of Materials in Nuclear Power Systems*, ANS, 2009, pp. 1192–1203
4. A. Jenssen et al., Crack growth behavior of irradiated type 304L stainless steel in simulated BWR environment, in *Proc. 11th Int. Conf. on Environmental Degradation of Materials in Nuclear Systems*, ANS, 2003, pp. 1015–1026
5. T.M. Karlsen, P. Bennet, N.W. Høgberg, In-core crack growth rate studies on irradiated austenitic stainless steels in BWR and PWR conditions in the Halden reactor, in *Proc. 12th Int. Conf. on Environmental Degradation of Materials in Nuclear System—Water Reactors*, TMS, 2005, pp. 337–348
6. G.S. Was, P.L. Andresen, Stress corrosion cracking behavior of alloys in aggressive nuclear reactor core environments. Corrosion **63**(1), 19–45 (2007)
7. Z. Jiao, G.S. Was, Impact of localized deformation on IASCC in austenitic stainless steels. J. Nucl. Mater. **408**, 246–256 (2011)
8. Y. Chimi et al., Effects of locally deformed structure on oxide film properties in neutron-irradiated austenitic stainless steel, in *Proc. 17th Int. Conf. on Environmental Degradation of Materials in Nuclear Power Systems—Water Reactors*, CNS, 2015
9. Y. Chimi et al., Correlation between locally deformed structure and oxide film properties in austenitic stainless steel irradiated with neutrons. J. Nucl. Mater. **475**, 71–80 (2016)
10. L. Thomas et al., Crack-tip characteristics in BWR service components, in *Proc. 13th Int. Conf. on Environmental Degradation of Materials in Nuclear Power Systems—Water Reactors*, CNS, 2007
11. E. West, D. Morton, N. Lewis, Oxide film characterization along crack paths in stainless steel in aerated and deaerated water environments, in *Proc. 15th Int. Conf. on Environmental Degradation of Materials in Nuclear Power Systems—Water Reactors*, TMS, 2011, pp. 389–404
12. M.D. McMurtrey, G.S. Was, Relation between irradiation assisted stress corrosion cracking and discontinuous slip at grain boundaries, in *Proc. 17th Int. Conf. on Environmental Degradation of Materials in Nuclear Power Systems—Water Reactors*, CNS, 2015

Effect of Specimen Size on the Crack Growth Rate Behavior of Irradiated Type 304 Stainless Steel

A. Jenssen, P. Chou and C. Tobpasi

Abstract Crack growth rate (CGR) testing in BWR normal water chemistry was performed on compact tension (CT) specimens of two different sizes (B = 8 mm and B = 19 mm), machined from a Type 304 SS core shroud at a dose of ~1 dpa. The objectives were to study the effect of specimen size on the CGR, and to determine the K validity limit for a CT specimen dimension used in previous studies. The results show that for materials with significant strain hardening capacity remaining, there is no effect of specimen size on the CGR when testing is conducted at stress intensity factors valid according to ASTM E399 using the flow strength. For materials at higher dose in which the strain hardening capacity is lost or greatly reduced, a different K validity criterion might be applicable.

Keywords Stress corrosion cracking · Crack growth rate · Specimen size · K validity · Irradiated stainless steel

Introduction

Cracks in thick-section plant components, such as the core shroud in a BWR, are mainly under a plane strain condition. To generate relevant crack growth rate data in the laboratory, specimens where most of the crack front is under plane strain should be used. For similitude, the conditions during laboratory testing should be such that the results are directly transferrable to actual plant components. The K validity criterion in ASTM E399 [1], which is based on the specimen dimensions and the mechanical properties of the material, is designed to ensure mainly plane strain conditions at the crack tip. Consequently, it seems appropriate to also apply it to stress corrosion cracking (SCC) tests. However, in stress corrosion crack growth

A. Jenssen (✉)
Studsvik Nuclear AB, 611 82 Nyköping, Sweden
e-mail: anders.jenssen@studsvik.se

P. Chou · C. Tobpasi
Electric Power Research Institute, 3420 Hillview Ave, Palo Alto, CA 94304, USA

J.H. Jackson et al. (eds.), *Proceedings of the 18th International Conference on Environmental Degradation of Materials in Nuclear Power Systems – Water Reactors*, The Minerals, Metals & Materials Series, https://doi.org/10.1007/978-3-319-68454-3_77

rate (CGR) tests on austenitic stainless steels with high yield strength, either from cold work or radiation hardening, very high CGRs have sometimes been observed as K is increased, which indicates that the K validity criterion defined in ASTM E399 can be non-conservative, and thus not applicable to irradiated stainless steel [2]. An example of what has been interpreted as K invalidity in irradiated Type 316 stainless steel is presented in Fig. 1 [3].

Figure 1 shows the maximum allowed stress intensity factors according to two alternate K validity criteria, where the irradiation induced increase in yield strength has been reduced to account for deformation softening effects observed in irradiated stainless steel [2]. The allowed K according to ASTM E399 (curve not shown in Fig. 1) was above 50 MPa$\sqrt{m}$ at the stage of the test shown in Fig. 1. Also included in the figure are the K at the crack tip and the crack length. This figure shows that accelerated crack growth was observed just before K exceeded the alternate criterion according to ASTM E399 based on ΔYS/3, where ΔYS is the difference between the irradiated and unirradiated YS. The CGR measured after the onset of accelerated crack growth was inconsistent with the CGRs measured at somewhat lower K earlier in the test; a CGR about 100X faster than the one observed before the onset of accelerated growth was observed. This response is believed to be a result of K invalidity [2, 3].

The mechanical properties of highly irradiated stainless steels are characterized by localized deformation (channeling) and strain softening effects [2, 3], and this has been proposed as an explanation for K invalidity. For this reason, the alternate criteria shown in Fig. 1 have been proposed, where the K validity is determined by

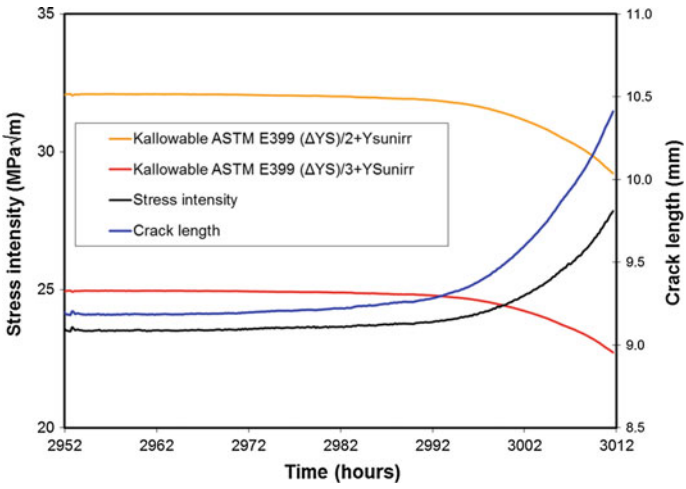

Fig. 1 Stress intensity (and crack length) during testing of a Type 316 SS at 7.8 dpa in simulated PWR primary water compared to the maximum allowed K according to two alternate K validity criteria. In the alternate K validity criteria, the irradiation induced increase in yield strength ($\Delta YS = YS_{irr} - YS_{unirr}$) has been reduced to account for deformation softening effects observed in irradiated stainless steel. [3]

discounting the increase in the irradiated over the unirradiated yield strengths [2, 4] defined as:

$$YS_{eff1} = (YS_{irrad} - YS_{unirrad})/2 + YS_{unirrad} \quad (1)$$

$$YS_{eff2} = (YS_{irrad} - YS_{unirrad})/3 + YS_{unirrad} \quad (2)$$

where $YS_{unirrad}$ is the unirradiated yield strength, and YS_{irrad} is the irradiated yield strength, both at the test temperature.

A large portion of the CGR data related to irradiated materials have been obtained with small compact tension (CT) specimens (thickness up to 8 mm), where the dimensions of the source material, or the limited space in test reactors, or the capacity of the hot cells prevented machining of larger specimens [4–8]. Consequently, it is of interest to determine if the data obtained with small specimens are transferable to thick section components. A study was therefore initiated with the objectives to determine the effect of specimen size on the crack growth rate of irradiated stainless steel, and to determine the K validity limit for CT specimens with dimensions B = 8 mm and W = 16 mm. Another objective of the study was to improve the understanding regarding what factors are important in determining the K validity in irradiated SS.

Material and Specimens

Thick-Section (25 mm) SS 2333 austenitic stainless steel (Swedish equivalent of Type 304 SS) from the core shroud of the Swedish boiling water reactor (BWR) Barsebäck 2 was tested in this study. The component was in service for 28 years, or 198,689 effective full power hours (EFPH), and during this time the material tested had accumulated a fast neutron dose of about 1 dpa. The chemical composition of the material is shown in Table 1.

Two specimen sizes were tested in this study; a smaller specimen with a thickness of 8 mm, and a larger specimen with a thickness of 19 mm; see Fig. 2. Two small (Specimens S4A and S4B) and one large specimens (Specimen L1) were tested. All specimens were machined in the T–L orientation (i.e., in the circumferential direction of the core shroud), and they were positioned such that one of the side surfaces of the specimen was immediately adjacent to the inner surface of the core shroud (highest dose).

Tensile testing was carried out to determine the mechanical properties of the material in the irradiated condition, and stress strain curves from these tests are

Table 1 Chemical composition of the test material

Heat #	C	Si	Mn	P	S	Cr	Ni	Mo	Co	N
RL2218	0.04	0.87	1.70	0.017	0.011	19.0	9.0	–	0.029	0.046

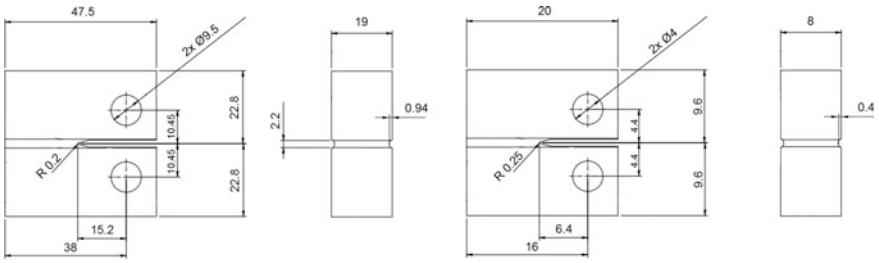

Fig. 2 Schematics of the specimens tested in this study

presented in the left-hand graph of Fig. 3. Data in 300 °C air for the material in the unirradiated condition was available from the heat certificate. Since the large specimen tested in this study used a larger fraction of the plate thickness (76%) compared to the small specimen (32%), the test material was characterized in the thickness direction to determine if variations existed that possibly could bias the results. The right-hand graph of Fig. 3 shows that the variation in tensile properties in the thickness direction of the plate is small. At the outer surface of the plate, the yield strength was somewhat lower, but at least from the inner surface to the mid-thickness of the plate there was virtually no variation in this property. Since the thickness of the largest specimen tested was 19 mm, combined with the fact that it was positioned towards the inner surface of the plate, the small variation in mechanical properties in this direction is judged to be insignificant. This conclusion is also supported by micro hardness measurements made across the thickness of the plate [9]. A summary of the tensile properties is provided in Table 2.

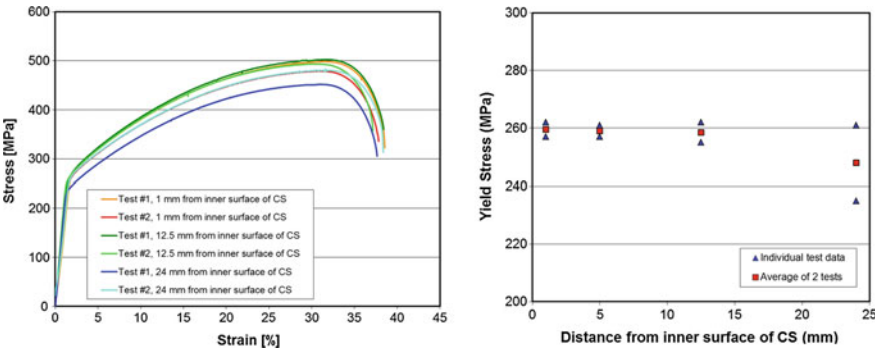

Fig. 3 Engineering stress strain curves in 288 °C air for the core shroud material at ~1 dpa at three different locations in the thickness direction of the plate (left), and yield stress at various distances from the inner surface of the core shroud (right)

Table 2 Mechanical properties of the test material in 288 or 300 °C air

Unirradiated (300 °C)			Irradiated (288 °C)[a]		
YS (MPa)	UTS (MPa)	TE (%)	YS (MPa)	UTS (MPa)	TE (%)
153	440	39	259	489	36

[a]Average of the two specimens located closest to the inner surface of the CS

Test Systems

Testing was performed in once-through autoclave systems of similar design installed in hot cells. The systems can test up to 19 mm thick CT specimens. Flow charts of these systems have been presented elsewhere [4, 5]. The autoclaves, which are made of stainless steel, were fed with high purity water with a conductivity of <0.06 μS/cm from the water purification system in Studsvik Nuclear's corrosion laboratory. Typically, the flow rate through the autoclave (free volume ≈ 1 L) was 7–8 L/hr. The addition of oxygen was made at the low-pressure side of the main pump. Conductivity and oxygen were monitored with Mettler Toledo Thornton Inc. Model 770 Max and Model 230-211 and 357-210, respectively at the outlet. Conductivity was also monitored at the inlet. Analyses for the presence of impurities in the water were made on grab samples at regular intervals. The corrosion potential (ECP) was measured on the CT specimen with a $Cu/Cu_2O/ZrO_2$ membrane electrode [10]. An Instron Model 3521 servo-hydraulic system, or a servo electric system of in-house design, both controlled with Instron Model 8800 control electronics, were used to load the specimens. A PC-based control and data acquisition system (based on LabView from National Instruments) was used to control the specimen load and to collect data from the various transducers. A direct current potential drop (DCPD) system was used to monitor crack growth on-line.

Test Procedures

After assembly of the specimen in the autoclave, the system was closed and high purity deaerated water flowed through the test loop at the test pressure. The autoclave was then heated up to 288 °C, and 2000 ppb of oxygen was added to the water. These conditions were maintained for at least a week until the outlet water chemistry stabilized and the specimen was pre-oxidized. Subsequently, in situ fatigue pre-cracking and transitioning to stress corrosion cracking (SCC) was initiated per the procedure shown in Table 3. As will be shown in the result section, modifications to the test protocol were made based on the crack growth response of the specimen.

Testing under constant K conditions (Stage 7) was conducted at $\sim$15 (Specimen S4A) and 23.5 MPa$\sqrt{m}$ (Specimen S4B) for the two small specimens. For the large specimen, testing at constant K was conducted at three different levels: $\sim$15, 23.3,

Table 3 Target conditions for in situ fatigue pre-cracking, SCC Transitioning, and testing at constant K

Stage	Water Chemistry	% of planned K_{max}	R	Frequency Hz	Crack Incr. mm
1	288 °C, 2 ppm O_2	~80	0.2	1 sine	~0.5
2	288 °C, 2 ppm O_2	100	0.6	1 sine	0.1
3	288 °C, 2 ppm O_2	100	0.6	0.1 sine	0.1
4	288 °C, 2 ppm O_2	100	0.6	0.01 sine	0.1
5	288 °C, 2 ppm O_2	100	0.6	0.001 sine	0.1
6	288 °C, 2 ppm O_2	100	0.6	0.001 + 9 ks hold	0.1
7	288 °C, 2 ppm O_2	100	1	Constant K	0.2–0.5

and 29 MPa$\sqrt{m}$. Steps with cyclic loading corresponding to Stages 1 through 6 in Table 3 (but at higher K) were introduced at each K level to mark the fracture surface so that cracking related to the different K levels could be distinguished.

When testing was completed, the system was cooled down while keeping a low load on the specimen. The crack was then advanced by fatigue loading to increase the crack length before the specimen was broken open. Actual crack lengths were determined by measuring crack lengths at 20 equidistant locations along the crack front and using the average of measured lengths at all locations. This information was used to correct the crack length versus time curves estimated by the DCPD system as well as the stress intensity factor. In addition, all specimens were subjected to fractographic examination using a scanning electron microscope (SEM) to determine the fracture mode and to document features of interest.

The DCPD error was relatively small in these tests, as the DCPD estimated final crack length was close to the actual (true) crack lengths. The errors in incremental growth were −3.7 and 5.3% in Specimens S4A and S4B, respectively, while the errors were 6.3, −2.4 and 7.0% for the three K levels tested with the large specimen. To correct the crack length versus time data obtained by the DCPD measurements, a non-linear correction was applied to the data as described in [6]. Compared to linearly corrected DCPD curves, the non-linear correction resulted in a lower correction factor at shorter crack lengths, and a higher factor at longer crack lengths. However, the difference between the linear and non-linear corrections was small, and for most CGRs the difference was 20% or less.

Crack Growth Rate Results

Small Specimen S4A

The crack growth response of Specimen S4A (small specimen) during the final SCC transitioning steps and at constant K is shown in Fig. 4. This figure shows that the

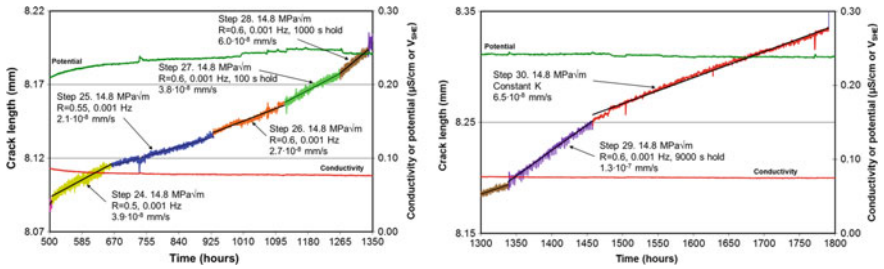

Fig. 4 Crack growth response of the small specimen S4A during the final steps of SCC transitioning (left) and constant K (right)

CGR increased slightly during the final steps of SCC transitioning (Steps 24–29), indicating time dependent SCC growth started to dominate the crack advance. The increase in CGR with time is possibly related to a gradual increase of intergranular cracking along the crack front (engagement). A reasonably linear CGR of $6.5 \cdot 10^{-8}$ mm/s was observed at a constant K of 14.8 MPa$\sqrt{m}$ (Step 30 in Fig. 4). Testing continued after Step 30, but this part of the test is not further discussed as no data at constant K were obtained.

The fracture surface of Specimen S4A is presented in Fig. 5, in which the crack fronts at the end of SCC transitioning, and the end of intergranular cracking, have

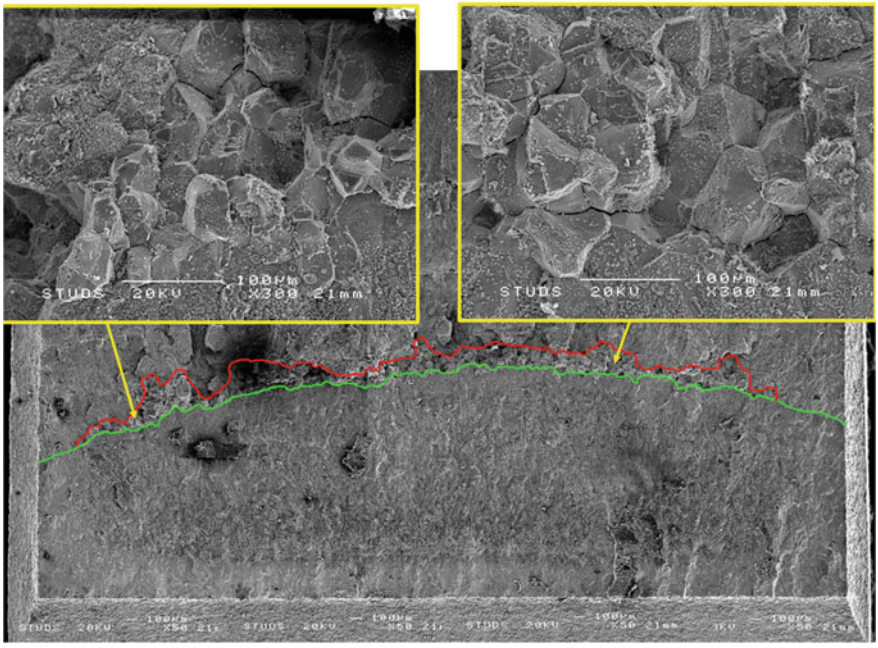

Fig. 5 Fracture surface of Specimen S4A where the crack fronts at the end of SCC transitioning and the end of intergranular cracking have been highlighted with, respectively, green and red lines

been highlighted with, respectively, green and red lines. Figure 5 shows that cracking extending from the machined notch was transgranular. This type of cracking extended on average 1.76 mm in the direction of crack growth, which is in good agreement with the DCPD measurement of the transition between Steps 28 and 29. Thus, it seems the fracture mode changed when the hold time at maximum load changed to 9000 s. Cracking related to Steps 29 and 30 was intergranular as shown by the details at higher magnification in Fig. 5. Intergranular cracking did not engage along the entire crack front (87% engagement).

Small Specimen S4B

Figure 6 presents the crack growth response of Specimen S4B during the final steps of SCC transitioning and testing at a constant K of $\sim$23.5 MPa$\sqrt{m}$. There was essentially no change in the CGR when the loading conditions changed from partial periodic unloading (PPU) with a hold time of 1000 s to constant K. A linear CGR of $1.1 \cdot 10^{-7}$ mm/s was measured for $\sim$500 h under constant K conditions (Step 18). The test was stopped after Step 18.

A montage of SEM micrographs over the fracture surface is shown in Fig. 7. The crack fronts at the end of SCC transitioning, and the end of intergranular cracking, have been highlighted with, respectively, green and red lines. Cracking extending from the machined notch was transgranular, although isolated intergranular facets were observed on the fracture surface related to cyclic loading. Transgranular cracking extended on average 1.07 mm from the machined notch, which is in very good agreement with the DCPD measurement of the transition between Steps 16 and 17. Thus, it seems the fracture mode changed when the hold time at maximum load increased from 1000 to 9000 s, consistent with the observation made for Specimen S4A as well as other studies [e.g., 11]. Cracking related to constant K was intergranular, as shown by the details at higher magnification shown in Fig. 7. Intergranular cracking engaged along nearly the entire crack front (97% engagement).

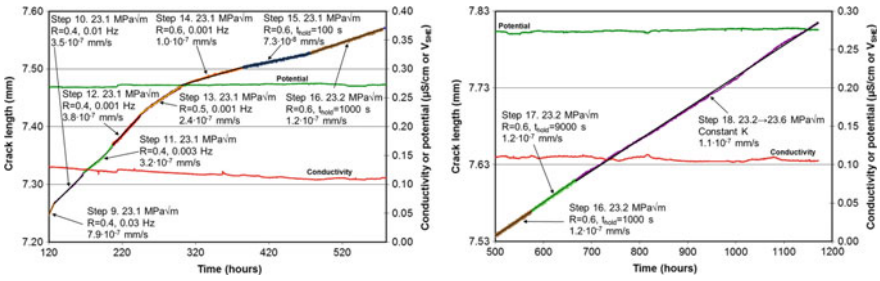

Fig. 6 Crack growth response of the small specimen S4B during the final steps of SCC transitioning and at constant K

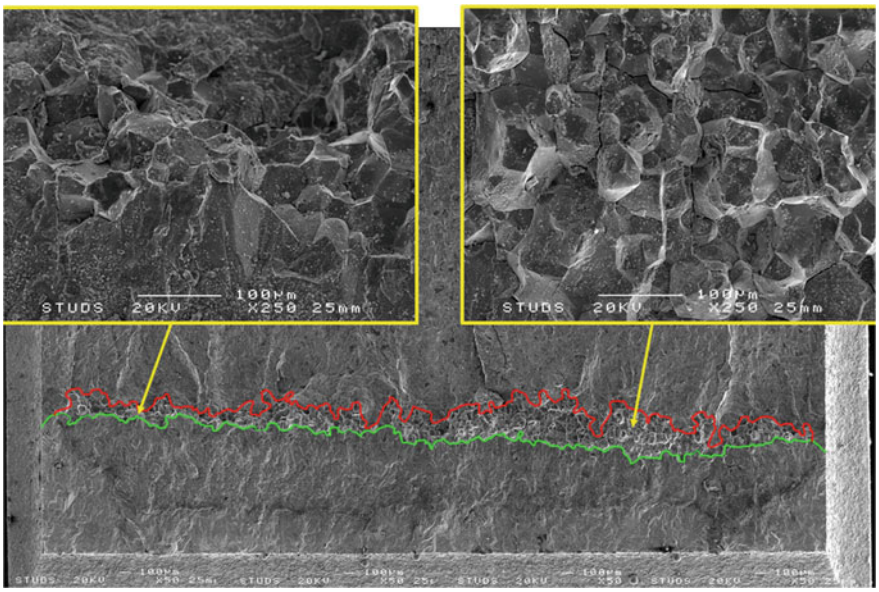

Fig. 7 Fracture surface of Specimen S4B where the crack fronts at the end of SCC transitioning and the end of intergranular cracking have been highlighted with, respectively, green and red lines

Large Specimen L1

The left-hand graph of Fig. 8 shows the crack growth response of Specimen L1 during testing at the first K level (15 MPa$\sqrt{m}$). The CGR did not change much when the loading conditions changed from PPU with a hold time of 9000 s to constant K. A linear CGR of 7.1 10^{-8} mm/s was measured for ~650 h under constant K conditions (Step 38). Following Step 38, the stress intensity was increased and the crack was advanced by fatigue (several steps with decreasing frequency, increasing R ratio, and finally PPU with hold time) to separate, on the fracture surface,

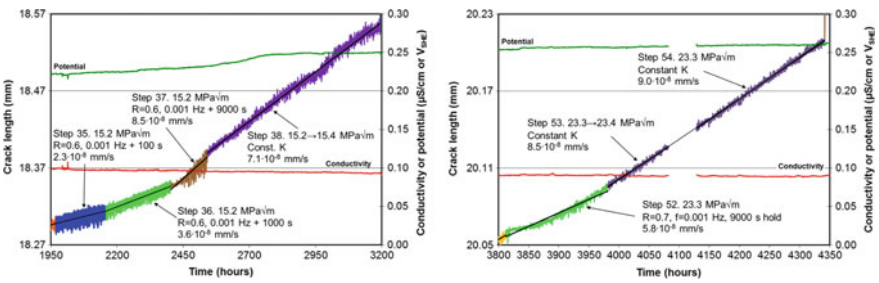

Fig. 8 Crack growth response of the large specimen L1 during testing at constant K of 15 MPa$\sqrt{m}$ (left) and 23 MPa$\sqrt{m}$ (right)

cracking related to this step from later steps of the test. The right-hand graph of Fig. 8 shows the crack growth response under constant K at the second stress intensity level of 23 MPa$\sqrt{m}$. Crack growth rates of 8.5 and 9.0 10^{-8} mm/s were measured under these conditions. At 4082 h, the PC collecting data from the test crashed, which is the reason for the gap in data and why test data at constant K was divided in two steps; but the load remained unchanged and constant when no data were recorded. A CGR of $8.8 \cdot 10^{-8}$ mm/s would be obtained if Steps 53 and 54 are combined (359 h test time).

Following testing at 23 MPa$\sqrt{m}$, the stress intensity was increased to 29 MPa$\sqrt{m}$ in the same fashion as during the previous increase in K. This marked the fracture surface, making it possible to separate cracking related to the two prior K levels, and it transitioned the fatigue generated transgranular crack to intergranular SCC. The CGR response during SCC transitioning at 29 MPa$\sqrt{m}$ is shown in the left-hand graph of Fig. 9. This figure shows that the changes in loading conditions (increasing R ratio and the introduction of PPU with hold times at maximum load) had limited effects on the CGR, indicating that time dependent SCC growth started to dominate the crack advance. At 4547 and 4570 h, the PC collecting data from the test crashed. No data were recorded in conjunction with these events which is the reason for the gaps in data. The load was cycled at R = 0.5 and f = 0.001 Hz during the periods when no data were recorded. A third interruption occurred at 5054 h when the autoclave system was shut down due to loss of power caused by a heavy thunderstorm. When the system was restarted, the specimen was held at constant load for ~50 h before starting Step 70. No growth was observed during the period at constant load. The crack growth responses following the shutdown were consistent with the CGRs measured prior to this event, indicating that the power failure had no or little effect on the CGRs measured later in the test.

The CGR response during the final step under constant K conditions is shown in the right-hand graph of Fig. 9. There was essentially no change in the CGR when the loading conditions changed from PPU with a hold time of 9000 s to constant K, if only the initial portion of Step 74 (dark blue portion of the curve) is considered. However, after about 90 h of testing at constant K, the CGR increased. A linear

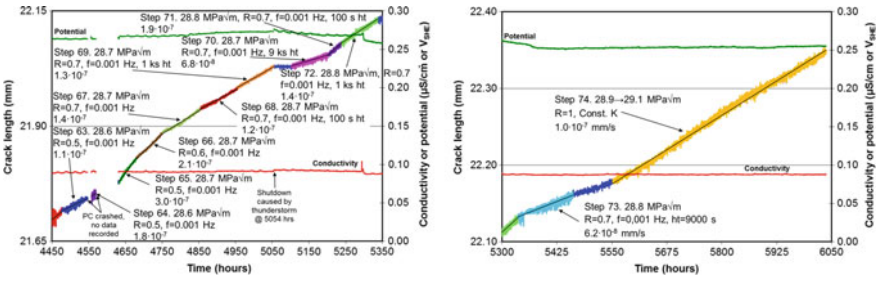

Fig. 9 Crack growth response of the large specimen L1 during SCC transitioning (left) and testing at constant K of 29 MPa$\sqrt{m}$ (right)

crack growth response corresponding to a CGR of $1 \cdot 10^{-7}$ mm/s was observed for the major portion of the time under constant K conditions.

A montage of SEM micrographs over the fracture surface is shown in Fig. 10. Three regions with intergranular cracking were observed, corresponding to the three test segments at constant K; see the colored lines highlighting the various regions. Cracking extending from the machined notch to the first region with intergranular cracking, and cracking between the intergranular regions, was transgranular. This type of cracking extended on average 2.95 mm from the machined notch, which is in very good agreement with the DCPD measurement of the transition between Steps 36 and 37. Good agreement between actual crack lengths and the DCPD measurement was also noted for the other two transitions from transgranular to intergranular cracking that occurred later in the test. Similar to the small specimens tested, the fracture mode changed from transgranular to intergranular when the hold time at maximum load increased from 1000 to 9000 s. Cracking at constant K values was intergranular, as shown by the details at higher magnification in Fig. 10. The engagement of intergranular cracking along the three crack fronts was 79% at the first K level, 95% at the second, and 93% at the third.

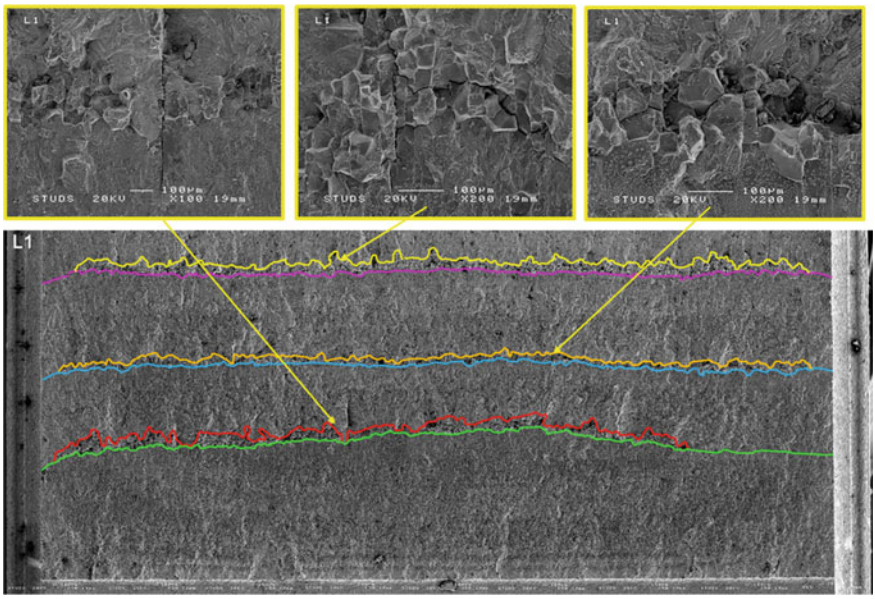

Fig. 10 Fracture surface of Specimen L1 where the various regions with intergranular cracking have been highlighted

Discussion

One objective of this study was to determine the K validity limit for small CT specimens. Figures 11 and 12 compare actual K during testing for Specimens, S4A, S4B and L1 with the various K validity criteria discussed in the introduction. In addition to determining whether a data point satisfies the various K validity criteria, the crack length versus time response must also be considered. K validity is indicated by consistent crack growth response with changes in K. Small changes in K leading to large increases in crack growth rates indicate K invalidity.

As shown in the right-hand graph of Fig. 11, Specimen S4B exceeded all three K validity criteria during testing at constant K of 23.5 MPa$\sqrt{m}$. The criteria per ASTM E399 and the ones based on YS_{eff1} and YS_{eff2} were exceeded by respectively 60, 102 and 122%. Specimen S4A, which was tested at 14.8 MPa$\sqrt{m}$, also exceeded all three criteria, and in this case by 3, 31 and 43%; see left-hand graph of Fig. 11. For both specimens, consistent crack growth responses during SCC transitioning and constant K were observed. In addition, there were no indications of accelerated CGRs. These observations suggest the CGRs obtained at constant K on the small specimens represent valid data.

K validity and K during testing of the large specimen are shown in the left-hand graph of Fig. 12. Regarding the lowest K level (15 MPa$\sqrt{m}$), K remained below all three validity limits. At the intermediate K level tested (23 MPa$\sqrt{m}$), the K validity criteria per ASTM E399 and the ones based on YS_{eff1} and YS_{eff2} were exceeded by respectively 4, 32 and 45%, whereas at the highest K level, these criteria were exceeded by 37, 73 and 90%. Consistent crack growth responses during SCC transitioning and constant K were observed for all three K levels investigated. In addition, there were no indications of accelerated CGRs, which suggests all data obtained on this specimen represent valid data.

The data obtained at constant K are plotted as a function of stress intensity in the right-hand graph of Fig. 12. Also included in this figure is the 75th percentile normal water chemistry (NWC) model for crack growth in irradiated stainless steel developed by Eason et al. [12].

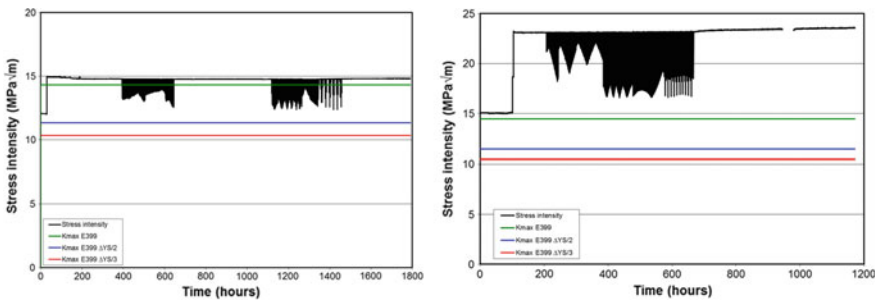

Fig. 11 Stress intensity factor during testing of Specimens S4A (left) and S4B (right) compared to various K validity criteria

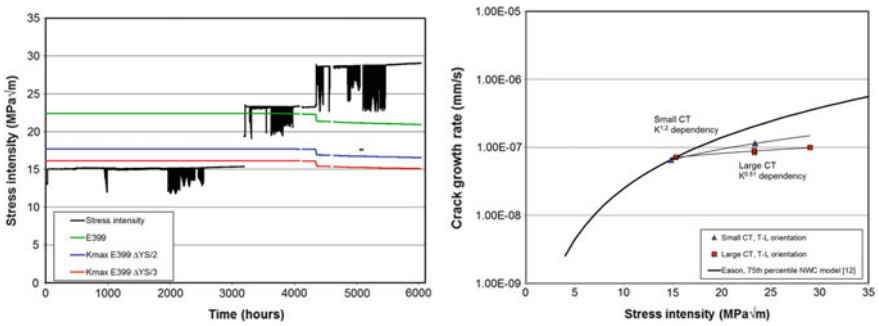

Fig. 12 Stress intensity factor during testing of Specimen L1 (left) compared to various K validity criteria, and CGRs under constant K versus stress intensity in simulated NWC for the specimens tested in this study (right), and the 75th percentile NWC model for crack growth in irradiated stainless steel [12]

The right-hand graph of Fig. 12 shows that at the lowest K level tested (15 MPa$\sqrt{m}$), both specimen sizes cracked at almost identical rates. The CGRs differed by 10%, a difference smaller than the variations normally observed among CGR data generated under nominally identical conditions. As discussed above, the large specimen was valid according to the K validity criterion as stated in ASTM E399, while the small specimen violated this criterion by 3%. Since there was no effect of specimen size at this K level, it can be concluded that data from both specimens were valid. Furthermore, it can be concluded that the K validity criterion per ASTM E399 is applicable to the material and dose tested in this study. By inference, the latter conclusion would also apply to other materials with significant remaining strain hardening capacity, e.g., stainless steels in the unirradiated condition or irradiated to relatively low doses.

At the intermediate K level (23 MPa$\sqrt{m}$), both specimen sizes cracked at similar rates, with the small specimen cracking a factor of $\sim$1.3 faster than the large specimen. Such a difference is smaller than the 2X variation typically observed among CGR data generated under nominally identical conditions. As reported in the beginning of this section, the large specimen exceeded the K validity criterion defined in ASTM E399 by 4%, while K for the small specimen was 60% above the limit. Based on the discussion in the previous paragraph, it can be concluded that the CGR determined with the large specimen must be valid, since the maximum allowed K was exceeded with about the same factor as the small specimen tested at the lowest K level. These results indicate that the K validity criterion defined in ASTM E399 can be violated with some margin. This is true for materials with significant remaining strain hardening capacity, and the situation is expected to be different for highly irradiated stainless steel, which have no or little work hardening capacity and can work soften. Testing of the large specimen at the highest K (29 MPa$\sqrt{m}$) resulted in a CGR similar to the data obtained at lower (and valid) K; the K-dependence of CGRs in this material is not very strong. This observation,

together with the discussion in the next paragraph, suggests the CGR obtained at 29 MPa$\sqrt{m}$ represent valid data.

The observation that the maximum allowable K defined in ASTM E399, to some extent, can be exceeded without giving rise to non-representative CGR data is in agreement with Andresen's findings [2], as well as data on unirradiated Type 304 SS [13] and Alloy X-750 [14]. Andresen concluded that the K validity criterion according to ASTM E399 is conservative and probably can be exceeded by 20 to 30%. In addition, for high work hardening materials, such as the material tested in this study, Andresen recommended the flow strength to be used in place of the yield strength to define the K validity. Using the flow strength (average of yield and ultimate tensile strengths) in place of the irradiated yield strength would increase the allowable K for the small CT specimen from 14.5 to 20.7 MPa$\sqrt{m}$; and for the large specimen from 22.4 to 32 MPa$\sqrt{m}$. If the limits based on flow strength can be exceeded by 20 to 30%, then K values in the range 24.8–26.9 MPa$\sqrt{m}$ and 38.4 to 41.6 MPa$\sqrt{m}$ would be allowed for respectively the small and large specimens. Thus, the results of this study are in line with Andresen's recommendation for work hardening materials.

The results of this study show that there is no effect of specimen size on the CGR when testing is conducted at valid stress intensity factors based on ASTM E399 and flow strength. Since significant strain hardening capacity remained in the material tested, the K validity can be based on ASTM E399 using the flow strength. In addition, the results indicate that the limit also can be exceeded by at least 20%. For highly irradiated stainless steels with no or little work hardening capacity left, experience show that the K validity according to ASTM E399 is not applicable. Because of the relatively low dose of the material tested in this study, it was not possible to propose K validity criteria appropriate for highly irradiated material. At present, the K validity criteria discussed in the introduction have to be used for materials irradiated to high dose. To better define a K/size criterion for materials irradiated to high doses, testing of specimens of different sizes, machined from thick section material with no or little strain hardening capacity left, would be needed.

The K dependencies shown in Fig. 12 ($K^{0.51}$ and $K^{1.2}$) are clearly lower than the $K^{2.486}$ dependency used in the NWC model for crack growth in irradiated stainless steel [12], and the $K^{2.3}$–$K^{2.5}$ dependencies reported by Andresen et al. [2, 15], and observed in other tests on irradiated stainless steels [4, 6]. The reason for this is unclear as there were no testing issues or anomalies related to the fracture surfaces that could explain the low K dependencies observed. It is noted that in this study, intergranular cracking did not develop across the entire thickness of the specimen, although the % engagement in many cases was close to 100%. In irradiated stainless steels at higher doses, the % engagement is typically 100% while cracking is highly intergranular. It is possible the K dependencies observed were biased low by engagement below 100%.

It is noted that the 75th percentile normal water chemistry (NWC) model for crack growth in irradiated stainless steel [12] envelops all data obtained in this study; see Fig. 12. The data obtained in this study were not used to develop the model.

A few studies on the effect of specimen size have been published, but they are restricted to unirriadiated materials. Sato and Shoji performed CGR testing on thermally sensitized and warm rolled Type 304L stainless steel in simulated BWR NWC, as well as on solution annealed and cold rolled Type 316L stainless steel in simulated PWR environment [16]. An effect of specimen size was observed in BWR environment, where lower CGRs were observed in the smaller specimens. By comparing the data versus the quantity $[(K/\sigma_{YS})^2/B_{eff}]$, where K is the stress intensity, σ_{YS} the yield strength at temperature, and B_{eff} the effective thickness of the specimen, it was verified that all but the smallest specimen satisfied the requirements of small scale yielding. Differences related to the crack tip chemistry caused by thickness induced variations of the mass transport kinetics between the crack tip and bulk water, of e.g., impurities, was mentioned as a possible factor contributing to the size effect observed. In contrast with the results obtained in BWR environment, no specimen size effect was observed in PWR environment if the requirements of small scale yielding were satisfied. They found that the CGR was independent of the specimen size if the quantity $[(K/\sigma_{YS})^2/B_{eff}]$ was below 0.45. This is essentially the K validity criterion defined in ASTM E399 which requires that $[(K/\sigma_{YS})^2/B_{eff}]$ remains below 0.4.

Itow et al. investigated the effect of specimen size at high values of K on the SCC CGR of sensitized Type 304 stainless steel in simulated BWR NWC using CT specimens with thicknesses 1" (25.4 mm) and 2" (50.8 mm) [17]. Testing was performed at constant load, and in the early stages of the test, the CGRs measured on the 1" specimen (61 MPa$\sqrt{m}$) agreed well with the 2" specimen (66 MPa$\sqrt{m}$). However, during the final stages of the test, the CGR in the smaller specimen (62 MPa$\sqrt{m}$) was about 10X faster than the growth rate in the large specimens. Thus, the effect of specimen size in this study was opposite to what Sato and Shoji observed [16]. Based on the flow stress of the heat of material tested and the specimen dimensions in question, the maximum allowable Ks according to ASTM E399 were 33 and 50 MPa$\sqrt{m}$ for the small and large specimens, respectively. Although both specimen sizes developed intergranular cracking, differences in the fracture surface appearance were noted. In the small specimen, multiple deep cracks extending perpendicular to the crack plane were observed, a feature that was not observed on the large specimen, or on the small specimen tested at lower K. The authors believed the multiple deep cracks were caused by SCC accompanied by plastic deformation.

Morton, Richey et al. tested side grooved CT specimens of as-received or thermally treated Alloy 600 with gross thicknesses ranging from 10.16 mm (0.4 inches) to 50.8 mm (2 inches) [18–20]. Testing was performed in hydrogenated deaerated water at hydrogen contents between 1 and 150 cc/kg and temperatures in the range 288 to 360 °C. An effect of specimen size was observed at K levels above 55 MPa$\sqrt{m}$, where the CGRs in the smaller specimens (B = 10.16 and 15.24 mm) were significantly faster compared to the larger specimens. Accelerated CGRs in the smaller specimens were observed when the quantity $[(K/\sigma_{YS})^2/B_{eff}]$ increased above $\sim$2. The fracture mode of all specimen sizes tested was intergranular. However, the two smallest specimen sizes tested showed limited evidence of ductile dimples.

Except for the size effect observed in BWR NWC by Sato and Shoji [16], the studies referred to above indicate that smaller specimens yield higher CGRs than larger specimens when K exceeds a certain limit. As discussed by Andresen [2], and indicated by the above referenced studies, this limit is dependent on the work hardening capacity of the material, so that different requirements would apply for solution annealed/thermally sensitized, cold worked, or irradiated materials.

In the study by Morton and Richey et al. [18–20], accelerated CGRs were observed in the smaller specimens when the quantity $[(K/\sigma_{YS})^2/B_{eff}]$ exceeded about 2. This observation is consistent with the results from the study by Itow et al. [17], where this quantity was ~ 3.2 for the small specimen and ~ 1.8 for the large. It is also, at least qualitatively, in agreement with Andresen's recommendations for high work hardening materials [2], such as solution annealed or sensitized stainless steel and Alloy 600, that the K validity according to ASTM E399 should be based on the flow strength, and that this limit can be exceeded by 20 to 30% without giving rise to accelerated CGRs. A value of 2 or less for the quantity $[(K/\sigma_{YS})^2/B_{eff}]$ indicates the limit can be exceeded by more than 20 to 30%, perhaps up to 40–50%.

Conclusions

The results show that there is no effect of specimen size on the CGR when testing is conducted at valid stress intensity factors. Significant strain hardening capacity remained in the material tested, and the results indicate that the K validity can be based on ASTM E399 using the flow strength. Thus, the maximum allowed K can be defined according to the following expression:

$$K < FS\sqrt{\frac{B_e or (a-W)}{2.5}} \tag{3}$$

where, FS is the flow strength calculated as the average of the yield and ultimate tensile strengths, B_e is the effective thickness calculated as $B_e = \sqrt{B\ B_{sg}}$ (B = gross thickness and B_{sg} = thickness at the side grooves), and (a-W) is the remaining uncracked ligament. The lesser of B_{net} and (W-a) should be used.

In addition, the results suggest that the limit shown in Eq. 3 can be exceeded by at least 20%. This observation is true for materials with significant strain hardening capacity left, and for materials at higher doses in which this capacity is lost or greatly reduced, the K validity must be defined differently. Because of the relatively low dose of the material tested in this study, no information on how to define the K validity for highly irradiated materials was obtained. Testing similar to this study on material irradiated to higher dose would be needed to better define K validity criteria for materials at high dose.

The CGRs measured under constant K (15–29 MPa$\sqrt{m}$) ranged from $6.5 \cdot 10^{-8}$ to $1.1 \cdot 10^{-7}$ mm/s. All data were enveloped by the 75th percentile NWC model for

crack growth in irradiated stainless steel. The K dependencies observed were clearly lower than the $K^{2.5}$ dependency used in this model, and the dependencies reported by others. The reason for this is not clear, but it could be related to the % engagement being less than 100%.

Acknowledgements The work presented in this paper was funded by EPRI. Material from the Barsebäck 2 core shroud was procured with the assistance of Pål Efsing and Björn Forssgren, Ringhals AB. Testing and post-test examinations were performed by many colleagues at Studsvik. All these contributions are gratefully acknowledged.

References

1. Standard Test Method for Linear-Elastic Plane-Strain Fracture Toughness K_{Ic} of Metallic Materials, E399, Annual Book of ASTM Standards, Volume 03.01 (ASTM International, West Conshohocken, PA, 2006)
2. P. L. Andresen, K/Size Effects on SCC in Irradiated, Cold Worked and Unirradiated Stainless Steel, Paper presented at the 11th International Symposium on Environmental Degradation of Materials in Nuclear Power Systems—Water Reactors. Stevenson, USA (ANS, August 2003), pp. 870–886
3. G.S. Was, Recent Developments in Understanding Irradiation Assisted Stress Corrosion Cracking, (Paper presented at the 11th International Symposium on Environmental Degradation of Materials in Nuclear Power Systems—Water Reactors. Stevenson, USA. (ANS, August 2003), pp. 965–985
4. A. Jenssen, J. Stjärnsäter, R. Pathania. Crack Growth Rates of Irradiated Commercial Stainless Steels in BWR and PWR Environments, (Paper presented at the 15th International Conference on Environmental Degradation of Materials in Nuclear Power Systems—Water Reactors, Colorado Springs, CO, August 2011)
5. A. Jenssen, P. Efsing, K. Gott and P-O Andersson, Crack Growth behavior of Irradiated Type 304L Stainless Steel in Simulated BWR Environment, Paper presented at the 11th International Conference on Environmental Degradation of Materials in Nuclear Power Systems—Water Reactors, Stevenson, WA. (ANS, August 2003), p. 1015)
6. A. Jenssen, J. Stjärnsäter, R. Pathania, Crack Growth Rate Testing of Fast Reactor Irradiated Type 304L and 316 SS in BWR and PWR Environments, Paper presented at the 14th International Conference on Environmental Degradation of Materials in Nuclear Power Systems, (Virginia Beach, VA, August 2009)
7. A. Jenssen, J. Stjärnsäter, R. Pathania, R. Carter, Crack Growth Rate Testing of Irradiated Type 304L and Type 316L in BWR Environments, Paper presented at the International Boiling Water Reactor and Pressurized Water Reactor Materials Reliability Conference and Exhibit Show, National Harbor, MD, (July 2012)
8. A. Jenssen, R. Pathania, R. Carter, Crack Growth in Irradiated Austenitic Stainless Steels in BWR Environments, Paper presented at Fontevraud 8 - Contribution of Materials Investigations and Operating Experience to LWRs' Safety, Performance and Reliability, Avignon, France, (September 2014)
9. Effect of Specimen Size on the Crack Growth Rate Behavior of Irradiated Type 304 Stainless Steel: Phase 1—Testing of Type 304 at 1 dpa. EPRI, Palo Alto, CA: 2012. 1023962
10. L.W. Niedrach, W.H. Stoddard, Monitoring pH and Corrosion Potentials in High Temperature Aqueous Environments. Corrosion **41**, 45–51 (1985)
11. BWRVIP-265: BWR Vessels and Internals Project, Crack Growth in High Fluence BWR Materials-Phase 2. EPRI, Palo Alto, CA: 2012. 1026508

12. E. D. Eason, R. Pathania, Irradiation- Assisted Stress Corrosion Crack Growth Rates of Austenitic Stainless Steels in Light Water Reactor Environments, Paper presented at the 17th International Conference on Environmental Degradation of Materials in Nuclear Power Systems—Water Reactors, Ottawa, Ontario, Canada, (August 2015)
13. A. Jenssen, C. Jansson and J. Sundberg, The Effect of Hold Time on the Crack Growth Rate of Sensitized Stainless Steel in High Temperature Water, (Paper presented at the 12th International Conference on Environmental Degradation of Materials in Nuclear Power Systems–Water Reactors, Snowbird, UT, August 2005)
14. A. Jenssen, P. Efsing and J. Sundberg, Influence of Heat Treatment, Aging and Neutron Irradiation on the Fracture Toughness and Crack Growth Rate in BWR Environments of Alloy X-750, Paper presented at the 12th International Conference on Environmental Degradation of Materials in Nuclear Power Systems—Water Reactors, Snowbird, UT, (August 2005)
15. P. L. Andresen, Similarity of Cold Work and radiation Hardening in Enhancing Yield Strength and SCC Growth of Stainless Steel in Hot Water, Paper presented at Corrosion 2002, NACE 2002, Paper #02509)
16. T. Sato and T. Shoji, Effects of Specimen Size and Thickness on CGR in High Temperature Waters, Paper presented at the 11th International Symposium on Environmental Degradation of Materials in Nuclear Power Systems—Water Reactors. Stevenson, USA. ANS, (August 2003) p. 862
17. M. Itow, M. Kikuchi and S. Suzuki, SCC Crack Growth Rates of Type 304 Stainless Steel at High K Region in Simulated BWR Environment, Paper presented at Corrosion 2000, Orlando, FL, NACE, 2000, Paper #00221
18. Morton, D. S., et al., In search of the true temperature and stress intensity factor dependencies for PWSCC. Paper presented at the 12th International Conference on Environmental Degradation of Materials in Nuclear Power Systems—Water Reactors, Snowbird, UT, (August 2005), pp. 977–988
19. Richey, E., Morton, D. S., Moshier, W. C., Influence of Specimen Size on the SCC Growth Rate of Ni-Alloys Exposed to High Temperature Water. Paper presented at Corrosion 2006. Houston, TX, NACE, 2006. Paper #06513
20. E. Richey, D. Morton and W. Moshier, Influence of Specimen Size on the SCC Growth Rate of Ni-Alloys Exposed to High Temperature Water, Report LM-05K151, Lookheed Martin, (October 2005)

Plastic Deformation Processes Accompanying Stress Corrosion Crack Propagation in Irradiated Austenitic Steels

M.N. Gussev, G.S. Was, J.T. Busby and K.J. Leonard

Abstract During stress corrosion crack propagation, stress values in the crack tip vicinity often exceed material yield stress limit. Plastic deformation processes may accompany and influence cracking. Here, stress corrosion crack propagation and deformation mechanisms were investigated using EBSD analysis. The investigated material was 304L Ti-enriched austenitic stainless steel irradiated to 10.4 dpa at 320 °C in the BOR-60 fast reactor. Crack growth tests were conducted in a simulated Normal Water Chemistry (NWC) environment in the temperature range 288–320 °C using compact tension specimens. By analyzing crack trajectory and grain structure in the crack vicinity, it was established that grain orientation with respect to the acting stress direction was not a key factor controlling crack propagation. No crystallographic orientation susceptible to cracking was identified. Also, EBSD analysis revealed strong inhomogeneity in plastic strain distribution along the crack path. Most crack-adjacent grains remained virtually strain-free whereas few grains experienced strong plastic strain. These areas were presumed to be "plastic bridges" or "ductile ligaments."

Keywords EBSD · Stress corrosion cracking · Deformation localization · Neutron irradiation · Austenitic steel

M.N. Gussev (✉) · J.T. Busby · K.J. Leonard
Oak Ridge National Laboratory, One Bethel Valley Road, MS-6151, P.O. Box 2008, Oak Ridge, TN 37831, USA
e-mail: gussevmn@ornl.gov

G.S. Was
University of Michigan, 2355 Bonisteel Blvd., Ann Arbor, MI 48109-2104, USA

J.H. Jackson et al. (eds.), *Proceedings of the 18th International Conference on Environmental Degradation of Materials in Nuclear Power Systems – Water Reactors*, The Minerals, Metals & Materials Series, https://doi.org/10.1007/978-3-319-68454-3_78

Introduction

Austenitic 300-series steels are widely used in the industry because of their favorable combination of mechanical and corrosion properties and their acceptable radiation tolerance. However, this class of materials suffers from several issues, with the stress corrosion cracking (SCC) susceptibility being one of the most widely recognized problems in the high-temperature operating environments, like Light Water Reactors (LWRs) [1–3]. It is expected that the SCC-related issues will become more severe with the aging of the LWR fleet.

Currently, crack growth rate (CGR) measurements are one of the most common tools for quantifying the material performance and cracking in the corrosion environments. The main outcome of the test is the CGR value as a function of corrosion environment, temperature, stress intensity, and material parameters. A rich literature exists on the different aspects of SCC propagation mechanisms in non-irradiated materials; however, the role of material structure on crack propagation and plastic deformation mechanisms are still not well understood for materials irradiated to high doses (10 dpa and more). Radiation-induced hardening and the change in the deformation mode from multiple active slip systems to dislocation channeling should influence the advancing crack and the plastic strain fields in the crack-surrounding area. The present work aims to investigate deformation mechanisms and evaluate plastic strain fields induced by stress corrosion crack propagation in neutron-irradiated stainless steel.

Experimental Procedure

A set of round compact tension (RCT) specimens were produced and irradiated in the framework of the Cooperative Irradiation-Assisted Stress Corrosion Cracking Research (CIR) Program [4, 5]. The specimens were irradiated in the BOR-60 fast reactor and tested by several research teams [6–8]. The details on testing history and crack growth results for the specimen studied here (MS-01 RCT specimen, damage dose 10.7 dpa) are given in [9]. The experiment setup is discussed in [10]. The specimen, Fig. 1, was pin-loaded and had side groves. The crack growth test was performed under Normal Water Chemistry (NWC) conditions [10], with temperatures varying from 288 to 320 °C. The stress intensity factor (K) increased from 16.28 MPa $\times$ $m^{0.5}$ at the beginning of the test to 29.33 MPa$\sqrt{m}$ at the test end.

For investigation of the microstructural influence on crack behavior, the post-tested fatigued apart RCT sample was sectioned to reduce the activity level; the rounded bottom part with the pin hole was removed. Details are shown in Fig. 2. The remaining slice with $\sim$2.5 mm thickness was cut once again to produce cross-sectional slices. The cross section plane location is identified in the figure; it was important to capture the maximal portion of the stress corrosion crack. The cross-section was located close to the middle plane of the RCT specimen and

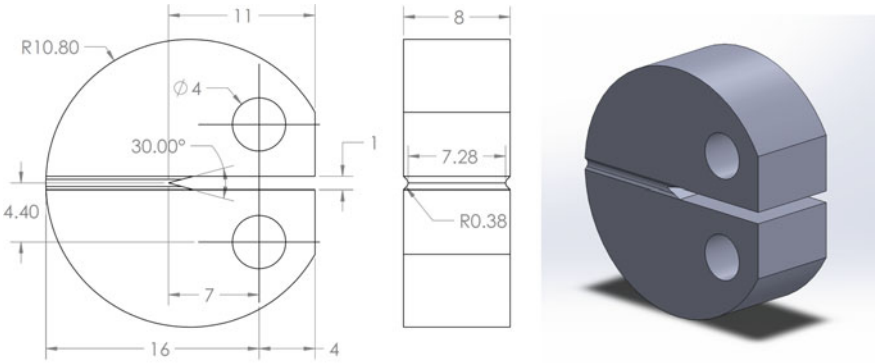

Fig. 1 Dimensions (in millimeters) and the shape of the RCT specimen

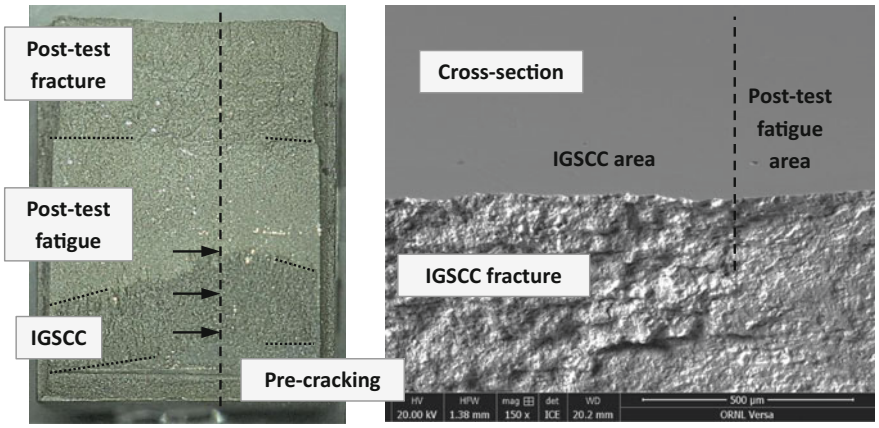

Fig. 2 Left: Specimen surface showing different fracture mechanisms (Pre-cracking, Inter-granular stress corrosion cracking, etc.); dashed line and black arrow show the location of the prepared cross-section. Right: a tilted view of the specimen cross-section prepared for EBSD analysis; one may see the transition between IGSCC area and post-test fatigue

represented, we believe, a plane strain state. The cross-sectional sample was prepared by mechanical grinding and polishing. The last mechanical polishing step was 0.5 μm sandpaper to keep the edges sharp and non-damaged. The final preparation step was electropolishing in a Struer A2 solution for 2 s (nominally 15–60 s would be used) to keep the sample edges as sharp as possible. Attempts at electropolishing for 5–10 s produced slightly rounded edges destroying the crack-adjacent layer of grains. It was believed for the given material under the given electropolishing conditions (2 s at 30 V DC), $\sim$3 μm of material was removed near the crack edge.

EBSD analysis was performed on a VERSA 3D FEG scanning electron microscope. The operational voltage was 20 kV. A rectangular grid was used; step size varied from 1 to 2 μm for general structure scan to 125 nm for high-resolution

scans in the crack-adjacent area. To characterize plastic strain distribution, several EBSD strain metrics were used: (1) Kernel Average Misorientation or KAM, (2) Grain Reference Orientation Deviation or GROD, and (3) Grain Average Misorientation or GAM. These metrics are widely described and analyzed in the literature [11–13]. Unless otherwise stated, all KAM, GROD, and KAM values discussed below in the text were calculated for a step size of 125 nm.

The possibility to introduce artificial damage was considered during specimen preparation. Bulk material was analyzed, and multiple scans were performed after the electropolishing during 15 s. It eliminated ~12–15 micron near-surface layer and provided strain- and scratch-free surface. KAM, GAM and other EBSD strain metrics for the bulk, well-polished material, were compared with the results for the crack-adjacent area.

Experimental Results and Discussion

After sample preparation, several EBSD scans were performed at a depth of ~1.5–1.7 mm below the fracture surface, below the SCC and other deformed areas, to analyze the material structure and phase composition. Figure 3 shows typical EBSD data for the bulk material. The irradiated material had relatively small average grain size, about 10 μm, and a pronounced bimodal grain size distribution. Small grains formed specific clusters and bands, and large grains often grouped together. Whereas the bimodal grain distribution was observed for all analyzed areas, the fraction and the average size of large grains varied slightly across the structure suggesting some minor structure inhomogeneity.

Two phases were identified: (1) austenite, face-centered-cubic, and (2) delta-ferrite, body-centered-cubic; phase identification was confirmed by hand analysis of Kikuchi patterns. The amount of delta-ferrite visible with EBSD was

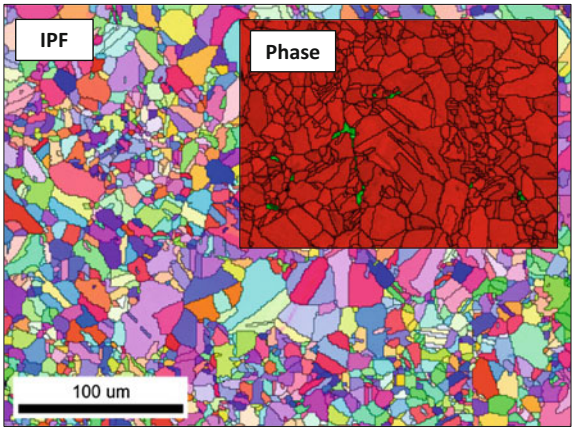

Fig. 3 EBSD IPF map showing grain morphology for the investigated material. Insertion demonstrates the Phase map for the same area (austenite is red, delta-ferrite is green)

estimated to be ~1–1.5%. Ferrite grains formed groups and colonies; the ferrite grains often had larger KAM values compared to the surrounding austenite grains. No visible texturing was observed. The bulk structure was found to be consistent with an annealed structure; no specific signs of pre- or post-irradiation cold work was observed using EBSD. The GROD values for most grains were between 0.1–0.2°. Average GAM parameter for the non-deformed bulk material was ~0.13–0.15°. Average KAM value for austenite was ~0.13–0.17°; ferrite grains in bulk often had slightly higher KAM values and were excluded from analysis.

Figure 4 shows an example of the EBSD data set collected along the crack propagation path. The scan was performed at a magnification of 1000× with 125 nm step (pitch). The separate scans taken along the crack path, overlapped at ~20–30 μm, allowing for stitching. The depth (distance from the crack edge) varied slightly for different scans from ~30–40 to 50–70 μm depending on the local crack trajectory. As expected, such depth should reveal plastic strain in the crack-adjacent layer and show strain gradients.

It is important to underline that, although the scan location was known, it was very difficult, if possible at all, to connect the collected EBSD data to the particular stress intensity factor value or other parameters during the CGR test [9]. The CGR testing provides an average crack length value [7, 10] whereas crack front often had a curved or complex shape (Fig. 2), so only rough K-value may be estimated.

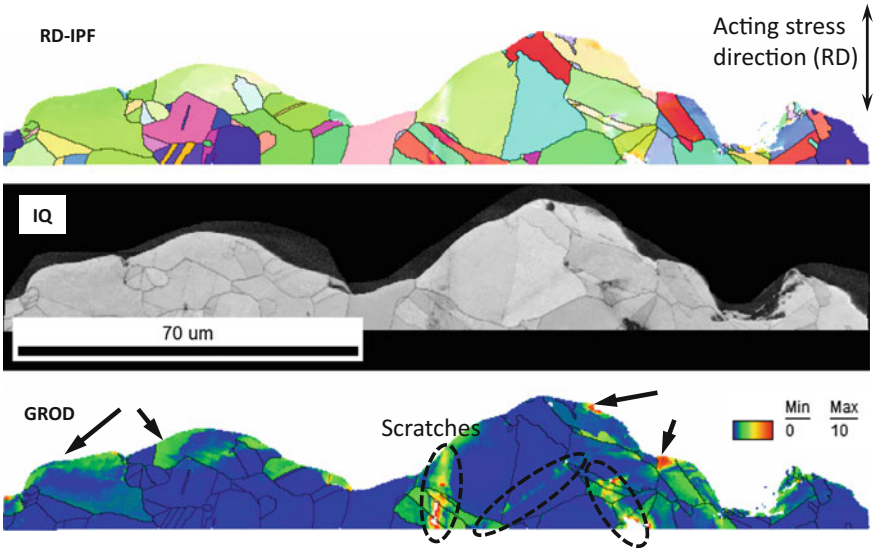

Fig. 4 Typical EBSD dataset for the crack-adjacent area: IPF (Inverse Pole Figure), colored in the RD (acting stress) direction, IQ (Image Quality), and GROD (Grain Reference Misorientation Deviation) maps. Black arrows mark locations with high local strain level; dashed ovals show scratches introduced during specimen preparation

As follows from the EBSD results, the crack-adjacent grains often have some signs of plastic strain; for the GROD map in Fig. 4, plastic strain is visible as a smooth change in color from blue to green and yellow. The width of the crack-adjacent area with signs of plastic strain is ~10–15 μm, and is slightly more in some cases. GROD value for the crack-adjacent grains may reach ~10° for some grains.

An important feature in Fig. 4 is the absence or very low level of misorientation in many crack-adjacent grains. Instead of high strain level in the neighboring grains, a significant grain fraction had practically zero misorientation variations.

Figure 5 shows an additional EBSD data set with one specific feature. Many grains in the GROD map are strain free (blue color); however, grains in the image center show pronounced local misorientation. The deformed grains are grouped together, contrasting with the neighboring weakly or non-deformed area. These highly deformed areas, termed below as "deformation hot spots," occupied ~10–15% of the overall analyzed crack path.

Figure 6 shows the "hot spot" from Fig. 5 in more detail providing GAM and KAM maps. One may see visible fluctuations in KAM and GAM color codes

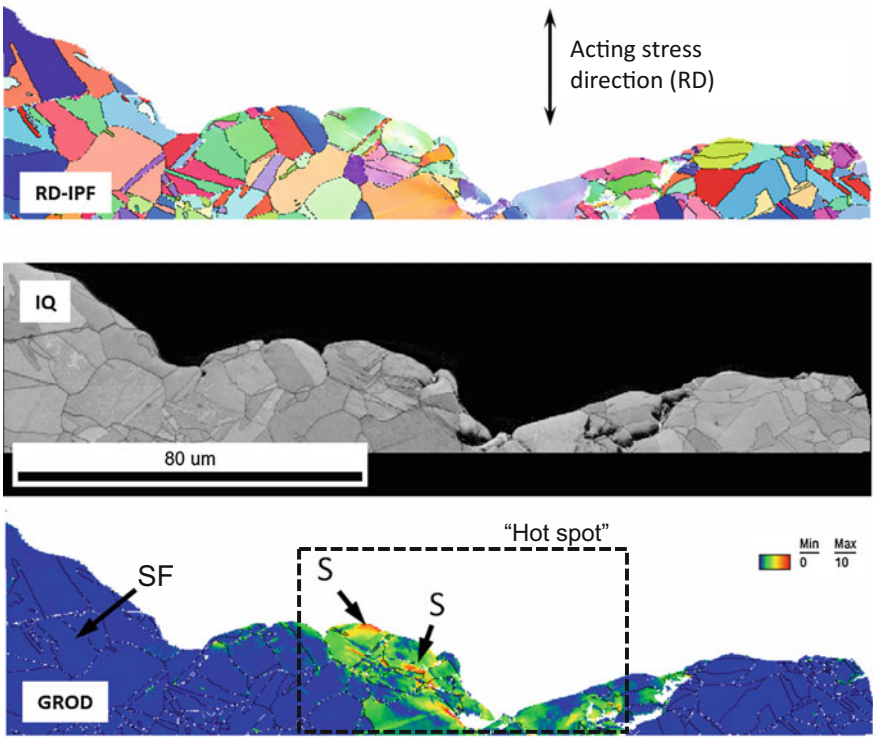

Fig. 5 EBSD data for the crack-adjacent area showing a spot with high local strain level. S: areas with high local misorientation (GROD). The GROD scale here was limited by 10°

images representing higher deformation values at this particular location, the depth of these features extending ~15–25 μm. These features suggest the presence of pronounced slip lines or dislocation channels. Dislocation channels (slip bands), as a rule, are not expected to appear in the image quality (IQ) maps. However, for this particular location, Fig. 6, some darker contrasting feature is visible in the IQ maps that correlate to the KAM and GROD maps. Grain boundary network map (overlayed on the IQ map of Fig. 6) also demonstrated several small grains separated by low-angle boundaries. One may argue these subgrains formed during cracking.

Figure 7 shows another unique region containing a small (~20–25 μm) secondary crack. Here, the IQ map shows some widening of the secondary crack away from the main crack; the lose of the crack edge material due to specimen preparation (electropolishing) may be estimated as ~2–3 μm or less for each crack side. Additionally, one may see that electropolishing induced rounding of the crack edges making the analysis of the crack surface oxidation unobtainable.

By analogy with the above-discussed results, one may see strong inhomogeneity of plastic strain in the GROD and KAM maps, Fig. 7; many grains were strain free, with GAM < 0.2°, which is close to the bulk value, whereas others experienced

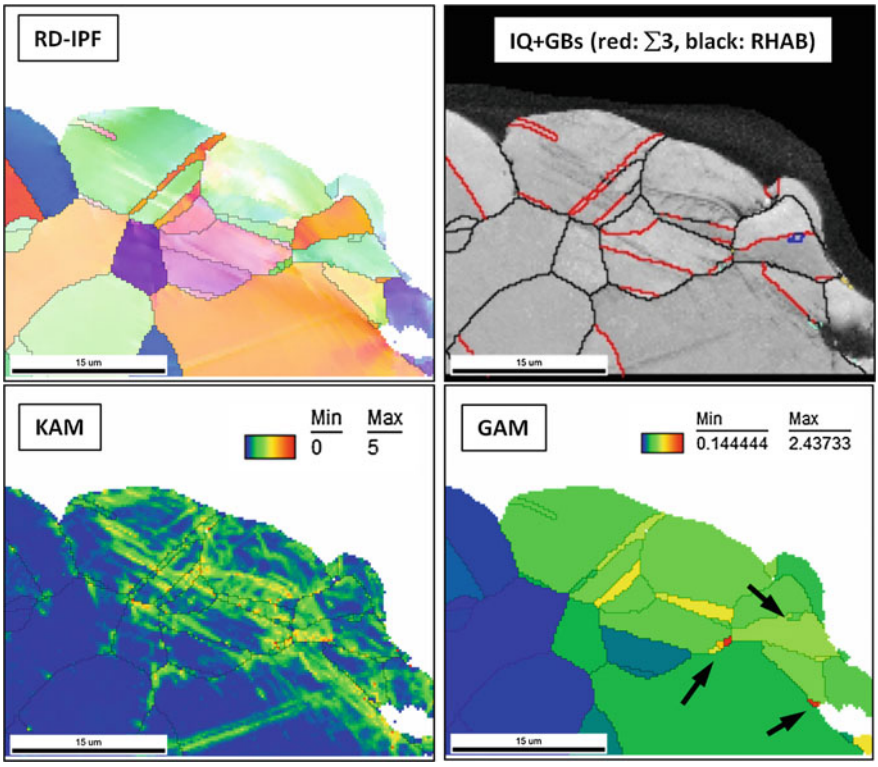

Fig. 6 EBSD data set for the highly-strained area (deformation "hot spot")

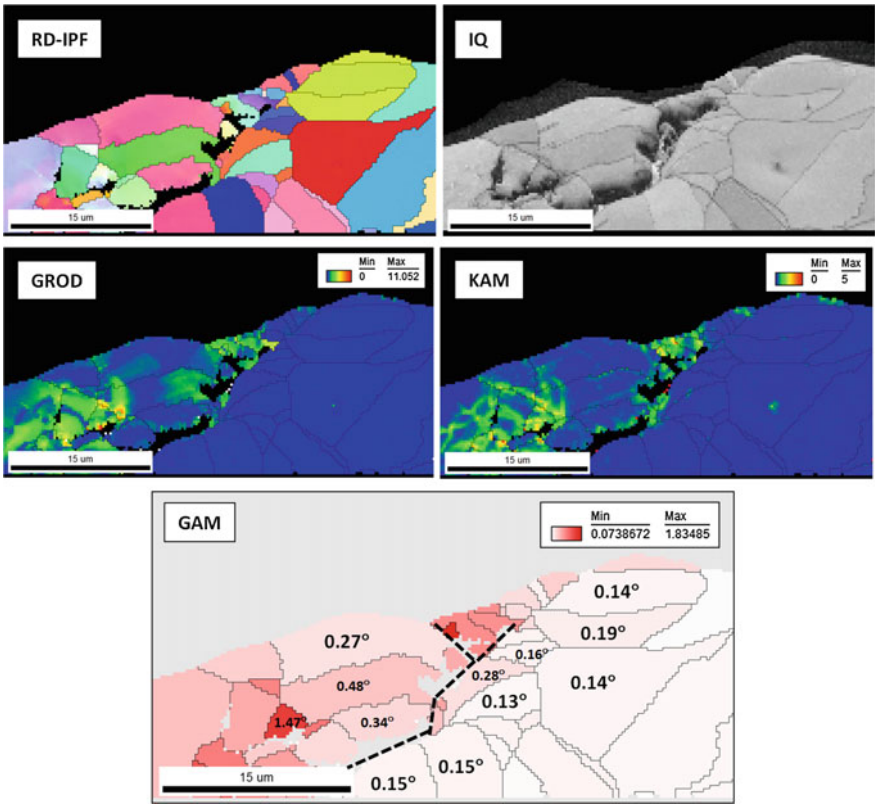

Fig. 7 EBSD dataset for the area with small secondary crack (dashed black line). Step size 125 nm. The map shows the GAM value for some crack-adjacent grains

pronounced plastic strain. These results suggest crack may propagate via the structure at stresses significantly lower than the material yield stress. In some cases, the crack tip movement through the structure did not induce plastic strain in many crack-adjacent grains.

To measure the thickness of the plastically deformed layer, a detailed analysis of the KAM profiles was conducted. To reduce local fluctuations and noise level, the KAM values were averaged for 10 pixels located at the same depth, and the profile was calculated in the normal direction relative to the fracture surface. Figure 8 shows several KAM profiles for the most typical areas. Profiles #1 and #2 intersect several strain-induced features at small depths (<5 μm), which look like low-angle (<5°) in-grain boundary (LAB). LABs provide a small local increase in KAM (from ~0.15 to 0.18°, i.e., bulk level, to ~0.4–0.5°). Below ~5 μm the material appeared to be unstrained, and the KAM profile curves (#1 and #2) were close to the bulk values (~0.18°). Interestingly, LABs often presented in the austenitic grains near the crack edge. These structure elements (LAB) might be seen as a sharp

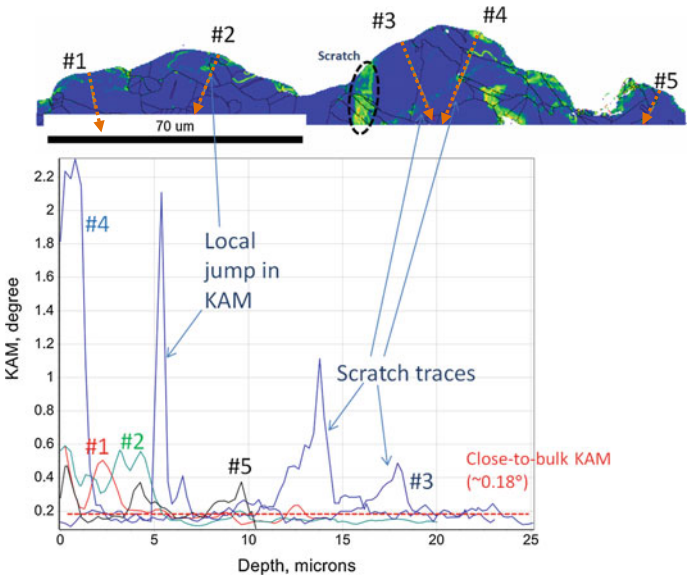

Fig. 8 KAM profiles (#1–5) for the EBSD scan shown in Fig. 4. The average width of 10 data points

local increase in KAM, and often were also visible in the IQ maps. The LABs were much rarer in bulk, far from the crack edge.

Profiles #3 and #5 were taken in the grains without visible plastic strain. Indeed, regardless of the depth, the KAM value remained around bulk values ($\sim$0.18°). It appears that material at these locations did not reveal plastic strains even in the crack vicinity. The local fluctuation in profile #3 at 10–15 μm of depth was caused by a scratch. Profile #4 had few maximums; the first maximum, at the crack edge, was most likely induced by plastic strain. The second, at $\sim$5–6 μm depth, corresponded to the LAB and the last one, at $\sim$13 μm depth was caused by surface scratching. Thus, as follows from the KAM profiles, most plastic strain was localized in the $\sim$5–10 μm layers.

The complex character of strain localization required further analysis to explain the appearance of multiple strain-free grains. Grain orientation to the acting stress strongly influences the elastic and plastic behavior of the grain (Schmid and Taylor factors). If crack propagation depends on the stress field near the crack tip, and on the grain Schmid factor, grain population in the crack-adjacent area may be different than that of the bulk. Figure 9 shows this comparison between the crack-adjacent grains and that of the bulk material. The number of data points was limited (only two scans were included in the figure) to keep the image readable. As follows from the plot, there is no pronounced difference between cracked and non-cracked grain populations. At least, this difference was weak and did not lead to the pronounced depopulation of any unit triangle area.

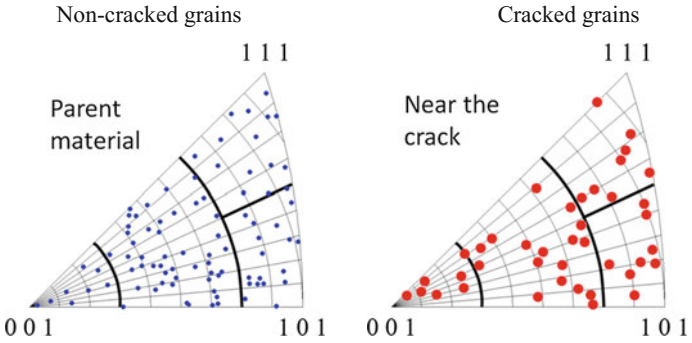

Fig. 9 The orientation of crack-adjacent grains compared to randomly selected grains in bulk. The IPFs are plotted with respect to the acting stress during the crack growth test

To analyze the grain orientation role in more detail, a series of EBSD scans (>250 crack-adjacent grains) were merged, and the orientation of the crack-adjacent grains was compared to the summary data for the grains farther from the crack (Fig. 10). As shown in the texture plots, the general texturing in the bulk material, far from crack, was weak enough, only $\sim 1.53 \times$ random. The most pronounced texturing component was an increased fraction of [001]-oriented grains in the crack propagation direction (A-group), [010] in Fig. 10. Two other specific areas (B, C) were just slightly above the average (~ 1.1 and $\sim 1.2 \times$ random, respectively).

Comparing the grain orientation patterns in bulk and near the crack, one may see that crack-adjacent grain orientations are, in general, close to the non-cracked ones. Grains with [001]-orientation with respect to the crack propagation direction (group marked as "A" in Fig. 10) have a texture index of $\sim 1.5 \times$ random in bulk

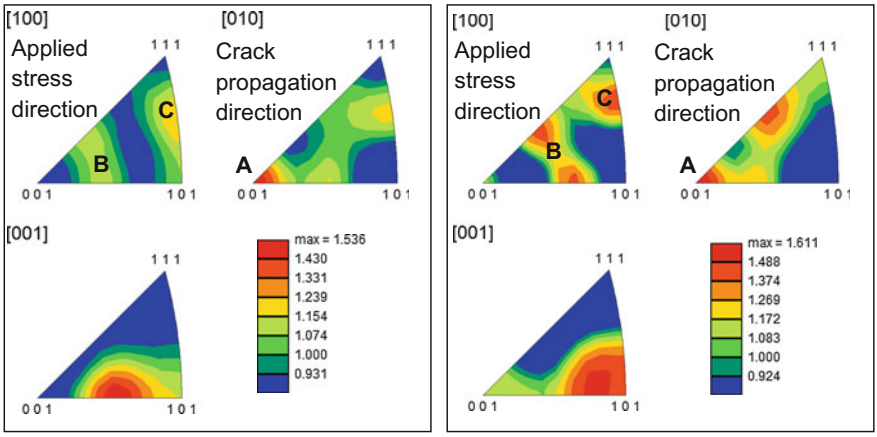

Fig. 10 The texture in the bulk non-cracked material (left) and summary texture plot for the crack adjacent grains. The summary plot for 8 scans (same step size and imaging conditions)

and ~1.6 × random near the crack. Two other specific areas (B and C) have similar texture indexes (B: ~1.1 × random in bulk and ~ 1.5 × random after cracking; C: ~1.2 × random in bulk and ~1.6 × random after cracking). Some weak secondary effects may be present; however, they appear to be insignificant.

At the moment, it is possible to conclude that grain orientation plays a weak, if any, role on the stress corrosion cracks advancing. No one grain population (e.g., grains with [111] or [001] orientation) dominated along the crack path.

Conclusions

In the present work, the stress corrosion crack propagation was investigated for a highly-irradiated (10.4 dpa) austenitic steel specimen. Using SEM-EBSD approach, plastic stain fields were evaluated in a neutron-irradiated round compact tension specimen of model 304 steel tested under NWC conditions. No pronounced crack branching was observed; only a few short, less than 40–50 μm secondary cracks were found in the structure.

EBSD analysis revealed strong inhomogeneity in plastic strain distribution along the crack path. Some crack-adjacent grains remained virtually strain-free whereas few grains experienced strong plastic strain. These areas were presumed to be "plastic bridges" or "ductile ligaments." The width of the plastically deformed areas along the crack was, in most cases, 5–10 μm or less; this value increased up to ~20–50 μm inside the plastic bridges.

Grain orientation with respect to the acting stress direction was not a major factor controlling crack propagation. No crystallography orientation susceptible to crack propagation was identified by this work.

References

1. K. Fukuya, Current understanding of radiation-induced degradation in light water reactor structural materials. J. Nucl. Sci. Technol. **50**, 213–254 (2013)
2. Z. Jiao, G. Was, Impact of localized deformation on IASCC in austenitic stainless steels. J. Nucl. Mater. **408**, 246–256 (2011)
3. G.S. Was, Y. Ashida, P.L. Andresen, Irradiation-assisted stress corrosion cracking. Corros. Rev. **29**, 7–49 (2011)
4. J. Massoud, P. Dubuisson, P. Scott, V. Chamardine, CIR II program: description of the Boris 6 and 7 experiments in the BOR-60 fast breeder reactor, *EPRI Report*, vol. 1011787 (2005)
5. P. Scott, Materials reliability program: a review of the cooperative irradiation assisted stress corrosion cracking research program (MRP-98), *EPRI Report*, vol. 1002807 (2003)
6. M. Ernestova, J. Burda, Crack growth testing of tailored alloys from Boris 6 and 7 irradiations, *EPRI Report*, vol. 1021235 (2009)
7. A. Jenssen, J. Stjärnsäter, R. Pathania, Crack growth rates of irradiated commercial stainless steels in BWR and PWR environments, in *15th International Conference on Environmental*

Degradation of Materials in Nuclear Power Systems-Water Reactors (Wiley Online Library, 2011), pp. 1229–1240
8. S. Van Dyck, IASCC mechanisms-controlling material factors: SCC crack-growth tests on selected Boris-6 tailored heats, *Palo Brussels, Belgium: SCK-CEN*, (2009)
9. G.S. Was, Y. Ashida, K.J. Stephenson, A. Flick, P.L. Andersen, Identifying mechanisms and mitigation strategies for irradiation assisted stress corrosion cracking of austenitic steels in LWR core components, *EPRI Report*, vol. 3002003105 (2014)
10. Y. Ashida, A. Flick, P.L. Andresen, G.S. Was, The key factors affecting crack growth behavior of neutron-irradiated austenitic alloys, in *15th International Conference on Environmental Degradation of Materials in Nuclear Power Systems-Water Reactors* (Wiley Online Library, 2011), pp. 1241–1254
11. M. Kamaya, K. Kubushiro, Y. Sakakibara, S. Suzuki, H. Morita, Y. Rika, D. Kobayashi, K. Yamagiwa, T. Nishioka, Y. Yamazaki et al., Round robin crystal orientation measurement using EBSD for damage assessment. Mech. Eng. J. **3**, 16–77 (2016)
12. S. Wroski, J. Tarasiuk, B. Bacroix, A. Baczmaski, C. Braham, Investigation of plastic deformation heterogeneities in duplex steel by EBSD. Mater. Charact. **73**, 52–60 (2012)
13. R. Yoda, T. Yokomaku, N. Tsuji, Plastic deformation and creep damage evaluations of type 316 austenitic stainless steels by EBSD. Mater. Charact. **61**, 913–922 (2010)

Part XII
PWR Oxides and Deposits

Effect of Grain Orientation on Irradiation Assisted Corrosion of 316L Stainless Steel in Simulated PWR Primary Water

Rigel D. Hanbury and Gary S. Was

Abstract Simultaneous exposure of 316L stainless steel to a proton beam and high purity water containing 3 wppm H_2 was used to study the effect of radiation on corrosion. Protons create displacement damage in the solid and radiolysis products in the water. Irradiations lasted 24 h at a damage rate of 7×10^{-7} dpa/s. The 316L was solution annealed at 1050 °C for 30 min, 5% cold worked, and heat treated at 1100 °C for 10 min resulting in 23 μm grains. Samples were pre-characterized by EBSD to correlate grain orientation with oxide properties measured by Raman spectroscopy and TEM. Following irradiation, hematite was identified exclusively in areas exposed to radiolyzed water, both under the beam and downstream. Inner oxide layers in the unirradiated region had a strong dependence on grain orientation, whereas the irradiated region has little to no grain orientation dependence.

Keywords Irradiation accelerated corrosion · Proton irradiation · 316L stainless steel · Grain orientation

Introduction

Light water reactors create a unique environment for corrosion due to high temperature water and radiation fields. Data on the corrosion of in-core components is scarce, so the effects of radiation on the corrosion of materials is not well understood. Simulation of the radiation environment is the best recourse for obtaining data on radiation corrosion. Several studies have found an increase in corrosion rate of stainless steels under irradiation [1–5].

Exposure of stainless steel to high temperature water results in a passive duplex oxide structure [6]. The protective inner layer consists of Cr-rich spinels, and the outer layer is faceted magnetite (Fe_3O_4) crystallites under PWR conditions. The inner layer forms a diffusion barrier for additional oxidation, so faster corrosion

R.D. Hanbury (✉) · G.S. Was
University of Michigan, 2355 Bonisteel Blvd, Ann Arbor, MI 48109-1204, USA
e-mail: rigelh@umich.edu

J.H. Jackson et al. (eds.), *Proceedings of the 18th International Conference on Environmental Degradation of Materials in Nuclear Power Systems – Water Reactors*, The Minerals, Metals & Materials Series, https://doi.org/10.1007/978-3-319-68454-3_79

kinetics tend to create thicker inner oxide layers. The grain orientation of stainless steel has a substantial impact on the inner oxide thickness observed over these grains [7, 8]. Outer oxide particles grow by precipitation of metal (mostly iron) ions from the solution and are faceted under more reducing conditions and equiaxed under more oxidizing conditions [9, 10].

Radiation can affect both the corroding material directly by displacement damage, and it can affect the corrosive medium via radiolysis. Radiolysis has a clear effect by changing the electrochemical potential (ECP) of the water by producing long-lived species like O_2 and H_2O_2 along with short-lived radical oxidizing species. The effect of radiolysis is suppressed—but not nullified—by the addition of hydrogen. Some radiolyzed water produced at the corroding interface will contribute to corrosion before being scavenged by hydrogen. The ion linear energy transfer (LET) greatly changes the yield of species produced by radiolysis; proton irradiation is a much closer approximation to neutron-induced radiolysis than gamma radiation [11, 12]. Therefore, ion irradiations are necessary for simulating the full effect of radiolysis on LWR core components.

Displacement damage in both the metal and the oxide is the other key feature of radiation corrosion. Sequential irradiation and corrosion of stainless steel has been shown to have very little, if any, impact on the corrosion rate [7]. Point defect diffusion in the metal and oxide may both contribute to enhanced oxidation rates of *in situ* radiation corrosion. Passive corrosion is a diffusion limited process; even a small change in diffusivity can alter the kinetics of corrosion.

In situ irradiation corrosion is one of the only experimental methods for testing the contribution of radiation effects to corrosion behavior. Proton irradiations have the advantage of creating cascade damage in the solid and high LET radiolysis product generation when compared to electron or gamma irradiations. Proton irradiation of 316L stainless steel has been shown to increase the system ECP [5, 13]. This paper is focused on exploring the effect of proton irradiation on the corrosion of 316L stainless steel, particularly grain orientation effects on corrosion.

Experiment

In order to study the effects of water radiolysis and displacement damage on corrosion behavior, an *in situ* radiation corrosion cell is used in the Michigan Ion Beam Laboratory. The design of this irradiation accelerated corrosion (IAC) cell is detailed in an earlier publication [14]. To achieve radiation effects at the corroding surface, the sample material acts as a window for protons entering the cell from the beamline. The sample also serves as a structural support for separating the high pressure water cell from the high vacuum beamline.

Sample Design

Deformation from water pressure is mitigated by introducing a 17-4 PH steel backing material to the sample holder. A sketch of the sample assembly with the backing material can be seen in Fig. 1. The combined thickness of the backing and sample materials is controlled such that 5.4 MeV protons are transmitted in the water at an energy of 1.5 MeV. The proton energy of 5.4 MeV was selected to avoid the 5.45 meV threshold for the $^{56}Fe(p,n)^{56}Co$ reaction that greatly increases residual activity. The backing also serves to decrease the radioactivity of the sample material by reducing the energy of protons impinging on the sample material.

The 17-4 PH backing material is prepared by cutting pieces from an 8 mm rod and thinning down to roughly 40 μm with 600 grit SiC paper. The 316L sample material is cut from a 4.45 cm diameter rod by slicing 300 μm wafers and 8 mm discs are mechanically punched from the wafer. These discs are then polished with up to 800 grit SiC paper, then polished down to 0.25 μm diamond solution, and finally vibratory polished with 0.050 μm colloidal silica. The opposite side is thinned to about 35 μm with up to 600 grit SiC paper such that the combined thickness of the two materials are 75 μm. Both thinned discs are sandwiched

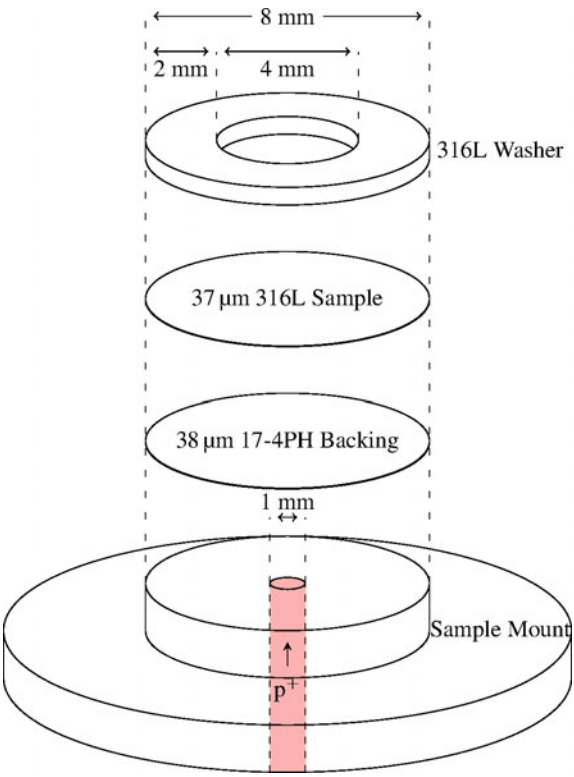

Fig. 1 Sketch of the IAC sample mount assembly with backing material

between a 316L sample mount with a 1 mm diameter aperture and a 316L washer as in Fig. 1 and spot welded around the perimeter. This assembly is pressurized to 14.5 MPa in room temperature water to ensure there will be no leak into the beamline and that there is minimal deformation of the sample material. Following this, the washer is ground down to about 100 μm to allow water flow across the sample surface in the corrosion cell. An EBSD map is then collected from the sample surface where the remaining washer thickness does not shadow the signal (about 2.5 mm diameter around the center). Finally, the sample assembly is cleaned in acetone, methanol, and ethanol before 10 min argon plasma cleaning to remove residual colloidal silica and carbon deposition from the EBSD mapping.

Corrosion Cell

For the experiment in this work, a 316L stainless steel was exposed to 320 °C water with 3 wppm H_2. The composition of the material used is given in Table 1. The 316L stainless steel was solution annealed at 1050 °C for 30 min, 5% cold worked, and heat treated at 1100 °C for 10 min resulting in 23 μm average grain size. After a 3 h heating period, a raster-scanned 5.4 MeV proton beam is used to achieve a dose rate of 7×10^{-7} dpa/s for 24 h, after which the cell immediately begins cooling.

Characterization

Raman spectra were collected using a Renishaw inVia confocal Raman microscope with a 633 nm laser. SEM surface imaging was performed using an FEI Nova. Cross-sectional specimens were prepared by FIB using an FEI Helios, and inner oxide thickness was measured using bright field imaging in conventional TEM with a JEOL 2010F. Each cross-sectional specimen was fully imaged, and the inner oxide thickness was measured continuously. Transmission Kikuchi diffraction was used to identify lift-out grain orientation for correlation with oxide thickness measurements. Energy dispersive X-ray spectroscopy (EDS) was performed on the cross-sectional samples with a JEOL 2100 in STEM mode.

Table 1 Composition of 316L alloy heat 626032 (in wt%)

C	Cr	Ni	Mo	Mn	Si	N	O	S	P
0.028	17.6	12	2.39	1.78	0.59	0.08	0.003	0.01	0.01

Results and Discussion

There are two main effects of irradiation that can be observed by comparing the irradiated and unirradiated region oxides with Raman spectroscopy in Fig. 2. First, hematite is clearly present in the irradiated region, whereas the unirradiated region is mostly hematite free [15]. A portion of the area not exposed to the beam has a strong hematite signal and corresponds to the radiolysis affected region downstream from the irradiated area. This area was not considered in this work as all analysis of the unirradiated region is from the remaining area with no hematite signal. The second effect is the shift in the spinel A_{1g} peak at 675 cm^{-1} in the unirradiated region to 661 cm^{-1} in the irradiated region. This shift implies a decrease in the nickel and chromium content of the spinel as this peak becomes more narrowly peaked at Fe_3O_4 [16].

Outer oxide particle distributions can be compared qualitatively from SEM images of both regions in Fig. 3. The coverage of outer oxide particles in the irradiated area is nearly 100% with smaller equiaxed particles. In the unirradiated region, the outer oxide consists of faceted particles with coverage that varies between grains. Grain boundaries can often be distinguished clearly in the unirradiated area by locating a sharp change in the number density and average size of outer oxide particles. Since the outer oxide morphology is homogeneous across grains in the irradiated region, there are no clear grain boundaries in SEM imaging. For this reason, EBSD prior to oxidation is an essential tool for gathering grain orientation data by selecting lift-out sites. The difference in morphology of the

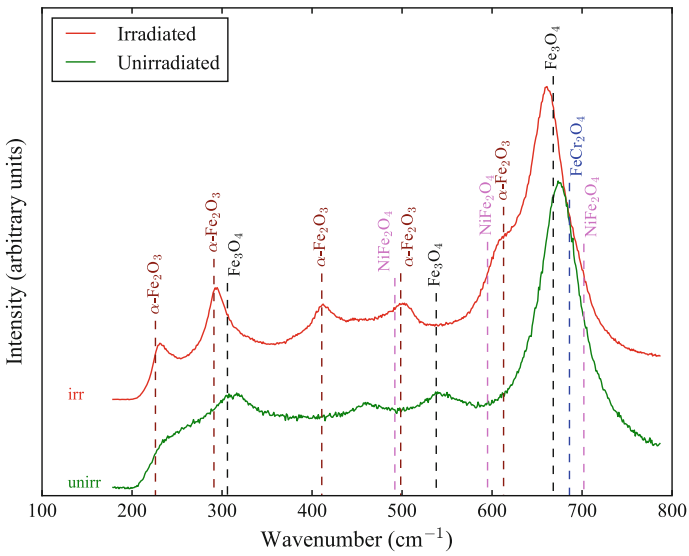

Fig. 2 Raman spectra comparison of the irradiated and unirradiated regions of 316L exposed to 320 °C water with 3 wppm H_2 for 24 h with a 633 nm laser; peak data from [15]

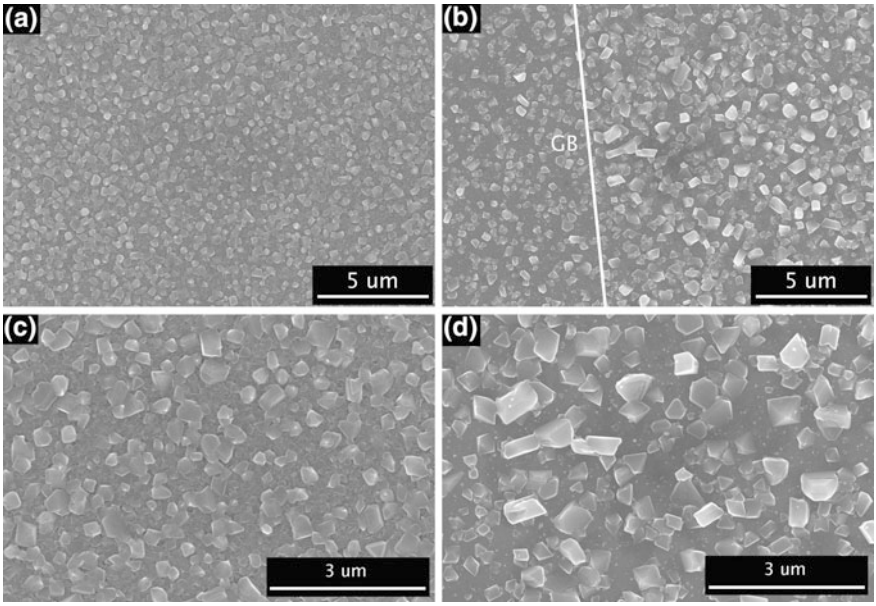

Fig. 3 SEM images of outer oxide coverage and morphology for both irradiated **a** and **c** and unirradiated **b** and **d** areas of 316L exposed to 320 °C water with 3 wppm H_2 for 24 h

particles between the two regions is likely due to the structure change from magnetite in the unirradiated region to hematite under irradiation that was confirmed by Raman spectroscopy.

A comparison of the TEM imaged oxides in the irradiated and unirradiated regions is in Fig. 4. The original metal surface can be seen at the interface between the inner and outer oxide layers in the unirradiated area. The irradiated region, however, the interface is wavy, indicating penetration into the underlying metal and dissolution of the alloy.

A collection of the inner oxide thickness and grain orientation measurements for various grains in both irradiated and unirradiated regions is in Fig. 5. There is a clear distinction between unirradiated grains regarding inner oxide thickness; unfortunately, there is insufficient data to make a correlation between specific grain orientations and oxide thickness. Oxide thickness measurements in the irradiated region, however, show little difference between grains. A ratio between adjacent grain inner oxide thickness illustrates the large differences in the unirradiated region and the small differences in the irradiated region in Fig. 6.

In Fig. 7, line-scans show that the irradiated region has an inner oxide largely depleted in chromium compared with the chromium rich inner oxide of the unirradiated region. The interface between the metal and the inner oxide has some chromium enrichment in a thin oxide film that likely forms during the cooldown of the corrosion cell. Chromium dissolution is indicative of transpassive corrosion, which is corroborated by the loss of the original metal surface.

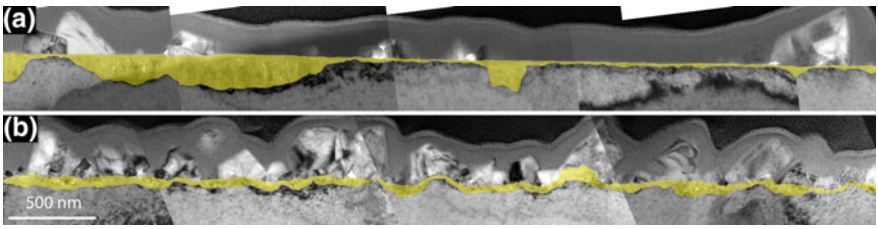

Fig. 4 Oxide layers imaged in conventional TEM in the unirradiated region **a** and irradiated region **b** of 316L exposed to 320 °C water with 3 wppm H_2 for 24 h

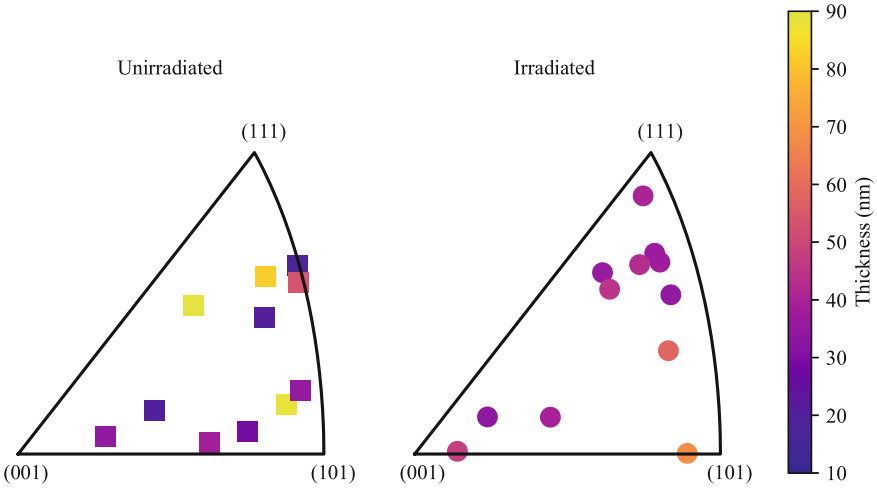

Fig. 5 Oxide thickness as a function of grain orientation for both irradiated and unirradiated areas of 316L exposed to 320 °C water with 3 wppm H_2 for 24 h

Data from Raman spectroscopy has confirmed the presence of hematite in the irradiated region oxide, and the change in outer oxide particle morphology from the SEM images indicates the change in phase from magnetite to hematite. This change in ECP is most likely due to oxidizing radiolysis products, and the effect has changed the operating thermodynamic regime to hematite stability. Depletion of chromium from the inner oxide layer was observed in the irradiated area using EDS and is supported by Raman spectroscopy. This also indicates a more oxidative potential where the solubility of chromium ions has reached the point of active dissolution. Inner oxide thickness depends heavily on chromium content, so grain orientation effects should be diminished with chromium dissolution. The loss of the original metal surface observed in cross-sectional TEM, and the intermediate thicknesses measured in the irradiated area both indicate dissolution. Therefore, passivity is lost under irradiation in favor of transpassive corrosion with both active oxide growth and dissolution. This conclusion matches earlier results on primarily

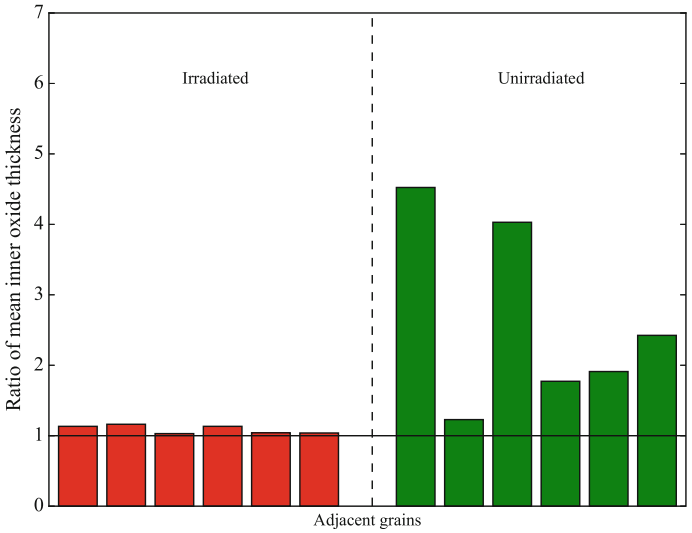

Fig. 6 Inner oxide thickness comparison between grains in both irradiated and unirradiated regions of 316L exposed to 320 °C water with 3 wppm H_2 for 24 h

higher dose rate (7×10^{-6} dpa/s) proton irradiation corrosion experiments on 26% cold worked 316L [5].

Dissolution is a significant form of corrosion in the irradiated area, but not in the unirradiated area. The effect of dissolution on the grain orientation dependence of corrosion cannot be determined yet since the rate of dissolution has not been measured. There is a stark contrast between inner oxide thickness above some grains in the unirradiated area (Fig. 5). Inner oxide layers in the irradiated area are much more uniform in thickness; however, dissolution may be responsible for suppressing any measureable grain-to-grain differences.

Assuming the oxide dissolution rate is driven by solubility and is nearly constant within the irradiated region, the expected oxide film behavior should reach an equilibrium thickness. When the oxide is first growing, the oxidation rate is greater than the dissolution rate, so an oxide film forms and presents a diffusion barrier to the rate of oxidation. Once the rate of diffusion becomes equal to the dissolution rate, the oxide film reaches a steady state thickness, and the corrosion rate becomes constant and equal to the dissolution rate. If the protectiveness of the inner oxide is dependent on the underlying metal grain orientation, then the equilibrium thickness will be inversely related to the protectiveness. However, once the diffusion barrier reaches its equilibrium thickness, no further change will accumulate between grains. Therefore, further work is needed to determine if there is an effect of grain orientation on corrosion under irradiation.

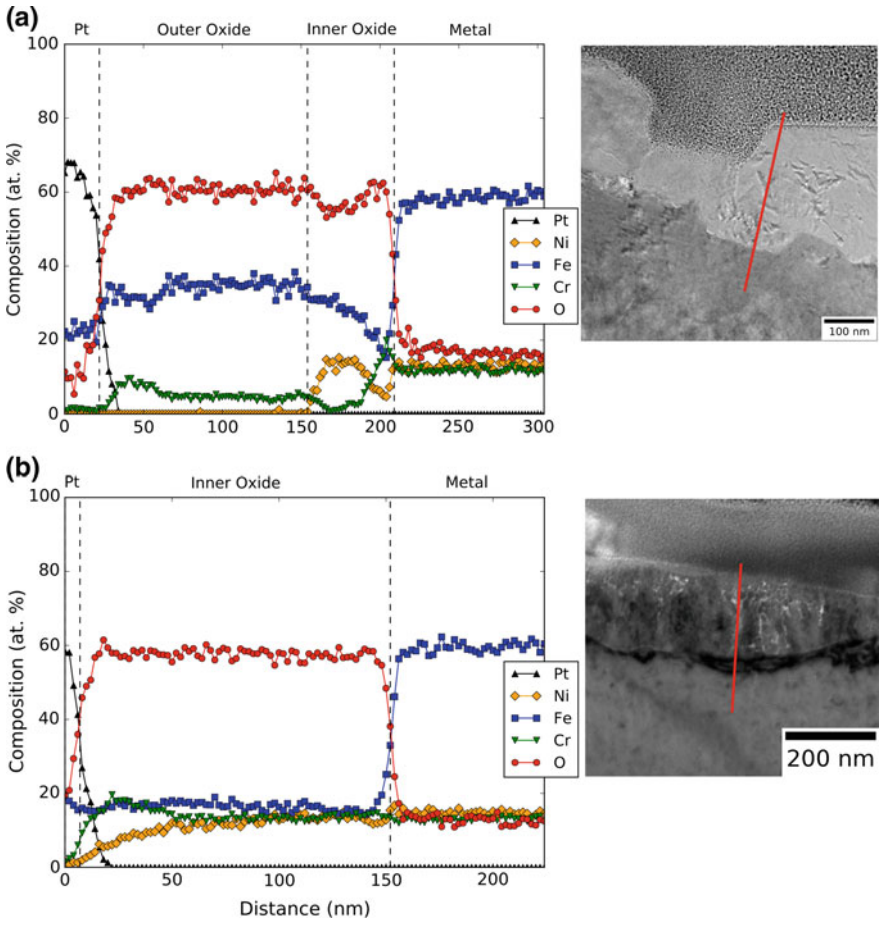

Fig. 7 STEM-EDS line-scans across oxides in the irradiated (above) and unirradiated (below) regions of 316L exposed to 320 °C water with 3 wppm H_2 for 24 h (Color figure online)

Conclusions

Simultaneous proton irradiation and corrosion of 316L stainless steel was performed in simulated PWR water and resulted in transpassive corrosion, consisting of oxide film growth and dissolution. The unirradiated region showed a strong dependence of inner oxide thickness to grain orientation, but proton irradiation resulted in a decrease of sensitivity to grain orientation-dependent oxide growth. Inner oxide thickness is more strongly dependent on dissolution conditions than grain orientation effects, causing no observable grain-to-grain differences in the irradiated region. Therefore, irradiation cause a suppression of grain orientation effects on oxide growth.

Acknowledgements The authors acknowledge the help of the staff and facilities of both the Michigan Ion Beam Laboratory and the Michigan Center for Materials Characterization. This work is supported by EDF Contract No. 8610-5920005571.

References

1. K. Ishigure, M. Kawaguchi, K. Oshoma, N. Fujita, in *The Effect of Radiation on the Corrosion Product Release from Metals in High Temperature Water*. Water Chemistry of Nuclear Reactor Systems 2 (Pergamon Press Ltd, 1981)
2. K. Ishigure, H. Ikuse, K. Oshima, N. Fujita, S. Ono, The effect of radiation on the corrosion product release from metals in high temperature water. Radiat. Phys. Chem. **21**(3), 281–287 (1987)
3. M. Lewis, J. Hunn, Investigations of ion radiation effects at metal/liquid interfaces. J. Nucl. Mater. **265**(3), 325–330 (1999)
4. S. Lapuerta, N. Millard-Pinard, N. Moncoffre, N. Bérerd, H. Jaffrezic, G. Brunel, D. Crusset, T. Mennecart, Origin of the hydrogen involved in iron corrosion under irradiation. Surf. Coat. Technol. **201**(19), 8197–8201 (2007)
5. S.S. Raiman, Irradiation accelerated corrosion of 316L stainless steel in simulated primary water. (Ph.D. thesis, University of Michigan, 2016)
6. B. Stellwag, The mechanism of oxide film formation on austenitic stainless steels in high temperature water. Corros. Sci. **40**(2), 337–370 (1998)
7. Z. Jiao, G. Was, in *15th International Conference on Environmental Degradation of Materials in Nuclear Power Systems-Water Reactors* (Wiley Online Library, 2011), pp. 1329–1338
8. R. Soulas, M. Cheynet, E. Rauch, T. Neisius, L. Legras, C. Domain, Y. Brechet, TEM investigations of the oxide layers formed on a 316L alloy in simulated PWR environment. J. Mater. Sci. **48**(7), 2861–2871 (2013)
9. Y.J. Kim, Characterization of the oxide film formed on type 316 stainless steel in 288 C water in cyclic normal and hydrogen water chemistries. Corrosion **51**(11), 849–860 (1995)
10. Y.J. Kim, Analysis of oxide film formed on type 304 stainless steel in 288 C water containing oxygen, hydrogen, and hydrogen peroxide. Corrosion **55**(1), 81–88 (1999)
11. B. Pastina, J.A. LaVerne, J Physic Chem A **103**(11), 1592–1597 (1999)
12. W.G. Burns, H.E. Sims, Effect of radiation type in water radiolysis. J. Chem. Soc., Faraday Trans. 1 **77**, 2803–2813 (1981)
13. M. Wang, S. Perrin, C. Corbel, D. Féron, Electrochemical behaviour of 316L stainless steel exposed to representative chemistry in pressurised water reactors under proton radiation. J. Electroanal. Chem. **737**, 141–149 (2015)
14. S.S. Raiman, A. Flick, O. Toader, P. Wang, N.A. Samad, Z. Jiao, G.S. Was, A facility for studying irradiation accelerated corrosion in high temperature water. J. Nucl. Mater. **451**(1), 40–47 (2014)
15. B.D. Hosterman, Raman spectroscopic study of solid solution spinel oxides (Ph.D. thesis, University of Nevada, Las Vegas, 2011)
16. S.S. Raiman, D.M. Bartels, G.S. Was, Radiolysis driven changes to oxide stability during irradiation-corrosion of 316L stainless steel in high temperature water. J. Nucl. Mater. **493**, 40–52 (2017)

Finite Element Modelling to Investigate the Mechanisms of CRUD Deposition in PWR

Jiejie Wu, Nicholas Stevens, Fabio Scenini, Brian Connolly, Andy Banks, Andrew Powell and Lara-Jane Pegg

Abstract Corrosion Related Unidentified Deposition (CRUD) in PWR may cause severe issues, such as Tube Support Plate (TSP) blockage, fuel cladding cracking, and subsequently increased radiation doses for workers. The primary objective of this work is to develop an all-inclusive deposition model, which will reproduce the morphology and elucidate the contributing electrokinetic mechanisms. In this paper the development and verification of a model of the streaming current linking the potential distribution and the fluid flow behaviour using the Finite Element Method (FEM) is presented. In the model, coupled anodic and cathodic regions were found at the inlet of a pipe restriction, associated with a region of recirculating flow following the front facing step (FFS). The corresponding current densities and overpotential at the metal/solution interface were calculated. The coupled anode and cathode may explain the observed deposition process—generating deposits at the front facing step first, followed by a region free of deposits and then repeating ripples of deposited material. At the restriction outlet, a cathode was found which balances the current loops. In this paper, the simulated initiation and propagation processes of the electrokinetic deposition are presented.

Keywords CRUD · Electrokinetic deposition · Streaming currents · Multi-physics modelling · Finite element method

Introduction

CRUD was first observed in one of the earliest Canadian reactors in 1950s [1]. It was found that corrosion products from structural components in nuclear plants tend to deposit in different locations, such as restrictions in steam generators and

J. Wu (✉) · N. Stevens · F. Scenini · B. Connolly
The University of Manchester, Manchester, UK
e-mail: jiejie.wu@manchester.ac.uk

A. Banks · A. Powell · L.-J. Pegg
Rolls-Royce Plc, Manchester, UK

J.H. Jackson et al. (eds.), *Proceedings of the 18th International Conference on Environmental Degradation of Materials in Nuclear Power Systems – Water Reactors*, The Minerals, Metals & Materials Series, https://doi.org/10.1007/978-3-319-68454-3_80

instrumentation [2], and fuel cladding [3], causing operational difficulties. Primary flow rate variations due to the deposit formation were observed in some French and US plants [4].

CRUD mainly consists of magnetite (Fe_3O_4) and nickel ferrite ($NiFe_2O_4$) [5]. There are two main kinds of deposits: (a) hard and adherent deposits due to the precipitation from dissolved cations from solution, and (b) porous and loose deposits generated from particulate species [6, 7]. This paper will only focus on the former deposition which is driven by an electrokinetic mechanism. In order to study the behaviour of this deposition, experimental research has been performed by Guillodo et al. [8], who proposed an electrokinetic mechanism of the deposit generation based on the work of Robertson [9] and Woolsey [10]. In Guillodo's work, the deposition was observed at the entrance to a 6 mm diameter restriction, and along the annulus close to the entrance, in high flow rate and high temperature primary coolant condition [4]. Work on CRUD deposition in micro-orifices with very high flow velocities has been performed by Scenini et al. [11]. The electrochemical potential distribution through the annulus of a test has been measured [12] and the anodic and cathodic behaviour of the current component at the front face of an orifice where the CRUD is known to deposit has been investigated [13].

The modelling of deposition is not widely studied. Some simulation research of the particulate deposition can be found in some references [14–16]. However, the numerical simulation of the electrokinetic deposition is not often seen. This paper aims to simulate the initiation and propagation processes of the electrokinetic deposition in pipe restrictions, looking at the current loops created by an electrokinetic current arising from flow over a charged surface in the region of a change in the internal geometry which acts to interrupt the flow profile. The polarization created by these loops is studied and, under the assumption that anodic polarization causes enhanced deposition, a hypothesis is proposed to explain the observed 'rippled' geometry reported for CRUD deposition.

Electrokinetic Mechanism

When a charged solid wall (metal) surface is exposed to an electrolyte, an Electrical Double Layer (EDL) with excess charge will be formed which consists of two layers; the *Helmholtz layer* and the *diffuse layer* as shown in Fig. 1. The *Helmholtz layer* is immobile and adherent to the wall surface. A slip plane can be found between these two layers, where the *diffuse layer* starts to move. The excess charge displacement in the diffuse layer caused by the fluid flow velocity generates a streaming current, I_s, along the wall surface as shown in Fig. 2a. The potential at the slip plane (Fig. 2b) with respect to the value in the bulk solution is known as zeta (ζ) potential [17]. Where the zeta potential value is negative, the wall surface is negatively charged and the EDL has excess positive charge.

When the fluid flows over sharp geometric disturbances as shown in Fig. 2c, the streaming current will change as the flow velocity changes. Where the solution

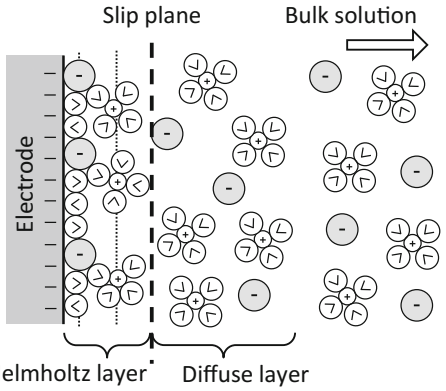

Fig. 1 Electrical Double Layer (EDL) [17–19]

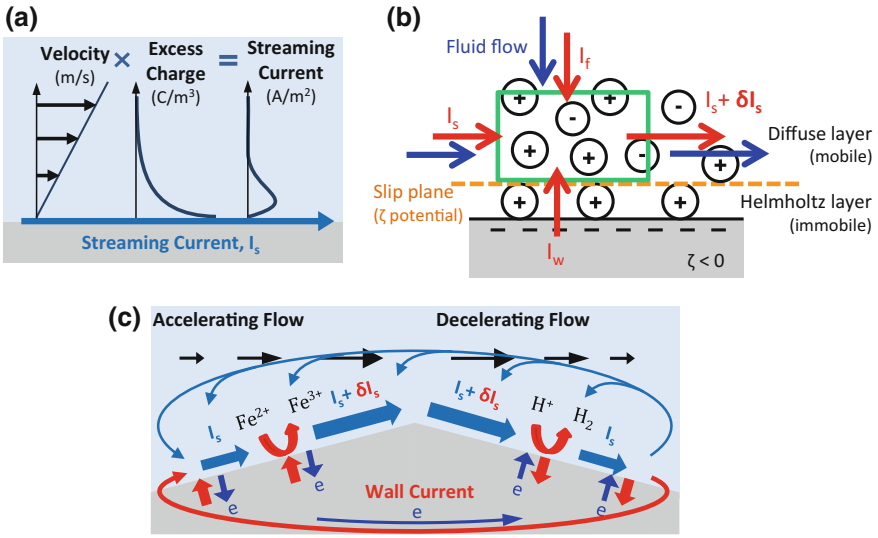

Fig. 2 Streaming current ($\zeta < 0$). **a** Generation. **b** Control volume [20]. **c** Variation over sharp disturbances ($\rho_s \gg \mathbf{R_{pol}}$)

resistivity, ρ_s, is much higher than the polarization resistance of the metal/solution interface, R_{pol}, a wall current, I_w, contributes to a streaming current increase, δI_s, at an accelerating region as an anodic current and conducts away the majority of the streaming current to the wall at a decelerating region as a cathodic current (Fig. 2b, c). The portion of the current loop in the metal is greater than that in the solution due to the greater conductivity of the metal. Therefore, the current from the bulk is negligible under the condition $\rho_s \gg R_{pol}$. Figure 2c also shows that the wall current passing through the interface and coupling with the streaming current generates current loops between the solution and wall.

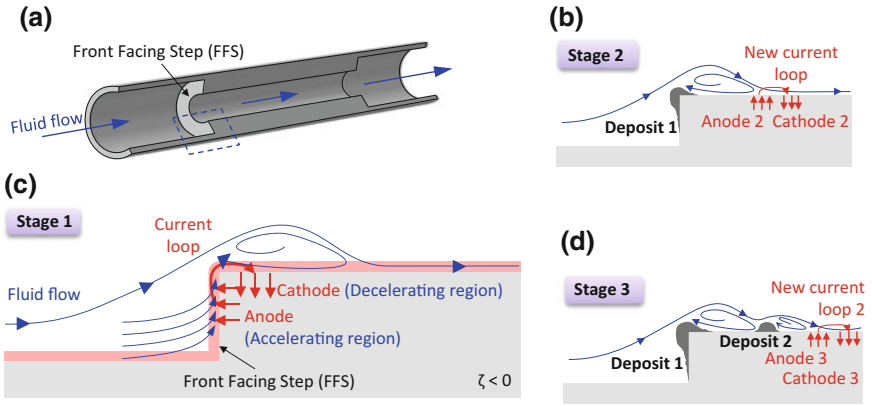

Fig. 3 Schematic plots of deposition initiation and propagation. **a** Geometry in 3D used in the model (grey—metal; blue arrows—fluid flow) **b** Deposition initiation (expansion of dashed box from a; red arrows—electric current) **c**, **d** Deposition propagation

Figure 3a shows the geometry step used in this work for a tube restriction (grey—metal; blue arrows—fluid flow) and Fig. 3b–d (red arrows—electric current) are the axisymmetric cross section expansions of the dashed box from Fig. 3a. The geometry step face at the inlet of the restriction is called the Front Facing Step (FFS) as shown in Fig. 3a. At the restriction, the accelerating fluid flow at the FFS generates an anode and the decelerating fluid in the flow recirculation zone adjacent to the step forms a cathode, as shown in Fig. 3b. The streaming current in the EDL links the anode and the cathode generating a current loop between the wall and the solution. The anodic reaction in this model is assumed to be the oxidation of iron generating magnetite which will modify the local solubility [8]. Therefore, initial deposit forms at this anodic region (Fig. 3c). After this, a new current loop is found following the recirculation zone due to the new accelerating and decelerating regions, which will generate a second deposit, as shown in Fig. 3d. Stages 1–2 schematically describe the deposition initiation process and stages 2–3 describe the deposition propagation.

Model Set-up

The thickness of the EDL is solution-dependent and varies from a few nanometres to a few hundred nanometres [21, 22]. In order to maximise the effect of the EDL in the electrokinetic deposition process, a geometry with a small size (μm) was used in this model (small when compared to other research tests [4, 7, 10]). A 2D cross-section of the simple step-geometry shown in Fig. 3a, which moves from a 20 μm inner diameter cylindrical tube to a restriction which is a 10 μm diameter tube with 100 μm length, is shown in Fig. 4a (not drawn to scale). The simulated

fluid (blue in Fig. 4a) is a solution of 0.03 mol/m^3 NaCl in water, which will be used to form excess charge in EDL, and the simulated generic metal (grey) is steel UNS G43400 (AISI 4340) with a very low surface polarization resistance ($\rho_s \gg R_{pol}$). The dashed box shows the most intricate and interesting area in this model. The average restriction velocities, $\bar{v}_{re}$, of 4, 20, 40, 60, 80, 120 and 200 m/s were investigated.

This model consists of three components: Transport of Diluted Species, Electrostatics and Electric Current. In the electrostatic module, an electric potential of −1 μV is applied along the restriction step as shown in Fig. 4a (red lines), with an electric ground applied as a boundary condition at the inlet and outlet at the beginning and end of the restriction in the x direction. The applied negative charge on the metal surface generates an EDL with excess positive charge in the fluid side of the interface and produces a negative ζ-potential as shown in Fig. 4b. The solution flow was modelled assuming time-averaged turbulent flow, and the velocity was multiplied by the excess charge to generate streaming currents in the near wall region (Fig. 2a) from upstream to downstream as the flow sheared the ions in the electric current module. Tafel behaviour was applied to the restriction boundary in this module to find the localised current densities.

$$\eta = V_m - V_s \tag{1}$$

$$j_a = j_0 \exp \frac{\alpha_a n F \eta}{RT} \tag{2}$$

$$j_c = j_0 \exp \frac{-\alpha_c n F \eta}{RT} \tag{3}$$

$$j = j_a - j_c \tag{4}$$

In Eq. (1)–(4), η is the overpotential, V_m is the potential of the metal and V_s is the potential of the solution. Anodic and cathodic current densities are denoted as j_a and j_c respectively, while j_0 is the exchange current density, which is set equal to 10^{-6} A/cm^2 as referenced from reactions on steel surface at high temperature [23].

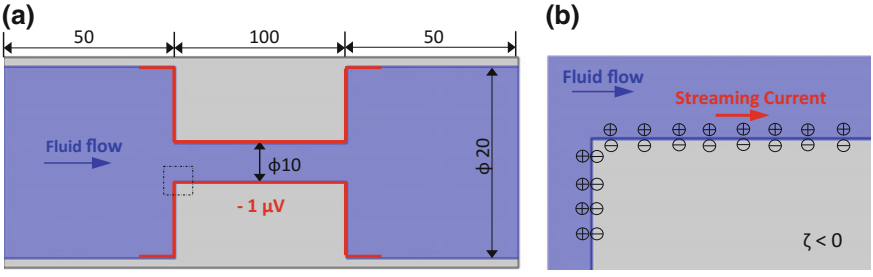

Fig. 4 **a** 2D cross-section of the geometry (μm) (red lines—applied electric potential; dashed box—area of interest). **b** Excess charge in the double layer generating streaming current

The anodic and cathodic transfer coefficients, α_a and α_c, are arbitrarily set to 0.5, which is a common value for simple electron-transfer reactions [19].

A few assumptions were made before the model set-up: the excess charge in the Helmholtz layer is included in the boundary condition; fluid flow is independent of the electric distribution and the velocity is not coupled to the species transport; EDL is too small to change the shape; only Tafel kinetics is applied for anodic and cathodic process; the solution conductivity is constant.

Results and Discussion

Deposition Initiation—Stage 1

Current Path

Figure 5a shows the current path detail at the inlet of the restriction which is the area in the dashed box in Fig. 4. The red/black normalised arrows are the currents in the solution/metal, respectively. The large red arrows represent the streaming current in the double layer, part of which flows upstream in the opposite direction to the bulk. This is due to the fluid flow recirculation zone shown in Fig. 5b, which

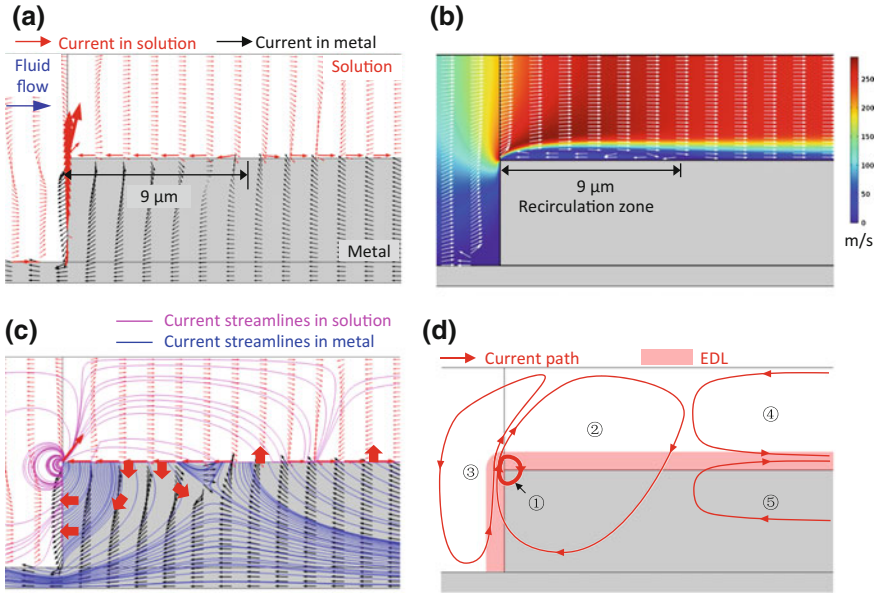

Fig. 5 Current and fluid flow at stage 1. **a** Current in solution and metal. **b** Fluid flow velocity field showing a 9 µm recirculation zone adjacent to the inlet, $\bar{v}_{re}$ = 200 m/s. **c** Current streamlines. **d** Schematic current path

carries the excess charge upstream. The size of the upstream streaming current is controlled by the size of the recirculation zone, which is 9 µm at an average restriction velocity of 200 m/s. This size is very close to the inner diameter of the restriction which is 10 µm. It should be noted that the normalised arrows in the solution and metal bulk don't represent the values of the local current which can be between six and eight orders of magnitude smaller than the streaming current along the wall surface.

Current streamlines in both solution and metal are shown in Fig. 5c. Current is conducted into the metal adjacent to the inlet; most of the current re-joins the solution through the FFS and the rest flows back to the solution further downstream. Due to the large difference in conductivity between the metal and solution, most of the streamlines (and thus current) can be found in the metal.

Figure 5d shows the schematic current path. The most active area is located at the inlet of the restriction where the accelerating streaming current at the FFS sweeping into the restriction meets the upstream streaming current inside the restriction at the inlet. The majority is conducted into the metal generating current loops between the metal and solution passing through the metal/solution interface. The most intense current loop is located at the sharp corner as loop 1. Loop 2 shows the edge of the current between the metal and solution at this region. The rest streaming current from FFS couples with the current in the solution bulk forming loop 3. It is deformed due to the accelerating flow in this area. The remaining streaming current in the EDL moves downstream, giving two additional loops, loop 4 and 5, extending to the outlet of the restriction.

The size of the model geometry has been chosen in this case to be small to allow the different physical processes involved to all be modelled in one mesh. The concentration of the current in small areas near the sharpest features interrupting the flow, to create local pairs of anodes and cathodes, suggests that this process is a localised one which may not be strongly affected by changes to the geometry away from the wall regions such as using larger pipes, provided the local shear rate at the wall and electrical behaviour of the walls is constant.

Overpotential and Normal Current Density

Figure 6a and b show the overpotential, $\eta = V_m - V_s$, and normal current density, $j_\perp = j_a - j_c$, along the restriction step from point D to E at different average restriction velocities, respectively (the same points in Fig. 6c). Overpotential between the metal and solution drives the current movement in the interface. Where $V_m > V_s$, the only way to balance the potential is to move electrons from solution to metal, which generates an anodic current. Where $V_m < V_s$, a cathodic current will be generated. Therefore, the interface exhibits anodic behaviour from point D to A, with current flowing from metal to solution, and cathodic behaviour from point A to B and at point C, with current flowing from solution to metal. The size of the cathodic region is the same as that of the recirculation zone (Fig. 5b) which is also 9 µm at an average restriction velocity of 200 m/s. The extreme values of anodic

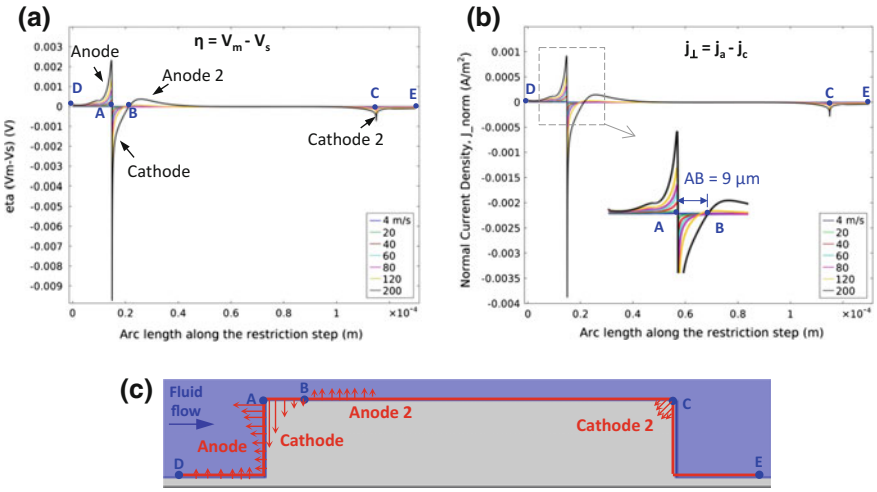

Fig. 6 **a** Overpotential along the restriction step. **b** Normal current density. **c** Current path between the solution and metal

and cathodic currents are located around point A (Fig. 6b) which is shown as loop 1 in Fig. 5d. Figure 6c shows current passing through the metal/solution interface at anodes and cathodes. The main deposit generation process discussed in this work is the oxidation of ferrous ions into magnetite which is an anodic reaction [8, 10]. Therefore, the first anode (from D to A in Fig. 6c) is assumed to be where the initial deposit is located at. It should be noted that we have termed this initial deposit as 'deposition initiation'. A second anode was found following the first cathodic region, which gives rise to the formation of a second deposit.

Overpotential and normal current density both increase with the increasing average restriction fluid flow velocities. This may be due to the high shear rate along the wall surface at high velocity, which moves more charge in the same time unit generating higher current density. More details of the dashed box of the normal current density are shown in Fig. 6b. The values of the current density and the sizes of the anodes and cathodes increase with the increasing velocities. This implies that the quantity and the size of the deposits at high velocity may be larger than those produced at low velocity in a certain velocity range.

Deposition Propagation—Stage 2

A 'bump' with 1 μm radius was added at the inlet corner of the restriction to simulate the initial deposit, which has the same metal material for simplification in the present model. The resulting behaviour of the fluid flow and electric current is shown in Fig. 7 which is similar to that of stage 1 in Fig. 5. A longer fluid

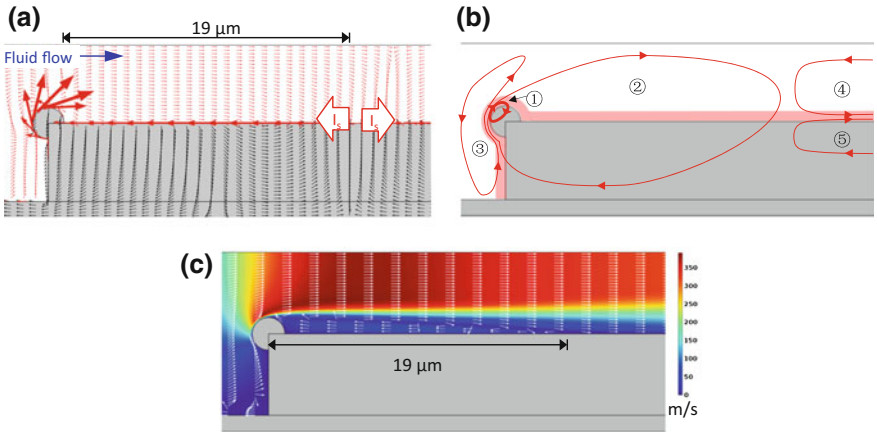

Fig. 7 Current and fluid flow at stage 2. **a** Current in solution and metal. **b** Schematic current path. **c** Fluid flow velocity field showing a 19 µm recirculation zone adjacent to the inlet, $\bar{v}_{re}$ = 200 m/s

recirculation zone (Fig. 7c), 19 µm at an average restriction velocity of 200 m/s, was found due to the greater geometric disturbance of the simulated deposit. The size of the fluid recirculation zone controls the size of the electric recirculation zone, giving the same size of the upstream fluid flow and streaming current (Fig. 7a). Similarly, the upstream streaming current joined the streaming current from the FFS conducting into the metal generating the strongest current loop, loop 1, which is located at the top of the simulated deposit. This may explain the growth of the initial deposit—initiating at the corner and continuing to grow into a deposit. Two additional big loops extending to the restriction outlet were found.

Deposition Propagation—Stage 3

A second 'bump' with 1 µm radius was then placed 19 µm away from the first simulated deposit inside the restriction to simulate the second deposit, where the second anode was located at stage 2, as shown in Fig. 8a. In the area between the restriction inlet and the front of the second deposit, similar characteristics of the fluid and electric current as stage 2 were observed.

Another recirculation zone with smaller size, 10 µm at an average restriction velocity of 200 m/s in Fig. 8d, was found following the second deposit, which brings the streaming current upstream as shown in Fig. 8a. The upstream streaming current joining the streaming current from the front of the second deposit was mainly conducted into the metal. Extra loops were found around the second deposit showing anodic and cathodic behaviour in the front and at the back, respectively, as shown in Fig. 8b. The densest current, loop 1 in Fig. 8c, is located at the top of the

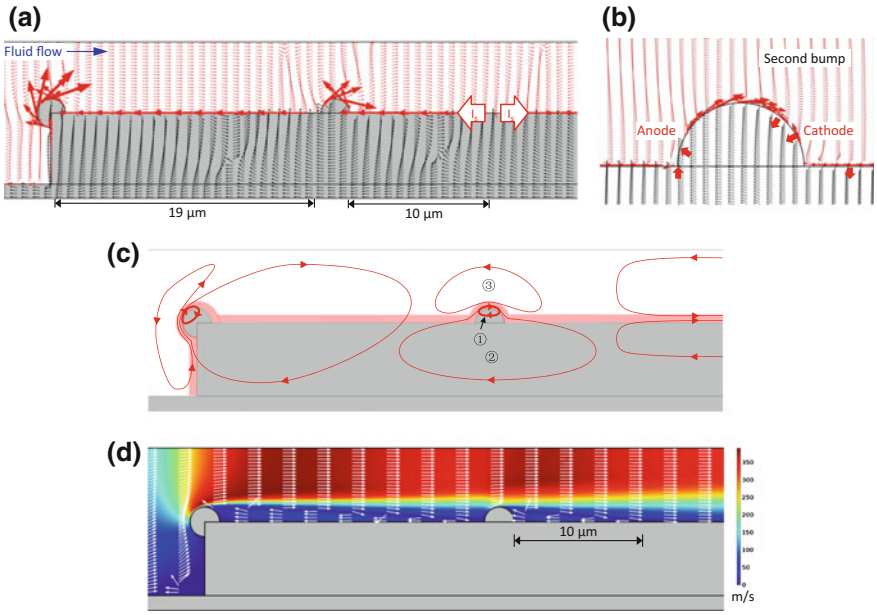

Fig. 8 Current and fluid flow at stage 3. **a** Current in solution and metal. **b** Current details around the second simulated deposit. **c** Schematic current path d Fluid flow velocity field showing a 10 µm recirculation zone following the second deposit, $\bar{v}_{re}$ = 200 m/s

second simulated deposit which is similar to the first simulated deposit. Loop 2 shows the edge of the current between the metal and solution in this region. The remaining of the streaming current flowing downstream generated two further loops extending to the end of the restriction.

Comparison Between Stage 2 and 3

Normal current density and current path of stage 2 and 3 at different average restriction flow velocities are shown in Fig. 9. For stage 2, the anodic region is located at the FFS and the front face of the initial deposit with current flowing from metal to solution and a cathodic region from the back of the initial deposit to point B with current flowing from solution to metal. A second anode was also found adjacent to the first cathode. This shows a similar electric current phenomenon as observed at stage 1.

For stage 3, an extra anode (Anode 2) and cathode (Cathode 2) were found around the second deposit as shown in Fig. 9c, d. A third anode (Anode 3) was found following the second cathode, which means a third deposit should be located

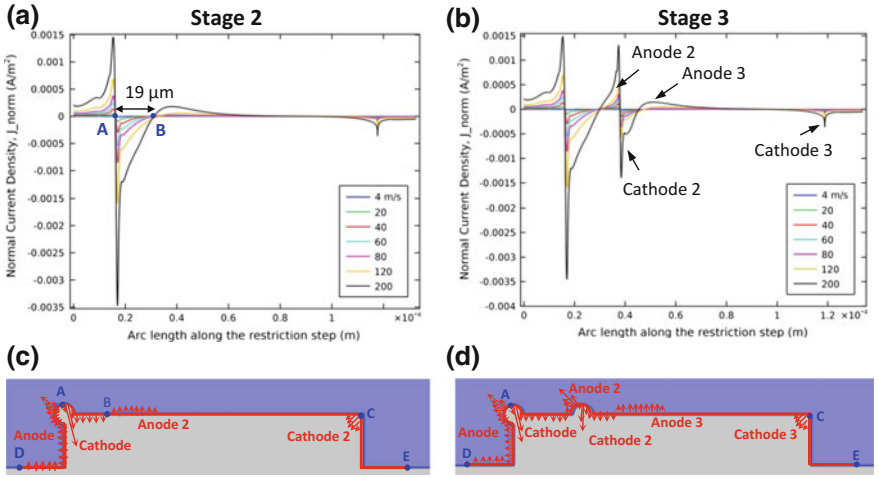

Fig. 9 **a** Normal current density along the restriction step at stage 2. **b** Current path between the solution and metal at stage 2. **c** Normal current density along the restriction step at stage 3. **d** Current path between the solution and metal at stage 3

in this area. The rest of the area along the restriction step showed a similar behaviour as observed at stage 2.

From stage 2 to 3, the location of a third deposit (Anode 3) was found after the second deposit 'formed'. This means that an extra anode (thus an extra deposit) always appears after a previous deposit generates. We call this phenomenon deposition propagation. Anode 2 and 3 simulate the deposit ripples inside that are observed in actual restriction in plants.

Conclusions

An electric model describing initiation and propagation of CRUD deposition in geometric restrictions was built and discussed in this paper. The anodic and cathodic characteristics along the restriction step surface were investigated. It was found that the recirculating fluid flow over surfaces following sharp disturbances (i.e. restrictions) gives rise to coupled anodic and cathodic regions when a charged Electrical Double Layer is present. An anodic region was found at the front facing step of the restriction followed by a cathodic region. A coupled second anode was adjacent to the cathode. After an additional simulated deposit was introduced inside the restriction at the locations of the anodic currents (e.g. from stage 2 to stage 3), an extra couple of cathode and anode was found within a fluid flow recirculation zone surrounding the simulated deposit. The length along the wall surface and the current density value of anode and cathode both increase with the increasing average restriction fluid flow velocities, which indicates that larger size and mass of

deposits may be found at the anodic area at higher velocity in a certain velocity range.

Where the solution resistivity (ρ_s) is high compared to the polarization resistance of the interface (R_{pol}), significant wall currents linking the anodic and cathodic regions passing through the solution/metal interface are predicted. Where CRUD deposition rate is assumed to be accelerated in anodically polarized regions, then a pattern of initiation and sequential propagation of deposits is predicted, which matches the experimentally observed build up on the external face of a step, and the rippled surfaces inside the flow restriction.

To the purpose of maximising the EDL effect on the deposition process, micrometre size geometry was used in this model. This should not affect the kinetics when it scales up to millimetre size in the future work. Restriction diameter effect and more details of velocity effect on the oxide formation will also be studied in the future work.

References

1. R.A. Castelli, *Nuclear Corrosion Modelling* (Oxford: Butterworth-Heinemann, an imprint of Elsevier, 2009), xi–xvii
2. EPRI, Characterization of PWR steam generator deposits, (Report EPRI TR-106048, Dominion Engineering, INC., McLean, Virginia, 1996)
3. IAEA, Current trends in nuclear fuel for power reactors—NTR supplement (Information document from 51st IAEA General Conference, Austria Center Vienna, Bruno-Kreisky-Platz, Vienna, 17 September 2007), 11
4. M. Guillodo et al., Formation of deposits in HT water under high velocity conditions : a parametric study (Paper presented at the Water Chemistry of Nuclear Reactor Systems Conference, San Francisco, California, 2004), 1941–1949
5. S. Odar, P. Rudling, Crud in PWR/VVER coolant Volume I—sources, transportation in coolant, fuel deposition and radiation build-up (Report LCC10 STR, ANT International, 2014)
6. M. Vepsalainen, T. Saario, Magnetite dissolution and deposition in NPP secondary circuit (Report VTT-R-09735-10, VTT, 2010)
7. C. Brun et al., Investigation on the relation between pressure drops and fluid chemical treatment (Paper presented at the Water Chemistry of Nuclear Reactor Systems Conference, Avignon, France, 2002)
8. M. Guillodo et al., Singular deposit formation in PWR due to electrokinetic phenomena—application to SG clogging (Paper presented at the 6th CNS International Steam Generator Conference, Toronto, Ontario, Canada, 2009)
9. J. Robertson, Corrosion and deposition due to electrokinetic currents (Report TPRD/L/3030/R86, CEGB, 1986)
10. I.S. Woolsey et al., Occurrence and prevention of enhanced oxide deposition in boiler flow control orifices (Paper presented at the water chemistry of nuclear reactor systems 5, Bournemouth, UK, 1989)
11. F. Scenini et al., Electro deposition of CRUD (Report R115529, University of Manchester, 2014)
12. F. Scenini et al., Investigation of the role of electrokinetic effects in corrosion deposit formation. Corros. Sci. **87**, 71–79 (2014)

13. F. Scenini et al., Electrochemical and direct build up measurements of oxide deposition in accelerated flow (Paper presented at the 20th NPC Conference, Brighton, UK, 2016)
14. M. Guillodo et al., Experimental and numerical study of deposit formation in secondary side SG TSP by electrokinetic approach (Paper presented at the Nuclear Plant Chemistry Conference, Paris, France, 2012), 1–14
15. C.W. Turner, M. Godin, Mechanisms of magnetite deposition in pressurized boiling and non-boiling water, (Report AECL-11046, Atomic Energy of Canada Limited Research, 1994)
16. C. Henry, J.P. Minier, G. Lefèvre, Towards a description of particulate fouling: from single particle deposition to clogging. Adv. Colloid Interface Sci. **185–186**, 34–76 (2012)
17. C. Brett, M. Brett, *Electrochemistry—Principles, Methods and Applications* (Oxford University Press, Oxford, UK, 1993), pp. 39–68
18. J. Bockris, A. Reddy, *Modern Electrochemistry 2* (Plenum Press, New York, NY, 1977), pp. 718–790
19. D. Pletcher, *A First Course in Electrode Process*, 2nd edn. (The Royal Society of Chemistry, Cambridge, 2009), pp. 1–47
20. A. Banks, A. Powell, L. Pegg, University of Birmingham, Continuum Blue, Rolls-Royce COMSOL Modelling (A talk presented in a meeting in University of Birmingham, 11 December 2014)
21. D. Li, Electro-viscous effects on pressure-driven liquid flow in microchannels. Colloids Surf. A Physicochem. Eng. Asp. **195**, 35–57 (2001)
22. K. Bohinc, V. Kralj-Iglič, A. Iglič, Thickness of electrical double layer. Effect of ion size. Electrochim. Acta **46**, 3033–3040 (2001)
23. E. Bardal, *Corrosion and Protection* (USA: Springer-Verlag London, 2004), 35–51

Properties of Oxide Films on Ni–Cr–*x*Fe Alloys in a Simulated PWR Water Environment

Xiangkun Ru, Zhanpeng Lu, Junjie Chen, Guangdong Han, Jinlong Zhang, Pengfei Hu, Xue Liang and Wenqing Liu

Abstract The iron content in Ni–Cr–*x*Fe (x = 0–9 at.%) alloys strongly affected the properties of oxide films formed in a simulated PWR primary water environment at 310 °C. Increasing the iron content in the alloys increased the amount of iron-bearing polyhedral spinel oxide particles in the outer oxide layer and facilitated the local oxidation penetration into the alloy matrix from the chromium-rich inner oxide layer. The local oxidation penetration was caused by the pile-up of the cation vacancies.

Keywords Nickel-based alloys · Simulated PWR water · TEM · Iron content · Oxide film · Local oxidation penetration

Introduction

Nickel-based alloys, such as Alloy 690 and 600, and weld metals, such as Alloy 52, 152 and 182, have been widely used in pressurized water reactors (PWRs). During the long-term operation of PWRs, environmentally-assisted cracking, such as stress corrosion cracking (SCC), has been one of the main issues limiting the performance life of many component materials [1–10]. Oxidation behavior is crucial for stress

X. Ru · Z. Lu (✉) · J. Chen · G. Han · J. Zhang
Institute of Materials, School of Materials Science and Engineering, Shanghai University, Shanghai 200072, People's Republic of China
e-mail: zplu@t.shu.edu.cn

X. Ru · Z. Lu
State Key Laboratory of Advanced Special Steels, Shanghai University, Shanghai 200072, People's Republic of China

P. Hu · X. Liang · W. Liu
Key Laboratory for Microstructure, Shanghai University, Shanghai 200444, People's Republic of China

J.H. Jackson et al. (eds.), *Proceedings of the 18th International Conference on Environmental Degradation of Materials in Nuclear Power Systems – Water Reactors*, The Minerals, Metals & Materials Series, https://doi.org/10.1007/978-3-319-68454-3_81

corrosion cracking initiation and growth. Environmental and engineering parameters, such as solution composition [11–13], dissolved oxygen (DO) [14–21], dissolved hydrogen (DH) [18, 20, 22–25], temperature [24, 26, 27], pH value [28, 29], material compositions [30–34], microstructures [35], mechanical properties [24, 36, 37] etc. have been found to have significant effects on the oxidation behavior of Ni-Cr–Fe alloys in high temperature water environments. Of these factors, dissolved hydrogen has been proven to be a very important one, as the primary water was maintained in a reducing state by adding hydrogen. Xu et al. [18, 20] have found that electrochemical potential, film resistance, morphology and composition of the oxide film exhibited obvious distinctions with the change of water chemistry. Kim et al. [23] found that increasing the DH concentration decreased the NiO Raman peak, whereas the Cr_2O_3 peak and spinel oxide peaks appeared as the DH concentration increased. The crack-initiation time decreased as the DH concentration increased [23]. Soustelle et al. [38] reported that the oxide film formed on Alloy 600 was nickel depleted and chromium rich under high hydrogen partial pressure, while the intermediate partial pressure of hydrogen, i.e., a corrosion potential close to the Ni/NiO equilibrium, resulted in the maximum thickness of the oxide film, the lowest chromium contents in the oxide film and the most dense external crystallite layer. Mendonça et al. [24] investigated the oxide film formed on Alloy 182 and observed the peak in SCC susceptibility at a certain temperature and DH around the electrochemical condition where the Ni to NiO transition takes place. The composition of materials plays an important role in their oxidation behavior. Das et al. [31] found that the iron and chromium atoms segregate faster than the nickel atoms at the Fe–Cr-Ni alloy surface. The oxide film formed on nickel-based alloys under simulated BWR water conditions indicated that an iron injection might cause the alloy to behave similarly to an alloy that had elevated iron content [32]. Schreiber et al. [33] found the preferential selective oxidation of Cr in nickel-based alloys in high temperature water, and similar results were proposed by Lim et al. [34]. Therefore, it is necessary to investigate the influence of the alloying elements in nickel-based alloys on the oxide films formed in hydrogen-bearing simulated PWR water environments.

The present work, based on using tailored Ni-Cr-xFe alloys (x = 0, 1, 3, 5 and 9 at. %), investigated the oxide films that formed in 310 °C simulated PWR water under hydrogenated conditions. The morphologies and chemical compositions of the oxide films were characterized by scanning electron microscopy (SEM), focused ion beam (FIB), transmission electron microscopy (TEM) and energy dispersive X-ray spectroscopy (EDS) measurements. The bulk effect of alloy composition on oxidation was emphasized in this work, while the role of metallic ions released from the autoclave body was often emphasized in the existing literature [39–42]. The effect of the immersion time was also investigated in this work.

Experimental

Materials

Five different model alloys (Ni_2Cr, Ni_3Cr, Ni_2Cr-1at.%Fe, Ni_2Cr-3at.%Fe and Ni_2Cr-5at.%Fe) and the commercial alloy TT690 are used in the present experiment. The practical contents of Ni, Cr and Fe in the Ni–Cr–*x*Fe alloys used in the present experiment are shown in Table 1. The model alloys were designed to maintain a constant Ni/Cr ratio to ensure the effect of iron could be investigated separately. The model alloys were prepared in an arc melting furnace under an argon atmosphere using a non-consumable tungsten electrode and a water cooled hearth. The model alloy ingots were forged and rolled at 1200 °C. The final heat treatment for the model alloys was solution treatment at 1100 °C for 20 min and water quenching. The final heat treatment for the TT690 alloy was at 715 °C for 10 h and air cooling. Rectangular specimens (length × width × thickness = 10 mm × 5 mm × 1 mm) for the immersion test were cut from the model alloys and the TT690 alloy by electric-spark line-cutting equipment. The target surfaces of the specimens were mechanically ground with waterproof abrasive paper up to 1500 grit successively. All specimens were cleaned, in turn, with deionized water, ethanol and acetone. To keep all of the specimens hanging in the autoclave, a small hole was processed in each specimen, and hooks covered with Teflon tubes in "S" style were applied.

Immersion Tests

A dynamic 5 L (net volume) stainless steel autoclave with a recirculating loop was applied for immersion tests in the simulated PWR water environment. The specimens were exposed to the simulated PWR water with 1200 ppm B (wt.) as H_3BO_3 + 2.0 ppm Li (wt.) as LiOH for 978 h. The temperature and pressure were adjusted to be 310 °C and 12 MPa to keep the solution in the autoclave liquid. The high-temperature water environment was referred to as the hydrogenated PWR primary water with a DH of approximately 30 cc/kg (wt.) and a DO < 5 ppb (wt.) representing the normal operating conditions.

Table 1 The practical contents of Ni, Cr and Fe in the investigated materials (wt%)

Materials	Ni	Cr	Fe
Ni_2Cr	65.66	34.29	0.05
Ni_2Cr-1at.% Fe	66.46	32.61	0.93
Ni_2Cr-3at.% Fe	65.04	32.40	2.56
Ni_2Cr-5at.% Fe	63.25	32.05	4.70
TT690	59.42	29.35	10.13
Ni_3Cr	75.20	24.77	0.03

Characterization of the Oxide Films

The morphologies of the surface oxide films were evaluated by a JSM-7500F field-emission SEM at 10 kV. The estimated chemical compositions of certain oxides in the outer oxide layer of the oxide films were analyzed on an EDS system installed on the SEM. The cross-sections of the surface oxide films were prepared by a Helios Nanolab 600i FIB system and analyzed using a 200 kV JEM-2010 field emission high resolution TEM equipped with an EDS system.

Results

Surface Morphologies and Compositions

After 978 h of immersion, the surface morphology difference was found among the specimens with different iron contents in the alloy matrices. The binary alloys Ni_2Cr and Ni_3Cr were mainly covered with continuous platelet-like oxides with a few polyhedral oxide particles scattered on the top, as shown in Fig. 1a, f. When increasing the iron content in the alloy matrices, the amount of polyhedral oxide particles increased, as shown in Fig. 1a–e. The surface of the TT690 specimen was fully covered with polyhedral oxide particles and no platelet-like oxide was present, as shown in Fig. 1e. The average diameter of the polyhedral oxide particles was approximately 190 nm for the model alloys (Ni_2Cr, Ni_3Cr, Ni_2Cr-1at.%Fe, Ni_2Cr-3at.%Fe and Ni_2Cr-5at.%Fe), but approximately 130 nm for the TT690 specimen. The Ni, Cr and Fe contents of the oxide films detected by SEM-EDS are shown in Table 2. Because of the low thickness of oxide films, the elemental content data by SEM-EDS included base signal and could not be treated as the accurate values of the oxide films. The iron content in the Table 2 was found to be $\sim$1 wt% higher than that in the alloy matrix. The iron detected in the oxide might come from both the 316L stainless steel autoclave and the metallic alloy. This should be noted when analyzing the oxidation mechanism.

Cross-Sectional Morphologies and Compositions

The comparison of the cross-sectional morphologies of specimens after 978 h of immersion is shown in Fig. 2. The cross-sectional morphologies show a two-layered structure of the oxide films for all the specimens. The high angle annular dark field (HAADF) images show that the interface between the inner oxide layer and alloy matrix was almost smooth for the iron-free alloy, as shown in

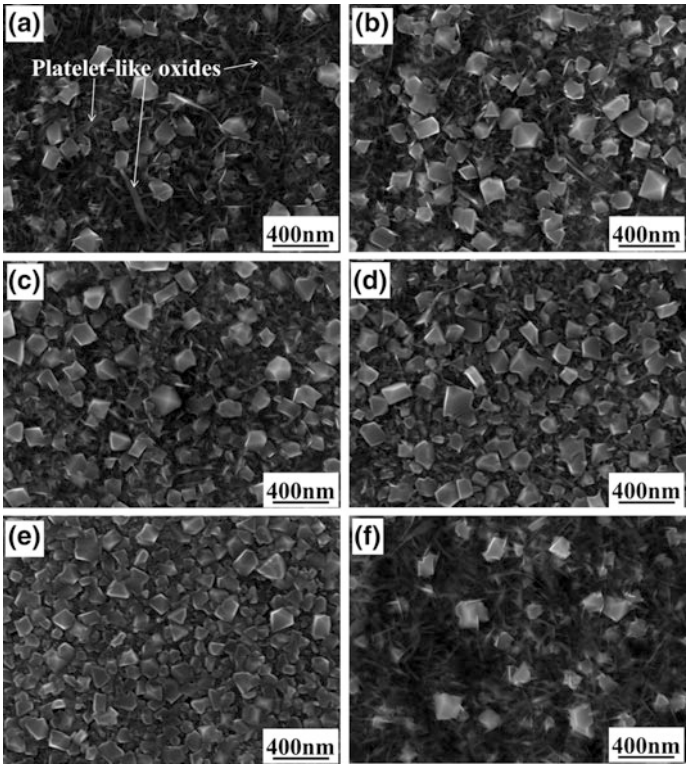

Fig. 1 SEM images of the oxide films on specimens immersed in the hydrogenated PWR primary water at 310 °C, with 30 cc/kg DH and DO < 5 ppb for 978 h: **a** Ni_2Cr, **b** Ni_2Cr-1at.%Fe, **c** Ni_2Cr-3at.%Fe, **d** Ni_2Cr-5at.%Fe, **e** TT690 and **f** Ni_3Cr

Table 2 The Ni, Cr and Fe contents in the oxide layer detected by SEM-EDS (wt%) after 978 h of immersion in the hydrogenated PWR primary water at 310 °C, with 30 cc/kg DH and DO < 5 ppb

Specimens	Ni	Cr	Fe
Ni_2Cr	66.46 ± 1.20	30.80 ± 0.85	0.88 ± 0.07
Ni_2Cr-1at.% Fe	65.78 ± 0.86	30.34 ± 0.21	2.09 ± 0.34
Ni_2Cr-3at.% Fe	64.80 ± 0.63	29.80 ± 0.48	3.73 ± 0.12
Ni_2Cr-5at.% Fe	62.68 ± 0.51	28.92 ± 0.49	6.50 ± 0.07
TT690	57.34 ± 0.18	30.01 ± 0.11	10.80 ± 0.11
Ni_3Cr	75.82 ± 0.26	22.05 ± 0.07	0.63 ± 0.12

Fig. 2a, b. After the iron content in alloy matrix was increased to 3 at.%, some small local penetration into alloy matrix from the inner oxide layer could be observed, as shown in Fig. 2c, d. The depth and amount of the local penetration increased while the iron content increased to almost 9 at. %, as shown in the TT690

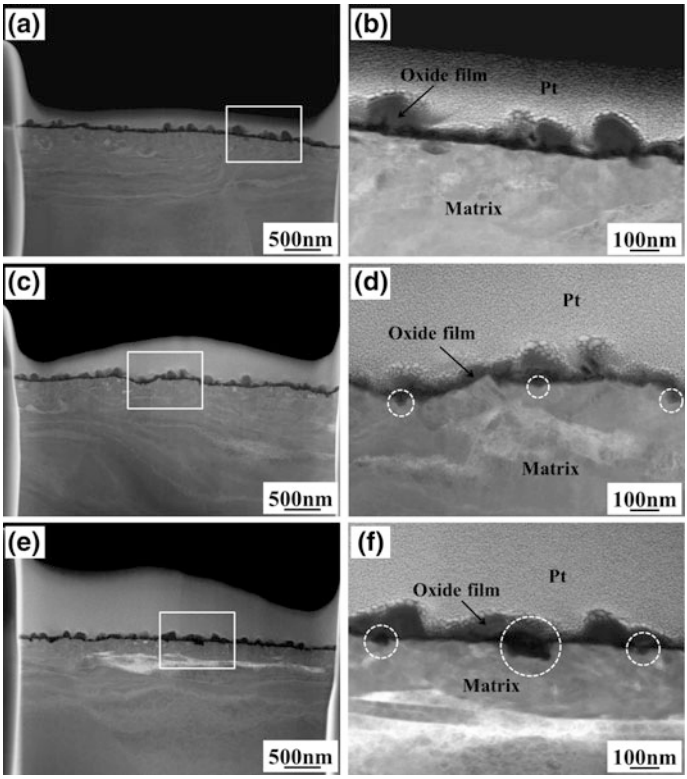

Fig. 2 HAADF images of the oxide film on specimens Ni_2Cr, Ni_2Cr-3at.%Fe and TT690 after 978 h of immersion in the hydrogenated PWR primary water at 310 °C, with 30 cc/kg DH and DO < 5 ppb: **a**, **b** Ni_2Cr; **c**, **d** Ni_2Cr-3at.%Fe; and **e**, **f** TT690. **b**, **d**, **f** are the enlarged images of the square areas in **a**, **c**, **e**, respectively. (The dashed circles show the penetration along the interface between the inner oxide layer and alloy matrix)

specimen in Fig. 2e, f. The high resolution transmission electron microscopy (HRTEM) images of the platelet-like oxides in the inner oxide layer on specimens Ni_2Cr and Ni_2Cr-3at.%Fe after 978 h of immersion are shown in Fig. 3. Only a few platelet-like oxides could be detected through the lattice fringes. The low thickness and the stack of the platelet-like oxides resulted in the difficulty of obtaining complete crystal lattices.

The TEM cross-sectional analysis of the oxide films on the specimens Ni_2Cr, Ni_2Cr-3at.%Fe and TT690 after 978 h of immersion in hydrogenated PWR primary water are shown in Figs. 4, 5 and 6. The diffraction patterns indicate that these polyhedral oxide particles in the outer oxide layer had a spinel structure, as shown in Figs. 4b, 5b, and 6b. The compositions of the analyzed oxides on different specimens are shown in Table 3. The elemental contents data show insignificant differences among the three specimens. The iron content in the alloy matrix had an insignificant effect on the composition of the polyhedral spinel oxide particles in the

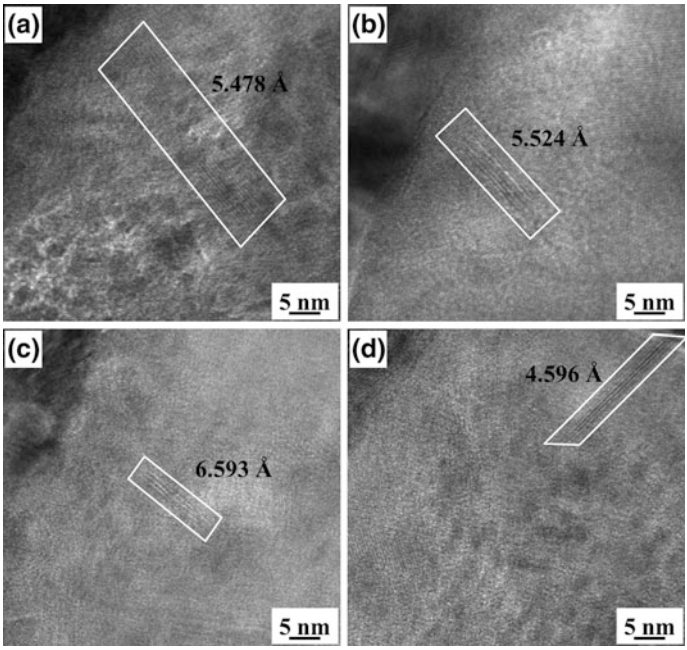

Fig. 3 HRTEM images of platelet-like oxides on specimen Ni_2Cr **a**, **b** and Ni_2Cr-3at.%Fe **c**, **d** after 978 h of immersion in the hydrogenated PWR primary water at 310 °C, with 30 cc/kg DH and DO < 5 ppb

outer layer after 978 h of immersion. The elemental distribution data of the oxide films on the specimens Ni_2Cr, Ni_2Cr-3at.%Fe and TT690 after 978 h of immersion in hydrogenated PWR primary water are shown in Figs. 4d, 5d and 6d, respectively. The arrows are used to mark the scanning targets for EDS linear analysis, as shown in Figs. 4c, 5c and 6c. Chromium was the dominant element in the inner oxide layer, while both iron and chromium played important roles in the oxide formation in the outer oxide layer, as shown in Figs. 4d, 5d and 6d. The EDS linear scanning results also showed that the nickel content was very low in both the inner oxide layer and the outer oxide layer. The estimated thicknesses of the inner oxide layer of specimens Ni_2Cr, Ni_2Cr-3at.%Fe and TT690 were 30, 50 and 40–90 nm, respectively. Table 4 provides the Ni, Cr, Fe and O contents of the inner oxide layer on TT690 after 978 h of immersion. Almost 40% chromium content and approximately 7% iron content were detected. Comparing with approximately 30% chromium content and 31% iron content in the polyhedral oxides in the outer oxide layer, the chromium enrichment and iron depletion were obvious in the inner oxide layer. The nickel content of the inner oxide layer in Table 4 might be biased by the nickel in the alloy matrix because of the low thickness.

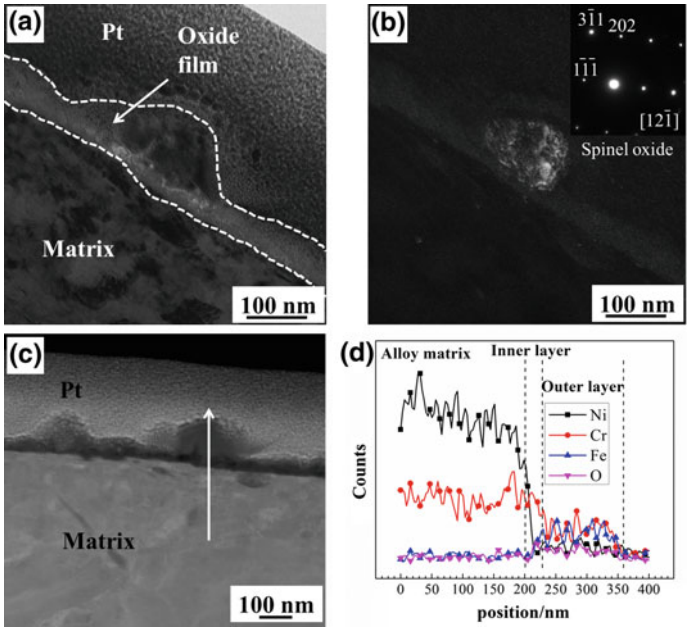

Fig. 4 TEM cross-sectional analysis results of the Ni_2Cr specimen after 978 h of immersion in the hydrogenated PWR primary water at 310 °C, with 30 cc/kg DH and DO < 5 ppb: **a** bright field image, **b** dark field image with diffraction pattern, **c** the EDS linear direction marked by the arrow and **d** the linear distribution of elements

Discussion

By comparing the morphology and composition analysis results, we determined that the iron content in the alloy matrix can affect the properties of the oxide film on Ni–Cr–*x*Fe (x = 0, 1, 3, 5 and 9 at. %) alloys in the simulated PWR primary water environment with 30 cc/kg DH at 310 °C.

Effects of the Iron Content in the Alloys on the Outer Oxide Layer

Figure 7 shows the schematic drawings of the oxide films formed on the specimens Ni_2Cr, Ni_2Cr-3at.%Fe and TT690 after 978 h of immersion in the hydrogenated PWR primary water. The oxide films on Ni–Cr–*x*Fe (x = 0, 1, 3, 5 and 9 at. %) alloys had a duplex layer structure. The Ni, Cr and Fe contents in polyhedral oxides on specimens Ni_2Cr, Ni_2Cr-3at.%Fe and TT690 after 978 h of immersion have similar atomic ratios of approximately 1: 2: 2. The diffraction patterns in Fig. 7

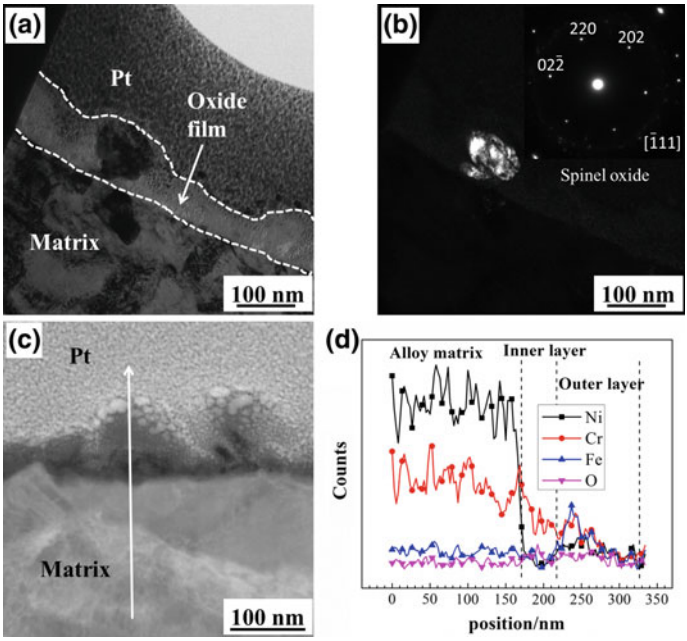

Fig. 5 TEM cross-sectional analysis results of the Ni_2Cr-3at.%Fe specimen after 978 h of immersion in the hydrogenated PWR primary water at 310 °C, with 30 cc/kg DH and DO < 5 ppb: **a** bright field image, **b** dark field image with diffraction pattern, **c** the EDS linear direction marked by the arrow and **d** the linear distribution of elements

indicate that the polyhedral oxides had a spinel-structure. Under the present test conditions, the dominant stable phase for pure nickel was metallic nickel, according to the thermodynamic data [43]. Sennour et al. [44] demonstrated the presence of the $NiFe_2O_4$ and $NiCr_2O_4$ in the oxidation products of Alloy 690 with thermodynamic calculations and a stability diagram. The existence of these oxide products could also be demonstrated by the E-pH diagrams for the Ni, Cr and Fe species in the pure metals and the Ni–Cr–Fe ternary system in water at different temperatures by Beverskog and Puigdomenech [45]. The main compositions of these polyhedral oxides were identified to be $NiFe_2O_4$ and $NiCr_2O_4$. The cation concentration near the alloy surface is crucially affected by the formation of the oxide film in high temperature water. For the formation of iron-bearing polyhedral oxide particles in the outer oxide layers, the concentrations of iron cations near the alloy surfaces are crucial. Both the iron cations that came from the autoclave body and the iron cations that came from the alloy matrix could contribute to the formation of the iron-bearing polyhedral oxides. The contribution of iron cations that came from the autoclave body can be demonstrated by the iron-bearing polyhedral oxides on iron-free specimens Ni_2Cr and Ni_3Cr, as shown in Table 2. Increasing the iron content in the alloy matrix would enhance the release rate of iron cations into solution, thus increasing the local concentration of iron cation near the alloys and

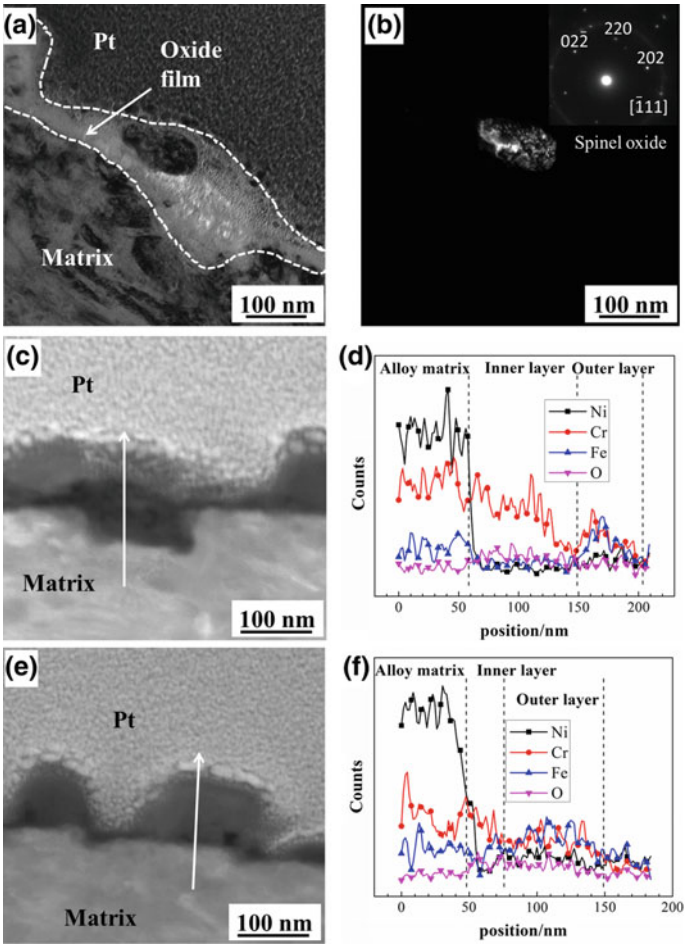

Fig. 6 TEM cross-sectional analysis results of the TT690 specimen after 978 h of immersion in the hydrogenated PWR primary water at 310 °C, with 30 cc/kg DH and DO < 5 ppb: **a** bright field image, **b** dark field image with diffraction pattern, **c**, **e** the EDS linear direction marked by the arrows and **d**, **f** the linear distribution of elements

Table 3 The Ni, Cr, Fe and O contents of oxide particles formed on Ni_2Cr, Ni_2Cr-3at.%Fe and TT690 specimens after 978 h of immersion in the hydrogenated PWR primary water at 310 °C, with 30 cc/kg DH and DO < 5 ppb, as obtained by TEM-EDS (wt%)

Specimens	Ni	Cr	Fe	O
Ni_2Cr	14.79 ± 0.68	30.57 ± 0.81	28.37 ± 0.79	26.27 ± 1.32
Ni_2Cr-3at.%Fe	16.37 ± 0.38	30.46 ± 0.44	26.94 ± 0.41	26.24 ± 0.71
TT690	12.72 ± 1.04	29.97 ± 1.30	31.10 ± 1.28	26.21 ± 2.09

Note The O content was obtained based on the stoichiometry in the analysis software INCA developed by Oxford Instruments

Table 4 The Ni, Cr, Fe and O contents of the inner oxide layer on TT690 after 978 h of immersion in the hydrogenated PWR primary water at 310 °C, with 30 cc/kg DH and DO < 5 ppb, as obtained by TEM-EDS (wt%)

Specimen	Ni	Cr	Fe	O
TT690	27.84 ± 1.10	38.03 ± 1.14	6.98 ± 0.70	27.17 ± 1.73

Note The O content was obtained based on the stoichiometry in the analysis software INCA developed by Oxford Instruments

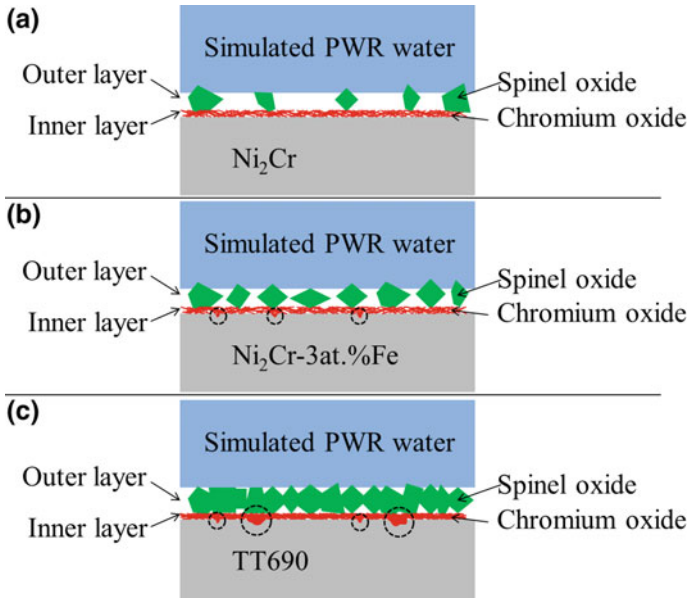

Fig. 7 Schematic drawing of the oxide films on the Ni-Cr-*x*Fe alloys after 978 h of immersion in the hydrogenated PWR primary water at 310 °C, with 30 cc/kg DH and DO < 5 ppb: **a** Ni_2Cr, **b** Ni_2Cr-3at.%Fe, and **c** TT690. The dashed circles show the penetration along the interface between the inner oxide layer and alloy matrix

favoring the formation of iron-bearing spinel oxides. The precipitation mechanism [44, 46] can illustrate the formation of the polyhedral spinel oxides. The formation of oxide films on Ni–Cr–Fe alloys in high temperature aqueous solutions is related to the varying diffusion rates of the metal ions in oxides, and the diffusion rates follow the order: $Fe^{2+} > Ni^{2+} >> Cr^{3+}$ [47–49]. The metallic cations diffuse from the matrix/film interface to the film/solution interface and react with water and the anions in the solution to form the outer oxide film. With increasing iron content in the alloys, more iron cations were released from the metal substrate and diffused through the inner oxide layer to form the outer oxide layer, resulting in more iron-bearing polyhedral spinel oxides in the outer oxide layer, as shown in Fig. 1.

With the iron content in the alloy matrix increased to ~9 at.% (TT690), a continuous outer oxide layer consisting of polyhedral oxide particles covered the alloy surface. The SEM morphology in Fig. 1e gives a clear view of the outer oxide layer on the specimen TT690. The average size of the polyhedral oxide particles on TT690 is a little smaller than that on the model alloys. The iron content increasing resulted in the increase of iron cations near the alloy surface and then increased the nucleation of the iron-bearing spinel oxides. The energy for the growth of the nucleation was limited by the energy cost of the nucleation.

Effects of the Iron Content in the Alloys on the Inner Oxide Layer

Increasing iron content in the alloy matrix slightly increased the thickness of the inner oxide layer. The inner oxide layers were chromium enriched and iron depleted compared to the outer oxide layers, as shown in Figs. 4, 5 and 6. The chromium-bearing oxides in the inner oxide layer were described to be CrOOH [50, 51], Cr_2O_3 [50, 52, 53] or chromium-bearing spinel oxides [44]. Marchetti et al. [54] found that the oxygen diffusion by short circuits in the oxide scale controlled the growth of the thin passive layer. Increasing the iron content in the alloy matrix can increase the iron cation concentration gradient between the matrix/film interface and the film/solution interface, accelerate the transport rate of iron cations, and give rise to the increasing migration rate of oxygen into the inner oxide layer and the growth of the inner oxide layer. The point defect model (PDM) [55] indicates that the growth of the passive film is based on the movement of defects, and the mixed-conduction model (MCM) [56] emphasizes the coupling between the ionic and electronic defect structure in the steady-state passive film. Both of the models illustrate that the formation of the oxide film is closely related to the migration of metallic cations. The increasing amount of anion transported into the inner oxide layer can result in a more serious corrosion along the interface between the inner oxide layer and alloy matrix. The PDM [57] also points out that the diffusion of metal cations can induce cation vacancies (or metal holes) [55] at the matrix/film interface, and these metal holes will submerge into the metal matrix. However, some metal holes start piling up and forming voids at the matrix/film interface when the diffusion rate of metal cations is larger than the submergence rate of metal holes. The increased iron content in the specimen Ni_2Cr-3at.%Fe induced the penetration into the alloy matrix from the inner oxide layer, and the higher iron content in the specimen TT690 gave rise to the more and deeper penetration.

Conclusions

The present work investigated the morphologies and chemical compositions of the oxide films grown on Ni–Cr–*x*Fe alloys at 310 °C in simulated PWR primary water with SEM, FIB, TEM and EDS. After 978 h of immersion, iron in the nickel-based alloys strongly affected the properties of the oxide films formed in simulated PWR water. The following conclusions can be drawn.

1. For iron-bearing nickel-based alloys, the local oxidation penetration into the alloy matrix from the inner oxide layer was interpreted by the pile-up process of the cation vacancies.
2. Increasing the iron content in the alloy could increase the general diffusion rate of the cations, accelerate the pile-up process of the cation vacancies, and ultimately increase the local oxidation penetration into the alloy matrix from the inner oxide layer. The iron content in the alloy had a less significant effect on the other regions of the chromium-rich inner oxide layer, except for the local oxidation penetration.
3. Increasing the iron content in the alloy significantly increased the amount of the iron-bearing polyhedral spinel oxide particles in the outer oxide layer.

Acknowledgements This work was supported by Shanghai Municipal Commission of Economy and Informatization No. T-221715003, the National Natural Science Foundation of China (51571138), and the International Cooperative Project sponsored by Science and Technology Commission of Shanghai Municipality No. 13520721200.

References

1. P.M. Scott et al., in *Comparison of Laboratory and Field Experience of PWSCC in Alloy 182 Weld Metal*. Proceedings of the 13th International Conf. On Environment Degradation of Materials in Nuclear Power Systems-Water Reactors (Whistler, British Columbia, 2007)
2. J. Hickling, A. Mcllree, R. Pathania, Materials reliability program (MRP) crack growth rates for evaluating primary water stress corrosion cracking (PWSCC) of thick-wall Alloy 600 materials (MRP-55). Revision 1, EPRI, Palo Alto, CA, EPRI Final Report (1006695), (2002)
3. G.A. White, J. Hickling, L.K. Mathews, in *Crack Growth Rates for Evaluating PWSCC of Thick-Wall Alloy 600 Material*. Proceedings of the 11th International Conf. On Environmental Degradation Materials Nuclear Power Systems-Water Reactors, (ANS, 2003), pp. 166–179
4. S. Yamazaki et al., The effect of prior deformation on stress corrosion cracking growth rates of Alloy 600 materials in a simulated pressurized water reactor primary water. Corros. Sci. **50**, 835–846 (2008)
5. M. Sennour et al., Advanced TEM characterization of stress corrosion cracking of Alloy 600 in pressurized water reactor primary water environment. J. Nucl. Mater. **393**, 254–266 (2009)
6. Z.P. Lu et al., Characterization of microstructure, local deformation and microchemistry in Alloy 600 heat-affected zone and stress corrosion cracking in high temperature water. Corros. Sci. **58**, 211–228 (2012)

7. Z.P. Lu et al., Characterization of microstructure, local deformation and microchemistry in Alloy 690 heat-affected zone and stress corrosion cracking in high temperature water. J. Nucl. Mater. **465**, 471–481 (2015)
8. Y.S. Lim et al., Primary water stress corrosion cracking behavior of an Alloy 600/182 weld. Corros. Sci. **100**, 12–22 (2015)
9. Y. Xie et al., Characterization of stress corrosion cracks in Ni-based weld alloys 52, 52 M and 152 grown in high-temperature water. Mater. Charact. **112**, 87–97 (2016)
10. G.S. Was et al., Corrosion and stress corrosion cracking in supercritical water. J. Nucl. Mater. **371**, 176–201 (2007)
11. S.E. Ziemniak, M. Hanson, Zinc treatment effects on corrosion behavior of Alloy 600 in high temperature, hydrogenated water. Corros. Sci. **48**, 3330–3348 (2006)
12. J. Huang et al., Influence of Zn on oxide films on Alloy 690 in borated and lithiated high temperature water. Corros. Sci. **53**, 3254–3261 (2011)
13. I. Betova et al., Effect of water chemistry on the oxide film on Alloy 690 during simulated hot functional testing of a pressurised water reactor. Corros. Sci. **58**, 20–32 (2012)
14. Z. Zhang et al., Influence of dissolved oxygen on oxide films of Alloy 690TT with different surface status in simulated primary water. Corros. Sci. **53**, 3623–3635 (2011)
15. W. Kuang, X. Wu, E.-H. Han, Influence of dissolved oxygen concentration on the oxide film formed on Alloy 690 in high temperature water. Corros. Sci. **69**, 197–204 (2013)
16. J. Wang et al., Comparison of corrosion resistance of UNS N06690TT and UNS N08800SN in simulated primary water with various concentrations of dissolved oxygen. Corrosion **70**, 598–614 (2014)
17. Z. Zhang et al., Influence of later-dissolved oxygen on microstructural changes in oxide films formed on Alloy 690TT in hydrogenated primary water. Corros. Sci. **94**, 245–254 (2015)
18. J. Xu, T. Shoji, The corrosion behavior of Alloy 52 weld metal in cyclic hydrogenated and oxygenated water chemistry in high temperature aqueous environment. J. Nucl. Mater. **461**, 10–21 (2015)
19. J. Xiao et al., Effects of dissolved oxygen on corrosion fatigue cracking of Alloy 690(TT) in pressurized water reactor environments. Int. J. Fatigue **74**, 65–70 (2015)
20. J. Xu, T. Shoji, The corrosion behavior of Alloy 182 in a cyclic hydrogenated and oxygenated water chemistry in high temperature aqueous environment. Corros. Sci. **104**, 248–259 (2016)
21. J. Tan et al., The effect of dissolved oxygen on fatigue behavior of Alloy 690 steam generator tubes in borated and lithiated high temperature water. Corros. Sci. **102**, 394–404 (2016)
22. Z. Zhang et al., Analysis of surface oxide films formed in hydrogenated primary water on Alloy 690TT samples with different surface states. J. Mater. Sci. Technol. **30**, 1181–1192 (2014)
23. T. Kim et al., Effects of dissolved hydrogen on the crack-initiation and oxidation behavior of nickel-based alloys in high-temperature water. Corros. Sci. **106**, 260–270 (2016)
24. R. Mendonça et al., Effect of temperature and dissolved hydrogen on oxide films formed on Ni and Alloy 182 in simulated PWR water. J. Nucl. Mater. **477**, 280–291 (2016)
25. S.Y. Persaud et al., High resolution analysis of oxidation in Ni-Fe-Cr alloys after exposure to 315 °C deaerated water with added hydrogen. Corros. Sci. **106**, 236–248 (2016)
26. H. Sun, X.Q. Wu, E.H. Han, Effects of temperature on the protective property, structure and composition of the oxide film on Alloy 625. Corros. Sci. **51**, 2565–2572 (2009)
27. G.J. Abraham et al., Electrochemical characterization of oxide film formed at high temperature on Alloy 690. Nucl. Eng. Des. **243**, 69–75 (2012)
28. D.J. Kim, H.C. Kwon, H.P. Kim, Effects of the solution temperature and the pH on the electrochemical properties of the surface oxide films formed on Alloy 600. Corros. Sci. **50**, 1221–1227 (2008)
29. J. Huang, X.Q. Wu, E.H. Han, Influence of pH on electrochemical properties of passive films formed on Alloy 690 in high temperature aqueous environments. Corros. Sci. **51**, 2976–2982 (2009)

30. S.Y. Persaud et al., The influence of the high Fe and Cr contents of Alloy 800 on its inter- and intergranular oxidation tendency in 480 °C hydrogenated steam. Corros. Sci. **106**, 117–126 (2016)
31. N.K. Das et al., Early stage SCC initiation analysis of fcc Fe-Cr-Ni ternary alloy at 288 °C: A quantum chemical molecular dynamics approach. Corros. Sci. **51**, 908–913 (2009)
32. J. Chen, et al., *High Resolution Electron Microscopy Study on Oxide Films Formed on Nickel-Base Alloys X-750, 182 and 82 in Simulated High Flow Velocity BWR Water Conditions*, ed. by A. Jasiulevicius Proceedings of the 15th International Conf. on Environmental Degradation of Materials in Nuclear Power Systems-Water Reactors (Wiley Online Library, 2011), pp. 371–383
33. D.K. Schreiber, M.J. Olszta, S.M. Bruemmer, Grain boundary depletion and migration during selective oxidation of Cr in a Ni-5Cr binary alloy exposed to high-temperature hydrogenated water. Scripta Mater. **89**, 41–44 (2014)
34. Y.S. Lim et al., Intergranular oxidation of Ni-based Alloy 600 in a simulated PWR primary water environment. Corros. Sci. **108**, 125–133 (2016)
35. S. Xia, B.X. Zhou, W.J. Chen, Effect of single-step strain and annealing on grain boundary character distribution and intergranular corrosion in Alloy 690. J. Mater. Sci. **43**, 2990–3000 (2008)
36. M. Payet et al., Corrosion mechanism of a Ni-based alloy in supercritical water: Impact of surface plastic deformation. Corros. Sci. **100**, 47–56 (2015)
37. S. Lozano-Perez et al., The role of cold work and applied stress on surface oxidation of 304 stainless steel. Corros. Sci. **56**, 78–85 (2012)
38. C. Soustelle, M. Foucault, P. Combrade, in *PWSCC of Alloy 600: A Parametric Study of Surface Film Effects*. Ninth international symposium on environmental degradation of materials in nuclear power systems-water reactors (TMS, Newport Beach, Ca, USA, 1999), p. 105
39. F. Carrette et al., Analysis and TEM examination of corrosion scales grown on Alloy 690 exposed to pressurized water at 325 °C. Surf. Interface Anal. **34**, 135–138 (2002)
40. A.Y. Daigo, Y. Watanabe, K. Sue, Corrosion mitigation in supercritical water with chromium ion. Corros. **63**, 1085–1093 (2007)
41. W. Kuang et al., Effect of alternately changing the dissolved Ni ion concentration on the oxidation of 304 stainless steel in oxygenated high temperature water. Corros. Sci. **53**, 2582–2591 (2011)
42. W. Kuang et al., Effect of nickel ion from autoclave material on oxidation behaviour of 304 stainless steel in oxygenated high temperature water. Corros. Sci. **53**, 1107–1114 (2011)
43. B. Beverskog, I. Puigdomenech, Revised Pourbaix diagrams for nickel at 25–300 °C. Corros. Sci. **39**, 969–980 (1997)
44. M. Sennour et al., A detailed TEM and SEM study of Ni-base alloys oxide scales formed in primary conditions of pressurized water reactor. J. Nucl. Mater. **402**, 147–156 (2010)
45. B. Beverskog, I. Puigdomenech, Pourbaix diagrams for the ternary system of iron-chromium-nickel. Corrosion **55**, 1077–1087 (1999)
46. L. Marchetti et al., XPS study of Ni-base alloys oxide films formed in primary conditions of pressurized water reactor. Surf. Interface Anal. **47**, 632–642 (2015)
47. R. Dieckmann et al., Defects and cation diffusion in magnetite (III.) tracerdiffusion of foreign tracer cations as a function of temperature and oxygen potential. Ber. Bunsen-Ges. Phys. Chem. **82**, 778–783 (1978)
48. R. Dieckmann, Point defects and transport properties of binary and ternary oxides. Solid State Ionics **12**, 1–22 (1984)
49. J. Robertson, The mechanism of high temperature aqueous corrosion of stainless steels. Corros. Sci. **32**, 443–465 (1991)
50. N.S. Mclntyre, D.G. Zetaruk, D. Owen, X-ray photoelectron studies of the aqueous oxidation of Inconel-600 alloy. J. Electrochem. Soc. **126**, 750–760 (1979)

51. J.B. Ferguson, H.F. Lopez, Oxidation products of Inconel alloys 600 and 690 in pressurized water reactor environments and their role in intergranular stress corrosion cracking. Metall. Mater. Trans. A **37**, 2471–2479 (2008)
52. A. Machet et al., XPS study of oxides formed on nickel-base alloys in high-temperature and high-pressure water. Surf. Interface Anal. **34**, 197–200 (2002)
53. F. Carrette et al., Analysis and TEM examination of corrosion scales grown on alloy 690 exposed to PWR environment. Mater. High Temp. **20**, 581–591 (2003)
54. L. Marchetti, S. Perrin, O. Raquet, M. Pijolat, Corrosion mechanisms of Ni-base alloys in pressurized water reactor primary conditions. Mater. Sci. Forum 529–537 (2008)
55. C.Y. Chao, L.F. Lin, D.D. Macdonald, A point defect model for anodic passive films I. Film growth kinetics. J. Electrochem. Soc. **128**, 1187–1194 (1981)
56. M. Bojinov et al., Electrochemical study of the passive behaviour of Ni-Cr alloys in a borate solution-a mixed-conduction model approach. J. Electroanal. Chem. **504**, 29–44 (2001)
57. L.F. Lin, C.Y. Chao, D.D. Macdonald, A point defect model for anodic passive films II. Chemical breakdown and pit initiation. J. Electrochem. Soc. **128**, 1194–1198 (1981)

Part XIII
PWR Secondary Side

Effect of Applied Potential and Inhibitors on PbSCC of Alloy 690TT

Brent Capell, Jesse Lumsden, Michael Calabrese and Rick Eaker

Abstract Alloy 690TT has been shown to be susceptible to lead stress corrosion cracking (PbSCC) at pH_T values of 9.1 and above and with no cracks occurring at lower pH_T values like 8.5. Previous work on PbSCC has been completed at the open circuit potential (OCP). A test program has been completed at applied electrochemical potentials for Alloy 690TT at pH_T values of 8.5 and 9.5. Testing has shown sporadic PbSCC occurrence at pH_T 8.5 which previously showed no cracking although an exact causal factor was not identified. At pH_T 9.5, applying a potential did not stop PbSCC from occurring, although at +75 mV applied potential there was the inclusion of an apparent incubation time where none had previously been observed. To minimize to PbSCC, scoping testing was completed on four candidate inhibitors at pH_T 9.5. Three of the four inhibitors tested (TiO_2, H_3BO_3, and CeB_6) showed reductions in maximum crack depths compared to testing without an inhibitor. Although promising, inhibitors still require additional testing before widespread use can be recommended.

Keywords PbSCC · Alloy 690TT · Inhibitor · Lead · Secondary side

B. Capell (✉)
Electric Power Research Institute (EPRI), 1300 West WT Harris Blvd, Charlotte, NC 28262, USA
e-mail: bcapell@epri.com

J. Lumsden · M. Calabrese
Teledyne Scientific and Imaging Company, 1049 Camino Dos Rios, Thousand Oaks, CA 91360, USA

R. Eaker
HKA Enterprises, 337 Spartagreen Blvd, Ducan, SC 29334, USA

J.H. Jackson et al. (eds.), *Proceedings of the 18th International Conference on Environmental Degradation of Materials in Nuclear Power Systems – Water Reactors*, The Minerals, Metals & Materials Series, https://doi.org/10.1007/978-3-319-68454-3_82

Introduction

Stress Corrosion Cracking (SCC) from the secondary side of steam generator tubing has been occurring in pressurized water reactors (PWRs) since the 1970's [1]. Since the first reports of SCC, researchers have been trying to understand the mechanism by which cracking occurs and trying to reduce the operational impact. One aspect of the SCC in secondary side environments that has been investigated is the role of lead (Pb) on the cracking process [2]. Examination of pulled tubes from service and laboratory studies have both demonstrated that Pb is associated with SCC [3, 4] and this paper will use the term PbSCC to indicate SCC linked to Pb in a secondary side (caustic) environment.

Analysis of pulled tubes from service has shown that Pb is often present near the crack tips [3]. The lead appears associated with cracked regions where the local composition can deviate from the base metal composition. These areas often have depleted regions in chromium or nickel. One theory for the mechanism by which lead acts is that it disrupts the ability for a protective oxide to form.

Laboratory studies of PbSCC have also been completed looking at the effect of various factors on the occurrence of PbSCC. EPRI and others have sponsored a number of studies investigating key parameters to try and provide insight into minimizing the risk of PbSCC on operational plants. One variable tested was the tubing material [5, 6]. Early steam generators in the US used Alloy 600MA but were found to be very susceptible to SCC (with and without lead) leading to development and use of the more resistant Alloy 600TT (thermally treated version of Alloy 600MA with intergranular carbides) and Alloy 690TT (with increased Cr). Additionally, some non-US plants have utilized Alloy 800NG, a stainless steel variant, as a tubing material. While these alloys have greatly improved in-plant performance compared to Alloy 600MA, laboratory testing suggests that neither alloy is completely resistant to PbSCC [6].

A second factor that has shown to have a strong effect on PbSCC is the pH_T of the environment. Alloy 690TT shows a threshold behavior for susceptibility to PbSCC. For pH_T values at and above 9.1 (at 330 °C and above), Alloy 690TT undergoes relatively rapid crack formation [6, 7]. At pH_T values under 9.1, Alloy 690TT appears highly resistant to PbSCC with no crack formation after 5000 h in a Reverse U-Bend exposure test. For Alloy 600MA and 600TT, pH does not have as strong effect and both alloys are susceptible to PbSCC for all pH values [7]. Similar to Alloy 690TT, at high pH_T Alloy 800NG is susceptible to PbSCC while at more neutral values of pH_T Alloy 800NG is very resistant to PbSCC [8].

While the effect of pH_T for Alloy 690TT has been measured, a secondary chemistry effect arises from the electrochemical potential (ECP) that is present during the cracking process. All the previous testing was completed at the open circuit potential (OCP). Shifts in ECP above and below the OCP can shift the stable surface oxide phases. Given that lead may act through passive surface film stability, a change in ECP could affect PbSCC resistance of Alloy 690TT. Examining this effect was the first goal of this test program.

Another aspect of PbSCC resistance is the use of inhibitors to reduce PbSCC. An inhibitor could act to reduce the negative behavior of lead. If an inhibitor can be shown to be effective in reducing PbSCC, this represents a new tool that PWR plants could implement to reduce cracking at plants. The first step of employing such an inhibitor is to perform scoping testing is to identify candidates and test these candidates to see if there is evidence they are effective. The second goal of this program was to perform scoping testing for candidate inhibitors for PbSCC of Alloy 690TT.

Experimental Description

Exposure testing was completed using Reverse U-Bend (RUB) specimens. The heat of material tested was D512507 and the composition of this heat is shown in Table 1. Additionally, limited testing of Alloy 600MA was performed during the inhibitor portion of the testing. The heat of Alloy 600MA used was M182702 and it was supplied in the mill-annealed condition. Both heats of material were received from production lots of steam generator tubing material. Samples were cut to length, split, and bent using the same processes as previously employed for prior EPRI sponsored testing.

Samples were fabricated by splitting 12.7 cm (5 inch) long segments of the tube longitudinally using the fixture to ensure the cut was made along the axis of the tubing. The split tube sections were bent around a "donut" shaped mandrel. The mandrel used were the same as that in previous EPRI testing of Alloy 600MA, Alloy 600TT, and Alloy 690TT RUB specimens that used the same diameter and thickness tubing [7]. After bending in the mandrel, the specimen is allowed to relax where the legs partially spread apart again. The specimens are reloaded using an Alloy 600 bolt through holes drilled in the base of the legs that is tightened until the legs are parallel. This produces a specimen where the sample is under considerable stress and the original inner diameter surface is in tension although the exact stress/strain conditions have not been well determined through a process like X-ray Diffraction (XRD).

The test solutions are shown in Table 2 depending on the desired test conditions. The test solutions the same those previously used [7] and are designed to be a representation for a concentrated crevice with highly faulted chemistry. The pH values were chosen because the PbSCC behavior was known at OCP at these values and the goal of this project is to understand how PbSCC response changes with applied ECP. For inhibitor testing, only pH_T 9.5 was used since no cracking occurs at OCP for pH_T 8.5. Test solution pH was controlled by varying the NaOH concentration and MULTEQ was used to predict the final solution pH [9]. Table 2 also shows the four inhibitor candidates tested in this program: Nickel Boride (NiB), Titanium Dioxide (anatase form) (TiO_2), Boric Acid (H_3BO_3), and Cerium Hexaboride (CeB_6). The concentrations of each of these was set at high levels to have the best chance of demonstrating effectiveness as an inhibitor.

Table 1 Chemical composition (in weight percent) for heats used in this study

Alloy	C	Mn	S	P	Si	Cr	Ni	Cu	Co	Al	Ti	Fe	N
690TT	0.019	0.19	<0.0001	0.010	0.29	29.4	60.1	0.04	0.008	0.08	0.28	9.5	0.008
600MA	0.026	0.27	<0.001	0.003	0.27	15.8	74.5	<0.01	0.003	NR[a]	NR[a]	8.6	NR[a]

[a]Value Not Reported

Table 2 Test solution chemistries

Test condition	NaCl	NaOH	Pb as PbO	Inhibitor
ECP testing				
$pH_{330\ °C}$ 8.5	3 m	0.049 m	500 ppm	NA
$pH_{330\ °C}$ 9.5	3 m	0.54 m	500 ppm	NA
Inhibitor testing—all at $pH_{310\ °C}$ 9.5				
None	3 m	0.45 m	500 ppm	None
NiB	3 m	0.48 m	500 ppm	2000 ppm
TiO_2	3 m	0.45 m	500 ppm	2000 ppm
H_3BO_3	3 m	0.55 m	500 ppm	1000 ppm
CeB_6	3 m	0.51 m	500 ppm	2000 ppm

A titanium autoclave was used to measure the effect of applied ECP. Up to four specimens were electrically isolated from the autoclave and attached to a potentiostat with a nickel reference electrode as shown in Fig. 1a. The autoclave was sealed and deaerated using a 95% Argon/5% hydrogen cover gas which was pressurized and purged at least three cycles to ensure the solution is deaerated. The cover gas composition corresponds to a starting dissolved hydrogen concentration of 6 ppm. The autoclave was heated up and the samples exposed at 330 °C for periods of time ranging from 432 h to a total of 4296 h. If an autoclave was shutdown, the solution inside was refreshed before the next exposure cycle.

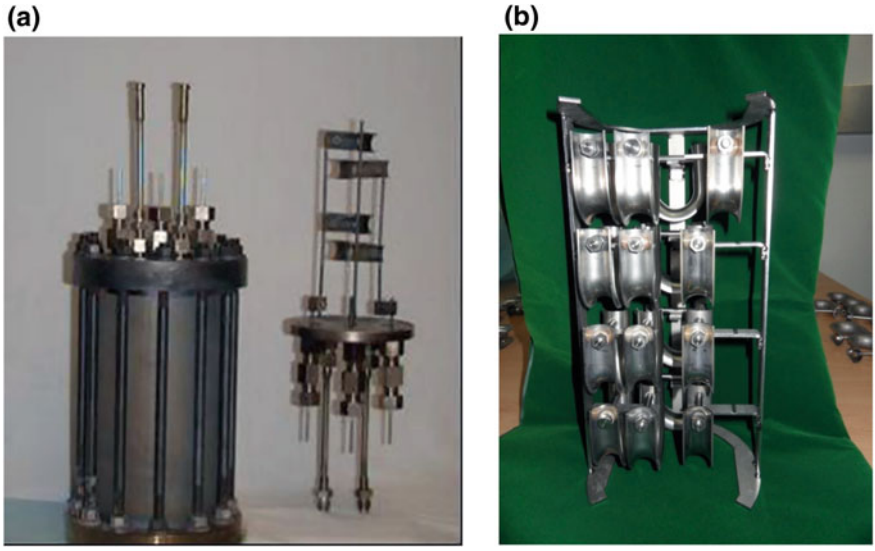

Fig. 1 **a** Autoclave and mount (shown upside down) for RUB specimens for applied ECP tests and **b** mount for inhibitors testing

For testing of inhibitors, the same testing procedure was used but exposures were performed in a different autoclave. The autoclave used for inhibitor testing was Ti but limited to a lower temperature resulting in inhibitor exposure being performed at 310 °C with exposure times up to 2000 h. A larger specimen tree, shown in Fig. 1b, was used which could expose up to 16 specimens for each run.

After the final exposure time, the samples were mounted and destructively examined to look for evidence of cracking. Previous testing showed that visual inspection of the specimen surface was not sufficient to find small cracks in the specimens.

Results and Discussion

Effect of Applied ECP—$pH_{330\ °C}$ 8.5

Previous testing of Alloy 690TT showed that at $pH_{330\ °C}$ 8.5 no cracking was observed for specimens up to 5000 h of exposure. Maximum crack depths after exposure from this study are shown in Table 3. Figure 2 plots the maximum crack depth as a function of exposure time. Figures 3, 4, and 5 show optical micrographs from samples after exposure with $pH_{330\ °C}$ 8.5. Figure 3 shows two specimens after exposure at $pH_{330\ °C}$ 8.5 with −75 mV applied potential with one specimen not having cracked while another specimen shows a transgranular crack. Figure 4 shows two specimens after exposure at $pH_{330\ °C}$ 8.5 with +50 mV applied potential with one specimen not having cracked while another specimen shows a transgranular crack. Figure 5 shows two specimens after exposure at $pH_{330\ °C}$ 8.5 with +75 mV applied potential with no cracks in either specimen.

At $pH_{330\ °C}$ 8.5, applying an ECP resulted in no cracks present for 17 of the 20 specimens. The three cracked specimens are spread sporadically across the applied potential and exposure time. The time aspect is especially interesting since cracks grew in some specimens while other specimens from the same batch or with substantially more exposure time showed no evidence of crack growth. In addition to crack presence not being fully dependent on time, at the same applied potential, some specimens cracked while duplicate specimens did not. At +50 mV potential, four specimens were tested for 1632 h and only one of four were found to have cracks.

Under OCP, no cracking occurred while under both positive and negative applied potentials, cracking was observed on a seemingly random set of specimens. This could indicate that applied potentials off OCP could impact the resistance of Alloy 690 to PbSCC, but that the change in resistance is more complex than simply the applied potential. One explanation for the sporadic occurrence of cracking is that there are local surface features which affect PbSCC development. For example, in Fig. 6b, the cracking appears to start at a slight depression in the surface that could be related to some kind of local surface deformation that allows PbSCC to

Table 3 Maximum crack depths in alloy 690TT RUB specimens after exposure with various potentials

Potential (relative to OCP)	$pH_{330\ °C}$ 8.5		$pH_{330\ °C}$ 9.5	
	Time (hrs)	Maximum crack depth (microns)	Time (hrs)	Maximum crack depth (microns)
0 mV (OCP) (previous reported)	2928	0	432	255
	2928	0	432	230
	5016	0	500	235
	5016	0	500	244
			912	310
			912	355
			1584	389
			1584	354
			1824	538
			1824	846
			2376	800
			2376	626
			2928	1016
			2928	974
−75 mV	1000	0	600	162
	1000	0	600	216
	2760	0	1600	375
	2760	126	1600	290
	3096	0	3072	Cracks[a]
	3096	320	3072	Cracks[a]
	4056	0	3072	Cracks[a]
	4056	0	3072	Cracks[a]
+50 mV	1632	265	432	226
	1632	0	432	197
	1632	0	1008	377
	1632	0	1008	319
			1440	198
			1440	279
+75 mV	1000	0	500	0
	1000	0	500	0
	3072	0	1536	0
	3072	0	1536	0
	4080	0	3264	140
	4080	0	3264	365
			3552	0
			4296	257

[a]For specimens at $pH_{330\ °C}$ 9.5 after 3072 h, cracking was present, but excessive surface oxidation made precise crack depth measurements impractical

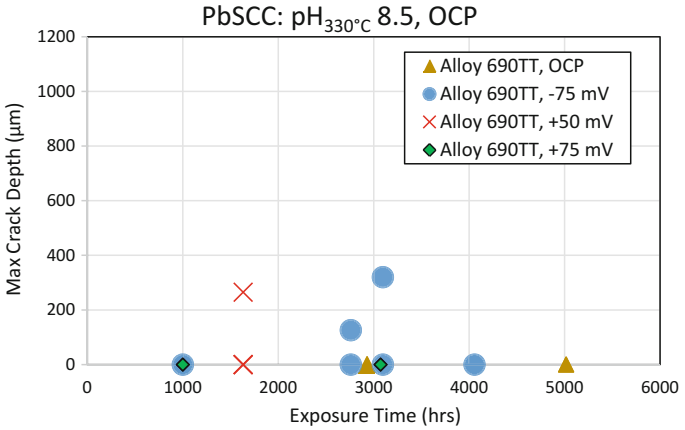

Fig. 2 Maximum crack depth as a function of exposure time for applied potentials at $pH_{330\ °C}$ 8.5

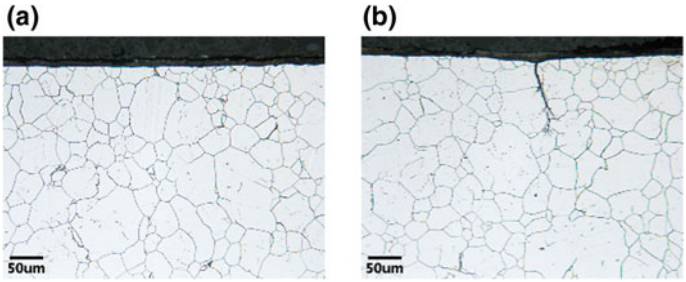

Fig. 3 Micrographs after exposure at $pH_{330\ °C}$ 8.5 with −75 mV applied potential for 2760 h with specimen **a** 7-29 not showing any cracks and **b** 7-30 showing cracking present

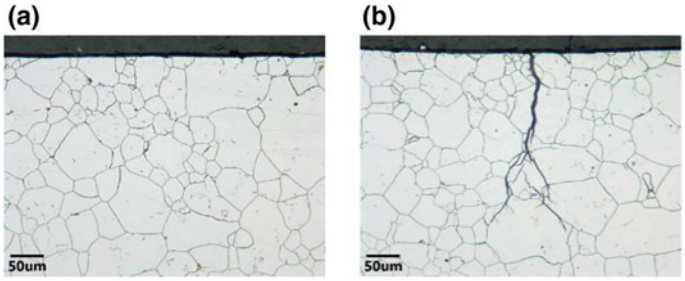

Fig. 4 Micrographs after exposure at $pH_{330\ °C}$ 8.5 with +50 mV applied potential for 1632 h with specimen **a** 7-38 not showing any cracks and **b** 7-27 showing cracking present

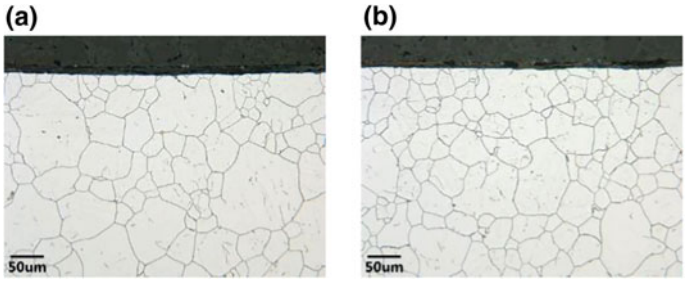

Fig. 5 Micrographs after exposure at $pH_{330\ °C}$ 8.5 with +75 mV applied potential for 4056 h no cracks present on specimen **a** 7-11 and **b** 7-12

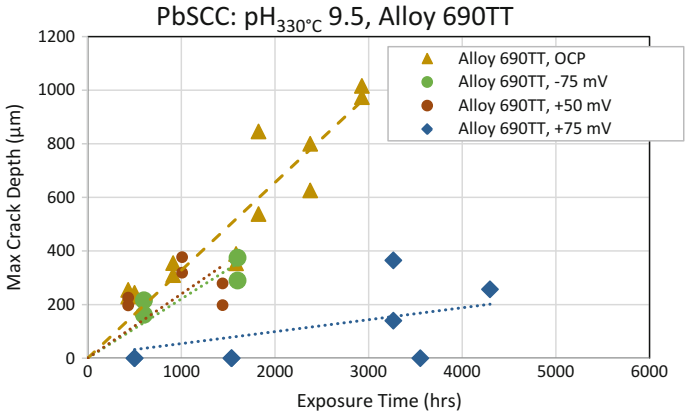

Fig. 6 Maximum crack depth as a function of exposure time for applied potentials at $pH_{330\ °C}$ 9.5

occur. This would indicate that ECP values just off OCP allow secondary factors to influence PbSCC resistance.

The behavior of PbSCC under off normal ECP has implications for operating conditions. This lack of cracking at OCP implies that operation at OCP best ensures that PbSCC will not occur while the sporadic appearance of PbSCC at both higher and lower applied potentials suggests that these conditions are not as resistant. Therefore, operation near the OCP appears to be the proper potential to minimize cracking and application of applied potential is likely to result in some additional risk, though not a certain risk, for formation of PbSCC.

Effect of Applied ECP—$pH_{330\ °C}$ 9.5

Previous testing of Alloy 690TT showed that at $pH_{330\ °C}$ 9.5 cracking appears to initiate very quickly after start of the exposure and progress at a linear rate.

Table 4 Maximum crack depth for various inhibitors and temperatures all at pH_T 9.5

Test condition		Time (hrs)			
	Inhibitor	0	1000	1500	2000
Alloy 690TT—310 °C	None	0	21.9	60.3	98
	NiB	0	75.8	134.4	178
	TiO_2	0	6.6	7.5	7.5
	H_3BO_3	0	32.9	50.8	59.5
	CeB_6	0	5.1	26.9	29.5
Alloy 690TT—330 °C	None	0	298	400	650
Alloy 600MA—310 °C	None	0	3.6	5.4	14.7
Alloy 600MA—330 °C	None	0	75.6	180	190

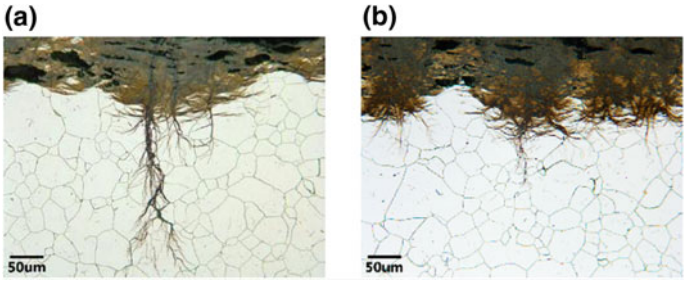

Fig. 7 Micrographs after exposure at $pH_{330\ °C}$ 9.5 with −75 mV applied potential for **a** specimen 7-3 after 1600 h showing transgranular cracks and **b** specimen 7-11 after 3072 h where transgranular cracking is present, but the large amount of surface oxide makes accurate crack depth imprecise

Maximum crack depths after exposure from this study are shown in Table 3. Figure 6 plots the maximum crack depth as a function of exposure time. Figures 7, 8, and 9 show optical micrographs from samples after exposure with $pH_{330\ °C}$ 9.5. Figure 7 shows two specimens after exposure at $pH_{330\ °C}$ 9.5 with −75 mV applied potential at two different times both showing transgranular cracks present. Also shown in Fig. 7b is that excessive surface oxidation has occurred making precise determination of the crack depth impractical for this exposure time. This occurred on all four specimens exposed at 4096 h. Figure 8 shows two specimens after exposure at $pH_{330\ °C}$ 9.5 with +50 mV applied potential with both specimens showing cracking that starts as transgranular, but progresses to intergranular after some depth. Figure 9 shows two specimens after exposure at $pH_{330\ °C}$ 9.5 with +75 mV applied potential with no cracks in one specimen after 3552 h and transgranular cracking in one specimen after 4296 h.

For −75 and +50 mV applied potentials, the crack growth rate is comparable to the OCP crack growth rate as demonstrated by the similarity to the OCP trend line. While there does appear to be a slightly lower growth rate at both these applied

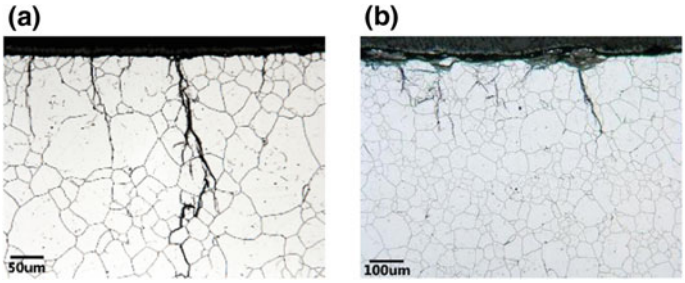

Fig. 8 Micrographs after exposure at $pH_{330\ °C}$ 9.5 with +50 mV applied potential for **a** specimen 7-35 after 1008 h showing cracking transitioning from transgranular to intergranular and **b** specimen 7-33 after 1440 h showing similar cracking behavior

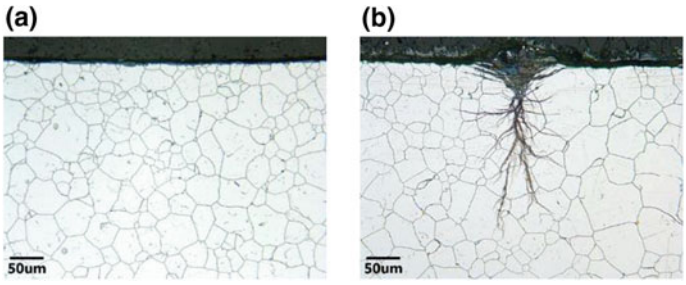

Fig. 9 Micrographs after exposure at $pH_{330\ °C}$ 9.5 with +75 mV applied potential for **a** specimen 7-24 after 3552 h showing lack of cracking and **b** specimen 7-23 after 4296 h showing typical transgranular cracking

ECPs, cracking appears to still be linear from the start of the test. For +75 mV applied potentials, a slightly different behavior was observed as shown by no cracking being observed in four specimens at times less than 1600 h followed by 3 of 4 specimens cracking at time longer than 3200 h. The lack of cracks at short times indicates that some incubation feature may be present. However, at sufficiently long times, cracking still occurs for +75 mV applied potentials. While the surface oxide film was not quantitatively evaluated, it does appear that the surface oxides with +75 mV applied potentials are not as thick. Thick oxides on Alloy 800NG were found to correspond to increased susceptibility to PbSCC in [8].

At $pH_{330\ °C}$ 9.5, applying a potential does not lead to immunity from PbSCC. For −75 mV and +50 mV, the crack growth rates are very similar to OCP. For +75 mV, the addition of incubation time implies that there is some protection from PbSCC, however, given enough time, this condition is still susceptible to PbSCC. Therefore, operation at a very high pH value should still be avoided to prevent PbSCC. This result reinforces the need to keep faulted crevice conditions at lower pH values to avoid susceptibility to PbSCC.

Inhibitor Scoping Testing

Maximum crack depths for the inhibitor testing are shown in Table 4 with all tests completed at $pH_{330\ °C}$ 9.5 because cracking was not observed in Alloy 690TT at $pH_{330\ °C}$ 8.5. Figure 10 shows the maximum crack depth as a function of exposure time at two temperatures for two alloys (Alloy 600MA and Alloy 690TT). Because the inhibitor testing temperature was lower than previously used, the difference in the observed crack growth rates was compared. As shown in Fig. 10, the crack growth at the lower temperature was lower for both alloys. The drop in maximum crack depth for Alloy 690TT dropped the uninhibited case to around 100 microns of crack growth after 2000 h exposure. At this level, significant decreases in crack growth were still be resolvable. For Alloy 600MA, the maximum crack depths at 310 °C have become quite low meaning that effective measurement of inhibitor effectiveness would be difficult.

The effectiveness of the inhibitor candidates can be seen in Fig. 11 which shows the crack depth trends with time for each of the candidates. Each candidate will be briefly discussed.

1. NiB: The observed crack depths for NiB were greater than those without an inhibitor. Therefore, NiB acts more as a crack accelerant than an inhibitor. Large additions of NiB should be avoided to decrease crack growth.
2. TiO_2: The maximum crack depth after 2000 h decreased from 98 microns without an inhibitor to 7.5 microns with TiO_2 as an inhibitor. This is a substantial reduction in crack depth. TiO_2 was chosen as a candidate because of past use for secondary side SCC control in earlier steam generators [10]. The effect on PbSCC specifically demonstrates that TiO_2 should be considered again for use if PbSCC can be determined to the cause of cracking. One issue noted

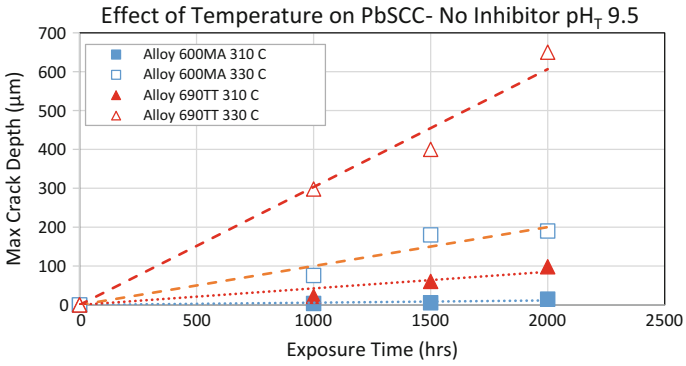

Fig. 10 Effect of test temperature on PbSCC between 330 °C and 310 °C for alloy 600MA and 690TT

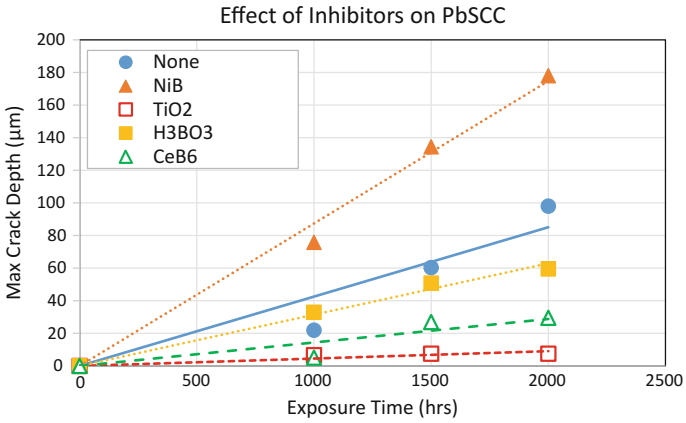

Fig. 11 Effect of Inhibitor on maximum crack depth as a function of exposure time at 310 °C at $pH_{310\ °C}$ 9.5

during this test program was the formation of white precipitate after the tests with TiO_2 (Fig. 12). The precipitate is present at the room temperature water line suggesting it was formed during cooling and was not present at high temperature. The jelly like precipitate was dehydrated and analyzed where it was found to contain Ti, Na, and O. As stated previously, TiO_2 has previously been added to operating plants but similar precipitates have not been reported. One explanation is that the concentration for this scoping study was 2000 ppm while previous use has been of the order 100–200 ppm, significantly less. While this study showed TiO_2 to be an effective inhibitor, more work will be required to understand the relationship between concentration, effectiveness, and precipitate formation.

3. H_3BO_3: Boric acid had lower crack depths at 2000 h compared to without an inhibitor, but the decrease was less than for TiO_2. This shows that boric acid does appear effective, but not as effective as TiO_2. However, no precipitates were observed as for TiO_2. Boric acid has also previously been used in plants to control secondary side SCC [11]. Overall, boric acid was effective in reducing PbSCC in this program.
4. CeB_6: The addition of CeB_6 reduced the maximum crack depths at 2000 h to 29.5 microns. While not as good as TiO_2, it was a substantial reduction, more effective than boric acid, and did not result in any precipitate formation. However, CeB_6 does not have any record of major in-plant usage. Additional materials compatibility testing would need to be performed prior to plant applications.

Overall, three of the four tested inhibitors showed a reduction in maximum crack depths compared to testing without an inhibitor. Of these, all have some advantages and some disadvantages. TiO_2 has the largest decrease in crack depths. Given past usage in plants, TiO_2 is considered a likely candidate.

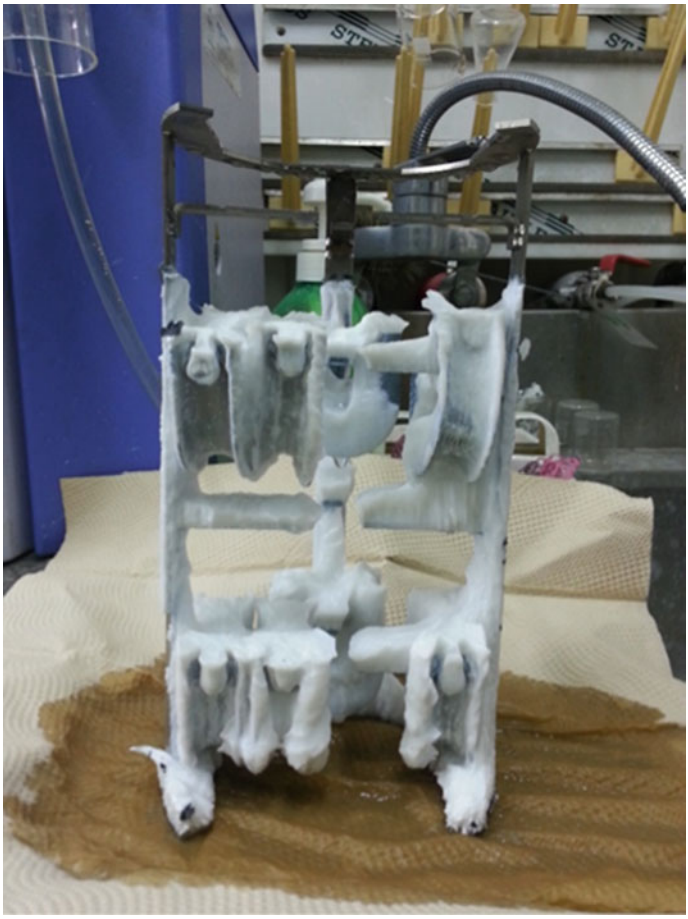

Fig. 12 White precipitate formed in inhibitor test with TiO_2

There are two key questions that need to be answered about TiO_2 (or any inhibitor) before plant use can be recommended. First, what is the relationship between concentration and effectiveness? Given the observed precipitate in TiO_2 tests but the lack of such precipitate during past plant use, dropping the concentration and examining if TiO_2 is still as effective is a necessary step to optimize plant usage. Second, the scoping testing completed had the inhibitor present during the entire test run. Any inhibitor may be started after the first signs of cracking have been observed. Therefore, determining the effectiveness of an inhibitor to stop initiated cracking is needed to understand when the inhibitors need to be used to be most effective.

Conclusion

Testing at a variety of applied potentials and with the additional of four candidate inhibitors was completed. The results of this study demonstrate:

1. At $pH_{330\,°C}$ 8.5, 3 of 20 specimens with applied potentials showed cracking where open circuit potential testing previously showed no cracking. The three cracked samples however were sporadically spread around applied potential and time which indicates a more variable link to cracking than simple potential and time. These results confirm that keeping to open circuit is the best course to reduce the potential for PbSCC to occur.
2. At $pH_{330\,°C}$ 9.5, PbSCC occurred at all applied potentials. For −75 mV and +50 mV, the cracking behavior was only slightly better than at open circuit potential. For +75 mV applied potential, cracking behavior seemed to show an incubation time, but cracks still developed after enough time. Reduction of cracking by applying potential is not effective to stop PbSCC and all high pH excursions should be appropriately managed by pH reductions down to a value where Alloy 690TT shows greater resistance.
3. Inhibitor testing showed that TiO_2, H_3BO_3, and CeB_6 were all effective in reducing crack depths compared to testing without and inhibitor. NiB lead to greater crack depths and should be avoided. Of the three effective inhibitors, TiO_2 lead to the greatest reduction in PbSCC, but also showed a white precipitate that likely formed during cooling and may be related to the high concentration used for testing. Additional technical work, including effect of concentration on effectiveness and ability to inhibit active cracks, is needed prior to full plant use.

References

1. Steam Generator Management Program: Steam Generator Progress Report—Revision 18, EPRI, Palo Alto, CA, 2013. 3002002201
2. Proceedings: 2005 EPRI/ANL/NRC Workshop on Effects of Lead and Sulfur on the Performance of Secondary Side Tubing of Steam Generators in PWRs, EPRI, Palo Alto, CA, 2005. 1012780
3. Summary of Analytical Electron Microscopy Observation of Intergranular Attack and Stress Corrosion Cracks in Alloy 600 Steam Generator Tubing, EPRI, Palo Alto, CA, 2005. 1011683
4. P.J. King, F. Gonzalez, J. Brown, Stress Corrosion Cracking Experience in Steam Generators at Bruce NGS. Proceedings of Sixth International Symposium on Environmental Degradation in Nuclear Power Systems—Water Reactors, the Minerals, Metals and Materials Society, Warrendale, PA, 1993, p 233–243
5. F. Vaillant, D. Buisine, B. Prieux, Comparative Behavior of Alloy 600, 690 and 800 in Caustic Environments. Proceedings of the Seventh International Symposium on Environmental Degradation of Materials in Nuclear Power Systems—Water Reactors, National Association of Corrosion Engineers, Houston, TX, 1995

6. Steam Generator Management Program: Conditions Causing Lead Stress Corrosion Cracking of Steam Generator Tubing: Alloy 690TT, EPRI, Palo Alto, CA, 2013. 3002000490
7. P. Wolfe, R. Eaker, J. Lumsden. PbSCC of Alloy 690TT and Alloy 800NG Steam Generator Tubing in Alkaline Conditions, Proceedings of the 16th International Conference on Environmental Degradation of Materials in Nuclear Power Systems—Water Reactors, National Association of Corrosion Engineers, Houston TX, 2013
8. Capell, B., Wolfe, R., Lumsden, J., Eaker, R. PbSCC of Alloy 800NG Steam Generator Tubing in Alkaline Environments, Proceedings of the 17th International Conference on Environmental Degradation of Materials in Nuclear Power Systems—Water Reactors, Canadian Nuclear Society, Toronto, Canada, 2016
9. MULTEQ: Equilibrium of an Electrolytic Solution with Vapor-Liquid Partitioning and Precipitiation: The Database Version 7.0, EPRI, Palo Alto, CA, 2012. 1025010
10. Titanium Dioxide Application Guidelines, EPRI, Palo Alto, CA, 1997. TR-108002
11. Correlation of Secondary-Side IGA/SCC Degradation of Recirculating Steam Generator Tubing with the On-Line Addition of Boric Acid, EPRI, Palo Alto, CA 1992. TR-101010

Corrosion of SG Tube Alloys in Typical Secondary Side Local Chemistries Derived from Operating Experience

Ian de Curieres

Abstract In spite of strong industry improvements (new alloys, more stringent chemistry control…), Outer Diameter Stress Corrosion Cracking (ODSCC) still occurs in modern SG alloys, although at a lesser extent than it used to affect 600MA tubes. Currently, alloy 600TT, and even 800NG, do indeed suffer from ODSCC. Since the chemistry of the secondary side of PWR NPPs improved, past tests do not enable to assess simply the risks for modern alloys (too extreme pH for instance). Thus, IRSN reviewed what typical chemical conditions could be met in actual steam generators. Based on this review, IRSN performed corrosion tests in these conditions to assess the potential risks for alloys 600TT and 690TT in "typical" top-of-tubesheet environments. This paper will present the safety, technical and industrial frames of these tests, as well as the first results. An emphasis will also be put on the scientific implications of these results.

Keywords Steam generators · Tubes · Corrosion · Secondary side · Lead · Sulphur

Acronyms

ODSCC	Outer diameter stress corrosion cracking
SCC	Stress corrosion cracking
IGA	Inter granular attack
SG	Steam generator
MA	Mill-annealed
SN	Sensitized
TT	Thermally treated
AVT	All volatile treatment
RUB	Reversed U-bend
FIB	Focused ion beam

I. de Curieres (✉)
IRSN, Fontenay-aux-Roses, France
e-mail: ian.decurieres@irsn.fr

J.H. Jackson et al. (eds.), *Proceedings of the 18th International Conference on Environmental Degradation of Materials in Nuclear Power Systems – Water Reactors*, The Minerals, Metals & Materials Series, https://doi.org/10.1007/978-3-319-68454-3_83

HOR	Hide-out-return
pH_T	High temperature pH
GC	Generalized corrosion
LME	Liquid metal embrittlement

Introduction

Secondary side corrosion of SG tubes (ODSCC, IGA…) used to be a significant issue in steam generators from the late 50s to the late 90s, prompting many industrial maintenance, inspection and component replacement efforts. In addition, many laboratory works were performed either to understand the involved mechanisms or to predict the behaviour of SG tube bundles. All of these elements were summarized in many published works, for instance [1–10]. Until the late 90s, the majority of ODSCC cases occurred in stainless steel or alloy 600MA/SN tubes. However, since the early 2000s, ODSCC affecting alloy 600TT tubes is reported worldwide [11–14], and even in alloy 800NG [15–17], sometimes after only about 10 years of operation. Currently, no ODSCC, nor IGA, has been reported on alloy 690TT tubes.

Although these new ODSCC instances are much less numerous than in alloy 600MA tubes, their occurrence could be expected based on past knowledge. However, some of their aspects are not that obviously understood, for instance:

- the kinetics of occurrence. Based on past tests, alloy 800 and 690TT would be supposed to have quite similar behaviours [18]. In the field, in spite of sometimes non-nominal conditions (e.g. denting), no evidence of cracking in alloy 690TT is encountered whereas there are approximately 200 tubes made of alloy 800 suffering from ODSCC [15, 17];
- the kinetics of cracking of alloy 800 has sometimes been quite fast, with indications of ODSCC detected after about 10 years of operation, which is quite faster than what could be inferred from laboratory tests;
- the chemistry of occluded areas was improved over time, by implementing stricter chemistry specifications, and its expected range should not have favoured cracking, at least not to the extent or celerity observed in Spanish SGs [17], for instance.

As for ODSCC of tubes made of alloy 600TT, cracks were discovered between a few years to 25 years of operation.

Even though most of these new cases lead to examination of pulled tubes, prediction of additional cases remains difficult, even with the assistance of laboratory model testing. The relatively few amount of cracked tubes requires very detailed examinations which are sometimes complicated to implement [14].

Among the reasons provided for explaining the uncertainties or differences in behaviour with past tests or experience are:

- the high temperature pH in the crevices (pH_T). It is often estimated by computations based on hide-out return (HOR) chemistry data obtained during outages. Such computations are based on the concentration of soluble ions obtained (Na, K, Cl….). However, recent works have demonstrated that this may fail to estimate the actual pH_T in the crevices. CNL indeed indicated that the presence of solid magnetite induces a buffering effect which modifies the calculated pH_T by 1.5 unit [19]. In addition, quite extreme pH_T used to be considered in past assessments (either <3.5 or >10), which are no longer relevant to current operating practices thanks to more stringent chemistry specifications.
- the chemical state of the tested environments. In most tests performed, the chemical conditions are in the liquid state with heavily concentrated solutions, especially with caustic species. High concentration factors are possible for most chemical species in the crevices, inducing very non-nominal conditions. However, the relevance of purely liquid solutions to model the conditions in crevices remains undetermined.

The industry performed a survey of actual chemistry conditions at the bottom of SGs, based on more than 20 years of operation [20]. They observed that in many SGs, a sludge pile was present on the tubesheet. This "sludge" is made of aluminosilicates, calcium species, various pollutants and a balance of magnetite (about 85–90% wt). Magnetite is also known to have a sponge-like ability with some well-known pollutants in high-temperature water [21], as well as having reducing capabilities on some chemical species [22]. In these conditions, the local chemistry is expected to be a mixture of solid particles, concentrated fluid and doped steam, including polluting species at various oxidized levels. Accordingly, the industry concluded that some new testing protocols were required to assess or understand the recurring ODSCC behaviour [20].

Based on these considerations, IRSN launched an experimental program, described hereafter, to progress in this field. The present works is one among many new and recent approaches dedicated to ODSCC, some of them being summarized in this conference [23].

Experimental Frame

In this works, the idea was to produce testing considering a tri-phasic system simulating the sludge piles, the concentrated crevice fluid and the boiling areas by wet steam, to assess the most susceptible areas in the SGs. This was achieved by using some capsules, filled at one third with some sludge. The composition of the sludge was derived from operating experience as described in [20]. The whole

experimental set is based on the one previously used by a vendor to perform skillfully and satisfactorily such corrosion testing [24].

The experimental set-up is the following one:

- use of RUB specimen of industrial SG tube materials, made of 1/6 of a SG tube. Such specimens have a stress level of about 550 MPa and 9% of plastic deformation at the apex;
- materials tested are 600TT and 690TT from vendors, with a few reference specimens in 600MA. The chemical composition and material properties of materials used are indicated in Tables 1 and 2;
- the RUB specimen are pre-oxidized in nominal all-volatile treatment (AVT) secondary water ($pH_{25\ °C}$ 9.6) at 320 °C for 600 h, as the sludge piles and pollutions are not present at the first start of the component, but rather come after a certain operating time;
- the corrosion test duration in the capsules is of 7000 h at 320 °C. In the presence of a sludge pile in the tubesheet of SGs, the outer-diameter temperature of SG tubes is the same as the inner diameter one, about 320 °C;
- in the capsules, a tri-phasic medium is produced: simulated sludge with pollutants, concentrated crevice fluid and wet steam. The compositions of the simulated sludge and the concentrated fluid are provided in Table 3, and the scheme of the capsules is in Fig. 1. The composition of the crevice simulating fluid is similar to that used in other tests based on hide-out-return (HOR) results and concentration factors [1–3, 25];
- in the capsules, gaseous hydrogen is periodically removed through a Ag-Pd thimble to maintain a globally stable hydrogen partial pressure in the capsules;
- hydrazine is initially added to suppress all oxygen trapped during the capsule closure, while heating the capsule;
- pollutants considered are either Pb, S or a mixture of both since they are observed to be the most critical ones either observed on pulled cracked tubes or in laboratory studies [25]. Their composition is derived from an analysis of past operating experience of removed sludge from SGs, after 25 years in France and the USA;
- 3 pH_T are considered as the screening parameter: 4, 7.5 and 9.[1] The pH_T are initially computed by the OLI software, considering all phases, either liquid or solid. At the end of the tests, some sampling of sludge and fluid are made to check the consistency between the calculations and the measurements on actual solutions/When S species are incorporated as reduced species, the amount is based on estimations performed previously [22].

The test matrix for the tests is shown in Table 4.

Once tests are performed, capsules are cooled down, and then opened. RUB specimen are then characterized by binocular lenses, SEM and TEM.

[1]At 320 °C, the equilibrium pH is around 5.5.

Table 1 Chemical composition of materials used for RUB specimens

Material	Heat	C (%)	Si (%)	S (%)	P (%)	Mn (%)	Ni (%)	Cr (%)	Cu (%)	Co (%)	Ti (%)	Al (%)	Fe (%)
600TT	WF489	0.027	0.27	0.001	0.012	0.83	73.1	16.2	0.02	0.018	0.24	0.16	8.9
690TT	116,201	0.017	0.173	<0.001	<0.015	0.33	58.0	29.84	<0.01	<0.035	0.37	0.048	11

Table 2 Mechanical properties of materials used and compliance with the manufacturing code

Material	Heat	Mechanical properties at 20 °C			Mechanical properties at 350 °C		
		Ys0.2 (MPa)	UTS (MPa)	El (%)	Ys0.2 (MPa)	UTS (MPa)	El (%)
690TT	RA127	310	707	51.2	237	595	46.9
690TT	116201	>240	>550	>30	>190	–	–
600TT	WF489	320	730	47.5	273	659	40.9
RCC-M 4103		>240	>550	>30	>190	–	–

Material	Heat	Grain size (μm)	$HV_{0.025}$
690TT	RA127	46	202
690TT	116201	55	196
600TT	WF489	23	200

Table 3 Chemical composition of environments

Sludges: Fe_3O_4 + 0.8% CaO + 5% of Al_2O_3/Sio_2 with Si/Al = 4
Liquid phase: H_2O + 3 ppm ETA + 1 ppmNH_3 + 3 M Nacl + N_2H_4

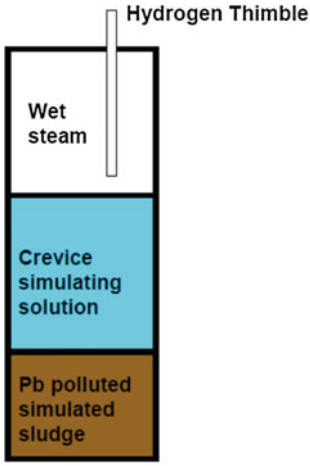

Fig. 1 Schematic presentation of the capsule tests, from [24]

Table 4 Test matrix

	pH_T = 4	pH_T = 7.5	pH_T = 9
2000 ppm of Pb in sludge as **PbO**	✓	✓	✓
2000 ppm of Pb in sludge as **(91% $PbSO_4$ 9% PbS)**	✓	✓	✓
8000 ppm of soluble SO_4^{2-} as **(91% Na_2SO_4 and 9% Na_2S)**	✓	✓	✓
Pb/S free sludge	✓	✓	✓

Preliminary Results

Checking of OLI Computation Relevance

Once capsules are opened, some sampling of the liquid and the solid sludge is possible. Some sampling was performed in each capsule and chemical analysis was done. Table 5 introduces the comparison between the measurements and the OLI calculations for 3 capsules.

The first finding is that there is a fairly good agreement between the measurements at room temperature (RT) and the OLI calculations for high temperature solutions. Considering that measurements are made for room temperature whereas predictions are made for a temperature of 320 °C, small discrepancies are possible, due to cooling effects or precipitation linked to solubility variations (case of Al, for instance). Thus, a factor of 2 of difference is not considered to be significant, since the orders of magnitude are the same.

Thus, this good agreement is a good indicator that the calculations performed by OLI are accurate, hence the pH_T estimated by this code are proper ones.

Surface Conditions After Pre-oxidation in Nominal AVT Water

Briefly, the RUB specimens, after the pre-exposure to nominal AVT water exhibit very classical surface conditions and oxides. They are presented in Fig. 2. The main finding would be that the alloy 600TT specimens have some surface flakes, made of Al and Si. These flakes are the consequence of residues of Al present on the surface due to the manufacturing process.

Results at the End of 2016

Currently, all capsules have gone through the 7000 h of corrosion testing. Due to the abundant amount of specimens (about 15 per capsule), examination at the SEM scale has not been performed on all specimens yet.

On first observation, it appeared that apart from 2 RUB specimens, cracks, when existing, are not visible with a naked eye nor with binocular lenses (see Fig. 3). The specimens' surfaces are covered with coloured thick oxides, reflecting the complex chemistries of the environments.

Table 5 Comparisons of computations by OLI and measurements on samples after corrosion testing. Top: in the liquid phase; bottom: in the solid phase

Amount of chemical phase (ppm)						
Structure	Capsule 1		Capsule 2		Capsule 3	
	Simulation 320 °C	Measurments RT	Simulation 320 °C	Measurments RT	Simulation 320 °C	Measurments RT
pH	4	3.8	7		4	5.3
Na (+1)	56,000	42,000	70,000		57,000	35,600
Ca (+2)	12,000	11,700	1613		5700	5300
Fe (+2)	–	520	–		144	420
Pb (+2)	4300	1072	45		4400	770
Al (+3)	0.008	0.5	0.23	NA	0.09	0.3
CI (−1)	101,000	83,000	98,000		99,000	62,000
Si (+4)	630	65	11,000		680	55
S(+6)	–	NA	–		30	860
S(+4)	–		–		0.02	NA
S(−2)	–		–		56	
Amount of chemical phase (w%)						
Structure	Capsule 1		Capsule 2		Capsule 3	
	Simulation 320 °C	Measurements RT	Simulation 320 °C	Measurements RT	Simulation 320 °C	Measurements RT
Al	5770	6300	5750	6230	5700	4750
Ca	–	8600	4900	10,100	4858	7900
Pb	–	660	1930	1400	–	240
Si	17,600	20,200	13,000	19,400	12,600	17,200

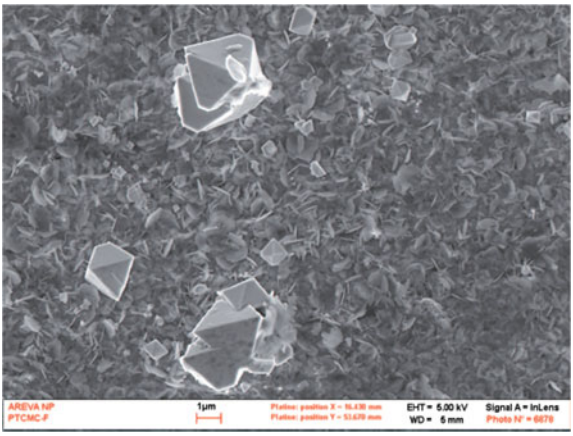

Fig. 2 SEM surface observation of a RUB specimen of alloy 600TT

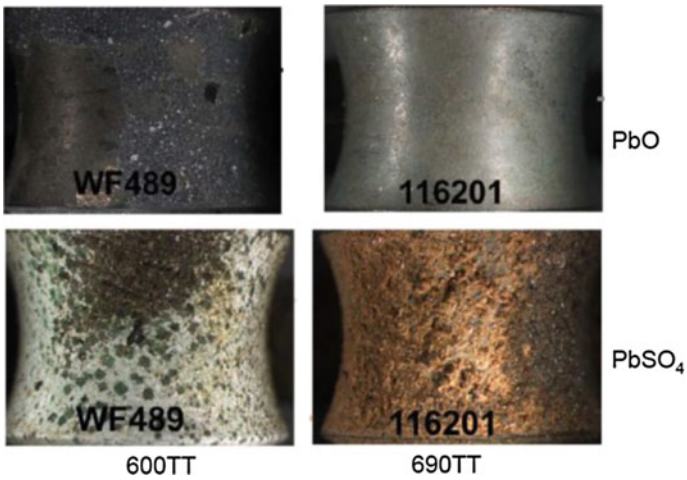

Fig. 3 Surface observation of 4 RUB specimens after the 7000 h corrosion testing

Accordingly, examinations were first focused on samples having been exposed to the pH_T of 4 and 7.5 in capsules with polluted sludges. The current results are presented in Table 6 hereafter. The examinations for other test conditions are pending.

The first result is that reference samples in alloy 600MA all cracked, quite heavily, sometimes (see Fig. 4), with cracking morphologies as observed in the field, validating the severity of the test conditions.

The second result is that in mildly acidic conditions in presence of typical sludge, all alloys suffer from ODSCC, even 690TT. IGA is also clearly initiated in

Table 6 Test results after SEM analysis for capsules at pH_T 4 and 7.5 with polluted sludge

		pH_T = 4			pH_T = 7,5		
		WF422 600MA	WF489 600TT	116201 690TT	WF422 600MA	WF489 600TT	116201 690TT
Pb (PbO)	Solid	C	C		C		
	Liquid	-		C	-	-	-
	Steam	-		C	-	-	-
Pb and S ($PbSO_4$/PbS)	Solid	C	C		C	C	
	Liquid	-	C	C	-	C	
	Steam	-	C	C	-	C	
S (Na_2SO_4/Na_2S)	Solid	C					
	Liquid	-	C	C	-		
	Steam	-	C		C	C	-

No analyzis -
GC and/or IGA
No indications
C Cracks observed from the surface

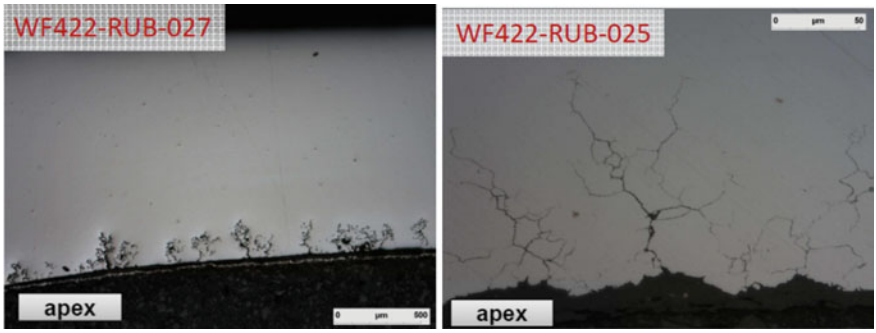

Fig. 4 Cracks in RUB reference specimens in alloy 600MA after the 7000 h corrosion testing

alloy 600 (both MA and TT). One other noteworthy result is that 690TT cracked in mildly acidic conditions, with only presence of S and no Pb.

However, in mildly alkaline conditions 690TT appears to have no issue whereas all grades of alloy 600 crack.

Microscopy Examinations of Cross-Sections of Specimen Tested at PH_T of 4

SEM Scale

SEM performed on cross sections of various specimens revealed many corrosion phenomena, not visible from the surface, including IGA, ODSCC and GC. Figure 5 illustrates some examples of observed corrosion phenomena.

SEM observation clearly shows that ODSCC actually occurs in 690TT specimens, and that it is purely intergranular, whereas it was mostly observed as transgranular in most tests, essentially caustic ones, for instance [26]. This is a rather new feature which is confirmed by the extent of cracking. Table 7 shows that in cracked 690TT specimens, there are 2–9 cracks per specimen, all intergranular. This implies that IGSCC of 690TT is not a particular phenomenon affecting one specific sample.

The crack depths do not exceed 180 µm in these cases, although some 600MA reference samples had through-wall cracks. Nonetheless, one should consider that the test duration does not exceed one year of operation. The temperature is that of actual crevices in the sludge pile area of tubesheets. The only accelerating factor is the stress/strain level (∼550 MPa and 9% of plastic deformation at the apex). Accordingly, this extent of cracking, although limited, implies a potentially significant crack extension within a few years of operation.

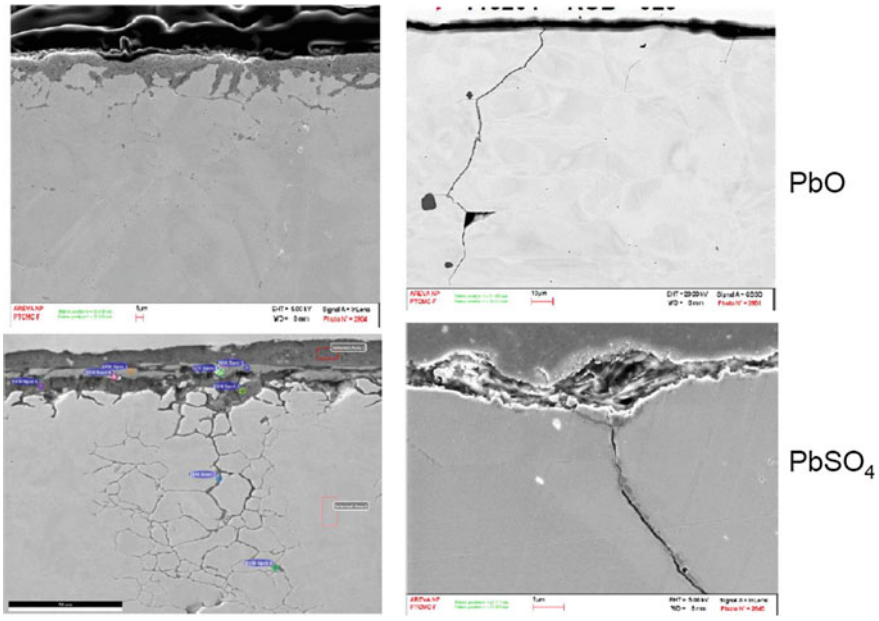

Fig. 5 SEM examinations of cross-sections of 4 RUB specimens. Left: 600TT, right: 690TT

Table 7 Summary of crack dimensions observed after SEM analysis for capsules at pH_T 4 and 7.5 with polluted sludge

		600TT		690TT	
		Max. depth	Crack density* (/mm)	Max. depth	Crack density* (/mm)
PbO	Liquid	180 µm	2	110 µm	0.9
	Wet steam	20 µm (IGA)	/	63 µm	0.5
$PbSO_4$	Liquid	180 µm	~3	60 µm	0.7
	Wet steam	78 µm	1	45 µm	0.32
Na_2SO_4	Liquid	79 µm	0.7	92 µm	0.2
	Wet steam	31 µm	0.3	/	/

*Depth >15 µm, specimen width ~10 mm

Cross sections examinations reveal that oxide layers are very thin, sometimes hardly visible (see for instance the pictures about 690TT in Fig. 3), except for some alloy 600TT specimens, affected by IGA or substantial surface corrosion. In the latter case, analyses with SEM-EDS show no detectable presence or Pb or S (apart from traces) in the surface oxide films, whereas Al or Si are detected. Figure 6 illustrates one isolated case where Pb is detected in the surface oxide films, by EDS, but nothing in the cracks at this observation scale.

The same conclusion can be derived for the crack oxides, thus precise observations required TEM investigations.

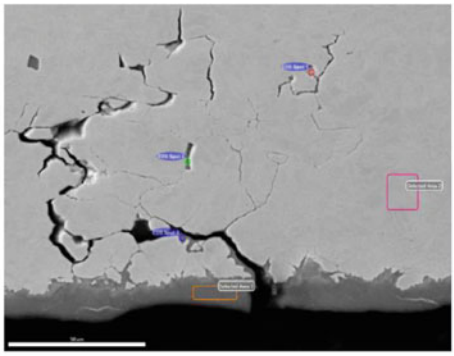

	O	Mg	Al	Si	S	Ca	Ti	Cr	Fe	Ni	Pb
WF489-027 | Area 1 | EDS Spot 1				0,7				16,8	9,6	72,9	
WF489-027 | Area 1 | EDS Spot 2	2,7	1,7	1,1					17,6	9	67,9	
WF489-027 | Area 1 | EDS Spot 3	1,6		1,4	0,6				16,6	9,3	70,5	
WF489-027 | Area 1 | Selected Area 1	21,8		0,6	1,3		0,5	0,5	27,1	15,8	31,5	0,7
WF489-027 | Area 1 | Selected Area 2	1,5			0,7				16,8	9,3	71,7	

Fig. 6 SEM EDS examinations of a cracked 600TT specimen exposed at pH_T of 4 to a typical sludge polluted with $PbSO_4$

TEM Analysis

After these SEM characterizations, TEM samples were prepared based on FIB sampling, with a focus on 690TT cracked specimens, exposed to pollutions in the sludge either as PbO or $PbSO_4$. These examinations were coupled with EDX ChemiSTEM ones to characterize the metallic elements. On a few cracks, similar results are obtained, visible in Figs. 7, 8 and 9.

In these cracks, grain boundary carbides are not clearly visible anymore, although they are observable ahead. The cracks comprise Cr rich (nearly pure)

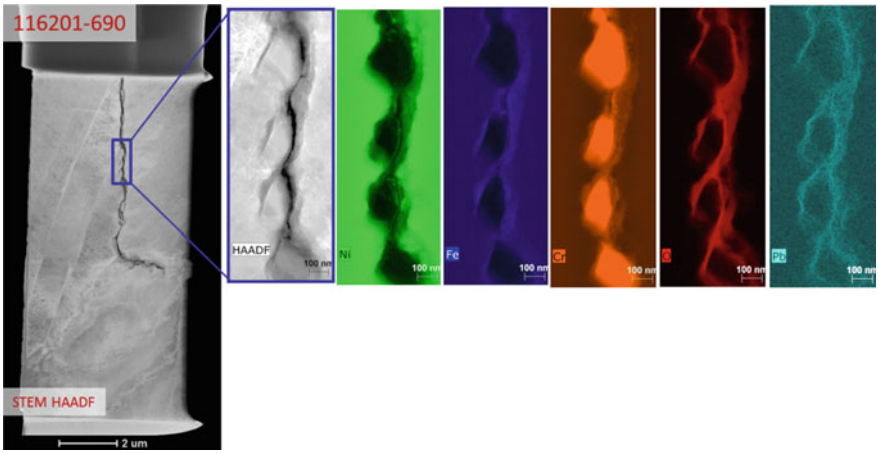

Fig. 7 TEM and EDX ChemiSTEM examinations of a crack in a 690TT exposed to PbO polluted sludge (liquid phase specimen)

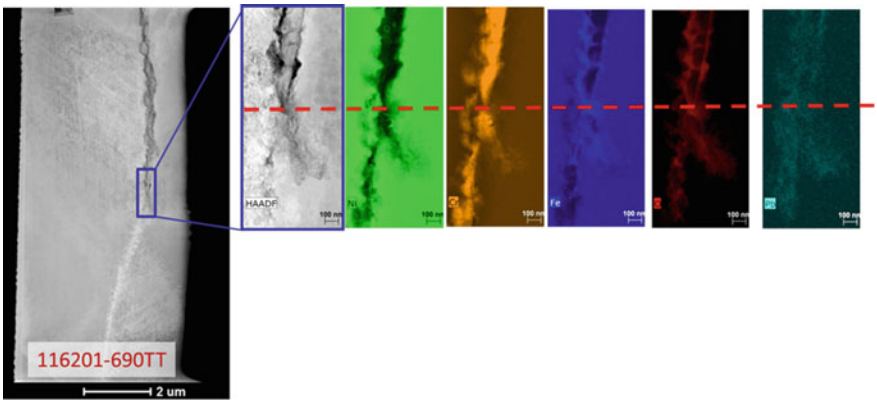

Fig. 8 TEM and EDX ChemiSTEM examinations of a crack in a 690TT exposed to $PbSO_4$ polluted sludge (liquid phase specimen). Crack tip indicated by the red dashed line

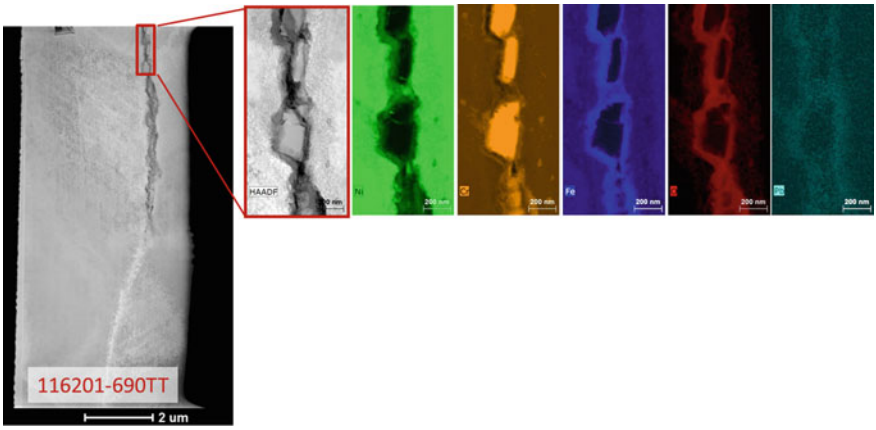

Fig. 9 TEM and EDX ChemiSTEM examinations of a crack in a 690TT exposed to $PbSO_4$ polluted sludge (liquid phase specimen). Crack lips predecessing the crack tip

nodules, surrounded by iron-rich oxides. Some Ni depletion occurs ahead of the crack tip (see Fig. 8), as well as the presence of oxygen.

Pb, when present, seems located in the crack lips iron rich oxides. In Fig. 8, it can be observed that Pb is detected up to 1 μm ahead of the crack tip, which will require a discussion. The amount of Pb in these oxides is estimated to be about 1–2 wt %.

Chemistry profiles across the nodules provide with the additional information below (Figure 10).

The nodules seem metallic and are made of about 90% wt of Cr, and 10% wt of Ni. The oxides on the crack lips are iron-rich, and both Ni and Cr depleted. Such iron-rich oxides also circle the nodules. Around these nodules and their oxidized circling, one observes fluctuations in the chemical composition on a distance of

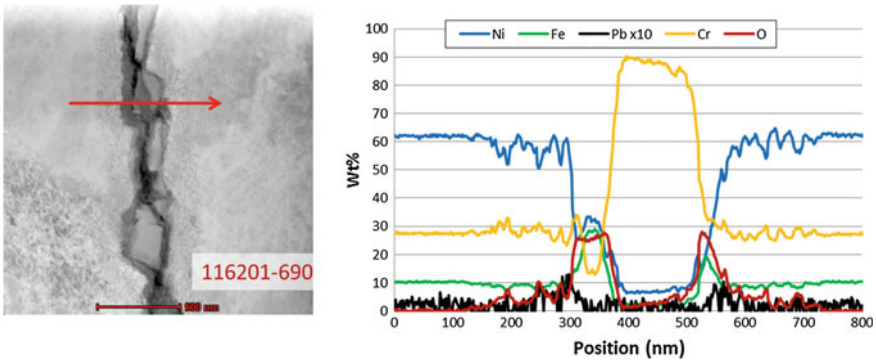

Fig. 10 TEM and EDX ChemiSTEM examinations of a crack in a 690TT exposed to $PbSO_4$ polluted sludge (liquid phase). Metallic profile across the crack

100 nm. These fluctuations seem to be slightly Ni depleted and/or Cr enriched. Some oxygen is also detected in this area, suggesting this might be some signature of oxidation around dislocations.

X-ray diffraction patterns performed on these Cr nodules show a variation in the lattice grid and parameters in pole figures. At the crack tip, the diagram is that of Cr carbides, typically $Cr_{23}C_6$. But, when the nodules are farther from the crack tip, the X-ray diffraction diagram resembles more Cr_2O_3 ones.

As for Pb, it appears to be located at the interface between the lip oxides and the base metal underneath. This is in full agreement with observations made on pulled tubes, in alloy 600, cracked in service [25]. The thickness of the Pb containing material is in the order of magnitude of 10 nm, according to these profiles.

Discussion

Considering the sampling of TEM and SEM investigation performed, the main results, and subsequent discussion, will be dedicated to tests at pH_T 4 conditions with Pb as the main pollutant.

The cracking mechanism remains to be determined. However, potential elements deserve to be paid attention to, for basic discussion points:

– Ni preferential dissolution, which may appear twice as a contributor. Firstly, in mildly acidic conditions with presence of Pb, preferential dissolution of Ni is a classical feature, already reported [25]. The electrochemical reaction involved is

$$Ni + Pb^{2+} \rightarrow Ni^{2+} + Pb$$

Grain boundary Ni depletion is a likely consequence of it, since diffusion is easier at this location. This phenomenon could be a contributing factor to ODSCC in Alloy 690TT. Secondly, this alloy is also subject to intergranular cracking in the absence of Pb, but with S. In this case, ODSCC is less intense (smaller cracks and a lower crack density). And preferential dissolution of Ni in the presence of S has been studied and confirmed long time ago [28, 29];

– liquid metal embrittlement (LME) could also be a contributing factor to the cracking mechanism. This is a potential mechanism since the melting point of metallic Pb is 327.5 °C, hence only a few degrees Celsius above the test temperature. It would explain the location of Pb at the metal-oxide interface and particularly its detected presence up to 1 µm ahead of the crack tip. Although this was observed in a sample in alloy 690TT, further tests will look for this feature in alloy 600TT. Looking for such a presence of Pb ahead of the crack tip on tubes removed from operation is a must-do;

- the Cr rich nodules are likely to be evolutions of initial grain boundary carbides. Indeed, carbides are visible ahead of the crack tip, but not anymore in the cracked grain boundaries. However, one may wonder whether there is no contribution from spinodal decomposition at all. Once Ni is depleted by preferential dissolution, its content may be as low as about 10–20% wt (see Fig. 8). In this case, the remaining alloy would be close to a basic 75% Cr and 25% Fe metal. At 320 °C, it could be possible that such an alloy would separate, by spinodal decomposition, into a nearly pure Cr phase and a Cr-rich Fe phase. This would induce microstructural features with similarities with what is observed. The pole figures performed tend to indicate that the nodules would rather be derivatives from grain boundary carbides, but the effect of the strong Ni depletion observed (as low as 10% wt instead of 60% wt) requires to be considered at least in terms of metallurgical effects on the grain boundaries and associated local stresses;
- On Fig. 8, the presence of oxygen is observable ahead of the crack tip, up to about 1 μm. This implies that a potential mechanism of intergranular internal oxidation may also be a contributor to the damage.

A candidate mechanistic model for explaining intergranular ODSCC of alloy 690TT could be proposed in a very first approach:

- grain boundary metallurgical weakening by preferential dissolution of Ni. This preferential dissolution may be due to the presence of Pb in acidic environments or the presence of S, as indicated previously;
- some oxidation of the Ni depleted grain boundary (interaction with Cr species);
- the grain boundary is weakened up to the point of cracking. The last weakening process could be by dissolution (lattice stresses due to the oxidation and strong Ni depletion, for instance) or by the presence of Pb (e.g. surface cohesion energy decrease by LME).

This candidate sequence may not be sequential but simultaneous; it is yet sheer basic assumption for explaining the cracking. More research works is required to assess the main proposed steps for this simplistic model.

Among the next research works, a specific focus should be made on determining the possibilities of liquid metal diffusion of Pb in these alloys. The fact that Pb is not in a volumic and metallic state, but somewhat dispersed and ionic should be taken into account as it might impact the diffusion mechanisms. Moreover, the possibility of local alloy degradation due to Ni depletion, and its metallurgical consequences should be investigated too.

Also, the effect of S alone or the fact that in mildly alkaline conditions (pH_T of 7.5) no cracking is detected in alloy 690TT specimens could indicate that pH effects may be the primary contributors, perhaps by favouring the Ni preferential dissolution. A wider picture shall be made after analysis of specimens tested at pH_T of 7.5 and 9. In addition, the effect of temperature could be refined by imposing a heat flux through the sample instead of the current heating procedure.

This shall be the focus of the next steps of research works on these specimens.

Eventually, one should consider testing alloy 800 in these conditions to both assess its susceptibility and compare the potential degradation mechanisms.

Conclusions

IRSN launched corrosion tests of alloys 600TT and 690TT used for SG tubes. These tests aimed at assessing the risks of IGA or ODSCC in the presence of chemistries typical of what may be encountered in the secondary side of steam generators. The only screening variable was the pH_T in crevices, chosen in the range of pH_T mentioned by various utilities, in order to establish domains of susceptibilities.

The current results clearly indicate an IGA/ODSCC susceptibility exists for industrial alloys in presence of "typical" sludge piles. The susceptibility is lower for 690TT than for 600TT, but not null. Even in moderately aggressive conditions (mildly acidic or alkaline pH_T in crevices), cracking is possible for SG tube alloys. In moderately acidic conditions, quite likely in actual steam generators, alloy 690TT may even crack in the absence of Pb, when S is present. The damage mechanism is unclear yet, but hypothesis and research program are determined to progress in the understanding of the physical mechanism.

For the author, there is no doubt that alloy 800NG would be affected at least at the same level than 690TT, based on the operating experience and review of past tests which showed similar behaviours for these alloys. This could be easily verified by testing alloy 800 specimens in the same type of tests.

Based on these results, it is quite significant that the cleanliness of secondary side of steam generators, in particular prevention or mitigation of the formation of sludge piles, is of primary importance for the integrity of the tube bundle. This loss of integrity is a safety issue.

More prospectively, these results indicate that even though utilities have improved the chemistry management in the secondary side, immunity of SG tube alloys is a delusion. Accordingly, considering the safety stakes associated with SG tubes degradation, IRSN considers that relaxing the criteria for secondary side chemistry would be inappropriate. Eventually, it is an obvious conclusion, or reminder, that in-service Non Destructive Examinations remain a key point of the surveillance and should not be relaxed, even if alloy 690TT is up to now immune to ODSCC in service.

Acknowledgements IRSN would like to thank the AREVA Technical Center in le Creusot who performed the tests and analyses.

References

1. R.W. Staehle, J.A. Gorman, Quantitative assessment of sub-modes of stress corrosion cracking on the secondary side of steam generator tubing in pressurized water reactors—Part 1. Corrosion **59** (2003)
2. R.W. Staehle, J.A. Gorman, Quantitative assessment of sub-modes of stress corrosion cracking on the secondary side of steam generator tubing in pressurized water reactors—Part 2. Corrosion **60** (2004)
3. R.W. Staehle, J.A. Gorman, Quantitative assessment of sub-modes of stress corrosion cracking on the secondary side of steam generator tubing in pressurized water reactors—Part 3. Corrosion **60** (2004)
4. P. Scott, F. Cattant, I. de Curieres, O. Raquet, Matériaux pour les tubes de GV de réacteurs à eau pressurisée et leur résistance à la corrosion sous contrainte en service (SFEN, ST2 commission, Paris, November 2008)
5. R. Wolfe, Field experience with steam generator tubing materials in the United States, in *Proceedings of the International Nuclear Components Conference*, Mississauga, Canada, November 2015
6. R.W. Staehle, Approach to predicting SCC on the secondary side of steam generators, in *Proceedings of the International Conference Fontevraud 5*, vol 2, edn., (SFEN, September 2002) pp. 1019–1035
7. M. Bouchacourt et al., Modélisation de l'IGA/IGSCC dans les générateurs de vapeur des centrales REP d'Electricité de France, in *Proceedings of the International Conference Fontevraud 4*, vol. 1, ed., (SFEN, September 1998), pp. 663–674
8. Y. Lu, Define optimum conditions for Steam Generator tube integrity and extended steam generator life, in *Proceedings of 15th International Conference on Nuclear Engineering*, Nagoya, Japan, April 2007
9. EPRI, *Steam Generator Reference Book* (1985)
10. I. de Curieres, *Environmental Degradations in PWR Steam generators, Chapter 8*, ed by J. Riznic Steam generators for Nuclear Power Plants, (Elsevier, May 25, 2017) pp. 183–213
11. USNRC Information Notice 2008–07 Cracking indications in thermally treated alloy 600 steam generator tubes, USNRC website
12. S.S. Hwang et al., Steam Generator Management Strategies in Korea, IAEA, Vienna, June 15–18, 2009
13. Y. Thebault et al., Experience of steam generator tube examination in the hot laboratory of EDF: analysis of recent events concerning the secondary side, paper A166-T06. in *Proceedings of the International Conference Fontevraud 7*, edn. SFEN, September 2010
14. M. Boccanfuso et al., The first two occurrences of external damage on alloy 600TT tubes in France. in *Proceedings of the 17th International Conference on Environmental Degradation of Nuclear Reactors*, CNS, Ottawa, Canada, August 2015
15. IAEA-TECDOC-1668, Assessment and management of ageing of major nuclear power plant components important to safety: Steam Generators, 2011 update, Vienna, Austria, 2011
16. R. Kilian et al., Operating experience with alloy 800 SG tubes in Europe, in *Proceedings of the 13th International Conference on Environmental Degradation of Nuclear Reactors*, CNS, Whistler, Canada, August 2007
17. R. Kilian et al., Examination of ET-indications of steam generator tubes from the Almaraz unit 2 NPP replacement steam generator SG3, in *Proceedings of the 17th International Conference on Environmental Degradation of Nuclear Reactors*, CNS, Ottawa, Canada, August 2015
18. F. Vaillant et al., Comparative behaviour of alloys 600, 690 and 800 in caustic environments, in *Proceedings of the 7th International Conference on Environmental Degradation of Nuclear Reactors* (Breckenridge, USA, August 1995), pp. 219–232
19. J. Ulaganathan et al., Mitigating effect of magnetite buffering on alloy 800 tubing degradation in acidic, sulfate-dominated, environments at 300 °C, in *Proceedings of the 17th International*

Conference on Environmental Degradation of Nuclear Reactors, CNS, Ottawa, Canada, August 2015
20. I. de Curieres, F. Vaillant et al., Lead pollution on the secondary side of steam generators: an overview , paper A127-T06, in *Proceedings of the international conference Fontevraud 7*, edn. SFEN, September 2010
21. S. Nasrazadani et al., Lead (Pb^{2+}) adsorption on magnetite (Fe_3O_4) at 200 °C, in *Proceedings of the 13th International Conference on Environmental Degradation of Nuclear Reactors*, CNS, Whistler, Canada, August 2007
22. S. Delaunay et al., Prediction of sulfur speciation in secondary circuit conditions—influence of magnetite and hydrazine at 275 °C, paper 237-P2-15, in *Proceedings of the International Conference on Nuclear Power Chemistry*, Paris, France, 2012
23. S. Persaud et al., Lead induced corrosion in SG tubing material, *in Proceedings of the 18th International Conference on Environmental Degradation of Nuclear Reactors*, Portland, Oregon, USA, August 2017
24. E. Aublant, O. Calonne et al., Lead induced corrosion in SG tubing material, in *Proceedings of the 16th International Conference on Environmental Degradation of Nuclear Reactors*, NACE, Asheville, USA, August 2013
25. *Proceedings: 2005 EPRI/ANL/NRC Workshop on effects of Lead (Pb) and Sulfur (S) on the performance of the secondary side tubing of steam generators in PWRs*, EPRI report no. 1012780, December 2005
26. M. G. Burke, R. E. Hermer, M. W. Phaneuf, Evidence for a corrosion/tunneling mechanism of lead-induced transgranular SCC of alloy 690 in PbO + 10% NaOH solution, in *Presented at the 13th International Conference on Environmental Degradation of Materials in Nuclear Power Systems—Water Reactors*, Whistler, BC, Canada, 2007
27. P. Marcus et al., The influence of Sulphur on the dissolution and passivation of a nickel-iron alloy—Part I. Corros. Sci. **24**(4), 259–268 (1984)
28. J. Oudar et al., Role of adsorbed sulphur in the dissolution and passivation of nickel and nickel-sulphur alloys. Appl. Surf. Sci. **3**(1), 48–67 (1979)

Investigation on the Effect of Lead (Pb) on the Degradation Behavior of Passive Films on Alloy 800

J. Ulaganathan and H. Ha

Abstract Alloy 800 has been demonstrated to be susceptible to Pb-induced degradation such as stress corrosion cracking (SCC) in laboratory experiments. Pb has been proposed to cause such degradation by affecting the formation of protective oxides comprising the passive films on the alloys. To understand the detrimental effects of Pb, Alloy 800 samples pre-passivated under all volatile treatment (AVT) conditions were exposed to alkaline environment of $pH_{280\ °C}$ 9.5 at 280 °C in the absence and presence of Pb. The Pb-free and Pb-containing passivated surfaces, along with bare surfaces as control samples, were characterized using electrochemical and surface analytical techniques. The results contrast the susceptibility of Alloy 800 to Pb-induced degradation reported in literature, where experiments are usually performed on bare surfaces with excess Pb, typically as PbO, present in the aqueous solutions; suggesting that the effect of Pb depends on whether it is present in solution or incorporated in the film.

Keywords Alloy 800 · Passive film · Pb · Cyclic polarization · Mott-schottky analysis · Atom probe tomography

Introduction

Alloy 800 has been the material of choice for steam generator (SG) tubing in several CANDU®,[1] and European power plants, and its in-service performance has been remarkably good for 30 to 40 years [1]. However, laboratory investigations performed under conditions simulating plausible extremes of SG heat-transfer crevice environments have shown Alloy 800 to be susceptible to Pb-induced degradation [2–4]. This has raised concerns about the risk of delayed onset of

[1]CANDU®—Registered trademark of Atomic Energy of Canada Limited (AECL).

J. Ulaganathan (✉) · H. Ha
Canadian Nuclear Laboratories, 286 Plant Road, Chalk River, ON K0J 1J0, Canada
e-mail: jagan.ulaganathan@cnl.ca

J.H. Jackson et al. (eds.), *Proceedings of the 18th International Conference on Environmental Degradation of Materials in Nuclear Power Systems – Water Reactors*, The Minerals, Metals & Materials Series, https://doi.org/10.1007/978-3-319-68454-3_84

degradation, in service, after long incubation periods. Moreover, the ubiquitous presence of Pb in SG deposits [5] necessitates rationalization of the lack of such degradation observed in service to date.

PbSCC testing of Alloy 800 reverse U-bend (RUB) samples exposed to Pb-containing alkaline environments showed rapid crack initiation (incubation period <200 h) at $pH_{330\ ^\circ C}$ 9.5 and delayed onset (incubation period >3000 h) of similar rapid cracking at $pH_{330\ ^\circ C}$ 8.5 [4]. Characterization by X-ray photoelectron spectroscopy (XPS) and Auger electron spectroscopy (AES) showed the presence of Pb in the passive films formed under these conditions [4]. The films formed under these conditions are known to have a bi-layered structure [6]. Pb was observed to penetrate the outer layer comprised of Fe- and Ni- based oxides [4]. However, the inner layer comprising Cr-rich oxides is the most important for the protection of the underlying alloy. Therefore, it is of interest to know if, and how, Pb can penetrate this inner layer and reach the metal/oxide interface to cause degradation.

During the growth of passive films, dehydration reactions occur resulting in the formation of mixed-oxides with spinel structure. Such spinel oxides are highly stable [7, 8] and can slow down the diffusion of ions through the oxide layers, thereby, decreasing the corrosion rate of the alloys. However, XPS analyses revealed that Pb exists predominantly as hydroxides rather than oxides in the Pb-containing passive films on Alloy 690 [9]. Additionally, grazing incidence X-ray diffraction (GIXRD) has shown spinel oxides to be present only in passive films formed in the absence of Pb, but not in the presence of Pb [9]. Similarly, secondary ion mass spectroscopy (SIMS) showed higher hydrogen content in passive films formed in the presence of Pb than that in the absence of Pb [9, 10]; and hydrogen has been shown to inhibit dehydration reactions during passivation, thereby resulting in films with higher fraction of hydroxides [11, 12]. Therefore, it has been hypothesized that Pb causes passivity breakdown by interfering with the formation of protective oxides in the passive films; thereby, promoting metal dissolution through the less protective Pb-containing passive films and increasing the susceptibility of the underlying alloy [9, 10]. Another hypothesis is the penetration of Pb through paths provided by stress-induced fracture of the inner layer of the bi-layered passive film.

This work was performed to understand the effect of Pb on the integrity of passive films on Alloy 800 formed under alkaline conditions. Usually, freshly prepared sample surfaces[2] are exposed to a Pb-containing environment, and the passive films are characterized at the end of the exposure. However, in operating power plants, oxide layers exist on the SG tubing surfaces from exposure to the high temperature aqueous conditions of the SG secondary side. Therefore, to better simulate the conditions in plants, samples pre-passivated under all volatile treatment

[2]In laboratory investigations, sample surfaces are abraded and are considered to be clean and oxide-free; but an air-formed film cannot be avoided and it is the air-formed film that gets exposed to the high temperature aqueous environment.

(AVT) conditions were exposed to Pb-free and Pb-containing alkaline environments to form Pb-free and Pb-containing passive films. The alkaline environment was chosen to simulate plausible extremes of SG heat-transfer crevice conditions. The Pb-free and Pb-containing passive films were characterized using electrochemical techniques and surface analytical techniques.

Experimental Details

Sample Preparation

Samples were prepared from a commercial Alloy 800 SG tubing with an outer diameter of 15.88 mm and a wall thickness of 1.13 mm. The chemical composition of the material from the mill certificate is provided in Table 1. The samples were cut as 10 mm long segments from the tubing. The outer surfaces of the samples were polished to a 1200 grit finish, cleaned with ethanol and acetone in an ultrasonic bath, rinsed with water, dried, and stored in an Ar-filled desiccator.

Pre-Passivation Under All Volatile Treatment Conditions

The samples were pre-passivated under AVT conditions at 280 °C for 25 days, so as to more resemble the surfaces of SG tubing in nuclear power plants. Batches of 40 to 50 samples were pre-passivated in a refreshed autoclave made of Hastelloy C. The feedtank consisted of $\sim$30 ppm[3] morpholine to maintain a $pH_{25\,^{\circ}C}$ of 9.5, 200 ppb[4] hydrazine as an oxygen scavenger to achieve <1 ppb dissolved oxygen, and continuous purging with ultra-high purity Ar gas. The autoclave was refreshed at a rate of $\sim$1.5 to 2 L h^{-1}, and was heated to 280 °C. The hydrazine concentration and $pH_{25\,^{\circ}C}$ were monitored downstream of the autoclave, and the feedtank chemistry was adjusted, as necessary. The pre-passivated samples were rinsed with water, dried, and stored in an Ar-filled desiccator.

Preparation of Pb-Free and Pb-Containing Passive Films

The pre-passivated samples along with bare samples (in some cases) were exposed to deaerated 0.1 mol kg^{-1} NaOH in the absence and presence of 500 ppm Pb as PbO at 280 °C for 1 week or 4 weeks. Both the Pb-free and Pb-containing alkaline

[3]ppm—parts per million by mass (mg kg^{-1}).

[4]ppb—parts per billion by mass (μg kg^{-1}).

Table 1 Composition of the alloy 800 from mill certificate

Heat Number	Composition (wt%)												
	Fe	Ni	Cr	C	Si	Mn	S	Ti	Al	P	Co	Cu	N
516809	43.2	32.78	21.87	0.017	0.46	0.50	0.001	0.48	0.29	0.012	0.01	0.02	0.16

Table 2 Conditions for the formation of Pb-free and Pb-containing passive films on pre-passivated and bare surfaces

Initial Condition of Sample Surface	Exposure Conditions		
	Pb as PbO (ppm)	Duration (weeks)	Environment
Pre-passivated	0	1	0.1 mol·kg^{-1} NaOH, 280 °C
		4	
Pre-passivated	500	1	
		4	
Bare	500	1	
		4	
Bare	Not exposed (control samples)		

environment had a $pH_{280\ °C}$ of 9.5. All the exposures were performed in a static autoclave made of Hastelloy C with stainless steel liner. After exposure, the samples were rinsed with water, dried, and stored in an Ar-filled desiccator. The different sample surfaces that were formed at the end of the exposures are briefly described below and the conditions of exposure are listed in Table 2.

- Pre-passivated, Pb-free films
- Pre-passivated, Pb-containing films
- Bare, Pb-containing films
- Bare surfaces as control samples.

Characterization of the Pb-Free and Pb-Containing Passive Films

The electrochemical behavior of the films were characterized by cyclic polarization and potentiostatic polarization at high temperature. The measurements were performed in a 2 L static autoclave made of Hastelloy C with stainless steel liner at 280 °C and saturation pressure. The measurements were performed in a three electrode cell configuration with PAR EG&G Model 263A/99 potentiostat. Platinum foil was used as the counter electrode. Alloy 600 was used as a pseudo-reference electrode for the high temperature measurements. The stability of the pseudo-reference electrode was confirmed by monitoring its potential with respect to a platinum electrode using an electrometer. The electrolyte was made of 0.1 mol kg^{-1} NaOH with a $pH_{280\ °C}$ of 9.5. The electrolyte was deaerated overnight with Ar gas before heating to 280 °C.

Cyclic polarizations were performed by scanning the potential anodically from 0 mV to 1000 mV with respect to open circuit potential (OCP) at a scan rate of 0.167 mV s^{-1}. The scan direction was reversed either at the peak potential or when the current density reached 1 mA cm^{-2}. Potentiostatic polarizations were performed at +1 V versus pseudo RE for 1 week. Prior to all the polarizations, the OCP was monitored for 1 h and was observed to be stable within few millivolts indicating that the passivated surfaces were stable. In addition, good reproducibility was observed with duplicate measurements.

The electronic properties of oxides in the passive films play a key role in the passivation process as the different anionic and cationic species are transported through the film via generation of point defects [13, 14]. Therefore, the semiconducting properties such as type and density of defects in the passive films were characterized using Mott-Schottky analysis [15, 16]. The measurements were performed in a three electrode cell configuration using the PAR potentiostat interfaced with a Solartron 1255 frequency response analyzer. The glass electrochemical cell was maintained at 30 °C by a water bath. A platinum foil counter electrode and a Ag/AgCl/satd. KCl reference electrode (RE) were used. The electrolyte was made of deaerated 0.1 mol kg^{-1} NaOH with a $pH_{25\ °C}$ of 13.

The Mott-Schottky analysis was performed with an AC signal of 10 mV peak-to-peak amplitude and 1 kHz frequency, over a potential range of 0.5 to −0.5 V versus RE at a scan rate of 50 mVs^{-1}. The potential range spans from the OCP to the transpassive dissolution region based on cyclic polarization of a freshly polished bare Alloy 800 sample in 0.1 M NaOH at 30 °C. Fast scan rate of 50 mVs^{-1} was used to avoid changes to the passive film under the applied potentials. As confirmation, the scan direction was reversed (−0.5 to 0.5 V vs. RE) and the capacitance data from both scan directions were observed to agree well. Also, good reproducibility was observed with duplicate measurements.

The composition of the films was characterized by XPS using a VG Scientific ESCALAB 220i-XL. Monochromatic Al K_α X-ray source (15 kV, 10 mA) with an elliptical spot size of ∼500 µm in the transverse (i.e., largest) diameter was used. The work function of the instrument was calibrated to give sputter cleaned metallic Au $4f_{7/2}$ and sputter cleaned metallic Cu $2p_{3/2}$ binding energy (BE) values of 83.91 eV and 932.67 eV, respectively. The base pressure in the analytical chamber was maintained in the low 10^{-10} Torr range. High-resolution Cr $2p_{3/2}$, Fe $2p_{3/2}$, Ni $2p_{3/2}$, O 1 s and C 1 s spectra were obtained using a pass energy of 20 eV, a step size of 0.05 eV over BE windows ranging from 20 to 40 eV, depending on the element. All XPS spectra were processed using CasaXPS Version 2.3.13 PR 1.6 [17]. The BE of all high-resolution spectra was corrected using the mainline of the C 1 s spectrum and a value of 284.8 eV.

AES depth-profiling of the films was performed using a PHI Model 670 Scanning Auger Nanoprobe. All spectral acquisitions were carried out using a 5 kV electron beam with approximately 5 nA probe current. The relative resolution (i.e., ΔE/E) of the instrument was less than 0.6%. The base pressure in the analytical chamber was maintained in the low 10^{-10} Torr range. The Auger electron spectra were acquired followed by depth-profiling using a 4.0 kV Ar^+ ion beam rastered over a 2 mm × 2 mm area. The sputter rate of the Ar^+ ion beam was calibrated using a Ta_2O_5 standard of known thickness. The profiles followed the

distributions of O, Fe, Ni, Cr, and Pb; and C to monitor for surface contamination. All profiles were processed using CasaXPS Version 2.3.13 PR 1.6 [17]. The relative atomic concentrations (at.%) were determined semi-quantitatively and normalized to 100%. Target factor analysis was used to correct for background noise from profiles of Pb, C, O, and Cr.

Atom probe tomography (APT) was performed using a local electrode atom probe 4000X HR (CAMECA Scientific Instruments, Madison, WI, USA) at the Canadian Center for Electron Microscopy (CCEM), Hamilton, Ontario, Canada. Data acquisition was conducted in ultra-high vacuum ($<4 \times 10^{-9}$ Pa) at a temperature of 59.7 K at the specimen holder. Field evaporation of the samples was induced by ultraviolet laser pulses (λ = 355 nm, 40–60 pJ, 200 kHz). A DC voltage was applied to the sample at all times, and was controlled between 2 and 9 kV to maintain a constant evaporation rate of 0.5% (0.005 ions per pulse). The Integrated Visualization and Analysis Software package v3.6.6 (CAMECA Scientific Instruments, Madison, WI, USA) was used to reconstruct acquired data with established reconstruction algorithms. Samples for APT analysis were prepared in a Zeiss NVision 40 focused ion beam (FIB) instrument (Carl Zeiss, Germany) using a "back-side" lift-out technique. This technique and the necessity for it is described in Section "Surface Analysis". The instrument is equipped with a rotating micromanipulator (Kleindiek Nanotechnik, MM3A-EM) capable of full rotation, in addition to the conventional translational movements. The samples were sharpened into needles using a 30 kV Ga^+ ion beam. Eight needles were extracted; six from the film on a pre-passivated surface and two from the film on a bare surface. The needles were approximately 20 nm in diameter at the tip and a few hundred nm in length.

Results and Discussion

Cyclic Polarization and Potentiostatic Polarization

Cyclic polarization in the alkaline environment (0.1 mol kg^{-1} NaOH) at high temperature (280 °C) showed that the electrochemical behaviors of the Pb-containing films were similar, irrespective of whether the film was formed on a pre-passivated surface or on a bare surface (Fig. 1). However, the Pb-containing films were observed to behave differently from that of the Pb-free films. The presence of Pb in the film suppressed the primary active peak and shifted the secondary anodic peak to lower potentials compared to that of the Pb-free film. The passive current densities were similar for both the Pb-free and Pb-containing films in the order of $\mu A\ cm^{-2}$. This shows that as long as the surface was passivated, irrespective of the presence or absence of Pb, metal dissolution from the surface remained low. The lack of deleterious effect of Pb on passivated surfaces has been previously observed in Alloy 600 and Alloy 690 exposed to 0.1 M perchloric acid ($HClO_4$) at room temperature [18].

However, adding Pb to the solution instead of being incorporated in the passive film showed a deleterious effect of Pb. Cyclic polarizations of bare samples performed with 100 ppm Pb in the solution showed higher active and passive current

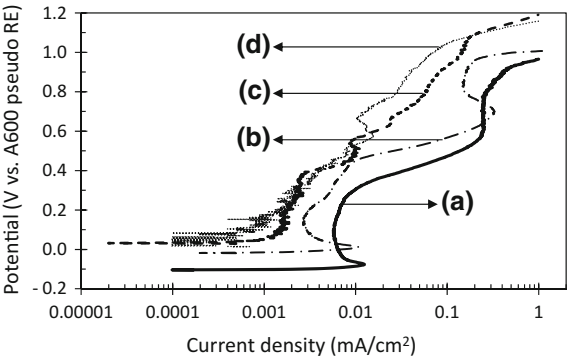

Fig. 1 Cyclic polarization of **a** bare surface, **b** Pb-free film formed on pre-passivated surface, **c** Pb-containing film formed on a pre-passivated surface, and **d** Pb-containing film formed on a bare surface in 0.1 mol kg^{-1} NaOH at 280 °C and a scan rate of 0.167 mV s^{-1}. Only the forward scans are plotted for clarity

densities than that in the absence of Pb in the solution (Fig. 2). Passivated surfaces too showed higher active and passive current densities when the cyclic polarization was performed with 100 ppm Pb in the solution (Fig. 2) compared to that performed in solution without addition of Pb (Dataset (b) in Fig. 1). Previously, the increase in active current densities was attributed to anodic stripping of metallic Pb deposited during cathodic pre-treatment of the samples rather than from the increased activation of the alloy by the dissolved Pb ions in the solution [19]. In this work, the bare samples were not cathodically pre-treated with this caution in mind, and also to be consistent with the measurements on passivated samples, which were not cathodically pre-treated to avoid the risk of altering the surfaces by reducing the oxides in the film. Therefore, the observed increases in active current densities is possibly from the increased activation of the alloy; but the possibility of contributions from anodic stripping of Pb deposited by under potential deposition (UPD) may not be ruled out.

The cyclic polarizations show that the effect of Pb on the electrochemical behavior of Alloy 800 in high temperature alkaline environments depends on whether Pb is present in solution or incorporated in the passive film; possibly lending support to the rationalization that the lack of Pb-induced degradation of Alloy 800 in service is due to the immobilization of Pb in the SG deposits [20, 21]. Additionally, the observations from the cyclic polarization shows that caution must

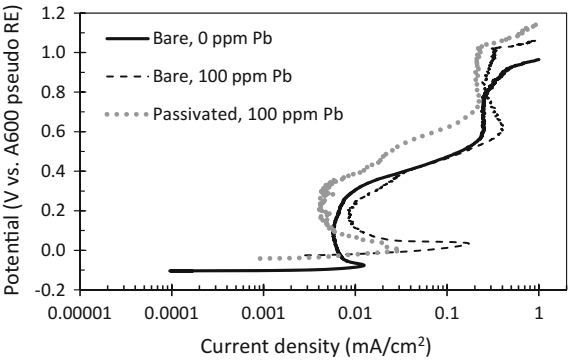

Fig. 2 Cyclic polarization of bare and passivated surfaces in 0.1 mol kg^{-1} NaOH without and with 100 ppm Pb as PbO in solution at 280 °C and a scan rate of 0.167 mV s^{-1}. Only the forward scans are plotted for clarity

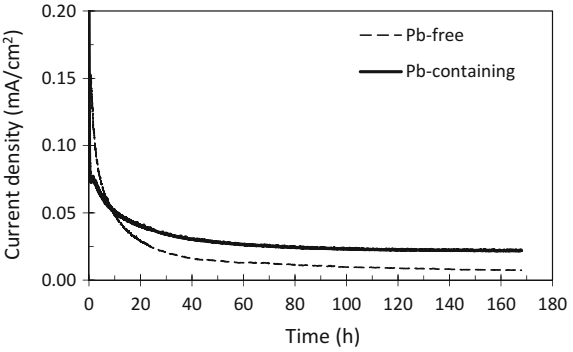

Fig. 3 Potentiostatic polarization of Pb-free and Pb-containing films on pre-passivated surfaces in 0.1 mol·kg^{-1} NaOH at 280 °C for 1 week under a potential of +1 V versus Alloy 600 pseudo RE. The absence of sudden bursts in the current density versus time curves indicates that pit initiation events did not occur on both the surfaces

be exercised while designing the electrochemical experiments and while interpreting the results to understand the effect of Pb on the degradation of SG tubing in operating plants.

Since the presence of Pb in the passive film did not show any deleterious effect on the alloy's uniform corrosion, its effect on localized degradation such as pitting was investigated. The degradation susceptibility of the Pb-free and Pb-containing passivated surfaces was characterized by potentiostatic polarization under large anodic overpotentials (i.e., highly oxidizing conditions) chosen from the cyclic polarization data. However, no sudden increases in the current densities indicating pit initiation were observed over a 1 week exposure to the alkaline environment (without any Pb in solution) at 280 °C, under an applied potential of +1 V versus RE (Fig. 3). The absence of pitting was further confirmed by examining the sample on the surface and in the cross-section using scanning electron microscopy (SEM). These results contrast the susceptibility of Alloy 800 to Pb-induced degradation reported in literature, where experiments are usually performed on bare surfaces with excess Pb, typically as PbO, present in the aqueous solutions. The non-susceptibility to localized corrosion observed in the potentiostatic polarization corroborates the cyclic polarization data, which showed the alloy to behave differently between experiments performed with the Pb in solution and with the Pb incorporated in the film.

Mott-Schottky Analysis

Figures 4 and 5 shows the capacitance (C) measurements on the Pb-free and Pb-containing passive films, plotted as C^{-2} versus potential. The C^{-2} values of the Pb-free films (Fig. 4) were smaller than that of the Pb-containing films, by three to four orders of magnitude (Fig. 5). In the case of the Pb-containing films, the C^{-2} values were higher for the films formed on the pre-passivated surfaces than those formed on bare surfaces, suggesting a possible difference in the interaction of Pb with pre-existing and freshly growing films. Additionally, with increasing exposure durations, C^{-2} was observed to increase for the Pb-free films (Fig. 4) and decrease for Pb-containing films (Fig. 5). These observations indicate the influence of Pb on

the electronic properties of the passive films on Alloy 800 formed under alkaline conditions. Previously, the electronic properties of passive films on Alloy 800 and Alloy 690 formed under simulated SG crevice-type environments have been observed to be influenced by the presence of impurities such as lead, sulphate, thiosulphate, and chloride [9, 10, 22, 23].

The linear regions in the C^{-2} versus potential plots (Figs. 4 and 5), representing the Mott-Schottky behavior, showed both negative and positive slopes implying both p-type and n-type behaviors of the films; which is characteristic of the bi-layer structure of the films formed on Alloy 800 under alkaline conditions. Figure 6 shows the defect densities, estimated using the Mott-Schottky relationship, for the Pb-free and Pb-containing films formed from 1 week exposure to the alkaline environments. Similar trend was observed for the films formed from 4 week exposure. It was observed that the incorporation of Pb lowered the defect densities, both donors (N_D) and acceptors (N_A), in the passive films. However, the decrease in defect density was observed to be less pronounced on a freshly growing film (bare surface) than on a pre-existing film (pre-passivated surface).

According to many passive film growth models [24], fluxes of point defects such as oxygen and/or cation vacancies and interstitials are necessary for the growth of passive films. Based on these models, the decrease in defect densities with the incorporation of Pb in the passive films suggests an effect of Pb on the passivation

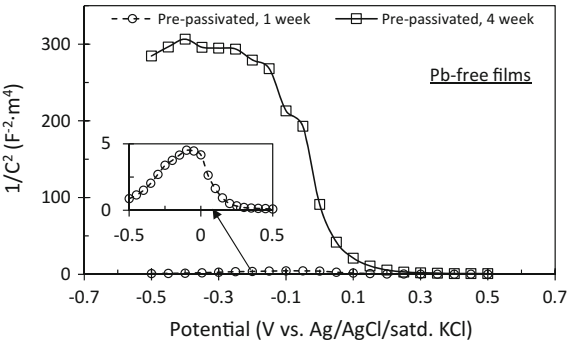

Fig. 4 Mott-Schottky plots for Pb-free passive films formed by exposing pre-passivated surfaces to 0.1 mol·kg^{-1} NaOH at 280 °C for 1 week and 4 weeks

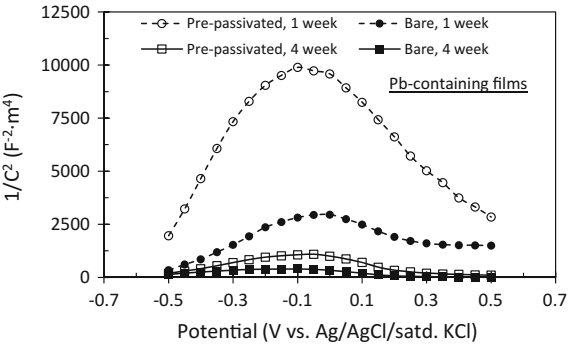

Fig. 5 Mott-Schottky plots for Pb-containing passive films formed by exposing pre-passivated and bare surfaces to 0.1 mol·kg^{-1} NaOH + 500 ppm Pb as PbO at 280 °C for 1 week and 4 weeks

kinetics. On the one hand, irrespective of the presence or absence of Pb, similar low passive current densities from the passivated surfaces were observed from the cyclic polarizations in this work. On the other hand, PbSCC susceptibility of bare surfaces has been observed in simulated Pb-containing SG crevice environments [2–4]. These two aspects suggest to the possibility that the decrease in defect density from the incorporation of Pb affects the repassivation kinetics of a film damaged by factors such as stress rather than the passivation kinetics of an undamaged film.

Surface Analysis

Characterization of the passive films by XPS showed that the composition of both the Pb-free and Pb-containing films were similar, except for the presence of Pb species in the Pb-containing films. Deconvolution of the Cr $2p_{3/2}$, Fe $2p_{3/2}$, and Ni $2p_{3/2}$ spectra by peak fitting (Fig. 7) indicated that the passive films were comprised of predominantly Cr^{3+}-containing oxides (Cr_2O_3), and Ni^{2+}- and Fe^{3+}-based spinel oxides ($NiFe_2O_4$) [25, 26]. For the films formed by exposure to the alkaline environment in the presence of Pb, a second Fe^{3+} oxide and/or hydroxide (γ-Fe_2O_3/FeOOH) component was observed. The Pb 4f spectra (Fig. 8a), acquired from the Pb-containing films, exhibited a doublet structure that is attributed to spin orbit coupling (i.e., $4f_{7/2}$ and $4f_{5/2}$ components). The peak fitting of the spectra indicated the presence of only one Pb species, having BE values consistent with a Pb^{4+}-containing hydroxide ($Pb(OH)_4$) [27]. Similar Pb hydroxide species have been observed previously by others [9, 10]. Analyses of the corresponding O 1 s spectra (Fig. 8b) confirmed the presence of both oxide (O^{2-}) and hydroxide (OH^-) species. The AES analyses (not shown here) also confirmed the presence of Pb in the Pb-containing films. From the AES depth profiles, the thickness of the films was estimated based on the depth at which the atomic concentration of oxygen dropped by 50% from that on the surface. The passive films on the pre-passivated samples were thicker than those on the bare samples; and the films from 4 week exposure were thicker than those from 1 week exposure. For the same exposure duration, the

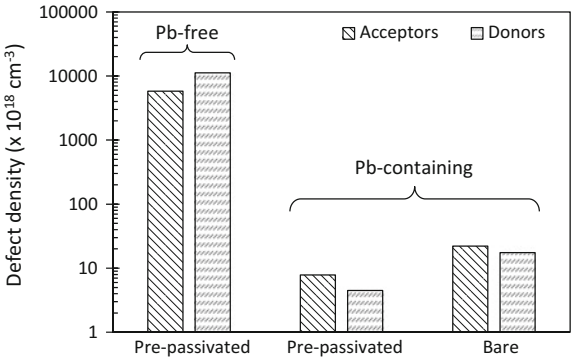

Fig. 6 Acceptor and donor densities estimated from the Mott-Schottky plots for the Pb-free films formed on pre-passivated surfaces, and Pb-containing films formed on pre-passivated and bare surfaces

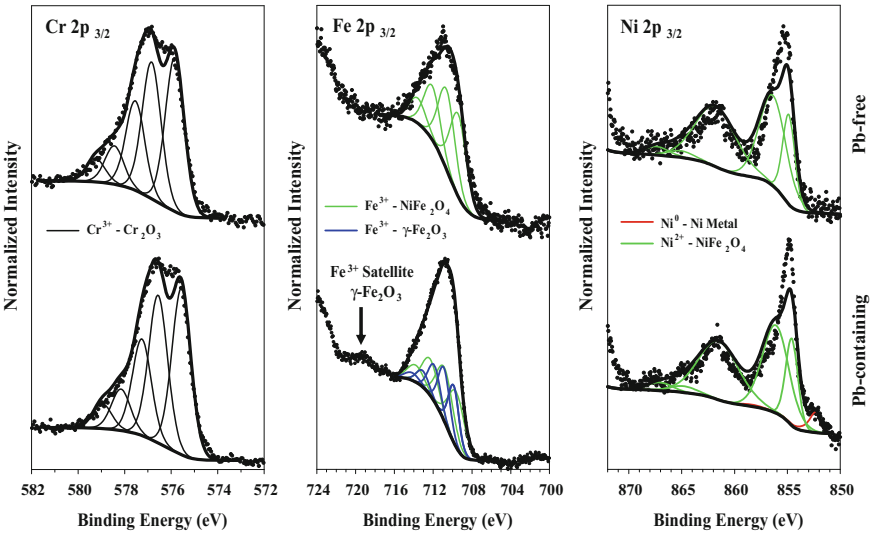

Fig. 7 Deconvolution by peak fitting of the Cr $2p_{3/2}$, Fe $2p_{3/2}$, and Ni $2p_{3/2}$ core level spectra from XPS analyses showing similar compositions for the Pb-free and Pb-containing passive films formed on pre-passivated surfaces

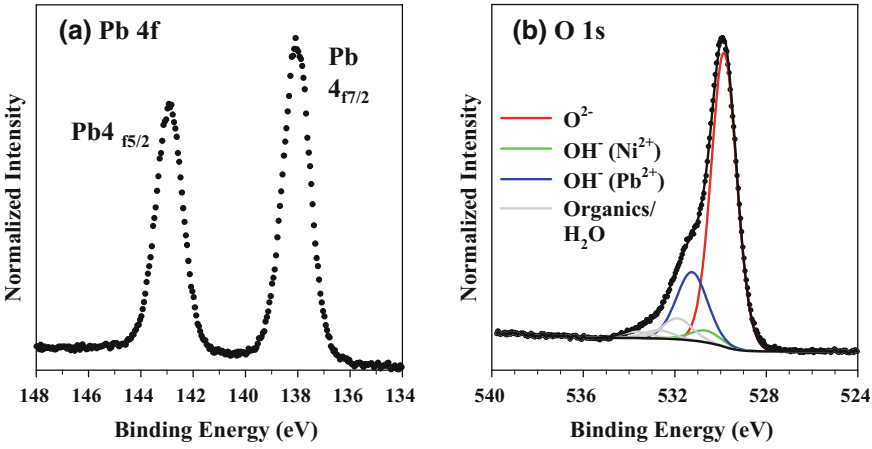

Fig. 8 **a** Pb 4f and **b** O 1s spectra from XPS analysis showing Pb to be present predominantly as hydroxide. Spectra are from the Pb-containing film formed on pre-passivated surface

Pb-containing films were thicker than the Pb-free films. The average thickness of the films estimated from measurements performed at two areas on each sample is listed in Table 3.

The APT analyses performed on the Pb-containing films on pre-passivated and bare surfaces provided insights on the transport of Pb through the passive film.

Table 3 Average thickness of passive films estimated from the AES depth profiling performed at two areas on each sample

Surface Condition	Exposure Duration (weeks)	Average thickness (nm)
Pre-passivated, Pb-free film	1	347
Pre-passivated, Pb-containing film	1	431
Pre-passivated, Pb-containing film	4	453
Bare, Pb-containing film	1	271
Bare, Pb-containing film	4	315

Samples were extracted from the metal/oxide interface using a "back-side" lift-out procedure so as to orient the needles with the surface oxide at the bottom and the sub-surface metal at the top of the needle (Fig. 9). Such a procedure was used to limit the ambiguity from any O retention by the metallic regions while performing the analysis from the oxides into the metal [28].

Figure 10 shows a three-dimensional (3D) APT reconstruction performed from the tip (sub-surface metal) to the base (metal/oxide interface) of the needles extracted from the Pb-containing films on the pre-passivated and bare surfaces. In both the cases, a thin (<5 nm) inner layer of Cr-rich oxide adjacent to the metal matrix and an outer Ni- and Fe-rich oxide was observed. Analysis of the elemental composition showed that the Cr:O atomic ratio in the Cr-rich oxide was very close to that of Cr_2O_3. The Ni-Fe-rich oxide had a composition of ~35–40 at.% Ni and ~12 at.% Fe with <2 at.% Cr. A slight enrichment in Ni and depletion in Cr was observed in the alloy immediately adjacent to the metal/oxide interface.

Figure 11 shows a two-dimensional (2D) longitudinal slice (5 nm in thickness) from the 3D reconstruction shown in Fig. 10. In this 2D slice, the distribution of Pb is overlaid on the distribution of Ni, and that of Fe and Cr. Such an analysis revealed that the Pb was present predominantly in the Ni-Fe-rich oxides with some presence in the Cr-rich oxide. However, it is worth mentioning that the presence of Pb in the thin Cr-rich oxide might be because of overlapping signals between the Ni-Fe-rich oxide and the thin Cr-rich oxide. Attempts to resolve this are underway. The observation of Pb in the oxides shows that Pb was able to penetrate through the thick outer oxide layers to reach the inner Cr-rich oxide. This observation was made on both the pre-passivated and bare surfaces; suggesting that Pb had no difficulty in penetrating through a pre-existing film. Nevertheless, the cross-sectional analysis revealed that Pb did not penetrate through the more protective Cr-rich oxide to reach the underlying alloy surface. It should be emphasized that the samples in our study were not subjected to any external stress during exposure to the Pb-containing alkaline environment. In contrast, other APT analyses have revealed Pb at the metal/oxide interface of RUB samples subjected to PbSCC testing in similar Pb-containing alkaline environment [29]; alluding to the necessity of high stress levels to mechanically damage the inner Cr-rich layer, thereby, providing a path for Pb to reach the metal/oxide interface. Future work is being planned to determine the stress levels required to rupture the inner Cr-rich oxides, along with similar APT analyses to determine the behavior/location of Pb in such situations.

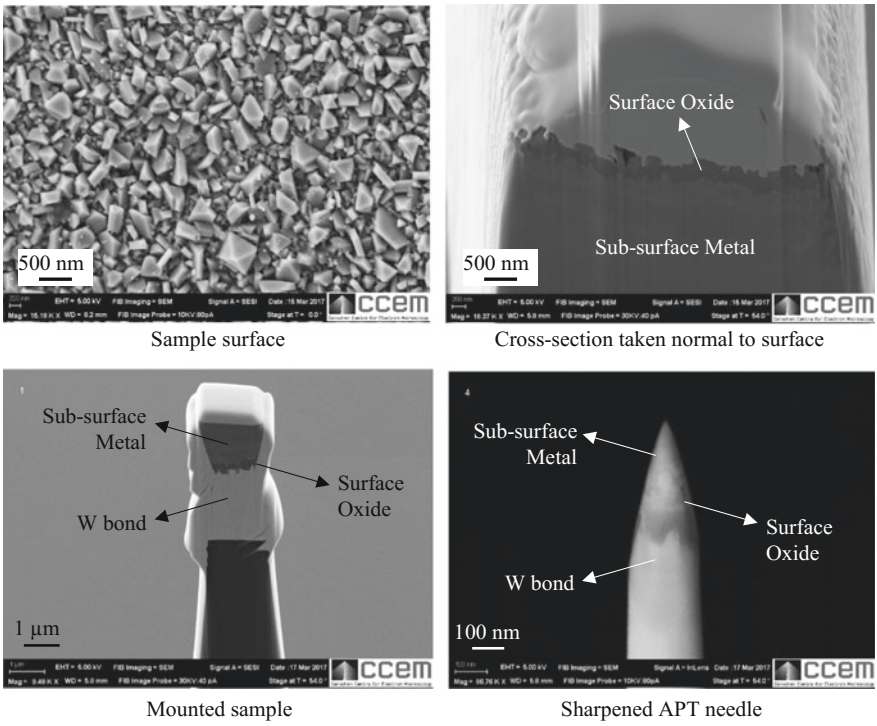

Fig. 9 SEM images showing the FIB "back-side" lift-out procedure to prepare the needles for APT analysis

Conclusions

Electrochemical and surface analytical techniques were used to characterize Pb-free and Pb-containing passive films formed under alkaline conditions at 280 °C on Alloy 800 samples that were pre-passivated in AVT conditions. Cyclic polarization showed that both the Pb-free and Pb-containing films performed equally well in terms of the passive current densities, indicating that the incorporation of Pb in the outer oxides did not affect the passivity of the underlying alloy. Additionally, Alloy 800 samples with Pb-containing films on the surface were not susceptible to localized degradation such as pitting during one week exposure to the alkaline environment under a large anodic overpotential at 280 °C. However, the presence of excess Pb in the solution increased the active current densities during cyclic polarization of the bare surfaces as well as pre-passivated surfaces. Therefore, it is inferred that the effect of Pb depends on whether Pb is present in the solution or incorporated in the film.

Based on the Mott-Schottky analysis and the existing passive film growth models, the lowering of defect densities from the incorporation of Pb in the films suggests an effect of Pb on the kinetics. The following aspects—(i) similar low

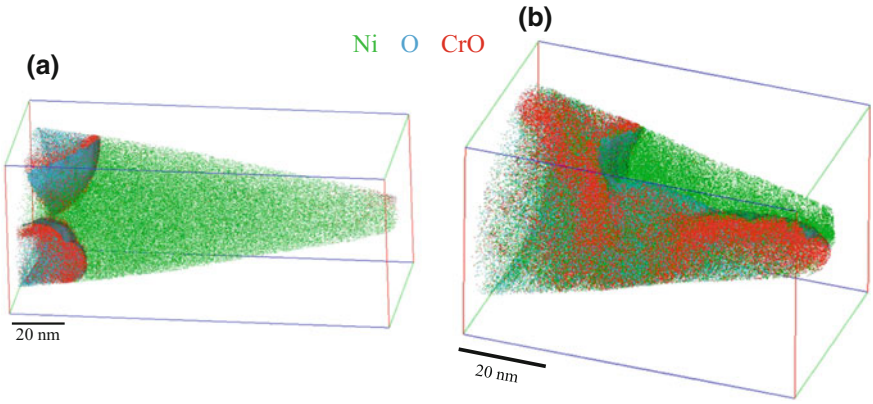

Fig. 10 Three-dimensional APT reconstruction of the needles extracted from the Pb-containing films on (**a**) pre-passivated surface and (**b**) bare surface, formed by exposure to the alkaline environment for 4 weeks. The metal matrix is at the tip and the metal/oxide interface is near the base of the needle. In (**b**), the metal/oxide interface is not parallel to the base of the needle as the oxide crystals grew to different depths at the interface

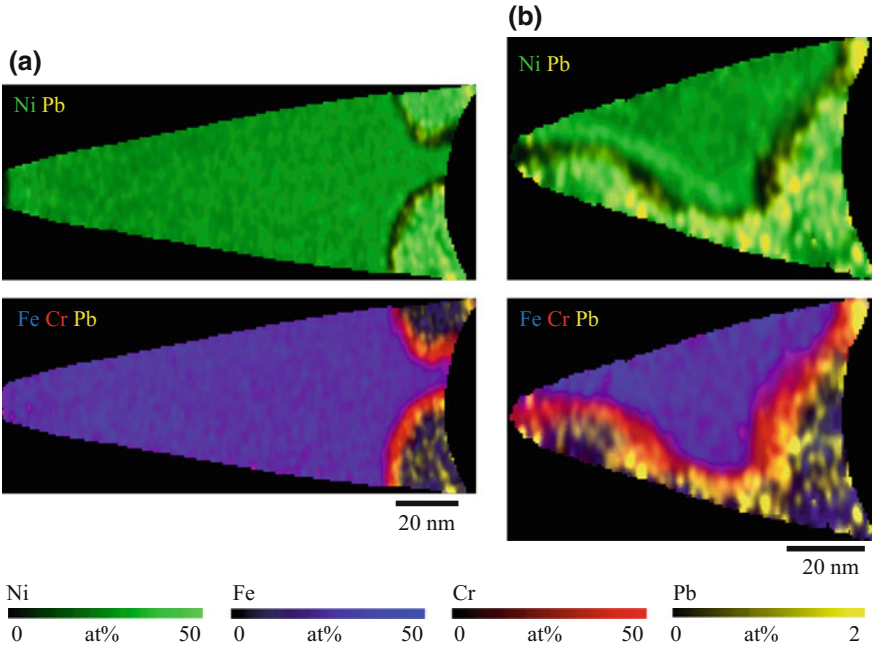

Fig. 11 Two-dimensional slice (5 nm in thickness) from the three-dimensional APT reconstruction in Fig. 10 showing the distribution of Pb overlaid on the distribution of the major alloying elements: Fe, Ni, and Cr. Data are from the needles extracted from the Pb-containing films on (**a**) pre-passivated surface and (**b**) bare surface, formed by exposure to the alkaline environment for 4 weeks

passive current densities from the passivated surfaces, irrespective of the presence or absence of Pb, observed in this work and (ii) PbSCC susceptibility of the bare surfaces in simulated Pb-containing SG crevice environments observed in literature —suggest that Pb possibly affects the repassivation kinetics of a film damaged by factors such as stress rather than the passivation kinetics of an undamaged film. This inference was further supported by the APT analysis at the metal/oxide interface, which showed that Pb was not present at the interface of the unstressed samples analyzed in this work, but was present at the interface of highly stressed RUB samples subjected to PbSCC testing [29].

Acknowledgements Many thanks are due to colleagues at CNL, especially A. Audet and H. Chaudhry for performing the room temperature and high temperature electrochemical measurements; C. Mayhew, H. Rudzinski, and B. Payne for the AES and XPS characterization; and J. Smith for review and technical discussion. APT was performed and analyzed by B. Langelier at the Canadian Center for Electron Microscopy, Hamilton.

References

1. R.L. Tapping, Materials Performance in CANDU Reactors: The First 30 years and the Prognosis for Life Extension and New Designs. J. Nucl. Mater. **383**, 1–8 (2008)
2. D. Gómez Briceño, M.L. Castaño, M.S. García, Stress Corrosion Cracking Susceptibility of Steam Generator Tube Materials in AVT (All Volatile Treatment) Chemistry Contaminated with Lead. Nucl. Eng. Des. **165**, 161–169 (1996)
3. H. Takamatsu, T. Matsunaga, B.P. Miglin, J.M. Sarver, P.A. Sherburne, K. Aoki, and T. Sakai, Study on Lead-Induced Stress Corrosion Cracking of Steam Generator Tubing under AVT Water Chemistry Conditions, Proceedings of the Eleventh International Conference on Environmental Degradation of Materials in Nuclear Power Systems—Water Reactors, American Nuclear Society (ANS), 1997, pp. 216–223
4. B. Capell, R. Wolfe, R. Eaker, J. Lumsden, PbSCC of Alloy 800NG Steam Generator Tubing in Alkaline Conditions, Proceeding of the Seventeenth International Conference on Environmental Degradation of Materials in Nuclear Power Systems—Water Reactors, Canadian Nuclear Society (CNS), 2016, pp. 713–727
5. C. Marks, C. Anderson, "Steam Generator Management Program: Steam Generator Deposit Characterization for Steam Generator Tube Degradation Prediction and Management", Technical Report 1018249, Electric Power Research Institute (EPRI), (2008 December)
6. B. Stellwag, The Mechanism of Oxide Film Formation on Austenitic Stainless Steels in High Temperature Water. Corros. Sci. **40**(2–3), 337–370 (1998)
7. B. Beverskog, I. Puigdomenech, Pourbaix Diagrams for the Ternary System of Iron-chromium-nickel. Corrosion **55**(11), 1077–1087 (1999)
8. R.J. Lemire, G.A. McRae, The Corrosion of Alloy 690 in High-temperature Aqueous Media —thermodynamic Considerations. J. Nucl. Mater. **294**(1–2), 141–147 (2001)
9. B.T. Lu, J.L. Luo, Y.C. Lu, Passivity Degradation of Nuclear Steam Generator Tubing Alloy Induced by Pb Contamination at High Temperature. J. Nucl. Mater. **429**(1–3), 305–314 (2012)

10. B.T. Lu, J.L. Luo, Y.C. Lu, Effects of pH on Lead-induced Passivity Degradation of Nuclear Steam Generator Tubing Alloy in High Temperature Crevice Chemistries. Electrochim. Acta **87**(1), 824–838 (2013)
11. S.-I. Pyun, C. Lim, R.A. Oriani, The Role of Hydrogen in the Pitting of Passivating Films on Pure Iron. Corros. Sci. **33**(3), 437–444 (1992)
12. J.G. Yu, C.S. Zhang, J.L. Luo, P.R. Norton, Investigation of the Effect of Hydrogen on the Passive Film on Iron by Surface Analysis Techniques. J. Electrochem. Soc. **150**(2), B68–B75 (2003)
13. S.R. Morrison, *Electrochemistry at Semiconductor and Oxidized Metal Electrodes* (Plenum Press, New York, USA, 1980)
14. M. Bojinov, G. Fabricius, T. Laitinen, K. Mäkelä, T. Saario, G. Sundholm, Coupling between Ionic Defect Structure and Electronic Conduction in Passive Films on Iron, Chromium and Iron-Chromium Alloys. Electrochim. Acta **45**(13), 2029–2048 (2000)
15. N.E. Hakiki, M. Da Cunha Belo, A.M.P. Simões, M.G.S. Ferreira, Semiconducting Properties of Passive Films Formed on Stainless Steels—Influence of the Alloying Elements. J. Electrochem. Soc. **145**(11), 3821–3829 (1998)
16. M. Da Cunha Belo, N.E. Hakiki, M.G.S. Ferreira, Semiconducting Properties of Passive Films Formed on Nickel-base Alloys Type Alloy 600: Influence of the Alloying Elements. Electrochim. Acta **44**(14), 2473–2481 (1999)
17. N. Fairley, Casa Software Ltd., 1999–2011
18. D. Costa, H. Talah, P. Marcus, M. Le Calvar, and A. Gelpi, Interaction of Lead with Nickel-base Alloys 600 and 690, Proceedings of the Seventh International Conference on Environmental Degradation of Materials in Nuclear Power Systems—Water Reactors, NACE, (1995) pp. 199–208
19. H. Radhakrishnan, A.G. Carcea, R.C. Newman, Influence of Pb^{2+} Ions on the Dissolution and Passivation of Nickel and Ni-21Cr in Acidic Solutions. Corros. Sci. **47**(12), 3234–3248 (2005)
20. R.W. Staehle, "Assessment of and Proposal for a Mechanistic Interpretation of High Nickel Alloys in Lead-Containing Environments", Proceedings of the Eleventh International Conference on Environmental Degradation of Materials in Nuclear Power Systems—Water Reactors, American Nuclear Society, 2004, pp. 381–424
21. R.W. Staehle, "Clues and Issues in the SCC of High Nickel Alloys Associated with Dissolved Lead", Proceedings of the Twelfth International Conference on Environmental Degradation of Materials in Nuclear Power Systems—Water Reactors, NACE, 2005, pp. 1163–1210
22. D.H. Xia, Y. Behnamian, H.N. Feng, H.Q. Fan, L.X. Yang, C. Shen, J.L. Luo, Y.C. Lu, S. Klimas, Semiconductivity Conversion of Alloy 800 in Sulphate, Thiosulphate, and Chloride Solutions. Corros. Sci. **87**, 265–277 (2014)
23. D.H. Xia, Y. Behnamian, L. Yang, H.Q. Fan, R.K. Zhu, J.L. Luo, Y.C. Lu, S. Klimas, Semiconductivity of Steam Generator Tubing Alloys in Simulated Crevice Chemistries Containing Lead and Sulphur. Corros. Eng., Sci. Technol. **51**(1), 37–50 (2016)
24. A. Seyeux, V. Maurice, P. Marcus, Oxide Film Growth Kinetics on Metals and Alloys—I. Physical Model. J. Electrochem. Soc. **160**(6), C189–C196 (2013)
25. M.C. Biesinger, B.P. Payne, A.P. Grosvenor, L.W.M. Lau, A.R. Gerson, R.S.C. Smart, Resolving Surface Chemical States in XPS Analysis of First Row Transition Metals, Oxides and Hydroxides: Cr, Mn, Fe, Co and Ni. Appl. Surf. Sci. **257**(7), 2717–2730 (2011)
26. B.P. Payne, M.C. Biesinger, N.S. McIntyre, X-ray Photoelectron Spectroscopy Studies of Reactions on Chromium Metal and Chromium Oxide Surfaces. J. Electron Spectrosc. Relat. Phenom. **184**(1–2), 29–37 (2011)

27. C.D. Wagner, A.V. Naumkin, A. Kraut-Vass, J.W. Allison, C.J. Powell, J.R. Jr. Rumble, NIST Standard Reference Database 20, Version 3.4 (Web Version) (http:/srdata.nist.gov/xps/) 2003
28. E.A. Marquis, B.P. Geiser, T.J. Prosa, D.J. Larson, Evolution of Tip Shape during Field Evaporation of Complex Multilayer Structures. J. Microsc. **241**(3), 225–233 (2011)
29. S.Y. Persaud, J.M. Smith, C.D. Judge, F.Long, A. Korinek, B. Capell, et al., "High Resolution Characterization of Pb-Caustic SCC in Alloy 800", *Manuscript Submitted for Publication,* 2017

Influence of Alloying on α-α′ Phase Separation in Duplex Stainless Steels

David A. Garfinkel, Jonathan D. Poplawsky, Wei Guo, George A. Young and Julie D. Tucker

Abstract Thermal embrittlement caused by phase transformations in the temperature range of 204–538 °C limits the service temperature of duplex stainless steels. The present study investigates a set of wrought (2003, 2101, and 2205) and weld (2209-w and 2101-w) alloys in order to better understand how alloying elements affect thermal embrittlement. Samples were aged at 427 °C for up to 10,000 h. The embrittlement and thermal instability were assessed via nanoindentation, impact toughness testing, and atom probe tomography (APT). Results demonstrate that the spinodal amplitude is not an accurate predictor of mechanical degradation, and that nanoindentation within the ferrite grains served as a reasonable approximate for the embrittlement behavior. Compositionally, alloys with a lower concentration of Cr, Mo, and Ni were found to exhibit superior mechanical properties following aging.

Keywords Duplex stainless steels · Spinodal decomposition · Embrittlement

D.A. Garfinkel · G.A. Young · J.D. Tucker (✉)
School of Mechanical, Industrial and Manufacturing Engineering, Oregon State University, Corvallis, OR, USA
e-mail: Julie.Tucker@oregonstate.edu

J.D. Poplawsky · W. Guo
Oak Ridge National Laboratory, Center for Nanophase Materials Sciences, Oak Ridge, TN, USA

J.H. Jackson et al. (eds.), *Proceedings of the 18th International Conference on Environmental Degradation of Materials in Nuclear Power Systems – Water Reactors*, The Minerals, Metals & Materials Series, https://doi.org/10.1007/978-3-319-68454-3_85

Introduction

Duplex stainless steels (DSS) are a two-phase (ferrite and austenite) subset of stainless steels that offer a desirable combination of strength, toughness, corrosion resistance, and affordability. DSS are currently used in chemical storage and processing, desalinization, and other industries where corrosion resistance is needed [1, 2]. There are additional applications in which DSS are not currently used, specifically nuclear power generation, wherein the combination of corrosion resistance and mechanical properties make them an attractive candidate material. However, thermal instabilities resulting in embrittlement in the temperature range of 204–538 °C currently inhibit usage in elevated temperature applications [1–4].

Thermal embrittlement in DSS is the result of a miscibility gap in the Fe–Cr system that leads to an unmixing of Fe and Cr into two phases (no change in crystal structure), one being Cr-enriched and Fe-depleted (α′), the other being Cr-depleted and Fe-enriched (α) [5]. This transformation, which occurs exclusively in the ferrite phase, typically through spinodal decomposition, results in embrittlement and hardening primarily through a lattice mismatch between the α and α′ regions. Because of the separation into these two phases, the transformation can be referred to as α-α′ separation. Other precipitates in the ferrite, specifically G-phase, have also been suggested as modest contributors to mechanical degradation, however, others question if G-phase has any effect [6–8].

In order to create an optimal DSS with the desired ferrite/austenite phase fraction and material properties, careful alloying of many elements is required [1, 2]. The thermal instability behavior and ensuing mechanical degradation in DSS is highly dependent on alloying: subtle differences in composition can lead to significant differences in aging behavior. Many elements have been suggested as contributing to the thermal instability, though, Cr, Ni, Mo, and Si have been singled out as especially detrimental [5, 6, 8]. While N has been found to reduce the damaging effects of aging [8].

It is the purpose of this study to observe the unique responses of different DSS alloys to thermal aging. Both the kinetics (α-α′ separation) and the resulting mechanical degradation (hardening and impact toughness) were compared with compositional factors to determine the relationship between alloying, thermal instability and mechanical degradation. Further, by using techniques such as nanoindentation and atom probe tomography (APT), the ferrite phase was isolated from the bulk in order to study its performance without the influence of the ferrite/austenite phase fraction or grain structure, to provide the most direct observation of α-α′ separation.

Methods

Materials

Five DSS alloys were studied: three commercial, hot-rolled wrought alloys, 2101, 2205, and 2003, and two weld alloys, 2209-w and 2101-w. The weld deposits were made through multi-pass gas tungsten arc welding (GTAW) process in which large

weld pads (approximately 13 cm wide × 11 cm high × 16 cm long) were created using 2101 and 2209 filler metal. The 2101-w and 2209-w welds were made on the corresponding base metal, 2003 and 2205 respectively, then the weld pads were cut from the base metal.

Bars of all five alloys were aged isothermally at a temperature of 427 °C for up to 10,000 h, air cooled, and then machined into test samples. Three of these alloys, 2003, 2101-w and 2101 are considered lean grade DSS alloys, while the other two, 2209-w and 2205, are considered standard grade alloys. The composition of each alloy is included in Table 1.

Atom Probe Tomography

APT was conducted on samples of each alloy following thermal aging at 427 °C for 1, 100, 1000, and 10,000 h. An additional sample that was aged for 10 h was analyzed for alloys 2101, 2209-w, and 2101-w. More information regarding APT equipment and settings can be found in Ref. [9].

APT was used to quantify α-α′ separation through the measurement of spinodal amplitude: the difference in Cr composition between the α and α′ regions. Two methods were utilized to determine the amplitude, or ΔCr, of the spinodal decomposition: (1) the Langer-Bar-on-Miller (LBM) non-linear theory of spinodal decomposition method [10], and (2) the proxigram method. The LBM method was used to quantify early stages of spinodal decomposition, and the proxigram method was used to quantify the late stages. More information on these methods can be found in Ref. [11].

Nanoindention

Nanoindentation was conducted on a Micro Materials NanoTest Vantage Nanoindenter. Testing was conducted on unaged samples of all five alloys as well as samples aged at 427 °C for 10,000 h. Using a Berkovich tip, testing included at least 10 indents within the ferrite grains and at least 3 in the austenite grains for each sample. A dwell time of 40 s and a loading rate of 0.2 mN/s was utilized. A target indent depth of 130 nm was chosen for depth control on the weld alloys,

Table 1 Chemical composition of the five alloys studied (wt%)

Alloy	Fe	Cr	Ni	Mo	Mn	Si	N	C	Cu
2101	Bal.	21.49	0.21	0.21	5.00	0.79	0.21	0.029	0.30
2003	Bal.	21.42	3.70	1.75	1.22	0.37	0.180	0.010	0.13
2205	Bal.	22.44	5.69	3.11	1.80	0.42	0.17	0.020	0.43
2101-w	Bal.	23.40	7.30	0.24	0.7	0.44	0.163	0.011	0.13
2209-w	Bal.	22.96	8.77	3.08	1.74	0.036	0.15	0.014	0.16

while a target depth of 400 nm was used for the wrought alloys to account for the difference in grain size.

Results

Cr Distribution

One convenient method to observe α-α′ separation qualitatively is by taking small 'slices' from the reconstructed APT samples and viewing the Cr distribution. Figure 1 shows Cr maps (blue dots) in 40 × 15 × 5 nm^3 slices, with 5 nm representing the depth into the page. Images of the 1, 1000, and 10,000 h samples aged at 427 °C for all five alloys are included. Figure 1 shows that the originally homogeneous distribution of Cr present in unaged samples transitions into Cr clustering following aging. This trend is present in all five alloys, and is a clear indication of α-α′ separation. The α′ regions are seen as the Cr-rich clusters and the α regions as the Cr-depleted regions. Also in Fig. 1, the α′ regions demonstrate an obvious progression with aging; the Cr regions increase in size and spacing with increased aging time. Another important observation is the interconnected α-α′ structure in all five alloys, which confirms the method of α-α′ separation as spinodal decomposition as opposed to nucleation and growth. The interconnected nature of the α-α′ separation is not clear in all images in Fig. 1 but was verified for all alloys in the full three dimensional reconstruction of the APT tip.

When comparing the aging behavior of the five alloys, there is an obvious difference between the weld and wrought alloys. Alloys 2101-w, and 2209-w, along with 2101, exhibit much larger and farther spaced α′ regions than 2003 and 2205. After 10,000 h of aging, an average spacing between 12 and 15 nm was found in 2101-w, 2209-w, and 2101, whereas 2205 and 2003 had an average spacing between 5 and 7 nm. Finally, though it is difficult to observe in Fig. 1, it appears that alloys 2101, 2101-w, and 2209-w have a higher density of Cr in the α′ regions than is seen in 2003 and 2205. The large, dense, widely spaced decomposed regions are an indication of more significant thermal instability in the weld alloys compared to the wrought alloys.

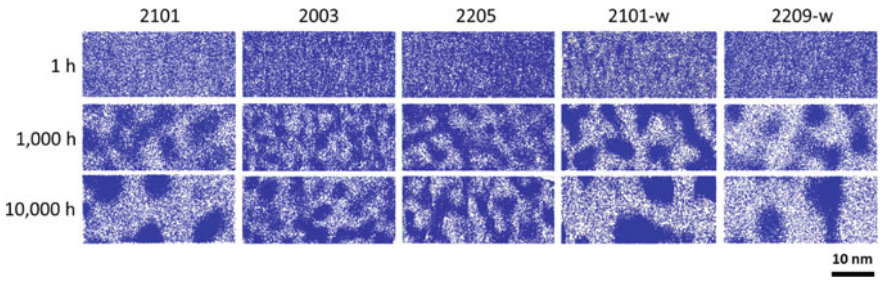

Fig. 1 Cr distribution (blue dots) with aging (1, 1000, and 10,000 h) at 427 °C of all five alloys. Note that the viewing size is 40 × 15 × 5 nm^3 with 5 nm representing the depth into the page (Color online figure)

Amplitude

The difference in Cr composition between the α and α′ regions can be used to quantify α-α′ separation. Figure 2 demonstrates the ΔCr measurements for each alloy utilizing the results from the LBM method for the early stages of aging (1 and 10 h), and the proxigram method for the later stages (100, 1000 and 10,000 h). Trends are in general agreement with those observed in Fig. 1: spinodal decomposition is enhanced with aging, and the weld alloys, along with 2101, demonstrate the greatest degree of decomposition. Other trends that are more difficult to see in Fig. 1, become apparent in Fig. 2. For example, in Fig. 1 there is a seemingly negligible difference in aging behavior between 2003 and 2205, however, Fig. 2 demonstrates a significantly larger ΔCr in 2205. Additionally, the measured amplitude for 2101 is closer to that found in 2209-w than would be expected from Fig. 1.

Nanoindentation

The overall change in hardness in the ferrite from unaged to 10,000 h of aging for all five alloys is shown in Fig. 3. Again, the weld alloys exhibit an inferior performance (most hardening), compared to the wrought alloys. However, the results shown in Fig. 3 are not in complete agreement with Figs. 1 and 2. Alloy 2101 experiences the least hardening despite a larger spinodal amplitude than the other wrought alloys. Additionally, 2209-w demonstrates the most hardening, while 2101-w has the largest spinodal amplitude. Not shown in Fig. 3, hardness testing in austenite grains showed no trends of hardening, as would be expected.

Hardness testing serves as a convenient method to approximate embrittlement behavior. It is also preferred to toughness testing due to the potential to isolate changes in mechanical properties within the ferrite grains. However, the results of the two tests are not always in agreement. Charpy impact toughness testing was conducted in addition to nanoindentation on all five alloys and was used to validate nanoindentation as an approximation method.

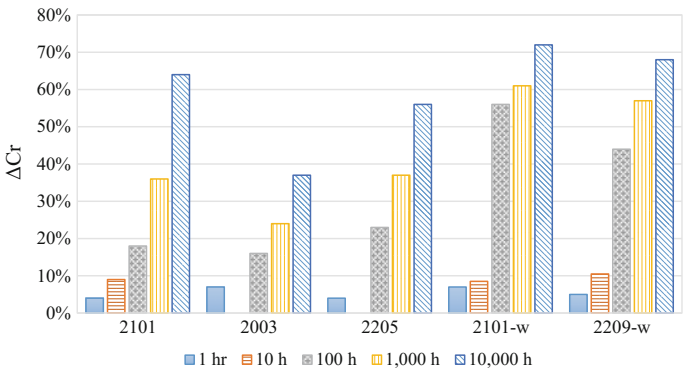

Fig. 2 Combination of amplitude results from LBM and proxigram methods. 10 h samples of 2003 and 2205 were not analyzed, and thus are left blank

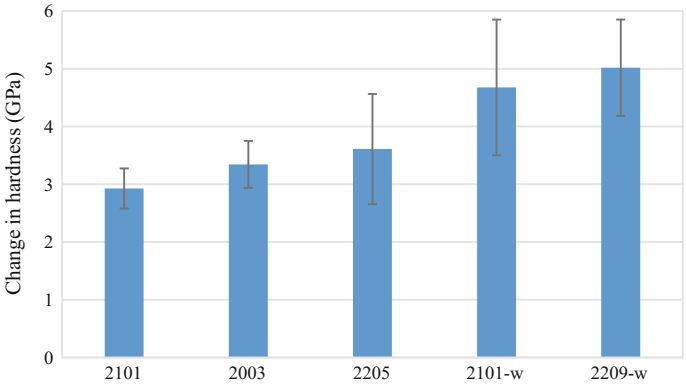

Fig. 3 Change in hardness within the ferrite grains from unaged to 10,000 h of aging for all alloys, error bars show ± one standard deviation

Figure 4 shows the testing temperature required for an impact toughness of 35 ft-lbs after aging at 427 °C: a higher value signifies a more brittle material. Image analysis of scanning electron micrographs revealed that the wrought alloys had a much higher ferrite phase fraction (~50%) compared to the weld alloys (~20%). For that reason, the Charpy impact toughness results for the weld alloys and wrought alloys were considered separately. The results are in general agreement with nanoindentation results, with the only discrepancy being the performance of 2101, which experienced the least hardening, but had a performance between that of 2003 and 2205 in Charpy testing. It should also be noted that 2101 has the least data points, which makes comparison difficult. Thus, the nanoindentation results are not a perfect representation of the embrittlement behavior, however, nanoindentation does serve as a reasonable approximation for embrittlement for the five alloys tested. Additional results from mechanical testing on alloys 2205, 2003, 2101-w, and 2209-w can be found in Ref. [12].

Discussion

The most significant relationship connecting α-α′ separation to the bulk composition was that of Cr and ΔCr. Figure 5a shows a clear correlation between the bulk Cr composition and ΔCr (10,000 h of aging), with one major outlier (2101). This behavior confirms that within the spinodal region, increasing the Cr composition leads to enhanced α-α′ separation through a larger amplitude. The outlier behavior of 2101 can likely be attributed to its relatively unique chemical composition-very high Mn (5 wt%), and very low Ni (0.21 wt%)-possibly shifting its behavior compared to the more similar alloys. In Fig. 5b, the amplitude is compared with the change in hardness. Here it is seen that there is no clear relationship between the amplitude and the change in hardness. The absence of a correlation between amplitude and hardness is unexpected, as a greater amplitude corresponds to more

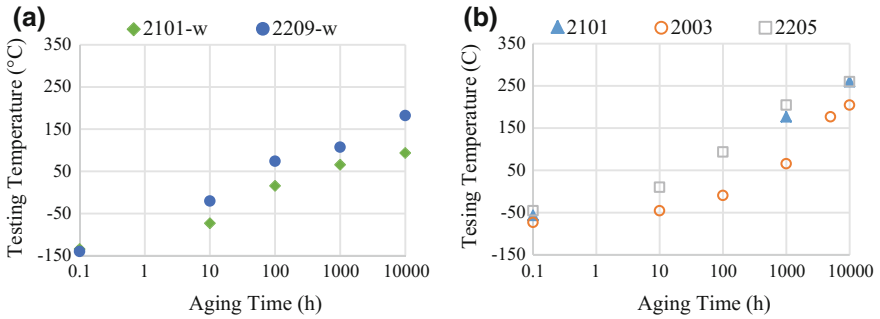

Fig. 4 Testing temperature required for an impact toughness of 35 ft-lbs as a function of aging time at 427 °C for the weld (**a**) and wrought (**b**) alloys

significant decomposition, and thus would be expected to lead to more hardening. It is possible that there is a threshold effect causing a rapid increase from the wrought alloys to the weld alloys after a spinodal amplitude of ~65.

Many of the commonly used alloying elements such as Cr, Ni, Mo, Mn, N, and Si have been suggested as contributing to thermal instability and embrittlement [5, 6, 8]. In the present study, all alloying elements were compared to the change in hardness individually (not shown). Both bulk and ferrite (APT) compositions were considered. Ni, Cr, and Mo each demonstrated an overall increasing trend between composition and hardening, though the majority of the trends were weak. The closest correlating behavior between the elements mentioned above belonged to Ni. Mn demonstrated essentially no relationship to hardening, while Si and N exhibited a negative correlation to hardness. It should be noted that N was not detected by APT in the ferrite, instead its contribution can be explained by its relationship with Ni: Increasing N stabilizes the austenite phase, and thus less Ni is required in the alloy, which leads to the opposite relationship between N and hardening as Ni. Finally, a decrease in Fe led to an increase in hardening, which suggests that alloying enhances hardening.

Although, there are apparent trends when considering single elements, the correlations remain relatively weak. Previous literature suggests a correlation between

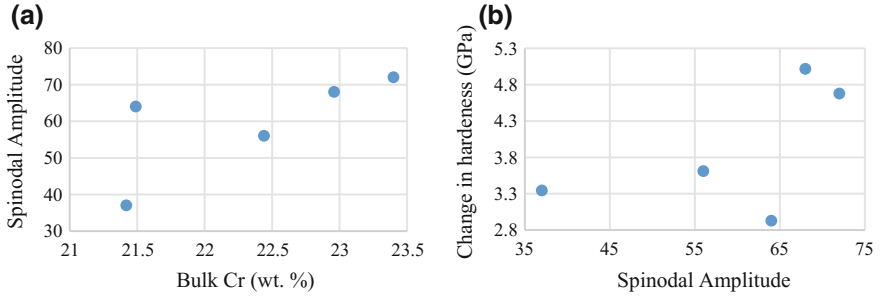

Fig. 5 Relationship between the spinodal amplitude and the bulk Cr composition of the five alloys aged for 10,000 h (**a**) and relationship between amplitude and change in hardness (**b**)

the combined Cr, Mo, and Si concentration in DSS and the embrittlement behavior [8]. When examining this relationship using the nanoindentation and APT data, it was found that an increase in this combined composition within the ferrite grains correlated to an increase in hardening. However, because Si demonstrates a decreasing influence on hardening when isolated, removing it from the comparison improved the correlation. The relationship between the combined Cr and Ni composition on hardening is shown in Fig. 6a. There is a clear trend of increasing hardness when increasing the composition of Cr and Ni.

Additionally, other alloying elements were included with Cr and Ni to determine if there was a stronger relationship. Specifically, Mo is of interest due to the superior aging performance of Mo-free alloys compared to Mo-bearing alloys [8]. Figure 6b shows the relationship when including Mo. The inclusion of Mo has little effect on the linear fit R^2 value ($\sim$0.85), however, unlike the initial relationship, when including Mo there is an increase in hardness in each alloy with increasing composition. In Fig. 6a 2209-w has a greater hardness than 2101-w despite a lower Cr + Ni composition. Also seen in Fig. 6b, there is a clear linear behavior between the bottom three data points (wrought alloys) and a similar behavior between the top two data points (weld alloys).

The connection between the combined Cr and Ni composition on spinodal decomposition is rather straightforward. Cr initiates α-α′ separation due to the Fe–Cr miscibility gap, while Ni has been suggested as augmenting α-α′ separation by enhancing Cr diffusion [8]. The bulk Cr composition was shown to correlate well with spinodal amplitude in Fig. 5a. When comparing the spinodal amplitude with the Cr composition within the ferrite, this relationship was not as clear. However, by adding Ni into the comparison, the correlation became much stronger.

In order to demonstrate the contribution of Ni on spinodal decomposition, another concept must be introduced: the partitioning behavior of alloying elements other than Fe and Cr. Table 2 shows the difference in composition of Ni, Mo, Mn, and Si in the α region compared to the α′ after 10,000 h of aging. Results were obtained using APT proximity histograms with compositions of 30 and 15 at.% Cr

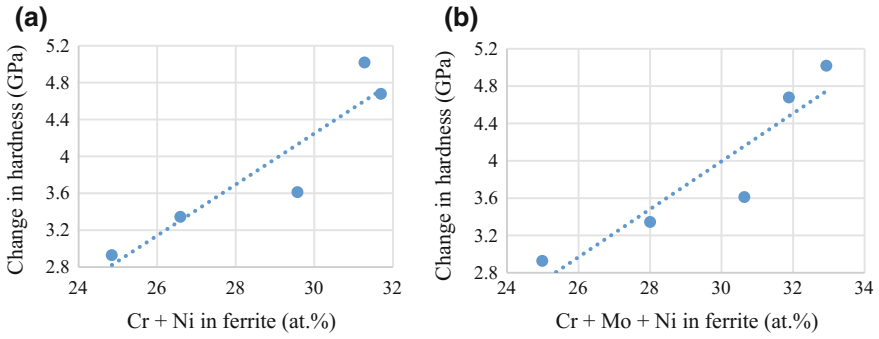

Fig. 6 Comparison of combined composition of Cr + Ni (**a**) and Cr + Ni + Mo (**b**) with the change in hardness

Table 2 Partitioning tendency of Ni, Mo, Mn, and Si in the five alloys after 10,000 h of aging

Alloy	Ni (α/α′)	Mo (α/α′)	Mn (α/α′)	Si (α/α′)
2101	1.6/0.7	0.2/0.3	3.7/6.3	1.6/2.7
2003	3.4/2.5	1.2/1.6	0.9/1.5	1.0/1.3
2205	4.8/2.2	1.7/2.5	1.5/1.2	1.2/1.0
2101-w	5.7/1.8	0.2/0.3	0.4/0.8	0.9/1.0
2209-w	9.4/2.1	0.8/1.9	2.2/0.8	0.7/0.3

used as cutoffs for α′ and α, respectively. Ni is shown to segregate to α in all alloys, which should increase diffusion of Cr to α′, and thus enhance the spinodal amplitude. However, as seen in Fig. 5b, the spinodal amplitude does not demonstrate a clear correlation with hardness.

This discrepancy can be partially explained by considering the influence of Mo. Table 2 shows that Mo partitions to α′ in all alloys. The relatively large size of Mo in α′ increases the lattice constant, and thus enhances the lattice mismatch; enhancing the lattice mismatch would be expected to lead to increased hardening.

The results in Fig. 6 can now be better understood by combining the effects of Cr, Ni, and Mo. Cr and Ni enhance spinodal decomposition which initiates hardening, while Mo segregates to α′ leading to an enhanced lattice mismatch, and thus greater hardening. Though, the difference in behavior observed in Fig. 6 when adding Mo to Cr and Ni does not significantly alter the relationship with hardening. This suggests another contribution from Cr, Ni, and possibly Mo outside of spinodal decomposition.

Though it is not within the scope of this paper, G-phase was found in four of the five alloys (2101, 2101-w, 2205, and 2209-w), and the largest volume fractions were found in the worst performing alloys. Additionally, Ni and Mo are both G-phase formers, so a hardening effect associated with G-phase would fit well with the relationship shown in Fig. 6 [6, 8]. Thus, the data in this study suggests that G-phase is contributing to the hardening/embrittlement of these alloys. As was mentioned earlier, only minor contributions from G-phase on mechanical properties have been found, however, it has been suggested that there is a volumetric threshold where influences become more significant [7, 8].

Conclusions

Five DSS alloys, consisting of both lean and standard grades, were studied following thermal aging. APT and mechanical testing were performed to observe the differences in phase transformation and mechanical degradation behavior in these alloys. Results demonstrated that all alloys experienced spinodal decomposition, and all alloys experienced both hardening and embrittlement. Combining the APT results with both the compositional information and mechanical testing yielded several significant insights.

- Spinodal amplitude correlates well with bulk Cr composition in similar alloys.
- Spinodal amplitude did not correlate well with hardening behavior.

- Nanoindentation and Charpy impact toughness results were not in complete agreement, however, nanoindentation did prove to be a reasonable approximation for the tested alloys while being able to eliminate effects of grain structure and ferrite/austenite phase fraction.
- Lean grade alloy 2003 demonstrated the best performance when considering both phase stability and impact toughness, while lean grade alloy 2101 experienced the least hardening.
- The combined Cr + Ni and Cr + Ni + Mo compositions provided the best correlation with the hardening behaviors. Cr and Ni were shown to enhance the spinodal amplitude and the segregation of Mo to α' increases the lattice mismatch. Additionally, the contribution of Ni and Mo to G-phase formation appears be influencing hardness.
- The data in this study suggests that G-phase is contributing to the hardening/embrittlement of these alloys.

Acknowledgements APT was conducted at Oak Ridge National Laboratory's Center for Nanophase Materials Sciences (CNMS), which is a U.S. DOE Office of Science User Facility.

References

1. R. Gunn, *Duplex Stainless Steels: Microstructure* (Elsevier, Properties and Applications, 1997)
2. H.D. Solomon, T.M. Devine, *Duplex Stainless Steels: A Tale of Two Phases*. American Society for Metals (1982)
3. J. Charles, Duplex stainless steels, a review after DSS'07 in Grado, presented at the Revue de Métallurgie, (2008)
4. J. Lai, S.H. Shek, K.H. Lo, *Stainless Steels : An Introduction and Their Recent Developments*. (Bentham Science Publishers, 2012)
5. F. Danoix, P. Auger, Atom probe studies of the Fe–Cr system and stainless steels aged at intermediate temperature: a review. Mater. Charact. **44**(1), 177–201 (2000)
6. M. Guttman, Intermediate temperature aging of duplex stainless steels. A Review, (1991)
7. S.L. Li et al., Annealing induced recovery of long-term thermal aging embrittlement in a duplex stainless steel. Mater. Sci. Eng. A, **564,** 85–91 (2013)
8. J. Bonnet, J. Bourgoin, J. Champredonde, D. Guttmann, M. Guttmann, Relationship between evolution of mechanical properties of various cast duplex stainless steels and metallugical and aging parameters: outline of current edf programmes. Mater. Sci. Technol., **6**, 221 (1990)
9. D.A. Garfinkel, J.D. Poplawsky, W. Guo, G.A. Young, J.D. Tucker, Phase separation in lean-grade duplex stainless steel 2101. JOM, **67**(10), 2216–2222 (2015)
10. J. Zhou, J. Odqvist, N. Thuvander, Peter Hedstom, Quantitative evaluation of spinodal decomposition in Fe-Cr by atom probe tomography and radial distribution function analysi. Microsc. Microanal. **19**(19), 665–675 (2013)
11. W. Guo, D.A. Garfinkel, J.D. Tucker, D. Haley, G.A. Young, and J.D., Poplawsky, An atom probe perspective on phase separation and precipitation in duplex stainless steels. J. Nanotechnol. (2016)
12. G.A. Young, J.D Tucker, N Lewis, E. Plesko, P. Sander, Assessment of lean grade duplex stainless steels for nuclear power applications. Proc. 15th International Conference Environment Degradation Materials Nuclear Power Systematics-Water React (2011)

Stress Corrosion Cracking of Alloy 800 in Secondary Side Crevice Environment

Maria-Lynn Komar and Guylaine Goszczynski

Abstract Alloy 800 nuclear grade (NG) is a material of choice for replacement steam generators (SG) due to its inherent resistance to primary water stress corrosion cracking (SCC). However, the long term performance of SGs depends on the performance of the material in upset conditions. Various degradation modes have been observed in Alloy 800NG under simulated secondary crevice environments (SCE) in C-ring and CERT experiments. Furthermore, the first incidences of SCE SCC have been observed in Alloy 800NG SG tubes in nuclear power plants and may be the sentinel events at the onset of more extensive cracking in the future. Understanding the parametric dependencies of SCC obtained under representative SCE and plausible transient conditions are keys to predicting future SG performance, validating mitigation strategies, and addressing life extension issues. The results of SCE crack growth rate (CGR) testing of Alloy 800NG in conditions representative of an acid-sulfate chemistry upset condition will be presented.

Keywords Alloy 800 · Stress corrosion cracking · Initiation · Growth rate · Acidic crevice environment

Introduction

Stress corrosion cracking is a known SG aging related degradation mechanism, and an area of continuing concern for the nuclear power industry [1–6], particularly as decisions regarding life extension are being made. Due to severe SCC susceptibility in primary water [7–10], steam generators made with nickel-based Alloy 600 have been replaced with alternate materials such as Alloy 690, a higher chromium nickel based alloy, or Alloy 800, an iron based alloy. As CANDU stations have favoured Alloy 800NG for SG replacement and refurbishment, a valid basis for long-term prediction of in-service performance of Alloy 800NG SG tubing material under

M.-L. Komar (✉) · G. Goszczynski
Kinectrics Inc., 800 Kipling Ave., Unit 2, Toronto, Ontario M8Z 5G5, Canada
e-mail: maria-lynn.komar@kinectrics.com

J.H. Jackson et al. (eds.), *Proceedings of the 18th International Conference on Environmental Degradation of Materials in Nuclear Power Systems – Water Reactors*, The Minerals, Metals & Materials Series, https://doi.org/10.1007/978-3-319-68454-3_86

plausible CANDU secondary side conditions is required. In general, Alloy 800NG has only been observed to crack under extreme conditions in the laboratory [11], although recent field experience has indicated that degradation can occur in crevices [11–13] particularly where the material is cold worked. Much work has been done to characterize degradation mechanisms in Alloy 800NG in various environments, including benign environments such as all-volatile treated (AVT) water [13, 14], primary water reactor environments [7, 9, 10] and simulated crevice environments [13, 15–19]. While acid-sulfate environments have been identified as particularly damaging [18, 19], the effect of temperature on degradation rates has not been determined. This paper presents results for constant stress intensity crack growth rate tests performed on Alloy 800NG in an acidic crevice environment outside the safe pH-ECP safe zone [15, 16] at 280, 300, and 320 °C.

Test Method

Materials

Alloy 800NG plate material with chemistry, microstructure, and mechanical properties representative of SG tubing were used in these tests. The Alloy 800NG material was fabricated to satisfy the chemistry specification for Alloy 800NG [20] and thermomechanically processed to produce a microstructure representative of SG tubing material [21].

Chemical composition of the Alloy 800 material is reported in Table 1. The material was cast, hot rolled between 1050 and 1200 °C, then solution annealed at 1065 °C for 10 min followed by forced-air cooling. The hot rolled bar was then cold-rolled 72% followed by recrystallization annealing at 975 °C for 15 min and water quenched. Mechanical properties, grain size and hardness for the Alloy 800NG material are reported in Table 2.

Environment

The tests were performed in an environment simulating a potential CANDU SG acidic crevice (AC) chemistry upset condition [15, 16, 22–24] outside the recommended pH-ECP zone. The particular crevice chemistry used was a precipitate free modification of the standard AC chemistry used extensively by COG and the CANDU industry. The composition and pH of the standard and modified AC

Table 1 Chemical composition (wt%) of Alloy 800NG material [21]

Material	Heat #	C	Ni	Cr	Fe	Cu	Ti	Al	Si
Alloy 800	M722675	0.02	34.1	21.9	41.9	0.42	0.58	0.014	0.23

Table 2 Mechanical properties of Alloy 800NG material [21]

Property	25 °C	360 °C
0.2% Yield strength, MPa	312–326	241–262
Ultimate tensile strength, MPa	579–586	500–514
Elongation, %	47–51	40–41
	Longitudinal	Transverse
Grain size, μm	13 ± 1	15 ± 2
Microhardness	153 ± 5	157 ± 3

chemistries are given in Table 3. The pH of the solution at test temperature was calculated [25] using the MULTEQ model. Testing was performed in a static autoclave under de-aerated conditions.

Crack Growth Rate Test Method

Constant stress intensity tests on pre-cracked compact tension (CT) samples under active loading and continuous monitoring of crack length using direct current potential drop (DCPD) [3, 13] are well established as most appropriate for CGR measurements to determine the activation energy of SCC propagation [7].

Compact tension specimens were made according to the geometry shown in Fig. 1. Pre-cracking was performed in air at 1 Hz with a starting load ratio ($R = K_{min}/K_{max}$) of 0.2, which was incrementally increased to 0.4 and 0.6 while keeping maximum stress intensity K_{max} constant at 30 MPa$\sqrt{m}$.

Two samples of Alloy 800NG were simultaneously transitioned then tested at constant stress intensity in a Cortest autoclave. Each sample was independently loaded, monitored, and controlled using custom software. Transitioning from fatigue cracking to SCC was performed in situ by reducing the frequency from 1 to 0.001 Hz, introducing a sequence of hold times at K_{max} while periodically

Table 3 Acidic crevice chemistry environment

Chemical	Modified	Standard COG/CANDU [21, 23]
	Molality	Molality
NaCl	0.55	0.3
KCl	0.05	0.05
$CaCl_2$	0.0015	0.15
$NaHSO_4.H_2O$	0.06	0.05
Na_2SO_4	–	0.15
pH@RT (meas)	1.63	1.74
pH@RT	1.63	1.91
pH@280 °C	2.47	2.60
pH@320 °C	2.57	2.69

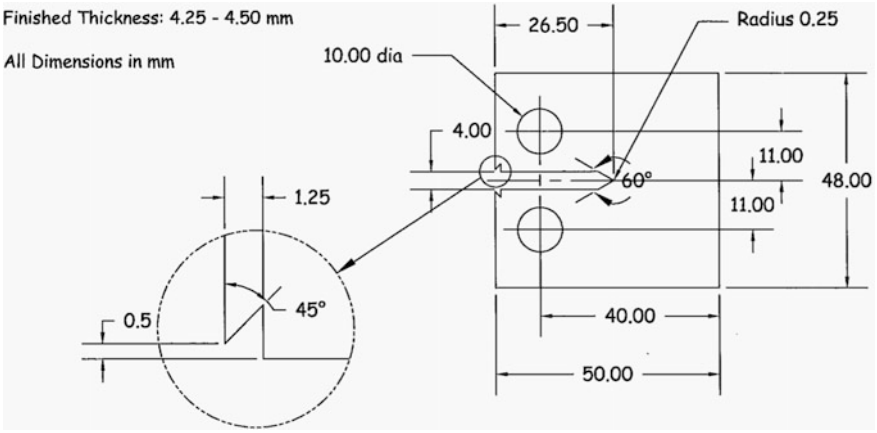

Fig. 1 Compact tension sample geometry

unloading to R = 0.6, and finally by switching to constant stress intensity. To ensure that CGR was not singificantly affected by variation in stress intensity (K) arising from differences between the crack length calculated from DCPD and the actual crack length, testing was performed at K = 30 MPa$\sqrt{m}$, which is in the expected plateau region of the da/dt versus K curve based on Alloy 600 PWSCC data [26]. During testing the crack length was continuously monitored using DCPD, and load was actively adjusted to ensure that K remained within the desired range, 25–35 MPa$\sqrt{m}$. Crack growth rate was measured at three temperatures, 320, 300 and 280 °C. Between each temperature the crack was advanced in a fatigue cycle, followed by repeating the transitioning steps prior to holding at constant stress intensity.

After testing, the samples were broken open and the instantaneous DCPD crack length data was adjusted to fit the crack length measured on the fracture surface. Crack growth rate was calculated from the slope of the corrected DCPD crack length plot during stable growth for the time at which the sample was held at constant stress intensity. Details of the parameters used in each stage, and the measured crack growth rates are reported in Table 4.

Results and Discussion

Fracture Surface Characterization

After completion of the test the samples were opened and the fracture surfaces examined by scanning electron microscope (SEM). Two features are notable on the fracture surface. Figure 2 shows that at 320 °C intergranular stress corrosion cracking (IGSCC) was continuous across the width of the samples while at 300 and

Table 4 Crack growth rate testing parameters and CGR results

						T3-CT5		T3-CT7	
Stage	Waveform	R	Freq. (Hz)	Hold/Fall/Rise (s)	Avg. Temp. (°C)	Avg. K_{max} (MPa$\sqrt{m}$)	CGR (mm/s)	Avg. K_{max} (MPa$\sqrt{m}$)	CGR (mm/s)
Sine 1	Sine	0.6	0.5		320.8	30.8	1.0×10^{-5}	30.6	1.1×10^{-5}
Trans 1	Trapezoid	0.6		100/400/500	320.9	32.3	-2.1×10^{-8}	31.9	-2.6×10^{-8}
Trans 2	Trapezoid	0.6		9800/100/900	319.1	31.9	-8.6×10^{-9}	31.5	-8.5×10^{-8}
Trans 3	Trapezoid	0.6		20600/100/900	318.8	31.9	3.7×10^{-9}	31.4	6.4×10^{-9}
Power outage	Hold unloaded				319.0	6.2		6.3	
PPU 1	Trapezoid	0.6			318.8	32.0		31.6	1.6×10^{-8}
SCC 1	**Const. K**				**318.8**	**31.2**	**4.9×10^{-8}**	**30.9**	**3.3×10^{-8}**
Decrease to 300 °C under constant load and acquire new reference									
Sine 2	Sine	0.6	0.5		300.9	31.1	3.0×10^{-6}	31.1	3.9×10^{-6}
Trans 4	Trapezoid	0.6		100/400/500	300.7	32.0	5.2×10^{-8}	31.8	2.4×10^{-7}
Trans 5	Trapezoid	0.6		9800/100/900	300.2	32.0	2.9×10^{-8}	31.8	3.4×10^{-8}
SCC2	**Const. K**				**300.1**	**31.8**	**1.8×10^{-8}**	**31.7**	**2.4×10^{-8}**
PPU2	Trapezoid	0.6		20600/100/500	Not performed				
Decrease to 280 °C under constant load and acquire new reference									
Sine 3	Sine	0.6	0.5		279.5	32.0	4.2×10^{-6}	31.7	4.0×10^{-6}
Trans 6	Trapezoid	0.6		100/400/500	279.6	32.9	6.5×10^{-8}	31.9	1.5×10^{-7}
Trans 7	Trapezoid	0.6		9800/100/900	279.3	32.8	2.1×10^{-8}	31.9	2.8×10^{-8}
SCC3	**Const. K**				**279.0**	**32.7**	**4.1×10^{-9}**	**31.8**	**7.5×10^{-9}**
PPU3	Trapezoid	0.6		20600/100/500	279.4	32.8	-1.5×10^{-9}	31.9	1.3×10^{-8}
Cool down to room temperature and acquire new reference									
Post test	Sine	0.4	1.0		19.5	24.1	7.1×10^{-6}	22.8	4.2×10^{-6}

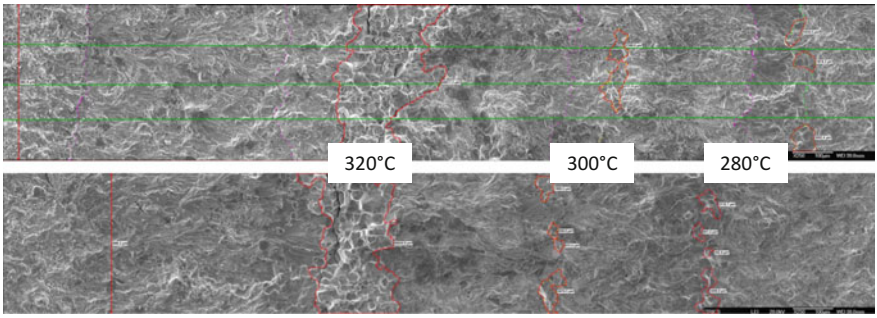

Fig. 2 Fracture surfaces, I800-T3-CT5 (top) and 1800-T3-CT7 (bottom) 250X

280 °C IGSCC was discontinuous. This indicates that while Alloy 800NG is much more resistant to IGSCC at 280 and 300 °C than at 320 °C in an aggressive acid-sulfate environment, it is not immune.

Furthermore, the fracture surfaces at 320 and 300 °C appear considerably different than the fracture surface at 280 °C as illustrated in Fig. 3. At both 320 and 300 °C the fracture surface is covered in a thick layer of fine platelets, while at 280 °C these platelets are absent and the oxide on the surface appears thin and smooth. It is not known if these differences are due to the differences in kinetics of oxidation due to the temperature, or due to the effects of hydrogen evolved from the corrosion process in the static autoclave. Further, more detailed characterization of the oxides on the fracture surface is required.

Temperature Dependence of Growth Rate

Figure 4 shows crack length versus time and K_{max} and temperature versus time plots and Fig. 5 shows the CGR versus inverse temperature plot for both samples tested. The CGR for Alloy 800NG in the acidic crevice environment follows an Arrhenius relationship.

All Ni base alloys appear to show a peak in crack growth rate close to the H_2 fugacity line associated with the Ni/NiO phase boundary [27–30]. The CGR response of each material at any ΔECP from the Ni/NiO transition is described by the height of the peak relative to the CGR at the tails which are hydrogen/ECP invariant, the half width of the peak, and the ECP offset of the peak from the Ni/NiO transition. These parameters are unique to each material, but invariant of temperature. Alloy 800, however, is not a Ni-based alloy, and is closer in composition to stainless steel, which has not demonstrated a CGR dependence on dissolved hydrogen [31].

The dependence of CGR on ΔECP (height, half-width, offset) is not known for Alloy 800NG, and in particular, for the crevice environment. Consequently, it is not known if the CGR in Alloy 800NG was affected by the dissolved hydrogen in the

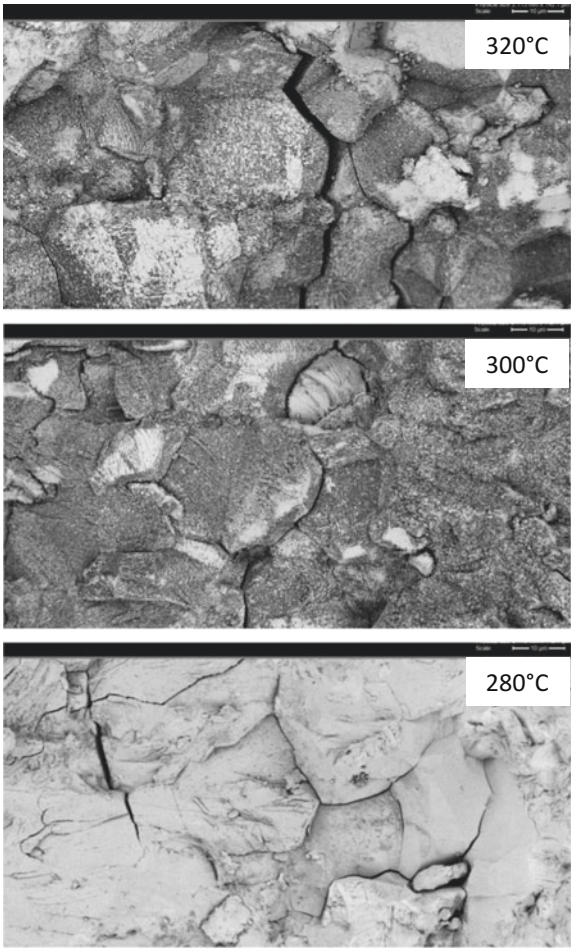

Fig. 3 I800-T3-CT5 constant K SCC fracture surface at 320, 300, 280 °C

crevice environment at the three temperatures tested. Changes in the fracture surface between 320 and 280 °C noted above suggest that temperature may not have been the only variable affecting CGR for Alloy 800NG in the crevice environment. Consequently, the Arrhenius plot of the data likely represents an apparent activation energy which reflects the interdependent effects of temperature, crevice chemistry, and dissolved hydrogen.

It is well known that the chemical environment in a SG varies significantly: steaming of hydrogen in the boiling region, release of hydrogen from decomposition of hydrazine, release of hydrogen from corrosion processes in crevices lead to locally different dissolved hydrogen concentrations [32]. Similarly, local variations in temperature and composition of the environment due to hideout and the formation of crevices may lead to different behaviour. Understanding the temperature dependent effects of hydrogen and changes in crevice chemistry on degradation

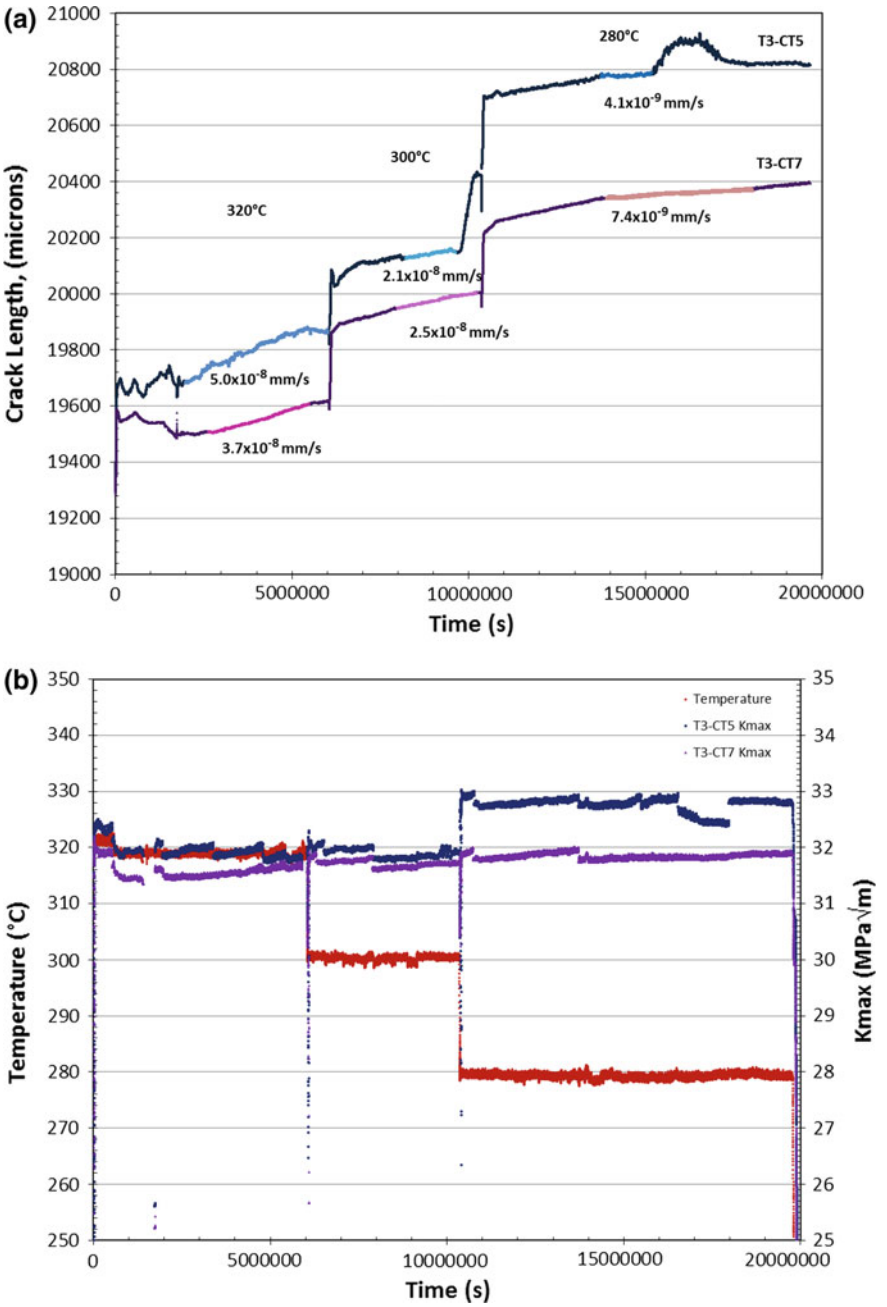

Fig. 4 Alloy 800 crack growth test in acidic crevice environment, **a** crack length versus time and **b** temperature and K_{max} versus time

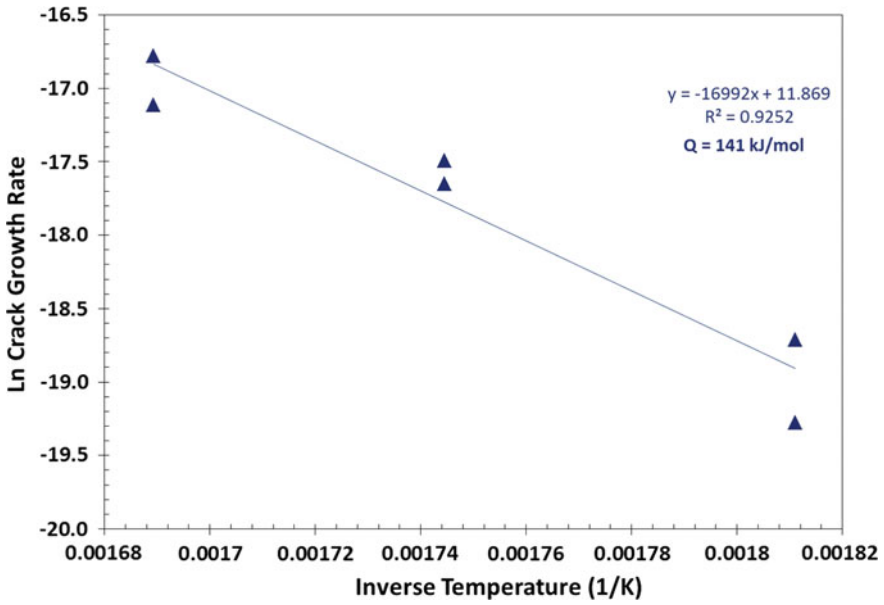

Fig. 5 Arrhenius plot of crack growth rate for Alloy 800 in acidic crevice environment

mechanisms in the secondary side of the SG are key factors in predicting the long term performance of steam generators.

Conclusions

Under constant stress intensity loading in an acidic environment outside the optimal pH-ECP zone, CGR in Alloy 800NG followed an Arrhenius relationship with temperature consistent with a thermally activated process.

The current measurements were conducted under constant environment, which is representative of the changes in a crevice when temperature changes. However, the effects on CGR of dissolved hydrogen released from corrosion processes, and changes in ECP at different temperatures in the crevice environment are not known. This means that the apparent activation energy may include the effects of temperature on crack growth, temperature dependence of dissolved hydrogen on ECP, and dependence of ECP on CGR.

A detailed, parametric understanding of the complex interaction between pH, hydrogen evolved from corrosion processes, electrochemical potential, temperature, dynamic strain, and surface and crack tip processes in the crevice environment is required to fully understand the factors that control SCC in SG alloys in crevice environments and to allow the true activation energy for SCC in Alloy 800NG to be measured.

Acknowledgements The authors gratefully acknowledge Peter Andresen of GE R&D for his expert advice on CGR testing, and Sandy MacKay of Ontario Power Generation for performing the MULTEQ calculations of the standard and modified crevice chemistry pH.

References

1. B. Alexandreanu, O.K. Chopra, and W.J. Shack, Crack Growth Rates and Metallographic Examinations of Alloy 600 and Alloy 82/182 from Field Components and Laboratory Materials Tested in PWR Environments, NUREG/CR-6964 ANL-07/12 Argonne National Laboratory, May 2008
2. Status Review of Initiation of Environmentally Assisted Cracking and Short Crack Growth EPRI, Palo Alto, CA: December 2005. 1011788
3. Y.Z. Wang, R.W. Revie, R.N. Parkins, Mechanistic Aspects of Stress Corrosion Crack Initiation and Early Propagation, CORROSION 99, NACE
4. E. Richey, D. Morton, M. Schurman, SCC Initiation Testing of Nickel-Based Alloys Using In-Situ Monitored Uniaxial Tensile Specimens, LM-05K043, May 17, 2005
5. Materials Reliability Program Crack Growth Rates for Evaluating Primary Water Stress Corrosion Cracking (PWSCC) of Alloy 82, 182, and 152 Welds (MRP-115), EPRI, Palo Alto, CA: 2004. 1006696
6. P. Andresen, *Stress Corrosion Cracking: Mechanisms and Current Status Theme Meeting on Mechanisms, Occurrences, and Mitigation of Corrosion Degradation in NPP* (Mumbai, India, 2011)
7. E. Serra, *Stress Corrosion Cracking of Alloy 600, EPRI NP-2114-SR* (Electric Power Research Institute, Palo Alto, CA, 1981)
8. R. Bandy, D. van Rooyen, Tests with Inconel 600 to Obtain Quantitative Stress-Corrosion Cracking Data for Evaluating Service Performance, BNL-NUREG-31814, (Upton, NY: Brookhaven National Laboratory, September 1982)
9. G. Was, K. Lian, The Role of Time-Dependent Deformation in Intergranular Crack Initiation of Alloy 600 Steam Generator Tubing Material NUREG/GR-0016, (Washington, DC: United States Nuclear Regulatory Commission, March 1998)
10. R.W. Staehle, Bases for Predicting the Earliest Penetrations Due to SCC for Alloy 600 on the Secondary Side of PWR Steam Generators, NUREG/CR-6737, (Washington, DC: United States Nuclear Regulatory Commission, September 2001)
11. Steam Generator Management Program: Alloy 800 Steam Generator Tubing Experience, (Palo Alto, CA: Electric Power Research Institute, 2012). 1024992
12. R. Kilian, R. Zimmer, R. Arenz, J. Beck, T. Schonherr, M. Widera, in *Operating Experience with Alloy 800 SG Tubing in Europe.* Proceedings 13th International Conference on Environmental Degradation in Nuclear Power Systems—Water Reactors, (Whistler, British Columbia, Canada: April 19–23, 2007)
13. D. Gómez-Briceño, M.S. García-Redondo, F. Hernández, in *Update of Alloy 800 Behaviour in Secondary Side of PWR Steam Generators.* Proceedings Fontevraud 7 Contribution of Materials Investigations to Improve the Safety and Performance of LWRs, (Avignon, Popes' Palace, France: September 26–30, 2010)
14. M. Wright, in *Establishing Threshold Conditions for Lead-Induced Cracking of Steam Generator Tube Alloys*. Proceedings Water Chemistry of Nuclear Reactor Systems, BNES, 1996
15. Y. Lu, in *Minimize Corrosion Degradation of Steam Generator Tube Materials—Updated ECP/pH Zone for Alloy 800 SG Tubing*. 5th CNS International Steam Generator Conference, (Toronto, Ontario, Canada: November 26–29, 2006)

16. Y. Lu, in *Define Optimum Conditions for Steam Generator tube Integrity and Extended Steam Generator Service Life*. 15th International Conference on Nuclear Engineering, ICONE 15–10854 (Nagoya, Japan: April 22–26, 2007)
17. E. Pierson, J. Stubbe, P. Someville, in *Resistance En Milieu Acide Des Materiaux Alternatifs Pour Tubes De GV (Alliages 690 Et 800)*, Fontevraud 3 International Symposium (Avignon, France: French Nuclear Energy Society, September 12–16, 1994) p. 556
18. D. Gómez-Briceño, M.S. García, F. Hernández, *Effect of Secondary Cycle Sulphuric Acidic Injection on Steam Generator Tubes*. Fontrevaud 3 International Symposium (Avignon, France: French Nuclear Energy Society, September 12–16, 1994) p. 565
19. J.M. Sarver, B.P. Migling, J.V. Monter, Constant Extension Rate (CERT) Testing of alloy 690 and 800 Nuclear Steam Generator Tubing. International Conference Fontevraud III, 1994
20. Tubetech NK38 TH 33111 02 Part 2 Technical Specification for DNGS Incoloy 800
21. M.L. Turi, G. Ogundele, G. Goszczynski, A.K. Jarvine, Stress Corrosion Cracking in Alloy 800 in Secondary Side Crevice Environment, in 16th International Symposium on Environmental Degradation of Materials in Nuclear Systems -Water Reactors, (The Minerals, Metal and Materials Society TMS, 2013), Doc Number: ED2013–3311
22. M. Mirzai, C. Marushka, S. Pagan, O. Lepik, G. Ogundele, M. Wright, G. Kharshafkjian, 1997 Stress Corrosion Cracking/Corrosion Fatigue/Fatigue in Alloy 600, in Proceedings Of 8th International Symposium on Environmental Degradation of Metals in Nuclear Power Systems—Water Reactors, vol 1. (La Grange Park, Illinois: American Nuclear Society Inc.) p. 11
23. M.D. Wright, M. Mirzai, in *Lead-Induced SCC Propagation Rates in Alloy 600*, ed. by F.P. Ford, S.M. Bruemmer, G.S. Was. 9th International Symposium on Environmental Degradation of Materials in Nuclear Power Systems—Water Reactors, (The Minerals, Metals and Materials Society, 1999) p. 657
24. Y. C. Lu, in *Effect of Lead Contamination on Steam Generator Tube Degradation,* ed by T.R. Allen, P.J. King, L. Nelson TMS. Proceedings of the 12th International Conference on Environmental Degradation of Materials in Nuclear Power System—Water Reactors (The Minerals, Metals & Materials Society, 2005)
25. S. MacKay, Ontario Power Generation, Private Communication, May 5, 2011
26. O.K. Chopra, W.K. Soppet, W.J. Shack, Effects of Alloy Chemistry, Cold Work, and Water Chemistry on Corrosion Fatigue and Stress Corrosion Cracking of Nickel Alloys and Welds, NUREG/CR-6721, ANL 01/07, Argonne National Lab, March 2001
27. Advanced Testing Techniques to Measure the PWSCC Resistance of Alloy 690 and its Weld Metals, EPRI, Palo Alto, CA, and U.S. Department of Energy, Washington, DC: 2004. 1011202
28. Materials Reliability Program, *Mitigation of PWSCC in Nickel-Base Alloys by Optimizing Hydrogen in the Primary Water (MRP-213)* (EPRI, Palo Alto, CA, 2007), p. 1015288
29. P.L. Andresen, F.P. Ford, K. Gott, R.L. Jones, P.M. Scott, T. Shoji, R.W. Staehle, R.L. *Tapping, Expert Panel Report on Proactive Materials Degradation Assessment*, BNL-NUREG-77111–2006, US NRC, February 2007
30. D.S. Morton, S.A. Attanasio, G.A. Young, in *Primary Water SCC Understanding and Characterization Through Fundamental Testing in the Vicinity of the Nickel/Nickel Oxide Phase Transition*, Proceedings 10th International Conference on Environmental Degradation of Materials in Nuclear Power Systems—Water Reactors, NACE, 2001
31. D. Morton, G. Newsome, E. West, C. Ehlert, in *SCC Growth Rate Testing of Cold Worked Stainless Steel in Hydrogen Deaerated Water*, 17th International Conference on Environmental Degradation of Materials in Nuclear Power Systems—Water Reactors August 9–12, 2015, Ottawa, Ontario, Canada
32. R.W. Staehle, J.A. Gorman, Quantitative assessment of submodes of stress corrosion cracking on the secondary side of steam generator tubing in pressurized water reactors: Part 1, critical review of corrosion science and engineering. Corrosion **59**(11), 931 (2003)

Using Modern Microscopy to "Fingerprint" Secondary Side SCC in Ni–Fe Alloys

S.Y. Persaud, J.M. Smith, C.D. Judge, M. Bryk, R.C. Newman, M.G. Burke, I. de Curieres, B.M. Capell and M.D. Wright

Abstract Aggressive aqueous environments (Pb, S, pH extremes) used in laboratory tests have been shown to induce stress corrosion cracking (SCC) in Ni–Fe–Cr alloys. These conditions are used to simulate the extremes of secondary side crevice environments that are unlikely to occur under normal operating conditions but laboratory testing can still be used to establish sensitivities to abnormal chemistry conditions. Advances in modern microscopy have enabled the characterization of these secondary-side SCC systems at near-atomic resolution, helping to reveal mechanistic characteristics unique to each SCC mode. International progress investigating secondary-side SCC phenomena using analytical transmission electron microscopy (TEM) is reviewed in this paper. The unique chemistry and degradation associated with different modes of SCC are identified and compared among Ni–Fe–Cr steam generator tube alloys of interest (Alloy 690 and Alloy 800). It is revealed that each SCC mode exhibits distinctive characteristics, or a "fingerprint", which can be used to identify the aggressive environment responsible for inducing SCC.

Keywords Stress corrosion cracking · Transmission electron microscopy · Nickel alloys · Secondary side · PbSCC · Sulfur-assisted cracking

S.Y. Persaud (✉) · J.M. Smith · C.D. Judge · M.D. Wright
Canadian Nuclear Laboratories, 286 Plant Road, Chalk River, ON K0J 1J0, Canada
e-mail: suraj.persaud@cnl.ca

M. Bryk · R.C. Newman
Department of Chemical Engineering and Applied Chemistry, University of Toronto, Toronto, ON M5S 3E5, Canada

M.G. Burke
Materials Performance Centre, University of Manchester, Manchester M13 9PL, UK

I. de Curieres
IRSN, Institut de Radioprotection et de Sûreté Nucléaire, Fontenay-aux-Roses, France

B.M. Capell
Electric Power Research Institute (EPRI), 1300 West WT Harris Blvd, Charlotte, NC 28262, USA

J.H. Jackson et al. (eds.), *Proceedings of the 18th International Conference on Environmental Degradation of Materials in Nuclear Power Systems – Water Reactors*, The Minerals, Metals & Materials Series, https://doi.org/10.1007/978-3-319-68454-3_87

Introduction

Ni–Fe–Cr alloys are used for steam generator (SG) tubing in nuclear power plants due to their demonstrated high resistance to general and localized corrosion. Alloy 600 (Ni-16Cr-9Fe) was historically the material chosen due to its high resistance to chloride-induced stress corrosion cracking (SCC) and is still used in some plants. However, the alloy was found to be susceptible to SCC in both the relatively pure, reducing water on the primary side and the impurity-containing water in the secondary side crevices of SGs; thermally treated (TT) Alloy 600 has demonstrated better resistance to SCC in these environments, due to precipitation of intergranular Cr carbides, but is still considered susceptible. In current and future plants, Alloy 800 (Fe-21Cr-33Ni) or Alloy 690 (Ni-30Cr-10Fe) are generally regarded as the alloys of choice for SG tubes in CANDU and pressurized water reactors (PWRs), respectively; in terms of environmental degradation, the performance of the alloys has been exemplary after decades of in-service exposure to high temperature aqueous environments [1–3].

Secondary side water is maintained at temperatures ranging from 250 to 280 °C and contains ppt levels of impurities, such as S, Pb, and Cl [4–6]. Although impurity concentrations in bulk SG secondary side water are very low, accumulation to higher concentrations can occur at heat-transfer crevices associated with tube supports, sludge and the top of the tubesheet. Local SG crevice chemistry is complex, and can have a pH ranging from acidic to alkaline. SCC of the SG tubing materials Alloy 800 and Alloy 690 has been demonstrated in laboratory studies in harsh environments containing Pb [6–22] and/or S [6, 23–31] in very alkaline or acidic conditions. Many of these experiments are intended to simulate the extremes of secondary side crevice environments to purposely induce cracking and are unlikely under normal operating conditions of secondary side water nowadays.

In simulated secondary side crevice environments, a number of unique SCC mechanisms are plausible depending on material composition and exposure conditions, pH extremes, and/or presence of Pb and S. The different combinations of environment and materials have resulted in a large literature-base associated with SCC of Alloy 690 and Alloy 800 in secondary side water conditions and proposals for a number of cracking mechanisms [6–21, 23–31]; secondary side SCC of historically used Alloy 600 is actually the benchmark material for these types of studies. However, in the present study, discussion is confined to current and future SG tubing alloys of interest to limit scope. Secondary side SCC studies have generally focused on a particular SG tubing material in a high temperature aqueous environment containing one known aggressor: Pb, S, or extreme pH. The scientific complexity will increase as SCC studies progress towards environments with a mixture of impurities (i.e. Pb and S). Therefore, there is a need to develop a database of "fingerprints" for secondary side SCC which outline the expected crack tip chemistry and SCC mechanism associated with different, known SCC systems (e.g. Alloy 800 in acid sulfate, Alloy 690 in Pb-caustic, etc.). Analytical transmission electron microscopy (ATEM) provides the requisite spatial resolution and

elemental sensitivity to characterize (or "fingerprint") crack tips to allow for differentiation between secondary side SCC mechanisms and chemistries.

Over the past 15 years, advances in electron microscopy have resulted in nano-scale crack tip analysis becoming almost routine [18, 25, 29, 32–39]. Several studies have illustrated that studying crack tip chemistry using ATEM can provide insight into mechanisms of cracking, such as He bubble embrittlement of Alloy X-750 [40] and primary water SCC (PWSCC) of stainless steels [32, 33, 39, 41, 42] and Ni alloys [36, 43–49]. This paper reviews the application of high resolution techniques to the study of Alloy 690 and Alloy 800 secondary side SCC. In addition, the unique crack tip chemistries and SCC mechanisms for different secondary side SCC systems are compared.

Development of Methodology

Although the spatial resolution and elemental sensitivity benefits for studying SCC and other localized corrosion phenomena using ATEM were recognized several decades ago [47, 50], studies were limited by difficulties associated with TEM sample preparation of site-specific specimens. Since the mid-1990s, technological advances have gradually resulted in TEM sample preparation improvements. Development for preparation of site-specific TEM lamellae progressed from mechanical polishing and ion-beam thinning [41, 47, 48], to the use of a single-beam focused-ion beam (FIB) [32, 39, 41], to eventual use of a dual-beam FIB and, more recently, a plasma FIB. The latter two instruments generally produced fewer artefacts, improved efficiency, and reduced risk of sample loss during preparation. As a result, the use of ATEM to study environmentally-assisted cracking (EAC) of nuclear-relevant materials has increased dramatically over the past two decades, and sample preparation is now regarded as reliable and nearly routine.

Locating appropriate cracks for extraction and analysis can prove challenging. Generally, conventional FIB lift-out from the surface is not applicable because crack tips are located well into the material (hundreds of microns). Instead, samples are cut to reveal the cross-section of the crack so a tip can be easily located. Following this, in-plane FIB extraction is applied to capture a region parallel to the top-surface containing a crack tip and area ahead. Several procedures for in-plane crack tip extraction have been published [29, 32, 35]. Figure 1 describes the procedure for in-plane crack tip extraction, specific to secondary side acid sulfate cracking of Alloy 800, by Persaud et al. [29].

In spite of the improvements in reliability and efficiency of crack tip extraction and TEM sample preparation, there are still some inevitable drawbacks:

- The local chemistry of the crack tip may change during cool down and/or after removal from the isolated high temperature aqueous environment. Also, crack tip chemistry could be affected by sample preparation or after exposure to air during TEM sample transfer (i.e. oxidation of reduced sulfur species).

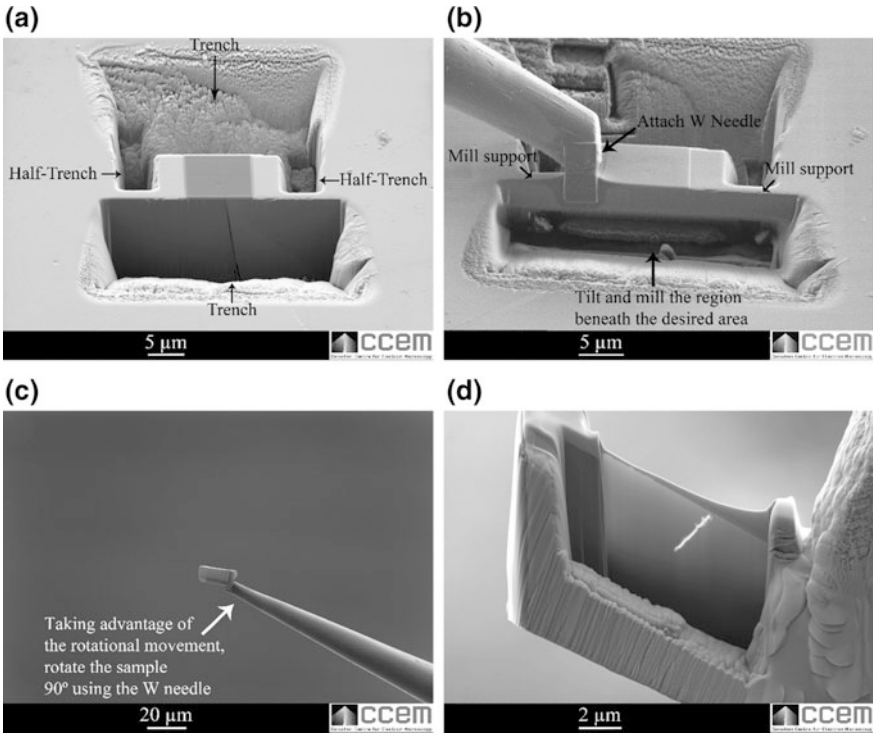

Fig. 1 Secondary electron (SE) images showing the FIB extraction procedure for a site-specific TEM sample containing a crack tip from an Alloy 800 C-ring sample exposed to 0.55M $NaHSO_4$ solution for 60 h at 315 °C from Persaud et al. [29]

- The depth of crack penetration could vary within the thickness of the section extracted, resulting in the crack spanning the entire length of the TEM sample (i.e. no crack tip) or no crack being present after thinning.
- It is difficult to determine whether a chosen crack tip has blunted or is still susceptible to propagation. Smith et al. recently made progress on this issue by applying ATEM to study Alloy 800 acid sulfate SCC in a sample with controlled and monitored crack growth [31]; direct current potential drop (DCPD) was used to ensure that the crack tip extracted had not blunted and was still susceptible to propagation.
- To date, ATEM examinations of crack tips identify local chemistry associated specifically with crack propagation, and not initiation. The overall mechanism of crack initiation could be dependent on chemical changes and/or defects present near the sample surface, missed by ATEM examination of crack tips well away from the material surface.

Given the variability possible in studying crack tips, the best approach is statistical, i.e. to study several crack tips using ATEM and report on consistent features.

High resolution imaging and chemical analysis using energy dispersive x-ray spectroscopy (EDX) and electron energy loss spectroscopy (EELS) have been used extensively to characterize cracks in ATEM. Relatively recent EDX advancements, such as the implementation of Si Drift Detectors (SDDs) and new multi-SDD configurations for significantly improved solid angles for X-ray detection, as well as improvements in hardware leading to improved signal-to-noise ratios for X-ray collection, have increased EDX elemental sensitivity to nm-scale spatial resolution. The technique is excellent as a pure chemical identification tool, now applicable to minor impurities, such as Pb and S, localized to nano-scale regions at very low concentrations (<4 at.%). For local bonding information and detection of lighter elements (up to the first row of transition metals) EELS is generally regarded as superior to EDX, whereas EDX is superior to EELS with respect to spectrum quantification. Recent advances in EELS technology allows for characterization of micro-scale areas using step sizes of <1 nm. Specific to secondary side SCC of Ni alloys, local chemistry changes in oxides, bonding of impurities at interfaces, and/or identifying local enrichments/depletions are particularly useful in EELS, although it must be recognized that such detailed analysis requires ultra-thin TEM specimens (<50 nm).

In recent years, evidence for SCC mechanisms associated with cracking in Ni alloys exposed to nuclear-relevant environments has been ascertained by applying the FIB and ATEM methodology outlined in this section. Some examples include: selective intergranular oxidation as the mechanism of PWSCC in Alloy 600 [36, 39, 43–47, 49], intergranular oxidation of stainless steels [32, 33, 39, 41], and He bubble formation and embrittlement of Alloy X-750 [40]. With regards to secondary side SCC of Alloy 600, Bruemmer et al. first used ATEM to show that up to 8 wt% Pb was present at oxide-metal interfaces at crack tips [37, 38]. They speculated that Pb likely accelerated the SCC of Alloy 600 and essentially provided the first "fingerprint" for a secondary side SCC system, Pb-assisted cracking of Alloy 600 in near neutral water. The FIB and ATEM methodologies described in this section are now being applied to study the complex chemistry associated with secondary side SCC of Alloy 690 and Alloy 800 SG tubing; the accumulated literature will be reviewed in the forthcoming sections, culminating in comparisons of the local chemistry changes unique to each secondary side SCC system.

Caustic Cracking

SCC in high temperature pure caustic ($pH_{300\ °C} > 10$) solutions is a well-known degradation mode for Alloy 690 and Alloy 800 SG tubing [5, 51–66]. However, the relevance of caustic SCC has diminished since the transition from phosphate-based to all volatile treatment (AVT) SG secondary side water chemistry

in the 1970s [4, 5], which has precluded the requisite high pH values required for caustic SCC. Regardless, several fundamental studies investigating caustic SCC of SG tubing alloys have been done, some involving the use of high resolution electron microscopy to characterize crack tips and surface oxides/films [59, 62, 65]; these studies allow for development of a general "fingerprint" for caustic cracking in SG tubing alloys.

Alloy 800

Classical caustic cracking of Alloy 800 in high temperature water ($pH_{300\ °C} > 10$) was studied by Newman et al. [59, 65, 66]. The cracking mode is generally transgranular under aggressive loading; however, in practice (or in slower laboratory testing) SCC is intergranular. In $pH_{300\ °C} > 10$ solutions, dissolved Cr and Fe species are thermodynamically favourable. As a result, de-alloying (selective dissolution) of Cr and Fe is prevalent, resulting in a remnant Ni-rich nanoporous surface film. The scanning electron microscope (SEM) image in Fig. 2a highlights the nanoporous Ni-rich film formed on the surface of an Alloy 800 sample after exposure to 50% caustic solution at 280 °C from Bryk et al. [65]; the nanoporous ligament structure is evident in Fig. 2b. De-alloying can extend preferentially along defects or grain boundaries located beneath the nanoporous surface film. Newman et al. have stated that the presence of a brittle, nanoporous Ni-rich surface film results in a film-induced cleavage SCC mechanism [67, 68] for classical caustic cracking in Alloy 800 [59, 65, 66].

Bryk et al. performed further ATEM examinations on caustic SCC tips extracted from Alloy 800 C-ring specimens exposed to 280 °C 50% caustic solution [65]; Fig. 3 shows a typical transgranular crack, but the visible porosity forms after the crack has passed. Porosity is evident spanning the entire length of the crack. EELS

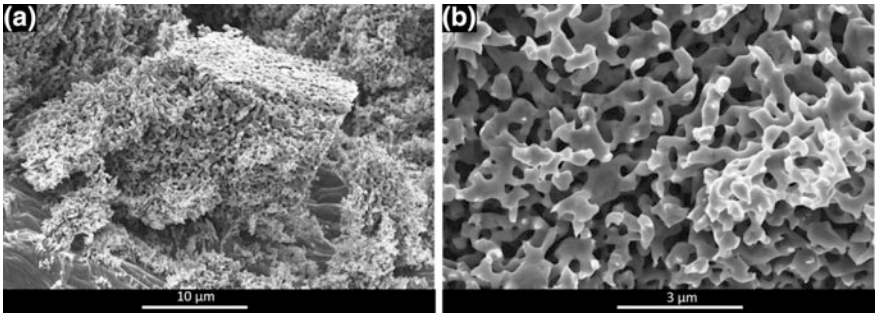

Fig. 2 SE images at low (**a**) and high (**b**) magnification of the coarse nanoporous Ni-rich layer present on Alloy 800 after exposure to 50% caustic solution at 280 °C from Bryk et al. [65]. This layer is not believed to be present at the crack tip, but is formed after Cr and Fe are completely dissolved, allowing for coarsening by surface diffusion

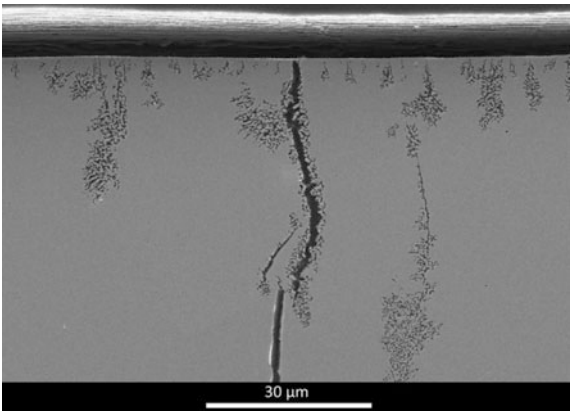

Fig. 3 SE image of the cross-section of an Alloy 800 C-ring after exposure to 50% NaOH solution at 280 °C for 6 h from Bryk et al. [65]. A lacey structure is observed throughout the cross-section and along the crack walls. It is believed that very fine porosity likely forms initially at the crack tip and the observed lacey structure is produced after Cr and Fe are completely dissolved, allowing for coarsening by surface diffusion and formation of gross porous Ni

elemental maps for a caustic SCC tip in Alloy 800 from Bryk et al. are provided in Fig. 4 [65]. Ni enrichment is revealed at regular intervals along crack walls, suggesting a nanoporous Ni-rich layer was originally present prior to fracture; Bryk et al. suggest that subsequent fracture of the brittle de-alloyed layer would have led to micro-cleavage into the underlying and uncompromised metal substrate [65], in line with a film-induced cleavage mechanism [67, 68]. The lack of Cr and Fe in the crack and on the fracture surface confirms that the elements are selectively dissolved, even in cracks located several hundred microns from the alloy surface. Using the ATEM analysis a "fingerprint" can be developed to identify Alloy 800 SCC in high temperature pure caustic environments ($pH_{300\ °C} > 10$), if such an environment were to be present:

- The cracking mode is generally transgranular and Ni-enrichment is present along the crack walls due to de-alloying.
- Oxide(s) are not present in the crack tips (due to the solubility of Fe and Cr) at the temperature of exposure but may form during cooldown.
- Porosity is observed on the surface of Alloy 800 and extends downwards from the alloy surface, likely along favourable defect paths and grain boundaries.
- Very fine porosity likely forms initially, with significant retention of Cr and Fe. Eventually, Cr and Fe are completely dissolved, which allows for coarsening by surface diffusion and formation of the gross porous Ni layer.
- Sharp micro-cleavage 'jumps' are likely to be visible in some cracks, in line with a film-induced cleavage mechanism [67, 68].

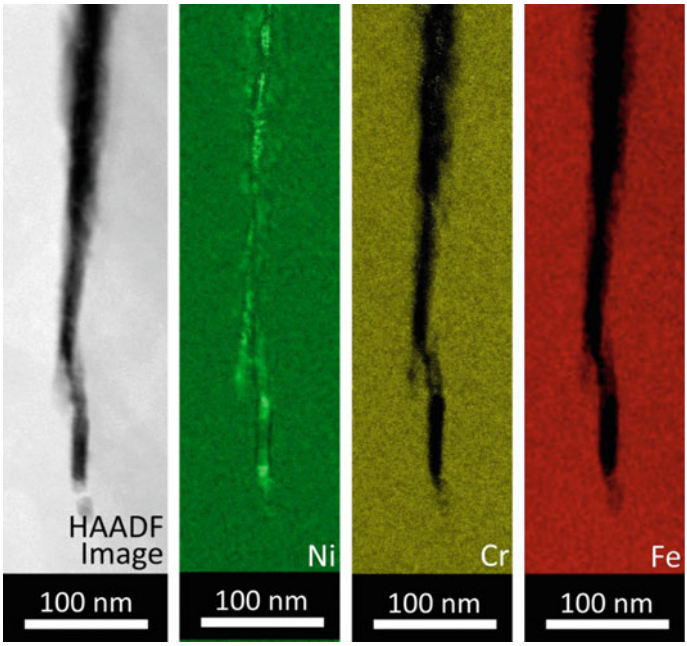

Fig. 4 High Angle Annular Dark Field-Scanning Transmission Electron Microscopy (HAADF-STEM) image and corresponding EELS elemental maps for a caustic crack in an Alloy 800 C-ring after exposure to 50% NaOH solution at 280 °C for 6 h from Bryk et al. [65]. Discontinuous Ni enrichment is observed along the crack. Also, Fe and Cr are selectively dissolved resulting in oxides not being present in the open crack

Alloy 690TT

Unlike Alloy 800, ATEM characterization of pure caustic ($pH_{300\ °C} > 10$) SCC in Alloy 690 has not yet been performed. However, Alloy 690 is well-known to be susceptible to caustic SCC [4–6, 53, 56, 62, 64] with the cracking mode reported to be transgranular, intergranular, or a mixture, depending on the alloy microstructure. Jiang et al. [62] recently characterized the surface chemistry of thermally-treated (TT) Alloy 690 after exposure to a 264 °C 50% NaOH solution. Thermal treatment of Alloy 690 is often performed to produce intergranular Cr carbide precipitates, which are thought to increase degradation resistance of the alloy. Jiang et al. reported a porous metallic Ni layer at the oxide-metal interface of Alloy 690TT after exposure to caustic solution, with the surface oxide being $Ni(OH)_2$ [62]. The porous metallic Ni layer is suggested to be a result of the thermodynamic conditions being favourable to Cr and Fe dissolution in pure caustic solutions, similar to conclusions from Newman et al. in Alloy 800 [59, 65, 66] and the original work of Deakin et al. on 316 stainless steel [58]. As a result, the reactive elements are selectively dissolved (de-alloying), leaving behind a porous, metallic Ni film on Alloy 690TT. It is not self-evident that de-alloying of Alloy 690TT should occur

given the low concentrations of Cr and Fe compared with the usual parting limit. However, given the similarities in surface chemistry, the "fingerprint" associated with classical caustic cracking of Alloy 690 may be similar to Alloy 800 caustic SCC. Further work should be performed to evaluate the local chemistry and morphology of pure caustic cracking in Alloy 690, especially given the difference in alloy composition (increased Cr content), the possible effect of intergranular Cr carbide precipitation, and the relation to the parting limit for dealloying.

Lead-Caustic Cracking

The addition of Pb to high temperature caustic solutions has been shown to increase the crack growth rate in Ni–Fe–Cr alloys dramatically [9–12, 15, 18–20, 22, 37, 38, 69, 70]; as mentioned, the discussed Pb-caustic environments are not representative of normal bulk water operating conditions. These laboratory test environments aim to simulate the extreme end of plausible secondary side crevice environments. The role of Pb in SCC is still open to speculation, but there is general agreement that the element impairs the ability of Ni–Fe–Cr alloys to re-form a passive Cr-rich oxide film after initial oxide rupture, either through incorporation in the oxide(s) or electrodeposition on the bare metal surface [12, 13, 15, 18–20, 37, 38]; This effect may be considered analogous to the known effect of low melting pointing elements on the activation of aluminum corrosion [71, 72] (i.e. the suspected aggressive element diffuses around on the alloy surface and disturbs the formation of the oxide network). Significant work has been performed investigating the SCC of Alloy 690 and Alloy 800 in Pb-caustic solutions ($pH_{300\ °C}$ 8–9.5) [12, 15, 18–20]. Pure caustic SCC of Alloy 690 is known to persist to $pH_{300\ °C}$ values as low as 8, but the addition of Pb significantly increases the crack growth rate [18]. In Alloy 800, the addition of Pb has recently been demonstrated to extend the SCC $pH_{300°C}$ threshold to 8.5 [12, 15, 19]. The Pb-SCC alkaline pH domain for Alloy 690 and Alloy 800 suggests that a continuum exists between pure caustic cracking ($pH_{300\ °C} > 10$) and Pb-caustic cracking; therefore, the "fingerprint" for the latter cracking mode may exhibit similarities with the former, but subtle changes in local crack tip chemistry are likely to account for Pb interference on oxide formation.

Alloy 800

Capell et al. [12] induced Pb-caustic SCC in Alloy 800 reverse U-bend (RUB) samples over the $pH_{330\ °C}$ range of 8.5–9.5. Exposures were carried out at 330 °C in a solution comprised of 3 mol/kg NaCl, NaOH for pH control, 6 ppm H_2, and 500 ppm of Pb added as PbO. Initiation and initial crack penetration was generally transgranular with eventual transition to intergranular cracking as cracks grew to greater than 50 μm in length. Immediate and rapid cracking was observed

at $pH_{330\ °C}$ 9.5, whereas an incubation period of several hundred hours occurred before similar rapid cracking at $pH_{330\ °C}$ 8.5 [12]. Further ATEM characterization of crack tips and surfaces in the Alloy 800 RUB samples of Capell et al. [12] was performed by Persaud et al. [22] to determine the mechanism of SCC, the role of Pb, and identify possible precursors to SCC. Intergranular SCC ATEM results from Alloy 800 RUBs exposed to $pH_{330\ °C}$ 9.5 will be highlighted in the present review; Fig. 5 is a FIB-SEM image of a TEM lamella containing an intergranular Pb-caustic crack [22]. The FIB-produced TEM sample contained a crack tip, a triple point, and a relatively large portion of a mature Pb-caustic intergranular crack. Transgranular SCC branching is visible in the upper portion of the TEM sample in Fig. 5.

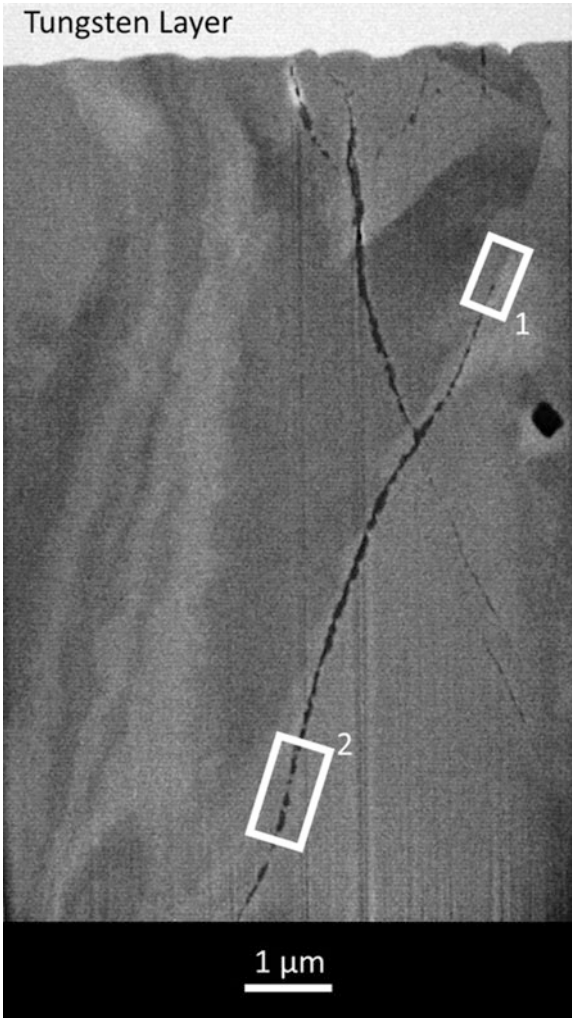

Fig. 5 FIB SE image of a TEM sample containing an intergranular crack from an Alloy 800 RUB after exposure to 330 °C caustic solution ($pH_{330\ °C}$ 9.5) with 6 ppm H_2 and 500 ppm of Pb added as PbO [22]. The regions "1" and "2" were subsequently analysed in detail (Fig. 6)

Figure 6 shows EELS and EDX elemental maps extracted from spectrum image datasets for the Alloy 800 intergranular crack tip, region 1 in Fig. 5 [22]. Discontinuous Ni enrichment (up to 70 wt%) is observed along the crack wall. EELS results indicate that a Cr-rich oxide is formed at the base of the crack tip with a mixed Fe and Cr oxide formed in more well-developed areas. Also, a gradient in Ni and Fe content is observed ahead of the crack tip (extending 300 nm ahead—not shown). EDX provides complementary elemental analysis revealing that Pb is present at the oxide-metal interface and does not overlap with oxygen. In the exposure conditions soluble Fe and Cr_2O_3 are energetically favourable species for Fe and Cr, respectively. Pb likely impairs the passivity of Cr_2O_3 by depositing on the bare metal surface after initial oxide rupture. In this way, Pb deposition likely retards the re-passivation kinetics of Cr_2O_3. In the absence of a passive oxide, soluble Fe can be selectively removed from ahead of the crack tip. The resulting de-alloyed area is likely susceptible to fracture under stress. Based on the described

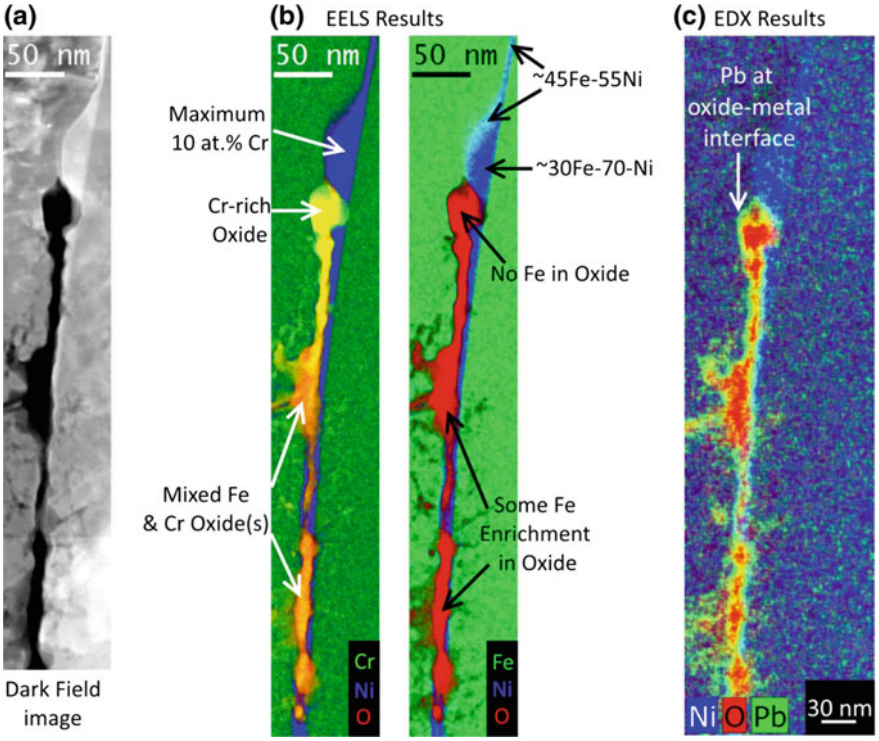

Fig. 6 **a** HAADF-STEM image, **b** EELS and **c** EDX combined elemental maps for the intergranular Pb-caustic ($pH_{330\ °C}$ 9.5) crack tip in the Alloy 800 RUB, region 1 in Fig. 5 [22]. A concentration gradient in Ni and Fe content is observed in EELS elemental maps just ahead of the crack tip, likely a result of selective dissolution of Fe (de-alloying). EDX results reveal that Pb is segregated to the Cr-rich oxide-metal interface

SCC process, Persaud et al. [22] propose a hybrid film-rupture/de-alloying SCC mechanism for Pb-caustic SCC ($pH_{330\ °C}$ 8.5–9.5) of Alloy 800.

Figure 7 shows additional EELS and EDX elemental maps for the more mature Alloy 800 Pb-caustic intergranular crack, region 2 in Fig. 5 [22]. Discontinuous metallic Ni regions (>90 at.% Ni) are located along the crack, located approximately 300 nm apart; these regions indicate the individual steps in the film-rupture/de-alloying SCC mechanism [22]. EELS results reveal that the oxide nearest the metal is Cr_2O_3 while a predominantly Fe-rich oxide is present towards the centre of the crack, likely re-deposited during cool down. EDX confirms that Pb is preferentially segregated to oxide-metal interfaces and metallic Ni regions. The elemental maps in Figs. 6 and 7 highlight the complementary nature of EELS and EDX. The accumulated ATEM results allow for development of an Alloy 800 Pb-caustic SCC "fingerprint" based on crack tip chemistry and morphology that may be relevant if such an environment were to be present:

- Discontinuous regions of metallic Ni are present along cracks.
- A Cr-rich oxide is formed nearest the metal matrix with a re-deposited Fe-rich oxide towards the centre of cracks.

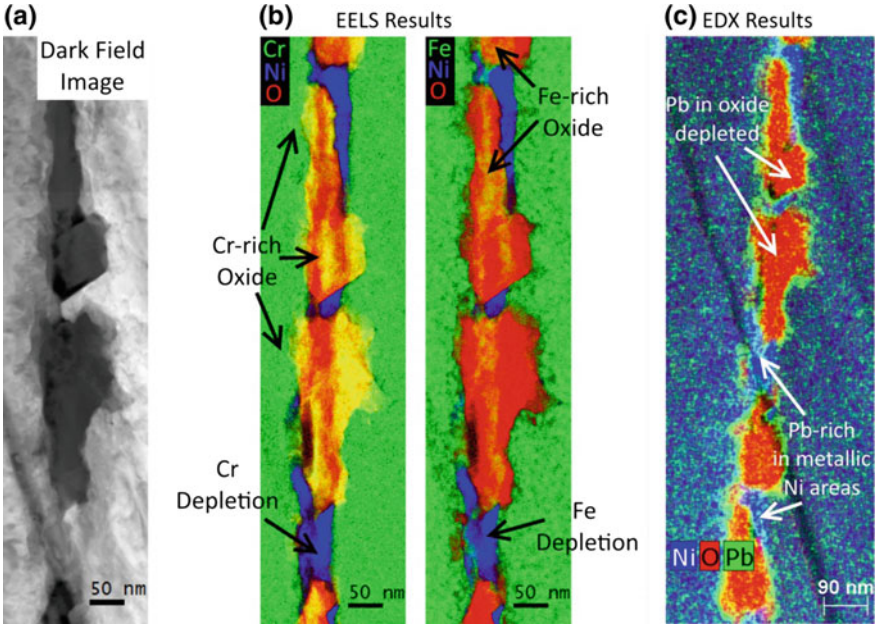

Fig. 7 **a** HAADF-STEM image, **b** EELS and **c** EDX combined elemental maps for the mature intergranular Pb-caustic ($pH_{330\ °C}$ 9.5) crack in Alloy 800, region 2 in Fig. 5 [22]. EELS analysis reveals that metallic Ni is present along the crack at equidistant intervals [22], suggesting a cyclic SCC mechanism. EDX results show that Pb is segregated to the Cr-rich oxide-metal interface and may deposit preferentially on Ni-rich regions

- Pb is present at oxide-metal interfaces and may preferentially deposit on Ni-rich areas of cracks.
- Cracks are generally relatively fine with evidence of grain boundary migration just ahead of crack tips.
- Distinct, nearly equidistant steps may be visible along the crack, differentiated by the location of metallic Ni regions.

Alloy 690TT

ATEM characterization of Pb-caustic SCC of Alloy 690TT has been performed by Burke et al. [18]. They exposed Alloy 690TT C-rings and RUBs to 10% NaOH solution with 10 g/L PbO added in a static autoclave at 307 °C. The solution used by Burke et al. [18] did not contain added hydrogen so conditions were more oxidizing than Alloy 800 RUB exposures of Capell et al. [12], discussed previously in Section "Alloy 800". As a result, the electrochemical potential may be near the Ni/NiO equilibrium electrode potential or in the NiO regime. Burke et al. reported predominantly transgranular cracking in stressed Alloy 690TT samples due to the presence of intergranular Cr carbide precipitates; in the absence of carbides, the cracking mode for Alloy 600 and Alloy 690 in caustic environments has been reported to be primarily intergranular [5, 6]. The presence of intergranular Cr carbides likely results in the corrosion process associated with SCC becoming more favourable within grains rather than along grain boundaries. Figure 8 shows bright-field (a) and dark-field (b) TEM images for a FIB-prepared sample containing a transgranular Pb-caustic crack from an Alloy 690TT RUB sample from

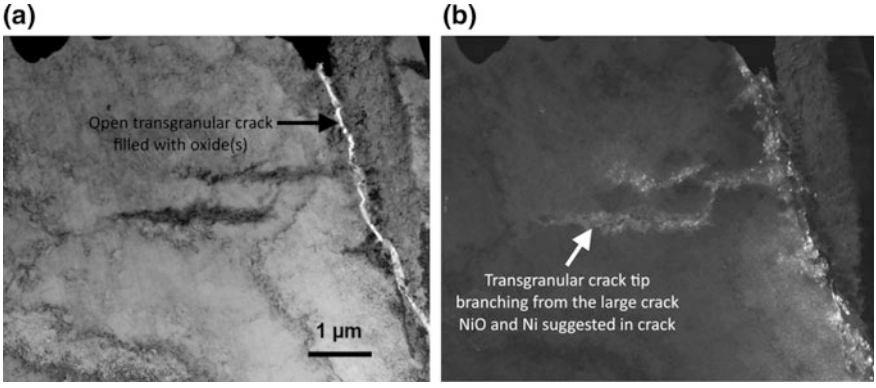

Fig. 8 Bright-field (**a**) and dark-field (**b**) TEM images for a transgranular crack in a stressed (RUB) Alloy 690TT sample exposed to 307 °C 10% NaOH solution with 10 g/L Pb from Burke et al. [18]. Selected area electron diffraction confirmed the presence of epitaxial NiO in the transgranular crack [18]

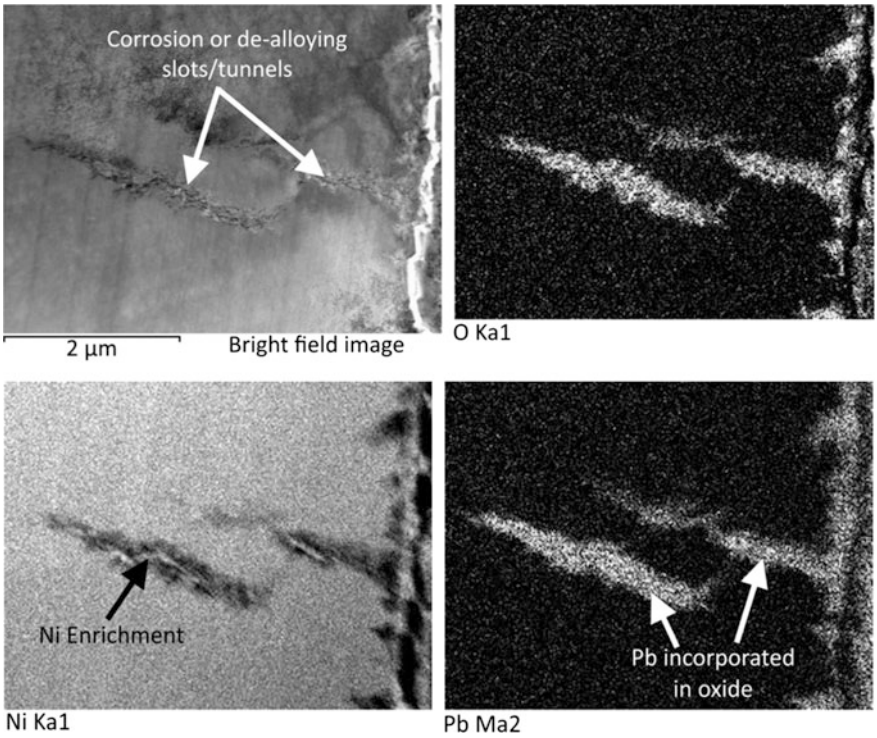

Fig. 9 Bright-field STEM image and corresponding STEM-EDX maps for a transgranular crack tip in the Alloy 690TT sample after exposure to 307 °C 10% NaOH solution with 10 g/L Pb from Burke et al. [18]. Pb is incorporated in the oxide and Ni-enrichment is observed. Corrosion and/or de-alloying occurred favourably along coarser "slot"-like features that were parallel to {110} planes. Burke et al. [18] suggest that linking up of these "slots" produces the macroscopically observed transgranular fracture facets

Burke et al. [18]. Selected area electron diffraction confirmed that NiO filled the centre of the crack, likely a result of the electrochemical potential being above the Ni/NiO equilibrium electrode potential line.

EDX elemental maps for a transgranular crack from an Alloy 690TT Pb-caustic RUB sample are shown in Fig. 9 [18]. Pb appears to be incorporated in the oxide, but the resolution is insufficient to determine whether segregation to a specific interface is occurring. Burke et al. [18] suggest that in addition to NiO, metallic Ni may be may be present in transgranular cracks, indicating the possibility of de-alloying. Also, they suggest that a series of aligned corrosion "tunnels" or "slots" are formed at or ahead of transgranular crack tips, highlighted in Fig. 9 [18]. The "slot"-like features are transgranular facets that are oriented such that they are parallel to {110}. An additional perspective on the Pb-SCC mechanism was provided through the evaluation of a crack-tip transverse cross-section from a partially-cracked C-ring specimen. The crack-tip section revealed the presence of

numerous fine aligned features, consistent with local regions of oxidation as shown in Fig. 10. Burke et al. propose that corrosion through dissolution or de-alloying along "slot"-like features leads to a corrosion tunnelling mechanism, described by Swann et al. [73], for Pb-caustic transgranular SCC in Alloy 690TT. The linking of "slots" would eventually result in the transgranular fracture facets. Whether the corrosion "tunnels" are porous metallic Ni formed through de-alloying or formed as a result of oxidation of Ni, Fe, and Cr is unclear.

The results of Burke et al. [18] suggests a unique "fingerprint" for Pb-caustic transgranular SCC of Alloy 690TT. The local crack tip chemistry and morphology

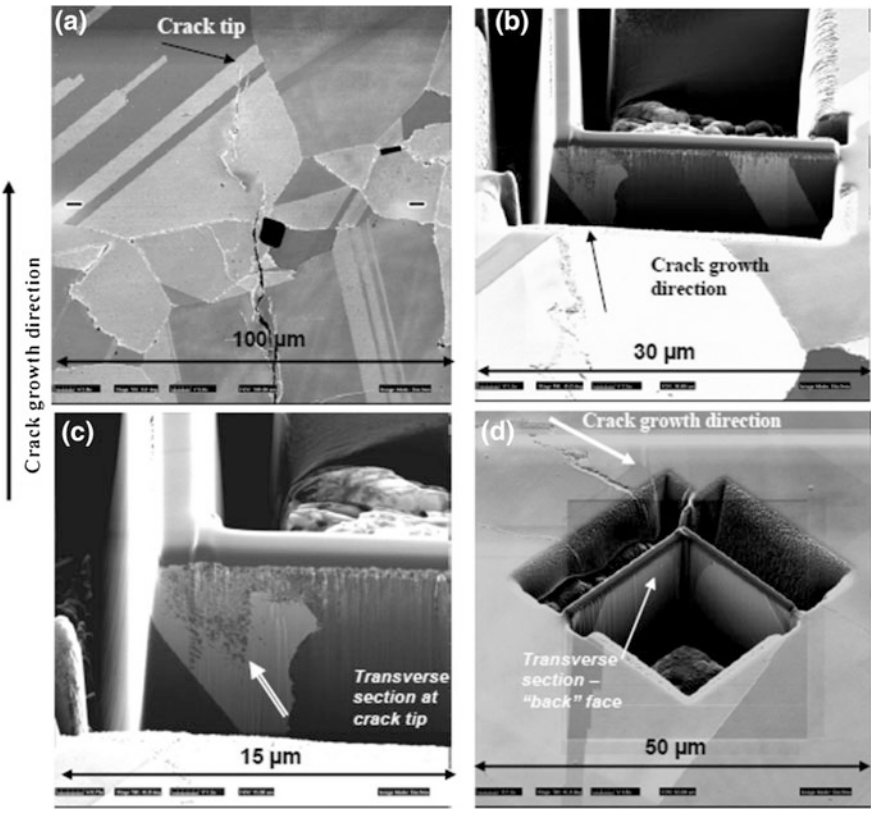

Fig. 10 FIB secondary electron images obtained from a C-ring cross-section sample from Burke et al. [18] showing **a** the primary transgranular crack and crack tip (crack propagation direction labeled); **b** the as-FIBed section of the crack tip taken perpendicular to the crack growth direction (crack propagation direction labeled); **c** higher magnification view of the section in (**b**) showing "slot-like" features beneath the crack tip cross-section surface (arrowed) (oxide is visible above the slots); and **d** view of the opposite side of the thin section shown in (**c**). Note that there is no evidence of the "slot-like" features on the opposite surface of the thinned cross-section section, indicating that this transverse section had intersected the SCC tip itself (crack propagation direction is also arrowed)

exhibit some similarities with Alloy 800 Pb-caustic cracking and probably pure caustic cracking of Alloy 690TT; the "fingerprint" likely incorporates the following features:

- Pb is present in crack tips and may be incorporated in the oxide. However, the possibility of preferential segregation to specific interfaces should be investigated further.
- NiO and possibly metallic Ni fill the centre of transgranular cracks with the formation of dissolved Fe and Cr species being thermodynamically favourable.
- "Slot"-like features are present ahead of transgranular cracks which are parallel to {110}. The corrosion process is suggested to occur along the "slot"-like features resulting in a corrosion tunneling/slot formation SCC mechanism [18].

Acidic Cracking with Pb and/or S

SCC of Alloy 690 and Alloy 800 has been induced in mildly acidic ($pH_{300\ °C} \sim 4$, neutral $pH_{300\ °C} \sim 5.6$) high temperature aqueous solutions with added S and/or Pb [6, 23–31]; such acidic environments aim to simulate the extreme end of secondary side crevice environments and are unlikely under normal bulk water operating conditions. It is generally accepted that the role of Pb and S is to reduce the passivity of oxides formed on Ni–Fe–Cr alloys [11–15, 70, 74–76]. Pb is likely incorporated in the surface oxide or deposited on the alloy surface, similar to the effect of Pb when added to caustic solutions, discussed in Section "Lead-Caustic Cracking". Reduced sulfur species have been shown to adsorb on metal surfaces resulting in a dipole (δ+) charge on the metal [77–80]. As a result, the corrosion rate, especially for Ni, is increased due to reduction in the activation energy necessary for active metal dissolution. Alternatively, thermodynamically stable sulfide compounds (e.g. NiS or Ni_3S_2) could form which disturb the formation of a passive oxide layer [77–80]. Studies which apply ATEM characterization to cracking of Ni alloys in acidic solutions with added Pb and/or S have emerged in recent years [25, 29–31] and some examples will be reviewed in the present section.

Alloy 800

Persaud et al. exposed Alloy 800 C-rings to 315 °C 0.55 M $NaHSO_4$ solution ($pH_{315\ °C} \sim 4$) for 60 h and intergranular cracking was observed to depths in excess of 300 μm [29, 30]. A SEM image of a typical crack is shown in Fig. 11 [29, 30]. Cracks were observed to propagate from pits formed on the surface and pits were present through the entire length of cracks. The crack morphology indicates that the acid sulfate conditions used by Persaud et al. are near the threshold between pitting and cracking. EELS results for an acid sulfate crack from Persaud et al. are

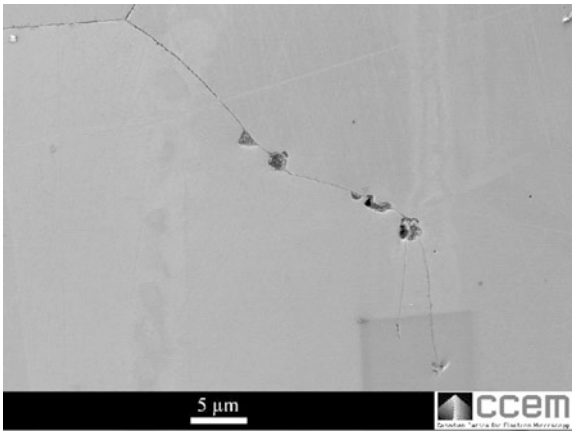

Fig. 11 SE image of a crack in an Alloy 800 C-ring after exposure to 0.55M $NaHSO_4$ for 60 h at 315 °C from Persaud et al. [29]. The cyclic manner in which propagation out of pits occurs along the crack is evident

shown in Fig. 12 [29, 30]. The crack is heavily corroded and filled with oxides. EELS characterization allows for identification of a 3–4 nm thick Cr-rich oxide closest to the matrix with a Fe and Cr mixed oxide formed toward the centre of the crack. Persaud et al. [29, 30] provide preliminary EDX analysis, which may imply that sulfur is present at Cr-rich oxide-metal interfaces, but technological limitations led to inconclusive results. Given the oxide structure, high corrosion rate, and possible presence of sulfur, Persaud et al. suggested a slip dissolution mechanism for SCC [29, 30]. As the mechanism proceeds, sulfur likely contributes by enhancing metal ion dissolution and impairing oxide passivity, allowing for easier oxide rupture; the presence of reduced sulfur species is likely a result of sulfate reduction, which has been reported in high temperature acidic solutions [28–30].

Smith et al. [31] recently extended the studies of Persaud et al. on acid sulfate SCC of Alloy 800. They exposed notched Alloy 800 tensile specimens to 0.55 M [SO_4^{2-}] solution at 280 °C using a direct current potential drop (DCPD) technique to monitor and control crack growth [31]. Through this, they ensured that any crack tips analyzed using ATEM were extracted from growing cracks (i.e. not blunted). ATEM characterization by Smith et al. [31] was done using STEM-EDX with multiple SDDs for improved x-ray collection and elemental detectability as compared to the analysis by Persaud et al. [29, 30]. As a result, sulfur could be identified, even at low concentrations (<4 wt%) in localized regions (<10 nm). A high angle annular dark field-scanning transmission electron microscopy (HAADF-STEM) image of a TEM sample from Smith et al. containing an intergranular acid sulfate crack with a pit located at the base of the crack tip is shown in Fig. 13 [31].

EDX elemental maps for the cracked grain boundary from Smith et al. are provided in Fig. 14 [31]. Sulfur and titanium are present, segregated towards the centre of the crack. The presence of sulfur and titanium was observed across several acid sulfate cracks characterized by Smith et al. EDX results from the large pit at the base of the crack tip in Fig. 13 are provided in Fig. 15 [31]. Sulfur is observed to definitively segregate to the pit-metal interface; the concentration of sulfur at the

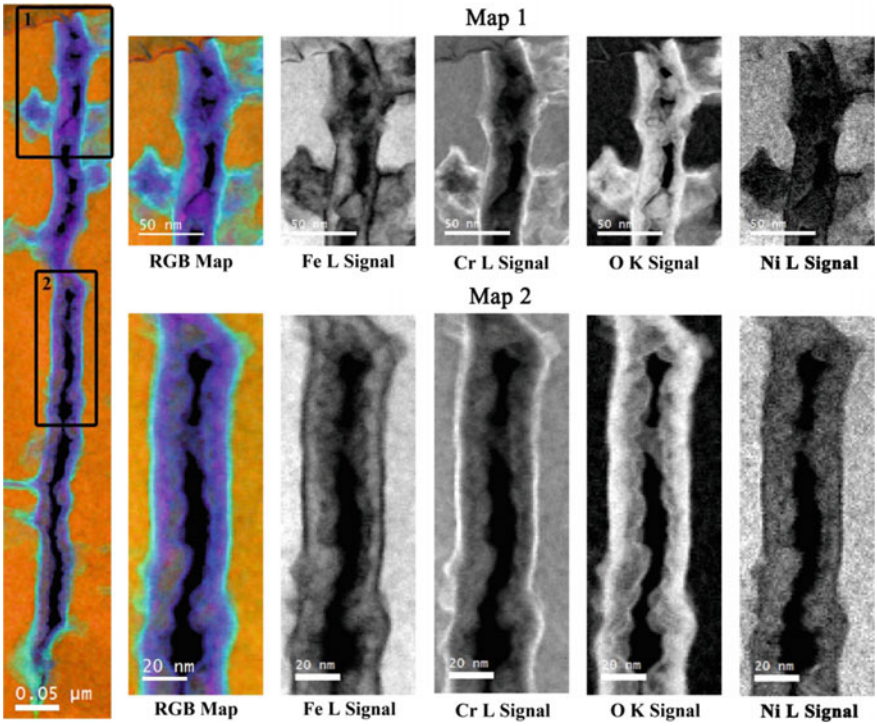

Fig. 12 EELS elemental maps for an acid sulfate crack tip in an Alloy 800 C-ring after exposure to 315 °C $NaHSO_4$ solution for 60 h from Persaud et al. [29]. Red (Fe), green (Cr), blue (O) mixed colour maps highlight the oxides formed in the crack tip. Map 1 and 2 are high magnification maps with the relative signal shown for each element (bright areas indicate enrichment) along with RGB maps. Ni is not included in the RGB map, but an energy-filtered image is shown for reference. There is a duplex oxide structure with a thin 3–4 nm Cr oxide formed near the matrix and a thicker Fe and Cr rich oxide formed toward the centre of the crack (Color figure online)

interface was found to be up to 4 wt%. The pit was filled with a Cr-rich oxide that was likely held together by carbon contamination from deposition during the FIB sample preparation procedure. Ni is not present in cracks or pits suggesting that the element is dissolved during exposure. The presence of sulfur in cracks and at the pit-metal interface suggests that the element is an active contributor to enhancing the dissolution rate of Ni. In addition, there was no indication of a protective oxide having formed at the pit-metal interface, likely also an effect of sulfur adsorption on the bare metal. The ATEM results of Persaud et al. [29, 30] and Smith et al. [31] allow for identification of a unique "fingerprint" for SCC of Alloy 800 in high temperature mildly acidic sulfate solutions that may be applicable if such environments were to be present:

- The surface exhibits signs of general corrosion and pitting with intergranular cracks propagating out of pits. Pits are also present along the crack path.

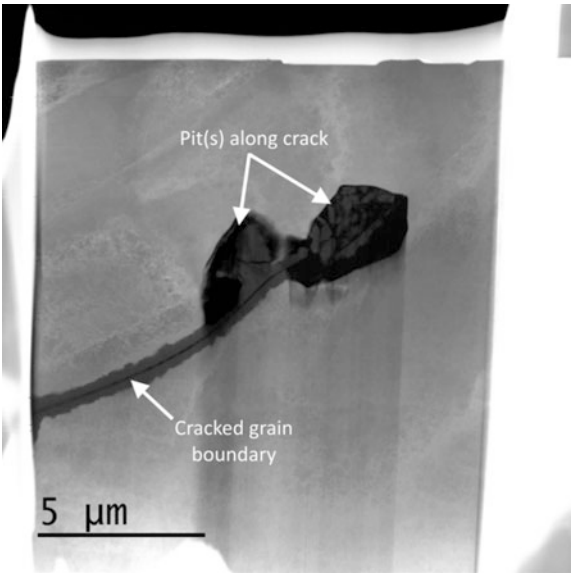

Fig. 13 HAADF-STEM image of an intergranular crack tip extracted from an Alloy 800 sample after exposure to 300 °C 0.55 M [SO_4^{2-}] ($pH_{300\ °C} \sim 4$) environment for 280 h from Smith et al. [31]. Pits were captured in the TEM foil along with a cracked grain boundary. Carbon contamination from FIB sample preparation (deposition) is present in the pit, which likely allowed the pit to maintain its integrity during preparation

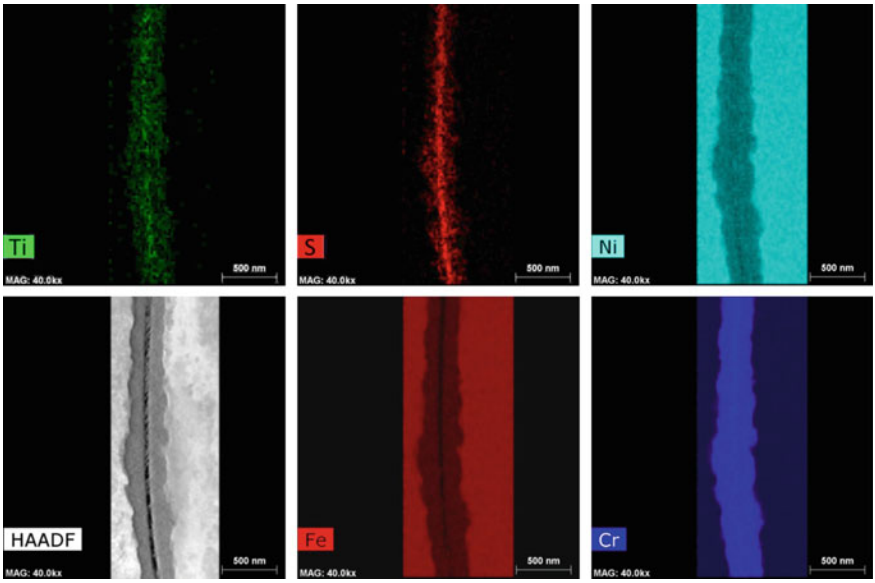

Fig. 14 EDX elemental maps from along the cracked grain boundary in the Alloy 800 acid sulfate crack tip TEM sample, in Fig. 13, from Smith et al. [31]. Sulfur and titanium are present in the centre of the crack. A Cr-rich oxide is present closest to the matrix, along the crack walls

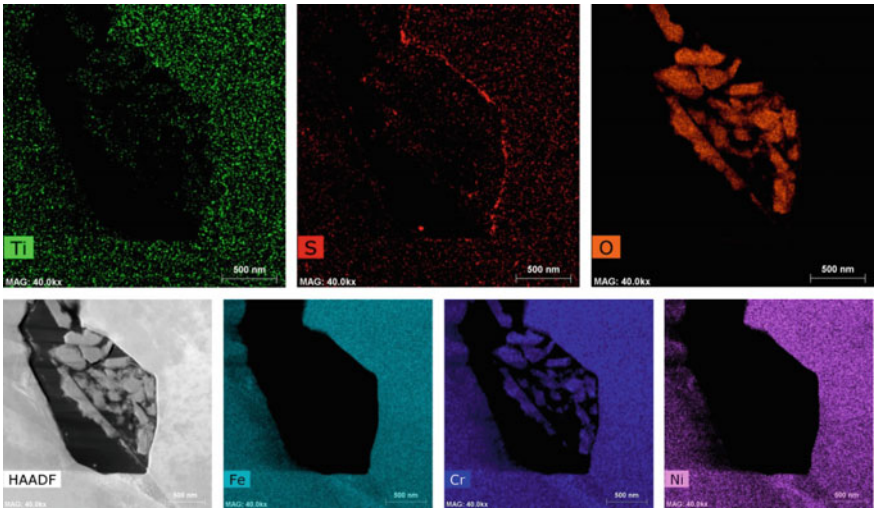

Fig. 15 EDX elemental maps obtained from a pit-like feature detected in the Alloy 800 acid sulfate crack in Fig. 13 [31]. Sulfur is present at the interface between the pit and the metal, suggesting it influences pit growth/SCC. A Cr-rich oxide is present in the centre of the pit

- The oxide structure in cracks generally consists of a mixture of Cr- and Fe-rich oxides, with a Cr-rich oxide formed nearest the matrix.
- Sulfur is segregated to the centre of cracks and is at the pit-metal interface. Sulfur likely impairs oxide passivity and enhances dissolution of metals.
- Ni is not present in cracks, likely soluble due to the pH of the environment and the presence of sulfur.
- Based on the local crack tip chemistry and morphology, a slip dissolution mechanism has been suggested for SCC [29, 30].

Alloy 690TT

Recent ATEM characterization of SCC in Alloy 690TT exposed to high temperature mildly acidic solution has been performed by de Curieres et al. [25]. They examined cracks formed in RUB Alloy 690TT samples after exposure to 320 °C mildly acidic ($pH_{320\ °C} \sim 4$) solution, with added impurities to simulate the conditions that may be present in secondary side crevices; the solution contained 3 ppm ETA, 1 ppm NH_3, 3M NaCl, N_2H_4. In addition to this crevice-simulating fluid, some solids simulating sludge deposits, as seen in actual components, were added to tests. These deposits contain 2000 ppm of Pb or S contamination (91% $PbSO_4$ and 9% PbS). SCC was observed in Alloy 690TT RUB samples to a maximum depth of 110 μm with a density of approximately 1 crack/mm. de Curieres et al.

[25] reported several forms of degradation including, general corrosion, intergranular attack, and intergranular SCC.

EDX elemental maps for a crack tip from an Alloy 690TT RUB sample from de Curieres et al. [25] are provided in Fig. 16. There is significant Cr enrichment in and just ahead of the Alloy 690TT crack tip (~50 wt%). An oxide is formed along the crack wall which is predominantly Fe-rich, but may contain small amounts of Cr. Ni is depleted in the crack and ahead of the crack tip (~35 wt% Ni), suggesting that Pb or S may enhance the dissolution rate of the element through preferential oxidation of Ni. Pb (~1.5 wt%) is observed at and ahead of the crack tip, preferentially segregated to the oxide-metal interface. The local crack tip chemistry suggests that the acidic pH, Pb segregation to oxide-metal interfaces, and the presence of sulfur (enhanced Ni dissolution) may contribute to SCC.

STEM-EDX elemental maps obtained from the same crack but at a location closer to the outer surface of the Alloy 690TT RUB from de Curieres et al. are provided in Fig. 17 [25]. Seemingly metallic Cr-rich "features" or "particles" (85 wt% Cr, no observable C) are present throughout the crack. The intergranular Cr carbides, which were originally present have "broken down", but the precise mechanism for this process is not well understood; de Curieres et al. speculate it could be a result of preferential interaction of Pb and S with intergranular Cr carbides or a form of liquid metal embrittlement [25]. Pb is observed to segregate to oxide-metal interfaces with line scans across the crack in Fig. 17. Also, Pb is present ahead of the crack tip, in Fig. 16, suggesting that the element does not totally overlap with oxygen (i.e. Pb is likely metallic) [25]. The oxides surrounding the Cr particles and in the corroded crack are predominantly Fe-rich. The

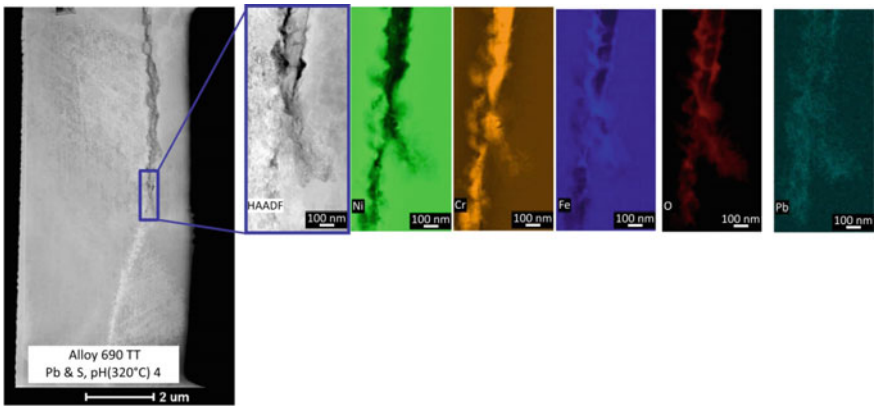

Fig. 16 STEM-HAADF images and EDX elemental maps obtained from a crack tip in an Alloy 690TT RUB sample after exposure to 320 °C simulated secondary side crevice solution with 2000 ppm of Pb and S (91% $PbSO_4$, 9% PbS) from de Curieres et al. [25]. Ni depletion was observed immediately ahead of the crack tip with Cr-enrichment within the crack. In some cases, the Cr is not oxidized and is present as seemingly metallic Cr. Pb is detected, segregated preferentially to oxide-metal interfaces

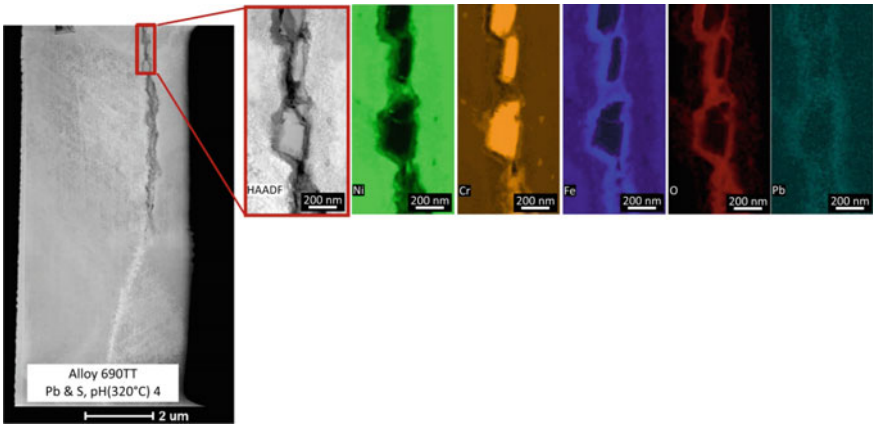

Fig. 17 STEM-HAADF images and EDX elemental maps for a crack from an Alloy 690TT RUB sample after exposure to 320 °C simulated secondary side crevice solution with 2000 ppm of Pb and S (91% $PbSO_4$, 9% PbS) from de Curieres et al. [25]. Seemingly metallic Cr regions are present in the crack, likely a result of Cr carbide breakdown. Pb is detected at the oxide-metal interface and the oxide formed in the open crack is generally Fe-rich

accumulated observations from de Curieres et al. allow for development of a "fingerprint" for the SCC of Alloy 690TT in a mildly acidic simulated secondary side crevice solution with added Pb and S, relevant if such an environment were to be present:

- Intergranular SCC, intergranular attack, and general corrosion occur and cracks are generally open with corroded fracture surfaces.
- Ni depletion and/or Cr particles are present throughout the crack and ahead of the crack tip. The Cr carbide breakdown process and its role in SCC is currently unknown.
- An Fe-rich oxide is present around Cr-rich particles and in the open crack.
- Up to 1.5 wt% Pb is present at the oxide-metal interface in cracks, which likely impairs oxide passivity and accelerates Ni dissolution. Ni dissolution is likely also enhanced by the presence of S.

"Fingerprint" Concept and Future Outlook

Comparing the local chemistries, morphologies, and SCC mechanisms of cracks formed in simulated secondary side crevice SCC systems discussed in the present review really demonstrates the idea and benefit of the "fingerprint" concept. For example, Fig. 18 shows a compilation of EDX and EELS elemental maps for crack tips from stressed Alloy 800 samples exposed to pure caustic (a), Pb-caustic (b), and acid sulfate (c) environments [22, 29, 30, 65]. The SCC mode for pure caustic

cracking in Alloy 800 is transgranular with metallic Ni enrichment located discontinuously along the crack path, as shown in Fig. 18a; de-alloying of reactive elements produces Ni enrichment and results in a film-induced cleavage SCC mechanism and absence of stable Fe and/or Cr oxides. Similarly, the Alloy 800 Pb-caustic ($pH_{300\ °C}$ 9.5) SCC tip in Fig. 18b reveals signs of de-alloying. However, at $pH_{300\ °C}$ 9.5 stable Cr oxides are energetically favourable, which results in Pb segregation to oxide-metal interfaces, and resulting impaired oxide passivity, being required to initiate SCC. Therefore, the local crack tip chemistry differences for Pb-caustic and pure caustic SCC can be identified relatively easily by comparing the oxide structure and the behaviour of Pb in Fig. 18a and b. When compared to Alloy 800 SCC in alkaline environments, the acid sulfate SCC tip in Fig. 18c exhibits essentially no similarities; in contrast to the former SCC modes, acid sulfate cracking of Alloy 800 likely occurs through a slip dissolution mechanism, initiates at pits, is accelerated by the presence of reduced sulfur species (from sulfate reduction), and Ni dissolution occurs while Fe and Cr may form stable oxides. In summary, the comparison of Alloy 800 secondary side SCC using ATEM, in Fig. 18, illustrates the variation in SCC "fingerprints" possible in the same material exposed to simulated secondary side crevice solutions, depending on pH and contaminants present.

A similar comparison of secondary side SCC "fingerprints" can be done for Alloy 690TT using ATEM results discussed in the present review. EDX elemental maps comparing crack tips for Alloy 690TT secondary side SCC in Pb-contaminated caustic and acidic environments are shown in Fig. 19 [18, 25]; the acidic environment also contained sulfur, but the contribution of the element could not be clearly determined from ATEM examination. It is worthwhile mentioning that the same results are observed in Pb-only polluted sludges, emphasizing the potential role of S as an aggravating factor in acidic conditions. The Pb-caustic Alloy 690TT SCC tip in Fig. 19b is transgranular, may contain metallic Ni, and is proposed to occur through a corrosion or de-alloying slot/tunnelling SCC mechanism [18]. In contrast, the Pb contaminated acidic Alloy 690TT SCC tip, in Fig. 19a, is intergranular, results in Cr carbide break-down, and Ni depletion is observed in the crack and ahead of the crack tip [25]. Similar to Alloy 800, the "fingerprints" for SCC of Alloy 690 in Pb-caustic and acidic environments with Pb and S exhibit distinct differences and demonstrate the benefit of developing a database. In addition, the secondary side SCC ATEM results in the present study also reveal that unique SCC "fingerprints" are possible across different SG tubing materials, even if the environment of exposure is similar. For example, the local crack tip chemistries and morphologies associated with Pb-caustic cracking of Alloy 800, in Fig. 18b, and Alloy 690, in Fig. 19b, exhibit distinct differences, such as cracking mode, stable alloying elements, and influence of intergranular carbide precipitation.

In the future, improved techniques and instrument advancements enabling superior spatial resolution and elemental sensitivity will be applied and developed for studying SCC. For example, atom probe tomography (APT) has recently been used for characterizing SCC in stainless steels [34] and Pb-caustic SCC in Alloy

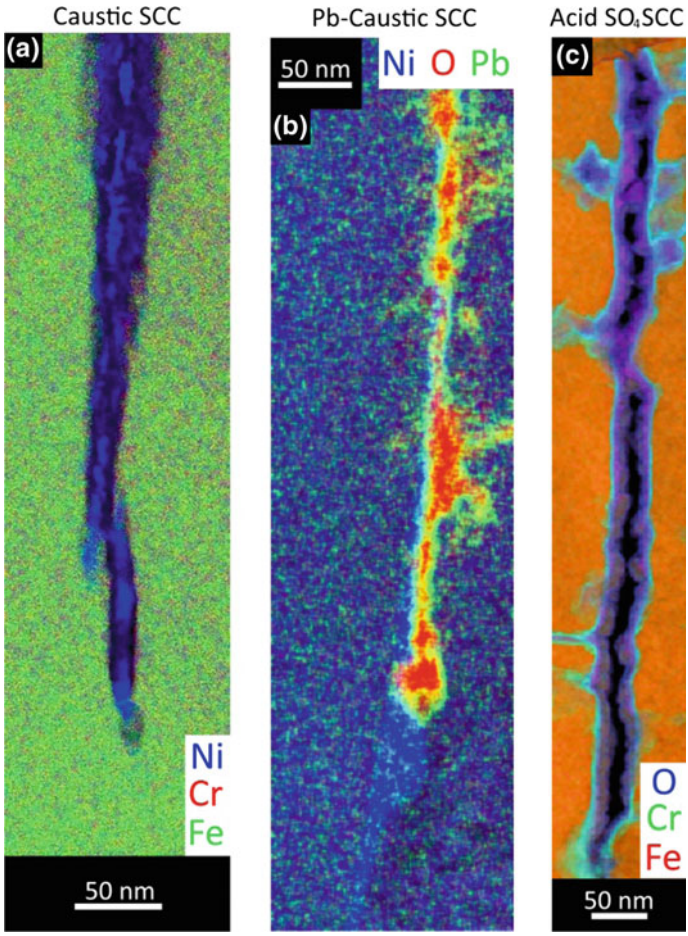

Fig. 18 A comparison of the local chemistry and morphology, or "fingerprint", for Alloy 800 secondary side SCC in three different high temperature simulated crevice solutions [22, 29, 65]. The images highlight crack tips from pure caustic (**a**), Pb-caustic (**b**), and acid sulfate (**c**) environments. In the same material, the local crack tip chemistries and SCC mechanisms are different across all three environments

800 [81]. In the latter study, multiple APT examinations were successfully performed, including one-side of a fracture surface containing Pb, shown in Fig. 20 [81], and an intact crack tip, shown in Fig. 21a [81]. The superior elemental sensitivity of APT allowed for nanoscale quantification of the Na concentration (<0.4 at.%) in the crack tip at the oxide-metal interface, in Fig. 21b [81]. The application of APT to characterization of cracks is still relatively novel and limited to very small volumes, but demonstrates how defining accurate "fingerprints" for known SCC systems will continue to improve in the future.

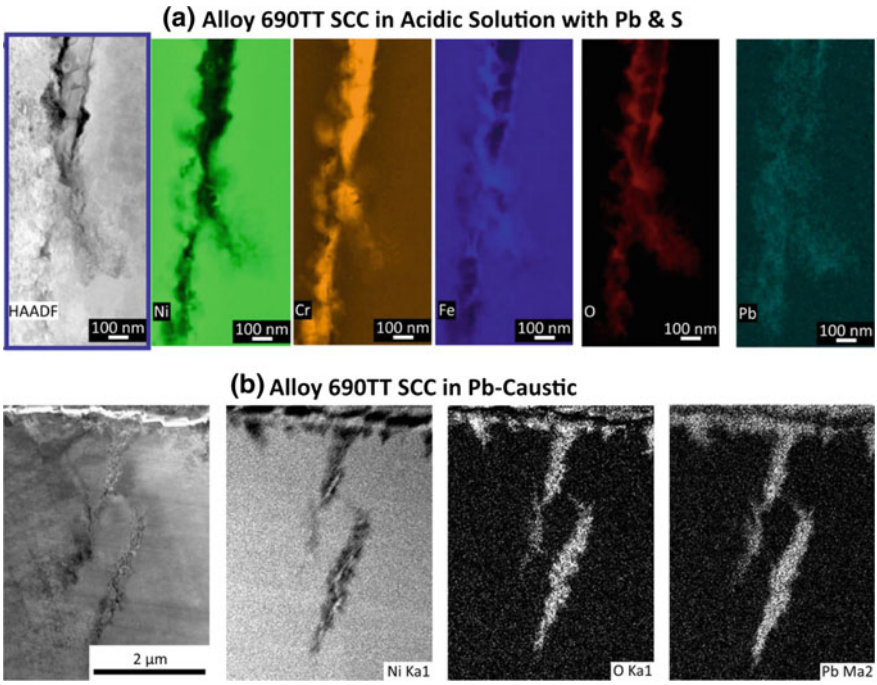

Fig. 19 A comparison of the SCC local chemistry and morphology, or "fingerprint", for Alloy 690TT exposed to an acidic environment containing Pb and S contamination (**a**) [25], and Pb-caustic conditions (**b**) [18]. The cracking mode, SCC mechanism, and behaviour of metal alloying elements and impurities are completely different in each environment

Summary and Conclusions

The present study highlights the application of ATEM to the characterization of secondary side SCC in SG tubing materials; such environments are unlikely under normal operating conditions, and are not an active degradation mode of concern, but developing an understanding of the local chemistry and mechanisms for each form of SCC is beneficial should future degradation occur. A comprehensive review was conducted evaluating ATEM results from several authors to identify local crack tip chemistries and infer SCC mechanisms for each known secondary side SCC system. From the accumulated information, "fingerprints" were generated which outlined local chemistry, cracking mode, and crack morphology associated with each secondary side SCC system. The comparison of "fingerprints" across different environments and materials revealed that unique characteristics are present for each form of secondary side SCC. As a result, this review has illustrated the benefit of developing a database of "fingerprints" for secondary side SCC of SG tubing alloys and provided a collection of ATEM results currently available. In addition, the approach demonstrated in this paper can likely be applied to studying SCC across a broad spectrum of materials and environments.

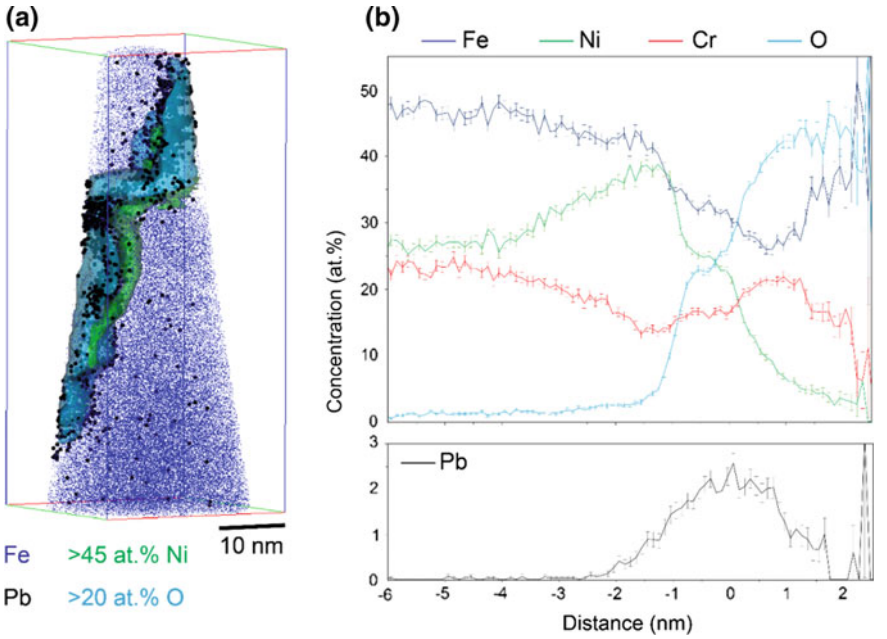

Fig. 20 **a** 3D APT data from Persaud et al. [81] for a transgranular Pb-caustic crack in Alloy 800 showing Fe and Pb ions, with Ni (>45 at.%) and O (>20 at.%) surfaces, indicating areas of enrichment. **b** A proximity histogram from the O iso-concentration surface showing concentration profiles leading into the oxide

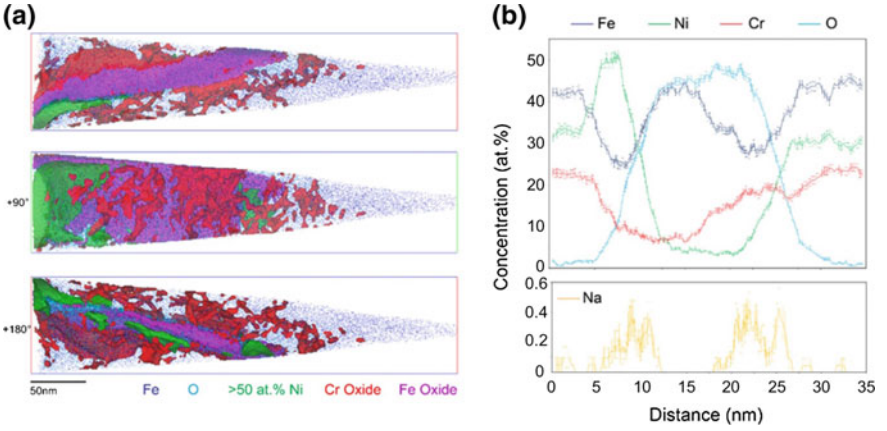

Fig. 21 **a** 3D APT data from Persaud et al. [81] for an intergranular Pb-caustic crack showing Fe and O ions, with iso-concentration surfaces for Ni, CrO, and FeO ionic species. Three different rotated views normal to the specimen axis are depicted, revealing the oxidized crack, the Ni enrichment at the crack tip, and the network of fine Cr oxides surrounding the crack. **b** A 1D concentration profile running normal to the intergranular crack. The oxide is composed of Fe and Cr rich regions. Na is enriched at the oxide-metal interface

Acknowledgements The authors are grateful to the CANDU Owners Group (COG) Steam Generator Integrity (SGI) program, the University Network of Excellence in Nuclear Engineering (UNENE), and the Electric Power Research Institute (EPRI) for providing funding for different portions of this work. TEM analysis was skillfully carried out at the Canadian Centre for Electron Microscopy (CCEM), the AREVA Technical Center, and Fibics Inc. The APT analysis was carried out by Dr. Brian Langelier and the APT system used in this work was funded by the Canada Foundation for Innovation as part of the Centre for Advanced Nuclear Systems.

References

1. M.D. Pandey, S. Datla, R.L. Tapping, Y.C. Lu, The estimation of lifetime distribution of Alloy 800 steam generator tubing. Nucl. Eng. Des. **239**(10), 1862–1869 (2009)
2. R. L. Tapping, Steam generator aging in CANDUs: 30 years of operation and R&D, presented at the in *5th CNS International Steam Generator Conference*, Toronto, ON, Canada, 2006
3. R.L. Tapping, Y.C. Lu, M.D. Pandey, Alloy 800 SG tubing: current status and future challenges, in *Proceedings of the 13th International Conference on Environmental Degradation of Materials in Nuclear Power Systems—Water Reactors*, ed. by T.R. Allen (Canadian Nuclear Society (CNS), Whistler, BC, Canada, 2007), pp. 2033–2051
4. R.W. Staehle, J.A. Gorman, Quantitative assessment of submodes of stress corrosion cracking on the secondary side of steam generator tubing in pressurized water reactors: Part 1. Corrosion **59**(11), 931–994 (2003)
5. R.W. Staehle, J.A. Gorman, Quantitative assessment of submodes of stress corrosion cracking on the secondary side of steam generator tubing in pressurized water reactors: Part 2. Corrosion **60**(1), 5–63 (2004)
6. R.W. Staehle, J.A. Gorman, Quantitative assessment of submodes of stress corrosion cracking on the secondary side of steam generator tubing in pressurized water reactors: Part 3. Corrosion **60**(2), 115–180 (2004)
7. E. Aublant, O. Calonne, M. Foucault, I. de Curieres, Lead induced corrosion in SG tubing materials, in *Proceedings of the 16th International Conference on Environmental Degradation of Materials in Nuclear Power Systems—Water Reactors*, ed. by P.L. Andresen, M.D. Wright, G.O. Ilevbare (NACE International, Omnipress, Asheville, NC, 2013)
8. S.S. Hwang, H.P. Kim, J.S. Kim, Degradation of alloy 600 steam generator tubes in operating pressurized water reactor nuclear power plants. Corrosion **59**(9), 821–827 (2003)
9. B.T. Lu, J.L. Luo, Y.C. Lu, Correlation between film rupture ductility and PbSCC of Alloy 800. Electrochim. Acta **53**(12), 4122–4136 (2008)
10. B.T. Lu, J.L. Luo, B. Peng, A. Palani, Y.C. Lu, Condition for lead-induced corrosion of alloy 690 in an alkaline steam generator crevice solution. Corrosion **65**(9), 601–610 (2009)
11. J. Lumsden, A. McIlree, R. Eaker, R. Thompson, S. Slosnerick, Effects of Pb on SCC of Alloy 600 and Alloy 690 in prototypical steam generator chemistries. Mater. Sci. Forum **475–479**, 1387–1392 (2005)
12. B. Capell, R. Wolfe, J. Lumsden, R. Eaker, PbSCC of Alloy 800NG steam generator tubing in alkaline environments, in *Proceedings of the 17th International Conference on Environmental Degradation of Materials in Nuclear Power Systems—Water Reactors*, ed. by P.L. Andresen, M.D. Wright, J. Jackson (Canadian Nuclear Society (CNS), Ottawa, ON, Canada, 2015)
13. H. Radhakrishnan, A.G. Carcea, R.C. Newman, Influence of Pb++ ions on the dissolution and passivation of nickel and Ni-21Cr in acidic solutions. Corros. Sci. **47**(12), 3234–3248 (2005)
14. X. Ru, R.W. Staehle, A theory for the role of line-contact crevices and their chemistries in promoting SCC in Alloy 690, in *Proceedings of the 16th International Conference on Environmental Degradation of Materials in Nuclear Power Systems—Water Reactors*, ed. by P.L. Andresen, M.D. Wright, G.O. Ilevbare, (NACE International, Omnipress, Asheville, NC, 2013)

15. R. Wolfe, R. Eaker, J. Lumsden, PbSCC of Alloy 690TT and Alloy 800NG steam generator tubing in alkaline conditions, in *Proceedings of the 16th International Conference on Environmental Degradation of Materials in Nuclear Power Systems—Water Reactors*, ed. by P.L. Andresen, M. D. Wright, G.O. Ilevbare, (NACE International, Omnipress, Asheville, NC, 2013)
16. D. Gomez-Briceno, M.L. Castano, M.S. Garcia, Stress corrosion cracking susceptibility of steam generator tube materials in AVT (all volatile treatment) Chemistry contaminated with lead. Nucl. Eng. Des. **165**, 161–169 (1996)
17. S.S. Hwang, J.S. Kim, J.Y. Kim, Role of lead in electrochemical reaction of Alloy 600, Alloy 690, Ni, Cr, and Fe in water. Met. Mater. Int. **9**(4), 389–394 (2003)
18. M.G. Burke, R.E. Hermer, M.W. Phaneuf, Evidence for a corrosion/tunneling mechanism of lead-induced transgranular SCC of Alloy 690 in PbO+ 10% NaOH solution, in *Proceedings of the 13th International Conference on Environmental Degradation of Materials in Nuclear Power Systems—Water Reactors*, ed. by T.R. Allen, (Canadian Nuclear Society (CNS), Whistler, BC, Canada, 2007), pp. 851–873
19. B. Capell, R. Wolfe, J. Lumsden, R. Eaker, Steam generator management program: lead stress corrosion cracking of nuclear grade Alloy 800. Report 3002002853, Electric Power Research Institute (EPRI), Palo Alto, CA, 2014
20. S. Choi, J. Lumsden, Steam generator management program: electrochemical evaluation of lead stress corrosion cracking (PbSCC) mechanism. Report 1020993, Electric Power Research Institute (EPRI), Palo, Alto, CA, 2010
21. Z. Zhang, J. Wang, E.-H. Han, W. Ke, Effects of surface state and applied stress on stress corrosion cracking of Alloy 690TT in lead-containing caustic solution. J. Mater. Sci. Technol. **28**(9), 785–792 (2012)
22. S.Y. Persaud, J.M. Smith, C.D. Judge, F. Long, A. Korinek, B.M. Capell, M.D. Wright, High resolution characterization of Pb-SCC in Alloy 800 exposed to 330 °C mildly caustic environments, *Manuscript Submitted for Publication,* 2017
23. A.J. Baum, W.M. Connor, S.D. Piskor, W.J. Stenger, Acid sulfate corrosion in PWR steam generators. Report NP-7346-M, Electric Power Research Institute (EPRI), Palo Alto, CA, 1991
24. J.P.N Paine, W.H. Cullen, M.J. Partridge, Susceptibility of Alloys 600 and 690 to acidified sulfate and chloride environments. Report TR-104045, Electric Power Research Institute (EPRI), Palo Alto, CA, 1994
25. I. de Curieres, SG tube alloys corrosion tests simulating typical secondary side deposits in *18th International Conference on Environmental Degradation of Materials in Nuclear Power Systems—Water Reactors*, Portland, Oregon, USA, 2017
26. Z. Fang, R.W. Staehle, Effects of the valence of sulfur on passivation of Alloys 600, 690 and 800 at 25 & #xB0;C and 95 & #xB0;C. Corrosion **55**(4), 355–379 (1999)
27. D. Gomez-Briceno, M.S. Garcia-Redondo, F. Hernandez, Update of Alloy 800 behaviour in secondary side of PWR steam generators. Paper A079-T06, presented at Fontevraud 7, Avignon, France, 2010
28. J.F. Newman, Stress corrosion of Alloys 600 and 690 in acidic sulfate solutions at elevated temperatures. Report NP-3043, Electric Power Research Institute (EPRI), Palo Alto, CA, 1983
29. S.Y. Persaud, A.G. Carcea, J. Huang, A. Korinek, G.A. Botton, R.C. Newman, Analytical electron microscopy of a crack tip extracted from a stressed Alloy 800 sample exposed to an acid sulfate environment. Micron **61**, 62–69 (2014)
30. S.Y. Persaud, A.G. Carcea, R.C. Newman, An electrochemical study assisting the interpretation of acid sulfate stress corrosion cracking of NiCrFe alloys. Corros. Sci. **90**, 383–391 (2015)
31. J.M. Smith, K. Daub, M.D. Wright, The environmentally assisted cracking of cold-worked Alloy 800 and higher-chromium variants in mildly acidic sulphate environments, in *Proceedings of the 17th International Conference on Environmental Degradation of Materials in Nuclear Power Systems—Water Reactors*, ed. by P.L Andresen, M.D. Wright, J. Jackson, (Canadian Nuclear Society (CNS), Ottawa, ON, Canada, 2015)

32. S. Lozano-Perez, A guide on FIB preparation of samples containing stress corrosion crack tips for TEM and atom-probe analysis. Micron **39**(3), 320–328 (2008)
33. S. Lozano-Perez, P. Rodrigo, L.C. Gontard, Three-dimensional characterization of stress corrosion cracks. J. Nucl. Mater. **408**, 289–295 (2011)
34. M. Meisnar, M. Moody, S. Lozano-Perez, Atom probe tomography of stress corrosion crack tips in SUS316 stainless steels. Corros. Sci. **98**, 661–671 (2015)
35. M.W. Phaneuf, G.A. Botton, Analysis of degradation in nickel-based alloys using focused ion beam imaging and specimen preparation combined with analytical electron microscopy, presented at Fontevraud 5—Contribution of Materials Investigation to Problems Encountered in Pressurized Water Reactors, Paris, France, 2002
36. D.K. Schreiber, M.J. Olszta, L.E. Thomas, S.M. Bruemmer, Grain boundary characterization of Alloy 600 prior to and after corrosion by atom probe tomography and transmission electron microscopy, in *Proceedings of the 16th International Conference on Environmental Degradation of Materials in Nuclear Power Systems—Water Reactors*, ed. by P.L. Andresen, M.D. Wright, G.O. Ilevbare, (NACE International, Omnipress, Asheville, NC, 2013)
37. L.E. Thomas, S.M. Bruemmer, Summary of analytical electron microscopy observation of intergranular attack and stress corrosion cracks in Alloy 600 steam generator tubing. Report 1011683, Electric Power Research Institute (EPRI), Palo Alto, CA, 2005
38. L.E. Thomas, S.M. Bruemmer, Observations and insights into Pb-assisted stress corrosion cracking of Alloy 600 steam generator tubes, in *Proceedings of the 12th International Conference on Environmental Degradation of Materials in Nuclear Power Systems—Water Reactors*, ed. by T.R. Allen, P.J. King, L. Nelson, (The Minerals, Metals & Materials Society (TMS), Salt Lake City, UT, 2005), pp. 1143–1154
39. S. Lozano-Perez, J.M. Titchmarsh, TEM investigations of intergranular stress corrosion cracking in austenitic alloys in PWR environmental conditions. Mater. High Temp. **20**(4), 573–579 (2003)
40. C.D. Judge, N. Gauquelin, L. Walters, M. Wright, J.I. Cole, J. Madden, G.A. Botton, M. Griffiths, Intergranular fracture in irradiated Inconel X-750 containing very high concentrations of helium and hydrogen. J. Nucl. Mater. **457**, 165–172 (2015)
41. Y.Z. Huang, S. Lozano-Perez, R.M. Langford, J.M. Titchmarsh, M.L. Jenkins, Preparation of transmission electron microscopy cross-section specimens of crack tips using focused ion beam milling. J. Microsc. **207**(2), 129–136 (2002)
42. Y.Z. Huang, J.M. Titchmarsh, TEM investigation of intergranular stress corrosion cracking for 316 stainless steel in PWR environment. Acta Mater. **54**(3), 635–641 (2006)
43. G. Bertali, F. Scenini, M.G. Burke, Advanced microstructural characterization of the intergranular oxidation of alloy 600. Corros. Sci. **100**, 474–483 (2015)
44. D.K. Schreiber, M.J. Olszta, D.W. Saxey, K. Kruska, K.L. Moore, S. Lozano-Perez, S.M. Bruemmer, Examinations of oxidation and sulfidation of grain boundaries in alloy 600 exposed to simulated pressurized water reactor primary water. Microsc. Microanal. **19**(3), 676–687 (2013)
45. S.Y. Persaud, A. Korinek, J. Huang, G.A. Botton, R.C. Newman, Internal oxidation of Alloy 600 exposed to hydrogenated steam and the beneficial effects of thermal treatment. Corros. Sci. **86**, 108–122 (2014)
46. S.Y. Persaud, J. Smith, A. Korinek, G.A. Botton, R.C. Newman, High resolution analysis of oxidation in Ni-Fe-Cr alloys after exposure to 315 °C deaerated water with added hydrogen. Corros. Sci. **106**, 236–248 (2016)
47. S.M. Bruemmer, L.E. Thomas, High-resolution analytical electron microscopy characterization of corrosion and cracking at buried interfaces. Surf. Interface Anal. **31**(7), 571–581 (2001)
48. L.E. Thomas, S.M. Bruemmer, High-resolution characterization of intergranular attack and stress corrosion cracking of Alloy 600 in high-temperature primary water. Corrosion **56**(6), 572–587 (2000)

49. G. Bertali, F. Scenini, M.G. Burke, The intergranular oxidation susceptibility of thermally–treated Alloy 600. Corros. Sci. **114**, 112–122 (2017)
50. H.W. Pickering, P.R. Swann, Electron metallography of chemical attack upon some alloys susceptible to stress corrosion cracking. Corrosion **19**(11), 373t–389t (1963)
51. P.M. Scott, P. Combrade, On the mechanisms of secondary side PWR steam generator tube cracking, in *Proceedings of the 8th International Conference on Environmental Degradation of Materials in Nuclear Power Systems—Water Reactors*, (American Nuclear Society (ANS), Amelia Island, FL, 1997), pp. 65–73
52. G. Santarini, J.Y. Boos, Corrosion of austenitic stainless steel in hot concentrated aqueous NaOH solutions. Corros. Sci. **19**(4), 261–281 (1979)
53. I.-G. Park, C.-S. Lee, S.S. Hwang, H.-P. Kim, J.-S. Kim, Caustic stress corrosion cracking of Alloys 600 and 690 with NaOH concentrations. Met. Mater. Int. **11**(5), 401–409 (2005)
54. R.C. Newman, R.R. Corderman, K. Sieradzki, Evidence for dealloying of austenitic stainless steels in simulated stress corrosion crack environments. Br. Corros. J. **24**(2), 143–148 (1989)
55. X. Liu, J. Shao, G. Cargnolino, D.D. Macdonald, Selective grain-boundary dissolution of Alloy 600 in a concentrated caustic solution at 140 & #xB0;C. J. Mater. Energy Syst. **7**(3), 223–236 (1985)
56. D.-J. Kim, H.P. Kim, S.S. Hwang, Susceptibility of Alloy 690 to stress corrosion cracking in caustic aqueous solutions. Nucl. Eng. Technol. **45**(1), 67–72 (2013)
57. S.S. Hwang, U.C. Kim, Y.S. Park, The effects of Pb on the passive film of Ni-base alloy in high temperature water. J. Nucl. Mater. **246**(1), 77–83 (1997)
58. J. Deakin, Z. Dong, B. Lynch, R.C. Newman, De-alloying of type 316 stainless steel in hot, concentrated sodium hydroxide solution. Corros. Sci. **46**(9), 2117–2133 (2004)
59. Z.L. Coull, Exploring de-alloying in Fe-Ni-Cr alloys and its relationship to stress corrosion cracking in nuclear high temperature water environments. Doctorate of Philosophy, Department of Chemical Engineering and Applied Chemistry, University of Toronto, 2010
60. R. Bandy, D. Vanrooyen, Mechanisms of stress corrosion cracking and intergranular attack in Alloy 600 in high temperature caustic and pure water. J. Mater. Energy Syst. **7**(3), 237–245 (1985)
61. J.S. Baek, J.G. Kim, D.H. Hur, J.S. Kim, Anodic film properties determined by EIS and their relationship with caustic stress corrosion cracking of Alloy 600. Corros. Sci. **45**(5), 983–994 (2003)
62. H. Jiang, J. Xiao, Technical note: investigation of oxide film formed on Alloy 690 (TT) tubes in alkaline water. Corrosion **73**(4), 320–325 (2017)
63. J. Hickling, N. Wieling, Electrochemical aspects of the stress corrosion cracking of Fe-Cr-Ni alloys in caustic solutions. Corros. Sci. **20**(2), 269–279 (1980)
64. W. Yang, Z. Lu, D. Huang, D. Kong, G. Zhao, J. Congleton, Caustic stress corrosion cracking of nickel-rich, chromium-bearing alloys. Corros. Sci. **43**(5), 963–977 (2001)
65. M.A. Bryk, D. Artymowicz, A.G. Carcea, R.C. Newman, Nanoporosity formation in alloy 800 investigated with respect to stress-corrosion cracking in high-temperature caustic solutions, presented at the *36th Annual Conference of the Canadian Nuclear Society* (Canadian Nuclear Society (CNS), Toronto, ON, Canada, 2016)
66. Z.L. Coull, R.C. Newman, Selective dissolution and oxidation zones in Ni-Cr-Fe space and their relationship to stress corrosion cracking, presented at NACE CORROSION 2007, Nashville, TN, 2007
67. K. Sieradzki, R.C. Newman, Brittle behaviour of ductile metals during stress-corrosion cracking. Philos. Mag. A **51**(1), 95–132 (1985)
68. K. Sieradzki, R.C. Newman, Stress-corrosion cracking. J. Phys. Chem. Solids **48**(11), 1101–1113 (1987)
69. S.S. Hwang, H.P. Kim, Y.S. Lim, J.S. Kim, L. Thomas, Transgranular SCC mechanism of thermally treated alloy 600 in alkaline water containing lead. Corros. Sci. **49**(10), 3797–3811 (2007)

70. D.J. Kim, H.C. Kwon, H.W. Kim, S.S. Hwang, H.P. Kim, Oxide properties and stress corrosion cracking behaviour for Alloy 600 in leaded caustic solutions at high temperature. Corros. Sci. **53**(4), 1247–1253 (2011)
71. F. Sato, R.C. Newman, Mechanism of activation of aluminum by low melting point elements: part 1—effect of zinc on activation of aluminum in metastable pitting. Corrosion **54**(12), 955–963 (1998)
72. F. Sato, R.C. Newman, Mechanism of activation of aluminum by low-melting point elements: part 2—effect of zinc on activation of aluminum in pitting corrosion. Corrosion **55**(1), 3–9 (1999)
73. P.R. Swann, Dislocation substructure vs transgranular stress corrosion susceptibility of single phase alloys. Corrosion **19**(3), 102t–114t (1963)
74. D.-J. Kim, B.H. Mun, H.P. Kim, S.S. Hwang, Investigation of oxide property on Alloy 600 with the immersion time in a high-temperature leaded alkaline solution. Met. Mater. Int. **20** (6), 1059–1065 (2014)
75. S.W. Kim, H.P. Kim, Electrochemical noise analysis of PbSCC of Alloy 600 SG tube in caustic environments at high temperature. Corros. Sci. **51**(1), 191–196 (2009)
76. U.C. Kim, K.M. Kim, E.H. Lee, Effects of chemical compounds on the stress corrosion cracking of steam generator tubing materials in a caustic solution. J. Nucl. Mater. **341**(2–3), 169–174 (2005)
77. P. Marcus, Sulfur-assisted corrosion mechanisms and the role of alloyed elements, in *Corrosion Mechanisms in Theory and Practice*, ed. P. Marcus, 2nd edn (Marcel Dekker Inc., New York 2002), pp. 287–310
78. P. Marcus, E. Protopopoff, Potential pH diagrams for sulfur and oxygen adsorbed on nickel in water at 25 and 300 & #xB0;C. J. Electrochem. Soc. **140**(6), 1571–1575 (1993)
79. P. Marcus, H. Talah, The Sulphur-induced breakdown of the passive film and pitting studied in nickel and nickel Alloys. Corros. Sci. **29**(4), 455–463 (1989)
80. J. Oudar, P. Marcus, Role of adsorbed sulphur in the dissolution and passivation of nickel and nickel-sulphur alloys. Appl. Surf. Sci. **3**(1), 48–67 (1979)
81. S.Y. Persaud, J.M. Smith, B. Langelier, B. Capell, M.D. Wright, An atom probe tomography study of Pb-caustic SCC in Alloy 800. *Manuscript Submitted for Publication*, 2017

Appendix
18th International Conference on Environmental Degradation of Materials in Nuclear Power Systems—Water Reactors: Questions and Answers

Editors' Note: The following comprises questions and answers corresponding to presentations made during the August 13–17, 2017 conference. Conference organizers experimented with a cloud-based, comment sharing software package called ThinkTank in an attempt to facilitate capture of Q&A for future reference. Because this software relies on audience input to the software and subsequent author response, not all questions were captured and not all captured questions were answered. Presentations are broken down by day and session. The title of the presentations is provided, followed by the author's name and then numbered questions. Responses follow each of the numbered questions and are denoted by lower case letters (a, b).

Monday, August 14, 2017

Session: Plenary

A Technology Driven Future

Scot Greenlee

1. You mentioned that framework has been in place for Risk Based Engineering Programs for several (4?) years, but has only been used a couple of times so far. What has held this opportunity to reduce the scope of 'safety related' systems from wider implementation to date?

J.H. Jackson et al. (eds.), *Proceedings of the 18th International Conference on Environmental Degradation of Materials in Nuclear Power Systems – Water Reactors*, The Minerals, Metals & Materials Series, https://doi.org/10.1007/978-3-319-68454-3

a. The 10CFR50.69 framework has been in place for about 10 years. The rule was put in place after South Texas Project applied for something very similar to 50.69 which NRC approved. There are two primary reasons that others have not applied. First, it is a lot of work to screen each system so many decided that the amount of work was too much to absorb. Second, most of us did not recognize the full benefit of adopting the rule. Now that the full benefit is understood, the costs are not seen as unreasonable and so most of us will move forward with adopting the rule.

Session: Accident Tolerant Fuel Cladding

Accident Tolerant FeCrAl Fuel Cladding: Current Status Towards Commercialization

Kevin Field

1. Is any sort of accelerated testing being considered for investigating the irradiated properties?
2. I am curious of the role of added Mo in C26 M. Will it cause more trouble of thermal ageing?
3. Is the 4.25″ dia. VIM in this case a condition of the scale of this production, or a technical requirement due to melt segregation?
4. How does this pathway compare to that used for FeCrAl alloys for other industries?
5. APMT exhibits good corrosion resistance, but your results on mechanical properties in both the unirradiated and irradiated states show severe embrittlement. Has this alloy been eliminated from future consideration?
6. Have you studied or seen any difference between Zr and FeCrAl regarding the adherence of released Nickel from other components in the primary system? I.e. the sensitivity for formation of CRUD.

Mechanical Behavior of FeCrAl and Other Alloys Following Exposure to LOCA Conditions Plus Quenching

Evan Dolley

1. The RT strain to failure of APMT is several percent, compared to virtually no plastic strain in the tensile tests reported by Kevin Field in the first talk in this session. Any idea why there should be such a large difference?
2. Any thoughts on the cause of the stringers? Characterization of these stringers? Given that APMT is a powder metal alloy.
3. Did you look at the composition of the light grey streaks in the bottom picture?

Investigating Potential Accident Tolerant Fuel Cladding Materials and Coatings

Kevin Daub

1. Did you develop a procedure to coat thin walled tube samples and are there any complications to maintain homogeneous coating on the tube?

Steam Oxidation Behavior of FeCrAl Cladding

Bruce Pint

1. How are you planning to investigate the reaction with other components in the core?

In Situ Proton Irradiation-Corrosion Study of ATF Candidate Alloys in Simulated PWR Primary Water

Peng Wang

1. Question about test geometry, on mechanism, does diffusion affect result?
2. Audience: role of electrochemistry?
3. Audience: also see effect of radiation on alloy? What if "dial it up"?
4. Audience: what about aging specimen at 475 °C to form alpha prime before test?

Hydrothermal Corrosion of SiC Materials for Accident Tolerant Fuel Cladding with and Without Mitigation Coatings

Stephen Raiman

1. Audience: comment on mass change of NiCr coated sample
2. Audience: what to do about uncoated edges? What can do to improve coating?

Characterization of the Hydrothermal Corrosion Behavior of Ceramics for Accident Tolerant Fuel Cladding

Peter Doyle

1. Audience: same before for SIC/SiC CMC samples?
    a. CMC SiC/SiC samples were not tested in this study. All SiC samples were pure SiC.
2. Any plans to do shorter experiments on silica?

a. Short experiments on silica were performed following this work, and they show corrosion rates similar to Terrani et al. J. Nucl. Mater. 465 (2015) 488–498.

Corrosion of Multilayer Ceramic-Coated ZIRLO Exposed to High Temperature Water

Gary Was

1. Audience: what is CTE of coating?
2. Audience: why is oxide thicker under coating?
3. Audience: did you look at Zirlo to see H from oxidation in SCW?

Session: General SCC and SCC Modeling—Part 1

Calibration of the Local IGSCC Engineering Model for Alloy 600

Thierry Couvant

1. How were the measurements of maximum oxide penetration depth made? Were they done using FIB x-sectional analyses? How many grain boundaries needed to be analyzed to get good sampling statistics?

Prediction of IGSCC as a Finite Element Modeling Post-analysis

Thierry Couvant

1. When applying this modeling approach to stainless steel, is it assumed that the SCC mechanism is similar to A600, i.e. is it still assumed that GB oxidation is a precursor to SCC initiation?

Session: PWR Nickel SCC—SCC

Scoring Process for Evaluating Laboratory PWSCC Crack Growth Rate Data of Thick-Wall Alloy 690 Wrought Material and Alloy 52, 152, and Variant Weld Material

Amanda Jenks

1. By eliminating PPU are you also eliminating the effect of thermal stress transients?
   a. The end goal is to develop CGR equations for steady state crack growth in plants, not necessarily transients. Most PPU data are under much faster transients than plants would see, regardless.

2. Have you looked at where the data that were scored out (i.e., >3) would change the model parameters with the scored in data considered more reliable?
    a. So few data were scored out (<5% of the overall database) that it is unlikely using the scored out data would affect the current results. Additionally, most of the scored-out data were obtained at the same K, T, and H_2 levels (levels that were average for the rest of the database), such that they would not fill in any data gaps that could improve the fits.
3. Was there a correlation of scoring with CGR?
    a. For the Segment Credibility score, CGRs >1E−10 m/s all got very good scores, but below this, there was no correlation with CGR.
4. Nice presentation.
5. Question asked during session: Is there any intention to score the quality of the end use of the data? e.g. if the component has a high K compared to a low K on plant?
    a. This scoring process by the Data Evaluation Group was only intended to reflect the testing quality of the data, not the relevance to plant components. The Applications Group subsequently evaluated the applicability of the laboratory tests to plant conditions to ensure that the data used to develop the disposition equation, to the extent possible, were directly relevant to plant conditions.
6. Question 2: Should PPU data be included in any disposition curves since components are more likely to see this on plant rather than constant load or K?
    a. Plant conditions are typically under constant loading conditions, in that they only experience transient conditions every 18–24 months when the cycle ends. This is different from the lab PPU data, which see transients several times per day. So no, there are no current plans to evaluate PPU data further.

Applicability of Alloy 690/52/152 Crack Growth Testing Conditions to Plant Components

Warren Bamford

1. Many of the problems are from unexpected conditions. Can't we imagine unexpected events that will give us higher than expected CW?
2. Some alloy 600 and alloy 182 surface cold work examples revealed a high damage layer reaching 1 mm in depth. How sure are we such thicker layers of cold work damage are not present in the alloy 690/152/52 replacements?
3. This is a question directed to the individual that asked question #2 above: Can you elaborate on how this depth of damage was induced? In what I would consider "normal" machining/grinding activities, I've measured CW layer

depths up to only about 0.15–0.20 mm. Thus, I have to think that what you report was "abusive" grinding, which we now hopefully avoid.
4. Just to note that it is not necessarily just the product forming that should be considered with orientation it is also the orientation that the additional strain has been applied.
5. Just a concern about repair welds that may have been more common when alloy 690 was first put into service. In my opinion, we have not characterized or tested alloy 152/52 repair welds in sufficient detail to understand remaining plastic strain and potential for increased susceptibility to SCC.
6. The data that you presented does not include the "rogue" heats that the following talk (Andresen") noted. How can you address the unexpected events of which he "rogue" metals might represent?
7. Questions asked during session: Could surface damage up to 1 mm depth occur in Alloy 690 CRDM components?
8. Does stress relief heat treatment after bending operations remove strain and stress? i.e. is it a strain anneal?

SCC of Alloy 152/52 Welds Defects, Repairs and Dilution Zones in PWR Water

Peter Andresen

1. You mentioned "rogue heats". How should this be related to in the previous presentation by that doesn't take this into account?
    a. The approach used in the 690 Expert Panel—and all similar efforts for other materials—is to model the 75th percentile of response, not either the low or high growth rate extreme. The 75th percentile has worked well for SCC of structural materials in plants, even though the 75th percentile is closer to the mean response than the 95th percentile. What is of greater concern is that we don't understand the composition or processing or grain boundary chemistry that gives rise to the higher susceptibility.
2. Question asked in session: In the as-received solution annealed condition the particularly high crack growth rate is seen for a water quenched material, could this be the cause of the high rate seen?
    a. George Young noted that the high growth rate material reported on my slides as "Morton, 20%CW" was water quenched following the solution anneal. Since this is not an uncommon practice, and since it should yield less segregation at grain boundaries, it's not easy to see how this explains high growth rates—but it should certainly be investigated.

Status of U.S. NRC Research Activities for Alloy 690/52/152 Crack Growth Rate Testing

Greg Oberson

1. Comment during session: Cracks in the dilution zone appear to see high crack growth rates. In plant components cracks weren't seen in dilution zones. There may be a residual strain effect here.
2. PPU even with long hold times were seen to accelerate rates, whereas for 82/182 data this was only seen for times below 1 h. Therefore different exclusion rules apply for 690/52 compared to 82/182.
3. What is the current inspection frequency and amount?
4. Do you take account of any foreign codes?
5. What is the plant for reviewing the EPRI report produced? How will you move forward and resolve any questions raised? Can you discuss the timescales for this process?

Stress Corrosion Cracking of 52/152 Weldments Near Dissimilar Metal Weld Interfaces—Possible Paths for Fast IG SCC Propagation

Bogdan Alexandreanu

1. Cr has been shown to be a key factor in many, many careful, single-variable experiments. It seems like that you don't see a clear correlation with Cr because you're looking at isolated areas on a few cross-sections, not continuously along the crack front. Have you considered measuring Cr along (or near) the crack tip on the fracture surface. Of course, Cr doesn't control all of SCC, so other factors could be complicating the picture.
    a. One (important) observation from these tests was that crack direction versus test plane was a also a key parameter; as such, in many cases, cracks were found to propagate off-plane, along the dendritic grains, but the CGRs measured by DCPD were low. The CGR plot does not account for the crack direction. Cr concentration were measured along the crack paths on cross sections, however, it is not clear that they are representative for the entire front
2. Have you considered using a technique FRASTA to 'reconstruct' the development of the fracture surface during your test?
    a. No, I have not

3. Cross-sections give one microscopic slice across the width of specimens. What techniques are available to look at chromium in these slices? Would stero-imaging be possible to look at how crack grew? Could you look down into the sample rather than in cross-section?
   a. Will have to look into it, the tested specimens are available
4. Are you saying crack can continue in first and second layer and then stop when it encounters the rest of the weld? What are the implications for weld overlays?
   a. The second and subsequent layers have been indeed more resistant to SCC
5. Composite specimens showed cracking in 182 and dilution zone but stopped at higher chromium—are second and subsequent layers less susceptible to cracking?
   a. A crack can advance very fast (E−10 m/s) in the first layer, then it can slow or stop in subsequent layers
6. What are the practical implications of your results for weld-overlay repairs? Do you expect the crack growth to continue or slow down and stop beyond the second layer?
   a. The crack would be expected to slow down or stop beyond the second layer.

Stress Corrosion Crack Growth Rate: Testing of Composite Material Specimens

David Morton

1. You show growth of cracks into an adjacent weld pass, with lines marking the exact location of the weld pass—with the incremental growth of microns. Do you really think you can define the location of the welding pass on that scale?
   a. It was difficult, and it often required extrapolation from adjacent locations, but there was a notable difference between the 8N12 and EN52 weld passes.
2. What was the maximum growth in the Alloy 52?
   a. The small SCC pockets with maximum depth of 1 mm would be difficult to detect with NTD.
   b. We have tested EN52i in welds with high strain and have not observed appreciable SCCGRs.
3. Could this be detected by NDT?
4. One reason for local crack growth is high strained regions. When repair welded on top or additional cold work applied this changes the strains in the weld, have you looked at these highly strained materials?

5. Have you measured the residual strain? This is the most important factor
   a. We have measured the yield stress of all welds and have performed EBSD characterization of several welds.
6. You tested in Alloy 625, which grade of material was tested?
   a. We tested EN625 weld metal not wrought Alloy 625.
7. What was the maximum crack extension observed in the EN52i weld metal and would it be detectable with UT?

Investigation of Hydrogen Behavior in Relation to the PWSCC Mechanism in Alloy TT690

Takumi Terachi

1. I don't think your Ni coated surface makes any difference. First, H_2 dissociates and permeates through Ni readily, and is a dominant source of H permeating through the metal. Second, the external surfaces of the crack play a small role compared to corrosion that occurs in the crack.
   a. Although we could not covered by Ni plating on fatigue pre-crack, the result indicated obvious suppression in Ni-plating specimen. This is our preliminarily results then now we try to confirm the phenomenon. Thanks for the comments.
2. By vacancy, do you mean voids as created from metal crystal defects?
   a. It looks cavity like defects formed by crack of carbide. But I believe cavities formed by migration of vacancy have more important for crack initiation.
3. If the mechanism is enhanced vacancy diffusion due to hydrogen, why does the crack growth rate drop back down soon after the hydrogen is added?
   a. We are trying to clarify the role of hydrogen and the points you mentioned is not clear for me as well. One of the possible explanation is blunting the crack tip and stress distribution.
4. When looking for crack tips, we did often find "cavities" ahead of the active crack tips (alloy 600). When we removed the metal mass between the crack tips and the "cavities" by FIB, we realized that the "cavities" were actually the cross sections of other cracks that went 3 dimensional. Did you see something similar before?
   a. Thank you for the comment and example data. We observed so many cavity like defects shown in the slides. From the number the defects, we believe that it formed inside of materials.

5. On slide 10, you are using CT specimens and so isn't the bending strength increasing not the creep deformation?
   a. From the cross-sectional observation, hydrogen seems affect the plasticity at crack tips.
6. Primary creep is increased by increased hydrogen.
   a. Hydrogen caused deformation continued only 4 h. This duration is corresponds to change of gas condition, then I believe the influence for primary creep is not dominant.
7. On slide 5, you have a high density of cavities before the test starts, are you just opening cavities that you couldn't see before rather than forming cavities?
   a. Shapes of cavity and crack of carbide are not identical. Observed cavity is normally round shape then I believe it formed by vacancy migration.
8. When you changed from argon to hydrogen do you go from NiO to Ni stable phase? Does this affect the results?
   a. Hydrogen partial pressure is changed from NiO to Ni stable phase when we inject hydrogen. The deformation is continued only 4 h, then I think surface oxidation is not the dominant factor.

Session: PWR Nickel SCC—Initiation—Part 1

Crack Initiation Data of Alloy 600 in PWR Water

Peter Andresen

1. In the figure on the left, failure happened at the head/shank junction. Is it a favorite site for initiation in this type of specimen?
   a. This did not occur often, and in any event, this specimen shows that there were several other areas that were nearly as extensively cracked as the primary crack near the shoulder.

SCC Initiation Behavior of Alloy 182 in PWR Primary Water

Mychailo Toloczko

1. I think 'compromised boundaries' in 182 may be dominating the scatter in your data. 25 years ago, Lars Ljundberg polished and etched over a dozen heats of 182 weld metal, and found that etchant leached back out of many boundaries and stained the area along many boundaries. There was no visual evidence that the boundary was not 'solid', but it clearly wasn't. You should work on techniques such as this—and perhaps simple 5–10% straining tests that might open up 'weak' boundaries—as a way to get more insight into this issue.

2. What are the reasons for the large variability in initiation times of replicate specimens?

    a. Raj, our current belief is that it could be due to two factors. One is that there is a wide range in SCC in susceptibility from grain boundary to grain boundary as well as from region to region within alloy 182 welds. Second is that the presence of preexisting defects could be contributing to the very low values. These defects are scattered throughout the weld and not all specimens may intersect these defects.

3. What was the driver for segregation of iron at aligned boundaries?
4. Where type II boundaries present?
5. Do you know the specific quantity of elements at different parts of the fracture surface given that it is not a polished surface?
6. Are the areas of susceptibility irregularly aligned and so can't align with plane of fracture specimen?

In Situ Evaluation of Multiple Stress Corrosion Cracks by X-Ray Computed Micro-Tomography and Digital Image Correlation

Jose Bolivar Vina

1. What is the length resolution of the Z-projections? Would you be able to determine the GB plane angle if you were to catch a crack right at the stage of initiation? With that information, you would be able to resolve stresses onto a fully defined GB which could tell you a lot about the importance of stress in the crack initiation process for this alloy.

    a. Resolution of Z-projection → the resolution of the scan was 2.34 μm/voxel, however, you cannot determine the crystallographic orientation (i.e. GB plane angles) by working under this configuration. With x-ray μCT, you can only determine the crack path. For obtaining such kind of information (orientations and GB angles) you have to work with the DCT technique but there are several experimental limitations (resolution, sample size …)

SCC Crack Initiation in Nickel Based Alloy Welds in Hydrogenated Steam at 400 °C

Catherine Guerre

1. According to your results, most of the cracks are located at the root of weld with the smaller grains. This observations indicate that smaller grains are related to the cause of SCC.

    a. The characterizations of the surface of the cracked U-bend specimen showed that many cracks are located in places where there are smaller grains.

By SEM and EBSD, we observe that most of the small grains are located at the root of the weld beads or weld passes (not the root of the weld). We also observe that if the roots of the weld passes are made of larger grains, they are also more susceptible to SCC initiation. We concluded that these areas (roots of the weld passes) are more susceptible to SCC initiation. But the roots of the weld passes can also consist of larger grains, and there can be small grains in the center of the weld passes (not more susceptible to SCC). No direct correlation could be established between grain size and susceptible grain boundaries. What we assume is that there could be a correlation between the roots of the weld passes and susceptible grain boundaries, whether the roots are made of small or large grains. Therefore, we tried to identify what could explain that the roots of the weld passes are more susceptible to SCC initiation. For weld A, chemical analysis by SIMS and EPMA showed a higher quantity of phases containing S, Ti and Al. Our hypothesis is that there are chemical heterogeneities in the weld and that there are more S, Ti and Al at the roots of the weld passes. The enrichment of S, Al and Ti during weld solidification could also be correlated with changes in the grain boundary microchemistry. Therefore, we suggest that this chemical heterogeneities could modify the grain boundaries strength and their electrochemical activity and therefore it could change the SCC susceptibility of the grain boundaries (at the roots of the weld passes).

2. What are the results for Weld A/HT?

    a. SCC tests were not performed on weld A after post weld heat treatment. SCC tests were only performed on these three alloys.

Session: Irradiation Damage—Stainless Steel

Effect of Strain Rate and High Temperature Water on Deformation Structure of VVER Neutron Irradiated Core Internals Steel

Anna Hojna

1. Widera: the work confirms that Ti stabilized behaves ductile at 5.2 dose.
2. P. Chou: Is typical not to observe dislocation channels?
3. Could you please explain briefly why the shift could be an indication of a gas but nothing else?

    a. Of course, the blueshift of Plasmon could also be an indication of something else. Blue shift of Plasmon could be related, for example to the properties of the electron density in the metal. That is why the conditional is used in the sentence. We performed STEM EELS analysis on several cavities. However,

we did not observe the blueshift of Plasmon peak in all cavities. Therefore, we have assigned the blueshift of the Plasmon to be associated with the presence of gas in the cavities.

4. What is the threshold stress required to initiate IASCC in this material?
    a. No IASCC crack initiation test has been performed with this steel. Russians rely on data of A304.

Radiation-Induced Precipitates in a Self-ion Irradiated Cold-Worked 316SS Used for PWR Baffle-Bolts

Jan Michalicka

1. Gabriel Meric de Bellefon: did you observed segregation on GB.
    a. Yes, the RIS was observed on all sinks, including HAGB, twin boundaries, dislocations and even primary precipitates. Along HAGBs was a uniform RIS observed, also at most twin boundaries. But RIS in form of granular precipitates was observed along some twin boundaries (especially at 500 °C).
2. Kim: gamma prime.

In Situ and Ex Situ Observations of the Influence of Twin Boundaries on Heavy Ion Irradiation Damage Effects in 316L Austenitic Stainless Steels

Gabriel de Bellefon

1. TEM preparation
    a. FIB for in situ
    b. Electropoloshing for ex-situ
2. AREVA: loop moving if it is sessile?
    a. It can be a perfect loop
3. ORNL: clusters?
    a. Good point, point defect clusters might be attracted by twin boundaries (rather than point defect)
4. Peter Chou/limit of absorption of twins
    a. Further work should look at the stability of twins in HAZ of welds

5. Are you optimistic about increasing the radiation resistance of stainless steels by introduction of twin boundaries?

    a. Yes. Thermo-mechanical treatment of stainless steel can introduce a high density of deformation twin boundaries without compromising mechanical properties. A high density could influence radiation tolerance positively.

In Situ Microtensile Testing for Ion Beam Irradiated Materials

Hi Vo

1. The single-grain tensile test results are highly dependent on the orientation of the grain with respect to the stress direction. How could such results be compared with the macro tensile test results?
2. Why fracture of GB is not smooth?

    a. I think this might be due to the unevenness of the oxide layer and also the presence of the carbide.

3. Thickness of oxides?

    a. The statistics of the thickness of the oxide across the grain boundary has not been obtained. Other studies have shown that the oxide thickness is inhomogeneous. Thank you.

4. How calculate number of dislocations?

    a. The number of dislocations has not been calculated for the grain boundary testing study.

5. Is the fracture along oxide/matrix interface or within the oxide?

Development of High Irradiation Resistance and Corrosion Resistance Oxide Dispersion Strengthened Austenitic Stainless Steels

Takahiro Ishizaki

1. How do these increases in mechanical properties compare to the Petch Equation?
2. Please comment more the statistical treatment and the results, what data did you use?
3. It is stated in bullet point 3 that the crack initiation resistance of the ODS steel was higher than 316L. However, based on your cracking results, it looks like

there are many more cracks in the ODS steel. Therefore many more cracks are initiated in the ODS steel, which would mean that the ODS steel is MORE susceptible to crack initiation. Have you looked at all into crack density measurements or fraction of grain boundaries which are cracking in the ODS steels compared to 316L or at what orientation of grains where cracks are forming like at random high angle boundaries?
4. On point 4: Due you have any plans to test the IASCC resistance following the irradiation, as thus far I believe you have examined the change in RIS, not necessarily the change in IASCC susceptibility after irradiation.

Session: Irradiation Damage—Swelling

Formation of He Bubbles by Repair-Welding in Neutron-Irradiated Stainless Steels Containing Surface Cole-Worked Layer

Masato Koshiishi

1. How did you measure your He concentration? Is it just based on calculation?
   a. He concentration was measured by the mass spectrometry at PNNL.

Emulating Neutron-Induced Void Swelling in Stainless Steels Using Ion Irradiation

Cheng Sun

1. Was the ion beam defocused or raster scanned?
2. What was approximate dpa rate of the used beam?
3. Were the $M_{23}C_6$ carbides found primarily in the grains or at grain boundaries?
4. Any correlation of voids with carbides in CG steels?
5. Given the data for the tempered martensite, the fit curve does not seem to fit the swelling response very well. Is this due to the lack of data points or is the behavior of the tempered martensite significantly different from the delta-ferrite?

Void Swelling Screening Criteria for Stainless Steels in PWR Systems

Sarah Davidsaver

1. What is the incubation dose from the model?
   a. As can be seen on this slide, at 320 °C there is not one.

Theoretical Study of Swelling of Structural Materials in Light Water Reactors at High Fluencies

Stanislav Golubov

1. Could you, please, specify in more detail the phenomenon of the "residual gas" in the material in therm of its origin? What sources of that gas can be expected. Do you have suggestions for mitigation of residual gas effects to void swelling in therm of development of more swelling resistant alloys?

Tuesday, August 15, 2017

Session: PWR Nickel SCC—Initiation—Part II

The Effect of Surface Condition on Primary Water Stress Corrosion Cracking Initiation of Alloy 600

Sonya Pemberton

1. Just to be clear, the specimens were first CW 15% and then machined. Correct?
   a. That is correct.
2. What size of "initiation crack" you compare in the graph?
   a. We think the cracks are 100–200 μm deep when we detect initiation by DCPD (the times plotted). After the test cracks are millimeters long on the surface up to about half way through the specimen ($\sim$2–3 mm) if we see specimen failure. The longer we grow the crack after DCPD detected initiation, the larger the crack we measure after the test.
3. Will you also be testing as-annealed condition along with the lower levels of cold work?
   a. We are currently testing with no cold work for one test with abusive machining (replica of machining conditions used for Test 5) to see if we can get initiation at low strains from machining damage alone.

Microstructural Effects on SCC Initiation in Cold-Worked Alloy 600 in Simulated PWR Primary Water

Ziqing Zhai

1. Can we relate initiation time to 'block' location?
2. Was it possible that the two samples had the "same" initiation time of the large grains that you mentioned, but the large grain that went into the surface

promoted other cracking in the other surrounding smaller grains in that specimen?
3. Examinations were performed in the past on steam generator divider plates where scc initiated, but large grain boundaries were not reported as preferential initiation sites. So, I don't think that de can conclude that a duplex grain size always promotes SCC.
4. Tests and crystal plasticity calculations on A600 with duplex grain size were performed at EDF. They revealed that stress concentrations can be reached at the large/small grains interfaces due to different mechanical behaviors in tension: only one slip system active in the large grain, several systems active in the small grain. This could explain why you observed more IGSCC at large grain boundaries.

Session: PWR Nickel SCC—Aging Effects

A Kinetic Study of Order-Disorder Transition in Ni–Cr Based Alloys

Baptiste Stephan

1. Can you comment on the starting condition of your alloys? Previous work has indicated that cooling rate (water quenching vs. furnace cooled) has a significant effect on the nucleation time and apparent activation energy for hardening via ordering.
   a. Our alloys were air cooled so the ordering starting times should be between furnace cooled and water quenched alloys. But it will be very difficult to compare directly with your results as the composition (traces elements) is a bit different between your alloys and ours. It seems that our ordering incubation times are longer than yours with furnace cooled alloys (I have to check the details) and I find it quite surprising.
2. Is iron the only parameter driving ordering kinetics?
   a. No, lots of parameters are important such as: thermal treatment, cold work and traces elements in your alloy
3. F. Vaillant proposed much lower Q values ($\sim$80 kJ/mol) in prior work. Can you explain the differences with your results?
   a. I think F. Vaillant worked with water quenched materials and made assumptions on activation energies (but I have to check). In this work we have an apparent activation energy that is much higher and it certainly comes from the thermal treatment (air cooling) that was used.
4. Do you believe that the conclusion that iron does not affect ordering below 425 °C, drawn from alloys with 3% max Fe, will hold valid for higher more

realistic Fe levels? Do you plan to perform work on materials with higher Fe content?

a. DSM, your question is very interesting, a strong hypothesis we've made is that we will have the same activation energies and pre-exponential factors for the 0–3% Fe range and the 3–10% range. Of course we cannot be sure of that. We are not planning to work on model alloys with higher Fe content but we will compare our results with 690 data made by Delabrouille. My feeling is the pre exponential factor (so ordering incubation times at low temperature) will be influenced by alloying elements and not by Fe content but it has to be verified.

5. What is the level of confidence in the extrapolation? This seems a very optimistic result, and although it may be the median extrapolation, one ought to consider a lower confidence limit. Of course, your "aging in progress" tests will help to validate the extrapolation.

a. For now, the level of confidence is very low, meaning that we have a big error associated with the 3 million h incubation time result. So yes, this is very optimistic (all the hypothesis we've used and how the extrapolation is done are given in the proceeding), the most critical parameter that we have to calculate is log A: an error of plus or minus 2 gives you an error of plus or minus 2 orders of magnitude in the ordering incubation time! So this parameter has to be precise first.

The Role of Stoichiometry on Ordering Phase Transformations in Ni–Cr Alloys for Nuclear Applications

Fei Teng

1. EDM cutting introduces little stress, but mechanical polishing can leave some residual stress. Do you think this could have had an effect on phase transformations and hardening?

a. Yes, mechanical polishing will leave residual stress, but it will not have phase transformation and hardening effect. This can be proved by diffraction pattern of TEM. In nanoindentation data, we didn't observe any hardening effect from polishing.

2. Very interesting result, so it means that ordered domains are not purely stoichiometric (Ni_2Cr composition). Will you take that in consideration in your first principle calculations?

a. Theoretically, ordered phase should be purely stoichiometric (Ni/Cr=2 ere), however, it seems Ni and Cr have different evaporation rate in APT, which causes the variance in composition. For this reason, I may not consider this into first principle calculation.

3. The phase fraction reported is much higher than the measured/observed phase fraction by TEM. How do you propose to address this in your model?

   a. The biggest reason for the difference is that modeling result includes both short range ordering and long range ordering. Also, the size of sample in modeling is still small (about one single precipate size). In future, we plan to increase the modeling size and add a cutoff on cluster that can be considered as LRO. After that adjustment, the two result should be closer.

4. Do you have plans to address "material" issues on the low-temperature ordering kinetics using your model? For examples, effects of cold work and excess vacancies would be interesting.

   a. Yes, we do. Actually that is our final goal that we want to do by using FEM based model MOOSE. In future, we are trying to model an SCC specimen in MOOSE and once we reach that point we can try to add other effect such as cold work and excess vacancies into the "specimen" and see their effect. But this is still a long time plan, and we are still trying to push the model forward.

The Effect of Hardening via Long Range Order on the SCC and LTCP Susceptibility of a Nickel-30Chromium Binary Alloy

Tyler Moss

1. Could you please tell the reference for your last bullet here?

   a. [11] W.J. Mill, C.M. Brown, M.G. Burke, "Fracture Behavior of Alloy 600, Alloy 690, EN82H Welds, and EN52 Welds in Water" (Report B-T-3303 Bechtel Bettis, 2007)

2. How do you determine your blunting line for J calculations given the changing mechanical properties as a result of ordering?

   a. See a description of the method here: W.J. Mill, C.M. Brown, M.G. Burke, "Fracture Behavior of Alloy 600, Alloy 690, EN82H Welds, and EN52 Welds in Water" (Report B-T-3303 Bechtel Bettis, 2007)

3. By faceted IG, do you mean that the cracking is mainly IG with some TG facets or what? Also, did you do any higher magnification fractography? It would be very interesting to see the fine morphology of the fracture surface in order to get an idea on the mechanism for the decreased fracture toughness. Do you already have an explanation for the increased LTCP susceptibility?

   a. There is a mixture of IG and cleavage TG fracture in the aged sample. The mechanism may be linked to enhanced planar slip interaction along grain boundaries, enhancing the hydrogen embrittlement.

PWSCC Initiation of Alloy 600: Effect of Long-Term Thermal Aging and Triaxial Stress

Seunghyun Kim

1. If the primary effect of the 400 °C aging is precipitation of grain boundary carbides, why would there be an increase in the bulk yield stress?
    a. According to the calculation result from orowan mechanism, yield stress and ultimate tensile strength could be increased due to precipitate morphology changes during thermal aging. Alloy 600 has low residual stress, therefore, precipitate hardening might be the most significant factor that could make some difference in mechanical property.

Stress Corrosion Cracking of Alloy 718 Subjected to Various Thermal Mechanical Treatments in Primary Water

Mi Wang

1. What is the driving mechanism for dissolution of the delta-phase precipitates?
    a. We don't have a clear explanation yet. We think that the delta phase become very brittle after it get oxidized in primary water. With the applied stress and a plastic deformation to 4%, it can easily dissolve into water. On the other hand, if the delta phase doesn't get oxidized, like in Ar gas, even with the same the stress and strain level, the delta can still stay at their locations.
2. Recent work was performed by AREVA and INL on fuel springs and delta phase, which if you have not reviewed it yet, I suggest you do.
3. A clarification: In your second conclusion, did you really mean to claim insensitivity to heat treatment within Group I or should this only be insensitivity to cold work?
    a. It is insensitive to chemical composition (two heat, normal and optimized) and to the cold work within the ranges studied.

Time to Fracture Studies of Alloy 718 in PWR Chemical Conditions with Neutrons

Joseph Long

1. Any idea how deep the IG attack is? Are they cracks or surface? The scale of the features here seem to be smaller than the grain size suggested by the next slide. Is this instead some fracturing of an oxide film?
    a. We don't know how deep they are. Some of them could be quite shallow. On the other hand, it seems implausible that there would have been only a few

regions of intergranular attack that were nearly co-planar, but there were no others of significant depth

2. Was metallography performed on the samples prior to irradiation to determine presence (or absence) of delta precipitates?
   a. It was not and that would have been beneficial. Material of the same alloy and heat treatments, though not the same heat, is available and could be put under a TEM.
3. Did you see and evidence of low temperature crack propagation during shut-down and startups?
   a. Not that I'm aware of, although I'm not sure what that would have looked like. For this alloy, even PWR conditions are below its intended service temperature.

Development of Short-Range Order and Intergranular Carbide Precipitation in Alloy 690 TT upon Thermal Aging

Hannu Hanninen

1. I'm a bit surprised that you suggest a grain size reduction due to TT and I can't imagine a mechanism for this. Can you elaborate?
2. Considering the prior SA+TT at much higher temperatures, why is a recovery process proposed during the thermal ageing? Is this related to the grain growth that is occurring? Actually, it is also unclear to me why grain growth would be occurring.

Session: Irradiation Damage—Nickel Based and Low Alloy

High Resolution Transmission Electron Microscopy of Irradiation Damage in Inconel X-750

Colin Judge

1. What is the effect of gamma irradiation versus neutron irradiation?
   a. Not that I'm aware of, although I'm not sure what that would have looked like. For this alloy, even PWR conditions are below its intended service temperature.
2. Did you observe IG cracking? Was this room temperature or elevated temperature? What is the effect of gamma prime disordering on strength?
   a. We observed entire IG cracking. The testing was performed at room temperature, but we did confirm that testing at the irradiation temperature also resulted in IG cracking. Gamma prime disordering will lead to softening of

the material, which is counter balanced by hardening by loops and bubbles. The net result is no significant change in hardening of the material.

3. What is the effect of hydrogen? Are you planning to do APT?
   a. Hydrogen is expected to contribute to embrittlement, but is difficult to identify the contribution. APT has been attempted on material with bubbles, but leads to difficulty in the reconstruction at the bubble locations.
4. What was the heat treat and have you looked at the effect of heat treatment?
   a. Solution treatment at 1093–1204 °C (no hold time specified), and precipitation hardened at 732+/−14 °C for 16 h, followed by air cooling. The effect of heat treatment was not considered in this investigation.

In Situ SEM Push-to-Pull Micro-Tensile Testing of Ex-Service Inconel X-750

Cameron Howard

1. What was the orientation of the tensile specimens relative to the spring coils?
   a. All tests performed at UC Berkeley were done such that the tensile loading direction was along the azimuthal direction of the springs. This is due to the fact that sample preparation methods polished the components so that they were mounted in a "C" shape shown in the slide.
2. It is stated that the strain rate used for these experiments is on the order of 10^{-3}. Is it possible to run the experiment slower, to be similar to the rates used in stress corrosion cracking slow strain rate tests ($\sim 3*10^{-7}$)?
   a. I believe the slowest displacement controlled loading rate for the Hysitron instrument is on the order of ~ 5 nm/s, which would get the strain rate down to $\sim 10^{-4} \times 10^{-7}$ strain rates would require specimens on the order of 1–10 mm with this set up which are too large. However, loading can be paused such that any specimen remains under any desired constant load to perform creep-like tests.
3. Did you test different specimen sizes to determine effects of surface/ other side effects? Any attempts to use Hysitron's high T stage?
   a. He implanted tensile specimens on the order of 5 μm × 5 μm × 20 μm have been tested in a parallel study. Size effects appear to be minimal in non-irradiated specimens. High temperature tests at reactor operating temperatures using the PI 88 are considered as future work.

Microstructural Characterization of Proton-Irradiated 316 Stainless Steels by Transmission Electron Microscopy and Atom Probe Tomography

Yun Soo Lim

1. Do you have any further plans to better characterize the Ni–Si solute clusters? i.e. size, density, and composition?
   a. Yes, we do. We are planning to get more quantitative data on the size distribution, number density and so on of Ni–Si clusters.
2. Did you (or are you going to) analyze the clusters/precipitates in TEM? Have you observed the clusters in form of crystals in TEM dark-field images?
   a. We tried to find clusters/precipitates in TEM. But we couldn't identify the spots or streaks originated by them in the diffraction pattern yet, possibly because they are very small or TEM conditions are not fit well. We'll continue to analyze them by TEM.
3. Consumed metal weight due to corrosion is a sum of weight loss and total oxide film weight.
   a. Yes, you are right.
4. Depending on actual material and coolant condition, oxide film thickness or weight loss alone could not define how much a metal corrodes and one cannot compare the degree of corrosion of two samples by using such a rate data. Therefore, it could be problematic to define corrosion rate by ignoring the oxide film weight.
   a. Before we measured the corrosion rate of a specimen, the specimen had been immersed in an undiluted HCl solution for about 1 min to remove the surface oxide film, therefore to get the corrosion rate of material itself.
5. Was the chemical polishing method used on the APT tips?
   a. No. We applied the chemical polishing only to FIB TEM specimens.
6. Is the ion milling condition enough to polish FIB damage? In my case, longer treatment is done.
   a. I'm not sure whether the ion milling mentioned is the optimum condition or not. We tried it for longer periods such as 20 and 30 min. But, we couldn't get better results. Therefore, we suggested a possible method, called chemical polishing, to remove FIB damage.

Session: PWR Oxides and Deposits

Irradiation Accelerated Corrosion of Stainless Steel in Simulated PWR Primary Water

Rigel Hanbury

1. The amount of hydrogen did not seem to suppress the radiolysis so hematite was formed. Why was that?
   a. Radiolysis is suppressed by hydrogen since the dissolved oxygen content of the outlet stream is below detectable levels. Due to the high dose rate of the proton beam, many radiolysis products achieve a concentration high enough to affect the ECP before they can be scavenged by the hydrogen.
2. In this study, you evaluated variability in oxide thickness for in situ irradiated material and unirradiated material. Have you looked at the variability in oxide thickness in specimens that were irradiated under vacuum and then exposed to an aqueous environment to isolate the role of the irradiation induced microstructure versus radiolysis on the oxidation behavior of the material?
   a. In this study, we have no plans to perform an ex-situ irradiation and subsequent corrosion. In the 15th Environmental Degradation conference, Jiao and Was submitted a paper finding no significant difference in oxide thickness between 5 dpa and unirradiated 316. At a final damage of 0.06, we do not expect the irradiation-induced microstructure to impact the oxide thickness or general corrosion behavior.

Finite Element Modelling of CRUD Deposition in PWR

Jiejie Wu

1. For a particle to deposit and stay at the surface, the shear stress on the particle plays a role. Which one is more dominant, the electrical or mechanical force? (I notice the very high flow velocity you used in the model)

Session: General SCC and SCC Modeling—Part II

Protection of the Steel Used for Dry Cask Storage System from Atmospheric Corrosion by TiO_2 Coating

Jing-Ru Yang

1. Has carbon steel been selected as the dry cask material for spent fuel storage in Taiwan?

a. In Taiwan, dry storage systems were used Stainless Steel as components. In our research, we tried to obtain slower increasing of electrochemical corrosion potential for carbon steel after stopping UV illumination. Thus, it can cost down for construction of dry storage system. This is the reason why we select carbon steels as materials for this research.

Predictive Modeling of Baffle Former Bolt Failures in Pressurized Water Reactors

Gregory Banyay

1. Is type 347 in an annealed or cold worked condition?
   a. Type 347 bolts are annealed.
2. What if the reason for the different behavior between plants using 316 and 347 bolts?
   a. Bolts made from 316 have one head type and bolts made from 347 have a different head type, so it's really the combination of material and head design/type which constitutes the difference in terms of bolt reliability.
3. Any indication whether certain heats are more susceptible to IASCC than other heats?
   a. No particular indications pertaining to heats, in and of themselves … it's really the bolt design that influences the susceptibility to IASCC.
4. What differentiates 3 Loops from 4 Loops? Is the stress which has been calculated in the FE model?
   a. Stress computed from the finite element model significantly influences the differences in behavior shown here between 3-loop and 4-loop designs.
5. The stress decreases with time because of irradiation induced stress relaxation. What triggers the onset of cracking?
   a. The Weibull scale (characteristic life) is affected by not only stress but also dose. Also, the stress relaxation only applies to the loss of preload; the bolt still has to bear the pressure-loading and so the stress remains fairly high even after the preload is relaxed. Also, the preload relaxation is somewhat asymptotic.
6. Are these predictions material specific e.g. 347 SS versus 316?
   a. The predictions are specific to a given bolt design at a given plant. No specifics pertaining to which bolt or which plant are provided in our conference paper in order to protect intellectual property, etc.

7. Does this figure represent replacement of all BFBs? Or inspection of all and replacement of some?
    a. This represents replacement of all failed BFBs. So it's interesting to observe that the 95th fractile predicts a non-negligible proportion of bolts would fail in the time step immediately following the "re-start"; these would be the original bolts that would have failed had the simulation been carried along to the next time step (i.e., another fuel cycle or so).

Technical Basis and SCC Growth Rate Data to Develop SCC Disposition Curve for Alloy 82 in BWR Environments

Katsuhiko Kumagai

1. Briant and Hall showed that 182 and 82 can undergo precipitation reactions during PWHT, which tends to increase the yield strength. It would be valuable to have more data on YS effects of PWHT on various welds and heats.
2. How do you explain point C fracture surface?
3. Is PWHT used in Japanese units?

Session: Special Topics II—Processes

Investigation of Pitting Corrosion in Sensitized Modified High-Nitrogen 316LN Steel After Neutron Irradiation

Diana Merezhko

1. How much material has been produced?

Erosion-Corrosion Impacts on Light Water Reactor Piping

Consuelo Guzman-Leong

1. What pipe configurations were addressed by the geometry factor?
    a. Based on literature reviews, geometry factors were determined for the following configurations: "T" pipe junctions, pipe bends, pipe constrictions, expansions, concentric reducers, and blinded tees.

2. The chloride concentration in the solid-liquid mixtures considered in developing the erosion-corrosion model was asked.
   a. Test data that was used in the modeling included solutions having chloride concentrations between ~ 2 and $\sim 150{,}000$ ppm.
3. Were HX tube fouling effects considered in the modeling?
   a. Fouling impacts on the tube velocity were not considered. It is anticipated that fouling may cause velocity increase, which would lead to an increase in wall thinning rates. Fouling effects on wall-thinning rates would be a great topic to investigate in future modeling efforts.
4. Was pressure of the piping factored into the prediction of the probability of exceeding the user-defined wall thickness?
   a. Minimum wall thickness requirements as prescribed in ASME Section III are not embedded in the probabilistic calculations. The investigator would need to consider ASME code-specified minimum wall thickness requirements when selecting the wall thickness (a user-defined input) to be analyzed by the probabilistic erosion-corrosion model.
5. Was overall conductivity (e.g. contribution from impurity ions) of the coolant considered in the Corrosion Model, in addition to pH?
   a. Although a range of test data covering a range of alkaline and acidic solutions (with and without abrasives) was considered in the modeling, the conductivity of these solutions was not a parameter that was assessed in the modeling.

Effect of Molybdate Anion Addition on Repassivation of Corroding Crevice in Austenitic Stainless Steel

Shun Watanabe

1. For a future application in a nuclear reactor RPV, for how many hours or days have you to apply the MoO_4 solution at 50 °C?
   a. The necessary time frame depends on molybdate concentration and potential of metal. If you add ten times more molar concentration of molybdate ion to chloride ion when the potential is as high as 200 mVSCE, for instance, about ten hours are required to repassivate a corroding crevice.

Wednesday, August 16, 2017

Session: PWR Nickel SCC—Alloy 60 Mechanistic

Diffusion Processes as a Possible Mechanism for Cr Depletion at SCC Crack Tip

Cecilie Duhamel

1. In PWR, where does "O" come from? Do you mean oxygen in water molecule that gets incorporated into oxide film (as described by PDM point defect model)?
   a. Yes, this is the oxygen coming from water molecule.
2. More a comment than a question: the trend line shown for 500 °C suggests that the ratio of Deff to Db becomes less than 1 at low strain rate. The actual data on the other hand seems to show an asymptotic approach to 1 at low strain rates. It would thus seem appropriate to show a non-linear trend line that reflects this.
   a. Actually, we would need more data at the lowest strain rates to have a better description of the strain rate dependency of the diffusion coefficient. However, our belief is that there's a kind of «threshold» strain rate (which is temperature-dependent) below which we don't have any more effect of dislocation motion on diffusion rather than an asymptotic trend. But again, this needs to be confirmed.
3. Do you assume the oxide film growth as parabolic w/time (kc used here)? Should not it be log(t)?
   a. Yes, we assumed here a parabolic film growth based on the literature data from Lefaix et al., Corr. Sci (2011) on surface oxidation of Alloy 600 in primary water. In addition, the time we consider in our modeling (6000s) is too short to reach an asymptotic regime.
4. The driving force for GB migration under vacuum is the formation of a surface Cr oxide. How good was your vacuum? You must have oxide formation. In our work carried out in H_2 environment where no oxide formed we never saw GB migration.
   a. The vacuum was around 10^{-7} mbar. With this vacuum condition, the oxygen partial pressure is still high enough to allow chromium oxide formation at the surface. Actually, the driving force for DIGM is grain boundary diffusion of Cr that diffuses to get oxidized at the surface.
5. Nice presentation. This work does a very good in explaining the observations of Cr depletion ahead of SCC tips. Is the presence of Cr depletion ahead of SCC necessary for crack advance? We have observed Ni enrichment ahead of cracks more frequently in slow growing/arrested SCC and have not observed Ni enrichment in fast growing cracks.

a. The motivation for our present work is based on previous studies on TEM characterizations of various SCC crack tips (Sennour et al, JNM 2009). In this study, it was shown that the asymmetric Cr_2O_3 formation, coupled with the asymmetric Cr depletion, was characteristic of what were supposed active cracks.

Role of Grain Boundary Cr_5B_3 Precipitates on Intergranular Attack in Alloy 600

Daniel Schreiber

1. Have you looked at any of the other B&W heats for this type of precipitation? (That is, those with high CGRs and those with lower CGRs?)
2. It would be interesting to complement this with a look as SG tubes, which have C on the order of 0.02%. I don't recall seeing any analyses related to boron or borides for these.

Exploring Nanoscale Precursor Reactions in Alloy 600 in H_2–H_2O Vapor Using In Situ Analytical Transmission Electron Microscopy

Giacomo Bertali

1. The largest difference that may occur to oxide film when exposure is done in vapor versus in liquid water is the fact that, in liquid water, oxide dissolves quickly in water and oxide composition may become very different than in gaseous corrosion. How do you account for that difference?

Electrochemical and Microstructural Characterization of Alloy 600 in Low Pressure H_2-Steam

Liberato Volpe

1. In steam, oxide film builds up without release of metal cations from oxide as it does in coolant environment. How is this considered in your experimental design?
   a. The oxidation behavior in water and in steam are different, and for this specific reason the preferential intergranular oxidation behavior (which is believed to be responsible for SCC) was investigated in hydrogenated steam and compared with the phenomenology reported by Molander et al. in water. A good correlation between the two was identified.

2. This reaction system is a kinetically controlled. The transition mentioned here seems to refer to a thermodynamic system. How do these two phenomena come together?

    a. It is correct to say that the oxide penetration is kinetically driven and that changing the hydrogen to steam ratio changes the thermodynamics. However, the purpose of this investigation was to understand how the oxidation kinetic varied at different redox potential.

3. The work by Molander (Studsvik) was done in simulated PWR coolant, which is very different environment than in steam with regard to how oxide dissolution in coolant versus being built up without release in your system.

    a. A good correlation was identified between the work by Molander et al. in water and the extent of oxide penetration measured by FIB. This similarity therefore suggests that the hydrogenated steam we employed produce results that are relevant to PWR conditions.

4. Was there greater external film oxidation in the NiO regime?

    a. We are still analyzing these coupons and currently we haven't yet all the data, however we expect a thick oxide layer in the most oxidizing environment.

Effect of Dissolved Hydrogen on the Crack Growth Rate and Oxide Film Formation at the Crack Tip of Alloy 600 Exposed to Simulated PWR Primary Water

Jiaxin Chen

1. This plot is not comparing constant load with constant load. If I understand the presentation correctly the CL could not be measured at higher hydrogen as issue with measuring crack progression, i.e. it is slower. This was also not measured during a single test with hydrogen variation, which is how the other data has been produced. Happy to discuss.

A Mechanistic Study of the Effect of Temperature on Crack Propagation in Alloy 600 Under PWR Primary Water Conditions

Zhao Shen

1. Has anyone else reported a peak for 690?

    a. Thank you for your question! By far I didn't find a peak for Alloy 690 IN THE open journal. I think this might be because this experiment is very time consuming and to see the peak you need to do a series of experiments. Actually, Arioka has done a series experiments in order to understand how

the extent of cold work affects the peak position and he found the peak for all of the Alloy 690 with different extent cold work but with different peak position.

2. The values for oxygen: are the error bars from software output only? How did you succeed in avoiding the inclusion of metal part when you approached the oxide/metal interface?

   a. Thank you for your question! The error bars are not only come from the software measurement but also include the part from statistical errors since the chemical composition in the Cr-rich oxide is averaged from all of the tested crack tips. As to how to avoid the metal part, I found it's not very difficult in this study because the size of the Cr-rich oxide ahead of the crack tips was relatively big, which makes it not very difficult to separate the oxide from the metal.

3. You mentioned some difficulties in the used TKD technique (time consuming …). Did you considered to use the STEM precession electron diffraction technique and its benefits to analyze the local strain around the crack tips?

   a. Thank you for your question! I said if you want to measure the absolute dislocation density, it's very time consuming, but we only measure the deformation intensity, which is much easier and convenient. I think the most difficult part for the TKD, it's not the technique itself but the sample preparation, which requires the sample thickness to be around 50–70 nm and without obvious bending. My samples have been 20% cold worked so it's very easy for them to bend during the fib milling and that's why I mentioned that I have prepared even more than 10 crack tips for each specimen but only 3 or 4 of them can work. If there is obvious bending in the thin TEM sample, we cannot measure the very localized plastic deformation zone. As to your mentioned STEM precession electron diffraction technique, I have read a paper about this technique from Manchester. Yes, it's very interesting but I think it's also very time consuming. If we don't mind the time I still think the HRTKD might be more appropriate. But for my work, I don't need to get the absolute dislocation density, I just need to get relative value which is far more than enough in my work.

Session: PWR Nickel SCC—Alloy 690 Mechanistic

Grain Boundary Damage Evolution and SCC Initiation of Cold-Worked Alloy 690 in Simulated PWR Primary Water

Ziqing Zhai

1. High, moderate, low: could these be more quantitative?

PWSCC Susceptibility of Alloy 690, 52 and 152

Takaharu Maeguchi

1. These long term Alloy 690 and EN52 tests are showing the excellence SCC resistance of these materials. Results are also suggesting that the possible degradation modes of LRO and void formation are insignificant. Have you or are you planning to perform characterization work to confirm the lack of LRO and void formation in the test specimens.

Relationship Among Dislocation Density, Local Strain Distribution, and PWSCC Susceptibility of Alloy 690

Hong Pyo Kim

1. Why isn't the dislocation density in the grain interior changing between 20 and 40% thickness reduction? I would expect that the density would be much higher by 40% CW.
    a. Dislocation density in grain interior increases with increase in thickness reduction from 20 to 40%. But dislocation density near grain boundary decreases with increase in thickness reduction from 20 to 40% due to generation of twinning near grain boundary at 40% thickness reduction. Please see slide 17.

Morphology Evolution of Grain Boundary Carbides Precipitated Near Triple Junctions in Highly Twinned Alloy 690

Hui Li

1. How did you characterize the misorientation angle in the APT needles?
    a. I use EBSD to characterize the misorientation angle of the grain boundaries. And then use FIB to prepare the APT needle samples containing typical grain boundary.
2. Is 15 °C a typographical error on this slide? Should it be 715 °C?
    a. Yes, it should be 715 °C.

The Mechanistic Study on the Stress Corrosion Crack Propagation for Heavily Cold Worked TT Alloy 690

Toshio Yonezawa

1. Data from Dr. Arioka are 16%Cr. Could you comment on a reason why 16%Cr without carbide have low CGRs than 26%Cr with carbide?

a. In Arioka et al's paper, detail material characterization data and crack growth rate monitoring were not reported. So, I cannot explain the correct reason, but these materials should be without GB carbides and relatively soft materials. These factors must be affected on SCC growth rates.

2. The slide indicates that the stress is not influence to the formation of cavities. Are there any possibility that stress gradient is more important than stress?

   a. In this paper, we denied the possibility of creep damage for PWSCC mechanism. Creep damage is well known to be stress dependency, not stress gradient. If you would like to the effect of stress gradient on SCC mechanism, you had better.
   b. In this paper, we denied the possibility of creep damage mechanism for PWSCC. Creep damage is well known to be stress dependency, not stress gradient. If you would like to explain the effect of stress gradient, it is better not to persist to creep mechanism.

Session: PWR Stainless Steel SCC and Fatigue—SCC—Part I

Microstructural Effects on Stress Corrosion Initiation in Austenitic Stainless Steel in PWR Environments

David Tice

1. With regard to the different cracking behavior observed between tests B1 and B2, do you believe that this is just due to the difference in strain, or may there have also been an effect from the changes in strain rate.

   a. I think the level of strain is dominant. we have repeated test B1 at 2E−8 s^{-1} and see similar behavior.

2. Given that you saw worse cracking in the OPS polished case, would you think that polished surfaces would be worse than ground surface in plant in the absence of dynamic strain?

   a. For long term exposures, probably not. The thin outer layer is rapidly consumed by oxidation. TG initiation can occur in the heavily deformed layer below and could eventually produce IGSCC after intersecting a grain boundary. However, it is difficult to extrapolate SSRT to plant loading conditions although there have been attempts to do so. See paper by J Bai et al ("The use of tapered specimens …") in Weld session (Wed 1:20 PM) at this conference.

3. What is the min value of stress that allowed you to observe cracking?

   a. SCC occurred for plastic strains above about 3%, increasing significantly at 5% stain. This corresponds to about 600 MPa in this work hardened material.

Oxidation and SCC Initiation Studies of Type 304L SS in PWR Primary Water

Fabio Scenini

1. Is there any influence of the thickness of the fine grain surface layer on initiation?
   a. This is something that we have not investigated. However we would expect that it would have an effect in real plant exposures.

SCC Initiation in Stainless Steels with Machined Surface in PWR Primary Water

Litao Chang

1. Do you mean that oxidation kinetics is increased in presence of ultra-fine grains at the surface?
   a. Yes, the oxidation kinetics was increased with the presence of ultra-fine grains. The inner oxide layer on the machined surface is thicker than that on the finely polished surface.
2. Have you tested specimens with the grinding marks are parallel to the tensile stress? I would expect the susceptibility to be remarkably smaller than in a case when the marks are perpendicular to the tensile stress.
   a. No, I did not test one sample with marks parallel to the loading direction.

Session: BWR SCC and Water Chemistry

SCC of XM-19 in 288 °C BWR Water and J-R Response in 288 °C Air

Peter Andresen

1. What is the motivation for SCC CGRs for XM-19? What kind of component do you have a concern?
   a. The primary interest is for shroud repair components, which use a combination of Alloy X-750 and XM-19. The XM-19 is a long bar that is exposed to various water chemistries and fluencies.

2. Action level 1 for sulfate is 5 ppb. We recently revised Action level 1 chloride from 5 to 3 ppb based on CGR studies. Have your studies included sulfate levels below 10 ppb?

   a. In these studies, we only examined the effect of 10 and 30 ppb sulfate (vs. pure water). In many other studies, we have considered values ranging from 5 to >50 ppb chloride or sulfate on austenitic materials. Broadly speaking, tolerance to water chemistry depends strongly on the Cr content, and in our studies on Alloy 52/152 weld metals ($\sim$30% Cr), there was no effect of 2 ppm O_2 and 50 ppb chloride or sulfate (vs. hydrogenated water). For 15–20% Cr materials (304/316/600/182/82), there would be a significant effect of this chemistry, but little at <10 ppb sulfate or chloride. For heavily sensitized materials (say, 5% min Cr at the grain boundaries), the effect of chemistry would be greater. Low alloy steel (a ferritic material) has a number of differences compared to SS or Ni alloys, but—simplistically—at low Cr, it is more sensitive to water chemistry. Our work on 9 and 12% Cr ferritic steels showed much less effect of 5–10 ppb chloride that RPV steels.

On the Effect of Preoxidation of Nickel Alloy X-750

Silvia Tuzi

1. How does the pre-oxidized film change after operation in the reactor?

Microstructures of Oxide Films Formed in Alloy 182 BWR Core Shroud Support Leg Cracks

Jiaxin Chen

1. How did you estimate the age of the crack from this study?
2. Was the crack still growing? Or, stopped?

Effect of Chloride Transients on Crack Growth Rates in Low Alloy Steels in BWR Environments

Xiaoyuan Lou

1. Can you comment on the difference between the memory effects associated with stainless steels versus low alloy steels?
2. Are S levels for these materials corresponding to high S line? Or, low S line?
3. Is there an explanation for the increased activation times observed for low Cl levels at increased K levels?

Electrochemical Behavior of Platinum Treated Type 304 Stainless Steels in Simulated BWR Environments Under Startup Conditions

Chu-Yung Yuan

1. Do you have either Pt surface loading or Pt particle size-distribution for the treatments?
2. It appears you inject H_2O_2 directly into the autoclave, but how close to the specimens. H_2O_2 decomposes quite quickly, and it's unclear what the actual concentration is at the specimens. Isolating the specimens—e.g., in an internal chamber of Teflon—can help.
3. The ECP of Pt is always higher in O_2, so your results need to be accompanied by Pt loading or Pt particle-density data.

    a. The Pt loadings are:

        i. Pt-90 0.399 μg/cm^2
        ii. Pt-150 2.257 μg/cm^2
        iii. Pt-280 3.183 μg/cm^2.

4. The difference in polarization response in H_2O_2 is pretty subtle, and the curves might easily be extrapolated to the same ECP.

    a. We are still working on the analyses on H_2O_2.

5. Our extensive data in O_2, H_2, and H_2O_2—as single or mixtures—shows that even pure Pt never has a higher ECP than SS in relevant combinations. Looking at single oxidizing species is misleading.

    a. I specifically remember that some data reported by Yong Kim also showed an elevated ECP on a Pt treated sample in oxygen only coolant at 288 °C. I think our data are consistent with what the catalysis theory predicts. However, I do agree with you in that in a solution with mixed O_2, H_2O_2, and H_2, elevated ECPs may not be easily observed.

6. What was the Pt loading per unit surface area at the three temperatures?

    a. The Pt loadings on different samples

        i. Pt-90: 0.399 μg/cm^2
        ii. Pt-150: 2.257 μg/cm^2
        iii. Pt-280: 3.183 μg/cm^2.

7. We have also done polarization analyses on electrochemical behavior of H_2 on Pt-treated samples, but the results have been presented in the past. We did not do analyses on other redox species because their concentrations are comparatively small.

Investigations of the Dual Benefits of Zinc Injection on ^{60}Co Uptake and Oxide Film Formation Under Boiling Water Reactor Conditions

Samuel Holdsworth

1. How dose Zn make an influence on SCC resistance of 316L SS?
2. Do you expect to see any benefit of polishing on Co uptake in HWC + Zn samples?

SCC Mitigation in Boiling Water Reactors: Platinum Deposition and Durability on Structural Materials

Pascal Grundler

1. Were all three exposed at the same time, and in proximity to each other? We have not observed as large of a difference.
   a. All three specimens were exposed during the same test (#I) at the same Location, e.g. the autoclave (see slide 5).
2. The upper graphs for the three materials are not as dramatically different as the lower graphs. Perhaps more statistics are needed.
   a. Of course the evaluation of more micrographs to have a higher number of particles to analyze is always desirable. However, the data sets presented here are large enough to provide reliable information.
3. What is the effect of flow rate on Pt deposition based on your data?
   a. Once corrected for the different amounts of Pt injected in the two tests, there is a trend towards higher loadings with increasing flow velocity in the specimen holders.
4. What might the effect of the oxide space charge layer on Pt deposition? Earl Johns.
   a. I would expect the Pt to preferentially deposit on the positive side of the layer, the n-doped side of the p–n junction.

Session: Stainless Steel Aging and Class

Influence of δ-Ferrite Content on Thermal Aging Induced Mechanical Property Degradation in Cast Stainless Steels

Thak Sang Byun

1. Were you able to determine the reason for the wide range of scatter in the data?
    a. The tensile samples used were SS-3 design with gage section dimensions of 0.75 mm × 1.62 mm. Only a few to several grains are through the thickness. I believe this small specimen geometry and highly inhomogeneous microstructure caused the significant scattering.

Microstructure and Deformation Behavior of Thermally Aged Cast Austenitic Stainless Steels

Yiren Chen

1. Delta ferrite has a higher Cr content, but because it has a much higher Cr diffusion rate it lead to higher Cr depletion during sensitization heat treatments.
    a. The diffusion rate of Cr is much higher in the delta ferrite, which is the reason of a shallower Cr-depletion profile on the ferrite side of the phase boundary (compared to that on the austenite side). This is one of several mechanisms used to explain the better sensitization resistance exhibited by the ferrite/austenite dual-phase microstructure.
2. Did you do any tests as a function of aging time? i.e. less than 10 k h
    a. Not at this point. But, we are planning for additional tests on specimens with different thermal aging conditions.

Effect of Long-Term Thermal Aging on SCC Initiation Susceptibility in Low Carbon Austenitic Stainless Steels

So Aoki

1. Did you look at the trace elements that may exist in these two alloys?
    a. No, I didn't. I must investigate further on the grain boundary segregations of trace elements such as P and S with atomic resolution by Three Dimensional Atom Probe (3DAP).
2. Did you use any more global measurement techniques to check for carbides/cr depletion? Or did you check a large number of GBs in your TEM foils?

a. No, I didn't either. I think further investigations would be necessary on the grain boundary by means of TEM or 3 dpa.

Effect of Thermal Aging and Low Dose Neutron Irradiation on the Ferrite Phase in 308L Weld

Yong Yang

1. How long was the duration during the neutron irradiation?
   a. About 4000 h.
2. What was the welding method?
   a. submerged arc weld.

Microstructural Evolution of Welded Stainless Steels on Integrated Effect of Thermal Aging and Low Flux Irradiation

Martin Bjurman

1. What was the welding method for the weld of the Zorita?
   a. The component was fabricated during the 60s, records are not available and the welding method is unknown. The weld geometry is an X-joint, 40 mm thick.

Session: Zirconium and Fuel Cladding

Corrosion Fatigue Crack Initiation in Zr-2.5Nb

Heidi Nordin

1. The oxide down the crack—how does it compare to oxide on the surface?
2. Question about water chemistry—you used heavy water, so wouldn't the hydrides be deuterides?
3. How thick was the oxide?
   a. The oxide on the sample was about 0.5 μm. Within the crack it was typically 0.2–0.5 μm except for the case of the pre-hydride specimen where blunting near the crack tip was observed. In this region the oxide is closer to 1 μm.
4. The corrosion study was done in heavy water, so the hydride observed in this study was deuterium?
   a. The corrosion testing was done in heavy water. In most cases, the deuterium pickup during the short duration of the tests was very low. For the pre-hydrided specimens, the solid phase observed would have been hydrides.

For the case were there was high deuterium ingress through the PD leads, technically the solid phase was deuterides. However, as explained in the paper, the terms hydrogen and hydrides refer to all isotopes of hydrogen and all solids precipitated once solubility has been exceeded, respectively.

5. For the pre-hdyrided sample, did the author see any evidence of "hydride"?
    a. For the pre-hydrided sample all the regions shown in red on the EELS images fro slides 13 and 14 were hydrides.

Cluster Dynamics Model for the Hydride Precipitation Kinetics in Zirconium Cladding

Donghua Xu

1. Do electropolishing induced hydrides have an even distribution throughout the sample (thick/thin regions, surface effects) and are they representative of 'real' hydride nuclei.
2. In the experiments, mentioned hydrides were artifacts from electropolishing. These should have been only on surface, if found in the sample, are they really artifacts?
3. If you look at experimental image, dislocations and stress field around hydrides. Are these in the model?

Modeling Corrosion Kinetics of Zirconium Alloys in Loss-of-Coolant Accident (LOCA)

Léo Borrel

1. What transport mechanisms are considered for through the oxide layer, and what uncertainties are considered?
    a. Hydrogen migrate in the oxide via interstitial. No complete uncertainty analysis has been performed yet.

Progressing Zirconium-Alloy Corrosion Models Using Synchrotron XANES

Michael Moorehead

1. Would the presence of hydrogen/hydrides affect the oxidation of either the base metal or the Nb particles? What might happen to a hydride near a growing oxide interface?
    a. I would not expect hydrogen to greatly impact the oxidation of Nb as Nb experiences delayed oxidation in comparison to the zirconium matrix

meaning that Nb oxidation occurs away from the oxide/metal interface where hydrides often form.

2. Do you think the presence of hydrides would have an effect on the oxidation of Nb (QA session)?

   a. See answer 1a above.

3. When you say the zirconium presence in beta-Nb ppts results in kinetic limits, what does that mean mechanistically (QA session)?

   a. Overall this isn't fully understood, but the idea is that since the location at which beta-Nb begins to oxidize in the ZrO2 layer is dependent on the oxide thickness, the oxidation of beta-Nb is not exclusively dependent on the oxygen gradient across the entire oxide—else it would occur at the same position in every case (say 30% the normalized oxide thickness). This may be caused by slower diffusion of oxygen through beta-Nb than the surrounding oxide which would mean that it's further kinetically limited.

Advanced Characterization of Hydrides in Zirconium Alloys

Sean Hanlon

1. During in situ TEM, can you comment on effect of electron irradiation on the hydrides?

   a. The accelerating voltage of 200 kV used in this study is well below the threshold voltage for displacement damage according to reference 8 in the paper. We therefore expect that the electron beam had no irradiation effects on the hydrides or the matrix.

2. Is there a change in the matrix from the electron irradiation?

   a. Same as above. An alternate reference is: Griffiths, M. "Displacement energies for Zr measured in a HVEM." Journal of Nuclear Materials 165.3 (1989): 315–317.

3. Is there a change in the matrix from the electron irradiation?

   a. Yes, the temperature of the sample was uniform during the 300 °C exposure; there were no temperature gradients present, which would significantly affect the hydrogen distribution. The hydrogen produced by corrosion was mostly in solution at the exposure temperature, with hydrides likely present only in the region very near the growing oxide layer.

4. Why was the hydride distribution non-uniform (QA session)?

   a. We have postulated that the tensile stress in the matrix below the growing oxide layer stabilizes a much higher concentration of hydrides than seen in the bulk of the sample, and/or shifts the solubility curve of hydrogen such

that hydrides are stable at much higher temperatures given a nominal overall hydrogen concentration. There are also complex thermodynamics occurring at the oxide-matrix interface that could affect hydride stability, but are beyond the scope of this work. Other than the small surface region (a few microns to a few 10s of microns the oxide interface) the hydride distribution appeared to be a uniform 10 ppm.

5. The FIB preparation can modify hydrides—what would you suggest to minimize this effect?

   a. We are still uncertain what part of the FIB preparation is the cause of this transformation. If local heating is the cause, a cooled sample holder, reduction of the beam current, or a modified lift-out technique that allows for better heat transfer would help minimize the effect. If the effect is due to irradiation damage or ion implantation then the accelerating voltage could be reduced or ion source changed. It is also possible that the transformation effect is due to proximity to the oxide rather than the FIB—this is the basis of ongoing investigations.

6. With in situ heating, saw hydrogen revolutionize with a lot of dislocation motion. Can you discuss this motion?

   a. Several other papers at this conference presented theories that hydrogen assists the motion of point defects and dislocations in various materials. The in situ heating video and images shown present a qualitative demonstration of how dislocations move in the presence of dissolving hydrides where hydrogen concentration in solution is relatively large. This type of hydrogen assisted motion might explain other phenomena such as DHC crack tip blunting, where high local hydrogen concentrations in the crack tip plastic zone might allow for enhanced creep and provide resistance to DHC at lower temperatures than otherwise predicted. A more quantitative study of this motion could be beneficial for confirming some of these proposed hydrogen effects as well as validating molecular dynamics models.

7. How was the bulk hydrogen measured? 10 ppm bulk seems quite low for the reported oxide layer.

   a. The bulk hydrogen measurement was measured by differential scanning calorimetry (DSC), which is calibrated against previous hot vacuum extraction mass spectrometry results. The error on this result is +/−3 ppm. The ‘bulk’ sample was fabricated by cutting all exposed surfaces with a slow

speed diamond saw; there was no oxide layer present. The apparent high hydrogen layer near the oxide surface is too small to measure using either DSC or HVEMS.

Effect of Alloying Elements and Stress on Hydrogen Diffusion in Zr Alloys

Yongfeng Zhang

1. What is the effect of elastic strain versus plastic strain?

Session: Welds, Weld Metals, and Weld Assessments

Effect of Thermal Aging on Fracture Mechanical Properties and Crack Propagation Behavior of Alloy 52 Narrow-Gap Dissimilar Metal Weld

Matias Ahonen

1. Why are you using Alloy 52?
   a. This mock-up is representative to the EPR construction, where Alloy 52 is used for the safe-end weld as the welding consumable.
2. Do you expect any dilution?
   a. The microstructural features are presented in detail in Teemu Sarikka's presentation. In general, dilution is low in the case of narrow-gap welding due to the low heat input.

Microstructural Characterization of Alloy 52 Narrow-Gap Dissimilar Metal Weld After Aging

Teemu Sarikka

1. Did the authors checked the microstructural change due to thermal aging which lead to the reduction of fracture resistance and shift of DBTT?
   a. Yes, that is what we have been working on in this in general. As for the decrease in fracture resistance, we do not really know at the moment and we are further working with that. As for the shift in ductile-to-brittle transition temperature, we think that it is due to phosphorus segregation to the low-alloy steel grain boundaries, which was the original assumption.

Session: Special Topics I—Materials—Part I

Evaluation of Additively Manufactured Materials for Use as Nuclear Plant Components

Ron Horn

1. Why choosing PB over SLM?
    a. I assume you are referring to Powder Bed (PB) and Selective Laser Melting (SLM). In essence SLM is a form of the "umbrella" or family of processes of PB. PB (DMLS, DMLM, SLM, etc.) is arguably the most mature Additive Manufacturing process available and is a cornerstone of GE's Additive Manufacturing portfolio, so machine data and knowledge are readily available for application to nuclear.
2. What processing parameters were used here?
    a. GE proprietary parameters were used in DMLM manufacturing.
3. What component are you thinking should be printed in the core?
    a. Applicable components are limited somewhat by size (at least with current DMLM machine capabilities). But any complex geometrical feature (most likely something that was previously cast) is a candidate. Or and new or iterations of design which have complex value add features, which are difficult or impossible to manufacture with conventional manufacturing techniques.
4. I assume your machine the samples after building since the surface of the samples is not as nicely as it should be for a tensile test?
    a. Yes. However, from a tensile prospective we have tested as built surfaces with similar results.
5. Is the image on the left the DMLM material, or wrought?
    a. Both images are DMLM. Left is micro after Stress Relief, Right is after HIP +Soln Anneal.
6. Have you evaluated the final microstructure for delta phase precipitates? These will not have a large impact on bulk mechanical properties, but WILL greatly impact performance in reactor.
    a. Final microstructure evaluation is ongoing with respect to precipitates. SCC and IASCC at INL is also planned which will aid in this discussion.
7. What process does GE use to treat the surface finish of the as-built parts?
    a. Final surface treatment may be somewhat application specific. But intent/desire is to use the as built surface wherever possible.

Hot Cell Tensile Testing of Neutron Irradiated Additively Manufactured Type 316L Stainless Steel

Paula Freyer

1. Why PB and not SLM?
    a. We do not understand this question. Powder bed (PB) and selective laser melting (SLM) are used interchangeably.
2. How are you anticipate of dealing with the surface issues of actual components?
    a. Various production components have different surface finish requirements. The selection of a surface finish treatment, if deemed necessary, will be component specific.
3. Do you have any information on what you would expect if you performed HIP —in terms of final results?
    a. We have HIPPED samples and done subsequent mechanical testing. We are not seeing a significant improvement in properties. We believe if fatigue strength is concern, HIPPING may help.
4. Is dimensional stability maintained on the larger components?
    a. Dimensional stability is dependent on the geometry of the part in addition to the size of the part. We have been able to maintain dimensions on prototype components to within acceptable tolerances.
5. Did you see any irradiation effects from the Co in the medical grade 316L?
    a. The medical grade stainless does not contain Co. It is the conventional 316 plate material that contains Co.
6. You said you want to put an AM part in a reactor in 2018. What component? What parts are of interest?
    a. The plan is to insert a thimble plugging device into a commercial reactor in 2018.
7. Where are you in the Schaeffler diagram with this composition?
    a. This information can be located online via a Google Search of the keywords Schaeffler Diagram and S31673.
8. What are the build parameters? In order to really qualify a part I would think it is key to be open on the precise build parameters so parts are reproducible.
9. Have you tried printing the specimens directly rather than machining them out of blocks? How do we know the properties measured aren't impacted by the EDM machining processes?
10. Z-axis would be essential it would be great seeing this data!

Thursday, August 17, 2017

Session: PWR Stainless Steel SCC and Fatigue—SCC—Part II

High-Resolution Characterisation of Austenitic Stainless Steel in PWR Environments: Effect of Strain and Surface Finish on Crack Initiations and Propagation

Gemma Pimentel

1. What was the duration of corrosion in simulated PWR coolant?
   a. Response: Between 500 and 1000 h.
2. Might there be some type of galvanic interaction that carbon coating enabled—causing increased oxidation on the austenite phase?
3. Do you think the beneficial effect of carbon contamination on 304SS SCCI in deaerated water is similar to the beneficial effect of sulfur (i.e., both enhance corrosion which in turn mitigates SCC)?

SCC of ASS Under off-Normal Water Chemistry and Surface Conditions—Part I

Nicolas Huin

1. Have you considered having an interaction of variables? Often there are a combination of variables—e.g. CW + tint + surface oxide removal.
   a. No we did not.
2. What is the diameter of the rub specimen?
   a. diameter $\sim$19.7 mm.
3. There has been some work on heat tint that has shown that there can be preferential Cr depletion at grain boundaries. When you were doing the heat tint simulation did you observe any $M_{23}C_6$ carbides in grain boundaries?
   a. We did not observe any $M_{23}C_6$ precipitation, but the precise characterizations are ongoing. I'll come back to the details in another conference presentation.

4. Regarding the previous comment/question—there can be Cr depletion at the grain boundaries.
   a. See answer 3a above.
5. I think the surface hardened layer is originated from the rapid solidified material on the top, they are not cold worked.
   a. In fact the deformation at the surface is related to the rapid solidification as well as the RUB forming process.

SCC of Austenitic Stainless Steels Under Off-Normal Water Chemistry and Surface Conditions—Part II

Matthias Herbst

1. The surface scratches on this specimen appears to be a bit different from the ones that Nicholas showed in the prior presentation. How consistent are these surfaces?
   a. Each material respond differently to the forming process. This specific presented RUB did not originally present some scales.
2. Was the change in hardness the same for both the inner and outer surfaces?
   a. We did not measure the hardness on the inner side ….
3. Is the hardness shown here and the residual stresses measured after bending?
   a. Yes it is.
4. Were there any recast zone cracks observed in the EDM surfaces prior to any exposure times?
   a. Usually it is what we observe.

Session: PWR Stainless Steel SCC and Fatigue—Fatigue

The Effect of Load Ratio on the Fatigue Crack Growth Rate of Type 304 Stainless Steels in Air and High Temperature Deaerated Water at 482 °F

Denise Paraventi

1. Are the datasets inclusive? For example, do the new 304 curves include the data originally used by Mills, or is it n independent fit?
   a. The fits shown are from only the data presented in this paper. Thus the new curves do not include the data used by Mills in his original fit. Comparisons are shown between the Mills fit/dataset and these new data, so where the models (and therefore the underlying data) differ can be seen in the figures.

Corrosion Fatigue Behavior of Austenitic Stainless Steel in Pure D_2O Environment

Ronald Ballinger

1. Does not the use of ammonium hydroxide introduce a source of hydrogen, albeit perhaps relatively small? Perhaps LiOD could be used instead if this was seen as significant.
   a. The effect of the ammonium hydroxide as a possible source of hydrogen is judged small compared to the internal hydrogen already present in the specimens.

Session: PWR Secondary Side

Environmentally Assisted Fatigue Crack Growth of Austenitic Stainless Steels in PWR Environments

Stuart Medway

1. Have you found intermediate sulfur steels that will recover their full enhancement during the phase? Thoughts on why that may be?
   a. Yes. Thought to be related to depletion of sulfur.
2. Will you be comparing the data to the trilinear model presented in the first presentation to determine the effect (if any) on the quantified level of enhancement?

Study on Hold-Time Effects in EAF

Matthias Herbst

1. Could you comment on what a "slightly higher lifetime" means in practice, e.g. in inspection interval of fatigue usage factor?
   a. Based on the results of our tests in air as well as in high temperature water, the effect of holds is in the range of up to 30% lifetime extension.

Effect of Applied Potential and Inhibitors on PbSCC of Alloy 690TT

Brent Capell

1. Will you also be looking at the effect of preoxidation?
   a. We had not immediately planned on including pre-oxidation, but will look into adding it.

2. For operating plant, it is not possible to add such high concentration. Do you have any plan on checking the applicable concentration of inhibiters?
    a. Additional testing with reduced concentrations is planned to help develop guidance for plant use.
3. According to the proposed cracking kinetics, there is no incubation period. Why?
    a. At the high pH of 9.5, the lead is sufficient to disrupt whatever actions are preventing the PbSCC at lower pH values. This is currently assumed to be a reaction with the protective film and there is assumed sufficient lead at the start of test to have the observed effect and therefore there is no incubation time.
4. It appears that the testing was done under static not refreshed chemistry conditions. Was this the case, and if so was there any check of the solution chemistry post-test?
    a. Yes testing was only done in a static autoclave. No testing of the solution posttest was performed. This is a check that can be added to future test programs to see what kind of effect the inhibitors are having.

Secondary Side Corrosion of SG Tube Alloys in Typical Secondary Side Chemistries

Ian de Curières

1. What is the reproducibility of stress at the top of the tested specimens?
    a. XRD measurements on various specimens show that the main stresses at the APEX are in the range 500–600 MPa.
2. Do you suspect any dependency of PBSCC to the stress level?
    a. As for any SCC phenomenon, there will likely be an effect of the stress. On first thought, we expect the same effect than the one observed by François Vaillant 20 years ago, i.e. an effect on the kinetics but not compulsorily a threshold effect.

Session: Plant Operating Experience

Root Cause Analysis of Cracking in Alloy 182 BWR Core Shroud Support Leg Cracks

Martin Bjurman

1. What is the reason for the shape of the crack?
    a. This shape is commonly seen in similar cases. Special for this case is that considering faster interdendritic cracking within each bead, the crack tended

to propagate within each bead, limiting the transitioning to neighboring beads.

2. What do you think has caused the high hardness? Cold work? Carbide precipitation? Is the carbon content of this material typical of 182?
   a. There is no clear cause of the high average hardness. Cold work is only present at the surface, the microstructure and precipitate structures are as expected, but we have not made extensive TEM-analysis of the base metal. The carbon content was not specifically measured and the original composition.
   b. There is no clear cause of the high average hardness. Cold work is only present at the surface, the microstructure and precipitate structures are as expected, noting that we have not made extensive TEM-analysis of the base metal. The carbon content was not specifically measured and the original records are not available.

Microbially Induced Corrosion in Fire Fighting Systems—Experience and Remedies

Ulla Ehrnstén

1. The main issue in any system is to hinder contamination of the system during maintenance etc. As MIC occurs only in very slow flowing of stagnant conditions, recirculation shall protect from MIC.
2. Are the systems in new plants periodically sanitized? If so, how.
   a. The new systems depend on the whole concept to hinder MIC and therefore sanitation is not needed.
3. How is microbial contamination of new or sanitized systems managed and prevented?
   a. The concept build on high quality water which is monitored, recirculation and stainless steel piping welded using shielding gas, thus avoiding heat tint in the HAZ.

Managing the Aging Degradation of Concealed Safety Relevant Cooling Water Piping in European S/KWU LWRs

Martin Widera

1. Why did you take the step of grit blasting the pipe specimen before examining oxides or taking thickness measurements?
   a. The sand blasting was done anyway before specimen preparation for light microscopy. Thus removing the thick oxides scales first also made UT

thickness measurements including coupling of UT sensor easier. The results are conservative.

Session: Cables and Concrete Aging and Degradation—Cables

Simultaneous Thermal and Gamma Radiation Aging of Electrical Cable Polymers

Leonard Fifield

1. Could you provide information on the "in situ" Gy total dose cables in the field are exposed to over say a 40 year span from historical data? What is a good a reference to look into the pervious approach used during qualification of these insulation high Gy dose with subsequent thermal decay and how does the max temp of 120 °C compare to the max temp of that work?
2. Was dose rate calculated based on distance or with dosimetry?
3. If each row of samples corresponds to one dose rate did you consider dose rate variability within each row?
4. How precisely do you need to know the position of each sample? Because they are curved, they are at varying distances from the source. What effect does this variation have on the dose rate?
5. Were the ends of the samples sealed?
6. What solvent do you use?
7. Gel Fraction is a measure of cross-linking. What is the base (time=zero; no exposure) XLPE insulation Gel fraction? What considerations for additive type/formulation of XLPE needs to be incorporated in future testing of Gel Fraction? Put differently, are you aware of what range of crosslinking is present in XLPE cable formulations and is that range broader than what your test method is capable of distinguishing from a precision perspective? Also, what caused the larger error on the 20 day 60 °C gel sample?
8. Will you compare different aging treatment (T-R, R-T, combined)?
9. Will you consider synergistic effects (radiation + temperature)?

Principal Component Analysis (PCA) as a Statistical Tool for Identifying Key Indicators of Nuclear Power Plant Cable Insulation Degradation

Chamila De Silva

1. How do you interpret the dataset plotted?
2. Can you extract information about relationship between each data set?
3. How do you use the interpretation of the data through PCA (i.e. validity of the tests)
4. Why did you pick these test methods for analysis?

How Can Material Characterization Support Cable Aging Management?

Marzieh Riahinezhad

1. Is Center of Excellence housed internal to Kinectrics? Or does it includes other members? (CANDU, universities, etc.)
2. Is NIR only good for yellow-jacketed cable? Or all cable jackets? (Does your database of NIR include data from all cable colors?)
3. How did you conclude that radiation was not the dominating aging mechanism?
4. Prediction of elongation of break for cable 3 is a number that is higher than the actual elongation. Does this imply that cable 3 should have already broke?

Aqueous Degradation in Harvested Medium Voltage Cables in Nuclear Power Plants

Robert Duckworth

1. How will the lab formulations compare to the field cables?
    a. The formulations will be compared through FTIR, NMR, xylene cross-linking to quantify similarities between the field cables and lab samples.
2. Did you consider using other frequencies for tan delta?
    a. For tan delta we are considering 0.01–0.1 Hz for comparison to current techniques.
3. What test data do you gather with PD? (i.e. PDEV, PDIV etc.)
    a. We will be testing for PDIV/PDEV for each cable with the goal to get a baseline for PD at the 2.5*Vo.
4. Will you perform wafering and microscopic characterization of the water trees?
    a. Yes.

Session: Cables and Concrete Aging and Degradation—Concrete

Frequency Domain Reflectometry Modeling for NDE of Nuclear Power Plant Cables

Samuel Glass

1. What is the input into the model in terms of cable properties (versus actual dielectric properties of the cable)?

a. The Ansys HFSS frequency-domain finite element simulation models consist of 3-D cable segments which have dielectric permittivity and loss tangent values assigned to the insulation material and an electrical conductivity value assigned to the conductors. We start with a uniform or slightly randomly varied (to represent normal manufacturing cable noise) insulation permittivity, and the insulation permittivity in the damaged region is varied from the nominal value. The S-parameters (scattering parameters) for the nominal and damaged sections over the simulated frequency range are exported from HFSS for use in the cascaded transmission line circuit simulation model shown on this slide.

2. Why isn't there a peak at zero feet in your simulation?

   a. The signal peak at the beginning of the cable varied for both the simulations and measurements performed during the FDR study and is a function of the impedance matching condition at the beginning of the cable measurement or simulation. For the LIRA measurements, the initial peak height is a function of the probe impedance compensation applied within the instrument since the input system impedance is not the same as the cable impedance and is affected by the short test lead probe section. For the Ansys finite element simulations (as in the example shown on the slide), the triad cable models consistently exhibited a significant initial peak while the coax cable models did not. This is likely due to the input port impedance being exactly equal to the nominal line impedance for the coax line since the coax cable cross-section is not a function of distance while the triad conductors rotate around their central axis. For the LIRA simulations, a low initial peak height was observed for most cases which indicates a similar impedance matching condition where the transmission line impedance at the beginning of the cable is the same as the nominal value along the cable length.

3. What is the influence of frequency on the response of the method?

   a. As explained more completely in the paper, the peak response and resolution is related to one-half wavelength in the maximum FDR bandwidth. For a 200 MHz bandwidth system, this is approximately 0.5 m or 1.5 ft. This supports the 1 and 2 ft. defect length peaks being similar and the highest compared to 0.25, 0.5 and 3 ft FDR responses.

4. According to this slide peak magnitude is a function of the size of the defect (i.e. not correlated to the level of degradation only)

   a. This is an excellent observation and probably the most important point of the presentation. The amplitude of the FDR response is a function of length and rate of change (impedance taper) of the degraded cable section. For a given FDR bandwidth, a longer defect section can be individually resolved into the beginning and end peaks which results in a different FDR response depending on the defect length even for identical aging conditions.

Aging Mechanisms and Nondestructive Aging Indicator of Commercial Filled Cross-Linked Polyethylene Cable Insulation Materials

Shuaishuai Liu

1. How does the result relate to the physical properties of the material (maximum radiation dose presented is quite low)?
2. Why use only high frequency? Low frequency has been shown to be sensitive to aging effects?
3. What physical change with aging does increase in loss tangent reflect? More lossy = less perfect structure?
4. Why not plot the imaginary and real part of the dielectric response? They both change with aging and the change may be less visible in the tan delta ratio (Professor Ohki).
5. If mp is characteristic of the material, why is it dependent on polymer crystal size?
6. Why not characterize the molecular weight of the material?

Successful Detection of Insulation Degradation in Cables by Frequency Domain Reflectometry

Yoshimichi Ohki

1. What do you mean by differential spectra? (subtract unaged spectrum?).
   a. Yes. I subtracted the unaged spectrum.
2. Non negligible influence of measurement frequency and temperature. How do you differentiate these effects from aging effects?
   a. The effects do not harm the location ability of the method.

Capacitive Nondestructive Evaluation of Aged Cross-Linked Polyethylene (XLPE) Cable Insulation Material

Zhihui Shao

1. What kind of degradation can the sensor measure?
2. How deep does the signal penetrate into the material?
3. What about the presence of a gap between the jacket and the insulation?
4. Would it work for multiconductor cables or shielded cables?
5. How do you deal with the properties of the jacket degrading faster than the insulation?

Session: Special Topics I—Materials—Part II

Corrosion Fatigue Testing of Low Alloy Steel in Water Environment with Low Levels of Oxygen and Varied Load Dwell Times

Cybele Gabris

1. How did these specimens prepared? Were they cut from the crack tip region by removing of side groove and polishing?
   a. These specimens did not have a side groove. A slice from the side of the specimen was removed. The slice was mounted and polished on the cut side.

Session: IASCC Testing—Characterization

Hydrogen Trapping by Irradiation-Induced Defects

Anne-Cécile Bach

1. Please, could you specify why you selected 500 °C as irradiation temperature?
   a. We choose to perform ion implantation at 500 °C in order to compensate for the effects of higher dose rate on microstructural evolution associated with ion irradiation.
2. Could you, please, further specify if the ion beam was defocused or raster-scanned and what dpa rate was produced by the ion beam approximately?
   a. The dose rate produced by the ion beam was about 2–4 $\times$ 10^{-4} dpa/s according to SRIM calculation. The maximal dose estimated was 4.5 dpa. For the ion beam, it was raster-scanned.
3. Do you think these diffusion coefficients are different in the high defect density 'trapped' region? (perhaps enhanced diffusion along dislocations, etc.) Could this explain some of the error in your model?
   a. Indeed it is possible, but using the same diffusion coefficient for H in the whole material leads to satisfactory simulations of H diffusion in the implanted and non-implanted materials. Moreover, H having a high diffusion coefficient, I think it would perhaps not be really affected by the defects but I will check this point in future simulations.
4. Do you expect cavities will be stronger traps than dislocations?
   a. Cavities could be stronger traps than dislocation loops but for now, I did not work on kinetic constants of trapping and detrapping by cavities so I cannot be sure. Further simulations and improvements of the model will provide more information about this point.

Grain Boundary Oxidation of Neutron Irradiated Stainless Steels in Simulated PWR Water

Koji Fukuya

1. Did you observed any difference in oxide structure (porosity for example) allowing to suspect ans effect of irradiation on oxide resistance to failure?
   a. There were no significant difference in oxide structure and compositions in TEM diffraction patterns and EDS analyses. But I agree trials for more detailed analysis will be needed.
2. What location of the C ring did you studied and is shown here?
   a. All observations in this study were made on the cross section of the tube as seen in No. 8. We selected cross sections for TEM observation so that the tensile stress was applied normal to a grain boundary.
3. Is GB oxidation the rate controlling step in initiation of IASCC?
   a. I believe so. As you know the time for IASCC initiation is extremely short for high doses plus high stresses, for example several hours for 74 dpa at 800 MPa. I suppose a very high oxidation rate might be possible in such conditions, although we need experimental evidence. At high stresses, GB oxidation is likely to be enhanced by tensile stress normal to the GB.

Session: IASCC Testing—Initiation and Growth

Irradiation-Assisted Stress Corrosion Cracking (IASCC) of Nickel-Based Alloy in Light Water Reactors Environments Part II: Stress Corrosion Cracking

Mi Wang

1. I understood, that ARRM aims to find a new material to replace austenitic stainless steel it means a material not suffering to IASCC. Can you propose a next step based on your results?
   a. The phase I of ARRM program is to select the potential materials by proton irradiation with two doses 5 and 10 dpa, followed by dual ion irradiation to higher dose (150 dpa). Based on the results of IASCC and microstructure changes, the materials will be selected to the next phase. Phase II will be neutron irradiation in a test nuclear reactor.
   b. We are going to test 10 dpa based on the 5 dpa results. Also, we are going to test 100 dpa duel ion irradiation for swelling

2. These high nickel alloys, if used in highly irradiated areas and in large surface areas, would contribute to high radiation levels both in the reactor core and in other areas of the plant due to corrosion product transfer and deposition. Was this not a consideration?

   a. That is right. It could be potential concern. But we are quite limited by the commercial alloys, which if it is good, and can be used immediately.
   b. Nickel-based alloys are limited to be used in the high irradiation area due to the activation. It will be a big concern if the CRUD contain active species deposited on the out-of-core region. Therefore, the high strength nickel-based alloy is only for structural application in the reactors, the region not to close to the in-core region. In the ARRM program, there is also a selection for low strength alloys (different iron-based alloys and etc.), those will be the potential replacement alloys in the in-core region.

3. Why do you observe dislocation channels on the PW surface and not on the NWC surface?

   a. Not yet. It is planned but apparently need more time.
   b. The SEM images I chose in this slide are in very low magnification. It gives an impression there is no dislocation channels in NWC. If you take a look at the next slide, you can find the dislocation channels are observed in all conditions. However, it is true that the dislocation channels seems to be much more significant in PW. It is probably due to the thicker oxide formed in NWC. Thus, the height of the channels will be less visible.

4. Do you have a reason that RIS does not occur for X-750 and 718 materials or there is just no data available?

   a. We don't have the data yet.

Irradiation-Assisted Stress Corrosion Cracking Initiation Screening Criteria for Stainless Steel in PWR Systems

Stephen Fyfitch

1. Are the calculated stresses in baffle bolts that have cracked in service consistent with this curve?

   a. In general, I believe they are, although we really have not been able to definitively calculate the exact stresses that failed baffle bolts have been loaded to. However, as Takura has shown, baffle bolt testing tends to show that the initiation stress is higher than that seen for flux thimble tubes.

Quantitative Measurement of Localized Stresses Near Dislocation Channel—Grain Boundary Interaction Sites in Irradiated Stainless Steel

Drew Johnson

1. The agreement in the normal stress measurements at the discontinuous channels is impressive, were the boundaries for these measurements randomly selected or were the taken on a subset of grain boundaries with a limited range of grain boundary inclinations?
2. What will be the effect of grain boundary inclusions on the GB stresses?

IASCC Susceptibility of 304L Stainless Steel Irradiated in a BWR and Subjected to Post-irradiation Annealing

Justin Hesterberg

1. Are these room temperature tests?
    a. No, 288 °C. The dislocation channel densities were taken from the CERT specimens for IASCC susceptibility test which were performed under simulated BWR-NWC conditions.
2. Shapes of the curves indicate different mechanical behavior of the materials, some showing plato, the last even hardening. Did you observed some cracks initiated during the test interruptions? Could the crack growth influenced the curve shape? Maybe the crack number is another parameter to evaluate IASCC.
    a. It is believed that the changes in the shapes of the curve is representative of the removal of the irradiation defects, thus causing a transition from the strain softening behavior (as-irradiated) to the strain hardening (PIA 550 °C: 20 h). The purpose of the test interruptions was intended to identify crack initiation sites, before severe crack propagation. Unfortunately, due to the severe environment (BWR-NWC) crack propagation was very rapid, and we were only able to observe a crack initiation site for the PIA 500 °C: 1 h, where a crack initiation site was identified after straining to $\sim 1\%$ plastic strain, which was then observed to grow during later strain increments. The total number of cracks was counted for each specimen, however, due to the rapid crack propagation, the total number was quite low (<5 for as-irradiated, which had the most crack initiation sites).

Effect of Specimen Size on the Crack Growth Rate Behavior of Irradiated Type 304 Stainless Steel

Anders Jenssen

1. Irradiated CGR data in Japan showed similar low K dependence to your results. It may be consistent with significant branching of cracks in highly irradiated components.

   a. The fractographic examination of the specimens did not indicate significant crack branching, while the material was irradiated to a relatively low dose ($\sim$1 dpa). As discussed in the paper, the reason for the low K dependency is unclear, although % engagement less than 100% is mentioned as a possible explanation.

2. Do you think there is any technical significance for the curvature of the crack front?

   a. The crack front in one of the small CT specimens was slightly curved, while the other specimens had straight crack fronts meeting the straightness requirements in ASTM standards. Since the data obtained on the specimen with a slightly curved crack front was consistent with data from the other specimens, it appears crack front curvature had no or little effect on the results.

Author Index

J.H. Jackson et al. (eds.), *Proceedings of the 18th International Conference on Environmental Degradation of Materials in Nuclear Power Systems – Water Reactors*, The Minerals, Metals & Materials Series, https://doi.org/10.1007/978-3-319-68454-3

Subject Index

J.H. Jackson et al. (eds.), *Proceedings of the 18th International Conference on Environmental Degradation of Materials in Nuclear Power Systems – Water Reactors*, The Minerals, Metals & Materials Series, https://doi.org/10.1007/978-3-319-68454-3

D